Photo: Roughan & O'Donovan

UCC
Coláiste na hOllscoile Corcaigh, Éire
University College Cork, Ireland

CIT
Institiúid Teicneolaíochta Chorcaí
Cork Institute of Technology

CRI10
Concrete Research in Ireland 2010

BRI10
Bridge & Infrastructure Research in Ireland 2010

The Joint Symposium Proceedings

UCC and CIT 2nd and 3rd September 2010

Editors: Nóra Áine Ní Nualláin, Des Walsh, Roger West, Eamonn Cannon, Colin Caprani and Bryan McCabe.

BRI10 Bridge & Infrastructure Research in Ireland
CRI10 Concrete Research in Ireland

Joint Symposium
University College Cork
Cork Institute of Technology
2nd- 3rd September 2010

PROCEEDINGS

Co-Editors

Nóra-Áine Ní Nualláin	**Des Walsh**	**Roger West**
Eamonn Cannon	**Colin Caprani**	**Bryan McCabe**

Published in 2010
ISBN No. 978-0-9542973-3-6

This publication is part of the proceedings of the joint symposium on
Bridge & Infrastructure Research in Ireland 2010
Concrete Research in Ireland 2010
held in University College Cork and Cork Institute of Technology
on September 2nd and 3rd, 2010

Copies of these proceedings are available from:
Des Walsh
Department of Civil, Structural & Environmental Engineering,
Cork Institute of Technology
des.walsh@cit.ie

Cover photograph courtesy of Roughan & O'Donovan Consulting Engineers

website: www.bcri.ie
by Starlight Solutions

Organising Committee of BCRI10

Dr Nóra Áine Ní Nualláin,	University College Cork, Conference Co-Chair
Des Walsh,	Cork Institute of Technology, Conference Co-Chair
Dr Roger West,	Trinity College Dublin, Conference Secretary
Eamonn Cannon,	NUI, Galway, Chair CRI10
Dr Colin Caprani,	Dublin Institute of Technology, Chair BRI10
Dr Bryan McCabe,	NUI, Galway, Geotechnical Chair
Dr Paul Archbold,	Athlone Institute of Technology
Prof Muhammad Basheer,	Queens University Belfast
Dr Michael Creed,	University College Cork
Dr Paul Fanning,	University College Dublin
Dr Annette Harte,	NUI, Galway
Dr Niall Holmes,	Queens University Belfast
Martin Mannion,	Cork Institute of Technology
Dr Alan O'Connor,	Trinity College Dublin

Scientific Committee

Dr Paul Archbold, AIT
Dr Yun Bai, QUB
Prof Muhammed Basheer, QUB
Prof Biswajit Basu, TCD
Richard Bradley, Irish Cement
Fintan Buggy, ROD
Brian Byrne, IT, Carlow
Eamonn Cannon, NUI, Galway
Patrick Casey, ARUP
Dr Colin Caprani, DIT
Prof Tom Cosgrove, UL
Dr Michael Creed, UCC
Dr Albert Daly, NRA
Peter Deegan, Banagher Concrete
Dr Tony Dempsey, ROD
Dr Shane Donohue, UCD
Dr Aidan Duffy, DIT
Liam Buffy, NRA
Dr Eric Farrell, TCD
Dr Paul Fanning, UCD
Peter Flynn, Arup
Dr Ken Gavin, UCD
Dr Amanda Gibney, UCD
Dr Dave Gill, AGL Consulting Engineers
Dr Jamie Goggins, NUI, Galway
Dr Arturo Gonzalez, UCD
Hugh Griffin, Arup Griffin
Dr Annette Harte, NUI, Galway
Dr Michael Hartnett, NUI, Galway
Dr Joe Harrington, CIT
Paul Healy, OCSC
Dave Holleran, Oran Precast
Dr Niall Holmes, QUB
Joseph Kindregan, DIT
Dr Denis Kelliher, UCC
Dr Debra Laefer, UCD
Dr Mike Long, UCD
Brendan Lynch, Irish Cement
Dr Bryan McCabe, NUI, Galway
Brian Madden, OCSC
Martin Mannion, CIT
Dr Michal Majka, Iarnród Éireann
Frank McGuire, RPS
Dr Ciaran McNally, UCD
James McNeill, Balfour Beatty
Dr Danny McPolin, QUB
Prof Karsten Menzel, UCC
John J Murphy, CIT
John T Murphy, Mott McDonald
Dr Sreejith Nanukuttan, QUB
Dr Nóra Áine Ní Nualláin, UCC
Prof Eugene O'Brien, UCD
Dr Alan O'Connor, TCD
Dr Dermot O'Dwyer, TCD
Conor O’Donnell, AGL Consulting Engineers
Dr Brendan O'Kelly, TCD
Jack O’Leary, Malachy Walsh and Partners
Brian O'Rourke, CIT
Dr Trevor Orr, TCD
Dr Sara Pavia, TCD
Dr Declan Phillips, UL
Dr Sarah Prichard, Buro Happold
Dr Niamh Power, CIT
Paul Quigley, ARUP
Kieran Ruane, RPS
Peter Seymour, ECOCEM
Dr Paraic Rattigan, ROD
Dr Mark Richardson, UCD
Dr Su Taylor, QUB
Des Walsh, CIT
Michael West, Iarnród Éireann
Dr Roger West, TCD

Foreword

As President of University College Cork and President of Cork Institute of Technology, we are delighted to welcome you to this joint symposium: Bridge and Infrastructure Research in Ireland 2010 / Concrete Research in Ireland 2010. This two day event is being co-hosted by the Department of Civil and Environmental Engineering (UCC) and the Department of Civil, Structural and Environmental Engineering (CIT).

This co-hosted conference is being held in the context of the close relationship between UCC and CIT as evidenced, for example, by the successful creation of the joint CIT/UCC Cork Centre for Architectural Education (CCAE) which will graduate its first cohort of students this year. We are delighted with this development and our other collaborative work across a range of disciplines which is contributing to the ongoing development of higher education in the region and beyond.

The first symposium on Bridge Research in Ireland was held in University College Dublin in 2002. The inaugural colloquium on Concrete Research in Ireland was held in Trinity College Dublin in 1997. Three bridge and five concrete colloquia were held before the events came together for a very successful inaugural joint symposium at NUI Galway in 2008. This is the first occasion on which either event has been held in Cork.

The collaborative nature of the symposium presents practitioners and researchers with an opportunity to present and discuss their research work on concrete, bridges, infrastructure and geotechnical engineering. UCC and CIT are pleased to host the second joint symposium; whilst maintaining the traditions of the event the UCC and CIT organisers have sought to enhance its growth, development and appeal. Seventy six papers will be presented over the two days with the postgraduate activity of eight colleges being represented; three outstanding keynote speakers have been scheduled.

We are delighted to host the event; we hope you enjoy the symposium and your visit to Cork.

Dr Michael Murphy
President
University College Cork

Dr Brendan Murphy
President
Cork Institute of Technology

August 2010

Preface

On behalf of the Organising Committee of BRI10 and CRI10, we are delighted to welcome you to this joint symposium on bridge, infrastructure, concrete and geotechnical engineering research in Ireland. We are most grateful to our joint hosts, the Department of Civil and Environmental Engineering at UCC and the Department of Civil, Structural and Environmental Engineering at CIT, for facilitating this event.

We have invited three keynote speakers, each very eminent in his own field. Prof Mark Stewart, of the University of Newcastle, Australia will deliver the second Joe O'Donovan Memorial Lecture on a Bridge theme; Mr. Peter Anthony of Horgan Lynch, Cork and Dr Eric Farrell of Trinity College Dublin will deliver the Concrete and Geotechnical keynotes respectively. The keynotes will be supplemented by over seventy papers to be presented in parallel sessions on bridges, infrastructure, concrete, geotechnics and materials on a wide variety of topics and from a number of sources. We look forward to sharing information and learning from all participants. We would like to thank all authors for their valued contributions and for responding so well to the various deadlines imposed by the organisers.

On your behalf, we would also like to offer our thanks to the members of the Scientific Committee, who have been diligently advising on technical matters, reviewing the papers and many of whom have agreed to co-chair the various sessions.

Thanks also are due to the Conference Offices, technical staff, administration and postgraduate students of UCC and CIT who have provided huge support in running the event. Special thanks are also due to the Webmaster, Paul Killoran of Starlight Solutions, who has produced an excellent website which has made the administration so much easier for the organisers and the authors alike.

Finally, we are most grateful to all of our sponsors – Arup, Balfour Beatty Ground Engineering, BAM, ECOCEM, Engineers Ireland (Cork Region), Horganlynch, Irish Concrete Society, Malachy Walsh and Partners, Mott McDonald, Roughan & O'Donovan, RPS and Sisk Ireland who have willingly supported this event, despite the difficult economic times which prevail. The intention of those who, fifteen years ago, initiated this continuing series of symposia, was to provide a forum for researchers and industry to meet to exchange views and especially to encourage young researchers to participate. We should remember that the support of our sponsors makes that possible at an affordable cost.

This event is the fourth bridge and sixth concrete colloquium in a very successful series and, with your continuing participation, we hope this format for sharing knowledge and renewing friendships will continue for many years to come.

Co-Editors

Nóra-Áine Ní Nualláin **Des Walsh** **Roger West**
Eamonn Cannon **Colin Caprani** **Bryan McCabe**

Table of Contents

LIFE-CYCLE COST OPTIMISATION OF MAINTENANCE STRATEGIES FOR RC STRUCTURES IN CHLORIDE ENVIRONMENTS

M.G. STEWART[1] & J.A. MULLARD[2]
[1]Centre for Infrastructure Performance & Reliability, University Newcastle, Australia
[2]Robert Bird Group, Hamilton, Australia

Abstract

Corrosion of the reinforcing steel can cause cover cracking and eventual spalling of Reinforced Concrete (RC) surfaces resulting in costly and disruptive repairs. The present paper will compare the effect of maintenence and repair strategies on the timing, extent and cost of remediation actions over the service life of a RC structure in a chloride environment. The paper presents a probabilistic reliability analysis which is used to predict the likelihood and extent of corrosion-induced cracking to RC structures. A spatial time-dependent reliability model has been developed where concrete properties, concrete cover and the surface chloride concentrations are treated as random fields. This allows for the calculation of the probability that a given extent of damage will occur for any time period. Maintenance strategies and repair efficiencies are incorporated in a Monte-Carlo event-based simulation analysis, allowing a comparison in terms of cost and number of repairs over the service life of a RC structure. Thus, the expected timing and extent of repairs can be predicted for various initial design parameters, inspection intervals, repair thresholds, maintenance strategies and efficiency of repairs. Results are presented for a RC bridge deck subject to a marine environment. The life-cycle cost analysis considers construction, repair and user delay costs. This predictive capability enables the extent of future repair costs to be more realistically estimated and the optimal maintenance strategies determined.

Keywords: life-cycle cost, corrosion damage, structural reliability, risk, optimisation

1. Introduction

It is widely recognised that the corrosion of steel in concrete is one of the most significant and costly durability problems for RC structures. The economic impact of deteriorating RC structures can be minimised through the optimisation of maintenance strategies. To allow designers and asset owners to fully investigate the economic consequences of different maintenance strategies, an integrated life-cycle cost analysis must be conducted that incorporates key maintenance parameters. For example, it has been shown that inspection interval, repair threshold, maintenance technique and repair efficiency can strongly influence the life-time performance of RC structures (Mullard and Stewart 2009). Inspection interval and repair threshold are relatively arbitrary parameters which are often set by the controlling authority and as such, the focus of the present paper is primarily on optimising maintenance strategies with regards to maintenance technique and repair efficiency.

Life-cycle cost (LCC) analysis for reinforced concrete structures has been well studied (e.g., Val and Stewart 2003, Li 2004, Yang et al. 2006, Breysse et al. 2009). The statistical variability of life-cycle cost can often be of more significance to decision makers than the average cost (Val and Stewart 2003). For example, it may be shown through analysis that a particular structure has a low mean life-cycle cost but if variability is high there is a significant probability that the actual cost will greatly exceed mean (expected) costs. Since damage and repair costs are influenced by the extent (area and location) of damage, then reliability models that include spatial variability are needed (e.g., Sudret 2008, Vu and Stewart 2005, Mullard and Stewart 2007, Kenshel 2009, Stewart and Suo 2009), and their effect on LCC can be more realistic (Stewart 2006). It has been established that probabilistic modelling is well suited for predicting corrosion damage in RC structures due to the uncertain nature of concrete dimensions, concrete properties and the deterioration process. It follows that prediction of life cycle costs should also be modelled probabilistically so that the uncertainties in the deterioration process can be adequately captured in the estimation of costs.

The design, construction and inspection costs for RC structures are typically readily quantifiable and as such, the focus of research is predicting the expected cost of failure which is linked to the likelihood and extent of corrosion damage, repair cost functions and user delay costs. To estimate the expected cost of failure in an accurate and realistic manner, the following key issues need to be addressed: deterioration modelling, spatial variability, influence of repair efficiency and maintenance strategies, and repair and user delay costs.

The paper reviews a probabilistic reliability analysis which is used to predict the likelihood and extent of corrosion-induced damage to RC structures. Corrosion damage is deemed to occur when corrosion-induced crack widths of 1 mm are evident on the RC surface. The spatial time-dependent reliability model considers concrete properties, concrete cover and the surface chloride concentrations as spatially variable random fields. This allows for the calculation of the probability that a given extent of corrosion damage will occur for any time period. Three repair techniques will be considered: (i) patch repair, (ii) preventative repair, and (iii) complete rehabilitive overlay. Incorporated into each of the above maintenance strategies are two repair efficiency factors which take into account varying time to corrosion initiation and corrosion rate of the repair material. Maintenance strategies and repair efficiencies are incorporated in a Monte-Carlo event-based simulation analysis, allowing a comparison in terms of cost and number of repairs over the service life of a RC structure. Results are presented for a RC bridge deck subject to a marine environment. The life-cycle cost analysis considers repair and user delay costs which are both functions of extent (area) of damage. This predictive capability enables the extent of future repair costs to be more realistically estimated and the optimal maintenance strategies determined.

2. Spatial Time-Dependent Reliability Model

In order to assess the performance of a RC structure over its lifetime the key processes involved in deterioration are integrated into a spatial time-dependent reliability analysis. The key deterioration processes are:

i. Corrosion initiation and propagation
ii. Crack initiation and propagation
iii. Influence of maintenance strategies

The proportion of a concrete surface with crack widths exceeding the limit crack width at time t (d_{crack}) for a single Monte Carlo simulation realisation is

$$d_{crack}(t) = \frac{n\left[t > T_{i(j)} + T_{sp(j)}\right]}{k} \times 100\% \quad (1)$$

where $T_{i(j)}$ and $T_{sp(j)}$ are the time to corrosion initiation and time to excessive cracking of element j, respectively, and n[] denotes the number of elements for which t> $T_{i(j)}+T_{sp(j)}$. Monte Carlo simulation analysis can then be used to infer the distribution of $d_{crack}(t)$. For full details of the deterioration models see Vu and Stewart (2000), Stewart and Mullard (2007) and Mullard and Stewart (2010). The spatial time dependent reliability analysis presented herein contains a number of highly non-linear limit state functions and a large number of random variables, spatial random fields and spatially dependent random variables. As such, a closed form solution is not tractable and Monte Carlo Simulation techniques are used in the analysis to provide the predictive outcomes. The process is described by the following steps:

- The RC structure is discretised into a number of elements of size Δ
- A random field is generated for each spatial variable where the value of the random field for each element is represented by a spatially correlated random variable generated from the corresponding probabilistic distribution. Once all spatial, spatially dependent, standard random and deterministic variables are defined, the stochastic deterioration models predict the timing of corrosion damage for each element. The extent of damage at a given time can therefore be calculated and checked against the repair threshold.

3. Life-Cycle Cost Analysis

Total life cycle cost can be described as:

$$LCC(T) = C_D + C_C + C_{QA} + C_{IN}(T) + E_{SF}(T) \quad (2)$$

where C_D is the design cost, C_C is the construction cost, C_{QA} is the cost of quality assurance/control, $C_{IN}(T)$ is the cost of inspections, and $E_{SF}(T)$ is the expected cost of maintenance (including repair and user delay costs) of corrosion-induced damage during service life T.

The aim of the current study is to investigate the effect of maintenance strategies on the life cycle cost of RC structures. As such, design, construction, quality assurance and inspection costs will be assumed to be equal for all cases analysed. The economic performance is then governed primarily by the influence of maintenance technique and repair methods. In these terms, the life-cycle cost considering only maintenance actions can then be defined by

$$LCC(T) = E_{SF}(T) \quad (3)$$

The expected cost of maintenance can be described as (Val and Stewart 2003)

$$E_{SF}(T) = \sum_{i=1}^{T/\Delta t} \Delta P_{f,i} \frac{C_{repair}}{(1+r)^{i\Delta t}} \quad (4)$$

where Δt is the time between inspections, $\Delta P_{f,i}$ is the probability of damage incident between the (i-1)th and ith inspections which is a function of time since last repair, r is the discount rate, and C_{repair} is the cost of damage including maintenance and repair costs, user delay and disruption costs, and other direct or indirect losses arising from damage to infrastructure. For example, an asset owner should be able to quantify the unit repair cost ($\$/m^2$), and if the area of damage is known then repair cost can be estimated. Damage may re-occur during the remaining service life of the structure, i.e., multiple repairs may be needed. The maximum possible number of damage incidents is $n_{max} = T/\Delta t$. At the time of first repair, $\Delta P_{f,i}$ can be expressed in terms of the repair threshold (X_{repair}) and the extent of damage (d_{crack}) as:

$$\Delta P_{f,i} = \Pr\left(d_{crack}(t) \geq X_{repair} \middle| d_{crack}(t-\Delta t) < X_{repair}\right) \tag{5}$$

where X_{repair} is the repair threshold when repair is undertaken. The probabilities used in the estimation of the expected maintenance costs are calculated using Monte Carlo Simulation techniques. The Monte Carlo simulation analysis assumes:

- When the repair threshold has been exceeded the first maintenance action is conducted as defined by the maintenance strategy. The original and the repaired area of RC structure then deteriorate at their corresponding rates (as defined by the deterioration models and any repair durability specifications).
- Repair is carried out immediately after corrosion damage has been discovered;
- The repaired RC structure will continue to deteriorate until the repair threshold is again exceeded at which time the second maintenance action is conducted. This cycle of deterioration and repair will continue until service life is reached.

Cost values are assigned to each maintenance action and consequence during the service life of the RC structure and therefore for any given analysis the performance in terms of the number, extent and life-cycle cost of maintenance actions can be calculated.

4. Maintenance Strategies

There are numerous parameters that can define a maintenance strategy but the current paper will focus on two primary influences: maintenance technique and repair efficiency.

4.1 Maintenance Techniques

The maintenance technique is defined herein as the nominated method of repair for a corrosion damaged RC structure. Three maintenance techniques are investigated:

Standard patch repairs (Maintenance technique M1)

Maintenance technique M1 is a patch repair technique where the corrosion damaged concrete elements are removed and replaced by a repair material once the extent of damage $d_{crack}(t)$ exceeds the repair threshold (X_{repair}). Thus, after each maintenance action the extent of damage on the RC structure is returned to zero as all damaged elements have been removed and replaced. The repaired area of concrete will then deteriorate at a different rate to the non-repaired concrete and this rate will be governed by the type of repair material and the efficiency of the repair. A schematic of the deterioration and repair process for maintenance technique M1 is shown in Figure 1. At time (t_1) the first maintenance action is undertaken (m = 1) where the damaged material is removed and replaced with a patch repair material and thus the extent of corrosion damage on the structure is returned to zero. Depending on the inspection interval, the actual repaired damage (x_m) may exceed the repair threshold (X_{repair}) as it is likely that the limit state has been exceeded at some time between inspections and the damage continued to increase over some portion of Δt. After a maintenance intervention the total deterioration rate of the RC structure is the superposition of the deterioration rates for the repaired and un-repaired areas and this will continue until the repair threshold is exceeded again so that m=2 at time t_2.

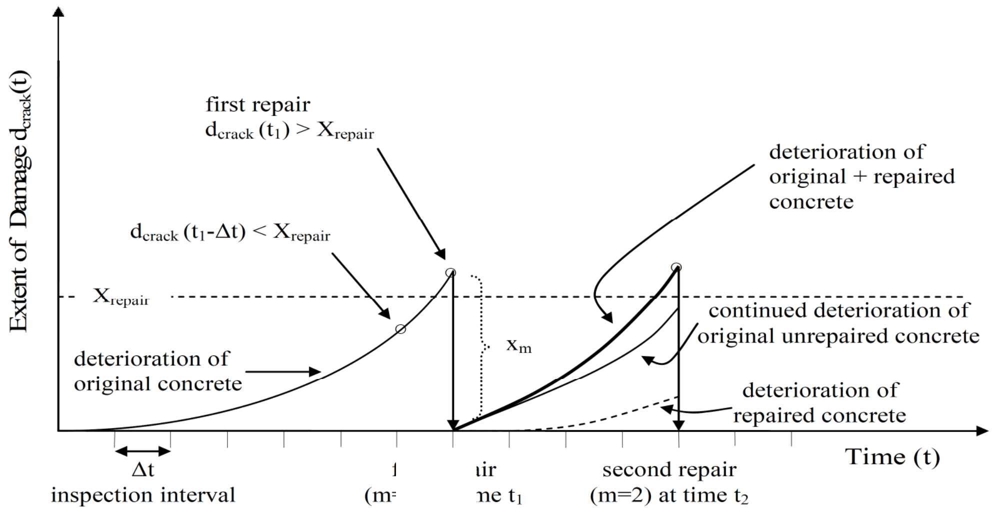

Figure 1 - Schematic of Maintenance Technique M1.

Preventative patch repairs (Maintenance technique M2)

Maintenance technique M2 is a preventative patch repair technique whereby a larger area of the RC structure is repaired in order to increase the time to subsequent maintenance actions. In addition to the damaged area being repaired, areas on the RC surface immediately adjacent to the damaged area are also replaced as these are likely to be close to the repair threshold due to the spatial nature of corrosion damage. The deterioration rate up to the first repair is the same as for maintenance technique M1, but the repaired area is much greater as the areas surrounding the damaged elements are also repaired. The additional repaired area has the effect of slowing the net rate of deterioration of the concrete after first repair and thus extending the time to the second repair when compared with maintenance technique M1. Figure 2 presents a schematic showing a two-dimensional RC surface that has been discretised into a number of elements.

Complete rehabilitative overlay (Maintenance technique M3)

A complete rehabilitative overlay is the removal and replacement of the entire RC surface over the reinforcing bars. Typically the concrete cover is removed to approximately 25 mm past the steel bars (which are then cleaned of corrosion products) and a repair material is installed. The original RC structure deteriorates until the repair threshold (X_{repair}) is exceeded at which time the complete area of the RC surface is removed and replaced with a rehabilitative overlay. The total repaired area is thus equal to the total area of RC surface. The overlay material then begins to deteriorate until a second maintenance intervention is required. This process is repeated until the end of the structures life and so multiple repairs are possible.

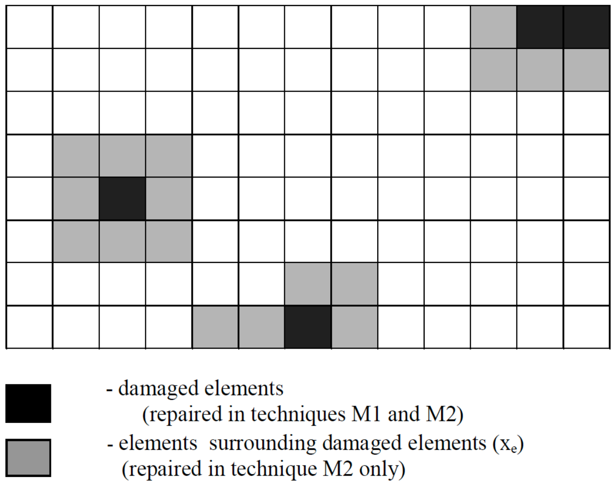

Figure 2 - Schematic of Repair Areas for Maintenance Techniques M1 and M2.

Figure 3 shows a probability histogram illustrating the comparative difference between maintenance techniques with regards to total number of maintenance actions required. The structure analysed is a 100 m^2 RC surface (cover = 40 mm, F'_c = 50 MPa) over a 120 year design life and it is clear that maintenance technique has a significant influence on the expected number of maintenance actions. The number of maintenance actions can be correlated to the total repaired area, with the maintenance techniques that repair the larger area at each maintenance action having fewer total repairs over the 120 year period. It is clear from Figure 3 that for minimising the total number of repairs, maintenance technique M3 is the preferred option. The larger repaired area of maintenance technique M3, however, has cost consequences and thus in purely economic terms it may not be the optimal solution. This is examined through a life cycle cost analysis to be discussed in the following sections.

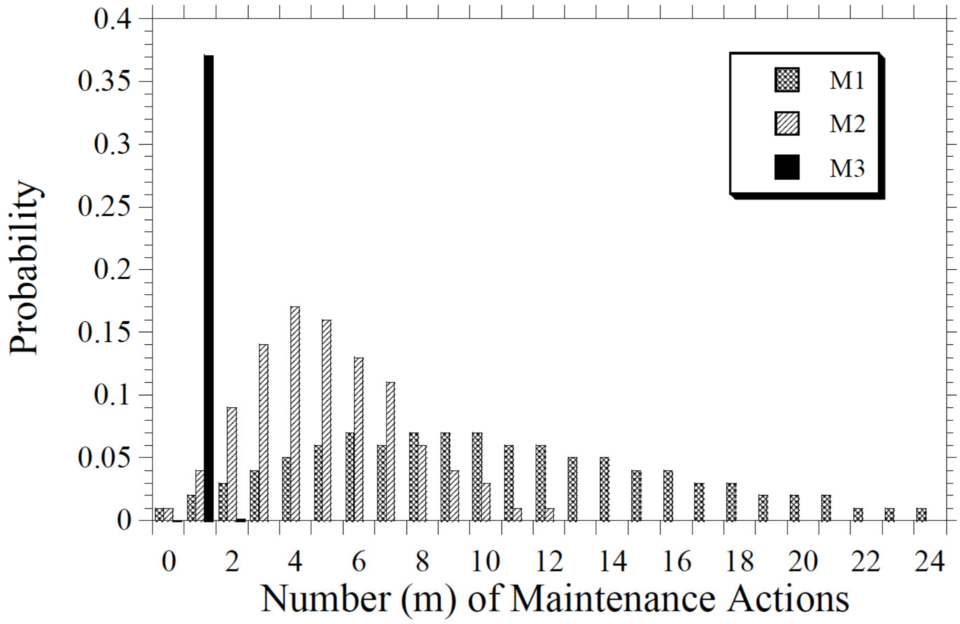

Figure 3 - Probability Histogram of Number of Maintenance Actions.

4.2 Repair Efficiency

The efficiency of repairs can influence the future performance of RC structures in two main ways; by effecting either the time to corrosion initiation or the magnitude of the corrosion rate of the repaired area. These repair efficiency factors are (Mullard and Stewart 2009):

1. Repair efficiency factor effecting corrosion initiation – the time to corrosion initiation of a repair material is defined as:

$$T_{i(repair)} = T_i + \Delta_{Ti} \qquad T_{i(repair)} \geq 0 \tag{6}$$

   where $T_{i(repair)}$ is the time to corrosion initiation for the repair material, T_i is the time to corrosion initiation for the baseline repair material (equal in quality to the original concrete) and Δ_{Ti} is the repair efficiency factor for corrosion initiation. Δ_{Ti} is given in years and will be a positive number for good repair efficiency.

2. Repair efficiency factor effecting corrosion rate – the corrosion rate in the repair material is defined as:

$$i_{corr(repair)} = i_{corr} \times \frac{100 + \gamma_{icorr}}{100} \tag{7}$$

   where $i_{corr(repair)}$ is the corrosion rate of the steel reinforcing embedded in the repair material, i_{corr} is the corrosion rate for a baseline repair material (equal in quality to the original concrete) and γ_{icorr} is the percentage increase in corrosion rate (i.e. a negative value of γ_{icorr} represents an decrease in corrosion rate). For example, a γ_{icorr} value of 10 represents a 10 % increase in the corrosion rate.

Three specific repair methods are analysed: concrete surface treatment; corrosion inhibitor; and cathodic protection. The effectiveness and efficiency of these repair methods has been estimated from the literature (see Mullard 2010 for full review) and the corresponding repair efficiency factors representative of U.S. and Australia practices are show in Table 1.

Table 1 - Repair Durability Specifications.

Repair Durability Specification	Δ_{Ti} (years)	γ_{icorr} (%)
Baseline case (patch repair same as original construction)	0	0
Concrete surface treatment	15	0
Corrosion inhibitor	7	-50
Cathodic Protection#	0	-100

It is assumed that the cathodic protection is active for the life of the structure and hence the corrosion rate is always zero.

4.3 Maintenance Strategies

Ten maintenance strategies will be assessed within the spatial time-dependent reliability analysis, see Table 2. For example, maintenance strategy 6 uses the complete rehabilitative overlay maintenance technique (M3) at a 12% repair threshold and a concrete surface treatment is applied to the overlay material.

Table 2 - Summary of Maintenance Strategy Parameters.

Maintenance strategy	Inspection interval Δt	Repair threshold (X_{repair})	Maintenance technique	Repair method	Repair efficiency	
					Δ_{Ti} (years)	γ_{icorr} (%)
1	1 year	2 %	M1	None	0	0
2	1 year	2 %	M2	None	0	0
3	1 year	12 %	M3	None	0	0
4	1 year	2 %	M1	CST	15	0
5	1 year	2 %	M2	CST	15	0
6	1 year	12 %	M3	CST	15	0
7	1 year	2 %	M1	CI	7	-50
8	1 year	2 %	M2	CI	7	-50
9	1 year	12 %	M3	CI	7	-50
10	1 year	12 %	M3	CP	0	-100#

CST – Concrete surface treatment, CI – Corrosion inhibitor, CP – Cathodic protection
- Assumes the cathodic protection is maintained for the life of the structure

4.4 Repair Cost Functions

For the current analysis, all initial design and construction costs can be ignored as the same structure is being considered with ten different maintenance strategies. As such, only the cost of maintenance actions will be considered to influence the total LCC.

The cost of patch repairs using ordinary Portland cement is:

$$C_{repair-patch} = 1.1 C_R A_{repair} \tag{8}$$

where A_{repair} is the area being repaired ($=x_m A$ where A is total area), and C_R is the unit repair cost. The cost function includes the fixed cost of repairs (i.e. fixed cost is assumed to be 10% of the total cost). The value of C_R (in 2009 Australian dollars) used herein is $400/m^2 for all maintenance techniques.

The cost of installing a concrete surface treatment (silane) is:

$$C_{repair-silane} = 1.2 C_R A_{repair} \tag{9}$$

The value of C_R (in 2009 Australian dollars) used is $18/m^2.

The cost of installing a calcium nitrate corrosion inhibitor for the repaired area is:

$$C_{repair-inhib} = C_R A_{repair} \tag{10}$$

There is no fixed cost associated with this repair durability specification as it is simply added to the concrete/repair material during batching. The value of C_R for 10 kg/m^3 of calcium nitrate corrosion inhibitor is, for a 250 mm thick slab equates to $18/m^2.

The cost of installing a cathodic protection system during rehabilitative overlay is:

$$C_{repair-CP} = C_{fixed} + 12 C_R A_{repair} \tag{11}$$

where C_{fixed} is the initial fixed cost and C_R is the unit application cost. An additional fixed cost (20% of the total cost) is also included. It is assumed herein that monitoring is conducted during regular inspections and no additional yearly maintenance or monitoring costs are incurred. C_{fixed}=$15,850 and C_R=$264/m^2.

The cost functions for the maintenance strategies presented herein are:

- Repair costs for maintenance strategies 1, 2 and 3 - use Eqn (8).
- Maintenance strategies 4, 5 and 6 - summation of cost functions (8)+(9).
- Maintenance strategies 7, 8 and 9 - summation of cost functions (8)+(10).
- Maintenance strategy 10 - summation of cost functions (8)+(11).

For more details see Mullard (2010).

The actual value of these costs may, in practise, vary significantly depending on such factors as the type and location of the structure and local labour/material availabilities. The data used herein to represent fixed costs for patch repairs uses a percentage of the overall cost to define the value of the fixed cost component. This may not be valid for smaller patch repair areas where the fixed costs may contribute a more significant portion of the total cost. If more accurate or site specific data is available for a particular structure, this information can then be incorporated into the framework developed in this study.

4.5 User Delay Costs

The costs associated with user delay during maintenance actions can be significant (Li 2004). Yunovich et al. (2001) assessed user delay costs where the cost data relates to a four lane bridge with an average daily traffic of 24,000 vehicles and no alternative route for diversion. When one lane is closed for maintenance, the user delay cost associated with the extra time taken to cross the bridge is estimated by Yunovich et al. (2001) to be \$60,877 per day based on a single lane closure and general queue theory. This value will be adopted herein.

4.5 Assumptions

For all maintenance techniques the following assumptions are made with regards to modelling the repair process:

- severe corrosion induced cracking is always detected when the structure is visually inspected.
- repair material is assumed to have the same spatial parameters as the original concrete for both cover and surface chloride concentration. This can be expected as the finished surface level and the location of the repair area on the structure does not change.
- repair efficiency is the same for all repairs over the life of the structure.
- total repaired areas during service life may exceed the original surface area as some elements may be subject to multiple repairs throughout their service life.

5. Application

The RC bridge deck considered is a 250 mm thick cast-insitu slab (see Figure 4). The deck span is a simply supported single span of 20 metres and the width of the deck is 20 metres (including 4 traffic lanes, a bicycle lane and a pedestrian walkway), resulting in a total RC deck area of 400 m^2. The deck slab is reinforced longitudinally and transversely with 16 mm reinforcing bars and 'fair' durability design specifications are assumed (cover = 50 mm, F'_c = 40 MPa). The chloride environment is assumed to be 'high marine' and only the top surface of the bridge deck is modelled as it is assumed that the soffit of the RC deck is protected by the bridge girders and permanent formwork and will therefore not be subject to chloride induced corrosion as it is protected from wind borne chlorides. A discount rate of 5% is used to account for all future costs. Normally distributed statistical parameters are shown in Table 3.

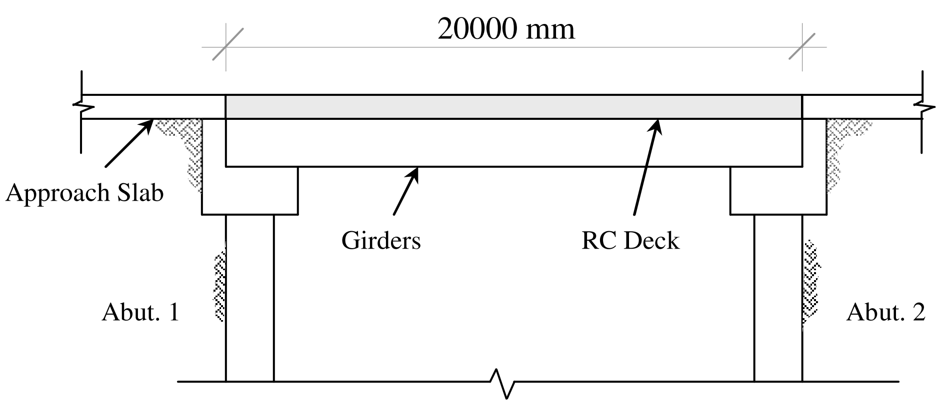

Figure 4 - Typical Bridge Structure used for Analysis of RC Bridge Deck.

Unless otherwise noted, the parameters used in the analysis of the RC bridge deck are those shown below (for a full description of all variables and statistical parameters, refer to Mullard (2010)):

- Discretised element size $\Delta = 0.5$ m
- Scale of fluctuation for concrete cover $\theta = 2.0$ m
- Scale of fluctuation for concrete compressive strength $\theta = 2.0$ m
- Scale of fluctuation for surface chloride concentration $\theta = 2.0$ m
- Size of limit crack width $w_{lim} = 1.0$ mm

Table 3 - Statistical Parameters.

Parameter	Mean	COV
C_o (Surface Chloride concentration)	3.05 kg/m^3	0.74
C_r (Critical Chloride concentration)	2.4 kg/m^3	0.2
Model Error (diffusion coefficient)	1.0	0.2
Model Error (corrosion rate)	1.0	0.2
Model Error (crack propagation)	1.04	0.09
Top Cover	+3.2 mm	σ=9.5 mm
Concrete Cylinder Strength f'_{cyl}	F'_c+7.4 MPa	σ=6 MPa
Workmanship Factor (k_w) $f'_c=k_w f'_{cyl}$	0.87	0.06
Concrete Tensile Strength $f'_{ct}(t)$	$0.53(f'_c(t))^{0.5}$	0.13
Elastic Modulus $E'_c(t)$	$4600(f'_c(t))^{0.5}$	0.12

The application of user delay in the spatial time-dependent reliability model is described by the schematic in Figure 5. It should be noted that the cost and extent of user delay adopted herein may not be appropriate for RC bridges where traffic volumes and user costs differ from the case presented in this study. The results presented, however, indicate the portion of life cycle cost due to user delay alone and as such, this cost can be increased or decreased (proportionally) according to estimated costs for a particular case.

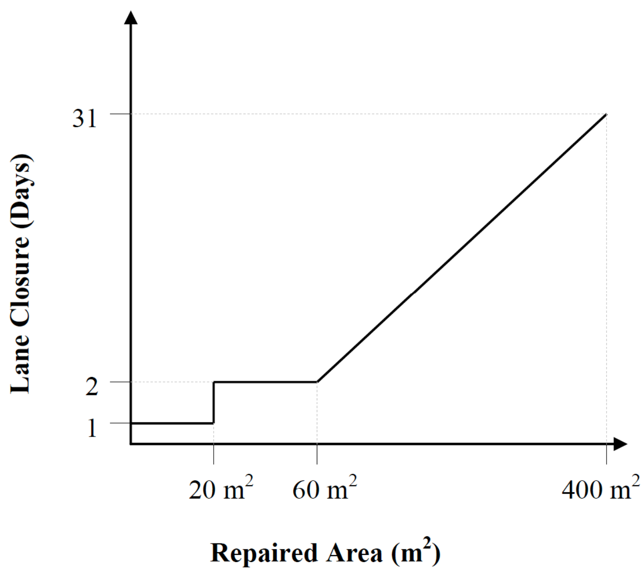

Figure 5 - Schematic of User Delay Costs

Figure 6 shows the probability of at least 'm' maintenance actions being required during a 120 year service life for the ten maintenance strategies investigated. Of the parameters considered, the most significant influence on the probabilities is maintenance technique and clearly defined groupings can be identified for the strategies using maintenance techniques M1, M2 and M3.

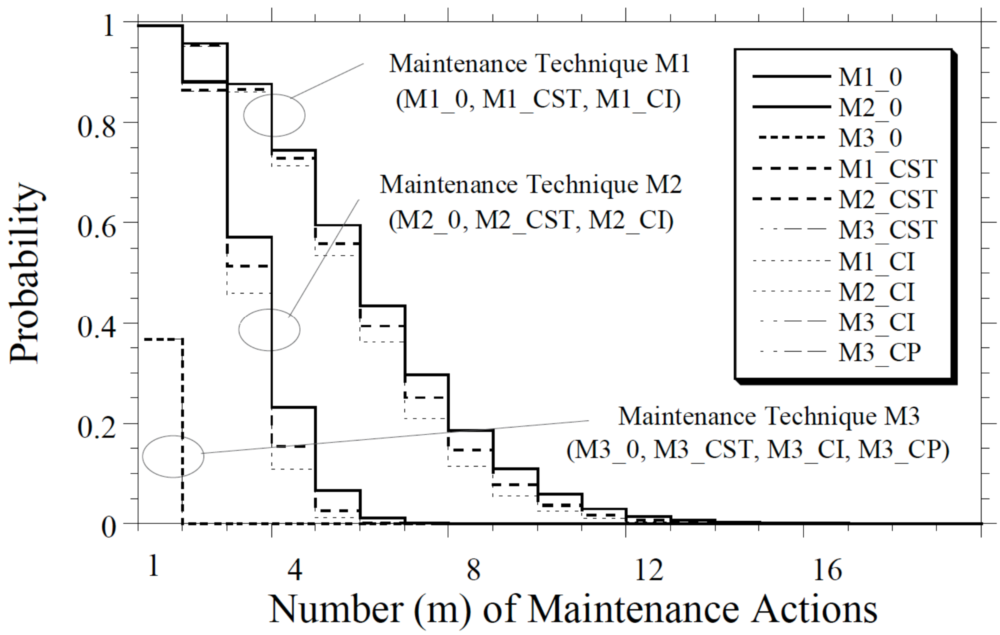

Figure 6 - Probability of At Least m Maintenance Actions for Different Maintenance Strategies.

The economic performance of each of the maintenance strategies can be compared using the average LCC data presented in Table 4. The average LCC of repair is influenced by the cost of repair, the number of repair actions required over the service life and the time at which they occur. Obviously repairs that occur later in the service life have a reduced influence on the average LCC due to the effect of the 5% discount rate. In terms of LCC of repair only, the maintenance strategies using maintenance techniques M1 and M3 are more economical than those using maintenance technique M2. Clearly, for economic optimisation there must be a balance between the length of delay in maintenance actions and the extent of damage repaired at that time (i.e. in terms of LCC of repairs, a longer delay in the timing of maintenance will more readily offset a larger repair area).

Table 4 - Summary of LCC for Different Maintenance Strategies.

Maint. Strategy	Average number of maint. actions (m)	Average area repaired during maint. actions (A_{repair})	Average LCC of repair costs	Average LCC of user delay costs	Average total LCC
M1_0	5.3 (0.47)	8.5 m^2	\$ 784	\$ 14,913	\$ 15,697 (0.72)
M2_0	2.8 (0.41)	54.5 m^2	\$ 2,552	\$ 18,889	\$ 21,441 (0.65)
M3_0	0.4 (1.31)	400 m^2	\$ 730	\$ 12,522	\$ 13,252 (1.57)
M1_CST	5.0 (0.46)	8.5 m^2	\$ 802	\$ 14,460	\$ 15,262 (0.71)

M2_CST	2.6 (0.38)	51 m^2	$ 2,524	$ 18,110	$ 20,634 (0.63)
M3_CST	0.4 (1.31)	400 m^2	$ 788	$ 12,522	$ 13,310 (1.57)
M1_CI	4.8 (0.45)	8.5 m^2	$ 763	$ 13,955	$ 14,718 (0.7)
M2_CI	2.4 (0.37)	52 m^2	$ 2,460	$ 17,764	$ 20,224 (0.62)
M3_CI	0.4 (1.31)	400 m^2	$ 773	$ 12,522	$ 13,296 (1.57)
M3_CP	0.4 (1.31)	400 m^2	$ 1,194	$ 12,522	$ 13,716 (1.57)

Notes: 1. Numbers in brackets are COVs. 2. The LCC's calculated in this study are in 2009 Australian dollars based on information and estimates from a number of sources.

The influence of repair durability can also be seen in Table 4. For maintenance strategies using maintenance technique M1 (maintenance strategies M1_0, M1_CST and M1_CI) the use of no repair durability improvement, a concrete surface treatment and a corrosion inhibitor have life-cycle costs for repair of $784, $802 and $763 respectively. For the case using the corrosion inhibitor, the effect of delayed maintenance (fewer average occurrences) offsets the cost of application and it has a lower LCC than for the case of no repair durability improvement. For the case of the concrete surface treatment, however, the cost of application outweighs the benefit of reduced maintenance actions and it has a higher LCC than for the case of no repair durability improvement. The influence of repair durability specifications is greater when maintenance technique M2 is used as a larger area of the RC surface is repaired. Maintenance strategies using maintenance technique M3 (maintenance strategies M3_0, M3_CST, M3_CI and M3_CP) do not benefit from repair durability improvements with the case of no repair durability improvements having the lowest LCC of repair. This is because for strategies using maintenance technique M3, the probability of second repairs over a 120 year design life is 0.0 meaning that no benefit is achieved by the application of either a concrete surface treatment or a corrosion inhibitor. Table 4 shows that user delay costs dominate LCC. Clearly these results are sensitive to the value of the discount rate, the cost of repair and the time and cost of user delay.

The variability of the LCC generated from a predictive model are important and can aide in the decision making process when assessing different maintenance strategies. The COVs of the predicted life-cycle costs are also shown in Table 4 and it can be seen that maintenance strategies using maintenance technique M3 (maintenance strategies M3_0, M3_CST, M3_CI and M3_CP) have a high COV.

Another measure of variability can be expressed by 5^{th} and the 95^{th} percentile values which can assist decision makers by providing the limits within which 90% of all outcomes will fall, see Figure 7. It can be seen that although maintenance strategy M3_0 has the lowest mean LCC, the variability is high and thus higher likelihood of incurring costs significantly higher than the mean. This information on the variability of performance and life-cycle costs clearly gives decision makers a more thorough basis for selecting maintenance strategies and may in fact alter the optimal solution from that based on mean data alone if the decision maker is risk averse or risk prone. For example, a risk averse decision maker may be more concerned about the likelihood of large costs than mean values. This is particularly apt for individual assets. However, for a portfolio of many assets, the decision maker should be risk neutral (use expected values) as this will provide the most cost-effective outcome across many assets. In other words, a risk neutral approach leads to decisions where the most benefit is achieved.

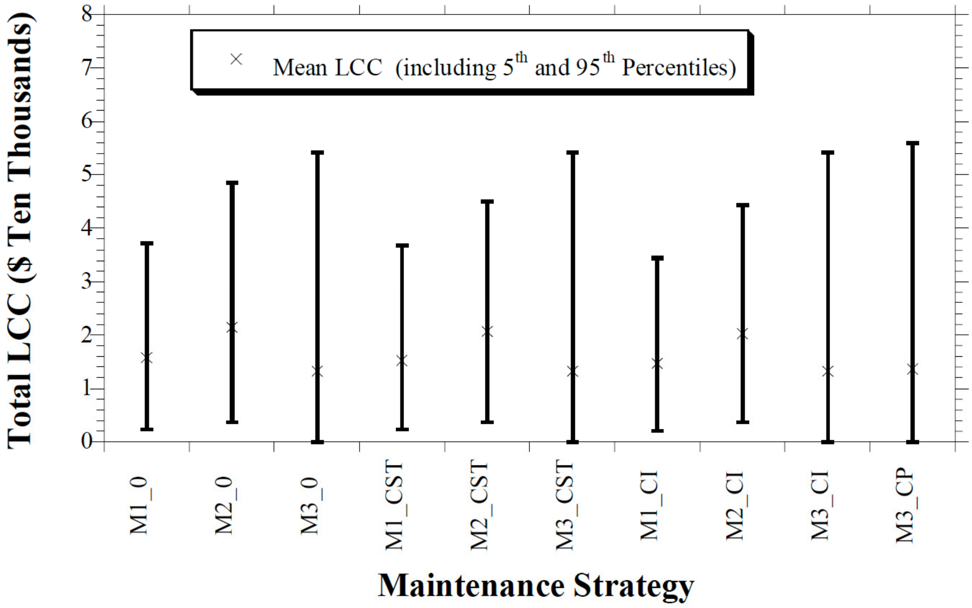

Figure 7 - 90th Confidence Intervals for LCC.

6. Conclusions

The spatial time-dependent reliability analysis conducted herein was used to predict the timing and extent of maintenance actions and the maintenance based life-cycle costs of a RC bridge deck. The Monte-Carlo based analysis technique allowed the variability of predictions from the complex deterioration and maintenance models to be calculated thus potentially providing decision makers with important and highly useful data to aide in the optimisation of maintenance strategies. Based on the analysis of the RC bridge deck, it was found that repair efficiency can affect the timing and extent of future maintenance actions and thus the total life-cycle costs over a 120 service life. User delay can be a more significant proportion of life-cycle costs than the actual cost of repair itself. Finally, knowledge of the probabilistic variability of predicted life-cycle costs can be an important factor in determining optimal and cost-effective maintenance strategies.

6. References

Breysse, D., S. M. Elachachi, E. Sheils, F. Schoefs and A. O'Connor (2009). Life-cycle Cost Analysis of Ageing Structural Components Based on Non-Destructive Condition Assessment. *Australian Journal of Structural Engineering* 9(1): 55-66.

Kenshel, O.M. (2009), *Influence of Spatial Variability on Whole Life Management of Reinforced Concrete Bridges*, PhD thesis, Department Of Civil, Structural & Environmental Engineering, Trinity College Dublin, August 2009.

Li, Y. (2004). *Effect of Spatial Variability on Maintenance and Repair Decisions for Concrete Structures*. Netherlands, Delft University.

Mullard, J.A. and Stewart, M.G. (2009). Stochastic Assessment of Timing and Efficiency of Maintenance for Corroding RC Structures. *ASCE Journal of Structural Engineering*, 135(8):887-895

Mullard, J.A. (2010). *Spatial time-dependent reliability analysis and optimisation of maintenance strategies for RC structures subject to corrosion damage*. Discipline of Civil, Surveying and Environmental Engineering. PhD Thesis, The University of Newcastle, Australia.

Mullard, J.A. and Stewart, M.G. (2009), Stochastic Assessment of the Timing and Efficiency of Maintenance for Corroding RC Structures, *Journal of Structural Engineering*, ASCE, 135(8):887-895.

Mullard, J.A. and Stewart, M.G. (2010), Corrosion-Induced Cover Cracking: New Test Data and Predictive Models, *ACI Structural Journal*, (in press).

Stewart, M.G. (2006), Spatial Variability of Damage and Expected Maintenance Costs for Deteriorating RC Structures, *Structure and Infrastructure Engineering*, 2(2):79-90.

Stewart, M.G. and Mullard, J.A. (2007). Spatial Time-Dependent Reliability Analysis of Corrosion Damage and the Timing of First Repair for RC Structures, *Engineering Structures* 29, 1457-1464.

Stewart, M.G. and Suo, Q. (2009), Extent of Spatially Variable Corrosion Damage as an Indicator of Strength and Time-Dependent Reliability of RC Beams, *Engineering Structures*, 31(1):198-207

Sudret B. (2008), Probabilistic models for the extent of damage in degrading reinforced concrete structures, *Reliability Engg and System Safety*, 93(3):410-422.

Val, D.V. and Stewart, M.G. (2003), Life Cycle Cost Analysis of Reinforced Concrete Structures in Marine Environments, *Structural Safety,* 25(4): 343-362.

Vu, K. and Stewart, M.G. (2000), Structural Reliability of Concrete Bridges Including Improved Chloride-Induced Corrosion Models, *Structural Safety*, 22:313-333.

Yang, S.-I., D. M. Frangopol and L. C. Neves (2006). Optimum maintenance strategy for deteriorating bridge structures based on lifetime functions. *Engineering Structures* 28(2): 196-206.

Yunovich, M., N. G. Thompson, T. Balvanyos and L. Lave (2001). Corrosion Costs and Preventative Strategies in the United States, CC Technologies Laboratories, Inc. to Federal Highway Administration (FHWA).

FINITE ELEMENT MODEL UPDATING USING CROSS-ENTROPY

J. DOWLING, A. GONZÁLEZ, E.J. OBRIEN & B. WALSH
University College Dublin, Dublin, Ireland

Abstract
This paper presents the potential of the cross-entropy method to surmise the properties of a simply supported beam using as input the response of the structure to a moving load. The beam model is discretised into a number of elementary beams with assumed initial statistical distributions of stiffness. Then, an optimisation procedure based on cross-entropy is employed to minimise differences between simulated measurements and the results of the theoretical finite element beam model. The procedure consists of generating a large sample of stiffness distributions for each elementary beam, and selecting those fitting the measured response best. Then, the parameters of the statistical distribution of stiffness assumed for each elementary beam (mean and standard deviation) are updated using the stiffness values of those combinations of elementary beams giving a best solution. It is an iterative procedure where the mean value of each distribution tends towards the true stiffness in successive iterations. The level of accuracy is limited by the quantity and quality of the available measurements. Therefore, the standard deviation of the final stiffness for each beam element (once further iterations do not lead to a reduction of the error) provides an estimation of the reliability of the prediction. Here, the method is demonstrated for the characterisation of the stiffness distribution of a beam from the simulated response to a moving load. First, deflections are calculated using a finite element beam model with assumed initial stiffness properties. There will be a record of simulated responses per measurement point that cross-entropy will try to imitate by adjusting and improving estimations of stiffness in successive iterations. The results show cross-entropy can be used as a valuable tool to estimate structural parameters and it has huge scope for applications in model calibration, bridge weigh-in-motion and monitoring.

Keywords: Finite-Element Updating, Cross-Entropy, Bridge Parameter Estimation

1. Introduction

The assessment of the material properties of structures through site measurement, without dissecting the structure, is a vibrant field of study. These parameters can be used to model and assess/monitor the structure or for direct damage detection. The ability to measure deflections or strains on site and infer the materials flexural rigidity (EI) or density (ρ) would allow an accurate and calibrated finite element model of the structure to be built.

Many non-destructive methods of inferring a bridge's structural parameters have been developed, particularly in the field of damage detection. For example, natural frequency based methods (Chen et al. 1995), mode shape based methods (Ewins 1984) and neural network based methods (Pandey and Barai 1995) to mention a few approaches. For a comprehensive review of damage detection algorithms using dynamic measurements, see Carden and Fanning (2004).

Walsh and González (2009) propose using the Cross-Entropy (CE) method (Rubinstein and Kroese 2004) in conjunction with static measurements to obtain the distribution of flexural stiffness within a discretized Finite Element (FE) beam model. The CE method can simply be described as an iterative procedure composed of two steps (de Boer et al. 2005); firstly a random data sample is generated and secondly the method by which the random data is generated is altered so as to produce a better fitting sample in the next iteration. It is a form of 'brute-force' optimization algorithm, which takes advantage of modern computational capacity to generate many possible solutions, gradually converging to the most probable solution. This paper will use the CE method for determining those properties necessary to construct the stiffness and mass matrices of a FE model.

2. Beam Model

A FE model was programmed with Matlab (Mathworks Inc. 2005) to calculate the response of a simply supported beam to a forcing function. The beam contained a number, *N*, of beam elements; hence *N+1* nodes; with each node having 2 Degrees-of-Freedom (DoF): rotation and vertical displacement. The DoFs of an 8m simply supported beam are shown in Figure 1 (The displacement of the vertical DoFs over the supports are set to zero for a simply-supported beam).

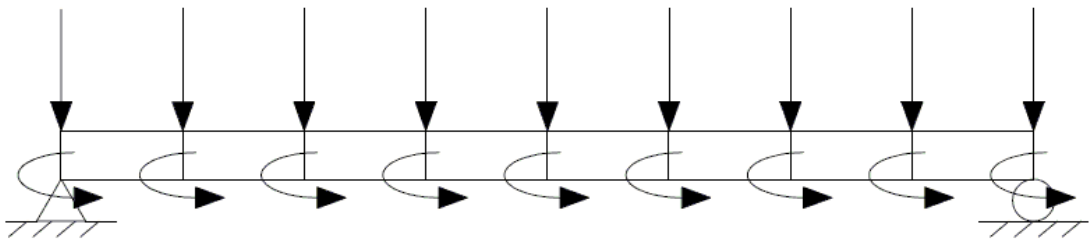

Figure 1 – FE Beam dipicting Degrees of Freedom

The 8m beam depicted in Figure 1 is split into eight 1m long beam elements giving (8+1)×2 = 18 DoFs. This FE model can be used to calculate the static response to the applied load and to derive the stiffness matrix from the simulated measurements, as in the earlier work of Walsh and González (2009). The model can also be used to calculate the dynamic response to a moving load and to derive mass and stiffness properties from this simulated response as proposed in this paper.

3. The Cross-Entropy Algorithm for FE Beam Models

The CE algorithm used to determine the material properties was developed through a number of trial generations, progressing from one to the next with increasing complexity. An initial study of the CE method pertaining to a FE model was conducted by reviewing the static CE algorithm of Walsh and González (2009). This algorithm calculated the flexural stiffness values of FE elementary beams (i.e., product of modulus of elasticity and second moment of area, EI). Secondly, change the forcing function from static to time-varying, and use the dynamic response to calculate the EI values. And finally, include the mass matrix in the solution and attempt to calculate the material density ρ in addition to the EI values.

The implementation of the CE method in conjunction with the FE model involves re-writing the matrices of the equation of motion so the material properties can be input variables. The general equation of motion for structural dynamics is given in Equation (1).

$$[M]\{\ddot{u}\} + [C]\{\dot{u}\} + [K]\{u\} = F(t) \tag{1}$$

In Equation 1, *[M]*, *[C]* and *[K]* are the system's mass, damping and stiffness matrices respectively, *{u}* is the vector of displacements and *F(t)* is the forcing function. In order to limit the number of unknowns in the CE algorithm, the influence of damping will be neglected for all the simulations described here.

3.1 Stiffness and Mass Matrices

The static CE algorithm solves the equation of motion in a simplistic form, considering only the stiffness matrices as in Equation (2).

$$[K]\{u\} = F(t) \tag{2}$$

The CE algorithm solving for both, EI and the material ρ, must consider the mass matrix in addition to the stiffness matrix. Equation (3) will be employed for this dynamic simulation.

$$[M]\{\ddot{u}\} + [K]\{u\} = F(t) \tag{3}$$

The global mass and stiffness matrices of Equations (1)-(3) are obtained from assembling the elementary stiffness (k_e) and elementary mass (m_e) matrices. The elementary matrices, k_e and m_e for beam elements with 2 DoFs per node, are shown in Equations (4) and (5) (Bathe 1996, Logan 2007),

$$k_e = EI\begin{bmatrix} 12/l^3 & 6/l^2 & -12/l^3 & 6/l^2 \\ 6/l^2 & 4/l & -6/l^2 & 2/l \\ -12/l^3 & -6/l^2 & 12/l^3 & -6/l^2 \\ 6/l^2 & 2/l & -6/l^2 & 4/l \end{bmatrix} \tag{4}$$

$$m_e = \rho/420\begin{bmatrix} 156Al & 22Al^2 & 54Al & -13Al^2 \\ 22Al^2 & 4Al^3 & 13Al^2 & -3Al^2 \\ 54Al & 13Al^2 & 156Al & -22Al^2 \\ -13Al^2 & -3Al^2 & -22Al^2 & 4Al^3 \end{bmatrix} \tag{5}$$

where l and A are elementary beam length and area respectively. The deflection measurements used as input to the CE algorithm are shown for reference in Figure 2. The deflections shown in Figures 2 (a) and (b) are the input signals to the CE algorithm described by Equations (2) and (3) respectively. The inclusion of the matrix *[M]* in the solution creates a more complicated deflection signal with the participation of the inertial forces of the beam. The magnitude and velocity of the load used were 200 kN and 10m/s respectively.

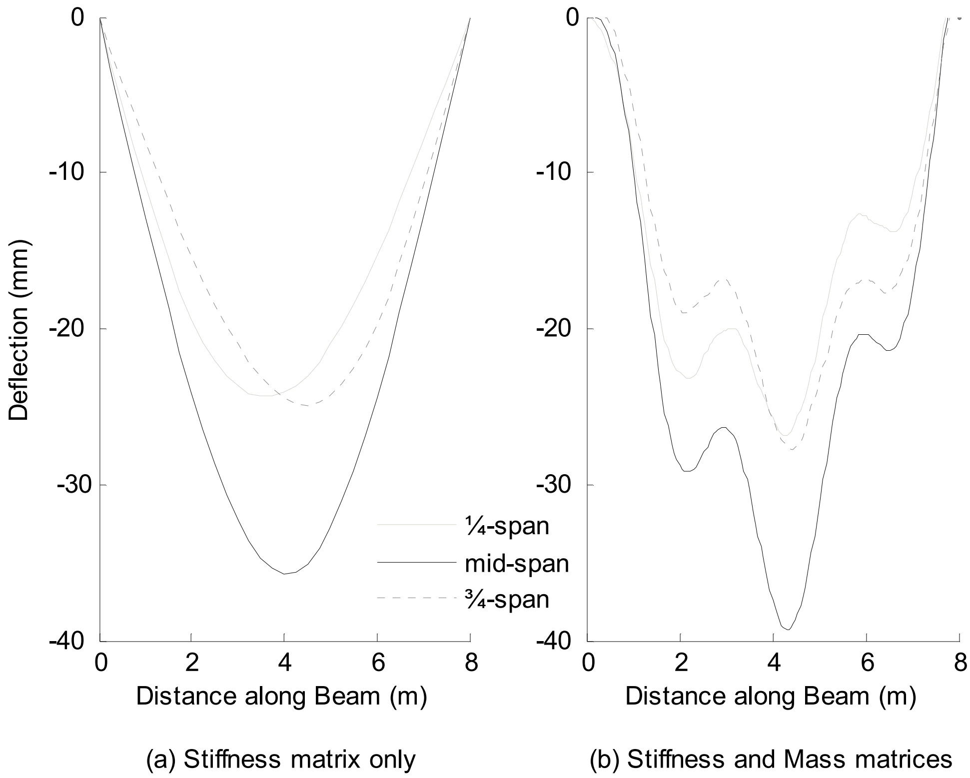

Figure 2 – Simulated Deflections

3.2 EI estimates, TBs and EIPs

The first step in the CE algorithm is to create the initial distribution of values, some initial EI distribution for each element of the beam (these distributions will be defined by mean (μ) and standard deviation (σ) values). Let's call this initial set of EI distributions an EI Profile (EIP). Some initial input is required to the system, a best-engineering estimate of the materials EI value. Variations larger than 30% from theoretical values are not expected except for large amounts of damage.

From the EIP a number, K, of Trial Beams (TBs) with elementary EI beam values randomly sampled from the EIP are generated. Deflection measurements are then taken at three locations along the beam to test the algorithm: ¼-span, mid-span and ¾-span for the applied loading. Clearly, the smaller the number of measurement locations, the larger the number of possible combinations of model parameters satisfying the solution and the more difficult the optimisation problem. An objective function is defined as the sum of the squares of the differences between the deflections measured for each TB and the deflections measured for the actual beam. An 'elite set' (Rubinstein and Kroese 2004) is defined as the top 5% TBs giving the lowest objective function values. The mean and standard deviation EI values of this elite set are then used to create the EIP for the next iteration of TBs. A tolerance is then specified to establish when convergence has been reached, i.e., 0.01% difference in successive objective functions.

Starting with the initial normal distribution of EI values for each of the N beam elements, the algorithm progresses; updating the μ and σ values, informed by the elite set from the previous iteration until convergence has occurred. At this point mean values are adopted as the predictions for the EI values and the standard deviations are a measure of the degree of confidence in these predictions (typically the more available measurements the smaller the standard deviation.

The inverse problem of estimating structural parameters given a structure's response to a loading event has no unique solution. There are multiple sets of EI and density values that may produce the desired structural response. Hence a common problem encountered along the route to the solution of the algorithm is that it may converge to a false-solution. This is a well documented issue with the CE method and the technique used to prevent early convergence is one penned the 'Noisy' CE Method by Szita and Lörincz (2006), which was first proposed as the method of 'injecting' extra variance into the samples by Botev and Kroese (2004). This technique simply involves adding noise to the updated standard deviation between iterations. This 'widens' distributions at the start of the iterations reducing false convergence. The magnitude of the added variance reduces as the number of iterations progresses, until at some simulation the variance is no longer artificially inflated.

4. Moving-Load Algorithm, Damage Simulation

This section presents the results of the CE algorithm in predicting stiffness distribution taking as input the simulated responses from Equation (2) (Figure 2(a)). Figure 3 presents the results of four CE algorithm simulations. Each simulation attempted to model different locations and severities of damage to the beam in the form of a local reduction in stiffness. The 8m beam used in the simulation was split into 8 metre long elements. The dotted line in Figure 3 shows the initial input to the CE algorithm; the light solid line shows the actual values; the heaviest solid line with empty circular markers are the final predicted EI values from the algorithm.

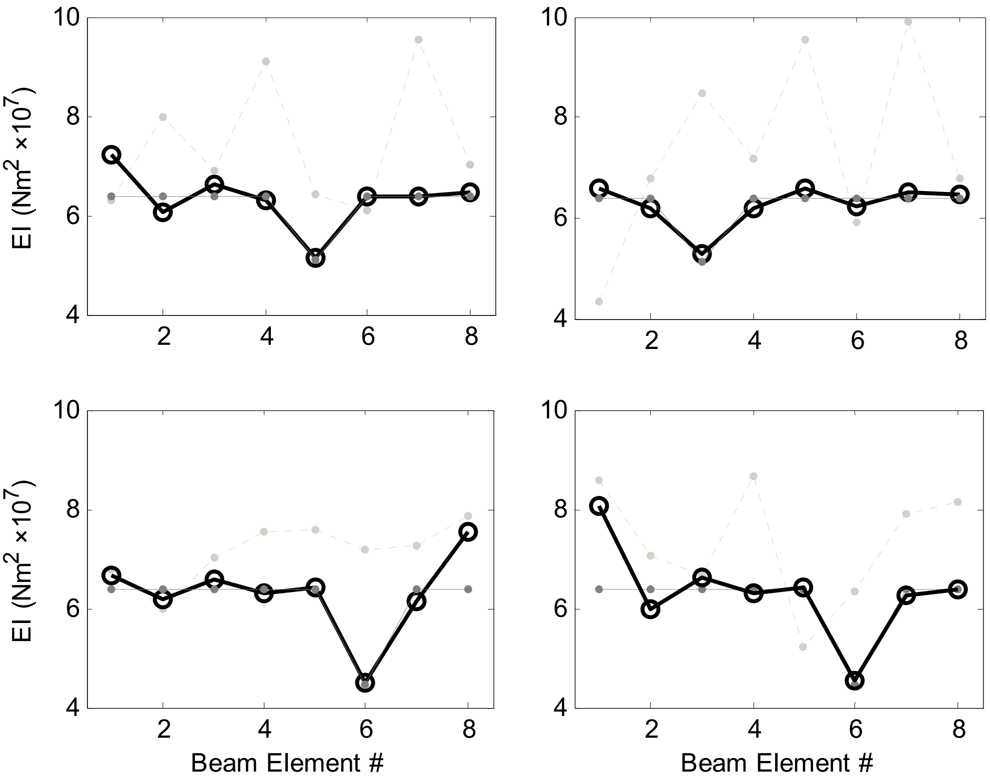

Figure 3 – EI Predictions for Four Simulations (dotted line: initial input; light solid line: actual values; heaviest solid line with empty circular markers: final predicted EI)

It has been noted in a previous study by Walsh and González (2009) that the predictions of the elements near the supports suffer due to the small magnitudes of the deflection values at these locations. This problem can be overcome with the use of inclinometers. With the exception of these end elements the predictions are very good; the location and magnitude of the damaged elements being identified correctly in every case.

5. Inclusion of Mass Matrix [M] in the Solution

The matrix *[M]* (Equation (3)) is included here as an unknown input to be predicted by the algorithm. This addition includes the material density in the list of unknowns solved in the CE algorithm. It was decided to solve for a single density value, that is, assume that the density of all beam elements being constant in a preliminary investigation. This increases the number of unknowns merely from the previous eight stiffness values to nine. The simulated input has been shown in Figure 2(b).

In programming the 'Noisy' CE algorithm it is accepted that sometimes the objective function of the optimisation algorithm may enlarge, that is, some trial solutions may be worse than in previous iterations. Figure 4, shows the objective function for such a simulation. In this simulation 'injection' occurred for the first 49 convergences, with the 50th convergence the simulation ended (at approximately iteration 4,000). The peaks in Figure 4 are at the iteration number where injection occurred, with the objective function values at convergence typically of the order of 10^{-4}.

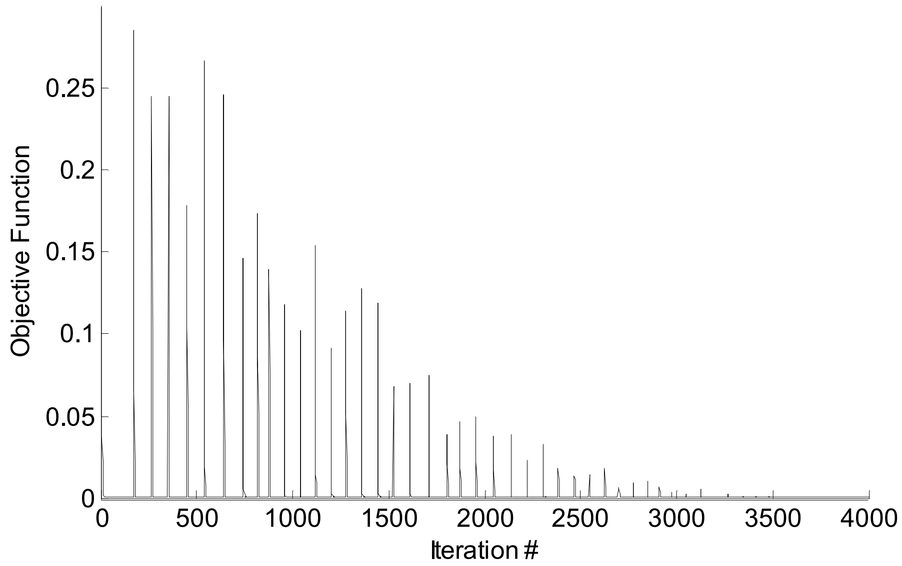

Figure 4 – Objective Function Values

The magnitude of the 'injection' was reduced as the iterations progressed. The final algorithm predictions are taken from the TB which gives the minimum objective function value, which may not necessarily be the final iteration. The predictions for this simulation are shown in Figure 5.

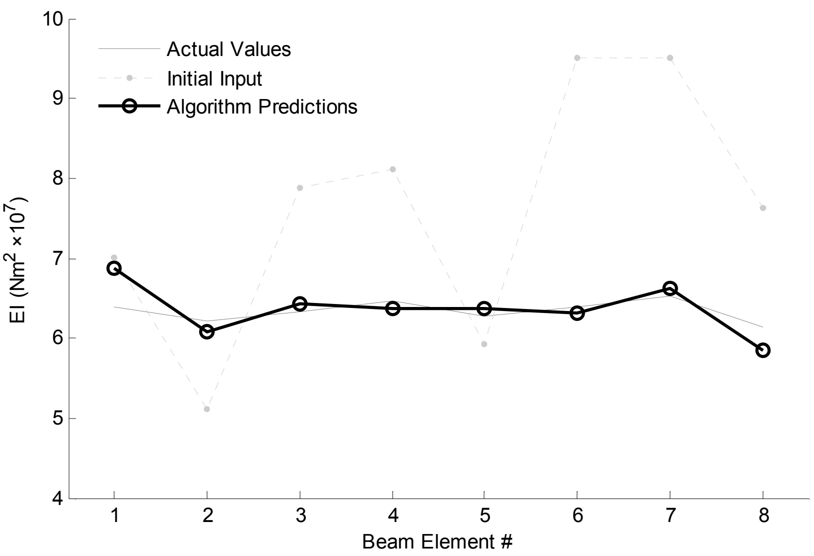

Figure 5 – Simulation Predictions, including [M]

The elementary beam EI values being sought in this simulation are distributed randomly about some mean, attempting to model healthy elements subject to usual material variation. This is imitating a scenario where the CE algorithm is being used for model calibration. The simulation prediction of material density was 24,040 kg/m^3, overestimating the actual value of 24,000 kg/m^3 by only 0.2%. There was a mean error of 2.7% in the prediction of the EI values (or a mean error of 1.5% when not considering the end elements.)

6. Conclusion

A CE algorithm has been shown to predict the flexural stiffness and density values of a FE beam with great accuracy. There is scope for incorporating other inputs such as strain measurements or additional unknowns, i.e., allowing the material density of each element to vary independently, or increasing the complexity of the structural model to 2-D or 3-D. It is a relatively easy-to-implement method compared to other statistical FE updating procedures, that has shown to be able to infer the stiffness and mass matrices of a FE model from measurements, which can be subsequently used for calibration of Bridge Weigh-in-Motion systems or applications in Structural Health Monitoring.

Acknowledgements

The authors wish to express their gratitude for the financial support received from the 7th European Framework ASSET Project towards this investigation.

References

Bathe, K.J. (1996), *Finite Element Procedures in Engineering Analysis*, Prentice Hall, Englewood Cliffs.

Botev, Z. and Kroese, D. (2004), 'Global likelihood optimization via the cross-entropy method, with an application to mixture models' in *Proceedings of the 2004 Winter Simulation Conference*, eds. R.G. Ingalls, M.D. Rossetti, J.S. Smith and B. A. Peters, Washington, DC, USA, 529-535.

de Boer, P., Kroese, D.P., Manor, S. and Rubinstein, R.Y. (2005). 'A Tutorial on the Cross-Entropy Method', *Annals of Operations Research,* 134, 19–67.

Carden, E.P. and Fanning, P. (2004), 'Vibration based condition monitoring: a review', *Structural Health Monitoring*, 3, 355-377.

Chen, H.L., Spyrakos, C.C. and Venkatesh, G. (1995), 'Evaluating structural deterioration by dynamic response', *Journal of Structural Engineering*, 121(8), 1197–1204.

Ewins, D.J. (1984), *Modal Testing: Theory and Practice*, Research Studies Press Ltd, England.

Logan, D.L. (2007), '*A First Course in the Finite Element Method, 4th Edition'*, Thompson, Tampa, USA.

Matlab Version R14 (2005), *User's Manual*. The Mathworks Inc., Massachusetts, USA.

Pandey, P.C. and Barai, S.V. (1995), '*Multilayer perception in damage detection of bridge structures*', Computers and Structures, 54(4), 597–608.

Rubinstein, R.Y., Kroese, D.P. (2004), *The cross-entropy method*. Springer, New York, USA.

Szita, I. and Lörincz, A. (2006), 'Learning Tetris Using the Noisy Cross-Entropy Method', *Neural Computation,* 18, 2936–2941.

Walsh, B.J. and González, A. (2009), 'Assessment of the Condition of a Beam Using a Static Loading Test', *Key Engineering Materials,* 413-414, 269-276.

A REVIEW OF GAIT PARAMETERS PERTINENT TO PEDESTRIAN LOADING

P. ARCHBOLD & B. MULLARNEY
Structures & Materials Research Group (STRAIT), Athlone Institute of Technology, Ireland

Abstract

Much work at present is aimed at establishing accurate load models for pedestrian loading, particularly on flexible structures, which are subject to excitation from such sources. This area of research is relatively new in the engineering community, with the vast majority of published data on the topic appearing since 2000, stimulated by a number of high-profile examples of excessive footbridge vibration.

Several forcing functions are proposed in the literature to simulate this type of loading but have been shown to have varying degrees of success in doing so. It is considered that understanding of the principal properties of human walking actions or gait must contribute to development of any robust load models.

Biomechanical research, aimed at achieving this understanding has identified a number of these properties, which are referred to as gait parameters. Also of importance in terms of human-structure interaction is how some of these parameters may be altered when subjected to external factors, such as footbridge vibrations. This paper introduces some of these parameters and reports values from a substantial review of references in the literature. A brief summary of some of the theoretical control mechanisms is also presented.

Keywords: Gait Parameters, Pedestrian Loading, Walking Control

1. Introduction

The issue of pedestrian loading on footbridges and more specifically the subject of pedestrian-structure interaction is beginning to attract significant attention from researchers within the engineering community. This is largely in the wake of several notable instances of excessive vibrations in footbridges being recorded in recent times.

The author has previously addressed this issue and developed interactive load models for an individual pedestrian, which successfully capture the interaction between the pedestrian and a vibrating structure and also the magnitude of the vertical vibrations induced in a particular test structure by the pedestrian (Archbold, 2004; Fanning et al., 2005).

Current work is focussing on trying to predict the load behaviour from crowds of pedestrians. One approach being undertaken is developing stochastic load models based on statistically accurate information in relation to individual pedestrian behaviour within crowds (Keogh et al., 2010). In order to verify and calibrate these statistical models, accurate and reliable data on the actions and processes involved in human locomotion are required.

Gait refers to the typical walking behaviour of pedestrians and can be broadly defined by a number of parameters. There is currently a dearth of reliable information in relation to these gait parameters due to the fact that much of the work on gait analysis up to now has been carried out in the field of biomechanics.

This paper presents an overview of several reported parameters of gait or walking action which have an influence on how pedestrians exert forces on structures and how they may also be adapted during the interaction process.

2. Gait Parameters

Although human locomotion is a very complex process, Davis et al. (2000) describe walking or "gait" as a cyclic activity for which certain discrete events have been defined as significant. In biomechanical terms, these parameters are classed as either spatial or temporal and a list of these parameters is contained in Table 1. Some of these parameters are also represented diagrammatically in Figure 2(a) and Figure 2(b).

Table 1 – Spatial and Temporal Gait Parameters

Spatial Gait Parameters	Temporal Gait Parameters
Step Length	Pacing Frequency/Cadence
Step Width	Swing Phase
Foot Landing Position/ Toe-in Toe-out Angle	Stance Phase/Support Phase
	Ground Reaction Force

In terms of pedestrian loading on structures, the gait parameters of relevance depend on whether vertical or lateral excitation is being considered. Step length, pacing frequency and the resultant vertical ground reaction force are the parameters which influence vertical loading. Meanwhile, step width, foot landing position, pacing frequency and the resultant lateral ground reaction forces determine the dynamic lateral loads applied. Each of these parameters will be examined in this paper.

2.1 Step Length

Step Length, l_s, (Figure 2(a)) refers to the distance from the heel strike of one foot to the heel strike of the other foot. There has been some confusion in the literature between step length and stride length, which is the distance between the heel strike of one foot and the next heel strike of the same foot. Stride length can simplistically be taken as approximately twice the step length but this may hide the fact that there can be variability between the right and left step lengths respectively.

Some authors claim that step length increases with age up to a point and then begins to diminish. This finding has been supported by analysis of the results published in 18 references (Assi et al., 2009; Bachmann & Ammann, 1987; Barker et al., 2006; Bennett et al., 2006; Bilney et al., 2003; Cho et al., 2004; Drerup et al., 2008; Dubost et al., 2008; Henriksen et al., 2004; Menz et al., 2004; Morris et al., 2007; Oberg et al., 1993; Parvataneni et al., 2009; Ricciardelli et al., 2007; Ryu et al., 2006; Sanhaci & Kasperski, 2005; Terrier et al., 2005; Wheeler 1982.).

Figure 1 shows the mean reported values from the current literature surveyed. The mean step length for children and young adults is 0.59m, rising to 0.67m for mature adults and dropping down to 0.61m for adults over the age of 60. Furthermore, the step length is relatively consistent with standard deviations of 8%, 11% and 9% respectively for each of the three groups.

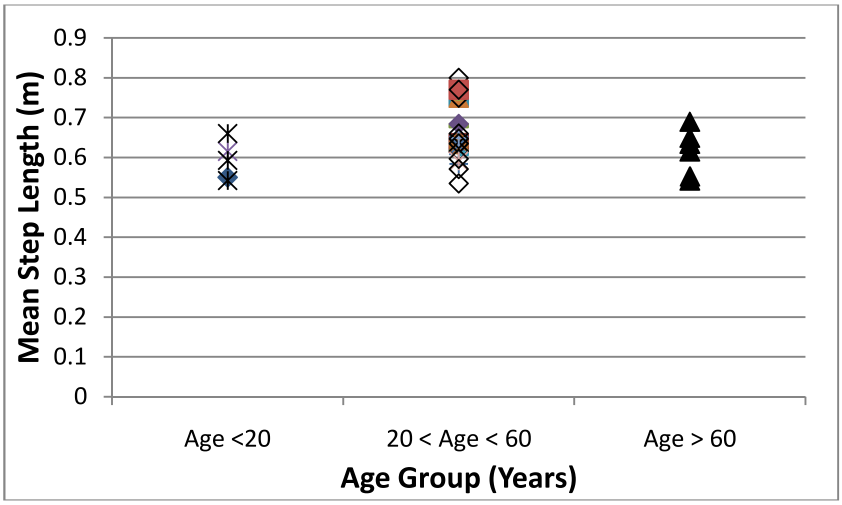

Figure 1 – Mean Reported Values of Step Length

Kerr and Bishop (2001) proposed a relationship between the height of the test subject, h, and the step length, l_s, for normal walking conditions. This relationship is defined as:

$$l_s = 0.45h \quad (1)$$

Grundmann and Schneider (1990) report tests carried out by Inman (1981) and Andriacchi (1977), which both give similar results. Andriacchi (1977) recorded time-distance measurements and ground reaction forces in relation to walking speed for normal test subjects and patients with knee disabilities. These measurements yield a relationship between the mean values of step length, l_s, the body height, h, and the pacing frequency, f_s as:

$$l_s = (0.24h)f_s \quad (2)$$

Both expressions give reasonably similar predictions of step length based on the height of the subject for the pacing rates concerned. Analysis of the results reported herein yields a relationship between step length and height of:

$$l_s = (0.4)h \quad (3)$$

Insufficient data was available to determine any connection between pacing frequency or walking speed and step length.

2.2 Step Width

Step width is defined as the distance between the centre lines of the two feet (Figure 2(a)). Reported values of step width have proven to be far more variable than step length, with standard deviations up to 30%. Further, there is less reported data on this particular spatial parameter. 5 references yield values between 0.09m and 0.19m for adults, with no apparent link between subject height and step width. Interestingly, values reported by Cho et al. (2004) and Ryu et al. (2006) suggest that Korean adults exhibit greater step widths than others reported. Donelen et al. (2001) and Bauby & Kuo (2000) both linked step width to stride length reporting that the step width was approximately equal to 12% and 13% respectively of the stride length.

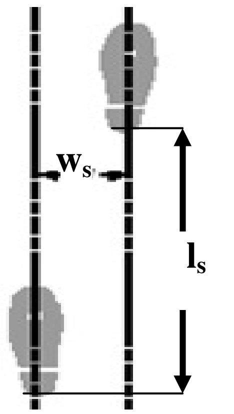

Step Width (w_s) &
Step Length (l_s)
(a) Spatial Parameters

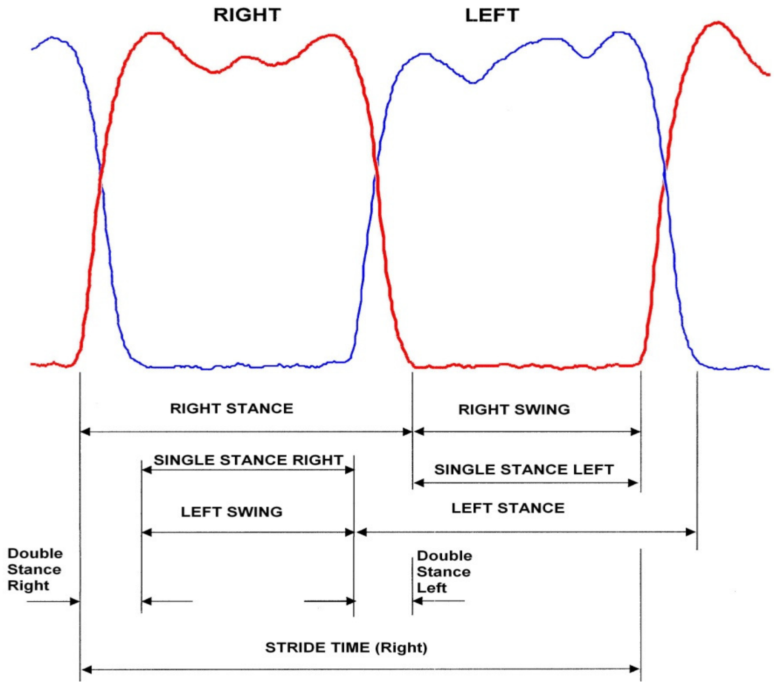

(b) Temporal Parameters

Figure 2 –Gait Parameters

2.3 Foot Landing Position

Simpson and Jiang (1999) reported tests, which revealed that foot landing position influenced the force applied by the pedestrian. They categorised their test participants into categories of "toe-in", "neutral" and "toe-out" depending on their foot landing position during straight line walking as shown in Figure 3. Values for foot landing position are reported in degrees, with positive representing toe-out and negative representing toe-in. Reported values for foot landing position range between +14.3^o (toe-out) and -3.8^o (toe-in) (Simpson & Jiang, 1999). This parameter presents the most variability of all of the spatial gait parameters in healthy test subjects.

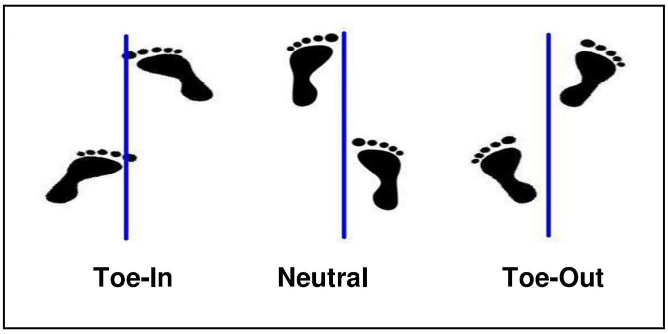

Figure 3 - Foot Landing Position (FLP) Categories (Simpson & Jiang, 1999)

2.4 Pacing Frequency

Pacing frequency is the most relevant of the temporal gait parameters in terms of pedestrian loading. It is defined as the inverse of the time taken from the initial contact of the left foot with the ground to the initial contact of the right foot immediately thereafter and corresponds to the rate of application of vertical forces. In biomechanical terms, this parameter is often measured as cadence, which is the number of steps per minute rather than the number per second.

Reported values of normal pacing frequencies indicate that the average pacing rate is between 1.8Hz and 2.2Hz. Keogh et al. (2010) reviewed 7 references and derived an average pacing frequency of 1.96Hz, with a standard deviation of 0.21Hz. This paper presents the results based on a survey of a further 20 sources of information and the results are presented in Figure 4.

These results show a decrease in pacing frequency with age. The under 20 group have an average of 2.02Hz, while the 20-60 year olds and the over 60's display 1.92Hz and 1.91Hz respectively. Interestingly, the results from Oberg et al. (1993) indicate that there may be a gender consideration relating to pacing frequency, with women walking at an average of 2.1Hz and men at an average of 1.98Hz for normal walking velocity.

The pacing frequency is quite intuitively dependent on the walking velocity, but for the normal range considered here, it has proven to be quite consistent, with standard deviations of the order of 6%.

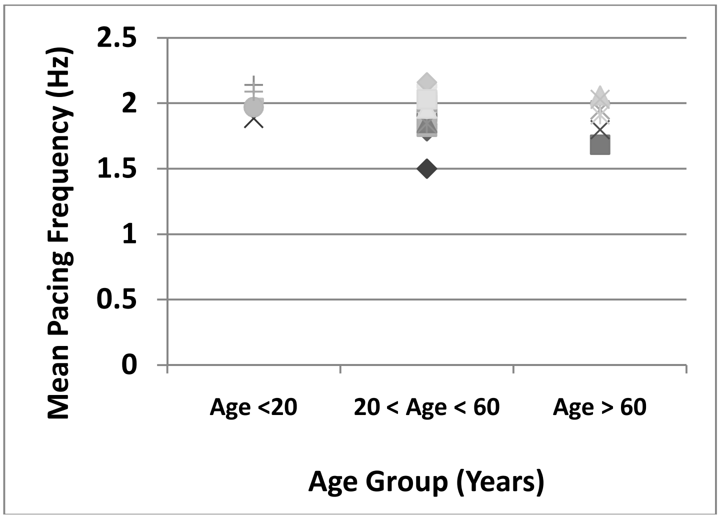

Figure 4 – Mean reported pacing frequencies

2.5 Stance & Swing Phase

The stance phase and swing phase respectively refer to the time elements of a step action where the foot is either in contact with the walking surface or moving (swinging) to its next intended location. These parameters are of least consequence in terms of pedestrian loading and there is little reported data on their values. Indicatively, the stance phase occupies approximately 65% of the step time and the swing phase 35%. No further analysis of these parameters is presented herein.

Table 2 presents a summary of the reported values for the relevant spatial and temporal gait parameters for healthy mature adults.

Table 2 – Reported Values for Temporal and Spatial Gait Parameters

Parameter	**Max. Average**	**Min. Average**	**Mean**	**Std. Dev.**
Step Length (m)	0.80	0.54	0.67	11%
Step Width (m)	0.19	0.09	0.14	29%
Foot Landing Position (^{o})	14.3 (Toe-out)	-3.8(Toe-in)	5.4	144%
Pacing Frequency (Hz)	2.16	1.50	1.92	6.7%

2.6 Ground Reaction Forces

Essentially, ground reaction forces (GRF's) measure the forces applied to a surface by a person walking across it. As such, ground reaction forces are the primary interest in studying loading applied by persons traversing a structure. Walking imparts forces in three orthogonal planes – forward/backward, lateral and vertical. In biomechanics literature, these three planes are labelled the saggital, medio-lateral and vertical respectively. Bachmann & Ammann (1987) reported that vertical force is of greatest magnitude, followed by the saggital and then the medio-lateral forces. In terms of pedestrian loading, the saggital plane is not considered to be of consequence as the structure will almost certainly be rather stiff in the direction of walking.

Vertical Ground Reaction Forces

Figure 2(b) shows a typical vertical ground reaction force, with the blue line representing the force exerted by the left foot and the red line representing the force exerted by the right foot. The total vertical GRF is a summation of these individual traces. The magnitude of the GRF is directly related to the mass of the person and there are some reports linking it to walking speed or pacing frequency. However, further examination of any possible links is required.

The total vertical GRF trace represents the dynamic vertical force applied by a pedestrian on a fixed surface and is generally approximated as a sine curve. This function can be reasonably well defined (Fanning et al., 2005) by:

$$F(t) = G + r_1 G\sin(2\pi f_s t) \qquad (4)$$

where:

F(t) is the forcing function

G is the weight of the person

r_1 is the dynamic force component factor, which is dependent on the actual pacing frequency

f_s is the pacing frequency (Hz)

t is the time of load application

Lateral Ground Reaction Forces

Medio-lateral GRF's indicate the amplitude and frequency of lateral loading (perpendicular to the direction of walking) imparted by pedestrians traversing structures. The frequency of lateral loading is approximately half the pacing frequency as it relates to consecutive strikes from the same foot. Figure 5 shows a trace of the medio-lateral GRF's produced from consecutive footsteps. Also shown is a sine curve, which may be used to approximate this force function. Medio-lateral GRF's depend not only on mass and pacing frequency, but the other spatial gait parameters of step width and foot landing position appear to be important also. Moreover, these are the most variable parameters, which leads to greater uncertainty in estimating the lateral loading applied by walking pedestrians. For example, it has been shown that two pedestrians of similar height and weight, while causing similar vertical vibrations in a flexible footbridge, have caused considerably different lateral vibrations (Archbold, 2004).

Perhaps surprisingly, foot landing position, rather than step width, appears to be the more dominant factor in determining pedestrian lateral forces. "Toe-out" participants have been shown to impart a lateral force up to 4 times that of "toe-in" participants. (Simpson & Jiang, 1999).

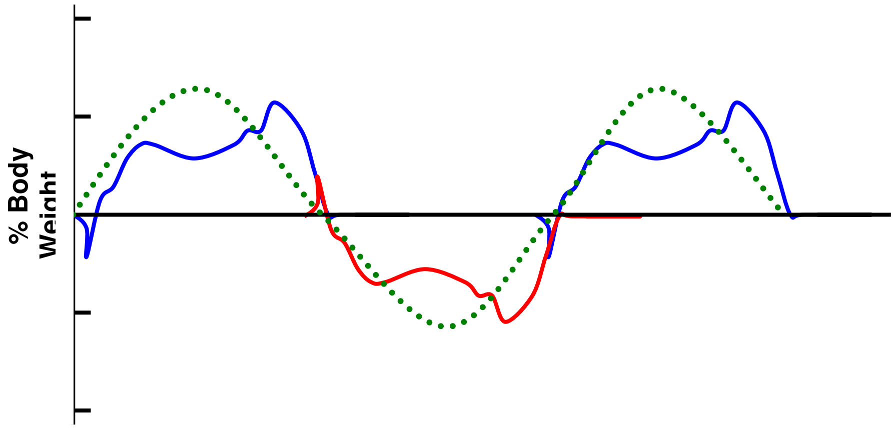

Figure 5 – Medio-lateral GRF trace from consecutive footsteps

Archbold (2004) proposed the following function to describe the lateral forces applied by walking pedestrians on a rigid surface:

$$F_L(t) = (-0.05f_s + 0.12)P_f G sin(\pi f_s t) \qquad (5)$$

Where:

$F_L(t)$ = Lateral force function
f_s = pacing frequency
P_f = FLP (foot landing position) factor (0.5, 1.0 or 2.0 for toe-in, normal & toe-out respectively)

Note that the frequency of this function is half that of the vertical force function.

6. Biomechanical Control of Locomotion

Despite the fact that a great deal is known about human walking, there is still not a single definitive theory to explain the phenomenon. Vaughan (2003) described a number of existing theories seeking to explain the evolution of understanding of bipedal walking.

One of the theories of control is that locomotion is the translation of the centre of gravity along a pathway requiring the least expenditure of energy. Saunders et al (1953) produced a landmark document from which many conventional ideas about normal human walking originate. This document theorises that there are six "determinants" of normal gait that were claimed to minimise the displacement of the body's centre of mass (BCOM) and smooth its trajectory, thereby saving energy.

Differences in opinion have arisen on some of these issues in recent times. Gard & Childress (2001) carried out a programme of research into vertical centre of mass movements during walking using both experimental data obtained from gait analyses performed on able-bodied subjects and theoretical data derived from a rocker-based inverted pendulum model of walking. They claim that, rather than minimising the displacement of the centre of mass, the human alters knee flexion and pelvic obliquity in order to act as a shock absorption mechanism.

Menz et al. (2003) studied acceleration patterns of the head and pelvis during walking. Thirty healthy test subjects walked on a level corridor and on an artificial grass surface underlain with foam and wooden blocks placed in a random manner in order to create an irregular and unpredictable walking surface. Acceleration measurements were then taken from both the head and pelvis. The authors maintain that an individual's comfortable walking speed is selected to minimise *variability* of accelerations, thus ensuring that accelerations of the head and pelvis are smooth and rhythmic. The principal aim is not to minimise centre of mass *movement* as previously theorised but to produce the most regular pattern of movement.

These new theories may give more insight into the interaction between a walking human and a vibrating structure and help to explain phenomena such as the "lock-in" phenomenon, when the pacing frequency is close to the natural frequency of the structure.

The third theory presented by Vaughan (2003), which is of significance to this research, concerns the maturation of gait in children. It is hypothesised that when a young child is taking his or her first steps, his or her biomechanical strategy is to minimise the risk of falling. Vaughan (2003) labels this theory a "risk aversion hypothesis". It is suggested that the initial aim to minimise the risk of falling could also be a significant factor in the altering of human gait when subject to external forces e.g. a vibrating structure. Children present a wider gait than mature adults – it may be thus suggested that adults will widen their step when experiencing lateral instability, which can then increase the medio-lateral forces they exert.

An important theory regarding control and effect is then presented by Vaughan (2003), where artificial neural networks (ANN) are applied to understanding how the central nervous system operates. The irony of this theory is that ANN's were originally inspired by the workings of the central nervous system and now they are being used to gain a greater insight into the system. This idea has great relevance in that it attempts to explain how changes in the environment, such as external perturbations, may produce changes in the walking pattern, which in turn may impact on the environment.

7. Summary

Spatial and temporal gait parameters, which affect the ground reaction forces exerted by walking pedestrians have been examined through a substantial review of current literature. These values offer guidance for researchers attempting to develop accurate load models to simulate pedestrian loading. A brief introduction to theoretical human locomotion control theory has also been provided. Two of these theories imply important considerations in terms of human-structure interaction, with one suggesting that the legs will act as a "shock-absorption" system, while the other suggests that step width is increased to counter any lateral instability. These will directly influence the vertical and lateral forces respectively applied by pedestrians to moving surfaces.

References

Andriacchi, T.P. (1990), 'Dynamics of pathological motion: applied to the anterior cruciate deficient knee', *Journal of Biomechanics* **23** (Supplement), 99 -105.
Andriacchi, T. & Alexander, E. (2000), 'Studies of Human Locomotion: Past, Present and Future', *Journal of Biomechanics*, **33**, 1217 –1224.
Archbold, P. (2004), '*Novel Interactive load Models for Pedestrian Footbridges'*, PhD Thesis, University College Dublin.
Assi, A., Ghanem, I., Lavaste, F. and Skalli, W. (2009), 'Gait analysis in children and uncertainty assessment for Davis protocol and Gillette Gait Index', *Gait & Posture,* **30**(1), 22-26.
Bachmann, H. & Ammann (1987), Vibrations in Structures Induced By Man and Machines, *International Association for Bridge and Structural Engineering*, Structural Engineering Document, Zurich.
Barker, S., Craik, R., Freedman, W., Herrmann, N. and Hillstrom, H. (2006), 'Accuracy, reliability, and validity of a spatiotemporal gait analysis system', *Medical Engineering & Physics,* **28**(5), 460-467.
Bauby, C. & Kuo, A. (2000), 'Active control of lateral balance in human walking', *Journal of Biomechanics*, **33**, 1433 - 1440.
Bennett, D., Ogonda, L., Elliott, D., Humphreys, L. and Beverland, D.E. (2006), 'Comparison of gait kinematics in patients receiving minimally invasive and traditional hip replacement surgery: A prospective blinded study', *Gait & Posture,* **23**(3), 374-382.
Bilney, B., Morris, M. and Webster, K. (2003), 'Concurrent related validity of the GAITRite® walkway system for quantification of the spatial and temporal parameters of gait', *Gait & Posture,* **17**(1), 68-74.
Chiu, M. & Wang, M. (2007), 'The effect of gait speed and gender on perceived exertion, muscle activity, joint motion of lower extremity, ground reaction force and heart rate during normal walking', Gait & Posture, **25,** 385–392.
Cho, S.H., Park, J.M. and Kwon, O.Y. (2004), 'Gender differences in three dimensional gait analysis data from 98 healthy Korean adults', *Clinical Biomechanics,* **19**(2), 145-152.
Dallard, P., Fitzpatrick, T., Flint, A., Low, A. & Ridsill-Smith, R. (2001), 'The Millennium Bridge, London: problems and solutions', *The Structural Engineer*, **79**(8), 15 – 17.
Davis, R.B., DeLuca, P.A., Ounpuu, S. (2000), *The Biomedical Engineering Handbook: Second Edition* Ed. Bronzino, J.D., CRC Press LLC.
Donelen, M.J., Kram, R. and D., K.A. (2001), 'Mechanical and metabolic determinants of preferred step width in human walking', in *Proceedings of the Royal Society of London: Series B*, UK, 268, 1985-1992.
Drerup, B., Szczepaniak, A. and Wetz, H.H. (2008), 'Plantar pressure reduction in step-to gait: A biomechanical investigation and clinical feasibility study', *Clinical Biomechanics,* **23**(8), 1073-1079.
Dubost, V., Annweiler, C., Aminian, K., Najafi, B., Herrmann, F.R. and Beauchet, O. (2008), 'Stride-to-stride variability while enumerating animal names among healthy young adults: Result of stride velocity or effect of attention-demanding task?', *Gait & Posture,* **27**(1), 138-143.
Fanning, P. Archbold, P. & Pavic, A. (2005), 'A Novel Interactive Pedestrian Load Model for Flexible Footbridges', in *Proceedings from the Society for Experimental*

Mechanics 2005 Annual Conference and Exposition on Experimental and Applied Mechanics, Portland, Oregon, USA, June 7th – 9th 2005.
Gard, S. & Childress, D. (2001), 'What determines the vertical displacement of the body during normal walking?', *Journal of Prosthetics and Orthotics*, **13**(3), 64.
Grundmann, H & Schneider, M. (1990), 'Stochastic Representation of Footbridge Vibrations Taking into Account Feedback Effects', *Structural Dynamics*, Eds Kratzig et al, Rotterdam.
Henriksen, M., Lund, H., Moe-Nilssen, R., Bliddal, H. and Danneskiod-Samsøe, B. (2004), 'Test-retest reliability of trunk accelerometric gait analysis', *Gait & Posture,* **19**(3), 288-297.
Kerr, S.C. & Bishop, N.W.M. (2001), 'Human induced loading on flexible staircases', *Engineering Structures*, **23**, 37 – 45.
Keogh, J., Archbold, P., Caprani, C. & Fanning, P. (2010), 'Estimating the Characteristic Response of a Flexible Footbridge Due to Crowd Loading', Proceedings of 5th Symposium on Bridge and Infrastructure Research in Ireland, Cork, September 2010.
Menz, H.B., Lord, S. & Fitzpatrick, R. (2003), 'Acceleration patterns of the head and pelvis when walking on level and irregular surfaces', *Gait and Posture,* **18,** 35 - 46.
Menz, H.B., Latt, M.D., Tiedemann, A., Mun-San-Kwan, M. and Lord, S.R. (2004), 'Reliability of the GAITRite® walkway system for the quantification of temporo-spatial parameters of gait in young and older people', *Gait & Posture,* **20**(1), 20-25.
Morris, M.E., Bilney, B., Matyas, T.A. and Dalton, G.W. (2007), 'Short-term relationships between footstep variables in young adults'', *Gait & Posture,* **25**(2), 229-235.
Oberg, T., Karsznia, A. & Oberg, K. (1993), 'Basic gait parameters: Reference data for normal subjects, 10-79 years of age, *Journal of Rehabilitation Research and Development,* **30** (2), 210–223
Parvataneni, K., Ploeg, L., Olney, S.J. and Brouwer, B. (2009), 'Kinematic, kinetic and metabolic parameters of treadmill versus overground walking in healthy older adults', *Clinical Biomechanics,* **24**(1), 95-100.
Ricciardelli, F., Briatico, C., Ingolfsson, E. and Georgakis, C. (2007), '*Experimental validation and calibration of pedestrian loading models for footbridge',* translated by Porto.
Ryu, T., Soon-Choi, H., Choi, H. and Chung, M.K. (2006), 'A comparison of gait characteristics between Korean and Western people for establishing Korean gait reference data', *International Journal of Industrial Ergonomics,* **36**(12), 1023-1030.
Sanhaci, C. and Kasperski, M. (2005), 'Random loads induced by walking': in Proceedings of 6th International Conference on Structural Dynamics EURODYN, Paris.
Saunders, J.B., Inman, V.T., Eberhart, H.D. (1953), 'The major determinants in normal and pathological gait', *Journal of Bone and Joint Surgery* **35**-A, 543–558.
Simpson, K. & Jiang, P. (1999), 'Foot landing position during gait influences ground reaction forces', *Clinical Biomechanics,* **14**, 396 - 402.
Terrier, P., Turner, V. and Schutz, Y. (2005), 'GPS analysis of human locomotion: Further evidence for long-range correlations in stride-to-stride fluctuations of gait parameters', *Human Movement Science,* **24**(1), 97-115.
Vaughan, C. (2003), 'Theories of bipedal walking: an odyssey', *Journal of Biomechanics*, **36**, 513 – 523.
Wheeler, J.E. (1982), 'Prediction and control of pedestrian-induced vibrations in footbridges', Journal of the Structural Division, **108**(9), 2045-2065.

ESTIMATING THE CHARACTERISTIC VERTICAL RESPONSE OF A FLEXIBLE FOOTBRIDGE DUE TO CROWD LOADING

J. KEOGH[1], P. ARCHBOLD[2], C. C. CAPRANI[1] & P. FANNING[3]
[1]Dept. of Civil & Structural Engineering, Dublin Institute of Technology, Ireland
[2] Structures & Materials Research Group (STRAIT) Athlone Institute of Technology, Ireland
[3] School of Architecture Landscape & Civil Engineering, University College Dublin, Ireland

Abstract
The issue of excessive vibration of footbridges due to pedestrian loading is now well documented. Bridge vibrations produced from a crowd of pedestrians have been estimated by modifying the effect caused by a single pedestrian by an enhancement factor to take crowd synchronization into account. In this paper this approach is extended to account for the fact that all pedestrians will not have the same pacing frequencies, and the effects of distributions of pacing frequency and other parameters on the enhancement factor are investigated. It is shown that this more faithful representation of pedestrian crowd walking behaviour gives reduced vibration response compared to the fully homogenous crowd case. Based on these results, enhancement factors for predicting the response due to a crowd from the predicted accelerations of a single pedestrian are proposed. Further, the results are compared with published test results to indicate that the model is reasonable.

Keywords: Bridges, Pacing frequency, Pedestrian, Stride, Synchronization, Vertical

1. Introduction

Recent developments in the design of structures, and increasing pressure on designers to deliver more aesthetically-pleasing structures, have led to longer and lighter footbridges. Increasingly, these structures are experiencing serviceability problems due to excessive vibration. This occurs when the natural frequency of the structure is within the range of pedestrian excitation frequencies. This can lead to discomfort for pedestrians traversing the bridge. Well known examples of footbridges that experienced vibrations due to the dynamic loading of pedestrians are, the Millennium Bridge, London (Dallard et al, 2001), the Pont du Solferino, Paris (Danbon and Grillaud, 2005) and the T-Bridge, Japan (Fujino et al, 1993).

1.1 Pedestrian Induced Vertical Loading

In this work, only the vertical vibrations induced by pedestrians are examined. Kala et al (2009) carried out research to investigate the vertical component of pedestrian force on a rigid surface using three sensors placed 0.9 m apart. They also examined the force transmitted by the heel to toe strike on impact with a solid walking surface and report that an increase in pacing velocity led to an increase in step length and peak force.

Pacing frequency is one of the most important parameters and corresponds to the application of vertical forces. It is classified as the inverse of time from the initial contact of the left foot with the surface to the initial contact of the right foot immediately thereafter (Archbold, 2008). Pacing frequency is often described using a normal distribution, and numerous parameter values have been published, Table 1. From these, 'meta-parameters' for the distribution have been derived. Where a range is given, a mean and standard deviation using a confidence interval (CI) of 95% are calculated.

Table 1 – Parameters of Normal distribution of pacing frequency from the literature.

Reference	Mean (Hz)	Standard Deviation (Hz)	Coefficient of variation
Dallard et al (2001)	1.9	0.25	0.13
Matsumoto (1978)	2.0	0.173	0.087
Grundmann and Schneider (1990)	2.0	0.22	0.11
Bachmann and Ammann (1987)	2.0	0.13	0.065
Pachi and Ji (2005)	1.83	--	--
Ebrahimpour et al (1996)	1.8	--	--
Kramer (1979)	2.2	0.3	0.14
Derived Meta Parameters	1.96	0.209	0.1064

1.2 Crowd Loading

The dynamic loading from a crowd for low-frequency footbridges has not been researched extensively (Kala et al, 2009). In a crowd loading situation, vibrations produced by one pedestrian may be reduced or damped by the presence of others due to destructive interference. Conversely, constructive interference can also take place. Grundmann et al (1993) highlighted that under crowd loading, footbridges with a natural frequency close to 2 Hz are likely to experience higher levels of vibration than those induced by a single pedestrian. This is as a result of the synchronisation of the steps of some of the pedestrians in the group.

The level of synchronisation within a crowd is reported with respect to the number of pedestrians on the bridge, N. Grundmann et al (1993) use a value of $0.135N$, Fujino et al (1993) use $0.2N$, whilst Bachmann and Ammann (1987) use $\sqrt{N}$. However, none of the quoted values have been applied to structures other than those from which they were obtained. Further, the literature does not cover higher levels of synchronization. Recent tests carried out on the Sean O'Casey Bridge, Dublin, suggest that there is a threshold vibration response beyond which the vibration response levels off as the number of pedestrians increases (Fanning and Healy, 2008). This result highlights the need for further investigation into crowd loading on bridges.

2. Numerical Modelling

2.1 Problem Formulation

The work presented here is based on a moving force model, similar to those employed in current design standards. This model may be conservative, as it does not consider interaction between the pedestrian and the moving bridge surface (Archbold, 2004).

Bridge

The bridge is considered to be a simply-supported, 50 m long beam. The section properties used are: mass of 500 kg/m; width of 2 m, and; depth of 0.6 m. A flexural rigidity of $EI = 7.2\times10^9$ Nm^2 was used. Thus the fundamental natural frequency of the bridge is 2.38 Hz. This is similar to the bridge used by Archbold (2008). Damping is taken to be 0.5% for the first two modes, with Rayleigh damping assumed thereafter. It is acknowledged that this will dampen the influence of higher modes.

Pedestrians

Adult pedestrian weight was represented by a log-normal distribution with a mean of 4.28 kg and a standard deviation of 0.21 kg. This is equivalent to an average weight of 72.2 kgs (Portier et al, 2007). Although design codes prescribe a stride length of 0.90 m, the stride length is taken here to be normally distributed with a mean of 0.66 m (Barela et al, 2008), and based on a coefficient of variation of 10%, a standard deviation of 0.066 m. As reported in Table 1, the pacing frequency is considered as normally distributed with a mean of 1.96 Hz and standard deviation of 0.209 Hz.

Crowd

A crowd length of 100 m and a width of 2 m were used to establish a representative crowd on the bridge at any point in time. The phase angle of the pedestrians is uniformly random in the interval 0 to 2π. Crowd densities of 0.75 p/m^2 (where 'p' is the number of pedestrians) and 1.5 p/m^2 are used, thus giving an average number of 150 and 75 pedestrians respectively on the bridge during the simulation. Pedestrians' starting locations are based on a Poisson arrival process and are described by the exponential distribution. The mean gap is a function of density and is 0.33 m/p and 0.66 m/p for the densities 0.75 p/m^2 and 1.5 p/m^2, respectively.

Synchronization

The proportion of pedestrians taken to be synchronized; that is, walking in step, is termed the level of synchronization and therefore ranges from 0 to 1. The synchronization levels quoted by Grundmann et al (1993), Fujino et al (1993) and Bachmann and Ammann (1987) given previously, are specifically examined in this work. More specifically, seven synchronization levels of 0, 0.135, 0.2, 0.5, 0.75 and 1.0 are considered, in addition to that of Bachmann and Ammann (1987), which depends on *N*. The pedestrians deemed to be synchronized are given the same pacing frequency and phase angle. These parameters are randomly selected according to their respective distributions previously given. The synchronized pedestrians are randomly distributed throughout the crowd.

2.2 Finite Element Modelling

A finite element model of the bridge was developed in Matlab. The beam was modelled using 10 one-dimensional beam elements, with lumped mass assumed. Transient solutions are obtained using the Newmark-β method. Each pedestrian is described by a moving force which varies with time (Archbold, 2004) according to:

$$P(t) = W\left[1 + r\sin\left(2\pi f_p t\right)\right] \tag{1}$$

In which, W is the pedestrian weight, f_p is the pacing frequency, and r is the dynamic force component, given by:

$$r = 0.25 f_p - 0.1 \tag{2}$$

Each moving force is distributed to the adjacent nodes according to the beam element shape functions as described in Wu et al (2000). The forces on the bridge due to the crowd at any point in time are taken as the superposition of the individual pedestrian forces.

The finite element model was verified using a closed form solution for a single moving force (Frýba, 1999) and for two moving pulsating forces using a corresponding finite element model in ANSYS.

2.3 Vibration Response

The vibration response in this work is assessed using a 5-second root-mean-square (RMS) moving average value from the acceleration history. The maximum of this RMS from any one particular scenario is taken as the response of the bridge to that particular loading scenario.

2.4 Enhancement Factor

Following investigations into the enhancement factors used by Grundmann et al (1993), Fujino et al (1993) and Bachmann and Ammann (1987), the crowd loading enhancement factor is defined as:

$$m = \frac{R_C}{R_{SP}} \tag{3}$$

In which R_C is the response due to the crowd and R_{SP} is the single pedestrian response. In this manner, the response due to a crowd can be estimated from that of a single pedestrian. Since the response due to a single pedestrian is easier to model, the idea of the enhancement factor has the potential to be used in codes of practice.

3. Results and Discussion

3.1 Single Pedestrian Response

Critical Parameter for Single Pedestrian Excitation

The response of the structure to a single pedestrian was investigated by considering permutations of randomly distributed and deterministic parameters. When each parameter is not varied according to its distribution, it is assigned the mean value, described previously. As expected, it was found that the response is most sensitive to the pacing frequency. The response function to pacing frequency was established by a pacing frequency sweep from 1.3 to 2.8 Hz, and is given in Figure 1(a). To estimate the distribution of RMS response to the population of pedestrians, varying only the pacing frequency, 10^6 pacing frequency samples were taken, and the corresponding RMS noted. The resulting distribution of RMS is given in Figure 1(b).

From Figure 1(a), it can be seen that there is a significant increase in the response at 2.36 Hz, which is close to the natural frequency of the bridge (2.38 Hz), as may be expected. As the frequency of the beam is two standard deviations away from the mean pacing frequency, less than 5% of the pedestrians walk at this frequency. Figure 1(b) shows that there are a high number of incidences of low RMS. This is as a result of the mean pacing frequency being lower than that of the bridge.

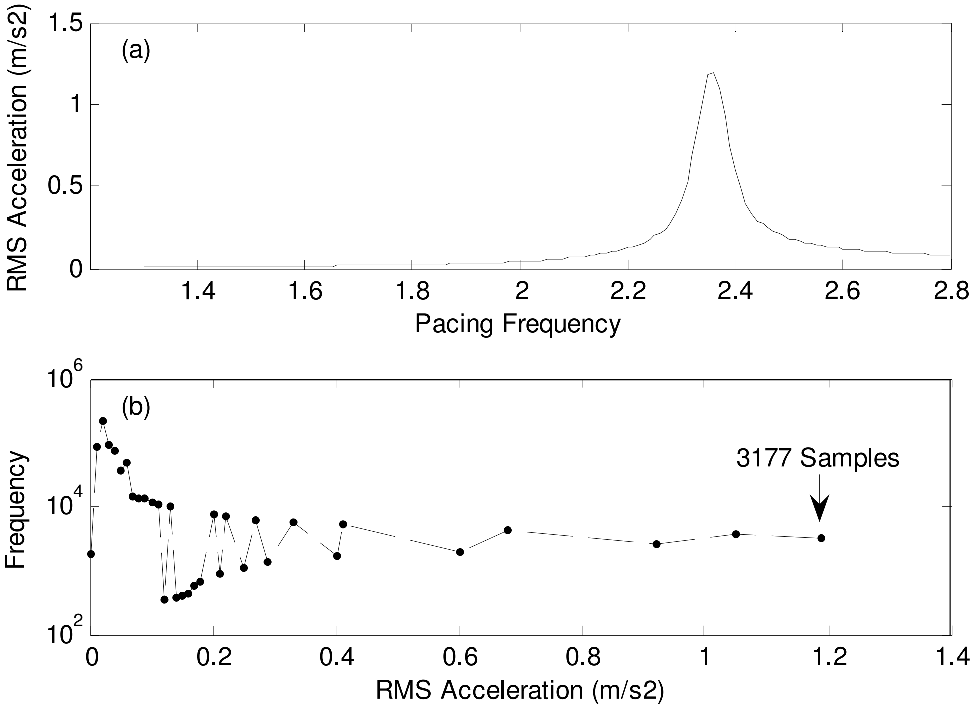

Figure 1 – Single pedestrian: (a) Response function; (b) distribution of RMS accelerations from 10^6 samples (only non-zero values shown).

Characteristic Single Pedestrian Response

Since there is not a single representative pedestrian, the response of the bridge for 1000 crossings of single pedestrians, with all parameters varied according to their representative statistical distributions, is determined. The characteristic response, R_{SP}, is defined as that below which 95% of samples are expected to fall, and is found in this case to have a value of 0.28 m/s^2. This is well below the limits prescribed in common design codes.

3.2 Crowd Loading Response

Typical Crowd Response

The response of the bridge to a typical crowd is given in Figure 2. This crowd has a density of 0.75 p/m^2 and 20% synchronization. From Figure 2, it can be seen that the peak acceleration response occurs when a cluster of synchronized pedestrians arrives onto the bridge at about 25 seconds. The midspan response then builds until it reaches a peak at about 38 seconds, when about 75 pedestrians are on the bridge. Consequently, the peak RMS is noted about 5 seconds later at 43 seconds.

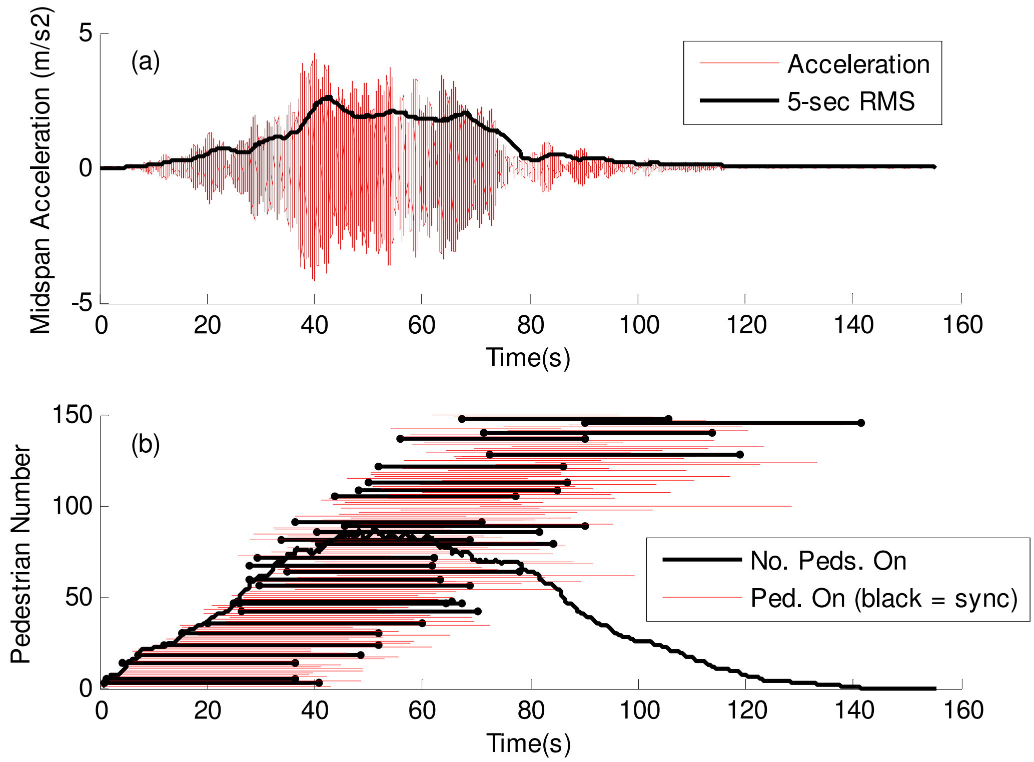

Figure 2 – Typical crowd response for 20% synchronization and 0.75 p/m^2.

Characteristic Crowd Response

For the crowd densities of 0.75 p/m^2 and 1.5 p/m^2, and for each of the 7 levels of synchronization given earlier, 1000 sample crowd responses were determined. The characteristic response (the 95-percentile) was then determined for crowd scenario. The corresponding enhancement factors are determined from Equations (3) with the value of R_{SP} found previously as 0.28 m/s^2. The results are given in Figure 3.

Figure 3 represents an improvement on existing enhancement factors which can state that if the synchronization is zero, the enhancement factor is zero. This implies that the response due to each pedestrian in a crowd is cancelled by that of another. Further, Figure 3 shows that the enhancement levels off for the lower crowd density. This may correspond to the threshold response identified in Fanning and Healy (2008).

Figure 4 compares the enhancement factors obtained in this work to those of:

- Bachmann and Ammann (1987), $m_B = \sqrt{N}$, with synchronization of $1/\sqrt{N}$;
- Grundmann et al (1993), $m_G = 0.135N$, with synchronization of 13.5%;
- Fujino et al (1993), $m_F = 0.2N$, with synchronization of 20%;

The results show a reasonable correlation with the work of these authors at the specified levels of synchronization. The enhancement factors for a density of 1.5 p/m^2 found here are higher than those reported by Bachmann and Ammann (1987) and Grundmann et al (1993), but lower than those reported by Fujino et al (1993). The present enhancement factors are higher than those of the other authors for the crowd density of 0.75 p/m^2.

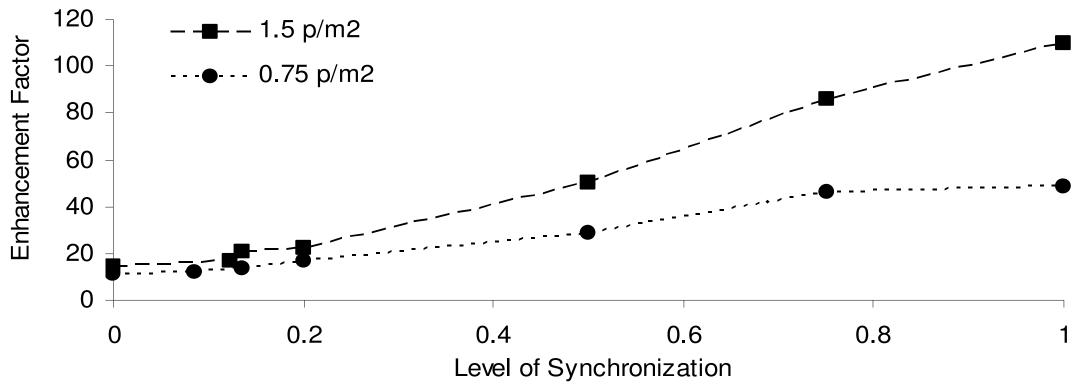

Figure 3 – Crowd loading enhancement factors for two densities.

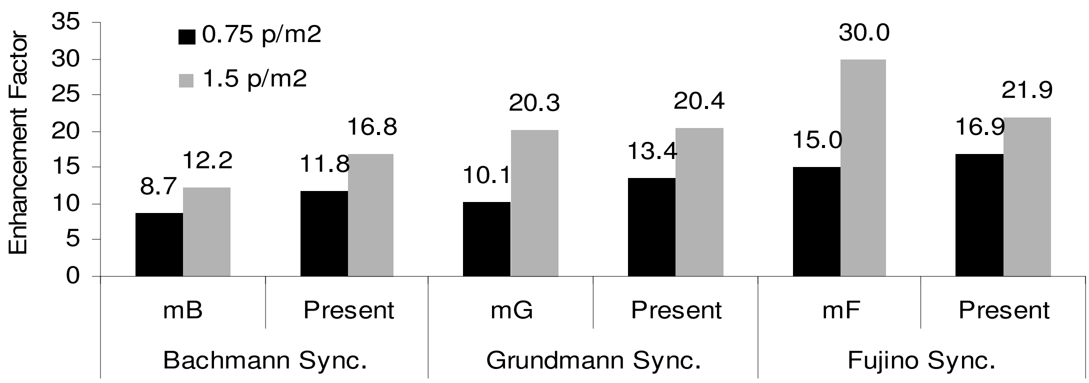

Figure 4 – Comparison of enhancement factors with those from literature

4. Summary

This research used a moving force finite element formulation to determine the vertical response of a bridge due to pedestrian excitation. Statistical distributions of pedestrian parameters were used to derive characteristic responses, for various synchronization levels and crowd density. The response to a single pedestrian was examined in detail, and a characteristic response established. The enhancement factors to be applied to the single pedestrian response, to obtain the characteristic crowd response were derived.

It was found that the enhancement factor is not zero for zero synchronization. Further, the enhancement factors found compare reasonably well to those of the literature. Additional research is required to investigate the levelling off of the crowd response for the lower crowd density as found by Fanning and Healy (2008).

5. Acknowledgment

The authors would like to acknowledge the Dublin Institute of Technology ABBEST Scholarship Programme for funding this research.

References

Archbold, P., (2004), *Novel Interactive load Models for Pedestrian Footbridges*, PhD Thesis, University College Dublin.

Archbold, P. (2008), 'Evaluation of Novel Interactive Load Models of Crowd Loading on Footbridges', *Proceedings of 4th Symposium on Bridge and Infrastructure Research in Ireland*, National University of Ireland, Galway, 35-44.

Bachmann, H. and Ammann (1987), 'Vibrations in Structures-Induced By Man and Machines', *IABSE*, Structural Engineering Document, Zurich.

Barela, A.M.F. and Duarte, M. (2008), 'Biomechanical Characteristics of Elderly individuals Walking on Land and on Water', *Journal of Electromyography and Kinesiology,* **18**(3), 446-454.

Dallard, P., Fitzpatrick, T., Flint, A., Low, A., Ridsdill Smith, R.M., Willford, M. and Roche, M. (2001), 'London Millennium Footbridge: pedestrian-induced lateral vibration', *ASCE Journal of Bridge Engineering*, **6**(6)**,** 412-417.

Danbon F. and Grillaud, G. (2005), 'Dynamic behaviour of a steel footbridge. Characterization and modelling of the dynamic loading induced by a moving crowd on the Solferino Footbridge in Paris', *Proceedings Footbridge 2005*.

Ebrahimpour, A., Hamam, A., Sack, R.L. and Patten, W.N. (1996), 'Measuring and Modeling Dynamic Loads Imposed by Moving Crowds', *ASCE Journal of Structural Engineering*, **122**(12), 1468 – 1474.

Fanning, P.J. and Healy, P. (2008), 'Sean O' Casey Bridge: Testing for Vibration Serviceability', *Proceedings of 4th Symposium on Bridge and Infrastructure Research in Ireland*, National University of Ireland, Galway, 61-69.

Frýba, L. (1999), *Vibration of Solids and Structures under Moving Loads*, 3rd Edn., Thomas Telford, London.

Fujino, Y., Pacheco, B.M., Nakamura, S. and Warnitchai, P. (1993), 'Synchronization of human walking observed during lateral vibration of a congested pedestrian bridge', *Earthquake Engineering and Structural Dynamics*, **22**(9), 741-758.

Grundmann, H. Kreuzinger, H., Schneider, M. (1993) 'Dynamic calculations of Footbridges*', Bauingenieur*, **68**(5), 215–225.

Grundmann, H and Schneider, M. (1990), 'Stochastic Representation of Footbridge Vibrations Taking into Account Feedback Effects', in W.B. Krätzig et al. (Eds.), *Proc. Eur. Conf. on Structural Dynamics*, *Eurodyn '90*, Bochum, Balkema, Rotterdam.

Kala, J., Salajka, V. and Hradil, P. (2009), 'Footbridge Response on Single Pedestrian Induced Vibration Analysis', *International Journal of Applied science, Engineering and Technology*, **5** (4), 269-280.

Kramer, H. and Kebe, H.W. (1980), 'Man-Induced Structural Vibrations', *Der Bauingenieur*, **54**(5), 195 – 199.

Matsumoto, Y., Nishioka, T., Shiojiri, H. and Matsuzaki, K. (1978), 'Dynamic design of footbridges', *IABSE Proceedings*, **2**, Paper P-17/78, Zurich.

Pachi, A. and Ji, T. (2005), 'Frequency and velocity of people walking', *The Structural Engineer*, **83**(3), 36–40.

Portier, K., Tolson, J.K., and Roberts, S.M. (2007), 'Body weight distributions for risk assessment', *Risk Analysis*, **27**(1), 11-26.

Wu, J.J., Whittaker, A.R. and Cartmell, M.P. (2000), 'Use of finite element techniques for calculating the dynamic response of structures to moving loads', *Computers and Structures*, **78**(6), 789-799.

DYNAMIC ANALYSIS AND ASSESSMENT OF HISTORIC RAILWAY BRIDGES

M. MAJKA
Structural Design Section, Iarnród Éireann, Dublin, Ireland

Abstract

The paper discusses the application of modern computational dynamic analysis to the assessment of the dynamic performance of historic railway bridges. The phenomena, such us dynamic amplification, serviceability-critical bridge and train accelerations, as well as bridge-train interaction and resonance are outlined and discussed. The background to the current serviceability requirements, based on Eurocode and UIC recommendations is provided and these requirements are discussed. This is followed by applications demonstrating the use of the dynamic analysis in the assessment of railway bridges. Examples include a historic way-beam bridge that was analysed to assess safe operational speeds, based on serviceability criteria. The second application demonstrates a preliminary feasibility study on increasing the line speed on the main Dublin-to-Cork line to 200 km/h and its effect on the existing bridges. The bridge stock is analysed and grouped into different categories, depending on their dynamic susceptibility. The methodology behind the high-level assessment and the main conclusions are presented and discussed. Means of improving the accuracy of the dynamic analysis and assessment, including field testing and model calibration, are examined.

Keywords: Bridge Dynamics, Bridge-Train Interaction, Dynamic Amplification Factor, Dynamic Assessment

1. Introduction

1.1 General

The dynamics of bridges subjected to moving loads has been attracting much attention in recent years. This can be attributed mainly to worldwide developments of high-speed railway lines, a common drive to upgrade existing railway infrastructure for higher speeds and loads, as well as to ageing of the infrastructure that requires proper planning of maintenance efforts and budgets. All of these activities require specialist knowledge, as well as accurate and efficient methods to calculate and assess the dynamic performance of structures carrying moving loads.

The design codes are often found to be very conservative when used for the assessment of existing structures and historic bridges in particular. This can be attributed to the fact that the design codes are developed in a very general manner to encompass a wide range of structures, load cases and other conditions. However, the use of the codes can be optimised with a better knowledge of local conditions, e.g. type of rolling stock using the bridge, type and condition of the railway track on the bridge, etc. It is worth emphasising that the refinement of the assessment, through a bridge and train specific dynamic analysis, can be achieved without compromising the safety levels of the structure. It only provides refined dynamic factors, acceleration levels and deformations, based on more specific bridge and train information.

This paper discusses the background to investigations carried out in recent years by Iarnród Éireann on the basis of the UIC Code 776-1R (UIC 2006) and UIC Code 776-2R (UIC 2009). These industry codes were later incorporated into the current Eurocodes. Also presented are some of the case studies on existing railway bridges and their major findings.

1.2 Historic Background

Despite the increased interest in the recent times, research on the dynamic response of bridges under moving loads has a long history behind. One of the first studies in the area was carried out as a result of a collapse of a bridge across the River Dee, just outside Chester in England, on 24 May 1847. The cast-iron girders of the end span of the bridge designed by Robert Stephenson failed suddenly under a train causing five fatalities and nine serious injuries. The accident was followed by an investigation by the Royal Commission on the use of iron in railway structures (Willis 1849). This included a series of experiments on a bridge subjected to passages of a variously loaded carriage travelling at different speeds. Willis (1849) was also one of the first researchers who appreciated the existence of the dynamic effects, as stated by Stokes (1849): "*The remarkable result was obtained that the deflection of the bridge increased with the velocity of the carriage, as least up to a certain point, and that it amounted in some cases to two or three times the central statical deflection […]*". Willis (1849) proposed a pioneering mathematical description of the problem using differential equations, where the bridge was represented as a massless beam and the load was treated as a single moving mass travelling at constant speed. The solution of these equations was provided by Stokes (1849) using the series expansion method. The problem was later approached in 1922 by Timoshenko, as summarised by Timoshenko and Young (1955) along with a discussion on the vibration of bridges, impact and effects of track irregularities and flats on wheels. The early approaches to the problem were also described by Inglis (1934). The most comprehensive analytical treatment of vibrations caused by moving loads was given in the classic monograph by Frýba (1999), first edition published in 1972.

A great part of research on the dynamics of bridge-train systems was carried out under the auspices of the International Union of Railways (UIC – *Union Internationale de Chemins de Fer*). Initially, the work was carried out by the Office for Research and Experiments (ORE) and then by its successor, the European Rail Research Institute (ERRI). ORE's studies on bridge dynamics originated as early as the 1950's with "*Question D 23 – Determination of dynamic forces in bridges*" which was concluded in the final report (ORE 1970). The project involved theoretical studies, analytical modelling and experimental testing of real-life railway bridges. In combination, the study provided the basis for determining the dynamic factors for railway bridges subjected to actual service trains, together with formulas for calculating the dynamic factor. This factor was defined as $(1+\varphi)$, where the dynamic increment over the static loading φ consists of two components. The first component φ' accounts for the effects of trains travelling at speed and the resulting vibrations that may exceed the static effects. The second component φ'' takes account of the effects resulting from track irregularities. The study also provided methods of determining the dynamic increment, based on the properties and features of the bridge, train and railway track. The findings of the ORE study were incorporated into the UIC Code 776-1R, firstly published in 1974, recent edition UIC (2006). This code became the basis of the railway loading models used in many national design codes, including British Standards, and also formed the basis of the current Eurocode 1 (NSAI 2009). Another UIC-lead project was initiated in the 1980's to provide guidance on serviceability criteria for bridges to satisfy requirements for passengers comfort. The "*Question D 160 – Permissible deflection of bridges*" was concluded in 1988 with clearly defined deflection levels for bridges (ORE 1983-88). The knowledge on the dynamics of railway bridges was further enhanced within the ERRI Project D 214 "*Rail bridges for speeds > 200 km/h*", with major findings summarised in ERRI (1999). The project investigated a number of issues, including dynamic response and interaction, resonance, methods of calculation of the dynamic response, damping in railway bridges, and effects of track irregularities. This combined work resulted in establishing uniform rules for design of bridges for high-speed railways that were codified in the UIC Code 776-2R (UIC 2009), and implemented into the Eurocodes, see NSAI (2009) and NSAI (2010) for details. These rules include guidance on whether the dynamic analysis is required or not, methods of determining dynamic properties of bridges and trains, requirements for structural capacity, as well as serviceability requirements, including deformation limits for bridges and permissible acceleration levels for bridges and trains.

2. Numerical Model for Dynamic Bridge-Train Interaction

A number of different approaches to modelling and analysis of bridges subjected to moving loads exist. These vary from simple analytical models for which a closed form solution can be obtained to elaborative finite element models with many of degrees of freedom. All the methods possess certain advantages and disadvantages, however, the finite element method has proven to be the most versatile and powerful tool for this type of application. Nevertheless, the existing commercial packages are not free from certain limitations regarding this specific type of analysis, such as the lack of dedicated vehicle models, computational effort required for the analysis, etc. In order to overcome some of those limitations and shortcomings, the author developed and extensively verified, both numerically and experimentally, a customised finite element-based bridge-train interaction model DBTI (Dynamic Bridge Train Interaction), as summarised by Majka (2006). Within the DBTI model, bridges are represented by beam-type finite elements and vehicles are modelled as multi-body dynamic systems. The solution is provided by means of the direct integration Newmark's method combined with an iterative scheme to incorporate bridge-train interaction. The DBTI model was employed to carry out all the analyses presented in the paper. Properties of the analysed bridges were established on the basis of historic drawings and site surveys, whereas dynamic properties of the rolling stock were established on the basis of manufacturers' data and experimental tests.

3. Case Studies

3.1 The Nore Viaduct, Thomastown

The dynamic assessment of the bridge was carried out as part of the overall assessment of the structure. The bridge, Figure 1, is located near Thomastown in Ireland and carries a single railway track over the River Nore. The structure, completed in 1877, consists of 2 no. masonry arches on each approach and the main 61m span being a wrought-iron bowstring arch. The original bridge was constructed with a waybeam deck, where the railway track, consisting of longitudinal timber sleepers (waybeams) continuously supporting the rails, was fixed directly to the open deck of the bridge. This type of bridge, despite being well proven over the years, suffers from durability problems with the waybeams. This results in a deterioration of the track quality requiring more stringent inspection and maintenance regimes, which have significant cost implications. Taking this into account, a programme was put in place in the early 2000's to refurbish most of the waybeam bridges within the Iarnród Éireann network. This was to be carried out by the provision of modern decks on those bridges with either ballasted tracks or slab tracks with embedded rails.

(a) (b)

Figure 1 - The Nore Viaduct in Thomastown: (a) elevation; (b) new composite deck

The bridge was modelled as a three-dimensional bow-string arch with its individual members modelled as three-dimensional beam finite elements. The dynamic analysis of the Nore Viaduct began with the modal analysis, which yielded the fundamental bending frequency f_B = 4.86Hz. The transient analysis of the bridge was then carried out for a train currently operating the line that was identified as causing particularly pronounced dynamic effects. This train is formed by two no. of 67t Iarnród Éireann locomotives type 141, followed by twenty 31t bulk cement wagons. The axles of the wagons are closely and almost evenly spaced with repetitive distances between the axles of d_1 = 3.40m and d_2 = 3.70m. The passage of a train over a bridge causes the bridge to be subjected to repetitive loading from the consecutive axles of the train. At some particular speeds, called the critical speeds, the frequency produced by the repetitive action of the train axles can match natural frequencies of the bridge and excite the resonance vibrations, which in turn can significantly increase the dynamic response of the bridge. As discussed by Frýba (1996), the largest amplification may occur when the fundamental frequency of the bridge is excited, i.e. when the speed reaches:

$$V_{cr} = d\ f_B \tag{1}$$

where d is the repetitive distance between the axles, also referred to as the characteristic length. In the case of the train under consideration here, this characteristic length takes two values, d_1 = 3.40m and d_2 = 3.70m, resulting in the critical speed in the region between 16.5m/s and 18.0m/s. This theoretical prediction corresponds very well with the results of the numerical analysis, obtained using the DBTI model and presented in Figure 2a. This figure shows the displacement-based dynamic amplification factor DAF_U, which describes the amplification of the dynamic displacements of the bridge in comparison with the static displacements. The DAF_U shown in Figure 2a reaches its very sharp peak of 1.095 at a speed of 17.50m/s (63.00km/h), indicating an amplified dynamic response at this particular speed. This maximum value of DAF_U is very close to the dynamic factor $1+\varphi$ for real trains given by Eurocode 1 (NSAI 2009), which takes the value of 1.099. The time-histories of the bridge displacements from Figure 2b show high-amplitude vibrations at the speed of 17.50m/s, whereas the traces for two other speeds of 1.00m/s (quasi-static load) and 44.45m/s are very alike. The high-amplitude vibrations increase with the number of axles travelling over the mid-span of the bridge and starts decreasing slowly due to the structural damping, when the train leaves the bridge. The described phenomenon has serious practical implications, particularly when the critical speeds are lower than the operational speed on the bridge. The railway administrations commonly limit the dynamic response of some bridges by imposing speed restrictions, however, some additional checks should also be considered to establish whether or not the imposed restrictions match with the critical speeds.

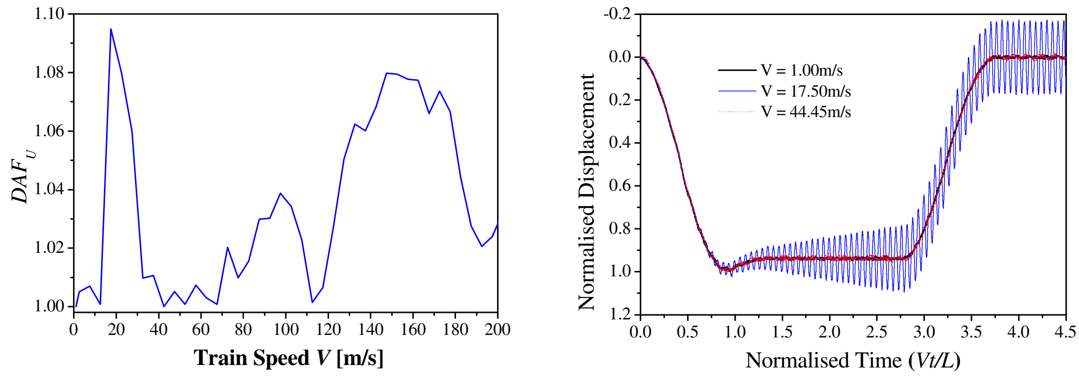

(a) (b)

Figure 2 – Results of the DBTI dynamic analysis of the Nore Viaduct: (a) DAF_U versus speed; (b) normalised displacement versus normalised time.

In order to limit the dynamic response of the Nore Viaduct, it was recommended to exclude the range of identified critical speeds by limiting the maximum speed to 30 mph (13.4 m/s). Similarly, the speed producing significant dynamic response could also be excluded by imposing the minimum speed for this particular type of train. The latter solution is of limited practical applicability, however it shows that two different approaches to the problem are possible. The bridge was strengthened and equipped with a slab track and embedded rail system in 2004, which significantly reduced its susceptibility to the dynamic loading.

3.2 Dublin – Cork Line Speed Review

A preliminary study was carried out for the Dublin-to-Cork line on the dynamic effects of increasing the service speed of trains from the current 90 mph to 100 mph (approx. 160 kph), and successively on to 125 mph (approx. 200 kph). This involved a desktop study to identify the types of railway underbridges on the line and gathering basic information on those structures, such as structural material, span, type of railway track, depth of ballast, etc. Among the stock of nearly 200 railway underbridges, over 50 % are backfilled structures, predominantly masonry arches, see Figure 3, which are generally regarded as non-sensitive to the dynamic excitation. Therefore, the study focused on the remaining 50 % of bridges and out of those, 68 bridges (34 %) were identified as potentially susceptible to the speed increase.

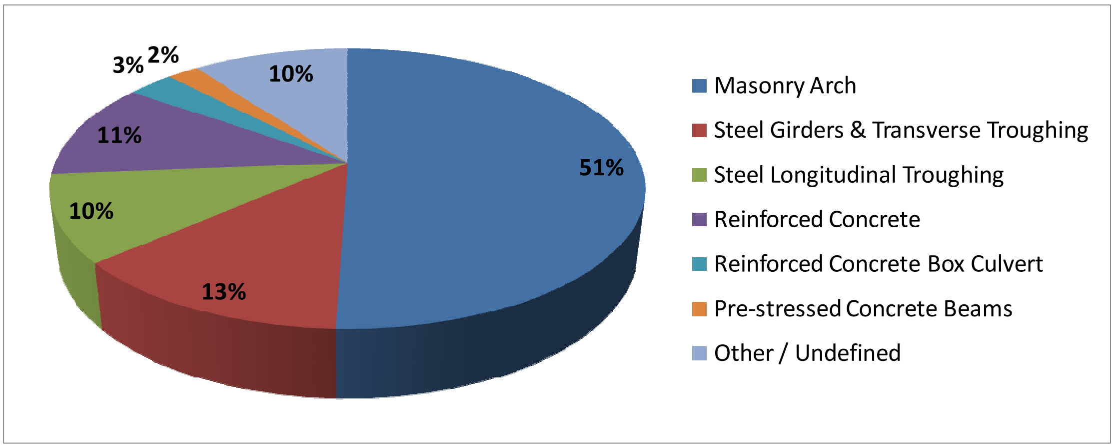

Figure 3 – Bridge stock on the Dublin to Cork railway line – breakdown showing the different bridge types among approximately 200 underbidges on the line.

The main areas of concern were as follows:

1) the increase in the dynamic factor and the resulting increase in stresses
2) the risk of resonance at the increased speed due to matching frequencies of underbridges and the Mark 4 train recently introduced into service
3) excessive accelerations and deformations of bridge decks as an effect of speed, leading to ballast instability and influencing running safety of rolling stock, as well as passengers comfort.

The first area of concern was investigated by estimating the increase in the dynamic factor DF = $1+\varphi$ due to an increase in speed of traffic, as prescribed by Eurocode 1 (NSAI 2009). The dynamic factor for real trains, as specified in Eurocode 1, is only valid for bridges with the fundamental frequency of vibrations within certain prescribed limits. The values of the DFs for the lower and upper bound frequencies were calculated for the speeds of 90, 100 and 125 mph. Next, the increase in the DFs resulting from the increase in the speed from 90 mph to 100 mph and 125 mph was calculated, see Figure 4. In the former case, the increase in DFs was only minor and did not exceed 0.050 for bridges with spans not exceeding 20 m and with the lower-bound frequency of vibrations. This reduced down to 0.023 for short span bridges (≤ 4 m) with the upper-bound frequency. In the latter case, the maximum increase did not exceed 0.190 for the lower-bound frequencies and reduced down to 0.086 for the upper-bound frequencies. The corresponding increase in stresses at the speeds of 100 mph and 125 mph, was found not to exceed 3.8 % and 14.1 %, respectively. In both cases bridges with a span of 20m and fundamental frequency close to the lower bound were found the most susceptible to the increase in the speed of traffic.

This quick and efficient method of estimating the increase in dynamic effects caused by the increase in the speed of railway traffic was facilitated formerly by UIC (2006) and currently by NSAI (2009). It is the author's experience, that the dynamic factors for existing and historic railway bridges can be reduced by carrying out a train and bridge specific dynamic analysis adhering to the Eurocode principles. Even further reductions can be achieved by the experimental calibration of the numerical models, in particular the damping ratios, which significantly affect the levels of vibrations.

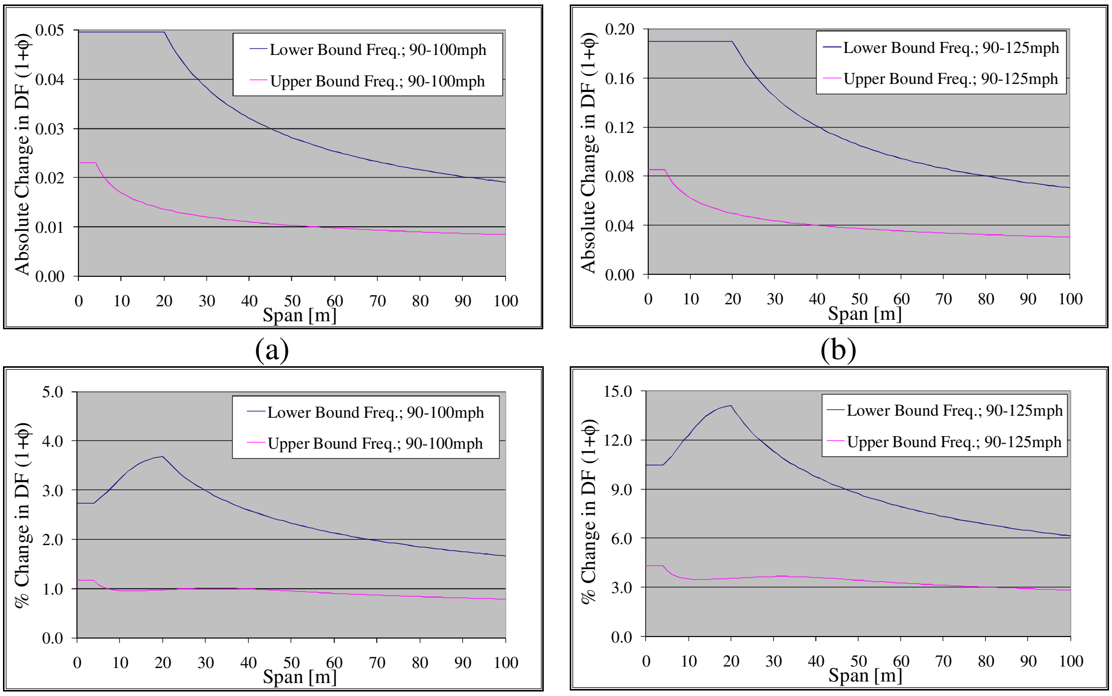

(c) (d)

Figure 4 - Changes in the Dynamic Factor 1 + φ calculated in accordance with Eurocode 1 for the lower and upper bounds of the bridge fundamental frequency caused by increasing speed of trains from: (a) 90mph to 100mph – absolute change; (b) 90mph to 125mph – absolute change; (c) 90mph to 100mph – % change; (d) 90mph to 125mph – % change.

The second area of concern, i.e. the risk of resonance, was also investigated at a high level. The resonance in railway bridges can arise from the repetitive action of the axles of moving trains. The resonance reaches its maximum when the time intervals between two successive loads are equal to the fundamental period of natural vibrations of the bridge, as shown in Equation (1). Ranges of bridges potentially susceptible to resonance were identified based on the prescribed characteristic lengths d_1, d_2, d_3 of the Mark 4 train and typical values of the fundamental frequency f_B for different types of bridges, see Frýba (1996) for details. In order to provide a safety margin for the assessment, the length of susceptible spans was extended by ±20 % beyond the identified span lengths. In total, 40 no. steel plate girder / troughing bridges with ballasted track, and 8 no. concrete bridges with ballasted track were found to be resonance-prone. It was recommended to carry out the full bridge-train interaction analysis for those bridges to establish the levels of vibrations and to assess their dynamic performance. This would also address the third area of concern, i.e. the risk of excessive accelerations and deformations of bridge decks. The level of bridge deck acceleration can be verified in a simplified manner against the limiting value of the speed-to-fundamental frequency ratio, as prescribed in Eurocode 1. However, for any bridge with the speed-to-fundamental frequency ratio beyond the limits of Eurocode 1, dynamic analysis is required.

4. Conclusions

The paper presented the application of modern computational dynamic analysis to the assessment of the dynamic performance and susceptibility of historic railway bridges. A brief background to the current serviceability requirements, based on Eurocode and UIC recommendations was provided and these requirements were discussed. The application of the dynamic analysis to the assessment of a historic railway bridge was described. A methodology behind a high level assessment of the dynamic effects of increasing the service speed of trains was presented. It is a conclusion of this paper, that the current Eurocodes provide a framework for the use of the advanced dynamic analysis by facilitating the bridge and train-specific dynamic analysis, and allowing for the refinements to the dynamic response to be achieved. It is worth emphasising that this approach has been used by Iarnród Éireann for quite some time prior to the introduction of the Eurocodes, on the basis of the industry UIC codes.

Acknowledgements

The author wishes to acknowledge assistance provided by Iarnród Éireann and NUI Galway in the preparation of this paper. The views expressed in the paper are those of the author and not necessarily those of Iarnród Éireann.

Reference

ERRI (1999), *D214/RP9, Rail bridges for speeds > 200km/h, Part B - Proposed UIC leaflet*, European Rail Research Institute, Utrecht, The Netherlands.

Frýba, L. (1996), *Dynamics of Railway Bridges*, T. Telford, London, UK.

Frýba, L. (1999), *Vibration of Solids and Structures under Moving Loads*, Thomas Telford, London, UK.

Inglis, C. E. (1934), *A Mathematical Treatise on Vibrations in Railway Bridges*, Cambridge University Press, Cambridge, UK.

Majka, M. (2006), *Dynamic response of railway bridges: Analysis of bridge-train interaction using numerical and experimental techniques*, PhD Thesis, National University of Ireland, Galway, Ireland.

NSAI (2010), *EN 1990 - Eurocode 0: Basis of structural design*, European Committee for Standardization, Brussels, Belgium.

NSAI (2009), *EN 1991:2 - Eurocode 1: Actions on structures - Part 2: Traffic loads on bridges*, European Committee for Standardization, Brussels, Belgium.

ORE (1970), *D23/RP17, Determination of dynamic forces in bridges - General survey of the work of the D23 Committee and preparation of general formulae for calculating the dynamic effects*, Office for Research and Experiments, Utrecht, The Netherlands.

ORE (1983-88), *D160/RP1-6, Permissible deflection of bridges*, Office for Research and Experiments, Utrecht, The Netherlands.

Stokes, G. G. (1849), 'Discussion of a differential equation relating to the breaking of railway bridges', *Trans. Cambridge Philosophical Society*, **8** (5), 707-735.

Timoshenko, S. P. and D. H. Young (1955), *Vibration Problems in Engineering*, Van Nostrand Reinhold Company, New York, N.Y., U.S.A.

UIC (2006), *Code 776-1R Loads to be considered in the design of railway bridges*, Union Internationale des Chemins de Fer, Paris, France.

UIC (2009), *Code 776-2 Design requirements for rail bridges based on interaction phenomena between train, track, bridge*, Union Internationale des Chemins de Fer, Paris, France.

Willis, R. (1849), 'Appendix to the report of the commissioners appointed to inquire into the application of iron to railway structures', *H.M. Stationary Office, London, England.*

LOAD-DEFLECTION PERFORMANCE OF GFRP REINFORCED THIN FRC PANELS

P.J. CULLIVAN & P. ARCHBOLD
STRAIT, Structures & Materials Research Group, Athlone Institute of Technology, Ireland

Abstract
Fibre Reinforced Concrete (FRC) reinforced with Glass Fibre Reinforced Polymer (GFRP) rods has potential for employment in applications such as permanent formwork for bridge deck construction. FRP offers advantages over traditional steel reinforcement in this regard due primarily to its resistance to corrosion, while the presence of fibres in the concrete helps to increase the toughness and handling ability of these formwork panels. Moreover, these panels are necessarily thin sections, with an overall depth in the range of 50 mm and as such they present real challenges to designers. Furthermore, there is currently a lack of definitive design guidance on the use of FRP reinforcement in concrete members. In light of this, one of the primary areas of concern in relation to the structural behaviour of FRP reinforced concrete members is the serviceability performance. Many of the methods proposed in the literature for estimating the serviceability performance tend to underestimate the short-term deflection of the sections under applied loading. This paper describes an experimental programme to measure the load-deflection response of GFRP reinforced FRC permanent formwork panels. The results from this test programme are presented and analysed and compared with existing numerical models reported in the literature for estimating this response. Modifications to the application of existing models to account for the behaviour of these innovative elements are also proposed.

Keywords: Deflection, Fibre Reinforced Concrete, Flexural Load Testing, GFRP

1. Introduction

Recent developments in bridge construction have led to more onerous demands on support structures such as permanent formwork. In an attempt to meet these demands, some practitioners have employed Fibre Reinforced Concrete (FRC) in these permanent formwork panels in order to provide extra toughness, but this yields a complex anisotropic structural composite. Limitations to relatively short spans, due to modest flexural capacity, may be overcome by reinforcing the FRC panels (Kim *et al*, 2009).

The use of traditional steel reinforcement, particularly in corrosive or moisture-prone environments, may present durability problems, leading to expensive remedial works to maintain the integrity of the overall structure. Aref *et al* (2005) quote the US Department of Transportation (1999), who estimate the average annual cost to maintain bridge conditions in the United States for the 20-year period of 1998–2017 to be US$5.8billion and the average annual cost to improve bridge conditions to be almost double this amount at US$10.6billion. This issue of bridge maintenance and repair is one which is becoming more prominent in Ireland in recent times in the wake of a surge in the overall bridge stock as part of recent heavy investment in transport infrastructure. A key step in reducing future maintenance costs is the reduction of potential durability issued with current construction materials.

Fibre reinforced polymers (FRP's) are rapidly gaining recognition as reinforcing materials in concrete structures, to rival steel reinforcement. Typical constituent fibres used are glass (GFRP), carbon (CFRP) and, more recently basalt (BFRP). They offer a number of advantages over steel reinforcement, due primarily to their non-metallic nature and are thus considered as ideal reinforcement materials for the FRC permanent formwork panels. However, because of a lack of definitive design codes for this innovative composite material, design of elements such as formwork panels has been largely empirical to date.

FRP tends to fracture suddenly and as such FRP-reinforced sections are designed to be over-reinforced in tension to ensure that failure occurs through the gradual crushing of the compressive concrete (Nanni, 2003; ACI, 2006). Moreover, FRP possesses a higher tensile strength than steel, but is also a highly elastic material, which gives rise to significantly larger deflections than in steel reinforced sections.

This paper examines the short-term load-deflection performance of GFRP reinforced FRC permanent formwork panels and compares the actual behaviour to that predicted by current models from literature.

2. Load-Deflection Prediction Models

Several methods have been proposed in the literature to account for the performance of a section before and after cracking has occurred.

2.1 Integration Method (Razaqpur *et al*, 2000)

Razaqpur *et al* (2000) proposed an integration method for calculating deflection. The entire length of the member was initially considered fully cracked having a constant moment of inertia (I_{cr}). Deflections where then corrected by applying a rationally derived correction term. This correction factor accounts for the uncracked regions of the member. And the authors argued that the effect of tension stiffening of FRP reinforced concrete members was not significant. This method is unique to each load case and support condition, possibly limiting its widespread application.

2.2 Modified Effective Second Moment of Area.

Benmokrane *et al* (1996), Toutanji and Saafi (2000) and ACI 440 (2006) recognised that Branson's (1977) equation (adopted by ACI Committee 318 (2008)) exhibited a much stiffer response for FRP reinforced concrete members. Hence a number of researchers proposed modifications to the effective second moment of area (I_e).

Benmokrane *et al* (1996) noticed that while Branson's initial equation under estimated deflection for GFRP reinforced concrete members, the response was parallel to the experimental response. To account for this, reduction factors were applied to the theoretical value of I_e. An attempt was made to attribute these reduction factors to the nature of FRP reinforcement. The resulting theoretical load-deflection response compared reasonably well to the limited experimental data.

Toutanji and Saafi (2000) incorporated the effects of FRP's different mechanical properties in the exponent m in order to keep the form of Branson's equation. Using linear regression an expression was derived for m from experimental data for six beams. This expression is based on the reinforcement ratio and the ratio of the modulus of elasticity of FRP to steel reinforcement. Good agreement was found between experimental data and the proposed method.

ACI Committee 440 design guide (2006) uses an empirically derived I_e proposed by Branson (1977) and modified by Gao *et al* (1998) to account for FRP's different modulus of elasticity and bond properties to determine the flexural rigidity and hence the instantaneous deflection under service loads for concrete members reinforced with FRP. This effective second moment of area represents a gradual transition between the un-cracked transformed second moment of area (I_u) to a fully cracked second moment of area (I_{cr}) as the service load increases beyond the moment at which first cracks appear (M_{cr}). This equation however is based on a statistical fit of experimental data and does not build upon the underlying principles of tension stiffening and has been debated by various researchers.

2.3 Tension Stiffening Effects (Bischoff, 2007)

Bischoff (2007) proposed a rational approach compared to the empirical approach adopted in ACI 440 (2006) to account for the tension stiffening effect of concrete between the cracks. Barris *et al* (2009) reported good fit between this method and experimental results from testing of 12 GFRP reinforced concrete beams.

A feature of each of the above models is that they relate to normal concrete and do not make provision for the effect of fibres on the mechanical properties of FRC.

3. Experimental Programme

This paper presents the results and discussion of an experimental programme to determine the short-term load deflection response of FRC permanent formwork panels with and without Glass FRP (GFRP) reinforcing bars. Details of the material properties and experimental setup are outlined in 3.1 and 3.2 below.

3.1 Material Properties

The FRC mix was designed to have a compressive strength of 60 N/mm^2 and contain 5kg/m^3 polypropylene fibres. According to manufacturer's data, the GFRP bars have a relatively low modulus of elasticity (40.8 GPa) and a high tensile strength of 825 MPa.

3.2 Experimental Setup

12 no. test samples, nominally 750 mm wide by 750 mm long and ribbed in profile (Figure 1(b)) were used in order to measure the short-term load-deflection response of these permanent formwork panels. 6 no. panels were nominally unreinforced, while the other 6 were reinforced with one 6 mm diameter GFRP rod placed in each rib, providing a total area of reinforcement of 169 mm^2. The simply supported panels were each subjected to a four point flexural load as shown in Figure 1 (a). A constant moment zone is evident between the two applied point loads. The applied load (P) measured using a load cell, was applied simultaneously using a hydraulic jack to two point loads. The load was applied to achieve a rate of deflection of 0.5 mm/minute up to a load when first cracks form, increasing to 2 mm/minute after cracking. The panel was instrumented with linear variable differential transducers (LVDT's) placed at mid-span to measure vertical deflection and at the supports to measure horizontal displacement. All data was recorded using automated data acquisition.

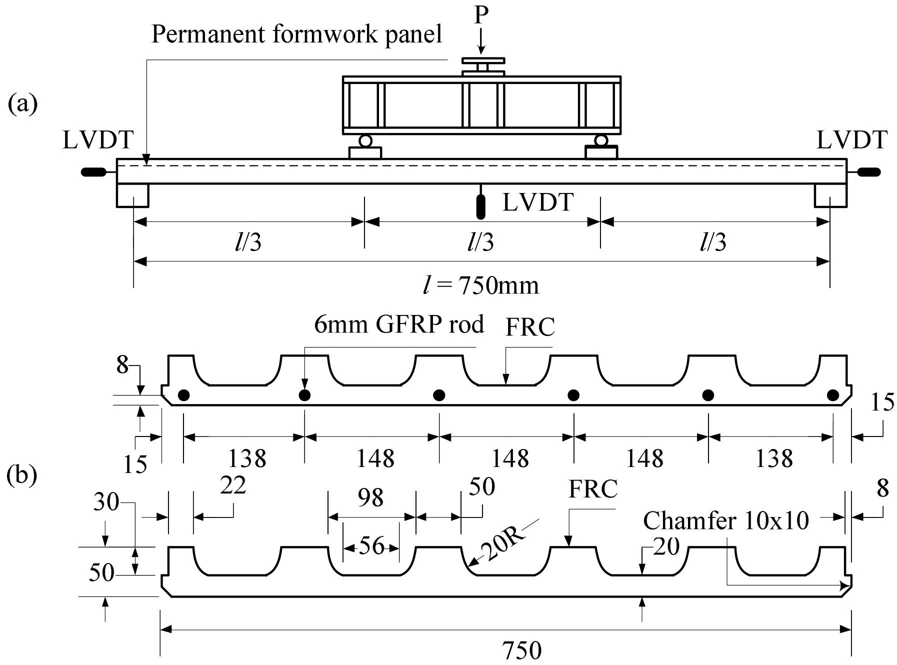

Figure 1 – (a) Experimental setup (b) Section through permanent formwork panels

4. Results and Discussion

All of the panels tested yielded similar results in terms of their response to applied load. For clarity, the results of three reinforced and three unreinforced samples are presented herein.

4.1 GFRP Reinforced Panels

Figure 2 below illustrates the measured and predicted load-deflection response, while Table 1 contains a summary of some of the pertinent data recorded for the GFRP reinforced panels. Cracking initiated at an average load of 7.9 kN (P_{cr}). This equates to a mid-span cracking moment (M_{cr}) of approximately 1 kNm. After cracking the load increases linearly (2 mm/minute) with a reduced flexural rigidity up to an average failure load of 27.6 kN. A reinforcement ratio of 0.99% and a balanced ratio of 0.55% were computed. The sections are therefore over reinforced facilitating the preferred failure mode of crushing of the concrete. This failure mode was observed for all three sections.

The deflection of each panel typically represents two discrete stages of the structural response. In the un-cracked state the section is considered homogenous and generally behaves linear elastically from zero load up to the load at which first cracking occurs. During the cracked phase as cracking increases the member stiffness progressively decreases from that of the uncracked state approaching that of a fully cracked section. This reduced member stiffness causes the rate of deflection per unit load to increase.

GFRP3 (Figure 2) was loaded at a steady rate up to a deflection of 14.6 mm and a load of approximately 19.8 kN (71% of failure load), and then unloaded at the same rate to a load of 0 kN. A deflection of 2.79 mm was recorded at zero load; however a further incremental recovery was experienced, with a final permanent deflection of

2.35 mm. The unloading and reloading did not have a significant effect on the ultimate load capacity of the panel.

Table 1 – Summary of Data Recorded for GFRP Reinforced FRC Permanent Formwork Panels

Specimen	ρ_f (%)	ρ_{fb} (%)	P_{cr} (kN)	P_u (kN)	Observed Failure Mode
GFRP1	0.99	0.562	8.190	27.910	Crushing of concrete
GFRP2	0.99	0.519	7.200	27.080	Crushing of concrete
GFRP3	0.99	0.562	8.300	27.900	Crushing of concrete

The values for I_u and I_{cr}, the uncracked and cracked second moments of area respectively, together with theoretical and experimental flexural rigidity are given in Table 2 below. Values for the I_u and I_{cr} were determined to be 4.2 x 10^6 mm^4 and 0.25 x 10^6 mm^4 respectively. The theoretical concrete modulus, E_c was calculated using $E_c = 4{,}700\sqrt{f'_c}$ (= 38 GPa) (CSA, 2004; ACI, 2006). This expression was empirically derived for normal concrete and may have limited applicability for FRC.

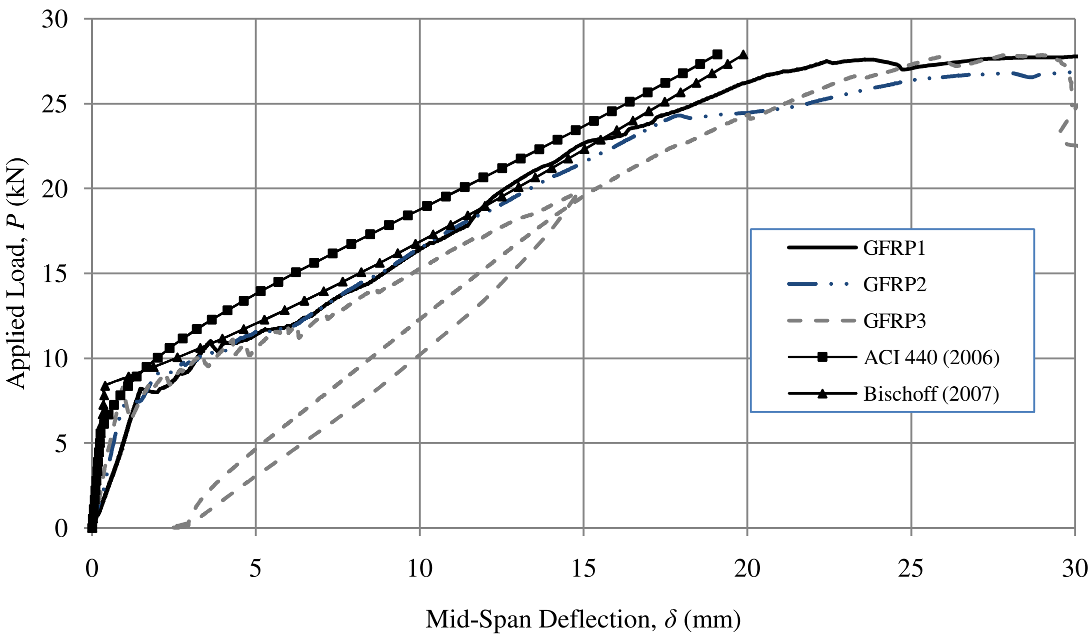

Figure 2 – Typical Measured and Predicted Load-Deflection Response of GFRP Reinforced Panels

The theoretical uncracked flexural rigidity (E_cI_u) shown in Figure 3, was estimated to be 159 x 10^9 Nmm^2 which is 2.9 times greater than the average measured flexural rigidity. This leads to a significant underestimation of the deflection for a given load. This underestimation is particularly relevant where serviceability considerations are likely to govern the design.

As discussed later, maximum allowable deflections in these panels would be of the order of 3.6 mm. From examination of Figure 2, both of the theoretical models grossly overestimate the allowable applied load in this instance.

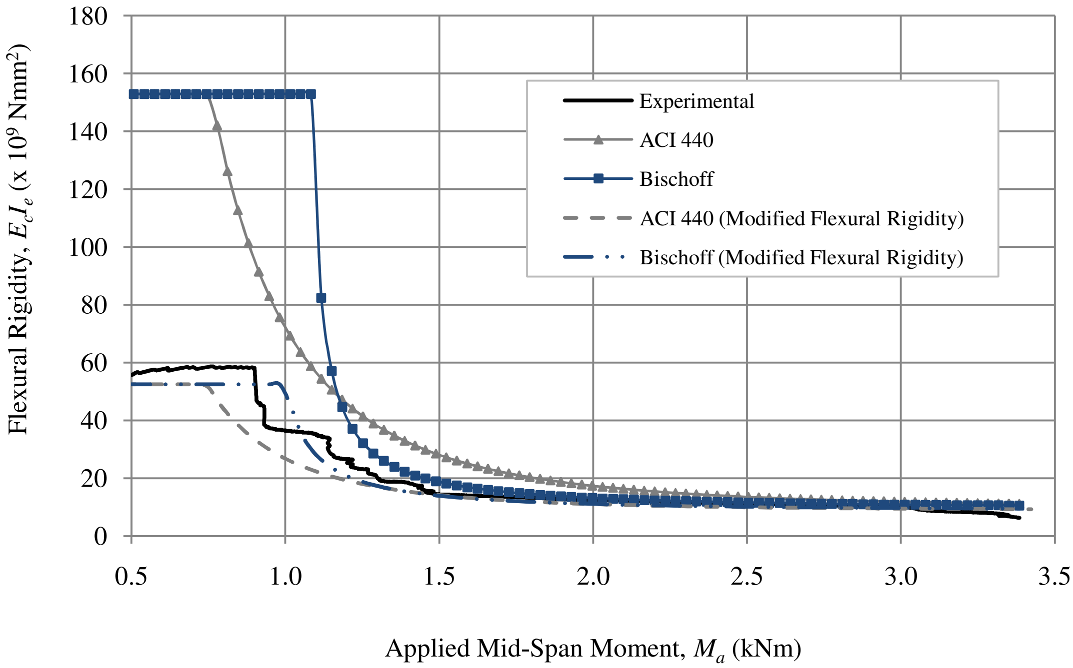

Figure 3 – Flexural Rigidity vs. the Applied Mid-Span Moment for GFRP2

Table 2 – Section and Rigidity Properties of Panels

Specimen	Full Section			Contributing Section		
	I_u (x 10^6 mm^4)	I_{cr} (x 10^6 mm^4)	$E_{c,\,th} I_u$ (x 10^9 Nmm^2)	$I_{u,\,Mod}$ (x 10^6 mm^4)	$I_{cr,\,Mod}$ (x 10^6 mm^4)	$E_{c,\,exp} I_u$ (x 10^9 Nmm^2)
GFRP1	4.172	0.251	159	2.621	0.538	40.154
GFRP2	4.172	0.251	159	2.583	0.400	57.023
GFRP3	4.172	0.251	159	2.586	0.413	67.541

Modified Flexural Rigidity

It is now assumed by the authors that the contribution of concrete between the ribs in the tensile zone is negligible. This concrete exists in tension and does not contribute to the compressive strength of the section. The average modified I_u and I_{cr} was therefore recalculated to be 2.6 x 10^6 mm^4 and 0.45 x 10^6 mm^4 respectively, based on the area deemed to be contributing to the section's moment resistance.

An inverse analysis was then conducted to derive an expression for E_c from the experimental data, which yielded a revised value of E_c = 21.3 GPa ($E_c = 2{,}510\sqrt{f'_c}$). This suggests that the design value $E_c = 4{,}700\sqrt{f'_c}$ grossly overestimates E_c for the FRC specimens examined. However, Barris *et al* (2009) carried out E_c testing to ASTM C 469/87 and found the value for E_c for six high strength normal concrete specimens to be significantly lower than code provisions ($E_c = 3{,}500\sqrt{f'_c}$). Kim *et al* (2009) reported large variability in the E_c for FRC (2% Fibres) and reported average modulus of elasticity of 32 GPa for concrete with a compressive strength of 65 N/mm^2. Further, E_c is suggested in several design guidelines to be in the range of 15–20 GPa for FRC (PCI, 2001; Wrigley, 2001; GRCA, 2003), so the revised estimate appears to be reasonable. Based on this a modified flexural rigidity was computed which compared more favourably with the measured value (Figure 3).

Moreover, the modified theoretical models, using the revised flexural rigidity display a much improved fit with the measured data (Figure 4). The difference between both theoretical methods is not significant; however Bischoff's method models the tension stiffening effect post cracking more accurately.

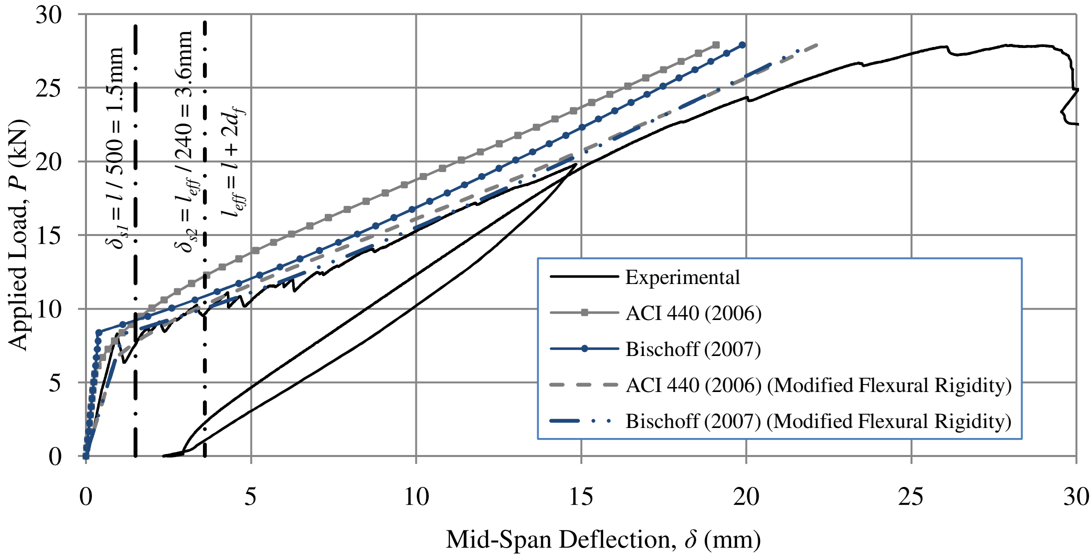

Figure 4 – Load-Deflection Response for GFRP3

4.2 Unreinforced FRC Panels

For these panels, once first cracking occurs little ductility is recorded and a brittle failure occurs at an average load of 8.3 kN (≈ +/-4.6%). The failure load for FRC panels approximately coincides with the cracking load for the GFRP reinforced panels. An average experimental Young's modulus of 20.2 GPa was observed for the FRC panels. This compares well with the GFRP reinforced sections (21.3 GPa).

4.3 Serviceability Limits on Deflection

While reinforcing with GFRP rods increases the ultimate load capacity of these panels to 27.6 kN (M = 3.5 kNm), serviceability requirements are likely to control the allowable applied load. For steel reinforced sections with brittle finishes it is normal to limit the deflection to span/500 (1.5 mm). Bank *et al*'s (2009) model specification for permanent formwork panels however allows a less stringent limit, limiting the service deflection to the effective span/240 (3.6 mm). Thus to satisfy serviceability the applied load should not exceed an applied load of approximately 10 kN, which is roughly 36% of the ultimate load.

Figure 5(a) shows the load-deflection responses in the region of the serviceability limits. The measured and predicted loads corresponding to these deflection limits are also presented in Figure 5(b).

ACI 440 predicted applied loads of 9.2 kN and 12.3 kN at deflection limits of 1.5 mm and 3.6 mm respectively, while the panels tested only achieved 84% and 94% of these limits respectively, recording the stated deflections under average loads of 7.8 kN and 10.3 kN. Meanwhile Bischoff's method predicted an applied load of 9.2 kN and 10.9 kN for the same limits, again overestimating the predicted load by up to 15%. While Bischoff's method predicts the applied load at a deflection limit of 3.6 mm reasonably well, ACI 440's method significantly overestimates deflection at this limit. The modified ACI 440 (7.7 kN and 10.3 kN) and Bischoff's method (8.5 kN and 10 kN) show much improved results for both deflection limits.

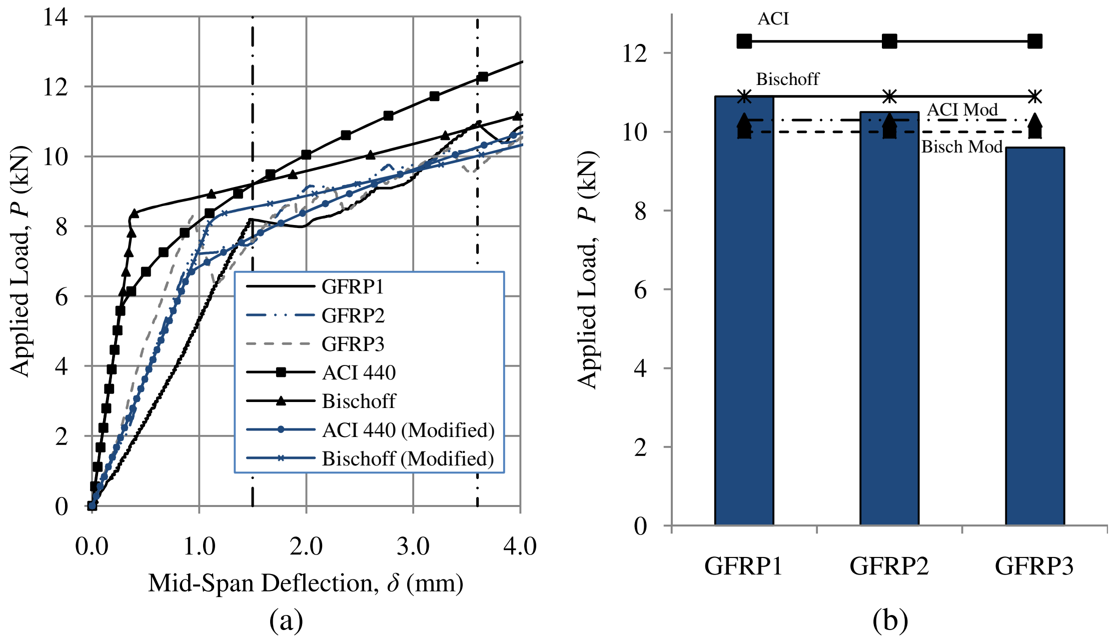

Figure 5 – (a) Load – deflection response with serviceability limits (b) Measured and Predicted loads (kN) at a serviceability limit of l_{eff} / 240 = 3.6 mm

5. Conclusions

The results of load-deflection tests on FRC permanent formwork panels reinforced with GFRP rods have been presented. Both the unreinforced and reinforced FRC panels displayed a similar cracking load.

GFRP reinforcement significantly increases the ultimate load capacity to 27.6 kN for the permanent formwork panels. However considering serviceability, the applied load is likely to be limited to approximately 10 kN, 36% of the failure load. A steel reinforced design would typically yield a serviceability requirement in the range of 60 to 70 % of the ultimate load.

Existing models in the literature underestimated the actual response of these ribbed panels, particularly in the area close to recommended serviceability deflection limits. A modified second moment of area was calculated and combined with a revised value for the FRC modulus to reproduce the measured flexural rigidity accurately.

Both ACI 440 (2006) and Bischoff's (2007) models significantly underestimate deflection prior to cracking and at loads approaching failure. Both methods do show improved results when using the modified flexural rigidity with Bischoff's model the preferred method as it more accurately models the tension stiffening effect of the panels tested.

Further testing is currently underway to determine empirical values for the material properties used in these panels, in particular, the mechanical properties of the FRP rods and the Young's modulus of the fibre reinforced, self compacting concrete. Determination of these parameters is essential in verifying the load-deflection models proposed herein.

6. Acknowledgements

This project is supported by the Technological Research Sector - Strand I Post-graduate R&D Skills Programme, funded by the Irish Government and part-financed by the European Union under the National Development Plan, 2007-2013. The authors would like to thank Peter Deegan of Banagher Concrete Ltd and Alan O'Connor and the technical staff of the laboratories in Trinity College Dublin for their assistance with this project.

References

ACI Committee 440 (2006) Guide for the Design and Construction of Concrete Reinforced with FRP bars (ACI 440.1R-06), American Concrete Institute (ACI) Committee 440.

ACI Committee 318 (2008) Building Code Requirements for Structural Concrete (ACI 318M-08) and Commentary, American Concrete Institute (ACI) Committee 318.

Aref, A.J., Kitane, Y. & Lee, G.C. (2005) 'Analysis of hybrid FRP-concrete multi-cell bridge superstructure', *Journal of Composite Structures,* **69**, 346-359.

Bank, L.C., Malla, A.P., Oliva, M.G., Russell, J.S., Bentur, A. & Shapira, A. (2009) 'A model specification for fiber reinforced non-participating permanent formwork panels for concrete bridge deck construction', *Journal of Construction and Building Materials,* **23**, 2664-2677.

Barris, C., Torres, L., Turon, A., Baena, M. & Catalan, A. (2009) 'An experimental study of the flexural behaviour of GFRP RC beams and comparison with prediction models', *Journal of Composite Structures,* **91**, 286-295.

Benmokrane, B., Chaallal, O. & Masmoudi, R. (1996) 'Flexural response of concrete beams reinforced with FRP reinforcing bars', *ACI Structural Journal,* **93**, 46-55.

Bischoff, P.H. (2007) 'Rational model for calculating deflection of reinforced concrete beams and slabs', *Canadian Journal of Civil Engineering,* **34**, 992-1002.

Branson, D.E. (1977) *Deformation of Concrete Structures,* McGraw-Hill

CSA (2004) *Design of concrete structures. Standard A23.3-04*, Canadian Standards Association (CSA).

Gao, D., Benmokrane, B. & Masmoudi, R. (1998) 'A calculating method of flexural properties of FRP-reinforced concrete beam: Part 1: Crack width and Deflection'. Technical Report, Department of Civil Engineering, University of Sherbrooke, Canada.

GRCA (2003) *Glass fibre reinforced cement formwork : specifier and designers handbook,* Glassfibre Reinforced Cement Association

Kim, G.B., Pilakoutas, K. & Waldron, P. (2009) 'Finite element analysis of thin GFRC panels reinforced with FRP', *Journal of Construction and Building Materials*, **23**, 930-942.

Nanni, A. (2003) 'North American design guidelines for concrete reinforcement and strengthening using FRP: principles, applications and unresolved issues', Journal of *Construction and Building Materials,* **17**, pp. 439-446.

PCI (2001) *Recommended practice glass fiber reinforced concrete panels*, Precast/Prestressed Concrete Institute (PCI) Committee on Glass Fiber Reinforced Concrete Panels

Razaqpur, A.G., Svecova, D. & Cheung, M.S. (2000) 'Rational Method for Calculating Deflection of Fiber-Reinforced Polymer Reinforced Beams', *ACI Structural Journal,* **97**, 175-184.
Toutanji, H. & Saafi, M. (2000) 'Flexural Behavior of concrete beams reinforced with glass fiber reinforced polymer (FRP) bars', *ASCE Strucutral Journal,* **97**, 712-719.
US Department of Transportation, F.H.A., and Federal Transit Administration (1999) *Status of the Nation's highways, bridges and transit: conditions and performance*, Report to Congress, May 2000.
Wrigley, R.G. (2001) *Permanent Formwork in Construction (C558)*, Construction Industry Research And Information Association (CIRIA).

FINITE ELEMENT MODELLING OF TRANSVERSE LOAD SHARING BETWEEN HOLLOW CORE FLOOR SLABS.

D.F. HODGE, B.D. O'ROURKE & J.J. MURPHY
Department of Civil, Structural & Environmental Engineering, Cork Institute of Technology, Bishopstown, Cork, Ireland

Abstract
This paper describes the use of the structural analysis software LUSAS (Version 14.3-9) to create 3D finite element (FE) models, to simulate the transverse load sharing over a number of precast hollow core floor slabs. Adjacent slabs are grouted together with mortar or concrete, thus providing a joint through which loads can be distributed transversely. Load sharing factors are used to convert concentrated loads to uniformly distributed loads for design calculations. Graphs of load distribution factors are incorporated in the current standards and guidelines, such as BS EN 1168:2005, which have been determined based on the theory of elasticity, and the Fédération Internationale de la Précontrainte (FIP) recommendations, which have been based both on analytical calculations and test data. Comparisons of the load distribution factors for linear loading have shown that there is a variation of up to 15% in the factors obtained from a number of sources.

An extensive FE modelling study has been conducted on many slab sections under various loading conditions. Both reinforced and prestressed models were generated and a non-linear concrete material model was used to model both the precast units and the joint material. Experimental testing has been conducted on precast reinforced slabs to validate the FE models. Also independent test results obtained from a peer reviewed source have been used to establish confidence in the models. The theoretical and FE analyses, along with experimental results, have been compared and numerical and graphical results are presented. These results have been compared with the recommended values.

Keywords: Finite element modelling, Hollow core, Load sharing, LUSAS

1. Introduction

Precast concrete hollow core slabs are used extensively as structural flooring systems within modern buildings. Their use offers advantages when compared to in-situ construction, such as high quality of product, reduced construction times and better economy. The slabs may be prestressed or reinforced, generally spanning simply supported and of 1.2m nominal width. Adjacent slabs are grouted together with mortar or concrete. Structural concrete topping can be added to improve the strength and may be included in the design calculations. Load sharing assumptions can be made to convert concentrated loads to uniformly distributed loads for calculation checks. This design approach is recognised in design codes of practice. Graphs of load distribution factors are incorporated in the current standards and guidelines, such as BS EN 1168:2005, which have been determined based on the theory of elasticity, and the Fédération Internationale de la Précontrainte (FIP) recommendations (1988), which have been based both on analytical calculations and test data. Figure 1 shows a comparison of the load distribution factors for linear loading on a central slab. It has been noted that there is a variation of up to 15%, in the critical factors obtained. Experimental and analytical research has been carried out in the past by Stanton (1987, 1992), Moss (1995), and Song et al (2009).

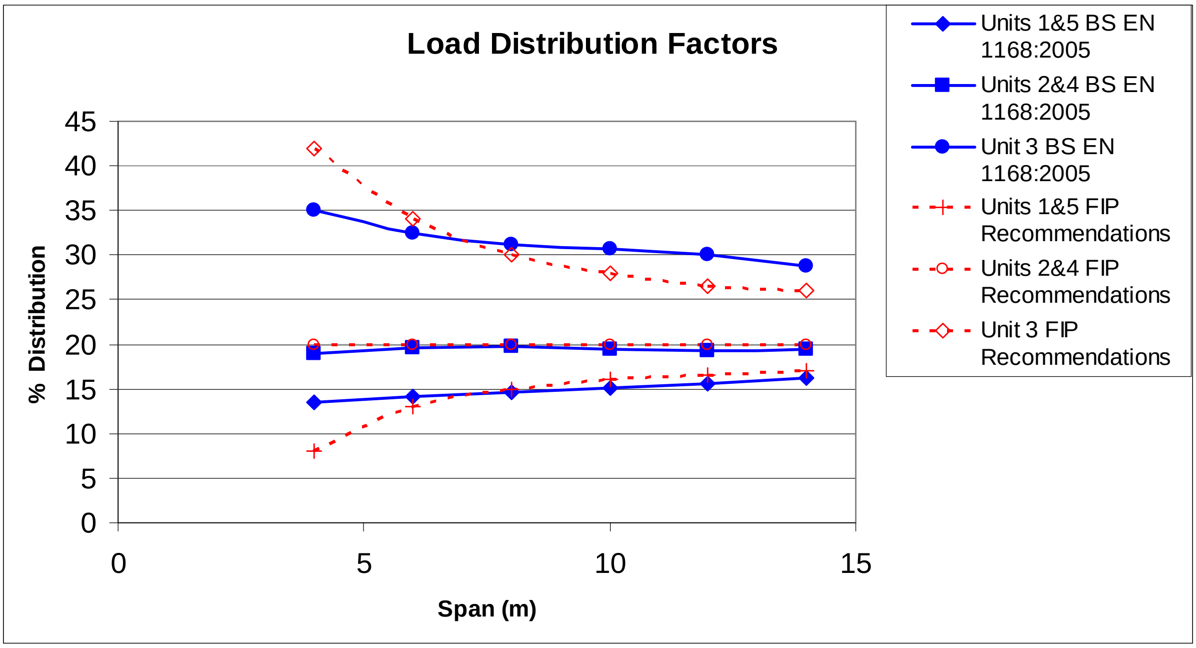

Figure 1 - Percentage load distribution factors for a linear load applied on a central slab

2. Scope and Objective

This paper describes the use of the structural analysis software LUSAS to create 3D solid continuum finite element (FE) models, to simulate the transverse load sharing of a number of precast hollow core floor slabs joined together using mortar / concrete infill. Stanton (1987) carried out similar work with the units being modelled as plates connected by rotational hinges. Stanton (1992) states "To model every void explicitly would make the analysis to cumbersome". With developments in computing it is now possible to model the units and joint with their actual geometry. An extensive FE modelling study has been conducted on many slab sections under various loading conditions. Within FE analyses there are four primary types of models that can be created; 2D, Quasi 3D, 3D, and 3D solid volumes. 3D Volume modelling whilst the most complex, is the most suitable type for these analyses. All the FE models created consist of five hollow core slabs joined along adjacent edges using a mortar / concrete infill. Figure 2 shows how the slabs are numbered throughout this paper along with the loading arrangement. Four different load cases have been used in each individual model. These are: (A) Point load on unit 3, (B) Point load on unit 1, (C) Line Load on unit 3 (e.g. wall loading), (D) Line load on unit 1.

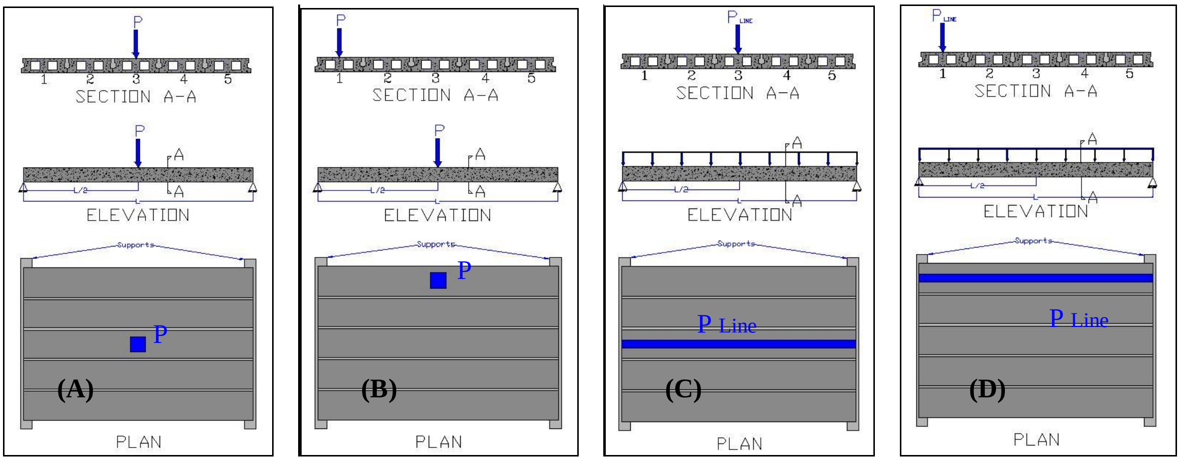

Figure 2 - Load Case Diagrams

Both reinforced and prestressed models were generated and a non-linear concrete material was used to model both the precast units and the joint material. Experimental testing has been conducted on precast reinforced slabs to validate the FE models. The test results presented by previous research (Moss, 1995) have been used to establish confidence in the models. In total 29 different models were created, each comprising five different sections of nominal width 1.2m. The depths of the units were 150mm, 200mm, 250mm, and 300mm. The objective of this study was to establish how conservative the current guidelines are, and whether more economical designs can be achieved using the results from FE analyses in situations where load sharing prevails. The theoretical and FE analyses along with experimental results have been compared and numerical and graphical results are presented.

3. LUSAS Finite Element Analysis

Three dimensional solid volume modelling of this arrangement of hollow core units is an extremely time consuming task involving pre-processing, processing and post-processing. A number of prestressed and reinforced units were modelled to simulate the load sharing of hollow core units. Figure 3 shows the displacement of a prestressed hollow core floor along with the stress profile of the reinforcement within a reinforced floor.

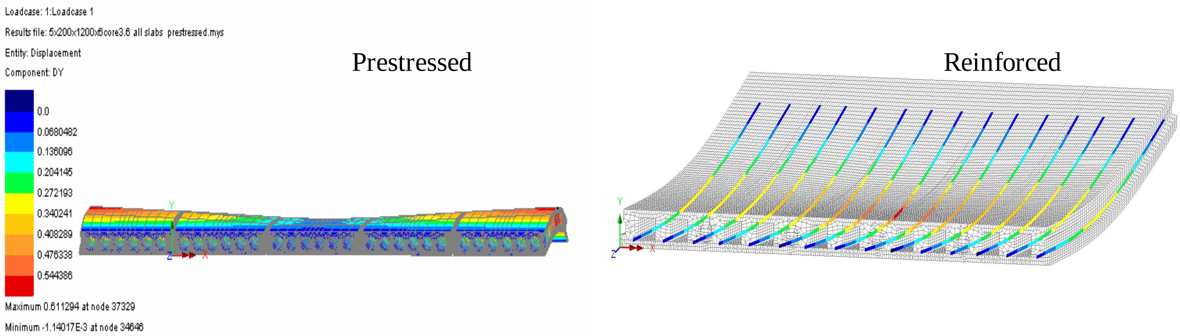

Figure 3 - Prestressed and Reinforced Models

The prestressed models were stressed using the “Pre-stress Wizard” facility within LUSAS. Within the wizard, properties such as creep, shrinkage, slippage, etc, can be entered. The lines representing the tendons need to be drawn in their location within the units and a solid pre-stressing wizard chosen. When creating the reinforced models, the lines representing the reinforcement must also be constructed as lines representing the volumes. This in effect means splitting the unit into two joined volumes along the reinforcement layer. This can cause considerable difficulties when meshing the models as the number of elements being created can be greatly increased. 3D solid bar elements were used to model the reinforcement. In the prestressed and reinforced models the concrete was represented using a non-linear concrete material model. This concrete model can represent both the tensile and compressive strength of the concrete along with concrete crushing and cracking characteristics. As a result of the large amount of time required to create and compute these models it was decided to create the same model geometry without pre-stressing tendons or reinforcement and with a linear elastic concrete. It was found that while the displacements and stresses were different from the reinforced/prestressed models, the load sharing percentages obtained were the same. This established that for this study, the rest of the modelling could be carried using linear elastic concrete units without pre-stressing or reinforcement. Table 1 shows the models that have been created and used within this study. To establish confidence in the models each of the units was first modelled individually before being joined and the displacements and stresses checked using traditional hand calculations. The maximum error found during this process was less than 0.5%. For the purpose of clarity within the result graphs, all sections have been modelled up to a span of 14m even though the shallower units cannot safely span up to 14m. In LUSAS (Version 14.3-9) there is a limit of approximately 250,000 elements. Aspect ratios also have to be taken into consideration. The aspect ratio is the ratio of the longest side of the element to the shortest. Generally largely distorted elements may result in inaccurate results, therefore LUSAS recommends that the aspect ratio be kept below 10. These limits caused considerable difficulties when working with the larger spans and careful consideration had to be given to the mesh density and element type and size.

Table 1 - Models used in this study

Span	**4m**	**6m**	**8m**	**10m**	**12m**	**14m**
150mm x 1200mm x 11core Echo	X	X	X	X	X	X
200mm x 1200mm x 11core Echo	X	X	X	X	X	X
250mm x 1200mm x 7core Ducon	X	X	X	X	X	X
300mm x 1200mm x 11core Echo	X	X	X	X	X	X
250mm x 1200mm x 6core Echo Prestressed		X		X		
150mm x 1200mm x 9core Moss Reinforced		X				
125mm x 400mm x 2core CIT Reinforced	3m span					

To model the hollow core units and the joints a cross section was first drawn in AutoCad and then imported into LUSAS. Within LUSAS, surfaces were created and then extruded to form volumes. 3D solid continuum elements called HX8M were used to mesh both the hollow core units and the concrete joints. These elements contain eight nodes and are of hexahedral shape. A consistent mesh density should be sought with perfect cube elements being formed, but with the curved voids this is impossible to achieve using any element type as none of the element types can be curved. The mesh was refined until a satisfactory mesh consistency was formed as shown in Figure 4. A linear concrete material was then assigned to both the units and the joints.

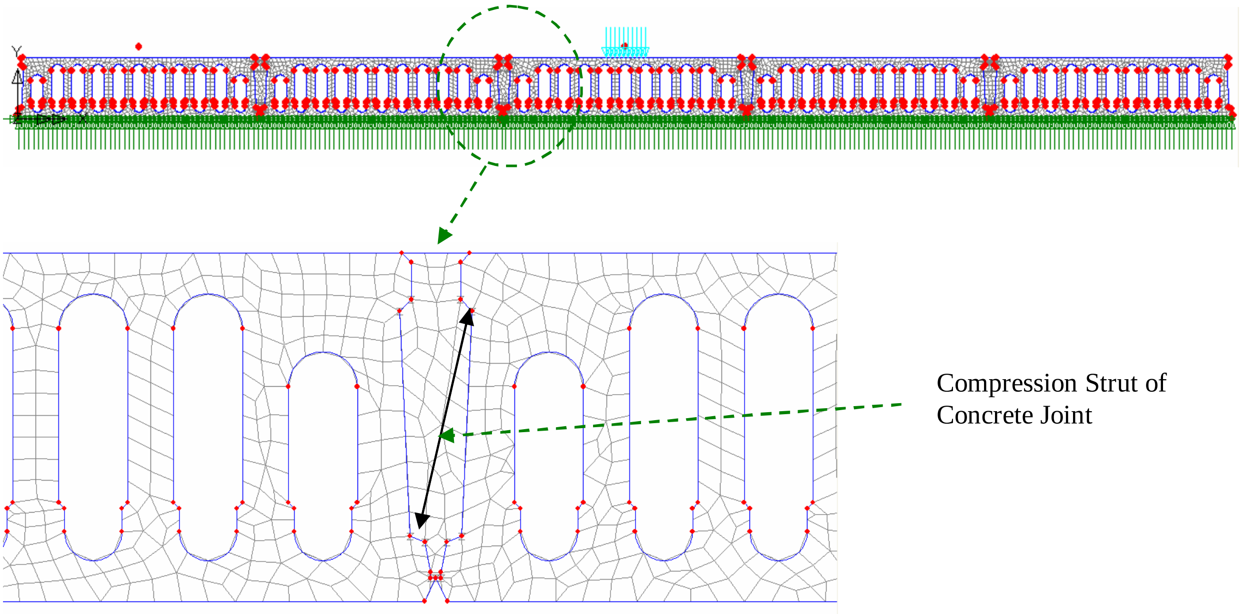

Figure 4 - Image of Volume Mesh

The hollow core units and the concrete joints were joined together using a joint element called JNT4. These joint elements join all nodes along a surface or line using springs. To prevent independent movement between the hollow core unit contact surfaces and the concrete joints' contact surfaces, these springs were assigned a very high stiffness value. To facilitate lateral transfer of the shear loads and represent the compression strut of the concrete joint, the joint elements were only assigned to the surfaces inclined to the horizontal. Supports were provided using a pinned support on one side and a roller support on the other. Point loads were applied as patch loads on a 200mm x 200mm patch, simulating a column load. Line loads were also applied as patch loads 215mm wide and running the length of the span, simulating a wall load.

4. Experimental Testing

A number of reinforced concrete slabs 125mm x 400mm x 2core were constructed and tested in the Heavy Structures Testing Laboratory at Cork Institute of Technology. The first test was undertaken on a single slab with a single load applied at centre span as shown in Figure 5. This was modelled in LUSAS as a reinforced model with non-linear concrete material assignment. The results for deflection at centre span for both the test and the model were very similar. The second test involved joining five slabs together using a mortar infill and applying a linear load on the centre slab as in load case (C), shown in Figure 2. Again the results obtained from the test, and the FE modelling, were in broad agreement. Finally, the floor section that was taken from Moss, 1995 [3] was modelled in LUSAS and the results compared with the results obtained from that paper. It was not possible to model the Moss floor section completely accurately because the complete design information was not included in the paper. However, the load sharing percentages calculated from the paper and the LUSAS model were found to be in broad agreement.

The present work is primarily an analytical approach, which is to be followed with a testing schedule of a full scale floor deck. The four load cases outlined in Figure 2 will be investigated and measurements of displacements and reactions recorded and then compared to the corresponding FE model. The floor deck will then be covered with a composite structural screed to establish what effect this will have on the load sharing characteristics.

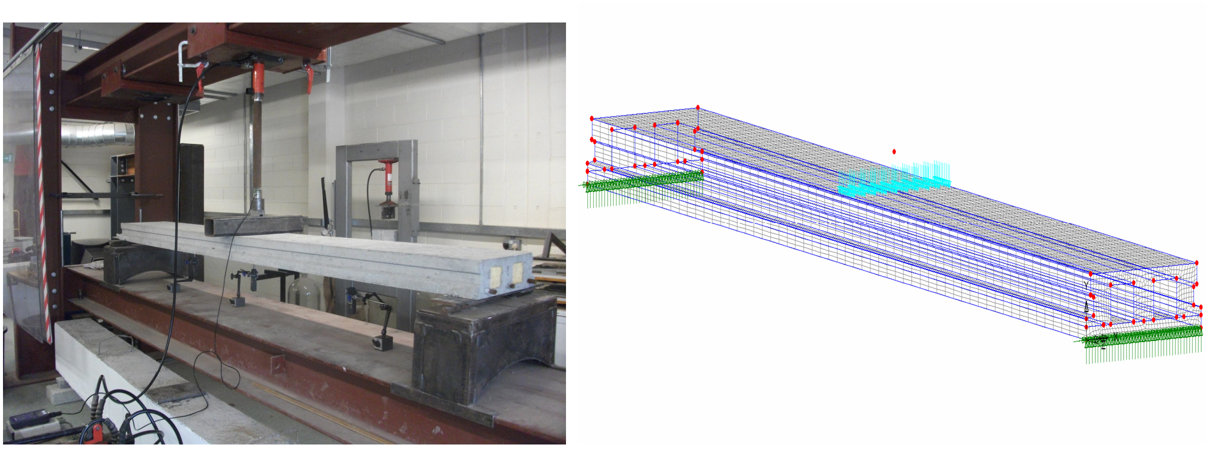

Figure 5 - Image of single slab being tested along with its LUSAS model

5. LUSAS Results

In this paper, load sharing is defined as the ability to transfer load from the loaded slab; thus a higher load sharing indicates that a greater proportion of the load is transferred to the unloaded units. The load sharing behaviour of the joined units outlined in Table 1 was calculated using the central displacements of each unit. These displacements were added together and a percentage load sharing per unit calculated. Within LUSAS a 2D slice was taken through the 3D models at centre span and the displacement of selected central nodes displayed. Figure 6 shows the results displayed for a line load on a 150mm x 1200mm x 11core Echo section of span 4m. The FIP recommendations provide graphs for a linear load on unit 3 and for linear loads on unit 1 in a three unit configuration. BS EN 1168:2005 gives graphs for all the load cases being considered in this paper along with guidance that the load being carried by the loaded slab should be modified by multiplying the percentage of the load on the directly loaded member by 1.25 if a screed is not being used. The FIP recommendations include this 25% in the graphs which can be excluded if a screed is used. For clarity all the results relating to both BS EN 1168:2005 and the FIP recommendations shown in the graphs in this paper include the 25% increase on the loaded slab.

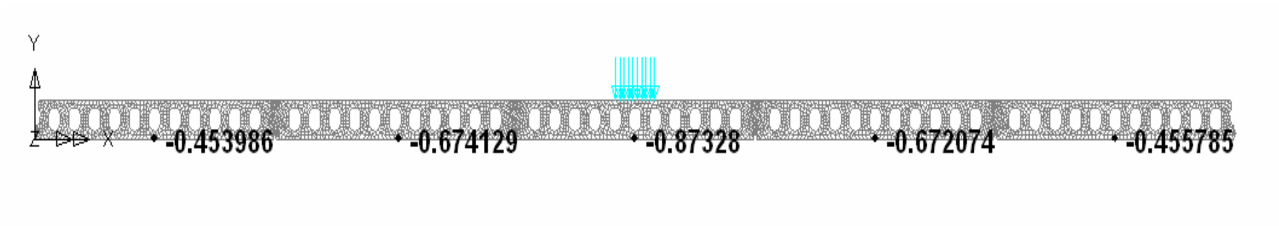

Figure 6 - Slice through 3D model showing displacements at selected nodes

5.1 Reaction Results

While Section 5.2 relies on displacements to calculate the load distribution graphs, it is important to realize that these graphs could lead to distribution factors, which may be unsafe when determining the shear capacity of the unit. To illustrate this, the vertical end reactions have been obtained from LUSAS for the 200mm x 1200mm x 11core model spanning 6m. Load cases (A) & (C) from Figure 2 have been considered. Table 2 shows the results from LUSAS for load case (A) where there is a 50kN applied load. The reaction results from LUSAS indicate that the loaded unit is taking 34.5% of the applied point load. The displacement results from LUSAS show 24% while the BS EN 1168:2005 graph shows 32.5%. In this load case the BS EN 1168:2005 graph shows good agreement with the LUSAS reaction results on the loaded unit.

Table 2 – Reactions from 200mm x 1200mm x 11core model load case (A)

Units	End Reaction (kN)	% Distribution Factor
1 & 5	3.446	6.9
2 & 4	12.895	25.8
3	17.233	34.5

Table 3 shows the results from load case (C) which comprised a line load of 10 kN/m. In this case the reaction results indicate that the loaded unit is taking 52% of the applied linear load. The displacement results from LUSAS show 23% while both the BS EN 1168:2005 and the FIP recommendations show approximately 34%. It can be clearly seen that if the displacement distribution factors were used in this loading arrangement the shear design may be unsafe.

Table 3 – Reactions from 200mm x 1200mm x 11 core model load case (C)

Units	End Reaction (kN)	% Distribution Factor
1 & 5	2.166	3.6
2 & 4	12.225	20.4
3	31.173	52

Figure 7 shows the results for Load case (C), which is a linear load being applied to the central unit. The floor deck consists of 200mm x 1200mm x11core echo units. There are graphs representing LUSAS, BS EN 1168:2005 and the FIP recommendations. From the graph it can be seen that the LUSAS results determined on the basis of displacements and those determined on the basis of reactions differ significantly. For a 4m span there is a difference of over 36% in the factors obtained from both calculations. For a maximum span of approximately 10m there is still a substantial difference of 20%. In comparing the LUSAS reaction results to BS EN 1168:2005 and the FIP recommendations it can be seen that there are also large discrepancies with a 28% and 21% difference respectively. Further analysis of the results from LUSAS for displacements, reactions and stresses, for all four load cases is ongoing. From work to date it appears that it is only in relation to line loads that there are major discrepancies.

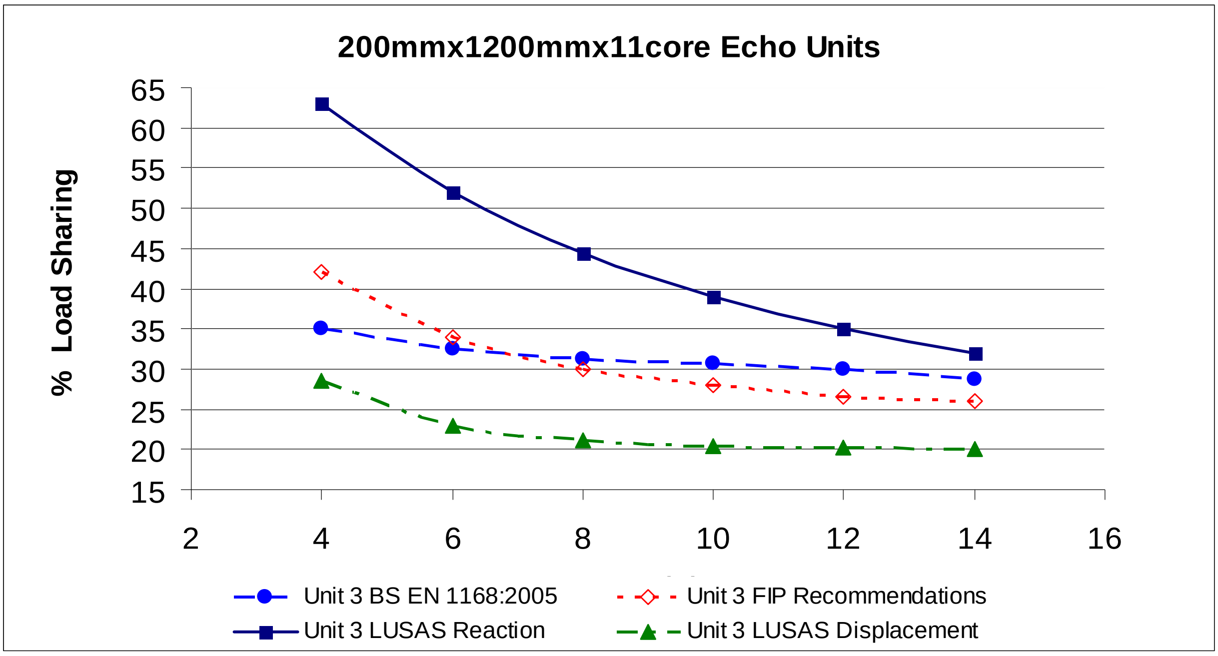

Figure 7 – Results for Load case (C) Linear load on unit 3

5.2 Displacement Results

The graphs shown in Figure 8 represent both the BS EN 1168:2005 load distribution factors along with the results from the FE analyses for load case (A). The lines of interest are those lines representing the loaded unit as this is the one from which the design loading will be obtained. In this case the loaded unit is number 3 and it can be seen from the graphs that the BS EN 1168:2005 load distribution factors are conservative when compared to the LUSAS model values. On the 4m spans, the LUSAS models give a 5-10% higher load sharing value than BS EN 1168:2005. In medium to long spans (>6m), the LUSAS model results show a consistent 6% increase in the load sharing values. Taking the LUSAS model results from the four graphs it can be seen that there is an increase in the load sharing percentages as the section depth decreases.

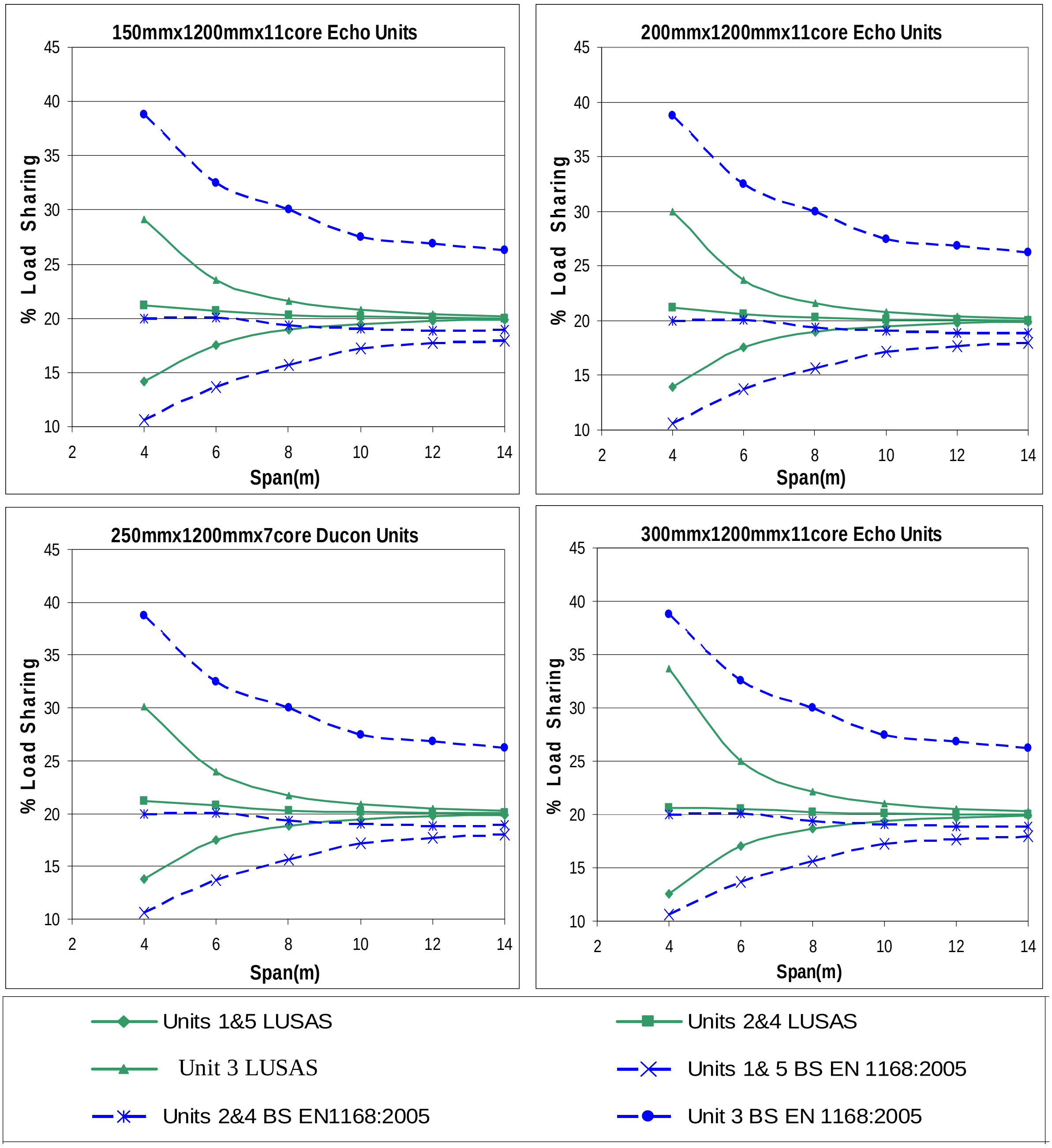

Figure 8 - Results for Loadcase (A) Point load on unit 3

Figure 9 shows the results for Loadcase (B), with a point load applied on the edge unit 1. On the 4m spans, the LUSAS models give a 6.5-12% higher load sharing value than BS EN 1168:2005. On medium to long spans (>6m) the increase is approximately 7%.

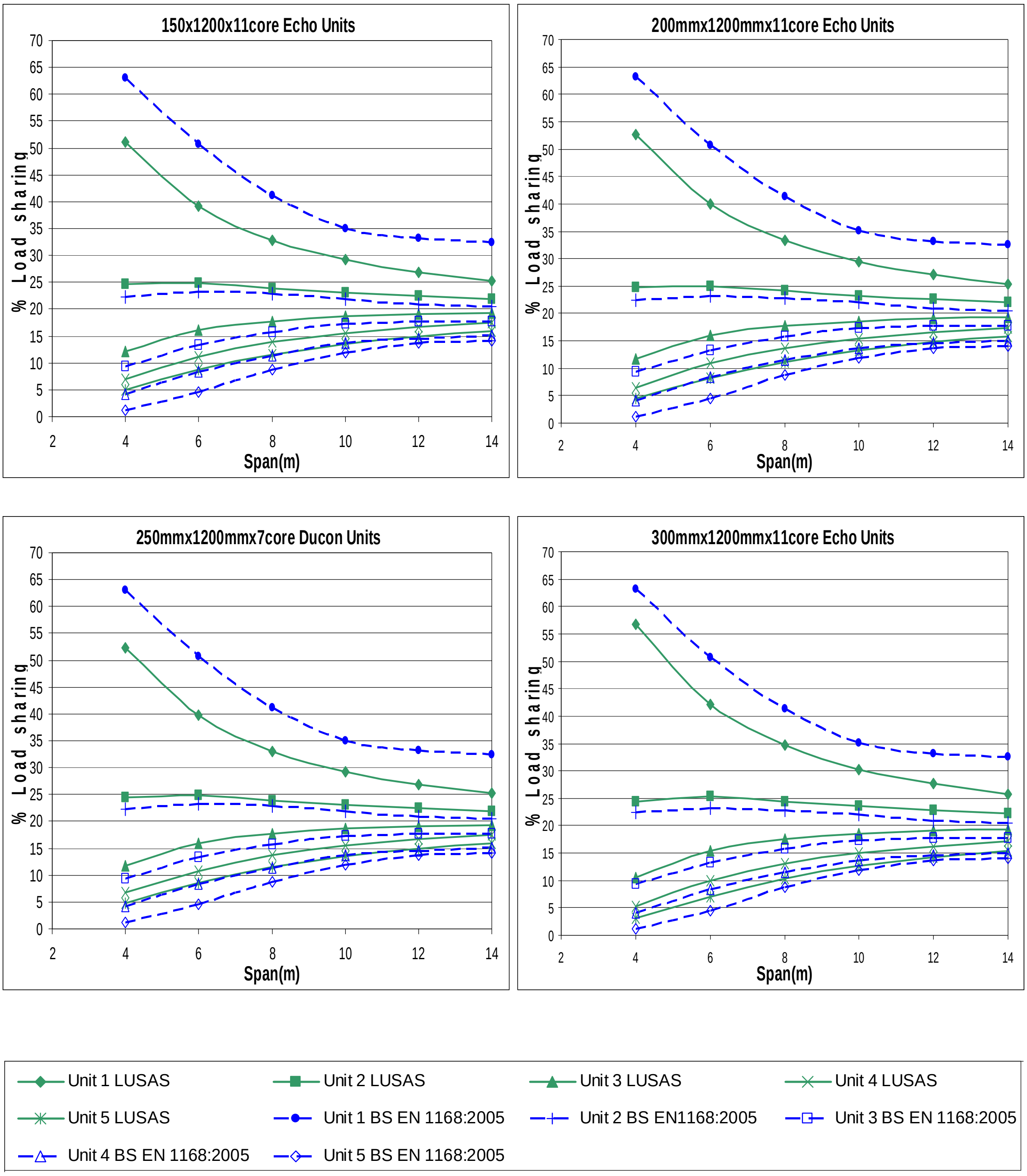

Figure 9 - Results for Loadcase (B) Point Load on Unit 1

Figure 10 shows the results for Loadcase (C), which is a linear load being applied to the central unit. There are graphs representing LUSAS, BS EN 1168:2005 and the FIP recommendations. The FIP recommendations are conservative on the shorter spans applying up to 7% more load onto the loaded element. The BS EN 1168:2005 load distribution factors are more conservative on longer spans (>6m). On the shorter spans (<6m), the LUSAS results show an increase in the load sharing percentage ranging from 7% to 4% when compared to BS EN1168:2005 and 14% to 11% when compared to the FIP recommendations. On the longer spans (>6m), the LUSAS results increase the load sharing by 9% when compared to BS EN 1168:2005 and by 6% when compared to the FIP recommendations.

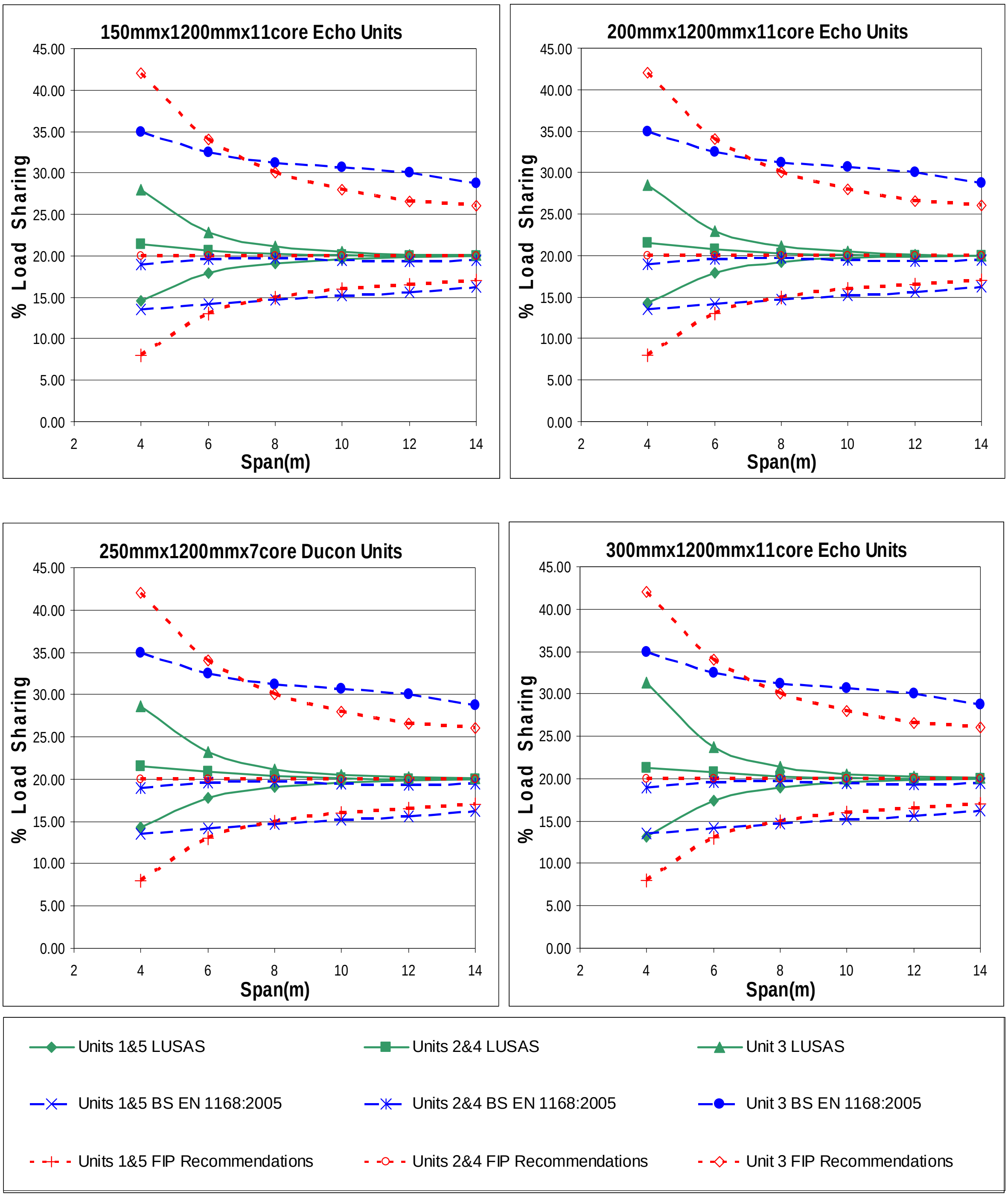

Figure 10 - Results for Loadcase (C) Linear load on unit 3

Figure 11 shows the results for loadcase (D), which is a linear load on the edge unit. On the 4m spans, the LUSAS models give a 7-12% higher load sharing value than BS EN 1168:2005. On medium to long spans (>6m) the increase is approximately 7%.

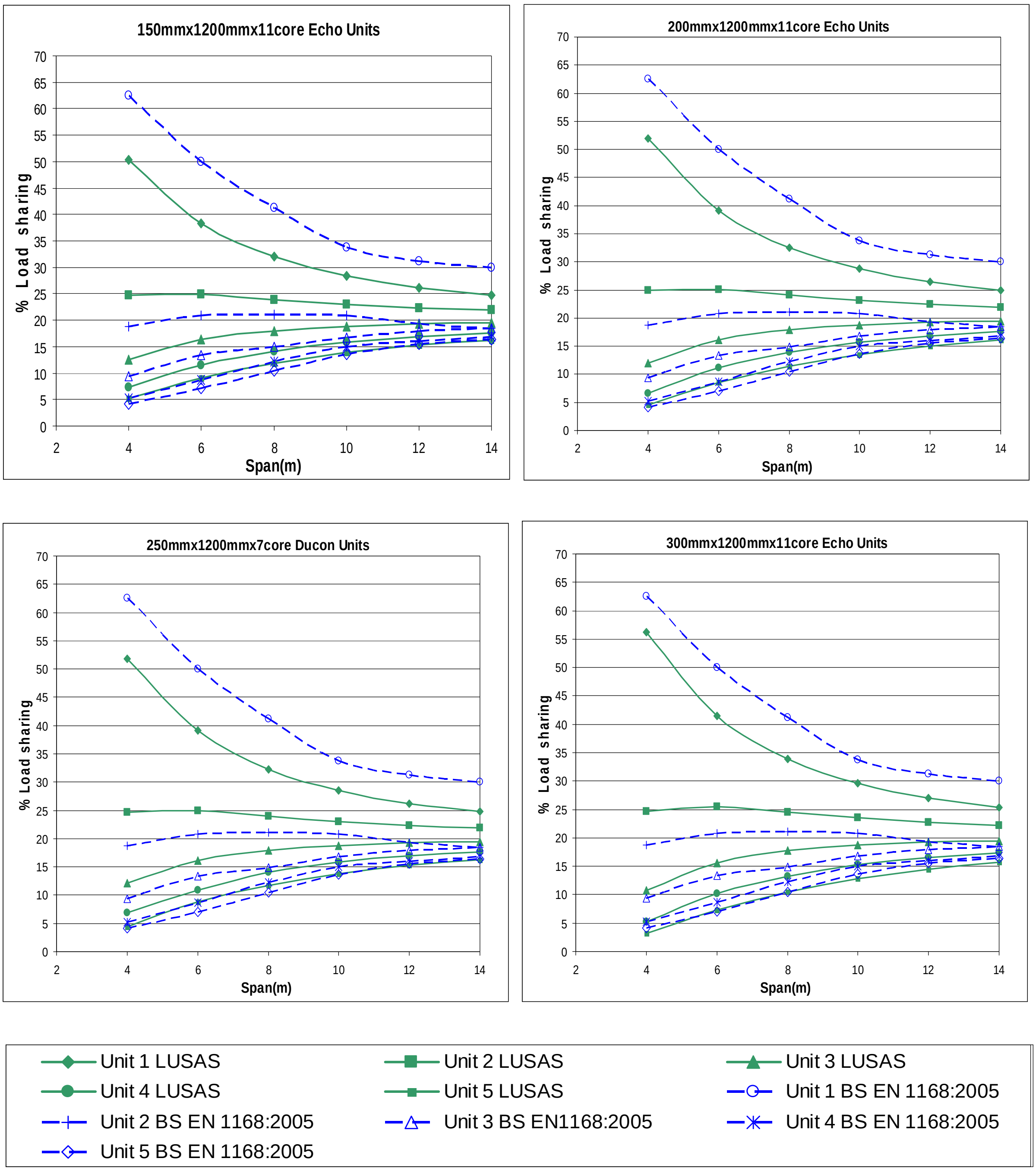

Figure 11 - Results for Loadcase (D) Linear load on unit 1

6. Conclusion

From the finite element analyses carried out and the test data obtained in this study, comparisons with the guidance from BS EN 1168:2005 and the FIP recommendations, the following conclusions can be made.

(1) Finite element modelling can be used to successfully model the transverse load sharing between hollow core floor slabs. It has been shown to provide consistently correct results in the cases of prestressed or reinforced hollow core units. Finite element modelling is effective as changes in span, load case, and section size can be modelled, and large amounts of reliable data collected.

(2) The load sharing provided by both BS EN 1168:2005 and the FIP recommendations are conservative in comparison with the finite element analyses displacement results for all the studied units and loading arrangements. While the design guidance given is conservative, it is possible that more economical designs could be achieved by the use of finite element modelling.

(3) Shear design needs to be carefully considered when using load distribution graphs.

References

British Standards, BS EN 1168:2005, *Precast concrete products - Hollow core slabs*.
Fédération internationale de la précontrainte (1988), *Precast prestressed hollow core floors*, Thomas Telford.
R. M. Moss, (1995), 'Load testing of hollow plank concrete floors', *The Structural Engineer*, Vol. 73, No. 10, pp. 161-168.
Jong-Young Song, Kim S. Elliott, Ho Lee, and Hyo-Gyoung Kwak (2009), 'Load Distribution Factors for Hollow Core Slabs with In-situ Reinforced Concrete Joints', *International Journal of Concrete Structures and Materials*, Vol.3, No.1, pp. 63-69.
John Stanton (1987), 'Proposed Design Rules for Load Distribution in Precast Concrete Decks', *ACI Structural Journal*, Vol. 4, No.5, pp. 371-382.
John Stanton (1992), 'Response of Hollow-Core Slab Floors to Concentrated Loads', *PCI Journal*, Vol. 37, No.4, pp. 98-113.

MOISTURE MOVEMENT IN CONCRETE DURING DRYING AND AFTER COVERING – A REVIEW

N. HOLMES[1] AND R.P. WEST[2]
[1] School of Planning, Architecture and Civil Engineering, Queens University of Belfast, Northern Ireland
[2] Department of Civil, Structural and Environmental Engineering, University of Dublin, Trinity College, Dublin, Ireland

Abstract
This paper presents a review of research recently completed at Trinity College into moisture movement in concrete floor slabs on grade. The review covers the main findings of the research including the problems associated with relying on the 75% relative humidity threshold to be achieved before applying an impermeable covering. Due to accelerated drying practices on construction sites, significant problems with floor coverings, such as blistering of vinyls and rising tiles, are ongoing. However, one of the findings of the research is the introduction of a new ASTM code of practice which allows a 'snapshot' of the long-term relative humidity at the time of covering. By measuring the relative humidity at 40% of the slab thickness (for one-face drying), the results from this work confirms that it gives a good prediction of the long-term equilibrium relative humidity underneath coverings.

The paper also presents the experimental work and the finite element study undertaken in the research, which shows good agreement with each other.

Keywords: Accelerated drying, concrete floor slabs, drying, finite element modelling residual moisture, moisture redistribution.

1. Introduction

Concrete slabs dry when they are exposed to an environment with an ambient humidity lower than in the concrete. Drying will continue until equilibrium is reached between the concrete and the environment in which it dries and impermeable floor coverings are applied to concrete floor slabs when the relative humidity (*rh)* reaches 75% at the surface, as determined using a surface hygrometer or similar (BSI, 1996). However, it is common on some sites to force dry the concrete leading to residuals of moisture deep in the concrete. This leads to damage to floor coverings such as rising of tiles, blistering of paints and de-bonding of vinyls and has been reported previously (West & Holmes, 2001; Holmes and West, 2002 and 2003). Also, methods to avoid these problems have been presented in the literature (Hedenbland, 1996; Suprenant and Malisch, 1998).

The reason for these damage types is that accelerated drying only influences the near surface region with little or no drying deep in the concrete. A large residue of moisture exists deep in the slab, which, upon sealing, will equilibrate and result in a higher long-term *rh* through the depth. This will generate vapour pressure and leads to high moisture content under the covering which results in the problems described above.

One of the findings from this research is the new ASTM code of practice F2170-02 (ASTM F2170-02, 2002) where it is now recommended that prior to sealing, a measurement of the *rh* is made at 40 or 20% of the depth, for 1- or 2-direction drying respectively. The results from the experimental study as part of this work, and from a finite element study (West and Holmes, 2005), have demonstrated that this is a reasonable depth to assess if long-term problems will be an issue. This has also been confirmed experimentally in a recent study at QUB (Glendinning, 2010).

This paper presents a summary of the outcomes of an extensive experimental programme in which a number of concrete slabs of varying thickness and w/c ratio were allowed to dry in a natural (laboratory) and artificially accelerated (control room) environment. The results from this will show that when accelerated drying is employed, drying is only really occurring near to the surface with relatively little drying deeper in the concrete (West & Holmes, 2001; Holmes and West, 2002 and 2003). Indeed, despite drying taking place for the same amount of time for identical slabs in the two environments, when 75% *rh* is achieved on the surface, a higher residual moisture level remains in the specimens in the control room. This has been confirmed from subsequent finite element analysis (West and Holmes, 2005), which will be presented also.

The results will also show that upon sealing, the measured *rh* at 40% of the depth, or 60mm for the 150mm thick slabs, provides a good estimate of the long-term equilibrated *rh*. This will provide users with an indication of possible covering failure problems long-term.

2. Experimental Details

The experimental programme monitored the *rh* through the depth of six 700x700x150mm thick slabs with w/c ratios of 0.4, 0.5 and 0.6 with mix details as in Table 1. All of the concrete was made with Ordinary Portland Cement of and were allowed to dry naturally (in the laboratory) and artificially (in a control room).

The ambient conditions experienced during drying for the slabs in the natural and artificial environments for the 150 thick slabs varied between 11 to 20^{0}C and 40 to 70% respectively. The ambient humidity and temperatures in the control room varied between 36 to 41^{0}C and 12 to 19%.

The slabs were cured under plastic for 24-hours after mixing and moist cured under wet hessian for 3-days. The concrete was prepared for testing by painting the four sides and the base, 3 coats per face, with an impervious coating. This ensured that 1-dimensional drying was occurring. To measure the *rh* through the depth of the concrete, six 16mm diameter holes were drilled into each slab to depths of 15, 40, 65, 90, 115 and 135mm using a masonry drill. The drilling of the holes did generate some heat but it is expected that it did not affect the moisture condition adversely. A plastic tube (Figure 1(a)) was inserted into the holes which traps an area of humidity approximately 5mm above the base of the hole. The prepared slabs ready for testing are shown in Figure 1(b).

Table 1 Mix constituents per m^3 for the concrete slabs.

Slab No Lab. and Control Room	w/c ratio	Fine aggregate (kg)	10mm aggregate (kg).	20mm aggregate (kg).	Cement (kg).	Water (l)
1 & 4	0.4	633	345	689	487.5	195
2 & 5	0.5	706	353	706	390	195
3 & 6	0.6	787	348	695	325	195

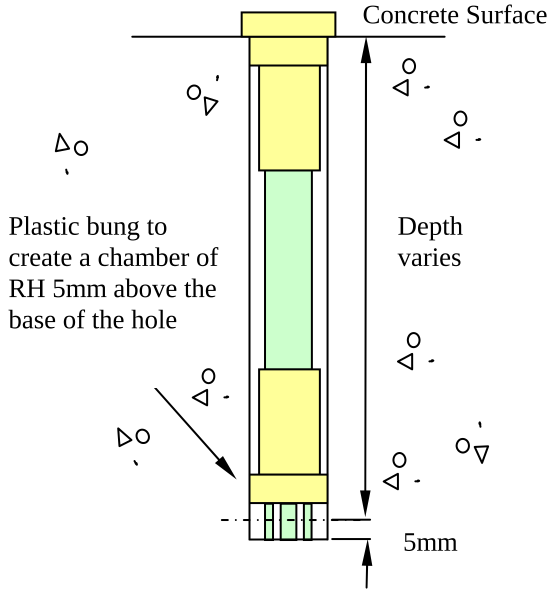

(a)

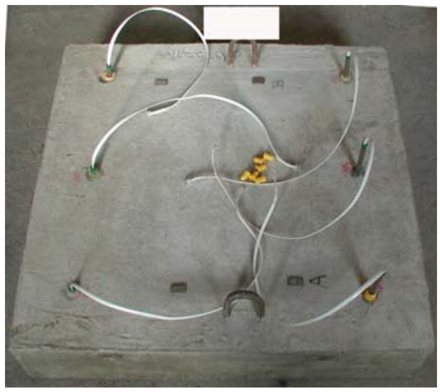

(b)

Figure 1 (a) Tube inserted into the 700x700x150mm thick concrete slabs (NTS) and (b) a sample slab with probes inserted

3. Testing Details

The *rh* in the concrete was measured at the surface and at depths of 10, 35, 60, 85, 110 and 130mm. The humidity was measured using portable humidity probes that were inserted into the plastic tubes (Fig. 2(a)). The probes were attached to a hand-held instrument, namely the Relative Humidity Reader (RHR) (Figure 2(b) (Tramex, 1980). The *rh* reading is shown on an LCD display. The *rh* was measured at regular intervals until the surface reached 75%, at which point the surface was sealed with an impermeable vinyl floor covering. The surface *rh* was measured using a plastic hood, (Figure 3) which is glued to the surface of the slab, sealing in evaporating moisture.

4. Experimental Results

rh profiles during drying up to the point of sealing, can be found in previous publications (West & Holmes, 2001; Holmes and West, 2002 and 2003). Figures 4 and 5 present the *rh* profiles through the depth at the point of sealing (ie. 75% surface *rh*) and the changing *rh* profiles during moisture redistribution, for the w/c=0.5 naturally and artificially dried slabs respectively.

It may be observed that a dashed line has been drawn along the depth of 60mm, or 40% of the depth. As shown, in most cases, this line appears to insect the cross-over point between the *rh* profiles at sealing and when it is almost equilibrated. In Figure 4 and 5, the *rh* at 60mm on sealing gives a very good approximation of the long-term uniform *rh*.

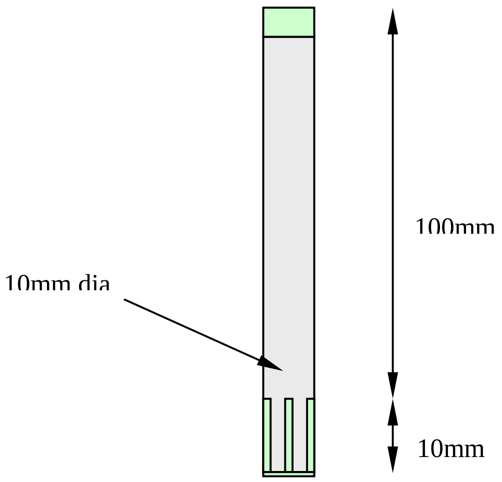

(a)

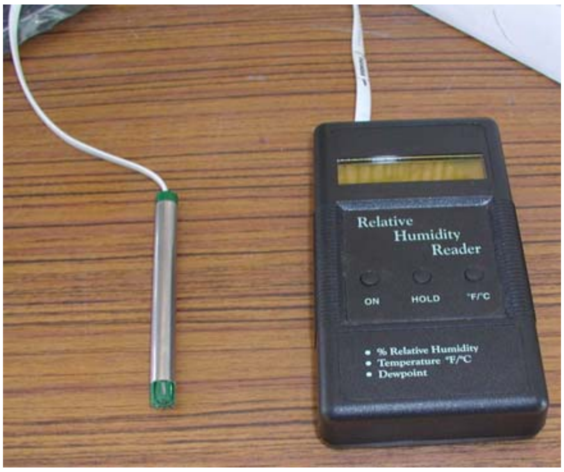

(b)

Figure 2 (a) Humidity probe used to measure the *rh* and (b) RHR meter (and probe).

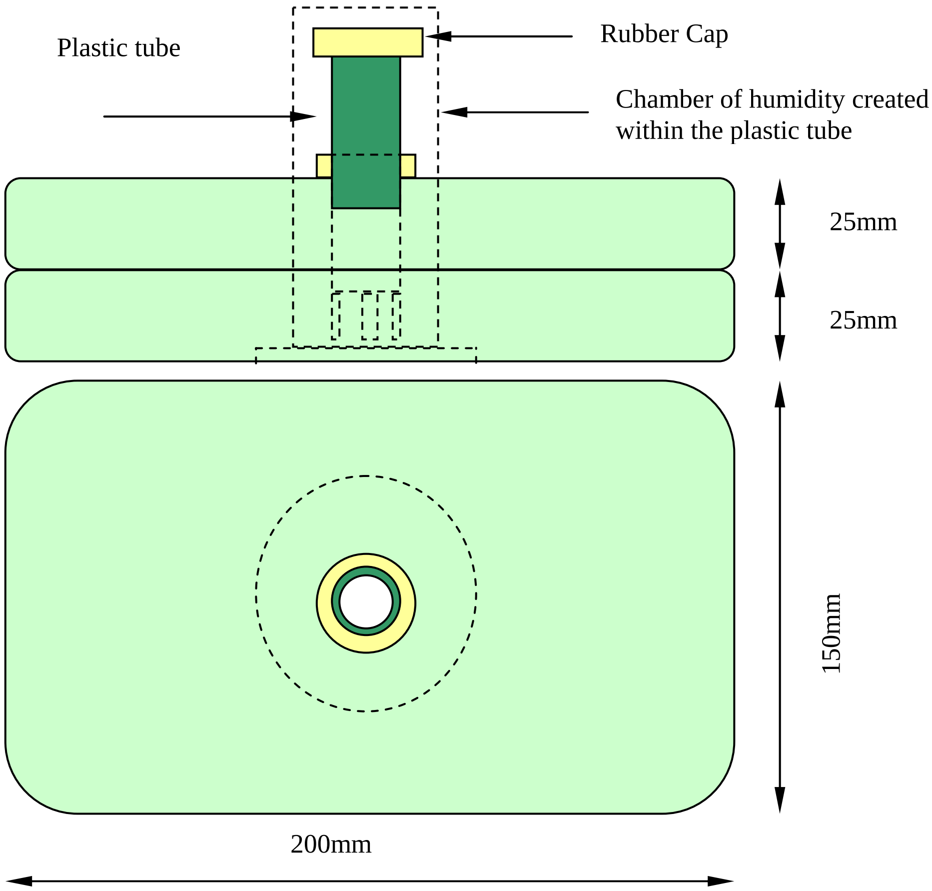

Figure 3 Apparatus used to measure the surface *rh* for the slabs (NTS).

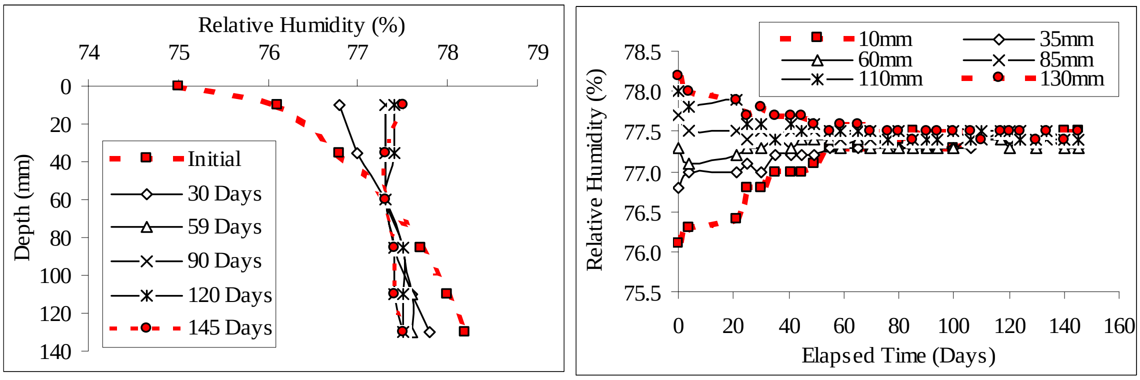

(i) (ii)

Figure 4 Experimental results for the laboratory dried slab with a w/c ratio of 0.5 with *rh* profiles (i) through the depth and (ii) over time after covering has been applied.

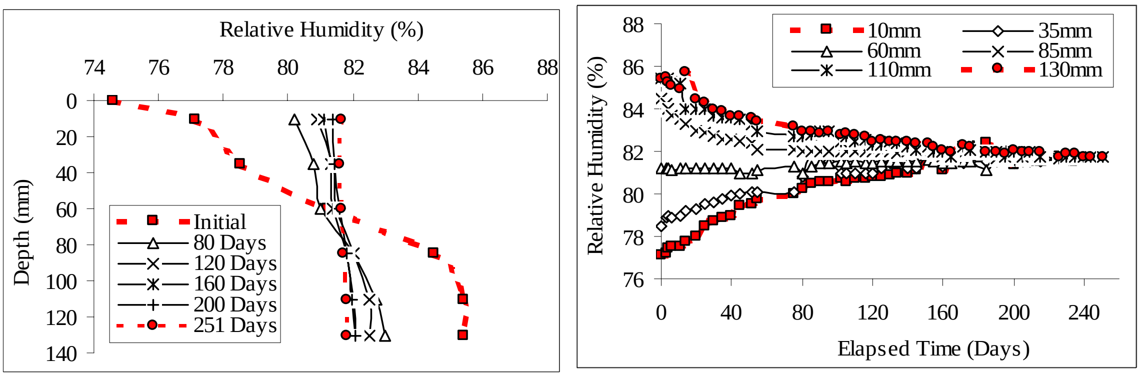

(i) (ii)

Figure 5 Experimental results for the control room dried slab with a w/c ratio of 0.5 with *rh* profiles (i) through the depth and (ii) over time after covering has been applied

5. Finite Element Study

In order to numerically predict and confirm if this 40% point is applicable, a finite element study was conducted using a commercially available package, DIANA. This model has the capability of modeling the non-linear diffusion of moisture within the concrete and its evaporation from the surface. The results from the model for drying up to 75% have been presented at a previous BCRI conference in 2003 (West and Holmes, 2003).

The mesh selected for the sealed specimen analysis is shown in Figure 6. It consists of 700 no. 8-noded quadrilateral (CQ8HT) elements for diffusion in the concrete. The major change in this model is the sealed surface, which previously had an evaporation boundary condition assigned too it.

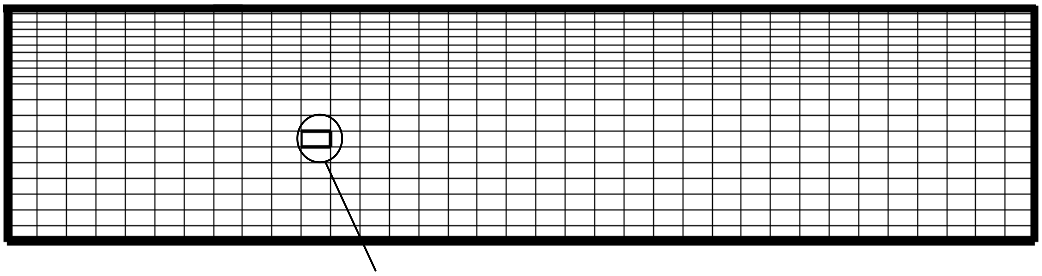

CQ8HT Element for diffusion in concrete

Figure 6 Mesh set-up for the 700x150mm thick concrete floor slab. Mesh consists of 700 CQ8HT diffusion elements and a sealed surface boundary condition.

5.1 Material Properties

The only material property which has to be specified here is the rate of moisture diffusion through the concrete. The equation to describe the diffusion between two neighboring nodes in DIANA is given in Equation 1, also known as Fick's second law (Fick, 1855). In Equation 1, P is the unknown (here the internal RH) and λ is the diffusion coefficient (m^2/sec) shown as a function of the internal RH. The diffusion coefficient (D) in this analysis is calculated using Equation 2, which has been developed from experimentally determined *rh* profiles with depth x over time t in various concrete slabs during drying (Bazant and Najjar, 1972; Kim and Lee, 1999; Shimomura and Maekawa, 1997)).

$$\frac{\partial P}{\partial t} = \frac{\partial}{\partial x}\left(\lambda(P)\cdot\frac{\partial P}{\partial x}\right) \qquad \text{Equation 1}$$

$$D(h) = D_1\left[\alpha + \frac{1-\alpha}{1+\left(\dfrac{1-h}{1-h_C}\right)^n}\right] \qquad \text{Equation 2}$$

where D_1 represents $D(h)$ when h is 100%, α is a parameter that represents the ratio D_0/D_1 where D_0 is the minimum $D(h)$ for h = 0%, h_C is the pore humidity at $D(h) = 0.5D_1$ and n is an experimentally determined exponent. Here α = 0.05, h_C = 0.80 and n = 15 are assumed (Bazant and Najjar, 1972; Kim and Lee, 1999) Despite the fact that D is dependant on numerous factors, such as the ambient temperature and humidity, the main influence on D is the internal moisture concentration, or the internal RH in this case. This equation calculates D, initially constant (up to approximately 85%) but it rapidly decreases with *rh* to approximately 75%, where it remains constant thereafter, as shown in Figure 7.

This equation gives a good representation of the actual moisture movement in the concrete during drying where initially the saturated conditions allows the moisture to 'diffuse' through the pores easier than when the moisture condition in the concrete changes to an unsaturated condition, particularly when the RH falls below 75%. Values for D shown in Figure 7 are based on previous published data and calibrated for the model to best suit the experimental results. Previous authors (Akita *et al*, 1997; Bazant and Najjar, 1972; Kim and Lee, 1999; Shimomura and Maekawa, 1997) have suggested D lies between 10^{-9} to 10^{-11} m^2/sec for normal dense concretes with w/c ratios between 0.4 and 0.6 during drying. D for the three w/c ratios are different due mainly to two factors. As the w/c rises, the amount of capillary pores increases as, theoretically speaking, only a w/c ratio of 0.44 in a sealed environment (Neville, 1995) is required for full hydration and with a rise in capillary pores, a more open pore structure and the rate of moisture movement also increases. Secondly, as drying proceeds, the rate of moisture movement will decrease, as the change from saturated conditions early on to non-saturated conditions later causes a decrease in moisture diffusion, as shown in Figure 7, due to a change in the concentration gradient.

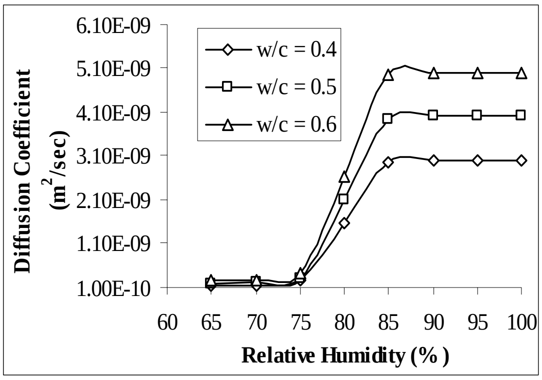

Figure 7 Typical diffusion rates used in the finite element analysis

5.2 Finite Element Results

Figure 8 shows the *rh* profiles (a) through the depth at various times and (b) at 10 and 130mm from the surface in the slabs w/c = 0.5 respectively. These slabs were previously dried in the laboratory and covered when the *rh* readings reached 75% on the surface. As may be observed, the finite element results compare very well with the experimental results and, in terms of the long-term predictions, are within 0.5% of each other. These results demonstrate, following calibration of the finite element model, that *rh* profiles during drying (Holmes and West, 2005 and 2003) and after application of an impermeable covering for NPC mixes can be accurately predicted. At 60mm, the *rh* at the time of sealing and at equilibrium are approximately equal for both the experimental results and, reassuringly, for the finite element results. For example, at 60mm in Figures 8, the *rh* is approximately 77.4 when sealed and at final equilibrium. This further demonstrates that the model can accurately predict the long-term behaviour of the residual moisture after sealing with reasonable accuracy for OPC concretes mixes.

Similar comparisons between the predicted and experimentally measured *rh* profiles for the slabs originally dried in the controlled room are shown in Figure 9 using the same diffusion coefficients as previously (Figure 7) for the three w/c ratios. The results again compare well.

Again, at 60mm, the initial *rh* at sealing gives a good indication of the long-term equilibrium. In Figure 8, the *rh* at 60mm on sealing is approximately 86% and at equilibrium is approximately 84.5. Despite the minor difference between the *rh* at sealing and at equilibrium

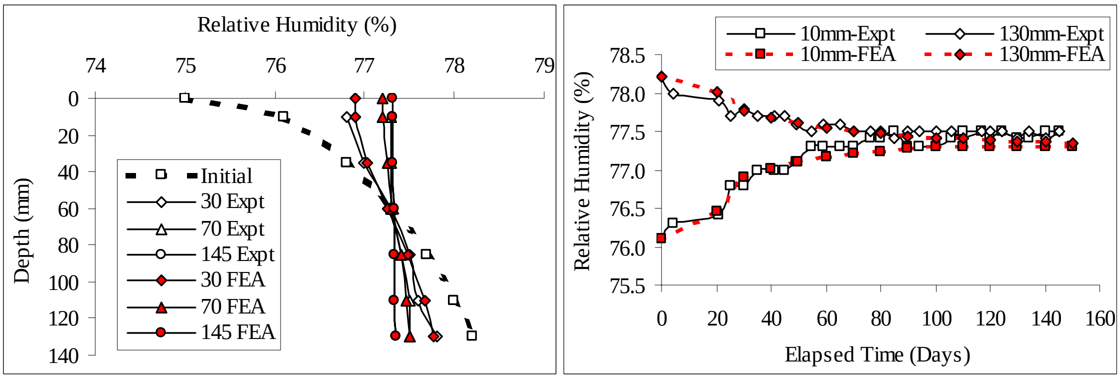

(i) (ii)

Figure 8 Finite element predictions for the laboratory dried slab with a w/c ratio of 0.5 with *rh* profiles (i) through the depth and (ii) over time.

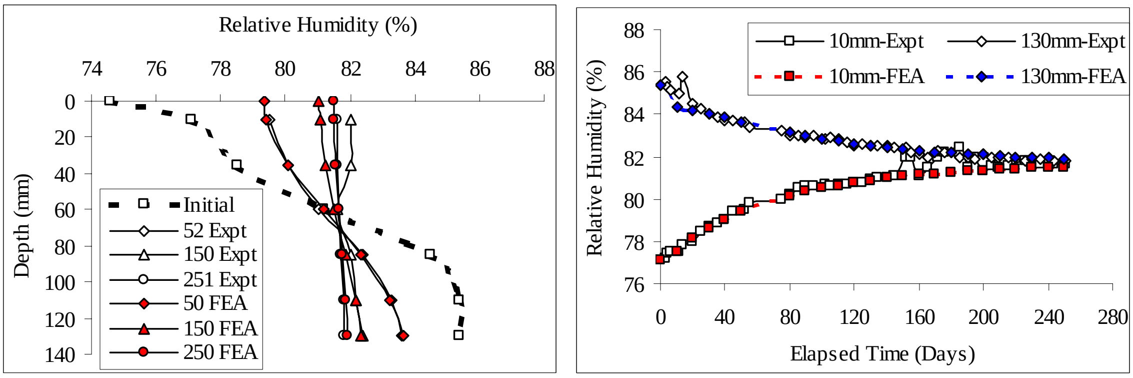

(i) (ii)

Figure 9 Finite element predictions for the control room dried slab with a w/c ratio of 0.5 with *rh* profiles (i) through the depth and (ii) over time.

in these cases (within 1.5%), 40% of the depth still appears to be a suitable point to predict the long-term *rh* through the depth following equilibrium.

This reflects a major contribution to the area of moisture behavior and it offers a real possibility of predicting *rh* trends both during drying (as shown by Holmes and West; 2003 and 2005) and after application of impermeable coverings in concrete slabs, as demonstrated here. This will aid floor-covering personnel to have an accurate estimate of the point to apply a floor covering and an indication of the *rh* distribution through the depth. It is anticipated, therefore, that by using the finite element model developed here and measuring the *rh* at 40% of the depth at the point of sealing will give an indication of the long-term equilibrated *rh*. So the existing method of using a hygrometer for 48 hours to establish whether 75% has been reached on the surface can be replaced with a 5 minute test using a probe inserted into a pre-drilled hole. If the reading at 40% of the depth (for one face drying) is between 75 and 78% *rh*, irrespective of the drying regime, then it is deemed to be safe to cover the concrete. This will both ultimately lead to a reduction in the cases of floor failures, as current practices to assess the moisture condition of concrete prior to the application of coverings produces uninformative and incomplete results. This can be achieved without the need for expensive monitoring practices.

6. Conclusions

The aim of the current research is to demonstrate how the long-term *rh* in a concrete slab can be predicted by measuring it at 40% of the depth, for 1-dimensional drying, as now recommended by the ASTM. Results presented here from *rh* readings both at the surface and at 40% of the depth, indicate that the long-term re-distributed *rh* can be reasonably predicted by measuring the *rh* at this depth.

When the surface *rh* reached 75%, the slabs were covered with an impermeable covering. The *rh* through the depth was continued to be monitored as the residual moisture redistributed. It was observed in the experiments for the majority of the slabs that the long-term *rh* under a covering is approximately the same as the *rh* at *circa* 40% of the slab depth at the time of covering, irrespective of the drying regime. This is an important finding because it suggests that when deciding when to cover a slab safely, the *rh* at 40% of the slab depth should be measured and not the surface *rh* alone, as is current practice. If floor covering suppliers are satisfied with a long-term *rh* of, say, 75 to 78%, at which long-term problems are unlikely to occur, then that should be the target value at 40% of the depth. Indeed, the ASTM have developed a new standard in which for drying through one face, it recommends that the *rh* should be measured, using probes like those here, at 40% of the slab depth. This recommendation was informed by the results presented here.

A commercial finite element model (DIANA) was developed with calibrated diffusion coefficients to predict the *rh* in the slabs after sealing. This model, gave good comparisons with measured *rh* profiles during drying and with other published values employing similar drying conditions which demonstrated the robustness of the model. This model was then set-up to model the application of the covering by applying an impermeable boundary condition on the surface with the previous evaporation boundary condition now redundant. Using both the initial condition from the measured *rh* profiles when the surface was 75%, and from the predicted *rh* profile, the predicted *rh* profiles during redistribution are within 5% of each other.

The new recommendations by the ASTM to measure the *rh* at 40% of the depth (for one-face drying) appears to be suitable as it represents the stationary point where the *rh* over time after covering remains relatively unchanged. It is concluded, therefore, that placing probes at 40% of the slab depth to measure the *rh* will give a good approximation of the long-term *rh* in the concrete following covering. This will aid flooring contractors in deciding at what point in time it is safe to apply a floor covering.

7. References

- Akita, H, Fujiwara, T. and Ozaka, Y. (1997), A practical procedure for the analysis of moisture transfer within concrete due to drying, *Magazine of Concrete Research*, Vol. 49, No. 179, pp. 129-137.
- ASTM F2170-02 (2002), *Standard test method for determining relative humidity in concrete floor slabs using in-situ probes*.

- Bazant, Z.P. and Najjar, L.J. (1972), Nonlinear water diffusion in non-saturated concrete, *Materials and Structures*, Vol. 5, No. 25, pp. 3-20.
- British Standard Institution BS 8203 Part 1, (1996), *Installation of Resilient Floor Coverings*, London.
- Fick, A. (1855), Über Diffusion *Ann Phys*.
- Glendinning, M. (2010), Using accelerating drying on concrete floor slabs to avoid long-term problems to impermeable coverings, Final Year project, BEng, School of Planning, Architecture and Civil Engineering, Queens University Belfast.
- Hedenbland, G. (1996), Drying of construction water in concrete, *Swedish Council for Building Research*, Stockholm, pp. 12.
- Holmes, N and West, R.P. (2002), Moisture Migration in Concrete Slabs during Drying, Floors and Slabs, *Proceedings of the International Congress-Challenges of Concrete Construction*, University of Dundee, pp. 173-180.
- Holmes, N. and West, R. (2003), Moisture re-distribution in concrete under impermeable coverings, in Role of Concrete in Sustainable Development, International Congress on Celebrating Concrete: People and Practice, University of Dundee, eds. R.K. Dhir, M.D. Newlands and K.A. Paine, Thomas Telford Publishing, London, pp. 299-308.
- Kim, J.K. and Lee, C.S. (1999), Moisture diffusion of concrete considering self-desiccation at early ages, *Cement and Concrete Research*, Vol. 29, pp. 1921-1927.
- Neville, A.M. (1995), *Properties of Concrete*, 4th Edition, Addison Wesley Longman Ltd.
- Shimomura, T and Maekawa, K. (1997), Analysis of the drying shrinkage behaviour of concrete using a micromechanical model based on the micropore structure of concrete, *Magazine of Concrete Research*, Vol. 49, No. 181, pp. 303-322.
- Suprenant, B.A. and Malisch, W.R. (1998), Are your floors dry enough for floor coverings, *Concrete Construction*, pp. 671-677.
- Tramex Ltd. (1980), *Moisture Detection Equipment*, Dublin, Ireland.
- West, R.P. and Holmes, N. (2001), Experimental Investigation of Moisture Migration in Concrete, *Colloquium on Concrete Research in Ireland*, pp. 39-44, NUI Galway.
- West, R.P. and Holmes, N. (2003), Finite element modelling of moisture in concrete during drying, Proceedings of the 2003 *Colloquium on Concrete Research in Ireland*, Editors P.A.M. Basheer and M.I. Russell, Queen's University of Belfast, pp. 157 - 165, 5th.
- West, R.P. and Holmes, N. (2005), Predicting moisture movement during the drying of concrete floors using finite elements, *Construction and Building Materials*, Vol. 19, No. 9, pp. 674-681.

THE NEW ENGINEERING BUILDING AT NUI, GALWAY AS A TEACHING TOOL FOR STRUCTURAL ENGINEERING

E. CANNON, J. GOGGINS
College of Engineering and Informatics, NUI Galway

Abstract:

The New Engineering Building (NEB) at NUIG will consolidate education and research activities in the various engineering disciplines into one building which will not only provide a learning environment, but will itself act as a teaching and learning tool. It will serve as a 'living laboratory' for engineering, where live data sets from numerous types of sensors will be used to illustrate structural engineering and building performance concepts in undergraduate teaching and in the development of full-scale research in structural engineering and energy.

This paper describes the instrumentation of several major structural elements in order to provide the interactivity required of the 'living laboratory'. Three elements were selected for instrumentation: a 40-tonne pre-tensioned box beam, a pre-tensioned double-tee unit and a novel precast two-way flat slab system. The processes of gauge selection, arrangement and installation are presented together some preliminary results.

Keywords: concrete, datalogging, double-tee, gauges, instrumentation, precast, pre-tensioned, prestressed, structural engineering, resistance, teaching, vibrating-wire.

1. Introduction

Figure 1 - Artist's impression of completed New Engineering Building at NUI Galway (NUI Galway, 2010).

The New Engineering Building (NEB) at NUI Galway (Figure 1), presently under construction, will unite all engineering activities on campus in a state of the art academic facility by September 2011. In addition to providing the facilities required of a learning environment, the building will itself function as a teaching and learning tool - it will be a ‘living laboratory’ for engineering. Live data sets from a variety of sensors types will be available for use in illustrating structural engineering and building performance concepts in undergraduate teaching, and in the development of full-scale research in structural engineering and energy. The building contains green-building initiatives which will provide working models for students. Several of the building’s constructional elements have consciously been left exposed, as visual learning tools (RMJM, 2008).

This paper concentrates on an aspect of the development of the NEB as a ‘living laboratory’ for structural engineering, dealing in particular with the embedded sensors – both those requiring to be installed prior to erection of structural elements and those fixed during construction on the NEB site. These are fundamental to the development of the building as an interactive teaching tool, reporting on the evolving dialogue of the structure with its environment (Cannon & Goggins, 2009).

2. The building structure

The gross floor area of the NEB is 14,100m^2. The building structure is composed predominantly of concrete, in-situ and precast, with some elements in structural steel. Superstructure loads are transferred to rock through end-bearing piles, while the ground floor slab rests on engineered fill. Some structural aspects of the project which are of particular interest are:

1. the extensive use of ggbs in place of CEM I concrete;
2. 40-tonne prestressed concrete transfer beams, precast by Banagher Concrete (Figure 2), positioned over the main lecture theatres;
3. prestressed double-tee units, precast by Banagher Concrete;
4. the Cobiax flooring system, a two-way spanning, void-formed, flat slab system utilising slabs manufactured by Oran Precast (Figure 3) and providing a high quality exposed soffitte finish;
5. deep structural steel plate girders, fabricated by Duggan Steel;
6. a highly visible structural steel floor suspension system in one corner of the building.

The instrumentation described in this paper refers principally to items 2 and 3 above.

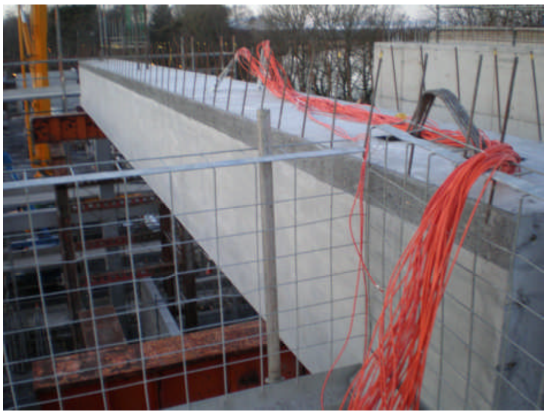

Figure 2 – 40-tonne prestressed concrete transfer beam.

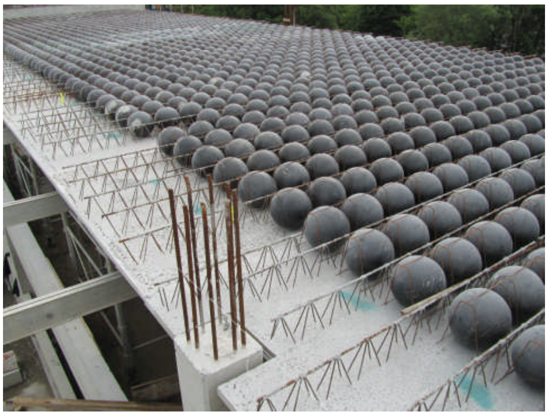

Figure 3 – Void-formed flat slab system prior to installation of top reinforcement mat.

3. Instrumentation:

3.1 Objectives

The general intention was to monitor a many aspects as possible of the response of the selected elements to their environment. This would include response to discrete loading events, time-dependent variation in strain due to creep, shrinkage and temperature change, possible restraint effects in the large transfer beam and in the Cobiax slab, and the load-sharing characteristics of the Cobiax slab.

3.2 Test elements and sensor arrangement

There was a severe time constraint in relation to the purchasing of gauges and datalogging equipment and also a significant time requirement for installation. Due to these factors and to budgetary constraints, instrumentation with embedded sensors was confined to three large-span elements. These were:

(i) a pre-tensioned concrete transfer beam located on the 2^{nd} floor on Grid line L from 3-7 (Figure 4);
(ii) a pre-tensioned double-tee unit located adjacently on the 2^{nd} floor between grid locations D3 to E7 (Figure 5);
(iii) a two-way spanning void-formed flat slab flooring system on third floor between grid locations A9 to C10 (Figure 6);

Elements (i) and (ii) were instrumented with vibrating-wire gauges at Banagher Concrete's premises, while element (iii) was instrumented with both VW and electrical resistance gauges, partly at Oran Precast's premises and partly on the NEB site.

Novel technologies such as fibre-optic sensors and Tensiomag® - for use with prestressing tendons - were explored, but were not feasible in this instance for reasons of time and budget. It is envisaged that additional instrumentation (e.g. accelerometers, inclinometers) will be installed later in the programme to measure aspects of performance in use.

The transfer beam contains 52 VW gauges distributed over 7 sections, five of which are grouped around a concentrated load near midspan, while the other two are near the supports (Figure 4). Most sections contain six gauges - two at top, middle and bottom - but two of the sections contain eleven gauges with the intention of extracting fuller detail regarding strain and temperature variation within the beam. This 970*1200 deep beam is located over one of the main lecture theatres and, given its large mass, its role in the heating and cooling of the space will be of interest.

The double-tee (Figure 5) contains 39 gauges in all - 13 at each of 3 sections. The narrowness of the rib and the arrangement of prestressing strand meant that only one gauge could be placed at any given height within the rib, but there is mirroring of provision between ribs. Nine gauges are arranged across the flange, with the aim of picking up possible variations in compressive strain across the flange, associated with shear lag (Moffatt & Dowling,1975).

Only basic details of the Cobiax units are provided in this paper.

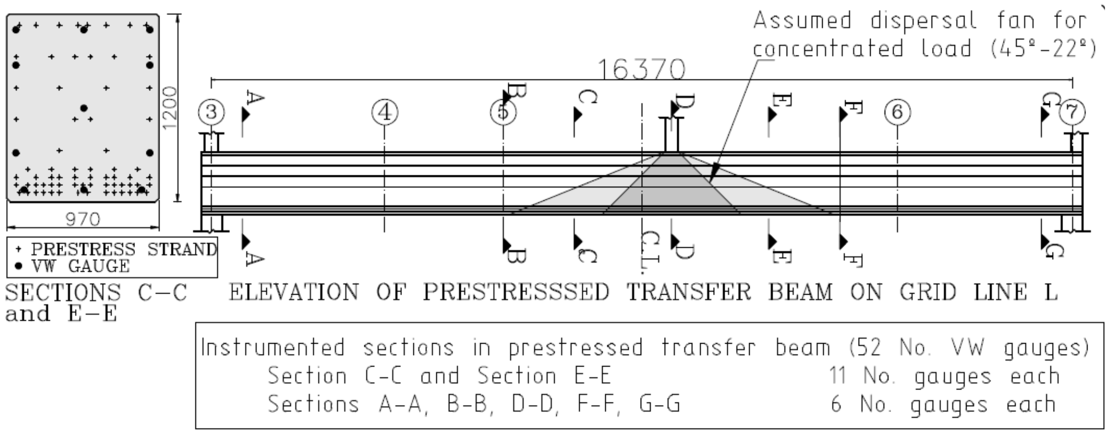

Figure 4 – Instrumentation of the prestressed transfer beam

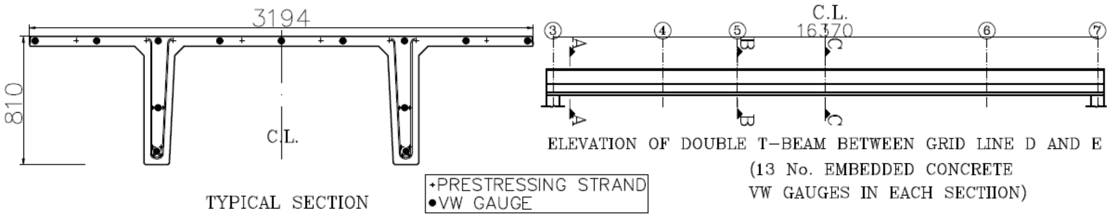

Figure 5 – Instrumentation of the precast double tee unit

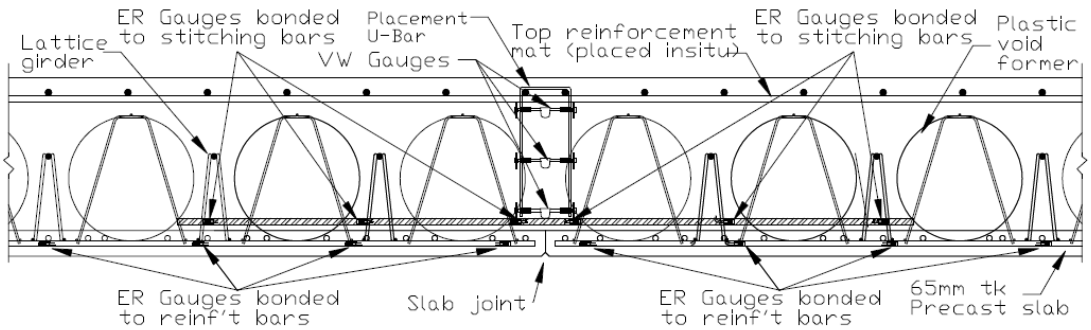

Figure 6 – Typical section of instrumentation in the void-formed flat slab system

3.3 Vibrating-wire gauges

The gauges incorporated in the transfer beam and the double-tee beam are vibrating wire strain and temperature gauges manufactured by Gage Technique, chosen for their robustness and reliability. They are of a type developed originally by the Transport and Road Research Laboratory (TRRL) in the UK (Figure 7) (Tyler, 1968). Vibrating-wire gauges have been extensively used in bridge and tunnelling projects (Tyler, 1973, Mortlock, 1974, Barr et al., 1987, O'Byrne, 1988, Cannon & O'Byrne, 2003). Their long term stability makes them suitable for measuring time dependent phenomena such as creep and shrinkage. Discussions with a specialist structural testing consultant regarding the range of sensor types currently available confirmed the continuing suitability of VW gauges for this task.

The gauge consists of a thin hollow tube of steel with circular flanges at each end. A piano wire inside the tube is stretched between two anchorage points at the ends. A change in the distance between the anchorage points causes a strain change in the wire and a corresponding change in its frequency of vibration. An electromagnet at the centre both plucks the wire and transmits the frequency of vibration of the wire to the recording device, which measures the period for 100 cycles of wire vibration. The gauge is usually operated within the range 500-1000Hz which is equivalent to a range of 2250 microstrain. A 5.5 inch gauge operating at 800 Hz is reported by the manufacturers as having a practical measuring resolution of 1.5 microstrain.

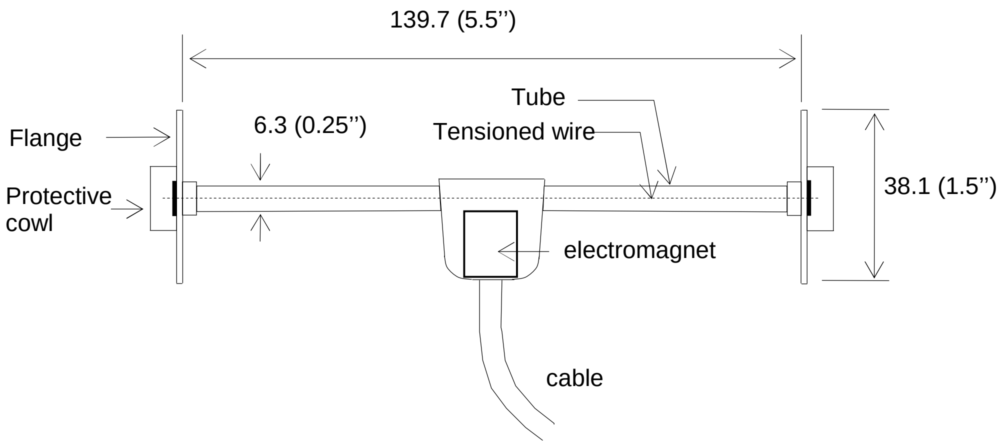

Figure 7 – Vibrating wire gauge.

Figure 8 – Vibrating wire gauges installed in void-formed flat slab in NEB

3.4 Electrical resistance gauges

Electrical resistance gauges (Tokyo Sokki Kenkyujo model FLA-6-120-11-3LT) were used to determine the stresses in reinforcing bars embedded in the Cobiax slabs. These gauges were installed on reinforcing bars in the Civil Engineering laboratory at NUIG at room temperature conditions. The reinforcing bar surface was prepared by removing thee ribs on the bars over a length of 25mm using a milling machine. The gauge was bonded to the bar using P2 TML strain gauge adhesive. A clamp was applied to the gauge and the adhesive was left to dry overnight, after which a VM waterproof tape was applied to protect from moisture and chemicals within the concrete. The reported operational life of the strain gauges and adhesive is a minimum of 30 years. All the gauges were tested in the laboratory before installing the bars on site. The gauges had 3m of 3-wire 0.11mm lead wire pre-connected; up to 15m lengths of 3-wire 0.5mm lead wires were used to connect these to the data acquisition system. The lead wires were installed inside plastic ducting within the concrete.

3.5 Data acquisition system

Campbell Scientific data acquisition system is used to acquire data from both types of gauge. The system for the pre-tensioned beams consists of a Campbell Scientific CR1000 datalogger. This is capable of controlling up to 128 VW gauges or 256 electrical resistance gauges through a series of AM16/32B multiplexers (up to 8 No. off, each capable of controlling up to 16 VW gauges or 32 electrical resistance gauges). In the case of VW gauges, a vibrating wire interface (AVW216) is required for each pair of multiplexers.

3.6 Installation

Installation of VW gauges is a laborious process which has to be fitted in around the work of joiners, steelfixers and general site operatives in preparation for pouring. The time required for installation will limit the scope of the instrumentation project unless the client is prepared for delays which will otherwise occur.

Survival of gauges and cabling is a concern before, during and after pouring. Where possible, cabling was bundled into PVC ducting within the element, and care taken where they emerged from the concrete. In the case of the transfer beam, poker vibrators represented a potential hazard to gauges and cabling, but due to the care taken by Banagher Concrete there was no disablement of gauges on this score. Formwork for the double-tee beam had external vibrators, which presented no risk.

4. Preliminary results

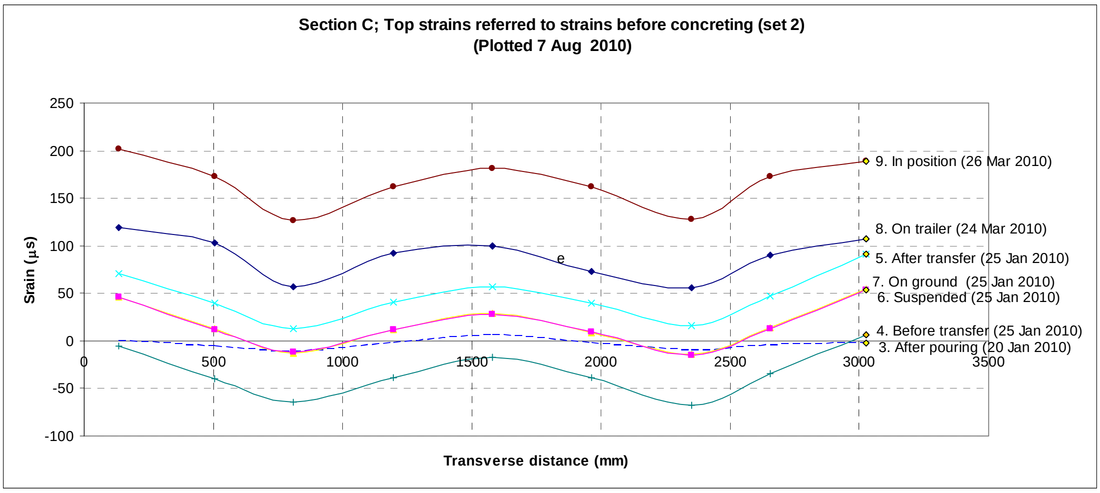

Figure 9. Changes in strain in top slab of double-tee at various dates.

Figure 9 shows strains in the top flange of the double-tee at various times in the first two months after casting. These are referred to a set of readings taken immediately prior to casting on Jan 20th, 2010 (Set No. 2). A set of readings was taken just after concreting, and four sets were taken on Jan 25th, the day on which prestressing transfer occurred and on which the element was lifted from its formwork. Ambient temperature on this day varied between 1.6°C and 3.1°C. Two further readings were taken two months later, one immediately prior to and the other just after placement of the double-tee in its final position.

No detailed analysis has as yet been carried out of these results, but notable features are:

(i) consistency in the variation of strain across the flange;

(ii) little strain change associated with pouring (broken line; Set No. 3);

(iii) development of tension across slab in the 5 days prior to transfer ((bottom line; Set No. 4). There are a large number of factors at play in this period, including significant changes in concrete temperature associated with heat of hydration; variations in ambient temperature; initial shrinkage, with different rates of development in ribs and flange, restraint from prestressing strand and the possibility of a degree of restraint from formwork. The lateral variation in strain – similar to shear lag – increases with distance from formwork. Further study is required of this phase;

(iv) relatively uniform increase in compression across the section at transfer (Set No. 5). There was a nett upward deflection at midspan at this juncture, indicating that the element was transferring from being continuously supported along its length to being supported at its ends;

(v) a reduction in compression when the element was lifted out of the shutters, associated with a reduction in the effective span (Set No. 6);

(vi) virtually identical strains a short time later when the element was lowered onto timber baulks on the ground, located in proximity of the lifting points (Set. No. 7);

(vii) a marked increase in compressive strain in the two months to March 24th, associated with early creep and shrinkage. These readings were taken when the double-tee was loaded onto a trailer prior to delivery to site and supported on timbers (Set No. 8);

(viii) a further increase in compressive strain two days later when the element was lowered into position and end supported (Set No. 9).

Figure 10 shows the variation in strain for all six gauges in the bottoms of webs i.e. at midspan, quarter point and near ends, for the dates mentioned above and referred to dataset No. 2 as before. The time scale is distorted; reading sets 1-3 occur on the same day (set 1 being a partial set relating to web gauges only and taken 3 hours before set 2), reading sets 4-7 occur 5 days later, and sets 8,9 occur two months later. Drawn to scale, the slope from 7 to 8 would be very much flatter than 4-5. Points worthy of note are:

(i) changes in compressive strain are considerably greater than for the flange;.

(ii) readings are highly consistent, notwithstanding the fact that bending moments at the three sections are different, with the greatest changes being noted between sets 8 and 9, when the element was lifted into its final position on site;

(iii) as occurred with flanges, there was little strain change registered for the webs at any of the sections as a result of concreting (sets 2-3);

(iv) there is some tensile strain developed in the webs over the 5 days prior to transfer (3-4);

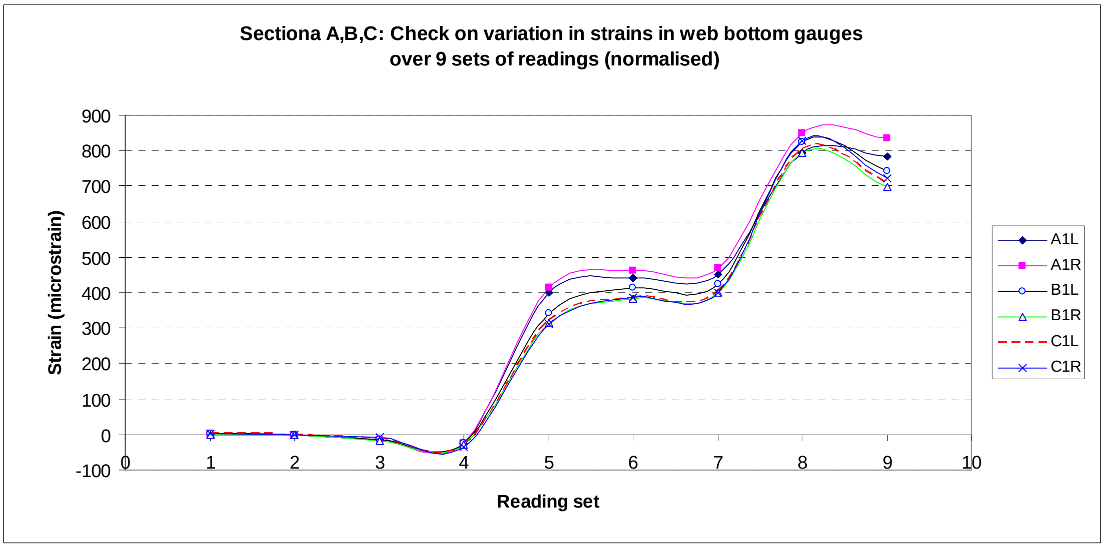

Figure 10. Variation in strain in gauges at bottoms of webs over initial two months.

(v) there is a significant development in compressive strain due to transfer of prestress, notwithstanding that the double-tee assumed its own self-weight loading at this juncture (4-5);

(vi) minor changes in strain resulting from suspension in mid-air (5-6) and lowering onto timber baulks on the ground(6-7);

(vii) significant changes in strain in the following two months, due to creep and shrinkage (7-8). There would not be a corresponding change in concrete stresses;

(viii) a reduction in compressive strain due to the element becoming end-supported on site (8-9).

5. Conclusions

The objective of the project was to instrument several elements in the New Engineering Building so as to provide useful insight into the real time-varying behaviour of concrete structures, for the benefit of undergraduate students and post-graduate researchers. It is considered that the proximity of the instrumented elements to lecturing spaces will confer a degree of immediacy on discussions of structural behaviour and energy performance, encouraging students to actively engage with the underlying engineering issues.

The period to date has been concerned with the completion of the instrumentation scheme, most recently for the Cobiax slab units, as and when the contractor's programme permitted. Instrumentation of the three structural members described in paragraph 3.2 is now complete, and datasets gathered laboriously on Gage Technique's manual data logger have been replaced by frequent and extensive datasets collected on Campbell Scientific dataloggers. Various load tests have been carried out since their installation, and will be reported on later. Whilst analysis of results is at a preliminary stage, results to date display an encouraging level of consistency. Much interesting work remains to be done by way of analysis and ancillary testing before the potential benefits of this project are realised.

Video and photographic records of the process of construction, installation and testing will be of continuing benefit in the education of future engineers in the New Engineering Building at NUI, Galway.

6. Acknowledgements

This support of the New Engineering Building committee, the buildings office and members of the College of Engineering & Informatics (Energy Management Group and Building Structures Group) is gratefully acknowledged. Consultants ARUP and RMJM facilitated us at various stages. The success of a project of this nature is crucially dependent on the cooperation of people on site; in this respect we were most fortunate in relation to the main contractor, BAM Building, subcontractors Banagher Concrete and Oran Precast, and the resident engineer, who facilitated us throughout. The Civil Engineering technicians and postgraduate students at NUI, Galway played major parts in bringing this project to its present state.

References

Barr, B., Waldron, P., Evans, H.R. (1987) ‘Instrumentation of glued segmental box girder bridges’, *Proceedings IABSE Colloquium, Bergamo*, 1987, Monitoring of large structures and assessment of their safety.

Cannon, E., O’Byrne, C. (2003) ‘In-situ instrumentation of concrete structures: a case study’. *Proceedings, Colloquium on Concrete Research in Ireland,* Queen’s University, Belfast, 2003

Cannon, E., Goggins, J. (2009) ‘Teaching tools – Instrumentation of New Engineering Building – Structural Engineering’. *Internal report*, College of Engineering & Informatics, NUI, Galway, 1 December 2009.

Moffat, K.R., Dowling, P.J. (1975) ‘Shear lag in steel box girder bridges’. *The Structural Engineer*, Oct 1975 pp. 439-448 (+ discussion Aug 1976 pp. 285-298)

Mortlock, J. D. (1974) *The instrumentation of bridges for the measurement of temperature and movement*. T.R.R.L. Report LR641, 1974

NUI Galway (2010) *New building*, http://www.nuigalway.ie/civileng/New_Building.html (28th April 2010).

O’Byrne, C. (1988) *The monitoring of strain in a prestressed concrete bridge of box girder construction.* MEngSc thesis, NUI, Galway, 1988

RMJM (2008) ‘*Teaching Tools’*. Project report, RMJM Architects, Edinburgh, July 2008.

Tyler, R.G. (1968) *Developments in the measurement of strain and stress in concrete bridge structures*. R.R.L. Report LR189, 1968

Tyler, R.G. (1973) *Long term strains in the Medway Bridge*. T.R.R.L. Report LR539, 1973.

NETWORK FOR DURABLE TRANSPORT STRUCTURES IN THE ATLANTIC AREA - DuratiNet

A. DALY[1], M. SALTA[2], F. SCHOEFS[3]& A.J. O'CONNOR[4]
[1]National Roads Authority, Dublin, Ireland
[2]LNEC, Lisbon, Portugal
[3]Nantes University, Nantes, France
[4]Trinity College Dublin, Dublin, Ireland

Abstract
The EU Atlantic Area Transnational Programme project DuratiNet is a three year research project (2009 - 2011) which aims to provide Durable Transport Structures in the Atlantic Area. The project boasts 15 partners from across the EU Atlantic Area, i.e. Ireland, France, Spain and Portugal. The backgrounds of partners range from Research Institutes such as the LNEC in Lisbon and the LCPC in Paris, to Universities such as Trinity College Dublin and Bordeaux University to SME's such as BEL and SIKA in Portugal to Infrastructure Owners and Managers such as the Irish National Roads Authority and Portuguese Road and Rail Authorities, to name but a few. These partners have come together under the project DuratiNet to facilitate the efficient exchange and transfer of knowledge in promoting the durability, safety and sustainability of transport infrastructures in the Atlantic Area. The project work packages are focused on (i) development of probabilistic maintenance decision tools for optimisation of repairs in transport structures, (ii) repair/rehabilitation of concrete and steel transport structures, (iii) condition assessment (i.e. using non-destructive and destructive techniques) and uncertainty modelling, (iv) the development of smart and green structural materials with extension to repair products and systems and (v) performance evaluation of repair systems and products. This paper will present the project objectives whilst presentation at the BCRI conference provides the opportunity to provide a mid term review of progress within the work packages of the DuratiNet project.

Keywords: Infrastructure, Concrete, Durability, Rehabilitation

1. Introduction

Transports are among the main development agents of the European economy, and for various reasons, they have a significant environmental impact. In fact, it is one of the main factors of environmental impact in so far as 30% of energy is consumed by transportation, 99% of that energy is derived from fossil fuels which gives the biggest contribution to carbon dioxide increase in the atmosphere. Consequently, in 2001, the European Union, in its white book entitled "European transport policy for 2010" (EU 2001) has drawn up a strategy to promote the development of mixed transportation networks, so as to reduce the environmental impact and to improve the energy efficiency, thus fulfilling Kyoto protocol. This will imply the development of intermodal transportation as an alternative to the current prevalence of road transport.

The implementation of European Union transportation policies (EU 2004) will lead to the construction of new transportation infrastructure at a railway and maritime level and to the need for repairing/rehabilitating the existing infrastructure in order to adapt them to the new transportation policy requirements. Even though the environmental impact of transportation is more directly related with energy consumption and with the associated energy types, it is also associated with other factors depending on the physical and economic sustainability of the varying infrastructure and, is therefore, significantly dependent on the choices made during the construction of new infrastructure or during the repair of existing ones. In fact, the sustainability of infrastructure must be carefully analysed, so that their maintenance will require the least possible cost and ensure a long service life, without the need for major repair/rehabilitation operations.

The project DuratiNet is focused on sustainability of transport structures in the Atlantic Region. Most of Atlantic Coast transport structures are exposed to the marine environment. This environment is of a highly aggressive nature for coastal infrastructure (ports and other structures directly associated with shipping) which are in direct contact with seawater. However, all road and railway structures in the Atlantic regions are (i) subject to the adverse effect of sea mists (ii) are aging and (iii) are deteriorated due to the highly aggressive marine environment which the main structural materials (i.e. reinforced concrete and steel) are particularly vulnerable to. Taking England as a case study, 59% of the country's bridges by number are between 39 and 49 years old, in France 32% of bridges are between 34 and 58 years old (Mahut & Woodward 2005). This aging bridge stock in Europe leads to very high maintenance costs in the Atlantic region.

The economic costs involved in the maintenance and/or repairing of infrastructural elements/networks are high and have strong impact on annual budgets of the owners and management authorities, requiring the development of a hierarchical system to prioritise repairing and maintenance. However, the associated environmental costs are no less significant despite being systematically overlooked. One part of this project seeks to address this problem in a manner discussed in section 2.5.

The development of new infrastructure projects is usually associated with significant investment, but, very often, these projects are analysed by only taking into account the minimisation of construction costs, whereas the service costs related to maintenance and rehabilitation, over the whole life, are in most cases disregarded, and thus fail to be considered in an optimised analysis of the project. In accordance with de Sitter's law (de Sitter 1983) the failure to adopt preventive measures that are to assure the durability of the structures, from the design and construction stage, may imply a 5 times factor increase in future maintenance costs. The DuratiNet project addresses this highly relevant issue of whole life cost optimisation which will positively impact on all the Atlantic areas of the co-operation. By promoting the transfer of knowledge, within the framework of the durability of transport structures, the project is a pioneering initiative with a transnational character in this area, which simultaneously encourages the adoption of joint strategies, both as regards the measures intended to prevent the deterioration of structural materials and as regards the optimisation of the maintenance and repair/rehabilitation actions on these structures.

The project involves the creation of a knowledge network, which is to be a mobilisation interface between research and development centres, the bodies responsible for managing the transportation structures (i.e. stake holders and end users of the research) and the repair companies as well as the companies developing products in this area (i.e. SME's). The project also aims to create an idea-generating network for the development of partnerships aimed at solving specific problems, namely those deriving from emergent needs of the quality control of products and repair systems of transportation structures going forward. This project is an initiative intended to improve the knowledge at different levels of the bodies operating in this area, i.e. research institutes, end users, stake holders and SME's. By adding to the knowledge base of both the efficiency and the serviceability of the repairs of transportation structures and reductions in maintenance costs, the project is expected to contribute to a reduction in the differences in the development of the Atlantic area and to improve the competitiveness of these regions, thus representing a contribution to the cohesive development of the European Union.

2. Project Outline

The main goal of the project is to create a network of excellence called DuratiNet to facilitate an efficient exchange and transfer of knowledge which will promote the durability, safety and sustainability of transport structures in the Atlantic Area. There are a number of short-term and long-term objectives. The short-term objectives which are to be accomplished in the three year duration of the project, will be focused on the development of a work plan geared towards the application of optimised maintenance methodologies for existing transport structures in the Atlantic Area, using durable and more environment-friendly repair materials and systems. The long–term objectives will be mainly focused on the creation of an Atlantic Area Cluster for the development of "Green and Smart Materials", for applications to transport structures, and on the perpetuation of a *Durati* web platform, for durable transport structures, and on the improvement of the data base for the benchmarking of service life models of structural materials, with data coming from previous works of the several partners and from MEDACHS project (Kenshel & O'Connor 2009).

The project will be executed through a partnership which includes 13 partners and 2 associated partners, from 5 countries and 7 Atlantic regions. The partners are as follows: 8 from partner research institutions, 4 from public management authorities in the area of transport, 1 is a non profitable institution for the development of construction science and the 2 associated partners are private companies, one of which is a contractor specialized in repair of structures and the second is a producer of repair products.

Partners from research institutions have different scientific and technical skills in the area of the project and their expertise is complementary. The input of different expertise and complementary skills in the partnership will allow for the revision of knowledge on repair and rehabilitation of structures. The best practices supporting the repair of reinforced concrete and steel transport structures will be examined and the reduction of their environmental impact using more "green" materials or procedures will be analysed according to the demands of the open market and the Construction Product Directives (CPD). Life cycle methodologies for structural materials will be developed and guidelines for the optimization of infrastructure maintenance and repair will also be prepared.

After revision of the knowledge on repair and rehabilitation of structures and by taking into consideration the specific aspects of the structures in the Atlantic Area, it will be possible to develop synergies for a critical identification of new needs, regarding applied research in the field of transport structure repair. The results achieved throughout the project will be used in recommendations for new developments and new research projects from national initiatives in each Atlantic Region or in co-operating activities in different European research and development programmes.

To accomplish the main goals of the project and to reach tangible results five specific objectives were defined. These objectives are outlined below in the sub headings.

2.1 Objective 1: Produce Guidelines on Reinforced Concrete and Steel Transport Structure Maintenance Optimization and Repair Materials

This objective will focus on producing guideline manuals for maintenance optimization and repair materials in infrastructure using universal methodologies and techniques for the optimization of the maintenance, inspection, assessment and repair for transport structures in the Atlantic regions (Figure 1).

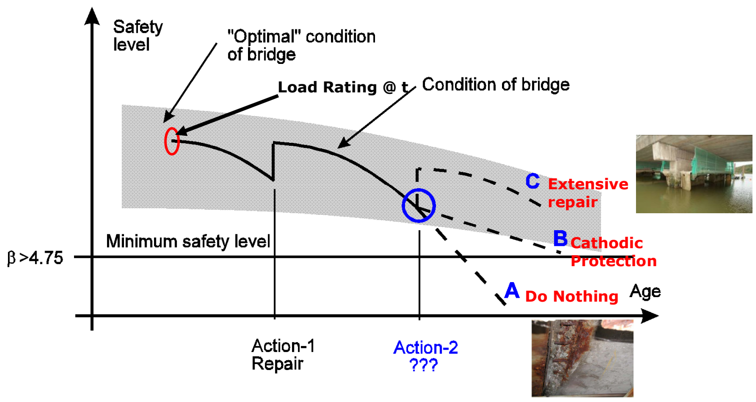

Figure 1 – Reliability based optimisation of maintenance/rehabilitation

Probabilistic models are then developed with a special focus on the spatial distribution. For steel structures in harbours, five zones have been selected and long-term corrosion models have been developed. Figure 2 presents the probability density function (PDF) for depth (mm) or corrosion. A complete reliability study can then be performed. Figure 3 illustrates the evolution of the stess-based limit state for a sheet pile wharf embedded at depth 25 m from the top, for the 95% fractile of corrosion at time 0, 10, 25, 50 years.

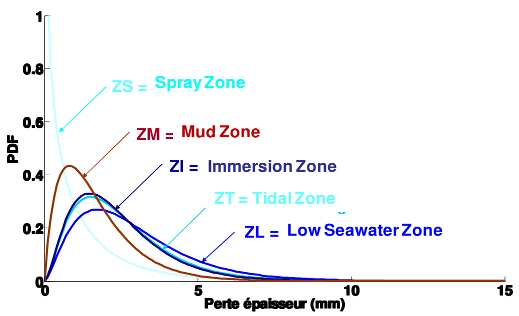

Figure 2 – Distribution of corrosion of steel structures in five areas after 25 years.

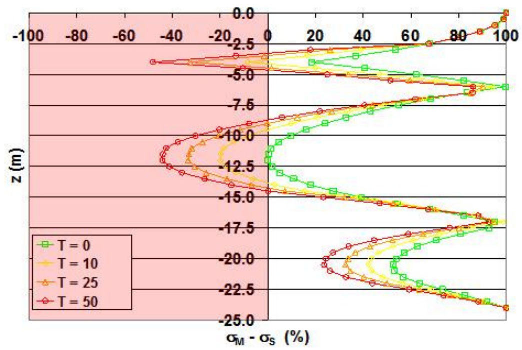

Figure 3 – Evolution of stress-based limit state with depth for a sheet-pile wharf

2.2 Objective 2: Create New Competences in Human Resources Capital at Level of Transport Structure Maintenance

Objective two is aimed at the organisation of different communication actions to promote the transfer of knowledge on repair and rehabilitation of structures. It also aims to create new competences at level of transport structure maintenance for agents with different skills adequate to the development and the application of new maintenance methodologies for efficient and durable repairs on transport structures in Atlantic Area. This will be achieved through regional workshops, and an international congress MEDACHS10/DuratiNet, for the dissemination of DuratiNet guidelines on optimised repair of concrete and steel. Short courses will also be provided concerning quality control and tests for materials and applied product characterization properties which would be of interest to contractors and material producers.

2.3 Objective 3: Identify New Expertise on Applied Research Concerning New Research and Quality Control Needs on Repair Products and Systems

This objective sets out to identify new expertise on applied research concerning quality control needs on repair products and rehabilitation processes coming from the application of the harmonized European Standards. This objective will see exploration into ageing data needs for service and residual life estimations on transport structures and the parameters for evaluation of repairs and environmental sustainability in this context. The work will be primarily concerned with identification of needs for repair products and rehabilitation processes. The objective will also see the analysis of data on evaluation of performance of repair materials and techniques coming from the experimental sites created during the Interreg iiib funded MEDACHS project (2004 - 2006) and their correlation with accelerated tests. Measure of performance generally relies on the assessment of Probability of Dectection, Probability of False Alarm and the building of Reiceiver Operating Characteristic curves. In the project, these concepts are based on the knowledge of the distributions of noise and signal. Figure 4 illustrates these distributions for three protocols P1, P2 and P3 used for the inspection of steel structures in harbours. In figure 4below the loss of thickness of a steel element in the mud zone after 25 years is presented. The plot is based on a long term deterioration model.

2.4 Objective 4: To Develop a Web Platform to Improve the Expertise and Knowledge in Repair Materials Service Life Prediction

This objective will see the construction of a “Web Platform” to facilitate the transfer of existent knowledge on the repair of transport structures and to improve the expertise and the knowledge on service life prediction of materials, including knowledge about performance and ageing of repair materials. It will have areas with free access to technical and scientific community and other areas which will only be used for internal project communication. A Database called (DBDURATI) will also be created containing data from existing structures or from large scale specimens on experimental marine sites, coming from the results of the previous Interreg iiiB MEDACHS (Farrell et al 2009) projects and from the expertise already existent inside the partnership.

For instance for protection of steel structures several techniques have been tested and ranked in view to be introduced in the risk analysis and maintenance optimization (Figure 5).

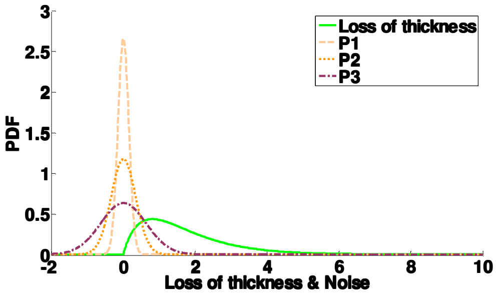

Figure 4 - Distribution of the noise for three protocols and of the corrosion (mud zone after 25 years).

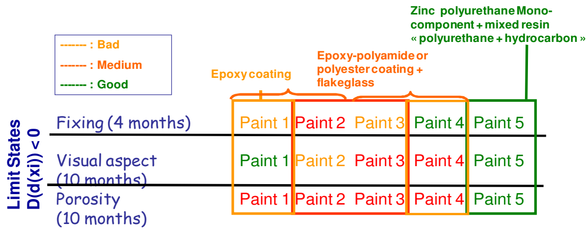

Figure 5 – Ranking of 5 paints following 3 limit states.

2.5 Objective 5: To Promote the Development and use of "Green and Smart" Structural Materials and Repair Products

This objective sets out to promote "green and smart" structural materials and repair products bringing about a reduction in energy needs during material production or application through the incorporation of waste and recycled materials and by-products, with increased long-life performance and without causing harm to workers or users. This objective addresses new challenges and research areas in innovative products for construction and repair.

The objective will incorporate three separate areas of study. The first study will involve a critical review of the use of "green" concrete mixes for new or repaired structures and the use of structural materials with improved durability. This study is concerned with the use of concrete mixes with reduced cement content, with waste products incorporation for encapsulation in concrete of harmful products and the use of recycled aggregates. The direct advantages on the environment at the level of energy consummation will be examined. The study will also examine the implications of these new concretes and repair materials on the performance of concrete structures. The second study within objective five will investigate the use of intelligent structural materials with active properties which address specific problems (i.e. self cleaning concrete and paints) and the use of permanent monitoring systems. The third area of study will examine the use of more resistant reinforcement materials than carbon steel, such as stainless steel and fibre reinforced plastics. These materials will be considered in terms of both repair and their use in new structures as preventive measure to increase the service life of structures.

The development and use of these kinds of products will be essential to promote and to strengthen synergies between environmental protection and economic growth within the area of repair and rehabilitation of transport structures. These activities will contribute to the creation of an Atlantic Cluster for the development of "Green and Smart Materials" and their more intensive use in infrastructure applications.

3. Progress to Date

The BCRI conference coincides well with the mid-term review of progress within the work packages of the DuratiNet project. To date guidelines have been prepared for reinforced concrete and steel transport structures dealing with the damage processes, inspection tests and repair method options for the different damage processes which occur during service life. The guidelines incorporate the relevant European Standards and the specifications used in each of the project's partner countries. Two forms of publications are being produced on the guidelines in order to cater for the different project end users. The first of these publications will contain extensive and detailed information about the damage processes and will describe several inspection tests with particular focus upon non destructive testing, (NDT), which have the ability to identify and quantify the types of damage occurring. This publication will also include a description of repair methods for mitigation of the damage processes which can occur in structures which are subject to the environmental conditions associated with the Atlantic Area.

The second publication will present the guidelines in a simpler format which will be available via an interactive web access system. The system will be based on several toolboxes with defect characterization for reinforced concrete and steel, general descriptions of inspection techniques and the advantages or limitations associated with each technique. The toolboxes will also contain details on the repair methods and the ability of the repairs to resist the various damage processes. It is expected that the web version of the guidelines manual will be completed during the second half of 2010.

4. Conclusions

The EU Atlantic Area Transnational Programme project DuratiNet is a three year research project (2009 - 2011) which aims to provide Durable Transport Structures in the Atlantic Area. As presented in this paper the project work packages are focused on (i) development of probabilistic maintenance decision tools for optimisation of repairs in transport structures, (ii) repair/rehabilitation of concrete and steel transport structures, (iii) condition assessment and uncertainty modelling, (iv) smart and green structural materials with extension to repair products and systems and (v) performance evaluation of repair systems and products. This paper presents an introduction with the presentation providing scope to provide a mid-term review of progress within the DuratiNet project.

5. Acknowledgements

The support of the European Union Interreg Atlantic Area Transnational Program through funding of the DuratiNet research project (Project No. 2008-1/049) is gratefully acknowledged.

6. References

de. Sitter, R.W., (1983), 'Cost for Service Life Optimisation – The Law of Fives', CEB Rilem Workshop Durability of Concrete Structures, Workshop Report pp. 131 – 134.

European Union, (2001), White Paper - "European transport policy for 2010: time to decide", http://ec.europa.eu/transport/strategies/2001_white_paper_en.htm

Farrell A., O'Connor A., Duffy L., Daly A., Kelly J. and Ryan P., (2009), 'Repair, Instrumentation and Monitoring of Ferrycarrig Bridge', *ICE Journal of Bridge Engineering*. Submitted for Publication.

European Union, (2004), EU Decision 884/2004/CE, (2004), eur-lex.europa.eu/LexUriServ/LexUriServ.do?uri=OJ:L:2008

Kenshel O. and O'Connor A., (2009), 'Assessing Chloride Induced Deterioration in Condition and Safety of Concrete Structures in Marine Environments', *European Journal of Environmental and Civil Engineering*, **13(5)**, pp. 593-612. *doi:10.3166/ejece.13.593-613.*

Mahut, B. and Woodward, R.J., (2005). 'Comparison of bridge management practice in England and France', Proceedings of the 5th International Conference on Bridge Management, editor Parke, G.A.R. and Disney, p., Thomas Telford, United Kingdom, pp 163-170.

EXPERIMENTAL INVESTIGATION OF CORROSION-INDUCED CRACK PROPAGATION IN REINFORCED CONCRETE

S. DOWNEY[1], A. O'CONNOR[1] & E. SHEILS[2]
[1]Dept. of Civil, Structural & Environmental Engineering, Trinity College Dublin, Ireland
[2]UCD Urban Institute Ireland, University College Dublin, Ireland
downeysw@tcd.ie

Abstract
The corrosion of steel in reinforced concrete can be considered in two phases – corrosion initiation and corrosion propagation. The rust product which forms on the surface of the steel bar as a result of corrosion has a larger volume than the steel which it replaces and induces tensile stresses in the surrounding concrete, subsequently causing cracking and spalling of the concrete during the corrosion propagation phase. This paper details the results of impressed-current accelerated corrosion testing on concrete slabs made with CEM II and blended cements. The performance of cement is compared based on the crack propagation rate and the extent of corrosion of the steel contained therein. Slabs have been prepared with substitutions of ground-granulated-blastfurnace-slag (GGBS) and pulverised fuel ash (PFA) for PC. The study has found that concrete containing a 30% substitution of PFA slows the rate of crack propagation, when compared with a standard OPC mix. Concrete containing 50% GGBS exhibits worse crack propagation performance to the OPC mix, despite it being acknowledged in the literature that the addition of GGBS inhibits corrosion initiation. However, for a given crack width (1.0mm) the PFA concrete experiences greater loss of steel mass, due to the longer time interval required to reach this width. The difference between PC and PC/GGBS samples is small. Both the crack width and corrosion of the steel must be considered in evaluating the whole-life cost of the structure.

Keywords: Corrosion, crack propagation, blended cements.

1. Introduction

One of the primary functions of the cover concrete in an RC section is the protection of the steel contained therein, particularly from aggressive agencies including chlorides. The most common sources of chlorides in structures are de-icing salts placed on roads, which affect highway structures, and those present in a marine environment. (Beasley 2003, Neville 1995) Chlorides may enter the concrete through either a diffusion or absoption process, (Conciatori et al 2008) which results in the breaking down the alkaline environment and passive layer and, in the presence of moisture and air, corrode the reinforcing steel. (Neville 1995) This is known as the corrosion initiation phase, the first of a two-stage process. As the rust product which forms on the surface of the steel bar as a result of corrosion has a larger volume than the steel which it replaces and induces tensile stresses in the surrounding concrete, subsequently causing cracking and spalling of the cover concrete during the corrosion propagation phase. (Sheils 2008, Beasley 2003) It is this propagation phase that is the subject of this paper.

While considering the effect on the whole-life cost of the structure of corrosion damage, a comparison must be made between the types of construction materials used. In searching for increased resistance to chloride attack, the performance of concretes with pulverised fuel ash (PFA) and ground-granulated-blastfurnace-slag (GGBS) has been examined in the literature (Yasmin 2000, Neville 1995), it is acknowledged that the time to corrosion-initiation can be delayed by the addition of such by-product materials in place of PC, due to both the chemical and physical effects which arise from their use. Of concern here is the chloride binding capacity, the alkalinity of the environment, and the pore structure of the concrete. However, there has not been such a focus on their performance in the corrosion propagation phase and this is an area which this research seeks to explore, to provide a basis for more informed decisions on construction and maintenance strategies, and the optimisation of material use to reduce the whole-life cost.
While the corrosion of the reinforcing steel may result in a loss of load-carrying capacity (Li et al. 2007, Yuan et al 2007, Perno et al 2005) the observations of previous corrosion-test studies (Sheils 2008, Li et al 2007, Vu et al 2005) highlight the serious aesthetic effects of corrosion (cracks and staining) and hence failure in the serviceability limit state may occur long before ultimate failure. Thus, the crack propagation on the surface, as a result of corrosion, is of primary concern here.
The issue of concrete strength has also been addressed in the literature. (Li et al 2007, Allan 1995) Whilst the expanded corroded product induces tensile stresses in the concrete, once the concrete has cracked, the tensile strength no longer governs the cracking behaviour. There is evidence to suggest that an energy-based or strain-based fracture mechanics criterion is more suitable, this will be explored in future research work.

2. Experiment Setup

The chosen accelerated corrosion experiment is the impressed anodic current method, the use of which is well established in corrosion testing. (Poursaee & Hansson 2009, Sheils 2008, Vu et al. 2005) The corrosion is achieved by applying an electric current (in this case, 30mA) to the reinforcing bar, through a current regulator which maintains a constant current over time, which acts as the anode. The cathode is formed by placing a stainless steel bar submerged in NaCl solution and the electric circuit is completed by the pore solution of the concrete, which acts as an electrolyte.

2.1 Concrete Specimens

For the purposes of this investigation, 3 standard concrete mixes were prepared, containing solely OPC, OPC substituted by 30% PFA and PC with a 50% GGBS substitution. The target strength was 42MPa and nominal water/binder ratio was 0.5 (taking into account the water content of the aggregate.) Calcium chloride ($CaCl_2$) was added to the concrete mix, at 3% of binder content. This had the side-effect of accelerating the initial hydration process and resulted in a noticeable loss of workability just minutes after the addition. The mix design is given below, in Table 1. The nominal water/binder ratio is 0.5 in the Saturated, Surface Dry aggregate state, but as the aggregate was dry before mixing, additional water was required.

Table 1 - Mix design, per 1m^3

Material	PC only	PC/PFA	PC/GGBS
Cement	390.000	310.00	190.00
PFA	-	135.00	-
GGBS	-	-	190.00
Water	218.523	198.49	213.89
Fine Aggregate	606.863	607.84	617.65
10mm Aggregate	381.188	376.24	386.14
20mm Aggregate	757.426	757.43	767.33
Density of mix	**2354.00**	**2385.00**	**2365.00**
CaCl2 (3%)	11.700	13.350	11.400

3 No. Slabs of each concrete were cast, each containing 2 No. 16mm. diameter steel bars placed at a cover depth of 25mm. The end of the bars protruded from the slab, so that the electrical connection could be made. Bar spacing was 150mm, sufficient that the cracks from adjacent bars would not interfere with each other, or cause total delamination of the cover concrete. (See Figure 1)

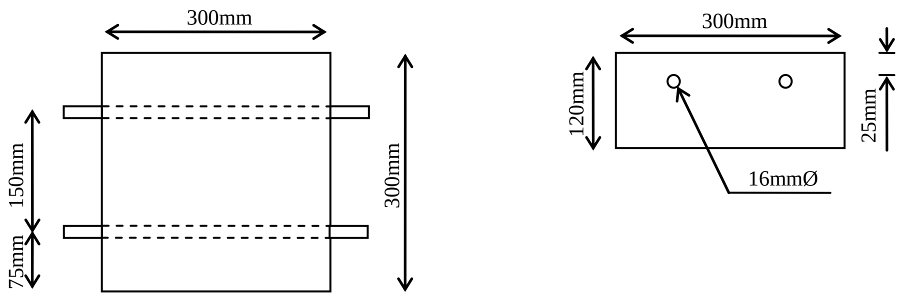

Figure 1 – Concrete specimen dimensions

2.2 Validity of Accerlerated Corrosion Testing

In order to generate cracks within a reasonable timeframe, a corrosion rate of 100µA/cm^2 was chosen. Although this is far higher than a feasible corrosion rate in real-world conditions, there is sufficient evidence in the literature (Poursaee & Hansson 2009, Sheils 2008, Vu et al. 2005) to show that results obtained using such a corrosion rate are still valid, with some consideration taken of the limitations of such an experiment as detailed by Pourasee & Hansson (2009) Specifically, such impressed current tests are suitable for examining the mechanical process of corrosion and cracking, but any observations of the chemical process may not be valid as different chemical products are formed and due to the short time period, there is not sufficient time for diffusion of the ions into the concrete resulting in acidic conditions near to the reinforcing bar. Further, the addition of $CaCl_2$ to the concrete mix to accelerate corrosion makes examination of the chemical constituents of the corrosion product or the contaminated concrete irrelevant, as the results may not be comparable to real-world conditions. However, as the objective of this work is to examine the cracking process, the impressed-current accelerated corrosion method is suitable to obtain the desired results.

2.3 Crack Measurement

The accelerated corrosion test equipment was set up as shown in Figure 2 after the specimens had been cured for 28 days at 20±2^{o}C. The soffit of the concrete specimen was immersed in a 5% NaCl solution to a depth of 20mm, as per Sheils 2008, Vu et al. 2005.)

Figure 2- Experiment setup

Initial crack observations were performed using a magnifying glass, which was continued until a point where a defined hairline crack was visible on the specimen. Once the crack had formed, crack measurement was performed by placing modified linear variable potentiometers across the crack. The potentiometer was fixed to each side of the crack using epoxy resin and the opening of the crack corresponded to a change in resistance of the potentiometer, and hence, a change in output voltage when a 12V input voltage was applied across the potentiometer. This voltage change corresponding to a change in crack width was calibrated against a Linear Variable Differential Transducer and the relationship found to be linear. Thus, an efficient system for measuring crack widths was formed using a data logger, set to record once per hour. Long-term drift and any other anomalies in the electrical circuit were monitored by stationary potentiometers, and found to be insignificant over the life of this experiment.

3. Results from Accelerated Corrosion Testing

3.1 Concrete testing

Upon 28 days curing, the concrete cubes and cylinders were subjected to compression and tensile splitting tests respectively. The results are summarised in Table 2 below.

3.2 Correction of data to constant corrosion rate

After all reinforcing bars had been removed and cleaned, it was found that for each bar, the corrosion rate, i_{corr}, as calculated in Equation 1, differed from the nominal corrosion rate (100μA/cm^2) desired in the experiment.

$$i_{corr} = \frac{(K \times W)}{(0.0166)(A \times T \times \rho_s)} (\mu A / cm^2) \quad (1)$$

where K is a constant, W is mass loss in grams, A is area in cm^2, T is the time of exposurein hours, and ρ_s is the density of steel, as defined in ASTM G1-90.

Hence, a normalisation procedure was performed to enable the data from each specimen to be compared, as per Sheils 2008 and Vu 2005. Experimental times for each crack width were multiplied by:

$$\frac{i_{corr}}{100\mu A/cm^2} \tag{2}$$

to relate them to an equivalent corrosion rate of 100μA/cm^2. The data which follows has been corrected according to this procedure.

3.3 Crack initiation

Approximately 48 hours after the beginning of the experiment, hairline cracks appeared on the surface of the PC and PC/GGBS slabs, directly above the reinforcing bar. Subsequently, similar cracks developed on the PC/PFA slabs after approximately 72 hours. Examination of the side of the specimens also revealed secondary cracks radiating from the bar inclined at 90 degrees to the main surface crack.

3.4 Crack propagation

Once the cracks had developed to a visible state and the datalogging equipment set up, 3600 hours of continuous crack propagation data was collected, with a clear trend to be seen. Over the lifetime of the experiment, the PC and PC/GGBS specimens exhibited similar crack propagation rates, while the PC/PFA specimens showed a slower rate of crack propagation. The results are shown below in Figure 3.

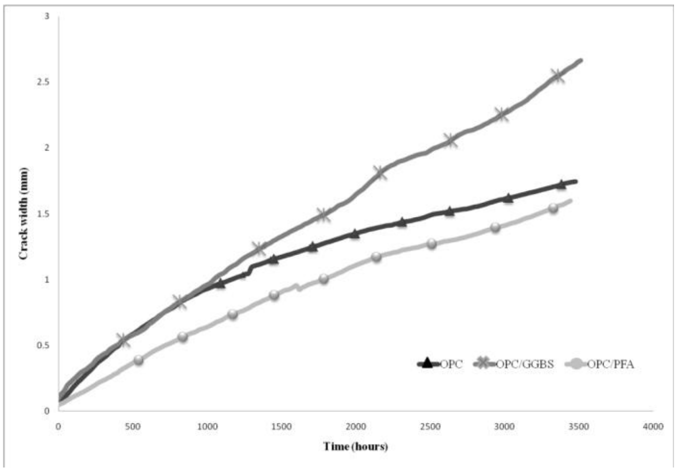

Figure 3 -Average Crack Propagation

3.5 Evaluation at 1.0mm crack width

When one of the specimens of each concrete type had reached an mean crack width of 1.0mm, the specimen was removed from the experiment and the steel bars removed for evaluation. The slabs used in this evaluation were chosen as the middle of the 3 slabs of each type, so as not to skew the average obtained from further crack propagation testing. The bars were cleaned and weighed in accordance with the standard ASTM G1-90 gravimetric weight loss method, and the mass of steel lost to corrosion was compared. The mass lost and the time at which the 1.0mm crack occurred are detailed in Figure 4. As the PC and PC/GGBS slabs reached the 1.0mm crack threshold earlier, less corrosion of the steel bar took place than in the PC/PFA specimen, and less mass loss was observed.

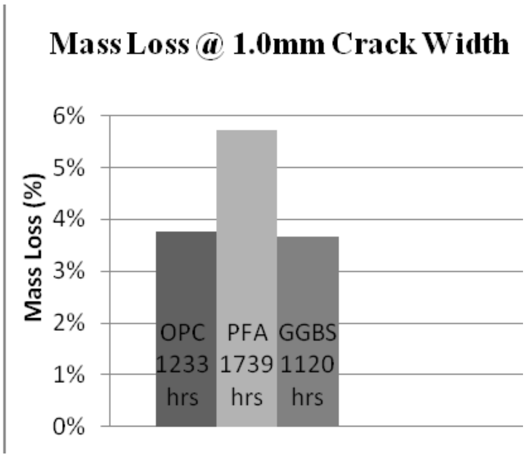

Figure 4 - Mass Loss at 1.0mm Crack Width

3.6 Evaluation after 3700 hours

The remainder of the specimens were removed from testing after 3700 hours of constant corrosion and again, the reinforcing bars were extracted and evaluated as per ASTM G1-90. Observing the remaining concrete slab, it was noticed that there were small pieces of steel which, although uncorroded, had broken free from the surface of the bar due to the surrounding steel corroding and producing a delaminating effect. This may result in a mass loss figure which is higher than the expected corrosion rate (as the steel was lost without being corroded) but the observation is valid as it is not impossible that such spalling may occur in real structures, and has been noted in previous attempts at accelerated corrosion testing. (Vu et al 2005) Figure 5 shows the similar rate of mass loss observed in each specimen, showing a similar corrosion rate was achieved in the specimens. Table 2, below, describes the actual corrosion rates and mass lost in the experiment.
Further, the results of one of the PC/GGBS slabs have been discounted due to an error in the testing procedure which delayed the onset of corrosion significantly. The effect of such a delay is clearly seen in the amount of steel lost over the test period.

Table 2- Measured concrete strengths and corrosion data

Specimen	Slump (mm)	f_c *MPa*	f_t *MPa*	% Steel lost	Loss @	i_{corr}	Time (real) (Hours)	Time (corrected) (Hours)
OPC1	120	47.75 σ=2.042	3.086 σ=0.215	11.86%	3700 hours	94.26	3700	3520
OPC2				3.77%	1.0mm	93.64	1350	1234
OPC3				10.66%	3700 hours	94.69	3700	3531
PFA1	110	45.9 σ=1.948	2.934 σ=0.14	11.59%	3700 hours	93.03	3700	3465
PFA2				10.32%	3700 hours	85.47	3700	3074
PFA3				5.71%	1.0mm	97.92	1700	1740
GGBS1	150	48.5 σ=0.469	2.915 σ=0.386	11.83%	3700 hours	95.71	3700	3571
GGBS2				4.16%	3700 hours	33.82	3700	1238
GGBS3				3.67%	1.0mm	94.65	1200	1120

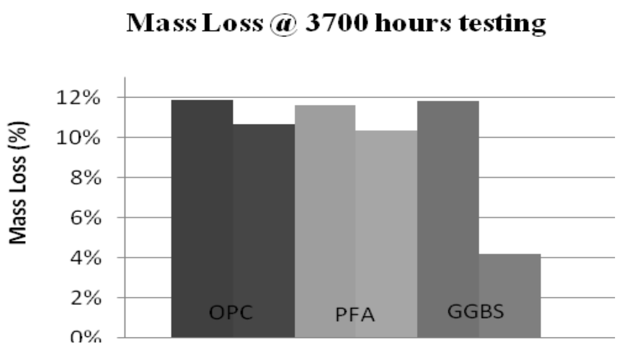

Figure 5 - Mass Loss for each slab after 3700 hours

3.7 Qualitative evaluation

As a maintenance intervention may be prompted due to the appearance of surface cracking, other visual features of the corroded specimens were noted, which may give some indication of the state of the structure. In particular, there was acute staining on the surface of the PC/PFA slabs, where rust product had risen up through the crack and spilled out onto the surface. This was observed to a lesser extent on the PC/GGBS slabs and lesser still on the PC slab. Of note also was the type of corrosion evident on the bars. Although the test is designed to assess general uniform corrosion, on each bar there existed a large area of pitted corrosion, situated directly below the crack, as a result of the greater exposure of this area of steel to the environment. (Figure 6)

Figure 6(a)- Surface staining **Figure 6(b)**- Pitted corrosion

4. Discussion and conclusion

The results of the crack propagation tests show that a concrete made with a 30% PFA substitution developed cracks at the slowest rate, but developed severe staining on the surface as the corrosion product rose through the crack by capillary action. The effect of this action is to reduce the stresses induced in the concrete and hence, slow the rate of crack propagation. That the other concretes did not exhibit such levels of staining suggests that more of the corrosion product tended to permeate into the concrete pores, subsequently filling or blocking them and causing a faster rate of crack propagation upon the development of further corrosion product. This action has been observed in previous studies (Sheils 2008, Allan 1995) and the pore characteristics of the concrete merits further investigation.

Analysis of the mass of steel lost at a crack width limit is also important as regards the application of the findings of this study in bridge maintenance optimisation. As the crack in the PC/PFA slab developed slowest, this also meant that there was time for the greatest amount of corrosion to occur, while the opposite was true in the PC/GGBS specimens. If it is the case that bridge maintenance actions are to be based upon cracks exceeding a particular limit at visual inspection, there exists the trade-off between early intervention when the crack develops at a fast rate (as in the PC/GGBS concrete) and later intervention when the crack is developing at a slower rate (as in the PC/PFA concrete,) then there is the risk that more corrosion of the reinforcing steel has occurred. Hence, there must be an assessment of the acceptable deterioration level of the steel and a serviceability criteria or crack width limit derived from it, (Zhang et al. 2009) which may be unique to the type of concrete being considered.

4.1 Further Research

This experiment was undertaken as part of a wider research project investigating the factors influencing the corrosion propagation phase in reinforced concrete. Future work will include changing the proportions of GGBS and PFA in the mix and variation of the specimen geometry. Consideration will also be given to emerging and specialist concrete technology to ensure that the research remains relevant over the entire lifetime of current and future infrastructure assets.

5. References

Allan, M. (1995) 'Probability of corrosion induced cracking in reinforced concrete' *Cement and Concrete Research Journal,* Elsevier, **26-6,** 1179-1190.

Beasley, K,J; (2003) 'Failure of Exposed Concrete Caused by Corrosion of Embedded Steel' *Journal Of Performance Of Constructed Facilities*, American Society of Civil Engineers, 107

Conciatori, D; Sadouki, H; Brühwiler, E. (2008) 'Capillary suction and diffusion model for chloride ingress into concrete.' *Cement and Concrete Research,* Elsevier, **38** 1401–1408.

Li, C.Q; Zheng, J. J; Lawanwisut, W; and Melchers, R. E. (2007) 'Concrete Delamination Caused by Steel Reinforcement Corrosion' *Journal of Materials in Civil Engineering*, American Society of Civil Engineers, July 2007, **19-7** 591-600.

Neville, A.M. (1995) *'Properties of Concrete, 4th Edition'* Pearson Prentice Hall

Perno, S; Rinaldi, Z; Valente, C; Pardi, L. (2005) 'Experimental evaluation of the load bearing capacity of corroded beams' in *BM5 International Conference on Bridge Management,* University of Surrey, England, 508-516.

Poursaee, A; Hansson, C.M. (2009) 'Potential pitfalls in assessing chloride-induced corrosion of steel in concrete' *Cement and Concrete Research,* Elsevier, **39** 391–400

Sheils, E. 2008 '*Optimisation of inspection planning for structures'* PhD. Thesis, University of Dublin, Trinty College.

Vu, K; Stewart, M.G; Mullard, J. (2005) 'Corrosion-Induced Cracking: Experimental Data and Predictive Models' *American Concrete Institute Structural Journal*, Sept/Oct 2005, **102-5,** 719-726.

Yasmin, A . *'An Analysis of Practices for Concrete Bridge Deck Durability*.' Thesis, Texas Tech University, December 2000.

Yuan, Y; Ji, Y; Shah S.P. (2007) 'Comparison of Two Accelerated Corrosion Techniques for Concrete Structures.' *American Concrete Institute Structural Journal* May/June 2007, **104-3,** 344-347.

Zhang, R; Castel, A; Francois, E.R. (2009) 'Serviceability Limit State criteria based on steel–concrete bond loss for corroded reinforced concrete in chloride Environment' *Materials and Structures* Springer, Netherlands, **42-10,** 1407-1421.

DEVELOPMENT OF STATE-BASED MARKOVIAN TRANSITION PROBABILITIES FOR BRIDGE CONDITION ESTIMATION

T.REALE, Dr. A.O'CONNOR
Dept. of Civil, Structural and Environmental Engineering, Trinity College Dublin, Dublin, Ireland

Abstract

In 2001, the EIRSPAN Bridge Management System (BMS) was introduced in Ireland to coordinate and integrate activities such as bridge inspection, repairs and rehabilitation work. Based on the Danish DANBRO system, the system includes the essential components of a BMS, considering the interrelated activities of inventory gathering, principal inspections, routine maintenance and rehabilitation works required for bridges. To date no optimisation procedures are utilised and instead a simple ranking system which identifies the bridges with the worst condition rating carrying the highest traffic volumes is used to help prioritise maintenance and repair decisions. However given the current economic climate, it is now more necessary than ever to ensure that bridge management is carried out as efficiently as possible. To this end, in 2009, the National Roads Authority of Ireland launched a research initiative with the primary objective of developing a bridge network lifecycle cost model in order to ensure optimal spend of limited budgets. Since the model is to be based on the EIRSPAN system, it has been decided to adopt a Markovian basis for its development. Hence the first step in the development of this model is the calibration of Transition Probability Matrices for the bridge components at a global structural level. This process forms the basis of this paper.

Keywords: Bridge Management Systems, Markov Processes, Transition Probability Matrices

1. Introduction

As bridges progress through their design lives and as volumes of traffic continue to increase unabatedly, bridge maintenance and management have become of increasing concern for governments and highway agencies worldwide as they struggle to achieve the optimum balance between budgetary spend and bridge network condition. Bridge Management systems have been used effectively in recent years to help achieve this optimum balance and at the time the decision was taken by the National Roads Authority (NRA) in Ireland to implement a BMS, several existing systems were examined and analysed including PONTIS (USA), BRIDGIT (USA), DANBRO (Denmark) and other systems developed by individual consulting firms. Ultimately it was decided that a customised version of DANBRO would best suit Ireland's needs and so this new BMS was then called EIRSPAN.

Czepiel (1995) stresses that in order to optimise the maintenance of a network of bridges and to ensure the minimisation of the whole-life cost of the structure, the components need to be repaired before the structure reaches an unsafe condition. In a lifecycle costing analysis, the decisions made at a certain point in time affect the decisions which shall be taken in the future. Therefore owners/managers of structures must not only make a decision based on present budget constraints but also take into account the future consequences and costs of present decisions. Management systems which focus on minimising the lifecycle cost rather than just a point in time cost of maintenance have thus been developed to aid the authorities when choosing maintenance interventions (Corotis et al., 2005). However, in order for engineers to have confidence in these systems, they must be able to reliably and uniformly rank and prioritise the inspections, maintenance and repairs in accordance with what is needed in the bridge network in addition to when exactly it is needed.

At present whole-life costing is technically available on a bridge by bridge basis in EIRSPAN but not as yet on a network level, and as the above research has shown, it needs to be available on a network level rather than a structure specific level in order to ensure optimal use of available resources. Consequently it was decided to further develop the present BMS by introducing a network lifecycle cost model into the system.

2. Types of Bridge Management Systems

Bridge Management systems themselves can be loosely categorised into two groups, (i) Markovian based and (ii) Reliability based. Both are powerful tools for whole-life optimisation of infrastructural networks but given the fact that the developed module needs to be incorporated into EIRSPAN, it was deemed best to adopt a Markovian Basis for developing the bridge network lifecycle cost model.

Markovian Based Bridge Management

Markovian based maintenance management is used in practice as part of existing BMS such as PONTIS and BRIDGIT (Frangopol et al., 2001; Czepiel 1995). As well as these existing BMS, research is continuing in this area to further develop these Markov Decision Processes (MDP) models. According to Scherer and Glagola (1994), ‘’MDP’s are a powerful and useful technique for bridge management systems’’. A Markovian model can be used to predict the deterioration of a structure from one condition state to another over time (Frangopol et al., 2001). With the development of Markov chains (Markov transition matrices) predictions can be made on the level of future deterioration of structures.

A Markov process has the property that the probability of an event occurring (i.e. moving to the next condition state) is independent of past states and only depends on the condition state it is in at the present point in time and the action applied to it (Scherer and Glagola, 1994; Cesare et al., 1992; Ang and Tang, 1984). This is known as the Markovian Property. Also, using a Markov process, the deterioration is modelled as discrete condition states rather than a continuous deterioration process. Although the condition of the structure is recorded using discrete states and at discrete times using a Markovian based methodology (unlike a reliability based approach), the physical process of deterioration of a structure is relatively stable, and inspections and maintenance are carried out at discrete times, therefore the state of a structure is only required at these discrete times (Corotis et al., 2005).
Therefore according to Markov theory:

$$P(t) = P_0 \times P^t \tag{1}$$

where:
$P(t)$ = The probability of being in a particular state i at time t.
P_0 = Initial State Vector
P = The Transition Probability Matrix – an example of which is shown in *Figure 1*.

$$\begin{bmatrix} T_{11} & 1-T_{11} & 0 & 0 & 0 \\ 0 & T_{22} & 1-T_{22} & 0 & 0 \\ 0 & 0 & T_{33} & 1-T_{33} & 0 \\ 0 & 0 & 0 & T_{44} & 1-T_{44} \\ 0 & 0 & 0 & 0 & 1 \end{bmatrix}$$

Figure 1: Example of Transition Matrix whereby the component is only allowed to deteriorate one state at a time and where maintenance and repair are not considered.

The Expected Value of the condition rating of a structure can then be easily computed from these probabilities by simply summing the probabilities of a structure being in each particular state by that state number.

Hence it can be seen that the transition probability matrix P has a huge impact on the overall expected condition rating of a structure. Therefore it is of the utmost importance that these probabilities are as accurate as is inherently possible.

3. State – Based Models

Markovian transition probabilities have been used extensively in the field of infrastructure management in the past. However existing approaches used to estimate these transition probabilities are quite empirical and suffer from numerous statistical limitations, namely being based on constant inspection time intervals and/or the Markov property assumption. Furthermore development of these models has been based on the observed discrete-state deterioration indicators without considering the element-specific but unobserved factors such as impacts from other elements, structural type, material properties etc.

Some of these limitations have been overcome in recent years by using a time-based approach as opposed to a state-based approach. The Markov performance prediction models used in state-of-the-art BMS's are discrete-time Markov Chain models which divide the time scale into fixed periods commonly known as transitions, the transition probabilities then are the probabilities of making each transition in the process. Time based models on the other hand model the system in continuous time and it is the time between the transitions of state which is treated as a random variable and called the "holding time'' (Ng, 1996). Research has shown (Mishalani and Madanat, 2002) that in the absence of large amounts of inspection and monitoring data over a significant period of time there are limits to the accuracy that can be achieved with these stochastic duration modelling techniques. For this reason, since the finished product has to have a real, tangible benefit to both transport officials and society as a whole and since Ireland and indeed many developed countries do not have sufficient data to make this approach economically feasible it has been decided instead to adopt a state-based method as a means of estimating suitable infrastructural transition probabilities within the context of the Irish National Road network.

4. Development of Transition Matrices

In order to develop a Markov Chain, states first have to be developed which can clearly describe the condition of the system and decisions can then be made based on the state a structure is in. As can be seen in Table 1 EIRSPAN assigns all structures in its database a condition rating from 0 (no or insignificant damage) to 5 (the component has failed or is in danger of total failure with possible implications for traffic safety). These states represent the initial condition for the structure in the transition matrix at time t_0. The transition states of a Markov Chain then represent the probability of moving between condition states due to either deterioration or maintenance actions.

Rather than defining a vector which records the state of all bridges in the network being considered (which would result in a very large number of computations), as in Scherer and Glagola (1994), the bridges are classified as a function of construction material, age, environment, loading intensity etc. in order to build up catalogues of groups of data. This reduces the number of possible computations and on this basis a separate Markov model and maintenance management policy is determined for each class of bridge. It is assumed that bridges within a class deteriorate at the same rate, given the same maintenance interventions.

Table 1- Condition States as defined in EIRSPAN
(EIRSPAN System manual No.3, 2008)

Condition State	Description
0	No or insignificant damage.
1	Minor damage but no need of repair.
2	Some damage, repair needed when convenient. Component is still functioning as originally designed. Observe the condition development.
3	Significant damage, repair needed very soon. i.e. within next financial year
4	Damage is critical and it is necessary to execute repair works at once, or to carry out a detailed inspection to determine whether any rehabilitation works are required.
5	Ultimate damage. The component has failed or is in danger of total failure, possibly affecting the safety of traffic. It is necessary to implement emergency temporary repair work immediately or rehabilitation work without delay after the introduction of load limitation measures.

This research project deals specifically with the Irish bridge network, hence while the developed procedures draw heavily on work that has gone before, they are specifically designed for use within the EIRSPAN system for Irish conditions. For instance it can be seen from Table 2 below (Duffy, 2004) that 40.1% of the national route bridge types in Ireland are stone bridges - one of the primary reasons Ireland needed to develop its own BMS as opposed to simply using another country’s system, as for example only 2.4% of the bridges in Denmark are masonry arch structures.

Table 2 - National Route Bridge Types, as in Duffy (2004).

Structure Type	Connaught/ Ulster	Leinster	Munster	Total
Masonry	328	214	335	877
Reinforced and Prestressed Concrete	195	408	284	887
Steel*	17	26	29	72
Corrugated Steel	48	45	30	123
Pipe Culvert	24	30	35	89
Not Registered	30	62	44	136
Total	642	785	757	2184

*Includes composite concrete and steel structures

4.1 Bridge Deterioration

Given the three distinct types of bridge in Ireland (i.e. Reinforced Concrete, Steel and Masonry Arch) and the varying deterioration mechanisms and repair options that apply to each one, different Markov model parameters will be developed for each of the three types.

Deterioration of RC bridges

RC bridges tend to deteriorate by spalling (see Figure 2), cracking, chloride induced corrosion of reinforcement, delamination and carbonation. Proximity to the coast increases the rate of many of these mechanisms since the concrete is subjected to much harsher exposure conditions and so considering Ireland’s significant coastline, distance from the sea is a factor when determining the bridge groupings.

Deterioration of Steel Bridges

Steel tends to deteriorate either by rusting due to the iron reacting with oxygen in the presence of water or air moisture or else by corrosion, often caused by the presence of chlorides.

Deterioration of Masonry Bridges

Very limited data exists for Masonry Arch Bridges in particular. Numerous difficulties exist with these bridges, not least of which is the lack of information surrounding their construction and design. Their performance in general is not well understood and many bridges exhibit individual character and behaviour which naturally makes the development of the Markov processes more difficult. Furthermore several bridges have historic importance which requires a specific management approach. Mortar loss and the height of the arch (see Figure 3) provide some indication of structural deficiency however and these factors will be incorporated into the developed deterioration model.

4.2 Method of Estimating Transition Probabilities

The developed transition matrices reflect the probability of an element (i.e. bridge deck, pier, abutment etc.) moving from one condition state to the next considering the specific physical mechanisms which cause the deterioration.

Previous methods (Jiang et al, 1988) of finding these transition probabilities have included the minimisation of the absolute difference between E(t) the expected value of the structure at time t and S(t) – the condition rating based on linear regression i.e.

Minimize: $\sum_{t=1}^{N} |S(t) - E(t)|$

subject to $0 \leq p_{ij} \leq 1$ for i,j = 1,2,...,n (2)

$$\sum_{i=1}^{n} p_{ij} = 1$$

where:
N = total number of transition periods
S(t) = facility condition at transition period t based on the regression curve
E(t) = expected value of facility condition at transition period *t* based on Markov chains:
However numerous arguments against the above method have already been outlined, not least the fact that it fails to capture the structure of the deterioration process as the change in condition state within an inspection state is not explicitly functioned as a function of explanatory variables. Furthermore, this use of linear regression as a deterioration model is inappropriate as the dependant variable – structure condition is discrete rather than continuous.

Consequently, it has been decided to use Poisson regression modelling for the purposes of developing these transition matrices. Using this model the number of drops in condition state per inspection interval shall be modelled by:

$$p(z_m = j) = \frac{e^{\lambda in} \lambda_{in}^{j}}{j!} \quad , \quad j = 0,1,23,...i, \; i = 1,2,....,k-1 \qquad (3)$$

where:
λ_{in} = deterioration rate of facility n in condition state i
j = number of drops in condition state in one inspection period

In order to develop the deterioration model, the deterioration rate is expressed as a function of explanatory variables X_n (as in Madanat and Wan Ibrahim, 1995) such as age, AADT (Average Annual daily Traffic), environment etc.
The relationship between λ_{in} and the explanatory variables then is given by

$$\lambda_{in} = e^{(\beta Xn)} \qquad (4)$$

where:
β = a vector of parameters to be estimated and
X_n is a vector of exogeneous variables.

As outlined previously the structural stock will already have been divided up into appropriate groups, therefore by adopting this approach one can simulate the different types and rates of both deterioration and maintenance as they apply to each structural group by simply altering the deterioration parameter λ_{in} by giving each structural group, i.e. RC, Steel or Masonry different input parameters to the Beta vector. Hence this Poisson model is exceptionally robust in that it will also allow us to efficiently, economically and accurately simulate the different environments and characteristics of each subset of bridges within each major structural group.

Figure 2: Example of Concrete Spalling

Figure 3: Example of a Masonry Arch Bridge in Co. Kerry, one of only two structures with an initial structure condition rating of 5.

5. Modelling Correlated Bridge Components

Following on from the aforementioned elemental transition matrices, the Markov process will then need to be extended to develop non-stationary transition matrices to consider correlated components within a bridge, i.e. where the condition of one element depends on the state of another element. The EIRSPAN system records a condition rating for each of 13 standard bridge components (i.e. Bridge Deck, Surfacing, Abutments, Expansion Joints, Bearings etc) with an overall rating given to the 14th component (Duffy, 2004). Non-stationary transition matrices are vital to identify the interrelationships, or absence of interrelationships, between these components. They will be a function of the structural form, material, age, environment etc.

Unfortunately a great deal of uncertainty exists when developing these procedures. Firstly, the initial inspection condition ratings themselves can be skewed due to the inherent variability in human perception. Secondly there is also an element of uncertainty associated with each type of maintenance intervention, due to variability in materials, environment, equipment, workmanship etc. To take this into account, the probability that a maintenance intervention improves the condition state of a structure from one state to another will need to be determined and used to update the transition matrix describing the effect of a particular maintenance intervention. The model will also continue to be validated with expert opinion in order to enhance the accuracy and validity of the results.

6. Conclusion

In conclusion, the method outlined above should prove extremely suitable in helping bridge officials in Ireland to better manage their entire bridge stock by enabling them to efficiently compute valid, reasonable expected condition ratings for the complete bridge network. Furthermore it is envisaged that with further work, the procedure could be expanded upon and integrated into a whole-life costing procedure in order to ensure optimal maintenance and repair strategies for the network.

7. Acknowledgements

This research is funded by the National Roads Authority of Ireland (NRA) and the author wishes to express sincere thanks for not only the financial support but also the invaluable help and information they have provided.

References

Ang, A. H-S. and Tang, W. N. (1984). "Probability concepts in engineering planning and design: Volume II, decision, risk and reliability." John Wiley and Sons, New York, USA.

Cesare, M.A., Santamarina, C., Turkstra, C. and Vanmarcke, E.H. (1992). "Modelling bridge deterioration with Markov chains." Journal of Transportation Engineering, 118(6), 820-833.

Corotis, R.B, Ellis, J.H. and Jiang, M. (2005). "Modelling of risk-based inspection, maintenance and life-cycle cost with partially observable Markov decision processes." Structure and Infrastructure Engineering, 1(1), 75-84.

Czepiel, E. (1995). "Bridge management systems literature review and search." *Northwestern University Infrastructure Technology Institute*, Technical Report No. 11.

Duffy, L. (2004). "Development of EIRSPAN: Ireland's bridge management system." *Proceedings of the Institution of Civil Engineers: Bridge Engineering*, 157(3), 139-146.

Frangopol, D.M., Kong, J.S. and Gharaibeh, E.S. (2001). "Reliability-based life-cycle management of highway bridges." *Journal of Computing in Civil Engineering*, 12(1), 27-34.

Jiang, Y., Saito, M., and Sinha, K. C. (1988). ''Bridge performance prediction model using the Markov chain.'' Transportation Research Record 1180, Transportation Research Board, Washington, D.C., 25-32.

Jiang, M., Corotis, R.B. and Ellis, J.H. (2000). "Optimal life-cycle costing with partial observability." Journal of Infrastructure Systems, 6(2), 56-66.

Madanat, S., Wan Ibrahim, W.H. (1995), 'Poisson Regression Models of Infrastructure Transition Probabilities', *Journal of Transportation Engineering*, vol. 121. No 3, 267-272.

Mishalani, R.G., Madanat, S. (2002), 'Computation of Infrastructure Transition Probabilities using Stochastic Duration Models', *Journal of Infrastructure Systems*, vol. 8, No. 4, 139-148.

National Roads Authority, (2008), *'' System Manual No.3 Principal Inspection, Revision C''*

Ng, S.-K. (1996). ''Survival analysis and semi-Markov bridge deterioration modeling.'' Ph.D. thesis, Univ. of Pittsburg, 272.

Scherer, W.T. and Glagola, D.M. (1994). "Markovian models for bridge maintenance management." *Journal of Transportation Engineering*, 120(1), 37-51.

PRACTICAL BRIDGE INSPECTION EQUIPMENT AND TECHNIQUES

THOMAS J. COLLINS
CEI Collins Engineers, Ltd., Dublin, Ireland

Abstract

The evaluation of in-service bridges requires the application of various inspection techniques and bridge engineering judgment backed by experience and expertise. In recent years, following a number of significant bridge failures, the bridge community has greatly expanded its knowledge of the causes and processes leading to bridge damage, distress and deterioration. While an experienced engineer's visual examination is still one of the most important tools in assessing bridge safety, there is often inconsistency between inspectors, and as bridges continue to deteriorate, there is a need for more thorough, repeatable and in-depth bridge inspection techniques to determine structural safety with certainty. While some of these techniques require special expertise, many can be employed by the bridge inspector with little or no additional training. This paper will discuss the advantages, limitations, costs, and criteria for selecting more sophisticated techniques for the inspection of concrete, masonry and steel structures, and for the investigation of scour and undermining at bridges.

Techniques to be highlighted, some of which may be applicable to more than one material or bridge type, include 3D laser scanning, ultrasonic thickness measurement, ultrasonic testing of anchor bolts, dye penetrant crack locating, accelerated low water corrosion (microbial induced corrosion) identification and testing, and impact echo testing. Techniques for identifying and quantitatively measuring scour, infilling of scour holes, and undermining of bridge foundations will include fathometers, underwater acoustic imaging, and sub-bottom profiling.

Practical guidelines will be presented, through actual inspection examples, to aid the engineer in determining if application of one or more of these techniques is appropriate and cost-effective or the inspection of a particular bridge

Keywords: bridge inspection, bridge deterioration, testing, monitoring

1. Introduction

The evaluation of in-service bridges requires the application of various inspection techniques and sound bridge engineering judgment backed by experience and expertise. In recent years, the bridge community has greatly expanded its knowledge of the causes and processes leading to bridge damage, distress and deterioration. While and experienced engineer's visual examination is still one of the most important tools in assessing continuing bridge deterioration and age support the need for more thorough and exhaustive bridge inspection techniques.

Today's bridge inspector must be equipped with a wide range of investigative techniques and equipment. Although they are not sufficient in themselves, specialized techniques and equipment are often necessary to determine structural safety with certainty. The following sections describe some of the more commonly used bridge inspection techniques and equipment that should be part of the modern bridge inspector's toolbox.

2. Scour and Substructure Inspection

2.1 Automated Hydrographic Survey System

There are several types of sounding or depth determination devices available for use during underwater investigations. Most common is the recording fathometer (Figure 1) which uses sound waves reflected from the channel bottom and records the depths virtually continually on a strip chart. It provides an expensive, effective means of recording channel depths but, due to the high frequency used, generally about 200 kHz. will not detect refilled scour depressions. Fathometers which operate at a lower frequency can be used to determine water depths and limited subbottom data; however, subbottom profiling equipment, as described below.

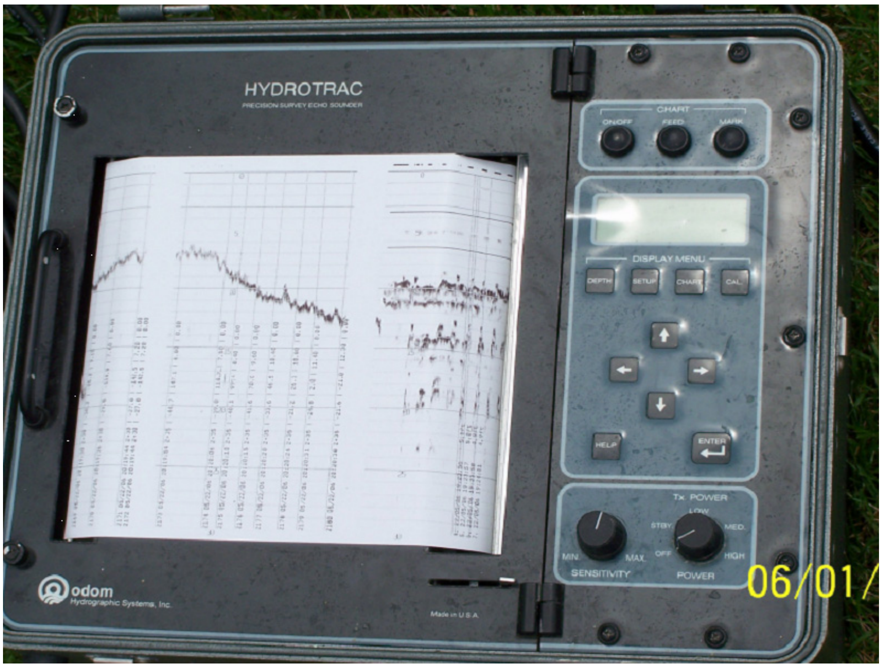

Figure 1 – Black and White Recording Fathometer

More advanced fathometer systems (Figure 2) include a global positioning system (GPS) receiver or a robotic total station. When a fathometer is coupled with one of these devices, water depths can be referenced to a local or national coordinate system. The primary benefit of a fathometer is its ability to develop accurate channel bottom profiles with a low cost, compact, and easy-to-use unit. The profiles can be used to locate and quantify scour depressions, areas of infilling, and channel bottom objects such as exposed footings or debris accumulations. Performing a fathometer survey prior to diving can direct the underwater inspector to potential problems as well as alert the inspector to below water hazards. Overlaying and comparing channel bottom profiles from multiple underwater bridge inspections taken over several years can alert engineers to possible channel related problems.

Figure 2 – Color Recording Fathometer with Transducer and GPS Antennae

2.2 Acoustic Imaging

Underwater acoustic imaging has been used for specialized offshore investigations for many years. Equipment now available provides greatly improved images of channel bottom conditions, undermining and exposed foundation (Figure 3). The use of acoustic imaging can also aid in the planning of diving operations by detecting areas of apparent damage and allowing concentration of diver operations in those areas.

There are a number of different types of scanning sonar devices with varying degrees of accuracy and detail available. Custom built sonar deployment and support apparatuses are used to position and stabilize the sonar unit to allow quantitative measurements of below water configurations, structural deficiencies and scour depressions with accuracy of less than one inch.

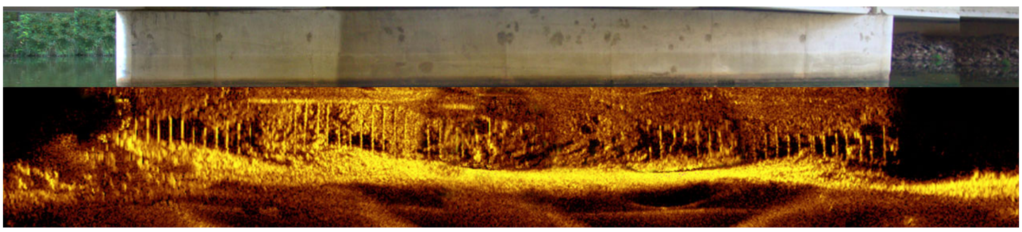

Figure 3 – Acoustic Image of Concrete Pier with Exposed Reinforcing Steel

2.3 Subbottom Profiling

The deepest scour holes will develop around foundation elements during periods of high waterway flow when it may be difficult and unsafe to determine their extent and severity. As water levels recede, scour holes may fill-in, making it difficult to determine, during routine inspections, the deepest scour that has occurred. The infill material will often be less dense than the undisturbed soil, and it may be possible, using subbottom profiling methods such as low frequency sonar and ground penetrating radar (GPR), to determine the maximum depth to which scour has occurred (Figure 4).

In bridge scour evaluations, the method can provide a continuous image of the channel bottom and subbottom sediment, including infilled scour features. High resolution subbottom systems have been used to detect and measure the thickness of dredged deposits, detect hard substrate, and identify buried objects such as cables and pipelines.

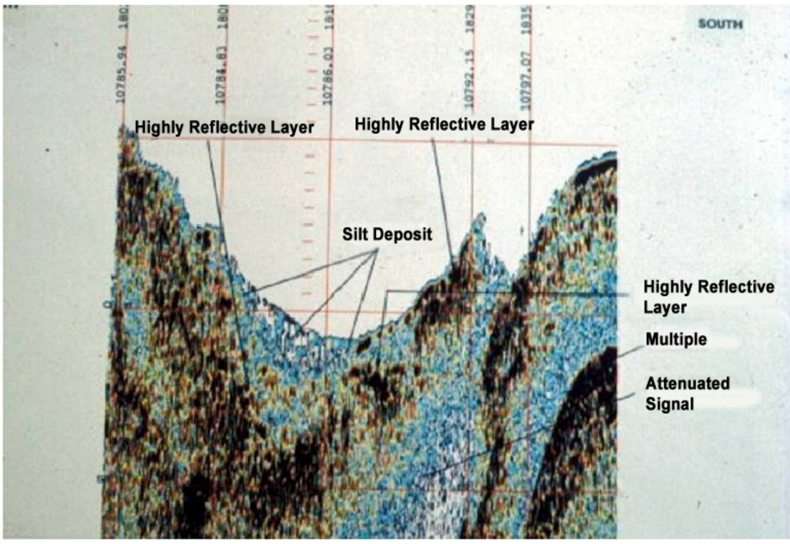

Figure 4 – Subbottom Profile of Scour Hole at Upstream Nose of Pier

3. Superstructure Inspection

3.1 Laser Scanning

Laser canning, also known as 3D scanning, or High definition surveying is a non-intrusive means of rapidly collecting detailed and accurate as-built data. It can rapidly capture high density survey quality data and provide more accurate and detailed as-built drawings than information obtained from manual measurements. It also eliminates the need climbing, ladders or other access equipment. The technology collects information for a structure or area in the form of a three dimensional image made up of millions of data points called a point cloud. Every pair of data points can provide measurements to within 6 mm accuracy. Figure 5 depicts one of hundreds of bridges scanned for Waterways Ireland as part of a program to document the configuration of bridges for which construction drawings were not available.

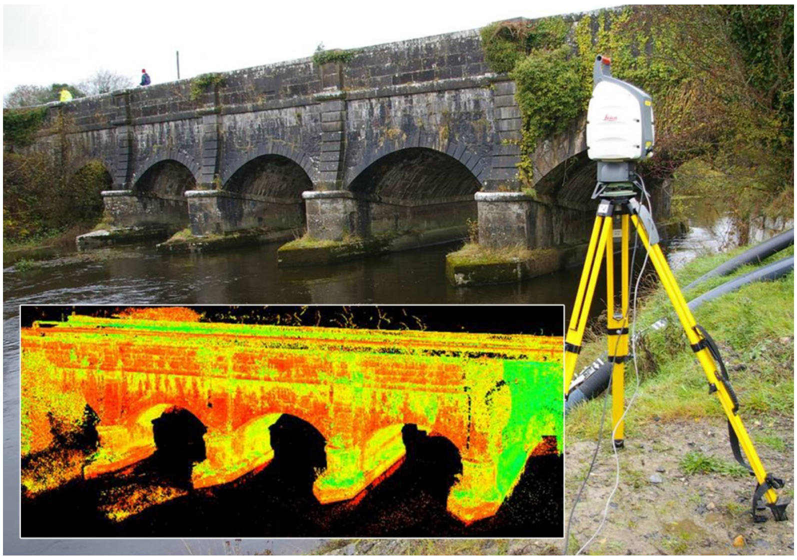

Figure 5 – Scanning Equipment and Point Cloud Data for Multi-Arch Bridge

3.2 Ultrasonic Testing Equipment

Steel Flaw Detection

Ultrasonic testing, as shown in Figure 6, has become the primary method of inspecting in-service pins of pin-and-hanger connections and pinned truss connections because of its ability to locate cracks and wear on the pin barrel without requiring the pin to be removed from the connection.

Figure 6 – Ultrasonic Pin Testing

Steel Thickness Measurement

An ultrasonic thickness measuring device, also known as a D-meter is a digital thickness measuring device. Although it can be calibrated for some other materials, it is generally used to measure the remaining thickness of steel members. It is also commonly used to detect breaks or flaws in anchor bolts. It is a simplified version of a flaw detector, typically using a straight beam transducer and showing a digital readout of the thickness of the member being measures. The transducer is placed on one side to the member to be tested and a sound wave travels from the transducer to the back face of the member, where it is reflected to the transducer. The device measures the travel time for the sound wave and converts it to a thickness. These devices can be used both above and below water as shown in Figure 7.

Figure 7 – Diver Using Underwater Ultrasonic Thickness Measuring Device

Ultrasonic Pulse Velocity Testing

Ultrasonic pulse velocity testing, operating at a much lower frequency than used for steel, may be used to assess the in-place condition of concrete and timber. By comparison to standards, the velocity at which an ultrasonic pulse travels through concrete can be used to estimate its compressive strength. It can also be used to detect areas with hidden defects within a concrete member such as voids, honeycomb, internal cracks and delamination planes. Transmitting and receiving transducers caqn be placed on opposite sides of the member for direct, or through, transmission measurement, or both transducers can be placed on the same side of the member, measuring the velocity along a V-shaped path. Ultrasonic pulse velocity testing, as shown in Figure 8, can also be used to estimate the compressive strength of in-service timber, both above and below water

Figure 8 –Ultrasonic Pulse Velocity Testing of a Timber Pile

3.3 Magnetic Particle Inspection

Magnetic particle testing (Figure 9) is used to locate cracks and damage to steel structures, primarily at welds. This method identifies defects that may not be visible to the eye. It consists of using a portable electromagnet to create a magnetic field on the surface of a steel member to which iron filings have been applied. The filings align with the magnetic field, but defects, such as cracks, are identified by discontinuities in the filing pattern.

Figure 9 – Magnetic Particle Testing of Steel Girder Flange

3.4 Dye Penetrant Testing

Dye penetrant testing is a widely applied and low cost inspection method for locating surface defects in non-porous materials. It can be used in the field to detect cracks in steel and aluminum members and welds, as well as cracks in castings and forgings. The steps involved include cleaning the surface, applying a dye and developed and removing excess dye. Capillary action draws the dye into cracks to aid in their detection.

3.5 Impact Echo Testing

Impact echo testing is a nondestructive inspection technique for concrete structures that can be used to determine the thickness and extent of flaws within concrete. It has been used to locate cracks, delaminations, voids and honeycomb. For bridge inspection work, one of its most important uses is locating voids in grouted ducts of post tensioned concrete girders (Figure 10). With impact echo techniques, rather than make random exploratory openings to locate possible voids, likely void areas can be located, improving the inspection efficiency.

Figure 10 – Inspector Using Impact Echo Equipment to Detect Voids in Grout Tubes

4.0 Summary

The specialized techniques described above are some of the many that are available to today's bridge inspector. Other useful techniques include concrete chloride testing, microbially induced corrosion testing, ground penetrating radar, and magnetic reinforcing steel locators. While their use may not be warranted for all structures, there are instances where they can provide needed information economically and efficient. The bridge inspector must be ready to employ the technology necessary to determine a bridge structure's condition with certainty as part of a good bridge management program. Use of these and similar techniques are essential to managing a cost effective bridge inspection and management program.

COMPOSITE REINFORCEMENT FOR BRIDGE DECK SLABS

G.THARMARAJAH, S.E.TAYLOR, D.ROBINSON & D.J.CLELAND
School of Planning, Architecture and Civil Engineering
Queen's University Belfast, Northern Ireland. BT9 5AG

Abstract

Expansive corrosion in steel reinforcement significantly reduces the design life and durability of concrete structures. Composite materials such as Glass Fibre Reinforced Polymer (GFRP) and Basalt Fibre Reinforced Polymer (BFRP) can provide a more durable alternative to steel reinforcement due to their resistance to corrosive environment, such as those experienced by a bridge deck slab. Replacing conventional steel with composite reinforcement in new structures can be beneficial and reduce the need for bridge repairs and associated costs. FRP reinforcement can be used successfully in laterally restrained slabs by recognising the benefits of arching action. This paper discusses tests carried out on laterally restrained FRP reinforced slabs and details the development of arching action theory and its application.
Keywords: FRP, GFRP, restrained slabs, CMA, corrosion

1. Introduction

In 1989, Wallbank (Wallbank, 1989) published a report based on a survey carried out on 200 U.K motorway bridges representative of 10% of bridge stocks. The report detailed the condition of the bridge structures and the expenditure for maintenance. It was estimated that the UK would spend £616.5 million to repair 10% of the bridge stocks which has deteriorated due to the corrosion of steel. Therefore, the cost to repair for all damaged bridges could be around ten times of the estimated cost or more. This could also be applied at a global level as this issue is applicable to many other countries. Among the 600,905 bridges across the United States, 12.1% of these were found to be structurally deficient (ASCE, 2009). It was estimated that U.S.A would need $8.3 billion/year in order to repair all the structurally deficient bridges due to corrosion damages and indirect costs such as traffic delays and loss of productivity would exceed $83 billion (Koch et al., 2001).

The corrosion in steel reinforced structures needs to be addressed with sustainable and durable solutions. In an attempt to reduce corrosion damage, several measures have been investigated such as high quality concrete which is less porous and less permeable, steel protection methods such as cathodic protection, epoxy coating and waterproofing the decks. However, the effectiveness of these methods in the long term raises concerns over its reliability (Keesler, et al., 1988; Clarke, 1999). There have been research and case studies in the last two decades to investigate the use of alternative durable materials, such as, FRP and stainless steel in reinforced concrete structures.

FRP materials and stainless steel are more durable and less corrosive alternatives to steel in reinforced concrete structures. The FRP materials can be further classified as Glass Fibre Reinforced Polymers (GFRP), Carbon Fibre Reinforced Polymers (CFRP), Aramid Fibre Reinforced Polymers (AFRP) and Basalt Fibre Reinforced Polymers (BFRP). Among these, stainless steel is twice as expensive as GFRP. CFRP and AFRP are also more expensive than GFRP and BFRP. Therefore, based on their availability and cost, GFRP and BFRP can be the most cost effective to replace steel.

2. Significance of the research

Since the 1950's, FRP has been used in the construction industry for strengthening and retrofitting existing structures. In the last two decades FRP has gained scope to replace the steel bars in the design of new non pre-stressed structures. During this period several tests have been carried out by researchers throughout the world to investigate its behaviour in slab, beam and parapet walls (Michaluk, et al. 1998; Benmokrane, et al. 2004; Ospina, et al. 2006). However, the low modulus of elasticity of FRP materials and brittle nature has raised concerns over the serviceability of the structures and ultimate strength. Due to these perceived drawbacks, FRP did not gain significant importance to replace steel. However, when the benefits of Compressive Membrane Action (CMA) are recognised the lower value of elastic modulus is insignificant.

3. Background to Compressive membrane action

Slab and beam bridge decks are one of the most common form of construction in the Europe and the rest of the world (El-Gamal et al., 2007). The deck slabs in these structures experience the beneficial influence of arching action (Tong et al. 1971 & Taylor et al. 2001 etc.). Since these slabs are restrained by end beams, the deflection of the slab needs to be incorporated with the in-plane expansion. The stiffer end beams restrain the in-plane expansion result in compressive membrane action/arching action (Figure 1). The influence of this arching action can be beneficially used in FRP reinforced slabs to enhance its serviceability and strength. A preliminary research by Taylor and Mullin has demonstrated the beneficial advantage of CMA in laterally restrained FRP reinforced slabs (Taylor and Mullin, 2006).

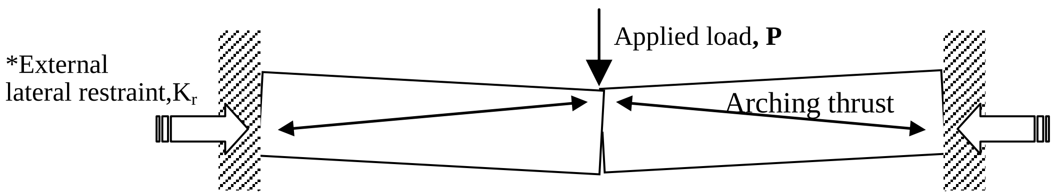

* External lateral restraint will be provided by end beams in bridge decks such as Y-, M- and W- beam and steel girder

Figure 1: Compressive membrane action in laterally restrained reinforced concrete slab

4. Experimental study

The behaviour of one way spanning FRP reinforced laterally restrained concrete slabs was investigated experimentally. The variables were the type of FRP reinforcement, bar diameter and percentage of reinforcement.

4.1 Properties of the materials

Both of the FRP material properties and concrete material properties were verified by testing relevant control samples. GFRP and BFRP bars were tested for tensile strength using an accurately calibrated tensile testing machine. As the FRP bar surface is different to that of steel and its strength perpendicular to the fibre direction is weak, FRP bars require specialised arrangements. A loading rate of 0.2kN/s was used and the FRP bars were coated with an epoxy adhesive to prevent any crushing within the anchorage region and to avoid any slip during the tests. The material values are listed in the Table 1.

Table 1 – BFRP material properties

Reinforcement	Tensile Tests loading rate 0.2kN/s			Manufacturer's reported values loading rate 1kN/s		
	Tensile Strength (MPa)	Elastic Modulus (GPa)	Ultimate Strain με	Tensile Strength (MPa)	Elastic Modulus (GPa)	Ultimate Strain μS
12mm GFRP	682.0	67.4	10120.0	>1000.0	>60.0	16666.0
12mm BFRP	920.0	54.0	17037.0	1200.0	50.0	24000.0

The concrete mix was based on a previous research study which investigated compressive membrane action in high strength concrete (Taylor, 2000). The concrete mix details are provided in the Table 2.

Table 2 – Concrete mix constituents (kg/m^3 concrete)

Target Strength N/mm^2	Cement	Super plasticizer*	Total Water	Total Aggregate	w/b ratio	a/b ratio	20mm agg.	10mm agg.	Sand
60-70	450	9	175	1825	0.38	4.06	639	547	639

***2% by mass of cement**

4.2 Test setup

A steel frame was used to provide the lateral restraint to the slabs and to represent the amount of restrain in a typical slab and beam bridge deck. The frame was tested to assess its lateral stiffness. Two slabs were reinforced with GFRP reinforcement and another two were reinforced with BFRP bars. The details of the test slabs are given in Table 3.

Constructed slabs were allowed to cure for 28 days by providing adequate moisture environment using a wet hessian. Control samples were tested for the compressive strength on the day of slab test and in accordance with BS EN 12390-Part 3. The slabs were tested using a 25mm wide knife edge line load applied at the mid span of the slabs. Deflection of the slabs was measured using 50 mm electronic displacement transducers placed below the loading line at the soffit of the slabs. Two 25mm transducers were used to monitor the movement of the steel frame in the lateral directions. The test setup is shown in Figure 2.

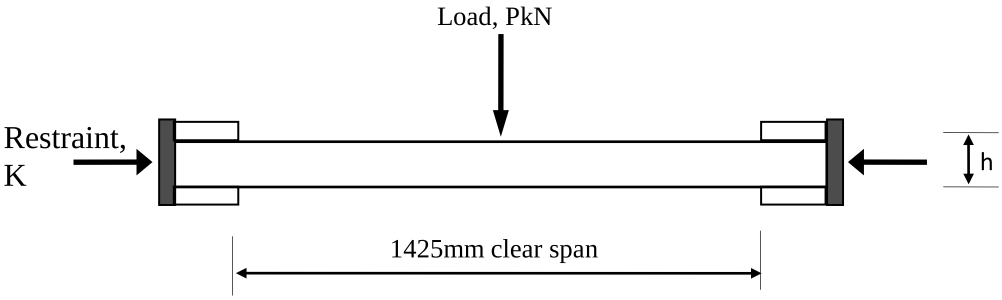

b = 475mm, h = 150mm and d = 117mm for 16mm bar and 119mm for 12mm bar

Figure 2 – Model Test Slab Set-up

Table 3: Test slab details

Test Slab No.	Dimensions of the slab length x width x depth [clear span] (mm)	Rebar diameter (mm)	Rebar percentage	Effective depth (mm)
GFRP 0.6%_12_125 T&B	1765 x 475 x 150 [1425]	12	0.6%	119
GFRP 0.6%_16_300 T&B	1765 x 475 x 150 [1425]	16	0.6%	117
BFRP 0.6%_12_125 T&B	1765 x 475 x 150 [1425]	12	0.6%	119
BFRP 0.6%_16_300 T&B	1765 x 475 x 150 [1425]	16	0.6%	117

A test load, equivalent to 40% of the predicted failure load, was applied to each slab and the recovery measured. The slabs were then tested to failure. Crack widths on the slabs were measured by embedding a vibrating wire gauge across the cracks formed during the test loads. Also, electrical resistance strain (ERS) gauges were used in reinforcing bars to monitor the strain development against applied load.

5. Results and Discussion

5.1 Serviceability behaviour of FRP reinforced slabs

Serviceability behaviour of FRP reinforced slab was a significant aspect of this research as the low modulus of elasticity, bond characteristics and brittle behaviour of the material have been perceived drawbacks in the service behaviour of FRP RC slabs. The load versus deflection characteristics of the slabs are plotted in Figure 3. The load versus deflection behaviour shows that all the slabs have almost similar stiffness up to the service load levels, independent of the type of reinforcement and modulus of elasticity.

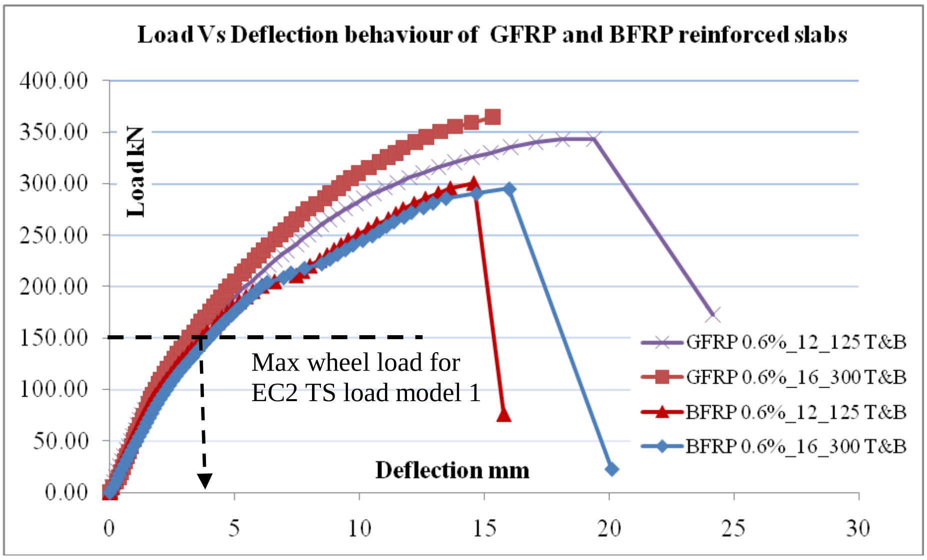

Figure 3: Deflection of the slabs against load applied

Deflections in Table 4 show that none of the tested slabs exceeded the span/350 level at the service wheel load of 150 kN recommended by the EU design code for a tandem system load model 1 (BS EN 1991_Part 2, 2008). Crack widths in the FRP reinforced slabs were below 0.4mm at the service load level. Codes are allowing larger crack widths for FRP reinforced flexural members as the limits are for aesthetics rather than durability as FRP reinforcement will not corrode (CSA, 2002). Although FRP reinforcement has ~25% of the modulus of elasticity of steel bar, these slabs show similar crack widths to previously tested steel RC slabs (Taylor, 2000) and this was due to the benefits of arching action (Figure 4).

Table 4 Summary of the tests

Test Slab	**Concrete strength (MPa)**	**Deflection at 150 kN**	**Maximum strain at 150 kN**	**Deflection at failure (mm)**	**Failure load (kN)**
GFRP0.6%_12_125T&B	68.1	3.5	< 20 % of Ultimate	19.4	343.5
GFRP0.6%_16_300T&B	65.7	3.2	< 20 % of Ultimate	15.4	364.9
BFRP0.6%_12_125T&B	69.3	3.7	< 12% of Ultimate	14.6	300.4
BFRP0.6%_16_300T&B	66.1	4.0	< 18% of Ultimate	16.0	295.1

The strain measurement in each bar show that the strain reached up to 20% of the ultimate strain value under the service load of 150 kN (Table 4). The difference between BFRP strain data and GFRP strain data provided in the table was due to the different ultimate strain value of the materials. In all the cases the strain measurement recorded below 2000 micro strain. This can be compared with the ISIS Canada manual (ISIS,2001) recommendation which states that the serviceability of FRP reinforced structures can be ensured, provided that the strain at service load remains less than 2000 micro strain. Therefore, the slabs can meet all the serviceability requirements.

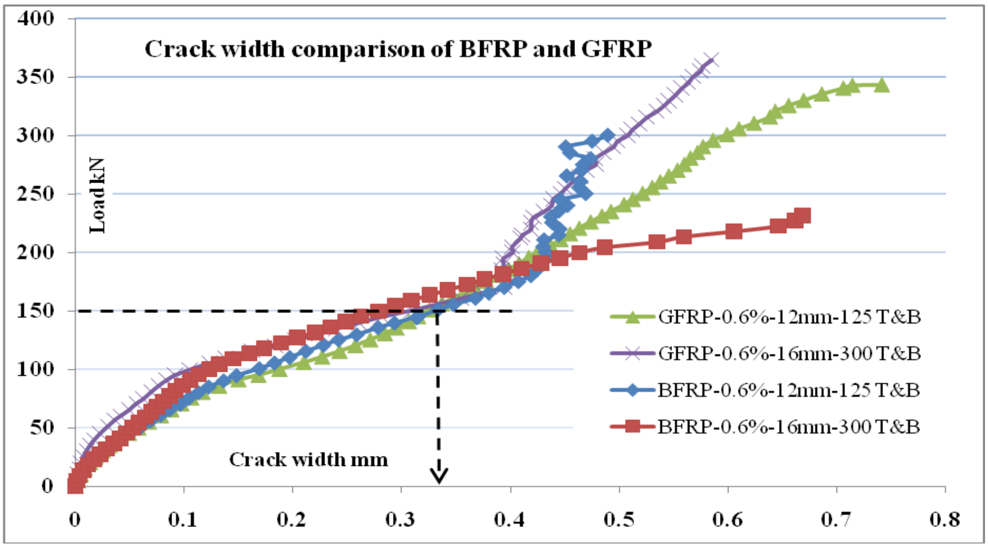

Figure 4: Crack width expansion against load

5.2 Ultimate load behaviour

Due to brittle behaviour, FRP reinforced slabs can fail by FRP rupture. In steel reinforced slabs, the ductility of the steel reinforcement ensures gradual energy dissipation due to yielding of the rebar. However, for FRP reinforced slabs, both the materials are brittle and could lead to a catastrophic failure.

In laterally restrained slabs, the influence of arching action ensures concrete crushing failure at the mid-span regardless of the reinforcement percentage. The typical failure mode of the laterally restrained slab is shown in Figure 5.

Figure 5: Typical failure of laterally restrained FRP reinforced slab

6. Arching action predictions

Arching theory developed at Queen's University Belfast can predict the strength of laterally restrained slabs and the arching action enhances the flexural strength of slabs. The theory was developed based on a spring analogy which takes into account stiffness of the external restraint and the influence of the concrete strength to predict the ultimate capacity of the slab. The arching theory has been found to give more accurate predictions of the ultimate capacity than EC2 (BS EN 1992-Part 2, 2005) for laterally restrained slabs, as the code does not consider the influence of arching action. A comparison of strength predicted by arching theory P_P and EC2, P_{EC} with the test load is given in Table 5.

Table 5 Comparison of strength predicted by arching action theory

Test Slab	P_t (kN)	P_p (kN)	P_{EC} (kN)	P_t/P_p	P_t/P_{EC}
GFRP0.6%_12_300 T&B	343.5	294.2	193.6	1.17	1.77
GFRP0.6%_16_125 T&B	364.9	170.0	272.6	1.34	2.14
BFRP0.6%_12_300 T&B	300.4	284.5	176.7	1.06	1.70
BFRP0.6%_16_125 T&B	295.1	275.3	173.1	1.07	1.70

Table 5 shows that the failure loads predicted by arching action theory is far better than the strength predicted by normal flexural strength calculations. The standard flexural equation is much too conservative for strength predictions in laterally restrained slabs.

7. Conclusion

This research aimed at investigating the beneficial influence of arching action on the serviceability behaviour of laterally restrained FRP reinforced slabs. The following conclusions can be drawn from this experimental and analytical investigation.

1. Both GFRP and BFRP reinforced slabs show improved service behaviour and strength compared to the previously tested and similar steel reinforced slabs (Taylor and Mullin, 2006) due to the beneficial influence of arching action.
2. The tested slabs have demonstrated strengths far in excess of the flexural theory predictions using the current standards.
3. Both GFRP and BFRP reinforced slabs satisfy all the serviceability requirements recommended by various codes such as Canadian Standards, ACI guidelines with even 0.6% reinforcement as it is discussed in section 5.
4. The variation of the ultimate failure load between BFRP and GFRP reinforced slabs was due to the different modulus of elasticity and rupture stress of bars as shown in Table 1.
5. The ultimate failure mode was the concrete crushing at the mid span for all the slabs which can give better warning than FRP rupture.
6. FRP reinforcement can be a durable alternative in bridge decks due to the benefits of arching action providing better serviceability and strength and helping to eliminate the perceived drawbacks of FRP materials.

8. Acknowledgement

The authors would like to gratefully acknowledge the support of Schöck Bauteile GmbH for supplying the GFRP bars and Magmatech for supplying the BFRP bars and technical staff at the university, K McDonald, W McRobers, J Hunter, T Foley and K McKnight.

9. References

ACMA. (2005). *Overview of the FRP Composites Industry - A Historical Perspective*. Retrieved March 19 , 2010, from http://www.mdacomposites.org

ASCE. (2009). *Report Card for America's Infrastructure.* American Society of Civil Engineers.

Benmokrane, B., El-Salakawy, E., Cherrak, Z., & Wiseman, A. (2004). Fibre reinforced polymer composite bars for the structural concrete slabs of a public works and Government Services Canada parking garage. *Canadian Journal of Civil Engineering* , 732-748.

Clarke, J. L. (1999). Fibre-Reinforced Plastic reifnorcement for Concrete. *Current Practice Sheet No.114*.

CSA. (2002). *S806-02 Design and Construction of Building Components with Fibre REinforced Polymers.* Ontario: Canadian Standards Association.

El-Gamal, S., El-Salakawy, E., & Benmokrane, B. (2007). Influence of reinforcement on the beahviour of concrete bridge deck slabs reinforced with FRP bars. *Journal of Composites for Construction, ASCE* , 449-458.

Keesler, R., & Powers, R. (1988). *Corrosion of epoxy coated rebars - Keys Segmental Bridge-Monroe County, Report No.88 - 8A.* Gainesville: Corrosion Research Laboratory, Florida Department of Transportation.

Koch, G. H., Brongers, M. P., Thompson, N. G., & Payer, J. H. (2001). *Corrosion Costs and Preventive Strategies In the United States - Report by CC Technologies Laboratories, Inc.* Federal Highway Administration (FHWA) Office of Infrastructure Research and Development.

Michaluk, C. R., Rizkalla, S. H., Tadros, G., & Benmokrane, B. (1998). Flexural Behaviour of One-Way Concrete Slabs Reinforced by Fiber Reinforced Plastic Reinforcements. *95* (3).

Ospina, C. E., & Bakis, C. E. (2006). Indirect Crack Control Procedure for FRP Reinforced Concrete beams and One way slabs. *Third International Conference on FRP Composites in Civil Engineering (CICE 2006).* Miami, Florida.

Taylor, S. (2000). *Compressive Membrane Action in High Strength Concrete Bridge Deck Slabs.* Queen's University Belfast: PhD Thesis.

Taylor, S.E. and Barry Mullin (2006), 'Arching action in FRP reinforced concrete slabs', Construction and Building Materials, 20, 71-80.

Taylor, S.E., Rankin, G.I.B., Cleland, D.J.(2001), 'Arching action in high-strength concrete slabs', *Proceedings of the Institution of Civil Engineers Structures and Buildings,* Institution of Civil Engineers,Vol.146,4, 353-362.

Tong, P.Y., Batchelor, B de V. (1971), 'Compressive Membrane Enhancement in Two-way Bridge Slabs', *American Concrete Institute*, SP 30-12.

Wallbank, E. (1989). *The Performance of Concrete in Bridges-A Survey of 200 Highway Bridges.* London: HMSO.

Taylor, S.E. and Barry Mullin (2006), 'Arching action in FRP reinforced concrete slabs', *Construction and Building Materials*, 20, 71-80.

SEISMIC ANALYSIS USING THE REAL-TIME HYBRID TEST METHOD

D.P.McCRUM & B.M.BRODERICK
Dept. of Civil, Structural & Environmental Engineering, Trinity College Dublin

Abstract
In this paper, the recently developed real-time hybrid test as a seismic analysis tool is described. The real-time hybrid test method is a test procedure for structural engineering that combines both numerical modelling and simultaneous physical testing, and is highly suited to the investigation of highly nonlinear systems, such as reinforced concrete or composite structures subjected to strong earthquake loads. Force/displacement commands computed from a numerical model are sent to the test actuator. Measured force and displacement responses are fed back from the test actuator at sub-timesteps and provide the information for solving the equations of motion for the numerical structure at the next timestep. In this paper, a real-time hybrid test undertaken on a composite steel and concrete column subjected to a seismic excitation is described. A validation finite element model of the real-time hybrid test undertaken using OpenSees is also presented. Finally, the paper describes an approach to the investigation of the response of the highly nonlinear and rate dependent behaviour in proposed future tests using a real-time hybrid test procedure.

Keywords: Hybrid Testing, Numerical Modelling, Real-time, Substructuring

1. General

The real-time hybrid test (RTHT) method is a newly developed testing technique that combines physical testing with simultaneous numerical modelling. The RTHT was developed from the pseudo-dynamic (PsD) method. The concept of the PsD test was first proposed by Hakuno *et al*. (1969) and was further developed by Takanashi *et al*. (1975). Typically, the important component of the test structure being analysed is physically tested (physical substructure) using high speed actuators, while the rest of the structure is numerically modelled (numerical substructure). The inertia forces and displacements are then fed back from the actuator(s) to the numerical model. The concept of the RTHT method is the same as that of the PsD method, however the test is performed at real-time rather than using the expanded timescale of the PsD test.

When the response of a particular component of a structure is highly nonlinear or rate dependent, it can be difficult to numerically model the component and subsequent structural response with a high degree of confidence. In many situations, the response can only be verified by physical testing. Traditional test methods such as quasi-static testing have the drawback that the component or structure response cannot be rate dependent because the slow rate of loading will not capture the rate dependent behaviour. Test methods such as shake table testing have the benefit that they are fully dynamic, however they are costly to purchase and maintain and have limitations related to scaling of test structure in order to fit payload capacity. The RTHT method is a cheaper alternative to the shake table test method. The critical component(s) to be tested are full scale and tested in real-time thus including rate dependent behaviour.

This paper presents the results of a RTHT undertaken on a composite column at the Structural Dynamics Laboratory at Trinity College Dublin, believed to be the first such test in Europe. Details of a time delay compensation technique for reducing the delay between the imposed command and desired calculated command will be presented. Proposed future testing will be briefly discussed.

2. Real-time Hybrid Testing Key Concepts

The fundamental principle of the real-time hybrid method is based on solving the equation of motion, using physically measured forces and displacements and numerically calculated displacements. Equation (1) gives the equation of motion in terms of the numerical and physical substructures for the RTHT method;

$$M_N \ddot{x}_{i+1} + C_N \dot{x}_{i+1} + R_{N_{i+1}} + R_{E_{i+1}} = F_{i+1} \tag{1}$$

where; M_N is the mass matrix, C_N is the damping matrix, $\ddot{x}_{i+1}$ is the nodal acceleration vector, $\dot{x}_{i+1}$ is the nodal velocity vector, $R_{N_{i+1}}$ is the numerical restoring force vector, $R_{E_{i+1}}$ is the experimental restoring force vector and F_{i+1} is the external excitation force applied to the system. The RTHT procedure and details of the data communication will be discussed further in Section 3.

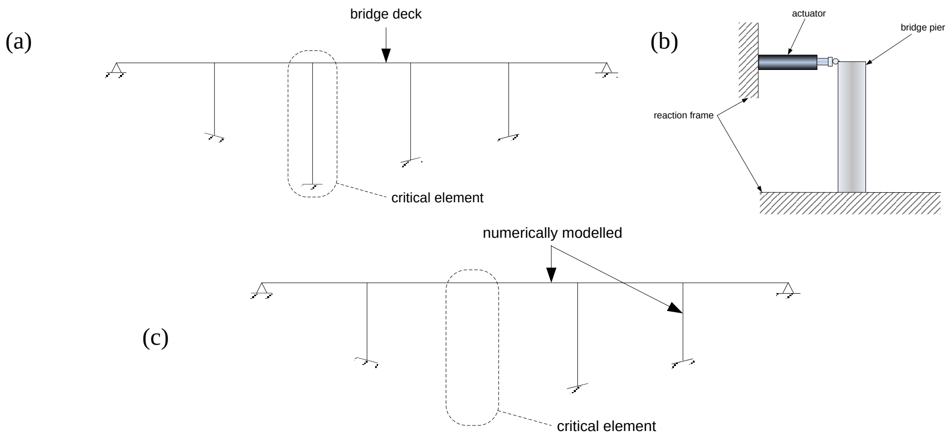

Figure 1 – Substructuring of the Hybrid Test Method (a) Entire Structure (b) Critical Element Test and (c) Numerical Model

A key aspect of the RTHT method is the concept of substructuring illustrated in Figure 1. Figure 1(a) indicates the entire structure being considered, Figure 1(b) indicates the critical element to be physically tested that has a highly nonlinear response and Figure 1(c) indicates the numerical model of the rest of the structure. It can be seen that the substructuring technique has huge benefits, where large scale structures can be both numerically modelled for the less important parts of the structure and physically test only the critical part of the structure. One such substructured test was undertaken on a bridge by Pinto *et al*. (2004) at the ELSA laboratory in Ispra, Italy. Two of the piers were physically tested (substructure) while the remaining four piers, abutments and bridge deck were numerically modelled (numerical substructure). A current development in RTHT is the geographical distribution of the physical test and numerical model, in which a numerical model is run in one location and the commands are sent via the internet to one or more other sites where the physical test in undertaken. Results are then sent back from the physical test via the internet to the numerical model.

2.1 Numerical Integration

As can be seen from Equation (1), the acceleration, velocity and displacement need to be calculated to give the command displacement for a future timestep. A considerable amount of research has been undertaken in the area of PsD and RTHT numerical integration techniques. Some techniques that are widely used in PsD and RTHT methods are the Newmark explicit method or the implicit α-OS method (Combescure & Pegon 1997). In early research into PsD testing, explicit numerical integration schemes were preferred because they were computationally very quick as the computation of the next timestep was based on information from the previous timestep. The issue with explicit integration schemes is that the stability of the method is based on the highest natural frequency i.e. the limit of stability is controlled by the timestep Δt. The method is stable when $\Delta t \leq T_{min}/\pi$; where T_{min} is the shortest period of the structure. The method is termed conditionally stable, but requires a short timestep.

Implicit schemes on the other hand require the acceleration at the end of the current timestep in order to calculate the next timestep. The calculation is achieved using an iterative procedure. The method needs to be very efficient in order to perform the calculation within a short enough time. Implicit schemes are more suitable for complex/stiff structures, when it can be difficult to estimate the highest natural frequency for estimating the required timestep for stability in an explicit scheme. Implicit schemes are unconditionally stable, and therefore the highest natural frequency is not of concern for stability. For this reason, implicit schemes are more commonly used in RTHT.

2.2 Errors and Delay Compensation

There are two main types of errors in hybrid testing; systematic and random. Systematic errors such as actuator force feedback error, or not imposing the command displacement promptly, can cause instability in the system and the test to fail. Other such systematic errors are actuator lag/overshoot. Random errors such as instrumentation noise cause instability but not of the same scale as systematic errors. Systematic errors are of more concern as they can cause rapid numerical failure.

When the system is subject to time delay and actuator lag, the system can quickly become unstable due to cumulative displacement error due to the imposed displacement lagging the desired calculated displacement. Due to the delay, the force measured and fed back is not that corresponding to the target displacement. Therefore, a delay compensation procedure is required to maintain the stability of the test procedure. A simplistic delay compensation procedure is presented in this paper. A RTHT was run and the delay between calculated displacement and actual displacement measured was approx 50ms. A constant 50ms delay was then applied to the calculated displacements in the model and no delay was assigned to the measured displacements, thus aiming to cancel out the delay. The delay causes an increase in the total energy in the system which is the same as that caused by negative damping. If the negative damping is greater than the structural damping, then the response will not converge. Therefore, removing any actuator delay is vitally important for an accurate solution. A more detailed delay compensation technique proposed by Horiuchi *et al.* (1996) using a third-order polynomial to predict the target displacement could be used.

3. Case Study: Composite Portal Frame

The physical test specimen used in the RTHT comprises of a composite column subjected to the N-S component of the El Centro displacement time history. The cross-section of the composite column is shown in Figure 2(a). The composite column is 2.5m in length with 80 N/mm^2 high strength concrete, Grade S275 203UC46 steel section and Grade 460 steel reinforcement. The shear links are 8mm dia. and the longitudinal reinforcement are 12mm dia. bars. The test specimen had been tested to failure in a cyclically loaded quasi-static test prior to the commencement of the RTHT. The idealised portal frame structure being tested and modelled is shown on the left hand side of Figure 3. The portal frame is 2.5m high and 3.0m wide.

3.1 Numerical Modelling Approach

Firstly, the numerical model used to predict the response of the test RTHT will be described. Figure 2(b) indicates the proposed composite column section from the portal frame to be modelled using OpenSees (McKenna *et al*. 2000), an object-oriented framework for finite element analysis. The Giuffré-Menegotto-Pinto Model with isotropic strain hardening was used to represent the steel material properties for both the UC section and reinforcement. The confined and unconfined concrete is modelled as a uniaxial Kent-Scott-Park material with degraded unloading/reloading stiffness and no tensile strength.

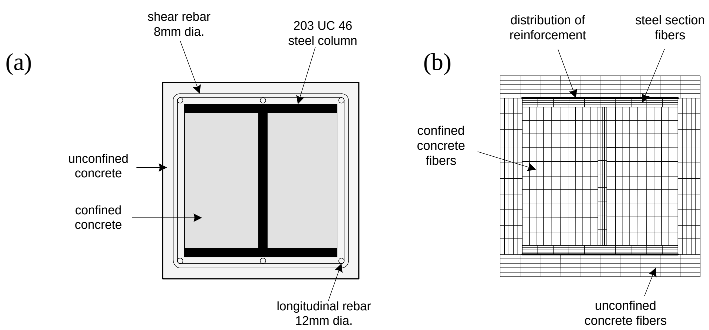

Figure 2 – (a) Composite Section (b) OpenSees Representation of Section

The column element has 7 No. integration sections along its length in order to capture the stress/strain distribution along the element accurately. The finite element sub-division of the section is 5 No. elements across each section and 10 No. elements along the length of each section as shown in Figure 2(b). The number of fiber elements is sufficient to capture the yielding and inelastic strains in the section. The longitudinal reinforcement is distributed along the outside of the steel flange sections as shown in Figure 2(b). The shear reinforcement is not considered. The nonlinear beam-column elements used in the analyses are based on small deformation theory, and the P-Δ effects are considered for the columns.

3.2 Real-time Hybrid Testing Approach

A RTHT was performed on an idealised portal frame structure with two composite columns. Figure 3 indicates the numerical representation of the portal frame in Mathworks Simulink. The Simulink software models, simulates, and analyses dynamic systems. The structural model is a two-dimensional portal frame with lumped masses at the column nodes as shown on the left hand side of Figure 3. The columns and beam are modelled in Simulink using an elastic spring to represent the member stiffness and a dash-pot to represent damping. In Figure 3, the physical substructure is Column 1 and the numerical substructure includes; Mass 1 & Mass 2, Beam 1 and Column 2.

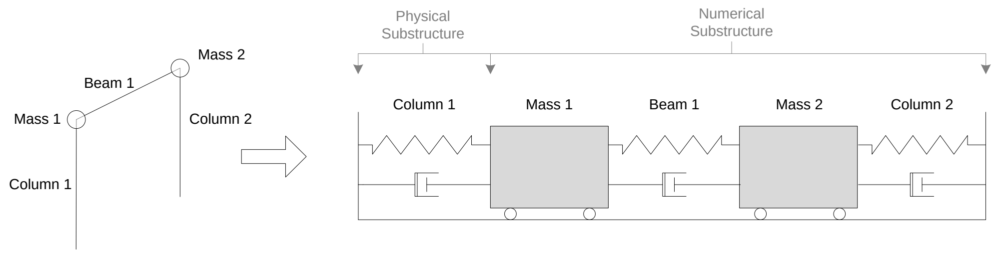

Figure 3 – Two-Dimensional Portal Frame Test Structure and Dynamic Model

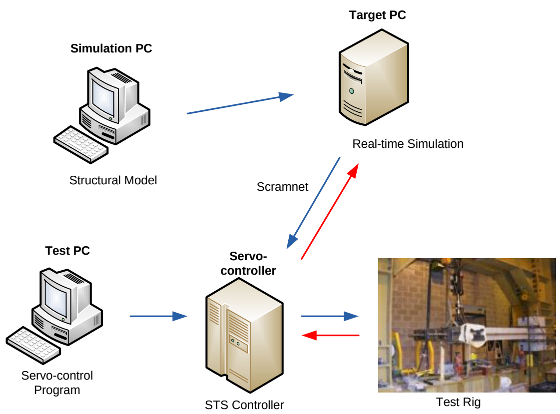

Figure 4 – Schematic of Hardware and Software for the RTHT

The RTHT communication between the hardware and software is shown in Figure 4. In the real-time test, Simulink is used to create the dynamic model of the structure. The structural model is created on the Simulation PC and then downloaded onto the Target PC through a fibre optic cable. The sole task of the Target PC is to run the model in real-time using Mathworks xPC Target. The Target PC has no user interface except for receiving commands from the Simulation PC. The Target PC sends commands to the Structural Test System (STS) controller via the shared reflective memory called SCRAMNet (Shared Common RAM Network). The Test PC provides the user interface to the Servo-controller and allows tuning and control of the actuator through a PID controller. The command force/displacement is then sent from the Servo-controller to the MTS actuator. The measured force and displacement are sent back to the Servo-controller and then back to the Target PC, where the data is used to calculate the next timestep command displacement, making the process close-looped.

4. Results

Figure 5 indicates the displacement command from the RTHT and the OpenSees model displacement. From Figure 5(a) it can be seen that the displacement predicted by the initial OpenSees model (described in Section 3.1) is not an accurate representation of the actual response. Figure 5(b) indicates the OpenSees model with damage incorporated. It can be seen from Figure 5(b) that the displacement predicted by the OpenSees model incorporating damage is a more accurate representation but still slightly overestimated. In OpenSees a zero length element with damage material properties for the steel rebar and section are used to more accurately model the bond slip and strain penetration at the base fixity. The global failure response (e.g. interstorey drift) can be used as the damage criteria, however the localised component damage response is also important. Without the physical test of the damaged specimen, one may have accepted the more simplistic undamaged model response, maintaining the need for testing complex structural problems.

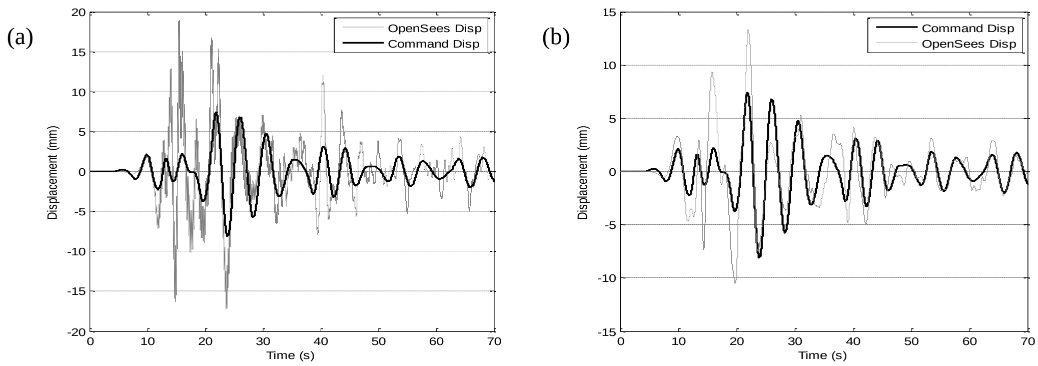

Figure 5 – Graph of Displacement vs. Time for OpenSees Model and Test Command (a) No Damage Modelled (b) Damaged Modelled

Figure 6(a) indicates the calculated and measured displacement when no delay compensation technique was employed. The delay and peak amplitude difference can be seen in Figure 6(b). The delay is 0.0598ms and the peak amplitude difference is 0.0162mm. Figure 7(a) indicates the calculated and measured displacement when a delay compensation technique was employed. The delay and peak amplitude difference can be seen in Figure 7(b). The delay is 0.052ms and the peak amplitude difference is 0.018mm. The delay compensation technique used did not have an effect on the delay. The delay compensation technique did have an effect on the maximum amplitude of the responses in which the delay compensation method resulted in larger amplitude. The difference in response can be seen when Figure 6(a) and Figure 7(a) are compared.

(a) (b)

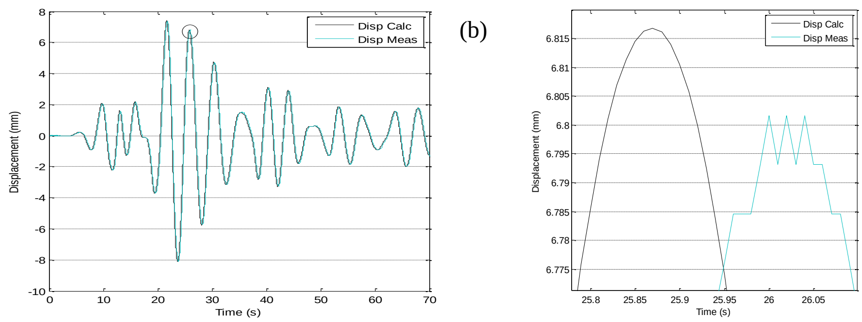

Figure 6 – Graph of Displacement vs. Time for Calculated and Measured Displacement with No Delay Compensation (a) Full Time History Response and (b) Close-up of Selected Peak

(a) (b)

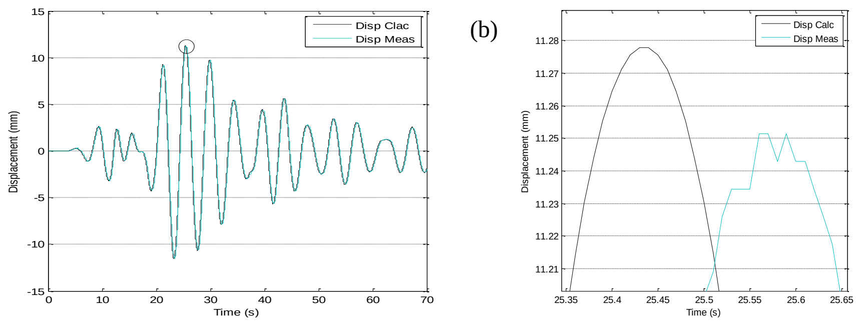

Figure 7 – Graph of Displacement vs. Time for Calculated and Measured Displacement with Delay Compensation (a) Full Time History Response and (b) Close-up of Selected Peak

5. Proposed Future Work

Figure 8 indicates the proposed RTHT to be carried out at the Trinity College Structures Laboratory using the hybrid test system. The Authors current research area is the numerical modelling and testing of concentrically braced frames. In Figure 8, the bracing members in the bottom storey of the multi-storey building suffer the greatest damage and are difficult to accurately model due to highly inelastic and rate dependent behaviour. It is proposed that the bottom storey braced frame will be tested as per Figure 8 (b) and the data from the test fed back into the numerical model. The hybrid test will provide more accurate information on how the multi-storey structure will respond as compared to a purely numerical model. Future testing will require a more detailed delay compensation technique than assigning a fixed delay as presented here.

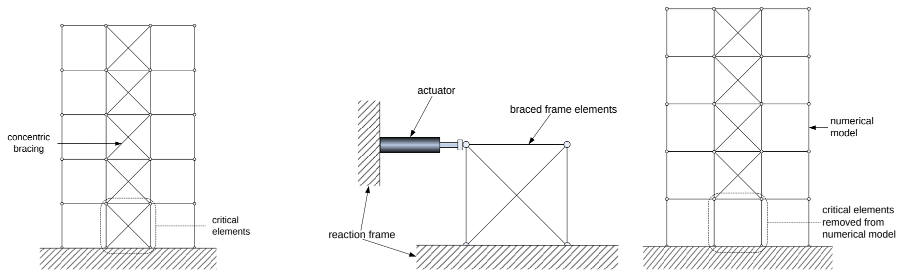

(a) Entire Structure (b) Critical Element (c) Numerical Model

Figure 8 – Proposed Hybrid Test Set-up

6. Conclusions

The RTHT method is a powerful procedure for dynamically testing a structure at full scale. The initial numerical model predicted the response of the damaged test specimen poorly, as would be expected when damage is not explicitly considered. When damage was incorporated in the model the results indicated a more accurate model, however the response was still somewhat overestimated. Thus, physical testing remains a key component for accurate prediction of complex structures. The simplistic delay compensation technique used in this study was found to have an insignificant effect on reducing the delay between the command and feedback displacement. The assumption that the delay will remain constant throughout the test is over simplistic and a more detailed delay compensation technique must be applied in future work.

Acknowledgements

This material is based upon work supported by the Irish Research Council for Science Engineering and Technology. The Authors would like to thank John Deenihan for the use of his test specimen and the Technical Staff for their help in performing the tests.

References

Hakuno, M., Shidawara, M. & Hara, T. (1969) Dynamic destructive test of a cantilever beam controlled by an analog-computer. *Trans. Jpn. Soc. Civ. Engrs*.:**171**, 1-9.

Horiuchi, T., Nakagawa, M., Sugano, M., & Konno, T. (1996). “Development of a real-time hybrid experimental system with actuator delay compensation.” *In Proc. 11th World Conf. Earthquake Engineering*, Paper No. 660.

McKenna, F., Fenves, G. L., and Scott, M. H. (2000). Open system for earthquake engineering simulation, University of California, Berkeley, Berkeley, CA 94720.

Pinto, A. V., Pegon, P., Magonette, G. & Tsionis, G. (2004) Pseudo-dynamic testing of bridges using non-linear substructuring. *Earthquake Engineering & Structural Dynamics*, **33**:11, 1125-1146.

Takanashi, K., Udagawa, K., Seki, M., Okada, T. & Tanaka, H. (1975) Non-Linear Earthquake Response Analysis of Structures by a Computer-Actuator On-Line System (Part 1 Detail of the System). *Transcript of the Architectural Institute of Japan*, **229**.

SEISMIC PERFRMANCE OF HIGH STRENGTH CONCRETE COMPOSITE COLUMNS SUBJECT TO INELASTIC FLEXURAL LOADING

J.E.DEENIHAN[1], B.M.BRODERICK[1]
[1]Department of Civil, Structural & Environmental Engineering, University of Dublin, Trinity College, Dublin, Ireland.

Abstract
An experimental investigation is undertaken to assess the seismic performance of high strength concrete (HSC) composite columns subjected to combined axial and cyclic lateral loading conditions. Current European design rules (Eurocode 8) require a concrete strength class between C20/25 - C40/50 N/mm^2 to be specified in dissipative zones of a composite structure. The aim of the research presented in this paper is to determine the conditions for which HSC (f_{ck} > 40N/mm^2) composite columns can be used in earthquake-resistant moment-resisting frames. This experimental programme is supported by the development of a numerical model based on Mander's stress-strain model to effectively determine the moment-displacement response of the composite section and the associated axial strain demands. The model is validated against the experimental data and it is shown to display good correlation with the results of the HSC experimental programme.

Keywords: Composite Column, High Strength Concrete, Inelastic Behaviour, Analytical Modelling

1. Introduction

Capacity design is based on the fundamental ability of structural elements to undergo large deformations within the inelastic range of material response. Structures subjected to seismic excitation require appropriate design and detailing to ensure adequate strength and ductility capacity of key members within the critical regions. The seismic energy dissipated is directly proportional to the ductility capabilities of the member. Composite columns provide superior axial and bending capacity compared with traditional reinforced concrete members. Member ductility is also vastly improved due to the high proportion of structural steel which is far more ductile than the brittle nature of concrete. The ductility and energy dissipation capabilities of fully-encased composite members incorporating normal strength concrete (NSC) has been widely investigated in recent decades [Wakabayashi (1987), Brettle (1973), Ricles & Paboojian (1994)]. Previous research has clearly identified the attractive performance of such structural members and has been implemented in earthquake resistant design codes worldwide.

Relatively little research has been covered into the area of high strength concrete (HSC) composite columns, but the seismic performance of these members is uncertain due to the inherent brittle nature of HSC. Composite columns incorporating HSC require careful detailing to effectively confine the core concrete, thus ensuring that the material ultimate strain is maximised thereby increasing the section ductility. Composite columns subject to axial and repeated cyclic loading depend on the combined performance of steel and concrete to withstand the applied loads. Concrete becomes more brittle as its strength increases, which contradicts the ductility requirements for dissipative seismic members. Some research is available for HSC composite columns subjected to repeated cyclic loading [El-Tawil & Deierlein (1999) and Chen et al (1992)], but as of yet the current European seismic design code [Eurocode 8 (2004)] is limited to a maximum concrete compressive strength of f_{ck} = 40N/mm^2.

This paper discusses the results of a series of tests conducted on a range of composite columns designed and detailed according to the current European practice [Eurocode 8 (2004)]. The experimental study focuses on the performance of fully-encased composite columns, of varying concrete compressive strength, subjected to axial compressive and lateral cyclic loading. Six such tests were carried out under major axis bending and subject to a constant axial force. Furthermore a computational model addressing the response of reinforced concrete under axial compression is modified to incorporate the effects of combined axial and lateral cyclic loading imposed on a composite cross section.

Subsequent sections of this paper set out a description of the experimental set-up together with details of the test specimens. The main experimental results are then presented and significant observations are summarised. Finally, the accompanying model is briefly introduced and its results compared with those obtained in the experimental programme.

2 Experimental Details

2.1 Testing Arrangement

The test set-up illustrated in Figure 1 (a) & (b) was designed to impose a constant axial load which followed the central movement of the specimen while it was subjected to increasing lateral displacements of increasing amplitude. The specimens were all subjected to strong axis bending. Figure 1 presents a schematic image of the reaction frame complete with in-situ specimen and all associated loading apparatus. The specimens were tested in a horizontal position to facilitate placement in the limited head-room. Four 900 kN capacity jacks were used to simulate the axial load, they were each connected to high strength McAlloy tension bars, which in turn reacted into a cross beam at one end of the specimen and outside the reaction frame at the base end, this cross beam in turn transmitted the applied loads into the reaction frame as illustrated below. The axial load was kept constant throughout each test but varied between tests.

The restraint illustrated in Figure 1 (a) was designed to prevent lateral displacement in the direction perpendicular to that of the load applied by the MTS actuator. It consists of a steel section, rigidly connected to the reaction frame, with a set of rollers resting against the vertical concrete faces of the test specimens. These rollers prevent movement in the horizontal direction and prevent any additional moment being required due to frictional effects.

The lateral load was applied using an MTS hydraulic actuator, operated under displacement control to simulate seismic loading at a height of 2.5m above the base of the column. The actuator had a 150 kN capacity a ±125mm stroke. The amplitude of displacements, Δ corresponded to displacement ductility demands of μ = 0.25, 0.5, 0.75, 1.0, 2.0, 3.0 and 4.0 in successive sets of cycles, where $\mu = \Delta/\Delta_y$, and Δ_y = yield displacement.

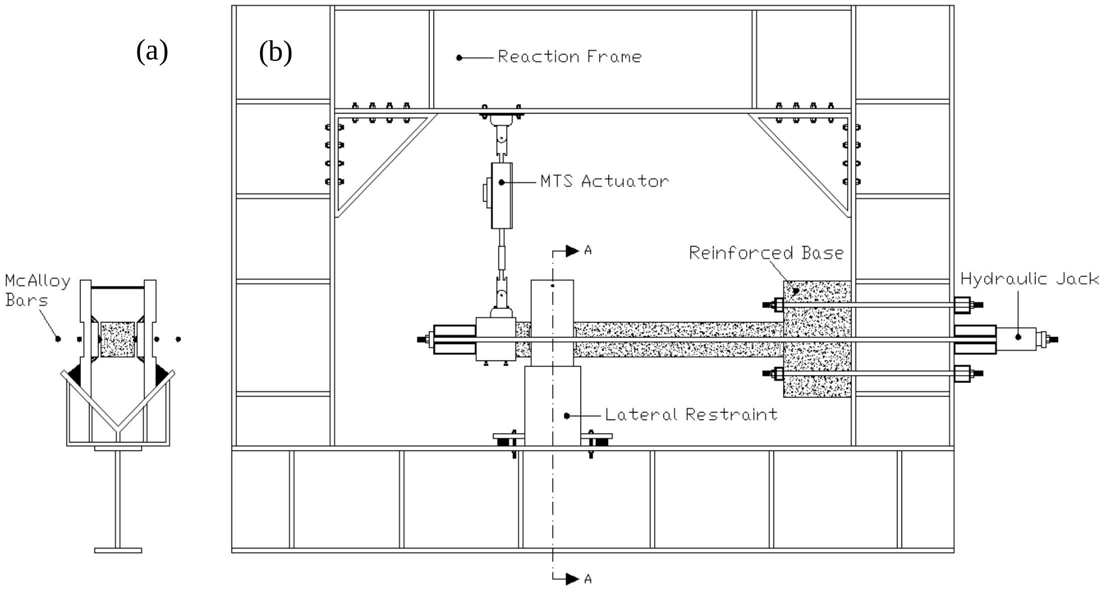

Figure 1 - Testing Arrangement (a) Section A - A (b) Reaction Frame and MTS Actuator Arrangement

2.2 Specimens and materials

Six fully-encased composite columns were tested in this experimental series, and all were designed and detailed according to European practice [Eurocode 8 (2004)]. The column length was anchored to a foundation block with detailing as illustrated in Figure 2.

The specimens consisted of a 203 x 46kg UC section, 2.7 m in length; 250 mm of this length being submerged into the base to anchor the composite section and to ensure full interaction between both structural elements. All structural sections were grade S275. A reinforcing cage was placed around the steel UC section to confine the partially confined concrete core and provide additional resistance and ductility to the section. The longitudinal reinforcing steel consisted of one T12 bar at each corner of the cross-section and two additional T12 bars along the line of the weak axis, in order to comply with the minimum reinforcement specified by the code [Eurocode 8 (2004)]. All reinforcing steel was grade S460; links were spaced at 72mm within the critical region, as defined by European seismic design guides, except for the final specimen which adopted a critical link spacing of 50mm. Beyond the critical region a common link spacing of 240mm was employed. Full details of the test specimens are given in Table 1.

Shear studs were welded to either face of the web of the steel sections at 250mm centres to ensure full interaction between the structural steel and concrete. A column base plate was located 250mm below the top of the reinforced concrete base to prohibit rotation about the end of the steel element and to ensure the formation of a plastic hinge within the column length. This base plate was in turn connected to an uplift plate, located 230mm below, via four M22 threaded bolts.

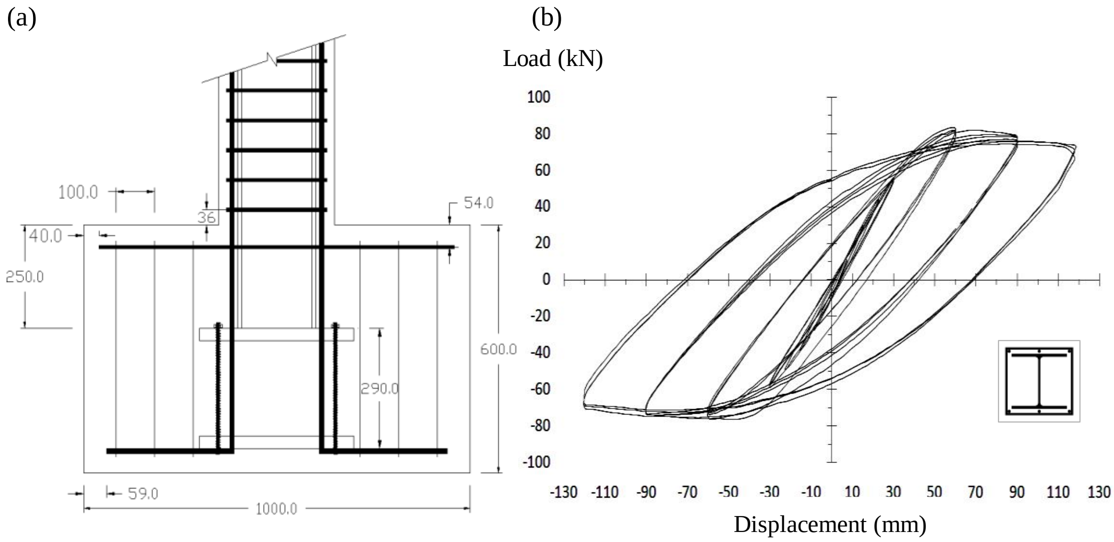

Figure 2 – (a) Test Specimen Details and Base-Plate Anchorage
(b) Experimental Load-Displacement (P-Δ) Hysteretic Response; Specimen JD3-ID3

3. Experimental Results

3.1 Test Series One

The first three test specimens were constructed using a lower grade concrete (C20/25). The horizontal top-of-column load-displacement relationship (hysteresis loops) for a selected test from this series is presented in Figure 2 (b). The applied lateral load and horizontal tip displacement is depicted by the vertical and horizontal axes respectively.

In Specimen JD3-ID3, one of the outer longitudinal bars initially yielded at a displacement ductility of $\mu = 0.75$, but all other longitudinal bars yielded at $\mu = 1.0$. Subsequent longitudinal cracking was followed by steel flange yielding at a displacement ductility of approximately, $\mu = 1.5$. Minor spalling of the cover was recorded at a displacement corresponding to $\mu = 2.0$, but most of the larger spall events occurred at $\mu = 3.0$. The specimen displayed little signs of deterioration in its hysteretic behaviour and it is evident that it is capable of dissipating energy is a stable manner. The test was terminated once the specimen reached the stroke limit of the actuator at a displacement corresponding to $\mu = 4.0$. The maximum moment recorded of $M_{max} = 213$ kNm, occurred at a displacement ductility of $\mu = 2.0$. Specimens JD1-ID2 and JD2-ID1 failed in a similar manner with individual elements yielding at similar displacement ductilities.

Table 1 - Specimen Details and Flexural Capacity

Specimen No.	f_{ck} ***(N/mm²)***	***P (kN)***	s_{crit} ***(mm)***	M_{max} ***(kNm)***
JD1-ID2	25	900	72	229
JD2-ID1	25	900	72	209
JD3-ID3	25	1200	72	213
JD4-ID5	85	1200	72	283
JD5-ID6	85	2000	72	344

3.1 Test Series Two

The second series of specimens were fabricated using a high-strength concrete (C70/85), which is significantly outside the scope of the European design code [Eurocode 8 (2004)]. Figure 3 (a) & (b) presents the hysteretic response for selected tests from this series. Identical displacement cycles were adopted for the high strength tests so as to facilitate energy dissipation comparisons between the specimens. The applied lateral load and horizontal tip displacement is depicted by the vertical and horizontal axes respectively.

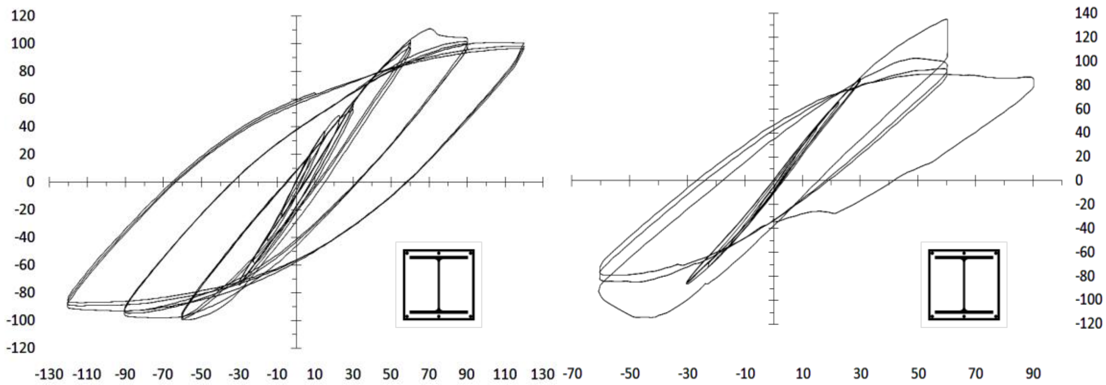

Figure 3 - Experimental Load-Displacement (P-Δ) Hysteretic Response; (a) Specimen JD4-ID5, (b) Specimen JD4-ID5

4 Analyses of Experimental Results

For the specimens tested in series one only minor variations in the hysteretic response were evident, the main noticeable difference was larger area enclosed within the 30mm (μ = 1) and 60mm (μ = 2) displacement cycle for specimen JD2-ID1. It indicates that this level of axial load is beneficial for increasing the area within the hysteresis curve thus maximising the potential energy dissipation of the specimen. The axial load increase produces a minor increase in the maximum moment achieved; this is consistent with the M-N interaction behaviour established by the design code.

Specimens JD3-ID3 & JD4-ID5 are identical in cross-section and level of applied axial load but possess a concrete compressive strength of 25 and 85 N/mm^2 respectively. A similar hysteretic response is recorded except exaggerated for the HSC specimen, due to its inherent additional strength. Both specimens were subject to a constant axial load of 1200kN. It is evident from this test that a concrete strength outside the upper limit of the design code, [Eurocode 8 (2004)] can effectively be incorporated in a design using the current confining provisions at this level of axial load (i.e. ≈ 20% Squash Load). This is not the case for higher axial load levels as is established by specimen JD5-ID6.

This specimen was subject to a constant axial load of 2000kN (i.e. ≈ 35% Squash Load). This axial load level resulted in an unstable hysteretic behaviour and a large drop off in the load carrying capacity of the section once the concrete element failed. The high axial load caused the concrete to fail brittly without warning. The specimen failed to achieve higher displacement ductilities similar to all other specimens, thus indicating that the current detailing provisions of Eurocode 8 (2004) are not suitable for HSC subject to this level of axial load, due to the brittle failure of the concrete and unstable hysteretic behaviour.

5 Model Formulation

The proposed model is developed from a widely employed stress-strain model for confined concrete subject to uniaxial compression [Mander et al (1988)]. It has been developed to accurately predict the influence of varying concrete confinement, axial load, and P-Δ effects to effectively determine the moment-displacement response of the composite section incorporating both normal and high strength concrete.

The model separates' the proposed section into a series of strips, identified primarily by its chief component, i.e. cover or confined concrete, steel flange etc. For any value of sectional curvature, the corresponding strains can be evaluated in each strip. Pre-defined stress-strain models for each constituent material enable the corresponding stress to be evaluated in each strip. Using this, the section moment curvature can be defined.

Assuming that all plastic deformation occurs in a concentrated area the section moment-displacement response can be determined using the well known relationship between displacement, rotation and curvature.

It is important to note that modified stress-strain curves for steel are necessary as it performances significantly different when confined by concrete, furthermore, in compression the concrete provides additional buckling resistance to the steel. Once the concrete had reached its yield strain the model needs to incorporate this loss of confining pressure.

5 Model Predictions

Figure 4 presents envelope curves for one NSC and two HSC tested specimens with the relevant model predictions superimposed. The model shows a very strong correlation with both sets of test results at all levels of displacement, thus proving an effective method to predict the performance of such specimens without the requirements for destructive testing. The model tends to underestimate the maximum achievable moment but is very effective in determining the post elastic capacity of the section. It is evident that the pre-yield stiffness can effectively be determined using this model.

It is clear from the data in Table 2 that the analytical model is a very effective method of predicting the performance of both the NSC and HSC specimens. The only substantial variation is for the HSC specimen subject to 2000kN of axial compressive force, once the concrete failed suddenly it lead to a sharp drop off in load carrying capacity thus decreasing the proposed models efficiency. Another important point to note is that the model tends to underestimate the maximum load applied to the specimen, generally by approximately 10%. This is conservative but needs to be considered where capacity design requires member strengths to be known so as to prevent undesirable plastic hinging.

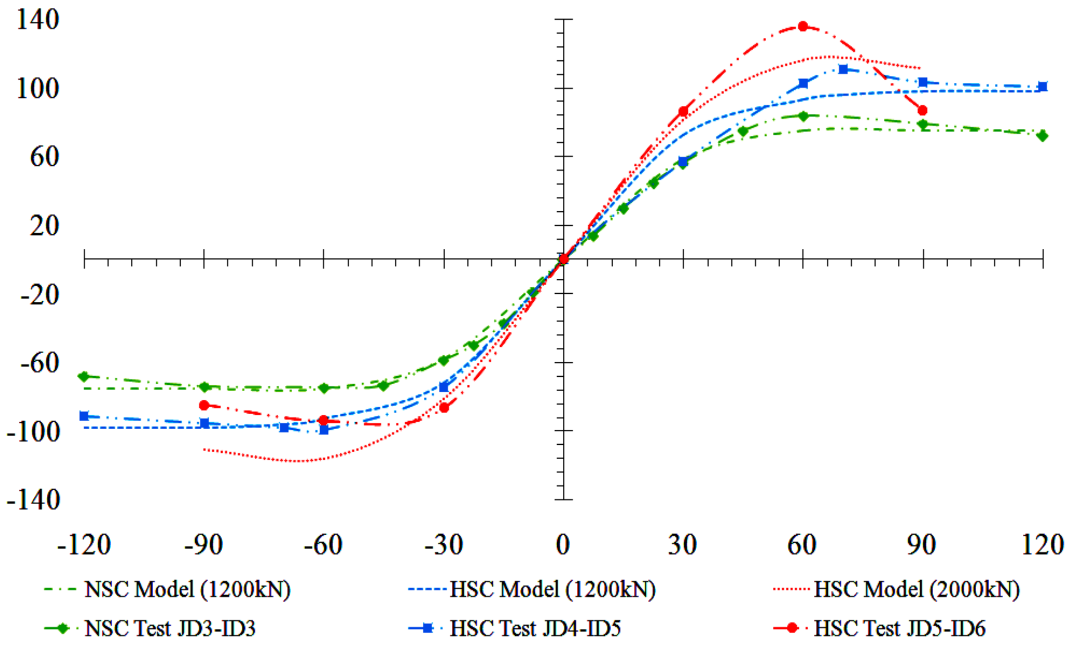

Figure 4 - Model and Experimental Load-Displacement Envelope's for NSC and HSC Specimens.

Table 2 presents the ratio between the predicted and calculated lateral loads at displacements of 30, 60, 90 and 120mm. The average between the ratios in both directions (i.e. negative and positive displacements) is presented to illustrate the overall efficiency of the model.

Table 2 - Ratio of Experimental and Analytical Values of Load Carrying Capacity

	30 (mm)	*60 (mm)*	*90 (mm)*	*120 (mm)*	*Yield Load (kN)*	*Yield Disp. (mm)*
NSC (P=1200kN)	0.984	1.054	1.019	0.933	75	46.5
HSC (P=1200kN)	0.912	1.084	1.013	0.978	102	60
HSC (P=2000kN)	1.065	0.989	0.783	----	122	49.5

6 CONCLUSIONS

The experimental programme indicates that composite columns possess good cyclic strength and ductility if adequately confined. The high strength series suggests that the current design provision can be implemented to incorporate HSC in the design of composite columns as long as the applied axial load is limited. Additional testing and analysis is necessary to verify this recommendation across a broad spectrum of sizes.

HSC composite columns subject to high levels of axial load fail brittly without excessive cracking prior to failure, this leads to a considerable drop-off in the load carrying capacity of the section.

Refined limitations on the maximum level of axial need to be introduced if HSC is to be introduced into composite column design.

The specimens' flexural capacity under combined flexural and axial loading exceeded the provisions of Eurocode 8 in all NSC tests, implying that the European code is conservative in strength prediction. The code predicts the HSC specimen's flexural capacity with varying accuracy thus should be used with caution as little to no safety factor may be built in; this suggests refined equations may be necessary for the development of suitably conservative M-N interaction curves for HSC sections.

The accuracy of the computational model varies between values of ± 9% for all levels of displacement for all specimen groups, excluding the failure point of Specimen JD5-ID6.

The computation model presented tends to underestimate the sections maximum flexural capacities but overall provides a very accurate estimate of the stiffness and performance of both the NSC and HSC specimens, particularly in the post elastic range, which is important for seismic response analysis.

ACKNOWLEDGEMENTS

This study was financially supported by the University of Dublin, 1252 Studentship Award and by the Department of Civil, Structural and Environmental Engineering, Trinity College Dublin. The authors would also like to thank the technical staff of the structures laboratories at Trinity College Dublin for their invaluable contributions to the planning and execution of the experimental research described in this paper.

REFERENCES

Brettle, H.J. (1973). Ultimate strength design of composite columns. *Journal of the Structural Division,* ASCE, New York, N.Y., **99:9**, 1931-1951.

CEN. (2004): EN 1998-1:2004. Eurocode 8: Design of structures for earthquake resistance – Part 1: General rules, seismic actions and rules for buildings, 2004.

Chen, C., Astaneh-Asi, A. and Moehle, J.P. (1992). Behaviour and design of high strength composite columns. *Proceedings of the Tenth Structural Engineering Conference,* ASCE, New York, N.Y., 820-823.

El-Tawil, S. and Deierlein, G.G. (1999). Strength and ductility of concrete encased composite columns. *Journal of Structural Engineering*, ASCE, New York, N.Y., **125:9**, 1009-1019.

Mander, J.B, Priestley, M.J.N, Park, R. (1988). Theoretical stress-strain model for confined concrete. *Journal of Structural Engineering*, ASCE, New York, N.Y., **114:8**, 1804-1826.

Ricles, J.M. and Paboojian, S.A. (1994). Seismic performance of steel-encased composite columns. *Journal of Structural Engineering*, ASCE, New York N.Y., **120:8**, 2474-2494.

Wakabayashi, M. (1987). A historical study of research on composite construction in Japan. *Proceedings of Composite Construction in Steel and Concrete Conference,* ASCE, New York, N.Y., 400-427.

DISPROPORTIONATE COLLAPSE IN BUILDING STRUCTURES

V. JANSSENS & D.W. O'DWYER
Dept. of Civil, Structural and Environmental Eng., Trinity College Dublin, Ireland

Abstract
The failure of the Ronan Point apartment tower focused interest in disproportionate collapse, and prompted the *'Fifth Amendment'* to the UK Building Regulations which was introduced in 1970. From this point on structures were required to exhibit a minimum level of robustness to resist progressive collapse. These rules have remained relatively unchanged for over 40 years. This paper presents a review of the concepts relating to structural collapse, and the robustness of structures. In general, there are three alternative approaches to disproportionate collapse resistant design: improved interconnection or continuity, notional element removal, and key element design. These techniques are outlined and their shortcomings are described. The treatment of robustness in the Structural Eurocodes is also summarised. The concepts outlined in this paper are not material specific, and therefore can be applied to all materials and types of structures.

Keywords: Accidental Actions; Collapse; Disproportionate; Progressive; Robustness

1. Introduction

On the morning of May 16, 1968, a minor gas explosion blew out the exterior walls of apartment 90 of the Ronan Point apartment tower. This triggered a progression of failures, resulting in the collapse of the southeast corner of the tower. This collapse revived the intellectual debate on structural collapse, and spurred a significant amount of research into disproportionate collapse and robustness of structures. As a result of this event, and the consequent report of the Commission of Inquiry, a number of countries implemented provisions to minimise the potential for disproportionate collapse. In 1970, the *'Fifth Amendment'* to the UK Building Regulations was introduced. This included a number of changes (Pearson and Delatte, 2005):

i. The possibility of structural collapse was considered for the first time. Hereafter, it was required that *"building[s] shall be constructed so that in the event of an accident the building will not suffer collapse to an extent disproportionate to the cause" (ODPM, 2004).* This requirement was initially limited to structures with five or more storeys, but in December 2004 was extended to all buildings.
ii. The requirement for a minimum level of ductility and redundancy throughout a structure was introduced.
iii. The requirement, for buildings with more than four storeys, to remain stable following the removal of a key element was introduced. If this requirement was not met the element must be designed to resist a pressure of $34kN/m^2$.

Following the recent terrorist attacks on the Murrah Federal Office Building, in 1995, and the World Trade Centre, in 2001, interest in this subject appears to have reached a peak. These events have highlighted the increased threat of terrorism worldwide and the need to consider hazards (explosions or detonations) that may not have been viewed as significant in the past.

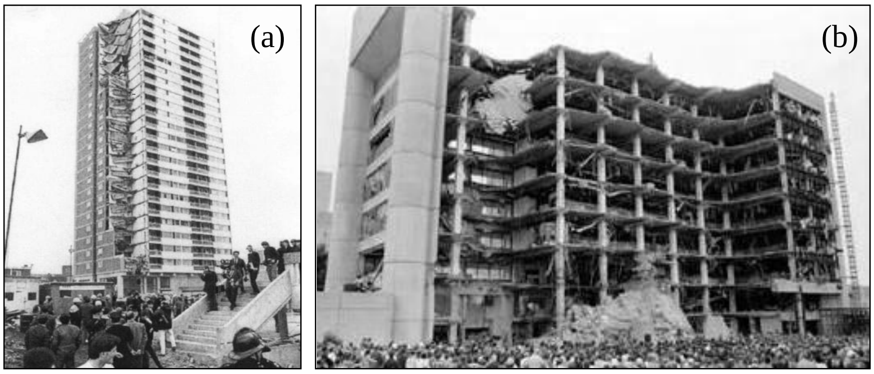

Figure 1 – Examples of Disproportionate Collapse (a) Ronan Point Apartment Tower (b) Murrah Federal Office Building

Additionally, recent developments in computerised design and high-performance materials have led to modern structures that are more optimised than their predecessors. This optimisation has led to a reduction in their inherent margin of safety. Therefore, modern structures are more vulnerable to the increasing range of loading conditions they are subjected to.

In view of all of these factors, the incorporation of rational procedures for mitigating the potential for collapse is an important part of the design of all structures. This is reflected in the numerous publications on disproportionate collapse and extreme loading that have appeared in the literature over recent years. A number of guidance documents have been published by regulatory authorities in the United States to assist design professionals in designing collapse resistant structures (GSA 2003, DoD 2009). In Europe, the Institution of Structural Engineering is due to publish a '*Practical Guide on Structural Robustness and Disproportionate Collapse'* in November 2010. However, these documents do not provide detailed advice on designing structures where the consequence of failure is high (i.e. class 3 structures). Further design guidance is needed in this area.

2. Designing for Disproportionate Collapse

In order to reduce the vulnerability of a structure to disproportionate collapse, one can adopt non-structural protective measures, structural protective measures or a combination of these measures. Non-structural protective measures improve a structure's resistance to extreme actions by non-structural means, such as structural monitoring or limiting public access. These measures will not be discussed further in this paper but the reader can refer to Starossek (2009) for more guidance. Meanwhile, structural protective measures improve a structure's ability to resist extreme events, by providing excess load resisting or energy absorbing capacity.

Robustness is a term used to describe *'the ability of a structure to withstand events like fire, explosions, impact or the consequences of human error, without being damaged to an extent disproportionate to the original cause'* (CEN, 2006). This definition does not distinguish between foreseeable and unforeseeable, or reasonable and unreasonable loading conditions. In more general terms, robustness is the structures ability to resist loading conditions outside the normal design envelope. These may include human error, malicious attacks, aircraft impact, external explosions and other low-probability high-consequence events. It is worth noting that the definition of robustness is under constant discussion within the engineering community and no single definition of the term exists at present (Starossek, 2009). Robustness can be considered to be related to the following structural properties:

Strength
One of the simplest methods of providing robustness is to provide critical components with the capacity to resist an extreme load. This concept is employed in the key element design method discussed in the following section. This excess capacity should be provided to the global structure, as well as to individual members and connections.

Ductility
The ability to deform while maintaining strength is crucial when designing collapse resistant structures. Utilising ductile members and connections, similar to those used in seismic design, can be beneficial in two ways. Firstly, by ensuring members directly affected by the triggering event behave in a ductile manner, energy will be absorbed as the structure deforms and the ensuing damage will be reduced. Secondly, using ductile members will assist in the development of alternative load paths, which allow the structure to bridge localised failure and redistribute the loads.

Redundancy
The provision of redundancy is generally associated with the provision of alternative load paths, which are absent from many structures mainly due to a lack of frame continuity and connection redundancy. For most structures, increasing the continuity will also result in an increase in the redundancy. Hence, the provision of redundancy may be considered dependant on the continuity throughout the structure. This is reinforced by the fact that for some recent building collapses (e.g. Ronan Point Collapse) the extent of failure could have been reduced, or even eliminated, had elements of the structure been interconnected more effectively.

3. Design Methods and the Provision of Robustness

As building designers cannot design for every hazard that a building may be subjected to in its lifetime, a general design approach is required to account for the risks associated with low-probability high-consequence events. There are, in general, three alternative approaches to designing structures to resist progressive collapse:

- Improved interconnection or continuity
- Key Element Design
- Notional Element Removal

These approaches can be classified in terms of indirect and direct design approaches.

3.1 Indirect Design Methods

Indirect design methods consist of various prescriptive measures of improving a structure's robustness. These methods have the advantage that they can be implemented without the need for any additional analysis. This is a significant benefit when dealing with unforeseen loading conditions, therefore indirect design methods are incorporated into most major codes and guidelines (CEN 2006, DoD 2009, GSA 2003). The provisions are usually in the form of prescriptive requirements for minimum joint resistance, continuity and tying between the members. But indirect approaches give no consideration to how a structure should behave if local damage occurs and may not actually increase the resistance of a structure to disproportionate collapse. Therefore, it is advised that these techniques are only used for standard structural configurations, and that a more detailed analysis would be carried out for complex or high occupancy structures.

This approach is often adopted in the form of minimum tying force requirements (CEN 2006). These requirements are based on the underlying philosophy that if all members are connected by joints with a specified capacity, the selected structural configuration will have adequate strength to resist disproportionate collapse. The structural elements should be effectively tied together to allow redistribution of the gravity loads following local failure. In general, both horizontal and vertical ties should be included, the capacities of which are determined separately to the design loads. The provision of horizontal ties is based on the concept that, following the loss if a support, the remaining structure will support the loads through catenary action (Alexander, 2004). However, Byfield and Paramasivam (2007) recently demonstrated that, for steel-framed buildings, industry standard beam-column connections possess insufficient ductility to accommodate the displacements required to mobilise catenary action.

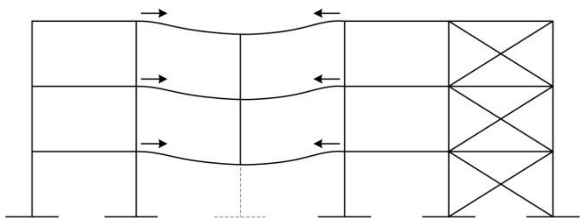

Figure 2 – Horizontal Ties Bridge Localised Failure by Catenary Action

Finally, it should be noted that the provision of continuity can be counter-productive in some cases. When an 1800kg TNT equivalent truck bomb exploded outside the Murrah Building the resulting blast destroyed one of the ground floor columns (Osteraas, 2006). The resulting progressive collapse destroyed nearly half of the building and was enhanced by the continuity of the reinforced concrete frame. In this case, the extent of collapse could have been reduced if the reinforcement had not been continuous throughout. The Charles de Gaulle collapse (Starossek, 2009) illustrates the usefulness of structural segmentation. The failure of a roof section initiated the collapse sequence, in which only 24m of the 680m long structure collapsed. The progression of collapse beyond this portion of the structure was prevented (unintentionally) by a movement joint at one end, and a weak joint at the other. Hence, the provision of horizontal and vertical ties are sufficient for standard buildings, but should not be relied on for high risk or high consequence structures. In these cases, the provision of weak links in large structures may be advisable.

3.2 Direct Design Methods

In contrast with indirect methods, direct design approaches rely heavily on structural analysis and can benefit significantly from the use of sophisticated analysis techniques; such as, nonlinear and/or dynamic analysis. Two commonly applied approaches to reduce the potential for disproportionate collapse are *key element design* and *notional column removal*. The key element design approach increases the strength of primary load carrying elements to resist failure under certain specified loading conditions. While designing for notional element removal requires a structure to be designed so that it can bridge local failure. These two methods are intended to be used in conjunction with one another, whereby the key element design approach is used only if a structure cannot sustain notional removal of the element in question (Ellingwood and Leyendecker, 1978).

Key Element Design

The key element design method requires that critical load carrying components are designed to withstand a specified level of threat which may be in the form of blast, impact or fire loading. Hence, the structure is provided with additional strength in areas that are believed to be prone to accidental loads (e.g. exterior columns at risk from vehicular collision), or in key elements that are crucial to the overall structural stability. These members should be able to develop their full resistance against an unanticipated load without failure of either the member itself or its connections. By activating the full resistance available in the key members, this approach maximizes their ability to deal with unforeseen hazards without having to redistribute loads.

One of the main issues with designing to resist disproportionate collapse is that the loading events in question are outside the scope of normal design. Due to the unforeseen nature of these events, we cannot accurately predict their magnitude and location. EN 1991-1-7 (2006) requires key elements be designed to resist a uniformly distributed load of 34kPa, applied in any direction to the element or attached components. This value is derived from the peak pressure in a gas explosion (Alexander, 2004), however clearly loads greater than this will result in failure of the element. Therefore, this approach may be of limited benefit in resisting collapse and is recommended for situations when designing for notional element removal is not possible (Ellingwood and Leyendecker, 1978).

Notional Element Removal

The notional element removal method was initially recommended following significant research during the 1970’s (Kaewkulchai and Williamson, 2004). This design approach focuses on the behaviour of a structural system, following the occurrence of an extreme event, and requires the structure to redistribute the loads following loss of a primary load bearing member. The basic procedure followed in the analysis involves removal of one, or more, primary structural components from the structure, which is then analysed to determine if the extent of collapse. This method promotes the use of regular structural configurations that exhibit ductility and energy absorption properties, desirable features for mitigating the risk of disproportionate collapse. An important advantage of this technique is that it is a threat independent approach. Therefore, the notional element removal method is valid for any hazard that may cause failure. This avoids one of the main difficulties faced by engineers in designing structures to resist disproportionate collapse: attempting to quantify an otherwise unknown loading event.

The design guidelines produced by the Department of Defence (DoD 2009) and the General Services Administration (GSA 2003), in the United States, both recommend the use of this technique (referred to as the alternative path method). These guidelines identify four alternative analytical approaches, of increasing complexity: linear static, nonlinear static, linear dynamic and nonlinear dynamic analysis. It is important to emphasise that the additional accuracy associated with more complex methods comes at a large computational expense, which can result in more expensive and longer design times for a project. Therefore, an analysis procedure where the analyses progress from simple linear static analysis to complex nonlinear dynamic analysis may be recommended. Using this method, the analyses would progress until the building meets the increasingly less conservative evaluation criteria, provided the method of analysis implemented meets the required guidelines (Marjanishvili, 2004).

1. *Linear Static Analysis*
   The simplest form of the notional element removal method involves performing a linear static analysis on the damaged structure. This involves applying the fully factored gravity loads to the damaged structure in a single step. The proceeding analysis is based on the assumption of small deformations. Dynamic effects can be indirectly considered by assuming an equivalent static load based on a constant amplification factor, typically taken equal to 2.0 (GSA 2003, DoD 2009).

2. *Nonlinear Static Analysis*
   Nonlinear static analysis improves on linear static analysis through inclusion of both geometric and material nonlinearities in the analysis. The inclusion of these nonlinearities is required to account for catenary/membrane effects, as well as to allow for accurate representation of inelastic response and P-Δ effects.
   Similar to the linear static approach, the nonlinear static approach applies a dynamic amplification factor to account for time-dependant effects. However the gravity loads are not applied in one step, instead a vertical pushover analysis is employed. This involves incremental application of the loads until the maximum loads are attained, or collapse occurs, and improves the accuracy of the results.

3. *Linear Dynamic Analysis*
   The sudden removal of a structural component results in an immediate change in the structural geometry. As a result of this gravitational energy is released and the internal strain energy, and kinetic energy, of the structure can be expected to alter rapidly. Therefore, dynamic effects are important when attempting to accurately represent the associated structural behaviour. Due to the localized nature of dynamic behavior, when using mode superposition all high modes of vibration should be included. Thus, direct step-by-step integration methods are preferable, since such algorithms account for all viable vibration modes (Marjanishvili, 2004).
   Linear dynamic analysis is unable to capture the nonlinear behaviour associated with collapse. Although linear dynamic analysis is easier to apply than nonlinear dynamic analysis, this method requires extensive judgment on the part of the designer to establish whether P-Δ and membrane effects are significant and to determine whether the computed results are realistic.

4. *Nonlinear Dynamic Analysis*
   The most rigorous approach for applying the notional column removal method is through the use of nonlinear dynamic analysis. This method dynamically removes a member from the structure, which is then analysed taking account of both the geometric and material nonlinearities. This allows larger deformations and energy dissipation through material yielding, cracking and fracture (Marjanishvili, 2004).
   Another important issue that must be addressed, in relation to disproportionate collapse, is the impact of failed members on other portions of the remaining structure. When a member fails, whether at one or both ends, the failed ends move independently of the main structure and may come into contact with other members (Kaewkulchai and Williamson, 2004). If contact occurs, additional mass and impact forces are dynamically imposed on the main structure, which may cause further failure.

4. Robustness and the Eurocodes

The design of structures to resist accidental actions is dealt with in EN 1991-1-7 (2006). This document outlines the design criteria for achieving robustness, according to its assigned consequence class. There are four possible classes listed (1, 2A, 2B and 3), with building type and the number of storeys as their main properties (DTLR, 2001). The recommended procedures are based on the design approaches discussed in the previous section, increasing in complexity as the consequences of failure increase. Table 1 summarises these recommendations.

Table 1 – Design criteria for meeting the robustness requirements (CEN 2006)

Consequence Class	**Recommended Procedure**
1	No further consideration, except to ensure that the robustness and stability rules given in EN 1990 to EN 1999 are met.
2a Lower Risk Group	In addition to the requirements for CC1, the provision of effective horizontal ties, or effective anchorage of suspended floors to walls, should be provided (*improved interconnection or continuity*).
2b Upper Risk Group	In addition to the requirements for CC1, the provision of: • Horizontal and vertical ties, in all supporting columns and walls should be provided (*improved interconnection or continuity*), or, • The *notional element removal* method should be applied to all key elements. If the notional removal of a column/beam would result in damage exceeding the lesser of 15% of the floor, or 100 m^2, the element should be designed as a *key element*.
3	A systematic risk assessment of the building should be undertaken taking into account both foreseeable and unforeseeable hazards.

Other than the information available in the Eurocodes, little other practical guidance is provided on ways of meeting these requirements. However, as these recommendations are based on UK practice, design guidelines based on the UK Building Regulations may be useful (e.g. Gulvanessian et al., 2009, Way, 2005)

4.1 Class 3 Structures

The recommended procedure for class 3 structures requires the designer to perform a systematic risk assessment of the structure. Further information on risk assessment can be found in the informative Annex B of EN 1991-1-7 and the '*Designers' Guide to Eurocode 1'* (Gulvanessian et al., 2009). However, the information available on risk assessment is more suitable for analysing foreseeable hazards. For unforeseen hazards, an approach based on limiting the extent of localised collapse may be more fitting.

5. Discussion

This paper forms an introduction to the subject areas of structural robustness and disproportionate collapse, with the references provided making a good starting point for any interested engineer. Current research in this area is ongoing and covers a wide range of topics. The authors have developed a dynamic structural analysis tool capable of modelling progressive collapse in framed multi-storey structures (Janssens and O'Dwyer, 2010). This program incorporates geometric and material nonlinearities, and could enable designers to easily check the effect of localised damage as part of a risk analysis. Elsewhere, COST Action TU0601 (Faber, 2006) is working to produce a risk-based approach for assessing robustness; Kim and Kim (2009) have published some results on the benefits of seismic connections in resisting collapse; and the insertion of shear fuses has been applied by Starossek (2009).

6. Acknowledgements

This research is supported by the IRCSET Embark Initiative.

References

Alexander, S. (2004), 'New Approach to Disproportionate Collapse', *The Structural Engineer,* **83**(23/24)**,** 14-18.

Byfield, M. P. & Paramasivam, S. (2007), 'Catenary Action in Steel-framed Buildings', *Proceedings of the ICE - Structures & Buildings*, **160**(5)**,** 247-257.

Department for Transport Local Government and the Regions (DTLR) (2001), *Proposed Revised Guidance on meeting Compliance with the Requirements of Building Regulation A3: Revision of Allot and Lomax Proposal*.

Department of Defence (DoD) (2009), *Unified Facilities Criteria - Design of Building to Resist Progressive Collapse, UFC 4-023-03*. www.wbdg.org

Ellingwood, B. R. & Leyendecker, E. V. (1978), 'Approaches for Design against Progressive Collapse', *Journal of Structural Division,* **104**(ST3)**,** 413-423.

European Committee for Standardization (CEN) (2006), *Eurocode 1 - Actions on Structures - Part 1-7: General actions - Accidental actions, BS EN 1991-1-7:2006*.

Faber, M. H. (2006), *Memorandum of Understanding (MoU) for COST Action TU0601: Robustness of Structures*. www.cost-tu0601.ethz.ch

General Services Administration (GSA) (2003), *Progressive Collapse Analysis and Design Guidelines for New Federal Office Buildings and Major Modernization Projects*. www.buildingsecurity.us

Gulvanessian, H., Formichi, P. & Calgaro, J. (2009), *Designers' Guide to Eurocode 1: Actions on Buildings: EN 1991-1-1 and -1-3 to -1-7,* Thomas Telford.

Janssens, V. & O'Dwyer, D. W. (2010), 'The Importance of Dynamic Effects in Progressive Collapse', in *Proc. of 34th IABSE Symposium*.

Kaewkulchai, G. & Williamson, E. B. (2004), 'Beam Element Formulation and Solution Procedure for Dynamic Progressive Collapse Analysis', *Computers & Structures,* **82**(7-8)**,** 639-651.

Kim, T. & Kim, J. (2009), 'Collapse Analysis Of Steel Moment Frames with Various Seismic Connections', *Journal of Constructional Steel Research,* **65**(6)**,** 1316-1322.

Marjanishvili, S. M. (2004), 'Progressive Analysis Procedure for Progressive Collapse', *Journal of Performance of Constructed Facilities,* **18**(2)**,** 79-85.

Office of the Deputy Prime Minister (2004), *Approved Document A: Structure*.

Osteraas, J. D. (2006), 'Murrah Building Bombing Revisited: A Qualitative Assessment of Blast Damage and Collapse Patterns', *Journal of Performance of Constructed Facilities,* **20**(4)**,** 330-335.

Pearson, C. & Delatte, N. (2005), 'Ronan Point Apartment Tower Collapse and its Effects on Building Codes', *Journal of Performance of Constructed Facilities,* **19**(2)**,** 172-177.

Starossek, U. (2009), *Progressive Collapse of Structures*, Thomas Telford Limited.

Way, A. G. J. (2005), *Guidance on Meeting the Robustness Requirements in Approved Document A (2004 Edition)*, The Steel Construction Institute.

ESTIMATION OF THE SAFE LOAD CAPACITY OF CANTILIVERED STONE STAIRS

D.W. O'DWYER & K. BASHORUN
Dept. of Civil, Structural and Environmental Engineering, Trinity College, Dublin, Ireland

Abstract
This paper presents a simple static analysis procedure for estimating the peak torques in a cantilevered stone stairs.

Cantilever stone stairs were constructed from the seventeenth to the early twentieth century, with occasional examples being constructed up to the present. Despite their name these stairs do act as pure cantilevers. Each tread transfers the load applied to it to the tread below with the resultant torques being resisted by combination of a torsional restraint at the wall and the development of horizontal forces between adjacent treads.

The paper describes this structural action in detail and explores how the inter-tread forces are influenced by the details of the stair construction.

The predominant failure mode for cantilevered stone stairs is sudden brittle failure when the applied torque exceeds the capacity of a tread. The paper identifies an appropriate method for calculating the allowable safe load for a stone tread. The approach presented is valid for the failure of brittle materials, where the volume of material under load influences the probably failure load.

Finally, the paper considers how the safety of cantilevered stone stairs should be assessed in practice. Thus the paper considers the accuracy of analyses in conjunction with errors in assessing the capacity of a tread.

Keywords: Analysis, cantilevered, capacity, failure, load, masonry, stone, stairs

1. Introduction

The recent collapse of the cantilevered stone stairs in the Natural History Museum in Dublin highlighted the risk of failure of these structures, see Figure 1. Cantilever stone stairs are very common in larger Irish buildings constructed from the seventeenth century until the early twentieth century. In the majority of these cases these stairs have given trouble free service and will continue to function safely. However, when cantilever stone stairs do fail it is often without warning. The brittle nature of such failures will be considered in detail later.

Cantilever stone stairs often form the fire evacuation routes in older buildings so their performance under a full imposed load is important. These structures are highly statically indeterminate and hence they are difficult to analyse. The finite element method can be used to solve complex structures such as cantilevered stone stairs. However, building a full three-dimensional computer model is complex and costly, and the output is still uncertain because the wall support conditions, the construction sequence and the material properties of the treads and wall are not known with certainty. Even where they can be analysed, assessing their safe load capacity is complex because of their brittle mode of failure, which is sensitive to the presence of localised weaknesses in the treads.

The complexity of a finite element analysis, the uncertainty as to the most appropriate input parameters and the volume and complexity of the output from a finite element analysis can obscure the fundamental behaviour of a cantilevered stone stairs. On the other hand, simple static analyses are easy to interpret, require assumptions to be stated explicitly and concentrate on the fundamental structural actions. The utility of static analyses for the analysis of indeterminate masonry structures is best illustrated by the work of Heyman on masonry arches (1982). In addition, a static analysis can be carried out very quickly. This paper presents a static analysis method for rebated cantilevered stone stairs. Previous authors have analysed cantilevered stone stairs using statics. However, in the case of rebated stairs the assumptions underlying the magnitude of the inter-tread horizontal forces and the location of the resultant of the inter-tread vertical contact forces were based on experience gained from experiments or finite element analyses. This paper gives a rational procedure for calculating these parameters, and these procedures agree with the results presented by previous authors.

Figure 1 – Flight of stairs which collapsed

2. Static analysis algorithm

Cantilever stone stairs support themselves and their imposed loading by developing vertical and torsion reactions at their embedded tread ends. Figure 2(a) shows a single flight of stairs in which each of the stair treads is built into the supporting wall at one end. Figure 2(b) shows a free body diagram and most, but for clarity not all, of the forces that could act on a single tread. This figure indicates a cantilever support reaction applied by the wall to the thread. In general the depth to which the treads were embedded into the wall was limited to prevent the development of such moments. Thus, M, is usually assumed to be zero. Similarly, the potential support reaction moment about a vertical axis, which is not shown in Figure 2(b), is also assumed to be zero.

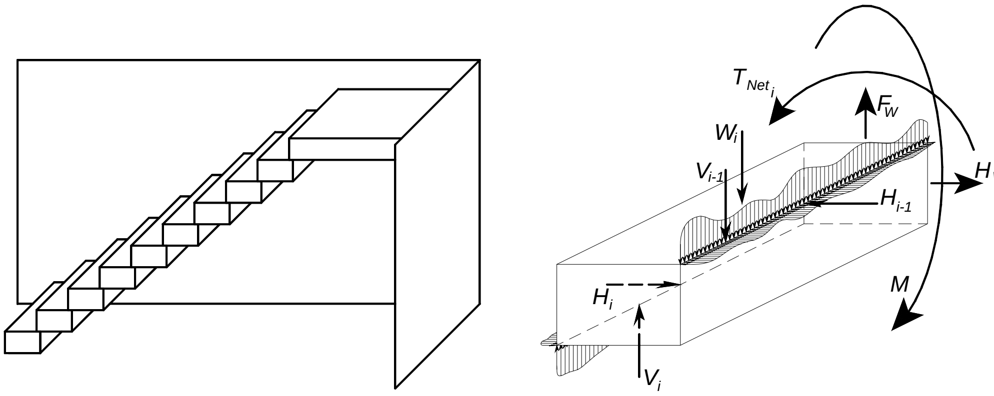

(a) (b)

Figure 2 – (a) Schematic of cantilevered stairs and (b) free-body diagram showing forces on a tread

Figure 2(b) indicates the continuous contact forces applied to the tread by the treads above and below. The details of the contact forces are complex and the locations of the resultants are not known (Price and Rogers 2005, Little et al. 2009). Calculating the magnitude of the horizontal resultants H_i and H_{i-1} is particularly complex and depends on the connection detail between treads.

The number of unknowns exceeds the number of static equilibrium equations and therefore cantilevered stone stairs are statically indeterminate structures. However, by assuming the locations of the resultants of the contact forces and assuming that the support reactions provided by the wall are limited to a torsional restraint and a vertical restraint, the number of unknowns is reduced and a static analysis becomes possible.

2.1 Assumptions

Consider the vertical loads acting on a single tread, such as that shown in Figure 3. Assume that at the wall end the tread is pin-supported and where it rests on the tread below it is supported on a linear elastic support. Let W be the self-weight plus imposed load acting on the tread and let V equal the resultant of the load applied by the tread above.

If flexure of the tread is ignored then the tread will rotate about the pin support until the reaction at the pin support plus the distributed support reaction are in equilibrium with the applied vertical loads. If the distributed support is linear elastic then the resultant of the contact forces, R_C, will occur two-thirds of the tread length out from the pin support. On this basis the resultant of the vertical contact forces between treads will be assumed to occur at a distance of two-thirds of the tread length from the face of the wall support.

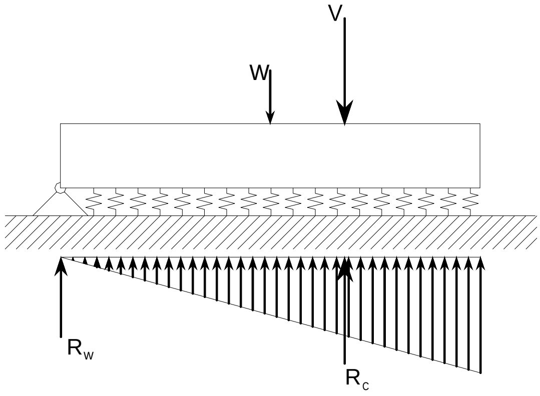

Figure 3 – Simple rigid body model for a single tread

The sum of the vertical reactions R_W and R_C must equal W plus V. V is the resultant of the vertical contact forces between the tread and the tread above: it also occurs at a distance of *2/3l* from the pin support. Taking moments about the pin support gives:

$$R_W = \frac{W}{4} \text{ and } R_c = \frac{3}{4}W + V \tag{1}$$

Rebated stairs can carry higher loads than non-rebated stairs due to the horizontal contact forces that can be developed between the treads. These horizontal forces apply a torsional couple to the treads and in the case of the lowest treads, which are most heavily loaded, this couple acts to reduce the torsional force due to the vertical loads. The challenge in analysing this behaviour is calculating the magnitude of the horizontal force developed between the treads. If the treads are restrained laterally by the wall then the analysis of these forces is complex because the horizontal forces can vary from tread to tread. However, it is reasonable to consider the behaviour of a cantilevered stone stairs where the wall does not apply horizontal reactions to the treads, this case results in a constant horizontal contact force between all the treads.

2.2 Rebated treads

Figure 4 shows a free body diagram showing the external forces acting on a flight of seven rebated treads. The bottom support tread, which rests on the ground, is not shown

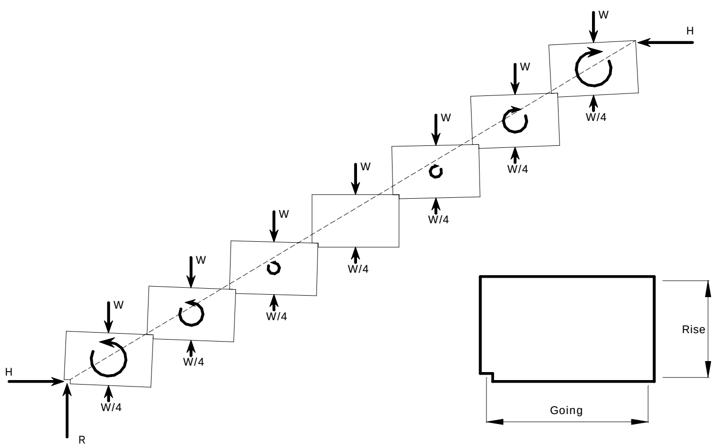

Figure 4 – A free body diagram of a flight of rebated treads

The external vertical forces acting on each tread comprise the gravitational load *W* and the support reaction at the wall of *W/4*. The vertical reaction force at the bottom tread is equal to $3/4$ of the sum of the vertical loads applied to the treads and the horizontal reaction at the bottom is equal to the horizontal reaction at the top. In addition to the vertical and horizontal forces, each tread also experiences a torque reaction applied by the wall. The torsion forces due to the horizontal forces act in the opposite direction to the torsions due to the vertical loads. In the lower treads the net torsions are anti-clockwise and in the upper treads the torsions are clockwise, see Figure 4. The magnitude of the torsions increase from the centre of the stairs. The clockwise and anticlockwise torsion forces approximately cancel, this can be seen from the fact that the top tread maintains contact with the landing: for this to occur, the sum of the clockwise and anti-clockwise tread rotations must be equal.

This free body diagram, taken in conjunction with the previous assumptions, can be used to estimate the magnitude of the horizontal reaction between treads. If moments are taken about the bottom corner of the lowest tread, and if the wall is assumed to apply no horizontal reaction to the treads and if the clockwise and anti-clockwise torques are assumed to cancel, then

$$H = \frac{3}{4} \times \frac{W}{N} \times \frac{Going}{Rise} \times \sum_{i=1}^{N} \left(i - 1 + \frac{1}{2} \right) = N \times \frac{3W}{8} \times \frac{Going}{Rise} \tag{2}$$

Where the *Going* and *Rise* are as shown in the Figure 4. In general, for the case where no vertical load is applied to the top tread, the vertical inter-tread contact force between tread *i* and tread *i-1*, where the treads are numbered from the top to the bottom, is equal to

$$V_i = \frac{3}{4} W \times i \tag{3}$$

Hence the torque on tread *i* due to the vertical component of the inter-tread contact forces is

$$T_{V_i} = \frac{3}{4} W \times (i-1) \times Going + \frac{3}{4} W \times \frac{Going}{2} = \frac{3}{4} W \times Going \times \left(i - \frac{1}{2} \right) \tag{4}$$

and the torque acting on tread *i* due to the horizontal component of the inter-tread contact forces, in stairs where a rebate allows such forces to be developed, is

$$T_{H_i} = -H \times Rise = -N \times \frac{3W}{8} \times Going \tag{5}$$

Thus, in a rebated stairs the net torque on tread *i* is

$$T_{Net_i} = \frac{3}{4} W \times Going \times i - \frac{3W}{8} \times Going \times (N+1) \tag{6}$$

Note that in a stairs with *N* treads the net torque in the top and bottom treads

$$T_{Nett_1} = -\frac{3W}{8} \times Going \times N + \frac{3W}{8} \times Going \tag{7}$$

$$T_{Nett_N} = \frac{3W}{8} \times Going \times N - \frac{3W}{8} \times Going \tag{8}$$

are equal in magnitude but opposite in direction. Furthermore, the ratio between the maximum torque in bottom tread on an unrebated stairs, T_{V_N}, and the torque in the bottom tread of a rebated stairs, T_{Net_N}, is

$$\frac{\frac{3}{4}W \times Going \times \left(N - \frac{1}{2}\right)}{\frac{3W}{8} \times Going \times (N-1)} = \frac{(2N-1)}{(N-1)} \qquad (9)$$

As the number of treads, *N*, increases this ratio approaches two. Previous authors have suggested that the peak torque in a rebated stairs is half that of a stairs with unrebated treads and that the torques in a rebated stairs increase from zero at the middle tread to equal and opposite torques in the top and bottom treads. Thus, the analysis presented in this paper gives a rational basis for the empirical advice given by Price and Rogers and other authors (Price and Rogers 2005, Little et al. 2009).

Once the maximum torque, which occurs at the wall, has been evaluated the distribution of torsional shear stresses acting on a section through the tread at the wall can be calculated. The analysis of solid prismatic sections under torsion is one of the classic solid mechanics problems (Timoshenko and Goodier 1970). A detailed description of this problem is beyond the scope of this paper.

3. Parametric Finite Element Analysis

The analysis outlined in Section 2 was based on a number of assumptions. The analysis is valid only if these assumptions are correct or at least close to the true situation. A series of FE analyses were performed using the *Ansys* finite element program to verify the static analysis method presented. Of course a finite element analysis is also an approximation and the possibility that the behaviour of real stairs that have been in-situ for hundreds of years may differ from that predicted by computer models.

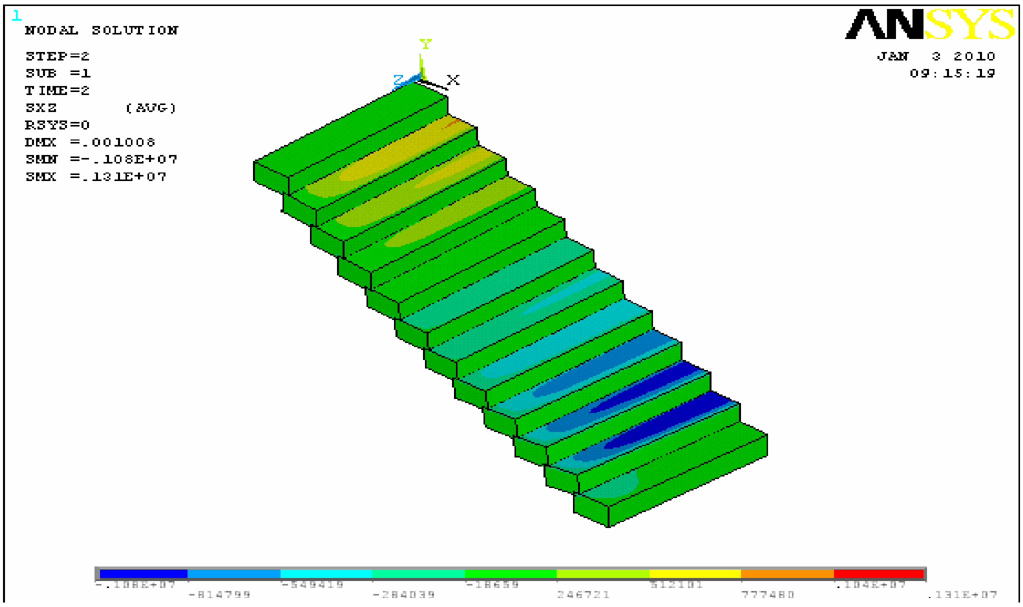

Figure 6 – Graphical output showing the shear stresses in a cantilevered stone stairs

A number of parameters were varied in this analysis including: tread length, number of treads, wall support conditions, tread profile, tread section size and presence of a rebate. Across all these models the static analysis was in broad agreement with the FE results, particularly for the most heavily stressed treads. Contact between the treads was modelled using specialised contact elements. The vertical contact forces observed in the model supported the assumption that the contact forces increase linearly along the length of the tread.

4. Failure criterion

Stone is a stiff brittle material that gives little warning of failure (RILEM TC QFS 2004). The appropriate failure criterion for stone or concrete is usually assumed to be Mohr's criterion, where failure occurs when the principal tensile stress exceeds the tensile capacity of the stone. This criterion can be modified to take account of tri-axial stress states but in the case of cantilevered stone stairs the principal tensile stresses are usually much larger than the stresses on the other principal planes.

The Mohr's failure criterion is widely used and in this instance the safety of a tread would be established by comparing the maximum tensile stress with the tensile capacity of the stone. However, brittle ceramics, and this category includes stone and concrete, are influenced by the size of the element (RILEM TC QFS 2004). Thus Mohr's criterion is not necessarily appropriate for cantilevered stone stairs.

4.1 Brittle failure criterion

Weibull (1939) was the first to describe the reliability of ceramic members. His approach is sometimes referred to as a weakest link theory because his analysis is similar to the classic problem of calculating the probability of failure of a chain (McLean and Hartsock 1989). Weibull's theory assumes that failure occurs if any small volume of a ceramic has a combination of inherent flaw and applied stress that would cause a crack to develop.

Weibull developed the following formulation to calculate the cumulative probability of failure, P_f, of a part comprising N elements of volume V_i.

$$P_f = 1 - \exp\left[\sum_{i=1}^{N}\left(\frac{\sigma - \sigma_u}{\sigma_o}\right)^m \frac{V_i}{V_o}\right] \tag{13}$$

σ is the stress in the volume, , σ_o is a normalizing material strength and is defined as the characteristic stress at which a reference volume of the material (V_o) would fail in uniaxial tension, σ_u is a stress below which the material would never fail (frequently taken conservatively as zero), and m is a parameter of the material (McLean and Hartsock 1989).

4.2 Material properties

To evaluate the probability of failure it is necessary to quantify σ_o and m. The procedure is described in EN 843-5:2006, which uses the maximum likelihood method to establish these two parameters. Once the characteristic strength σ_o of the material used in a stairs has been established then the probability of failure can be calculated. Because the stresses vary from tread to tread the overall probability of failure must consider each tread separately. In most cases the stairs will already be carrying its self-weight. Thus the overall probability of failure is equal to the probability of failure under full imposed loading minus the probability of failure under self-weight.

However, calculating the probability of failure of a stairs on the basis of either Weibull's approach or Mohr's criterion is only valid if the stone in the stairs is homogeneous and the treads do not contain large voids or defects. Stone is a natural material and it can be very difficult, if not impossible, to be sure that a tread does not contain irregularities. In many cases a visual inspection will confirm the presence of fossils. Therefore while an engineer can carry out preliminary analyses and estimate probable failure loads, the only sure means of verifying the safe load capacity of a cantilevered stone stairs is to apply a full load test.

5. Conclusions

The paper presented a static analysis method for analysing the forces in a rebated cantilevered stone stairs. The method provides a theoretical justification for the hypothesis that the maximum torsional stresses in a rebated stairs are approximately half those in an unrebated stairs. The assumptions that underlie the proposed static assessment method were validated by performing a parametric FEA.

The paper suggests the use of a Weibull, brittle failure, criterion when assessing the safe load capacity of cantilever stairs. This approach is an improvement on the traditional Mohr's Criterion approach.

The paper acknowledges that the stone used to construct cantilevered stone stairs is frequently inhomogeneous. If the material in the treads of a stairs contains significant localised weaknesses then failure criteria that assume a uniform homogeneous material may not be safe and there may be no alternative to load-testing the stairs.

References

Heyman, J. (1982), *The Masonry Arch*, Ellis Horwood series in engineering Science, Chichester.

Little, P., Hough, M. & Mullarkey, E. (2009), "Stone cantilever stairs - inspection and analysis of cantilever stairs," *The Structural Engineer*, **87**, Issue 8, 21 April 2009: 26-33

McLean, A.F., Hartsock, D.L., (1989), "Design with Structural Ceramics" In: Wachtman, J.B. (Editor): *Structural Ceramics: Treatise on Materials Science and Technology Volume 29*. Academic Press, Inc., New York, 27-97

Price, S. and Rogers, H. (2005), "Stone cantilevered staircases," The Structural Engineer, **83**, Issue 2 January 18th 2005: 29-36

RILEM TC QFS (2004), "Quasibrittle fracture scaling and size effect – Final report," *Materials and Structures/ Matériaux et Constructions*, **37**, October 2004: 547-568

Timoshenko, S.P. and Goodier, J.N., (1970), *Theory of Elasticity 3rd Edn*: McGraw-Hill, London

Weibull, W. (1939), "The phenomenon of rupture in solids," *Proceedings of the Royal Swedish Institute for Engineering Research*, **153**, 1-55

AN INVESTIGATION INTO THE VIBRATIONAL BEHAVIOUR AND DISPLACEMENT RESPONSE OF TYPICAL STEEL AND CONCRETE WIND TURBINE TOWERS

M.J. DAY & A. O'CONNOR
Dept. of Civil, Structural & Environmental Engineering, Trinity College, Dublin

Abstract
Wind turbine technology has developed rapidly in recent years; however, the impetus behind this has largely been on economics and although the tower is a low-technology component of the turbine, limited research has focussed on the tower structure itself. This paper focuses on the behaviour of typical steel and concrete wind turbine towers based on models in the literature. Two 90m tall towers were defined – suitable for turbines of 1.5MW and greater. Initially, the two towers were modelled using LUSAS finite element software. By performing an eigenvalue analysis, the towers were both classified as 'very soft' – in line with current design trends. The towers were subsequently loaded with simple load combinations, and in each case the peak resultant displacement at the top of the tower was determined. The results indicated that the concrete tower displaced less on average (54%) than the steel tower. Finally, the two towers were modelled using FAST aeroelastic code. The results showed that the concrete tower again out-performed the steel tower. Considering sustainability, transportability, economics and structural performance, this research indicates that concrete wind turbine towers can provide a viable alternative to steel towers for the next generation of multi-megawatt turbines in Ireland.

Keywords: Aeroelastic analysis, Concrete wind turbine towers, FAST, Simple load models, Steel wind turbine towers

1. Introduction

In 1997, the Commission of the European Union published a white paper calling for 12% of Europe's energy demand to be provided for by renewable technologies by 2010. In 2008, the EU increased this target: to provide 20% of energy from renewable sources by 2020. Ireland has set a more ambitious target of providing 33% of energy from renewable sources by 2020. Wind technology is already a proven cost-effective method of generating electricity and, through further development, will play a central part in meeting these criteria. With some of the best wind resources in Europe, Ireland is in an ideal position to develop these technologies.

In order to achieve the ambitious targets, wind installations in Ireland will need to be able to generate more electricity, more efficiently, than in the past. For the next generation wind turbines, tower design will have to play an integral part in reducing costs. These turbines will require taller, larger towers, but also tower structures that are more efficiently designed. This research investigates the response of concrete and steel wind turbine towers in this context.

The favoured design for the majority of Irish and European wind turbine towers is the steel tubular configuration – principally due to the mastering of their vibrational behaviour (Hau, 2006). This allows towers with very low stiffness to be designed, reducing materials and consequently offering an economic advantage. Steel prices were also favourable, however, the cost advantage has been eroding over the past five years with the price of steel jumping by 250% (Polyzois *et al.*, 2009).

According to Hau (2006), Singh (2007) and Tricklebank *et al.* (2007), concrete towers are becoming a viable option for taller turbine towers. Unlike steel towers, concrete construction allows tall towers to be built without unsolvable transport problems. In addition, developments in methods of prefabrication allow the long periods associated with concrete construction to be minimised. Concrete is also flexible and can be designed for the required exposure conditions. Tricklebank *et al.* (2007) indicate a design life of 40 to 60 years plus is feasible for concrete towers

This paper focuses on the vibrational and displacement behaviour of generic steel and concrete turbine towers. Based on models in the literature and available data from manufacturers, two towers (steel and concrete) were defined using LUSAS finite element software. The two towers were classified based on their vibrational behaviour. Subsequently, a number of simple load combinations were applied to the models, based on Det Norske Veritas & Wind Energy Department, Risø National Laboratory (DNV/Risø) (2001). The displacement behaviour of the towers under the load combinations was compared. Finally, the two towers were modelled using FAST aeroelastic code.

2. Tower and Turbine Characteristics

In order to define two towers – steel and concrete – models in the literature were taken as a guideline. In addition, manufacturer data was studied in order to make the models (and subsequent loading) as realistic as possible.

2.1. Tower Height and Nacelle Mass

Table **1** shows manufacturer data relating to a selection of turbines between 850kW to 3.6MW. This table shows that for the vast majority of wind turbine towers, the height of the towers is between 80 and 100m. 90m was chosen as a suitable height for the model towers – appropriate for turbines between 1.5MW and 3MW.

Table 1: Turbine manufacturer data for 3-bladed turbines

Turbine Manufacturer and Model	Rated Power (MW)	Tower Height (m)	Nominal (Range) Rotor Speed (rpm)	Rotor Diameter (m)	*Estimated* RNA mass (t)
Vestas V52	0.85	44-74	26.0 (14.0-31.4)	52	
Nordex S70	**1.5**	**65-85**	**(9.9-19.0)**	**70**	**~75**
Vestas V90	1.8-2.0	80-105	14.5 (9.3-16.6)	90	
Vestas V80	**2**	**60-100**	**16.7 (10.8-19.1)**	**80**	**~100**
Nordex N100	**2.5**	**100**	**(9.6-14.9)**	**100**	**~125**
Vestas V112	3	84-119	14.0 (6.7-17.7)	112	
GE 3.6sl	3.6	Site specific	(8.5-15.3)	111	

In order to determine the response of the tower models to a number of different loads, three turbines (highlighted in bold) were chosen to represent the range of turbines suitable for a 90m tower.

Although manufacturers provide a wide range of data regarding the performance and operating characteristics of turbines, other information such as the mass of the rotor nacelle assembly (RNA) is difficult to find. However, by collating all available information, an estimated RNA mass was defined and is included in the table.

The rotor speed and diameter of the three turbines – Nordex S70, Vestas V80 and Nordex N100 – were also required to define the dynamic loading on the turbine in Section 3 and the FAST models in Section 4.

2.2. Cross Sectional Dimensions

The dimensions of modern steel tubular towers are controlled by available manufacturing technologies and transportation limitations. Hau (2006) indicates that the manufacture of steel towers up to 4m in diameter is a conventional technology, however when towers exceed 90m in height, the required base diameter becomes greater than 4.5m. A base diameter of 4.5m was therefore chosen for this study. The diameter at the yaw bearing was chosen to be 3.5m to give a slight taper. The wall thickness at the base of the towers was set to 20mm (steel) and 300mm (concrete), with the wall thickness at the yaw bearing defined as 10mm and 150mm for the steel and concrete towers, respectively.

These values appeared to fit with models from the literature. Burton *et al.* (2001) give an example of a steel tower in which the wall thickness is 'increased…to 27.5mm.' Lavassas *et al.* (2003) model a 1MW steel tower with a height of 44.075m, a base diameter of 3.3m and top diameter of 2.1m; the wall thicknesses are 18mm and 10mm, respectively. Colwell & Basu (2009) use a tapering steel tower for their study, but employ a thickness of 18mm at the base and 10mm at the top of their 76m tower.

In concrete turbine tower design, the wall thickness depends on the method of construction (prestressed pre-tensioned, prestressed post-tensioned or reinforced), the strength of the concrete and the quantity of prestress and reinforcement. In this study, the model has been kept as generic as possible and was modelled as a reinforced concrete tower with no applied prestress.

Tricklebank *et al.* (2007) highlight a number of manufacturers who have developed concrete tower solutions: for hub heights up to 113m, Enercon have used precast reinforced concrete rings with wall thicknesses of around 350mm; Mecal and Hurks Beton use precast concrete elements with wall thicknesses of 250-350mm; GE Wind have used a wall thickness of 350mm for a 100m tower. Tricklebank *et al.* (2007) suggest suitable values for wall thickness of 300-400mm at the base of the tower, 150-175mm in the middle zone and a minimum thickness of 100mm in the top zone.

2.3. Material Properties and Fixity

The material properties of steel and concrete were defined as: E_{steel} = 200GPa, ρ_{steel} = 7850kg/m^3, $E_{concrete}$ = 30GPa, $\rho_{concrete}$ = 2400kg/m^3.

Both towers were analysed as fully fixed at the base; this is common practice according to Bazeos *et al.* (2002), and is based on the assumption that onshore towers have over-designed foundations in stiff soils. These models could also represent offshore towers, where the base of the tower begins at the top of the foundation section.

3. Finite Element Model

A simple finite element model (FEM) was developed using LUSAS software to model the two 90m towers. Thick non-linear beam elements (BMS3) were used in the analysis; this element was chosen as suitable following correlation of the free vibration behaviour of a cylindrical tower modelled in LUSAS with multi degree of freedom analysis.

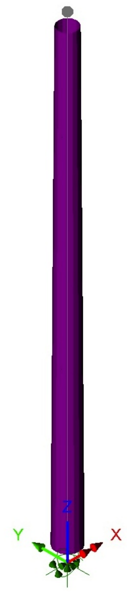

Figure 1: LUSAS model of tapered tower.

The geometric properties at the base and top of the towers were defined as circular hollow sections with appropriate diameter and cross section properties. Intermediate values were linearly interpolated by LUSAS.

In order to complete the eigenvalue analysis, a concentrated mass representing the RNA was defined at the top of the tower.

A schematic of the LUSAS model is shown in Figure 1a.

3.1. Free Vibration Response and Tower Classification

The primary concern in designing a wind turbine's tower is to ensure that the structure is not excited by resonance due to the frequency of the rotor forces, i.e. at rotational or blade-passing frequency. Hau (2006) identifies the relative position of the first natural bending frequency and the rotor exciting frequencies as the 'decisive criterion' for vibrational behaviour of the tower. The first natural bending frequency for both towers, determined from LUSAS eigenvalue analysis, is shown in Table 2.

Table 2: First bending frequencies of 90m steel and concrete towers

Applied RNA Mass (t)	Steel 1st Bending Frequency (Hz)	Concrete 1st Bending Frequency (Hz)
0	0.691	0.454
50	0.382	0.37
100	0.293	0.319
150	0.246	0.285

The relative positions of the bending frequencies of a turbine tower, in relation to the rated speed of the rotor and blade passing frequency, allow the tower to be classified. This classification ranges from extremely soft (first bending frequency less than rotational frequency to stiff (first bending frequency greater than blade passing frequency).

3.2. Simple Load Models

In order to simulate loading on the wind turbine tower structure, analysis was carried out in accordance with three models outlined as *simplified load calculations* in DNV/Risø (2001). Load models were developed to loosely represent each of the three turbines (1.5, 2, 2.5MW) outlined above. Each load combination was applied to the top node of the steel and concrete towers as concentrated forces/moments, and the displacements at the yaw bearing were determined.

These simple load models are included by DNV/Risø (2001) to provide tools for preliminary calculations and quick checks of results; advanced aeroelastic codes such as FAST (Section 4) are now available which makes simple load calculations unnecessary. However, this study focussed on the relative responses of steel and concrete towers, and in this context the actual loading itself is less significant.

Simple Load Basis (SLB)

The SLB is the simplest load definition method outlined by DNV/Risø (2001). It is an empirical equation, based on measurements from typical stall-regulated turbines. Load components are defined in each of the three orthogonal directions. Each component has a static and dynamic element, defined as functions of the rotor radius, turbine rated power rotor frequency.

Quasi-Static Method (QSM)

The QSM gives four design loads for a still-standing horizontal axis wind turbine in severe wind conditions – blade load, axial load, tilt moment and yaw moment. Each design load is calculated using a series of equations, which lead to definition of the load per unit length on the blade. These loads are purely static.

Parameterised Load Spectra Model (PLSM)

The PLSM is an extension of the SLB, however in this case the load components are expressed as the sum of a deterministic mean load $\overline{F}$ and a varying stochastic component, at the blade passing frequency, outlined in Equation 1.

$$F = \overline{F} + \frac{1}{2}F_{\Delta}\cos(2\pi n_C t) \qquad (1)$$

3.3. Results

The results from the LUSAS tapered tower models subjected to the DNV/Risø (2001) load combinations are shown in Table 3, which expresses the peak displacement of the concrete tower as a percentage of the peak displacement of the steel tower (i.e. the displacement of the steel tower is 100%).

For each load case, a time domain implicit dynamic analysis was performed on each tower over a period of 600 seconds with a time step of 1 second. The peak resultant displacement at the top of the each of the towers was noted.

Table 3: Selected results from LUSAS models

Loading		Relative displacement of concrete tower to steel tower
SLB	1.5MW Full Dynamic	67%
	2.0MW Full Dynamic	53.6%
	2.5MW Full Dynamic	42.8%
QS	1.5MW	52.66%
	2.0MW	54.95%
	2.5MW	52.66%
PLSM	1.5MW	96.32%
	2.0MW	55.9%
	2.5MW	18.8%

4. FAST

Developed by the National Renewable Energy Laboratory, the acronym FAST stands for fatigue, aerodynamics, structures and turbulence; it is an aeroelastic code certified by technical classification organisation Germanischer Lloyd for the design and analysis of onshore wind turbines.

FAST allows the user to completely define the physical properties of the turbine superstructure (platform, tower, nacelle, etc.), along with the ability to define and control the operation of mechanical aspects of the turbine operation (blade pitch, generator torque, nacelle yaw, etc.). FAST then analyses the wind turbine model under 4D wind conditions. The user has the ability to choose the required output data from the simulation.

4.1. FAST Models

The same 90m steel and concrete towers that were used for the FEM were redefined in FAST. The dimensions at the top and bottom of the tower were specified, allowing FAST to interpolate intermediate values; 64 nodes were used in the analysis.

FAST provides a number of test files, which can be used as a basis for defining individual turbine models. Test files 11-13, defined for testing a WindPACT 1.5MW turbine, were chosen. Elements of the turbine were redefined to resemble the Nordex S70 used for the LUSAS model.

Tests 11 (pitch failure in turbulence), 12 (extreme direction change) and 13 (turbulence) were simulated for both towers, along with two user-defined tests – turbine start-up and loss of grid connection. The tests were simulated for 20 or 40 seconds, depending on the size of the wind data file available.

4.2. Results

The findings from the FAST tests are shown in Table 4, which shows the relative resultant displacement values at the yaw bearing of the concrete tower in relation to the steel tower.

Peak displacements generally occurred before automatic blade pitching was initialised (which can be controlled in FAST), whereas the mean values indicate the average displacement values over the duration of the simulation.

Table 4: FAST test results

FAST Model Test	Peak/Mean value	Relative Displacement of Concrete Tower to Steel Tower
11	Peak	48.8%
	Mean	53.3%
12	Peak	47.4%
	Mean	53.1%
13	Mean	53.4%
Start up	Peak	58.9%
Loss of Grid Connection	Mean	64.1%

5. Conclusions

Table 5 shows the classification of both steel and concrete towers with various RNA masses, based on the nominal or average rotor speed of each of the turbines. The most likely tower classifications, based on the assumed RNA mass, are highlighted in bold.

Table 5: Tower classification (ES: Extremely Soft, VS: Very Soft, S: Soft, St: Stiff)

	90m Steel Tower				90m Concrete Tower			
Turbine Model	0t	50t	100t	150t	0t	50t	100t	150t
Nordex S70/S77 1.5MW	S	**VS**	**VS**	VS	VS	**VS**	**VS**	VS
Vestas V80 2MW	S	VS	**VS**	ES	VS	VS	**VS**	VS
Nordex N100 2.5MW	St	VS	**VS**	**VS**	S	VS	**VS**	**VS**

Both steel and concrete towers are classified as very soft when operating in conjunction with any of these three turbines. This agrees with Harrison (2006) who indicates that the most common stiffness concept is to have a first bending frequency at 1.5 times the rotor speed, i.e. very soft.

It can be seen from Table 3 and Table 4 that the results follow the same general trend: the peak (or mean) resultant displacement at the top of the concrete tower is less than that of the steel tower.

Considering the results from the LUSAS model simulations, the average relative displacement value for the concrete tower is 54.22% (53.52% excluding PLSM). The FAST analysis gives an average value of 53.56%.

Under the same load conditions, the concrete tower always performs better than the steel tower – displacing almost half as much at the top of the tower.

It should be noted that only the vibration behaviour and displacement response of the towers under loading were investigated in this study; other critical parameters such as breaking strength, buckling strength, stiffness were not explicitly determined and were assumed to be adequate based on the similarity to models from the literature.

According to Hammond & Jones (2008), the embodied energy of this 90m model steel tower is 3007GJ, whilst the value for the 90m concrete tower is 374GJ (12.4%); similarly, the amount of embodied CO_2 in the two towers are 339000kgCO_2 for the steel tower (virgin steel), compared to 39689kgCO_2 (11.7%) for the concrete tower (no replacement materials).

These towers would require 123.3t of steel and 187.2t of concrete, respectively. The total material cost for the two towers would depend on current market prices, however Tricklebank *et al.* (2007) indicate that concrete tower designs are at least competitive, with potential savings of up to 30%; slip-formed towers provide the greatest potential savings.

This research indicates that concrete turbine towers provide significantly better performance under loading than equivalent steel towers, with similar vibrational behaviour. Additionally, concrete towers have considerably lower embodied energy and CO_2 values. With limited steel manufacturing in Ireland and the availability of high quality local aggregates, concrete provides a more sustainable, economic alternative for the next generation of wind turbine towers in Ireland.

References

Bazeos, N., Hatzigeorgiou, G.D., Hondros, I.D., Karamaneas, H., Karabalis, D.L., Beskos, D.E. (2002) Static, seismic and stability analyses of a prototype wind turbine steel tower. *Engineering Structures,* 24(8) August, pp1015-1025.

Burton, T., Sharpe, D., Jenkins, N., Bossanyi, E. (2001) *Handbook of wind energy.* Chichester, John Wiley & Sons.

Colwell, S., Basu, B. (2009) Tuned liquid column dampers in offshore wind turbines for structural control. *Engineering Structures,* 31(2) February, pp358-368.

Department of Communications, Marine and Natural Resources (2007) *Delivering a Sustainable Energy Future for Ireland: the energy policy framework 2007-2020.* Dublin, Stationery Office.

Det Norske Veritas & Wind Energy Department, Risø National Laboratory (2001) *Guidelines for Design of Wind Turbines.* Copenhagen, DNV/Risø.

European Commission (1997) *Energy for the Future: Renewable Sources of Energy. White Paper for a Community Strategy and Action Plan.* Brussels, European Commission.

European Wind Energy Association (2009) *Pure Power: Wind energy targets for 2020 and 2030.* Brussels, EWEA.

Hammond, G.P. & Jones, C.I. (2008) *Embodied energy and carbon in construction materials.* Bath, University of Bath.

Harrison, R., Hau, E., Snel, H. (2000) *Large Wind Turbines Design and Economics.* Chichester, John Wiley & Sons.

Hau, E. (2006) *Wind Turbines: Fundamentals, Technologies, Application, Economics.* 2nd ed. Berlin, Springer.

Jonkman, J. M. & Buhl Jr., M. L. (2005) *FAST User's Guide NREL/EL-500-29798.* Golden, NREL.

Lavassas, I., Nikolaidis, G., Zervas, P., Efthimiou, E., Doudoumis, I.N., Baniotopoulos, C.C. (2003) Analysis and design of the prototype of a steel 1-MW wind turbine tower. *Engineering Structures,* 25(8) July, pp1097-1106.

Polyzois, D.J., Raftoyiannis, I.G., Ungkurapinan, N. (2009) Static and dynamic characteristics of multi-cell jointed GFRP wind turbine towers. *Composite Structures,* 90(1) September, pp34-42.

Singh, A.N. (2007) Concrete construction for wind energy towers. *Indian Concrete Journal,* 81(8) August, pp43-49.

Tricklebank, A.H., Halberstadt, P.H., Magee, B.J., Bromage, A. (2007) *Concrete Towers for Onshore and Offshore Wind Farms.* Camberley, The Concrete Centre.

FEASIBILITY OF CONCRETE WIND TURBINE TOWERS

A.QUILLIGAN, A.O'CONNOR
Dept. of Civil, Structural & Environmental Engineering,
Trinity College Dublin, Ireland

Abstract

In just a few short years wind turbine outputs have increased from a mere few hundred kilowatts up to a current maximum of 7.5MW (Enercon E-126). These advances, however, mean that with increasing turbine outputs there is also a similarly dramatic growth in rotor diameters and, therefore, tower heights. As tower heights go beyond 100m (e.g. Enercon E-126 has a 135m hub height) there are a number of limiting issues surrounding the current preference for a steel solution. This has led to numerous proposals for the use of prestressed concrete and/or hybrid materials in the construction of wind turbine towers with hub heights beyond 100m. The aim of this paper is to investigate the consequences of increasing tower heights, as well as increasing rotor and nacelle masses, on current wind turbine tower construction methods. This is in essence the genesis of a comparative study of steel and concrete as viable tower solutions at heights greater than 100m. Discrete modelling of the tower, blades and a coupled system of a tower with rotating blades is carried out in order to compare the response frequencies. It is proposed to verify these discrete models using both finite element software as well as an aero-elastic code called FAST which has been developed by the U.S Department of Energy. Further to this, the advantages of using prestressed concrete as a wind turbine tower solution in Ireland and internationally is presented.

Keywords: Concrete wind turbine towers, Steel wind turbine towers, Discrete Modelling, Finite Element Modelling, Aeroelastic Analysis.

1. Introduction

With the looming consequences of the Kyoto Protocol and the obvious signs of climate change globally, renewable energy is now both a political and social issue of primary importance. At the forefront of this renewable energy push is wind energy with its primary use in electricity generation. In recent years the global generating capacity has grown at 20% - 30% per year, having surpassed 90GW in 2007 (50 times the installed capacity of 1990). This growth is expected to continue for the foreseeable future with an estimated global investment projected to total more than $1 trillion (US) by 2020, bringing global installed capacity to more than 600,000 MW. In recent months the British government issued contracts to develop wind farms with a total capacity of 32GW over the next ten years. This offshore project alone has a projected investment of €110 billion.

Ireland is located at the western tip of the continent of Europe at the mercy of the Atlantic Ocean and is therefore well endowed with a good wind resource. Wind turbines and wind energy have become widely debated topics in recent times, particularly in Ireland where there is a general recognition of the potential to harness the vast power of the wind. An Irish government energy white paper entitled Delivering a Sustainable Energy Future for Ireland (Dempsey 2007) sets out the Irish government's energy action plans towards 2020. A primary target is that 33% of Ireland's electricity consumption will be generated from renewable sources by 2020 although the European Wind Energy Association (EWEA) estimates that this figure could in fact be closer to 50% as outlined in table 1 (Zervos and Kjaer 2009).

	Installed 2008		Installed 2020 (Estimated)			
	(MW)	(%) of total electricity	Low (MW)	(%) of total electricity	High (MW)	(%) of total electricity
Ireland	1,002	9.3%	6,000	47.8%	7,000	55.4%
UK	3,241	2.3%	26,000	18.6%	34,000	24.9%
Denmark	3,180	20.3%	6,000	42.5%	6,500	46.2%

Table 1 - EWEA Predicted Scenarios for Installed Capacity in Ireland for 2020

Ireland's wind energy resource is approximately four times that of the European continent with an estimated technical resource of 613TWh per year of which only 2.8TWh was harnessed in 2007, less than half a percent of the estimated technical resource (Harris and Hesmondhalgh 2004). To further outline the potential for wind generation it can be seen that in 2003 Ireland's annual electricity consumption came to 27TWh. As Ireland attempts to attract international investment and work towards creating a "smart" economy, a clean renewable electricity network is a considerable bonus for any companies who look at the possibility of moving to Ireland. Further to this, with the introduction of interconnectors to the U.K and France, both planned and under construction, this could see Ireland becoming a net exporter of clean renewable electricity in the near future.

As turbines become bigger and more powerful, reaching higher into the atmosphere to obtain greater wind speeds, there are also obstacles which require research and ingenuity in order to further advance wind power capabilities. Hau (2006) states that manufacturing steel tubular towers with a diameter of up to about 4m is a conventional technology that does not make any great demands on the equipment of the manufacturers. At heights of more than 90 m, the tower base diameter becomes greater than 4.5 m and the required thickness of the steel exceeds 40 mm. Shaping the steel sheets, i.e. roll-bending them, will then require special machines which are not always available in normal structural steel works. Added to this, due to the large diameter, the lower tower sections can no longer be transported by road. Tricklebank et al. (2007) also suggests prefabricated or cast-in-situ concrete as a solution to the unsolvable transport problems encountered by onshore steel wind turbine towers which may be understood from Figure 1.

Figure 1 - Transport of Steel Tubular Tower Section (approx 4m ø)

2. Concrete as a Tower Solution

The preliminary aim of this research is to generate a detailed comparison of the performance of concrete wind turbine towers with their steel counterparts. There are a number of reasons for addressing such a project:

- Continually increasing hub-heights and greater masses necessary for more modern and powerful turbines are stretching steel to its physical limit. Tricklebank et al. (2007) states that concrete is an adaptable construction material which can be easily fine tuned by alterations in mix design and prestress to optimise parameters such as strength, stiffness and density. It also states that transportation problems can be easily overcome by using precast concrete sections which incorporate simple jointing details allowing sections to be designed and transported to site limited only by size and weight.
- The non-existence of a steel industry in Ireland means that steel towers are designed, fabricated and imported from abroad which adds massively to transport costs and is a lost opportunity in terms of local employment. This is countered by the existence of considerable resources, expertise and manufacturing capability in both the pre-cast and cast-in-situ concrete industries in Ireland. Concrete can also be manufactured locally using readily available materials which results in a major impact on transport costs.
- A more sustainable and environmentally friendly solution is possible with concrete as concrete possesses a much longer service life of between 60 and 100 years (steel towers are designed for 20 to 30 years (Hau 2006)). This is due to concrete's better resistance to fatigue and the ability to fine tune its stiffness properties to suit particular loading conditions. Concrete can also be produced efficiently from recycled materials (i.e. Ground Granulated Blast Furnace Slag - GGBS and recycled aggregates) and towers could be easily decommissioned and recycled at the end of their service lives. This is particularly straightforward when the prestressing tendons are located outside of the concrete section and this also allows easy access for inspection and repair of the strands.
- A concrete alternative presents a major opportunity to tackle the environmental problem while using indigenous materials, resources and expertise, resulting in the generation of significant employment. This will also permit the opportunity to refine capabilities in this sector, allowing Ireland to become a global leader in concrete wind turbine tower construction and exporting these services to other nations striving to reach their renewable energy targets.

3. Discrete Modelling

In order to gain a comprehensive understanding of the vibration properties of a wind turbine system it is first necessary to look at the individual flexible elements of the system. These include, at a basic level, the rotating blades and the tower carrying the nacelle and rotor. Initially the free vibration of each of the elements individually will be considered. This can subsequently be extended to include the system of the tower coupled with the rotating blades.

3.1. Free Vibration of Towers

In reality, the towers which are considered represent systems of infinite degrees of freedom (DOF); however, the number of DOF required to accurately represent the free vibration of the system may be reduced and a lumped mass multi degree of freedom (MDOF) system ensues. The free vibration of such a system is represented by:

$$[m]\{\ddot{x}(t)\} + [k]\{x(t)\} = 0 \tag{1}$$

Where [m] denotes the mass matrix, [k] is the stiffness matrix and x(t) is the nodal displacement vector. This corresponds to an eigenvalue problem, the solution to which are the eigenvalues and the eigenvectors which represent the natural frequencies and mode shapes respectively.

3.2. Free Vibration of Blades

In reality wind turbine blades are extremely complex components, with both mass and stiffness varying along their three global axes. These components are much too complicated to be perfectly replicated in such a simple model. It is, therefore, suggested to model the blades as prismatic members for the purposes of this investigation.

There are two types of free vibration motion which are of interest in looking at rotor blades, termed flapping motion and lead/lag motion. Flapping occurs in the direction of wind flow while lead/lag occurs in the perpendicular direction (the direction of rotation of the blades). The flapping motion generally occurs at lower frequencies due to the reduced stiffness of the blades in this direction.

When analysing the free vibration of the blades there are a number of additional influences to be considered. As the blades rotate, they experience an outward axial force, known as centrifugal stiffening, which has the effect of increasing the stiffness of the blade (Murtagh 2005). Also, as the blade rotates the direction of the self weight force changes. When the blade is horizontal, there is no component of the force acting along the centroidal axis of the blade. Otherwise, however, there is a force acting along the blade which increases stiffness when its direction is outward (when the blade tip is below the hub) and reduces stiffness when it acts towards the centre of the rotor (blade tip above the hub). These additional influences are accounted for in a geometrical stiffness matrix which is added to the flexural stiffness matrix when analysing the model:

$$[K_B{}'] = [K_B + K_{GB}] \tag{2}$$

where $[K_{GB}]$ represents the geometrical stiffness matrix which is dependent on the blade rotational frequency as well as the angle the blade makes to the horizontal and is outlined in the following equation:

$$[K_{GB}] = \begin{bmatrix} \frac{N_1}{l_1} & \frac{-N_1}{l_1} & \cdots & 0 \\ \frac{-N_1}{l_1} & \frac{N_1}{l_1} + \frac{N_2}{l_2} & \cdots & 0 \\ \vdots & \vdots & \ddots & \frac{-N_{N-1}}{l_{N-1}} \\ 0 & 0 & \frac{-N_{N-1}}{l_{N-1}} & \frac{N_{N-1}}{l_{N-1}} + \frac{N_N}{l_N} \end{bmatrix} \tag{3}$$

where N_i represents the axial force due to a combination of centrifugal stiffening and self weight, l_i denotes the distance between nodes 'i' and 'i+1' and N is the total number of nodes.

Equation (1) is again applicable to the system of the rotating blades and, by solving this, the free vibration frequencies and mode shapes for the blades may then be acquired.

3.3. Coupled Tower/Nacelle and Blades

A rotating, three bladed rotor fixed to the top of a wind turbine tower represents a multi-body MDOF system where the vibration of the rotating blades has a significant influence on the vibration motion of the tower. Once the free vibration properties of all of the individual elements have been established independently, they can then be coupled together mathematically. Murtagh (2005) makes the assumption that vibration of the tower/nacelle and the blades occur in their fundamental mode shapes only, allowing each system to be reduced to a single degree of freedom system (SDOF). This is justified by suggesting that the higher modes contribute insignificantly to the dynamic response. The complex MDOF problem is therefore reduced into a more simple two DOF system with the blades and tower/nacelle each representing a DOF.

The modal mass of the tower/ nacelle can be acquired by the following equation:

$$M_n = [\emptyset]_n{}^T [m] [\emptyset]_n \tag{4}$$

where [m] is the mass matrix for the tower/nacelle and $[\emptyset]_n$ is the mode-shape corresponding to the n^{th} natural frequency. When n = 1 we get the modal mass for the first mode of vibration. The modal stiffness can then be calculated by multiplying the modal mass by the square of the natural frequency:

$$K_n = \omega_n{}^2 M_n \tag{5}$$

When the rotating blades vibrate, they impart a shear force into the tower and it is this force which strongly couples the motion of the blades to the tower. When vibrating in flapping mode, the full force is transmitted to the tower while when in lead/lag mode only the horizontal component is of interest. In the flapping case this force is calculated as follows:

$$V_{BF} = \omega_{BF1}^2 [M_B][\emptyset]_{B1} \tag{6}$$

Where ω_{BF1} is the first natural frequency of the blade in the flapping direction, while $[M_B]$ and $[\emptyset]_{B1}$ denote the blade mass matrix and the first mode shape of the blade respectively. The lead/lag force is calculated in a similar fashion except only the horizontal component of the force is taken.

In order to account for the three blades this force is multiplied by three for the flapping case and two for the lead/lag case as the blades act in and out of phase with each other during lead/lag motion. This force can then be used to calculate the modal stiffness value for the blades;

$$F = K_s u(L_B, t) \tag{7}$$

Where $u(L_B, t)$ is the relative displacement of the tip of the blade. For the first bending frequency this value is assumed to be one. The modal mass can again be calculated in a similar way to the stiffness for the case of the tower using equation (5). Now that all of the elements of the 2 DOF problem are assembled the system may be easily solved using equation (1).

4. Finite Element and Aeroelastic Modelling

In order to verify the results of the discrete model it is necessary to accurately generate a benchmark to which the results may be compared. One option would be to gather data from wind turbine manufacturers who have already calculated the vibration properties of the elements during the design process. However, due to major competition between wind turbine manufacturers, this information is kept as a closely guarded secret and little information has been found to date.

Finite element modelling is a proven and tested means of analysing complex structures to great accuracy. A simple FE model of the tower will quickly yield the natural frequencies for comparison with the discrete tower model. Not only can the results for the blades be compared in this way but a more detailed representation of an actual wind turbine blade may be modelled using the finite element method. The results of this may subsequently be used to improve the original discrete model, in particular for the coupled case. With some effort a complete model, including all elements of the wind turbine, will be generated to verify the results of the discrete coupled model. Finite Element modelling will, therefore, play a significant role in the analysis of the dynamic behaviour of both the steel and concrete wind turbine towers investigated in this research. Outside of dynamic behaviour these models can also be easily manipulated to investigate structural performance in various loading conditions.

The National Wind Technology Centre (NWTC) which is part of the U.S Department of Energy has produced a number of certified design codes which are available to the public on their website http://wind.nrel.gov/. One such code is FAST (Fatigue, Aerodynamics, Structures and Turbulence) which is a comprehensive aeroelastic simulator capable of predicting both fatigue and extreme loads for two and three bladed horizontal axis wind turbines. FAST allows all aspects of the wind turbine to be modelled as a MDOF coupled system in the time domain. This includes many of the mechanical components inside the nacelle which are not of considerable interest to this particular research. Different variations of wind loading can be specified, including turbulent wind inflow. Various scenarios of operation can also be implemented, including turbine shutdown, rapid change of direction, loss of generator torque and when the rotor is stationary. It is obvious that this aeroelastic code has many more capabilities than is required for this research but it does offer a certified benchmark to which results may be compared. Further to this, FAST may be linked with the mathematical modelling software Matlab (www.mathworks.com/) which is used for the discrete modelling phase. It will be possible to use many of the capabilities of FAST as part of the discrete model in the future. This will be most beneficial when analysing the wind loading time-histories.

5. Conclusions

With its long service-life relative to steel, and its superior properties in terms of structural performance and reusability, concrete is establishing itself as both a more sustainable as well as more efficient solution compared to steel, particularly for towers of heights beyond 100m. Coupled with the large transport costs involved in importing steel towers and the possibilities for a concrete alternative are easily recognised.

Furthermore, if the ambitious targets of 55% electricity generation are to be met by 2020, it would make sense to utilize indigenous industries and expertise as much as possible, therefore generating more employment and trade in the national economy.

Banagher Concrete in Co. Offaly, who part fund this project, have obtained a license for a proven precast concrete tower construction system. It is vital that these systems become more established in the wind energy market in the near future. It is planned to add five to six thousand MW of installed capacity in the next ten years. Besides the environmental advantages of such an undertaking, this could also greatly boost employment in the struggling construction sector, form a new branch of the smart economy and have a more sustainable solution by moving towards a concrete alternative.

In terms of modelling both steel and concrete wind turbine towers, this is a necessary step in analysing the performance of both solutions. Using the three techniques outlined in this paper along with any available information sources will ensure that an accurate and fair comparison may be drawn between steel and concrete towers.

Collaboration with the companies who will implement the construction of these turbines such as ESB, Bord Na Móna or Bord Gáis Energy is planned in the future of this project.

References

Dempsey, N. (2007). Delivering A Sustainable Energy Future For Ireland. D. o. C. M. a. N. Resources.

Harris, D. and S. Hesmondhalgh (2004). A Study on Renewable Energy in the New Irish Electricity Market, Sustainable Energy Ireland.

Hau, E. (2006). Wind Turbines: Fundamentals, Technologies, Applications, Economics, Springer, Berlin.

Murtagh, P. J. (2005). Dynamic Response of Wind Turbine Tower Assemblies. Civil & Environmental Engineering. Dublin, Trinity College Dublin. **Ph.D**.

Tricklebank, A. H., P. H. Halberstadt, et al. (2007). Concrete Towers for Onshore and Offshore Wind Farms, The Concrete Centre**:** 56.

Zervos, A. and C. Kjaer (2009). Pure Power: Wind energy targets for 2020 and 2030, European Wind Energy Association.

LESSONS LEARNT – PROBLEMS TO SOLVE

E.R. FARRELL

Dept. of Civil, Structural & Environmental Engineering, Trinity College Dublin, Ireland

Abstract

The infrastructural developments which were part of the 'Celtic Tiger' saw a massive increase in both the number and scale of large engineering projects in this country and, consequently, a requirement for an increased understanding of the behaviour of Irish soils. These developments included the construction of deep basements in many parts of the country, large scale dewatering projects, motorways, embankments, windfarms and tunnels. The increased scale of the projects saw the use of more sophisticated in-situ and laboratory testing for these projects, and the increased affluence generated more funding for geotechnical research.

This paper will review the geotechnical knowledge gained in recent years and the contribution that research has made to the construction of our infrastructure. The deficiencies in our geotechnical knowledge will be discussed and areas which require further development will be highlighted.

Keywords: boulder clay, classification, piling, spt, peat slide.

1. Introduction

The increased construction activity, together with the increased number of large public and private infrastructural projects that accompanied the improved economic conditions in Ireland during the 'Celtic Tiger' years, offers an excellent opportunity to review limitations in our geotechnical and geological knowledge and to assess the contribution of geotechnical research. The larger projects generally require more sophisticated and more detailed methods of analysis, with a consequential requirement for a better understanding of the behaviour of soils and rock. Many of these projects were designed by overseas consulting engineers not particularly familiar with our soils, which frequently highlighted the special features of Irish soils.

A complete review of the recent geotechnical experience proved a daunting task, consequently this Keynote Address is limited to the author's experience in research and in practice. Only brief reference is made to the research of my colleagues in Trinity College, Dublin or to that from the other research centres. Many different geotechnical issues could be discussed and the topics selected for this paper are:-

- Use of the term 'boulder clay'
- Description and classification of boulder clays
- Development in soil models and numerical methods
- Piling in glacial soils, including glacial sands and gravels
- Research into construction methods on peat
- Model for 'Flow slide' of peat caused by progressive failure

2. Use of the term boulder clay

Glacial soils include a variety of deposits laid down during the glacial period, for example some were associated with glaciers (lodgement and englacial tills) and others with lakes (glacial lacustrine) or rivers (glacial fluvial) which were formed as the ice melted. The lodgement and englacial tills are the most abundant and have interesting and somewhat unique geotechnical properties. These tills have a very characteristic grading which is almost linear when plotted on the semi-log particle size distribution curve – see Figure 1, with about an equal proportion of sand and gravel size particles. The fines content, which comprises the silts and clay size particles, is generally about 30% to 40% with low to very low plasticity indices (IP), and would be classified as low plasticity clay or silt. These soils would be colloquially termed ‘boulder clay’. Considering that there are few if any boulders in much of this till the term would appear to be inappropriate but its properties are generally understood by geotechnical engineers and there is no better alternative. These boulder clays have several unique features compared with typical ‘clay’ soils, some of which are listed on Table 1. There unique features affect the design of slopes and excavations in and embankments on these deposits.

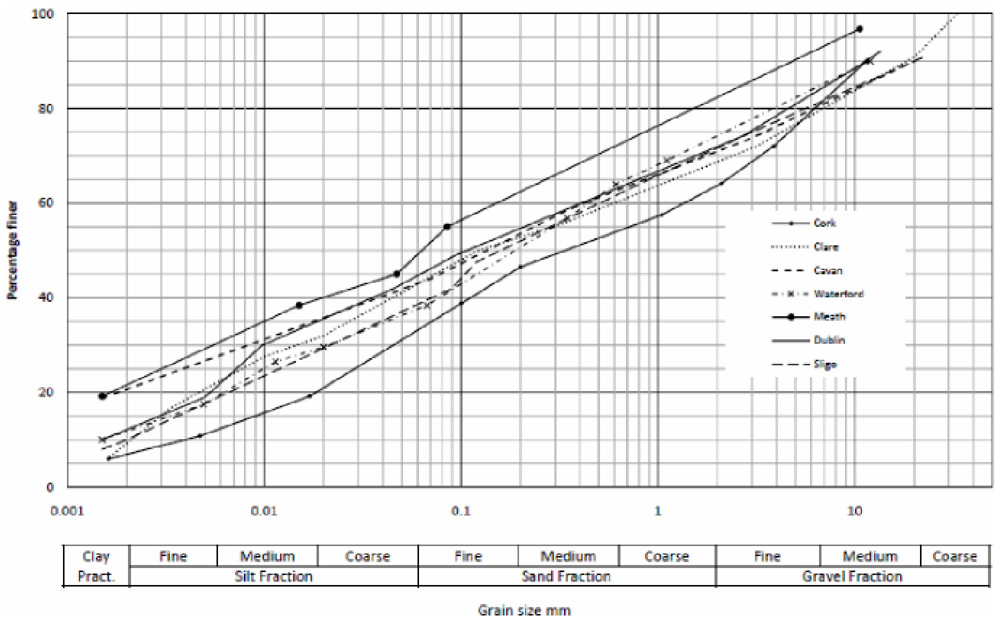

Figure 1 (after Hanrahan, 1977)

3. Description & Classification of boulder clays

The determination of the engineering parameters of boulder clays can be very difficult. Standard penetration tests can give some indication of the in-situ strength, however engineering experience has shown that the actual performance of these soils in many design situations is satisfactory even when ground and laboratory tests indicate that the in-situ strength is low. For example, relatively high road embankments (up to 13m on the Kildare Bypass) have been successfully constructed on such soils without the need for significant ground improvement measures. The experience would suggest that the consolidation was relatively high in the field and the compressibility relatively low, however it is difficult to determine the actual parameters required for geotechnical calculations by either in-situ or laboratory tests due to the stone content. Pressuremeter and Marchetti Dilatometer tests were tried on the Kildare Town Bypass and elsewhere, without success and laboratory tests to date generally lack the larger stones due to limitation on the size of the test apparatus. Consequently, engineering decisions are frequently reliant on good judgement.

Given the continuing reliance of ‘engineering judgement’ in the assessment of the engineering behaviour of some of the tills, it is important that the soil descriptions and classification systems adopted enable a boulder clay to be identified from boreholes and trial pit logs. Boulder clays are generally described in this country as a ‘sandy gravelly Clay’, or ‘sandy gravelly Silt’ in current practice, however these descriptions are not in compliance with BS5930: 1999 which requires minor constituents to be described as ‘slightly sandy/slightly gravelly’ if less than 35% by weight, and also states that ‘*Descriptions with cumulative proportions of the various fractions exceeding 100% are incorrect’*. Geotechnical engineers or engineering geologists from outside this country frequently adopt the more correct descriptions such as slightly gravelly sandy Clay; however such a description is not readily identified as a boulder clay. Particle size distribution curves would, of course, enable the true nature of the soil be identified, however the results of such tests are not always available. In order to overcome this disparity, it is suggested that the classification system be altered such that when the combined percentage of sand and gravel exceeds 50%, the term sandy and gravelly should be used if both of the individual constituents exceed 20%.

Eurocode 7: Pt 2 (IS EN 1997-2, 2007), which came into force earlier this year, refers to IS EN ISO 14688-1 and EN ISO14688-2, the former covering the Identification and Description of soils and the latter covers the Principles for a Classification. The suggestion made above regarding the qualifying terms ‘sandy’ or ‘gravelly’ conforms with the latter document (on Table B1) however that document suggests that 40% fines would be required in order for a boulder clay to be classified as such. In fact, as none of the constituents of our boulder clay make up 40% by weight, no main term would be appropriate. It is considered that this boundary for Irish soils should be 35%.

It is important that ‘engineering’ be brought into the systems used for the description and classification of soils. For example, BS 5930 allows for descriptions to be varied based on the ***personal assessment of its engineering behaviour***, without defining what aspect of the engineering behaviour is relevant. What is the significant difference between a gravelly Clay and a clayey Gravel? A fundamental requirement of a ‘clay’, in the author’s opinion, is its ability to stand unsupported in a relatively shallow excavation, say 3m high, in a ‘temporary condition’, provided it has the required undrained shear strength, in other words it requires a reasonable standup time. This ‘standup time’ is related to its ability to hold suction pressures and therefore to its permeability and stiffness. From experience and from the variation in permeability, a fines content of 35% or greater in a Boulder Clay would be expected to satisfy this requirement and would be expected to be called a Clay. In the experience of the author, a slope failure during the construction of a project in the black boulder clay which had 20% fines content confirmed the lack of ability to maintain the suctions, and a description of very clayey Sand/ Gravel would have been more appropriate - see Table 2. It is useful to recall that the Casagrande Classification system, which is the basis of the classification between a silt and clay adopted today in most countries, was developed from the descriptions of experienced geotechnical engineers who were circulated with representative samples. It is considered that Irish geotechnical engineers should ensure that any soil description or classification system adopted here include the essential engineering features of our boulder clays such that 'engineering judgement' can be correctly applied to the resulting descriptions and classifications.

Significant Engineering behaviour of 'Boulder Clay'
Generally called a 'Boulder Clay', although typically boulders are very occasional.
Few true 'clay' minerals, mainly 'rock flour' particles.
Can be very dense, with bulk densities of up to 2.47Mg/m^3 measured for the very stiff/hard lodgement tills.
The dense lodgement till can be very stiff, particularly at low strains compared with many clays.
Relatively high effective stress parameters for a 'clay'
Little degradation in effective stress parameters at large strain (residual).
Low IP, consequently can be difficult to work in wet weather, particularly with low fines.
Can behave as a fine 'cohesive' or coarse 'cohesionless' soil depending on its fines content.
Generally low compressibility and low creep.

Table 1 Unique features of 'Boulder Clays'

% fines	Description	Classification
≥ 35%	Sandy gravelly Clay (or Silt) if it is a 'boulder clay' type grading. Fines define as Silt if dilates in the standard 'pat' test.	Main term - Clay or Silt depending on I_P and w_L in line with current practice. Sandy or gravelly if each is >20% and when the combined is in excess of 50% by weight.
< 35% fines	Very clayey (or silty) Sand/Gravel	Called a Sand/Gravel if both exceed 20%.

Table 2 Suggested changes in classification of soils.

4. Dublin boulder clays

One of the success stories of the collaboration of research and industry is the work carried out on the Dublin boulder clays. This is a lodgement till which has extremely high undrained shear strength and stiffness properties compared with other stiff clays, for example, when compared with London Clay. Some of the basic research work in the 80s and 90s highlighted the low 'clay' content of this deposit (Hartford, 1987) and the large scale footing trial at the Tallaght Town Centre (Farrell, 1989) confirmed its high bearing capacity. The high stiffness at low strains was confirmed by Tracy (1996) site trials and further information on the properties were contributed by the laboratory work of Lawler (2002). The Dublin Port Tunnel project was a major contributor to knowledge in this area, both in terms of stratification (Skipper et al, 2005) and in terms of strength and stiffnesss (Menkiti et al., 2004; Long & Menkiti, 2005). These construction experiences gave further confirmation of the unique very high stiffness and high undrained shear strength of the boulder clay that had been well known locally. This work also highlighted the importance of soil suctions in maintaining these strengths and stiffnesses. This knowledge was used effectively to develop cost- effective and safe construction options.

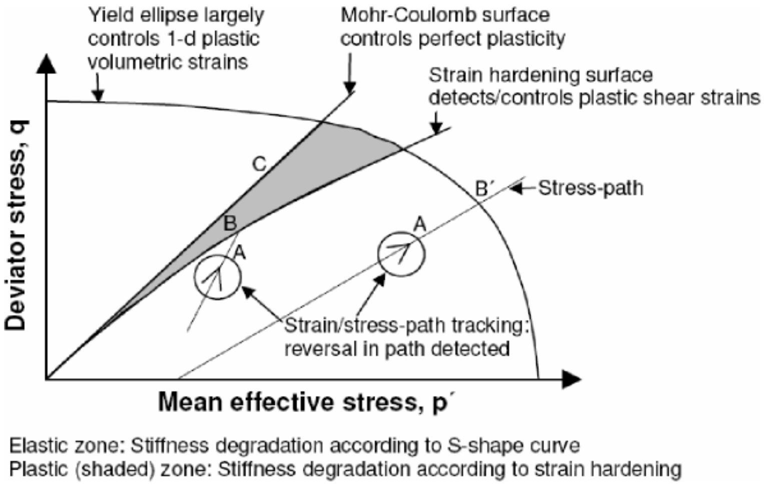

Figure 2 Sophisticated numerical modelling of soils.

Numerical modelling is becoming an increasingly important design tool in geotechnics, however it is important the soil models used in analyses incorporate the important aspects of the soil response modelled. The response of the Dublin Boulder Clay to a loading or excavation is complex as it depends on the stress history, the current stress state and on the magnitude and direction of loading (see Figure 2). Traditionally these differences in behaviour have been included in computer analyses by adjusting the input parameters for each specific design situation, which is obviously a significant limitation. The alternative is to adopt a more complex soil model that considers these factors, such as the commercially available HSS model (Lochaden et al., 2008), which is based on good quality laboratory and field data. While this HSS models many aspects of laboratory and field tests very well, further work is required as it gives a poor representation of the stress/strain recorded in some recently conducted undrained shear strength tests. The use of these sophisticated soil models is certainly the way forward, however it is necessary to develop methods of relating the required parameters to routine test parameters and, very importantly, to monitor controlled field trials to confirm that the computer models are correctly predicting the soil's response. Future model will no doubt incorporate anisotropy.

5. Earthworks in glacial soils

The description and classification of the boulder clay discussed earlier related to identifying soils which behaved as 'undrained' in the short term. There is of course a second, very important, soil classification system in use in this country, namely that given in the NRA Specification for Road Works, 2000, which uses geotechnically non politically correct terms such as 'non-cohesive' and 'cohesive' (the modern view is that 'cohesive' soils should be described as 'fine soils' in recognition of the part that suction pressure play in the cohesive behaviour). This different classification system is entirely logical as it is in reference to the requirements for the compaction of earthworks. In that context, soils having less than 15% fines being considered as 'non-cohesive' and, among other properties, their acceptability for use in fill is not primarily related to their in-situ moisture content as this could be altered by predrainage. 'Cohesive' soils are not therefore 'clays or silts' as defined in BS 5930. The NRA classification system has generally worked well for earthworks, the main difficulties arising from the low fines Boulder clay, particularly when the fines have low plasticity indices.

A major review should be undertaken into the reliability of the earthwork ground investigation information in relation to the actual performance of the material. The impression is that the laboratory test data carried out at the tender stage of many projects gave extremely low CBR values which conflict with strength assessment from $_{NSPT}$ and from the description on the logs. The most important information relating to the assessment of the acceptability of glacial soils is the CBR at in-situ moisture content and this information was frequently sparse or misleading in many of the tender ground investigations. The MCV is an empirical test which should be calibrated against the required design parameters, e.g limiting CBR and dry density. It does not directly measure any relevant parameter.

6. Piling in glacial soils, including glacial sands and gravels.

Two aspects of pile design/performance will be discussed in this section:-

- N_c in glacial till for bored/CFA and for driven piles, where $N_c c_u A$ is the end bearing pile capacity

- Interpretation of N_{SPT} in granular soils

Recent research has contributed significantly to a better understanding of the performance of piles in various types of soil. For example, the instrumented piles tests carried out at St James' Hospital (Farrell and Lawler, 2008) and at Ballsbridge (Gavin and Cadogan, 2008) have shown the distribution of shaft stress along CFA piles founded in the Dublin lodgement till. CFA and bored piles are easier to instrument than driven piles, consequently the Croke Park pile test (Farrell et al., 1998) is the only instrumented driven pile test to date. Most of the instrumented pile tests were in the Dublin boulder clays. Examples of the recorded shaft resistance for a driven pile and a CFA pile are given on Figures 3 and 4.

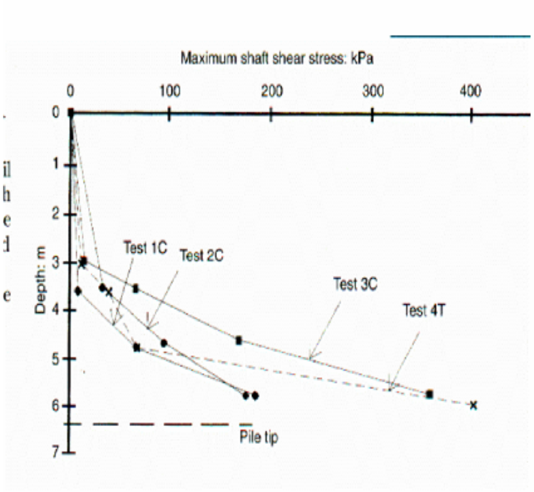

Figure 3 Shaft resistance along driven pile

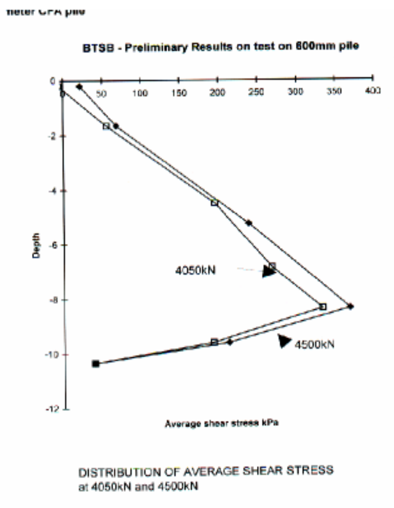

Figure 4 Shaft resistance along CFA pile

This research has also illustrated the significant difference between the value of N_c obtained from CFA and driven piles, with values of 7 to 9 being typical for the former type of pile and over 60 for the latter – see Figure 5. Intuitively differences are to be expected as driven piles would displace and therefore be expected to increase the effective stresses in the ground. However the variation in N_c is large and given that the majority of research data tends to be relate to the very stiff Dublin boulder clays, there could be a tendency for designers to expect the very high N_c values to apply for driven piles in other boulder clays in this country. The author has experience of one site three 425mm driven cast-in-situ piles 'failed' in a boulder clay (Pile 1, 48mm @750kN; Pile 2, 23mm @ 1100kN; Pile 3, 15.5mm@ 380kN). Back analysis using 〈 taken as 0.6, c_u taken as 5.5 N_{SPT} kPa, indicated an N_c value of about 15, which is closer to the value of 9 applicable to CFA piles. This back analysis was based on the N_{SPT} values, which were generally between 20 and 40 in the boulder clay and a c_u of 295kPa was recorded in a UU test in the deposit. The N_c factor for the driven cast-in-situ piles could have been affected by stress relief as the outer casing is withdrawn, however driven precast concrete piles penetrated considerably deeper. There has been a suggestion in some quarters that piles founded in boulder clay should be designed using drained parameters, for example using the chart of Berezantzev et al. (1961), particularly for boulder clays with I_P <15, however this is not supported by this experience nor by theoretical considerations. In practice, the lack of a satisfactory design method to determine the appropriate N_c factor is overcome by driving piles to a set, however this makes it difficult for designers and contractors to estimate the required length prior to the actual construction stage of a project.

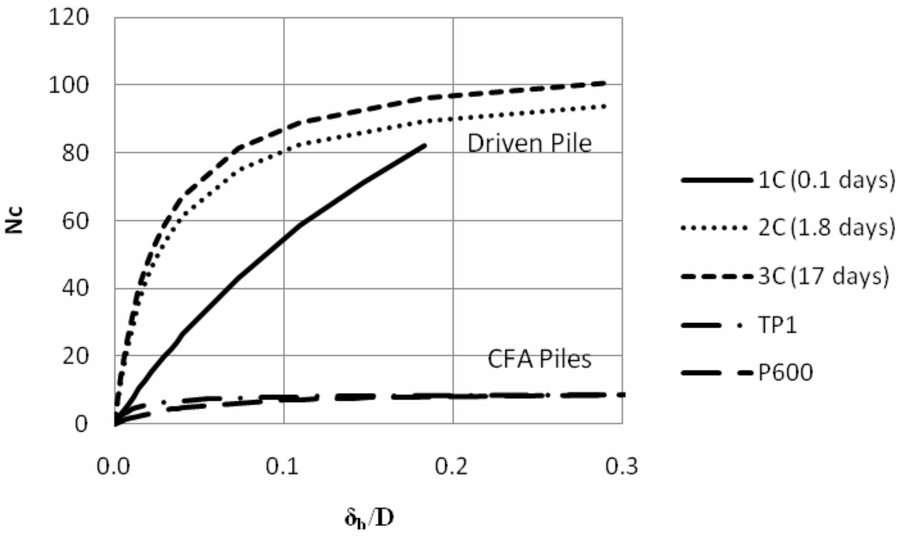

Figure 5 Differences in N_c values for CFA and driven piles (from Galbraith, 2010)

Despite the advances in geotechnical engineering, most pile design is based on the N_{SPT} value from the standard penetration test. The CPT does give more reliable results, however the nature of our boulder clays and glacial outwash gravels frequently limit the penetration that can be achieved. This limitation can be appreciated from Figure 6 which show layers of cobbles within an overall sandy or gravelly deposit. There have been several sites where N_{SPT} values recorded in initial ground investigation for projects were subsequently shown to be incorrect. On two sites in particular, the correct N_{SPT} values were half of those reported in the initial ground investigation. This error became apparent from the results of preliminary pile tests, which highlights the importance of such tests and also highlights the limitations in the method of execution and reporting of the results of the standard penetration test.

The source of the errors in the N_{SPT} can arise from the equipment or from the practical execution of the test. The recently introduced ISO 22476-3:2002, Standard Penetration Test, requires the energy level transmitted to the rods to be checked, something which is rarely done in this country. Such tests have been carried out in the laboratory and in the field as part of research projects in Trinity College (O'Keefe, 2007) by inserting a rod instrumented with accelerometers and strain gauges to measure the dynamic energy imparted– see Figure 7.

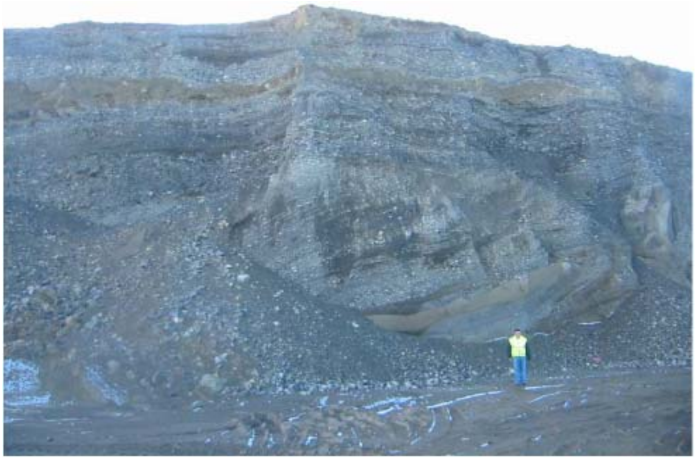

Figure 6 Layers of cobbles within glacial outwash deposit.

Figure 7 Instrumented SPT rod to measure energy transferred.

These tests indicated that about 74% of the energy is transmitted to the rods; thus the normal assumption of 60% is conservative. The normal trip hammer arrangement releasing the mass, which is used in this country, can be visually inspected to ensure that it is working properly; consequently this should not be a major source of error. Other possible sources of equipment errors are the use of incorrect or buckled rods, which again can be checked visually. One major cause of error which arose during the supervision of two ground investigation contracts in which the author was involved, which is illustrated in Figure 8 was the inadvertent carrying out of the standard penetration test within the borehole casing itself. This can be difficult to check as it requires an accurate measurement of the length of casing in the ground, a measurement of the depth to the top of soil in the boreholes and of the SPT and accompanying rods. Apart from possible measurement errors by drillers, 'blowing' sands and gravels can rise up borehole from the 'bailing' process. The standard penetration test is crude, however it is used for 90% of geotechnical design in this and in other countries. The stony nature of our soils generally rules out the more reliable CPT, therefore consideration should be given to improving the reliability of the SPT. Full details of equipment and method of test are given in laboratory tests and it should not be unreasonable for a similar test report to be prepared for each and every SPT. It is surprising that methods of automatically recording the necessary details of the SPT have not been developed in order to eliminate the gross errors that can be very detrimental to design.

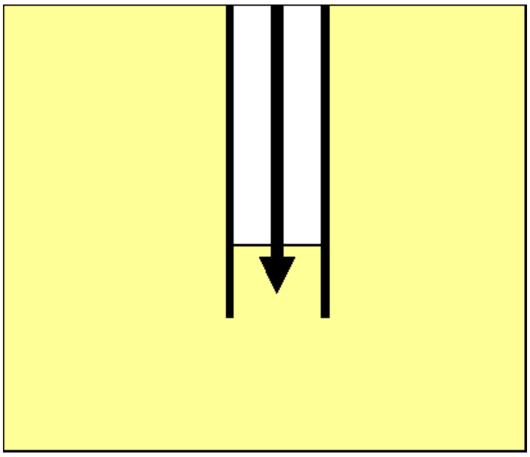

Figure 8 Risk of carrying out the SPT with the casing

7. Construction on peat

Peat continued to give rise to complex design situations and many aspects of its behaviour remain an enigma. The NRA has decided that it does not want the uncertainties arising from its behaviour and generally requires all organic soils under high quality roads to be removed. This has meant that the peat has been excavated and replaced, or alternatively the road in supported on piled load transfer platforms (LTP). Generally the LTP has been constructed using high strength low strain geosynthetic reinforcement. In such construction, access for the piling rigs over the very soft peats is obtained by constructing a working platform, normally comprising about 0.5m of granular material and geogrids, and the compressibility of the peat is clearly evident when it settles away from the LPT with time. The geosynthetic reinforcement is designed on the basis of arching of the embankment fill and on the resistance offered by the tensile resistance of the geosynthetic and any contribution from the ground beneath. Peat stretches the design limits of geotechnical structures and experience from soft ground construction in other countries does not necessarily relate to the extreme compressibility of peat.

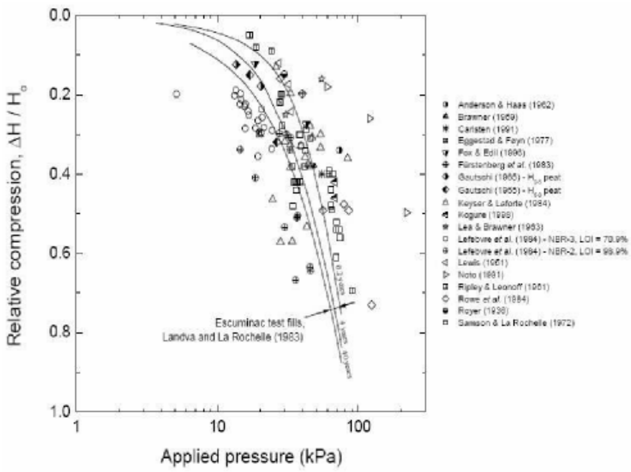

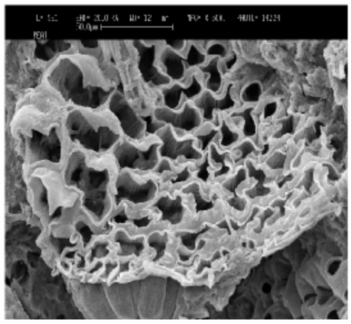

Figure 9 Compression versus applied pressure (Landva & La Rochelle, updated by O'Loughlin, 2007)

The geotechnical behaviour of peat is very dependent on its genesis, however much of the raised and blanket bogs in Ireland have moisture contents of the order of 1000% and organic contents in excess of 95%. A useful indicator of the compressibility of such peats can be obtained from a record of case histories of the compression of peat against increase in vertical effective stress which is shown on Figure 9 (after O'Loughlin, 2007). For example, a 5m thick peat layer would be expected to compress by 2m under an increase in vertical effective stress of 30kPa. This compressibility is not surprising considering that the peat is made up of plant remains, as shown on Figure 9 (from Hebib and Farrell, 2003). Apart from this 'primary' settlement, high creep rates can be expected. These settlements can be reduced by surcharging, however this has stability and time issues.

Extensive research has been carried out into methods of improving peats. Trinity College was part of the €4m Brite EurAm project into the stabilisation of organic soils in the late 1990s. Methods of peat stabilisation are illustrated on Figure 10a & b. The stabilisation research included the testing of large samples of peat, see Figures 11a and 11b, as well as standard laboratory tests (Hebib and Farrell (2003) and Hebib & Farrell (2004)). This research on Irish peats showed that high percentages of cement were required to improve significantly improve the required engineering parameters. These methods, which are relatively commonly used in Scandinavia, have not been proved to be cost competitive when applied to Irish projects. Research does not always give positive results. The results of vacuum consolidation trial – see Figure 12, are at an early stage and it is hopeful that this will be an option for improving rampart roads.

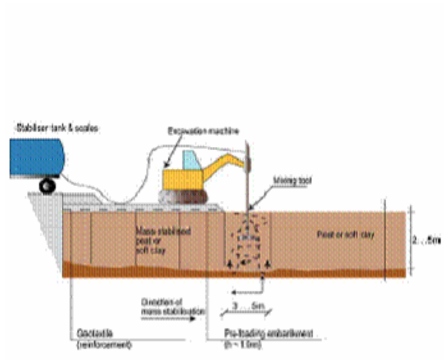

Figure 10a Mass Stabilisation

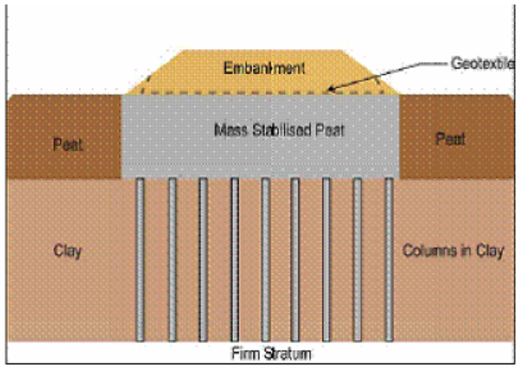

Figure 10b Column and mass stabilisation

Figure 11a large peat samples

Figure 11b Preparing for testing chamber

8. Stability of peat slopes

The stability of peat slopes has been a particular headache and as yet there is no definitive method of determining its shear strength. Boylan and Long (2009) have researched simple shear tests laboratory and ball cone field tests, with some interesting results. Research in Trinity College has also involved simple shear tests and other tests, but also attempts to test block samples of peat as shown on Figure 13. The object of these block sample tests is to assess the strength at very low effective stresses, similar to those which occur in the ground. The testing arrangement is simple, as shown on Figure 13, however the compressibility and permeability of the peat is such that there is significant distortion within the sample itself during shear.

Figure 12 TCD/NRA vacuum consolidation trial.

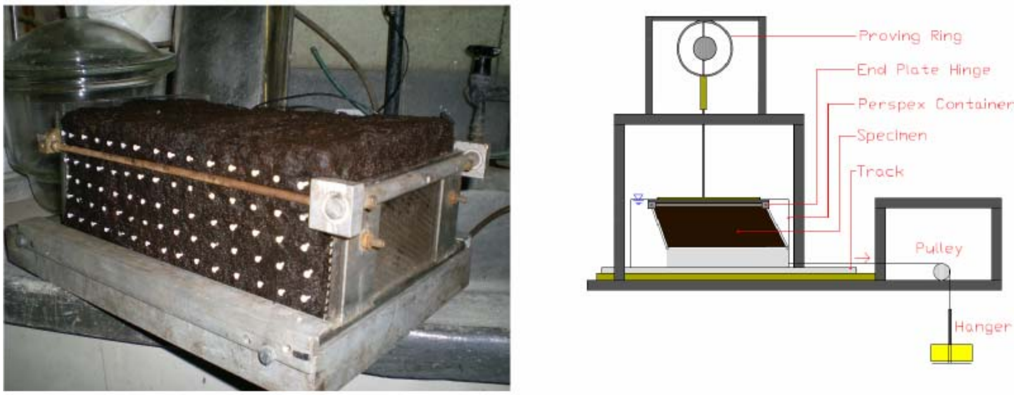

Figure 13 Testing of block samples of peat (Gardiner, 2010)

Peat is an unusual material in that it can be very strong under some loading conditions and weak in others. This is related to the structure of the peat and to its genesis. For example, Derrybrien experienced a major landslide in 2003, see Figure 14, yet 2m of fill was successfully supported on a 'floating' road construction where the bog was 4.65m thick. The moisture contents in the peat were generally in the range of 800% to over 1000%. The undrained shear strength was 5.2kPa to 7.6kPa with an average of 6.09kPa using the 65mm dia by 130mm high vane and 3.2kPa to 9.3kPa with an average of 5.09kPa using a larger 135x270mm vane. It is considered that the fibre content of the upper layers, together with the higher permeability, contributed to essentially reinforce the ground.

Figure 14 Flow slide in peat (Derrybrien, 2003)

Figure 15 Peat supporting 2m of fill on 'floating road' construction.

9. Flow failure mechanism

Despite the significance of peat slope failures as major geo-hazard, insufficient consideration has been given to the mechanism that gives rise to its most dangerous feature, namely the large area of peat mobilised by relatively minor geotechnical events which give rise to peat flow slides. These would be considered to be one form of bogflow as defined by Dykes and Warburton (2007). Progressive slides generally start at the toe of the slope and work back, for example, caused by river erosion. This mechanism is not the cause of most of the peat slides that have occurred recently, although it has been the cause in the past due to peat mining.

One cause of peat flow slides in such large mass is considered to be due to the strength of the upper levels which usually have a high fibre content and which prevent local failures. The peat flow slides occur on relatively flat slopes, consequently a local failure of a limited mass would not be a major geohazard. However, if something causes a reduction in the strength in a weak layer at depth in the peat, for example by overstressing a sensitive layer or by local uplift pressures, and if the peat cannot fail, then a force is transferred to the mass downhill. This mechanism is illustrated by the finite element analysis (FEA) on Figure 16 to 18. Initially the slope is stable and an infinite slope analysis gives the shear stress (τ) as γDL Sin β /L, where γ = unit weight of peat, D= thickness and L = length of a block of peat considered. Thus for 2.5m thickness of peat with γ=10.5 kN/m^3, the basal shear stress is 2.6kPa for β =5.7^o, which is consistent with the results of the FEA analysis as shown on Figure 19. Should some local event cause disturbance of a sensitive weak layer at depth such that its remoulded undrained shear strength is less than that required, the additional force is transferred to the remaining mass of peat. However it is not transferred uniformly, but is concentrated near the edge of the weakened zone, causing an increase in shear stress at the margin and the danger of a progressive failure at depth, as shown on Figure 19. This mechanism was modelled in the FEA for an extreme case for a 10m long length of remoulded soil with c_u=0.1 kPa, with the peat being assigned a c_u=20kPa to avoid a local shear failure.

There is evidence on at least one site that a peat flow slide was caused by this mechanism as the failure was in a sensitive clay layer at the base of the peat.

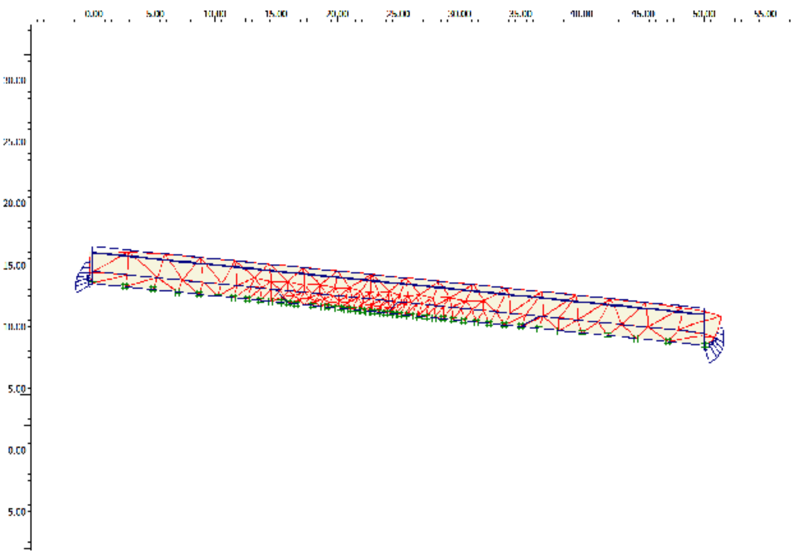

Figure 16 FEA modelling 3m of peat on 5.7 degree slope

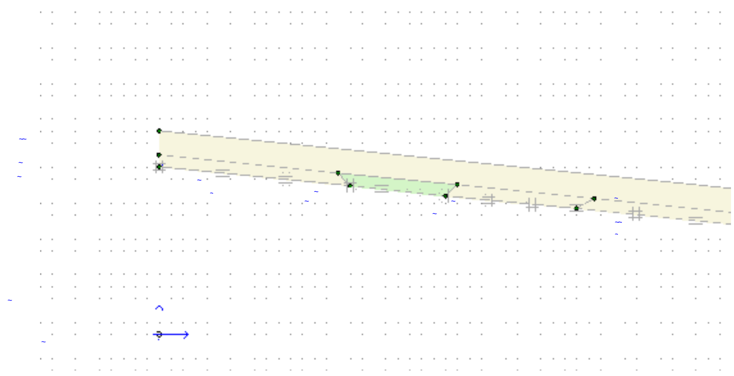

Figure 17 Remoulded basal layer introduced.

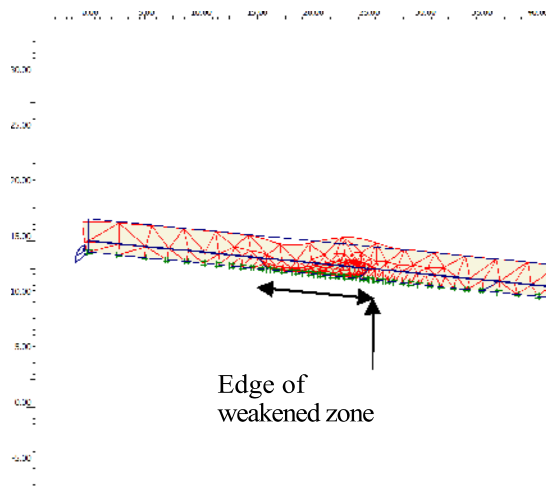

Figure 18 Deformed mesh with weak layer

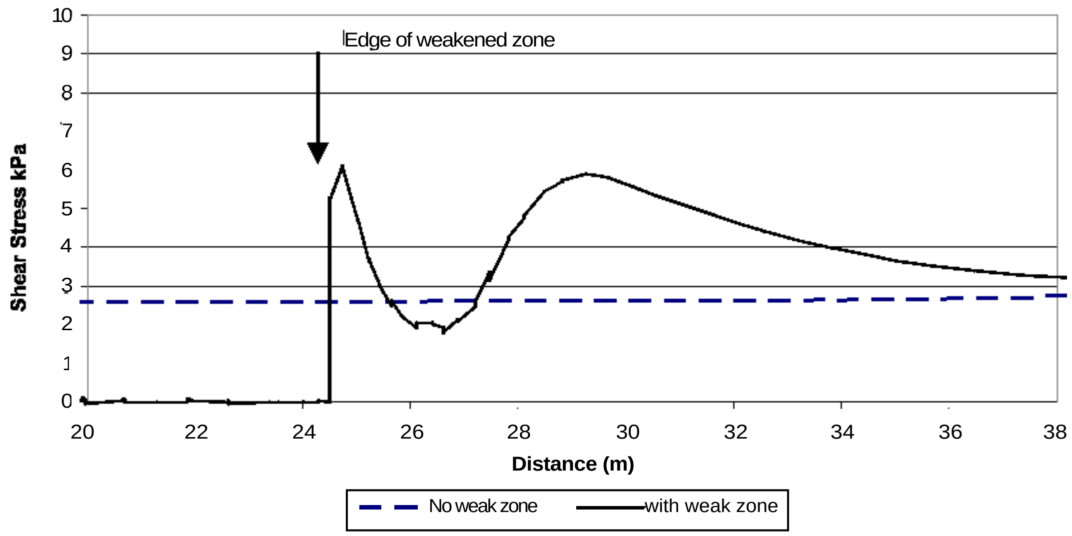

Figure 19 Comparison of shear stress distribution at 2.5m depth with and without remoulded section.

Summary

1. Irish boulder clays have unique geotechnical properties which affect geotechnical design options. However it is frequently difficult to obtain the required parameters from either in-situ or from laboratory tests due to their stony nature, consequently 'engineering' judgement is frequently required. It is considered that the current soil classification system used in this country, BS5930, does not allow for proper identification of these soils. IS EN ISO 14688-1 and IS EN ISO 14688-2 are referenced in Eurocode 7 (IS EN 1997-2:2007) which came into force this year and consideration should be given to developing a classification system for this country which is based on 'engineering' requirements and which allows these soils to be identified from descriptions on borehole and trial pit logs.

2. The knowledge of the geotechnical parameters of the Dublin boulder clays has increased significantly due to research in the laboratory and from careful recording of field performance. This has enabled the fundamental properties to be measured which can feed into the development of sophisticated numerical models.

3. A major review should be undertaken into the reliability of the earthwork ground investigation information in relation to the actual performance of the glacial soils.

4. Research in pile performance in boulder clays to date is mainly concentrated on CFA piles and also in the Dublin area, with only one instrumented pile test on a driven pile. The research to date, and practical experience, would suggest that the N_c factors for driven piles are high in the very stiff/hard Dublin boulder clay but there is uncertainty regarding its values in other boulder clays and this makes it difficult to predict pile lengths prior to construction.

5. Pile design in boulder clays and in sands/gravels is still mainly based on the standard penetration test. Major errors in N_{SPT} values have been experienced in some construction projects and greater consideration should be given to documenting and developing simple methods of checking the conditions in which the test is carried out.

6. The compressibility of peat has been highlighted by some of the recent construction projects. Research into methods of stabilising peats has not developed cost efficient methods to date, however vacuum consolidation may offer some options.

7. A flow failure mechanism is proposed to explain the genesis of the large peat slides.

References

Berezantzev, V.G., Khristoforov, V.S and Golubkov, V.N. (1961), 'Load bearing capacity and deformation of piled foundations', in *Proc. 5th International Conference SMFE*, Paris, Vol. 2, 11-15.

Boylan, N and Long, M. (2009), 'Development of a Direct Simple Shear Apparatus for Peat Soils', *ASTM Geotechnical Testing Journal*, 32 (2): 126-138.
Dykes A.P. and Warburton J. (2007), 'Mass movements in peat: a formal classification scheme', *Geomorphology* 86: 73-93
Farrell, E. R. and Lawler, M.L. (2008), 'CFA pile behaviour in very stiff lodgement till', *Geotechnical Engineering* 161 (GEI): 49-57.
Farrell, E. R., Lehane, B, and Looby, M. (1998), 'An instrumented driven pile in Dublin boulder clay.', *Geotechnical Engineering* 131: 233-241.
Farrell, E. (1989), 'Settlement parameters of Dublin black boulder clay', *Ground Engineering*, 22 , 5, 30-35.
Farrell, E. and Lawler, M. (2007), 'CFA pile behaviour in very stiff lodgement till', *Geotechnical Engineering*, 161, 49-57.
Galbraith, A. (2010), PhD, University of Dublin, *Trinity College*, in progress.
Gardiner, J. (2010), MSc, University of Dublin, *Trinity College*, in progress.
Gavin, G. K., and Cadogan, D. (2008), 'Axial resistance of CFA piles in Dublin Boulder Clay', *Geotechnical Engineering* 161 (GE4): 171-180.
Hartford, D.N.D. (1987), 'Some aspects of the engineering behaviour of well graded soils', PhD thesis, *Trinity College* , University of Dublin.
Hebib, S. and Farrell, E. (2003), 'Some experiences on the stabilization of Irish peats', *Canadian Geot. Jnl.,* Vol. 40, No. 1, 107-120.
Hebib, S. and Farrell E. (2004-2005), 'Stabilisation of Irish Soils' *Trans. Instn. Engrs. Ireland*, 128, 52-72.
Lawler, M.L. (2002), 'Estimating the ground deformations associated with earthworks and foundations in boulder clay'. PhD thesis, University of Dublin, *Trinity College*.
Lochaden, A.L.E, Farrell E.R., and Orr T.L.L. (2008), 'Comparing numerically modelled tunnel induced ground movement with field measurement', *Bridge and Infrastructure Research in Ireland*.
Long, M. and Menkiti, C.O.M. 2007. Geotechnical properties of Dublin boulder clay. *Geotechnique*, 57 (7): 595-611.
Menkiti, C.O., Long, M., Kovacevic, N., Edmonds, H.E., Milligan, G.W.E. and Potts, D.M. 2004. Trial excavation for cut and cover tunnel construction in glacial till—a case study from Dublin. *In Proceedings of the Skempton Memorial Conference, Advances in Geotechnical Engineering*. Vol. 2, pp. 1090–1105.
O'Keefe, W., J., 2007, Energy levels in SPTs in Ireland, MSc thesis, Trinity College , University of Dublin,.
Skipper, J., Follett, B., Menkiti, C. and Long, M. 2005. The engineering geology and characterisation of Dublin boulder clay. *Quarterly Journal of Engineering Geology and Hydrogeology*, 38: 171-187.
Treacy, P. 1996. Deformations around a deep excavation in boulder clay. M.Sc. dissertation, Trinity College Dublin, Dublin, Ireland.

ESTIMATING EXTREME LOAD EFFECT FROM A COMBINATION OF TRAFFIC STATES

C.C. CAPRANI
Dept. of Civil & Structural Engineering, Dublin Institute of Technology, Ireland

Abstract
Recent research has shown that the dynamic amplification factor (DAF) to be applied to free-flowing traffic-induced load effect may not be as high as previously thought. Therefore congested traffic states may govern load effect at lower bridge lengths than currently assumed. Thus there is a need for a methodology that incorporates both traffic states, their relative frequency of occurrence, and any form of DAF that may arise. This paper presents such an approach, and gives results for a range of bridge lengths, load effect, and DAF approaches. It is shown that the influence of DAF is minimal beyond about 50 m bridge lengths. Further, in the range of about 40 to 50 m bridge lengths, a combination of the two traffic states must be considered.

Keywords: Bridge; Congestion; Dynamic Amplification; Free-flow; Load; Traffic

1. Introduction

As a critical part of a nation's infrastructure, highway bridges must be maintained and kept operational, even as they deteriorate due to ageing. The loading to which bridges are subject is known to be an area in which significant savings may be made due to the conservatism inherent in many bridge loading standards. Using measured traffic data, the load effect, or effects, on a particular bridge, or a range of bridges, can be estimated with confidence. Recent research has found that the type of traffic that causes the critical loading scenario may not be as previously thought.

Free-flowing traffic dynamically interacts with the bridge structure, accentuating the loading. Congested traffic does not do this, due to its lower speeds, but is denser. Therefore for typical bridges lengths of about 25 to 45 m, the critical form of loading may not be clearly defined. In particular, the governing form of traffic depends both upon the level of dynamic interaction and the density in which vehicles are present on the bridge. Recent advances (Gonzalez et al (2008) and Caprani (2005)) in the statistical analysis of dynamic interaction have shown that the dynamic increment may not be as high as once thought.

With recent simulation models able to model both forms of traffic, the problem becomes one of the statistical modelling of the two different processes to arrive at a single characteristic load effect value. This must be done is such a way that the dynamic amplification factors appropriate to the problem can be incorporated in arriving at an overall distribution of load effect.

This paper proposes a way to incorporate both free-flowing and congested traffic into a single statistical framework based on extreme value theory. It is also how different loading scenarios (e.g. 1-truck, 2-truck, etc.), and different dynamic amplification factors, can be taken into account.

2. Simulation of Bridge Traffic Load Effect

2.1 Basis of Work

This work is based on Weigh-In-Motion measured traffic from the A6 motorway, near Auxerre, France. The traffic characteristics are modelled as described in Caprani (2005) and Monte Carlo simulation is used to generate new traffic, closely matching the statistical distributions of the measured traffic.

The free flow model used in this work is that described in OBrien and Caprani (2005). Measured parameters such as speed and hourly flow rates are maintained throughout the simulation.

For congested flows, the gap between vehicles is considered as a stochastic variable. A 5 m gap with a coefficient of variation of 5% is adopted, due to its prevalence in the literature (Caprani 2005).

2.2 Load Effect Calculation

To determine load effects, traffic is generated according to one of the flow models and passed over the influence lines of the load effects of interest in time-steps of 0.1 seconds. Cars are neglected in this work, but their effect on the spatial disposition of the trucks is allowed for in both the free-flowing and congested traffic models.

The bridge lengths and load effects considered in this work are as follows:

- Lengths: 20, 30, 40, 50, 60 m;
- Load Effects:
    - LE1: Mid-span bending moment in a simply-supported beam;
    - LE2: Central support hogging moment in a two-span beam;
    - LE3: left hand shear in a simply-supported beam.

For this work, one full bridge lifetime (50 years) of free-flow and congested flow traffic was generated. It is considered that there are 250 working days per year, and thus 12 500 days of traffic is required. For the free-flowing traffic, 12 500 days of traffic is generated and the daily maximum load effects noted. For the congested traffic, it is considered that there are two hours of full congestion per day, and thus there are 12 500 sets of 2 hours of congestion generated. Load effects are recorded separately for each type of loading event (1-truck, 2-truck, etc.) in both the free-flow and congested traffic scenarios. A sample histogram of overall load effect is shown in Figure 1: peaks corresponding to the different loading event types can be seen.

3. Extreme Value Statistical Analysis

3.1 Background

There are two main methods of extreme value theory (EVT) (Coles 2001). The block maxima approach, which uses the maximum of the data obtained for a block (a period of time), and the Peaks Over Threshold approach, which deals with exceedances over a high threshold.

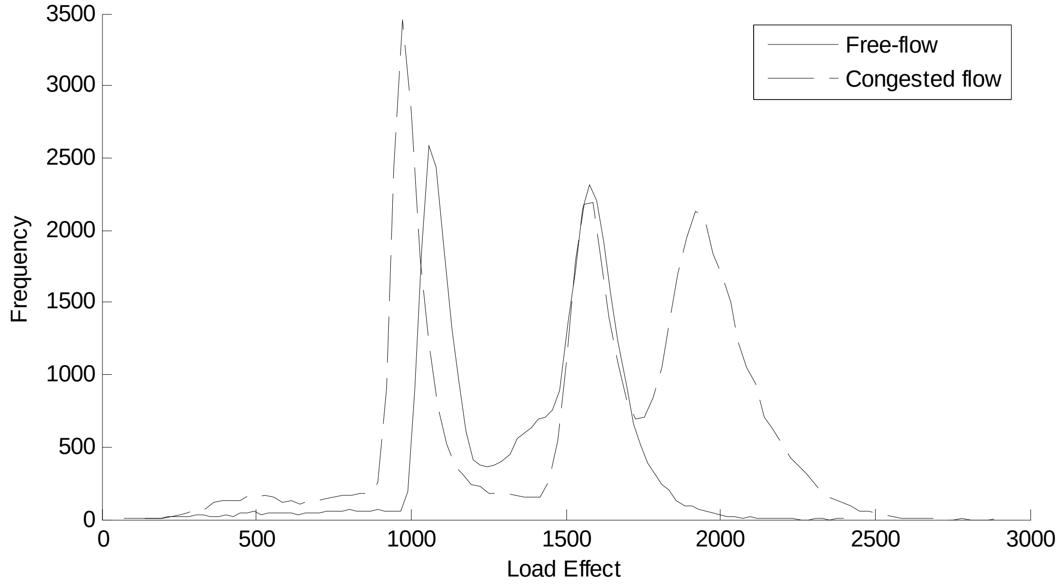

Figure 1 – Sample histogram of load effect: bridge length 40 m, Load Effect 2.

Importantly, the choice of EVT method is usually subjective whilst the results of the two methods are generally different. Recently, the Box-Cox-GEV model has been proposed by Bali (2003). This model encompasses both the GEV and GPD distributions and thus the two main approaches of EVT. Therefore, in applying this model, the data itself determines the most appropriate form of EVT analysis.

3.2 The Box-Cox-GEV Distribution

Bali (2003) gives the Box-Cox-GEV (BCGEV) extreme value distribution:

$$H(s) = \left(\frac{1}{\lambda}\right)\left(\left[\exp\left\{-\left[h(s)\right]_+^{1/\xi}\right\}\right]^{\lambda} - 1\right) + 1 \tag{1}$$

$$h(s) = 1 - \xi\left(\frac{s-\mu}{\sigma}\right) \tag{2}$$

The parameters of this distribution are those of the GEV distribution (μ, σ, ξ) and a 'model parameter', λ. As $\lambda \to 1$, the BCGEV converges to the GEV distribution. Conversely, as $\lambda \to 0$, by L'Hopital's Rule, the BCGEV converges to the GPD.

Maximum likelihood estimation of the BCGEV is not robust. Therefore, estimation has been carried out using nonlinear regression, as proposed by Bali (2003). Arranging the data in increasing order, $s_1, \ldots, s_r, \ldots, s_n$, we compare the expected value of $H(s)$ for each data point to its empirical value:

$$E\left[H(s)\right] = \frac{r}{n+1} \tag{3}$$

Substitution of Equation (1), followed by twice taking logarithms and by adding a residual (or error) term, η, we get the nonlinear regression equation:

$$\log\left[\left(-\frac{1}{\lambda}\right)\log\left(1+\lambda\left(\frac{r}{n+1}-1\right)\right)\right]=\frac{1}{\xi}\log\left[1-\xi\left(\frac{s_r-\mu}{\sigma}\right)\right]+\eta \tag{4}$$

Minimizing the sum of the squared residuals gives the parameter estimates. Then, because the GEV and GPD models are nested in the BCGEV model, the data determines whether the GEV, GPD or BCGEV model is most appropriate. It is to be noted that inference of the model parameter is not reliable and a one-dimensional grid search is undertaken, determining the optimum parameter to second order.

The threshold, *u*, is applied to the data, *x*, of length, *n*, by left-censoring, and the *k* number of exceedances noted. The BCGEV distribution is estimated for this reduced data set, *H*(*x*), and the overall distribution, *G*(*x*), is then determined using the Theorem of Total Probability as follows:

$$G(x)=\left[1-G(u)\right]H(x)+1\cdot G(u) \tag{5}$$

Writing $\theta=1-G(u)$, the probability of the threshold being exceeded, we then have:

$$G(x)=(1-\theta)+\theta\cdot H(x) \tag{6}$$

An obvious estimator for θ is the proportion of exceedances, k/n, and Coles (2001) points out that this is in fact the maximum likelihood estimator for θ. This result is similar to that obtained by Castillo et al (2005).

3.3 Accounting For Different Types of Loading Events

Caprani et al (2008) point out that the parent population of bridge load effect is not identically distributed and develop the Composite Distribution Statistics (CDS) approach to this problem, applicable to the extreme values, given by:

$$G_C(x)=\prod_{j=1}^{n_t}G_j(x) \tag{7}$$

In which n_t is the number of event types, $G_j(.)$ is the distribution of the *j*-truck loading event and $G_C(.)$ represents the CDS distribution. Whilst Caprani et al (2008) consider only the GEV distribution for $G_j(.)$, the BCGEV distribution is used here.

The BCGEV distribution can account for thresholds on the data, as explained previously. Since an overall threshold could eliminate some potentially important loading events, and since the goal of the threshold is to better model the individual tails, separate thresholds are applied to each loading event. In this work, a threshold of 1.5 standard deviations to the right of the mean is applied to each loading event type.

Figure 2 illustrates the distributions of load effect, the thresholds, and the CDS distribution used for estimation of the characteristic return level for a sample case.

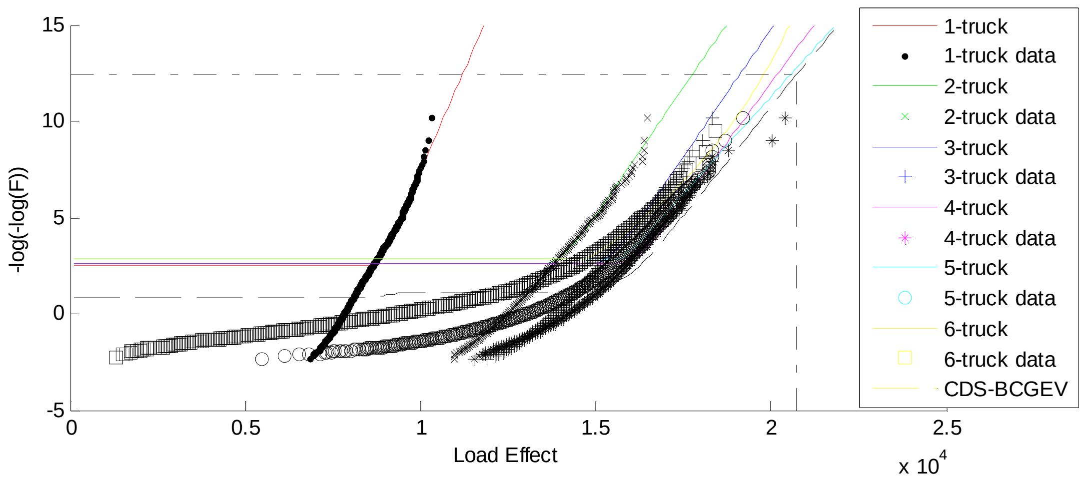

Figure 2 – Gumbel paper plot of congested flow distributions for 60 m, LE1.

3.4 Accounting for Different Traffic Scenarios

Formulation

Combining the distributions of load effect for free-flow (allowing for dynamic effects) and congested flow is done by recognizing that the relative frequencies of occurance are already included as part of the daily maximum distributions. The joint probability that a load effect will be less than a certain value x is then given by:

$$G_T(x) = \left[D(\cdot)\,G_{C,FF}(x)\right]G_{C,CF}(x) \tag{8}$$

In which $G_T(x)$ is the total distribution of load effect, $G_{C,FF}(x)$ is the composite distribution of load effect from free-flow traffic, $G_{C,CF}(x)$ is the composite distribution of load effect induced by congested traffic and $D(.)$ is the dynamic amplification factor (which may be a function of a number of parameters).

Dynamic Amplification Factors

To fully determine the total load effect distribution from Equation (8), a DAF function, $D(\cdot)$, must be specified. To investigate the implications of different forms of DAF function, the following have been used in this work:

- *EC*: The Eurocode DAF, as incorporated into Load Model 3 (Caprani 2005);
- *EC80*: Similar to the EC, but with an 80% reduced dynamic increment, as may be feasible for bridge assessments, perhaps (Caprani & OBrien 2008);
- *BR*: The DAFs of Brühwiler and Herwig (2008), suggesting no DAF at ultimate limit state for ductile failures (LE1, LE2), and a DAF for brittle failures (LE3);
- *ADR*: A distribution of DAF which recognizes the reduced dynamic increment of heavier loading events, adapted from that of Caprani et al (2010);
- *None*: The unusual case of no DAF being applied, used for comparison.

These various DAFs are shown in Figure 3. The ADR DAF does not vary by length or load effect – a large simplification, but does account for reduced DAF at higher load effects. The BR DAF is only defined for Load Effect 3.

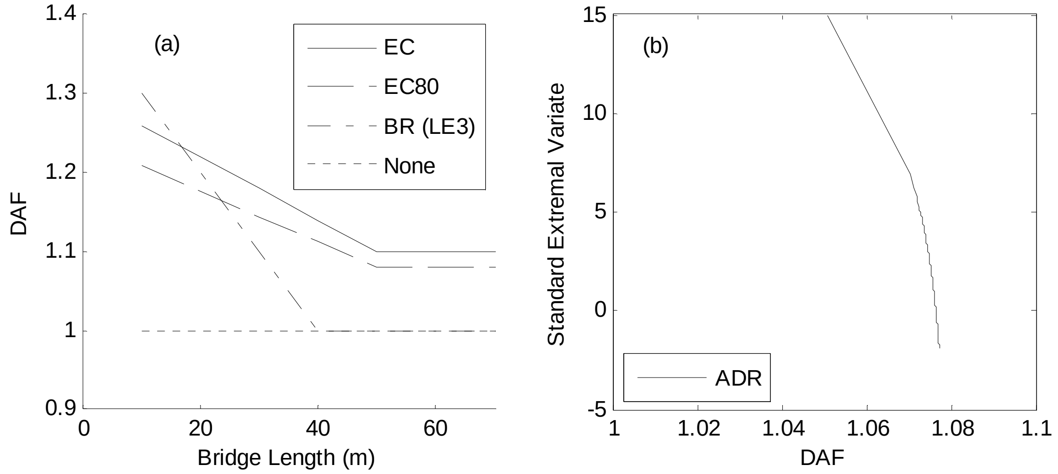

Figure 3 – Various DAF models considered: defined on the basis of (a) length and load effect, and (b) probability.

Implementation

The CDS distributions of congested and free-flow load effect are numerically determined. The total distribution of load effect is then also numerically determined using Equation (8). Figure 4 illustrates a case where both traffic scenarios contribute to the characteristic load effect. It can be seen that this load effect is greater than either traffic state would produce individually, and so allows for their joint occurances.

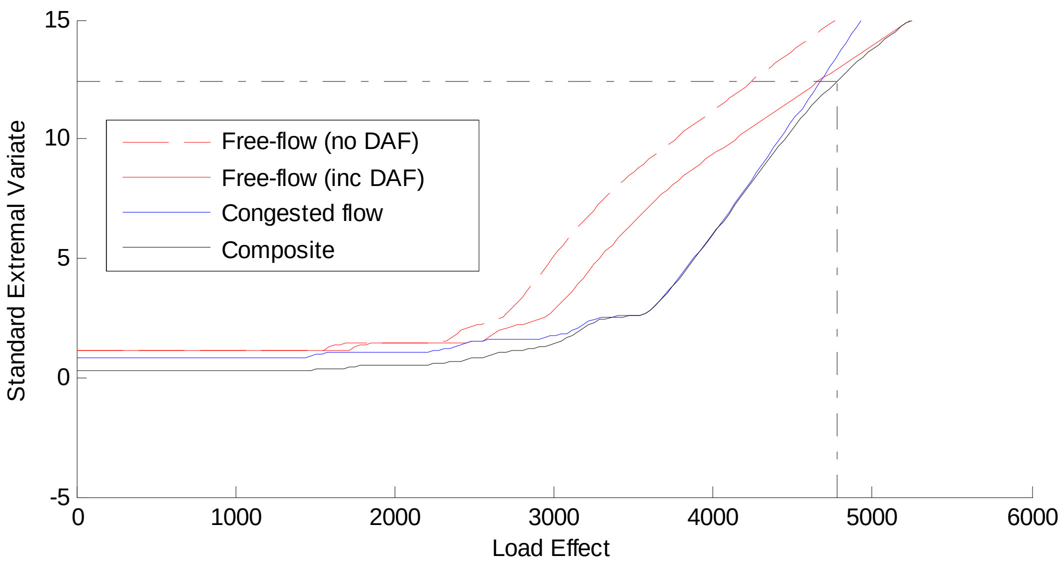

Figure 4 – Free, congested, and composite distributions for 50 m, LE2 (DAF EC).

4. Results

The characteristic values determined are normalized to the free-flow load effect result. This enables easier comparison of the influence of congested traffic and DAF by bridge length and load effect. Figure 5 shows these values for each load effect.

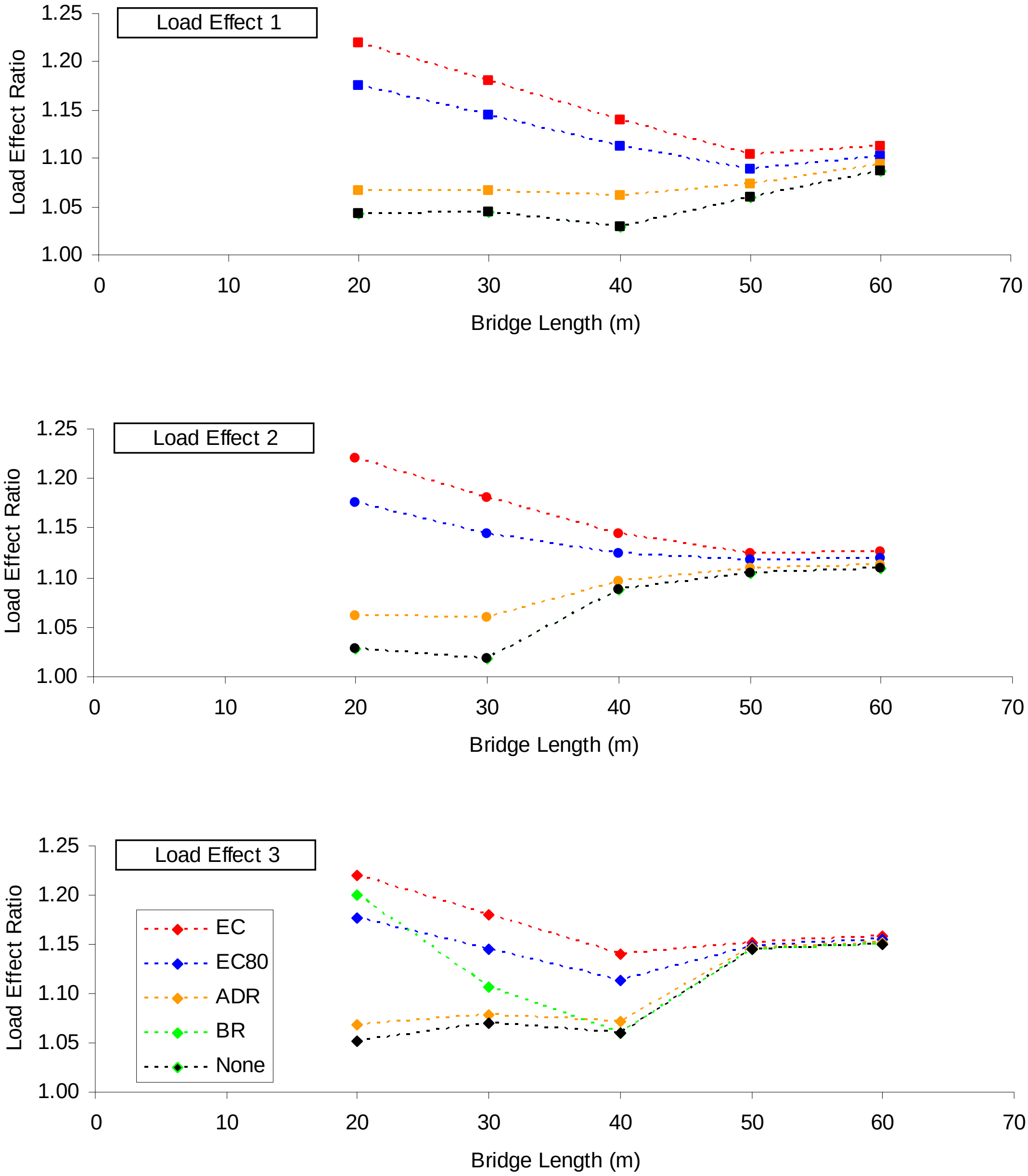

Figure 5 – Normalized characteristic load effects with various DAF models.

It can be seen from Figure 5 that the influence of dynamic amplification reduces as the bridge length increases. However, it can also bee seen that, depending on the DAF model used, load effects for shorter lengths are quite sensitive to dynamic effects. Even in the case of little DAF (for example the BR or ADR models), the composite load effect can be higher than that of free or congested traffic effect alone. This is due to the joint probability of occurance and suggests that both forms of traffic loading scenario must be simulated for bridges of length about 35 to 50 m, depending on the load effect of interest. Further, congested traffic seems to be more important for longer bridge lengths for Load Efects 2 and 3, and not as important for Load Effect 1. This may be due to the difficulty in locating vehicles close to the peak of the influence line for Load Effect 1, whilst the other influence lines have two peaks, or are broader.

5. Summary

This work has demonstrated a methodology to incorporate both free-flow and congested flow traffic scenarios, allowing for various dynamic amplification models, such that an overall distribution of bridge traffic load effect is obtained. It has shown how a more general extreme value theory model can be adapted for the bridge traffic load effect problem.

The results here indicate that free-flow traffic is of importance for lengths around 50 to 60 m, given the relative frequency of occurrence of this traffic scenario. It is also shown that load effects for shorter lengths are sensitive to the DAF model used. Further, in the range of about 40 to 50 m bridge lengths, a combination of the two traffic states must be considered so that it is reconized that the critical load effect may come from either traffic state.

References

Bali, T.G. (2003), 'The generalized extreme value distribution', *Economics Letters*, **79,** 423-427.

Brühwiler, E. and Herwig, A. (2008), 'Consideration of dynamic traffic action effects on existing bridges at ultimate limit state' in *Bridge Maintenance, Safety, Management, Health Monitoring and Informatics* eds. H.M. Koh and D.M. Frangopol, Seoul, Korea, 3675-3682.

Caprani, C.C., (2005), *Probabilistic Analysis of Highway Bridge Traffic Loading*, Ph.D. Thesis, School of Architecture, Landscape, and Civil Engineering, University College Dublin, Ireland, available from www.colincaprani.com.

Caprani, C.C., OBrien, E.J. and McLachlan, G.J., (2008), 'Characteristic traffic load effects from a mixture of loading events on short to medium span bridges', *Structural Safety*, **30**(5), 394-404, dx.doi.org/10.1016/j.strusafe.2006.11.006.

Caprani, C.C**.**, González, A., Rattigan, P.H. and OBrien, E.J., (2010), 'Assessment dynamic ratio for traffic loading on bridges', *Structure and Infrastructure Engineering*, in print, dx.doi.org/10.1080/15732471003667645.

Castillo, E., Hadi, A.S., Balakrishnan, N. and Sarabia, J.M. (2005), *Extreme Value and Related Models with Applications in Engineering and Science*, Wiley.

Coles, S.G., (2001), *An Introduction to Statistical Modeling of Extreme Values*, Springer-Verlag.

González, A., Rattigan, P.H., OBrien, E.J. and Caprani, C.C., (2008), 'Determination of bridge lifetime dynamic amplification factor using finite element analysis of critical loading scenarios', *Engineering Structures*, **30**(9), September, 2330-2337 dx.doi.org/10.1016/j.engstruct.2008.01.017.

OBrien, E.J., and Caprani, C.C., (2005), 'Headway modelling for traffic load assessment of short-to-medium span bridges', *The Structural Engineer*, **83**(16), 33-36.

SITE SPECIFIC MODELLING OF TRAFFIC LOADING ON HIGHWAY BRIDGES

B. ENRIGHT[1] & E.J.OBRIEN[2]
[1]Dept. of Civil & Structural Engineering, Dublin Institute of Technology, Ireland
[2]School of Architecture, Landscape & Civil Engineering, University College Dublin, Ireland

Abstract
Accurate traffic loading models based on measured weigh-in-motion (WIM) data are essential for the accurate assessment of existing bridges. Much work has been published on the Monte Carlo simulation of single lanes of heavy vehicle traffic, and this can easily be extended to model the loading on bridges with two independent streams of traffic in opposing directions. However, a typical highway bridge will have multiple lanes in the same direction, and various types of correlation are evident in measured traffic, such as groups of very heavy vehicles travelling together and heavy vehicles being overtaken by lighter ones. These traffic patterns affect the probability and magnitude of "multiple presence" loading events on bridges, and are significant for the maximum lifetime loading on the bridge.

This paper analyses traffic patterns using multi-lane WIM data collected at four European sites. It describes an approach to the Monte Carlo simulation of this traffic which seeks to replicate the observed patterns of vehicle weights, same-lane and inter-lane gaps, and vehicle speeds by applying variable bandwidth kernel density estimators to empirical traffic patterns. This allows the observed correlation structure to be accurately simulated but also allows for unobserved patterns to be simulated. The process has been optimised so as to make it possible to simulate traffic loading on bridges over periods of 1,000 years or more, and this removes much of the variability associated with estimating characteristic maximum load effects from shorter periods of either measured or simulated data. The results of this analysis show that the patterns of correlation in the observed traffic have a small but significant effect on bridge loading.

Keywords: Bridge, correlation, simulation, traffic loading, weigh-in-motion

1. Introduction

Much work has been done on modelling bridge loading due to two-lane same-direction traffic. In the work by Nowak (1993), a number of simplifying assumptions were made – for example that 1 in 15 heavy trucks has another truck side-by-side, and that for 1 in 30 of these multiple truck events, the two trucks have perfectly correlated weights. A heavy truck was defined as one with a gross vehicle weight (GVW) in the top 20% of measured truck weights. As Kulicki et al. (2007) note, the assumptions used were based on limited observations, and the assumptions on weight correlation were entirely based on judgment, as almost no data were available. Moses (2001) presents a simple traffic model for estimating multiple presence probabilities as a function of average daily truck traffic (ADTT), and then selects conservative values, some being based on subjective field observations, for calibrating load factors for bridge assessment. Sivakumar et al. (2007) refine the definition of side-by-side events to include two trucks with headway separation of ± 18.3 m (60 ft), and also consider the influence of the bridge length. Sivakumar et al. (2008), citing Gindy and Nassif (2006), extend this further by classifying multiple-presence events as side-by-side, staggered, following or multiple. They present statistics, derived from weigh-in-motion (WIM) measurements, for the frequency of occurrence of these events for different truck traffic volumes and bridge spans. They describe a method for estimating site-specific bridge loading which uses multiple-presence probabilities calculated either directly from WIM data or estimated from traffic volumes using reference data collected at other sites. It is assumed, surprisingly enough, that the GVW distribution is the same in both lanes, and that there is no correlation between weights in adjacent lanes.

In the development of the Eurocode for bridge loading (EC1 2003), characteristic load effects were estimated by extrapolating directly from results for measured traffic, and also by extrapolating from Monte Carlo simulation of traffic, with each lane being simulated independently (Bruls et al. 1996; O'Connor et al. 2001).

Croce and Salvatore (2001) present a theoretical stochastic model based on a modified equilibrium renewal process of vehicle arrivals on a bridge and note that while existing numerical models are particularly efficient when single-lane traffic flow is considered, they are unsatisfactory for multi-lane traffic, and have often employed drastic simplifications. In their model, convolution is used to combine load effect distributions for traffic in multiple lanes.

This study is based on WIM data collected at four European sites. A detailed analysis of the data reveals that for groups of adjacent vehicles in both lanes, there are patterns of correlation and interdependence between vehicle weights, speeds and inter-vehicle gaps. A Monte Carlo simulation model has been developed for evaluating bridge loading due to traffic in two same-direction lanes. This simulation seeks to reproduce the sometimes subtle patterns of correlation that are evident in measured traffic while also adding an element of randomness so as to vary the loading. This study focuses on short to medium span bridges, up to 45 m long, where free-flowing traffic with dynamics is taken to govern (Bruls et al. 1996).

2. Observed traffic

2.1. WIM data

The WIM data used as the basis for this study were collected at four European motorway sites, as summarized in Table 1. At each site, traffic in two same-direction lanes was measured. As would be expected, the volumes of truck traffic in the fast lane are much lower than in the slow lane, with the percentage of trucks travelling in the fast lane varying from 3.8% in Slovenia to 7.7% in the Netherlands. A notable feature of the data at all sites is the number of extremely heavy vehicles.

Table 1 – Summary of WIM data

Country	Netherlands		Czech Republic		Slovenia		Poland	
Time period	Feb to Jun 2005		May 2007 to May 2008		Sep to Nov 2006		Jan to Jun 2008	
Lane	Slow	Fast	Slow	Fast	Slow	Fast	Slow	Fast
Total Trucks	596 568	49 980	684 345	45 584	142 131	5 621	398 044	31 636
ADTT*	6 545	557	4 490	261	3 158	135	3 708	314
Maximum GVW	165.6	75.2	129.0	128.0	131.3	58.4	105.9	69.9
No. over 60 t	1680	36	322	54	15	0	584	3
No. over 100 t	238	0	10	2	1	0	1	0

* Average daily truck traffic per lane on week days

2.2. Patterns in measured traffic

There are distinctive patterns observable in the measured traffic. Similar patterns occur at each site, to a greater or lesser degree, and the challenge of reproducing these site-specific patterns in simulation is the focus of this paper. For short to medium span bridges, loading events featuring one truck in each lane are particularly important. To assess if there is any dependence between the weights of these vehicles, each fast-lane truck in the measured data is notionally paired with the nearest truck in the slow lane, and the gap is measured in seconds between the front axles of the two vehicles. At all sites, many fast-lane trucks are within 2 seconds of a slow-lane truck – 75% in the Netherlands, 72% in the Czech Republic, 55% in Slovenia and 46% in Poland. The differences between sites may be attributable to driver behaviour at each location. The average GVW of the truck in the fast lane and of the nearest truck in the slow lane are plotted against the inter-lane gap for the Netherlands in Figure 1(a). There is a significant peak in the fast lane GVW when the gap is around zero – i.e. when the trucks are very close – and a similar pattern is evident in the Czech Republic. It appears that a heavy truck in the fast lane tends to be associated with a nearby truck in the slow lane, i.e. it is passing another truck. In Poland (Figure 1(b)), there is a peak in the fast-lane GVW and also in the slow-lane GVW when the trucks are close, suggesting that both the passing truck and the truck being passed are heavier than average. The Slovenian data suggest that the passing truck tends to be lighter than the average for the fast lane. The graphs in Figure 1 show results for both the observed data and for simulated traffic where the simulation uses the methods outlined in this paper. At all sites, the simulated traffic reproduces the observed site-specific patterns very well.

There is also some correlation between the weights of successive trucks in the same lane, particularly in the slow lane where most trucks are found. The coefficient of correlation between the GVW of all leading trucks and all following trucks is typically in the range 5% to 10%. The correlation tends to increase as the weights of both trucks increases. In Figure 2, pairs of successive trucks are selected if both their weights are above a certain threshold (25 t, 30 t, etc.), and the correlation coefficient calculated for all such pairs is plotted against the threshold value. The trend is particularly pronounced in the Czech Republic (Figure 2(a)) and in the Netherlands. In Slovenia (Figure 2(b)) and Poland, the trend is present, but less obvious. There are widely-used techniques for modelling correlation in Monte Carlo simulation, such as that described by Iman and Conover (1982), and the use of copula functions (Nelsen 1999). In the authors' experience, it is very difficult to simulate the correlations evident in Figure 1 and Figure 2 using these techniques. The simulation method described in this paper successfully reproduces the observed correlations.

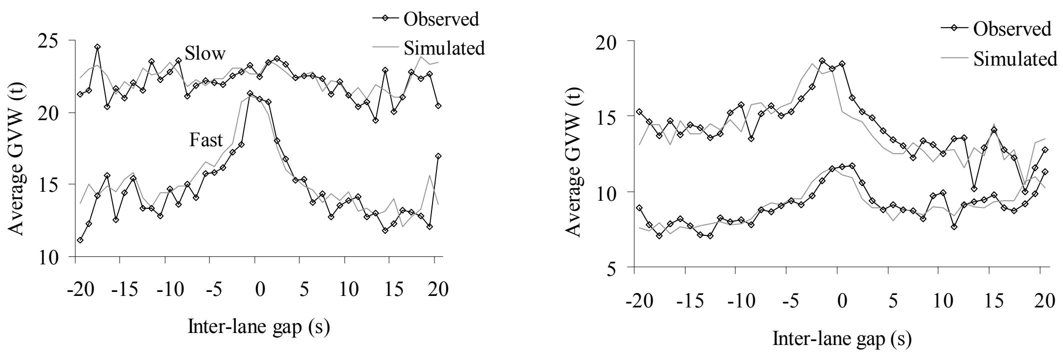

(a) Netherlands (b) Poland

Figure 1 – Inter-lane GVW correlation

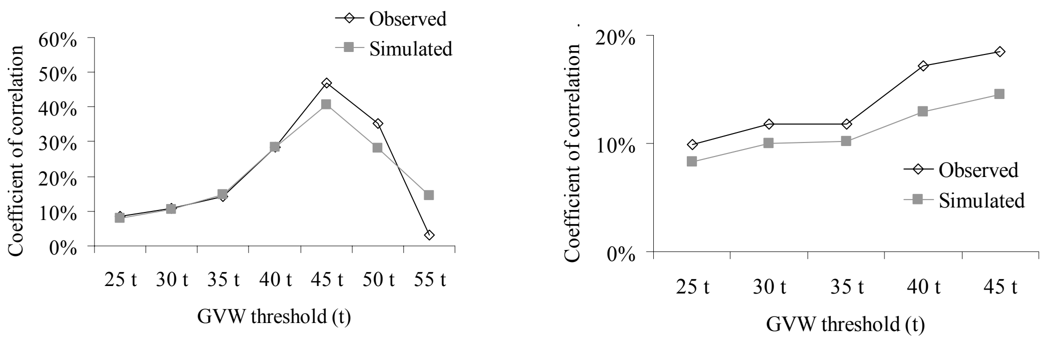

(a) Czech Republic (b) Slovenia

Figure 2 – Slow-lane GVW correlation

Other patterns evident in the observed data include a relationship between speed and GVW, with heavier trucks tending to travel at slightly lower speeds. There is some evidence of larger gaps behind heavier trucks. It is also apparent that successive inter-vehicle gaps are not independent, particularly at lower traffic volumes where platooning causes small gaps to occur in clusters. The simulation of the spatial layout of traffic in two same-direction lanes requires the correct modelling of three inter-dependent gap distributions – the in-lane gaps in each of the slow and fast lanes, and the inter-lane gaps. If the in-lane gaps are simulated independently for both lanes, the resulting inter-lane gap distribution will be a poor match for the observed. Similarly, if the slow-lane and inter-lane gaps are simulated based on the observed data, the resulting fast-lane gaps will not match the observed.

3. Simulation of traffic

The principle of bootstrapping is to draw random samples repeatedly from the observed data (Efron and Tibshirani 1993). In this case, the samples used are "traffic scenarios", with each scenario consisting of between five and eight slow-lane trucks in succession, with any adjacent fast-lane trucks. In preparation for simulation, the WIM data are analysed and all scenarios are identified. The parameters recorded for each scenario are flow rate, gaps, GVWs and speeds. The flow rate is represented by the number of slow-lane trucks in the current hour, rounded to the nearest 10 trucks/hour. The gaps needed to define the scenario are the gaps within each lane, and one inter-lane gap which positions the first fast-lane truck relative to the leading slow-lane truck in the scenario, as shown in Figure 3. The number of parameters needed to describe a single scenario (i.e. the dimensionality of the problem) varies with the size of the scenario, but in the typical scenario shown in Figure 3, a total of 21 different parameters are needed – the GVWs and speeds of seven trucks, six gap values and a flow rate. Correlations between parameters are implicitly included in each scenario.

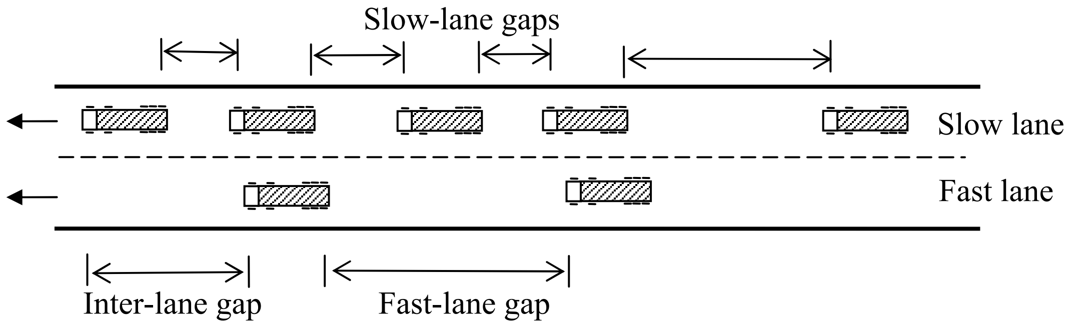

Figure 3 – Traffic scenario

In the simulation of traffic, the traffic flow rate at any time is based on the measured average hourly flow rate. Traffic scenarios appropriate to the current flow rate are drawn randomly from the observed traffic. This bootstrap process would be expected to produce bridge loading very similar to the measured traffic. Variations from the observed scenarios are introduced in a number of ways. Each time a scenario is selected in the simulation, the GVWs, gaps and speeds that define it are modified using variable-bandwidth kernel density estimators, as described below. When a GVW has been selected for a particular vehicle, the number of axles is randomly chosen from the measured distribution for that weight. The axle spacings, and distribution of the GVW to individual axles, are also generated randomly from measured distributions for vehicles with different numbers of axles.

The term "kernel density estimator" describes the use of kernel functions to provide a better estimate of a probability density function from sample data (Scott 1992). A simple histogram gives an estimate of the density at discrete points, but is influenced by the choice of the bin size and origin. Replacing each data point by a kernel function and summing these functions gives a better estimate. Different kernel functions can be used – they are typically symmetric unimodal functions such as the Normal density function. In Monte Carlo simulation, the "smoothed bootstrap" method – re-sampling the observed data and adding some noise – is the same as generating random variates from the kernel density estimate, but without needing to compute the estimated density. In this study, the smoothed bootstrap is applied to three variables – GVW, gaps and speeds. Each value x_i taken from the observed traffic scenarios is modified by adding some noise:

$$X_i = x_i + K\left[h(x_i)\right] \tag{1}$$

where K is a kernel function, centred at zero with a variable bandwidth h which depends on the value of x_i. For each random variable being modelled, a suitable bandwidth must be chosen – if the bandwidth is too small, not enough variability will be introduced to the empirical data, whereas too large a bandwidth will oversmooth the data, as shown for example in Figure 4(a). Scott (1982) discusses adaptive smoothing where the bandwidth of the kernel function is varied and cites the approach developed by Abramson (1982):

$$h_i(x_i) = \frac{h}{\sqrt{f(x_i)}} \tag{2}$$

where $f(x_i)$ is the empirical density function. This approach is adopted here, and allows for additional smoothing where the observed data are sparse, as illustrated in Figure 4(b) for fast-lane gaps in the Czech Republic. The choice of bandwidth h is somewhat arbitrary, and is based on the avoidance of oversmoothing (as in Figure 4(a)).

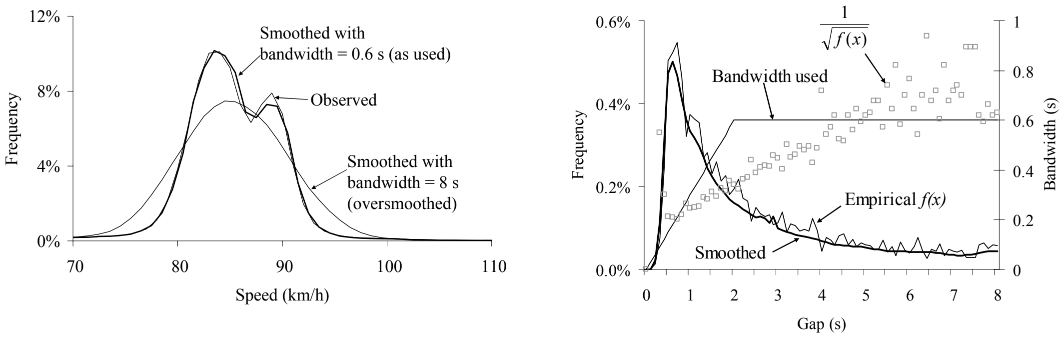

(a) Oversmoothing of speed – Netherlands – Slow lane

(b) Variable bandwidth, Fast lane gaps – Czech Republic

Figure 4 – Kernel bandwidth

4. Results

To assess the effects of correlation, an uncorrelated simulation model was also developed in which GVWs, slow-lane gaps, inter-lane gaps, and speeds are drawn independently for each truck from the observed distributions. In order to compare the simulation models, comparison is made between bridge loading by measured traffic and by simulated traffic on bridges of different lengths – 15, 25, 35 and 45 m. Daily maximum values are calculated for each loading event type for three load effects – mid span bending moment on a simply supported bridge (LE1), support shear at the entrance to a simply supported bridge (LE2), and for bridges which are 35 m or longer, hogging moment over the central support of a two span continuous bridge (LE3). Loading events are classified according to the number of trucks present in each lane on the bridge when a maximum load effect occurs.

For comparison purposes, the two simulation models – smoothed bootstrap and uncorrelated – were run for 2000 days, and the simulated and measured results plotted on Gumbel paper. An example is shown in Figure 5(a) for events with one truck in each lane on a 35 m bridge in the Netherlands, and this illustrates that the smoothed bootstrap gives a significantly better fit to the measured data. An analysis of all spans, load effects and event types described above shows that in general the smoothed bootstrap gives a better fit to the measured data for multi-truck events. For one-truck events, both methods perform equally well.

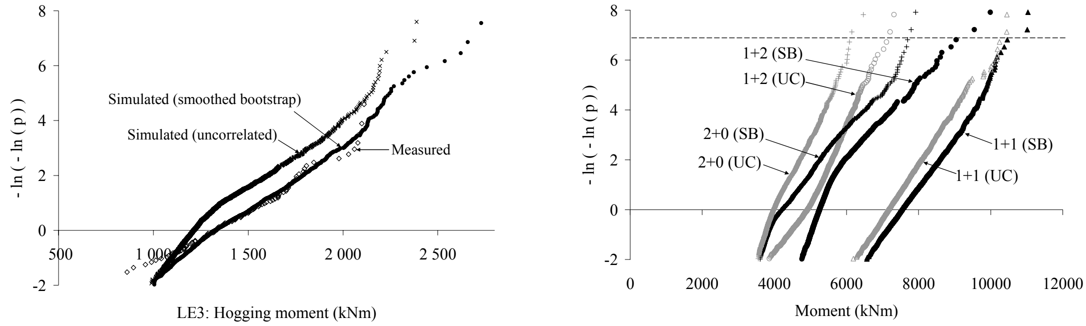

(a) Goodness of fit (b) Lifetime loading – 35 m bridge

Figure 5 – Daily and annual maximum load effects – Smoothed bootstrap (SB) vs. uncorrelated (UC) models

To see what effect the different modelling assumptions have on the characteristic maximum loading, both methods were used to simulate 2500 years of traffic. In the Eurocode for bridge loading (EC1 2003), the value with a 5% probability of exceedance in 50 years is specified for design which is approximately the value with a return period of 1000 years. Sample results are plotted in Figure 5(b) which shows simulated annual maxima on a 35 m bridge in the Czech Republic with high lateral distribution. Three event types are shown –one truck in each lane (1+1), two trucks in the slow lane (2+0), and one truck in the slow lane with two trucks in the fast lane (1+2). For single-truck events (not shown), both models give the same results, but for events involving two or more trucks there are significant differences between the two simulation models, with the smoothed bootstrap method giving more conservative results than the uncorrelated model. The increases in characteristic maximum load effects due to correlation in models were calculated for the four spans and three load effects considered at the sites in the Netherlands and the Czech Republic. Correlation effects were found to account for an increase in 1000-year loading of up to nearly 8%, with typical values of around 5%, particularly when lateral distribution is high. Confidence intervals estimated using a parametric bootstrap indicate that these differences are statistically significant.

5. Conclusions

There are subtle patterns of correlation evident in measured traffic data. This inter-dependence between weights, speeds and inter-vehicle gaps for adjacent trucks affects the estimation of lifetime maximum bridge loading. A multi-dimensional smoothed bootstrap approach is presented here which re-samples observed traffic scenarios and uses kernel functions to introduce additional variation. The traffic scenarios are defined so as to capture patterns that may be significant for bridge loading, and to maximise variability in the simulation. The method is relatively simple to implement for any new site, and could be extended to three or more lanes. It is effectively the same as sampling from empirical distributions (for GVW, gaps and speed), but with correlation and some additional smoothing and randomness. It potentially could be used to model congested or partly congested traffic, if sufficient data were available. The choice of bandwidth for the kernel smoothing functions is somewhat arbitrary, although results for characteristic bridge loading are, within reason, not too sensitive to this choice. The model presented provides a better fit to measured data across the range of key loading event types than is obtained with a model which does not include any correlation effects. The effects of correlation on characteristic maximum loading may be as high as 8% for the range of bridge spans considered.

References

Abramson, I. S. (1982), 'On bandwidth variation in kernel estimates - a square root law', *The Annals of Statistics*, 10 (4), 1217-1223.

Bruls, A., Croce, P., Sanpaolesi, L. and Sedlacek, G. (1996), 'ENV1991 – Part 3: Traffic Loads on Bridges; Calibration of Load Models for Road Bridges', *Proceedings of IABSE Colloquium*, *Delft, The Netherlands*, IABSE-AIPC-IVBH, 439 - 453.

Croce, P. and Salvatore, W. (2001), 'Stochastic model for multilane traffic effects on bridges', *Journal of Bridge Engineering, ASCE*, 6 (2), 136-143.

EC1. (2003), *Eurocode 1: Actions on structures, Part 2: Traffic loads on bridges*, European Standard EN 1991-2:2003: European Committee for Standardization, TC250, Brussels.

Efron, B. and Tibshirani, R. (1993), *An Introduction to the Bootstrap* Chapman and Hall/CRC.

Gindy, M. and Nassif, H. H. (2006), 'Multiple Presence Statistics for Bridge Live Load Based on Weigh-in-Motion Data', *Transportation Research Board 86th Annual Meeting*, *Washingotn D.C.*

Iman, R. L. and Conover, W. J. (1982), 'A distribution-free approach to inducing rank correlation among input variables', *Communications in Statistics – Simulation and Computation*, 11 (3), 311 - 334.

Kulicki, J. M., Prucz, Z., Clancy, C. M., Mertz, D. and Nowak, A. S. (2007), 'Updating the calibration report for AASHTO LRFD code', NCHRP. Washington D.C.: Transportation Research Board.

Moses, F. (2001), 'Calibration of load factors for LRFR Bridge Evaluation', NCHRP Report No. 454. Washington D.C.: Transportation Research Board.

Nelsen, R. B. (1999), *An introduction to copulas*, Springer, New York.

Nowak, A. S. (1993), 'Live load model for highway bridges', *Structural Safety*,13,53-66.

O'Connor, A., Jacob, B., O'Brien, E. J. and Prat, M. (2001), 'Report of current studies performed on normal load model of EC1 Part 2. Traffic loads on bridges', *Revue Française de Génie Civil*, 5 (4), 411-433.

Scott, D. W. (1992), *Multivariate density estimation : theory, practice, and visualization*, Wiley, New York.

Sivakumar, B., Ghosn, M. and Moses, F. (2008), 'Protocols for Collecting and Using Traffic Data in Bridge Design', W-135, NCHRP. Washington D.C.: Transportation Research Board, [online] available from: http://onlinepubs.trb.org/onlinepubs/nchrp/nchrp_w135.pdf, accessed 2 July 2009

Sivakumar, B., Moses, F., Fu, G. and Ghosn, M. (2007), 'Legal truck loads and AASHTO Legal Loads for Posting', NCHRP Report 575.

A NEW CONGESTED TRAFFIC LOAD MODEL FOR HIGHWAY BRIDGES

C.C. CAPRANI, C. CAREY & B. ENRIGHT
Dept. of Civil & Structural Engineering, Dublin Institute of Technology, Ireland

Abstract
Long span highway bridges are critical components of any nation's infrastructure. Therefore accurate assessment of highway bridge loading is essential, and it is well known that congested traffic governs load effect for such bridges. Current congestion models use conservative assumptions about traffic and inter-vehicle gaps. This research investigates congested traffic flow through the use of traffic microsimulation which has the ability to reproduce complex traffic phenomena based on driver interactions. A time series model has been developed to produce a speed time-series similar to the results of the microsimulation. The speed time-series from the new model, combined with the established speed-gap relationship from the microsimulation, form the basis of a more computationally efficient congested traffic model. It is shown that the new model replicates aspects of microsimulation traffic well. However, the resulting load effects do not match as well as expected, and so further development of the model is required.

Keywords: Bridge; Congestion; Gap; Loading; Microsimulation; Speed; Traffic.

1. Introduction

Long span bridges usually form a critical part of a country's highway infrastructure. Since they are difficult and expensive to construct in the first place, they therefore only exist where there are clear economic imperatives. To remove such a structure from service, even if only temporarily, would therefore cause large-scale disruption. The economic costs associated with this are usually several orders of magnitude greater than any rehabilitation costs. Thus the prime motivation is to minimize disruption through accurate assessment of the structure's rehabilitation needs.

In any highway bridge structure assessment, live loading is one of the most variable parameters and so its accurate assessment can have significant impact on the rehabilitation needs of the structure. For long-span bridges, congested traffic is known to be the critical live loading scenario. Therefore its accurate modelling is essential for minimizing rehabilitation and its associated costs.

The modelling of congested traffic that has been described in the literature has been based on some simplifying and conservative assumptions. For example, Nowak and Hong (1991) modelled assumed gaps of 15 ft (4.57 m) and 30 ft (9.14 m). Vrouwenvelder and Waarts (1993) use two models: for distributed lane loads a gap of 5.5 m is used, whilst for full modelling a variable gap of 4 to 10 m is used. And in the background studies to the Eurocode (EC1.2 (2003)), Bruls et al (1996) and Flint and Jacob (1996) use a 5 m gap between vehicles.

This work examines congested traffic flow through the use of traffic microsimulation, which has the ability to reproduce complex traffic phenomena based on driver interactions. Congested traffic can be induced in microsimulation through artificial speed limits. A speed-gap relationship for different traffic densities can be determined. The traffic microsimulation model is computationally expensive and so only limited amounts of data can be obtained whereas long run simulations are required for bridge loading assessment. This work develops a computationally efficient congested traffic model based on the speed-gap relationships.

2. Traffic Modelling

2.1 Site and Vehicle Characteristics

This work uses weigh-in-motion (WIM) data obtained from the A4 (E40) at Wroclaw, Poland. In total over 17 weeks of traffic was recorded, including cars, from 1 January 2008 to 5 June, 2008. Both lanes of traffic in one direction were measured.

In this work, the arrival of each successive vehicle in a lane is considered to be a Markov process. The transitional probability matrices for each lane are calculated from the measured WIM data. These matrices are then used to generate the each successive vehicle arrival.

The properties of each vehicle are modelled as described by Enright (2010). For example, a bivariate distribution is used to model gross-vehicle-weight (GVW) and the number of axles of the vehicle; axle spacing distributions (such as tri-modal normal) are defined for each vehicle type; and axle weights are defined using bi-modal normal distributions representing the percentage GVW carried.

2.2 Vehicle Overhang Database

The bridge loading caused by a stream of congested traffic is static in nature, due to the low speeds involved. For a given set of vehicles, larger load effects will result from more closely spaced vehicles. In particular, higher load effects will result from closer front and rear axles of successive vehicles. The parameters influencing the gap between adjacent front and rear axles are not only those of driving characteristics, but include the vehicle front and rear overhangs (i.e. distance from the front and rear of the vehicle to the front and rear axles respectively).

Vehicle overhangs are difficult to obtain from site measurements. Therefore, for this research, a database of vehicle information was compiled from information supplied by European vehicle manufacturers. Over 1000 vehicles are included in this database. These vehicle dimensions, along with other published data (Page and Ricketts 1997), were used to categorize vehicles by axle configuration.

3. Congested Traffic Model Development

3.1 Microsimulation Analysis

In order to account for the influence of driving behaviour on the gaps between vehicles in congested traffic, traffic microsimulation has been used. The Intelligent Driver Model (IDM) developed by Treiber and others (Treiber et al., 2000a, Treiber et al., 2000b) is used for this purpose. The program, *EvolveTraffic* (Caprani and OBrien 2008, Caprani 2010), implements the IDM and is used for this study.

The WIM data are processed using *EvolveTraffic*. Congested traffic is induced, similar to Treiber (2000b), using artificial speed limits (10, 15, 20 and 25 km/h).

These induce varying densities of 74 to 102 vehicles/km/lane. As the density increases over about 74 vehicles/km/lane congestion results. Kerner et al. (2004) state that when the average traffic speed is less than 24 km/h it can be considered as congested.

The 'virtual' road used in this study is 3 km long, with two lanes in the same direction. At 2800 m a speed limit, 200 m in length, is imposed to induce congestion. The data outputted from the microsimulation includes traffic speeds at 10 s intervals. Also, individual vehicle data, including the vehicle time-stamp and the vehicles length, including overhangs are output, which allow inter-vehicle, bumper to bumper gaps to be calculated. By averaging the inter-vehicle gaps over 10 second intervals, a speed-gap time-series is found (Figure 1).

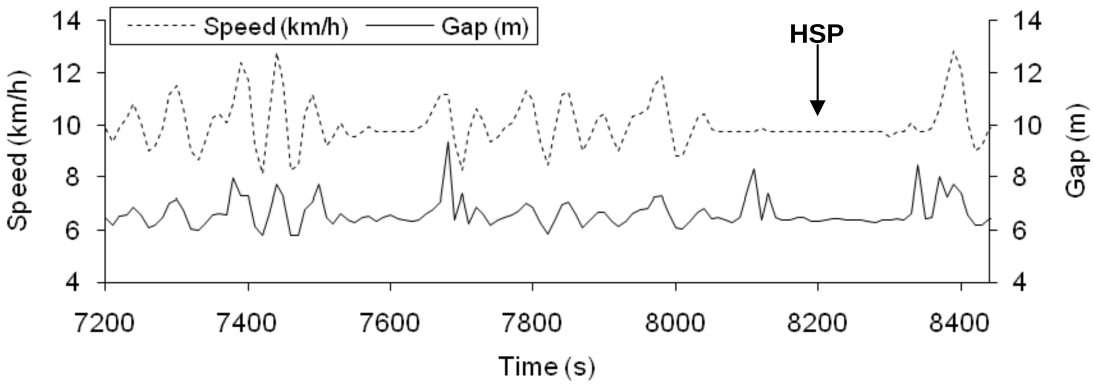

Figure 1 – Typical observed speed and gap time-series (see Section 3.3 for HSP).

3.2 Congested Traffic Speed-Gap Relationship

Traffic theory suggests that the speed-gap relationship is not monotonic: different gaps are found for similar speeds; depending on the phase (acceleration or deceleration) the traffic is experiencing (Kerner et al 2004). However in the congested traffic flow produced by the microsimulation, no hysteresis in the speed-gap relationship was observed (Figure 2), as the acceleration and deceleration phases are of low amplitude (below 0.2 m/s^2).

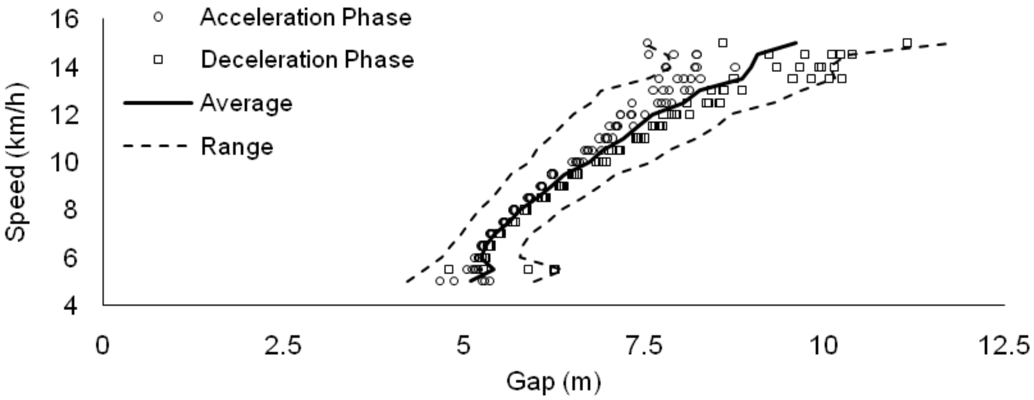

Figure 2 – Observed speed-gap relationship for density range 80-86 veh/km/lane.

3.3. Congested Traffic Speed Model

In the microsimulation modelling, periods for which traffic travels at a constant speed, labelled here as homogeneous speed phases (HSP), were observed (see Figure 1 for an example). Due to the non-stationary caused by the presence of HSPs, an autoregressive time-series model, such as ARIMA (Boxx et al. 2008) is not an appropriate model. Therefore, to model speed, the change of speed is calculated at each time-step and plotted against the current speed of each vehicle (Figure 3). This bivariate distribution is discretized for the speed ranges shown. Thus, given a particular speed, and whether the traffic is accelerating or decelerating, the change in speed can be estimated probabilistically. The phase the vehicle is experiencing is modelled using a Markov transition matrix for each speed range (Table 1).

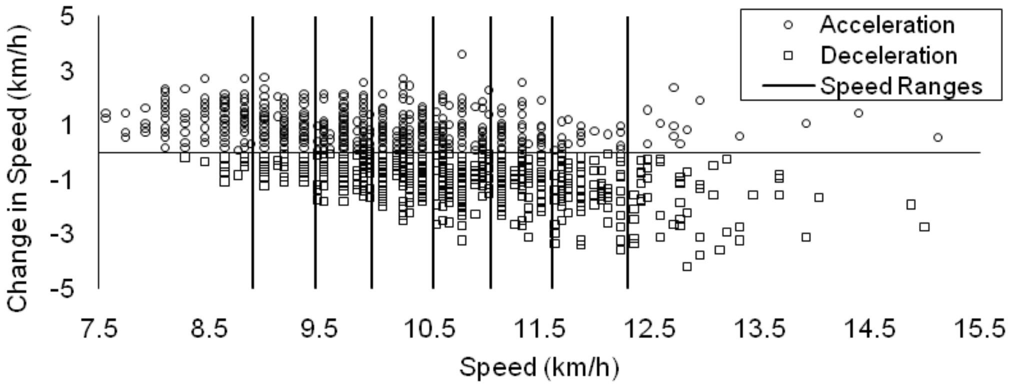

Figure 3 – Speed and phase identification (density range 74-79 veh/km/lane).

Table 1 – Traffic phase transition matrix for a density of 74-79 veh/km/lane.

Phase Transition*	Speed Range (km/h)						
	0-8.9	**8.9-9.5**	**9.5-9.8**	**9.8-10.5**	**10.5-11.1**	**11.1-12.0**	**12.0+**
A - A	1.00	1.00	0.98	0.69	0.53	0.34	0.26
A - D	0.00	0.00	0.02	0.31	0.47	0.66	0.74
D - D	0.08	0.34	0.53	0.85	0.96	0.98	1.00
D - A	0.92	0.66	0.47	0.15	0.04	0.02	0.00

* A – Acceleration; D - Deceleration

For a given traffic density there are specific speeds at which HSPs occur. The speed time series were analysed to identify the HSPs and determine the distribution of their duration. Further, the speed time series were analysed for the probability of an HSP occurring, for each particular speed.

3.3 Congested Traffic Model

The complete congested traffic load model proposed is determined from the congested traffic speed model and the established speed-gap relationship, with some variation applied (Figure 2). The following steps implement the model:

1. Randomly select a speed, based on the overall distribution of speeds;
2. Check if the speed is in a HSP, and if so the HSP duration;
3. From the bivariate relationship of Figure 3, determine the change in speed to find the speed in 10 s time;
4. Determine the particular phase (acceleration/deceleration) for the next speed, from the transition matrix (Table 1) given the current phase.

4. Application of Proposed Congested Traffic Model

4.1 Comparison with Microsimulation

To determine the accuracy of the proposed congested traffic model, relevant macro-statistics are compared to those from the full microsimulation in Figure 5 and Table 2. A typical speed time series obtained from the proposed model is shown in Figure 4, alongside a sample from full microsimulation.

The occurrence of different vehicle types in the proposed model is compared to those from the full microsimulation in Figure 6. The percentage differences in the occurrence of different vehicle types increases with the number of axles. This can be attributed to the relatively small number of such vehicles.

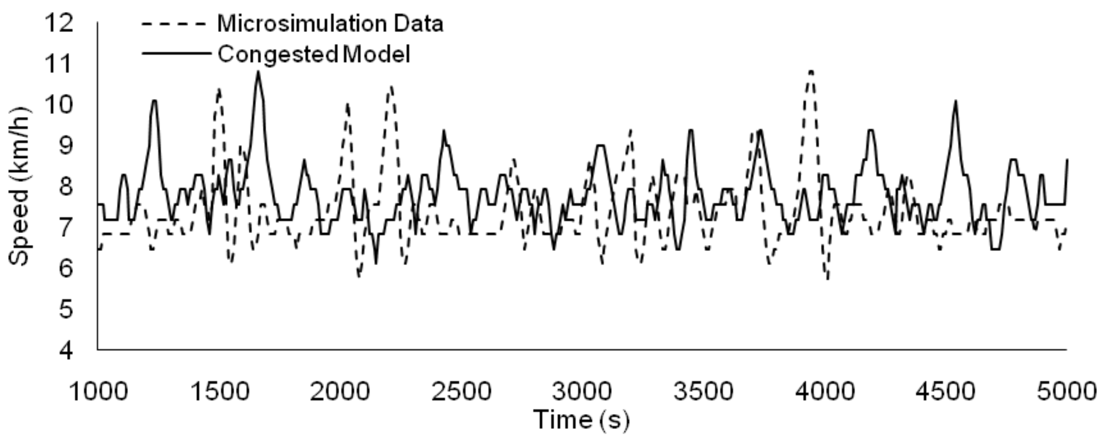

Figure 4 – Speed time-series from microsimulation and from congested model.

Table 2 – Proposed model and microsimulation statistics.

		Maximum	Minimum	Mean	Standard Deviation
Speed (km/h)	Microsim.	15.12	5.4	7.66	1.11
	Model	15.23	5.36	7.63	1.09
Gap (m)	Microsim.	12.64	1.54	5.67	0.74
	Model	12.88	1.71	5.71	0.77

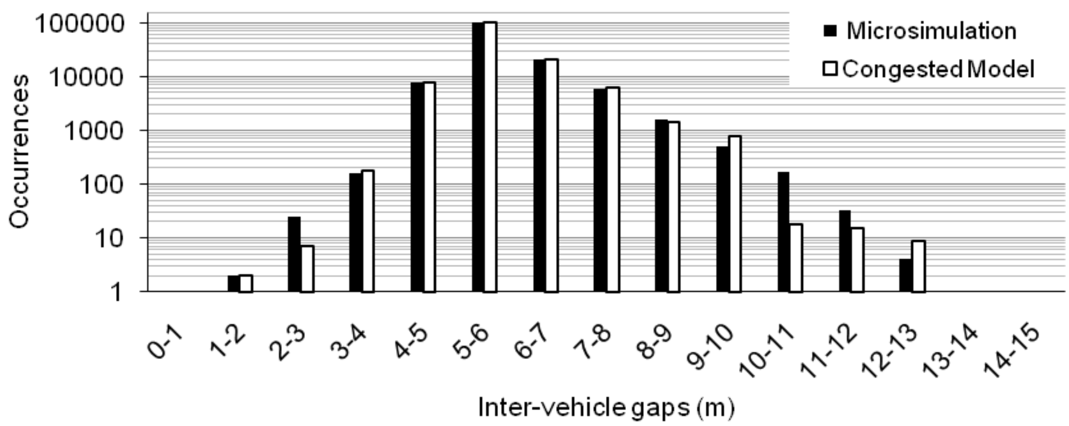

Figure 5 – Comparison of inter-vehicle gap distributions.

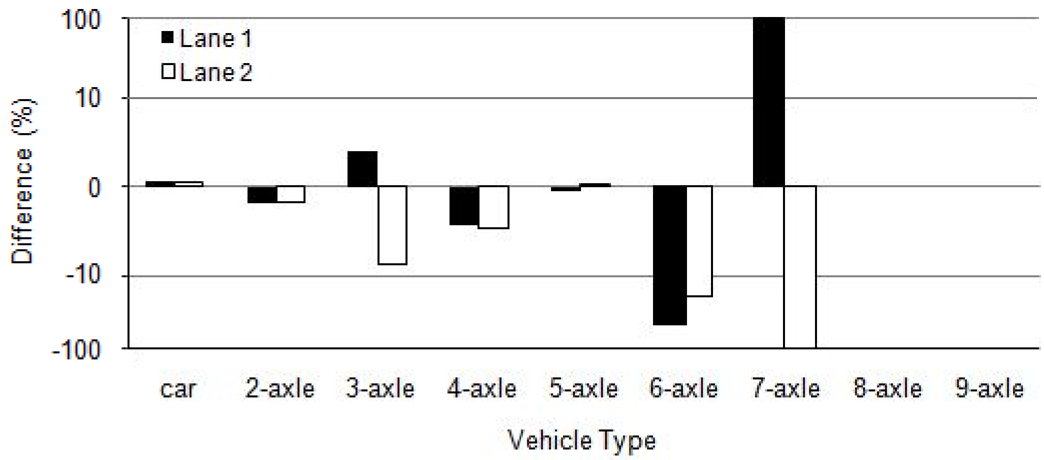

Figure 6 – Comparison of vehicle-type occurrence.

4.2 Comparison of Load Effects

The load effects resulting from the proposed congestion model are compared with those imparted by congested traffic from the microsimulation model, based on the WIM data. The bridge lengths and load effects considered are:

- Lengths: 40, 60, 80, 100 m;
- Load Effects:
    - LE1: Mid-span bending moment in a simply-supported beam;
    - LE2: Central support hogging moment in a two-span beam;
    - LE3: left hand shear in a simply-supported beam.

The simulations are 200 hours of congested flow, representing 100 days of traffic. Maximum-per-day load effects are fit with a Generalized Extreme Value distribution and the 1000-year return level of load effect estimated.

The return levels of load effect are calculated for the proposed model and from the full traffic microsimulation. The results are expressed as a ratio in Figure 7. This figure shows that load effects are consistently underestimated by the proposed model.

The GVW distributions used in both models are identical. Therefore, since LE3 gives a measure of the total load on the bridge, and since this is relatively uniform, it appears that an insufficient number of vehicles are present on the bridge. Thus it appears that the inter-vehicle gaps generated in the proposed model are not small enough for extreme loading scenarios.

The congested model underestimates load effects 1 and 2 also. Thus it appears that the generated gaps are not small enough at the critical influence line locations. However, given that the macro-statics of Table 2 show that the gap distributions are similar, it may be that the mode does not associate small gaps with heavy vehicles to the same extent that traffic microsimulation does. Perhaps, since heavier vehicles have less capacity to accelerate or decelerate, the gap distribution may be different for such vehicles than it is for light vehicles. Therefore the inter-vehicle gaps should be related to the vehicle GVW and are not just based solely on the vehicle speed.

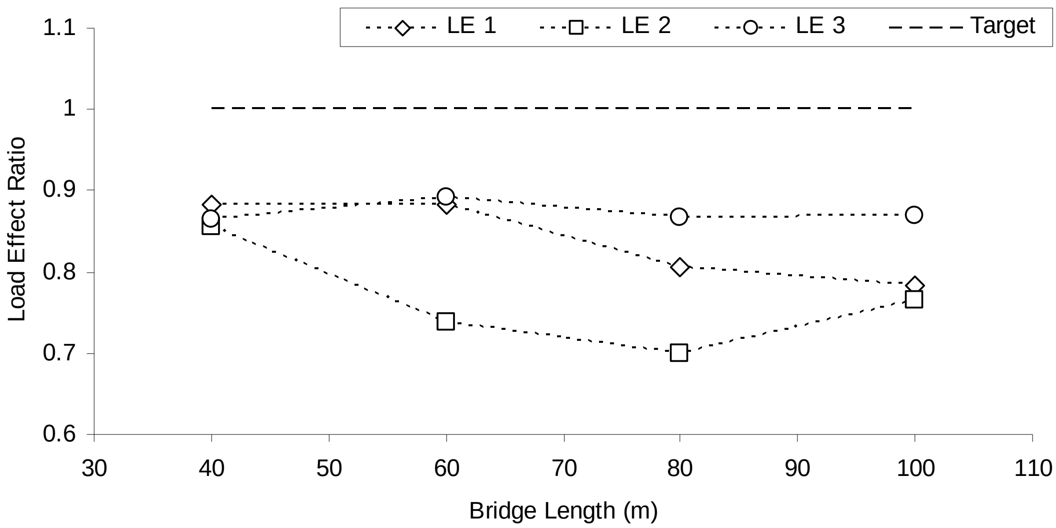

Figure 7 – Ratio of extreme load effect found from the congested model to that of the traffic microsimulation applied to the WIM data.

5. Summary

A new congested traffic model for long-span bridge loading is presented. This model is based on microsimulation of site-measured data, in order to create realistic congested traffic streams. This congested traffic was analysed and a speed time-series model and a speed-gap relationship for given traffic densities were defined. A Markov process is used to generate vehicles from the WIM data. The congested traffic model output is compared to that from microsimulation and is shown to compare well. Extreme load effects were determined for both models. It is found that the congested traffic model underestimates load effects. As a result, it is concluded from this work that a relationship between inter-vehicle gaps and load intensity may exist.

6. Acknowledgment

The authors would like to acknowledge the Dublin Institute of Technology ABBEST Scholarship Programme for funding this research.

References

Box, G.E.P., Jenkins, G.M. and Reinsel, G.C. (2008), *Time Series Analysis: Forecasting and Control*, Wiley.

Bruls, A., Croce, P., Sanpaolesi, L. and Sedlacek, G. (1996), 'ENV1991 – Part 3: Traffic Loads on Bridges; Calibration of Load Models for Road Bridges', *Proceedings of IABSE Colloquium*, Delft, The Netherlands, IABSE-AIPC-IVBH, 439-453.

Caprani, C.C. and OBrien, E.J. (2008), 'The governing form of traffic for highway bridge loading', *Proceedings of 4th Symposium on Bridge and Infrastructure Research in Ireland*, eds. E. Cannon, R. West and P. Fanning, National University of Ireland, Galway, pp. 53-60.

Caprani, C. (2010), 'Using Microsimulation to Estimate Highway Bridge Traffic Load', *Proc. 5th Intl. Conf. on Bridge Maintenance, Safety and Management*, IABMAS, Philadelphia, July, in print.

Enright, B. (2010), *Simulation of traffic loading on highway bridges*, PhD Thesis, School of Architecture, Landscape, and Civil Engineering, University College Dublin, Ireland.

Kerner, B. S., Rehborn, H., Aleksic, M. & Haug, A. (2004), 'Recognition and tracking of spatial-temporal congested traffic patterns on freeways', *Transportation Research Part C: Emerging Technologies*, 12(5), 369-400.

Nowak, A.S. and Hong, Y.K. (1991), 'Bridge live load models', *Journal of Structural Engineering*, ASCE, 117(9), 2757-2767.

Page, J. and Ricketts, N.J. (1997), *Traffic Data for Highway Bridge Loading Rules*, Rep. 251, Transport Research Laboratory, Crowthorne, Berks.

Treiber, M., Hennecke, A., and Helbing, D. (2000a), 'Microscopic Simulation of Congested Traffic', in: *Traffic and Granular Flow '99*, Eds. D. Helbing, H.J., Herrmann, M. Schreckenberg, and D.E. Wolf, Springer, Berlin, 365-376.

Treiber, M., Hennecke, A. and Helbing, D. (2000b), 'Congested Traffic States in Empirical Observations and Microscopic Simulations', *Physical Review E*, 62(2), 1805-1824, arXiv:cond-mat/0002177v2.

Vrouwenvelder, A.C.W.M. and Waarts, P.H. (1993), 'Traffic loads on bridges', *Structural Engineering International*, 3/93, 169-177.

DYNAMIC AMPLIFICATION FACTORS FOR BRIDGES WITH VARIOUS BOUNDARY CONDITIONS

C.H.CAREY, E.J.OBRIEN & A.GONZALEZ
School of Architecture, Landscape and Civil Engineering, University College Dublin, Ireland

Abstract
It is important that the assessment of bridges be as accurate as possible. Dynamic amplification is one area in which the codes are sometimes overly conservative. Bridge dynamics is well researched but the majority of this research has concentrated on simply supported bridges. This paper examines the effect that introducing support rotational restraint has on bridge dynamic amplification factors. Finite element models are used with rotational springs at the bridge supports. This paper examines the effect of vehicle velocity on the dynamic amplification for the different end restraints.

Keywords: (Boundary Conditions, Dynamic amplification, Speed)

1. Introduction

Bridge design is often excessively conservative. Conservatism is relatively inexpensive in new construction but can lead to unnecessary repair or replacement of existing bridges, with consequent waste of maintenance funds and non renewable resources. Standards and codes of practice make significant allowances for dynamics. For example, the Eurocode (admittedly for the design of new bridges) allows for a 20-70% increase in stress (Dawe 2003)

Dynamic amplification takes into account the phenomenon that the stress produced at a given point in a bridge when a vehicle is moving across it, differ from that generated, had the vehicle been stationary. The change in stress is a consequence of the complex relationship between a moving vehicle, the road profile and the bridge underneath. This relationship is dependent on many parameters including the natural frequencies of the bridge, the road surface and, the vehicle(s) causing the loading. There is much literature on these factors and their effect on bridge dynamics. This paper concentrates on the effect of speed and boundary conditions.

The term used to measure the dynamics in this paper is dynamic amplification factor (DAF), defined by Zhang et al. (2001) as,

$$DAF = \frac{E_{tot}}{E_{stat}} \tag{1}$$

where E_{stat} is the maximum static load effect induced at a point in the bridge by a stationary vehicle and E_{tot} is the maximum total (static plus dynamic) load effect induced by the same vehicle when it is moving.

1.1 Boundary Conditions

Most of the literature on bridge dynamics has been carried out on bridges with simple supports or certainly on bridges with one set of support conditions (Nowak and Hong 1991; Brady et al. 2006). Salawu and Williams (1995) acknowledge that significant assumptions are usually made with regard to the boundary conditions. Even for bridges incorporating spherical or pot bearings, some resistance to rotation is frequently evident in site measurements (Doebling et al. 1997).

Although most of the literature uses one set of boundary conditions, generally the simply supported case, there are some that investigate changes in the support conditions. Fryba (1971) is the most notable of these sources and the equations he developed are used to verify the finite element model used in this paper. Akin & Massood (1989) present a method of determining beam response to a moving mass with varying support conditions. They look at displacement at a certain point for different beams while varying the boundary conditions.

This paper examines the change in frequency as a result of a change in boundary conditions. Law et al. (1995) suggest that the fundamental frequency of a T-beam slab bridge deck is not sensitive to changes in boundary conditions. This is in contrast to Mertlich et al. (2007) who report that reducing the end rotational restraint had a significant impact on the natural frequencies. Brownjohn et al. (2003) report a considerable increase in frequency for a bridge that underwent rotational restraint and the installation of a guardrail. They go on to say that it is the increased rotational resistance that has had the greater influence on the bridge frequency.

1.2 Rotational Springs

Rotational springs are used in this paper to model rotational resistance at the supports. This approach is used in many scenarios such as to analyse the effect of increasing support stiffness after bridge upgrading works (Brownjohn et al. 2003) or, similarly to this paper, to use the adjustable stiffness of the springs to model a range of end conditions (Wu and Law 2004). In many cases rotational springs are used to fit finite element models to the experimental data (Doebling et al. 1997; Zhang and Aktan 1997; Sanayei et al. 1999; Feng et al. 2004). All of these authors acknowledge that the boundary conditions affect the dynamic characteristics. Salawu (1997) notes that dynamic characteristics may respond to changes in boundary supports.

2. Fryba Beam model

This paper represents the vehicle moving across the bridge as a simple point force traversing a beam. This is a simplification and can have a significant influence on the results (Akin & Massood 1989) but using such models facilitates a focus on the influence of specific parameters (Brady 2004). The bridge is 25m in length (l), has a span to depth ratio of 1/20 with square cross section meaning the second moment of area (I) is 1.38m^4. The Youngs modulus (E) is 3.6x10^{10}N/m^2 and density (μ) is 2446kg/m^3. The stiffness (k) of the rotational springs that model the boundary conditions changes. Fryba (1971) provides a closed form solution to the Bernoulli-Euler equation for a beam. He first presents a solution for simply supported boundary conditions but goes on to give a general equation for displacement at a point x and time t that can be adapted depending on the boundary conditions:

$$v(x,t) = \sum_{j=1}^{\infty} \frac{P}{V_j} v_{(j)}(x) \left\{ \frac{1}{\omega_{(j)}^2 + \omega^2} \left[\left(\sin \omega t - \frac{\omega}{\omega_{(j)}} \sin \omega_{(j)} t \right) \left(-\cos \lambda_j + A_j \sin \lambda_j \right) + \left(\cos \omega t - \cos \omega_{(j)} t \right) \left(\sin \lambda_j + A_j \cos \lambda_j \right) \right] + \frac{1}{\omega_{(j)}^2 + \omega^2} \left[\left(\sinh \omega t - \frac{\omega}{\omega_{(j)}} \sin \omega_{(j)} t \right) \left(-B_j \cosh \lambda_j - C_j \sinh \lambda_j \right) + \left(\cosh \omega t - \cos \omega_{(j)} t \right) \left(B_j \sinh \lambda_j + C_j \cosh \lambda_j \right) \right] \right\} \quad (2)$$

where the values A_j, B_j, C_j and λ_j are constants dependent on the boundary conditions, P is force, ω is the load circular frequency, $\omega_{(j)}$ is the natural circular frequency of the beam, and where:

$$v_{(j)}(x) = \sin \frac{\lambda_j x}{l} + A_j \cos \frac{\lambda_j x}{l} + B_j \sinh \frac{\lambda_j x}{l} + C_j \cosh \frac{\lambda_j x}{l} \quad (3)$$

and

$$V_j = \frac{\mu l}{2} \left\{ 1 + A_j^2 + B_j^2 + C_j^2 + \frac{1}{\lambda_j} \left[2C_j - 2A_j B_j - B_j C_j - \frac{1}{2}\left(1 - A_j^2\right) \sin 2\lambda_j + 2 A_j \sin^2 \lambda_j + \left(B_j^2 + C_j^2\right) \sinh \lambda_j \cosh \lambda_j + 2\left(B_j + A_j C_j\right) \cosh \lambda_j \sin \lambda_j + 2\left(-B_j + A_j C_j\right) \sinh \lambda_j \cos \lambda_j + 2\left(C_j + A_j B_j\right) \sinh \lambda_j \sin \lambda_j + 2\left(-C_j + A_j B_j\right) \cosh \lambda_j \cos \lambda_j + B_j C_j \cosh 2\lambda_j \right] \right\} \quad (4)$$

Using the relation, $M(x,t) = -EI \frac{\partial^2 v(x,t)}{\partial x^2}$ (5), an equation can be derived for moment which accounts for boundary conditions.

3. Finite Element Model

In order to implement the finite element method, both the stiffness and mass matrices must be defined. For the elements that do not have rotational springs attached, the stiffness matrix, k_e, is defined by Rockey et al. (1983) and is given below. Variations of the element stiffness matrix must be defined to allow for a rotational spring at the left ($k_{eS\text{-}L}$) or the right ($k_{eS\text{-}R}$) end of the beam.

$$k_{eS-L} = \begin{bmatrix} A & H & -A & Q \\ B & G & -B & D \\ -A & -H & A & -Q \\ C & O & -C & R \end{bmatrix} \quad (6) \qquad k_e = \frac{EI}{l_e^3} \begin{bmatrix} 12 & 6l_e & -12l_e & 6l_e \\ 6l_e & 4l_e^2 & -6l_e & 2l_e^2 \\ -12 & -6l_e & 12 & -6l_e \\ 6l_e & 2l_e^2 & -6l_e & 4l_e^2 \end{bmatrix} \quad (7)$$

$$k_{eS-R} = \begin{bmatrix} A & Q & -A & H \\ C & R & -C & O \\ -A & -Q & A & -H \\ B & D & -B & G \end{bmatrix} \quad (8)$$

where,

$$A = \frac{3EI}{l_e^3} + \frac{3\pi}{2l_e} \quad (9) \qquad B = \frac{3}{2l_e} \Big/ \left(\frac{l_e}{4EI} + \frac{2}{k} \right) \quad (10) \qquad C = Al_e - B \quad (11) \qquad D = \frac{1}{\frac{l_e}{2EI} + \frac{4}{k}} \quad (12)$$

$$R = \frac{3EI}{l_e} + \frac{D}{2} \quad (13) \quad Q = \frac{D+R}{l_e} \quad (14) \quad G = \frac{1}{\frac{l_e}{4EI} + \frac{1}{k}} \quad (15) \quad H = \frac{3G}{2l_e} \quad (16) \quad O = \frac{G}{2} \quad (17)$$

Where l_e is the length of each element and k is the stiffness of the spring. The mass matrix, also defined by Rockey et al. (1983), is the same for all elements. Moment can be calculated after finding the strain ($\varepsilon(x)$) using:

$$\varepsilon(x) = \frac{-y}{l_e^3}\left[\left(6l_e - 12(x_e)\right)u_i + \left(4l_e^2 - 6l_e(x_e)\right)\theta_i + \left(-6l_e + 12(x_e)\right)u_{i+1} + \left(2l_e^2 - \right.\right.$$
$$6lexe\theta i{+}1 \quad (18)$$

and,

$$M = \frac{EI}{y}\,\varepsilon(x) \quad (19)$$

Where x_e is the distance from the left hand edge of the element that the strain is measured, u_i is the displacement degree of freedom at node i and θ_i is the rotational degree of freedom.

4. Finite Element Model agreement with Fryba Beam model

As seen in Figure 1 the Finite Element (FE) and the Fryba (1971) beam model are in good agreement. The level of matching is dictated by the number of elements used in the FE model and the number of mode shapes considered when using the Fryba method. It can be seen that there are a series of progressively larger peaks in dynamic amplification with speed. Whether dynamics increases or decreases with speed depends on where typical highway speeds fall on this graph and the critical speeds are directly related to bridge first natural frequency.

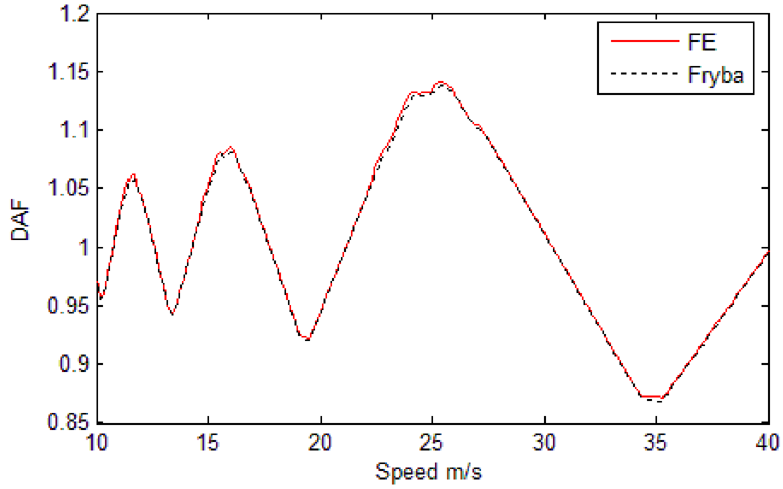

Figure 1 - Variation of Dynamic Amplification (DAF) with Speed: Comparison of Finite Element and Fryba models; Simply Supported End Conditions

5. Pinned versus Fixed

Figure 2 shows the variation of DAF with speed for both pinned and fixed boundary conditions. One of the first things of note is the difference in magnitude of DAF between the pinned and fixed bridges. It can be seen that the peaks for the pinned end conditions are considerably higher than for the fixed. The highest vales are 1.45 and

1.33 for the pinned and fixed bridges respectively. These values occur at 230 km/h and 431 km/h which are clearly not realistic speeds for road traffic (critical speeds will be different for bridges with different fundamental frequencies). The next peaks of 1.15 and 1.06 happen at 91 km/hr and 183 km/hr which illustrate that not only does the fixed beam have lower magnitude DAF but that these values are more difficult to reach for normal traffic as they occur at higher speeds.

Considering beams that have a stiffness in between pinned and fixed, it can be seen that the peak dynamic amplification factor decreases with an increase in stiffness and that higher speeds are needed to reach the peaks. This is shown by the trend to the right in Figure 3 for the final peak shown for each bridge. This indicates that changing the resistance to rotation has an effect on the frequency of the bridge; something which is investigated further in the next paragraphs.

Figure 4 shows the peak DAF's and corresponding critical speeds for each of the five boundary conditions used in Figure 3. The straight lines show that the peak DAF's decrease as the critical speed increases in an approximately linear way. The slopes of the lines joining the peaks increase with each peak, but only slightly.

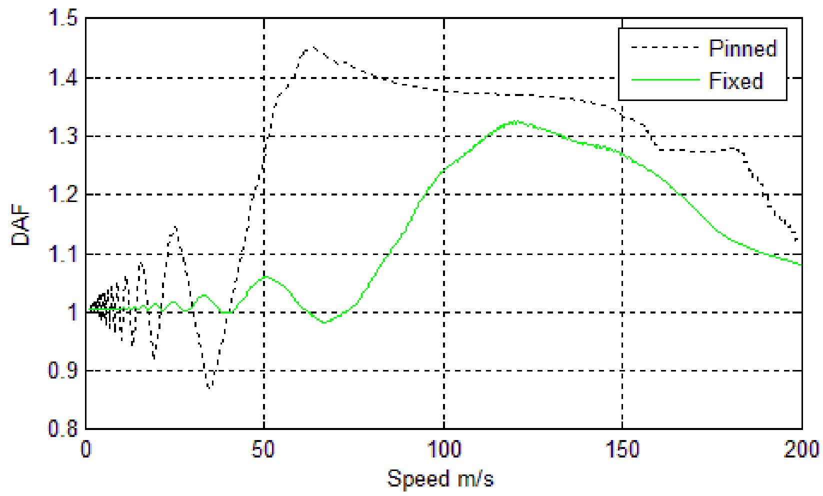

Figure 2 - Variation of Dynamic Amplification with Speed: Fixed vs Pinned End Conditions

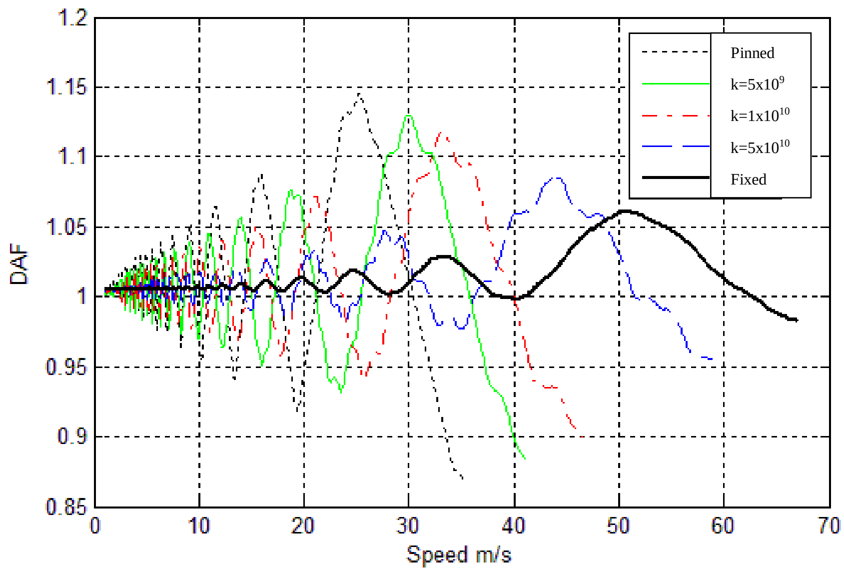

Figure 3 - Variation of Dynamic Amplification with Speed: Various End Condition Rotational Stiffnesses

Brady (2004) reports that for a given bridge, when the moving force reaches a certain velocity, it coincides with a critical bridge frequency and a peak DAF results. It is therefore important to look at what effect the increase in stiffness has on the bridge frequency. This is done by examining certain points in Figure 3 and creating the bending moment versus time responses for the relevant velocities. From these, the bridge frequency can be calculated. The resulting frequencies are presented in Table 1:

Table 1 - Change in Frequency with End Rotational Stiffness

Boundary Stiffness	Pinned	$5x10^9$	$1x10^{10}$	5×10^{10}	Fixed
Frequency (Hz)	3.54	4.19	4.68	6.25	7.55

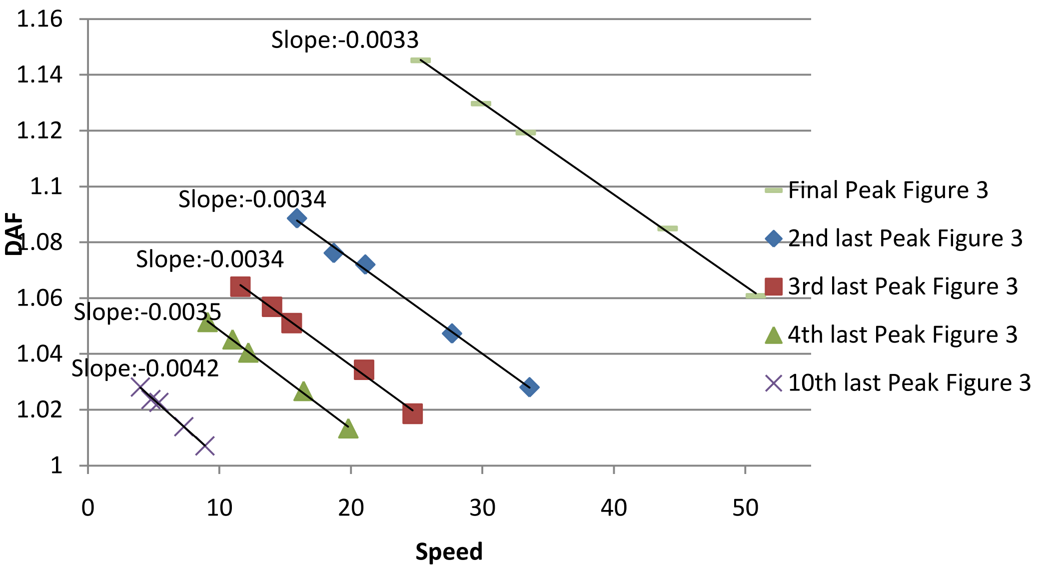

Figure 4 - Peak values of Figure 3

It can clearly be seen that increasing the resistance to rotation at the ends of the bridge increases the first natural frequency. This is consistent with Figure 3; the shift to the right illustrates that a higher speed is needed to produce the equivalent peak in each end stiffness. These peaks occur at certain frequency ratios, defined as the ratio load circular frequency to first beam circular frequency.

Accordingly, a higher speed for the same peak indicates that that bridge has a higher first natural frequency. Figure 5 is similar to Figure 3 but, in this case, the horizontal axis is rescaled by dividing by bridge fundamental frequency. This aligns the peaks to a considerable extent, removing the influence of changing frequency.

It is clear from Figure 5 that the peaks do not occur at the exact same frequency ratio. This behaviour is consistent with what is shown in Figure 4. The slope of the lines linking the peaks are not exactly the same. This implies that if the graphs were normalised so that the final peaks of the five bridges were directly under each other, then the other peaks would not line up accordingly.

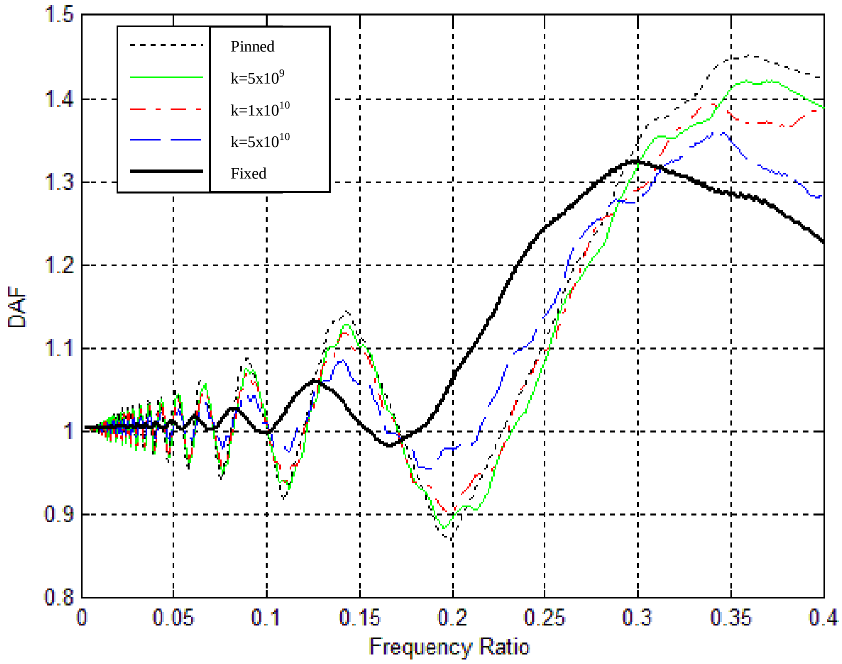

Figure 5 - Frequency Ratio vs Dynamic Amplification

6. Conclusion

The majority of the literature investigating dynamic amplification has looked at bridges with simple supports. By modelling rotational springs at the supports it is possible to model different levels of rotational restraint and hence to show the effect of the different boundary conditions on dynamic amplification. It is shown in this paper that by introducing rotational restraint the magnitude of dynamic amplification factor (DAF) reduces and occurs at higher vehicle speeds.

7. Acknowledgement

This research is supported by the Irish Research Council For Science Engineering And Technology (IRCSET) and the Irish Research Council For The Humanities And Social Science (IRCHSS).

8. References

Akin, J. E. and Massood, M. (1989), 'Numerical Solution for Response of Beams with Moving Mass', *Journal of Structural Engineering*, Am. Soc. Civ. Engnrs, **1**, 120-131.

Brady, S.P. (2004), *The influence of vehicle velocity on dynamic amplification in highway bridges*, PhD thesis, University College Dublin, Ireland.

Brady, S. P., OBrien, E. J. and Znidarič, A. (2006), 'Effect of Vehicle Velocity on the Dynamic Amplification of a Vehicle Crossing a Simply Supported Bridge', *Journal of Bridge Engineering*, Am. Soc. Civ. Engnrs, **2**, 241-249.

Brownjohn, J.M.W., Moyo, P., Omenzetter, P. and Lu, Y. (2003), 'Assessment of Highway Bridge Upgrading by Dynamic Testing and Finite-Element Model Updating', *Journal of Bridge Engineering*, Am. Soc. Civ. Engnrs, 3, 162-172.

Dawe, P. (2003), *Research Perspectives: Traffic Loading on Highway Bridges*, Thomas Telford, London, United Kingdom.

Doeling, S.W., Farrar, C.R. and Goodman, R.S. (1997), 'Effects of Measurement Statistics on the Detection of Damage in the Alamosa Canyon Bridge', *Proceedings of the 15th International Modal Analysis Conference*, 919-929.

Feng, M.Q., Kim, D.K., Yi, J-K and Chen, Y. (2004), 'Baseline Models for Bridge Performance Monitoring', *Journal of Engineering Mechanics*, **5**, 562-569.

Fryba, L. (1971), *Vibration of Solids and Structures under Moving Loads*, Noordhoff International Publishing, Groningen, The Netherlands.

Law, S.S., Ward, H.S., Shi, G.B., Chen, R.Z., Waldron, P. and Taylor, C. (1995), 'Dynamic Assessment of Bridge Load-Carrying Capacities', *Journal of Structural Engineering*, Am. Soc. Civ. Engnrs, **3**, 478-487.

Mertlich, T.B., Halling, M.W. and Barr, P.J. (2007), 'Dynamic and Static Behaviour of a Curved-Girder Bridge with Varying Boundary Conditions', *Journal of Performance of Constructed Facilities*, Am. Soc. Civ. Engnrs, **3**, 185-192.

Nowak, A.S. and Hong, Y-K. (1991), 'Bridge Live-Load Models', *Journal of Structural Engineering*, Am. Soc. Civ. Engnrs, **9**, 2757-2767.

Rockey, K.C., Evans, H.R., Griffiths, D.W. and Nethercot, D.A. (1983), *The Finite Element Method a Basic Introduction for Engineers*, Granada Publishing Limited, Frogmore, United Kingdom.Salawu, O.S. and Williams, C. (1995), 'Review of full-scale dynamic testing of bridge structures', *Engineering Structures*, **2**, 113-121.

Salawu, O.S. (1997), 'Detection of Structural Damage through changes in frequency: a review', *Engineering Structures*, **9**, 718-723.

Sanayei, M., McClain, J.A.S., Wadia-Fascetti, S. and Santini, E.M. (1999), 'Parameter Estimation Incorporating Modal Data and Boundary Conditions', *Journal of Structural Engineering*, Am. Soc. Civ. Engnrs, **9**, 1048-1055.

Wu, D. and Law, S.S. (2004), 'Model error correction from truncated modal flexibility sensitivity and generic parameter; II: experimental verification', *Mechanical Systems and Signal Processing*, **18**, 1401-1419.

Zhang, Z. and Aktan, A.E. (1997), 'Different Levels of Modelling for the Purpose of Bridge Evaluation', *Applied Acoustics*, **3**, 189-204.

Zhang, Q-L, Vrouwenvelder, A. and Wardenier, J. (2001), 'Dynamic Amplification factors and EUDL of bridges under random traffic flows', *Engineering Structures*, **23**, 663-672.

LOAD EFFECT OF SINGLE-LANE TRAFFIC SIMULATIONS ON LONG-SPAN BRIDGES

A. LIPARI[1], C.C. CAPRANI[2] & E.J. OBRIEN[1]
[1]School of Architecture, Landscape and Civil Engineering, University College Dublin, Ireland
[2] Dept. of Civil & Structural Engineering, Dublin Institute of Technology, Ireland

Abstract
It is well acknowledged that long-span road bridges (about 50 m long and more) are governed by congestion traffic rather than free-flow conditions. A conventional model for the design of new long-span bridges is to place over the bridge a load model representing a platoon of heavy vehicle with the gaps between them reduced to a minimum. This assumption is too conservative for existing bridges, given the large disruption costs faced by their closure for rehabilitation. In order to model the close gaps between vehicles, characteristic of congested traffic, microsimulation is needed to accurately capture drivers' behaviour. In this work, a microsimulation model is studied and found to replicate many different known forms of congestion. As a first approach to the topic, single-lane simulations of identical vehicles have been carried out in order to obtain load effect on a sample bridge. This load effect is studied with reference to the form of traffic causing the load effect. It is found that the most extreme load effect may not be caused by purely congested traffic but also by non-stationary congested conditions.

Keywords: bridges; loading; long-span; microsimulation; traffic

1. General

It is well acknowledged that long-span road bridges (50 m long and more) are governed by congested traffic rather than free-flow conditions. In free flowing traffic, vehicles have large gaps between them, while congestion implies long queues of closely spaced vehicles. Greater load effect results, even though there is no amplification for dynamic effects (Buckland, 1981).

A conventional model for designing new bridges is to reduce the gaps between trucks to a minimum. However, this assumption is too conservative for existing bridges, given the large cost associated with disruption caused by rehabilitation works. Therefore it is imperative that as the long-span bridge stock ages, more accurate estimation methods of congested traffic are found.

As the traditional macroscopic models, which describe the flow in terms of aggregate quantities, are not able to capture this phenomenon, micro-simulation is needed to capture drivers' behaviour in congested conditions. Further, since drivers do not usually stay between larger vehicles, cars may move out from between trucks, as traffic becomes congested. This can result in the formation of truck platoons in the slow lane (OBrien et al, 2009). Again microsimulation is the only tool than can adequately describe such movements.

In this paper, the flow of identical vehicles running on a single-lane road is studied. The different traffic states are identified and a sample load effect is calculated for each of these traffic histories. In this way, the influence of driver behaviour on long-span load effect can be understood, before application to more complex models and traffic streams.

2. Microsimulation Model

2.1 The Intelligent Driver Model

In order to carry out the traffic microsimulation, a program called *EvolveTraffic* has been extensively used. *EvolveTraffic* implements the Intelligent Driver Model (IDM) developed by Treiber et al. (2000a, 2000b). The IDM is a car-following model, which simulates driver behaviour in time through an acceleration function which optimizes overall braking:

$$a(t) = a\left[1 - \left(\frac{v(t)}{v_0}\right)^{\delta} - \left(\frac{s^*(t)}{s(t)}\right)^2\right] \tag{1}$$

where a is the maximum acceleration; v_0 is the desired speed; $v(t)$ the current speed; δ the acceleration exponent; $s(t)$ the current gap to the vehicle in front, and; $s^*(t)$ the minimum desired gap, given by:

$$s^*(t) = s_0 + s_1\sqrt{\frac{v(t)}{v_0}} + Tv(t) + \frac{v(t)\Delta v(t)}{2\sqrt{ab}} \tag{2}$$

In which, s_0 is the minimum bumper-to-bumper distance; s_1 the 'elastic' jam distance; T the safe time headway; $\Delta v(t)$ the velocity difference between the current vehicle and the vehicle in front, and; b the comfortable deceleration.

There are seven parameters in this model to capture driver behaviour. Most of these have a physical interpretation, and can be estimated through measurement and estimation. For simulation purposes, the length of the vehicle must also be known as it affects the spatial disposition of vehicles. Individual vehicles can be given their own driving parameters. However, in order to understand the fundamental behaviours, a traffic flow of identical vehicles with identical driver behaviour is considered further in this work.

2.2 Congested Traffic States

Treiber et al. (2000a, 2000b) have shown that congestion can be effectively generated by either decreasing locally the desired speed v_0 or increasing the safe headway T. It has been also shown that such local parameter variations act as an equivalent on-ramp bottleneck, which instead would require an injecting flow and a lane-changing model. In this paper, inhomogeneity is generated by increasing the safe time headway T downstream, say T', which Treiber et al. (2000b) state to be more effective than decreasing v_0.

A bottleneck strength δQ can be defined as difference between the inflow Q_{in} and the outflow Q_{out}

$$\delta Q(T') = Q_{in} - Q_{out}(T') \tag{3}$$

Depending on the inflow and the bottleneck strength, the downstream traffic can take up the identifiable traffic states explained in Table 1. A combination of these congested states may also occur and these are highly dependent on the previous traffic history.

Table 1 – Traffic States Definitions

Acronym	Explanation of traffic state
FT	Free traffic
MLC	Moving localized cluster, which moves upstream
PLC	Pinned localized cluster, which remains near the inhomogeneity
TSG	Stop and go waves
OCT	Oscillatory congested traffic
HCT	Homogeneous congested traffic

It is also possible to output the usual macroscopic quantities of interest, such as flow and density. In fact, *EvolveTraffic* counts the number of vehicles passing over specified virtual detectors, that is it returns the flow Q, and outputs the speed as well. The traffic density is found using the space mean speed, for n vehicles, defined as:

$$\bar{v} = \frac{n}{\sum_{i=1}^{n} \frac{1}{v_i}} \tag{4}$$

Through the fundamental relation of traffic, the density, ρ, is thus found as:

$$\rho = \frac{Q}{\bar{v}} \tag{5}$$

Phase diagrams are very informative for investigating the different forms of congestion that can occur, as they show the spatio-temporal variation of density along the roadway.

2.3 Model and Simulation Parameters

For this study, the vehicle stream is taken as being homogenous (i.e. all cars). Each vehicle is given the same set of driver behaviour parameters, shown in Table 2. These parameters are based on those used by Treiber et al. (2000b) and are found to give good match to real traffic.

A single-lane 5000 m long road is used in this work. The safe time headway is T from 0 to 2700 m (see Table 2), then increases gradually to 3300 m until it reaches the value T'. We examine a range of values of T'.

Table 2 - Model parameters of the IDM model

Parameter	**Value**
Desired velocity, v_0	120 km/h
Safe time headway, T	1.6 s
Maximum acceleration, a	0.73 m/s^2
Comfortable deceleration, b	1.67 m/s^2
Acceleration exponent, δ	4
Minimum jam distance, s_0	3 m
Elastic jam distance, s_1	0 m
Vehicle length, l	4 m

Eight different values of T' (1.9, 2.05, 2.2, 2.5, 2.8, 3.4, 4.0 and 4.6 s) and two inflows Q_{in} (1580 and 1200 veh/h) are considered for the simulations, each of which is 30 minutes long. All the vehicles have an initial velocity of 30 km/h.

Nine output detectors are set at 500 m intervals from 1000 m. However, after the inhomogeneity gradient finishes at 3300 m, the traffic is uncongested. Therefore the results of the detectors from 1000 to 3000 m are most relevant. Figure 1 gives an illustration of typical stop-go waves in congested traffic.

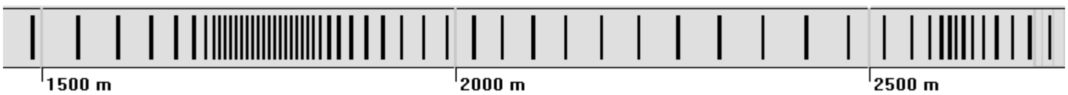

Figure 1 – Typical traffic behaviour: the black lines are vehicles (not to scale).

3. Traffic Behaviour

3.1 Bottleneck Strength and Safe Time Headway

For the values of T' considered, the bottleneck strengths (found from Equation (3)) are plotted in Figure 2. As can be seen, in the main, three different kinds of congestion have been found: stop-and-go waves (TSG), oscillating congested traffic (OCT) and a complex state with stationary congested traffic near the inhomogeneity, and oscillatory congestion further upstream (HCT/OCT). Such a state has been found in Treiber et al. (2000b) as well.

It is worth noting that the flow does not break down until the safe time headway is increased to 2.05 s (Q_{in} = 1580 veh/h) and 2.8 s (Q_{in} = 1200 veh/h). Below these threshold values, the change in T only has the only effect of reducing the flow. As may be expected, the 1200 veh/h curve lies beneath the 1580 veh/h, since a significant increase in the safe time headway is needed to generate congestion for lower flows.

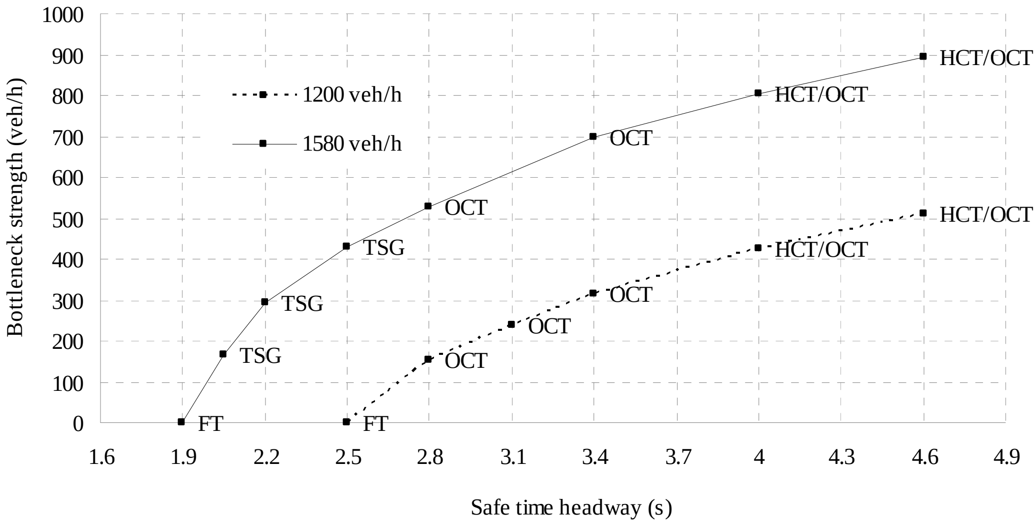

Figure 2 – Variation of bottleneck strength with safe time headway (for the explanation of the abbreviations see Table 1).

3.2 Identifying Traffic Phases

The traffic phase diagram is extremely useful for diagnosing traffic states. Figure 3 shows four phase diagrams corresponding to those obtained for Q_{in} of 1580 veh/h and T' of 1.9 s (FT), 2.2 s (TSG), 2.8 s (OCT), and 4.6 s (HCT/OCT). In these diagrams, the flat areas correspond to free traffic since the density is the same.

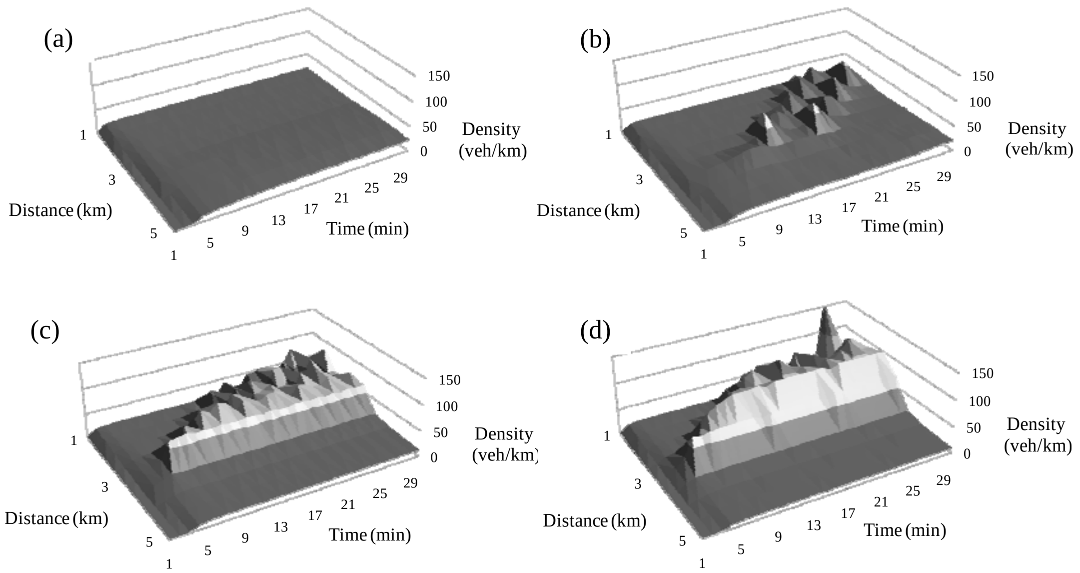

Figure 3 - Phase diagrams for Q_{in} = 1580 veh/h and various safe time headways: (a) 1.9 s; (b) 2.05 s; (c) 2.8 s; (d) 4.0 s.

Figure 3(a) shows free-traffic, with a slight density increase after the inhomogeneity due to the flow slowing-down; in Figure 3(b) it is easy to identify two stop-and-go waves. Figure 3(c) shows a typical oscillating traffic with a rough surface, while

Figure 3(d) shows a smooth-edged wall near the inhomogeneity (HCT), in front of the oscillating surface (OCT). These are similar to those of Treiber et al. (2000a, 2000b).

4. Load Effects due to Single Lane Traffic

4.1 Comparison of Approaches

There are two approaches to calculating load effects: *time-based* - a traffic 'image' is taken at the same location during the simulation; or *space-based* - a traffic image is taken on a stretch of road every time interval.

In the latter case, the spatial distribution of the vehicles can be directly output. Thus it is simple to calculate the load effects on a bridge. However, changes in gaps due to differing vehicle velocities cannot be taken into account, and this may affect the resulting load effect. On the other hand, the time-based image represents the actual *EvolveTraffic* virtual detectors' measurements, and can also uses data collected from typical real traffic measurements. However, this has the disadvantage that vehicle gaps must be monitored. In fact, for longer spans, if vehicles keep their own velocity, it is very likely that physically-impossible overlapping will occur in non-stationary conditions. Therefore, it is preferable to set a constant velocity, thus effectively 'freezing' the *time* headways, effecting a space-based solution. However, this 'homogenous' velocity is not straightforward to set. For instance, a sensible option would be to choose an average speed. In this case, this method provides reliable results when the actual velocity is close to the average one, but in non-stationary conditions, where there can be a wide range of velocities, two cases are likely to occur:

- the actual velocity is lower than the average (for instance, during a stop-and-go event): then the space headways will be overestimated and the load effects underestimated. In this case, as we are interested in congestion conditions, important pieces of information may be missed;
- the actual velocity is higher than the average (for instance, during free-flowing traffic): then the space headways will be underestimated and the load effects overestimated, which may be even higher than the ones during congestions.

4.2 Present Approach

Load effects are calculated on a sample bridge with 100 m span. The bridge is taken to be simply-supported and the overall bending moment at mid-span is calculated through the influence line theory. Each vehicle is represented as a single concentrated load of 2 t (19.6 kN).

The time-based approach is used, but the authors propose to find a spatial vehicle distribution by multiplying the time headways between the current vehicle and the front one by the current vehicle's own speed, thus effectively "freezing" the *space* headways. There is still some degree of approximation, as one vehicle may change its speed crossing the bridge, but the approximation of the constant speed is dropped and therefore the program can beneficially adapt to the different kinds of traffic.

As a result of this approach, for each vehicle passing over the 2000 and 2500 m detectors, we find the space headways between the current vehicle and as many following vehicles as occur on the bridge.

Moreover, rather than passing the whole traffic data across the bridge, the current leading vehicle is positioned over the last bearing. This assumption significantly reduces the amount of data, but is non-conservative in free-traffic, as it strongly depends on the free-flowing space headway. However, as the number of vehicles on the bridge increases, this difference becomes smaller and smaller, providing reliable results for congested traffic.

Figure 4 summarises the different time-based approaches discussed above. A traffic sample with slightly oscillatory congestion has been analysed. It can be seen that the moments calculated with the proposed approach are similar to those calculated by setting a constant velocity equal to the average of the traffic. Also shown are the moments calculated with variable velocity which, as can be seen, leads to higher bending moments for the reasons described earlier.

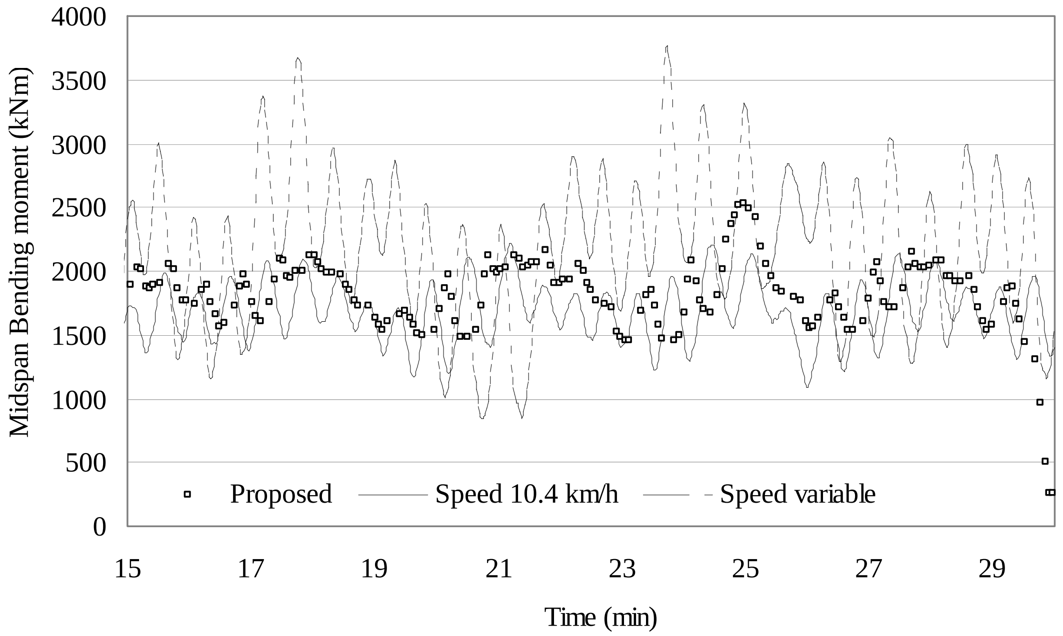

Figure 4 – Comparison of methods of calculation of load effect.

5. Results and Conclusions

Figure 5 shows the bending moments obtained for Q_{in} = 1580 veh/h at the 2500 m detector for the most congested situations (T' = 3.4, 4.0, 4.6 s). Figure 6 shows how the maximum moment is related to the safe time headway and the bottleneck strength. It can be noted that the OCT state for Q_{in} = 1200 veh/h and T' = 2.8 s does not affect the traffic at the detector 2000 m, providing a free-flow traffic moment load effect. Also, the homogeneous congestion conditions in the HCT/OCT states do not reach the 2000 m detector, although give almost the same moment values in both conditions.

It can be also seen that for high safe time headways the result tends to reach approximately the same bending moment of approximately 2550 kNm, regardless of the inflow and the corresponding bottleneck strength.

On conclusion, this research provides a valuable basis for further extension to multi-lane traffic micro-simulations. The method is also applicable to real traffic data (vehicle composition and distribution) to obtain load effects.

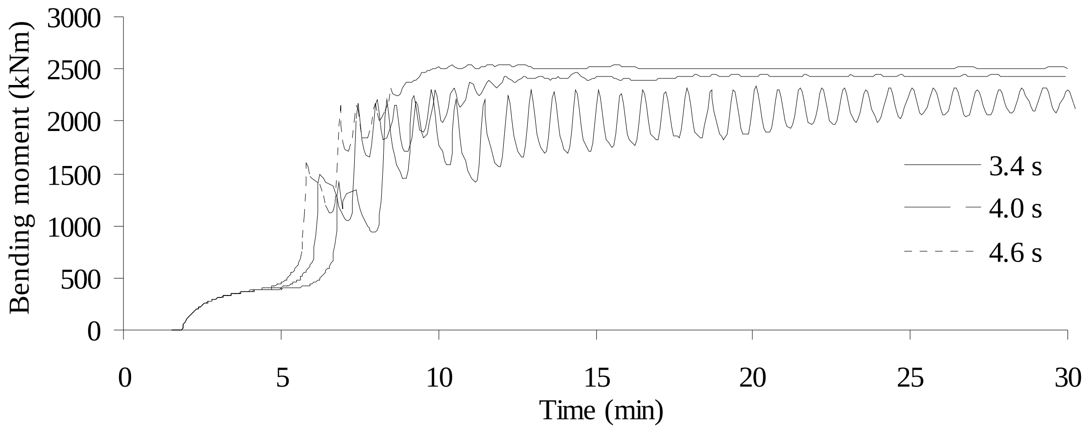

Figure 5 – Mid-span bending moment for Q_{in} = 1580 veh/h at the 2500 m detector.

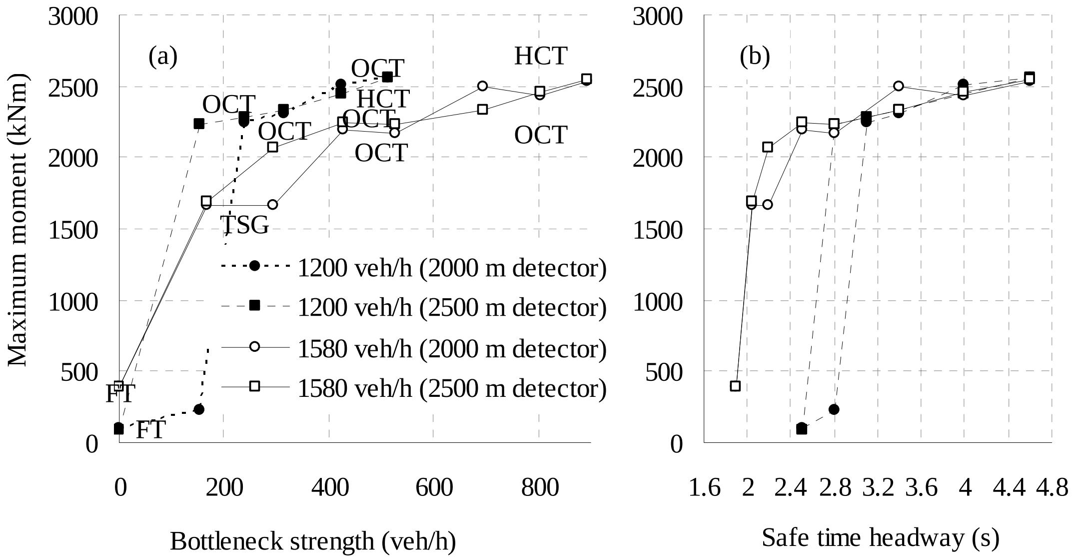

Figure 6 – Variation of maximum moment with: (a) bottleneck strength, and; (b) safe time headway. In (a) only changes in the type of congestion are marked.

References

Buckland, P.G. (1981), 'Recommended design load for bridges', *Journal of the Structural Division,* ASCE, Proc. Paper 15405, 1161-1213.

OBrien, E., Hayrapetova, A., Walsh, C. (2009), 'The use of micro-simulation for congested traffic load modelling of medium- and long-span bridges', *Structure and Infrastructure Engineering*, in print.

Treiber, M., Hennecke, A. and Helbing, D. (2000a), 'Microsopic Simulation of Congested Traffic', in *Traffic and Granular Flow '99*, eds. D. Helbing, H.J. Ermann, M. Schrechenberg and D.E. Wolf, Springer, 365-376.

Treiber, M., Hennecke, A. and Helbing, D. (2000b), 'Congested Traffic States in Empirical Observations and Microscopic Simulations', *Physical Review E,* **62**, 1805-1824.

A FEASIBILITY STUDY OF DRY SOIL MIXING FOR A BLANKET BOG

P.QUIGLEY[1] & J.O'BRIEN[2]
[1]Arup, 50 Ringsend Road, Dublin 4, Ireland
[2]Arup, 15 Oliver Plunkett Street, Cork, Ireland

Abstract
Much of Ireland is covered by peat and many of Ireland's new roads and developments pass over various types of bogs. Dry Soil Mixing (DSM) has been considered for a number of projects in lieu of traditional methods such as piling or excavation and replacement. This paper describes the feasibility study for a DSM project on a blanket bog in North West Mayo. A description of the site, the ground conditions and the field and laboratory results is given. The results indicated that the geotechnical behaviour is largely governed by the cementitious binder concentration. A discussion on the merits of DSM for Irish peats is also presented.

Keywords: blanket bog, dry soil mixing, peat

1. Introduction

The presence of peat presents developers with numerous difficulties. Peat is significantly more compressible than typical soft soils and generally unsuitable as a bearing stratum. The National Road Authority generally prohibits national roads being placed on organic soils, such as peat, that undergo significant secondary/creep settlements. The typical solutions for roads and developments over peat are to excavate the peat and replace it with a suitable fill or to pile through the peat into a suitable bearing stratum.

Recently DSM has been used as an alternative method. DSM involves mixing the soft soil with a cementitious binder. A mixing tool is driven into the ground to a target depth and binder in the form of powder is injected into the soil as the mixing tool is rotated at high speed. The natural water content in the soil allows the hydration of the binder, resulting in an increase in the shear strength and stiffness of the soil. A surcharge (typically 1m of fill used to form a working platform) is placed on the peat to assist the strength gain.

The Eurosoil Stab project was set up in 1997 to harmonise much of the testing and design protocol. Trinity College Dublin (Hebib 2001, Hebib and Farrell, 2003) carried out an experimental study of deep soil mixing using fen and raised bog peat in the midlands as part of the Eurosoil Stab project. DSM has been used to support rail embankments over peat using interlocking columns for the Chanel Tunnel Rail Link and, more recently, a rail embankment in the UK (Keller, 2010). Much of the work was carried out on fen and raised peat. This paper describes the feasibility study for DSM of a blanket bog for the Bellanaboy Gas Terminal on a site in North West Mayo.

2. Site and ground conditions

The site chosen for the Bellanaboy Gas Terminal is located on a gently sloping hill and was covered by blanket bog. The peat varied in thickness from 1.3m at the top of the hill to 8m downslope. The site was previously an agricultural research station and much of it was covered by grass and drained by a series of ditches. The top surface of the bog had a 1.3% to 2.0% gradient while the underlying, more competent, ground was slightly steeper and irregular (2 to 4% gradient). The ground conditions can be summarised as peat over a brown relic topsoil over a grey/blue mineral sandy gravely silt over a grey/green slightly gravely silty fine sand over a mica schist bedrock.

The peat was logged using the von Post classification for humification. The decomposition scale ranged from H1 to H10 with maximum fibre and minimum decomposition represented by H1 to minimum fibre content and maximum decomposition represented by H10. The peat was divided into three zones, namely H1 to H3, H4 to H7 and H8 to H9 (no H10 peat was logged on site). Each zone represented greater levels of decomposition and, to some degree, decreasing strength. The H1-H3 layer increased in thickness up slope and the H8-H9 layer thinned to nothing upslope. The H8-H9 layer thickened downslope and is considered to be, in part, fen peat.

The CPT and shear vane results indicated the peat to have a stronger upper zone (0 to 0.5m thick). This is believed to be due to the high fibre content of the peat. Below this zone was a middle weaker zone which increased in strength with depth. At the base of the peat was the H8 or greater peat where sample recovery was most difficult due to the low shear strength. Shear strengths measured in the fibrous peat were typically 10 – 15kPa and 4 – 8kPa in the middle and lower layers of peat, although a number of shear vane results recorded values of 0.5kPa.

The previous use of the site as an agricultural research station had resulted in areas with elevated concentrations of phosphate. Samples of peat with elevated levels of phosphate were also taken for mixing trials. Some typical parameters for peat used in the mixing trials are presented in Table 1.

Table 1 – Typical peat parameters used in the mixing trial

Properties	**Location**	
	PS21	**PS35**
Natural water content (%)	1090	1019
Organic content (%)	97.7	98
Von Post classification	H6-H7	H7-H8
pH	4.9	4.6

3. Mixing trials

A series of samples were taken from trial pits and boreholes using a Russian Peat sampler at various locations across the site. The peat was logged and representative samples of the peat and samples of Irish cement were shipped to Sweden. The laboratory investigation was carried out by the Swedish Geotechnical Institute (SGI). The peat was logged again using the Von Post method before the samples were mixed and the natural moisture content was recorded. The pore water from a proportion of the peat was extracted for chemical testing. The binder was then added and mixed into the peat using a dough mixer for about 5 minutes. The mixture was placed into plastic tubes and loaded using a steel bar with a diameter slightly less than plastic tube. The steel bar had graduations which allowed the vertical compression of the peat to be measured. Filter stones were placed at both end of the tubes to allow drainage from the tubes. The test specimens were then stored under water with a surcharge of 18kPa at

20 degrees C. The surcharge was placed 45 minutes after the mixing was finished. The axial strain in the specimens was monitored during curing.

A Grade 32.5 cement sourced from a builder's merchants was used in the initial trials (boreholes PS21-22). The later tests were carried out using a Grade 42.5 cement. The cementitious binder was confined to Irish produced Ordinary Portland Cement (OPC) as imported cements may have elevated concentrations of heavy metals and the developer did not wish to pursue alternative binders.

A number of tests were carried out using 100kg/m^3 of sand combined with 50, 100 and 150kg/m^3 of cement to investigate if the inclusion of a cheaper binder could improve the strength of the stabilised soil.

4. Results

The strength and stiffness of the specimens was measured using unconfined compression testing (Figure 1). A number of one dimensional compression tests were carried out also.

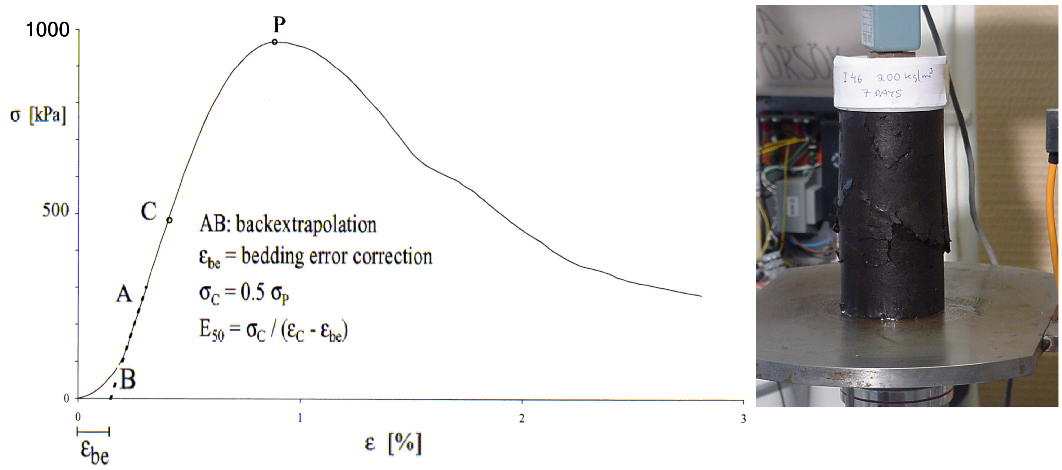

Figure 1 Methodology for determining strength and stiffness (left) with typical specimen (right)

4.1 Shear strength

Figure 2 shows the change in undrained shear strength with time for Borehole PS35. The strength gain in the soil was largely complete by 28 days. The 28 day undrained shear strength increased approximately proportionally to the OPC concentration in the stabilised soil (Figure 3). A target field strength of 40kPa was chosen for design; consequently the laboratory results needed to be of the order of 2.5 – 3 times the target strength to account for the differences in the quality of the mixing in the field work. The results suggested that a binder concentration of 200 to 300kg/m^3 of OPC would be required to reach the target strength. The addition of sand had a negligible effect on the results for cement concentrations of 50, 100 and 150kg/m^3.

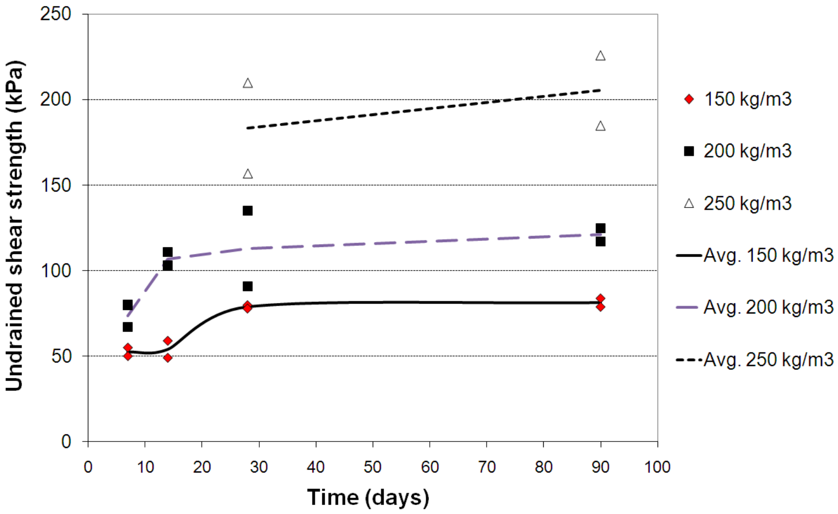

Figure 2 Change in undrained shear strength with time for PS35 2.1-3.1m.

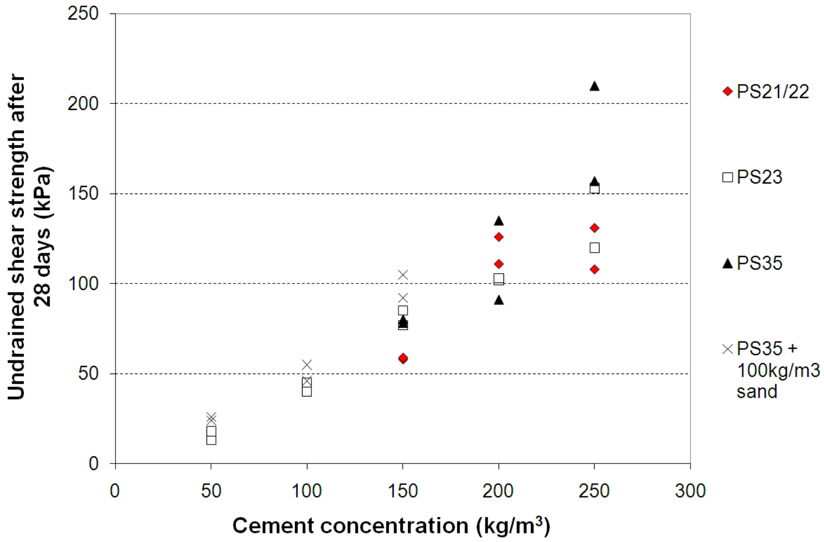

Figure 3 Undrained shear strength at 28 days after stabilisation for all specimens.

4.2 Stiffness

The stiffness of stabilised peat (E_{50} – see Figure 1 for definition) followed a similar pattern to the undrained shear strength with an increase in stiffness proportional to the OPC concentration (Figure 4). The inclusion of sand had a negligible effect on the stiffness for cement concentrations of 50, 100 and 150kg/m^3. The stiffness was largely unchanged following 28 days (Figure 5). The stiffness could be approximately related to the undrained shear strength using:

$$E_{50} = 180c_u \tag{1}$$

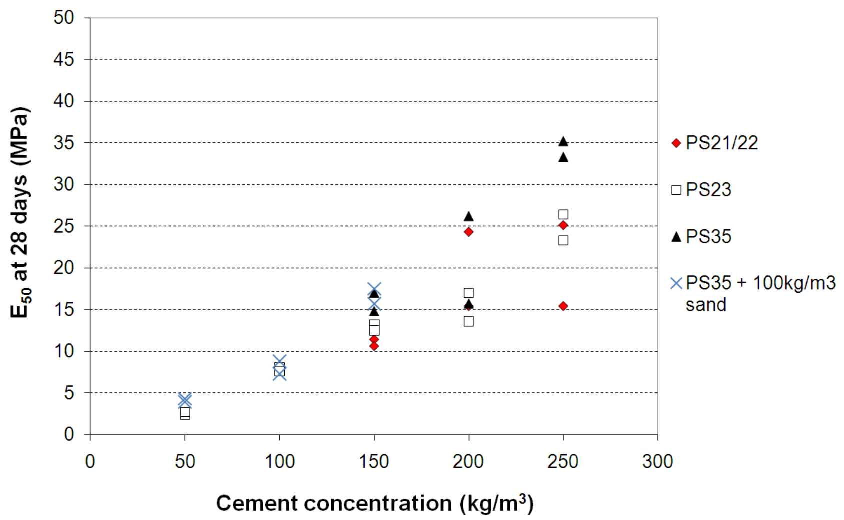

Figure 4 Comparison of E_{50} at 28 days for all boreholes.

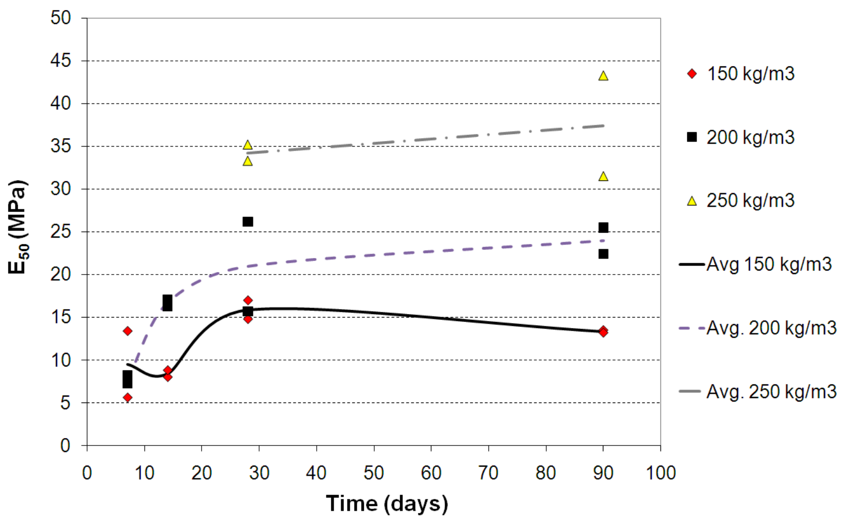

Figure 5 Variation in E_{50} with time for PS35 2.1-3.1m

4.3 Compressibility

Figure 6 shows that the compression of the samples during the initial curing time. At an OPC concentration of 150kg/m³ and above there was sufficient binder to minimise further compression after day 1. The lower OPC concentrations the axial strain increased over the next 5 to 6 days.

Three oedometer tests using a standard 75mm diameter by 20mm high specimens were carried out on peat stabilised with 200kg/m³ of cement (Figure 7). The yield stress appeared to vary between 100kPa and 150kPa. Figure 8 shows a plot of the compressibility coefficient (m_v) versus axial stress. The compressibility dropped up to the yield stress of 100 – 150kPa and then increased slightly post yield.

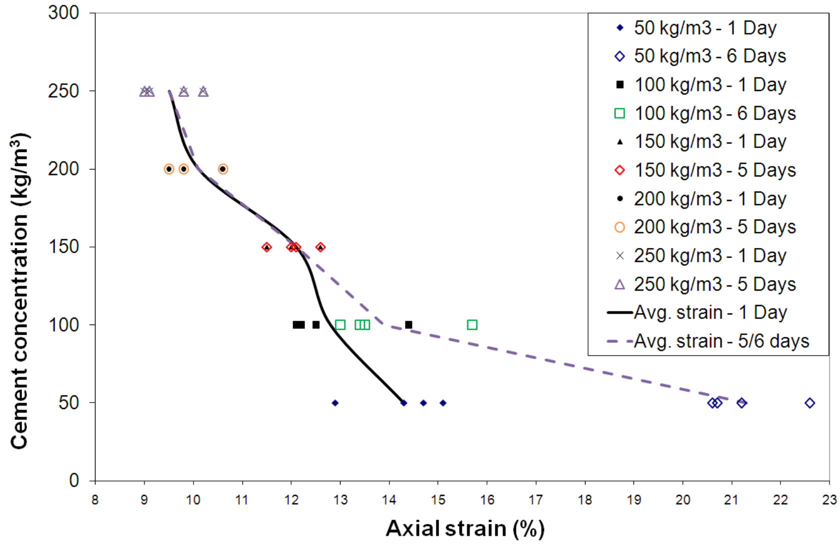

Figure 6 Variation in axial strains during curing for PS23 0.7-1.7m.

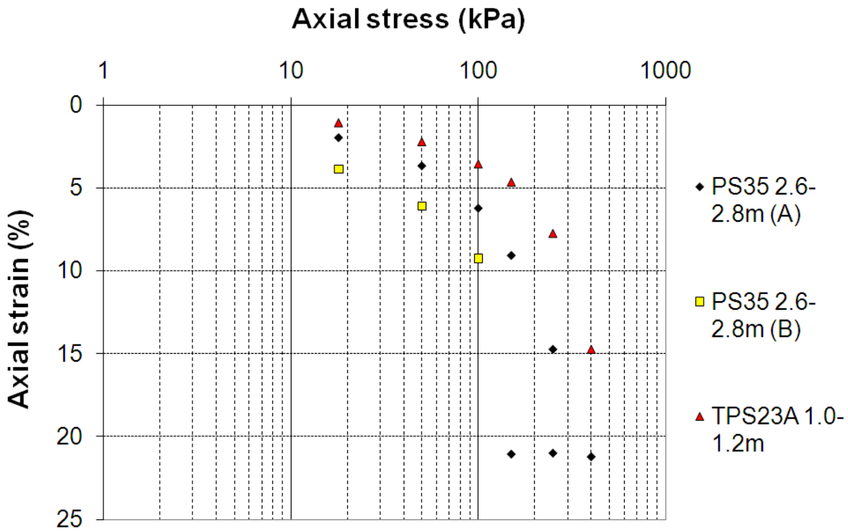

Figure 7 Stress strain curves from oedometer specimens tested at 28 days

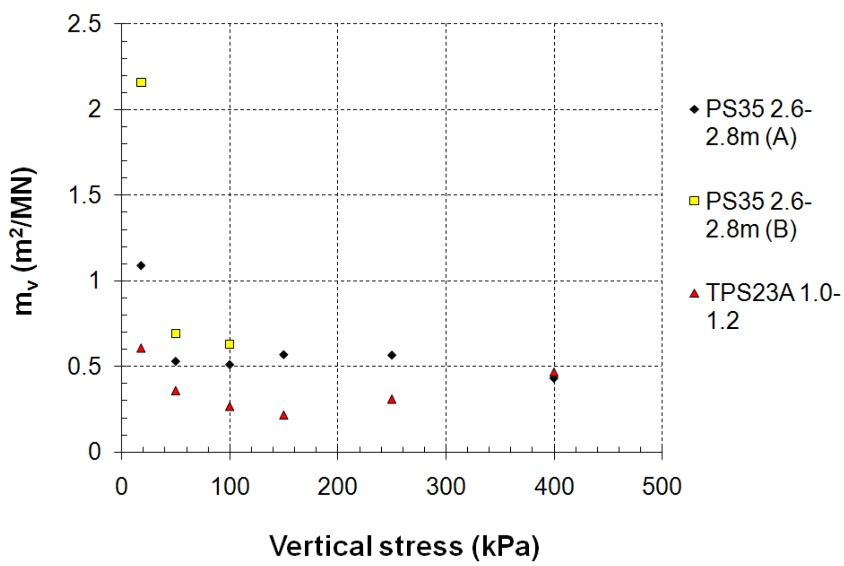

Figure 8 Plot of consolidation coefficient and applied vertical stress.

The secondary consolidation coefficient, C_α, was measured on the deformation of the specimens between 4 and 24 hours after each load increment increase. The variation is shown in Figure 9 and shows a gradual increase up to 100 to 150kPa and a subsequent rapid increase post yield. Typical C_α values for virgin peat vary between 3 to 6%.

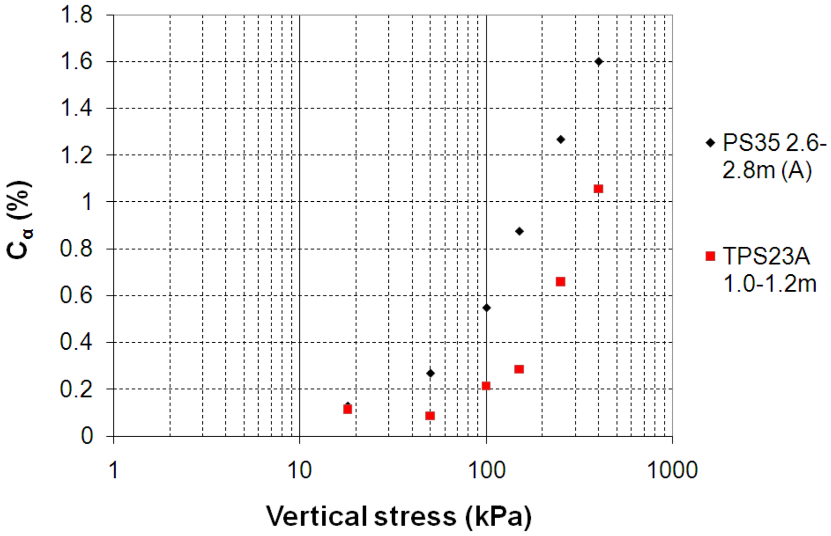

Figure 9 Plot of secondary consolidation coefficient and applied vertical stress.

5. Sustainability

There is an increasing awareness of sustainability issues in construction and sustainability is likely to have a greater influence in the choice of construction method. A common comparison tool in evaluating the sustainability of construction methods is the embodied energy (EE). Embodied energy is the energy required to manufacture and supply to the point of use, a product, material or service and is measured in Joules. O'Riordan (2007) presented a comparison of the EE for three embankment construction methods on soft clays/silts (a geotextile reinforced embankment with vertical drains, a piled embankment, and DSM using 100kg/m^3 of OPC covering 90% of the embankment footprint) in the UK. The results indicated that alternative binders with a lower EE or reducing the coverage to 50% would be required before the DSM method approached EE parity with the piled embankment solution. For a peat stabilisation project in Ireland the increased concentration of binder required (200-300kg/m^3) and the increased transport energy would widen the difference between the methods. Hebib and Farrell (2003) investigated the use of binders with a lower EE such as pulverised fuel ash, blast furnace slag, gypsum and lime, with varying success depending on the pore water chemistry.

6. Construction

Tender documents were drawn up for the enabling earthworks for the site. However, the selected contractor proposed an alternative design using excavate and replacement of the shallow peat and a piled raft road over the deeper deposits of peat. The alternative proposal was more advantageous in terms of the technical and programme requirements and was successfully adapted. One of the key disadvantages for peat stabilisation was the location of the site relative to potential sources of cement.

The constructability review also noted that DSM is usually carried out by mass stabilisation or column stabilisation. Mass stabilisation is carried out by a tool fixed to an excavator jib and can treat ground to about 6m from the top of the working platform. If the mixing tool is able to reach the deepest soft deposit then it's likely that excavate and replacement/displacement of the soft peat is also feasible and probably cheaper for blanket bogs. Column stabilisation can go deeper but the columns must overlap to achieve sufficient continuity across the soil mass.

7. Conclusions

The results indicated that the shear strength and stiffness of the stabilised peat was proportional to the cement concentration. The cement particles are likely to have formed a matrix within the peat, with the peat providing little contribution to the overall strength. The addition of sand provided only a minimal increase in the compressive strength and stiffness, suggesting that the binder concentration would have to be increase significantly before the addition of sand becomes effective. Sing et al. (2008) found that the significant addition of 25 to 50% by volume of the wet peat of siliceous sand with a combined binder concentration of 300kg/m^3 was effective. The results from the study were broadly similar to results published by Hebib and Farrell (2003). EuroSoil Stab (2002) indicates that the shear strength measured in the laboratory is greater than the same field binder concentration by a factor ranging between 2 and 5. From the above study it was estimated that approximately 200 to 300kg/m^3 of Ordinary Portland Cement would be required to provide a minimum undrained shear strength of 40kPa. Field trials would be required to verify these results.

Further work is required to provide more economical and sustainable DSM solutions.

8. Acknowledgements

The authors would like to thank Shell Exploration and Production Ireland for their support and kind permission to publish the results. The authors would also like to acknowledge Alan Phear (Arup), Turlough Johnston and Petra Rochs Perks (AGEC) and Per Evert Bengtsson (SGI) for their considerable contributions. The views expressed in this paper are the authors' alone.

References

EuroSoilStab, (2002), *Design guide: soft soil stabilisation.*, BRE.

Hebib, S. and Farrell, E.R. (2003), 'Some experience on the stabilization of Irish peats', *Canadian Geotechnical Journal, Vol. 40, 107-120.*

Hebib, S. (2001), *Experimental investigation on the stabilisation of Irish peat*, Ph.D. thesis, University of Dublin, Trinity College.

Keller (2010). http://keller-uk.com/news/keller-geotechnical-winners-ground-engineering-awards

O'Riordan, N., (2007), 'Technical sustainability of construction on very soft ground', in *Proc. Soft Ground Engineering*, eds. Long, Jennings, Rutty, Geotechnical Society of Ireland.

Sing, W.L., Hashim, R. and Ali, F.H. (2008), 'Behavior of stabilized peat soils in unconfined compression tests', *American Journal of Engineering and Applied Sciences* 1 (4), 247-279.

CONTROL OF SECONDARY CREEP IN SOFT ALLUVIUM SOIL USING SURCHARGE LOADING

T. CONROY[1], D. FAHEY[1], F.BUGGY[2] and M.LONG[1]
[1]School of Architecture, Landscape & Civil Engineering, University College Dublin, Belfield, Dublin 4 (Contact: mike.long@ucd.ie)Ireland.
[2] Roughan & O'Donovan Consulting Engineers, Sandyford, Dublin 18

Abstract
The construction of embankments over soft alluvium deposits of varying depths presents designers with many significant problems, most notably short term stability and long term settlement. High levels of consolidation settlement but also high rates of secondary compression often lead to significant long term settlements of the embankments. In order to overcome the problem of secondary compression a surcharge loading regime for the embankments, combined with perforated vertical drains to reduce the time for primary consolidation to take place could be implemented. This paper presents an investigation into the amount of surcharge that is required to achieve a specified improvement in the rate of secondary compression. The surcharge level required can be calculated on the basis of the procedure presented by Charles C. Ladd (1971) which involves the analysis of the results of several long duration oedometer tests at different levels of surcharge loading. Special long term oedometer tests which mimic the typical site loading regime for the construction of an embankment were carried out at University College Dublin. The laboratory test results are used to calculate the rate of secondary compression for normally consolidated soils (C_α), and the improved rate of secondary compression (C'_α) following removal of the surcharge load. The UCD results have been correlated with Ladd's method and historical data to assess the applicability of the method to an Irish alluvium soil. The results and their implications for design will be presented in this paper.

Keywords: Creep, Surcharge loading.

1. Introduction

The principle of surcharge loading is that the soil is temporarily loaded to an effective stress (σ'_{vs}) which is higher than the final effective stress (σ'_{vf}) which it will experience under the permanent embankment load. This means that the soil will become 'artificially' over consolidated (OC) when under the final embankment load. This is illustrated in Figure 1 (part A). The advantage here lies in the fact that OC soils exhibit lower creep rates than normally consolidated (NC) soils. Figure 1 (part B) shows the typical loading sequence which is carried out when surcharge loading is used. The soil is loaded to stress level σ'_{vs} and allowed to consolidate. The value of C_α is calculated as the slope of the curve between times t_p and t_r. The load is then removed and the soil is now at stress level σ'_{vf}. Swelling occurs following unloading until creep reappears at some time t_s, a new lower creep rate C'_α is now observed and can be calculated from the linear portion of the graph after t_s. Since C'_α is smaller than C_α the rate and amount of secondary compression is reduced. The magnitude of this reduction depends on the amount of surcharge loading used.

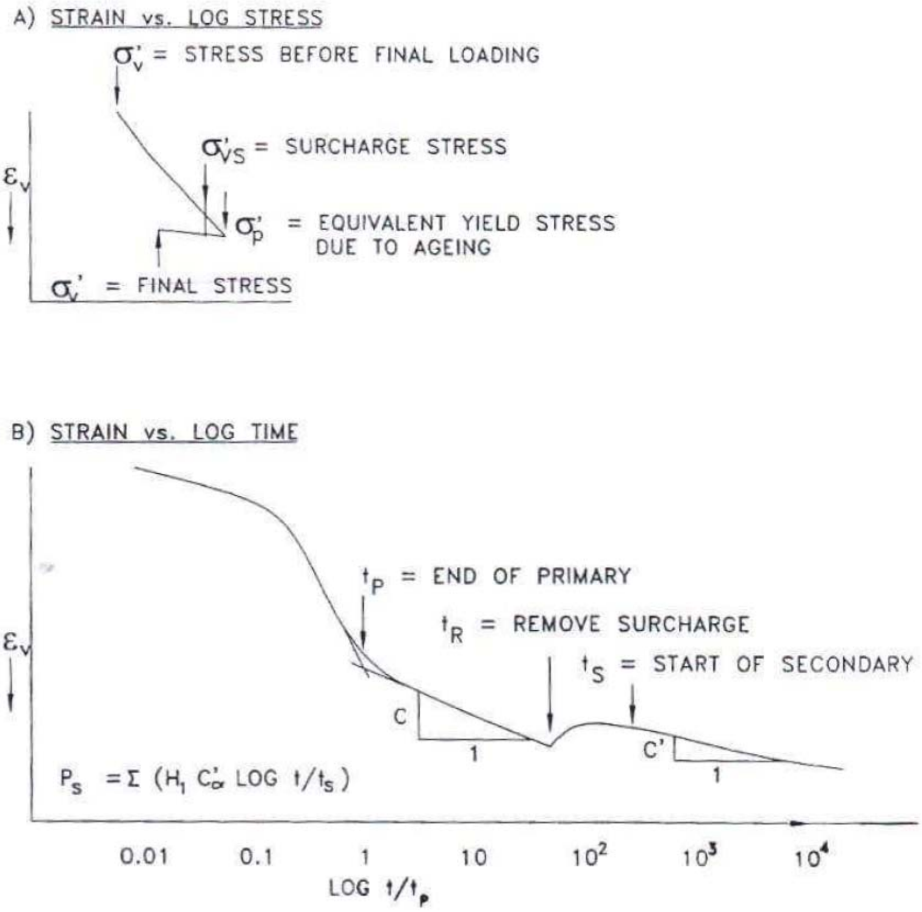

Figure 1 – Effects of surcharging on secondary compression, Ladd (1971)

This paper looks at the method of predicting the effect of surcharge loading in reducing the rate of secondary compression as proposed by Ladd (1971) and whether this method is applicable to soft alluvium soils from the Shannon Estuary in Ireland. Using data collected on several cohesive soil deposits, Ladd (1971) found that the ratio of C'_α to C_α is directly related to the level of surcharge loading applied to the soil. Figure 2 shows Ladd's relationship between C'_α / C_α and adjusted amount of surcharge (AAOS) where:

$$AAOS = \frac{\sigma'_{vs} - \sigma'_{vf}}{\sigma'_{vf}} \quad \text{where:} \qquad (1)$$

σ'_{vs} is the effective stress under surcharge and,
σ'_{vf} is the final effective stress following removal of surcharge and completion of all loading.

Ladd's results show maximum and minimum limits of expected improvement for any level of surcharge loading. From this data a mean line is also constructed which fits the data very well. If C_α for a soil is known then this graph can be used to calculate the amount of surcharge needed to achieve a required C'_α or to predict the reduced C'_α that will be achieved based on a known amount of surcharge

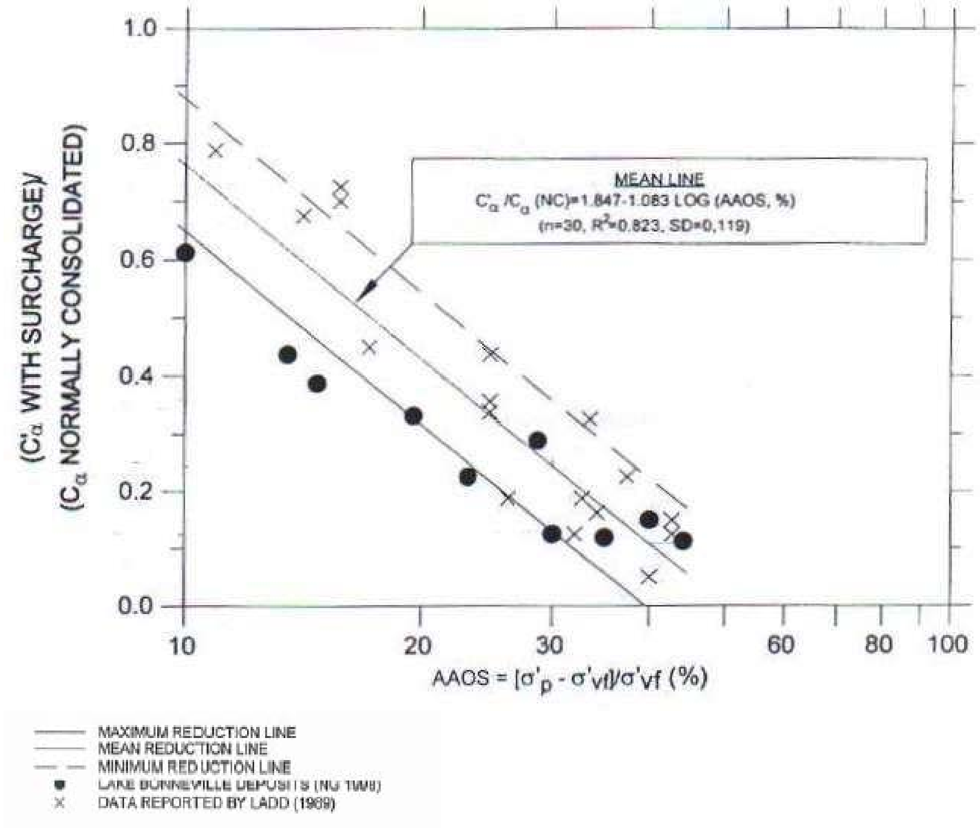

Figure 2 - C'α/ Cα vs. AAOS % Saye et al (2001)

Other authors who have investigated the effects of surcharge loading on creep behaviour include Mesri and Nash. Mesri's analysis of the improvement of C_α is based on his C_α /C_c concept as presented by Mesri and Castro (1987). This constant value of C_α /C_c for a soil is applicable to both compression and recompression and could be used in conjunction with C_c values along recompression curve to calculate the corresponding values of $C'_{\alpha.}$

Nash and Ryde (1999, 2000) developed models based on the work of Yin and Graham (1989, 1996) and Bjerrum (1972) which models creep as a set of isotaches on a strain versus stress plot. Each isotache represents a different constant creep rate. The Yin and Graham model makes use of the λ-κ model used in critical state soil mechanics to define the instant elastic-plastic behaviour. This results in the normally consolidated line being replaced by a reference time line (RTL). Creep rate at a particular time can be determined from a set of isotaches through the introduction of the concept of "equivalent time" t_e which is the time taken to creep under constant effective stress from the RTL to the present state. A feature of both the Mesri and Nash approaches is that the post surcharge creep rate C'_α is not constant but slowly increases to approach the original creep rate of NC soil after sufficient time has passed. The time required to fully recover C_α is variable and is dependant on the strain which occurs during surcharge, itself a function of the surcharge load.

2. Laboratory Test Methodology

A series of oedometer tests (using 76mm diameter 19mm depth ring) were carried out at University College Dublin on samples of soft alluvium soil obtained from piston tube sampling at 1.5 - 2m depth in the Shannon Esturary. The samples collected had a water content of 60%, a plastic limit of 41%, a liquid limit of 86%, a plasticity index of 45% and a liquidity index of 0.422. The organics content was approximately 5%. Soil underneath the crest of a wide embankment essentially experiences 1D compression and so oedometer testing apparatus is particularly suitable for modelling the behaviour of the soil. Three tests were carried out in 2009 and six tests in 2010. These tests were carried out in order to simulate the surcharging of the soil which could be carried out in the field during the construction of an embankment. Firstly the samples were consolidated to 160kPa to ensure the soil is behaving in the NC state. The soil is then loaded up to the surcharge stress σ'_{vs} which depends on the AAOS required. The surcharge load is left in place for two days to ensure that C_α can be accurately calculated. The sample is first unloaded to reflect the removal of temporary surcharge fill and then a small reload is applied representing the road pavement foundation and construction. The reload increment is then left in place to monitor the behaviour of the now OC soil under its final load. This final loading increment requires a long duration in order to calculate C'_α. The tests carried out by the authors along with the AAOS and duration of the tests are shown in Table 1. Care was taken to ensure that all surcharge loads applied were well in excess of the preconsolidation pressure of the natural deposit so that C_α is calculated for NC conditions. A typical test loading sequence is shown in Table 2.

Table 1 - Summary of tests carried out

Test	AAOS (%)	Duration (days)	C_α	C'_α	$C'\alpha/ C\alpha$
1	15	54	0.0081	0.0055	0.6784
2	15	54	0.0116	0.0056	0.4844
3	20	46	0.0107	0.0055	0.5154
4	25	54	0.0099	0.0028	0.2855
5	39				0.0780
6	39				0.0447
7	40	55	0.0117	0.0010	0.0814
8	50	48	0.0097	0.0001	0.0098
9	56				0.0771

Table 2 – Typical loading schedule of test 3 (AAOS = 20%)

Increment	Load (kPa)	Duration (days)	Comment
1	10	1	
2	20	1	
3	40	1	
4	160	1	
5	240*	2	Surcharge
6	190	1	Unload
7	200	46+	Reload

* load represents 20% AAOS, and this value changes for the different AAOS level

3. Results

The results of two of the oedometer tests, 20% and 50% AAOS, are shown in Figure 3 and Figure 4 respectively.

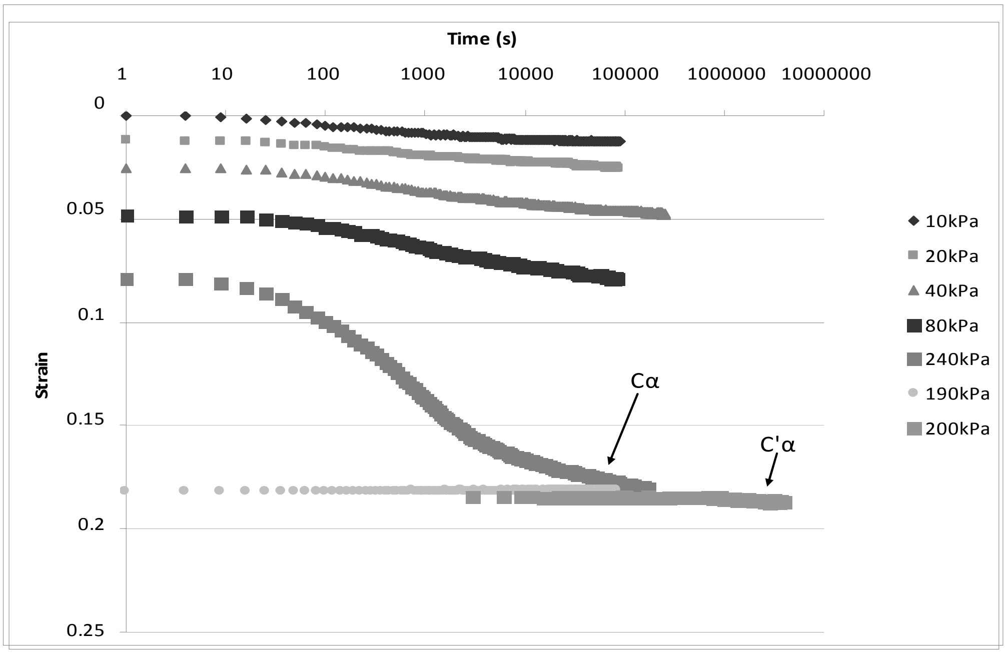

Figure 3 – strain vs. time for 20% AAOS

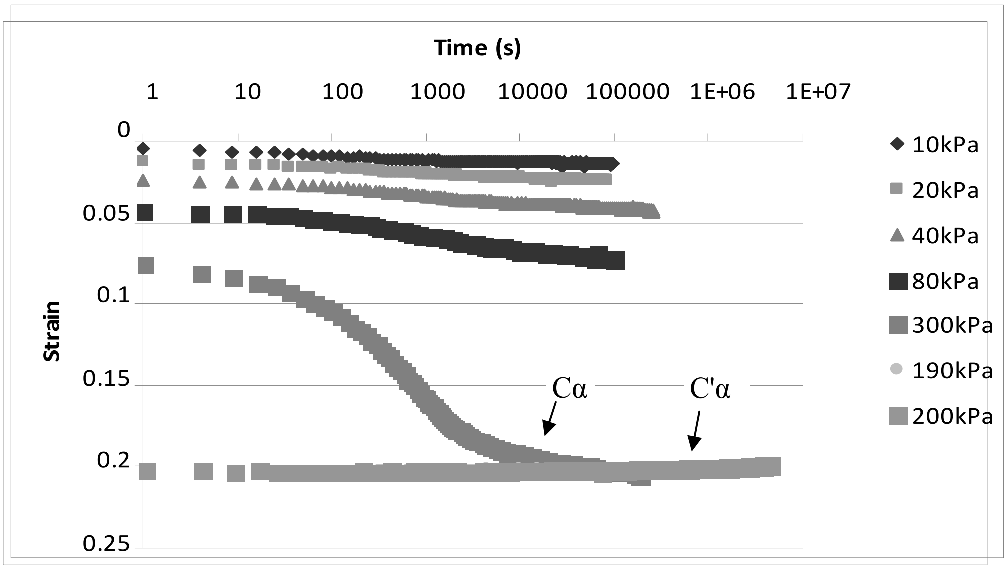

Figure 4 – strain vs. time for 50% AAOS

From these graphs it is clear that the value of C'_{α} is less than C_{α}, therefore less secondary compression would be expected after the surcharge load has been applied and removed. These graphs also confirm that there is a delay between the removal of the surcharge load and the reappearance of creep. Comparing these graphs it can be seen that creep reappears sooner for the 20% AAOS test than the 50% AAOS test, also the effect of surcharge level can be clearly observed. The 50% test show almost no creep and the strain vs time curve for the final load increment (200kPa) is almost horizontal, compared to the 20% test which still shows a significant rate of creep although less than the creep rate observed for NC soil at the maximum load.

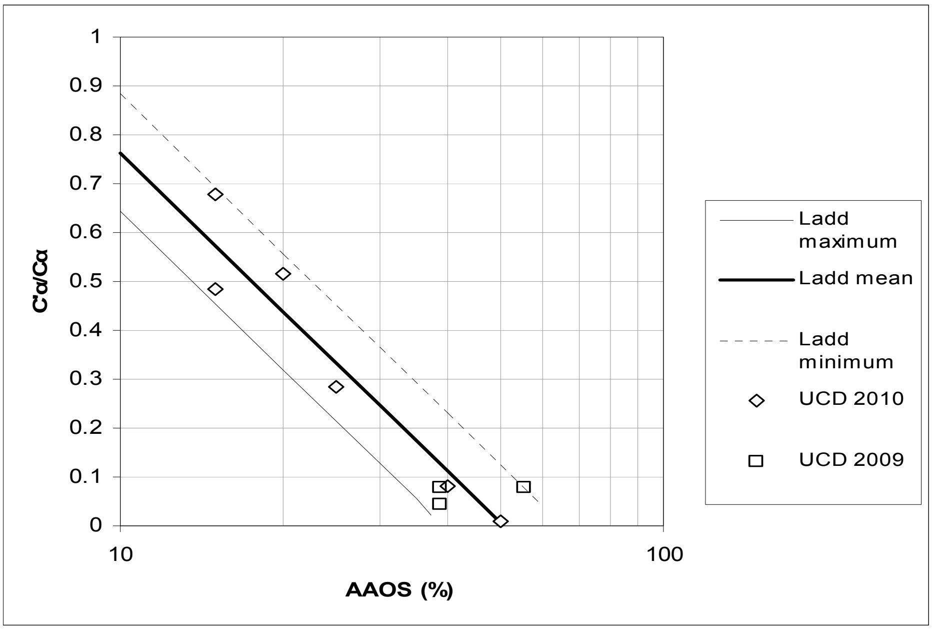

Figure 5 - C'_α/C_α vs. AAOS % for Shannon Estuary Alluvium (UCD 2009, 2010)

Further to the results recently obtained at UCD, the authors researched a number of the original papers from which Ladd used data to correlate a relationship for C'_α / C_α and AAOS. The data from four of these papers along with the results for the soft alluvium obtained from the Shannon Estuary and Ladd’s mean plus upper / lower limit lines are plotted on a graph of C'_α / C_α vs. AAOS as shown in Figure 6. To this entire data set of 31 points a mean trend line is added which is almost parallel to Ladd’s mean line and gives a slightly greater improvement in C_α for a given AAOS level. The fact that the trend obtained is so similar to Ladd’s, and that Ladd’s mean line is slightly more conservative than this new relationship using all of the data from the soft alluvium, suggests that Ladd’s mean line trend is suitable and readily applicable to use in design of surcharge loading regimes for the Shannon Estuary soft alluvium and similar Irish soils.

It should be noted that the authors used all the original data available from the four papers Salt Lake City - Saye et al. (2000), Barcelona - Alonso, Gens and Lloret (2000), New York - Stewart, Lacey and Ladd (1994) and Hong Kong - Koutsoftas et al. (1987). The only exception to this was the Barcelona paper which included AAOS tests of 4.4, 7.6 and 100%. These values were omitted because it was felt that the results for C'_α / C_α were potentially erroneous especially at the lower AAOS values and because the test durations were only of the order of 10 to 12 days which may not have been sufficiently long enough to ensure that the post surcharge creep rate had fully reappeared. There was also no other data from other sites close to these values to compare the results to.

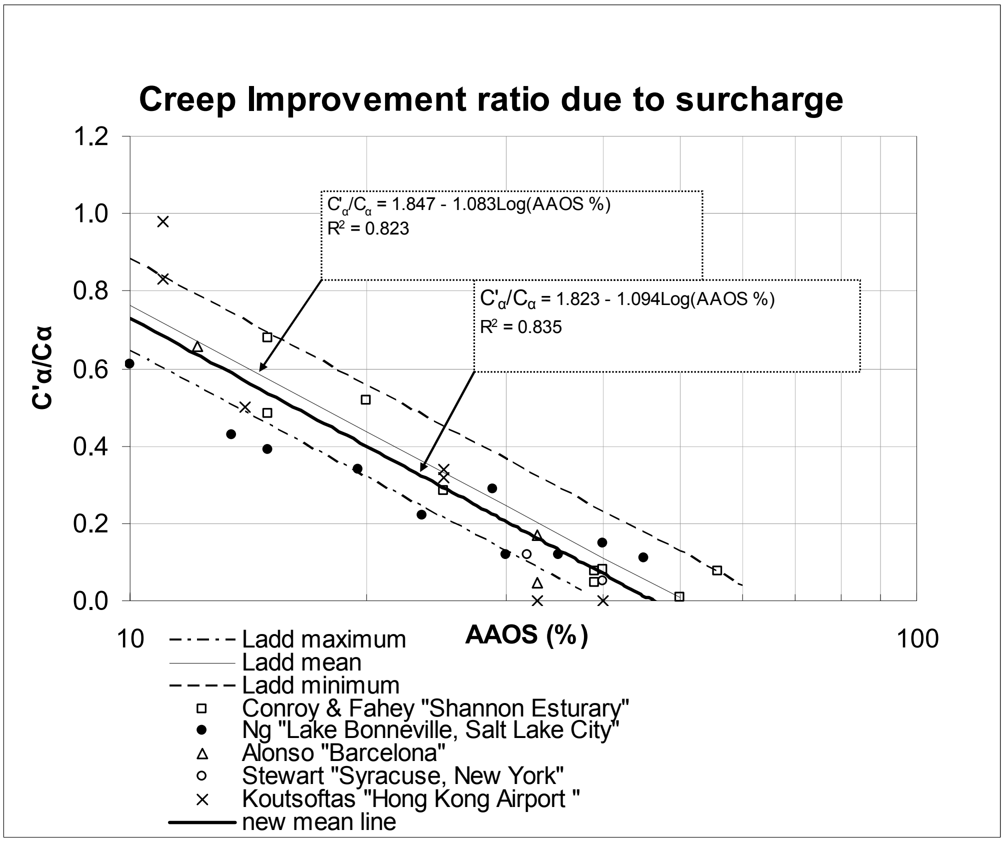

Figure 6 - C'_α/C_α vs. AAOS % for various sites

4. Conclusions

The results obtained and the trends observed in Figures 3-6 provide good evidence that Ladd's method of analysing the improvement in C_α for a given level of surcharge is applicable to the soft alluvium soils with modest organic contents such as those found in the Shannon Esturary in Ireland. Ladd's method may be used as a good rule of thumb when designing surcharge loading regimes for the design of embankments over clay soils.

It is advisable however where possible to carry out site specific tests to validate the values of surcharge to be used. This will not only flag any potential problems i.e. if improvement is not as good as expected, but also in the case where the improvement is better than expected and data obtained lies close to the maximum improvement line then potential economical savings may be made due to the need for a lower level of surcharge.

It is emphasised that the data and trends presented in this paper relate primarily to inorganic silts and clays or soils with relatively low organic content (5%) such as the Shannon Estuary site in Ireland. Surcharge has been attempted in highly organic soils such as mucks and peats. Some authors such as Yu & Frizzi (1994) have reported good performance of surcharged organic soils, albeit that the range of improvement is generally less and a greater variablility of results is observed compared to Ladd's data.

There have also been cases of poorer than expected post surcharge performance in muskeg as published by Samson & La Rochelle (1985), so it would appear that there is greater uncertainty in organic soils and Ladd's mean or limit lines are not considered appropriate for such soils..

5 References

Alonso, E. E., Gens, A. & Lloret, A. 2000. "Precompression design for secondary settlement reduction." *Géotechnique*, Vol 50, No. 6, 645-656.
Bjerrum, L. 1972. "Embankments on soft ground." *State of the Art report. Proc. Spec. Conf. on Performance of Earth and Earth-supported structures, Purdue University*, 1:1-54, ASCE.
Conroy, T & Fahey D. 2010 "The use of surcharge loading to reduce creep settlement underneath embankments" *unpublished final year project*
Koutsoftas, C., Foott, R. & Handfelt, L.D. 1987. "Geotechnical Investigations Offshore Hong Kong." *Journal of Geotechnical Engineering, ASCE*, Vol. 113, No.2.
Ladd, C. C. 1971. "Settlement Analyses of Cohesive Soils." *Research Report R71-2*, Department of Civil Engineering, M.I.T., Cambridge, Massachusetts.
Mesri, G., & Castro, A. 1987. "C_α/C_c concept and K_o during secondary compression ." *Journal Geotechnical Engineering, ASCE*, Vol. 113(3), 230-247.
Nash, D. F. T. & Ryde, S. J. 1999. "Modelling the effects of surcharge to reduce long term settlement of an embankment on soft alluvium". *13th European Conference on Soil Mechanics and Foundation Engineering,* **3**, pp. 1555-1561.
Nash, D. F. T. & Ryde, S. J. 2000. "Modelling the effects of surcharge to reduce long term settlement of reclamations over soft clays". *Coastal Geotechnical Engineering in Practice,* pp. 483-488.
Samson L. 1985. "Post construction settlement of an expressway built on peat by precompression." *Canadian Geotechnical Journal*, 22 (2) pp 308 – 312.
Samson L. & La Rochelle P. 1972. "Design and Performance of an expressway constructed over peat by preloading." *Canadian Geotechnical Journal*, 9(4). Pp 447 – 466.
Saye, S. R., Ladd, C. C., Gerhart, P. C., Pilz, J. & Volk, J.C. (2001) "Embankment Construction in an Urban Environment: the Interstate 15 Experience." *Foundations and Ground Improvement, ASCE,* 842-857.
Stewart, J. P., Lacy, H. S. & Ladd, C. C. (1994) "Settlement of Large Mat on Deep Compressible Soil" *Geotechnical Special Publication no. 40*, ASCE, 842-859
Yin, J-H. & Graham, J. 1989. "Viscous-elastic-plastic modelling of one-dimensional time-dependant behaviour." *Canadian Geotechnical Journal*, 26(2):199-209.
Yin, J-H. & Graham, J. 1996. "Elastic visco-plastic modelling of one-dimensional consolidation." *Géotechnique,* 46(3):515-527.
Yu, K.P. & Frizzi R.P. 1994. "Preloading organic soils to limit future settlements." *Vertical and Horizontal Deformation of Foundations and Embankments, ASCE,* 476-489.

PEAT IMPROVEMENT UNDER VACUUM PRELOADING: A NOVEL APPROACH FOR BOG ROADS IN IRELAND

J.P. OSORIO[1], E.R. FARRELL[1] & B.C. O'KELLY[1]
[1]Dept. of Civil, Structural & Environmental Eng., Trinity College Dublin, Ireland

Abstract
This paper presents the preliminary findings of a TCD/NRA vacuum preloading field trial that is part of a research project into the construction options for improving rampart roads. Vacuum preloading is a construction method used to accelerate settlement and the increase shear strength by applying a vacuum pressure to the ground by means of prefabricated vertical drains, an impervious tight sheet and a vacuum pump. Consolidating the ground by applying a vacuum load has several advantages over other techniques, for example; no fill material is required; construction periods are generally shorter; and there is no need for chemical admixtures. This paper presents a review of the literature and describes the setup and initial stage of the TCD/NRA vacuum preloading field trial, that is currently being carried out at Ballydermot bog.

Keywords: Ground improvement, peat, bog rampart roads, vacuum preloading

1. Introduction

In Ireland, there is a need to improve bog roads and rampart roads to meet modern traffic demands and safety requirements and also to reduce maintenance costs. Rampart roads are bog roads in which the peat has been harvested for fuel from one or both sides, leaving the road surface, in some cases, many meters above the surrounding ground surface. Rampart roads often undergo considerable distortion due to the low shear strength and high compressibility of the bog foundation, which may pose a significant safety hazard (Osorio et al., 2008). Cuddy (1988) reported that the cost of maintaining a bog road at a similar performance level to that of a road constructed on a firm ground foundation differed by about a factor of ten. The most commonly used techniques in Ireland to improve bog roads are overlaying the existing pavement with crushed stone, hot-mixed or cold-mixed bituminous materials; reinforcement of pavement with geosynthetics and the use of lightweight or super-lightweight fills (Davitt et al., 2000). Currently, there is no consistent methodology for the design of such road improvements.

Peat ground-improvement techniques such as surcharging and chemical stabilisation have been researched in Ireland. Hanrahan (1954, 1964, 1976) presented research studies in peat pre-consolidation using a gravel embankment as a temporary surcharge and the installation of vertical drains to accelerate the consolidation process and produce a more uniform increase in the shear strength of the peat with depth. Hebib (2001) and Hebib and Farrell (2003) presented a study into methods of stabilising peats by the addition of binders, although this approach has not proven to be cost effective in practice. This paper presents vacuum preloading as a novel and viable technique for improving bog roads and describes the setup and initial stage of the TCD/NRA vacuum preloading field trial.

2. Background on vacuum preloading

Vacuum preloading is a construction method used to accelerate ground settlement by reducing the air pressure at the ground surface, thereby accelerating the consolidation process. In vacuum preloading applications, the ground surface is sealed with an impervious membrane and through a vacuum pump a negative pressure (with respect to atmospheric pressure) is created in a sand cushion beneath the sealing membrane and in prefabricated vertical drains installed in the ground (Mohamedelhassan and Shang, 2002). The vacuum preloading technique was initially proposed by Kjellman (1952) as a mean of improving clayey soils. Vacuum preloading has several advantages over embankment loading, for example; no fill material is required; construction periods are usually shorter; and there is no need for heavy machinery. In addition, the vacuum pressure method is an environmentally friendly methodology since it does not put any chemical admixtures into the ground (Chai et al., 2005).

The vacuum preloading technique has been used extensively in several countries in Europe, Asia and North America since the 1980s (Dam et al., 2006) to improve the ground for the construction of ports, airport runways, roads and an oil storage station (Chu et al., 2000, Tang and Shang, 2000, Masse et al., 2001, Hayashi et al., 2002, Gao, 2004, Qiu et al., 2007, Chai et al., 2008). The ground conditions are usually highly compressible clayey soils and hydraulic fills used for land reclamation projects.

3. TCD/NRA vacuum preloading field trial

The TCD/NRA vacuum preloading field trial is currently being undertaken at Ballydermot bog. The main objective is to evaluate vacuum preloading as a technique for improving peat ground and its feasibility for improving the conditions and reducing the maintenance costs for bog roads and rampart roads.

3.1 Ground conditions

Ballydermot bog is a raised bog located to the north of Rathangan, Co. Offaly. Milled peat production commenced at Ballydermot bog in the mid-1940s and is currently being exploited by Bord na Móna (Hebib, 2001). A typical soil profile at the test area is presented in Table 1. In March 2009, 24 stand pipes were installed at the test area to monitor the ground water table depth. During the initial recording period, summer and autumn 2009, the water table was generally at a depth of between 0.25m and 0.90m, with extreme values as deep as 1.05m and as high as 0.02m above the ground surface.

Table 1 - Simplified soil profile

Layer	Depth (m)	Description	Observations and properties
1	0 – 0.7	Man-made fill	Black peat; occasional plastic bags, gravel, pieces of geotextile, machine parts.
2	0.7 – 4.0	Pseudo-fibrous peat	w = 660 – 1085% G_S = 1.39 – 1.54 LOI = 96 – 99% pH = 4.5 – 6.2 Von Post = $H_4 – H_7$
3	4.0 – 7.0	Boulder clay	The clay fraction reduces with depth until only boulders are found.

3.2 Summary of TCD/NRA field trial construction

The vacuum preloading field trial test covers a 10x10m surface area. Initially, 0.4m depth of the fill layer was excavated over a 12x12m area and levelled. It is important to note that for this paper, all depths are taken from the original ground level. Ninety-eight prefabricated vertical drains (PVD) were pushed vertically into the peat to a depth of 2.65m using the bucket of a bog digger and an aluminium box section as the lance. This left approximately 1.35m depth of peat between the base of the PVDs and the peat-clay interface to prevent the escape of the vacuum (Figure 1). According to Hayashi et al. (2002), when using PVDs, no improvement effect is achieved unless the drain spacing is 0.90m or shorter. In order to evaluate how the difference in the spacing of the PVDs affects the improvement method, the test area is subdivided in two, one in which the drain spacing is 0.85m and a second one with a spacing of 1.20m (Figure 2). The instrumentation system, which was pushed into the ground after the installation of the PVDs, will be discussed later.

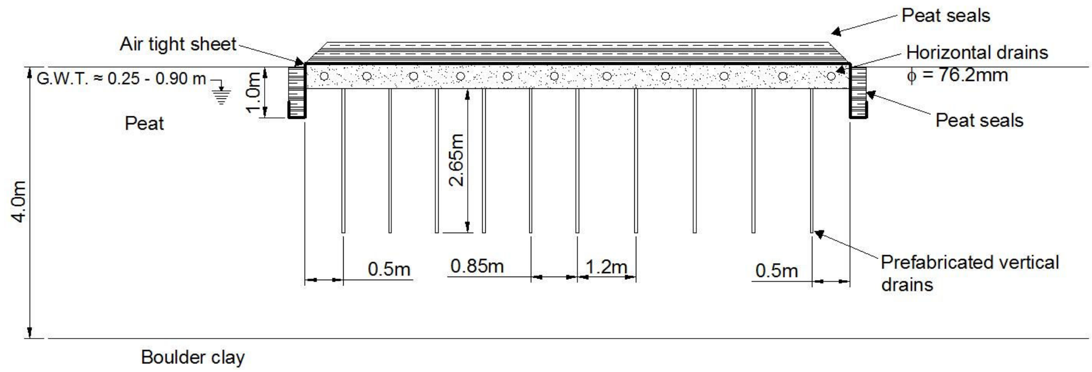

Figure 1 - Cross section of TCD/NRA vacuum preloading field trial

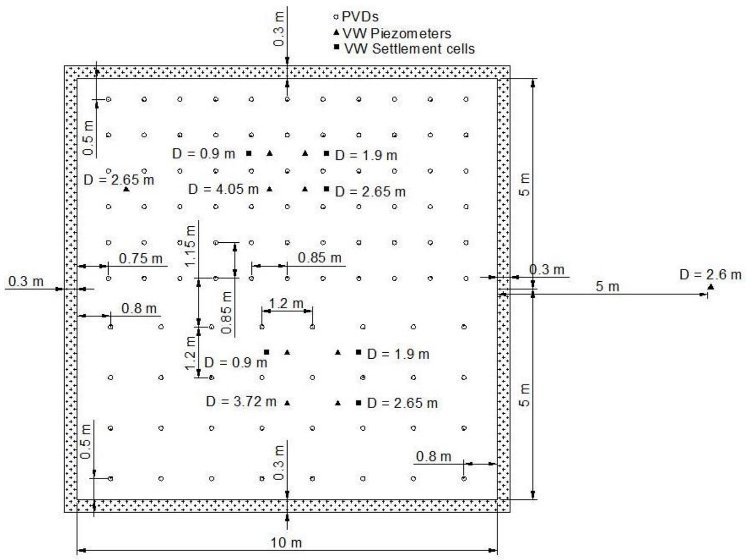

Figure 2 - PVD and subsurface instrumentation arrangement

A 0.15m deep sand bed was placed on the ground surface and a 0.30m deep gravel bed was placed above the sand bed. Corrugated and perforated flexible pipes, 76.2mm in diameter, were embedded horizontally within the gravel bed. The granular surface bed and the horizontal drains act as a drainage layer, transmitting the vacuum to the underlying peat as well as discharging pore water and air out of the treated soil mass (Figure 3). A 0.3m wide and 1.0m deep trench was then dug around the 10x10m test area and an airtight polythene membrane was laid over the test area. The membrane was keyed at the bottom of the trench by backfilling the trench and covering the top with peat in order to help maintain the seal and protect the membrane (Figure 1). Afterwards, the surface instrumentation was installed and the pumping system was connected. The vacuum is applied using a 38mm diameter jetpump connected to a 1.5kW centrifugal pump that can generate an 80kPa design preload vacuum pressure.

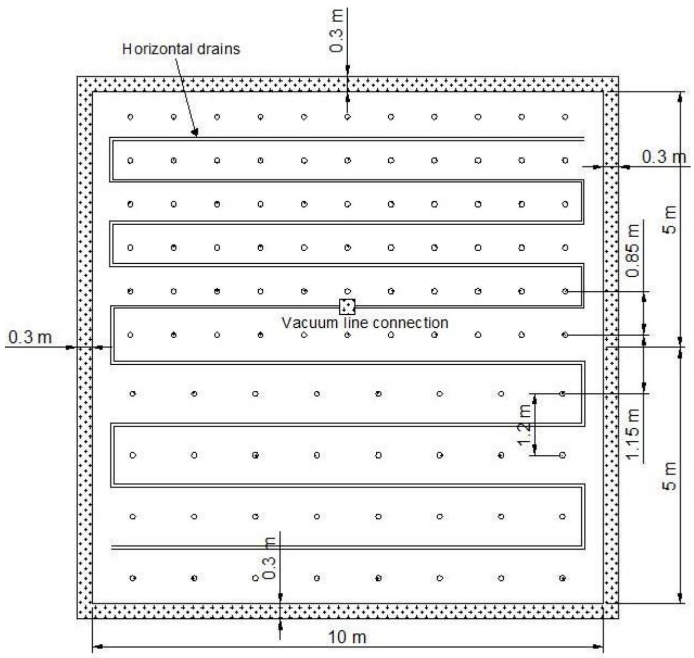

Figure 3 - Horizontal drains arragement

3.3 Instrumentation

The instrumentation system is designed to measure the settlement at different depths; positive and negative pore-water pressures at different depths; barometric pressure; surface and ground temperatures; water flow; ground water table and rainfall. The instrumentation system includes six push-in vibrating wire settlement cells; ten push-in vibrating wire piezometers (calibrated for both positive and negative pressures); a surface barometer/thermometer; 26 surface settlement plates; 17 stand pipes to monitor the ground water table level; a water meter and a rain gauge (Figures 2 and 4).

Due to the difference in PVD spacings, the two subareas required independent monitoring of settlement and pore pressures. Hence, three settlement cells and four piezometers were pushed in at the centre of each subarea at different depths (Figure 2). One of the remaining piezometers was located at the inner edge of the test area to study boundary effects, while the other was placed outside to observe if the vacuum pressure has any significant effect beyond the studied area. The surface barometer/thermometer and one of the settlement cells are connected to dataloggers allowing hourly monitoring of the test.

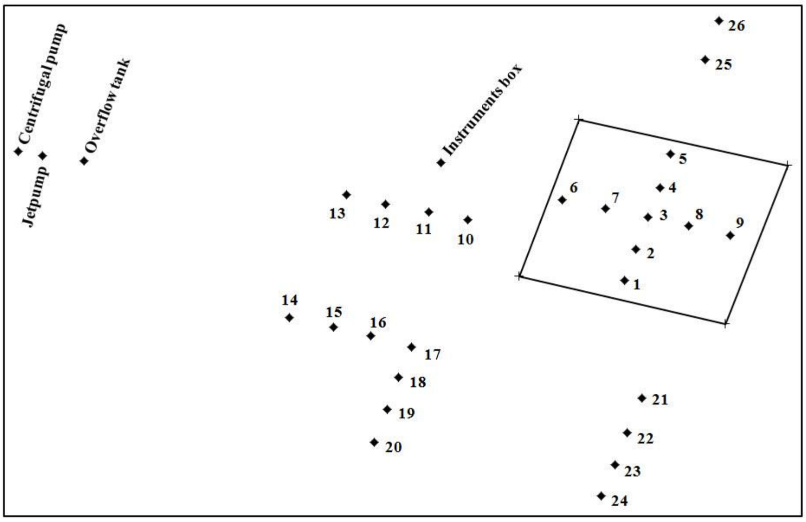

Figure 4 – Surface settlement plates and stand pipes distribution

Figure 4 shows that nine settlement plates are located inside the test area, with another 17 settlement plates located around it. A stand pipe was also pushed in next to each plate outside the test area allowing the ground water table depth measurement. These stand pipes replaced the ones installed before the test area was constructed, since most were lost during the construction.

A water meter was placed at the end of the water discharge pipe to measure the amount of ground water expelled from the soil mass which could be correlated with the settlement measures. The rain gauge was placed to record precipitation and to correlate it with the variations on the ground water table.

3.4 Test start and initial results

The TCD/NRA vacuum preloading field trial commenced on the 30th November 2009. The results from the first month are presented in this paper during which an average vacuum of 50kPa was achieved in the gravel layer. Figure 5 presents the settlements at different depths for both subareas. Figures 6 and 7 show the pore-water pressures recorded at different depths in both subareas.

Figure 5 shows that a surface settlement of 0.85m was recorded in the subarea of 0.85m spacing, and a surface settlement of 0.65m was recorded for the 1.20m spacing within a month.

Figure 6 shows that for the 0.85m spacing subarea there is a similar reduction in piezometric pressure at all depths within the peat layer of between 27.2kPa and 31.9kPa. However, the full 50kPa reduction in piezometric pressure was not transmitted to the monitor points in the peat layer. The piezometer located at 4.05m depth in the peat-clay interface presented a reduction of only 10.4kPa. It is important to remember that the PVDs were only installed to a depth of 2.65m. The piezometer located 5.0m outside the treated area did not show any reduction in the pore-water pressure, indicating that the vacuum does not affect the pressures outside the test area.

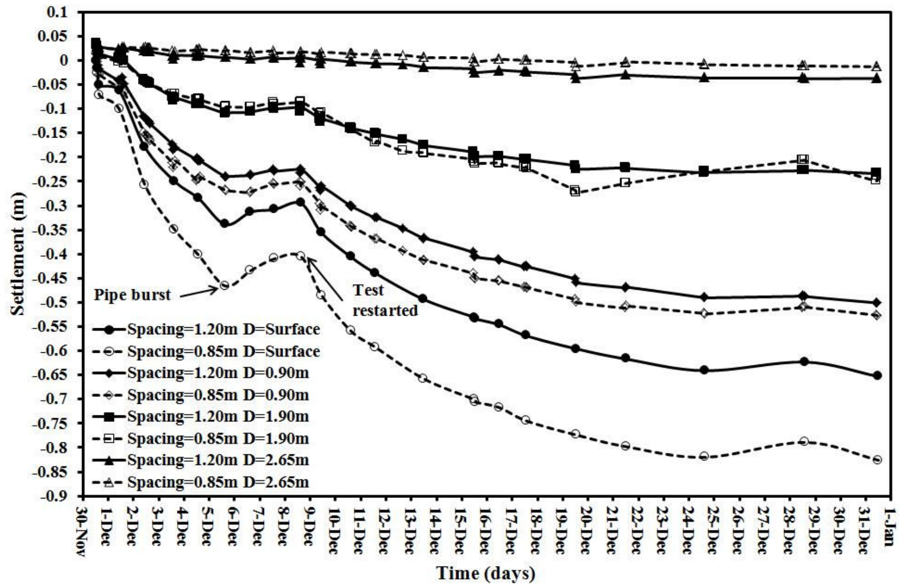

Figure 5 – Ground settlement at different depths for both spacing subareas

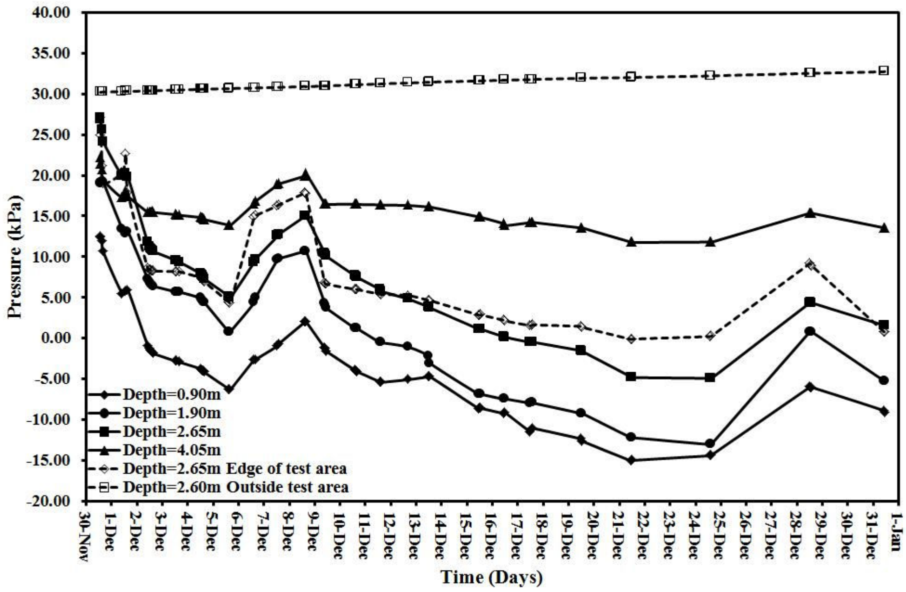

Figure 6 – Pore-water pressure variation for 0.85m PVD spacing subarea

Figure 7, obtained for the 1.20m spacing subarea, shows a similar trend with a piezometric drop of between 18.7kPa and 23.0kPa recorded at all depths, although lower in value, which can be explained due to the greater spacing between the PVDs. Note that at this subarea, the piezometric reduction with depth recorded by the instruments was similar, including the deepest piezometer which is located at a depth of 3.72m, i.e. 1.0m under the bottom of the PVDs and 0.30m above the peat-clay interface.

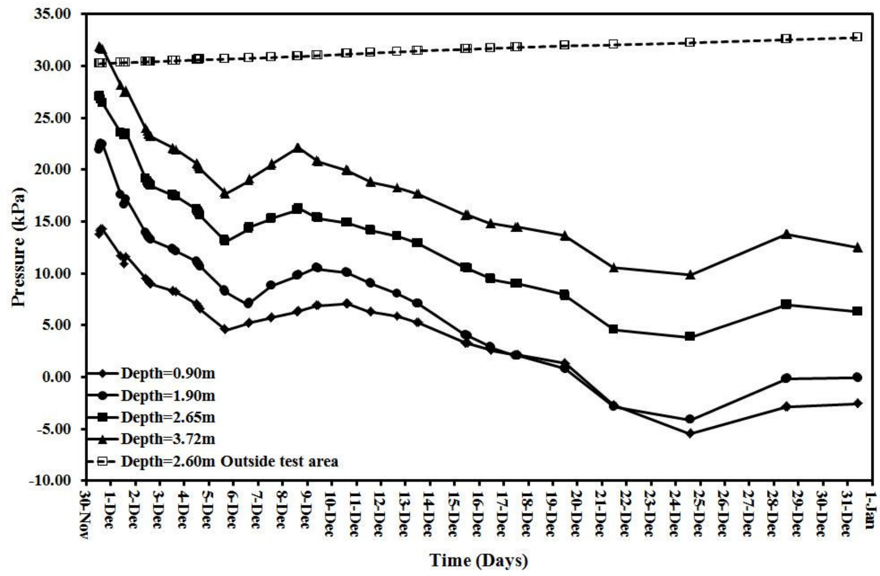

Figure 7 – Pore-water pressure variation for 1.20m PVD spacing subarea

4. Conclusions

The TCD/NRA vacuum preloading field trial was implemented and showed that this technique can be successfully used in peat soils. The average 50kPa vacuum level recorded at the ground surface in this trial is less than the maximum vacuum pressure achievable, which according to literature is generally considered to be about 80kPa, and additional measures are to be taken onsite to improve this. The vacuum distribution and drainage system comprising PVDs, horizontal drains and a granular bed, was effective in distributing the applied vacuum pressure and collecting the drained water. A surface settlement of about 0.85m was achieved under the average vacuum pressure of 50kPa within the first month where the PVD spacing was 0.85m. There was a noticeable difference in the time settlement plots, the pore pressure reduction, and the magnitude of settlement between the areas of different drain spacing. A uniform reduction in piezometric pressure with depth was observed, even 1.0m under the bottom of the PVDs. The findings indicate that a drain spacing of 1.2m can be effectively used to achieve significant ground improvement, albeit less than that achieved for a closer spacing. The main differences recorded were in the surface settlement readings and the reasons for this require further investigation. Further analysis will be carried out after the trial is over with the full set of data collected.

5. Acknowledgements

The research project ‘Design Approach for Improving Rampart Roads’ is funded by a Research Programme Fellowship (2007) from the National Roads Authority (Ireland). The authors would like to thank Bord na Móna for the use of the facilities at Ballydermot bog. The first author would like to kindly acknowledge Universidad de Antioquia for the leave of absence granted to work on this project and research awards in the form of an Ussher Award from Trinity College Dublin and the Geotechnical Trust Fund award from Institution of Engineers of Ireland.

References

Chai, J., Norihiko, M. and Begardo, D. T. (2008), 'Preloading clayey deposit by vacuum pressure with cap-drain: analyses versus performance', *Geotextiles and Geomembranes*, 26**,** 220 – 230.

Chai, J. C., Carter, J. P. and Hayashi, S. (2005), 'Ground deformation induced by vacuum consolidation', *Journal of Geotechnical and Geoenvironmental Engineering*, 131**,** 1552 – 1561.

Chu, J., Yan, S. W. and Yang, H. (2000), 'Soil improvement by the vacuum preloading method for an oil storage station'. *Geotechnique,* 50**,** 625 – 632.

Cuddy, T. (1988), *The Behaviour of Bog Road Pavements,* MAI thesis, Trinity College Dublin.

Dam, L. T. K., Sandanbata, I. and Kimura, M. (2006), 'Vacuum consolidation method - Worldwide practice and the latest improvement in Japan', *Technical Research Report of Hazama Corporation,* 38.

Davitt, S., Lynch, J., Mullaney, D. and Wall, W. (2000), *Guidelines on the Rehabilitation of Roads Over Peat,* Dublin, Dept. of Envir. and Local Government.

Gao, C. (2004), 'Vacuum preloading method for improving soft soils of higher permeability', *Ground Improvement,* 8**,** 101 – 107.

Hanrahan, E. T. (1954), 'Investigation of some physical properties of peat', *Geotechnique,* 4**,** 108 – 123.

Hanrahan, E. T. (1964), 'A road failure on peat', *Geotechnique,* 14**,** 185 – 202.

Hanrahan, E. T. (1976), 'Bog roads', *Irish Engineers,* 29**,** 3 – 5.

Hayashi, H., Nishikawa, J. and Sawai, K. (2002), 'Improvement effect of vacuum consolidation and prefabricated vertical drains in peat ground' in *Proc. 4th International Conference on Ground Improvement Techniques*, eds. R. Hawkins, P. Seco e Pinto, and L. Ribeiro e Sousa, Kuala Lumpur, Malasya.

Hebib, S. (2001), *Experimental Investigation on the Stabilization of Irish Peat*, PhD thesis, Trinity College Dublin.

Hebib, S. and Farrell, E. R. (2003), 'Some experiences on the stabilization of Irish peats', *Canadian Geotechnical Journal,* 40**,** 107 – 120.

Kjellman, W. (1952), 'Consolidation of clay soil by means of atmospheric pressure', in *Proceedings of the Conference on Soil Stabilization.* Cambridge, Massachusetts Institute of Technology.

Masse, F., Spaulding, C. A., Wong, I. C. and Varaksin, S. (2001), 'Vacuum consolidation: a review of 12 years of successful development', in *Geo-Odyssey.* Blacksburg, USA.

Mohamedelhassan, E. and Shang, J. Q. (2002), 'Vacuum and surcharge combined one-dimensional consolidation of clay soils', *Canadian Geotechnical Journal,* 39**,** 1126 – 1138.

Osorio, J. P., Farrell, E. R., O'Kelly, B. C. and Casey, T. (2008), 'Rampart roads in the peat lands of Ireland: genesis, development and current performance', in Proc. *1st International Conference on Transportation Geotechnics,* eds. E. Ellis, H.S. Yu, G. McDowell, A. Dawson and N. Thom, Nottingham, UK, 227 – 233.

Qiu, Q. C., Mo, H. H. and Dong, Z. L. (2007), 'Vacuum pressure distribution and pore pressure variation in ground improved by vacuum preloading', *Canadian Geotechnical Journal,* 44**,** 1433 – 1445.

Tang, M. and Shang, J. Q. (2000), 'Vacuum preloading consolidation of Yaoqiang airport runway', *Geotechnique,* 50**,** 613 – 623.

THE FEASIBILITY OF PRODUCING MANUFACTURED TOPSOIL FROM DREDGED MATERIAL FROM THE PORT OF WATERFORD

*C. SHEEHAN[1], J. HARRINGTON[2]
[1]Department of Civil, Structural and Environmental Engineering, Cork Institute of Technology, Bishopstown, Cork, Ireland.

[2]School of Building and Civil Engineering, Cork Institute of Technology, Bishopstown, Cork, Ireland.

Abstract

The Port of Waterford, Ireland has the largest annual maintenance dredge requirement of the Irish Commercial Ports at approximately 500,000 wet tonnes of material. All the material dredged is disposed to an offshore site. This paper presents an investigation into the feasibility of producing manufactured topsoil from dredged material from the Port of Waterford. This will not only reduce offshore disposal but will produce a viable commercial product from a source that has historically been categorised as a waste. The material produced may be used in a variety of ways (e.g. different types of agricultural use, landscaping, etc).

A survey of the local topsoil market was undertaken yielding information on topsoil cost, volume of material used annually and the concerns of the users regarding dredged material. The dredged material was analysed for its physical, chemical and nutrient characteristics. Fourteen different dredge material mixes were developed with two mixes of established topsoil for testing and growth trials. Dewatering and desalination of the mixes was undertaken with continuous monitoring. pH adjustment and organic amelioration, from household organic waste, was analysed. Growth trials were undertaken to compare the growth performance of the dredged material mixes with the established sources available on the marketplace. The creation of manufactured topsoil from dredge material was found to be technically viable with the treatment process developed improving both the germination rate and the overall biomass production.

Keywords:
Waterford Port, Dredge Material, Beneficial Reuse, Topsoil.

1.0 Introduction

1.1 Dredged Material Management in Ireland

Ireland's maritime transport industry accounts for over 99% of imports and exports (by volume) (Shields et al., 2005) and as an island nation Ireland's dredging industry is essential to the operation of its ports and harbours. Historically, the average annual maintenance dredge requirement for disposal at sea is approximately 1.2 million wet tonnes for the Republic of Ireland (OSPAR Commission, 1997-2006). Studies for Ireland (Harrington et al., 2004, Sheehan et al., 2008) have identified the limited amount of beneficial use of dredge material (DM) practiced, particularly for the fine grained fraction.

1.2 Proposal

This paper proposes the use of a mixture of coarse grained and fine grained DM from the Port of Waterford with local organic household waste to produce manufactured topsoil. Topsoil is situated in the upper strata of soil layers, usually 5 to 20cm in depth, and retains the majority of nutrients and moisture that is required by plant life to grow.

The proposal would reduce the volume of DM disposed off-shore from the Port of Waterford with potential applicability elsewhere in Ireland or internationally. Irish standards for topsoil are set out in the British Standard 3882:2007 (BS:3882, 2007) and are presented in Table 1. The most challenging parameters to comply with are the organic matter, pH and salinity, as sediment from an estuary generally has low organic content, a high pH and a high saline content. This research proposal includes dewatering and desalination monitoring, organic testing and amelioration, pH modification and growth trials. The local market for topsoil and the public’s perception of such a product is also presented.

Table 1 - Summary of British Standards for Topsoil

Parameter	Multi-Purpose Topsoil
Soil texture % m/m	
Clay Content %	5-35 %
Silt Content %	0-65 %
Sand Content %	30-85 %
Organic Matter % m/m	
Clay 5-20%	3-20 %
Clay 20-35%	5-20 %
Maximum Course content % m/m	
>2mm	0-30
>20mm	0-10
>50mm	0
pH	5.5-8.5
Plant Nutrient Content	
Nitrogen % m/m	>0.15 %
Extractable Phosphorus mg/l	16-100
Extractable Potassium mg/l	121-900
Extractable Magnesium mg/l	51-600
Exchangeable Sodium* %	<15
Visible Contaminants % m/m	
>2mm	< 0.5
…of which plastics	< 0.25

Note: *Need not measure if soil electro-conductivity <2800µS/cm

1.3 The Port of Waterford

The Port of Waterford has the largest annual maintenance dredge requirement of the Irish Commercial Ports at approximately 500,000 wet tonnes. The Port is operating under a 5 year Dumping at Sea License (2008-2013) with no current beneficial use of DM. The main areas of dredging (Figure 1) are around the main port facilities on the River Suir, at Cheek Point (CP) and further downstream in the main channel at Passage East (PE).

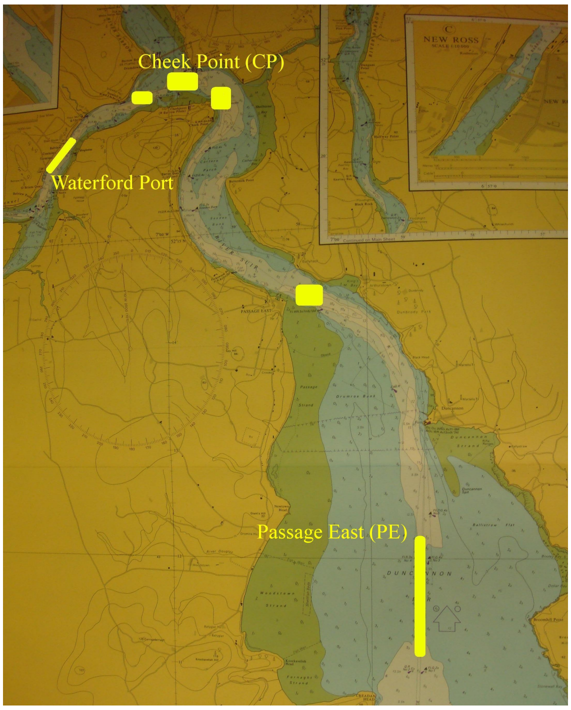

Figure 1 - Dredge Locations in Waterford Bay

2.0 Topsoil Market Survey

The local target market for topsoil in the greater Waterford City area was surveyed to establish if a market for topsoil existed and also to gauge the public's view of dredged material as manufactured topsoil. Hardcopy topsoil survey forms were sent to the target market in April 2008. The survey results from topsoil purchasers showed that the main end destination of the topsoil was with local contractors, the local authorities, landscapers and nurseries as well as a significant amount consumed annually by the general public. Most of this material was sourced from local topsoil companies and from local construction sites where land was stripped of topsoil. In general, the overall rating of topsoil received was considered in the good to very good category. However, overall 86% of respondents stated that they would consider using manufactured topsoil from dredged material and organic waste. The topsoil demand in the area based on survey results is estimated at between 25,000 to 50,000 tonnes annually.

A phone survey of 19 local topsoil suppliers regionally was also completed to establish the current price per tonne of topsoil in the area. The main survey results from the sellers of the material were the different ranges in topsoil cost with an average of €25.26 per tonne.

3.0 Characterisation of Dredged Material

Cheek Point (CP) was identified as the best source of fine grained material while the area of channel dredging by Passage East (PE) was selected for coarse material (Table 2). The fine/coarse mix gave a particle size distribution similar to high quality topsoil with good drainage with a silt and clay fraction allowing adequate water and nutrient retention. Samples were taken from both locations and tested physically, chemically and for their nutrient properties. The particle size distribution for Passage East indicates that the material is a silty loamy soil with low clay content (0.39%). Cheek Point's particle size distribution is finer but would be difficult to handle due to its silty nature and high insitu moisture content. The clay content is higher at 6.2% and would provide improved moisture and nutrient retention for any mix created. Both samples met the Dumping at Sea criteria (Cronin et al., 2006) indicating no contamination and a potentially valuable raw material not requiring treatment.

Electro-conductivity (EC) testing was also undertaken to determine salinity levels present in both samples. The fine grained material sampled from Cheek Point had an EC level of 19.26mS/cm while the coarser grained material from Passage East had a level of 15.36mS/cm.

Table 2 - Summary of Physical Test Results

Parameter		**Coarse Sample (Passage East)**	**Fine Sample (Cheek Point)**
BS 5930 Grading	Fines	58.2 %	85 %
	Sand	41.8 %	15 %
	Gravel	0 %	0 %
In situ moisture content		25.9 %	55.4 %
Organic content		0.53%	2.5%
Specific Gravity		2.61 Mg/m^3	2.55 Mg/m^3

4.0 Methodology for the Beneficial Use of Dredge Material

The initial DM assessment confirmed high water content, high saline content, an elevated pH level (8.23-8.74), compared to natural soils in Ireland, and low to moderate organic content. The overall goal of the treatment and growth trials is to achieve an optimum mix of dredge samples from the two locations identified to meet British Standard 3882:2007.

Several mixes were created with quantities of DM from both Passage East (PE) and Cheekpoint (CP) separated by weight into several different mix ratios from 80% PE/20% CP through to 20% PE/80% CP yielding a wide representative range (a total of seven mixes). Construction topsoil (CT) (the most popular source of topsoil material in the local area) from a local construction site was also used to monitor and compare its dewatering and desalination results with those of the DM mixes.

4.1 Dewatering & Desalination

Desalination is essential in this case for the creation of manufactured topsoil due to the high saline content of the DM. The dewatering and desalination process involves exposing the different mixes to the natural local climate (a process known as 'ripening') and monitoring moisture content and saline levels. This is essential to optimising turnover of the material and ensuring maximum production rates. Weed development was also recorded. Once the mixes reached a stable steady state moisture content and acceptable salinity [electro-conductivity (EC)] they were prepared for growth trials. Both the dewatering and desalination processes were undertaken in an exposed external location in Cork City for mixes of a depth of 200mm and daily rainfall levels were recorded (Figure 2). The dewatering process was undertaken for a 15 week period from the 25th July to the 17th November 2008 in an exposed area. All mixes created reached a stable moisture content level after three to four weeks reducing the moisture content from an average of 32.8% to 18.3%.

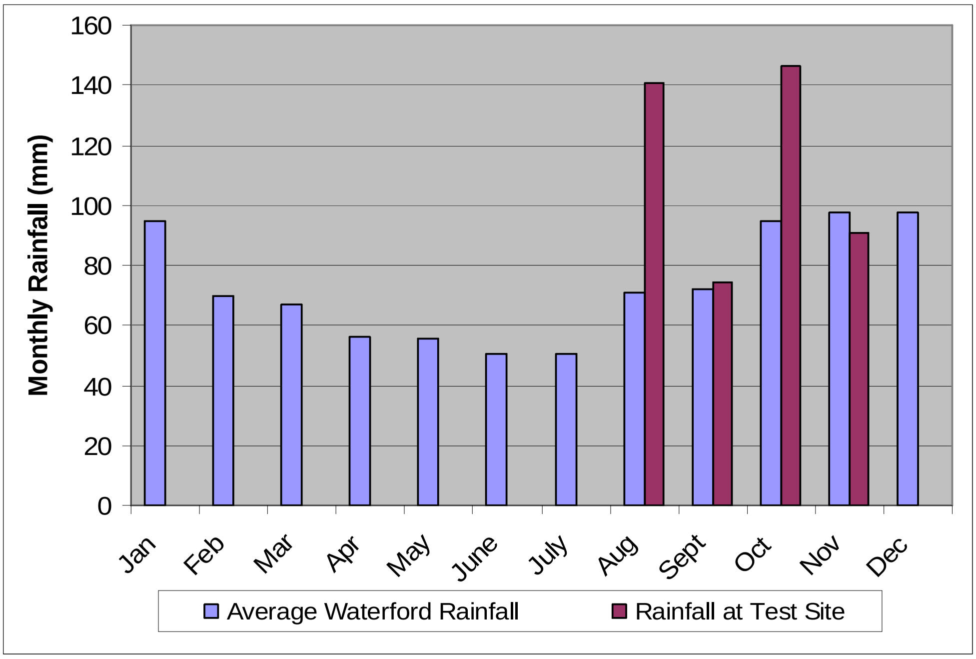

Figure 2 - Average Monthly Rainfall in Waterford Region & at the Test Site (Met Eireann, 2008)

The overall objective of the desalination process was to reduce the electro-conductivity (EC) to a target level suitable for plant germination and growth of 2 mS/cm (Kotuby-Amacher et al., 2000). EC readings were taken periodically during desalination to determine the saline content (Figure 3). The results show that, in general, it takes 2 to 3 months depending on the mix to reach the target EC level. The coarser mixes met the target more rapidly. It can be concluded from the dewatering and desalination stages that if the material is placed in a 200mm layer that the desalination stage is the defining factor due to the longer time duration requirement. Irrigation was required to increase the rate of desalination as the rainfall itself was insufficient over this time period.

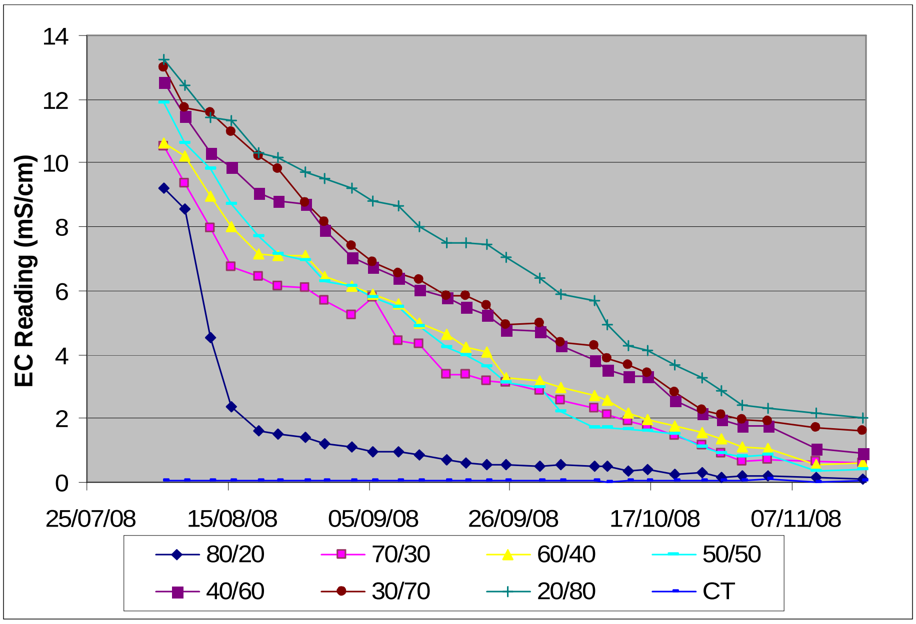

Figure 3 - Electro-Conductivity Readings during Desalination

4.2 Organic Amelioration and pH adjustment

The material mixes were split into two portions after dewatering and desalination. One portion was treated with chemicals (to lower pH) and mixed with compost from the local recycling centre (organic amelioration to boost the organic content of the mix). The other portion was left untreated for comparative analysis. Both were prepared for growth trials together with the construction site topsoil. A sample of high quality manufactured topsoil (Bagged Topsoil) was also obtained and used as a benchmark. Treated mixes are denoted in this paper with a 'c'. In total 14 DM mixes, one sample of construction topsoil and one sample of bagged topsoil were prepared.

A target of 6% organic content was chosen for this work (based on a literature review) and the required organic material could be recovered free of charge from a local compost recycling facility. Each mix was tested for its organic content and the amount of compost required was added to reach the target level of organic content. The amount of organics added ranged from 47.6kg/tn to 32.7kg/tn depending on the mix. The pH was also adjusted by this process, particularly so for the coarser mixes. A target pH level of 6.75 based on Gardiner and Garner's work (1953) was selected.

Aluminium sulphate [Al2(SO4)3] was added to each mix to reach the target pH and to optimise potential nutrient availability. A test amount (1g) of Aluminium Sulphate was added to a sample of each mix and the amount of pH adjustment recorded. From these results the amount of Al2(SO4)3 needed per mix to reach the target pH level was calculated and added prior to growth trials. The results show that the finer the mix the greater the amount of Al2(SO4)3 that is required, which has economic implications. Thus all the treated mixes, while having different particle size distributions, all had a pH level of 6.75 and an organic content of 6% prior to the commencement of growth trials. On average, the mixes without compost required approximately 27% more Al2(SO4)3.

4.3 Growth Trials

The growth trials were conducted indoors over a six-week period using common grass test species, the most common crop planted in the Republic of Ireland. A total of 384 seeds were planted in the 16 different mixes, 25mm below the surface. Artificial light was provided as well as water and rotation to ensure equal light coverage to all mixes. Seed germination data was collected daily to determine emergence rates and total percentage germination. Growth rates were also monitored by daily height measurements. Final height and dry above ground biomass were determined upon harvest.

The individual germination success rates of all the mixes highlighted the consistently better germination rates achieved by the treated mixes, relative to the untreated mixes. This is highlighted in Figure 4, which shows the germination results of the sum of the treated and untreated mixes. The treated mixes averaged 56.9% germination while the untreated DM mixes achieved an average of 31.5% germination.

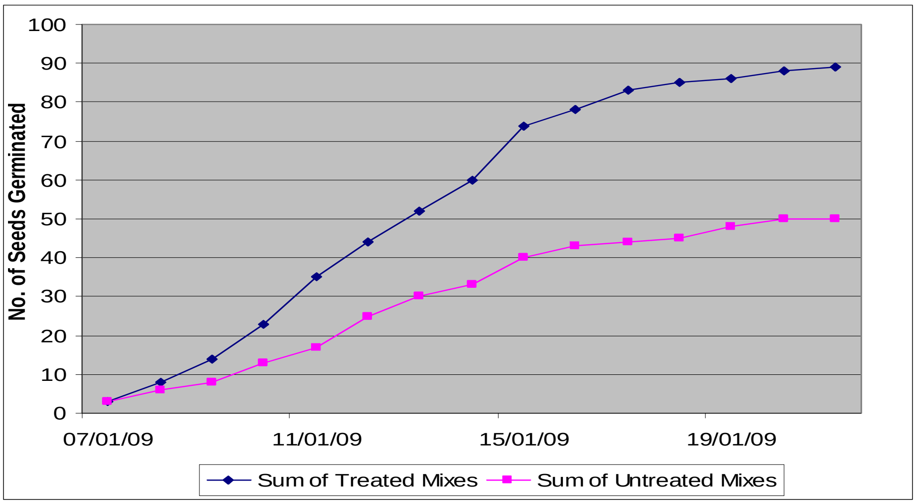

Figure 4 - Sum of Seed Germinations for Treated/Untreated Mixes

Daily height readings were taken during the growth period. The sum of the treated and untreated DM mix height growth levels show that the height development of the treated mixes is moderately better than the untreated mixes with the sum of the treated mixes ranging from 22mm to 73mm higher than the untreated mixes in daily monitoring. From this it was concluded that plant height development is not significantly effected by the treatment process post germination. Upon harvest the biomass of each mix was established (Figure 5). On average the treated mixes achieved 47.5% greater biomass than the untreated mixes. The biomass created by each mix is directly affected by the germination rate and the height development. The mix with the greatest production of biomass was the 60/40c mix, producing slightly more than the 50/50c mix.

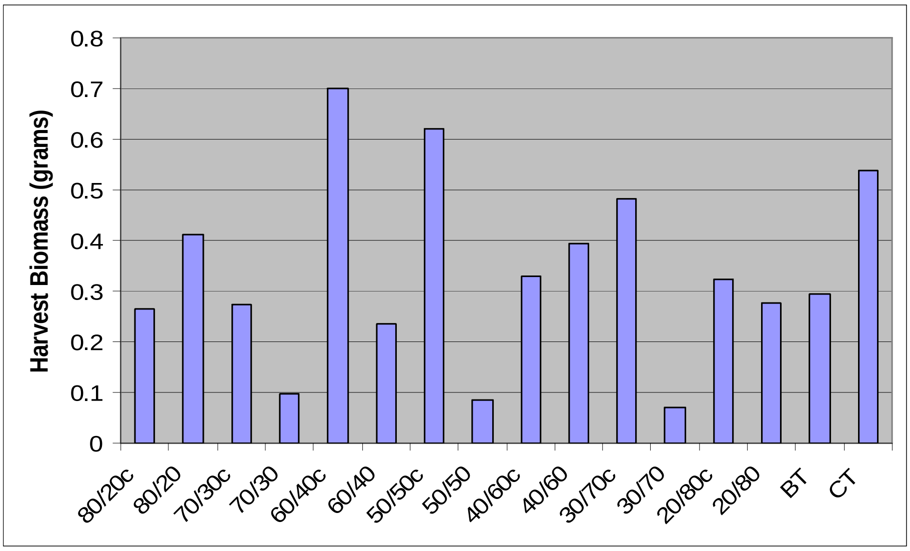

Figure 5 - Grams of Biomass per Mix upon Harvest

Table 3 ranks the dredge mix performance by germination rate, average growth height, sum of growth heights and biomass production. An overall ranking for each mix is also provided, giving each individual parameter equal weighting. Three of the top four rankings are for the treated mixes (60/40c, 50/50c, 30/70c) with construction topsoil ranked third. The highest ranked untreated mix was fifth (80/20).

Table 3 - Ranking of Growth Trial Results

Mix	Germination Rate	Average Growth Height	Sum of Growth Heights	Biomass Production	Overall Ranking
80/20c	6	14	7	12	10
80/20	4	10	5	5	**5**
70/30c	8	13	11	10	12
70/30	13	15	14	14	15
60/40c	**2**	5	**1**	**1**	**1**
60/40	12	6	13	13	13
50/50c	5	**2**	**2**	**2**	**2**
50/50	15	11	15	15	15
40/60c	10	12	10	7	10
40/60	14	**1**	12	6	7
30/70c	7	4	4	4	**4**
30/70	16	**3**	16	16	14
20/80c	9	8	8	8	7
20/80	11	7	9	11	9
BT	**1**	16	6	9	6
CT	**3**	9	**3**	**3**	**3**

Note: The lower the ranking the higher the performance, i.e. 1 designates best performance, 15 designates poorest performance
BT denotes Bagged Topsoil, CT denotes Construction Topsoil

4.4 Discussion

The data collected from the topsoil survey determines if there is a market for such a product. Analysis of the target market suggests that the public would be open to using manufactured topsoil with no negative views received from the survey returns.

Dewatering to a stable level for all mixes was established three weeks after storage and mixing was complete. Desalination took from eight to thirteen weeks depending on the permeability properties of the mix. It should also be noted that the ripening process was undertaken during the summer and autumn months. It is anticipated that results would be less advantageous over the winter and spring months due to reduced temperatures and greater precipitation.

The pH and organic testing programme found that for one tonne of the optimum mix (60% PE & 40% CP) 47.57kg of organic material and 37.19kg of Aluminium Sulphate was required to boost the organics to an acceptable level while ensuring that the pH was at such a level that growth in most of the plants was not negatively impacted. The addition of organics alone reduced the pH level by 0.5 to 0.75 depending on the mix. The effect of the addition of Aluminium Sulphate on the mixes depended on the differential between the original pH of the sample and the pH of the chemical itself, with supplementary additions providing less adjustment. The amount of organic amelioration and pH modification required was directly affected by the particle size distribution of each mix with coarser mixes requiring less Aluminium Sulphate.

The growth trial results showed that treated dredged material can compete with the standards of topsoil currently on the market. Germination rates of the treated dredged material were encouraging, although the untreated dredged material was less successful due to elevated pH and saline content. Both treated and untreated mixes, in general, had poorer germination results than both construction and bagged topsoil (with the exception of the optimum mix 60/40c mix). It can be concluded that the treatment of the dredged material increases germination rates (on average 56.4% better than the untreated) while producing more biomass per height grown. Untreated DM suffers from weakened germination but has comparable height and biomass results as highlighted by the ranking table presented. The best performing treated dredged material mixes (60/40c, 50/50c, 30/70c) had growth levels comparable with both construction topsoil and bagged topsoil. These results show that treated dredged material can be of a high quality and be competitive with the current market standard.

4.5 Conclusions

The results of the topsoil survey show a positive public perception of the DM product and the average price of topsoil was established to be €25.36 per tonne. The DM testing highlighted its topsoil characteristics post mixing, with good drainage and adequate nutrient and water retention capabilities. Dewatering and desalination of 200mm mix layers, with continuous irrigation, significantly improves the time required for these stages compared to previous research on layers of greater thickness (Thomas, 1990).

In all cases, the treated mixes compared favourably with current market standards for topsoil. The highest ranked treated mixes had satisfactory germination rates, height and biomass results and exceeded results for the construction topsoil. The untreated mix germination rates were impacted by their increased pH levels but had substantial height and biomass production upon germination. The treatment process implemented significantly boosted the germination rate of the treated DM mixes, which directly effects total grass height development and biomass production.

The ranking table (Table 3) presents a summary of the germination rate, average growth height, total height development and biomass production data collected from the growth trials. From this the optimum mix was identified as the treated 60/40 mix (60/40c). The results from the dewatering and desalination stage identified that the treated 60/40 mix would require at least 10 weeks to achieve the EC level required. Organic testing showed that 47.58kg of compost would be required per tonne to reach the desired organic content level for the 60/40 mix. 32.49kg of $Al_2(SO_4)_3$ per tonne would be required for the selected mixes to modify the pH level of the selected mix to maximise the nutrients available for plant growth. Based on the research undertaken the production of manufactured topsoil using DM (after treatment) is technically viable and compares well with market standards.

Acknowledgements
The authors wish to acknowledge the funding received from the Irish Environmental Protection Agency under the Science, Technology, Research and Innovation for the Environment (STRIVE) Programme 2007-2013.

References

British Standard:3882, 2007. *Specification for Topsoil and Requirements for Use*, British Standard 3882:2007, British Standards Institute, London, United Kingdom.

Cronin, M., McGovern, E., McMahon, T., Boelens, R., 2006. *Guidelines for the Assessment of Dredge Material for Disposal in Irish Waters*, Marine Institute, Galway, Ireland.

Gardiner, H.W. & Garner, H.V., 1953. *The Use of Lime in British Agriculture*, Published by Farmer and Stock Breeder Publication Ltd.

Harrington, J.R., Sutton, S., Lewis, A.W., 2004. 'Dredging and Dredge Disposal and Reuse in Ireland – A Small Island Perspective', in *Proceedings of World Dredging Congress XVII*, B4-5, pp. 1-14, Hamburg, Germany.

Kotuby-Amacher, J., Koenig, R., Kitchen, B., 2000. *Salinity and Plant Tolerance*, Electronic Publishing, Utah University, USA.

Met Eireann, 2008. Rosslare Climatic Monthly Data**,** The Irish Meteorological Online Service, December, 2008.

OSPAR Commission 1997-2006, *Dumping of Wastes at Sea 1997 to 2006*, London, UK.

Sheehan C., Harrington J.R., Murphy, J.P., Riordan J.D., 2008. 'An Investigation into Potential Beneficial Uses of Dredge Material in Ireland', *WEDA XXVIII and Texas TAMU 39th Dredging Seminar*, St. Louis, USA.

Shields, Y., O' Connor, J., O' Leary, J., 2005. *Ireland's Ocean Economy & Resources*, Marine Foresight Series No. 4, Marine Institute.

Thomas B.R., 1990. *Clyde Sediments : Physical Conditioning in Relation to Use as a Topsoil Product for Land Reclamation*, PhD Thesis, Department of Civil Engineering, University of Strathclyde.

PREDICTION OF SURFACE SETTLEMENTS ABOVE SHALLOW MICROTUNNELS IN MULLINGAR

B.G. CURRAN & B.A. McCABE
College of Engineering and Informatics, National University of Ireland, Galway, Ireland

Abstract
The disturbance to the ground caused by tunnel construction can lead to sub-surface ground movements. These movements manifest themselves at the ground surface in the form of a trough centered over the tunnel and extending in front of the advancing face. Many authors, including Schmidt (1969) and Peck (1969), have shown that the transverse settlement trough is well described by a Gaussian distribution curve while the longitudinal settlement trough has the form of a cumulative probability curve. Excessive surface and subsurface settlements, resulting from poorly-controlled tunnelling operations, can result in considerable damage to nearby buildings, overlying services and other infrastructure. This paper reviews semi-empirical methods used to predict short-term surface settlements, and appraises them in the light of new settlement measurements made during the construction of shallow microtunnels in gravel and clay in Mullingar, Co. Westmeath. This paper will serve as a useful reference for designers interested in constructing tunnels in similar materials around Ireland.

Keywords: Empirical method, Microtunnel, Settlement, Stability, Tunnelling, Volume loss.

1. Introduction

The increasing use of microtunnelling, especially in urban environments, has led to a greater need for accurate predictions of (i) the excavation stability; ensuring adequate support pressure is applied to prevent collapse and (ii) the pattern and magnitude of the ground settlement, to assess the potential damage to surrounding structures (Augarde *et al*., 2003). Ground settlement, the main focus of this paper, is traditionally predicted using empirical relationships derived from measured data which allow a reasonable degree of confidence for *greenfield* conditions. However, adjacent building foundations and services will interact with and possibly modify the profile of the settlement trough leading to difficulties in making realistic predictions of ground movements.

In 2009, Ward and Burke Construction Ltd. constructed almost 750m of pipeline in 8 drives, predominantly in clay and gravel, in Mullingar, Co. Westmeath as part of a Regional Sewage Scheme. Herrenknecht's AVN range of slurry shielded Tunnel Boring Machines (TBMs) were used. Support of the excavation is provided mechanically by the shield and the trailing product pipes and hydraulically by means of a water-based slurry, therefore minimizing possible ground movements. These machines are suitable for mixed or unstable ground conditions, where the excavation may collapse, as they provide constant support of the excavated face.

2. Stability

Accurate prediction of the stability of a tunnel is vital, as its collapse or blow-out, especially in the urban environment, can be catastrophic. According to Broms and Bennermark (1967), the stability ratio (or overload factor), N, in undrained conditions for a homogeneous clayey soil is given by Equation (1):

$$N = \frac{\sigma_s + \gamma z_0 - \sigma_T}{s_u} \tag{1}$$

where s_u is the undrained shear strength, z_0 is the depth to the tunnel axis, the cover plus half the diameter (C + D/2), σ_s is the surcharge pressure, σ_T is the tunnel support pressure and γ is the unit weight of the soil.

Based on laboratory tests along with field observations Broms and Bennermark (1967) concluded that the critical stability ratio at collapse, N_c, is about 6, a similar value reported by Peck (1969) and the ITA/AITES Report (2006). A high stability ratio can lead to the overcut (annulus around the pipe) being filled by squeezing ground leading to unwanted ground movements. This can be avoided by applying a sufficient volume and pressure of bentonite to the overcut during tunnelling and filling it with a cement grout on completion of works. Figure 1 allows the evaluation of the stability of a tunnel in terms of the zones described in the ITA/AITES Report (2006).

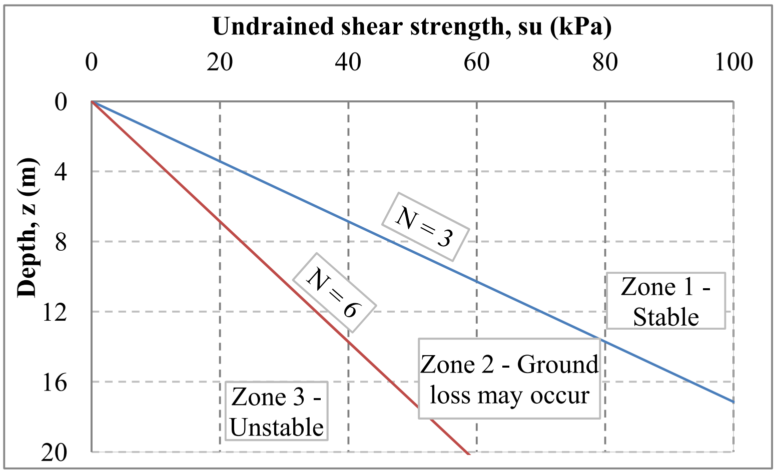

Figure 1 - Classification of short term stability

The stability ratio is only valid for cohesive soils with low permeability and does not apply to soils that exhibit insignificant or no undrained shear strength, e.g. gravel with low fines content. For tunnels in cohesionless soils without surcharge loading, the required support pressure is given by Equation (2) (Atkinson and Mair, 1981):

$$\sigma_T = \gamma D T_\gamma \tag{2}$$

where T_γ is the stability number, which is a function of the angle of friction of the soil, φ'. If the tunnel has a large surcharge and is at shallow depth the weight of the soil may be neglected and the required support pressure is given by Equation (3):

$$\sigma_T = \sigma_S T_S \tag{3}$$

(Atkinson and Mair, 1981) where T_S is the stability number.

3. Settlement

3.1 Causes of Ground Displacement

The deformation of soil surrounding a tunnel occurs in two stages. The initial short term settlement, which occurs within a few weeks of the passage of the TBM, is associated with the construction of the tunnel and is usually dominant. It includes:

i) Instability of the tunnel face due to poor control of the confining pressure.
ii) Stress release due to the overcut.
iii) Radial ground movements, caused by the tendency of the machine to plough or yaw if there are difficulties in maintaining its grade or line.
iv) A hydraulic gradient may weaken the mechanical condition of the soil at the excavation thereby increasing ground deformation.
v) Deflection of the lining as ground loading develops. As the product pipes are designed to resist lateral jacking forces the radial deformation of the pipes is likely to be satisfactory (ITA/AITES Report, 2006).

This is followed by a post-construction phase of time-dependent settlement. In clay it is due to consolidation as excess pore water pressure (that developed due to increased stress experienced as result of the tunnelling process) dissipates. The tunnel may also act as a drain, if it's lining is more permeable than the surrounding soil, causing consolidation settlement, as water enters it faster than can be replaced through the soil.

3.2 Transverse Surface Settlement

Martos (1958) proposed that the transverse settlement trough could be represented by an inverted Gaussian curve after examining the subsidence above mining excavations (Figure 2). Several authors including Schmidt (1969), Peck (1969) and New and O'Reilly (1982), demonstrated, through the analysis of case history data, that the settlement trough above tunnels in a *greenfield* site can be realistically described by the Gauss-distribution given by Equation (4). Although this semi-empirical method is frequently used it has no theoretical justification and contains several shortcomings as geotechnical parameters and the construction technique are not taken into account.

$$S_{(y,z)} = S_{(\max,z)} \exp^{\frac{-y^2}{2i^2}} \qquad (4)$$

$S_{(y,z)}$ is the vertical settlement at distance y from tunnel centre line and at depth z, $S_{(max)}$ is the max settlement over the centre line at depth z, y is the horizontal distance from the centre line, *i* is the transverse distance from the centre line to point of inflection of the trough.

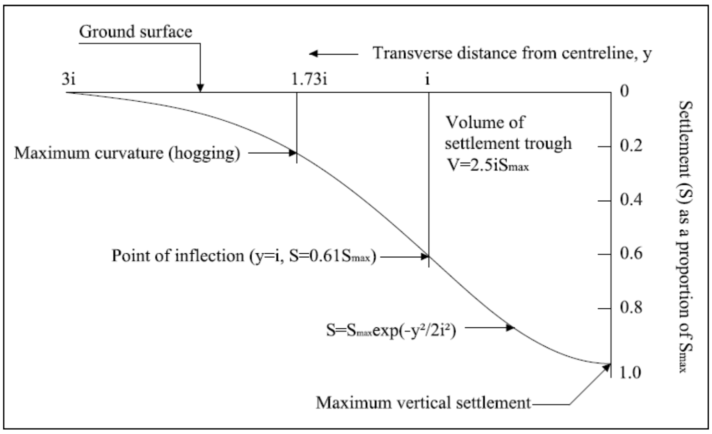

Figure 2 - Transverse settlement trough

O'Reilly and New (1982) assumed that all soil particles, in cohesive soils, move along radial paths towards the tunnel axis and that conditions of plane strain constant volume deformation applies. This theory of radial flow would suggest that the width of the settlement trough decreases linearly with depth and in order to conform to the condition of plane strain constant volume the ground movements increase linearly with depth to the tunnel axis.

O'Reilly and New (1982) proposed that *i* is a linear function of z_0, related through the empirical trough width parameter, K (Equation 5), and independent of the tunnel diameter except for shallow tunnels with cover to diameter ratios (C/D) less than uni

$$i = Kz_0 \qquad (5)$$

K varies between 0.4 – 0.5 for tunnels in stiff fissured clay, 0.5 – 0.6 in glacial deposits, 0.6 – 0.7 in soft silty clay and 0.2 – 0.3 in granular soils (O'Reilly and New, 1982). Mair and Taylor (1997) summarized a wide range of field data and concluded that K values vary between 0.25 and 0.45 in sands or gravels with an average of 0.35. Further empirical methods suggested by other authors are listed in Table 1.

Table 1 - Empirical formulae for predicting the trough width parameter, i

Author	Empirical Solution
Peck (1969)	$i/R = (z_0/2R)^n$ (n = 0.8 – 1.0)
Attewell & Farmer (1974)	$i/R = (z_0/2R)^n$ (n = 1.0)
Atkinson & Potts (1977)	$i = 0.25(z_0+R)$ – loose sand
	$i = 0.25(1.5z_0+0.5R)$ – dense sand & O.C. clay
Clough & Schmidt (1981)	$i/R = (z_0/2R)^n$ (n = 0.8)
O'Reilly & New (1982)	$i = 0.43z_0+1.1$ – cohesive soil
	$i = 0.28z_0-0.1$ – granular soil
Chapman et al. (2007)	$i = 0.5z_0$ – clay

The volume of the settlement trough, V_s, is derived by integration of Equation (4).

$$V_s = \int_{-\infty}^{\infty} S dy = \int_{-\infty}^{\infty} S_{(\max,z_0)} \exp^{\frac{-y^2}{2i^2}} dy = \sqrt{2\pi} i S_{(\max,z_0)} \qquad (6)$$

This can be expressed as a percentage of the cross-sectional area of the tunnel per meter length and is termed the volume loss, V_l. Mair (1996) suggests that with proper control losses of between 1-2 % for an unsupported excavation in stiff clay, 1-2 % in soft clay and as low as 0.5 % in sand can be achieved.

4. Analysis of Measured Settlements

4.1 Recorded Data and Ground Conditions

A total of 8 transverse settlement profiles are analysed in this paper. Relevant information is provided in Table 2; the time listed is that elapsing between the passing of the TBM and the first settlement records. The ground conditions experienced during MH 23-14 and MH 23-22 comprised of a dense gravel with an SPT-N value between 46 and 47 at a depth of 3.6 – 5.4 m. A firm gravelly clay (SPT-N = 20) was encountered at profiles 117-123 and 127-133 during drive MH 9-11 and a very soft sandy silt (SPT-N = 4) at profile 159-165.

Table 2 - Drive Parameters

Drive	Profile I.D.	Time (days)	Depth z_0 (m)	External Diameter D_E (m)	Weight of Soil, γ (kN/m^3)	Soil Description
MH23-24	26-32	18	5.06	1.46	20.5	Dense clayey Gravel with some cobbles (SPT-N = 47)
	36-42	26	3.6	1.46	20.5	
	47-53	24	5.05	1.46	20.5	
MH23-22	1-7	12	5.39	1.46	20.5	Dense clayey course Gravel with cobbles (SPT-N = 46)
	13-20	3	4.28	1.46	20.5	
MH 9-11	117-123	5	4.09	2.16	20	Firm slightly gravelly Clay (SPT-N = 20)
	127-133	4	3.95	2.16	20	
	159-165	4	3.53	2.16	16.5	Very soft sandy Silt (SPT-N=4)

4.2 Discussion

The volume loss, V_l, the maximum settlement, S_{max}, and the trough parameter K, for the monitored profiles are shown in Table 3. The measured volume loss is determined from Equation (6), where $S_{(max)}$ is measured directly onsite and i is estimated from Equation (5), with K varied until a best fit is formed with the measured profile. The volume of the settlement trough, assuming no volume change of the soil mass, varies between 0.5% and 4.5%. The larger volume losses of 3.3%, 2.7% and 4.5% were observed on site where boulders were encountered. The slow advance rate as the TBM grinds the boulder results in large volume losses as the ground above the tunnel is disturbed. However, in general the volume losses are acceptable (between 0.5 and 1.6%) highlighting effective construction control; and averages fall well below the conservative recommendation of 2.5% quoted by Mair (1996).

Large settlements recorded at profiles 117-123 and 127-133 (19.7 and 21.4mm) were possibly due to the low C/D ratio (see Table 3). When C/D < 2, special consideration must be taken to evaluate the settlement risk (ITA/AITES Report, 2006). There is no obvious trend of decreasing S_{max} with an increase in the depth to the tunnel axis or C/D ratio, although the range of tunnel depth and C/D values encountered at Mullingar is fairly narrow.

Table 3 - Measured transverse settlement trough parameters

Profile I.D.	V_l (%)	S_{max} (mm)	S_{max}/z_0	C/D	K
26-32	2.7	11.88	2.35	3.0	0.30
36-42	1.5	7.32	2.03	2.0	0.38
47-53	0.8	3.78	0.75	3.0	0.28
1-7	4.5	18.59	3.45	3.2	0.30
13-20	3.3	14.30	3.34	2.4	0.36
117-123	1.6	19.72	4.82	1.4	0.29
127-133	1.5	21.35	5.41	1.3	0.26
159-165	0.5	5.75	1.63	1.1	0.36

The plot of the trough width parameter against the depth to the tunnel axis in Figure 3, presents the Mullingar data and that from tunnels driven in the United Kingdom O'Reilly and New (1982) utilized in deriving their equation in Table 1 for granular soils. The three lines represent the upper and lower bounds and the mean value of K for granular soil according to Mair and Taylor (1997). The plot shows that the K values observed at Mullingar and at the drives utilized by O'Reilly and New (1982) are consistent with that suggested by Mair and Taylor (1997). As different construction methods were utilized in the drives in the United Kingdom it also adds evidence that the width of the trough is independent of the construction method as concluded by Mair and Taylor (1997)

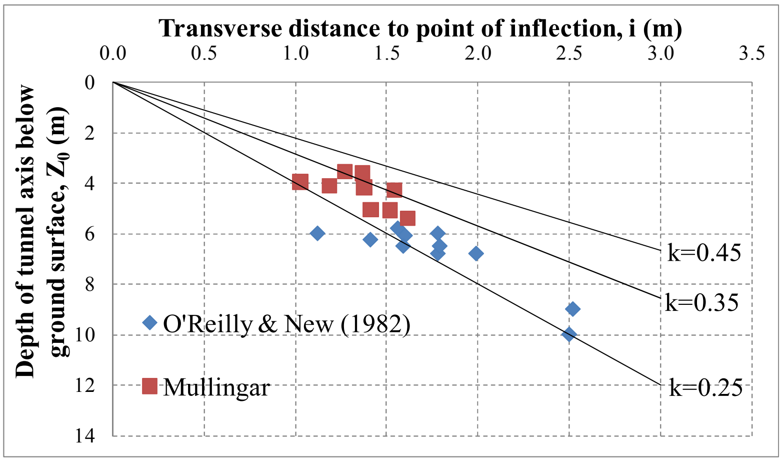

Figure 3 - Variation of i with z_0

Figure 4 compares the predicted transverse settlement troughs to those observed at Mullingar. In predicting the transverse settlement trough two parameters are required to characterize it, the distance to the point of inflection, i and the volume loss, V_l, both of which are assumed. The point of inflection is based on the empirical equations for granular soils in Table 1 and the empirical relationship in Equation (5) (K is equal to 0.3 for granular soils) and the volume loss is assumed to be a conservative 2.5%. The estimated settlement troughs are then determined by manipulating Equations (4) and (6). The empirical relationship in Equation (5) (i = kz) and O'Reilly and New's (1982) relationship tends to predict deeper, narrower ground settlement troughs in comparison to predictions that incorporate the C/D effect (Peck, 1969 and Attewell and Farmer, 1974). The predicted and observed troughs show a large difference mainly because the assumed volume loss is much greater than the observed one.

Table 4 lists the predicted S_{max} at each profile for the empirical relationship in Equation (5). S_{max} is over estimated in almost all cases, with very small under estimation of 8 and 10% and a large under estimation of 80% at profile 1-7, due to the problem boulders posed throughout the drives. As all settlements were recorded from settlement pins in the road, the inherent stiffness of the road's structure relative to the ground may attribute some part to the shallow troughs observed.

Table 4 – Estimated S_{max} (i = kz)

Profile I.D.	Max Settlement, S_{max} (mm)	S_{max}/z_0	$S_{max(Measured)}/S_{max(predicted)}$
26-32	11.00	2.17	1.08
36-42	15.46	4.29	0.47
47-53	11.02	2.18	0.34
1-7	10.33	1.92	1.80
13-20	13.00	3.04	1.10
117-123	29.79	7.28	0.66
127-133	30.84	7.81	0.69
159-165	34.51	9.78	0.17

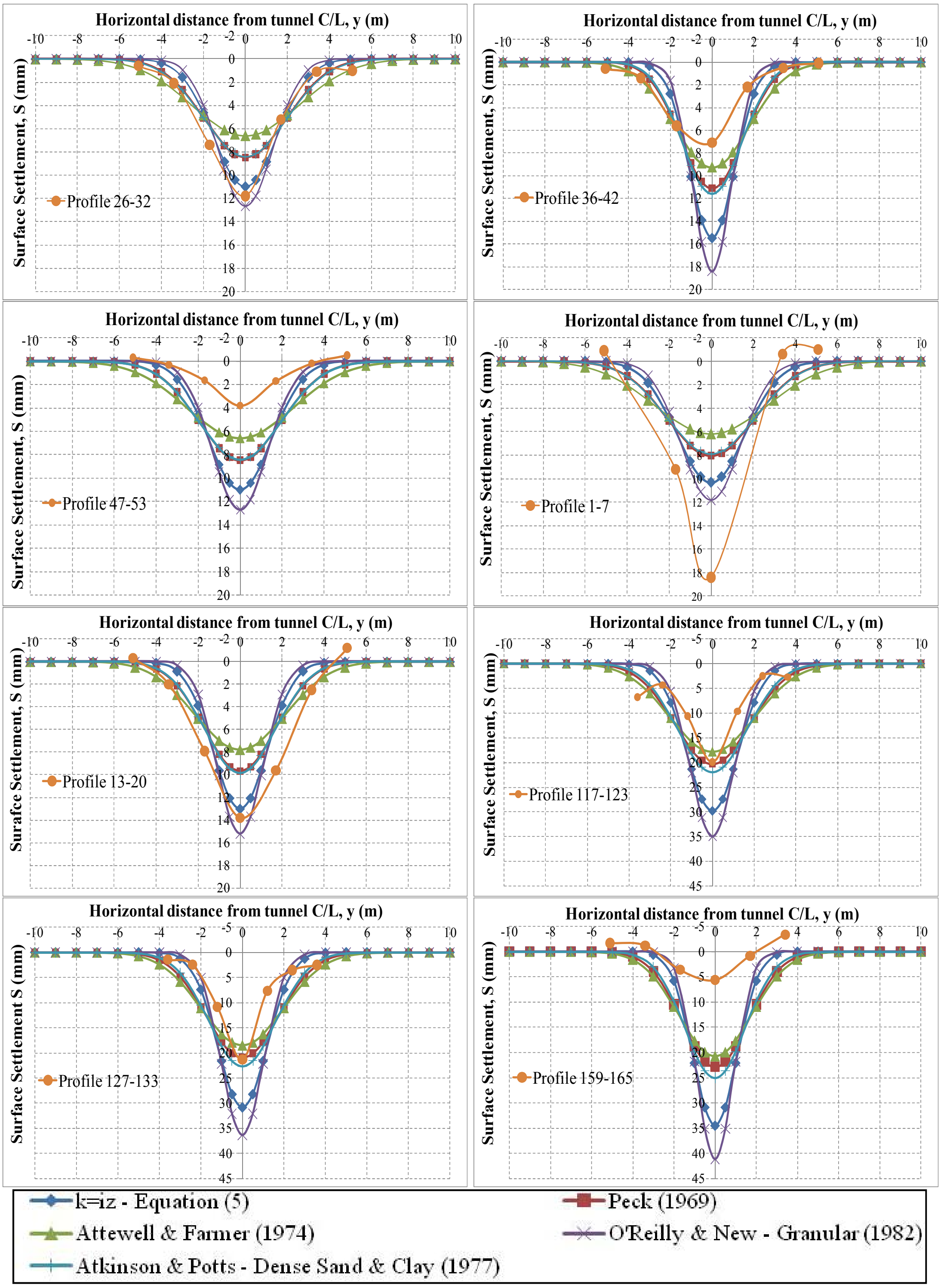

Figure 4 - Measured and predicted transverse settlement troughs at Mullingar

5. Conclusions

The new settlement data at Mullingar has been a useful contribution to Irish microtunnelling experience, and findings can be summarized as follows:

i) The use of settlement design parameters K = 0.3, for granular soils, and V_l = 2.5% generally leads to a conservative estimate of S_{max}.

ii) K values fall into the range between 0.25 and 0.45 for granular soils, as suggested by Mair and Taylor (1997).
iii) In general, the observed settlement troughs correspond to volume losses between 0.5 and 1.6%. These low values may be attributed to the use of a slurry shielded machine which allows proper control of the tunnel face.
iv) Larger volume losses can be accredited to the presence of boulder in mixed ground conditions.
v) The large settlements observed on site may be due to low C/D ratios.

6. Acknowledgements

The authors would like to acknowledge the funding received from Ward and Burke Construction Ltd, Kilcolgan, Co. Galway.

References

Atkinson, J.H. and Potts, D.M. (1997). 'Subsidence above shallow tunnels in soft ground', *Journal of the Geotechnical Engineering Division, ASCE*, **103**, 307-325.
Atkinson, J.H. and Mair, R.J. (1981). 'Soil mechanics aspects of soft ground tunnelling', *Ground Engineering*, **14 (5)**.
Attewell, P.B. and Farmer, I.W. (1974). 'Ground deformations resulting from shield tunnelling in London', *Canadian Geotechnical Journal*, **11**, 380-395.
Augarde, C.E., Lyamin, A.V. and Sloan, S.W. (2003). 'Stability of an undrained plane strain heading revisited', *Computers and Geotechnics*, **30**, 419-430.
Broms, B.B. and Bennermark, H. (1967). 'Stability of clay at vertical openings', *Journal of Soil Mechanics and Foundation Division, ASCE*, 1993, 71-95.
Chapman, D.N., Ahn, S.K. and Hunt, D.V.L. (2007). 'Investigation ground movements caused by the construction of multiple tunnels in soft ground using laboratory model tests', *Canadian Geotechnical Journal,* **44(6)**, 631-643.
Clough, G.W. and Schmidt, B. (1981). 'Design and performance of excavations and tunnels in soft clay' in *Soft Clay Engineering*, Elsevier, 569-631 (Chapter 8).
Mair, R.J. (1996). 'Settlement effects of bored tunnels'. Session Report, in *Proc. Int. Symposium on Geotechnical Aspects of Underground Construction in Soft Ground*, London, eds R.J. Mair and R.N. Taylor, Balkema, 45-53.
Mair, R.J. and Taylor, R.N. (1997). 'Bored tunnelling in the urban environment. Theme Lecture, Plenary Session 4', in *Proc. 14th International Conference on Soil Mechanics and Foundation Engineering*, Hamburg, Vol. 4.
Martos, F. (1958). 'Concerning an approximate equation of the subsidence trough and its time factors', in *International Strata Control Congress*, Leipzig, 191-205.
O'Reilly, M.P. and New, B.M. (1983). 'Settlement above tunnels in the United Kingdom – their magnitude and prediction', in *Proc. of Tunnelling 1982 Symposium*, Institution of Mining and Metallurgy, London (1982). 173-181.
Peck, R.B. (1969). 'Deep excavations and tunnelling in soft ground', in *Proc. 7th Int. Conf. on Soil Mechanics and Foundation Engineering*, Mexico City, **3**, 311-376.
Schmidt, B. (1969). 'Settlement and ground movements associated with tunnelling in soil'. PhD Thesis, University of Illinois, Urbana.
ITA/AITES Report (2006). 'Settlements induced by tunnelling in soft ground', *Tunnelling and Underground Space Technology,* **22(2)**, 119-149.

MONITORING BRIDGE DYNAMIC BEHAVIOUR USING AN INSTRUMENTED TWO AXLE VEHICLE

P.J. McGETRICK, A. GONZÁLEZ & E.J.OBRIEN

School of Architecture, Landscape and Civil Engineering, University College Dublin, Belfield, Dublin 4, Ireland

Abstract

Highway structures such as bridges are subject to continuous degradation primarily due to ageing, loading and environmental factors. A rational transport policy must monitor and provide adequate maintenance to this infrastructure to guarantee the required levels of transport service and safety. Increasingly in recent years, bridges are being instrumented and monitored on an ongoing basis due to the implementation of Bridge Management Systems. This is very effective and provides a high level of protection to the public and early warning if the bridge becomes unsafe. However, the process can be expensive and time consuming, requiring the installation of sensors and data acquisition electronics on the bridge. This paper investigates the use of an instrumented 2-axle vehicle fitted with accelerometers to monitor the dynamic behaviour of a bridge network in a simple and cost-effective manner. A simplified half car-beam interaction model is used to simulate the passage of a vehicle over a bridge. This investigation involves the frequency domain analysis of the axle accelerations as the vehicle crosses the bridge. The spectrum of the acceleration record contains noise, vehicle, bridge and road frequency components. Therefore, the bridge dynamic behaviour is monitored in simulations for both smooth and rough road surfaces. The vehicle mass and axle spacing are varied in simulations along with bridge structural damping in order to analyse the sensitivity of the vehicle accelerations to a change in bridge properties. These vehicle accelerations can be obtained for different periods of time and serve as a useful tool to monitor the variation of bridge frequency and damping with time.

Keywords: Bridge, Monitoring, Transportation

1. Introduction

For widespread implementation of Bridge Management Systems, a large number of bridges must be instrumented and monitored. Given the very large number of bridges that are not instrumented, some alternative method is needed to detect any change in behaviour of the structure which may indicate some form of damage. This paper investigates the use of a vehicle fitted with accelerometers on its axles to monitor the dynamics of bridges. The frequency of a bridge may vary significantly during short periods of time as result of environmental conditions, but a change in bridge frequency over long periods of time may be a clear sign of deterioration. Damping has also been shown to be a damage sensitive parameter (Curadelli *et al*, 2008; Modena *et al*, 1999). This approach reduces the need for any equipment to be installed on the bridge and would allow the assessment of bridge condition to become a simplified and considerably less time consuming process. It would bring about more efficient monitoring of the condition of existing bridges in a transport network while its development would enable maintenance to be undertaken at an earlier stage in degradation, which in general results in more economical repairs.

Yang *et al* (2004) theoretically verified the feasibility of extracting bridge dynamic parameters from the dynamic response of a vehicle passing over a bridge. The approach investigated by Yang *et al* employed a vehicle instrumented with accelerometers acting as a 'message carrier' of the dynamic properties of the bridge. The bridge was assumed to be a simply supported beam while a simplified sprung mass model represented the vehicle. The bridge natural frequency was extracted from the vehicle acceleration spectrum of the sprung mass and they found that the magnitude of the bridge natural frequency peak increased with vehicle speed but decreased with increasing bridge damping ratio.

Experimental investigations of this method have been carried out by Lin and Yang (2005) and González *et al* (2008). Lin and Yang validated the method in field tests using a two wheeled cart fitted with an accelerometer which was towed by a light two axle truck across a simply supported 30m span of a six span bridge. They found that the bridge frequency was easily identified at vehicle speeds less than 40 km/h (11.11m/s) but at higher speeds the bridge frequency becomes hidden by high frequency components from pavement roughness and cart structure. They also found that carrying out the field test while traffic was crossing the bridge had a beneficial effect as it increased the vehicle response.

The experimental analysis by González *et al* consisted of a field test on a main route near Oviedo, Northern Spain. A vehicle instrumented with accelerometers and GPS was driven over a long-span bridge (9 spans of lengths between 41 and 50 m, total length of 423.5 m) to obtain its frequencies. Their analysis of the technique also included a 3-D FEM vehicle-bridge interaction (VBI) model in which the method was tested numerically for various speeds, road roughness, damping levels and traffic conditions. They concluded that it is only feasible to extract the bridge frequency accurately from the dynamic response of the vehicle at low speeds and also when the bridge dynamic excitation is sufficiently high as the interference of road surface profile frequencies corrupt the spectrum and prevent the identification of the bridge natural frequency.

A theoretical investigation of the identification of bridge dynamic parameters using a 2-degree-of-freedom quarter-car model was carried out by McGetrick *et al* (2009). The aim of the investigation was to identify not only bridge frequencies of vibration but also a change in the bridge's structural damping. McGetrick *et al* conclude that the bridge's frequency of vibration and structural damping can be identified with ease from the dynamic response of the quarter car for a smooth road profile, while in the presence of a rough road profile the same properties become very difficult to identify.

González *et al* (2010) extended the analysis by McGetrick *et al* to a 4-degree-of-freedom half-car model and they found similar conclusions. Therefore, they noted that frequency matching between the axle hop of the vehicle and the natural frequency of the bridge is beneficial for the detection of that bridge frequency. The effect of a change in bridge damping on the vehicle response appeared reasonably small compared to the effect of a change in the road profile.

This paper builds upon the theoretical analysis carried out by González *et al*. The aim is to carry out a sensitivity study of some parameters that affect the dynamic response of the vehicle and as a result, the identification of the natural frequency of vibration of the bridge and changes in structural damping. A VBI simulation model is created in MATLAB for this purpose. The spectra of accelerations of the front axle are obtained from the dynamic response of the half-car as it crosses the bridge. The dominant frequencies of vibration are extracted from the acceleration spectra and compared to the exact bridge or half-car frequencies. As González *et al* included a study of various bridge span lengths this paper focuses only on a 15 metre bridge span. Bridge structural damping is varied from 0% to 5% (in steps of 1%). 0% bridge damping is only a reference point, although some long-span bridges may exhibit damping ratios as low as 0.3%. The vehicle properties varied in simulations are axle spacing (3.75 and 4.45 metres) and gross vehicle weight (9 and 18 tonnes). Two road conditions are tested: smooth and ISO Class A. The results will indicate the conditions in which this method can be used to monitor bridge dynamic properties with a sufficient degree of accuracy.

2. Vehicle – Bridge Interaction Model

A theoretical half-car model is used to represent the behaviour of the vehicle. The model has 4-degrees-of-freedom which allows for axle hop, sprung mass bounce and sprung mass pitch rotation. The body of the vehicle is represented by the sprung mass, m_s, and the front and rear axle components are represented by unsprung masses, m_{u1} and m_{u2} respectively. The axle mass connects to the road surface via a spring of stiffness K_t, while the body mass is connected to the tyre by a spring of stiffness K_s in combination with a viscous damper of value C_s modelling the suspension. Tyre damping is assumed to be negligible and thus is omitted. The model also accounts for the sprung mass moment of inertia, I_s, and the distance of each axle to the vehicle's centre of gravity, i.e., D_1 and D_2 in Table 1. The centre of gravity of the vehicle is taken to be equidistant from each axle ($D_1 = D_2$), i.e., body weight equally distributed between axles. The half-car property values are listed in Table 1 and are based on values obtained from work by Harris *et al* (2007) and Cebon (1999).

Table 1 - Half car properties

Property	Unit	Symbol i=1,2	GVW = 9 tonnes		GVW = 18 tonnes	
			Model	Model	Model	Model
Body mass	kg	m_s	7600		16600	
Axle mass	kg	m_{ui}	1100		1100	
Suspension Stiffness	N/m	K_{si}	1×10^6		1×10^6	
Suspension Damping	Ns/m	C_{si}	10×10^3		10×10^3	
Tyre Stiffness	N/m	K_{ti}	3.5×10^6		3.5×10^6	
Moment of Inertia	kg m^2	I_s	26462	35043	61485	81423
Distance of axle *i* to centre of gravity	m	D_i	1.875	2.225	1.875	2.225
Axle hop frequency	Hz	f_{axle1}	10.27	10.27	10.21	10.22

The half-car travels at constant speed, c, over a simply supported Euler-Bernoulli beam which has constant cross section and mass per unit length, μ = 28125 kg/m. It has span L = 15 metres, modulus of elasticity $E = 3.5 \times 10^{10}$ N/m^2, second moment of area J = 0.5273 m^4 and structural damping ξ which varies from 0% to 5%. The first natural frequency of the bridge, $f_{bridge1}$, is 5.66 Hz. Prior knowledge of this frequency is assumed here. In practice this can be obtained using a method described by Yang *et al* (2004), Lin and Yang (2005) and González *et al* (2008).

The simulation of the half-car crossing the beam is described by a system of coupled differential equations and is based on the approach proposed by Frýba (1999). The system of equations is solved using the Wilson-Theta integration scheme (Tedesco *et al*, 1999). The value of θ used is 1.420815.

3. Smooth Road Profile Results

The simulations in this section are performed using the VBI model outlined in Section 2 with a smooth road surface profile. The bridge structural damping is varied in the simulations along with the half-car mass and axle spacing. The exact frequencies of the bridge and half-car given in Section 2 will be compared to the frequencies in the spectra obtained from the vehicle accelerations. The scanning frequency used in all simulations is 8192 Hz.

3.1 Sensitivity of Vehicle Accelerations to Damping

An example of the power spectra of accelerations obtained from the front axle of the half-car as it crosses the 15 metre bridge are shown in Figure 1 for a vehicle velocity of 22m/s, 3.75m axle spacing and 18 tonne GVW. All simulated structural damping levels (0% to 5%) are represented on this figure. A clear peak is visible at 6 Hz which corresponds to the first natural frequency of the bridge, $f_{bridge1}$. The resolution of the acceleration spectrum is ± 0.25 Hz which causes a slight deviation between the spectrum peak and the dashed line representing the bridge frequency. The accuracy of this peak could be improved by driving the vehicle at a lower velocity to increase the number of measurements which would result in a higher frequency resolution.

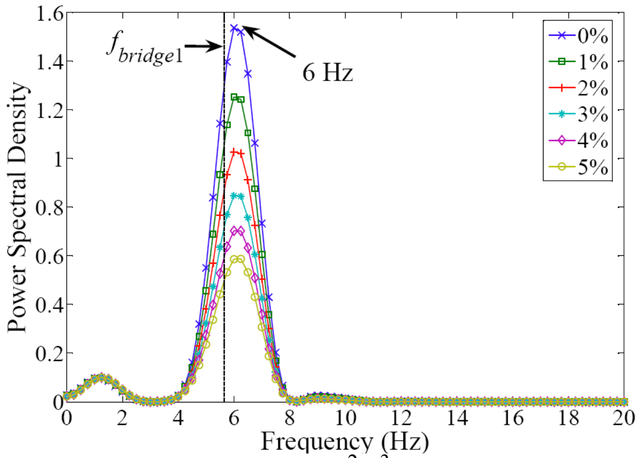

Figure 1 - Acceleration spectra (PSD in m^2/s^3) for front axle of 18 tonne half-car travelling over bridge with smooth road profile.

It can be seen that there is a decrease in Power Spectral Density (PSD) magnitude for increasing structural damping level at this peak. The sensitivity of this decrease to a 1% change in damping is greater for changes between lower levels of damping. For example, in this figure, for a change from 0% to 1% damping, the sensitivity of the PSD is 18.5% and from 1% to 2% the sensitivity is 18%. This sensitivity is obtained by calculating the difference between the PSD peaks and dividing it by the PSD peak magnitude at the lower damping level. This trend remained when other vehicle parameters were investigated.

The peak PSD is very sensitive to a change in damping when the bridge surface is smooth, which suggests that this peak could be used for periodic monitoring of bridge structural damping in these ideal conditions. It should be noted that results are shown for a vehicle velocity of 22m/s (80km/h) which corresponds to highway speeds, i.e. the instrumented vehicle would not cause traffic disruption while monitoring a bridge.

3.2 Effect of Vehicle Mass and Axle Spacing

Vehicle mass and axle spacing have been varied in simulations to investigate their effect on the ability to detect bridge frequency and structural damping from the acceleration spectrum. Results are shown in Figure 2 for a vehicle velocity of 22m/s. Only the spectra of axle accelerations for 2% and 3% damping are plotted, which is representative of the trend occurring for other damping levels. Figure 2(a) illustrates that as vehicle mass increases, the magnitude of the PSD at the bridge peak for a smooth profile increases which would improve sensitivity of the algorithm. Figure 2(b) illustrates that as axle spacing increases, the magnitude of the PSD at the bridge peak decreases which suggests that it is more favourable for the instrumented vehicle to have a shorter axle spacing. However, the relative sensitivities of the PSD peaks to changes in damping do not vary significantly with vehicle mass or axle spacing. For the 18t model with axle spacing of 3.75m, sensitivity between 2% and 3% is 17.5%, for the 9t model the equivalent value is 17.9% and for the 18t model with axle spacing of 4.45m the sensitivity is 17.2%.

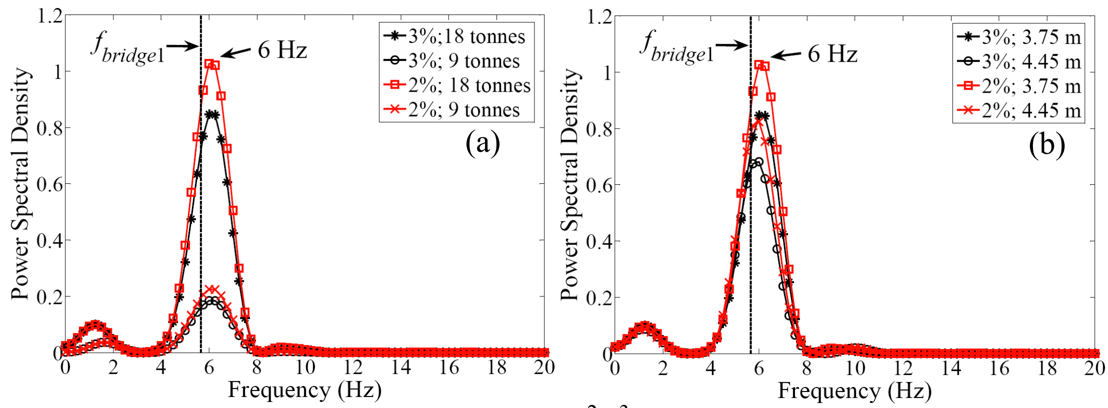

Figure 2 – Acceleration spectra (PSD in m^2/s^3) for front axle of half-car crossing bridge with smooth road profile varying: (a) vehicle mass (axle spacing is 3.75m) and (b) axle spacing (vehicle mass is 18t).

4. Rough Road Profile Results

A rough road profile is now included in the simulations. The road irregularities of this profile are randomly generated according to ISO (1995) for a 'very good' profile or road class 'A'. As for the smooth profile simulations, the structural damping is varied along with the half-car mass and axle spacing. The scanning frequency used in all simulations is 8192 Hz.

4.1 Sensitivity of Vehicle Accelerations to Damping

The spectra of accelerations obtained from the front axle of the half-car during the rough road profile simulation are shown in Figure 3(a) for a vehicle GVW of 18t with axle spacing 3.75m travelling at 22m/s. The resolution of the acceleration spectra is ± 0.25Hz. A large peak is visible in this figure which corresponds to the front axle hop frequency of the half-car, f_{axle1} (Table 1). However, there is no clear peak in the region around the first natural frequency of the 15 metre bridge. Also, it is not possible to distinguish between the different spectra for each damping level at the scale used in the figure. The rough road profile clearly interferes with the ability to detect bridge frequency and changes in structural damping and it governs the dynamic response of the vehicle. Comparing to the PSD magnitudes of Figure 1, the ISO class 'A' road profile produces a dynamic vehicle response which is approximately 200 times larger than the response due to a perfectly smooth road profile.

Despite the influence of the rough road profile and although it would be necessary to zoom into the figure to visualize the differences in PSDs, it is possible to capture changes in damping in the region of the first natural frequency of the bridge ($f_{bridge1}$). Thus, Figure 3(b) shows that by analysing the spectra at a frequency of 6Hz, which corresponds to the bridge peak obtained for a smooth profile in Figure 1, the PSD is still reasonably sensitive to changes in damping with an average sensitivity of 18%. The sensitivity to a 1% change in damping is greater for changes between lower levels of damping, a trend that was also observed in Section 3.1.

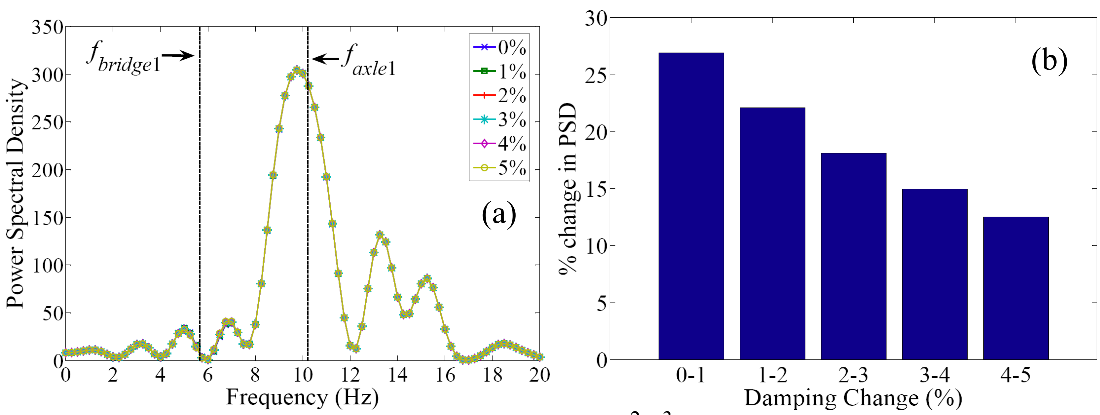

Figure 3 – (a) Acceleration spectra (PSD in m^2/s^3) and (b) Sensitivity of PSD of accelerations for front axle of 18 tonne half-car travelling over bridge with rough road profile.

4.2 Effect of Vehicle Mass and Axle Spacing

The relationships between vehicle mass and axle spacing and peak PSD magnitude in simulations with rough road profile are illustrated in Figure 4 for a vehicle velocity of 22m/s and two damping levels: 2% and 3%. Similarly to the smooth road profile, the peak PSD magnitude increases for increasing vehicle mass (Figure 4(a)). However, Figure 4(b) illustrates that as axle spacing increases the magnitude of the peak PSD for a rough profile does not vary significantly.

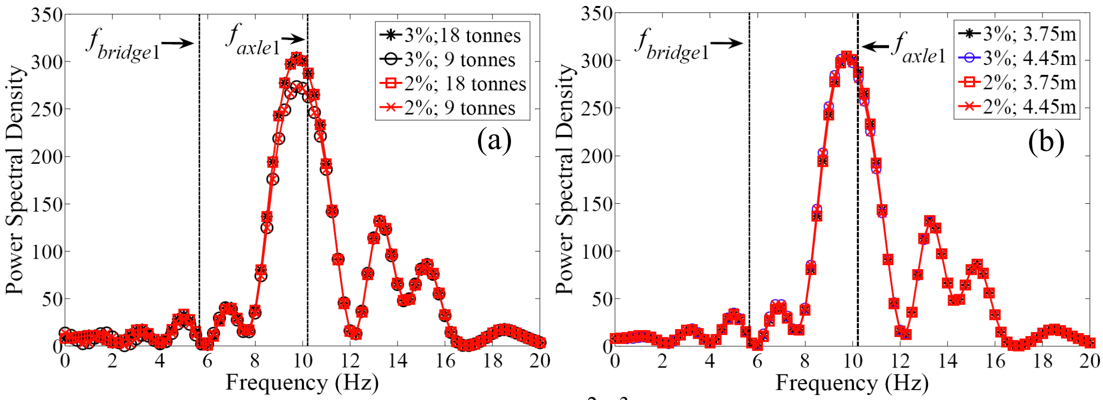

Figure 4 – Acceleration spectra (PSD in m^2/s^3) for front axle of half-car crossing bridge with rough road profile varying (a) vehicle mass (axle spacing is 3.75m) and (b) axle spacing (vehicle mass is 18t).

5. Conclusions

This paper has investigated the use of an instrumented two-axle vehicle to monitor the dynamic parameters of a bridge. The results show that it is possible to detect the bridge frequency from the vehicle vibration for smooth road profiles but it is more difficult to do so with rougher road profiles. This finding is in agreement with past studies. Using a heavier vehicle would increase the bridge deflection and thus increase the bridge influence on the vehicle vibration, improving results for a rough road profile. This paper has shown that the magnitude of PSD at the bridge frequency decreases with increasing bridge damping. This decrease is obtained and quantified easily for a smooth profile due to the presence of a dominant bridge frequency peak. For a rough road profile there is no such bridge peak but by analysing the spectrum in the region of the bridge frequency, changes in PSD exist due to changes in damping. The magnitude of the PSD for an axle of the half-car was found to increase for decreasing axle spacing for a smooth road profile and for increasing vehicle mass. Further study is required for the removal or reduction of the influence of the road profile roughness on the vehicle response to enable the development of an instrumented vehicle as an efficient low-cost method for monitoring bridge dynamic behaviour.

6. Acknowledgements

The authors wish to express their gratitude for the financial support received from the 7th European Framework ASSET Project towards this investigation.

References

Cebon, D. (1999), *Handbook of Vehicle-Road Interaction*, Swets & Zeitlinger, the Netherlands.

Curadelli, R. O., Riera, J. D., Ambrosini, D. and Amani, M. G. (2008), 'Damage detection by means of structural damping identification', *Engineering Structures*, **30**, 3497-3504.

Frýba, L. (1999), *Vibration of Solids and Structures under Moving Loads*, 3rd Edition, Noordhoff International, Groningen, Netherlands.

González, A., Covián, E. and Madera, J. (2008), 'Determination of Bridge Natural Frequencies Using a Moving Vehicle Instrumented with Accelerometers and GPS', *Proceedings of the Ninth International Conference on Computational Structures Technology*, Athens, Greece, paper 281.

González, A., OBrien, E. and McGetrick, P. (2010), 'Detection of Bridge Dynamic Parameters Using an Instrumented Vehicle', *Proceedings of the Fifth World Conference on Structural Control and Monitoring*, Tokyo, Japan.

Harris, N.K., OBrien, E.J. and González, A. (2007), 'Reduction of bridge dynamic amplification through adjustment of vehicle suspension damping', *Journal of Sound and Vibration*, 302, 471-485.

ISO 8608:1995 (1995), 'Mechanical vibration-road surface profiles-reporting of measured data', International Standards Organisation.

Lin, C. W. and Yang, Y. B. (2005), 'Use of a passing vehicle to scan the fundamental bridge frequencies. An experimental verification', *Engineering Structures*, **27**, 1865-1878.

McGetrick, P. J., González, A. and OBrien, E.J. (2009), 'Theoretical investigation of the use of a moving vehicle to identify bridge dynamic parameters', *Insight*, **51**(8), 433-438.

Modena, C., Sonda, D. and Zonta, D. (1999), 'Damage Localization in a Reinforced Concrete Structures by Using Damping Measurements', *Key Engineering Materials*, **167-168**, 132-141.

Tedesco, J.W., McDougal, W.G. and Ross, C.A. (1999), '*Structural Dynamics, Theory and Applications*', Addison-Wesley.

Yang, Y. B., Lin, C. W. and Yau, J. D. (2004), 'Extracting bridge frequencies from the dynamic response of a passing vehicle', *Journal of Sound and Vibration*, **272**, 471-493.

FACTORS AFFECTING TRAFFIC-GENERATED VIBRATIONS ON STRUCTURES AND THE MASONRY MINARET OF LITTLE HAGIA SOPHIA

A. ERKAL[1], D.F. LAEFER[1], P. FANNING[1], E. DURUKAL[2], U. HANCILAR[2] & Y. KAYA[2]
[1] School of Architecture, Landscape, and Civil Engineering, University College Dublin, Ireland
[2] Dept. of Earthquake Engineering, Kandilli Observatory and Earthquake Research Institute, Bogazici University, Istanbul, Turkey

Abstract
Increasingly buildings and their occupants are negatively impacted by traffic–induced vibrations. The continuous application of vibrations is particularly detrimental for historic masonry buildings and for very modern structures constructed of strong and light materials. Population and land development trends indicate greater proximity of traffic flow near buildings in coming years. This paper outlines the factors influencing the frequency content and the magnitude of vibrations on nearby structures in an attempt to enable local communities and their designers to be more proactive in vibration mitigation. Using these described factors, the paper assesses the effects of traffic-induced vibrations on a portion of a monumental masonry building: the minaret of Little Hagia Sophia Mosque (former Byzantine Church of the Saints Sergius and Bacchus) based on adjacent railway field measurements.

Keywords: Dynamic response, human annoyance, Little Hagia Sophia Mosque, masonry structures, minarets, traffic-induced vibrations

1. Introduction

Ground vibrations due to earthquake and blasting have been studied more extensively than other vibration sources such as road and rail since the effects of the former are more dramatic and sudden. However, transport-induced vibrations may damage adjacent buildings, cause human discomfort, and disrupt sensitive equipment and manufacturing, because of their long-term and repetitive nature. Global urbanization has brought unprecedented population densities adjacent to transportation routes, with increasing quantities of road and rail traffic (Figure 1). Although considerable numerical simulations and experimental studies have been conducted to predict the negative effects of these vibrations, the factors affecting the impact of traffic-induced vibrations and their consequences have not been fully categorized. Therefore, this paper aims to address and establish, in a systematic way, the factors influencing the range of frequencies and vibration amplitudes that are most detrimental to existing structures, by evaluating the response of the minaret of Little Hagia Sophia Mosque, because this tall and slender masonry structure is extremely close to a heavily trafficked train line and has not been investigated regarding train-induced vibrations. This will help conserve cultural heritage and assist in devising mitigation for existing disturbances.

2. Factors affecting the impact of transport-induced vibrations

A key component to assessing transport-induced vibrations is understanding under what conditions vibrations reach amplitudes exceeding those thought to disturb building occupants and damage buildings. Peak particle velocity (PPV), the maximum velocity of the wave transmission, is often used as the limiting factor (Table 1).

(a) Istanbul (b) Dublin

Figure 1 - Buildings Immediately adjacent to Transport Routes

Table - 1 Sampling of Published Vibration Threshold Values for Buildings and Occupants

Peak Particle Velocity (mm/sec)	**Effect on Human or Buildings**	**Ref.**
0.3	Perceptible for human	(Wiss 1981)
0.8	Distinctly perceptible for human	(Wiss 1981)
2.5	Strongly perceptible for human	(Wiss 1981)
5	Risk of architectural damage	(Whiffin and Leonard 1971)
10	Vibrations can cause minor structural damage on buildings	(Whiffin and Leonard 1971)

2.1 Factor 1: Vehicle features

Vehicle mass has a significant effect on traffic-induced vibration levels (Papagiannakis and Raveendran 1998). A larger mass leads to larger inertial forces on pavement, thereby producing larger ground-borne vibrations. These are primarily due to heavy vehicles. Vehicle dimensions are also important. For instance, the delay between the passages of each axle influences the frequency of loading and, thus, the frequency content of the ground-borne excitation. Additionally, in-situ measurements have shown that higher amplitude vibrations occur for higher vehicle velocities. Equally, the vibrational characteristics of the vehicle are significant. Jerry et al. (2006) provide the following examples: (1) a steel-leaf, spring suspension system of a truck produces more dynamic forces and vibrations than an air suspension systems; (2) stiff, over-inflated tyres bounce more readily over surface irregularities, thereby resulting in higher dynamic forces; and (3) the braking system and the rate of acceleration and deceleration also contribute to the generation of vibrations.

2.2 Factor 2: Vehicle–road –track interaction characteristics

The road and track surface conditions and their mechanical properties play a crucial role in the ultimate PPV levels. Specifically, flexible pavements absorb more energy than stiff pavements. Pavement roughness caused by cracks, potholes, bumps, and even uneven manhole covers (and similar often uncontrolled features) drive a dynamic response in a passing vehicle and hence contribute significantly to ground vibrations (Figure 2). These surface irregularities cause randomly occurring dynamic forces up to 15% higher than the corresponding static forces (DIVINE 1997). However, periodic and discrete pavement irregularities effects can be even more severe, causing more than an 80% increase in dynamic forces (Jerry et al. 2006). When potholes or bumps are more than 25 mm in depth/height or 150 mm in length these can cause ground peak particle velocities (PPVs) of around 5 mm/second, which is noteworthy as a PPV of 5 mm/sec has been proposed as a limit to prevent architectural damage in houses with plastered walls and ceilings (Whiffin and Leonard 1971). Similarly, since both train rail and wheels can have defects such as corrugation, stiffness variation, joints, and wheel flats, additional dynamic loads can be produced up to 50% of the wheel load (Profillidis 2000).

Figure 2 - Cracks on the Road Surface – Donnybrook, Dublin

2.3 Factor 3: Propagation of waves through soil

While traffic-induced stress waves propagate through soil, the propagation wave characteristics depend significantly on the distance from the source, the soil properties, soil profile and topography, and the adjacent structure characteristics. Vibration amplitude diminishes with distance due to expanding surface and material damping. Material damping is related to soil type, moisture content, and soil temperature (Dowding 1996). For example, dry sand and gravel soils have the highest capability to absorb vibration, while soft clays have the lowest (Watts 1992). There are even cases where the layered soils have caused wave amplification. As an example, Hunaidi and Tremblay (1997) reported that traffic vibrations appear worst in areas underlain by a soft silty clay layer between 7 m and 15 m deep. Furthermore, seasonal variations of the ground water table changes response properties as saturated soil result in lower compressibility and higher density (Schevenels et al. 2004).

2.4 Factor 4: Soil-structure interaction characteristics

While vibrations are transmitted from the ground to a building's foundation, both the foundation type and the soil-structure stiffness interaction play important roles. François et al. (2007) concluded that no building wall deformation occurs, if a building is resting on a soft soil, and the global structural response is dominated by rigid body kinematics. If the soil is stiff with respect to a building, however, the building walls deform in a quasi-static way, following the ground motion. Additionally, the presence of a (stiff) foundation prevents the transfer of energy into the structural system. Therefore, wall cracking caused by excessive deformations is more likely to occur when a soft structure rests on a stiff soil.

2.5 Factor 5: Structure features

If traffic-induced vibration frequencies are similar to those of a building's natural frequencies, resonance occurs (Hunaidi et al. 2000). In such cases, vibration reduction can be achieved by judicious stiffening of the structure for a particular vibration mode. For resonant excitation, the most critical case is excitation of the first natural frequency of the building (Ju 2009) – then, unfortunately, structural interventions to alleviate vibration response can be hampered due to the global response of the structure in its first mode of vibration. However it is usually the frequencies of the higher modes of vibration of structures that tend to coincide with the principal frequencies of traffic-induced ground motions. In particular, as buildings become taller, higher modes for individual floor levels are more likely to be excited by adjacent vibrations. Furthermore, when the modal mass participating ratios are sufficiently large at higher modes, significant amplification of vibration response is possible (Erkal et al. 2010a).

3. Case Study: Minaret of Little Hagia Sophia

To understand how these factors converge, a case study is presented. Minaret response to vibrations is a well-established concern, especially in seismic zones (Gentile and Saisi 2007). There have been a number of studies including El-Attar et. al's (2005) work on the potential benefits of base-isolation for reducing the seismic vulnerability of Mamluk-style minarets and Dogangun et. al's (2008) analysis on three masonry minarets of varying heights using two earthquake ground motions. They suggested fibre reinforced polymer composite wraps or reinforcement for retrofitting based on numerical investigation of dynamic behaviour and response. However, adjacent transport-induced vibration impacts on minaret structures remains unexplored. Here, the minaret of Little Hagia Sophia Mosque is assessed in relation to train traffic due to its extreme proximity to the railway (Erkal et al. 2010b, Yuzugullu and Durukal 1994).

A vibration measurement program was performed on the masonry structure Little Hagia Sophia Mosque located in the district of Eminonu in Istanbul, adjacent to the Sirkeci-Halkalı railway line. The mosque, formerly the Church of the Saints Sergius and Bacchus, was built in the period 527-536, AD, as a model for the Hagia Sophia. During the Ottoman Empire (1506-1513) it was converted into a mosque. In 1762 a minaret was first built but demolished in 1936. The current minaret was built in 1955. The height and slenderness of a minaret makes it particularly vulnerable to ground movements (Figure 3). This minaret of cut stone is only 10.5 m from the heavy railway line (north-south direction) as shown in Figure 4 in plan view with the mosque and minaret, and the instrumentation.

The instruments were placed equi-distantly along the minaret's height up to the minaret balcony (Figure 4-b). Seismographs are labeled as A-D, and the preceding number indicates the test no [e.g. 10A means instrument A in Test 10]; the other tests were conducted elsewhere on the property. Three perpendicular components of ground motions (east-west, north-south, and vertical) from four trains were measured. Four ultra-lightweight, digital output seismometers (CMG-6TD) were used. The seismometers are ideally suited for sites where there is medium level of background vibrations. Owing to the possible high stiffness of the masonry buildings and high frequency nature of vibrations, sampling rate was assigned at 500 samples per second to allow a broad range analysis; 2.5 times greater than the value chosen in the study of ambient vibration testing of a masonry bell-tower (Gentile and Saisi 2007).

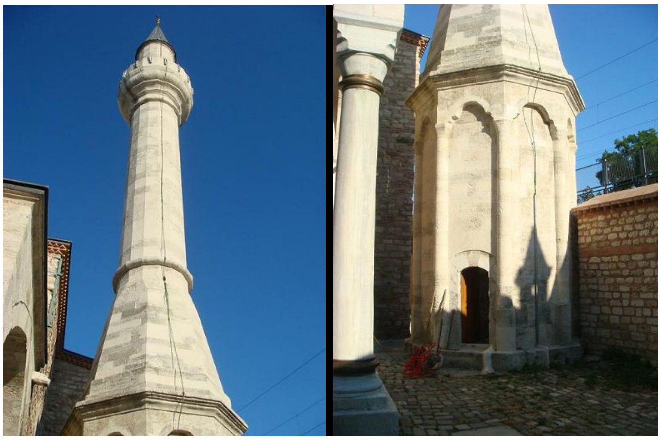

Figure 3 - Minaret as a Single Structure next to the Mosque

Regarding loading, 118 suburban and 6 intercity passenger trains in addition to 2 freight trains pass by the minaret (1 approximately every 10 minutes) daily (TCDD 2010). These transport 65,000-75,000 people using trains of 6 cars – 2 of which are locomotives, which pull from either end depending upon journey direction.

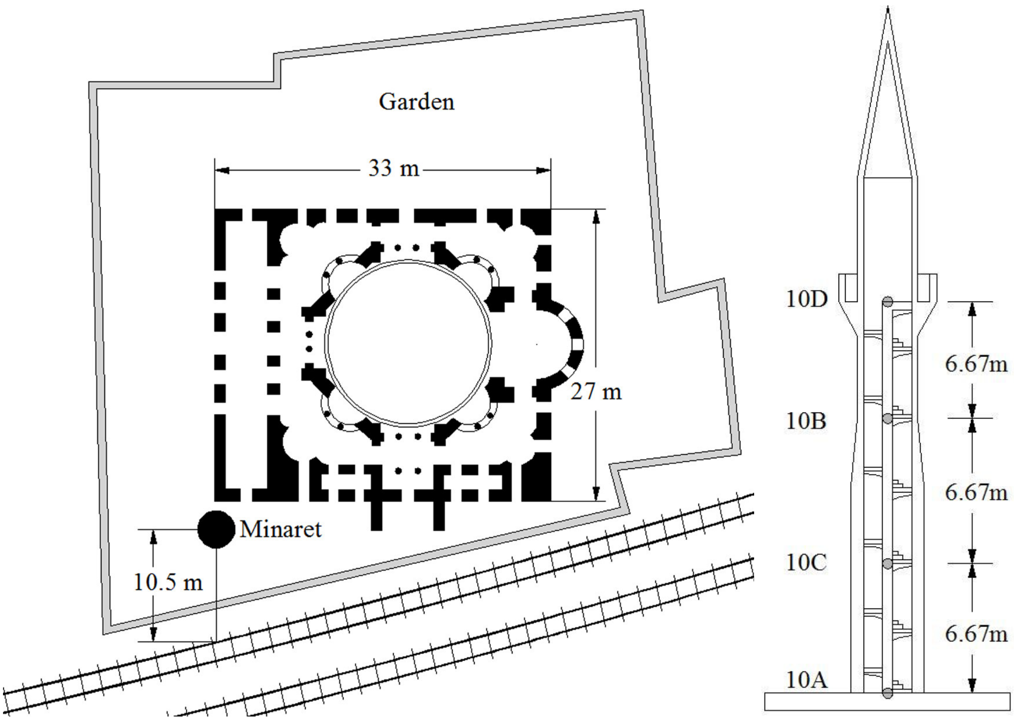

a) Mosque and minaret proximity to the railway b) Instrumentation

Figure 4 - Plan View and Profile of the Minaret

4. Discussion of the factors considering the minaret

Since most codes and studies rely on a PPV to evaluate the severity of traffic-induced vibrations, PPVs, were measured at four points of the minaret (Figure 5). Although the PPVs were not sufficiently large to generate severe structural damage, in some cases, the vibration levels exceeded the lowest damage PPV threshold found in literature (1mm/sec) (Domenichini et al. 1998), although this is exceptionally low compared to most of what is reported in the literature. Most of the PPV values were larger than 0.3mm/sec as being perceptible to human body (ISO 1989), and some of them larger than 0.8mm/sec as distinctly perceptible (Wiss 1981). Vibration levels were as high as 1.25mm/sec at the balcony level in the north-south direction (Figure 5).

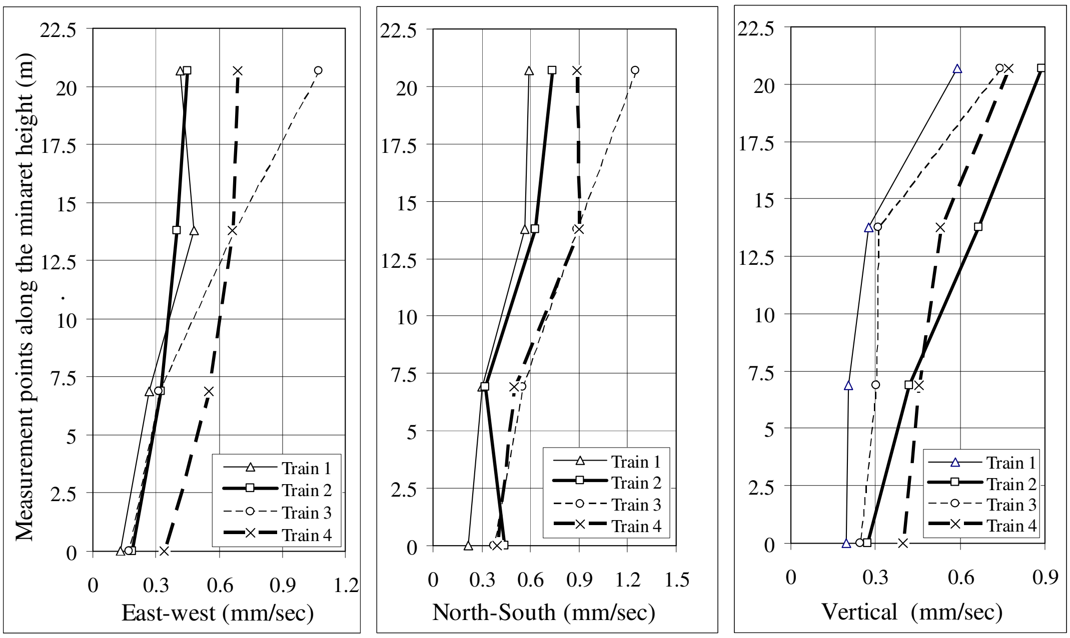

Figure 5 - PPV Vibration Levels along the Height of the Minaret

Regarding vehicle and rail features, the train weighs 3,200kN (carriage axle weight: 140kN and 4-axle locomotives weight: 160kN). Axle weight for freight train locomotives is 200 kN, which could be critical, as Celebi (2006) also mentions that the increase in passenger transport at high speeds, with heavy-loaded trains or giant lorries will cause strong ground and structural vibrations in intensively populated urban areas. This type of vibration in the frequency range of 4–50 Hz may cause some structures to resonate with their vibrating modes. In the study reported herein, train velocities spanned 70-90km/h, similarly to that reported by Xia et al. (2005), who noted that when train speed increased from 60km/h to 80km/h, maximum ground level vibration increased by 23%.

In relation to soil and soil-structure interaction features, the site's clay and marl of the early pliocene period is cohesive and composed of fine particles. The soil is very heterogeneous and heavily layered. A pit excavation beside the minaret showed the top 90 cm to be new fill with plant residue, silt, brick rubble, and bone. Beneath that was old fill with 20-30% of gravelled greyish limestone covered with clay-marl lithology and many coal and glass pieces to a depth of 2 m [Arun and Akoz 2003].

In terms of structural features, although the largest PPV values mostly occur at the higher levels, the response is not uniformly greater with height (Figure 5). This is attributable to the fact that the principal excitation frequencies associated with traffic activity are likely to be higher than the lowest natural frequencies associated with the minaret. In other words, contrubution of higher modes to the overall response of the minaret is significant. A similar observation was made by Dogangun et al. (2008), in the analysis of 3 masonry minarets (20, 25, and 30m in height). Based on modal analysis, they reported that the contribution of higher mode effects to total dynamic response was significant. Additionally, modal and time history analyses of the minarets have shown that the structural periods and the overall structural response are influenced by the minaret height and spectral characteristics of the input motion.

Conclusions and future work

Five factors influencing the transport-induced vibration characteristics on nearby structures have been explained and discussed in a systematic way in relation to a vibration-susceptible masonry tower structure - the minaret of Little Hagia Sophia Mosque in an attempt to enable communities to be more proactive in vibration mitigation. Current practice in building vibration assessment, due to traffic loading, is guided by a single threshold value. Therefore, there is an urgent need for further research to establish a parametric set of quantified input variables and to directly relate those to the five areas outlined in this paper. Such knowledge would allow a change in codes to mitigate the impact of traffic-induced vibrations in the design stage and to effective remedy methods for existing structures. Future work will include the finite element modelling and evaluation of vulnerable structures to traffic-induced vibrations for further comparison with field measurements.

Acknowledgments

Financial support from Enterprise Ireland (PC/2008/337) is greatfully acknowledged. We also thank the Earthquake Engineering Department in Bogazici University, Istanbul, and the tecnicians Mr Ahmet Korkmaz and Mr Nafiz Kafadar and to Prof. Dr. Zerrin Bayrakdar, Prof. Dr. Fevziye Akoz, Prof. Dr. Gorun Arun in Yildiz Technical University, Istanbul for information provided. Additionally, the General Directorate of the Foundations of Turkey is acknowledged.

References

Arun, G. and Aköz, F. (2003), 'Diagnostic Studies on Küçük Ayasofya Mosque – The Church of Sts Sergius and Bacchus', *International Conference on Construction*, Cluj, Romanya, 1-9.

Celebi, E., (2006), 'Three-dimensional modelling of train-track and sub-soil analysis for surface vibrations due to moving loads', *Applied Mathematics and Computation*, 179, 209-230.

DIVINE Programme, OECD, Dynamic Interaction of Heavy Vehicles with Roads and Bridges. DIVINE Concluding Conference, 1997, Ottawa, Canada.

Dogangun, A., Acar, R., Sezen, H. and Livaoglu, R. (2008), 'Investigation of dynamic response of masonry minaret structures', *Bulletin of Earthquake Engineering*, **6** (3) 505-517.

Domenichini, L., Crispino, M., D'apuzzo, M. and Ferro, R. (1998), ‘Road Traffic Induced Noise and Vibration’, *Proceedings of the XXIII PIARC Road National Conference*, Italy, 69-118.

Dowding, C.H. (1996) *Construction Vibrations*. Prentice-Hall, Inc.

El-Attar, A.G., Saleh, A.M. and Zaghw, A.H. (2005), ‘Conservation of a slender historical Mamluk-style minaret by passive control techniques’, *Structural Control and Health Monitoring*, **12** (2) 157-177.

Erkal, A., Laefer, D., and Fanning, P. (2010a), ‘Analyses and evaluation of building response to traffic-induced vibrations and related human disturbance’. *The Transportation Research Board 89th Annual Meeting*, Washington, D.C.,, Jan., 10-14.

Erkal, A., Laefer D., Fanning, P., Durukal, E., Hancilar, U. and Kaya, Y., (2010b in press) “Investigation of the Rail-induced Vibrations on a Masonry Historical Building” *SAHC-2010 Conference*, October 6-8, 2010, Shanghai, China.

François, S., Pyl, L., Masoumi, H.R., and Degrande, G. (2007), ‘The Influence of Dynamic Soil-structure Interaction on Traffic Induced Vibrations in Buildings’, *Soil Dynamics and Earthquake Engineering*, **27** (7) 655-674.

Gentile, C. and Saisi, A. (2007), ‘Ambient vibration testing of historic masonry towers for structural identification and damage assessment’, Construction and Building Materials, 21, 1311-1321.

Hunaidi, O., Guan, W. and Nicks, J. (2000), ‘Building Vibrations and Dynamic Pavement Loads Induced by Transit Busses.’ *Soil Dynamics and Earthquake Engineering*, **19** (6) 435-453.

Hunaidi, O., and Tremblay, M. (1997), ‘Traffic-induced Building Vibrations in Montreal’, *Canadian Journal of Civil Engineering*, **24** (5) 736-753.

International Standard Organization (ISO), (1989) Standard 2631-2, ‘Evaluation of human exposure to whole-body vibration Part 2: Continuous and shock-induced vibration in buildings (1-80 Hz).’

Jerry, J.H., Blaney, C.T. and Hein, D.K. (2006), ‘Mitigation of Highway Traffic-Induced Vibration’, *Annual Conference of the Transportation Association of Canada Charlottetown,* 1-13.

Ju, S.H. (2009), ‘Finite Element Investigation of Traffic Induced Vibrations’, *Journal of Sound and Vibration*, **321** (3-5) 837-853.

Papagiannakis, A.T., and Raveendran, B. (1998), ‘International Standards Organization-Compatible Index for Pavement Roughness’, *Transportation Research Record: Journal of the Transportation Research Board*, (1643) 110-115.

Profillidis, V.A. (2000), *Railway Engineering*, Aldershot Ashgate.

Schevenels, M., Degrande, G. and Lombaert, G. (2004), ‘The Influence of the Depth of the Ground Water Table on Free Field Road Traffic-induced Vibrations’, *International Journal for Numerical and Analytical Methods in Geomechanics*, **28** (5) 395-419.

TCDD, Turkiye Cumhuriyeti Devlet Demiryollari (2010), Railway Organization of Republic of Turkey, http://www.tcdd.gov.tr/

Watts, G.R. (1992), ‘The Generation and propagation of vibration in various soils produced by the dynamic loading of road pavements’, *Journal of Sound and Vibration*, **156** (2) 191-206.

Whiffin, A. C. and Leonard, D. R. (1971) *A Survey of Traffic-induced Vibrations*. Report, LR 418, Transport and Road Research Laboratory, UK. Department of Environment.

Wiss, J.F. (1981), 'Construction Vibrations: State-of-the-art.', *Journal of the Geotechnical Engineering Division, Proceedings of American Society of Civil Engineers*, **107**, (No. GT2), 167-181.

Xia, H., Zhang, N. and Cao, Y.M. (2005), 'Experimental study of train-induced vibrations of environments and buildings' *Journal of Sound and Vibration*, **280**, (No. 3-5), 1017-1029.

Yuzugullu, O. and Durukal, E. (1994), 'The Effects on Train Traffic on Küçük Ayasofya Mosque', *Proc. of the Int. Conf. on Studies in Ancient Structures*, İstanbul, Turkey, 1-40.

USING MEAN DYNAMIC FORCE PATTERNS IN CALCULATIONS OF REMAINING PAVEMENT LIFE

EUGENE O'BRIEN & ABDOLRAHIM TAHERI HOSSEINKHANI
University College Dublin

Abstract
A road develops permanent deformation or fatigue damage because of the stress and strain induced in its structure by surface loading and environmental change. Dynamic tyre forces generated by the vibration of moving heavy vehicles excited by road surface profiles are heavily influenced by vehicle speed, road roughness and vehicle properties. The traditional approach to pavement life assessment considers all axle weights that are anticipated and calculates the number of equivalent axles of standard weight. It takes no account of dynamic oscillation of axle forces about the static weight. A mechanistic-empirical approach is implemented here to simulate the deterioration of a pavement**.** Statistical Spatial Repeatability (SSR) is of great importance in road pavement design and assessment. This paper highlights the importance of spatial repeatability and statistical spatial repeatability in the damage evolution during the pavement life.

Keywords: Pavement Design, Statistical Spatial Repeatability, Truck Fleet Model.

1. Introduction and Context

Pavements deteriorate in response to forces applied by passing vehicles and as a result of environmental effects. The traditional approach to pavement life assessment considers all axle weights that are anticipated and calculates the number of equivalent axles of standard weight. It takes no account of dynamic oscillation of axle forces about the static weight. More significantly, the traditional approach to pavement assessment does not account for 'spatial repeatability', the fact that the mean pattern of dynamic forces applied by a fleet of trucks to a pavement, is repeatable. Many researchers (Hahn, 1985; Cole and Cebon 1992; Collop 1994; O'Connor et al. 2000) have presented evidence showing that for a given speed, the dynamic wheel force time histories generated by a particular heavy vehicle are concentrated and repeated at specific locations along the road for repeated test runs. Hahn (1985) suggests that because a large proportion of heavy vehicles tend to have similar geometry and dynamic characteristics, and tend to travel at a similar speed, spatial repeatability of pavement loading may be expected in normal traffic flow. Potter et al. (1994) show the 'road damaging' ability of vehicles by spatial repeatability**.** O'Connor et al. (2000) show that individual patterns of force are not repeatable for similar vehicles at similar speed but that the mean of many force patterns are repeatable.

A mechanistic-empirical approach is implemented here to simulate the deterioration of a pavement**.** This framework, illustrated in Figure 1 (Collop and Cebon 1995), may include a dynamic vehicle/pavement interaction calculation to find the pattern of forces applied to the pavement. This is combined with a material response model to find the resulting stresses. These in turn are used to calculate pavement damage in the form of permanent deformation and loss of stiffness through fatigue. The permanent deformation (rutting) influences the vehicle/pavement dynamic interaction and a feedback loop is necessary to update the profile and recalculate the pattern of applied forces.

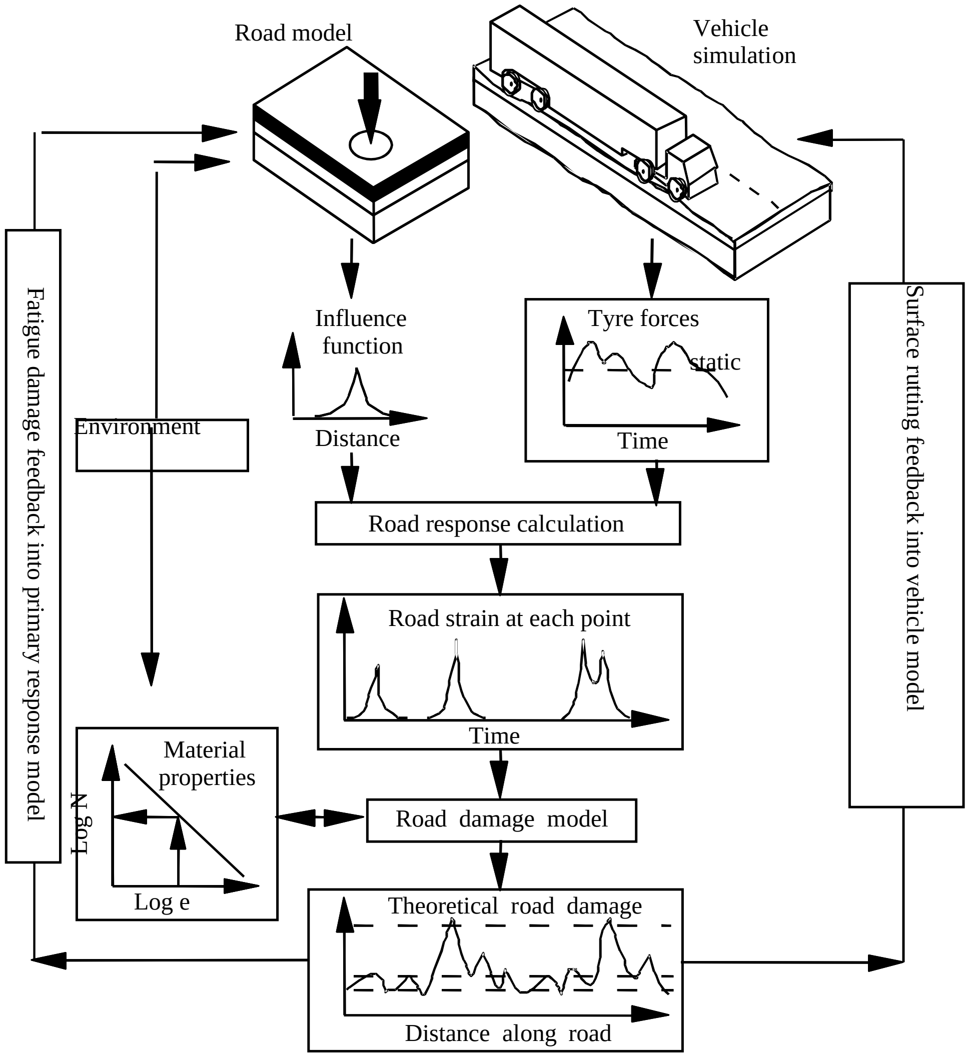

Figure 1 - Long-term pavement performance framework (Collop and Cebon 1995)

2. Statistical Spatial Repeatability

The vehicle/pavement dynamic interaction model, illustrated in Figure 2 for a quarter car (QC), is in effect a system of coupled differential equations. The differential equations describing the motion of the two-degree-of-freedom QC system are:

$$m_s \ddot{y}_u = k_s(y_u - y_s) + c_s(\dot{y}_u - \dot{y}_s) \tag{1}$$

$$m_u \ddot{y}_u = -k_s(y_u - y_s) - c_s(\ddot{y}_u - \ddot{y}_s) + k_t(y_r - y_u) \tag{2}$$

In this model, the unsprung mass (representing the mass of the wheels and axle) and

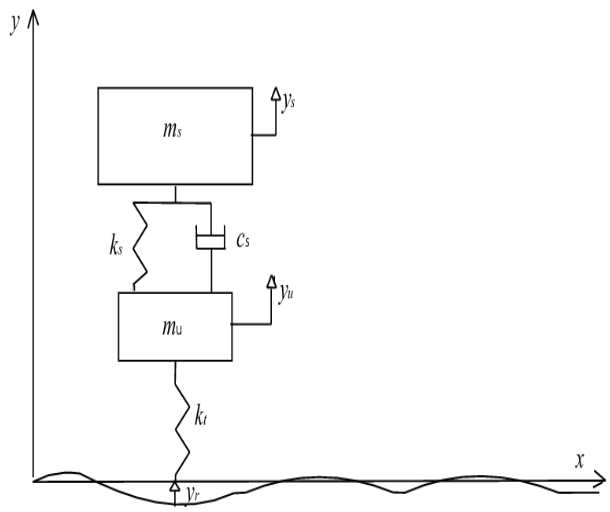

Figure 2 - Quarter car model of vehicle axle

sprung mass (representing part of the mass of the vehicle body) are denoted as mu and m_s respectively. The suspension system is represented by a linear spring of stiffness k_s and a linear damper c_s, while the tyre is modelled by a linear spring of stiffness k_t. The terms, $\dot{y}_u$, $\dot{y}_s$, $\ddot{y}_u$, $\ddot{y}_s$ are the corresponding velocities and accelerations.

The problem is complicated by the fact that there is significant variation in the vehicle fleet between the five parameters shown in Figure 2. To adequately address the problem of pavement damage in response to load, these five parameters need to be treated as random variables.

Figure 3 illustrates the average of 3 separate groups of 1000 wheel forces measured on a pavement in the Netherlands. The three patterns are similar, clearly illustrating what has been referred to as ‘statistical spatial repeatability’ (SSR) (O'Connor & E. O'Brien & B. Jacob, 2000), i.e., the repeatability of *mean* patterns of force applied by a fleet of vehicles. In Figure 3 it can be seen for example that the mean applied force is greater at 9 m than it is at 19 m. It can be inferred that the former point will be more damaged than the latter, unless/until the SSR pattern changes.

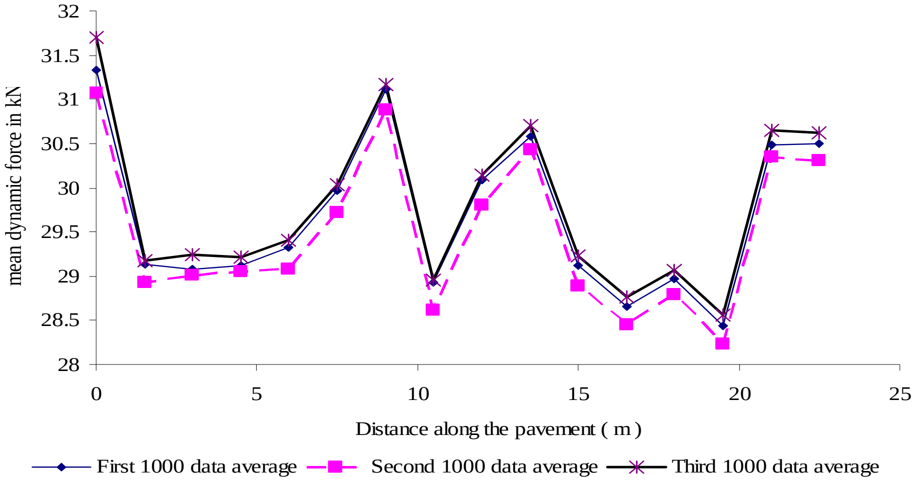

Figure 3 - Patterns of statistical spatial repeatability for third wheel taken from a fleet of five axle vehicles (data courtesy of DVS)

Statistical Spatial Repeatability arises from the fact that, while every wheel passing the road is different, there are similarities between them and, when results are averaged over a large number such as a thousand wheels, the road profile induces a similar mean pattern of motion and applied force. While it is computationally demanding, this process can be reproduced in numerical simulations.

Monte Carlo simulation is a numerical method of generating 'typical' combinations of parameters given the statistical distributions of each parameter. For the pavement damage problem, Monte Carlo simulation is used to generate millions of combinations of parameters for the quarter car and hence to calculate millions of patterns of applied (static + dynamic) force.

3. Pavement Damage Model

The procedure shown in Figure 1 can be divided into four main areas: Dynamic Vehicle simulation; Pavement primary response calculation; Pavement damage calculation and Damage feedback mechanism. The inputs to the model are:

(i) the details of the pavement being simulated (layer thicknesses, mix specifications etc);
(ii) the time increments to be used in the simulations;
(iii) the traffic loading and
(iv) the climatic conditions.

From these initial specifications, a length of pavement surface profile is divided along its length into many equally spaced sub-sections. A time domain vehicle simulation is used to generate dynamic tyre forces for vehicles as a function of distance. A set of primary response 'influence functions' is generated, for each pavement sub-section and each mode of damage, here using the simplified Method of Equivalent Thickness (Ullidtz and Larsen, 1983). The modes of damage that are included in the model are structural rutting and fatigue damage to the asphalt layers. These primary response influence functions are combined with the dynamic tyre forces, to give primary pavement response patterns, evaluated at a large number of equally spaced discrete points along the pavement. The primary responses are combined with the appropriate pavement damage models and the number of load applications, to predict damage (rutting and fatigue damage) as a function of distance along the pavement at any given time. An updated surface profile is then generated by subtracting the calculated rutting in the wheel path from the original profile used for that time increment. This mechanism accounts for the effects of changing surface profile on the pattern of statistical spatial repeatability and hence the pattern of mean dynamic tyre forces. The calculated fatigue damage is represented by reducing the elastic modulus of the asphaltic material for each sub-section. This mechanism reflects the effects of cumulative fatigue damage on the primary responses and hence subsequent pavement damage. The above process is then repeated for the next time increment, and so on, until the pavement has reached the end of its serviceable life.

In this paper, a quarter car model is used, with Monte Carlo simulation, to simulate patterns of dynamic force on the pavement.

4. Results

The quarter car model is used, with the pavement damage model described above, to demonstrate the way in which a typical pavement responds to millions of cycles of load. In this model, Monte Carlo simulation is used to reproduce the variation in the vehicle fleet dynamic properties (represented here with just 5 properties as illustrated in Figure 2) and hence the variation in patterns of applied force as each axle passes. Despite great variation between individual patterns of applied force, SSR means that there is a consistency in the *mean* patterns. To illustrate the evolving pattern of mean forces, this approach is applied to an initial road profile that is perfectly smooth except for a pothole that is 2.5 mm deep and extends over a length of 3 m as illustrated in Figure 4.

Figure 4(c) shows that even such a tiny pothole excites the dynamics of the quarter car. It has an initial (static) weight of 100 kN to represent a heavy axle. The dynamic forces oscillate considerably about this static weight – by more than 30% at one stage. Figure 4(b) shows how the road profile changes during the pavement life in response to the mean pattern of applied force. After 34 million passes, most of the profile has undergone a permanent deformation of almost 10 mm. However, deformations of double this amount have occurred in the pothole due to the high mean forces there. For a fixed set of properties (mass, stiffness, etc.), there are two natural frequencies in the quarter car model. In this simulation, each property is varying according to an assumed Normal distribution. Two mean frequencies can be seen in Figure 4, corresponding to mean axle hop (high frequency) and mean body bounce (low frequency) of the fleet. The axle hop is of high amplitude but its influence is local. The body bounce is of lower amplitude but its influence is more long lasting.

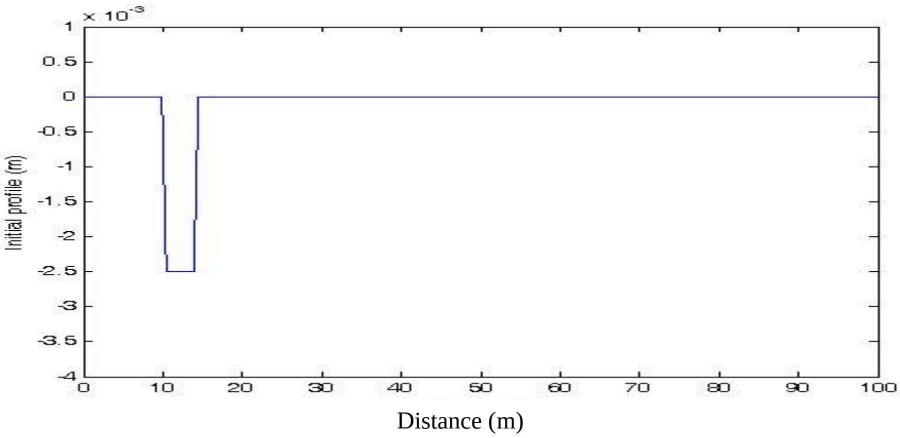

(a) Initial pothole profile

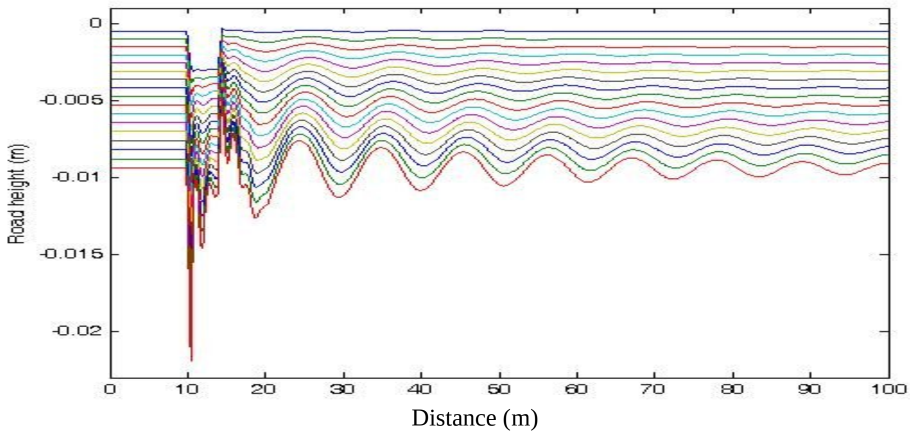

(b) Evolving surface profile due to damage

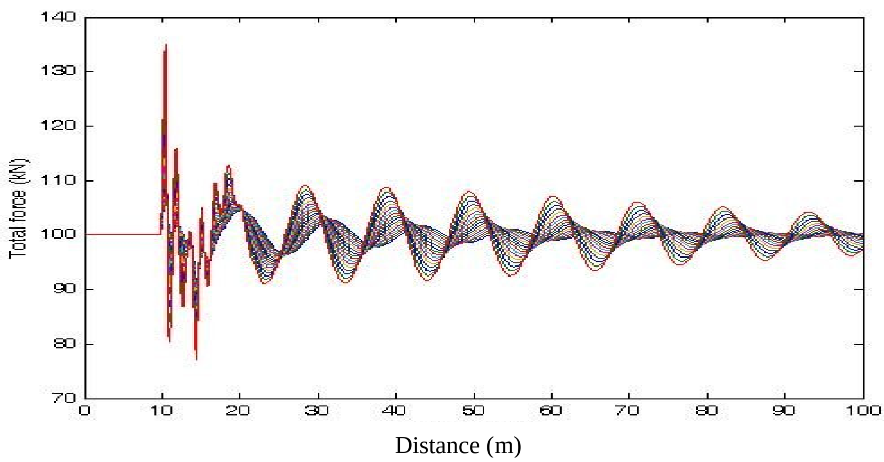

(c) Evolving of the Mean Applied Force Due to Damage

Figure 4 - Simulated evolution of pothole pavement profile and pattern of mean applied force throughout pavement life (every 2 million axles)

Figure 5 illustrates the evolving road surface profile and patterns of applied force for a randomly generated initial road profile of Class A (according to the ISO standard). Figure 5(a) illustrates how the road surface profile changes during the pavement life and Figure 5(b) shows the corresponding changes in the mean patterns of applied force. It can be seen that the profile undergoes permanent deformation at certain points (e.g., around 58.75 m) which results from a peak in mean force at that point. It is particularly interesting how both the road profile and the resulting pattern of forces change during the pavement life. For example, in the initial pattern of mean forces, there is no peak at 51 m; this develops later in its lifetime. The peaks in force come from the dynamic oscillation of the vehicle. They are therefore induced by a combination of the profile at a given time and the dynamic properties (including mean natural frequencies) of the QC vehicle.

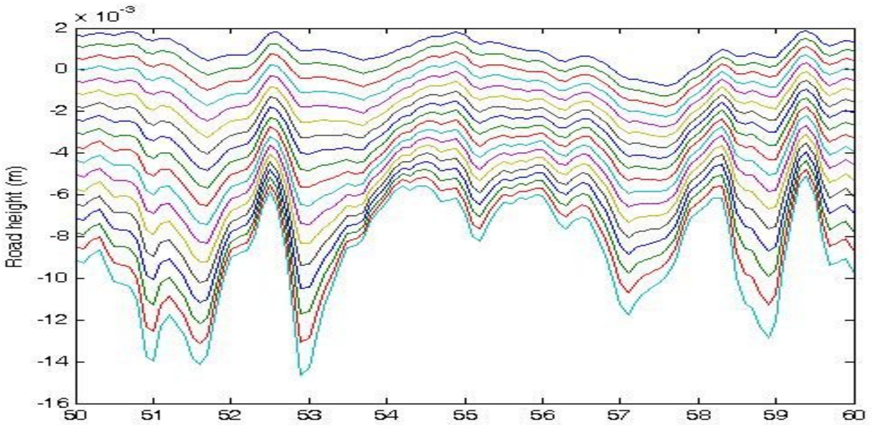

Distance (m)

(a) Evolving surface profile due to damage

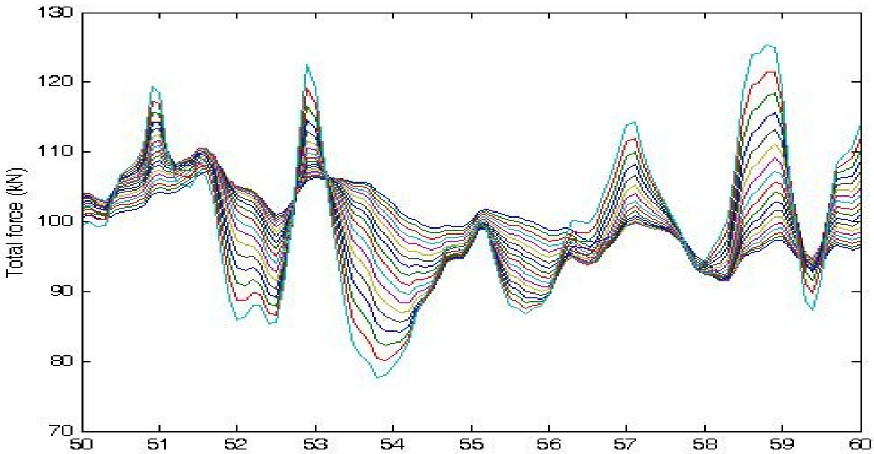

Distance (m)

(b) Mean total (static + dynamic) force patterns

Figure 5 - Simulated evolution of pavement surface and pattern of mean applied force for segment of pavement throughout pavement life (every 2 million axles)

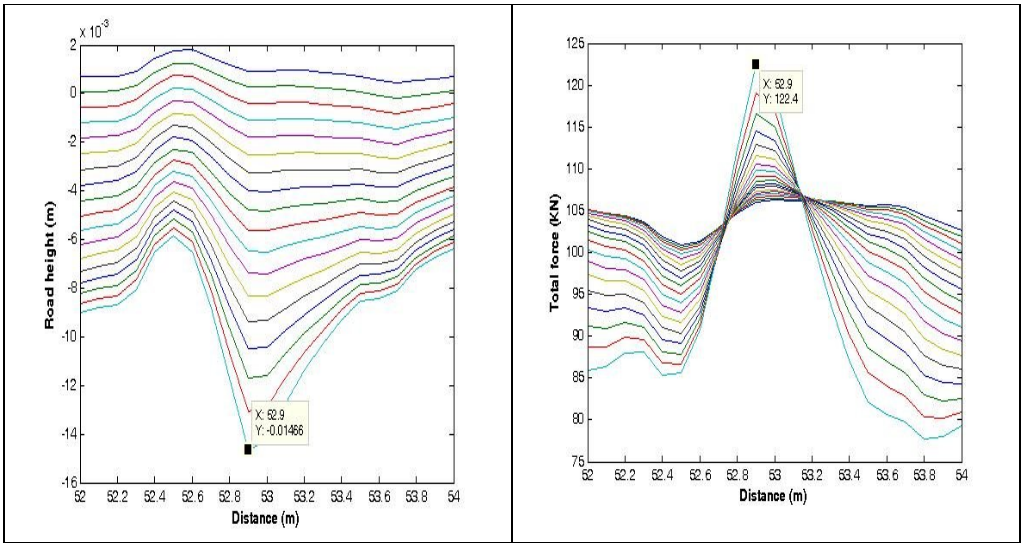

Figure 6 –Force and relating damage at x=52.9 m

5. Conclusions

This paper presents a mechanistic-empirical framework of pavement damage in response to applied forces. It highlights the importance of spatial repeatability and statistical spatial repeatability in the damage evolution during the pavement life. A simple pothole example shows that two vehicle fleet mean frequencies play an important role in pavement damage. For a more general profile, the process is not as clear cut but it can be seen that statistical spatial repeatability still plays a key role in the pavement damage process and should not be ignored in a pavement damage model. It is clear that the process of calculating many millions of dynamic responses is computationally very demanding.The above-mentioned method gives a fundamental concept to predict the road damage evolution using mean dynamic force pattern that saves a lot of computational time with significant accuracy.

References

Collop A.C. and Cebon D., (1995). ‘Parametric study of factors affecting flexible-pavement performance.’ *Journal of Transportation Engineering*, 485–494.

D.J. Cole, D. Cebon, (1992). ‘Spatial repeatability of dynamic tyre forces generated by heavy Vehicles’ , *Proc. Instn Mech. Engrs*, Part D, 206(D1), 17-27.

Hahn W.D., (1985). ‘*Effects of Commercial vehicle design on road stress-vehicle research result*’. Institut fur Kruftfahrwesen, University Hanover (Translated by TRRL as WP/V ED/87/38).

Potter, T.,E., C. , Collop, A., C., Cole D.,J., and Cebon D., (1994). ‘*A mat Tests: Results and Analysis*’. CUED/C-MECH/TR 61, University of Cambridge.

T. O’Connor, E.J. OBrien, and B. Jacob, (2000). ‘An Experimental Investigation of Spatial Repeatability’, *Heavy Vehicles Systems, International Journal of Vehicle Design*, Vol. 7, No.1. 64-81.

Ullitz P., Larsen B.K.,(1983).‘*Mathematical model for predicting pavement performance.*’ Transportation Research Board, Record no 949, pp 45-55, Washington D.C., U.S.A.

DETECTING DAMAGE IN A BEAM SUBJECT TO A MOVING LOAD USING LOCALISED VARIATION IN VIBRATION RESPONSE

D.HESTER[1] & A.GONZÁLEZ [2]

[1]School of Architecture Landscape and Civil Engineering, University College Dublin & O'Connor Sutton Cronin & Associates Ltd, 9 Prussia St, Dublin 7
[2]School of Architecture Landscape and Civil Engineering, University College Dublin

Abstract
There is a growing amount of research being carried out in the field of Structural Health Monitoring and in this context a number of authors have investigated ways of detecting damage in a beam by analysing its response to the passage of a moving load. The displacement response is typically used in investigations of damage detection using the response to a moving load, but in this paper the possibility of using the acceleration signal, relatively easier to measure on site, is examined. The starting point of the investigation was to compare the acceleration signals from healthy and damaged beams using numerical models. It is shown that in addition to the well understood changes in amplitude and frequency that occur when there is damage in the beam, there is a small discontinuity in the acceleration signal as the load passes over the damaged section. This discontinuity is not present in the acceleration signals of healthy beams so if it can be recognized in an acceleration signal it can be employed to identify damage. The difficulty is that the discontinuity is very small relative to the dynamic oscillations in the signal, however it is shown how the correct application of a moving average filter facilitates the identification of the damage location.

Keywords: Acceleration, bridge, damage detection, moving load

1. Introduction

The process of identifying damage in civil and mechanical engineering structures is referred to as Structural Health Monitoring (SHM). The past 10 years has seen a growing number of papers published in the area of SHM. This increased research is motivated by the potential for significant economic savings if the service life of existing structures can be maximized. Farrar and Woden (2007) give an overview of the whole area of SHM and they highlight that vibration-based damage assessment of bridges and buildings has been studied in the field of civil engineering since the early 1980's. Doebling (1996) gives a detailed review of vibration based condition monitoring. He also describes how the fundamental principle involved in all vibration based damage identification techniques is that the modal parameters (such as frequency and mode shapes) are determined by the physical properties of the structure (such as stiffness, mass and damping), therefore any changes in the physical properties of the structure will cause detectable changes in the modal properties.

This paper is focused on the specific case of detecting damage in a beam by analysing its response to the passage of a moving load. A number of authors have tackled this challenge in different ways. For example, Zhu and Law (2006) show that if the mid-span displacement is recorded as a load passes over a beam, the continuous wavelet transform of this record can be used to determine the position of the damage. Zhang (2009) reached similar conclusions by analysing the displacement response to a moving load using wavelet packet analysis. Liu (2007) records the response of the beam to a moving load and uses displacement readings to calculate modal curvatures, which are then used to indicate damage. All of these techniques work by identifying a local discontinuity in the displacement response that is present due to a localised loss of stiffness in the vicinity of the crack, (in this paper the term discontinuity is used to refer to a localised bump in the pattern of the signal due to the presence of damage). The difficulty with using displacement signals is that they are difficult to record to the required level of accuracy at high scanning frequencies in the field. Therefore in this paper the possibility of using the acceleration response is investigated. To successfully detect damage in an acceleration signal it is necessary to appreciate what effect damage has on the acceleration signal of the structure. A finite element model of a simply supported beam subject to a moving load is used to generate acceleration signals and to establish the fundamental differences between healthy and damaged acceleration signals that a damage detection technique should seek.

2. Mathematical Model of System

Damping is assumed to be small and not to affect the response in forced vibration significantly, so it is not considered in the simulations. The dynamic response of a discretized bridge beam model with negligible damping subject to a moving load is solved using the second order matrix differential equation given in Equation 1.

$$[\mathrm{M}]\left\{\frac{\mathrm{d}^2\mathrm{y(t)}}{\mathrm{dt}^2}\right\} + [\mathrm{K}]\{\mathrm{y(t)}\} = \{\mathrm{F(t)}\} \qquad (1)$$

where y is the vector of nodal displacements and rotations, [M] is the consistent global mass matrix, [K] is the global stiffness matrix and {F(t)} is the vector of applied forces. The first step is to populate the global stiffness and mass matrices for the bridge. The elementary stiffness and mass matrices for 1D beam elements are well established. The presence of a crack will have negligible effect on the mass properties of the structure so the global mass matrix of the damaged structure is assumed to remain the same as that of the healthy structure. However, the presence of a crack will result in a localised loss in bending stiffness in the vicinity of the crack and the global stiffness matrix for the structure needs to reflect this. Crack modeling approaches try to represent the loss in stiffness due to the crack (Dimarogonas 1996). The stiffness reduction technique used was that proposed by Sinha et al (2002), and it is based on the work of Christides and Barr (1984). Sinha's technique allows the estimation of the bending stiffness in the vicinity of the crack, then using these values of bending stiffness the elemental stiffness matrices of the damaged elements were calculated and the global stiffness matrix for the structure was populated. The ratio of crack height (h) to beam depth (d) is denoted as delta and it is used here to characterize the severity of damage.

Figure 1 shows a sketch of the model used. A constant load P (10 tonnes) crosses the structure at a given speed and {F(t)} defines the distribution of P to the degrees of freedom of the structure at each time 't'. {F(t)} is calculated by determining the position of the load (b(t)) at every time step and using the hermitian shape functions to apportion the applied load to the nodes of the beam element where the load is located. In order to perform a dynamic simulation of a load crossing the bridge it is necessary to convert the equilibrium equations of motion into a discrete time integration scheme. This scheme is solved using the Wilson-θ method. The results of the beam response to the moving load were found to be in agreement with those published by Mahmoud (2001) for different crack heights of a 50 m long beam.

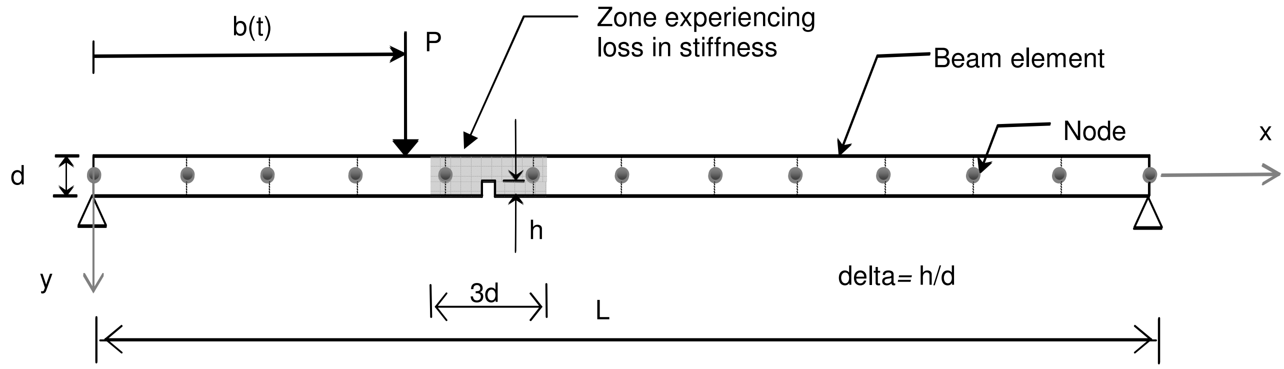

Figure 1- Sketch of Beam Discretized Model Subject to a Moving Force.

In this paper the structure is modelled as a 40 m simply supported span. The properties of the 40 m beam are those typical of a 15 m wide bridge consisting of 10 SY6 precast concrete beams spaced at 1.5 m centres with a 195 mm thick deck slab, resulting into an inertia of 6.02 m^4, a Young's modulus of $3.5x10^9$ N/m^2, and a total cross sectional area of 10 m^2. The first natural frequency of the healthy structure is 2.88 Hz. The speed of the load for all simulations is 6 m/s.

3. Effect of Damage on Acceleration Signals

Figure 2 shows the mid-span acceleration response of a healthy 40 m beam (delta = 0.0) as it is traversed by a constant load of 10 tonnes moving at 6 m/s. The x-axis in the figure shows the normalised position of the load on the bridge (0 and 1 when the load is at the start and end of the bridge respectively). The figure also shows the acceleration signal when the same bridge has a crack of delta equal to 0.4 at the third point of the span. When comparing the acceleration signals shown in Figure 2 the most obvious differences are that damaged acceleration signal (delta=0.4) has a larger amplitude and a lower frequency than the healthy signal (delta=0.0). The phenomenon of damage causing a global change in the amplitude and frequency of vibration of the structural response is well understood. However, this paper is more interested in the exploitation of local changes in the acceleration signal due to damage that may facilitate its identification. If the healthy signal was examined, the plots connecting the maximum or minimum peaks in the signal are approximately linear. The locus of the peaks of the damaged signal are also approximately linear, except when the load is at 0.33L (i.e. the location of the crack) where the peak appears to be marginally higher than both adjacent peaks. However, relative to the amplitude of the acceleration signal any change in the height of the peak as the load passes over the damage is very small and therefore difficult to identify. In an attempt to amplify the effect of the discontinuity in the acceleration signal (as the load crosses the damage), a sinusoid is fitted to the simulated signals. The purpose of doing this is that if the approximated sinusoid is subtracted from the acceleration signal any discontinuities present in the acceleration signal should stand out more obviously.

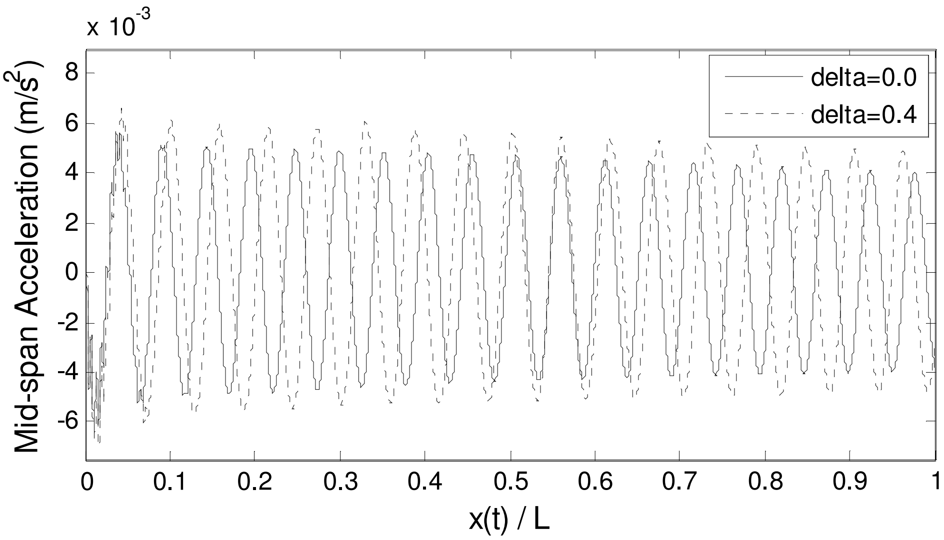

Figure 2 - Mid-span Acceleration of a 40m Bridge Traversed by a Constant Load Moving at 6m/s.

Figure 3 shows a sinusoid fitted to the healthy acceleration signal. A sinusoid is fitted to the damaged acceleration signal in the same manner. Figure 3 shows that if a linearly decaying sinusoid of the appropriate amplitude and frequency is used it can approximate quite closely the recorded acceleration signal. However, it is not an exact match the principal reason for this is that the acceleration signal has more than one frequency of vibration, where as the sine wave only has one frequency.

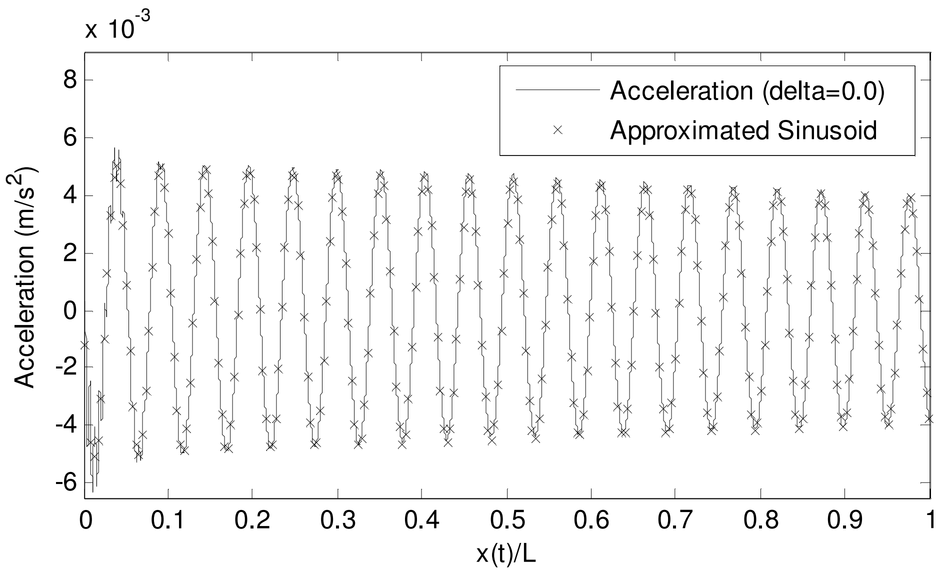

Figure 3 - Sinusoid Fitted to Mid-span Acceleration Signal of Healthy Bridge.

The result of subtracting the approximating sinusoids from both signals is shown in Figure 4 (the frequency of the approximating sinusoid is different for each signal). The continuous line in Figure 4 (delta=0.0) shows the result of subtracting the fitted sinusoid from the simulated acceleration signal in Figure 3. By doing so, most of the vibration of the first mode is removed (Note the y-axis limits in Figure 4 are almost an order of magnitude lower than in Figure 3). By examining the continuous line in Figure 4 it can be seen that in the early stage of the simulation (before the load reaches

0.2L) there is a significant amount of vibration from the higher modes and thereafter there is just periodic vibration at the first mode. In the damaged case (delta=0.4), the higher modes of vibration also dominate the early part of the motion however, unlike the healthy case the vibrations thereafter are not periodic, there is a peak at x(t)/L=0.33, i.e., some kind of discontinuity as the load crosses the damage.

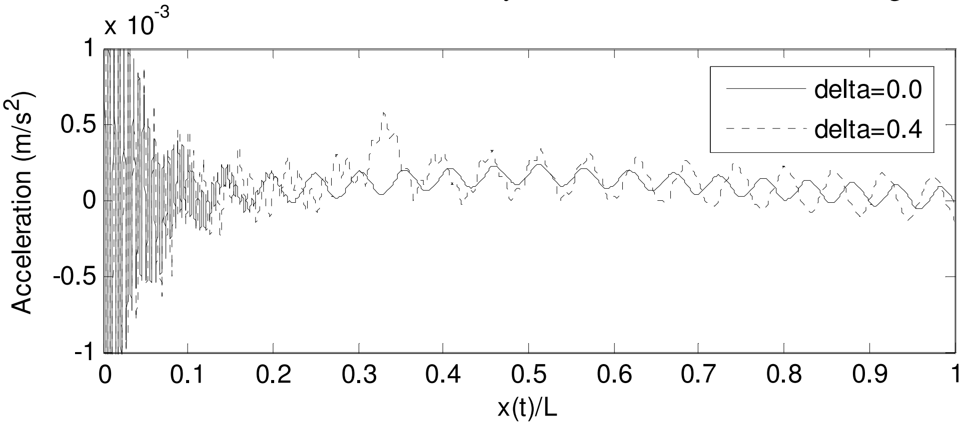

Figure 4- Sinusoid Subtracted from Mid-span Acceleration Signal.

To understand why there is a local discontinuity in the mid-span acceleration signal as the load crosses the damage it is useful to break the displacement signal from a damaged beam into its component parts. Each part is differentiated twice to get the component parts of the damaged acceleration signal. This procedure is illustrated in Figure 5. Figure 5(a) shows the mid-span displacement as a constant load of 10 tonnes crosses the bridge at 6 m/s. The bridge has a crack at the third point of the span with delta equal to 0.2. Again the x-axis in the figure shows the normalised position of the load on the bridge (0 and 1 when the load is at the start and end of the bridge respectively). Figure 5(b) shows the mid-span velocity of the bridge -this is obtained by differentiating the mid-span displacement signal with respect to time. Figure 5(c) shows the mid-span acceleration signal which is obtained by differentiating the velocity signal shown in Figure 5(b). Figure 5(d) shows the total mid-span displacement broken up into its component parts. 'static' refers to the displacement that would be experienced at mid-span if the load was moved incrementally across the 'healthy' structure and was applied statically at each location. The 'damage' component is the extra static displacement experienced at mid-span due to the damage. It must be noted that the 'damage' component is quite small compared to the 'static' component and the maximum value of the 'damage' component occurs when the load is at 0.33L. 'dynamic' is simply the dynamic component of the mid-span displacement. If the 'static', 'damage' and 'dynamic' components are added together, the total mid-span displacement shown in Figure 5(a) is obtained. Figure 5(e) shows the component parts of the velocity signal, and they are obtained by differentiating each of the three components of displacement with respect to time. The sum of the three velocity components in Figure 5(e) is equal to the total mid-span velocity shown in Figure 5(b). Finally, the three components of the acceleration signal are obtained by differentiating the components of the velocity signal with respect to time. Again the three acceleration components in Figure 5(f) sum to give the total mid-span acceleration shown in Figure 5(c). The 'static' component and the 'damage' component of the acceleration signal are very small relative to the 'dynamic' component, thus, they practically look like straight lines in Figure 5(f). However, Figure 6 shows the 'static' and 'damaged' components of acceleration plotted at a

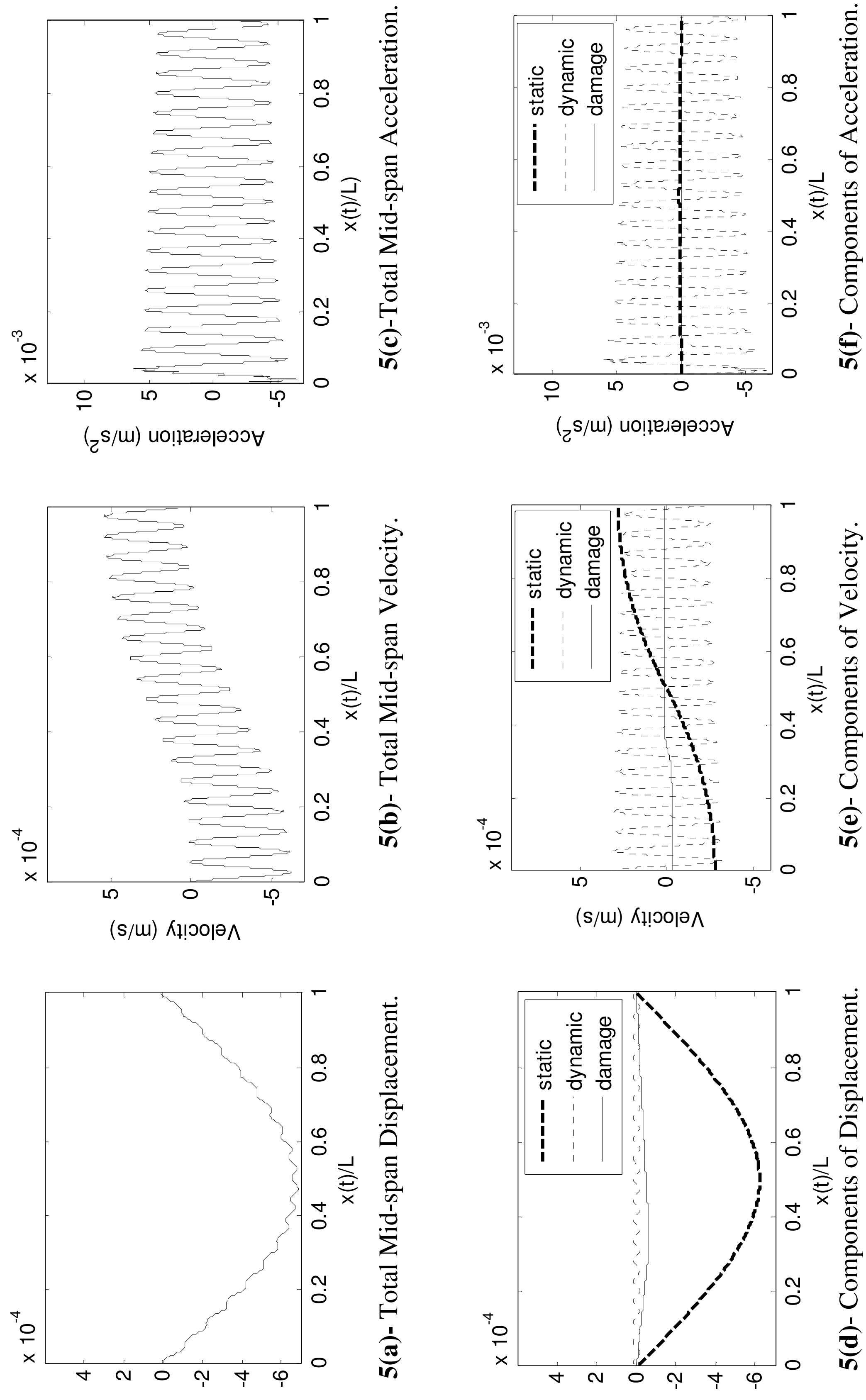

5(a)- Total Mid-span Displacement.

5(b)- Total Mid-span Velocity.

5(c)-Total Mid-span Acceleration.

5(d)- Components of Displacement.

5(e)- Components of Velocity.

5(f)- Components of Acceleration.

Figure 5- Total Response Signals and their Component Parts.

magnified scale and they are not straight lines. It can be seen that the static component increases linearly from zero to a maximum at the recording location and then decreases linearly back to zero. The damage component is zero everywhere except at the damage location. Therefore if an appropriate method of filtering out the dynamic component of the acceleration signal is employed it should be possible to locate damage in a bridge by analysing its acceleration signal.

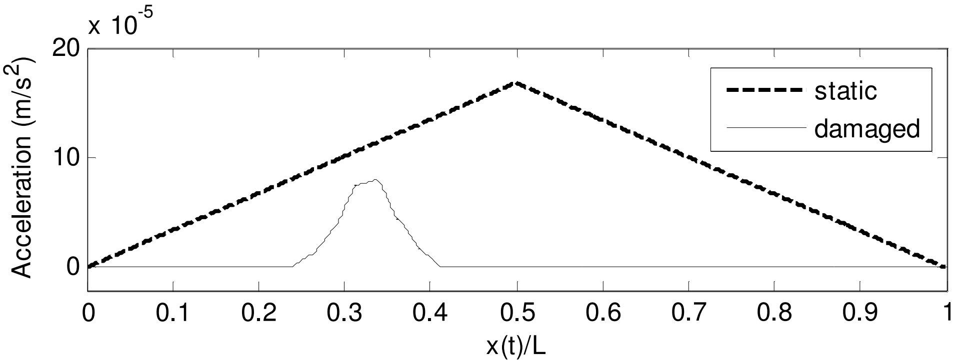

Figure 6 – Magnified View of Static and Damaged Components of the Acceleration Signal.

4. Filtering Acceleration Signal to Detect Damage

The acceleration signals shown in Figure 2 are vibrating almost exclusively at the first natural frequency of the structure and the contribution of other modes is very small. A Moving Average Filter (MAF) replaces each point in the signal with the average of several adjacent points. When the acceleration signal is vibrating primarily at one frequency, the dynamic oscillations can be removed using a MAF where the span of the filter is equal to one period of vibration. Figure 7 shows the result of applying a moving average filter to the acceleration signal from a healthy bridge and a bridge with a delta=0.2 crack at the one third point of the span. The span of the moving average filter was determined by doing a Fourier transform on the acceleration signal to determine the dominant frequency. In the healthy case (delta=0.0) once the dynamic component of the acceleration signal is removed all that remains is the triangular shaped static component, indicating that the beam is healthy. In the damaged case (delta=0.2), the triangular profile of the static component is still evident however this time there is a bump at x(t)/L=0.33 which indicates that there is damage at the 1/3 point of the span. Essentially the damaged plot in Figure 7 is the sum of the 'static' and 'damaged' components shown in Figure 6.

5. Conclusion

This paper has investigated the possibility of using the acceleration response of a beam subject to a moving load to detect damage. As part of this process the differences between healthy and damaged acceleration signals have been examined. As expected, there are global changes in amplitude and frequency in the damaged beam, but a small local discontinuity is also found in the acceleration signal as the load passes over the damage section. However, this discontinuity is very small relative to the dynamic oscillations in the signal. A moving average filter has been used to successfully remove the undesired influence of the main mode of vibration facilitating the location of the damage. Further research is needed to analyse the potential of the proposed algorithm to detect multiple damages in more complex mathematical models of the moving loads and the underlying structure.

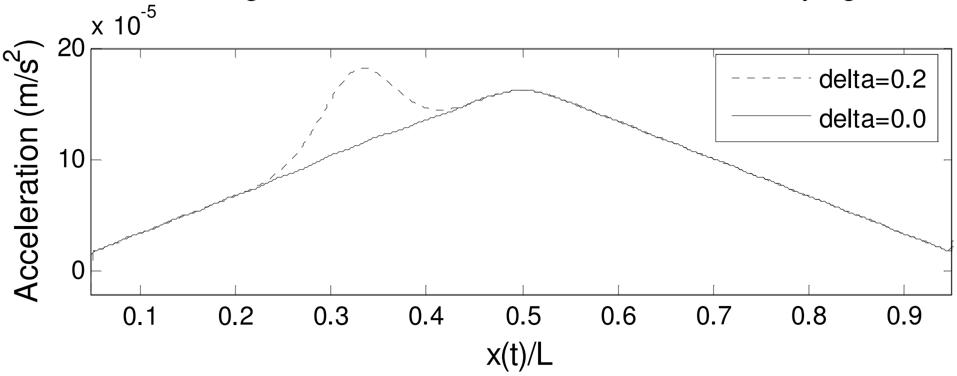

Figure 7 – Acceleration Signals from Healthy and Damaged Bridge Smoothed using Moving Average Filter.

Acknowledgements
The authors wish to express their gratitude for the support received from the 7th European Framework Project ASSET towards this investigation.

.

References

Christides, S. and Barr, D.S. (1984), 'One-dimensional theory of cracked Bernoulli-Euler beams', *International Journal of Mechanical Science*, **26**, 639-648.
Dimarogonas, A.D. (1996), 'Vibration of cracked structures: a state of the art review', *Engineering Fracture Mechanics*, **55**, 831-857.
Doebling, S.W., Farrar, C.R., Prime, M.B. and Shevitz, D.W. (1996) 'Damage identification and health monitoring of structural and mechanical systems from changes in their vibration characteristics: a literature review', *Los Alamos National Laboratory report*, LA-13070-MS.
Farrar, C.R. and Woden, K. (2007) 'An introduction to structural health monitoring' *Philosophical Transactions of the Royal Society*, **365**, 303-315.
Liu, F., Li, H., Yu, G., Zhang, Y., Wang, W. and Sun, W (2007) 'New damage-locating method for bridges subject to a moving load', *Journal of Ocean University of China,* **6(2)**, 199-204.
Mahmoud, M.A. (2001), 'Effect of cracks on the dynamic response of a simple beam subject to a moving load' in *Proceedings of the Institute of Mechanical Engineers, Part F: Journal of Rail and Transit*, **15**, 207-215.
Sinha, K.J., Friswell, M.I. and Edwards. S. (2002), 'Simplified models for the location of cracks in beam structures using measured vibration data', *Journal of Sound and Vibration*, **251**(1), 13-38.
Zhu, X.Q. and Law, S.S. (2006), 'Wavelet-based crack identification of bridge beam from operational deflection time history', *International Journal of Solids and Structures*, **43**, 2299-2317.
Zhang, W., Wang, Z, and Hongwei, M.A. (2009) 'Studies on Wavelet Packet-based crack detection for a beam under the moving load' *Key Engineering Materials,* **413-414**, 285-290
Liu, F., Li, H., Yu, G., Zhang, Y., Wang, W. and Sun, W (2007) 'New damage-locating method for bridges subject to a moving load', *Journal of Ocean University of China,* **6(2)**, 199-204.

FINITE ELEMENT MODELLING, DYNAMIC TESTING AND MODEL UPDATING OF A LABORATORY SCALE TIMBER FOOTBRIDGE

S. LIU & P. ARCHBOLD
STRAIT, Structures & Materials Research Group, Athlone Institute of Technology, Ireland

Abstract

Accurate finite element models are becoming increasingly important as they find use in applications such as structural condition monitoring techniques and inverse force analysis on existing structures. Prior to their use in any further applications, the finite element models must be verified through comparison with measured physical response data from the structure in question. Dynamic response characteristics – which can be used to calibrate and verify these finite element models – are determined through modal testing.

This paper describes the design and construction of a laboratory scale timber footbridge, together with the modal testing, finite element modelling and finite element model verification through comparison with the dynamic characteristics of the structure.

Keywords: Finite Element Model Updating, Modal Testing, Laboratory Scale Structure

1. Introduction

Finite element models of structures have many post-design applications, such as their use in structural condition monitoring techniques. Many of these techniques measure changes in dynamic structural response characteristics and compare them to results from intact structures, often derived from numerical models (Archbold & Liu, 2009). For such applications, the accuracy of the finite element model must first be verified through comparison with measured experimental structural response under known excitation.

1.1 Dynamic Testing

Dynamic or modal testing is defined as “the process involved in testing components or structures with the objective of obtaining a mathematical description of their dynamic or vibration behavior” (Ewins, 1984). Modal testing can be classed as either operational or controlled depending on the excitation mechanism employed during the test. For large scale structures such as suspension bridges, operational modal analysis, where the response of the bridge to ambient and traffic loading is measured is the only practical method. For smaller structures and machinery components, however, forced or controlled excitation sources are used. Typical results derived from modal testing include the natural frequencies, mode shapes and damping characteristics of the element being analysed.

1.2 Comparison of Dynamic Characteristics

The mode shape is a unique characteristic of a mechanical structure and it is known as the spatial description of the amplitude of each resonance (Palacz & Krawczuk, 2002). While the comparison of numerical values of natural frequencies is straightforward, a slightly more complex method must be used for the comparison of mode shapes.

Two commonly used methods for direct comparison of mode shapes are the Modal Assurance Criterion (MAC) and the Co-ordinate Modal Assurance Criterion (COMAC). The MAC measures the correlation between two sets of mode shapes, while the COMAC measures correlation between mode shapes at a selected measurement point on the structure.

The MAC is defined as a scalar constant relating the degree of consistency (linearity) between one modal and another (Allemang, 2002).

$$\mathrm{MAC}(\varphi_i, \varphi_j) = \frac{|\varphi_i{}^T \varphi_j|^2}{\varphi_i{}^T \varphi_i \varphi_j{}^T \varphi_j} \tag{1}$$

where φ_i and φ_j are two vectors of a discrete system or two eigenfunctions for a continuous system (Palacz & Krawczuk, 2002).

If the MAC has a value near zero, this is an indication that the vectors are not consistent; if it has a value near one, this is an indication that the vectors are consistent (Allemang, 2002).

The Co-ordinate Modal Assurance Criterion (COMAC) identifies the co-ordinates at which two sets of mode shapes do not agree. The COMAC factor at a point *i* between two sets of the mode shape in states $A\varphi^A$and $B\varphi^B$ is defined by

$$\mathrm{COMAC}(i) = \frac{\left[\sum_{j=1}^{N} \left|\varphi_{i,j}^A \varphi_{i,j}^B\right|\right]^2}{\sum_{j=1}^{N} (\varphi_{i,j}^A)^2 \sum_{j=1}^{N} (\varphi_{i,j}^B)^2} \tag{2}$$

where *N* is the number mode shapes, $\varphi_{i,j}^A$ and $\varphi_{i,j}^B$ denote the values of *j*th mode shape at a point *i* for the states *A* and *B* respectively.

This paper reports on the design and construction of a laboratory scale timber footbridge, which was constructed to examine some structural condition monitoring techniques and also for study into human-structure interaction. The results from dynamic testing of the structure and the finite element model development, updating and verification are also presented.

2. Test Structure

The test structure (Figure 1) employed in this research is a laboratory scale timber footbridge. Overall, the bridge is 3.0m long and 1.2m wide. The structure comprises two longitudinal beams (150mm x 75mm) at 800mm centres, with the decking made up of twenty-one transverse planks (17mm x 40mm), screwed to the beams. The timber for both was class C16. The bridge was supported directly on timber beams resting on a concrete floor slab.

Figure 1 - Test structure

3. Finite Element Modelling Strategies

Two finite element models of the bridge were constructed using ANSYS V11.0 Finite Element Software. The first model was a simplistic three-dimensional elastic beam element model and the second was constructed using 4-noded shell elements. In each case, the boundary conditions were such as to model the bridge as being simply supported.

The shell model was verified through comparison with estimated static deflection and predicted mode shapes from the beam model. The mode shapes were extracted using a Block-Lanczos extraction algorithm and 10 modes were extracted in each case. The estimated mid-span static deflections under self weight were 2.38mm and 2.22mm from the beam and shell models respectively.

The beam model did not capture any torsional modes of the structure, so comparison between predicted mode shapes consisted of examination of vertical and lateral modes only. The results of a Modal Assurance Criterion Analysis (Table 1 and Figure 2) show near perfect agreement between the models as expected.

Further discussion of the numerical model in this paper will refer only to the shell model, as it is more capable of simulating the total dynamic response of the test structure.

Table 1 - MAC Values from Numerical Strategies

Mode No.	1	2	3	4	5
1	**1.0000**	0.7166	0.6739	0.6697	0.6374
2	0.7166	**1.0000**	0.6488	0.7285	0.6262
3	0.6739	0.6488	**1.0000**	0.6462	0.6191
4	0.6697	0.7285	0.6463	**1.0000**	0.6262
5	0.6374	0.6262	0.6191	0.6263	**1.0000**

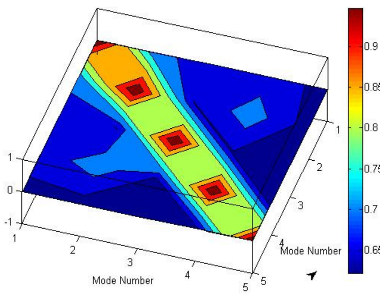

Figure 2 - Diagrammatic Representation of MAC Analysis

4. Dynamic Testing

The type of test, the extent of the test and the required quality of the results all follow from the defined objectives of the test (Maia *et al*., 1997). The main purpose of this test was to obtain the natural frequencies and mode shapes for the structure.

4.1 Test set-up

Four Monitran MTN/1800 accelerometers, with a sensitivity of 1.020V/g@80Hz were mounted on the bridge above the main beams, with two at mid-span and two at approximately ¼ -span. Data was recorded from these accelerometers through a Virtual Instrument (VI) developed in NI LabVIEW 8.5. The sample rate was 2000 readings/second, which was deemed sufficient from the initial finite element model predictions for the first five modes. The accelerations were post-processed within the VI to also output displacements and the data was exported for further post-processing. The test set-up is schematically represented in Figure 3.

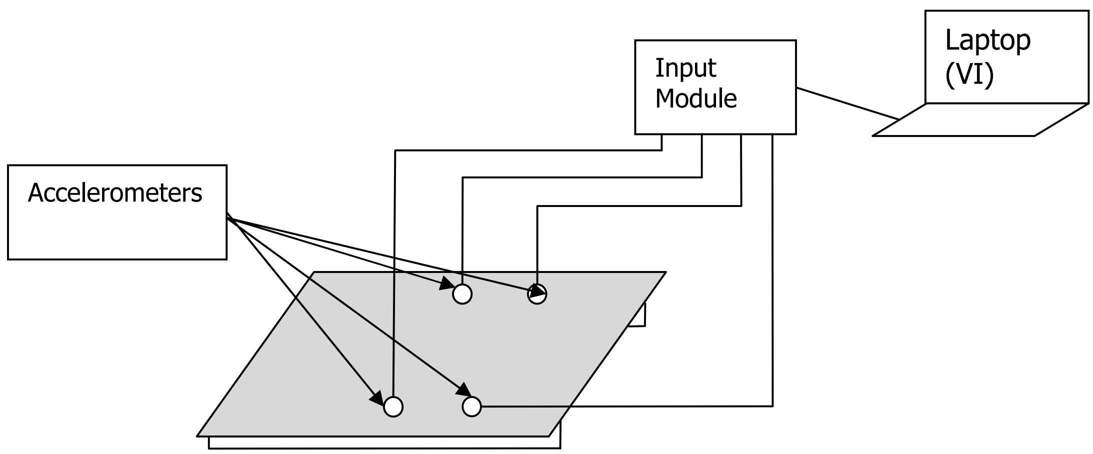

Figure 3 - Schematic Representation of Test Set-up

4.2 Test Procedure

Excitation was provided through hammer blows to the structure at mid-span, directly above one of the longitudinal beams. Each test consisted of three hammer blows at two second intervals and the test was repeated three times, giving nine sets of free vibration response data from the four accelerometer locations.

4.3 Dynamic Test Results

Figure 4 shows a typical response from the excitation tests. This data was then transformed from the time domain to the frequency domain through a Fourier Transform function to yield frequency data as shown in Figure 5. The results from one and two accelerometers respectively are shown for clarity in these diagrams. Averages of the natural frequencies recorded from each of the nine sets of response data are reported herein.

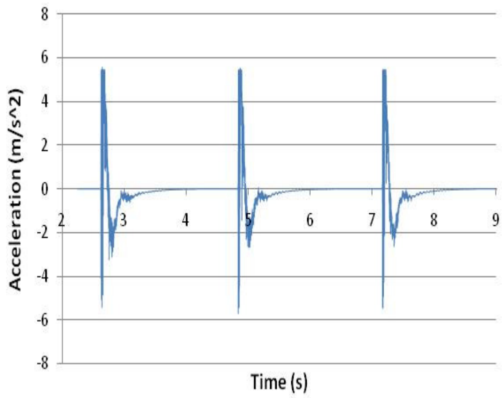

Figure 4 - Measured Accelerations

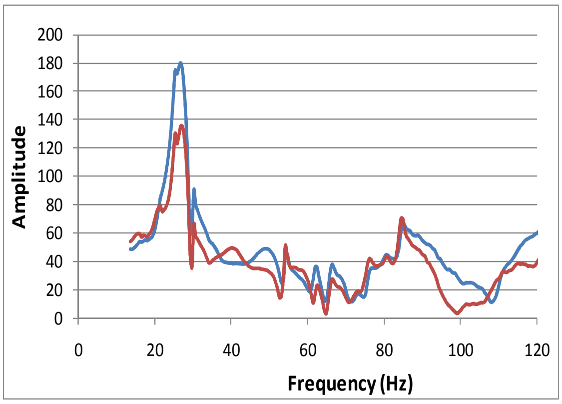

Figure 5 - Measured Natural Frequencies from Two Accelerometer Positions

Natural Frequency Comparison

The measured natural frequencies for the first five mode shapes are compared to those predicted from the original numerical model in Figure 6. The straight line represents an exact match between the measured and predicted natural frequencies, while the markers represent the actual correlation recorded for the first four mode shapes. Markers above the line reflect and overestimation of the natural frequency, while those below represent an underestimation. The numerical model underestimated the natural frequencies by as much as 23% for the second vertical mode, while overestimating the torsional frequencies.

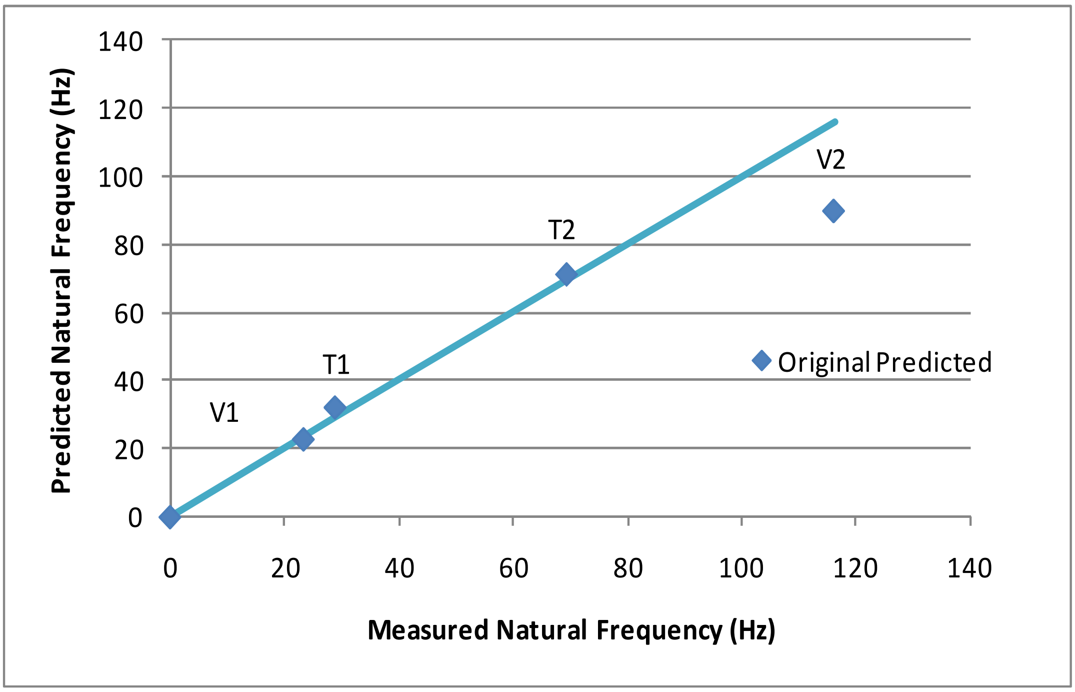

Figure 6 - Measured and Predicted Natural Frequencies

Mode Shape Comparison

As there were only four accelerometers used in the dynamic test, the accuracy of the plotted mode shapes is somewhat limited. Moreover, all of the accelerometers were placed in one half-span of the bridge. As a result only half-mode shapes are plotted. The plotted mode shapes and associated natural frequencies are contained in Table 2, along with the predicted modes from the finite element model. The notation V refers to vertical modes, while T represents torsional modes. They are then numbered sequentially. MAC analysis of these mode shapes also showed poor correlation, enhancing the need for updating of the original finite element model.

Table 2 - Predicted and Measured Mode Shapes

Mode Shape	**Predicted (Original)**	**Measured (Half Mode Shape)**	**Predicted (Updated)**
V1	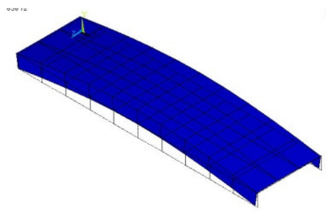 22.80Hz	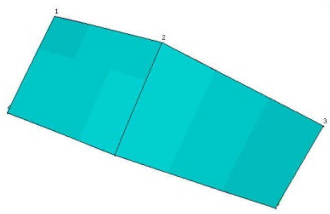 23.36Hz	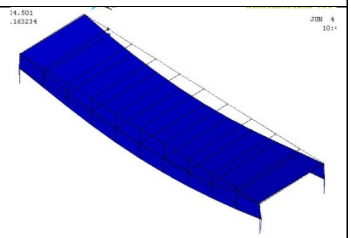 24.50Hz
T1	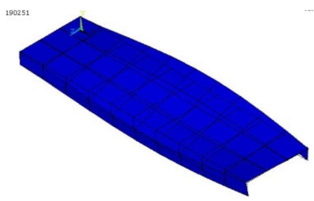 32.12Hz	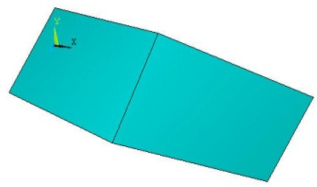 28.89Hz	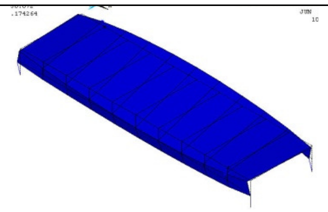 30.07Hz
T2	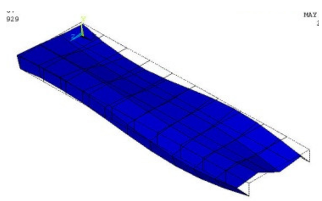 71.12Hz	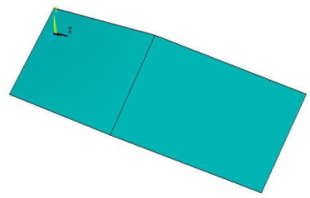 69.43Hz	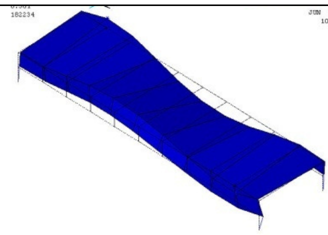 70.38Hz
V2	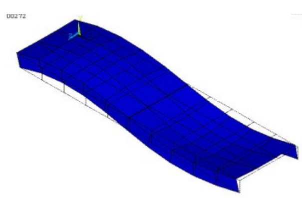 89.71 Hz	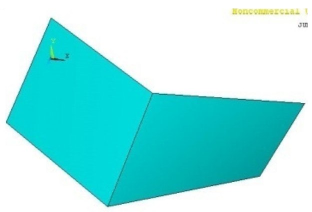 116.17Hz	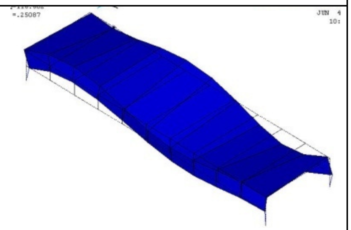 116.60Hz

5. Model Updating

The aim of model updating is to optimise certain parameters within the finite element model in order to better replicate the measured results. Updating can be carried out automatically through the use of a range of algorithms or manually. In this case, due to the simplicity of the model and the relatively small number of influencing parameters, the model updating was carried out manually. Prior to any updating, a sensitivity analysis was carried out on a number of chosen parameters to assess their influence on the overall results.

Density
An initial density of 600kg/m^3 was used in the development of the finite element model. Further to the dynamic testing, the density of the elements was measured in the laboratory and turned out to be 432.91kg/m^3 and 418.06kg/m^3 for the deck and beam elements respectively. This was updated and the model showed some improvement on the original.

Young's Modulus
Sensitivity studies on the Young's Modulus showed that increasing or reducing the value of this property affected all modes equally, as expected. Changing the Young's modulus thus could not account for the overestimation of some modes, combined with the underestimation of others. The actual value of Young's modulus was not empirically determined so a design value was chosen and the same value used for both the deck and the beams.

Support Conditions
The original model was assumed to be simply supported i.e. degree of freedom constraints were applied directly to the nodes at the supports. In updating the model, these boundary conditions were investigated. Support conditions generally are viewed as being critical in terms of the dynamic response of a structure. Here, spring elements were employed to model, not just the stiffness of the supporting beams, but the overall general stiffness values of the support conditions. The stiffnesses of the springs was seen to have an influence on the predicted responses and also assisted in terms of correcting the overestimation of some modes and the underestimation of others.

Further, two 25kg weights were applied to opposite corners of the bridge during testing to counter some warping of the structure which occurred during storage. These were not included in the original model but were modelled as mass elements in the updated model. These weights were placed directly over the structural supports and were more likely to affect damping properties than natural frequencies or mode shapes.

Updating Procedure
The chosen parameters were manually updated on an iterative basis in order to establish the best fit between the measured and predicted mode shapes and natural frequencies.

Of the parameters varied during the updating process, changes in the Young's Modulus and density respectively led to relatively modest, linear variations in the predicted dynamic response. The most effective parameter for improving the predicted response was the spring stiffness used in modeling the support conditions. Nonetheless, a combination of a considerable change in density and the introduction of spring supports proved to ultimately be the most appropriate model updating strategy.

Table 3 shows the original and final values for some of the chosen updating parameters, while Table 2 also shows the results of the updated mode shape and frequency predictions.

Table 3 - Original and Updated Input Parameters for Finite Element Model

Input Parameter	**Original Value**	**Final Value**
Density of Timber (Deck)	600kg/m^3	432.91kg/m^3
Density of Timber (Beam)	600kg/m^3	418.06kg/m^3
Young's Modulus of Timber	1 x 10^{10}N/m^2	1 x 10^{10}N/m^2
Support Spring Stiffness	N/A	576 x 10^6N/m
Support counter weights	N/A	25kg

6. Finite Element Model Verification

In order to assess the accuracy of the updated model, the dynamic characteristics are now compared to the measured values.

6.1 Natural Frequency Comparison

Figure 7 shows a comparison of the original, updated and measured natural frequencies. The error between the measured and predicted frequencies, in terms of least squares of the differences, improved from 6.4% to 1.6%, illustrating a high degree of correlation between the updated model and the physical test structure. Diagrammatically, it can also be seen from Figure 7 that there is better fit between the updated markers and the straight line than those of the original predicted values.

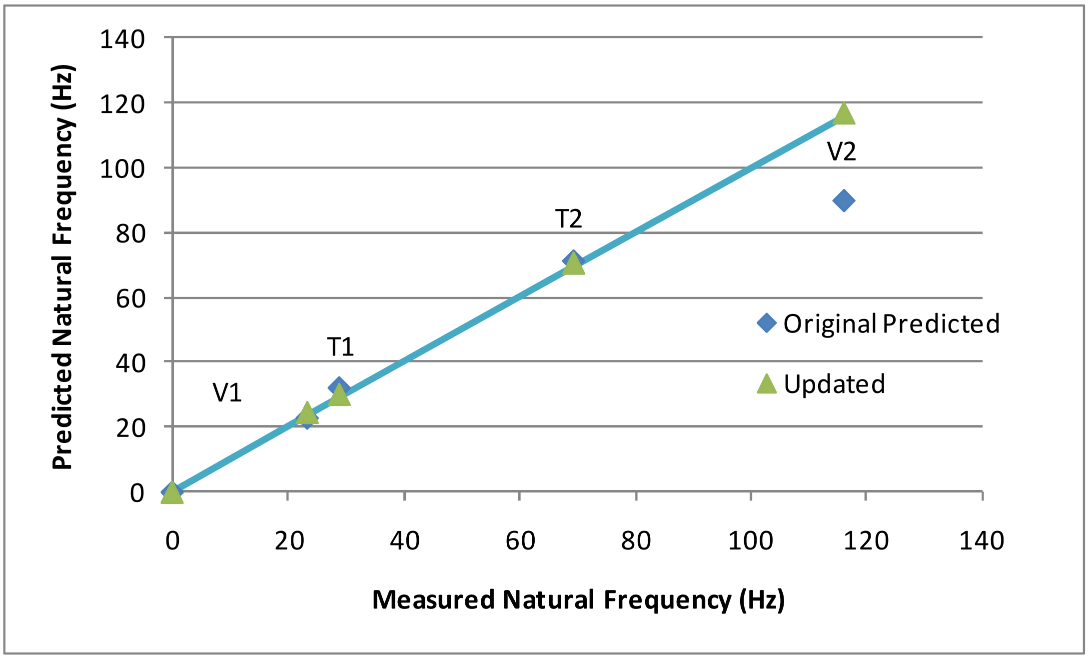

Figure 7 - Predicted and Measured Natural Frequencies after FE Model Updating

6.2 Mode Shape Comparison

A MAC analysis was performed to compare the mode shapes predicted in the updated finite element model with those measured through the modal testing of the structure. The results of this analysis are shown in Table 4 and Figure 8. It is noted that the MAC values, while yielding good results for the first three modes, tend not to be close to 1 for the higher modes. This may be as a result of the difficulty in accurately determining the amplitudes of vibration associated with the higher frequency modes. Application of suitable filters to the response signal may benefit the identification of these values and is currently under investigation.

Table 4 - MAC Values for Measured and Updated FE Model

Mode No.	V1	T1	T2	V2
V1	**0.9755**	0.9926	0.9355	0.6998
T1	0.9759	**0.9939**	0.9243	0.7049
T2	0.7890	0.7571	**0.8898**	0.2725
V2	0.5104	0.5451	0.3150	**0.5495**

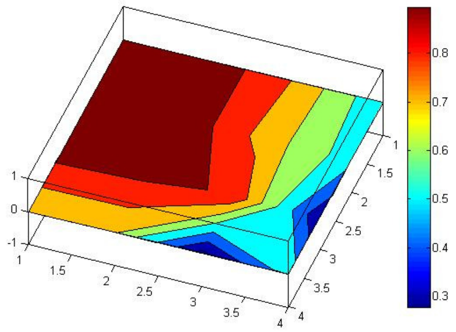

Figure 8 - MAC Analysis of Measured and Updated Mode Shapes

7. Summary

A laboratory scale test structure has been designed and constructed. Modal testing was carried out on the structure and the first four mode shapes and associated natural frequencies have been identified. Based on the findings of the modal testing, the finite element model has been updated to show improved correlation between the measured and predicted modes, together with an reduction in the error associated with the first four natural frequencies from 6.4% to 1.6%. This model offers greater potential for use in analysis of the structural response to both known and unknown excitation in the future.

8. Acknowledgements

This project is supported by the Technological Research Sector - Strand I Post-graduate R&D Skills Programme, funded by the Irish Government and part-financed by the European Union under the National Development Plan, 2007-2013.

References

Allemang, R.J. (2002) ‘The Modal Assurance Criterion-Twenty Years of Use and Abuse. University of Cincinnati, Cincinnati, Ohio’, based on a paper presented at *IMAC-XX, the 20th International Modal Analysis Conference, Los Angeles, CA*, February 2002.

Archbold, P. & Liu, S. (2009) Novel Methods in Condition Monitoring of Large Scale Structures, *Proceedings of the Twelfth International Conference on Civil, Structural and Environmental Engineering Computing*, Funchal, Madeira.
Carden, P. & Fanning, P. (2004). 'Vibration Based Condition Monitoring: A Review', *Structural Health Monitoring* Vol. 3(4) 355 – 377.
Doebling S.W., Farrar C.R., Prime M.B. & Shevitz D.W. (1996) '*Damage Identification and Health Monitoring of Structural and Mechanical Systems from Changes in Their Vibration Characteristics: A Literature Review*'. Los Alamos National Laboratory, LA-13070- MS, Los Alamos, New Mexico.
Ewins, D.J. (1984) *Modal Testing Theory and Practice*, Research Studies Press, Letchworth, Hertfordshire, England.
Maia, N.M.M., Silva, J.M.M., He, J., Lieven, N.A.J., Lin, R.M., Skingle, G.W., To, W & Urgueira, A.P.V. (1997) *Theoretical and Experimental Modal Analysis*. Research Studies Press Ltd. England, 127-128
Palacz, M & Krawczuk, M, Vibration Parameters for Damage Detection in Structures, 2002, *Journal of Sound and Vibration* (2002) 249(5), 999-1010.

GROUND PENETRATING RADAR AS AN INNOVATIVE TOOL FOR IDENTIFYING AREAS OF SCOUR AND SCOUR INFILL AROUND BRIDGE FOUNDATIONS

K.E.J.CAMPBELL[1], A.RUFFELL[2], D.HUGHES[2] S.TAYLOR[2], B.DEVLIN[1]
[1] CEI Collins Engineers Ltd, Northern Ireland
[2] Queens University, Belfast, Northern Ireland

Abstract
Inspections of structures below water level are essential to ensure the long-term serviceability of our bridge infrastructure and to avoid major damage or bridge failure. This paper outlines a recent investigation using Ground Penetrating Radar (GPR) in conjunction with a hydrographic sonar survey. GPR is ideally suited to the survey of waterways in shallow (<10 m) freshwater due to excellent transmission of radar waves, giving high quality images from small, manoeuvrable boats. The results of a recent GPR survey of a riverbed in the vicinity of a bridge are given and some initial interpretation of the data has shown that GPR is capable of illustrating subsurface profiles and thus useful for detecting scour infill around structures.

Keywords: (Bridge, Modelling, Monitoring, Underwater inspection)

1. General

The aim of this study was to determine whether Ground Penetrating Radar (GPR) could be used effectively for the investigation of a sub-bottom channel profile around structures such as bridge piers and to evaluate its usefulness in obtaining data regarding scour and scour infill. A range of frequencies and equipment set-ups were trialled with a view to exploring the technology further.

1.1 History and Background of Ground Penetrating Radar (GPR) and Water Penetrating Radar (WPR)

A brief summary of the science involved is given as it is beyond the scope of this paper to review in detail all GPR and electrical geophysical survey methodologies. GPR uses the transmission and reflection of radio waves (typically 25 to 1000 MHz based on resolution and depth penetration) in soil, rock, water and sediment. A GPR system requires a source and receiving antenna. The transmitter-receiver array is moved along a survey profile and radar traces are collected against a pre-set time or distance interval to produce a time-distance cross-section plot known as a radargram.

Alternatively, one antenna may be moved away from a static antenna to create a moveout profile. Radargrams possess two properties that are of interest; namely, reflections at interfaces between two geological media of differing dielectric permittivity; and radar wave attenuation as a function of fluid electrical conductivity (Reynolds, 1997). Antenna may be built to transmit and receive a range of frequencies, from low (e.g. 25 MHz) to very high (e.g. 2-3 GHz). Most common for subsurface surveying (including in freshwater) are antennae in the 50 to 500 MHz range. This study tested a range of antennae. If antennae are unshielded, the results of the GPR survey are prone to artefacts, such as metal poles but give a lightweight and flexible design. Shielding the antennae removes the problem of interference but creates an inflexible design. Antennae orientation can influence results, with different orientations achieving greater subsurface penetration but balanced with limiting out-of-plane reflections (Kruk & van der Slob, 2004).. For boat-borne GPR surveying, the dimensions of the boat often determine antennae orientation (Gorin & Haeni, 1989), making this less of an issue than in terrestrial surveying. GPR data can be extensively processed to remove artefacts and improve clarity: full descriptions of processing steps are covered in Reynolds (1997); Sharma (1997) and Daniels (2000). Variations in water conductivity and suspended matter affect radar wave propagation and reflection (Parker et al., 2009) and GPR may not work in brackish lakes and lagoons. This is because fresh and saltwater have similar dielectric properties and radar velocities but very different conductivities. This will result in radar wave attenuation in freshwater of 0.1 and 1000 in saltwater at which radar signals are lost. Parker et al (2009) give a summary of WPR. Two data outputs are possible: radargrams (vertical soundings of water and sediment) and plan views of amalgamated radargrams at various depths. These 'map like' outputs comprise digital data that can be subjected to manipulation in a Geographic Information System such as ARC-GIS (ESRI, 2010). Although WPR has been used to successfully image scour around bridge supports (Gorin and Haeni, 1989), the current work shows radargrams, raw plan views and selected processed data of bridge scours, and makes an evaluation of each data output type.

1.2 Description of the Site and Bridge

A site was selected which had suitable geographic factors, including freshwater with a low level of pollutants and potential for scour. The A3 Northway Dual Carriageway Bridge over the river Bann in Portadown, Northern Ireland was considered a suitable location. There are two additional bridges adjacent to the study site which could be included in future testing schemes. The 3 bridges have 4 types of construction in a ~300 m stretch of river.

The River Bann flows in a northerly direction (Figure 2) and is typically 20-40 m wide at this stretch and is popular for fishing, possibly indicating low levels of pollutants. It is also popular with pleasure craft and jet skiers. There is no marine or saline influence, as the site is inland and drains to Lough Neagh, a freshwater lake.

Depth-soundings were established and indicated that the river had an average depth in and around the bridges, of 3 m, with isolated locations measuring up to 5 m deep adjacent to the piers. This variability makes hydrographic surveying (such as echo sounding and WPR) more relevant, as discrete Fathometer Soundings or plumb-bob depths may not be representative of the entire area. Visual examination of the riverbed material indicated that it consisted of soft silt/mud with stones and cobbles.

(i)

(ii)

Figure 1 – (i) Location Map, 'A' shows the location of the car park and slipway, 'B' shows the location of the road bridge. (ii) View of the Bridge *A3 Northway Dual Carriageway (foreground)*

The use of GPR is highly relevant in such mixed subsurface soils as sediment type may be indicated, buried objects located and soft sediment depth estimated. In order to study the efficiency of the two main data outputs in GPR, both radargrams (for vertical measurements) and plan views were gathered. Radargrams were collected with unshielded 100 MHz antennae using a loose grid (Figure 2), with the same area surveyed using the 100 MHz shielded antennae.

The highway bridge structure is a multi-span reinforced concrete bridge. There are two piers located in the water each consisting of two circular reinforced concrete columns of 1.5 m diameter. The columns are spaced 10 m apart and the span between the 2 piers measures 20 m. Adjacent to the A3 Bridge is a railway bridge. Both railway bridge piers consist of three steel columns resting on a reinforced concrete pile cap which is supported by a number of concrete piles.

2. Investigation Methodology

In this study several antennae were trialed. A grid (shown in Fig 2) was used to cover the area under the bridges. The GPR equipment was set up in the base of a 3 person, 6 m long, 3 m-wide motorized dinghy. The first survey was conducted with the engine switched on and off (drifting in the wind or current when off) to confirm that the boat engine had a negligible effect on the radar data. The transmitters were mounted in the boat as they could not be submerged. The antennae required constant contact with the water and were positioned on the base of the boat for the following reasons: (1) Stability; (2) Protection from complete submersion; (3) Connection with the water surface and (4) Retention of the manoeuvrability of the boat without risk of damaging the equipment.

Figure 2 –Bridge site; shows the position of the proposed scan lines.

The first scanning lines (runs) were parallel to the longitudinal direction of the bridge as indicated by the numbering system for the data sets shown in Fig.2. Runs were carried out each side of the piers and a run along the centre-line of the bridge. These lines proved difficult to follow and thus the alignment is approximate. This is because the river current along with the presence of wind caused drifting resulting in the need for several attempts to achieve an acceptable alignment. The final alignment could be improved in future surveys by using a total station to determine the location of the boat against time as the scan progresses. This would then be cross referenced with the GPR files to determine more accurate results.

The runs parallel to the river bank proved to be easier in achieving a proper alignment as there was greater control into the direction of the flow. Runs were carried out each side of the piers along with two runs between the piers due to the wider spacing involved. The survey was extended to cover both the railway bridge structure and the A3 road bridge due to their proximity to each other. The results obtained for the railway bridge structure are not presented in this paper.

The data was stored before carrying out runs using another antenna with different settings and frequency. The second survey was carried out in an attempt to penetrate deeper into the sub-surface layers and compare with the results obtained with the previous survey. A shielded antenna was set up and a similar grid was used to survey around the two bridges again. However, this equipment produces 3D output and is generally used on land with defined grids and an odometer wheel to trigger the radar signals. This proved a challenge to overcome, and several options were considered. A grid of 30 m by 20 m was selected with different grid spacing to the previous surveys which necessitated the need for more lines being run. The equipment was positioned as normal but with a slightly different arrangement of the shielded antennae due to its size and shape. The odometer wheel was rotated by hand for the purpose of this initial investigation to demonstrate if the system could produce acceptable 3D results. An anchor and line system to turn the wheel automatically would be more accurate but was not considered during the trials due to time and availability restrictions. After several initial runs to assess the correct rotation speed of the wheel, scans were completed over a period of two hours. Two different antennae were used on the same grid set-up.

This equipment was also used to scan the abutment front face of both the road and rail bridges above water. The road bridge abutments consisted of reinforced concrete construction and the abutments of the adjacent railway bridge were of masonry construction. This GPR survey was carried out by holding the antennae against the structure and passing it along in horizontal and vertical directions.

3. Results and Discussion

The data files required post-processing to aid the interpretation of the data and specific identified items in the scan. Only four pre-processed and one post-processed data files collected are presented in this paper. Similar processing steps were applied to all the data for consistency of interpretation with one post-processed section shown in Figure 4.

The short cross-lines (463 to 467) in Figures 3 and 4 illustrate the change in topography across the river with some subsurface detail. Processing of the data, as in Figure 4, improves the radargram quality, allowing surface and subsurface objects such as rocks or debris to be identified and also gives an idea of sediment thickness. The longer "river-parallel" lines 469 to 474 showed more subtle changes in topography, with a similar improvement in sub-riverbed imaging on processed data.

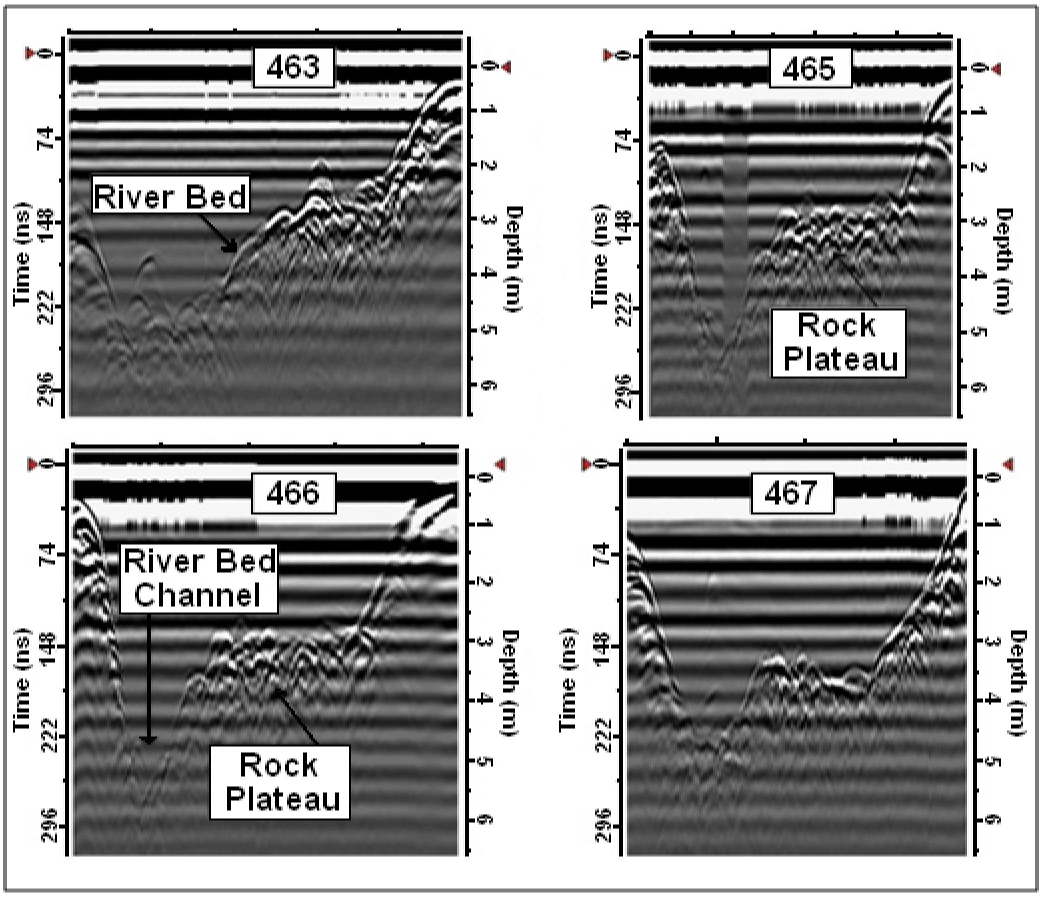

Figure 3 – Cross-river radargrams - unprocessed 100 MHz data

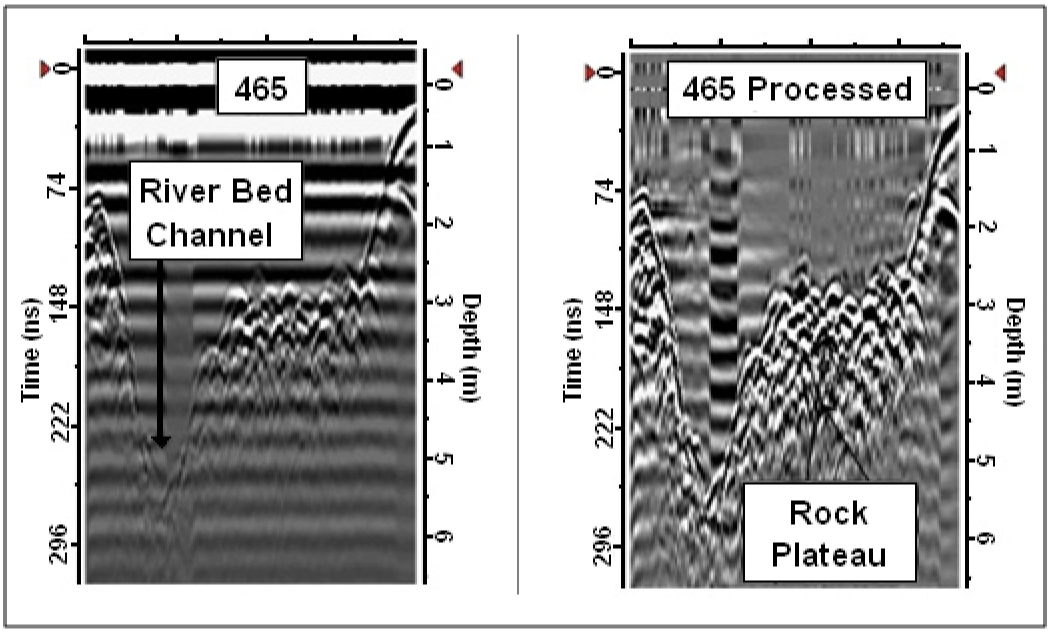

Figure 4-Cross-river profile processed with resultant improvement of imagery in the subsurface.

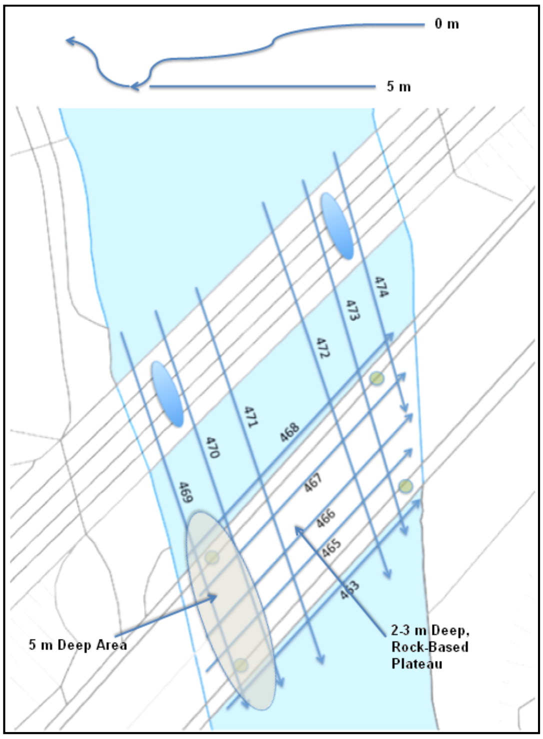

Figure 5 – Crude interpretation of the radargrams in terms of likely distribution of river-bed and sub-bottom features.

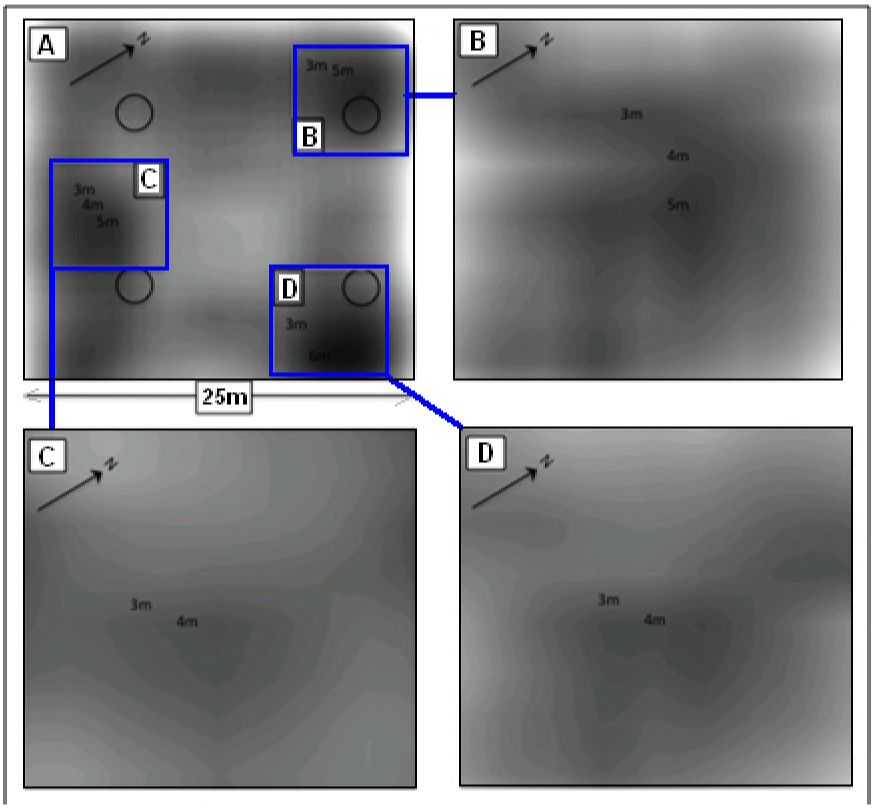

Figure 6– (a) Water depth slice under the road bridge (circular concrete supports) and three discrete areas of deeper water (b) Sediment depth in hollow B (c) Sediment depth in hollow C (d) Sediment depth in hollow D

When viewed together, the data allows a rudimentary view of the area under the bridge and its four supports to be interpreted. It was concluded that around the bridge piers there appeared to be deeper areas of water and a central area of rock at the river bed level (Figure 5). The plan view of water depth in the same survey area (Figure 6a) shows considerably greater detail, with the deep water area now resolved as a pair of hollows approximately 5 m deep (areas b and c), with a third area (d) not detected on the vertical soundings. These three depressions in the river bed are adjacent to the circular bridge supports. In order to gain some insight into the nature of these hollows, each was examined in detail and sediment thickness mapped (Figure 6). All three areas showing maximum sediment deposits are aligned NE, in parallel with the main flow direction of the river at this location.

4. Conclusions

- Whilst physical depth sounding with a plumb bob may be quick and inexpensive, it does not provide the comprehensive coverage of a hydrographic survey using echo sounding or GPR. GPR is advantageous in estimating sediment thickness, buried objects and depth to rock in confined locations such as those around a bridge pier.
- The gathering of radargrams, or vertical profiling, allows interpretation of the depths of the river bed to form a contour map (bathymetry), the presence of rock vs. sediment on the river (or lake) floor, and an estimation of the likely distribution of water and sediment depths. The unshielded antennae used to gather such data are small and lightweight.
- The gathering of time-slice WPR data gives a more accurate image of the distribution of both water depths and sediment thicknesses. The shielded antennae used to gather such data are large and heavy, making them more cumbersome in the field. In this case study, one area of deep water with a platform of rock outcrop was identified from the radargrams: this was investigated further using the time-slice data at three areas of deep water, each with 4 m-5 m of sediment.
- The three areas of infill are adjacent to the bridge supports, and oriented along the axis of river flow. Having a baseline survey of these depressions and the surrounding area allows for decisions to be made on how these sediment layers may or may not be developing. If it detects an increase in size of the depression, then this may suggest the presence of scouring and action can be taken. However if they do not change, it may be possible that these are natural depressions following historic events on which the bridge piles were subsequently placed and thus are not of concern.
- The combination of WPR survey types provides the most complete view of the river and the bridge supports. Both radargrams and time-slices are very suitable for future bridge surveys, using unshielded antennae triggered by an odometer wheel where no interference is likely and shielded antennae where cables, metal poles etc are observed. The results could then be verified by coring.

This paper demonstrates the applicability of the technique using existing non-adapted technology which gives excellent results useful for bridge assessment purposes and to assist in a suitable maintenance plan. Although the concept of using GPR on water or around bridges is not new, it is still a useful tool for 3D channel profiling.

Acknowledgements

The Authors would like to thank the Department for Regional Development Roads Service (NI) and Northern Ireland Railways (NIR) for their cooperation.

References

Beres, M. and Haeni, F.P. 1991. Application of ground-penetrating radar methods in hydrological studies. Ground Water, 29, 375-386.

Daniels DJ. 1996. Surface-penetrating Radar. *Institution of Electrical Engineers, radar Series* 6. 320pp.

ESRI. (2010, August). *ArcGIS 10: ESRI*. Retrieved 2010, from ESRI web site: http://www.esri.com/software/arcgis/arcgis10/index.html

Gorin, S.R. and Haeni, F.P. 1989. Use of surface-geological methods to assess riverbed scour at bridge piers. U.S. Geological Survey Water Resources Investigations Report 88-4212.

Haeni, F.P. 1996. Use of ground-penetrating radar and continuous seismic reflection profiling on surface water bodies in environmental and engineering studies. Journal of Environmental and Engineering Geophysics, 1, p.27.

Haeni, F.P., McKeegan, D.K. and Capron, D.R. 1987. Ground-penetrating radar study of the thickness and extent of sediments beneath Silver Lake, Berlin & Meriden, Connecticut. U.S. Geological Survey Water Resources Investigations Report, 85-4108.

Kovacs, A. 1991. Impulse radar bathymetric profiling in weed-infested fresh water. U.S.A. Cold Regions Research & Engineering Laboratory, CRREL Report 91-10.

Kruk J van der, Slob EC. 2004. Reduction of reflections from above surface objects in GPR data. *Journal of Applied Geophysics* **55**: 271-278.

Nobes, D.C., Rother, H., Kruk, J. van der and Jol, H.M. 2005. Radar 'lensing' by a small river: can a layer of surface water improve the signal? IN GPR 2004, Special Issue of Near-surface Geophysics, 4, 1, 69-74

Parker, R., Ruffell, A. and Hughes, D. 2010. Geophysics and the search of freshwater bodies: a review. *Science & Justice*, **50**, 53-65.

Reynolds, J.M. 1997. *An Introduction to Applied and Environmental Geophysics*. John Wiley and Sons Inc. Chichester. 796pp.

Sellmann, P.V., Delaney, A.J. and Arcone, S.A. 1992. Sub-bottom surveying in lakes with ground-penetrating radar. U.S. Army Corps of Engineers Cold Regions Research & Engineering Laboratory. CRREL Report 92-8. 18pp.

Sharma, P.V. 1997. Environmental and Engineering Geophysics. Cambridge University Press. 349pp.

CARBON FOOTPRINT COMPARISON OF MINI AND MICROPILING TECHNIQUES

J. AMOS[1]
[1]Balfour Beatty Ground Engineering, Basingstoke, UK

Abstract
Piling works are responsible for emitting a significant quantity of $C0_2$, primarily from the energy used in the manufacture of steel and concrete. Different piling techniques produce varying amounts of $C0_2$ and so the choice of pile type has an environmental impact. Being able to calculate the carbon footprint of a pile allows designers to assess alternatives and so consider sustainability as a factor in their choice-making. This paper describes a modified estimating system which places carbon calculation at the heart of the estimating process. It therefore allows choices to be made at an early stage with regards to using energy efficient piles. A case study is given where three pile types are compared to evaluate their relative carbon footprint.

Keywords: Carbon, Footprint, Piling

1. Background

An understanding of a customer's existing and future needs are essential in business. In order to gain an understanding Balfour Beatty Ground Engineering (BBGE) surveyed its customers to identify what would be the issues of most significance to them in the future. From the survey it was clear that customers would like clarity about the environmental impact of foundation construction. They wanted to understand what the Carbon Footprint of foundation construction is for any given project, so that this could be assessed and minimised.

To meet the customers requests a system was put in place whereby during the estimating process for any given project the carbon footprint of the foundation solution could be calculated routinely, as with other environmental factors such noise and vibration.

BBGE already possessed an in-house estimating application called SIESTA, which put simply uses a library of costs which are multiplied by material and production quantities to provide an overall cost. The system was modified to include calculation of the carbon emissions, using a library of appropriate emission factors for the material and production elements, and was called GREEN SIESTA.

2. Estimating Carbon Emissions

To identify and quantify the carbon-significant elements within their foundation systems BBGE employed NIFES (National Industrial Fuel Efficiency Limited), a specialist in measuring carbon emissions. All aspects of site operations were considered including: piling technique, rigs, material usage, concrete mix design, steel weight, transport methods and typical transport distances for plants and materials.

Where standards or protocols for measuring carbon existed these were followed. During the collation of the carbon library it became evident that there were no set criteria as to how the construction industry should measure embedded carbon - that is the total amount of carbon dioxide emitted from every stage of its production and distribution, from source to end product.

The NIFES figures showed that there was a significant variation in the estimated embedded carbon values for the various elements being considered. Therefore average UK market figures recommended by NIFES were used.

3. Primary Sources of Emissions

In basic terms the more energy involved in a product or process the greater the carbon footprint. The vast majority of this energy comes from the burning of fossil fuels.

3.1 Concrete

The largest contributor to $C0_2$ in foundations is concrete. Concrete is responsible for 60 – 70% of all the $C0_2$ within the construction of foundations (Nirmal et al, 2010). The $C0_2$ embedded within concrete is derived mainly from cement. The production of one tonne of cement produces on average 0.8 tonnes of $C0_2$, but varies depending on production process as shown in Table 1.

Table 1 – CO_2 emissions from cement manufacture

Method of Manufacture	Carbon Emitted
Wet kiln	970 Kg CO_2/te
Semi-wet kiln	930 Kg CO_2/te
Dry kiln	740 Kg CO_2/te
Semi-dry kiln	840 Kg CO_2/te

3.2 Steel

Steel is the second largest contributor to $C0_2$ in foundation production, accounting for 10 – 30% of the total. Mining and processing ore into steel is an energy intensive process.

As steel is traded on world markets its source can be difficult to trace and it can contain unknown amounts of recycled material. It is estimated that virgin steel produces 2.7 tonnes of $C0_2$ per tonne of product. However recycled steel produces 0.4 tonnes of $C0_2$ per tonne of product.

The figure used in GREEN SIESTA is a NIFES advised average of 1.82 tonnes of $C0_2$ per tonne of steel, taking into account the relative proportions of virgin and recycled steel.

3.3 Transport and Fuel

This can account for 10-15% of $C0_2$ in foundation production. This includes for haulage of materials and plant to site, as well as fuel used on site by rigs and other plant. Site fuel usage is approximated from the anticipated duration of the project and the average fuel used per day for the appropriate rig and plant.

For plant and material transport GREEN SIESTA takes into account distance, journey composition and a round trip to average out the emissions due to vehicles being heavily or lightly loaded.

4. How GREEN SIESTA works

During the tender estimation process a Bill of Quantities is produced. From this the GREEN SIESTA system then pulls down information from a library of carbon emission data for each component: concrete / grout, steel, spoil, fuel and mobilisation. This is used to calculate the total $C0_2$ produced for the piling system being estimated, which is then shown in graphical and tabular form.

5. CASE STUDY

In order to evaluate the relative carbon footprint produced by various piling techniques a site was chosen in central London where the piling work had been secured by BBGE. As the site had restricted access the comparison was limited to those techniques that would be used on such sites: micropiling (self-drilling hollow bar system), bottom driven (steel tube) minipiling and auger bored minipiling.

A micropile is installed using a hollow Ischebeck bar (40-127mm diameter) with cutting bits up to 280mm diameter. The bar is percussively drilled into the ground assisted by grout flushed through the hollow bar to the cutting bit. Once design depth is reached the grout continues to be pumped through the bar until the grout comes up to the surface by filling the annulus between the bar and the soil. The hollow drill bar therefore provides the permanent steel reinforcement within the pile.

A bottom driven steel tube minipile is formed by using a steel tube (220mm to 323mm diameter, 5mm thick) which is crimped/closed at one end. Lean mix concrete is placed at the bottom (crimped-end) of the tube and a drop hammer is used inside the tube to drive it into the ground. The tubes come in sections up to 3m long which need to be welded together as each section is progressively driven. When the tube is driven to design depth high slump concrete is tremied in followed by insertion of a single steel bar or cage reinforcement.

An auger bored minipile is constructed by an auger (up to 600mm diameter) drilling into the ground. The auger screws into the soil and is then lifted back to surface with the soil cast to the side. Casing is used as necessary to stabilise the bore. When design depth is reached concrete and reinforcement is placed into the empty bore and the casing extracted, if required.

The project in London consisted of a lightly loaded two storey structure to be constructed on an elevated section of walkway. Site constraints included an underpass and a service tunnel on each side of the piling area (Figure 1).

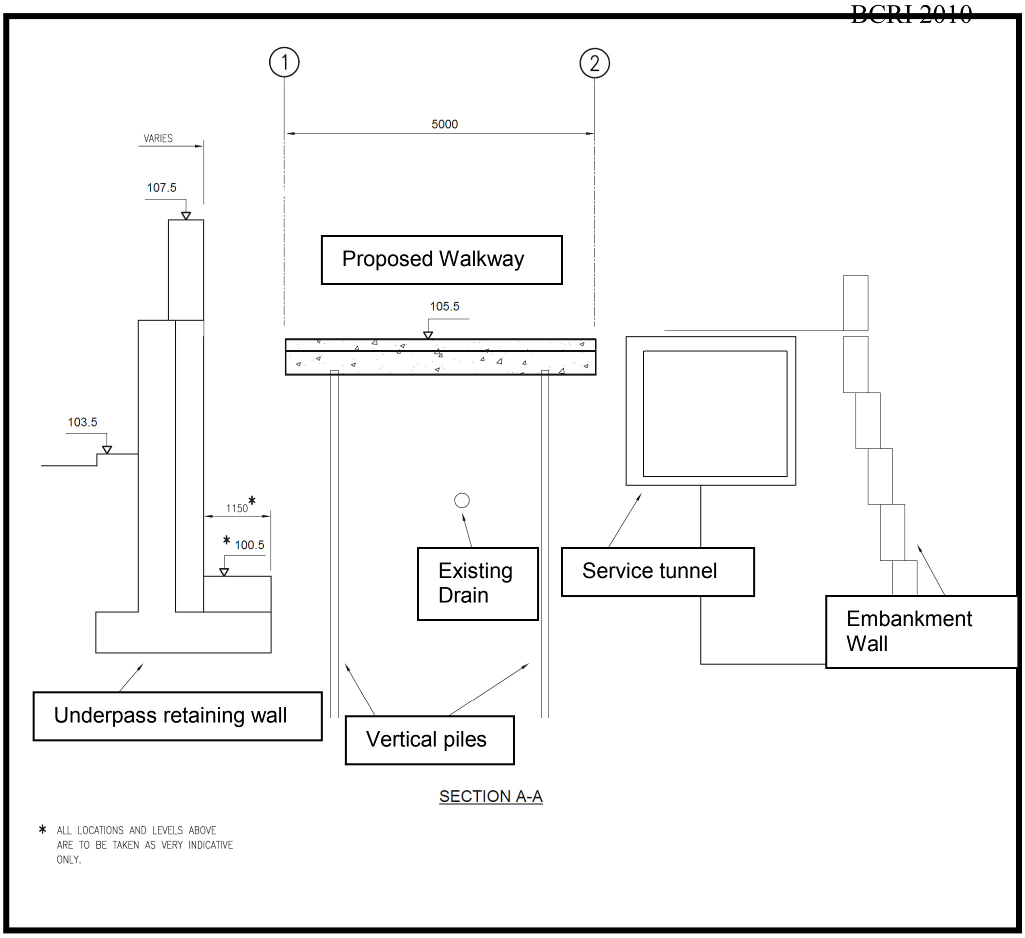

Figure 1 - Typical cross-section (N-S) through the site showing constraints.

In addition to the site constraints the ground conditions were problematic due to the thickness and nature of the Made Ground. A typical geological profile is presented in Table 2.

Table 2 - Typical Geological Profile

Stratum	Level of Top of Stratum (m AOD)	Level of Top of Stratum (m.bgl)	Typical Thickness (m)	Typical Description
Made Ground	104.7	0	9.2	FILL: Compact brown and grey sandy fine to coarse Gravel
River Terrace Gravels	95.5	9.2	4.0	Medium Dense brown fine to coarse SAND and fine to coarse angular to rounded GRAVEL with occasional cobbles.
London Clay	91.5	13.2	Proven to 16.8m	Stiff brown slightly sandy CLAY.

Groundwater was recorded approximately 5.0m BGL.

Three design options (Table 3) were considered for the carbon assessment comparison.

Table 3 - Design Considerations

Type	Diameter (mm)	Length (m)	F.O.S.	Safe Working Load (kN)	Testing
Micropile	40/16 hollow bar with 175mm clay bit	13.0	2	250	Non working pile test
Bottom Driven	220mm	11.0	2.5	250	Dynamic pile test
Auger Bored	300mm	20.5	3	250	None

A Bill of Quantities was produced for each of the solutions. The break down of the bill of quantities is presented in Table 4.

Table 4 - Quantities and Outputs for Micropile, Bottom Driven and Auger Bored Piles

Type	Grout / Cement	Steel kg	Spoil m3	Fuel litres	Mobilisation	Productivity
Micropile	Ordinary Portland Cement – 1.02t or 0.735m^3 grout (overbreak 230%)	110.00	0.4	23	Rigid HGV: 1 No. Approx mobilisation distance: 220 miles	120m per day. Approx 9 per day.
Bottom Driven	Readymix Concrete – 1.2t or 0.50m^3	215.00 for casing + 23.50 for cages (4 no. t12 bars x 6.0m	None	28.5	Rigid HGV: 1 No. Approx mobilisation distance: 220 miles	45.5m per day. Approx 3.5 per day.

Auger Bored	Ordinary Portland Cement 2.5t or 1.80m^3 grout (overbreak 125%)	23.5 for cages (4 no. t12 bars x 6.0m)	1.8	150	Articulated HGV: 1 No. & Rigid HGV: 1 No. Approx mobilisation distance: 220 miles	20-25m per day. Approx 1 per day.

On completion of the Bill of Quantities using the figures derived from GREEN SIESTA the total $C0_2$ for the project was calculated for each piling technique. The results of these are presented in Figure 2 and Table 5.

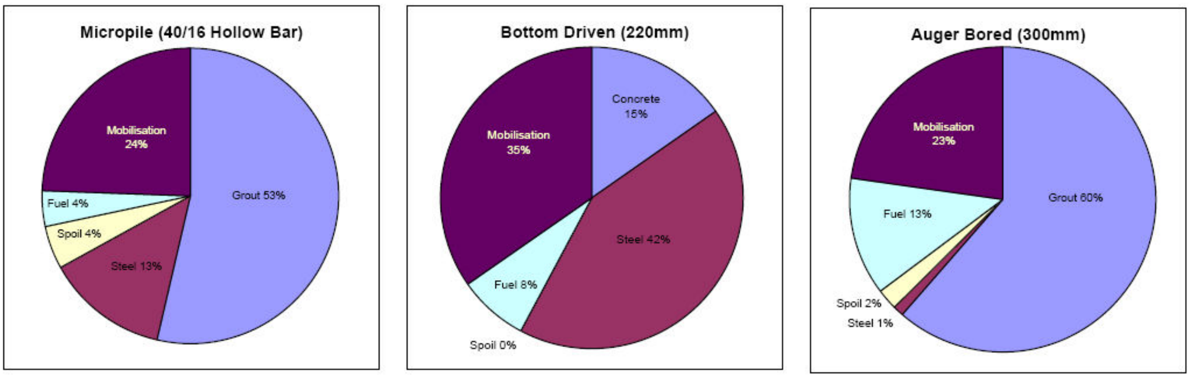

Figure 2 - Percentage of carbon dioxide embedded and emitted for each piling technique, using GREEN SIESTA.

Table 5 - Total carbon dioxide embedded and emitted for each piling technique, using GREEN SIESTA.

Type	Grout[1] / Cement[2]	Steel[3]	Spoil[4]	Fuel[5]	Mobilisation[6]	Total
Micropile	0.79te	0.20te	0.066	0.06	0.36	1.59te
Bottom Driven	0.16 te	0.44te	None	0.08	0.36	1.13te
Auger Bored	1.94te	0.04te	0.066	0.4	0.72	2.91te

1) GREEN SIESTA uses a NIFES advised average of 777kg CO_2/te
2) GREEN SIESTA uses a calculated average of 328kg CO_2/m^3
3) GREEN SIESTA uses a NIFES advised average of 1,820kg CO_2/te
4) Transport only. Based on 50 mile trip, 50% urban and 50% rural
5) Based on DEFRA recommendation of 2.630kg CO_2/litre
6) Round trips are assumed by an articulated HGV with 40% urban, 40% rural and 20% motorway driving

Whilst the bottom driven steel tube minipiling system produced the lowest amount of $C0_2$ the micropile solution was chosen as the most suitable for this project because of the following advantages it provided; the ability to overcome the anticipated obstructions in the Made Ground, programme and limited spoil generation.

6. Discussion

Considering each pile type in turn:

6.1 Micropile

The total embedded and emitted carbon produced by the micropile was 1.59 tonnes, which places it in second place out of the three. Whilst the system uses a relatively small volume of grout, the grout required contains higher cement content. This is reflected in the high $C0_2$ output. However the system was chosen as the preferred minipiling technique for this site because of other significant factors, principally its ability to quickly penetrate through the upper compact fill material producing minimal spoil, which would have been costly to dispose of.

6.2 Bottom Driven Pile

The total embedded and emitted carbon produced for the bottom driven pile was 1.13 tonnes. This was the lowest of the three piling techniques considered and so indicates that where the system is suitable from a technical viewpoint it can provide the most energy-efficient and sustainable choice. In addition it usually is the most cost-effective system. The highest portion of carbon attributed to the system is in the use of steel for the permanent casing and reinforcement. Whilst the volume of concrete used in the bottom driven pile is higher than the grout volume required by the micropile the overall amount of cement used in the concrete is less than in the grout and so the overall amount of $C0_2$ produced is less.

As the bottom driven pile is a displacement pile there was no additional carbon generated for the removal of the spoil. This can provide a significant advantage should the soil be contaminated and be expensive to remove from site.

6.3 Auger Bored Pile

The total embedded and emitted carbon produced for the auger bored pile was 2.91 tonnes. This is 2.5 times more carbon than the bottom driven pile and 1.8 times more carbon than the micropile. Auger bored is therefore the ‘worst offender’ for carbon production. This is due to the (relatively) inefficient design leading to its longer length. Whereas the bottom driven and micropile can derive the bearing capacity needed from the gravels the auger bored piling system uses lower skin friction adhesion factors which require it to extend down into the underling clay. Therefore, the increased pile length requires greater materials (particularly grout) and hence greater carbon content. It should also be noted that the additional transport required delivering the casings and flights to site for the auger bored method also contributed to its greater total carbon content.

6.4 General Issues

From the research conducted for this paper it is clear there are large variations in identified Carbon Emission for different construction processes and that there is no single agreed procedure for calculating this. For instance if the figures published for recycled steel are utilised this would have a dramatic reduction in calculated carbon content. Traceability of the source of the steel or identifying the percentage of recycled material within the steel or concrete is very difficult and so precise figures for every situation are not possible.

Furthermore it is evident that the design mix for the concrete/grout mix can have a significant impact on the amount of the total carbon produced e.g. if cement replacements such as PFA are used the amount of $C0_2$ can be reduced significantly.

Clearly the design of the pile and the ability to reduce the length of the pile required can bring rewards both financial and in reduction of carbon footprint. Consideration should be given to appropriate pile testing at an early stage of a project if appropriate so that design efficiencies can be made which possibly could lead to reduced pile length and reduced amount of materials (and carbon content) required.

7. CONCLUSIONS

The paper compares the carbon footprint of three restricted access minipiling techniques for a central London project. The results show that the carbon footprint of a pile can be easily estimated and from surveys of clients' requirements we know that this parameter is of interest to clients. Therefore if a client wished to choose a more sustainable foundation solution which has a lower amount of energy embedded into its production and construction, then this gives them the information which allows them to make this choice. As can be seen from the above Case Study the Carbon Footprint of a pile is only one of a number of factors that need to be taken account of and ultimately the chosen minipiling solution must fulfil its technical obligations under the contract first and foremost. In the Case Study the micro-pile was not the most energy-efficient system however it was best able to deliver the technical requirements and so was chosen on that basis. Interestingly the most energy efficient system (the bottom driven steel tube minipile) is usually the most cost-effective technique, so the sustainable option, when suitable, can also be the most affordable.

It is suggested that where possible, consideration should be given to the use of cement replacement materials (e.g. PFA) to further minimise carbon content.

Efficiencies in pile design, which can be supplemented by increased use of preliminary pile testing, can lead to shorter and more cost-effective piles being constructed. This also can bring obvious environmental benefits.

The Carbon Calculator demonstrated in the GREEN SIESTA system can be used with any foundation (piling or ground improvement) system to allow comparisons of carbon footprint to be made between them and so provide the client with the information they need to make a sustainable choice.

References

Tiwari, N.K., Scott, J.N. and Troughton, V.M. (2010), 'Sustainability in the Foundation Industry', in *Proc. EFFC/DFI Geotechnical Challenges in Urban Regeneration*. Excel Centre, London. May 2010.

FULL-SCALE STATIC LOAD TESTS ON INSTRUMENTED MICROPILES

A.P. GALBRAITH & E.R. FARRELL

Dept. of Civil, Structural and Environmental Engineering, Trinity College, Dublin

Abstract

This paper presents the findings of four maintained compression load tests carried out on instrumented micropiles on the Malahide Causeway in December 2009. The micropiles were installed and were constructed in a similar manner to those which had been installed for Irish Rail as part of the remediation works to the viaduct following a pier failure due to erosion in August 2009.

The load/deflection behaviour at the pile head is presented during the different stages of the tests and a methodology of converting measured strains at various depths to force in the micropile is described and used to develop force/depth profiles. These results are used to determine the magnitude of the interface shear stresses developed in each of the three principal strata through which the piles were installed.

In addition, two tests were carried out at each location in order to study the repeatability of installation as part of a general study into reliability in pile design.

Keywords: instrumentation, force/depth profile, micropiles, reliability, strain readings

1 Introduction

Micropiles are frequently used as part of remediation work for foundations, particularly where there is limited access, and it is generally considered that the construction method employed results in increased shaft resistance compared to traditional piles due to permeation of grout outside the nominal diameter of the pile, (Tonon and Mammino 2004), (Russo 2004). The remediation work of the Malahide Causeway offered an opportunity to instrument 4 No. micropiles, which were installed during November and December, 2009, to determine the distribution of strain with depth during loading and from this estimate the shaft resistance.

In addition to determining the force/depth profile for each pile, two tests were carried out at each location in order to study the repeatability of installation as part of a general study into reliability in pile design. These tests gave an indication of the repeatability of the method of installation of the micropiles and also an indication of the variability of the ground for the site under study.

2 Background

2.1 Test Pile Locations

The test piles were installed on two raised rock fill platforms, about 10 by 10m in plan area, on the West side of the viaduct. One platform was located on the Southern (Malahide) end of the viaduct and the other at about midspan. Two compression tests were carried out from each platform, Pile 1&2 from the North platform (between piers 6&7) and Pile 3&4 from the other, (between piers 10&11). The test level of the North and South platforms was around 1.2 and 2.0m OD respectively with the general level of the top of the causeway at about 0.7mOD. The causeway maintains the western water level at about +0.7m OD, however the tidal variation at the marine side is between about -1.5 and +1.0mOD (Malin).

2.2 Installation of Piles

The micropiles comprised an R51N (51mm diameter) hollow Dywidag bar with a full length external thread, that, in combination with a sacrificial drilling head (115mm diameter), becomes a self-drilling micropile.

Prior to their installation, a steel case of outer diameter 139mm and of wall thickness 3mm was installed to a depth of approximately 5m using the Odex method.

The micropiles were constructed by pumping grout through the 33mm bore of the R51N bars as they were drilled to the required depth. The ultimate strength and the stiffness of the hollow bar was 800kN and 214GPa respectively (Dywidag 2010).

The micropiles were instrumented by insertion of a 12mm diameter 16m long rebar on which electrical resistance strain gauges had been placed at 1m centres, with the first gauge 300mm from the end of the rebar (which would lie at the toe of the pile). This instrumented rebar was inserted into the now grout filled bore of the R51N bar immediately after the pile had been installed. Additional gauges were placed on one of the piles to give some indication of the reliability of the strain readings and also on possible bending effects.

Four No. micropiles were installed in this way and the details are displayed in Table 1.

2.3 Ground Conditions

The ground stratigraphy comprised causeway stone fill, over alluvium, over glacial till classified as a clay of low-intermediate plasticity (Figure 2.1), over limestone at depth well below the piles founding level. Ground test results and the stratigraphy at each test location, interpreted by Roughan and O'Donovan, consulting engineers to Irish Rail are presented in Figure 2.2 and Figure 2.3 respectively.

Table 1 - Pile Details

Pile	Location Pier	Pile Head Level [mOD]	Platform Level [mOD]	Pile Length [m]	Pile Toe Level [mOD]
1	6	1.4	1.15	14.75	-13.35
2	7	1.32	1.19	14.73	-13.41
3	10	2.43	1.98	14.94	-12.51
4	11	2.38	1.93	13.56	-11.18

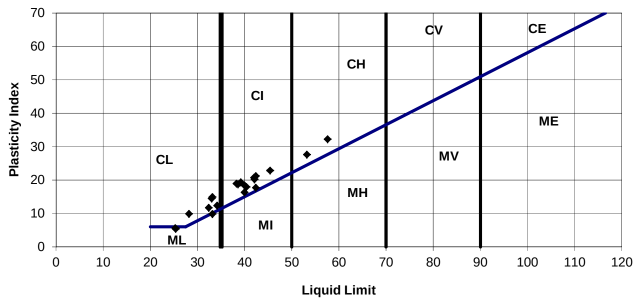

Figure 2.1 – Plasticity Chart

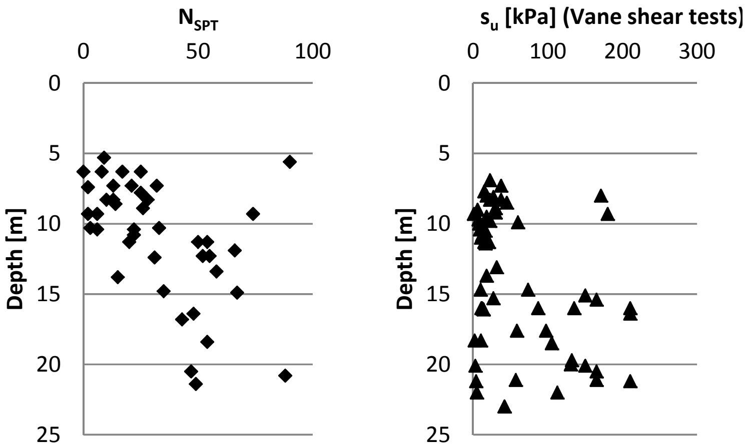

Figure 2.2 – Results of SPT and vane shear tests vs depth

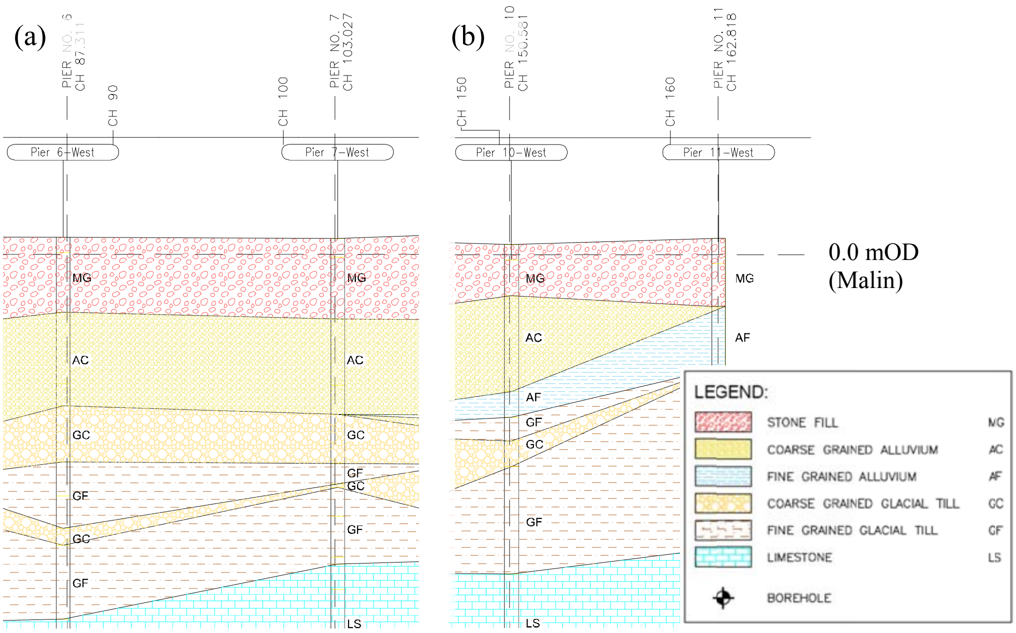

Figure 2.3 – Interpreted Stratigraphy, (a) Pier 6-7 (b) Pier 10-11 (equal horizontal and vertical scales from Roughan & O'Donovan)

2.4 Test Arrangement and Programme

The test arrangement was designed to allow testing of 2 No. micropiles simultaneously, using two separate hydraulic jack and pump systems, to achieve a maximum test load of 750kN over three load cycles. One long main reaction beam was used with three cross beams to span over two test piles, with six tension anchors to provide the reactive force to compressive loading of the test piles (Figure 2.4). These tension anchors were placed just in excess of ten test pile diameters - 1.4m, from each test pile and were constructed in the same fashion as the test piles.

It should be noted that when testing Pile 1 and Pile 2 the stool was deflected at higher loads, causing a reduction in the load on one of the piles. These problems resulted in the application of 5 load cycles to both Pile 1 and Pile 2 to achieve the desired test load.

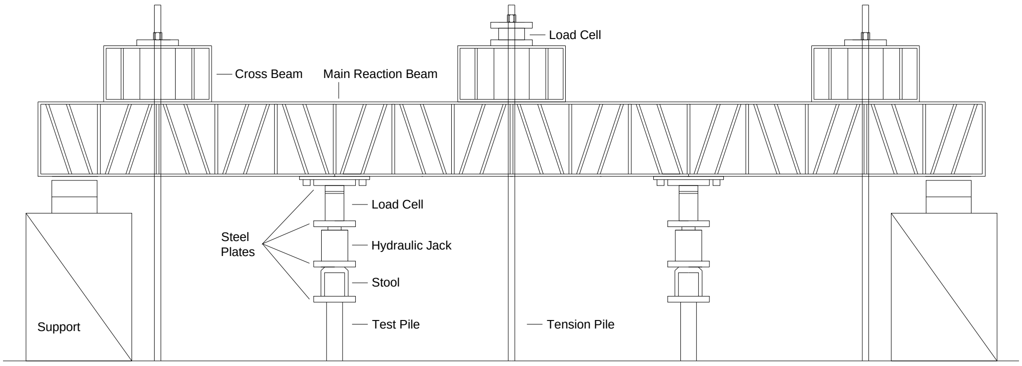

Figure 2.4 - Overall setup front elevation

3 Pile Test Results

The results of the pile load tests are presented in this section including the load/deflection behaviour force/strain behaviour measured at the pile head.

3.1 Pile head load/deflection

The measured pile head load/deflection data for each of the test piles is displayed in Figure 4.1 for each load cycle applied to the piles with unload cycles removed for clarity alongside a smoothed hyperbolic fit using Chins method, (Chin 1970). Pile 1 & Pile 2 were loaded to about 870kN and Pile 3 & Pile 4 to about 650kN.

It can be seen that the response of Pile 1 & Pile 2 was similar and the same is true for Pile 3 & Pile 4 while there is an obvious difference between the two sets of tests with Pile 3 & Pile 4 being deflected to greater head deflections at lower loads.

Figure 4.1 also shows the load/time cycles for Pile 3 & Pile 4, a similar incremental load/time approach was applied to Pile 1 and to Pile 2 though more cycles were required due to load drop off during one of the load cycles.

4 Interpretation and Discussion of Results

4.1 Force/depth profile

The strain readings were logged continuously during intermittent periods throughout the load test sequence and were interpreted to estimate a force/depth profile for each micropile tested. Some strain gauges yielded unreasonable values and were removed from the plots prior to any interpretation.

Force/strain relationship at pile head

The force/strain relationships recorded from the strain gauges located close to the pile head (within the Odex casing), for each of the test piles are displayed in Figure 4.2.

The force/strain data are approximated well by a straight line at strain values greater than about 200με. It should be noted that very large gauge readings were recorded on gauges closest to the pile head and these were discarded on the grounds that the load had not yet been distributed evenly over the cross section of the pile – the second closest strain gauge (at about 1.3m from the pile head) was then used in interpretation.

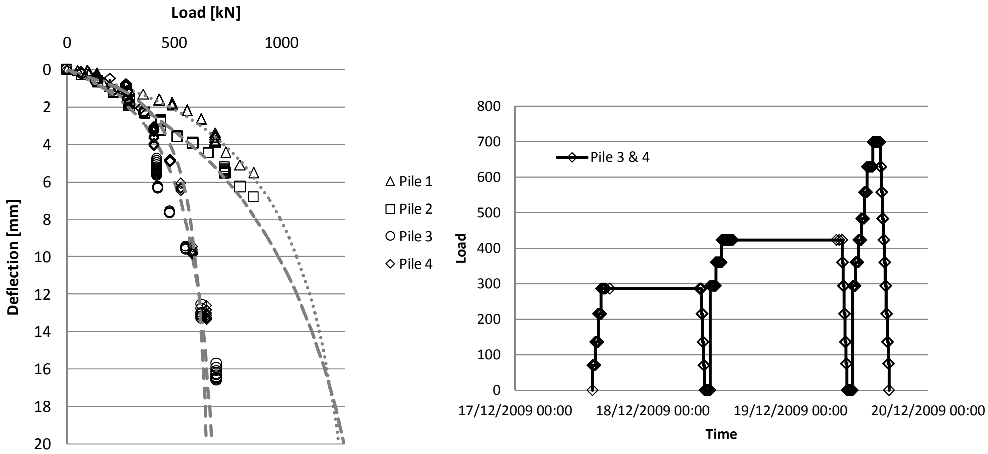

Figure 4.1 - Pile head load/deflection curves and load/time graphs

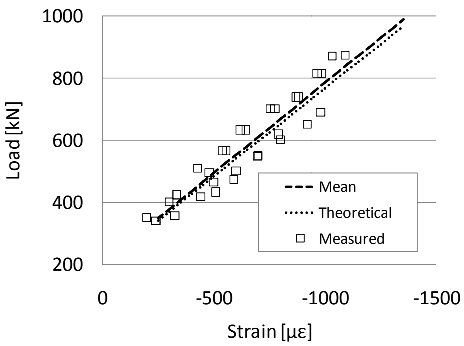

Pile [_]	EA [MN]	E [GPa]
1	599	39
2	643	42
3	530	35
4	409	27
Average	545	36

Figure 4.2 – Force/strain relationship and summary Pile 1 - Pile 4

The force/strain relationship shown on Figure 4.2 was used to convert strain readings directly to force where the cross-section remained constant, i.e. the uppermost 5m of each test pile where the outer steel casing was present. The force/strain relationship for the remainder of the pile was estimated by adjusting the values (where is the overall stiffness of the micropile of cross-sectional area) to allow for the change in cross section described in the following.

Verification of force-strain relationship within the upper 5m

The force, at any section may be calculated by the product of the measured strain, the gross stiffness of the pile and the gross cross-sectional area of the pile . It should be noted that will vary when the section changes.

The slope of the force/strain graph at the pile head, which is given on Figure 4.2, gives the gross value for the upper pile section which includes the 139mm diameter outer casing. The computed values using this plot are reasonable, ranging from 27-42GPa with a mean value of 36GPa. A theoretical load/strain curve is also displayed on Figure 4.2 and compares well with the value of interpreted using the measured strain. Uniform strain conditions were assumed and the average stiffness of the grout, for the closest match is 6GPa, not unreasonable for this early age water-cement mix (though no cube or cylinder tests were carried out on this material at the time of loading).

Calculating EA when the cross-section changes

A EA value was computed for the pile section below the casing by using the same material stiffness parameters for each element in the pile cross-section. It was found that the EA value for the section of the pile below the casing was around half that for the cross-section where the casing was present, therefore an EA equal to half that of the cased section was used for the remaining pile length, thus assuming a constant pile section comprising the R51N anchor, with the 12mm central bar, a grout fill central core with the outer grout surround extending to 115mm diameter. The resulting force/depth profiles are considered to be reasonable. In practice, the grouted pile section may vary with depth, however, most of the force would be taken by the anchor and the central bar, consequently the assumption of constant EA with depth is not unreasonable.

Interpreted force distribution

The interpreted force distribution profile for Pile 1 and Pile 3 are shown in Figure 4.3, as examples. A small percentage of the applied load reached the toe of Piles 1, 2 and 3, typically less than 10% with around 25% reaching the toe of Pile 4 at higher loads, these values are comparable to those interpreted by others in the case of similar piles under test, (Han and Ye 2006), not surprising – the ratio A_s/A_b is greater than 500 and it is well known that larger displacements are required to mobilise base resistance than shaft resistance.

4.2 Pile-Soil Interface Shear Stress

The shear stress profile, τ developed at any applied load may be estimated from the interpreted force/depth profile by division of the change in load, ΔF between strain gauges locations by the area of pile shaft A_s between the same strain gauges.

Each pile was considered in three parts, corresponding to the three principal soil layers, allowing estimation of τ developed within each of the layers.

Causeway Fill

The estimated shaft shear stress developed in the Causeway Fill was in the range 140 – 200kPa considering all four tests (see Figure 4.4). The value of 200kPa was estimated for Pile 2 only, with the other three piles tested developing around 150kPa in this layer, at their respective maximum applied loads.

The interpreted stress-deflection curve for the Causeway Fill would indicate that limiting shear stress may have developed in this layer in the case of Pile 1, Pile 3 and Pile 4 where it reached about 150kPa. In the case of Pile 2, shear stress seems to be increasing further and reached a maximum of 200kPa at the maximum applied load.

Alluvium

The Alluvium layer underlying the Causeway Fill developed little shear stress, in the range 0 – 25kPa in the case of Pile 1, Pile 3 and Pile 4. It is estimated that a greater shear stress, about 50kPa, was developed in the Alluvium layer in the case of Pile 2.

Glacial Till

Pile 1 and Pile 2 both developed around 100kPa in the Glacial Till layer at the maximum load application. Pile 3 developed around 110kPa, and Pile 4 developed almost double that of the other piles, about 200kPa.

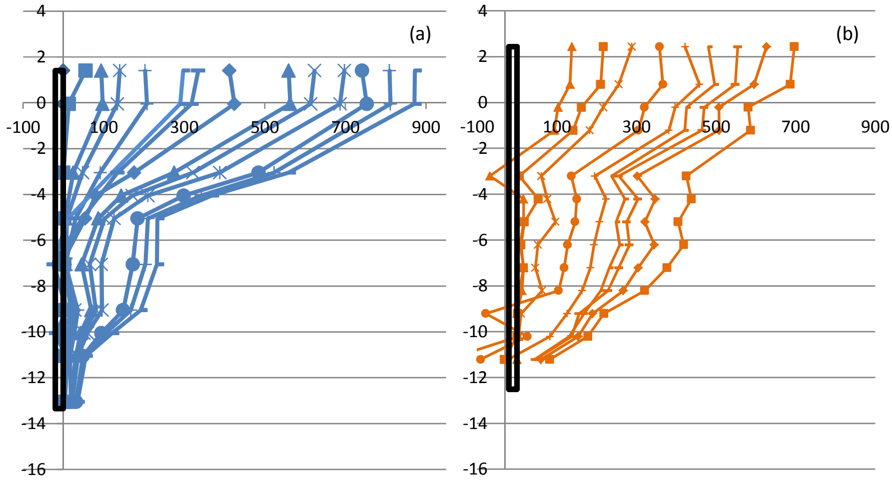

Figure 4.3 - Interpreted load/depth profile (a) Pile 1 & (b) Pile 3

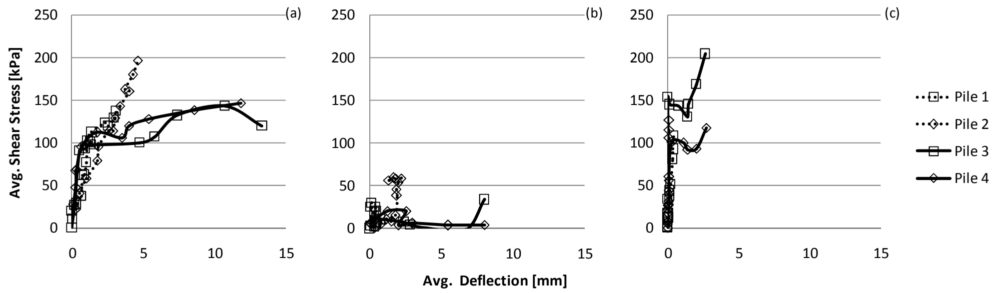

Figure 4.4 – Estimated stress-deflection in (a) causeway fill (b) alluvium (c) glacial till

Pile 1 and Pile 2 show no sign of reaching a limiting shear stress in the Glacial Till layer, where Pile 3 and Pile 4 indicate little gain in stress with increasing strain – this is to be expected due to higher deflections in the case of Pile 3 and Pile 4. Pile 3 and Pile 4 were deflected by 2.5 times that of Pile 1 and Pile 2 and so these piles would be expected to develop greater shear resistance in this lower Glacial Till layer (under a limiting value). The pile deflection in this lower Glacial Till layer is estimated to be around 2.5mm at a maximum.

5 Conclusions

Four micropiles were successfully instrumented with strain gauges and these gave a reasonable strain/depth profile at the various load stages.

Strain gauges placed on opposing sides of the central instrumented bar of Pile 4 gave readings within 95% of each other even at the maximum load application, indicating that strain readings were reliable.

A relationship between force and strain was developed using the data from strain gauges close to the pile head and this relationship was adjusted for the change in cross section of the micropiles at around 5m depth where the casing was terminated. The estimated force/depth profile was consistent with what would be expected for the strata penetrated.

The two piles on each platform yielded almost identical results with respect to the pile head load/deflection behaviour, indicating that the pile installation method is fairly repeatable.

The two sets of pile test results, however, exhibited very different behaviour despite the fact they were installed using the same piling rig. The distinct change in behaviour between the two sets of pile tests is considered to be due to the difference in ground conditions and this highlights the importance of considering the ground variation on a site when interpreting pile load test results.

The reliability of these micropiles is increased where the pile test results are considered as two separate sets of results (at each of the two separate locations) as opposed to one. Considering the results in this way has the effect that the resistance of the pile in both locations is increased for a particular level of confidence in the foundation.

Most of the applied load was resisted along the shaft of the pile with a small percentage of the applied load reaching the toe of Piles 1, 2 and 3 – typically less than 10% with around 25% reaching the toe of Pile 4 at higher loads.

It was observed that most of the applied head load was resisted by skin friction in the Causeway Fill (crushed rock) layer, where it was estimated that a shear stress of about 150kPa was developed, with up to 200kPa for Pile 2 only.

Practically no load was resisted in the Alluvium layer for Pile 3 and Pile 4 with low values of 25 and 50kPa estimated for Pile 1 and Pile 2 respectively at higher loads.

An average skin friction of around 100kPa was estimated to have developed in the Glacial Till layer for three of the piles with Pile 4 reaching 200kPa. The stress-strain curves for this layer show no signs of having reached a limiting shear stress. This suggests that the shear stress in this layer may have continued to increase with increasing strain had the piles been loaded further.

Acknowledgements

The Authors acknowledge Irish Rail for permission to use the results, to Jons Civil Engineering, P.J.Edwards and Co. Ltd for installation of the test piles, AGL Consulting and Roughan & O'Donovan.

This research is funded by the Irish Research Council for Science, Engineering and Technology (IRCSET) with Byrne Looby Partners under the Enterprise Partnership Scheme. The Authors also thank the Geotechnical Trust Fund for their support.

References

Chin, F. K. (1970). Estimation of the ultimate load of piles from tests not carried to failure. Proc. 2nd S.E. Asian Conference, Singapore.

Dywidag, S. I. (2010). "DYWI ® Drill System Technical Data." Retrieved 31/05/2010, 2010, from http://www.dywidag-systems.com/uk/products/geotechnical-systems/dywi-drill-system/technical-data.html.

Han, J. and S.-L. Ye (2006). "A field study on the behavior of micropiles in clay under compression or tension." Canadian Geotechnical Journal 43: 19-29.

Russo, G. (2004). "Full-scale load tests on instrumented micropiles." Institution of Civil Engineers 157(GE3): 127-135.

Tonon, F. and A. Mammino (2004). "Reliability-Based Design and Construction Issues for a Micropile Foundation in Costa Rica." Practice Periodical on Structural Design and Construction, ASCE 9(4): 227-236.

INSTRUMENTED STATIC PILE LOAD TESTING – FIELD PROCEDURES, DATA INTERPRETATION AND RECENT DEVELOPMENTS

P. DOHERTY[1], D. IGOE[1] & K. GAVIN[1]
[1]Geotechnical Research Group, Dept. of Civil Engineering, University College Dublin, Ireland

Abstract
Pile load tests are a necessary requirement of most piling projects to validate capacity and confirm the initial design assumptions. However instrumented pile testing offers significant advantages over conventional uninstrumented tests and are warranted in a number of circumstances, where the benefit of instrumentation offsets the additional expense. This paper describes the issues which arise when designing an instrumented load test. Interpretation of the instrumentation output is discussed in detail, with particular emphasis on selecting an appropriate pile modulus and the impact of residual loads. The final section briefly describes some recent advances in instrumented testing, highlighting the state of the art in geotechnical instrumentation, including osterberg testing, fibre optics and retrievable extensometers.

Keywords: Piling, Instrumentation, Foundation, Load Tests

1. Introduction

In recent years the complexity of civil engineering structures has increased dramatically, with buildings such as the Burj Khalifa tower in Dubai pushing the limits of what was previously thought possible. These revolutionary projects are becoming more commonplace and each innovative superstructure places additional requirements on the supporting substructure. Designing foundation solutions to meet these new challenges often requires significant innovation in terms of capacity, serviceability and constructability. In order to validate the reliability of novel foundations in-situ testing is becoming more common place – in particular instrumented load testing offers a practical means of validating design assumptions and confirming the suitability of the proposed piling solution.

2. Why conduct an instrumented pile test?

Conventional load tests, which utilise a load cell and displacement gauges at the pile head, are a mandatory requirement for most projects involving piled foundations, with a fraction of the production piles (typically 1-3%) tested to validate the geotechnical design. However, there are a number of situations where instrumented pile load tests (IPTs) provide a beneficial alternative to conventional load testing. These situations include:

- To validate the pile installation process and the construction methodology in situations where novel foundation solutions are being adopted
- For structures that are highly susceptible to movement and displacement limits are relatively tight, IPTs offer the most appropriate method of quantifying the pile stress-strain relationship.
- Where the ground conditions are uncertain, highly variable or unfamiliar.

• Interactive design where preliminary pile tests at the outset of the project can be used to refine the production pile design leading to efficient foundation solutions.

3. Designing an instrumented load test

The detailed design of an IPT is essential to achieve the required test results. Engineers are concerned with obtaining two design parameters, namely the unit skin friction, q_s, and the unit end bearing, q_b. A well designed test has the following key characteristics:

(1) The pile should be designed to fail under the applied loads to achieve the ultimate limit state, and thus allow quantification of the actual factor of safety. In addition, the reaction system should be designed to ensure adequate capacity and minimum compliance.

(2) The pile test should ideally be conducted by incrementally increasing the load to failure without unloading, as unloading loops can result in residual stress accumulation which can complicate interpretation of the instrument output.

(3) The test pile location should be conducted in ground conditions which are well known, ideally adjacent to an existing borehole or in-situ test profile. This will allow the resulting pile skin friction to be correlated to local rather than average soil properties. Once this correlation has been established it is easily extrapolated across the site using data from additional boreholes.

(4) The most common instrumentation system method in current use is strain gauges. Budget will play an important part in deciding the amount of instrumentation used, however the trade off between economy and performance should be carefully considered to ensure adequate instrumentation is incorporated into the pile. Each instrumentation level should incorporate four strain gauges offset by ninety degrees to minimise any bending effects due to eccentric loading or non-verticality in the pile.

(5) The uppermost strain gauges should be located near the pile head with no load transfer occurring between the applied load and this level. In practice, this can be implemented by debonding a small length of the pile shaft near the ground surface, by excavating the pile to the first level of gauges or by extending the pile above ground and incorporating this level of gauges in this region (see Figure 1). The load cell can then be used to calibrate/validate the strain gauge output. In the case of concrete piles, this level of gauges provides an accurate measure of the composite Young's modulus, which is strain level dependent.

(6) Strain gauge levels should be located at the interface of geological strata, such that the pile-soil load transfer can be quantified for a given soil type.

(7) Where strain gauges are to be used to quantify the base load, it is important to have multiple levels in close proximity to the pile base, as extrapolation is often required from the lowermost strain gauge level to the pile tip. This is particularly important for driven piles where a highly non linear shaft shear stress distribution can exist close to the pile tip and linear extrapolation can overestimate the base resistance.

(8) Accurate pile construction details should be recorded to aid interpretation of the pile test. In particular times between soil excavation and concrete placement should be recorded for bored piles and the blow counts recorded for driven piles.

(9) An accurate pile cross section is required for strain gauge interpretation and therefore strain gauges should be placed to avoid overlapping steel bars in the reinforcement cage of bored piles or to avoid other disconformities in the reinforcement structure.

(10) The reinforcement cage should be robust and not overly slender to minimise deformations during the cage lifting and placement operations, which might alter the vertical alignment of the strain gauges. For concrete piles, the gauges are protected by their intimate contact with the concrete/grout, however in the case of driven steel piles the gauges are housed internally or within welded channels, which provide adequate cover.

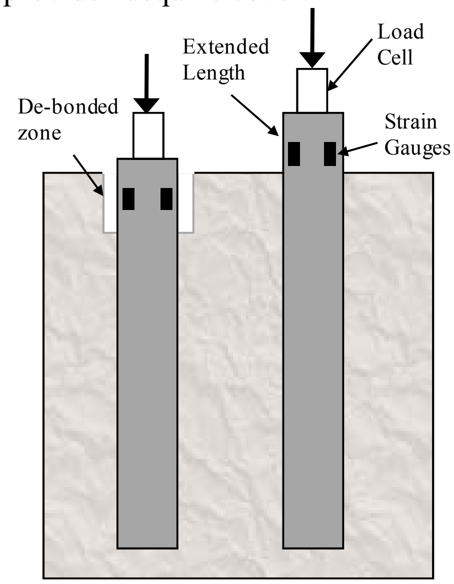

Figure 1 – Uppermost Layer of Strain Gauges

4. Instrumentation Selection

There are a number of alternative instrument choices available for measuring strain in piles. However, the most commonly used strain gauges in static load tests are vibrating wire (VW) gauges, which have a number of advantages over electrical resistance strain (ERS) gauges or semi-conductor types. The primary advantage of the VW gauge is the sensor output, which is a frequency rather than an electrical resistance or a voltage. This results in a more stable output which is unaffected by voltage drops resulting from poor electrical contacts. Additional benefits include resistance to moisture ingress and temperature changes, both of which significantly impact on ERS gauges. VW gauges are typically attached by welding or cable ties and this makes VW technology more robust and hence more suited to civil engineering applications than the electrical alternatives. Signal loss due to excess cable length can also be a significant issue for ERS gauges however VW applications are unaffected by changes in cable length due to the nature of the output. VW gauges are clearly the sensor of choice for static pile load tests, however the frequency with which VW gauges can be read is limited and as a result ERS gauges are required for dynamic application such as for measuring the dynamic installation resistance during pile driving. There are many adaptations of this technology for different civil engineering uses. Figure 2 shows the different types of strain gauges used for pile load testing, including ERS gauges, concrete embedment, arc weldable and sister bar strain gauges.

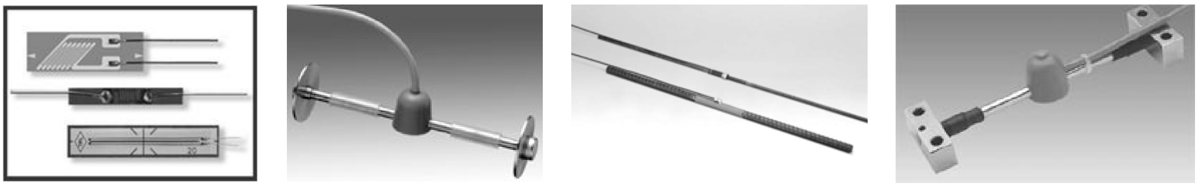

Figure 2 – Uppermost Layer of Strain Gauges (a) Foil ERS Gauges (b) VW Concrete Embedment (c) VW Sister Bar and (d) VW Arc Weldable Strain Gauges

As can be seen from Figure 2, concrete embedment gauges have two enlarged end plates which provide adequate grip for the concrete/grout and are ideally used for measuring the concrete strain in bored piles. These gauges are probably the easiest to install using cable ties and a slightly adapted reinforcement cage with pre welded parallel bars. This installation process is shown in Figure 3a for the reinforcement cage of an 800 mm diameter, 15 m long CFA pile installed in Killarney (See Gavin et al. (2009). An alternative arrangement for instrumenting bored or CFA piles is the "sister bar" strain gauge. This typically comprises a miniature VW strain gauge installed inside a 100 to 200mm length of high strength steel on the neutral axis. Two rebar extensions are then welded to either end of the strain measuring unit. These provide sufficient concrete contact to minimise local slippage and the impact of local unconformities. A schematic of the sister bar arrangement is illustrated in Figure 3b. The sister bars are welded alongside the longitudinal rebars of the reinforcement cage and thus measure the reinforcement strain rather than the concrete strain as in the case of embedment gauges. Sister bars, while typically more expensive than embedment gauges, offer higher durability and are often specified for situations requiring a very robust solution. Driven steel piles, usually adopt arc weldable strain gauges which are installed directly on the pile shaft within the preformed protection channels for both tubular and H-piles.

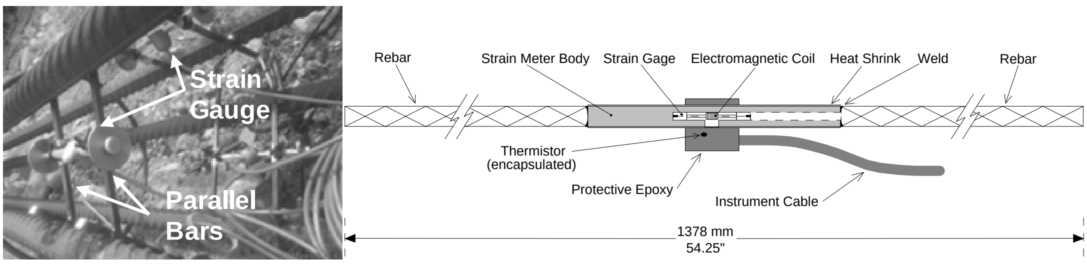

(a) (b)

Figure 3 - (a) Embedded Concrete Strain Gauges and (b) The Sister Bar Strain Gauge (after Deschamps & Richards, 2005)

5. Interpreting the Results

Determining the loads from the strain measurements requires a sophisticated analysis by a skilled engineer familiar with strain measurements and the potential errors that may arise. The Force, F, in an axially loaded pile of cross sectional area, A, can be related to the applied strain, ε, through Eqn. 1a.

$$F = EA\varepsilon \quad (1a)$$

$$F = (E_s A_s + E_c A_c)\varepsilon \quad (1b)$$

The Youngs' modulus, E, is the composite young modulus of the pile material. For a driven steel pile the value of E is simply the Youngs' modulus of steel, E_s, which is known to be a relatively constant parameter at approximately 200kN/mm^2 ±5%. However, the composite modulus of a concrete pile must consider both the reinforcement steel area, A_s, and concrete area, A_c as per Eqn. 1b. In contrast to steel, the Young's modulus of concrete, E_c, is not a constant but varies in proportion to both the compressive strength and more importantly the strain. The range of compressive loads applied to the pile during a load test will result in a significant spread in the operational value of E_c between the onset of the test and failure. This is also true for the distribution of load through the pile shaft, as the load reduces with depth and the corresponding strain reduces, the operational value of E_c will increase.

5.1 Determining an Appropriate Pile Modulus

To overcome the problem of determining a representative value of E_c, Fellenius (2001) proposed a method to determine the tangent modulus, M (see Eqn.2), of the concrete directly from the test data. This method works on the premise that once the pile shaft resistance is fully mobilised, the change in stress varies linearly with the change in strain, as per Eqn.'s 3 to 5. The pile secant modulus, E_{sec} can thus be determined by linear regression of the measured experimental tangent moduli as a function of strain, allowing the parameters for A and B to be quantified.

An example of such an analysis is shown in Figure 4 for a case history presented by Fellenius (2001) for a driven tapered concrete pile in sand. Clearly an assumed strain independent pile modulus would result in significant error in determining the load from the measured strains. The main difficulty in using this method of analysis is that complete mobilisation of the unit shaft resistance is required for accurate regression. Proof load tests mobilising only a small proportion of the ultimate shaft resistance will not provide sufficient data at large strains to accurately determine the A and B parameters. This is overcome by using the strain gauges in the initial debonded zone as a calibration tool for the remaining levels, which should provide an accurate strain-modulus relationship.

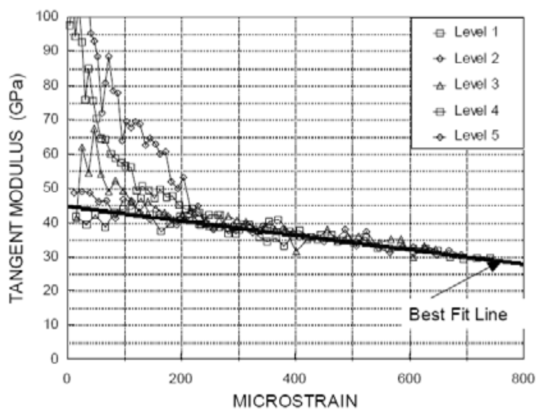

$$M = \frac{\Delta\sigma}{\Delta\varepsilon} = A\varepsilon + B \quad (2)$$

$$\sigma = 0.5A\varepsilon^2 + B\varepsilon \quad (3)$$

$$\sigma = E_{sec}\varepsilon \quad (4)$$

$$E_{sec} = 0.5A\varepsilon + B \quad (5)$$

Figure 4 - Dependence of Tangent Modulus on Strain (after Fellenius, 2001)

5.2 Residual Loads

Residual loads are present in both bored and driven piles and can significantly influence the ultimate distribution of load (Fellenius 2002). In driven piles the rebound and decompression of the soil beneath the pile base mobilize a tension shaft resistance which 'locks in' load at the pile base. In bored piles residual loads are caused by soil creep and settlement around the pile. In the past it has typically been commonplace to zero strain gauge readings prior to load testing, and hence ignoring any residual loads developed during the piles installation. The errors caused by this can lead to an overestimation of the shaft load by more than 40% (Alawneh and Malkawi, 2000) and results in an equal underestimation of the base load. Residual loads also significantly affect the load-displacement response of a pile as the base load may be partially mobilized prior to loading.

Figure 5a shows a profile of strain gauge loads along a driven square precast concrete pile in loose sand (Fellenius, 2002) during the final increment of a static load test. The strain gauge readings were zeroed prior to the test and hence the 'measured' values ignore residual loads. The 'true load' represents the values which are corrected for residual loads. Figure 5b shows the load-displacement curve for a static load test and demonstrates the potential error which can occur when residual loads are ignored. Although the total capacity is unaffected by residual loads, it is essential that residual loads are accounted for when separating the base and shaft load components. Residual loads can be measured in two ways:

1 Zeroing the strain gauges prior to installation and measuring the values at the end of installation;
2 Performing a tension load test to failure and comparing the unloaded strain gauge values before and after.

Method 1 is applicable provided the gauges do not experience drift of the zero position. Method 2 operates under the assumption that residual loads are completely removed during a tension load test to failure. Ideally the strain gauges should be zeroed prior to installation and the measured residual load verified with a tension test however this may be impractical depending on the load test program and future use of the pile.

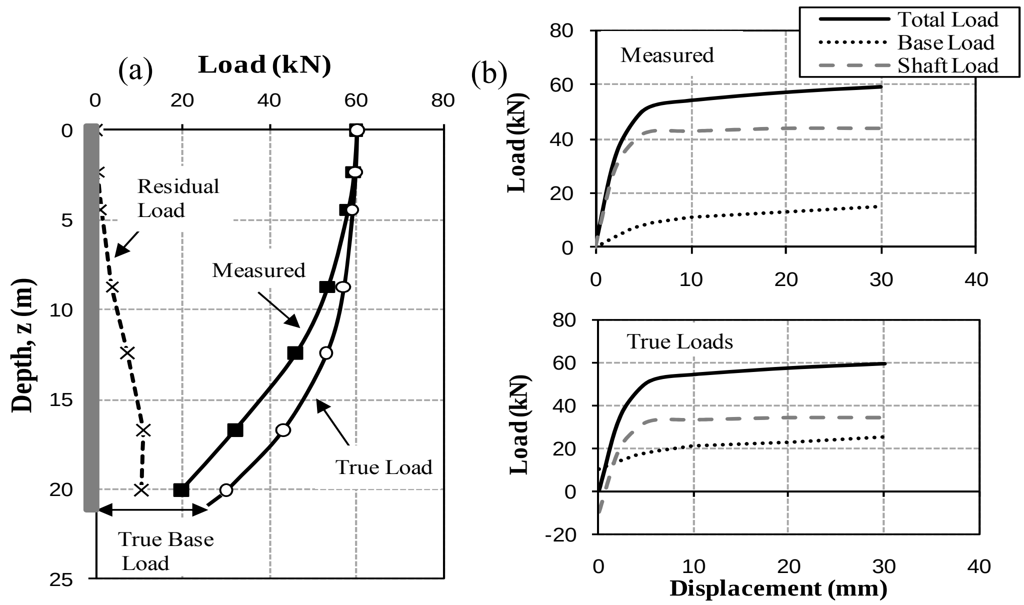

Figure 5 - (a) Typical Residual Load Distribution along a Driven Pile and (b) Load-Displacement Curves Ignoring and Accounting for Residual Loads

6 Recent Advancements

6.1 Retrievable Extensometers

While strain gauges measure the strain at a particular level (over a very short gauge length) extensometers measure the strain over a very long gauge length. Recent advancements in vibrating wire technology offers the possibility of using retrievable extensometers to measure deformation over the entire length of piles in segments. Some models can be installed in a steel or PVC pipe running along the length of the pile and are locked in place using a series of pneumatically expandable anchors between which the deformation can be measured. Upon completion of the test the pneumatic pressure can be released and the extensometer removed for re-use in another application.

6.2 Fibre Optics

Fibre optics provide an alternative to vibrating wire technology while maintaining greater stability than electrical resistance gauges and are especially suited for use in confined spaces. Like vibrating wire gauges they are unaffected by electrical disruption and voltage surges and are capable of signal transmission over long distances but also have the added advantages of being suitable for both static and dynamic applications. The strain output attained from fibre optic sensors is directly comparable with that obtained from VW gauges. The primary disadvantage of Fibre Optic gauges is the high cost of the data acquisition system and as a result its use is not commonplace.

6.3 Osterberg Cell Testing (O-Cell)

A relatively new load test method was suggested by Osterberg (1989) which utilises a sacrificial hydraulic jack installed at or near the pile tip. Hydraulic pressure, applied through the jack, loads the pile in compression from the pile tip, so that the shaft and base react against each other. Hydraulic pressure gages and tell tales provide a measure of the applied load and movement at the pile toe. This set-up is illustrated schematically in Figure 6. While Osterberg load tests are not routinely used in Europe and to the authors' knowledge have never been used in Ireland, they are now the method of choice for bored pile testing in the USA, amounting to approximately 90% of all static load tests (Schmertmann and Davis, 1997). The high capacity of large diameter piles over 10MN results in reaction systems that are uneconomical for conventional load testing and also potentially unsafe; as a result the O-cell test is an attractive alternative. The upscaling of Irish building projects with large foundation solutions may see future use of the Osterberg cell in the Irish market.

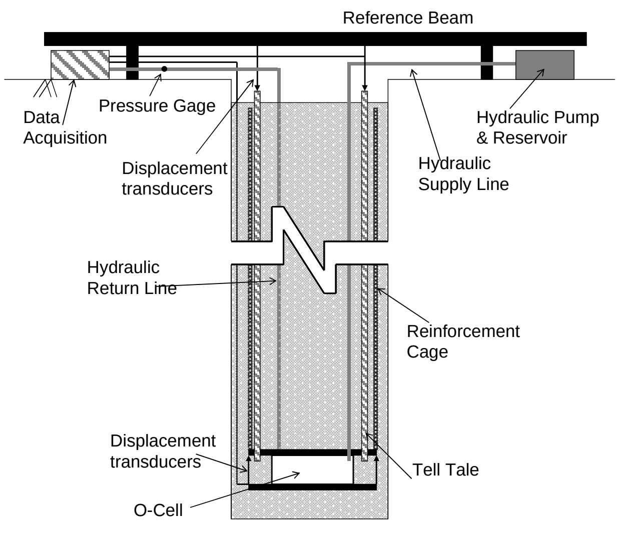

Figure 6 - Osterberg Cell Load Test

7. Summary

Instrumented testing provides a useful tool to confirm pile designs, specifically to determine unit shaft resistances, unit end bearing and pile movement-stress relationships. Carefully planning of the instrumented test is essential for successful data output; to aid designers in this respect best practice instrumentation procedures were described. Issues arising in interpreting the strain readings were discussed, including residual loads and appropriate pile modulus selection. Recent advancements in instrumentation procedures were also highlighted.

References

Alawneh, A. S. and Husein Malkawi, A. I. (2000), 'Estimation of post driving residual stresses along driven piles in sand', *Geotechnical Testing Journal*, Vol. 23, No. 3, pp. 313-326

Deschamps, R. and Richards T. D. (2005) 'Installation, measurment and interpretation of "sister bar" strain gauges in micropiles' *The International Association of Foundation Drilling "Geo-Quality Assurance and Control" Conferenc*e. Dallas, Texas.

Fellenius, B. H. (2001), 'From strain measurements to load in an instrumented pile', *Geotechnical News Magazine*, **19**, 1, 35 – 38.

Fellenius, B. H. (2002), 'Determining the resistance distribution in piles', *Geotechnical News Magazine*, **20**, 2, 35-38.

Gavin, K., Cadogan, D. and Casey, P. (2009) 'The shaft capacity of CFA piles in Sand' *ASCE Journal of Geotechnical and Geoenvironmental Engineering*, **135**, 6, 790-798

Osterberg, J. O. (1989), 'New device for load testing driven piles and drilled shafts separates friction and end-bearing', *Proceedings of Int. Conf. on Piling and Deep Foundations*, London, AA Balkema, pp. 421

Schmertmann, J. H. and Hayes, J. A. (1997), 'The Osterberg Cell and bored pile testing – A symbiosis', *Proc. of the 3rd Int. Geotechnical Engineering Conf.*, Cairo University, Egypt, 139-166

MODEL TESTING FOR ESTIMATION OF BASE RESISTANCE OF BORED PILES IN SAND

D.D.CADOGAN & J.O'DONOVAN
Department of Civil, Structural and Environmental Engineering,
Cork Institute of Technology, Cork, Ireland

Abstract
Estimates of the ultimate base resistance of bored piles in sand would appear to have improved as a result of the expanding database of load tests available, which has allowed the techniques for the calculation of base resistances to be reappraised and adjusted, if necessary. Such base resistances are typically estimated relative to displacements of the order of 10% of the pile diameter. Design methods commonly used in practice attempt to predict this measure of resistance, $q_{b\ 0.1}$, based on the results of a cone penetration test, q_c, with a factor α used to correlate these data values. This paper briefly reviews the current design methods used to estimate the base resistance of such piles and examines an ongoing experimental test programme being undertaken on a series of instrumented model bored piles at a test bed site, where the results of compression load tests, and the associated base resistance evaluations, are evaluated in regard to data gathered from Cone Penetration Test (CPT) tests at the site.

Keywords: Base Resistance, Bored Pile, CPT, Instrumentation, Piling, Sand

1 Introduction

Large diameter bored piles can be a very effective option where relatively high vertical loads are to carried by a foundation system in a built-up area, given their advantages in terms of vibration and noise mitigation relative to the use of driven or jacked piles in such situations. In this regard, it is important that sufficient experimental test work is undertaken in terms of developing and validating the design of bored piles, similar to the research programmes for the displacement form of pile, whereby instrumented model piles are used in order to improve our ability to predict the load-settlement behaviour of such piles. This is particularly important in relation to design methods which utilise correlations with Cone Penetration Test (CPT) data. However, given the nature of the installation of bored piles, a new model pile is required in the case of each individual test to be completed, which is a serious drawback in comparison to the use of instrumented displacement piles which can be reused in a relatively straightforward manner. It may be argued that there is a deficiency in regard to the extent of bored pile experiments undertaken at field test sites, as a result of this.

This paper focuses on compression tests carried out on two model bored piles, which form part of a test programme being undertaken at a sand and gravel quarry site near Cork City. An advantage of using such model piles is that the modification of factors such as pile length and diameter can be investigated. However, the model piles examined in this paper are geometrically identical but they are tested in soil where there is some variability in the soil profile (and thus the CPT profile) in a given footprint.

2 Design Techniques – Correlations with CPT Data

The presence of scale effects must be considered in relation to the shaft resistance of model bored piles in sand, as described by Lehane and Jardine (1994), Garnier and Kronig (1998) and Cadogan and Gavin (2006), which is due to the dilation of the soil around the curved surface of a pile. The magnitude of this will depend on the relative density and shear strength of the soil, as well as the diameter of the pile and its surface roughness. Small diameter piles experience relatively high values of dilation of the surrounding soil at failure point, and relatively advanced instrumentation such as total and pore pressure cells would be required to determine the shaft resistance of such piles to a reliable degree. In contrast, the use of instrumented piles has proven successful in calculating the base or end bearing resistance q_b of bored piles, given that dilation of the soil has little influence on the base resistance of such piles and the use of strain gauges will suffice in this case.

In the case of driven piles, the ease of use and relative availability of CPT test equipment has created an impetus to improve the reliability of methods to calculate the base resistance of piles in sand using such data. Randolph (2003) noted that the displacement necessary to mobilise a given proportion of the base resistance should be taken into account when correlating the pile base resistance with in-situ test parameters such as the CPT q_c values. One of the more common approaches is to estimate the base resistance at a 10% normalised displacement, $q_{b0.1}$, relative to the pile diameter. Where such design techniques are to be integrated with CPT data, the $q_{b0.1}$ and q_c values can be related through the use of a constant reduction factor α, as shown in Equation (1):

$$q_{b0.1} = \alpha q_c \tag{1}$$

The use of this reduction factor depends on a number of issues, the extent of which has been investigated previously – Lehane et al (2005) proposed that the α factor where used in the UWA-05 method for closed-ended driven piles is independent of the sand state, the pile diameter and the depth of the pile base, with a constant base resistance α factor value of 0.6 recommended for this form of displacement pile. However, Lee and Salgado (1999) have described how the α factor decreases as the relative density of sand at the pile base increases and as the pile diameter becomes greater in magnitude, while Jardine et al (2005) similarly suggested that α reduces in value as the pile diameter increases. In practice, local knowledge and experience may dictate the value of α used, as reported by De Cock et al (2003) following a review of pile design practice across Europe, where it was shown that the values used for α will typically not depend on the diameter of the pile to be installed or its length – it is suggested by De Cock et al that a mean value of 0.2 for α be used for bored piles.

Findings in relation to correlations between the comparable bearing resistance response of shallow footings on sand and q_c values are reported by Gavin et al (2009).

3 Fieldwork

The field tests were carried out at a sand and gravel quarry site located at Ovens, Co. Cork, as shown in Figure 1. The material at the test bed location is classed as medium dense sand to a silty sand, with localized narrow lenses of small gravel, shown on the

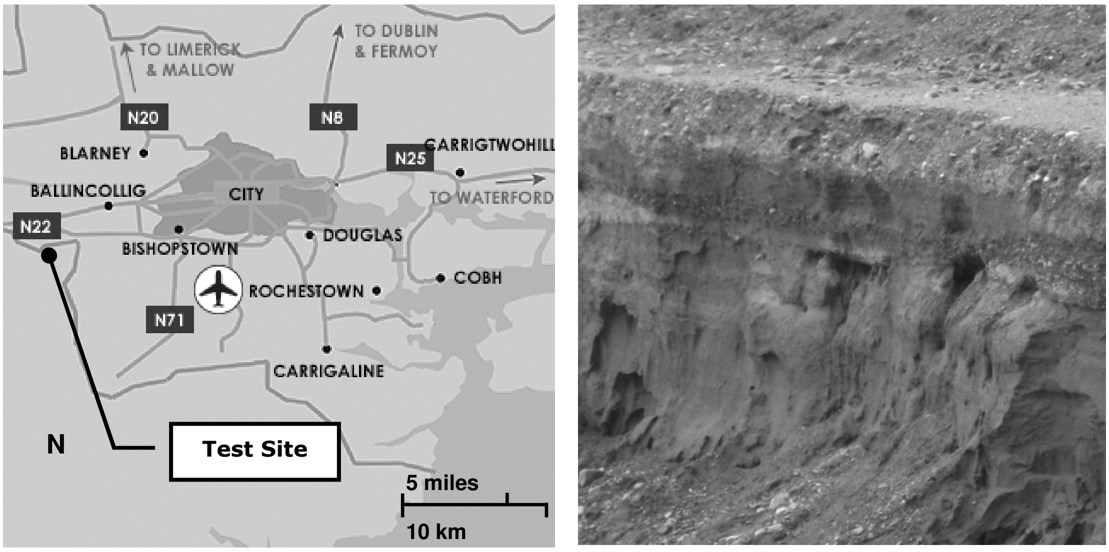

Figure 1 - Location of test bed site at Ovens, Co. Cork; and lenses in sand stratum

right-hand side of Figure 1. This soil has a unit weight of approximately 19-20kN/m^3, and it is in an over-consolidated state given its relative level within the site and previous soil extraction works at the location of the test bed. A number of CPT tests were undertaken at the site which confirmed this soil classification using interpretation based on Robertson et al (1986). Relative density values of 80%-100% in the upper 1m layer, and 60% to 80% in the lower levels, were derived using the procedure presented by Jamiolkowski et al (1985) and Jamiolkowski et al (2003). The CPT tests produced CPT q_c values in the range of 4-12MPa, as presented in Figures 2 and 3.

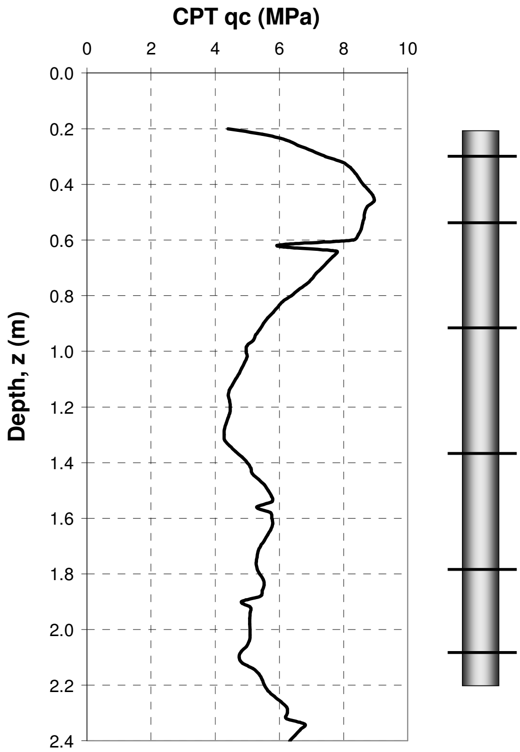

Figure 2 - CPT q_c values at location of pile TP1, and strain gauge locations on TP1

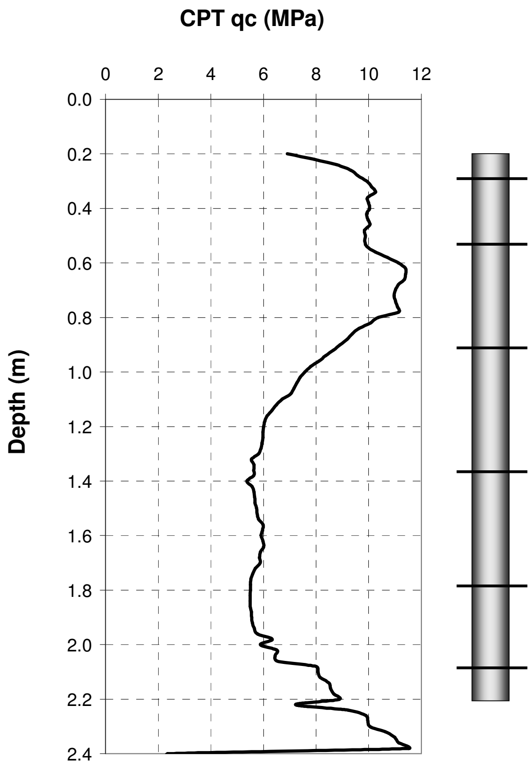

Figure 3 - CPT q_c values at location of pile TP2, and strain gauge locations on TP2

The water table level was relatively deep below the base of the piles. The natural water content obtained from samples taken above this water table level was approximately 8-9%, showing it to be partially saturated at that elevation on the site. A number of shear box tests were completed on samples of sand at various depths, whereby an angle of friction ranging from 34°-37° was determined from these tests for this stratum of soil.

3.1 Test Piles

Two model bored piles were installed at the test site. Piles TP1 and TP2 were both 2m long and 100mm in diameter. They were steel-reinforced grouted piles and they were formed using a hand auger. The boreholes remained unsupported whilst the piles were formed – this was possible due to the apparent cohesion in the soil, as evidenced by the almost sheer excavation faces retained from floor level in the quarry.

Each pile had a reinforcement frame which consisted of four no. T8 steel bars with welded links at an average of 150mm centres. Six levels of electrical resistance strain gauges (with four gauges at each level) were attached to the frame at the positions highlighted in Figures 2 and 3, adjacent to the CPT profiles. High strength grout of a 50 N/mm^2 nominal strength was used to form both piles and each was allowed to cure for a minimum of 18 days. The two piles were located approximately 7 metres apart.

It was critical that both the strain gauges and the cable connections were sealed against the ingress of water. A succession of layers of polyurethane varnish coating, wax, silicone gel and thermo-shrink wrapping was used to achieve this. A minimum of 15mm cover to the steel was provided at the sides and at the bottom of each pile.

As shown in Figure 4, the displacement of the pile head in each case was monitored using three Linear Variable Displacement Transducers (LVDTs) attached to an independent reference frame. The pile head load, strain gauge output, and displacement transducer/pressure sensor readings were recorded at a frequency of 0.1 seconds, using a Vishay System 7000 data acquisition system. An electronically-controlled hydraulic powerpack was used in conjunction with a load cell and a suitable jack to achieve and maintain the required applied loads on the piles.

(a) (b) (c)

Figure 4 – (a) test arrangement, (b) hydraulic powerpack, (c) data acquisition system

In addition, a specimen section was formed for each pile at the time of installation. These cores were reinforced as per the field piles and were 300mm in length and had strain gauges installed in a similar pattern. They were tested to failure in laboratory conditions in order to determine the stress-strain properties of the grout, while they also provided useful information in the calibration of the strain gauge outputs.

4 Test Results

The linear small-strain concrete modulus of the concrete was obtained from laboratory tests on the concrete cores fabricated as part of the process. In turn, the non-linear stiffness-strain response of the concrete was obtained from the strain gauge readings using the tangent modulus approach as described by Fellenius (2001).

The distribution of load in the pile was calculated from the strain readings, by assuming in general that the steel and grout experience equal strain, and thus the load at a position in the pile is obtained by multiplying the measured strain by the appropriate cross-sectional area and the individual elastic stiffnesses of the concrete and steel, respectively. The elastic stiffness of steel and the cross-sectional area reinforcement were known, while the elastic stiffness of the concrete would vary during a load test and the data provided by the tangent modulus procedure was used to this end.

5 Analysis of Results

The maximum load applied to pile TP1 at 10% relative displacement was 74kN, while the equivalent load for TP2 was 96kN. The plot of base resistance q_b to settlement for the two piles is given in Figure 5. Both piles exhibited a relatively stiff pressure-settlement response for pile head settlements below 1mm. Test pile TP2 mobilised the highest base resistance for all displacements, which tallies with the higher value q_c profile as shown in Figure 3.

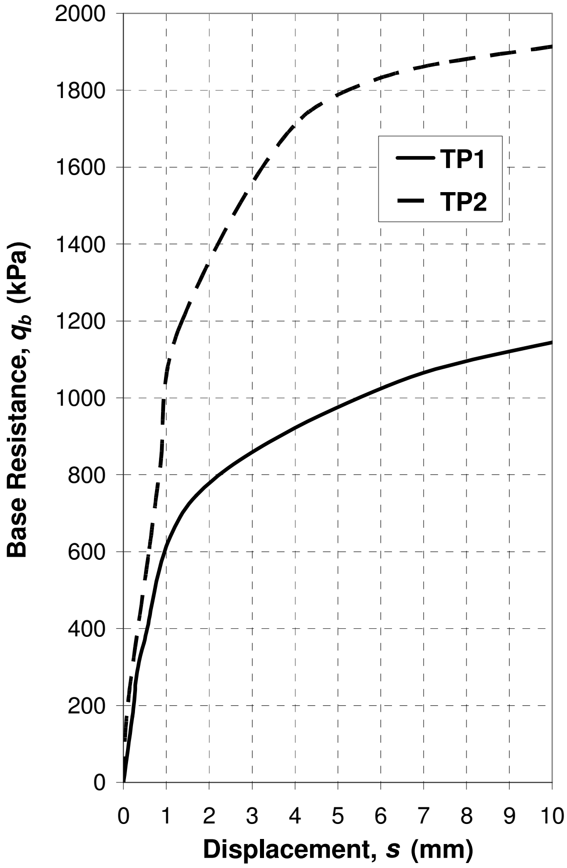

Figure 5 - Base resistance mobilised in model pile tests

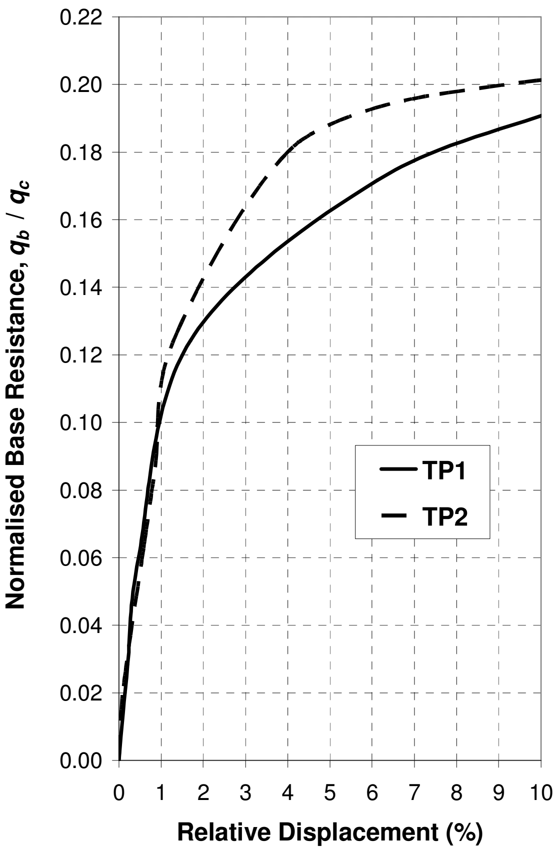

Figure 6 - Normalised end bearing resistance versus relative displacement

Figure 5 shows the maximum bearing pressure mobilised at a pile head settlement of 10% relative displacement for pile TP1 to be 1,150kPa and 1,900kPa for pile TP2.

As described by Yang (2006), the average CPT q_c values at the base of a pile in a sand to silty sand soil is to be measured from the base of the pile to a depth of between 1.5 and 3 pile diameters below it. In accordance with this, q_c at the base level was calculated to be 6,000kPa and 9,500 kPa for TP1 and TP2, respectively. These q_c values were used to normalise the q_b values which are plotted against the normalised displacement, as shown in Figure 6. The normalised response of the piles is seen to similar in both test areas for a relative pile head displacement of 10%, despite the varying soil profile at these pile locations as reflected in the CPT q_c profiles presented in Figures 2 and 3. This may be said to be consistent with results presented by Briaud (2007), who found that the pressure-settlement response of footings at a given site was unique when normalised as shown in Figure 6.

6 Summary and Conclusions

This paper reports the results of field tests carried out on instrumented model bored piles, whereby the installed strain gauges allow the shaft and base resistances mobilised during static loading to be isolated.

The base resistance mobilised by the test piles, normalised by the CPT q_c values, were found to be independent of the variability in the soil profiles, with the values for the reduction factor α seen to be close to the recommended value of 0.2 in general.

The results support the conclusions of the tests undertaken on similar instrumented model piles installed in sand, as described by Cadogan et al (2010), where it was shown that the base resistance-settlement response of bored pile foundations was independent of the pile diameter, pile length and soil q_c profile. The results of the tests on the two model piles examined in this paper would appear to agree with this third factor.

It was also shown by Cadogan et al (2010) that the load-settlement behaviour of full-scale piles may be predicted by performing model-scale footing tests at a given site and developing a unique pressure-settlement curve through the use of the results of these tests and CPT q_c test profiles. It is intended that further tests on model pile tests of varying dimensions will be carried out at the test site in Cork, as well as a series of footing tests, in order to investigate this further.

7 Acknowledgements

The authors wish to thank the following people for their contributions to the work described here: Jim Morgan of the Department of Civil, Structural and Environmental Engineering at Cork Institute of Technology, for his valuable assistance in undertaking the fieldwork; William Tobin, formerly of Cork Institute of Technology, who performed some of the work at the test site presented in this paper; and Darren Ward and Paul Duignan of Insitu Site Investigation in undertaking the CPT test programme. We also wish to thank Roadstone JAWood for the use of the quarry at Ovens, Co. Cork, and in particular Tim O'Mahony and Daniel Long.

8 References

Briaud, J.L. (2007), 'Spread footings in sand – load settlement curve approach', *ASCE Journal of Geotechnical and Geoenvironmental Engineering*, **133**, 905-920.

Cadogan, D. and Gavin, K. (2006), 'Field test on model bored pile in over-consolidated sand' in *Proceedings 3rd International Young Geotechnical Engineers Conference, Osaka, Japan, 12-16 September 2005*, eds. C.W.W. Ng, L.M Zhang and Y.H. Wang, Taylor and Francis, London, 1335-1340.

Cadogan, D., Gavin, K. and Tolooiyan, A. (2010), 'Physical model testing and FE analyses of base resistance of bored piles in sand' in *Proceedings 7th International Conference on Physical Modelling in Geotechnics, Zurich, June-July 2010*, eds. S. Springman, J. Laue and L. Seward, Taylor and Francis, London, 739-744.

De Cock, F., Legrand, C., and Huybrechts, N. (2003), 'Overview of design methods of axially loaded piles in Europe – Report of ERTC3–Piles, ISSMGE Subcommittee' in *Proceedings of the 13th European Conference on Soil Mechanics and Foundation Engineering, Prague, 25–28 August 2003*, eds. I. Vanicek, R. Barvinek, J. Bohac, D. Jirasko, and J. Salak. The Czech Geotechnical Society, Prague, 663-715.

Fellenius, B.H. (2001), 'Strain measurements to load in an instrumented pile', *Geotechnical News Magazine*, **19**, 35-38.

Garnier, J. and Kronig, D. (1998), 'Scale effects in piles and soil nails in sand' in *Proceedings Centrifuge 98*, Balkema, 205-210.

Gavin, K., Adekunte, A., and O'Kelly, B. (2009), 'A field inestigation of vertical footing response on sand', *Geotechnical Engineering*, Vol. 162 (5), 257-267.

Jamiolkowski, M.B., Ladd, C.C., Germaine, J.T. and Lancellotta, R. (1985), 'New developments in field and laboratory testing of soils' in *Proceedings of the 11th International Conference on Soil Mechanics and Foundation Engineering*, San Francisco, Vol 1, Balkema, Rotterdam, 57-153.

Jamiolkowski, M.B., Lo Presti, D.F. and Manassero, M. (2003), 'Evaluation of relative density and shear strength of sands from cone penetration test', *Soil behaviour and soft ground construction*, Geotechnical Special Publication No. 119, ASCE, 201-238.

Jardine, R.J., Chow, F.C., Overy, R., and Standing, J. (2005), *ICP design methods for driven piles in sands and clays*, Thomas Telford, London.

Lee, J. and Salgado, R. (1999), 'Determination of pile base resistance in sands', *Journal of Geotechnical and Geoenvironmental Engineering*, **125**, 673-683.

Lehane, B.M. and Jardine, R.J. (1994), 'Shaft capacity of driven piles in sand: a new design approach' in *Proceedings of 7th International Conference on the Behaviour of Offshore Structures*, Boston, 1, 23-36.

Lehane, B.M., Scheider, J.A., and Xu, X. (2005), *CPT based design of driven piles in sand for offshore structures*, Internal report no. GEO:05345, University of Western Australia.

Randolph, M.F., Dolwin, J., and Beck, R.D. (1994), 'Design of driven piles in sand', *Geotechnique*, **44**, 427-448.

Robertson, P.K., Campanella, R.G., Gillespie, D. And Greig, J (1986) "Use of piezometer cone data" in *Proceedings of In Situ '86, ASCE Specialty Conference on Use of In Situ Tests in Geotechnical Engineering*, Blacksburg, ASCE, New York, 1263-80.

Yang, J. (2006), 'Influence zone for end bearing of piles in sand', *ASCE Journal of Geotechnical and Geoenvironmental Engineering*, **132**, 1229-1237.

RELIABILITY OF ECCENTRICALLY LOADED SPREAD FOUNDATIONS DESIGNED TO EUROCODE 7: AN IRISH PERSPECTIVE

W.S. FORREST & T.L.L. ORR
Dept. of Civil Engineering, Trinity College, University of Dublin, Ireland

Abstract
Eurocode 7 is the new geotechnical design standard for Europe. It is based on the limit state design method with partial factors and characteristic values. For limit states involving failure in the ground, there are three Design Approaches (DAs) in Eurocode 7, each with a different set of partial factor values. Ireland has the distinction of being the only member state to permit the use of all three DAs in its National Annex (NA). The intention of the Eurocodes is that designs should achieve a minimum target reliability level for each limit state considered. This paper examines the reliability of an eccentrically loaded foundation on clay, designed using the partial factors and DAs prescribed in the Irish NA. The reliabilities of these designs are compared with the target reliability index and with the reliabilities of designs carried out to the NAs of Denmark, France, Germany and the UK.

Keywords: Eurocode 7, Limit State Design, Reliability, Spread Foundations

1. Introduction

The Structural Eurocodes are the new European Standards for the design of buildings and civil engineering works. They were adopted as the Irish National Standards in 2010. There are ten Eurocodes covering the following aspects of design: EN 1997 or Eurocode 7 for geotechnical design, EN 1990 providing the basis of design for all the Eurocodes, Eurocode 1 for actions, Eurocode 8 for earthquake resistance and Eurocodes 2, 3, 4, 5, 6 and 9 for designs involving different materials.

EN 1990 states that designs must be carried out using the partial factor method or an alternative method based on a probabilistic approach. The method presented in Eurocode 7 (Orr and Breysse 2008) is based on the limit state design concept with partial factors and characteristic values.

EN 1990 states that structural designs should aim to achieve a recommended minimum level of reliability, described by a specified value, known as the target reliability index (β), for both Ultimate Limit States (ULSs) and Serviceability Limit States (SLSs). β is directly equivalent to the probability of failure (P_f) and is a more meaningful measure of safety than the traditional deterministic Factors of Safety. In this paper, the advanced First Order Reliability Method (FORM) is used to determine the β values of spread foundations designed using the three Design Approaches (DAs) for different sets of partial factors and undrained shear strengths. These are compared with the reliabilities of foundations designed using the National Annexes (NAs) of different CEN Member States in order to evaluate the designs to Eurocode 7 using different NAs.

2. Eurocode 7

2.1 Limit State Design

Limit State Design (LSD) was first introduced in Europe in the 1950s (Becker 1996) and has been used in Denmark for over forty years. The fundamental concept of LSD is that all possible limit states for a structure must be considered and shown to be sufficiently unlikely to occur (Orr 2000). ULSs involve situations such as collapse or other forms of failure, including excessive deformation in the ground. The target β values for a Geotechnical Category 2 or a medium risk structure given in EN 1990 are shown in Table 1. SLSs correspond to the functionality or the appearance of a structure and have a higher probability of occurrence and hence lower target β values than ULSs.

Table 1 – Target β values for medium risk structure

	1 year		**50 years**	
	β	**P_f**	**β**	**P_f**
ULS	4.7	$1.3{\times}10^{-6}$	3.8	$7.2{\times}10^{-5}$
SLS	2.9	$1.9{\times}10^{-3}$	1.5	$6.7{\times}10^{-2}$

2.2 Design Approaches

For ULSs involving failure of the ground, termed GEO ULSs, Eurocode 7 offers three DAs with different sets of partial factors for the soil strength and resistances. The partial factor values as well as the Design Approach(es) that may be used in a particular CEN Member State are stated in the NA of that state. Table 2 lists the DAs being adopted in each Member State (Schuppener 2010) for the design of spread foundations. Ireland has chosen to adopt all three DAs.

Design Approach 1 (DA1) has two combinations of partial factors that need to be satisfied: Combination 1 (DA1.C1) aims to provide safe designs against unfavourable deviations of the actions from their characteristic values (Schuppener 2010) while Combination 2 (DA1.C2) aims to provide safe designs against unfavourable deviations of the ground strength properties from their characteristic values.

Table 2 - Design Approaches in the EU Member States (as of May 2008)

Design	**No/Incomplete ans.**	**All DAs**	**DA1**	**DA2**	**DA2***	**DA3**
Spread Found.	Bulgaria	Ireland	Belgium	Estonia	Austria	Denmark
	Cyprus		Italy	France	Germany	Netherlands
	Czech R.		Lithuania		Greece	Switzerland
	Hungary		Portugal		Poland	
	Iceland		Romania		Slovakia	
	Latvia		UK		Slovenia	
	Malta				Spain	
	Norway			Finland		
	Sweden			Luxembourg		

In Design Approaches 2 and 3 (DA2 and DA3) only one verification is required. In DA2 partial factors greater than unity are applied to the actions and to the bearing resistance, while partial factors of unity are applied to the ground strength properties. There are two methods of designing using DA2. In DA2 partial factors are applied to the characteristic actions at the start of the design calculation, while in DA2* as defined by Frank et al. (2004) partial factors are applied at the end of the design calculation. In DA3 a distinction is made between structural and geotechnical actions and different sets of partial factors are applied to the actions as well as partial factors being applied to the ground strength parameters.

2.3 Partial Factor Values

Table 3 shows the recommended GEO partial action factor values, which have been chosen by Ireland (IRL), and the alternatives to these recommended values that have been chosen by some CEN member states: Lithuania (LT) and The Netherlands (NL) have selected a lower value of 0.90 for permanent favourable actions ($\gamma_{G,f}$) compared with the recommended value of 1.00, Denmark (DK) has also chosen a value of 0.90, but only for geotechnical actions; several member states have decided to use a less conservative value for permanent unfavourable actions ($\gamma_{G,u}$) than the recommended 1.35 in DA1.C1 and DA3: Estonia (EST) and Denmark (structural) have adopted a value of 1.20, while Greece (GR), Germany (D), Finland (FIN), Denmark (for geotechnical actions) and Switzerland (CH) have selected a value of unity; Belgium (B) has chosen a value of 1.10 instead of the recommended 1.30 for variable unfavourable actions ($\gamma_{Q,u}$) in DA1.C2.

There have also been changes to the partial factors values chosen for soil strength in various Member States' NAs. Table 4 shows that Austria (A) and Germany felt that the recommended partial factor of 1.4 for the undrained shear strength, c_u (γ_{c_u}) was too conservative and have chosen a value of 1.25 instead; Switzerland and Greece have selected a more conservative value of 1.50, while The Netherlands and Denmark have adopted values of 1.75 and 1.80 respectively, owing to the high variation in c_u. In the Greek NA, a partial factor of 1.40 is applied to the tangent of the effective friction angle, tanϕ'. This is higher than the recommended value of 1.25, but Switzerland and Denmark have chosen a less conservative value of 1.20. The recommended partial factor value for the effective cohesion (c') is 1.25 and hence is the same recommended value for tanϕ'.

Table 3 - Partial action factors chosen by CEN Member States (Schuppener 2010)

	DA1.C1			**DA1.C2**		**DA2**			**DA3**			
	$\gamma_{G,u}$	$\gamma_{G,f}$	$\gamma_{Q,u}$	$\gamma_{G,u}$	$\gamma_{Q,u}$	$\gamma_{G,u}$	$\gamma_{G,f}$	$\gamma_{Q,u}$		$\gamma_{G,u}^{+}$	$\gamma_{G,f}^{+}$	$\gamma_{Q,u}^{+}$
IRL	1.35	1.0	1.5	1.0	1.3	1.35	1.0	1.5		1.35/1	1.0	1.5/1.3
B					1.1				CH	1.0		
EST	1.2								DK	1.2/1	1.0/0.9	
LT		0.9							FIN	1.0		
									D	1.0		
									GR	1.0		
									NL		0.9	

$^{+}$Actions in DA3 are structural/geotechnical, $\gamma_{Q,f} = 0$

However Switzerland, Denmark, and The Netherlands have selected alternative values of 1.50, 1.20 and 1.45 respectively in their NAs. France (F) and Spain (E) have adopted a partial factor value for the earth resistance ($\gamma_{R,e}$) of 1.50 compared with the recommended value of 1.40.

Table 4 - Partial factors for soil strength in the EU Member States (Schuppener 2010)

DA1.C2				**DA2**					**DA3**			
	$\gamma_{\tan\phi'}$	$\gamma_{c'}$	γ_{cu}		$\gamma_{\tan\phi'}$	$\gamma_{c'}$	γ_{cu}	$\gamma_{R;e}$		$\gamma_{\tan\phi'}$	$\gamma_{c'}$	γ_{cu}
IRL	1.25	1.25	1.40		1.00	1.00	1.00	1.40		1.25	1.25	1.40
				F				1.50	A			1.25
				E				1.50	CH	1.20	1.50	1.50
									DK	1.20	1.20	1.80
									D			1.25
									GR	1.40		1.50
									NL		1.45	1.75

2.4 Characteristic Values

The characteristic value is a fundamental part of the limit state design method. Eurocode 7 differentiates between the selection of characteristic values of actions (F_k) and characteristic values of ground strength properties (X_k). The characteristic values of actions are selected in accordance with EN 1990 and the following equation is used for a normally distributed action:

$$F_k = \mu_F + k\sigma_F = \mu_F(1 + kV_F) \tag{1}$$

where μ_F is the mean action , σ_F is the standard deviation, V_F is the coefficient of variation, and k is a factor, which determines the particular characteristic value. The subscript F donates an action. A k value of 1.645 represents the 5% fractile of an unlimited test series.

In the case of ground strength parameters, Eurocode 7 differentiates between limit states governed by large or small mobilised soil volumes. Where a large volume of soil is concerned, the characteristic value should be selected as a cautious estimate of the mean value (Frank et al. 2004), whereas, when a local failure is being considered, the characteristic value should be chosen as the 5% fractile of the test results. For a normally distributed parameter, the following equation is used where the subscript X donates a material property:

$$X_k = \mu_X - k\sigma_X = \mu_X(1 - kV_X) \tag{2}$$

Orr (2000) states that using purely statistical methods and not taking account of experience of the ground conditions will result in a characteristic value that is too cautious and cites Schneider (1997) who proposed a value of k = 0.5 in Equation (2), which has been found to be useful in practice. However for k = 0.5, from a purely statistical point of view, 13 samples would be needed to achieve 95% confidence in the mean value, as required by Eurocode 7 (Forrest and Orr 2010a). Often there are too few test samples taken at a site to make reasonable assumptions using purely statistical methods and hence well established experience normally needs to be incorporated in the selection of the characteristic value.

3. Foundation Designed to Eurocode 7

To assess the reliability of an eccentrically loaded spread foundation in clay designed to Eurocode 7, using the Design Approaches and partial factors adopted by Ireland and by Denmark, France, Germany and the UK, the example shown in Figure 1 is examined. This example is similar to one examined by Forrest and Orr (2010b). This square pad foundation for a building is at 0.8m embedment depth in clay with groundwater at great depth. The design foundation breadths were optimised for the different Design Approaches and sets of partial factors.

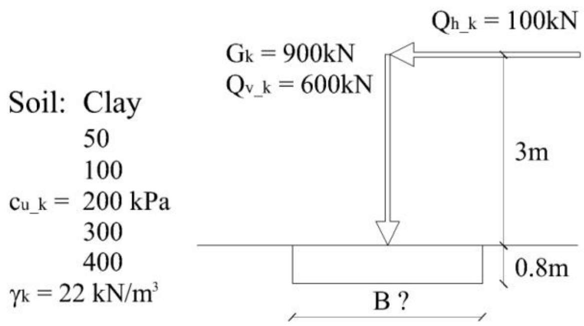

Figure 1 - Eccentrically loaded square foundation on clay

The design undrained bearing resistance, $R_{v,d}$, was determined using the calculation model in Annex D of Eurocode 7 consisting of the following equation:

$$R_{v,d} = A'((\pi + 2)c_{u,d}s_c i_c + q) \tag{3}$$

where A' is the effective foundation base area, s_c is a shape factor equal to 1.2 for a square foundation, q is the overburden pressure at the foundation base and i_c is an inclination factor given as follows, where H_d is the horizontal load:

$$i_c = \frac{1}{2}\left(1 + \sqrt{1 - \frac{H_d}{A'c_{u,d}}}\right) \tag{4}$$

The design sliding resistance $R_{h,d}$, was determined using the calculation model in Eurocode 7 consisting of the following equation:

$$R_{h,d} = A_c c_{u,d} \tag{5}$$

where A_c is the total base area under compression.

Eurocode 7 provides a geometric allowance in the case of spread foundations subject to actions with large eccentricities which state that where the eccentricity of the loading on a rectangular foundation exceeds 1/3 the width, tolerances of up to 100mm should be considered.

While this paper calculates the reliability of spread foundations designed using the different Design Approaches and the partial factors adopted by Ireland and some other countries, it should be noted that Eurocode 7 states that for conventional structures founded on clays, the ratio R_k/V_k should be calculated for undrained conditions and if this ratio is less than 3, then a settlement calculation should always be undertaken. Since the ratio R_k/V_k is often less than 3 using the recommended partial factors for all the DAs, therefore for undrained conditions, the SLS condition rather than the ULS controls the design breadth of spread foundations for conventional structures.

4. Reliability Analyses

The reliability indices of the designs using the different design Approaches and partial factors were determined using the advanced first-order reliability method. This method was originally proposed by Hasofer and Lind (1974) for normally distributed variables and was later extended for non-normal distributions by Rackwitz and Fiessler (1978). The reliability analyses were carried out using the following performance or limit state function that defines the limit state surface for bearing resistance failure.

$$Z_1 = A'((\pi + 2)c_{u,d}s_c i_c + q) - (G_d + Q_{v,d}) \qquad (6)$$

While both the bearing and sliding limit states were considered, bearing resistance failure was the controlling limit state in all the cases studied.

The random variables in the analyses and their distributions are summarised in Table 5. A lognormal distribution and a coefficient of variation of 35% was assumed for the undrained shear strength (c_u) of the clay which was found by Forrest and Orr (2010b) for the Dublin Boulder Clay. The mean and standard deviation values of the actions were estimated from their specified characteristic values. The variations of the strength parameters were reduced by spatial averaging along the potential slip surface using the method outlined by Forrest and Orr (2010a). A vertical scale of fluctuation of 2m for c_u was assumed (Phoon and Kulhawy 1999). The horizontal scale of fluctuation was ignored because it is approximately ten to twenty times the vertical scale of fluctuation (Puła 2007).

5. Analyses and Results

The reliabilities of designs carried out using the partial factors and DA set out in the Irish NA were compared with the target β value and designs from the NAs of Denmark, France, Germany and the United Kingdom, using the COMREL-TI 8.10 program (STRUREL 2004). The analyses were performed using two characteristic values for c_u, Schneider's (1997) cautious estimate of the mean $c_{u,k:Schneider}$ and the 5% fractile $c_{u,k:5\%}$, and assuming c_u has a log-normal distribution.

Figures 2 and 3 give the β values of spread foundations designed to the NAs of Denmark, France, Germany, Ireland and the UK. Figure 2 demonstrates that designs to the Danish NA (DA3) is the most conservative, due to γ_{c_u} = 1.8, and achieves the target β value of 3.8 when the $c_{u,k:5\%}$ value is used. The Irish DA3, using the recommended value γ_{c_u} = 1.4, is the next most reliable and has β values greater than

Table 5 - Summary of Random Variables

	F_k	$X_{k,mean}$	$X_{k,Schneider}$	$X_{k,5\%}$	Distribution	μ	σ	V
G	900				Normal	772.86	77.29	0.10
Q	600				Lognormal	431.79	86.36	0.20
γ		22			Normal	22	1.10	0.05
c_u			41.3	21.2	Lognormal	50	17.5	0.35
			82.5	42.4	Lognormal	100	35	0.35
			165	84.9	Lognormal	200	70	0.35
			247.5	127.3	Lognormal	300	105	0.35
			330	169.7	Lognormal	400	140	0.35

3.8 when c_u < 350kPa. DA2 is marginally less reliable than DA3 when the recommended partial factors are used as per the Irish and French NAs, since γ_{c_u}(DA3) = γ_R(DA2) = 1.4. DA2 is more reliable than the DA2* being adopted in the German NA. For this example, designs using the Irish and UK DA1 are the least reliable of the designs using the different DAs but still exceeds the target reliability when c_u < 280kPa. Overall, Figure 2 shows that, for lower values of c_u, the $c_{u,k:5\%}$ characteristic value can be overly conservative since β >> 3.8.

Figure 3 shows the reliabilities when the $c_{u,k:Schneider}$ value is chosen. Overall the reliabilities are reduced compared with Figure 2 since a less conservative characteristic value is chosen. The Danish DA3 achieves the target β value when c_u < 200kPa, as does the French/Irish DA2, and the Irish DA3 when c_u < 140kPa and 150kPa respectively. The Danish DA3 has the highest β values for the range of c_u analysed, followed by the Irish DA3 and then the French/Irish DA2. The German DA2* has higher β values than the Irish/UK DA1 when c_u < 210kPa, however the reliability of DA2* decreases with increasing c_u. This is due to the design being carried out initially using characteristic values, which decreases the horizontal load, thereby reducing the eccentricity, increasing the effective breadth and therefore decreasing the design breadth to achieve a less conservative design.

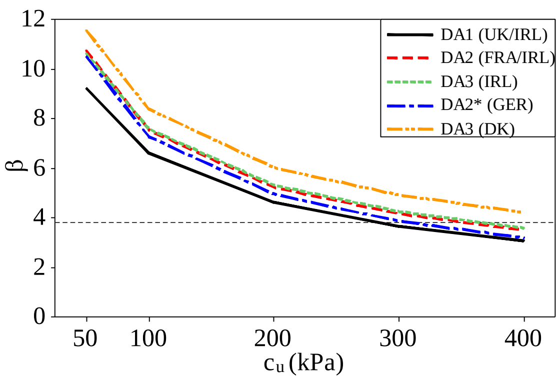

Figure 2 –Member States with $c_{u_{k,5\%}}$

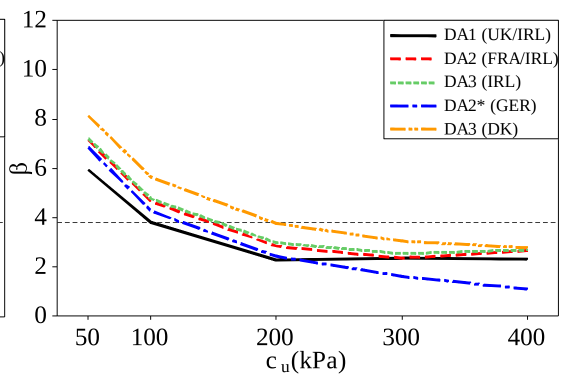

Figure 3 –Member States with $c_{u_{k,Schneider}}$

6. Conclusions

From the analyses presented in this paper, it has been shown that spread foundation on clay, designed to Eurocode 7, using the recommended partial factors, with log-normally distributed c_u and a coefficient of variation of 35%, achieve reliabilities greater than the target value for c_u less than a certain value. For the example chosen, the Danish DA3 partial factors give the most conservative design approach and the one closest to the target β, when Schneider's characteristic value is used. DA1 gives the least conservative designs when the $c_{u,k:5\%}$ value is used. DA2* gives the least conservative design when the $c_{u,k:Schneider}$ value was used and c_u > 210kPa.

This paper demonstrates that, in view of the large coefficients of variation that can occur in clay, foundations designed to Eurocode 7 for undrained conditions using any of the three Design Approaches may not achieve the target reliability due to the large inherent variability that exists in clay. To achieve the target β values, for undrained conditions, the $c_{u,k:5\%}$ value may need to be selected for foundation design, however in some cases this can be overly conservative.

It should also be noted that the design of shallow foundations is likely to be controlled by SLS requirements and a settlement calculation is also required when $R_k/V_k < 3$.

Acknowledgements

The authors would like to acknowledge funding received from the Irish Research Council for Science, Engineering and Technology and the Geotechnical Trust Fund of Engineers Ireland.

References

Becker, D. E. (1996). "Eighteenth Canadian Geotechnical Colloquium: Limit States Design for Foundations. Part I." *Canadian Geotechnical Journal* **33**: 956-983.

Forrest ,W. S. and T. L. L. Orr (2010a). "Reliability of Shallow Foundations Designed to Eurocode 7 " *Georisk,* Accepted, **In Press**.

Forrest, W. S. and T. L. L. Orr (2010b). Reliability of spread foundations on clay designed using the Eurocode 7 Design Approaches, in *Proc. 17th SEAGC*, Taipei

Frank, R., C. Bauduin, R. Driscoll, M. Kavvadas, N. Krebs Ovensen, T. Orr and B. Schuppener. (2004). *Designers' Guide to EN 1997-1 Eurocode 7: Geotechnical Design - General Rules*. H. Gulvanessian. London, Thomas Telford Ltd.

Hasofer, A. M. and N. C. Lind (1974). "Exact and Invariant Second-Moment Code Format." *Journal of the Engineering Mechanics Division* **100**: 111-121.

Orr, T. L. L. (2000). "Selection of characteristic values and partial factors in geotechnical designs to Eurocode 7." *Computers and Geotechnics* **26**: 263-279.

Orr, T. L. L. and D. Breysse (2008). Eurocode 7 & reliability-based design. *Reliability Based Design in Geo. Eng*. K. K. Phoon. London, Taylor & Francis**:** 298-343.

Phoon, K.-K. and F. H. Kulhawy (1999). "Evaluation of geotechnical property variability." *Canadian Geotechnical Journal* **36**: 625-639.

Puła, W. (2007). *On some aspects of reliability computations in bearing capacity of shallow foundations*. Wien; New York Springer.

Rackwitz, R. and B. Fiessler (1978). "Structural reliability under combined random load sequences." *Computers and Structures* **9**: 489-494.

Schneider, H. R. (1997). ‘Definition and determination of characteristic soil properties’ in *XII International Conference on SMGE*, Hamburg, Balkema.

Schuppener, B. (2010). "Eurocode 7 Geotechnical design. Part 1: General rules and its latest developments." *Georisk* **4**(1): 32-42.

STRUREL (2004). *COMREL and SYSREL:Users Manual*. Munich

USE OF NON-LINEAR LOAD-SETTLEMENT MODEL FOR PREDICTING PILE BEHAVIOUR

K.GAVIN[1], P. DOHERTY[1], J.BEVIN[2] and L.TWOMEY[2]
[1]Geotechnical Research Group, Dept. of Civil Engineering, University College Dublin, Ireland
[2] Geotechnical Group, Arup Consulting Engineers, Dublin, Ireland

Abstract
Whilst complex numerical analyses can be performed for geotechnical analyses of building foundations, these usually require sophisticated laboratory testing on high quality undisturbed samples in order to define the appropriate soil parameters. Because of the high stone and boulder content of glacial tills, site investigation for routine structures typically does not provide such data and Engineers often rely on simple correlations linking in-situ test results such as Standard Penetration Test (SPT) N values with values of soil strength and stiffness. This paper discusses the use of simple non-linear elastic models for the design of foundations, which can be implemented in a spreadsheet format. The input parameters can be obtained from in-situ tests such as Plate Loading Tests (PLT), Multiple Analysis of Surface Waves (MASW) and Cone Penetration (CPT) or SPT Tests. The application of the model to predict the axial resistance developed by pipe piles installed in glacial deposits found at Greystones, County Wicklow is described in this paper.

Keywords: Piling, Settlement, Foundation, Load Tests

1. Introduction

The ultimate capacity of a pile (Q_{ult}) is derived from a combination of unit skin friction (τ) developed over the shaft area and base resistance (q_b) developed at the pile tip.

$$Q_{ult} = \tau_{As} + q_b A_b \tag{1}$$

where A_s and A_b are the shaft and base areas of the pile respectively.

When using standard pile types (e.g. driven pre-cast concrete and CFA piles) local design experience is usually available which enable reasonably good estimates of q_s and q_b values (See Farrell et al 2001, Gavin et. al 2009) to be made. Where non-standard piles are used designers need to carefully assess the applicability of conventional practice. With moves towards limit state design it is often a requirement to provide some estimate of pile settlement. Settlement prediction models tend to range from the overly simplistic linear elastic type to complex non-linear elastic finite element methods. In the first type the models do not adequately represent real soil behaviour. In the second, the input parameters required for the constitutive models, which describe real soil behaviour, are rarely available.

The strong effect that soil plugging during installation has on the axial resistance developed by open-ended (pipe) piles installed in sand and clay was identified by Paikowsky and Whitman (1990). They described the process of soil plug formation wherein; during the initial stages of pile installation, the length of the soil plug (L_p) inside the pipe, equals the pile penetration depth (L) and the pile is said to be coring. As the pile penetration depth increases, frictional stresses between the inside wall of the pile and the soil plug, may cause partial plugging and in some cases the pile may become completely plugged. The development of the soil core during installation is quantified by the Plug Length Ratio (PLR) or the Incremental Filling Ratio (IFR):

$$PLR = L_p/L \tag{2a}$$
$$IFR = \Delta Lp/\Delta L \tag{2b}$$

They noted that although many full-scale piles have PLR values close to unity, partial plugging during installation may occur, which results in large increases in the axial resistance (and thus penetration resistance) of piles installed in sand, and large increases in the excess porewater pressure surrounding piles in clay.

This paper describes the installation and load testing of a 610 mm diameter, open-ended steel pipe pile at the Greystones harbour development in County Wicklow. Open-ended steel tubular piles are not widely used in Ireland, their use is often confined to maritime projects and there are no local case histories available with which to aid design. The pile design was undertaken by Arup Dublin using traditional design methods. An alternative estimate of the pile capacity was made using recent CPT based methods for estimating the resistance of open-ended piles which are included in the latest edition of the American Petroleum Institute (API) design guidelines for offshore structures. The ability of both design methods, when combined with a simple non-linear settlement model, to predict the behaviour of the test pile is described.

Figure 1- Aerial view of Greystones Harbour development

2. Site Description

The piles were installed to support a boardwalk which formed part of a development at Greystones harbour, County Wicklow (See Figure 1). The ground conditions were investigated using a series of shell and auger boreholes which found that a relatively uniform soil profile existed in the vicinity of the boardwalk, See Figure 2. An 8.5 m thick layer of stiff to very stiff boulder clay overlay a 5 m thick layer of very dense gravel which in turn overlay greywacke bedrock.

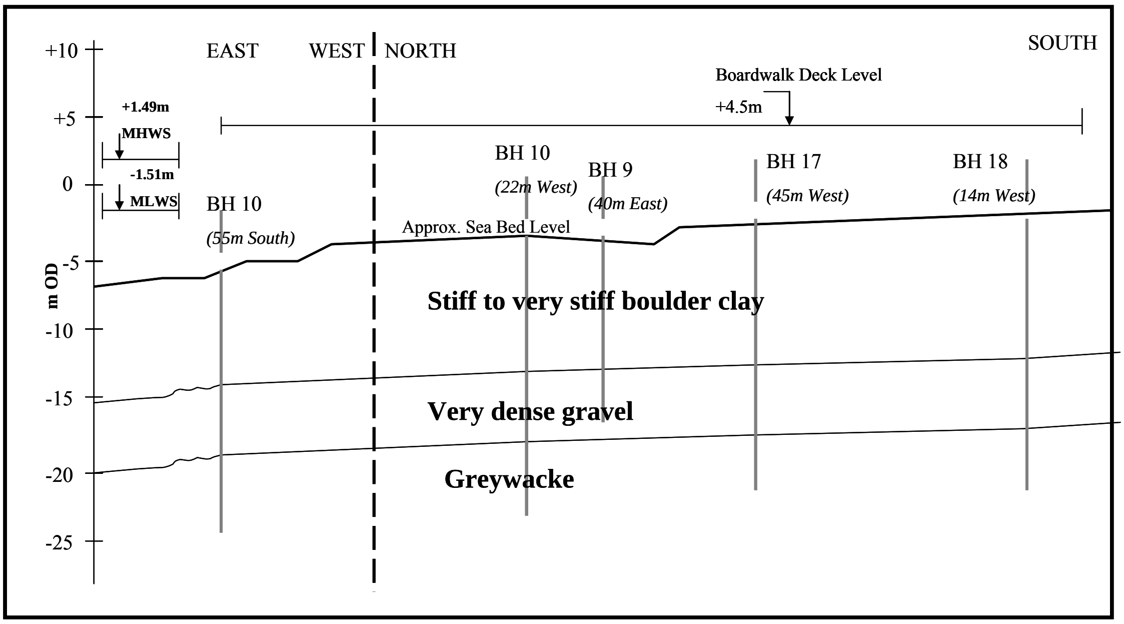

Figure 2 - Geological Cross-Section

The SPT N values recorded in the boulder clay, shown in Figure 3a varied from 30 to 85 (with an average of 53). SPT values in the dense gravel were more uniform and slightly higher than the boulder clay, with an average N value of 59. The results of Atterberg limit tests performed in the boulder clay (See Figure 3b) were consistent with depth, with a Plastic Limit (PL) of ~14%, a Liquid Limit (LL) of ~ 38% and a Plasticity Index (PI) of 24%. The in-situ water content was ~ 15% giving a liquidity index close to zero. A series of unconfined unconsolidated triaxial tests were performed on samples of boulder clay. The results were again relatively uniform with depth, revealing s_u values of ~150 kPa at depths between 1 m and 7 m. These are much higher than the s_u value of ~320 kPa suggested using standard correlations with N values (Stroud 1990). These latter higher values were used in the pile design.

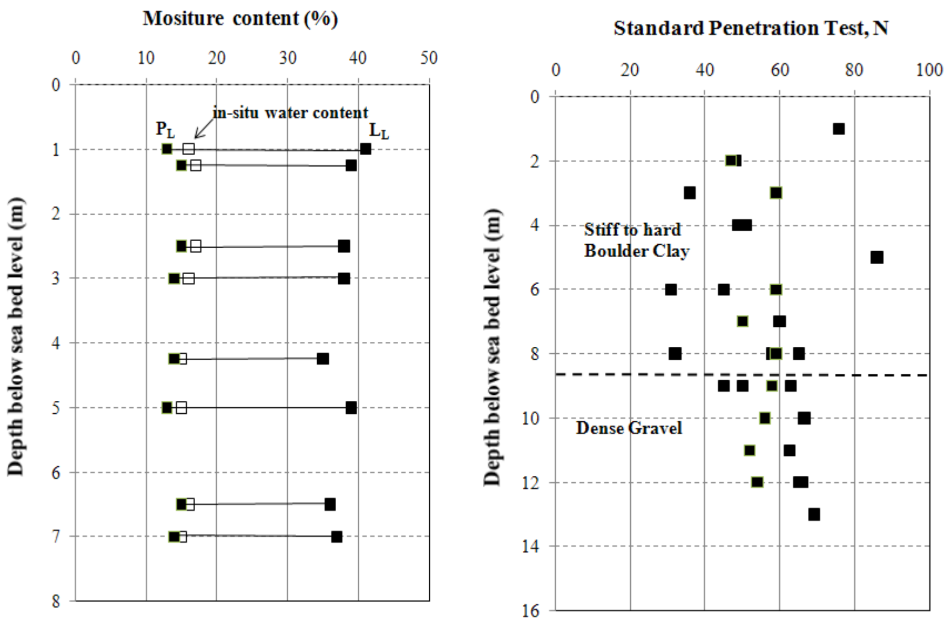

Figure 3 - Ground Conditions including (a) Plasticity Data and (b) SPT Data

3. Pile Details

The test pile was a 610 mm steel pipe pile with a 16 mm thick wall (See Figure 4a). It was driven using a 9 tonne hydraulic hammer with a drop height of 1200 mm from sea-bed level (-4.55 m AoD) to a depth of -14.9 m, giving a pile penetration of 10.35 m. The pile driving records shown in Figure 4, show that the driving resistance (reflected by the number of blows) increased with depth as the pile was driven through the boulder clay to a depth of 8.5 m. The driving resistance in the gravel layer was uniform at 45 blows/250 mm (or 5.6 mm per blow). The plug level was 0.43 m below sea bed giving a PLR value of 0.96, indicating that the pile was virtually fully coring.

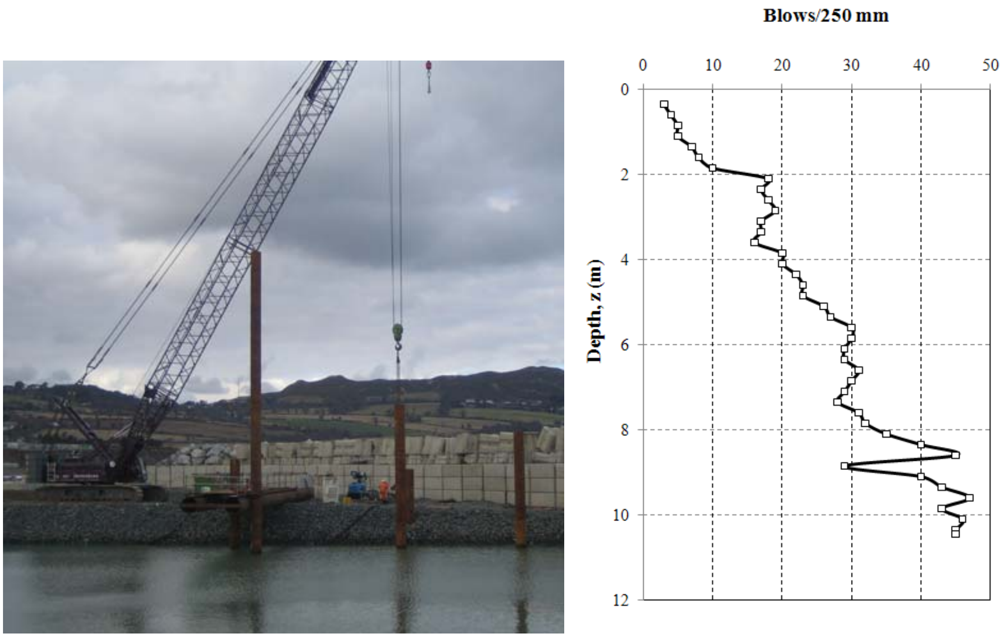

Figure 4 – (a) Pile installation and (b) driving records

4. Pile Design

The pile capacity was estimated using two approaches; the first was to estimate the resistance using correlations with the SPT N value, proposed by Meyerhof (1976). In the second approach recent deign equations linking the pile resistance to Cone Penetration Test (CPT) data was used.

4.1 Method 1

The maximum shear stress developed in the boulder clay and gravel layers was estimated using industry standard design approaches:

τ_{max} (kPa) = 0.5 s_u (boulder clay) e.g. CIRIA 504 (1999) (3a)

τ_{max} (kPa) = 2 N (Sand and Gravel) after Meyerhof (1976) (3b)

Conservative estimates of s_u = 300 kPa were made for the boulder clay layer, and N = 50 was assumed for the gravel. This gave unit shaft resistance values of 150 kPa and 100 kPa respectively.

Given the pile tip was founded in the dense gravel layer, and following the experimental observations of Lehane and Gavin (2001), the bearing resistance mobilised by the soil beneath the annular area (q_{ann}) of the pile was assumed to be equal to that mobilised beneath a closed-ended (full-displacement piles), whilst the resistance below the pile plug (q_{plug}) was assumed to be equivalent to that developed by a bored pile:

q_{ann} (kPa) = 400 N (4a)
q_{plug} (kPa) = 100 N (4b)

For a SPT N value at the pile base of 50, this gave a q_{ann} and q_{plug} values of 20,000 kPa and of 5,000 kPa respectively. Thus for 610 mm diameter, 10.5 m long pile embedded 2.0 m into the dense gravel layer the total pile capacity was:

(150 x 3.142 x 0.61 x 8.5) =2443 kN - shaft resistance in boulder clay (5)
(100 x 3.142 x 0.61 x 2.0) = 383 kN – shaft resistance in dense gravel
(20,000 x 0.0298) = 703 kN – base resistance beneath pile annulus
(5,000 x 0.264) =1558 kN – base resistance mobilised by pile plug
5087 kN

The approach is similar, but less conservative that that outlined in the Steel bearing piles guidance document (2008) as the latter ignores the contribution of the pile plug resistance if the pile is unplugged.

4.2 Method 2

Lehane and Gavin (2001), Gavin and Lehane (2003) and Foye et al. (2009) demonstrated experimentally that plugging increased both the shaft and base resistance of piles installed in sand and proposed correlations between pile resistance and IFR. Lehane et al. (2005) present the following correlations between the end resistance (q_c) measured in a CPT test and the bearing pressure mobilised at a pile head movement equal to 10% of the pile diameter ($q_{b0.1}$) and the maximum shear stress (τ_{max}) which was included in the latest API design manual for offshore piles:

$$q_{b0.1}/q_c = 0.15 + 0.45\, A_{reff} \quad (6a)$$
$$A_{reff} = 1 - \text{FFR}\,(D_i^2/D^2) \quad (6b)$$
$$\tau_{max} = \frac{q_c}{33}\, A_{r,eff}^{\;0.3} \left(\frac{h}{D}\right)^{-0.5} \tan\delta \quad (6c)$$

where : A_{reff} is the effective area, FFR, the final filling ratio is the final IFR value and D_i is the internal pile diameter. It should be noted that the bearing pressure predicted by equation 6a is the average pressure acting over the gross pile base area.

Since no CPT data were available at the site a correlation between q_c and SPT N proposed by Mayne and Kulhawy (1990) was used to estimate q_c values:

$$q_c\ (\text{kPa}) = 544\ N\ D_{50}^{\;0.25} \quad (7)$$

where: D_{50} is the mean particle size of the soil in mm. For a D_{50} value of 2 mm and a measured N value of 59, Eqn. 7 yields a q_c value of 38,100 kPa. The empirical nature of such a correlation introduces additional uncertainty into the analysis, however the presence of boulders in glacial till can prevent CPT tests being performed and therefore this correlation uncertainty is often unavoidable. For a pile diameter of 610 mm, wall thickness of 16 mm and FFR = 1, A_{reff} from equation 6b is 0.9 and therefore:

$$q_{b0.1} = 38{,}100 \text{ x } (0.15 + (0.45 \text{ x } 0.1) = 0.196 \text{ x } 38{,}100 = 7{,}466 \text{ kPa} \quad (8)$$

Whilst the shaft resistance in gravel is given using Equation 6, where a limiting value of h/D = 2 is specified and so the shaft resistance over the three pile diameters embedded in the dense gravel is given as:

$$\tau_{max} = 38{,}100/33 \text{ x } 0.9^{0.3} \text{ x } 2^{-0.5} \text{ x } 0.5 = 407 \text{ kPa} \quad (9)$$

The shaft resistance in the boulder clay was assumed to equal that given by method 1 and therefore the total pile resistance was:

(150 x 3.142 x 0.61 x 8.5) = 2443 kN - shaft resistance in boulder clay (10)
(407 x 3.142 x 0.61 x 2.0) = 1561 kN – shaft resistance in dense gravel
(7,466 x 3.142 x 0.61^2/4) = 2181 kN – base resistance beneath pile annulus
6186 kN

Because the total pile resistance is derived from two sources, namely; the shaft and base resistance, it is preferable if these components of the resistance are separated during load testing. In order to achieve this, relatively complex instrumentation is required and this was not available for this project. In the absence of such instrumentation it is important that the load-settlement response confirms the predicted response of both the base and shaft resistance mobilisation curves (which are quite distinct). The mobilisation of shaft resistance was modelled using an elastic solution proposed by Randolph and Wroth (1978):

$$\tau = \frac{2Gw}{4D} \quad (11)$$

where: G, the operational shear modulus was estimated from the expression proposed by Fahey and Carter (1993):

$$\frac{G}{G_0} = 1 - f\left(\frac{\tau}{\tau_{max}}\right)^g \quad (12)$$

where: G_0 is the small strain shear modulus, D is the pile diameter, f and g are curve fitting parameters, taken as unity in this instance.

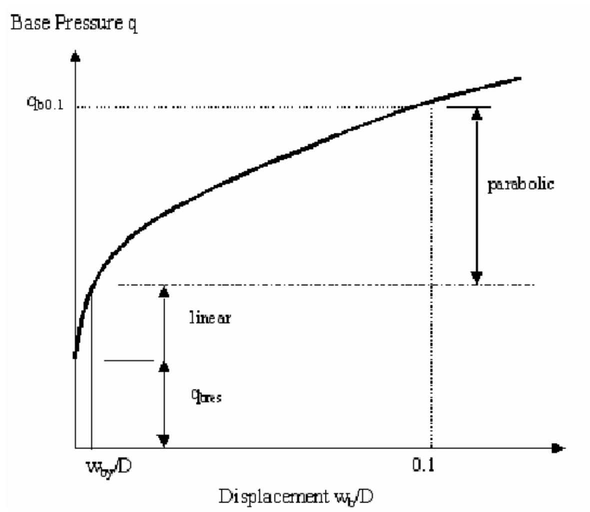

Figure 5 - Base pressure-settlement model (after Gavin and Lehane 2007)

The base pressure-settlement response was modelled using a 3 stage model proposed by Gavin and Lehane (2007). The model (See Figure 5) includes: (i) a stage when no base movement occurs until the residual base pressure (q_{bres}) set up during pile installation is exceeded. For fully coring open-ended piles, residual base stresses are low and can be ignored. (ii) A linear stage, with settlement controlled by the small strain elastic stiffness E_0. This operates until the normalised settlement exceeded the yield strain level. The yield strain w_{by}/D was assumed to be 1.5% for the test pile. (iii) A final non-linear stage up to w_b/D=10%, when the base pressure is $q_{b0.1}$ (that is, at w_b/D=10%).

The linear portion of the curve when $w_b/D < w_{by}/D$ can be described by:

$$q_b = [k\,(w_b/D)] + q_{bres} \tag{13}$$

$$k = (4/\pi)\,E_0/(1-\upsilon^2) \quad \text{for } w_b/D<w_{by}/D \tag{14}$$

The non-linear stage from w_{by}/D to w_b/D = 0.1 is of parabolic form, and the base stress at a given displacement can be determined from:

$$q_b = [k\,(w_{by}/D)^{1-n}\,(w_b/D)^n] + q_{bres} \quad \text{for } 0.1>w_b/D>w_{by}/D \text{ and } w_{by}/D \geq 0.003 \tag{15}$$

Unit shaft and base resistances were obtained from Equation 5 (for axial capacity method 1) and Equation 10 (for Method 2). E_0 for the very dense gravel was assumed to be 200 MPa and G_0 of 250 MPa was assumed for the boulder clay. Elastic shortening of the pile was included in the analysis. These values correspond to average stiffness values obtained for similar materials from geophysics such as Multi-channel analysis of surface waves (MASW).

5. Discussion

A computer controlled maintained static load test was performed on the test pile 8 months after installation. The maximum load applied of 5200 kN was twice the safe working load. The pile performed adequately in the load tests with a measured settlement of only 4 mm at the Safe Working Load, SWL (2600 kN) which increased to 12.24 mm at twice the working load. Comparison of the measured and predicted settlement profiles shows that although analyses using the axial resistance predicted using both Methods 1 and 2 provided excellent predictions of the axial resistance of the pile at load up to the SWL, the ultimate axial resistance was underestimated using method 1. Given that both Methods 1 and 2 provide very similar predictions for base resistance, which showed good agreement with CAPWAP estimates of base resistance, and the estimated shaft resistance in the boulder clay was comparable to measurements made on closed-ended piles by Farrell et al (1998), it would appear that the improved prediction offered by method 2 stems from a better shaft capacity prediction. Accurate modelling of very large shaft resistance values near the toe of open-ended piles was suggested by Gavin and Lehane (2003), Foye et al. (2009), and this feature of behaviour is included in both the Imperial College (IC-05) and University of Western Australia (UWA-05) design methods. Although the lack of instrumentation provided in this test precludes definitive proof that this was the mechanism which resulted in the good performance of the test pile, full-scale instrumented load tests are currently being commissioned by UCD with our industrial partners Mainstream Renewable Power to confirm these mechanisms.

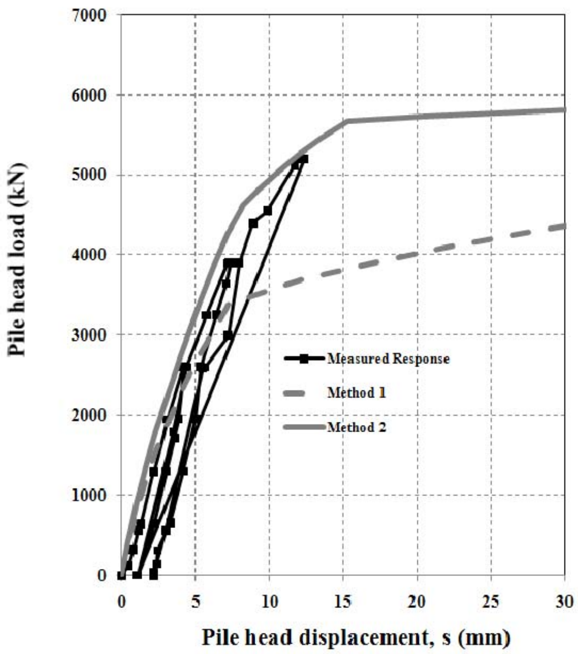

Figure 6 - Comparison of measured and predicted load-settlement response

SUMMARY

A case history was presented in which the predicted load-settlement response of a 610 mm open-ended pile, which was driven through boulder clay to found in a dense gravel layer, was compared to the measured response. A simple load-settlement prediction model was shown to provide excellent estimates of the measured pile response. Back-analyses of the pile test result suggested that large shaft resistance was mobilised by the test pile, particularly near the toe of the open-ended pile. Instrumented pile tests are currently underway to confirm this mechanism which can then be incorporated fully into design practice.

References

Farrell, E., Lehane, B. and Looby M. (1998) ‘Instrumented driven pile in Dublin Boulder Clay’ *Proceedings of the Institution of Civil Engineers–Geotechnical Engineering*, **131**, 4, 233-241.

Gavin, K. G. and Lehane B. M. (2007) ‘Base load-displacement response of piles in sand’ *Canadian Geotechnical Journal*, **44**, 9, 1053-1063.

Gavin, K. G., Cadogan, D. and Twomey L. (2008) ‘Axial resistance of CFA piles in Dublin boulder clay’ *Proceedings of ICE, Geotechnical Engineering*, **161**, 4, 171-180.

Jardine R. J., Chow F.C., Overy R. and Standing J. (2005) ICP Design Methods for Driven Piles in Sands and Clays. Thomas Telford, London.

Randolph M. and Wroth C. P (1978) ‘Analysis of deformation of vertically loaded *piles’ ASCE Journal of Geotechnical Engineering Division*, **104**, GT12, 1465-1488

Stroud M. A (1989) ‘The SPT test – Its application and *interpretation’ Institution of Civil Engineers Conference on Penetration Testing*, Birmingham. Thomas Telford, London, 29-49

Trenter N. A. (1989) Engineering in glacial tills. CIRIA, Report No. C504

CONCRETE IN THE BUILT ENVIRONMENT, PAST, PRESENT & FUTURE

Peter Anthony
Horganlynch & Partners, Cork

Abstract
The paper gives an overview of the use of concrete in the built environment over the ages, and for the modern age addresses its use as a visual architectural material. The development of the material from its origins in pre-Roman times to the material of today, and material of the future, are touched on. The relationship between architect and engineer is discussed and the contribution of the engineer in achieving the required aesthetic goals is explored.

Keywords: Architecture, Cecil Balmond, Concrete, History, Le Corbusier, O'Donnell and Tuomey, Peter Rice, Sustainability, The future,

1. The Past

The history of the built environment and the history of man are intertwined, the former being one of the significant physical manifestations of the development of the latter. The initial driver for man to build was the provision of shelter from the elements and attack, and the earliest forms of construction included interventions in rock by cave dwellers. Early constructions included primitive huts where the materials of construction included clay, wattles and grasses. Such forms of construction are still in use in some communities to this day.

Quarried stone was the first material used by man to create significant structures and they were generally built to contain the tombs of rulers. These structures adopted an early form of concrete in their composition to construct the core where a dry form of the material was compacted with rubble stone. The word concrete comes from the latin word *concretus* meaning compact or condensed.

The mathematician Imhotep who created the Pyramid of Djoser in the 27th. Century BC (see Figure 1) has been heralded as the first engineer.

Figure 1 – Pyramid of Djoser

The technology and use of stone and concrete developed over time, and by the first century AD had been used in the construction of the magnificently detailed and executed Roman forum (see Figure 2). The concrete used by the Romans, *opus* *caementicium*, was made from quicklime, pozzolana and an aggregate of pumice stone. Tests have shown that this concrete had as much compressive strength as modern Portland cement based concrete. This concrete gave a freedom to design that was not previously provided by brick and stone. Resulting structures such as the splendid Pantheon (see Figure 3) constructed in Rome in the second century AD remains as the largest unreinforced concrete dome standing to this day.

Figure 2 – Roman Forum

Figure 3 – Pantheon in Rome

In this period the Roman architect/engineer/builder Vitruvius produced the ten volume *De Architectura*, considered to be the most important treatise on Roman architecture and engineering. The iconic Vitruvian Man drawn by Leonardo da Vinci is based on the studies of the human body by Vitruvius.

The significant construction materials of Roman times, stone, together with unreinforced concrete in compression – used, for example in the The Markets of Trajan by Appolodorus of Damascus (see Figure 4) - remained so up to the eighteenth century.

Figure 4 - The Markets of Trajan by Appolodorus of Damascus

In Renaissance times significant buildings in stone and concrete included the Palazzo Chiericati in Vicenza by Palladio and the Church of San Spirito in Florence by Brunelleschi (Figure 5) who trained as a Master Goldsmith but was described as an architect/engineer.

Figure 5 – Church of San Spirito in Florence by Brunelleschi

The Victorian era introduced the age of iron and steel in construction with significant structures being created such as Paddington station (1854) by Isambard Kingdom Brunel who also created the dramatic Clifton Suspension Bridge (completed 1864) near Bristol, and St. Pancras Station in London (1864-68) by William Barlow (Figure 6) which has been recently restored to its original magnificence

Figure 6 – St. Pancras Station in London

Figure 7 – The Au Bon Marché Store, Paris

Gustav Eiffel produced some dramatic work in iron and steel including the Au Bon Marché store (1879) on the Left Bank in Paris (Figure 7), one of the first framed buildings ever constructed, and the Eiffel Tower (1889). Other significant buildings of the era include the recently restored Palm House at Kew Gardens in 1844 by Decimus Burton and Crytsal Palace by Joseph Paxton in 1851.

The American skyscraper story developed from the iron and steel era, initially in Chicago with Louis Sullivan and then in New York with Burnham's Flatiron Building (1902) being one of the classic earlier iconic examples of the genre (Figure 8).

Figure 8 – Flatiron Building in New York

While concrete was used in construction since pre-Roman times it did not become the significant material of construction it is at present until the development of reinforced concrete in the later 19th century and prestressed concrete in the early 20th century. A number of developments and inventions facilitated the emergence of concrete as the pre-eminent material of construction.

- In the 1750's John Smeaton pioneered the use of 'hydraulic lime' in concrete using pebbles and powdered brick as aggregate;
- Portland cement was patented by Joseph Aspdin of Leeds in 1824, the name deriving from the resemblance of the hardened cement to the building stone quarried on the Isle of Portland;
- In 1850 a Frenchman named Lambot constructed a boat using reinforced concrete and in 1854 Wilkinson patented a reinforced concrete floor slab design;
- François Coignet published a document in 1861 which defined the principles of what we now refer to as reinforced concrete.

Figure 9 - Hennebique House in Bourg-la-Reine

Hennebique House in Bourg-la-Reine, constructed between 1894 and 1904, was the first reinforced concrete building in France (Figure 9).

2. The Present Modern Age

Le Corbusier, one of the founding fathers of Modern Architecture, used reinforced concrete in a bold manner as the primary aesthetic of his architecture. Significant work produced by him which helped define the building stock we have today include the Unité d'habitation in Marseille (Figure 10) which, in addition to being a striking example of exposed reinforced concrete in architecture, was a significant social experiment in urban dwelling producing mixed results. His governmental building in Chandigarh India (Figure 11) is a classic example of the building aesthetic possible with reinforced concrete.

Figure 10 – Unite D'habitation Marseilles

Figure 11 – Governmental Building in Chandigarh, India

Some years ago while walking through the Harvard University Campus in Cambridge, Massachusetts, I came upon - and was mesmerised by - the Carpenter building (Figure 12), Le Corbusier's only building constructed in the United States. Not knowing the building or its architect at the time I was subsequently delighted to discover its provenance.

Another influence on the use of reinforced concrete in the built environment around this time was the Bauhaus movement in Germany. The movement was founded by the architect Walter Gropius to create an educational environment in which crafts and the fine arts could be taught together. This movement produced significant concrete buildings such as the Bauhaus' own Workshop in Dessau (Figure 13) as well as a generation of very gifted architects and artists.

Figure 12 – Carpenter Building, Harvard University Campus

Figure 13 – Dessau Workshop, Germany

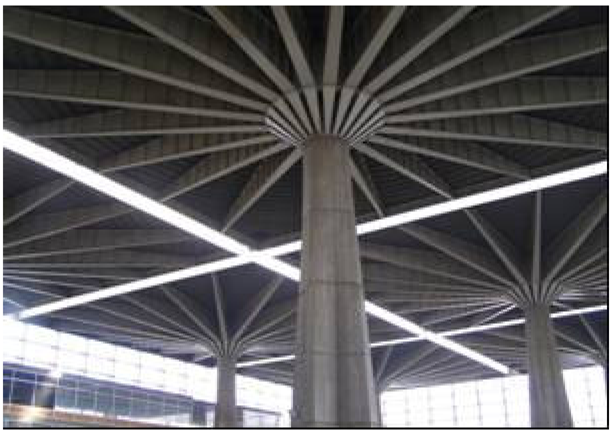

Figure 14 – The Exhibition Building in Turin

In the mid 20th century the Italian engineer Pier Luigi Nervi produced dramatic longspan structures such as The Exhibition Building in Turin (Figure 14) in steel and concrete. Significant other work included the Pallazetto dello Sport in Rome, and the striking St. Mary's cathedral in San Francisco.

The form of the architecture has sometimes been defined by the material and structural forms adopted to define space. The work of the engineer Heinz Isler using thin reinforced concrete shell structures (Figure 15) is of particular relevance. His work in free form finding and hyperbolic paraboloid shell construction resulted in a significant dramatic body of work and paved the way for the later work of Peter Rice on the Sydney Opera House project.

Figure 15 – Reinforced Concrete Shell Structure by Isler

One of the more significant buildings in the western world which define the era of exposed concrete providing the architectural aesthetic is Sir Denys Lasdun's National Theatre on the south bank of the river Thames in London (Figure 16). The brutalism of the raw exposed concrete is liked and loathed by the public with equal passion. In time the stark grey rawness of concrete-clad brutalist buildings fell out of favour, particularly in the UK.

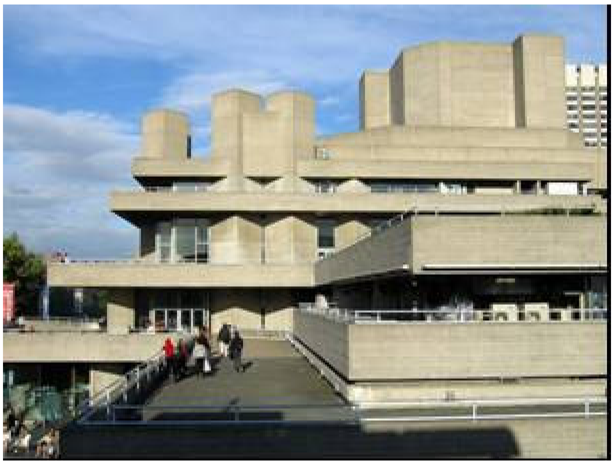

Figure 16 – The National Theatre on the South Bank of the Thames River, London

For the High-tech movement which followed the predominant materials of construction were steel and glass. However, an excellent example of the adaptability of concrete as a construction material and its use during the high-tech era is provided by the genius of Peter Rice. Rice had been involved with Renzo Piano and Richard

Rogers on the Pompidou Centre in Paris (Figures.17-19) in the early 1970's and developed the signature cast steel gerberettes to support the building floors. These large tactile elements define this ageless product of the high-tech era.


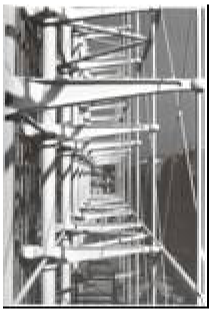
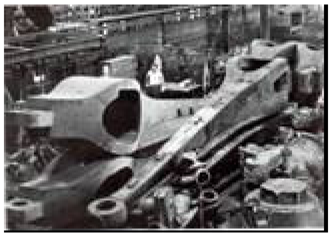

Figure 17 **Figure 18** **Figure 19**
Pompidou Centre

When Rogers designed the Lloyds building in London a decade later he wanted to recreate a similar aesthetic with exposed structure and services. He requested that the functionality and articulation of the structure be visible and clear to all. However London fire regulations prevented the use of structural steel for the structure and therefore Rice re-created a similar aesthetic using a combination of in-situ and precast concrete (Figures 20-22).



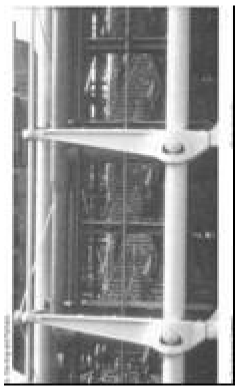

Figure 20 **Figure 21** **Figure 22**
Lloyds Building in London

Rice further colloborated with Renzo Piano on the Menil Collection Gallery in Houston, Texas (Figures 23-24) where he designed the roof structure to allow reflected light into the gallery space using a combination of cast steel truss sections and ferrocement light deflectors. Piano rightly described Rice as being:

"one of those engineers who has greatly contributed to architecture re-affirming the deep interconnection between humanism and science, between art and technology".

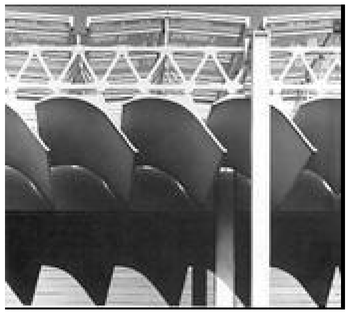

Figure 23 **Figure 24**
Menil Collection Gallery in Heuston Texas

While the era of concrete brutalism, as instanced by the National Theatre, is now gone, the role of concrete in the creation of architecture is still very relevant. The engineer can play a significant role in conjunction with the architect in the delivery of quality architecture using concrete.

At a conference in the South of France called *Art and Technology, East meets West* in the 1990's Richard Weinstein, Head of Architecture at UCLA, described engineers as being *Iagos*. Iago is the character in Shakespeare's Othello who kills romantic and sensitive aspirations by reiterating rational argument. Iago, as the agent of rationality above all else, succeeds in breaking the fragile ideas that are based on flights of fancy. In the end heartfelt passion is denied by building a barrier of pragmatism beyond which it is impossible to negotiate. Iago is thus the prototype for WH Auden's *Scientific Man* as described in *The Joker in the Pack*.

This analogy appealed to Rice as he firmly believed that the engineer should take an active part in the creative design process and not just kill it with the simplistic logic of engineering design and regulation.

The architect Ian Ritchie, one time partner of Rice's in RFR, the practice he established in Paris following his departure from Arup, recalls a discussion he had with Rice regarding the Louvre pyramid they were designing with IM Pei at the time. Rice observed that the maximum member size that they had developed for the courtyard roof structure had been based upon the diffusion of a shadow line created by an object between the light source and the ground plane as defined by the French mathematician and philosopher Jean Le Rond d'Alembert. Rice's consideration of structure went far beyond the normal textbook approach to member sizing and thereby enriched the final product as a result.

An engineer with a similar passion for structures in architecture, and with the intellect, inventiveness and flair of Rice is Cecil Belmond of Arup London. He has collaborated with many of the world's current major architects to produce ground breaking architectural structures. He has also collaborated with artists such as Anish Kapoor and others on largescale art installations.

Charles Jencks, the architectural critic said of him:
"Cecil Balmond brings this new understanding to the collaboration of engineer and architect. With Daniel Libeskind at the V&A he has worked out both a new chaotic spiral organisation and a new system of tiling, the fractiles. With Rem Koolhaas he has developed acentric cantilevers and new roof structures. He, like they, turn columns into beams and floors into walls and roof. The continuous structural surface

the hybrid floor, ramp, wall has become an identifying mark of the new paradigm, as conventional glass and steel curtain wall was for Modernism".

His concrete catenary roof for the Portuguese Pavilion for the 1995 Lisbon Expo designed with the architect Alvaro Siza is an excellent example of the structure defining the architecture (See Figure 25).

Figure 25 – Concrete Catenary Roof for the Porteguese Pavilion

The freedom of expression currently afforded by computers both in form definition, structural analysis and design has heralded a new era for concrete as a structural material due to its capacity to be moulded into shapes and forms not possible with many other materials.

The aesthetic requirements of the architectural profession with respect to concrete finish are not always at one with the technical requirements of the engineer with respect to the material.

The following photographs (Figures 26-27) illustrate the different approaches of architects and engineers to certain aspects of concrete as a visual construction material.

Figure 26

Figure 27

Bruder Klaus Chapel in Switzerland

The photographs are of the Bruder Klaus Chapel in Switzerland by the 2009 Pritzker Prize winning architect Professor Peter Zumthor. An engineer acting alone would probably have rejected the concrete in this building as being unacceptable due to honeycombing, separation and other defects which would affect the strength and long term durability of the concrete. However this was the exact aesthetic the architect was looking for. I wonder if the engineer for the project features the work on his web page or in promotional literature. However this project clearly illustrates where a broader view by the engineer is sometimes necessary to meet the desired aesthetic requirements.

The size and nature of the Irish market dictates that the engineers working in consultancy adopt a generalist approach to work and narrow specialization is rare. My own career has been almost exclusively involved in the design of structures but unfortunately mostly of a prosaic nature due to market requirements. However I have had the privilege of working on some significant architectural projects with very talented architects, Andrej Wejchert, Andy Devane, Shane de Blacam, Eric van Egeraat, Des McMahon, John Tuomey, Sheila O'Donnell and Neil Hegarty to name a few.

We recently worked on an entry for the West Cork Arts Centre in Skibereen with O'Donnell and Tuomey Architects. The site for the development has a very small footprint and the client's accommodation schedule was rather large. The architects addressed the brief by designing a tall slender concrete box representative of one the old towers guarding mediaeval towns. However rather than have a smooth sharp concrete aesthetic, they were looking to use what they termed “farmer's concrete” similar to the Zumthor chapel laid in layers as if a rammed earth structure. Structurally there were few issues as thick walls were called for, supporting small floor plates. However the achievement of the uncompacted concrete look caused us some soul-searching. We did not win the competition, which, on reflection, may be fortuitous!

One project we did complete with O'Donnell and Tuomey is the Glucksman Gallery in UCC, a project shortlisted for the Stirling Prize in 2005. The dramatic form of this gallery, which did not vary from initial hand sketch to finished product, would not have been possible without the use of a concrete supporting structure.

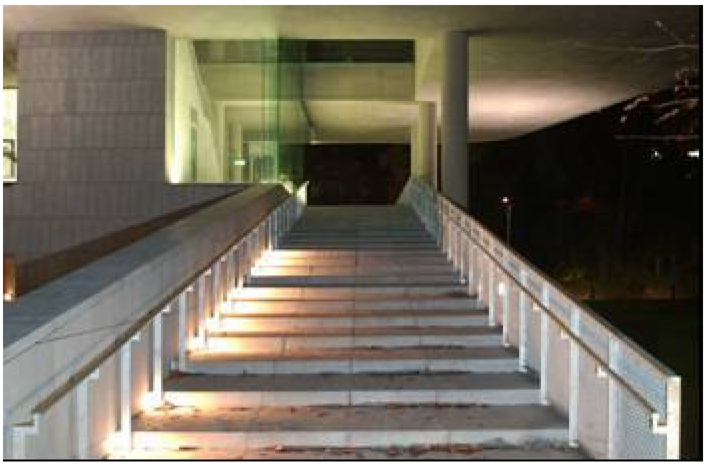

Figure 28 – Glucksman Gallery, University College Cork

This unique and spectacular building posed a number of significant and exciting engineering challenges. The overall structure can be considered as consisting of two significant masses, a solid conventional block to podium level with a larger plan mass hovering above this with both separated by a minimum of supporting columns located inboard of the edges of the upper mass.

The requirement for a relatively column-free zone at podium level and the existence of a large cantilevered structure over this level posed the main challenges.

These challenges were amplified by the asymmetric nature of the plan form. The construction to podium level is conventional with a piled reinforced concrete basement slab, load bearing reinforced concrete walls and reinforced concrete podium level slab. The mass of this section of the building acts as a physical counterbalance to the upper cantilever section. The underside of the slab over podium level presents a flat concrete soffit. However this masks a significant orthogonal grillage of upstand beams. A timber joist structure is laid on top of the concrete beam grillage to support the oak gallery floor boarding. This concrete slab and beam floor plate acts as an entablature structure to support the building over.

The structure above the entablature level over the podium consists of a reinforced concrete core wall and floor structure and perimeter structural steel column and floor beam grillage. The central core structure contributes to the overall building stability and helps balance the asymmetric cantilever loading.

Another O'Donnell and Tuomey project we are currently completing, the Lyric Theatre in Belfast, utilises a reinforced concrete frame and wall structure in a more prosaic manner. However I have no doubt that the finished product will be equally as dramatic as the Glucksman Gallery.

Figure 29 – Lyric Theatre, Belfast

Figure 30 – Concert Hall in the Canary Islands

Not even the briefest review of the use of concrete in current architecture would be complete without reference to the engineer/architect Santiago Calatrava. While better known for his signature asymmetric arch bridges, his love of form and use of materials, particularly concrete, makes his buildings very special indeed.

The striking concert hall in the Canary Islands shown above (Figure 30) demonstrates the sensual forms he has achieved in concrete.

3. The Future

The more significant challenges for the future to be addressed by you as engineers and researchers will be related to the environment and sustainability of the built environment.

The manufacture of cement is still a significant producer of CO_2. Significant strides have been made with respect to emissions reduction in the production of concrete by the part substitution of ground granulated blast furnace slag together with environmental advances in cement manufacture itself. Undoubtedly further research will bring further improvements and additional carbon dioxide reduction.

The capability of the built environment to respond to, and withstand, natural disasters such as earthquakes is an issue requiring more research. Someone astutely remarked that buildings, not earthquakes, kill people. While the principles of earthquake design are well developed, and design methods codified, either poor regulation or lack of implementation of standards still results in significant loss of life.

The insulating value of concrete is also an issue and currently there is conflict between concrete strength and its insulating value. There is a growing requirement from architects for concrete external walls to buildings with fair face finish on both sides. This can be achieved either by sandwiching insulation within a twin skin construction or utilising concrete which has inherent insulating properties. The problem with sandwich construction arises at junctions where continuity of insulation compromises structural integrity or continuity of structure compromises insulation creating cold bridges.

The problem with current insulating concrete is that the aggregates generally used are based on perlite, a siliceous rock which when heated expands considerably to create a highly voided material which provides the insulation. Unfortunately the resulting concrete is of low strength due to the low strength of the voided aggregate. Further research is required to develop a high strength insulating concrete.

When I commenced my career the concrete structural design code we used was BS CP114 and the concrete used generally for structures had a 28-day design strength of 21N/mm^2. Until recently with BS8110 and now with the Eurocodes we generally use concrete achieving 40N/mm^2 for normal work, virtually double the strength.

In recent years, projects such as the Burj Khalifa in Dubai have pushed the requirement for higher strength concrete. For example, a number of buildings in Seattle, Washington, contain concrete with a compressive strength of 131N/mm^2. The US Army Engineers have developed concrete strengths up to 240N/mm^2 in compression and 40N/mm^2 in flexure while developing hardened structures for military defenses. While projects such as the Burj Khalifa in Dubai may be few in number for the foreseeable future, Man will always want to build bigger and higher.

The use of Nanomaterials in concrete such as nano-particles of silica or nanotubes will help develop higher strength concretes. However these materials in turn require better mixing technologies. Further development of these technologies is required to facilitate everyday use at reasonable cost.

Durability of concrete has always been a significant concern with respect to the material and problems related to carbonation and chloride attack, high alumina cement concrete and lack of concrete cover to ferrous reinforcement has tarnished the reputation of the material. Considerable strides have been made to rectify the situation with recent code and specification improvements. However further improvements in this area will no doubt be forthcoming to increase the longevity of the material.

Working on projects with architectural concrete always requires considerable thought and design in relation to the concrete formwork. Jointing and required finish are always items of considerable discussion and debate. While the UK National Structural Concrete Specification provides good specification clauses and reference sites for normal Type A and Type B finishes, the specification of a Type C special architectural concrete finish always poses difficulties. A robust written specification for a particular aesthetic finish for a large area of concrete invariably leads to disputes. Sample panels can help, but it is always difficult to consistently replicate a sample panel produced under near ideal conditions on the work site. Further research and guidance in this area would assist the practicing engineer.

4. Conclusions

Concrete in one form or the other has been one of the most significant building materials since man began to build. The contribution of the engineer to the use of concrete in the built environment both as a collaborator with architects, and alone, is enormous and his or her contribution when considering the design issues in a holistic rather than a narrow way paves the way for the production of great architecture.

The challenges facing engineers working in concrete research are exciting and I have no doubt that the current material limitations will be pushed out continuously to help keep it as the predominant material of construction for the built environment into the future.

References

Rowland, D. Howe, T.N. (1999) *Vitruvius. Ten Books on Architecture*. Cambridge University Press, UK

Brown, André (2001) *The Engineer's Contribution to Contemporary Architecture: Peter Rice*, Thomas Telford, London

Rice, Peter (1998) *An Engineer Imagines,* Ellipsis Press, London

Chilton, J. (2000) *The Engineer's Contribution to Contemporary Architecture: Heinz Isler*, Thomas Telford, London

Balmond, C. (2002), *Informal*, Prestel, London

Shakespeare, W. (1603) *Othello*, (various publishe*rs)*

Auden, W.H. (Ed.) *(1938) The Oxford Book of Light Verse,* Oxford

Concrete Society (2004) *National structural concrete specification for building construction*. 3rd edition, Concrete Society, Surrey, UK.

INFRASTRUCTURE ASSET MANAGEMENT DATABASE SYSTEM FOR INFRASTRUCTURE OWNERS

B.M. DEVLIN
CEI Collins Engineers Ltd, Dublin, Ireland

Abstract
Asset management is the systematic and coordinated activities and practices through which an organisation optimally manages it assets, and their associated performance, risks and expenditures over the lifecycle for the purpose of achieving its organisational strategic plan.

This paper discusses the creation of an asset management database system for managing the inventory and maintenance of structures. The paper describes the data required to be input into the system and how it can be utilised to ensure that information pertaining to the configuration and condition of individual structures is readily available.

Good practice dictates that regular inspections of assets should be undertaken. The overall purpose of inspection and monitoring is to check that assets are safe for use and fit for purpose and to provide the data required to support effective maintenance management and planning. It is important for supervising engineers and inspectors to have a clear understanding of the objectives of inspections and how it fits into the management plan for the infrastructure in question. This paper outlines the various forms of inspections with their associated objectives. The development of inspection manuals and process models is also discussed, which are tools used to assist infrastructure owners achieve their goal of provision of a systematic and holistic framework for the management of assets.

Keywords: Asset Management System, Business Process Model, Database, Inspection, Inspection Manual.

1. Introduction

It is widely recognised that a well managed transport infrastructure is vital to the economic stability, growth and social well being of a country. Bridges and other infrastructure are fundamental to the transport infrastructure because they form essential links in the highway network. It is not therefore in the public interest to allow infrastructure to deteriorate in a way that compromises the functionality of the transportation network, be it through restrictions or closures caused by unsafe structures or the disruption of traffic through poor planning of maintenance work.

The purpose of an Asset Management System (AMS) is to enable storage, manipulation, management and retrieval of data and information and to support engineering processes, asset management planning and resource accounting and maintenance planning and management. An AMS should achieve this effectively and efficiently, align with recognised requirements (e.g., condition indicator), be compatible with other systems for data sharing/transfer (e.g., asset valuation) and be reflective of the size and nature of an authority's infrastructure stock. *(Management of Highway Structures – A Code of Practice, 2005).*

The essential elements that feed into an Asset Management Database System include the key dimensions and make-up of a structure, the various types of inspection records, any load assessment data and proposed work details with associated costings.

2. Inspection types

2.1 Visual Inspection

A Visual Inspection is a cursory inspection conducted at least annually by operation and maintenance personnel as part of their routine work activities. It is conducted visually, without special access equipment or traffic management. No pre-inspection data collection is required. Its purpose is to promote public safety and recognise short term maintenance requirements by identifying readily apparent defects such as settlement, potholes, accumulated debris, excessive vegetation, obvious damage, distorted or missing members, severely corroded members, large cracks, voids or scaled and spalled concrete.

This type of inspection should be routinely conducted by personnel when at a site for any reason, and may be used to report readily apparent conditions which might affect public safety or require immediate remedial actions. A Visual Inspection is normally conducted and documented at least once each year.

If conditions are found which require immediate attention, the inspector should take action to protect the safety of the public and the infrastructure in question, and report the conditions to the appropriate supervisor.

2.2 General Inspection

A General Inspection is a routine inspection conducted at least once each two years by engineers or approved operations staff who have undertaken the appropriate training. A General Inspection should also be carried out in the event of special incidents such as flooding, vessel impacts, vehicle collisions after the opening of a new structure and after major works have taken place at a structure. The inspection includes all visually accessible parts of the structure including adjacent structures and the waterway, if applicable. The General Inspection should include adjacent earthworks and waterways that may affect the structure, including evidence of flooding or other conditions such as the accumulation of debris or blockages which could lead to scouring of supports. Where available, records of the most recent Visual Inspection, General Inspection, Principal Inspection and Load Assessment should be reviewed before undertaking the inspection.

As part of a General Inspection, the inspector should highlight any defects that may require remedial actions. The inventory data should be reviewed and updated, if necessary.

2.3 Principal Inspection

A Principal Inspection is a detailed inspection conducted at least once each six years by engineering personnel or consulting engineers retained by the infrastructure owner. The inspection includes all inspectable parts of the structure, including adjacent earthworks and waterways that may be relevant to the behaviour or stability of the structure. A Principal Inspection is a close examination conducted with ladders and other access equipment, as necessary to be within touching distance of all bridge parts. Special testing equipment is not required, but simple tools such as hammers, scrapers, measuring tapes and scales should be used. It may also require traffic management measures to safeguard the inspectors and the travelling public. Records of the most recent Visual Inspection, General Inspection and Principal Inspection should be reviewed before undertaking the inspection.

A Principal Inspection may be combined with other activities such as a Special Inspection or planned maintenance activities to share special access equipment or traffic management activities. During a Principal Inspection, the inventory data may be reviewed and updated, if necessary.

3. Inspection Manual

The inspection manual describes the various types of inspections included in the overall inspection programme, the frequency at which these inspections should be conducted, and the qualifications of inspectors conducting each type of inspection. The manual is primarily concerned with the detailed process and procedures for conducting inspections, but the information presented is useful to inspectors conducting all types of inspections.

The purpose of the inspection manual is to ensure the proper safety inspection and evaluation of infrastructure, to standardise inspection and reporting procedures, and to provide guidance for complying with an Agency's policies and procedures. *(Waterways Ireland Inspection Manual, 2008).*

Typical contents of an inspection manual are as follows:

(a) TYPES OF INSPECTIONS
- Visual Inspection
- General Inspection
- Principal Inspection
- Structural Assessment
- Special Inspection
- Mechanical and Electrical Inspection

(b) FREQUENCY OF INSPECTIONS

(c) QUALIFICATIONS OF INSPECTORS

(d) INSPECTION PROCEDURES
- Preparation for Inspection

- Safety Practices
- Field Inspection Equipment
- Field Documentation

(e) EXECUTION OF INSPECTION
- Sample Structure Diagrams
- Condition Ratings

<u>APPENDICES</u>

APPENDIX 1 – Inspection Template
APPENDIX 2 – Detailed Inspection Guidelines for Various Elements
APPENDIX 3 – Inspection Reporting Guidelines
APPENDIX 4 – Sample Inspection Report
APPENDIX 5 – Inspection Procedure Chart and Text Descriptions

4. Business Process Model

In order for an AMS to function correctly and efficiently, it must harmonise with the existing organisational structure of the authority adopting it. Clear guidelines must exist as to what activities are required to be carried out, who should undertake those tasks, when they should take place and what resources are to be utilised. A collection of processes, textual descriptions and data constituents that describe the hierarchy and organisation of tasks and activities to be undertaken is called a business process model. In essence, a business process model provides a detailed blueprint to show the order of activities required to complete a procedure. In turn, that procedure may often be a small step in another overall process.

A business process model for an AMS organises and describes each of the activities that are undertaken by an authority responsible for a bridge network, in a format that can be understood by all personnel within the authority. Collins Engineers, in partnership with Waterways Ireland, have developed such a business process model to enable Waterways Ireland to successfully implement their Bridge Management System. *(Waterways Ireland Business Process Models 2008).*

4.1 Organisation of Process Procedures

A Business Process Model for an AMS is normally partitioned into two interlinking sections; one portion deals with the administration of inspection procedures, while the other relates to the management of bridge works. Two overall procedures organise the primary activities involved with these two headings and are named, ‘The Overall Inspection Procedure’ and ‘The Overall Work Management Procedure’. While these overall procedures are distinct from one another, they are closely related, with numerous interlinking tasks and activities. The Overall Inspection Procedure Chart is shown in Figure 1.

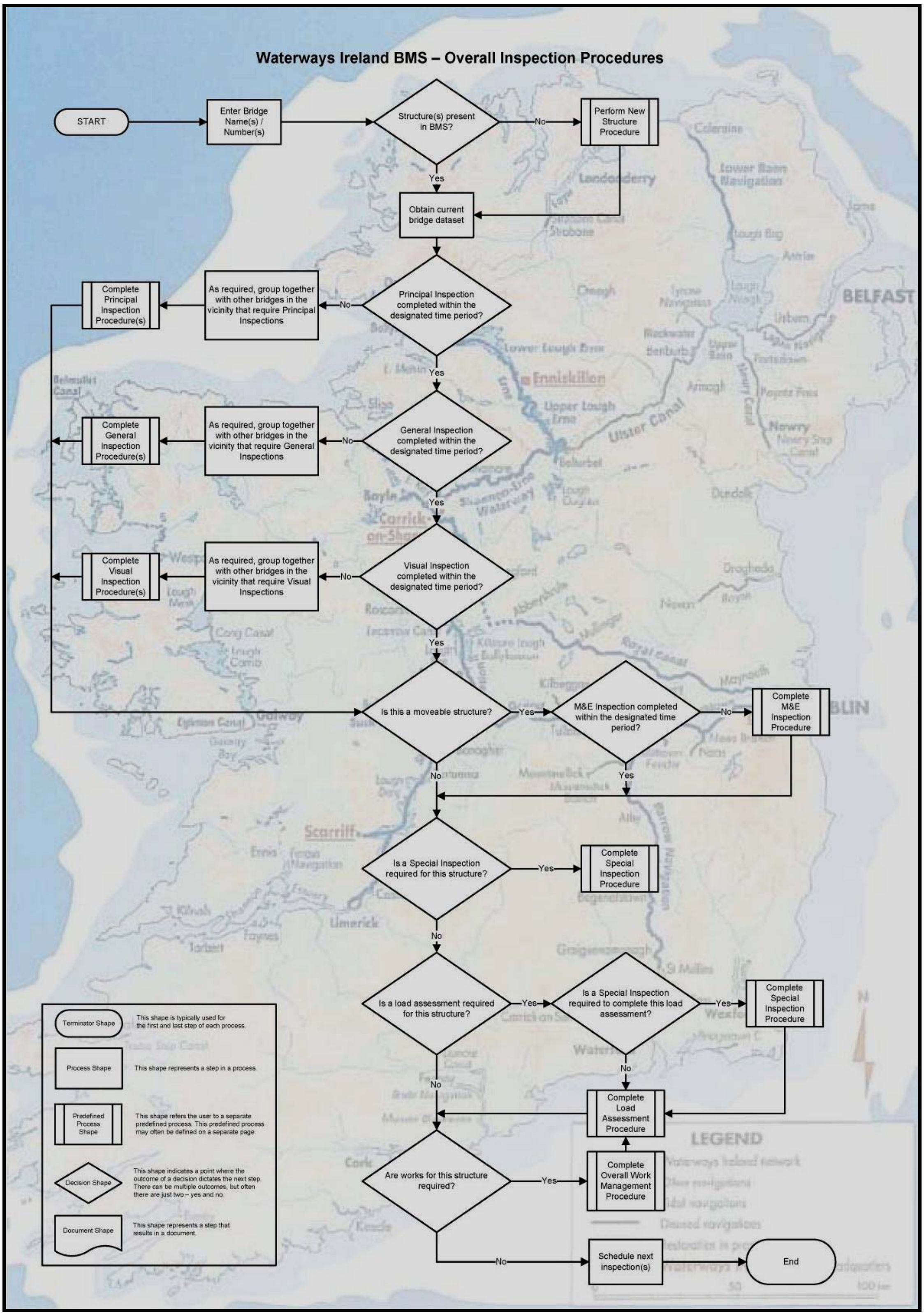

Figure 1 - Overall Inspection Procedure Chart

Within each of these primary partitions, several sub-processes exist which deal with the principal AMS tasks, such as the ‘New Structure Procedure’, ‘Principal Inspection Procedure’, ‘Emergency Works Procedure’ and the ‘Repair / Maintenance Procedure’. Again, many of these process procedures are closely inter-related, with one procedure often arising out of another. For example, the ‘Repair / Maintenance Procedure’ may often be undertaken as a result of a previously conducted ‘Principal inspection Procedure’ since repairs are often recommended following a Principal Inspection. These sub-processes are then further sub-divided, where necessary, down to the required level of detail.

5. Asset Management Database System

An asset management database enables an authority to record and maintain data and information about structures in a standard format. The database enables each asset to be uniquely identified by its structure ID and allows a number of attributes to be held against the ID. Examples of different fields within an asset database are given below. *(Structure Asset Management System Database, 2006).*

5.1 Inventory

This data entry interface allows the addition and editing of structure data, corresponding to the “Header Information”, “General Details”, and “Construction Details” sections of the database. Existing data fields can be renamed to suit the overseeing authority standards, such as Ordnance Survey Sheet, Local Authority Structure ID, Function of Structure, Type of Wearing Course, Mechanics of Moving Bridge Type, Verge Material, Air Draft, Components, and List of Services on the bridge. Refer to Figure 2.

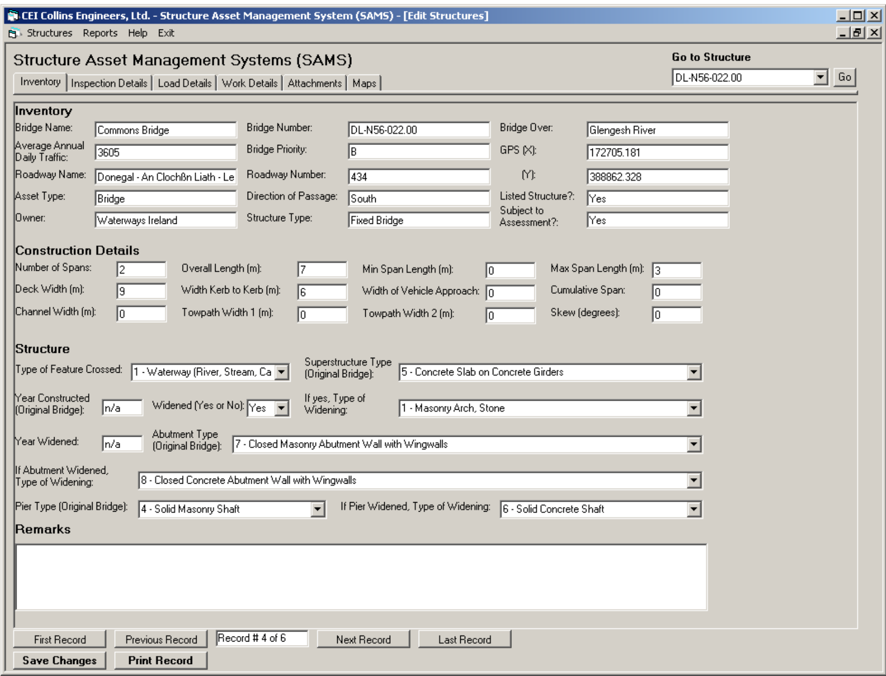

Figure 2 – Database: Inventory Field

5.2 Inspection Record

This data entry interface allows the entry of inspection records, which correspond to previously entered inspection requests. All historical inspection records are stored in the database and can be easily browsed. Photographs, pdfs, AutoCAD drawings, or any other electronic files can be attached to an inspection through the Attachments tab. The number and verbiage of the component groups is customisable (carriageway wearing surface, structural slab, expansion joints, etc.).

Condition ratings are normally entered at this stage. This allows the authority to query the database at a later stage to prioritise structures in need of maintenance. Refer to Figure 3.

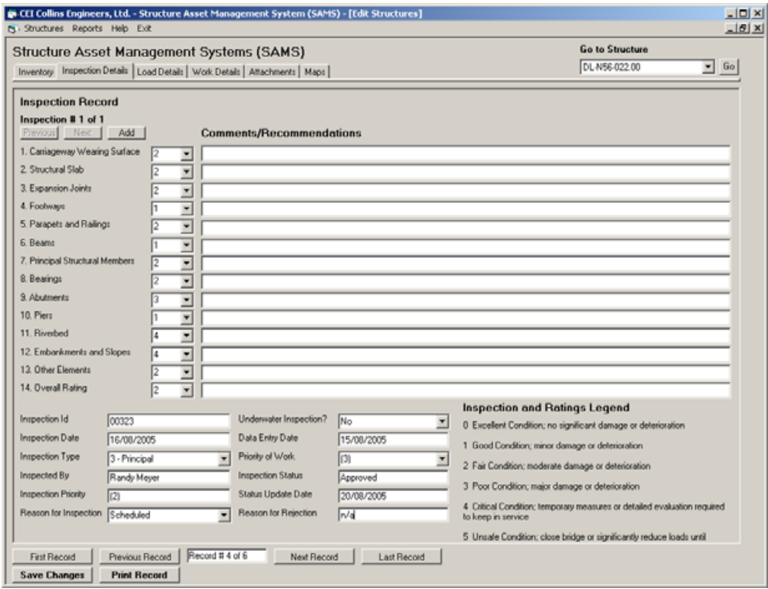

Figure 3 – Database: Inspection Record Field

5.3 Load Details

This data entry interface allows the addition and editing of load details, which correspond to a single structure. Multiple records can be added per structure, to allow for historical tracking of load ratings which may change over time. Photographs, pdfs, AutoCAD drawings, or any other electronic files can be attached to an inspection record through the attachments tab.

5.4 Work Details

This data entry interface will allow the addition and editing of work details, which link to specific inspection records. Multiple work details (jobs) can be added per inspection record. All historical work details are stored in the database and can be easily browsed. Photographs, pdfs, AutoCAD drawings, or any other electronic files can be attached to an inspection through the attachments tab. Refer to Figure 4.

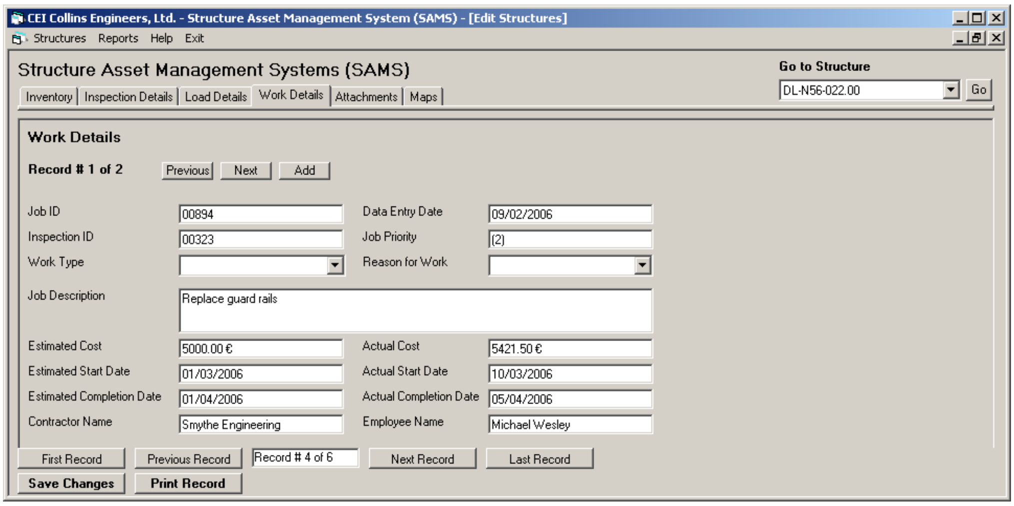

Figure 4 – Database: Work Details Field

6. Conclusions

This paper has given a brief overview of the organisation and business processes and information management and systems components of an Asset Management Regime. Implementation of an effective AMS enables infrastructure owners to plan and carry out works on structures that are appropriately targeted and contribute towards the strategic objectives and goals for the network in the most cost effective manner while bearing in mind responsibilities to other parties. *(Management of Highway Structures – A Code of Practice, 2005).*

7. References

CEI Collins Engineers Ltd (2006) '*Structure Asset Management System Database*'.
Roads Liaison Group (2005) '*Management of Highway Structures – A Code of Practice*'.
Waterways Ireland (2008) '*Waterways Ireland Business Process Models*'.
Waterways Ireland (2008) '*Waterways Ireland Inspection Manual*'.

MANAGEMENT OF CONCRETE HALF-JOINT BRIDGES

M. HALE[1], V. FAILS[2], N. FENNING, J. WHITE & D. ANSTICE
[1]Mouchel, Birmingham, England
[2]Roads Service, Ballymena, Northern Ireland

Abstract
From January 2010 the Northern Ireland Roads Service (NIRS), in conjunction with Mouchel, have been undertaking a detailed review of 12 concrete structures within their bridge stock, each of which contained half-joints.

A large number of half-joint structures were introduced to the UK during the 1960's and 1970's, during a rapid expansion of the motorway and trunk road network. Reinforced concrete half-joints pose a particular problem as they are not easily accessible for inspection and maintenance. This has led to a concern about the long-term durability and structural performance of these joints, due to the effect of chloride laden water penetrating through defective or leaking deck joints. The steel reinforcement in the joint area is therefore vulnerable to chloride attack and potential serious corrosion.

The objective of the study is to develop and carry out a programme of desk studies, prioritisation, further special inspections, structural assessment, design of strengthening/remedial works and the development of an overall management strategy. All work relating to the structures has been carried out in accordance with the guidance given in 'DEM 71/04'.

Keywords: Bridge and Transport Infrastructure, Bridges, Concrete, Deterioration, Management, Materials, Monitoring, Testing

1. Background

During the 1960's and 1970's, rapid expansion of the UK trunk road network led to the introduction of a large number of cantilever/suspended span bridges and a number of propped cantilever bridges.

These particular forms of structural half-joint are illustrated in Figure 1. The construction of reinforced concrete half-joints poses a particular problem as they are not easily accessible for inspection, maintenance or repairs. This has led to concern about the long-term durability and structural performance of half-joint structures, as highlighted by the collapse of the De la Concorde overpass in Montreal, Canada (Commission of Inquiry Report, 2007).

The principal cause of structural problems with reinforced concrete half-joints is attributed to defective and leaking deck joints in the carriageway above. This has allowed chloride contaminated water to be deposited on to the bearing shelf of the half-joint in the vicinity of the re-entrant corner. The steel reinforcement in this area is therefore vulnerable to chloride attack and consequential corrosion.

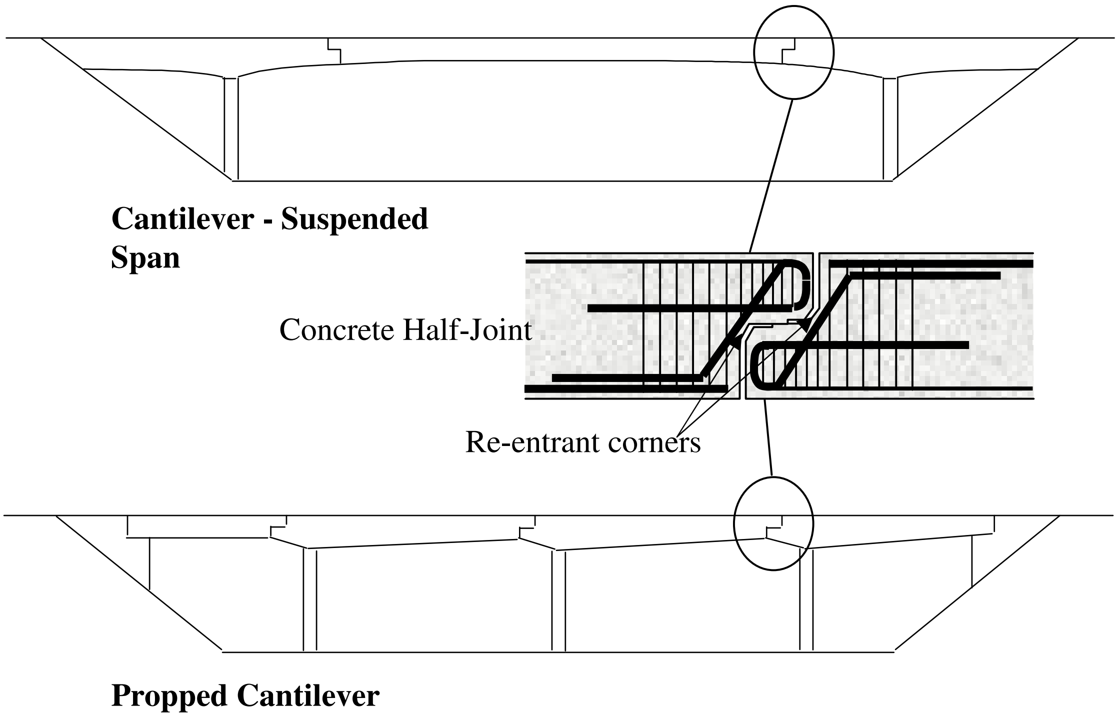

Figure 1 - Structural Forms of Half-Joints

Inspection of the road joints and the soffit of the half-joint will generally indicate whether or not the road joint has been leaking and hence the potential for chloride contamination. However, the lack of accessibility for investigation of the bearing shelf means that detailed investigation of the concrete and steel reinforcement is often very difficult. The lack of available test information has resulted in a reduced confidence as to the physical condition of these joints and their load carrying capacity.

The extent and severity of deterioration of the half-joints due to chloride contamination is dependent upon the type of joint, in particular how they were designed and detailed, and subsequently how they have been maintained.

As part of its strategy for the management of half-joint deck structures Roads Service issued 'DEM 71/04', which set out an interim management strategy for reinforced concrete and steel/concrete half-joint structures.

Mouchel were appointed by Roads Service with the objective of using the findings of previous desk studies, initial special inspections and assessments, along with other record information, to develop and carry out a programme of further special inspections. The results of the further special inspections would then be used to determine whether any additional work, such as monitoring, further inspection, assessment or remedial work is required, leading ultimately to the development of a management strategy for each structure, and the stock of structures as a whole.

This paper describes the testing undertaken, which was carried out in accordance with 'DEM 71/04' and current best practice including 'TR 60', the inspection procedures set out in ‘BD 63/07’ and the ‘Inspection Manual for Highway Structures’. A summary of the results and conclusions is provided, based on the findings, and any recommendations deemed necessary are presented.

1.1 Description of the structures

The 12 structures included in this study are a mixture of one, two and three span bridges. Methods of construction include: in situ reinforced concrete (r.c.), post-tensioned, and composite beam and slab deck, as detailed in Table 1 below.

Table 1 – Summary of structures included in the study and their form of construction

Structure Name (No. of Joints)	**Description**
Balloo (1)	2-span bridge. In situ r.c. cantilever slabs and suspended span is a composite precast beam and in situ concrete deck
Gracehill (2)	3-span bridge. Cantilever spans are r.c. and suspended span is a composite slab comprising precast beams and infill concrete
Parkmore Footbridge (2)	3-span bridge. Cantilever spans are post-tensioned and suspended span is reinforced concrete
Lake Road Footbridge (2)	3-span bridge. Cantilever spans are post-tensioned and suspended span is reinforced concrete
Moylinn East Footbridge (2)	3-span bridge. Cantilever spans are post-tensioned and suspended span is reinforced concrete
Pound (2)	3-span in-situ reinforced concrete deck
High Street (2)	3-span in-situ reinforced concrete deck
Derg (2)	3-span reinforced concrete in situ beam and slab deck
Strule (2)	3-span post-tensioned concrete deck
Lifford (2)	3-span post-tensioned concrete deck
Newbridge New (2)	3-span in-situ reinforced concrete deck
Folk Museum (1)	Single-span structure with 6 No. Preflex Beams and in situ reinforced concrete deck slab

2. Prioritisation

After a detailed review of the existing data, a report was produced that identified and justified the need for testing to be carried out at the half-joints of some of the structures. Using the Roads Service Bridge Management System (RSBMS) user manual, the condition of the half-joints were given a component rating based on the severity of defects encountered at the half-joints, and a priority ranking to determine the timing of any work required.

Two bridges; Pound and High Street, have both been recently repaired. For this reason, they were given both a component rating and priority ranking of 1 for their half-joints, as there were no significant defects, and no work was required.

Five bridges; Balloo, Parkmore, Lake Road, Moylinn East and Folk Museum were given a component rating of 2 for their half-joints, which means the defects are non urgent in nature and not affecting the function or the structural stability of the component. Therefore, the defects can wait until the next routine inspection in order to be assessed, and for this reason, these structures were given a priority ranking of 2, which means the work isn't urgent and should be carried out only when resources permit.

The remaining five bridges, namely Gracehill, Derg, Strule, Lifford and Newbridge New were given both a component rating and priority ranking of 3. The component rating of 3 for their half-joints means the defects are non urgent in nature but may affect the function or the structural stability of the component before the next inspection. The priority ranking of 3 means work needs to be carried out within 2 years. It was therefore recommended that further special inspections, in accordance with DEM 71/04, were carried out to these five structures.

3. Inspection methodology

Following the prioritisation exercise, the five bridges that were given a priority ranking of 3 underwent further special inspections in March and April 2010. The testing at each half-joint was carried out to an area within 1 metre either side of the joint along the soffit and the side faces. The test area was split into 500mm by 500mm grids, reduced to 250mm by 250mm where significant defects were observed. The testing was carried out directly to the superstructure and was conducted from an underbridge unit (see Figure 2) to allow the testing team to get within touching distance of the structure.

Figure 2 - Inspection of Half-Joints from an underbridge unit

A typical range of testing techniques were employed, consisting of a detailed hammer and visual survey, half-cell and cover survey, carbonation depth measurements, chloride, cement, alkali and sulphate content determinations, rebound hammer survey and core samples (taken for compressive strength tests and petrographic analysis).

The exact locations for the chloride, cement, alkali and sulphate content determinations, and carbonation depth determinations, were determined on site by Mouchel's supervisory staff. The testing locations for the chloride sampling were chosen to coincide with areas of high half-cell potential and/or areas where visual defects were present. In addition and where possible, one trial pit was excavated per joint, each approximately 1m² in plan area, and concrete testing, as described above, was carried out directly to the top surface of the deck. This was to check the condition of the waterproofing, top surface of the deck and the expansion joints.

4. Inspection Results

The main types of deterioration encountered were cracking, delamination and/or spalling, water staining, exposed reinforcement and leachate staining, which were present to varying degrees on all five bridges that were inspected. There are two main situations where deterioration is most prevalent. The first is water staining which would indicate a failure of the waterproofing and/or deck expansion joints (see Figure 3).

Figure 3 – Detail of water staining emanating from half-joint at Derg bridge

The second situation is delamination and/or spalling adjacent to the half-joints and at the deck ends, and would indicate that chloride induced corrosion is occurring, particularly to areas with low cover. This is most evident at Strule, where cracking is also an issue (see Figure 4).

Figure 4 – Detail of cracked half-joint nib at Strule bridge

The likelihood of corrosion occurring to the five bridges that were given a priority ranking of 3 was confirmed by the testing results. High half-cell potentials (lower than -350mV) and high chloride ion contents (in excess of 0.3% by weight of cement) were concentrated in localised areas of the half-joints although their presence was not widespread throughout the joints. Two of the structures; Lifford and to a lesser extent Derg, had carbonation depths that were either approaching or in excess of the cover measurements. This issue is a concern, as although there is no indication of carbonation induced corrosion at this time, it could occur in the near future. Additionally, the combination of chlorides and carbonation leads to more serious corrosion than chlorides or carbonation alone. It is thought that there may be some environmental factors that have contributed to the high carbonation readings for these two structures.

The sampling for alkali and sulphate content indicated that alkali aggregate reaction and sulphate attack were unlikely for all structures. This was verified by the results of the petrographic analysis. In addition, the compressive strengths from the core samples taken indicated that the concrete for all structures was of a suitable strength required for structural concrete.

5. Comparing DEM 71/04 with IAN 53/04

Whilst the DEM is based closely on the IAN, which is produced by the Highways Agency in England, there are subtle differences between them. First among them is the way the Roads Service and the Highways Agency (HA) manage their networks. England is split up into a number of 'areas' with the HA appointing highway service providers to act as managing agent contractors, or MAC's, for each area. In Northern Ireland, the network is more centrally managed, with a Project Manager given the specific task of overseeing the requirements of the DEM.

The main body of the DEM and the IAN are essentially the same or similar, with the most notable difference being the use of different bridge database systems to assist in managing the structures' inspection and maintenance regimes, as well as to provide a way of prioritising repair or remedial work. The HA use SMIS – Structures Management Information System, whereas Roads Service use RSBMS – Roads Service Bridge Management System. A large part of the annexes for the IAN are utilised with advice for the managing agents on how to use SMIS for inputting the relevant data for the half-joint deck strategy. Similar advice is not included in the DEM.

The other main difference is the approach to risk management. While the DEM uses a method of prioritisation that is based on the system in RSBMS, the HA SMIS system does not have this capability, and so two of the annexes are dedicated to a simplified method of prioritisation (which appears to be similar to the RSBMS method), and a more detailed and in depth approach based on a qualitative risk assessment.

5.1 Progress

The prevalent defects encountered on the five bridges are typical of bridges with half-joints, and in this context, it was not unexpected to find defects of this nature. Other than Strule, the defects are not of the same magnitude as Mouchel have encountered on half-joint structures in England. This may be due to a combination of factors, most likely to be the higher traffic volumes that use the trunk road network in England, and thus a more stringent winter maintenance regime. Another factor is that Mouchel has worked extensively on the half-joint structures located in the West Midlands; on the Midland Links viaducts, and also on the M50. These structures are among the earliest highway structures of the type, particularly on the M50.

6. Summary

Recommendations have been made specific to each structure so that the structures can continue to operate as intended and in a safe manner. High priority has been given to preventing further deterioration of half-joints, by maintaining drainage in working order and the integrity of deck waterproofing and expansion joints. Expansion joint replacement and renewal of waterproofing (where they have shown to have failed) are the most important preventative remedial actions to safeguard against further deterioration of a half-joint.

For Strule bridge, the findings of previous inspections, combined with the results of the further special inspection undertaken as part of this study, have been used to develop a proposal for remedial repairs and refurbishment.

For Lifford and Derg, it has been recommended that existing structural assessment reports are reviewed and new assessments should be carried out as appropriate, including an SV assessment. Assessments should include sensitivity analysis on the condition of the structure. This is to check whether the defects encountered have affected the structures' load carrying capacity. Additionally, it has been recommended that the carbonated concrete at Lifford be removed, with localised concrete repairs carried out to these locations.

The condition of the Gracehill and Newbridge New are relatively good, so at this stage they will be closely monitored at their next routine inspection.

The seven bridges that did not have a further special inspection completed as part of this study, should receive further special inspections either prior to, or at the time of their next routine inspection. In the case of Pound and High Street, the extent of the investigations would be minimal, being carried out simply to confirm that the repairs have been successful and the component rating was still valid.

A management strategy document will be produced to capture the most suitable, sustainable and cost effective options for each structure in terms of monitoring, inspection, routine and preventative maintenance, repair and strengthening, and contingency planning to take into account weight restrictions, highway closure, temporary propping and other emergency measures.

References

Gouvernement du Québec (2007), *Report of the Commission of Inquiry into the Collapse of a Portion of the de la Concorde Overpass*.

Highways Agency (2004), *Concrete Half-Joint Bridge Deck Structures, IAN 53/04*.

Roads Service (2008), *Concrete Half-Joint Bridge Deck Structures, DEM 71/04 (Rev 2)*.

The Concrete Society (2004), *Electrochemical tests for reinforcement corrosion, Technical Report 60*.

Highways Agency (2007), *Highway Structures: Inspection and Maintenance. Inspection. Inspection of Highway Structures, DMRB Volume 3 Section 1 Part 4, BD 63/07*.

The Stationery Office (2007), *Inspection Manual for Highway Structures*.

BRIDGE SCOUR INVESTIGATION: DEVELOPING A SCREENING AND HYDRAULIC VULNERABILITY RATING SYSTEM FOR BRIDGES

B.HERON[1] & C.BOWE [2]
[1]O'Connor Sutton Cronin Consulting Engineers, Dublin, Ireland
[2]Iarnród Éireann, Dublin, Ireland

Abstract

Bridge Management is an important area of bridge engineering due to the large outlay of capital expenditure on bridge maintenance, repair and replacement, by stakeholders in their bridge stock and the requirement that the bridges are kept in a serviceable condition for the entirety of their design life. Iarnród Éireann (IE) is responsible for the maintenance of several hundred bridges that span across rivers and streams. Recently as part of Iarnród Éireann's overall Bridge Management System a programme was initiated for assessing the vulnerability of IE bridges to scour and other related hydraulic forces. O'Connor Sutton Cronin Consulting Engineers were engaged to assist Iarnród Éireann in developing a screening and hydraulic vulnerability rating system so that any required maintenance could be prioritised.

This paper describes the screening and vulnerability rating system that was developed and how it relates to the two main industry standard documents on scour inspections (Hydraulic Engineering Circular No. 18 (HEC-18) and Bridge Advice Note 74/06 (BA 74/06). It will set out the desk study required and the on site inspections that are carried out by the bridge inspector in combination with an underwater dive team. Each step in the process will be set out in a series of logical step diagrams with a detailed explanation of each step.

Keywords: Bridge Management System, Bridge Scour, Iarnród Éireann, Vulnerability Ranking

1. Introduction

Iarnród Éireann is responsible for the maintenance of over 300 bridges that span across rivers and streams. As a bridge owner and operator who are following a bridge management regime they need to assess the risks of various deterioration mechanisms and their consequences in order to determine a suitable maintenance schedule within their overall budget.

One risk item that has come to prominence in recent times is the risk of structural damage to bridges as the consequence of river flooding and the resulting scouring that can occur due to these increasing flood events. Every structure over an existing watercourse that has support members within or adjacent to the waterways channel is likely to experience scour to some extent during a flood event. There are varying consequences that can occur due to scour, from safety considerations, requirements for additional maintenance works to the reconstruction of a bridge should a failure occur due to the undermining of a support member.

Therefore each and every rail bridge that is determined as being vulnerable to the effects of scour upon its structural foundations is required to be assessed for the potential scouring that can occur so that an appropriate action can be taken to ensure the ongoing stability and serviceability of the structure. If the assessment is undertaken in an appropriately structured manner, there is no reason why this cannot be achieved at a relatively low cost.

It was based upon this premise that O'Connor Sutton Cronin Consulting Engineers were engaged by Iarnród Éireann to assist them in developing a screening and hydraulic vulnerability rating system so that any required maintenance could be prioritised in the most economical manner within Iarnród Éireann's overall bridge management system.

2. Objectives

The overall aim of Iarnród Éireann's bridge management programme as it related to the risk of scour to its bridge inventory was to develop a system that would permit Iarnród Éireann to reduce the vulnerability of the network of rail bridges to failures caused by scour or related failure. No bridge structure over water has a zero probability of failure due to scour, as even the best protected structures can be undermined. However, tt is reasonable to put in place a system where there is a balance between the level of protection provided by the bridge owner to meet safety requirements and the maintenance costs of the structure.

The specific objectives that were set in relation to developing the screening and hydraulic vulnerability system were as follows:

- Review and assess the existing industry standard scour inspection processes and in particular if these processes could be integrated into Iarnród Éireann's bridge management programme;
- Develop a bridge screening process that could be used so that the overall inventory of bridges could be assessed to determine which are required to be progressed to the next stage of the process which determines the susceptibility of a bridge to scour;
- Develop a scour susceptibility scheme that determines whether a bridge is vulnerable to scour or other hydraulic forces;
- Develop a classification stage to evaluate the vulnerability of the structure to scour damage. The purpose of this was to provide a quantitative score for a structure so that it could be compared in a relative manner to other structures on the same rail line. In addition each structure could be placed in a hydraulic vulnerability class i.e. High, Medium or Low.

3. The Scour Problem

Scour is defined as the erosion or removal of streambed or bank material from bridge foundations due to flowing water (Kattell and Eriksson, 1998). Although it may be greatly affected by the presence of structures encroaching on the channel, scour is a natural phenomenon caused by the flowing of water over an erodible boundary.

In a river, scour is normally most pronounced when the stream or river bed and river banks consist of granular alluvial materials. However, it also occurs with cohesive materials, such as clay, and even deeply weathered rock can be vulnerable in some circumstances. Under constant flow conditions, scour will reach a maximum depth in sand and gravel bed materials in hours; cohesive materials in days; glacial till, sandstones, and shale in months; limestone in years and dense granite in centuries

(Richardson and Davis 2001). Under flow conditions typical of actual bridge crossings, several floods may be needed to attain maximum scour.

It is useful to classify the various types of scour that can occur at a bridge crossing. The total scour that can occur is comprised of three components, the following definitions are taken from Richardson and Davis, 2001:

1. Natural scour (aggradation and degradation) are long-streambed elevation changes due to natural or man induced causes which can affect the reach of the river on which the bridge is located. Aggradation involves the deposition of material eroded from the channel or watershed upstream of the bridge; whereas, degradation involves the lowering or scouring of the streambed due to a deficit in sediment supply from upstream;
2. General scour (contraction scour) is a lowering of the streambed across the stream or waterway bed at the bridge. This lowering may be uniform across the bed or non-uniform, that is, the depth of the scour may be deeper in some parts of the cross section. General scour may result from contraction of the flow, which results in the removal of material from the bed across all or most of the channel width, or from other general scour conditions such as flow around a bend where the scour may be concentrated near the outside of a bend. General scour may be cyclic and/or related to the passing of a flood;
3. Local scour involves the removal of material from around piers, abutments, spurs, and embankments. It is caused by an acceleration of flow and resulting in wake and horseshoe vortices induced by obstructions to the flow.

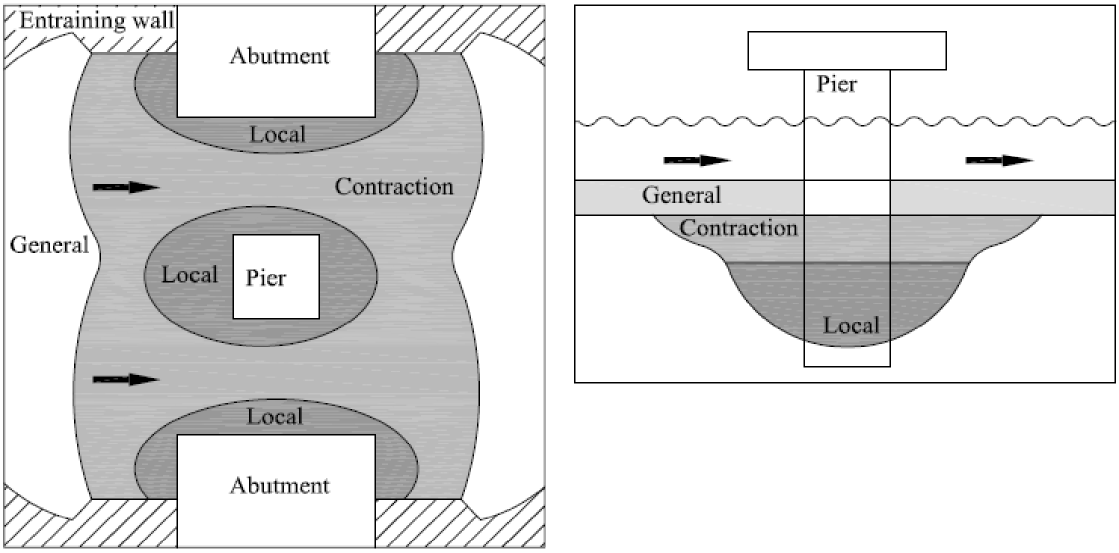

Figure 1 – Types of scour at a bridge (Whitbred et al, 2000)

These three scour components are added together to obtain the total scour at a bridge pier or abutment (see Figure 1). In addition, lateral migration of the stream must be assessed when evaluating total scour at piers and abutments.

4. Existing Assessment Methods

The main industry standards in the US and UK were reviewed to assist in developing a framework for carrying out an assessment and rating system. The two principle manual/ standards reviewed was the Hydraulic Engineering Circular No. 18 (HEC-18) – Evaluating Scour at Bridges, (Richardson and Davis, 2001) and BA 74/06 Assessment of Scour at Highway Bridges (DMRB 2006).

4.1 Hydraulic Engineering Circular No. 18 (HEC-18)

HEC-18 is the technical standard for knowledge and practice in the design, evaluation and inspection of bridges for scour in the US. This standard was developed by the Federal Highway Administration to provide each Department of Transport within the various states with a process within which they could each develop a programme for conducting scour evaluations.

The process developed by HEC-18 was the following 5 stage scour screening and evaluating process:

- Stage 1 – All bridges over waterways were to be screened into five categories (1) low risk, (2) scour susceptible, (3) scour critical, (4) unknown foundations, or (5) tidal;
- Stage 2 – Scour susceptible bridges and bridges with unknown foundations were prioritised by conducting a preliminary office and field examination of the list of bridges compiled in Stage 1;
- Stage 3 – Field and office scour evaluations were conducted on the bridges prioritised in Stage 2 using an Interdisciplinary Team of hydraulic, geotechnical and structural engineers;
- Stage 4 – Bridges identified as scour critical from the office and field review or during a bridge inspection in Stage 3 should have a plan of action developed for correcting the scour problem;
- Stage 5 – After completing the scour evaluations for the list of potential problems compiled in Stage 1, the remaining waterway bridges included in the states bridge inventory should be evaluated. In order to provide a logical sequence for accomplishing the remaining bridge scour evaluations, another bridge list should be established, giving priority status based upon the functional class of the highway the bridge is upon and the on bridges that serve as vital links on the transport network.

The two stages that were of most importance to O’Connor Sutton Cronin in developing a screening and evaluation process for Iarnród Éireann were Stage 1 and 2 of HEC-18. Stage 1 described a mechanism for the screening of a large bridge inventory and prioritising the order in which the field evaluation should occur.

Stage 2 of the HEC-18 process set down the requirements for the office review that provides a better basis for inspecting the bridge and the stream, while also detailing a framework for the site inspection and each element that should be carried out. The site inspection was broken down into the following elements (Richardson and Davis, 2001):

- Safety considerations;
- Recording and coding guide;
- General site/river conditions;
- Assessing the substructure condition;
- Assessing the scour potential at bridges;
- Underwater inspections;

- Post inspection documentation.

4.2 Assessment of Scour at Highway Bridges BA 74/06

The Advice Note BA 74/06 (DMRB, 2006) was intended by the Highways Agency in the UK as a means of assessing the potential for scour to damage a bridge. While it was developed by the Highways Agency primarily for use on road bridges, it was recognised that it could also be adopted for other bridge types.

The Advice Note set out a two stage process for the carrying out an assessment and analysis of bridges for scour. While also including further advice and recommendations for putting in place a plan of action for a bridge once its Priority Rating had been determined.

Stage 1 of BA 76/04 is the assessment stage. This stage is broken down into 3 elements:

- Collection of data regarding the bridge, its foundations, the river and any historical information available;
- Inspect the bridge site. This is the principle element of Stage 1. With requires the inspection of the river banks, main river channel, floodplain, and bridge waterway both upstream and downstream. There is a requirement for an underwater inspection as part of this inspection;
- Assess for scour potential. This is where it must be determined if there are any features that make the risk of scour endangering the bridge very low. If there are then the analysis need precede no further, otherwise the assessment should proceed to Stage 2.

Stage 2 is the analysis stage of the process and involves a calculation of the potential scour depths and then an assessment of the priority rating. There are 5 steps in the calculation as follows:

- Collect additional information relating to the details of the river channel. This may be mapping of the catchment or information from gauging stations;
- An estimation is made of the magnitude of the 200 year flood;
- Estimation on the depth and velocity of the flow at the bridge site;
- Estimation of the depth of the scour adjacent to the bridge footings;
- Based upon all of the above, assess the priority rating for the bridge.

5. Screening and Hydraulic Vulnerability System Developed

Following a review and a comparison of both BA 74/06 (DMRB, 2006) and HEC-18 (Richardson and Davis, 2001) it was noted that the ranking and priority procedures given in BA 74/06 relied on a significant amount of data collection with hydrology studies and hydraulic analysis to estimate flood flows, water depths and water velocities. This information is then used to estimate total scour depths with subsequent comparison with known foundation depths.

This requires considerable time and resources to provide a quantitative priority ranking of this type. In addition, where a significant number of the bridges have an unknown foundation depth it would not be possible to carry out this type of assessment without obtaining detailed Site Investigations.

While in comparison HEC-18's scour susceptibility assessment and hydraulic vulnerability calculation to provide a priority ranking system can be carried out through a combination of the following:

- A field appraisal of scour, through the completion a field appraisal questionnaire which reviews the main features of a river channel and its interaction with a bridge structure;
- A structural inspection to determine the current condition of a bridge, structural features that may render it susceptible to scour and the signs of any distress that may indicate that it is currently being affected by scour;
- An underwater inspection to determine the presence of existing scour and the condition of scour protection measures.

Therefore to meet the objective set by Iarnród Éireann to develop a structured assessment method at a low cost to prioritise their bridge management in directing resources in an efficient way, a system was developed that would incorporate elements of the Stage I assessment from BA 74/06 while adopting and developing a hydraulic rating score that could be used to prioritise what bridges were required to be brought to Stage II analysis in accordance with BA 74/06.

The approach developed was a combination of the scour susceptibility system outlined in HEC-18 which details a screening and vulnerability rating system using desk studies and the visual field appraisals described above. While the qualitative system for establishing a bridge rating was based upon the vulnerability rating charts developed by the US Forest Service as part of their scour evaluation program, (Kattell and Eriksson, 1998). These charts use the findings recorded in the field appraisal to carry out the numerical rating for each bridge.

The Forest Service, U.S. Department of Agriculture, manages a bridge stock of approximately 7,650 bridges on National Forest lands that bridge watercourses. Scour is almost the single most common cause for bridge damage and failure on National Forest lands (Kattell and Eriksson, 1998). To arrest this problem, the Forest service developed a process to review and evaluate all bridges over water to determine the scour potential of each bridge.

The logical step diagram shown overleaf (see Figure 2) sets out the various stages in the scour evaluation programme developed based upon the systems set out in HEC-18 and the Forest Service scour evaluation program. The screening and hydraulic vulnerability system is broken up into 3 distinct processes, i.e. screening, classification and vulnerability rating.

Stage 1 – Screening

The screening stage is the preliminary stage carried out by the bridge stakeholder to evaluate a large population of bridges using the information contained in the stakeholders bridge inventory and inspection system. The purpose is to determine which structures require a scour inspection. While structures not over water require no further action, the order of the remaining structures is prioritised for inspection based upon information available for the following:

- Pier, abutment or footing in channel or floodplain;
- Pier, abutment or footing on scourable material;
- Stream velocity (if known);
- Foundation type;
- Previous inspection reports.

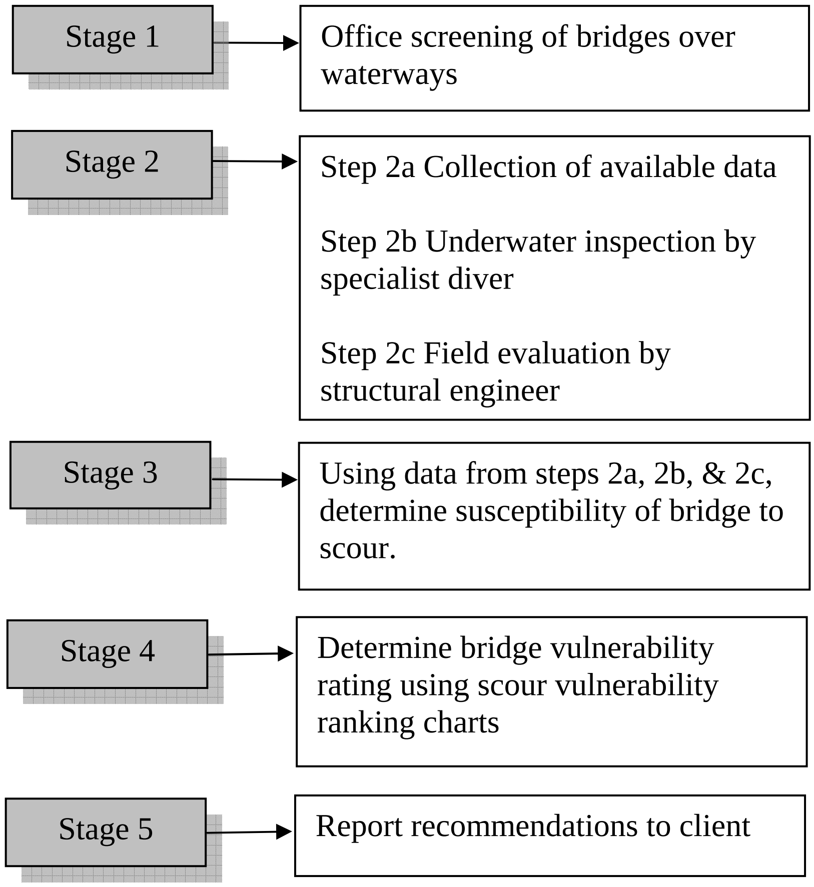

Figure 2 – Scour Appraisal Process

Stage 2 & 3 – Classifying

The purpose of the classification stage is to evaluate the vulnerability of a structure to scour damage on the basis of geologic, hydraulic and river conditions (NYSDOT, 2003). The product of this is to determine whether a structure can be designated as scour susceptible and to try to ascertain as to whether the structure is (1) low risk, (2) scour susceptible, (3) scour critical or (4) unknown foundations. This stage is carried out in 3 parts:

1. Collection of available data, i.e. bridge drawings, historic maps, previous underwater reports, river flood data, bridge inspection cards;
2. Field evaluation is carried out by the engineer to assess the general site conditions, assess the scour potential at bridges and assess the substructure condition;
3. Carry out an underwater inspection.

Through assessing the data gathered and comparing it to historical data, foundation information and riverbed characteristics, it is then possible to designate if the bridge is scour susceptible.

Stage 4 – Vulnerability Rating

The purpose of this vulnerability rating stage is to provide a uniform measure of the vulnerability of a structure to scour through a numerical analysis of the findings of the field appraisal, underwater inspection and desk top study carried out as part of the bridge classification stage.

This is carried out through the use of vulnerability ranking flow charts (see Figure 3), (Kattell and Eriksson, 1998). The specific parameters used in the vulnerability charts are based upon the variables that affect the level of scour at a structure where a calculation to be carried out. There are 4 charts used in this process:

1. General Conditions Flow Chart – This addresses parameters that have a general impact on the potential scour depth at a bridge based upon the river channel and its interaction with a bridge structure. The variables that are assessed for this flow chart are (i) River slope/velocity, (ii) Channel bottom stability, (iii) Channel bed material, (iv) Channel configuration, (v) Debris/ice problem, (vi) Near a river confluence, (vii) Affected by backwater, (viii) Historic scour depth, (ix) Historic maximum flood depth, (x) Adequate opening, and (xi) Overflow relief available. Each of these parameters relate to a variable that would be required to determine the level of general, contraction and local scour at a bridge;
2. Abutment Vulnerability Flow Chart – This chart is intended to evaluate the relative vulnerability of a bridge to scour considering factors that affect abutment scour. A separate evaluation is carried out for both abutments. As with the general conditions chart, the parameters evaluated in the abutment vulnerability charts reflect the variables that would affect the level of scour at a bridge site; (i) Presence of scour countermeasures, (ii) Abutment foundation type, (iii) Abutment location on river bend, (iv) Angle of inclination and (v) Embankment encroachment;
3. Pier Vulnerability Flow Chart – This chart is intended to evaluate the relative vulnerability of a bridge to scour considering factors that affect pier scour. A separate evaluation is carried out for each pier as the level of scour could vary at each pier. The parameters that are assessed reflect the variables that affect the level of scour at a structure; (i) Presence of scour countermeasure, (ii) Pier foundation type, (iii) Skew angle, (iv) Pier/pile bottom below streambed and (v) Pier width.

The product of this step is a vulnerability rating score which serves two purposes: first, it quantifies the potential vulnerability of a structure to scour damage relative to other bridges on the same rail line, and second, the score is used to place the hydraulic vulnerability rating into a High, Medium or Low hydraulic vulnerability class. Both of which permits the stakeholder prioritise any further maintenance work as part of their overall long term management plan.

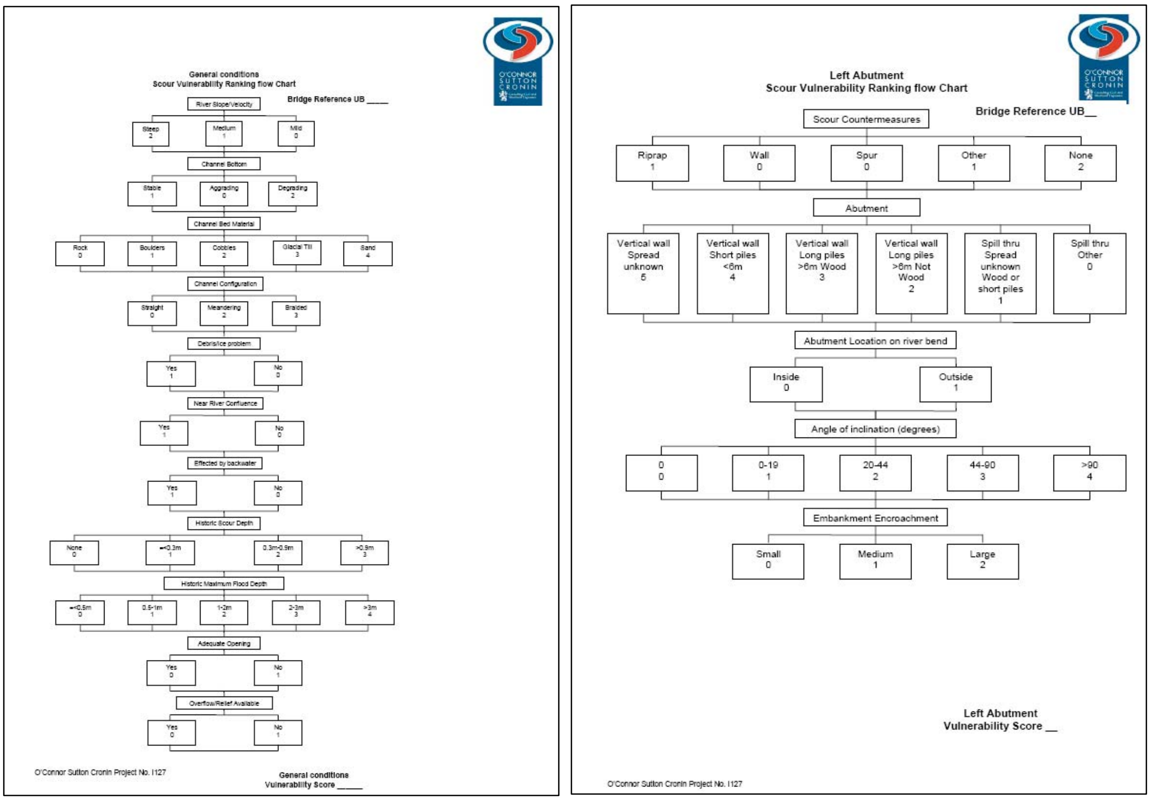

Figure 3 – General Conditions and Abutment Vulnerability Charts

6. Conclusion

It is not considered economically feasible for a bridge owner to protect all bridges to resist all conceivable floods; the purpose of a Bridge Management System should be to reduce risk to as low as reasonably possible. Bridge owners should be able ask themselves 'Have we done all that is reasonable to ensure safety?'

The system adopted by Iarnród Éireann provides a numerical assessment that can be used to carry out a vulnerability analysis on a large stock of bridges. This numerical analysis is based upon accepted calculations (Richardson and Davis, 2001) for determining the level of general, contraction and local scour that can occur at a structures substructure unit where it interacts with a watercourse, thereby using the parameters that influence the level of scour at a structure to determine the vulnerability of the same. Unlike a Stage I assessment in accordance with BA 74/06 which does not account for different types of bridge structure, the vulnerability ranking charts take into account the influence that the different bridge substructure elements have and their relationship to a river environment, be they multi-span or single span structures.

With the scour screening system and vulnerability assessment method developed it is felt that this will permit Iarnród Éireann to best allocate resources in the most efficient manner to ensure the serviceability of the rail network over its design life. It allows for the review of the inventory of river bridges in a cost effective manner, determines the scour susceptibility of the bridges and provides Iarnród Éireann with a mechanism to prioritise the bridges that need to be brought to a Stage II analysis by determining a hydraulic vulnerability rating.

References

Design Manual for Roads and Bridges BA 74/06, (2006). *Assessment of Scour at Highway Bridges*. Highways Agency, London.

Kattell, J. and Eriksson, M., (1998). *Bridge Scour Evaluation: Screening, Analysis, & Countermeasures*. US Department of Agriculture Forest Service. San Dimas, California.

NYSDOT, (2003). *Hydraulic Vulnerability Manual*. Structures design and construction division bridge safety assurance unit. New York State Department of Transportation.

Richardson, E.V. and Davis, S.R., (2001). *Evaluating Scour at Bridges*. 4th Edition, Hydraulic Engineering Circular No. 18, US Department of Transportation. Federal Highway Administration (HEC 18), Arlington, Virginia.

Whitbred et al. *Cost-Effective Management of Scour Prone Bridges*. Proceedings of the Institute of Civil Engineers, Transportation, May 2000.

QUANTIFYING IRELAND'S INFRASTRUCTURAL DEFICIT

MARY MOLONEY[1], KARSTEN MENZEL[2], EAMON MCKEOGH[2]

[1]Department of Civil, Structural and Environmental Engineering, Cork Institute of Technology, Cork

[2] Department of Civil and Environmental Engineering, University College Cork

Abstract

Ireland's construction output during the Celtic tiger years peaked at €38.4 billion in 2007. However, the extraordinary fact is that less than 20% of this was put into public infrastructure. Across the euro zone the Republic of Ireland was quoted as being a 'wealthy' country. However, nearly 65% of construction output during the period 2000 and 2007 was invested in the combined sectors of private residential (housing and apartments) and private non-residential construction. These assets have now depreciated by between 30% and 50%; many lie idle and cannot be sold. Ireland's Construction Industry contributed 24.7% of the country's GNP in 2006. The latest estimate for 2009 is that this figure is 14.5%, which is still above the average in the EU and US. During the time of great apparent prosperity Ireland did not invest sufficiently in its public infrastructure. Roads investment is the one category that bucks this trend. It is well recognised and widely published that for a country to maintain sustainable growth and prosperity it must invest in its infrastructure. Ireland failed to invest sufficient funds in public infrastructure during this time of peak construction output. The pace at which Ireland emerges from the current recession will depend in part on finding innovative funding mechanisms to fund infrastructural development.

This paper defines the term productive infrastructure and identifies the sectors that should be included in its scope, i.e. physical networks for power, rail road. It measures the investment that has occurred during the period 2002 – 2008 in Productive Infrastructure. It examines the global norms for investment in Productive Infrastructure and identifies Ireland's investment shortfall.

Key words:

Public infrastructure, roads, bridges, transport, infrastructure deficit, networks, public investment

1. Introduction

The OECD in its Economic Survey in 2006 (OECD and Development, 2006), noted that Ireland had undergone very rapid economic growth but that its infrastructure had not kept pace. This paper discusses the relevance of infrastructure to a country's growth, and identifies Ireland's global ranking in terms of the quality of its infrastructure and associated expenditure. The paper estimates how much should be spent to bring Ireland's infrastructure in line with its global position as a developed and innovation driven country (Schwab, 2009).

The paper reviews government expenditure figures for 2002 to 2008 (Ireland, 2008, Department of Finance, 2010, DKM, 2009) and demonstrates that rather than increase investment, the country has decreased its investment in key aspects of infrastructure that would support economic activity. Therefore, the question is by how much, and in what way is Ireland deficient in its current infrastructure? Furthermore, how much does Ireland need to invest to bring it in line with its OECD partners?

2. Infrastructure: physical networks that support economic activity

There are many services, facilities and sectors that can be included under the general heading of 'infrastructure'. It is necessary to define the term 'Infrastructure' as it will be used in this paper and to do so a number of publications were referenced.

An International Monetary Fund (IMF) working paper defines 'infrastructure' as "the physical networks that support economic activity" (Teresa Ter-Minassian, 2008). The IMF considers that infrastructure networks are transport, water, sanitation, power and telecommunications sectors.

Also the World Economic Forum in its Global Competitiveness reports (Schwab, 2009) identifies infrastructure as being transport, communications and energy systems.

The Irish Government has used three sub-headings to define its infrastructure investment: productive, socio and economic. In its 2007-2008 Public Capital Programme (PCP) (Ireland, 2008), the sub-heading of Productive Infrastructure includes the sectors of Energy, Transport, Environmental Protection and Communications. This Irish Government sub-heading closely matches the apparently accepted international definition of 'infrastructure', being the 'physical networks that support economic activity'. Therefore, in undertaking comparative reviews of what countries should spend on 'infrastructure' and measuring Ireland's performance, the relevant sectors under the Irish Government's 'Productive Infrastructure' sub-heading are included, namely power and energy[1], transport[2], environmental protection[3] and communications[4]. In international terms, the expenditures included under the other Irish Government sub-headings, namely socio and economic, are not considered to be 'infrastructure', per se. Therefore, the terms 'infrastructure' and 'productive infrastructure' are used interchangeably for the remainder of this paper.

[1] energy generation and distribution, sustainable energy programmes, energy conservation

[2] road construction and maintenance, semi-state bodies for bus, rail, port and air services, public transport projects, island access, road safety authority

[3] water and sewerage services, waste recycling and disposal facilities, fire and emergency services, carbon credits and landfill remediation

[4] information and communications technology programme, grants for digital terrestrial television, telecommunications and semi-states – an Post and Radio Teilifis Eireann

3. Infrastructure and Economic Growth

There have been a number of studies undertaken which clearly indicate that the quality of a country's infrastructure is intrinsically linked to its economic growth and that infrastructural investment is vital to maintain and improve a country's competiveness and growth (Teresa Ter-Minassian, 2008, OECD and Development, 2006, Schwab, 2009, Cecilia Briceno-Garmendia, 2004). These studies found a positive relationship between the stock of infrastructure assets and the rate of economic growth and prosperity.

Ter-Minassian and Hajdenberg identified that the impact that public investment had on an economy's growth depended on a number of factors. These included: the source of funding (increased taxation, government borrowings and/or private competition); the availability of other complementary investment in social areas of development; and the institutional context and quality of governance in which investments are made. The quality of the project evaluations and prioritisation, and the regulatory and operational framework within which infrastructural projects and services are provided – be they public or private investment or indeed in partnership, also have an effect on the level of growth derived from investment.

The World Economic Forum (WEF) (Schwab, 2009) also commented on the relationship between infrastructure investment and economic growth when it published its 2009 Global Competitiveness Report. This stated that extensive and efficient infrastructure is an essential and vital driver to a country's competitiveness. The WEF maintains that Productive Infrastructure determines the centre of economic activity and joins regions and countries together. The WEF went further, stating that the quality and effectiveness of infrastructure networks significantly impacts on a country's economic growth.

4. Ireland – A Developed Economy or Developing?

The WEF defines three stages of development for global economies. In increasing order of development, these are: factor driven, efficiency driven and innovation driven. The WEF identifies the stage of development from a country's GDP per Capita (US$) and its score in the WEF Global Competitiveness Index, GCI.

Since 2005 the World Economic Forum has measured the competitiveness of countries using a Global Competitiveness Index. This index is based on what the WEF considers are the 12 pillars of competitiveness. Infrastructure is included as one of these pillars. In measuring this pillar a number of infrastructural sectors are measured and surveyed. These are: the quality of the overall infrastructure, quality of roads, quality of railway infrastructure, quality of port infrastructure, quality of air transport infrastructure, available air seat kilometres, quality of electricity supply, and telephone lines.

Ireland was a global economic phenomenon in the period 2000 – 2008. Ireland's GDP per capita ranked it among the top 10 global economies in 2007-2009 (Schwab, 2009, Michael E. Porter, 2007, Michael E. Porter, 2008). However, in the WEF Competitiveness Report 2009, Ireland has slipped from an overall country ranking of 22nd in 2008 (Michael E. Porter, 2008), to 25th. This drop in overall country ranking was contributed to by the poor score for Ireland's infrastructure. The report ranked Ireland's infrastructure 65th out of the 133 countries assessed. The 2009 result is no exception; in each of the previous two reports, Ireland is positioned midway in the 133 countries for its quality of infrastructure.

In GDP per capita terms, Ireland is ranked 6th, close to countries such as Switzerland and Denmark; see Figure 1 below. However, Ireland's rating for the overall quality of its infrastructure places it alongside Sri Lanka, China etc; see Figure 2 below.

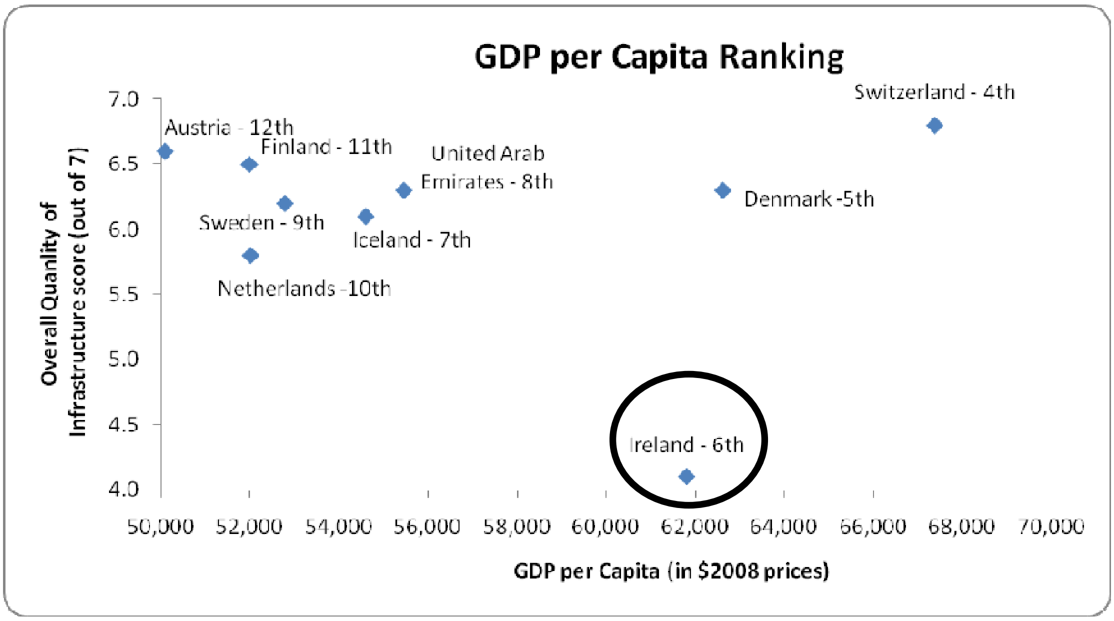

Figure 1 : World Economic Forum Global Competitiveness Report 2009 – Ireland's ranking (6th) alongside 4th (Switzerland) to 12th (Austria) Countries in it's GDP per capita and showing the Overall Infrastructure Score (Schwab, 2009)

Therefore, from the perspective of overall quality and effectiveness of infrastructure, the WEF findings would suggest that Ireland would be more correctly considered as an efficiency driven economy; or at best an economy in transition between being efficiency driven and innovation driven. This conclusion is in stark contrast to Ireland's GDP per capita ranking.

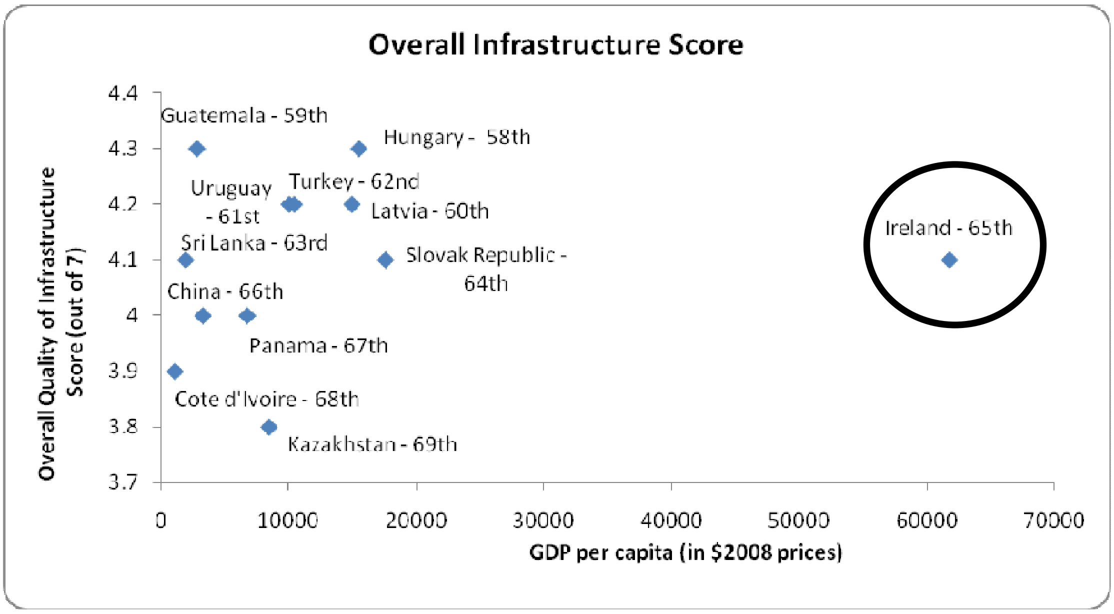

Figure 2: World Economic Forum Global Competitiveness Report 2009 – Ireland's Infrastructural ranking (65th) alongside the nearest ranking countries in overall quality of infrastructure scores – Hungary (58th) to Kazakhstan (69th) , and their relative GDP per capita (US$ 2008)[5]

The World Economic Forum 2009 report (Schwab, 2009) suggests that if an economy is very competitive, it will deliver a higher standard of living to its population. Also, the more productive the country the higher the level of return obtained by investments in that country's economy. Therefore Ireland should be striving to improve its standard of infrastructure, to increase its Global Competitiveness Index, increase its productivity and ultimately lead to a more sustainable growth rate in the economy.

In 2004, Kamps (Kamps, 2004), examined Ireland and 21 other OECD countries to ascertain the Nett Capital Stock. The paper looked at three years - 1980, 1990 and 2000 and ranked the 22 countries according to the level of investment in percentage GDP per capita at 1995 prices. Ireland had ranked 5th of the 22 in both 1980 and 1990. However, in 2000 Ireland ranked 22nd – last of the 22 countries examined. The report showed that Ireland's ratio of Government Capital Stock to GDP was 75.9 in 1980, 66.8 in 1990 and 35.2 in 2000.

The OECD (OECD and Development, 2006) in its economic survey of Ireland 2006, also identified Ireland as having one of the lowest stocks of public capital per head in the OECD. The OECD 2006 and Kamps 2004 suggest that Ireland's public capital stock per person in 2000 was 10% below its 1987 levels.

As the above discussion has demonstrated, the WEF competitiveness indices demonstrate continued under-investment into the period of 2001 to 2009. The question

[5] This may be affected by Ireland's population distribution between rural and urban areas. This will be will examined more closely in a further paper

is by how much has the under-investment been; and how much is required to address the deficit?

5. Ireland's historical infrastructural investment

In assessing the required future investment in infrastructure, the recent historical context is very informative. Kamps 2004 has demonstrated that the relative ratio of investment in infrastructure in Ireland nearly halved between 1990 and 2000.

The 2006 OECD (OECD and Development, 2006) country survey reported that the Irish Government was set to invest up to 5% of the national income in infrastructure. The OECD report projected that this level of 4-5% would have to be maintained from 2010 onwards, to bring Ireland's infrastructure up to standard with its OECD and Global partners.

However, the actual figures both before and since then have been considerably different. As Ireland's GDP rose during the period 2002 to its peak in 2007 as outlined in Figure 3, the country's relative investment in productive infrastructure decreased. Prior to 2006 the investment level was in the range of 3.25% to 3.5%; between 2006 and 2008 the level was in the region of 3.0% – 3.25%.

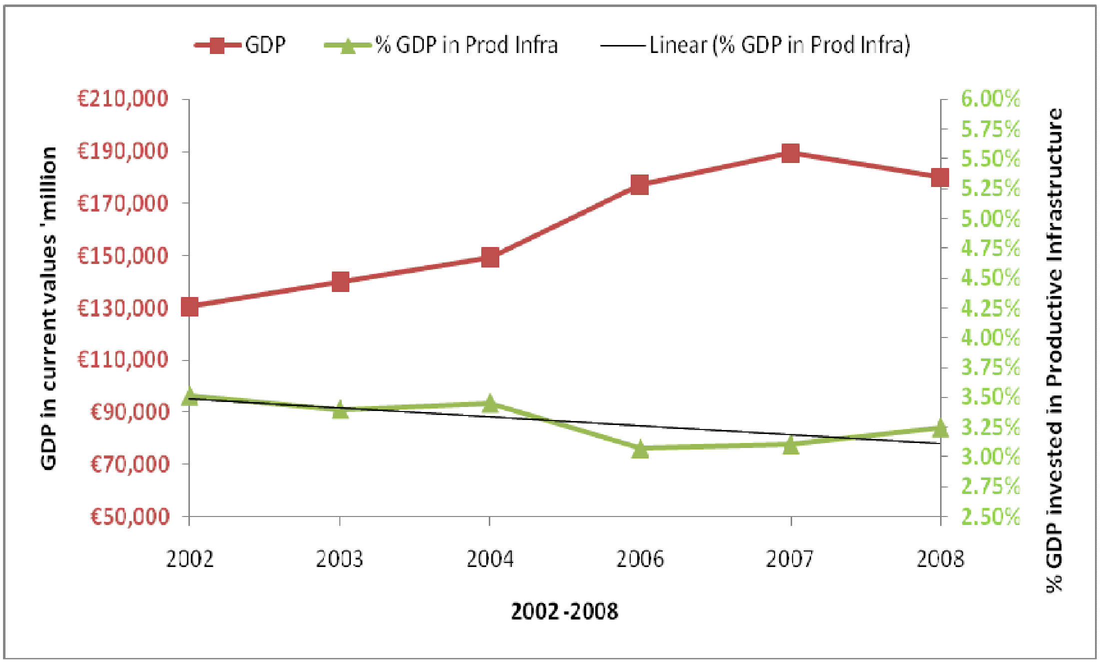

Figure 3: Ireland's GDP versus its % GDP investment in Productive Infrastructure from 2002 to 2008; Source: (Ireland, 2008, Department of Finance, 2010, CSO, 2010)

The projected 5% investment level has never been reached. Clearly, the level of infrastructure investment has been inadequate over a long period, a conclusion borne out by the successive WEF Reports (Michael E. Porter, 2007, Michael E. Porter, 2008, Schwab, 2009) and discussed above.

6. Ireland's present infrastructure investment levels

Detailed Irish Government investment figures up to and including 2008 have been used in the preparation of this paper. However, since 2008 the Irish Government has not published a capital investment programme. For this paper, capital investment figures were obtained from the Irish Department of Finance for 2009 outturn and 2010 estimated investment programme. However, these do not include 2009-2010 figures for non-exchequer, semi-state investment. Therefore the analysis included in this paper is up to and including 2008. These figures have been charted in figure 3 above, which clearly demonstrate that Ireland's investment in infrastructure has not kept pace with its economic growth.

These 2009-2010 Department of Finance figures do not use the category of 'Productive Infrastructure' but rather a grouping titled 'Economic/Productive Infrastructure'. Sectors that were previously included under social infrastructure have been moved to this sector, e.g. the schools investment programme. This does not display a true image of how much is being invested at present in productive infrastructure, as defined internationally.

7. Ireland's required infrastructure investment

A literature review of a number of articles (Teresa Ter-Minassian, 2008, Cecilia Briceno-Garmendia, 2004) suggests a clear link between the general income level of a country, its state of development and it ongoing investment needs. The latter would suggest that a low middle-income developing economy with a developing infrastructure should generally invest 5.5-7% of GDP in its productive infrastructure. A higher middle-income developing country would require circa 3% of GDP as ongoing infrastructure investment.

However, while the GDP of Ireland rose, the level of infrastructure investment remained static in percentage of GDP terms, at a level close to 3%. The 5% target referred to in the OECD 2006 Report was not achieved, despite the significant and growing productive infrastructural deficit. Therefore, even though Ireland has a high income per capita level, due to its present deficit of vital productive infrastructure, there remains a strong case for maintaining an elevated level of infrastructure investment in Ireland, similar to that of a low-middle income developing economy.

If 2006 is taken as a baseline for investment targets, then to address the widening infrastructure gap in the interim, and assuming modest growth of 2% over the period to 2020, it is estimated that investment would be required at a rate closer to 6.25% to redress the balance.

In other words, it is the conclusion of this paper that Ireland should now invest 5.5% - 7% of GDP in productive infrastructure, on a consistent basis, to improve its competitiveness and complete the transition to a true innovation-driven economy.

8. Ireland's Infrastructural Deficit – Conclusions

The World Economic Forum (WEF) (Schwab, 2009) identified that extensive and efficient infrastructure is an essential and vital driver to a country's competitiveness - the quality and effectiveness of infrastructure networks significantly impacts on a countries economic growth. This paper has identified a number of issues with Ireland's level of investment in productive infrastructure over the past decade.

1. It is estimated that Ireland under invested, by up to 30%, in productive infrastructure over the past 10-15 years. There should have been in the region of 1.5% to 2.5% additional GDP invested during the boom years of 2002 to 2007.

2. Ireland's ranking in the category of productive infrastructure sets it with developing or emerging economies. An appropriate level of infrastructure investment is now between 5.5% and 7.0% of GDP, considering the significant time lost over the period 2002-2007.

3. What is not clear is the role that *public* investment and growth has in a country's economy; therefore the role of private investment will be examined, in future work, for specific project categories

Further work will be carried out to identify what specific productive infrastructure projects need to be undertaken and prioritised. A methodology will be prepared to identify how these projects should be prioritised, so as to remove the 'bottle-neck' identified as far back as 2006 (OECD and Development, 2006) in Ireland's infrastructure.

References:

Cecilia Briceno-Garmendia, A. E., Nemat Shafik (2004) Infrastructure Services in Developing Countries: Access, Quality, Costs and Policy Reform. World Bank Policy Research Working Paper.

CSO (2010). Cork, Ireland, CSO.

Department of Finance, I. G. (2010) Capital Investment Programme - 2009 Provisional Outturn, 2010 estimate. Dublin.

DKM (2009) Review of the Construction Industry 2008 and Outlook 2009-2011. Dublin, DKM Economic Consultants.

Ireland, G. O. (2008) Public Capital Programme 2008. Department of Finance, I. G. (Ed.). Dublin, Government Publications Sales Office.

Kamps, C. (2004) New Estimates of Government Net Capital Stocks for 22 OECD Countries:1960–2001 IN Fund, I. M. (Ed.). Washington, DC, IMF Working Paper - Fiscal Affairs Department.

Michael E. Porter, K. S. (2008) The Global Competitiveness Report 2008-2009. Geneva, World Economic Forum.

Michael E. Porter, K. S., Xavier Sala-I-Martin (2007) The Global Competitiveness Report 2007-2008. Geneva, World Economic Forum.

OECD & Development, O. F. E. C.-O. A. (2006) OECD Economic Surveys - Ireland. OECD Publishing.

Schwab, K. (2009) The Global Competitiveness Report 2009-2010. Geneva, World Economic Forum.

Teresa Ter-Minassian, R. H., and Alejandro Hajdenberg (2008) Creating Sustainable Fiscal Space for Infrastructure: The Case of Tanzania. IMF Working Paper.

AN ASSESSMENT OF THE PHYSICAL PROPERTIES OF LIME-HEMP CONCRETE

F.MURPHY, S.PAVIA & R.WALKER
Dept. of Civil Engineering, Trinity College, Dublin, Ireland

Abstract

This work is part of a wider research programme that aims at producing alternatives to conventional building materials. The aim of this project is to investigate several physical properties of a sustainable, carbon-negative, lime-hemp biocomposites which can partially replace existing, non-biodegradable, non-sustainable, building materials of high embodied energy and high CO_2 emissions. The shrinkage, flexural and compressive strengths of these lime-hemp concretes, made with either calcium lime or a commercial binder with a cement content and varying lime:hemp proportions (1:9, 1:1 and 3:1), were investigated according to the relevant European standards. The shrinkage and strength development at 7, 28 and 90 days were monitored. The relationship between shrinkage and binder type, hemp content and water content was observed. The development of the flexural and compressive strengths shared several characteristics but their behaviour departed in relation to increasing hemp content with compressive strength continuously decreasing while flexural strength varied little between 50% and 75% hemp content.

Keywords: lime-hemp concrete, compressive strengths, flexural strength, shrinkage

1. Introduction

The construction industry is non-sustainable. It is responsible for the consumption of non-renewable raw materials and fossil fuels, and for high CO_2 emissions that adversely impact on the environment. In light of this, there is a critical need to develop sustainable alternatives to conventional building materials of high embodied energy responsible for high CO_2 emissions.

Lime-hemp composites, are providing such alternatives and can replace high embodied energy materials for certain applications. They have been used in construction in France since the 1990s, and there are now several hundred hemp buildings in the country. Lime-hemp concrete has also been gaining popularity in Ireland in recent years, and there are now over 20 buildings constructed in lime-hemp concrete and a further 100 that have been thermally upgraded (Pronchetti, 2010) throughout the country.

A lime-hemp concrete is a composite material, comprising of hemp shiv, which is the woody interior of the hemp stalk, and lime. Hydraulic lime, pozzolans and cements may also be added to the binder to reduce setting times. Lime-hemp concrete acts as a CO_2 sink and $1m^3$ of lime-hemp concrete wall can sequester over 100kg of CO_2 (Bevan and Woolley, 2008). Lime-hemp concrete also displays good thermal, acoustic and fire properties.

The physical properties of lime-hemp concrete are still not well known which affects their uptake into mainstream technology. As part of this research, three important physical properties are examined including shrinkage and flexural and compressive strength. Two binders were investigated: a hydrated lime and a commercial binder incorporating cement and other pozzolanic and mineral additions. The hydrated lime will set purely through carbonation while hydraulic additions in the commercial binder will result in a partial hydraulic set which is a faster process. The effect of the different hemp shiv contents, relating to different applications; wall, floor and plaster on the physical properties shall also be examined.

Shrinkage is unlikely to cause problems in properly constructed lime-hemp concrete walls (Bevan and Woolley, 2008). The phenomenon has not been widely investigated for lime and hemp shiv concretes, although hemp fibers (sheath of fiber inside the bark) are widely used to reduce shrinkage in plasters. Shrinkage tests to date, using hemp shiv, have produced varied results that have not proved representative of their performance in real life situations (Evrard, 2003).

The effects of hemp fibers on the flexural strength of lime, cement and gypsum binders has been investigated by Le Troëdec et al (2009), Sedan et al (2008) and Dalmay et al (2010) respectively. A similar flexural loading vs strain curve was observed by all authors in which, initially, the load is primarily supported by the matrix but following the occurrence of the first macroscopic damage, the load is transferred to the matrix/fiber interfaces, with a corresponding slight increase in stress uptake and a reduction in rigidity. Unlike brittle composites, after the peak load is achieved, there is a gradual load decrease on account of the progressive failure of the matrix/fiber bonds. In addition, Elfordy et al (2008) investigated a commercial lime binder and hemp shiv and established the relationship between increasing density and increased flexural strength.

The compressive strength of lime-hemp concretes has attracted more attention than flexural strength and has been investigated by Evrard, (2003); O'Dowd and Quinn (2005); de Bruijn et al, (2009) and Elfordy et al, (2008). Lime-hemp wall concrete is considered a non-load bearing material with compressive strengths typically under 1.2MPa, that is typically cast around a timber frame. It has low rigidity and accommodates major deformations without rupturing (Evrard, 2003).

2. Materials and Methods

2.1 Mixing

Different composites were produced by mixing hemp shiv with either hydrated lime CL90s complying with EN459-1 (2001) or a commercial binder (TH) which included hydraulic and pozzolanic additions. Each binder was mixed with hemp in three ratios by volume (Table 1) in accordance with the specific application. It is noted that the commercial binder is significantly denser than the hydrated lime. The water content was dependent on the amount of hemp in the mix, with 3.3litres of water per litre of hemp as advised by the supplier. The 10% hemp mixes (CL90H10& TH10), on account of the low hemp content required additional water in order to achieve an adequate workability which was determined experimentally.

The binder and hemp were dry mixed for approximately 10 seconds and the water gradually added in 100ml segments at regular intervals. Each batch was mixed for 10 minutes except for the 90% binder mixes which required a further 5 minutes of mixing to achieve workability. After mixing, the samples were transferred into prismatic moulds filled in three layers and tamped 25 times each. The final layer was levelled off with a steel trowel. They were stored under damp hessian for three days at temperature 20°C±2°C and relative humidity 95%±5% and then demoulded and transferred to a curing room at temperature 20°C±2°C and relative humidity 65%±5%.

Table 1 – Mix proportions by volume

Mix Name	Binder	Hemp:Binder:Water By Volume	Application % volume
CL90H75	CL90	1:0.33:0.3	Non-load bearing wall 75% hemp 25% binder
CL90H50	CL90	1:1:0.3	Floor 50% hemp 50% binder
CL90H10	CL90	1:9:2	Plastering 10% hemp 90% binder
TH75	Commercial Binder	1:0.33:0.3	Non-load bearing wall 75% hemp 25% binder
TH50	Commercial Binder	1:1:0.3	Floor 50% hemp 50% binder
TH10	Commercial Binder	1:9:2	Plastering 10% hemp 90% binder

2.2 Shrinkage

Testing was based on American cement standard ASTM C 596-96 (1996). One sample of each mix was tested. Measurements were recorded, on a daily basis, with gauges accurate to 0.002 mm following removal from the mould on day 3 and were concluded after 30 days by which time, changes in shrinkage for all samples were under 0.0025% per day.

2.3 Flexural and Compressive Strength

Flexural and compressive testing was carried out using a Zwick Testing machine. No standards currently apply to lime-hemp concrete and EN 459-2 (2001) was used to guide the tests. Four samples of each mix were tested. Loading rates of 1N and 10N per second were selected for the flexural and compressive strengths, respectively.

2.4 Modulus of Elasticity

The Young's modulus was used as a measure of the stiffness of the material and was determined by the slope of the linear part of the stress-strain curve both under compression and in flexion.

3. Results and Discussion

3.1 Shrinkage

Shrinkage is primarily due to the evaporation of water during drying, and therefore shrinkage was most significant at early ages (see figure 1). The decrease in length was significant, however, shrinkage was uniform and no significant cracks appeared in any of the samples.

Shrinkage was greatest in the first 10 days. By day 10, the CL90 samples had undergone over 90% of their total 30-day shrinkage while the commercial mix displayed a slower rate of shrinkage, ranging from 70-90% of the total 30-day shrinkage. The total shrinkage at 30 days for the commercial mix was found to be lower than that of the hydrated lime samples for all lime:hemp ratios. This was expected as mortar shrinkage decreases with increasing binder hydraulicity.

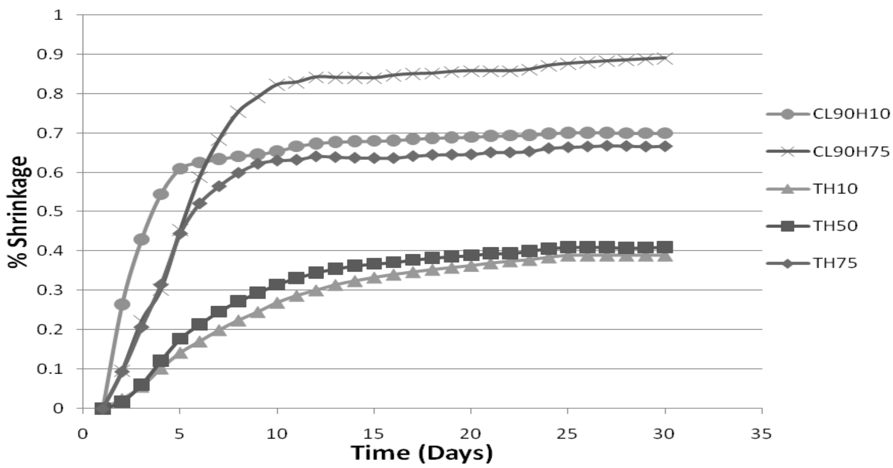

Figure 1 - Shrinkage

The difference in the 30-day shrinkage of the two 10% hemp mixes is greater than that of the 75% hemp mixes; this suggests that the binder type has a higher impact on the total amount of shrinkage than the hemp content.

An increase in shrinkage was observed for the 75% hemp mixes partly on account of the increased water content demanded by their higher hemp content. At early stages, the two 75% hemp samples displayed a similar rate of shrinkage as excess water evaporated. However, the commercial 10% and 50% hemp mixes have similar shrinkage despite the 50% mix having lower water content. This suggests that the hemp content must also contribute to shrinkage.

Shrinkage is a complex process that has an interdependent relationship with water content, binder type and hemp content. Binder type appears to have a stronger effect on total shrinkage than hemp content or water content. On site, the drying process can take several months thus shrinkage can also extend over several months. CL90H50 results are not included on account of experimental error.

3.2 Flexural Strength

The flexural strength development and mechanical behaviour of hemp composites in flexion are included in figures 2 and 3. This research found that flexural strength increased with increasing binder content between 25% and 50%. However, a further increase in binder content to 90% had little effect on flexural strength. This suggests a contribution from the lime-hemp bonds towards the flexural strength of the composite. The commercial mix was found to produce samples of significantly higher flexural strength than the CL90s samples. The values obtained are comparable to those from former aurthors: the flexural strength of TH75, which has an equivalent composition to the hempcrete blocks investigated by Elfordy et al (2008), had a similar flexural strength at 28days of 1.2MPa and 1.19MPa, respectively, for an equivalent density.

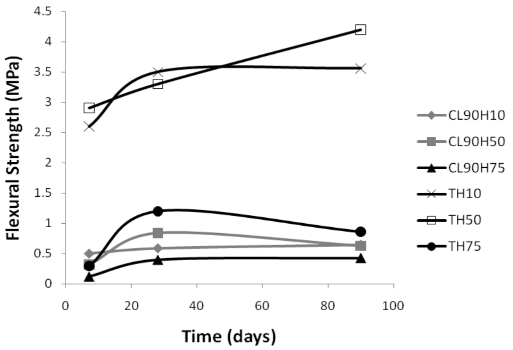

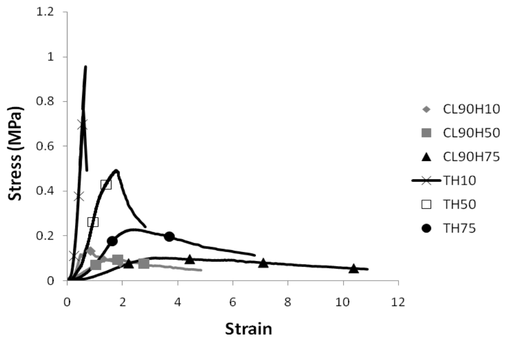

Figures 2 – Flexural strength development of hemp composites

Figures 3 –Mechanical behaviour of hemp composites in flexion

All samples rapidly attained flexural strength, achieving over 90% of their total 90 day flexural strength by 28 days (with the exception of the 50% commercial mix). The commercial samples developed their early flexural strength marginally faster than the CL90s samples, likely on account of the early formation of hydraulic products. All the low hemp content composites gained their flexural strength significantly faster than the high hemp content samples.

Flexural strength did not continuously increase with time for all mixes. A decrease was recorded for TH75 and CL90H50 between 28 and 90days. Similar behaviour was observed by Hanley and Pavía (2008) in which flexural strength was found to decrease in several hydraulic lime mortars between 28 and 56days. In the case of hydraulic binders, this may be attributed to the evolution of the hydration products formed over time. Behaviour after 90 days was not measured.

Figure 3 shows a representative example of the behaviour of the hemp composites under flexural loading. The 10% hemp mixes with commercial binder act in a brittle manner, and the flexural load vs strain relationship after the point of rupture displays a similar behaviour to that observed by Le Troëdec et al (2009) and other authors (as discussed in the introduction). This suggests that the hemp shiv particles act in a manner similar to hemp fibers at low concentrations.

The 50% and 75% hemp composites exhibit a lower load carrying capacity and progressive failure takes place in a ductile manner. The binder type has the greatest influence on stiffness, with the commercial samples having a greater Young's modulus at higher binder contents. The Young's modulus of the commercial composites was not observed to continuously increase with time, the TH10 and TH50 samples decreasing by 11% and 22% respectively between day 7 and day 90. In contrasts, the CL90s hemp composites (on account of carbonation) increased in stiffness overtime.

3.3 Compressive Strength

An increase in compressive strength was evident with increasing binder content, as found by Evrard (2003) and other researchers (Figure 4). However O'Dowd and

Quinn (2005) noted that increasing the hemp content beyond a 3:1 ratio had little further effect on reducing the compressive strength.

As expected on account of their hydraulic content, the commercial binder composites displayed higher ultimate compressive strengths than the CL90s ones. However, as the hemp content increased, the hydraulic strength of the binder was found to have less effect on the compressive strength of the composite: the 10% hemp commercial samples were approximately 5.5 times stronger than their equivalent CL90 mixes, however the 50% and 75% commercial samples were only 3.2 and approximately 2 times stronger, respectively, than their equivalent CL90s mixes. The low strength samples are approximates on account of variability of the standard deviation in measuring strengths under 2MPa.

The commercial samples, on account of their hydraulic component, had a higher rate of strength gain than the CL90 samples that relied solely on carbonation for strength development. In consequence, the rate of strength gain of the commercial samples increased at higher binder content while the rate of strength gain of the CL90 samples did not.

The compressive strength results obtained are relatively high when compared to other authors (Evrard, 2003 and de Brujin et al, 2009). Elfordy et al (2008) determined a relationship between increasing density and compressive strength and the high compressive strengths is likely linked to a high level of compaction resulting in high density samples.

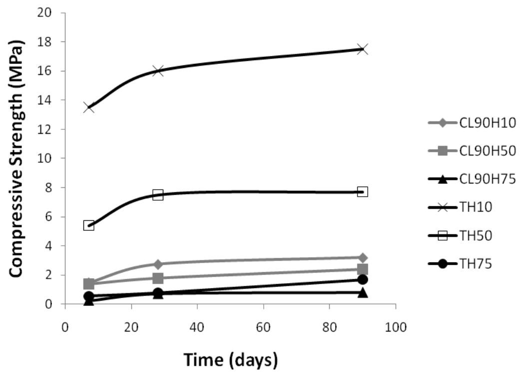

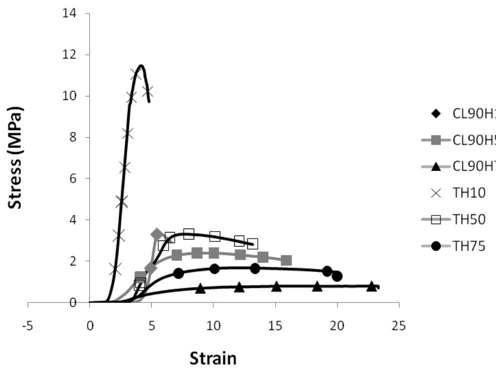

Figures 4 – Compressive strength development of hemp composites

Figures 5 –Mechanical behaviour of hemp composites under compressive loading.

Figure 5 shows the mechanical behaviour of the hemp composites under compressive loading. As for flexural strength, the 10% hemp samples act in the most brittle manner while at higher hemp contents, the behaviour is more plastic. The behaviour of the 75% hemp mixes is a continuous plastic deformation similar to that described by Evrard (2003), with an initial linear relationship between stress and strain followed by a failure of the binder matrix at a point where the behaviour becomes more ductile. This is likely due to the transfer of stresses to the matrix/hemp interface which allows the sample to continue accommodating load.

According to the stiffness measured with the Young's modulus, the commercial hemp composites achieve a much higher rigidity, as also noted by (de Bruijn et al, 2009) however, stiffness greatly decreases at high hemp contents. The results also show a general increase in stiffness over time.

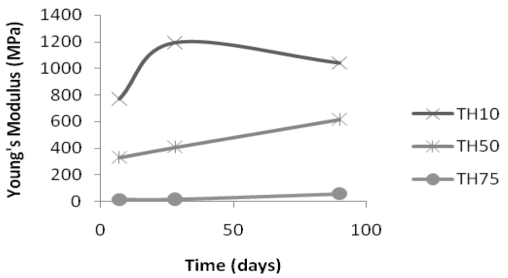

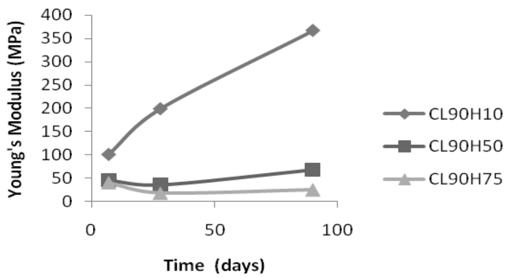

Figures 6 – Average Young's modulus for commercial binder samples subjected to compressive loading

Figure 7 - Mechanical behaviour of hemp composites under flexion

4. Conclusion

Shrinkage is strongly related to drying. It is heavily dependent on the binder nature and influenced in a lower extent by increasing hemp and water contents.

The mechanical behaviour of the hemp composites both in flexion and under compression shows similarities: the composites become more plastic as the hemp content increases. The nature of the binder appears to have a slight impact on mechanical character with the hydraulic component of the commercial binder imparting a more brittle behaviour to the composite at low hemp contents.

The flexural and compressive strength also share several similarities including their dependency on the binder nature at low hemp contents: the faster strength gain and higher ultimate values were observed at low hemp contents for the commercial mix. The composites gained their early flexural and compressive strength at a similar rate, ranging from 30% of the 90 day strength at 7 days for the high hemp content samples to 75% for the low hemp content mixes. The only exception was the CL90s low hemp content mixes which developed compressive strength slower than flexural strength. The commercial binder produced samples of higher stiffness however the effect of the binder was less evident at high hemp contents when the biocomposite's rigidity was significantly reduced.

The main difference between the flexural and compressive strength gain was the compressive strength increased with increasing binder content while the flexural strength achieved a maximum value at 50% hemp content. This suggests a contribution from the lime-hemp bonds towards the flexural strength of the composite.

References

ASTM C 596-96 (1996) Standard test method for drying shrinkage of mortar containing hydraulic cement. American Society for Testing and Materials

Bevan R., and Woolley T. (2008), *Hemp Lime Construction*, BRE Press.

de Bruijn, P.B., Jeppsson, K.H., Sandin, K., Nilsson, C., (2009), 'Mechanical properties of lime–hemp concrete containing shives and fibres' *Biosystems Engineering* **103** 474-479

Dalmay, P., Smith, A., Chotard, T., Sahay-Turner, P., Gloaguen, V., Krausz, P., (2010) 'Properties of cellulosic fibre reinforced plaster: influence of hemp or flax fibres on the properties of set gypsum' *J Mater Sci*, **45**, 793–803

Elfordy, S., Lucas, F., Tancret, F., Scudeller, Y., Goudet L., (2008) 'Mechanical and thermal properties of lime and hemp concrete ("hempcrete") manufactured by a projection process.'*Construction and Building Materials*, **22**, 2116-2123

EN 459–1 (2001), Building lime—part 1. Definitions, specifications and conforming criteria. British Standards Institution, London

Evrard, A., (2003) Hemp concretes: A synthesis of physical properties, Construire en Chanvre St. Valerin (in French)

Hanley, R., Pavı´a, S., (2008) 'A study of the workability of natural hydraulic lime mortars and its influence on strength' *Materials and Structures* **41** 373-381

O'Dowd, J., and Quinn D., (2005), 'An investigation of Hemp and Lime as a Building Material ', Bachelor of Engineering Thesis, UCD

Pronchetti, R., 31st March 2010, Lime Hemp Workshop, Co. Westmeath, Ireland

Sedan, D., Pagnoux, C., Smith, A., Chotard, T., (2008) 'Mechanical properties of hemp fibre reinforced cement: Influence of the fibre/matrix interaction', *Journal of the European Ceramic Society* **28**, 183–192

Le Troëdec, M., Peyratout, C.S., Chotard, T., Bonnet, J. P., Smith, A., Guinebretière, R., (2009) 'Physico-chemical modifications of the interactions between hemp fibres and a lime mineral matrix: impacts on mechanical properties of mortars' *Journal of the European Ceramic Society*, **29**, 10, 1861-1868

STABILISED SOIL BLOCKS – A COST-EFFECTIVE SUSTAINABLE CONSTRUCTION TECHNOLOGY

J. GOGGINS
College of Engineering & Informatics, National University of Ireland, Galway.

Abstract
The aim of this paper is to show that stabilised soil blocks (SSBs) are cost-effective sustainable masonry units that have the potential to be used both in developing countries and Europe. In fact, these blocks are extensively used in developing parts of the world, such as Western Zambia. The topography of Western Zambia is unusual in that there is little or no aggregate available for use in block making and as a result most blocks have to be made out of soil stabilised with cement. The process for making SSBs is to dry mix soil and cement, add water and then compress the conglomerate together in a mould to form a masonry unit.

This paper presents the findings from laboratory tests on the strength and durability of stabilised soil blocks. It is shown that this construction technology is not only cost effective and has a very low impact on the environment for use in buildings in Africa, but is also a viable technology for use in the Irish climate.

Keywords: Block, cement, masonry, soil, stabilisers, sustainable technology.

1. Introduction

One construction technology used in houses in developing countries that has very low impact on the environment is stabilised soil blocks (SSBs), which are formed by compressing a mixture of soil, cement and water. SSBs are extensively used in the construction of both structural and non-structural elements in many developing countries throughout the world, especially in rural areas. The blocks are low-cost as their main component, the soil, is usually sourced locally, often directly from the site of construction. Further, these blocks can be produced on site, saving in transportation costs. The main stabilisers used in their manufacture are cement, lime or a combination. Mulengu et al (2008) found SSBs containing cement gave higher strengths than those with lime. In any case, cement and lime have large amounts of embodied energy due to the product process required in their manufacture. Further, these materials can often be relatively expensive due to production and transportation costs.

Maize is the most widely grown staple crop in Africa – more than 300 million Africans depend on it as their main food source (Adesanya 1996). Adesanya & Raheem (2009) found that using burnt corn cobs, a waste product, in SSB the quantity of Ordinary Portland Cement (OPC) in these blocks can be reduced by up to 50%. Similarly, Basha et al (2005) found that rice husk ash (RHA) cannot be used solely for stabilisation of soil. On the other hand, the performance of SSBs can be intensified by using 6-8% OPC and 15-20% RHA. Reduction in plasticity index and increase in strength and resistance to immersion indicate an improvement. Further, a lesser amount of cement is therefore needed to achieve a given strength as compared to cement-stabilised soils. Since cement is generally far more costly then RHA this results in lower construction costs.

Cement kiln dust works well as a stabiliser for certain types of soils due to its calcium content. Ion exchange between soil and calcium-containing additives will result in the formation of more granular material that is less plastic, less sensitive to moisture changes, more resistance to wet-dry and freeze-thaw cycles, and has increased compressive strength (Maslehuddin et al 2009). Browne (2009) assessed various alternative stabilising options to produce low carbon earth blocks. Further tests on alternative stabilisers such as saw dust ash (SDA) and oats husk ash (OHA) are ongoing at NUIG.

In terms of masonry blocks, compressive strength is not the most critical characteristic. Assuming the soil is adequately compressed and suitable soil is used in the making of the blocks, avoiding the use of topsoil with high levels of organic matter, the target strength should be met. Durability is the main concern with SSBs. The ability of the soil in the blocks to resist prevailing rain, wetting and drying cycles, freezing and thawing cycles, and chemical attack are critical issues if they are to be applicable in a European climate.

This paper presents findings from experimental studies undertaken at NUIG to determine the performance of SSBs. In particular, the main objectives were to identify suitable soil, to investigate the variation in performance of blocks with varying cement content and with fibrous materials, and to highlight the effects of different curing methods on the strength of blocks.

2. Material properties

Before any SSBs can be made, careful attention must be paid to the selection of soil to be used in the blocks. Other than considerations like the cost, availability and transport, the soil must fulfil certain composition characteristic requirements. The soil should have a silt and clay content of less than 20% (ITDGZ, 2008). A particle size distribution ranging from medium gravel to fine sand is desirable. Soils outside this specification (e.g. more clayey soils) can still be used, but will require extra cement for stabilisation (ITDGZ, 2008). More precise parameters are given by Pave (2007), who provides a table of basic soil requirements for low strength blocks (≤4 MPa) and higher strength blocks (4-16 MPa) as shown in Table 1. Soil used must not contain organic material or harmful quantities of salts (Pave, 2007), which rules out the use of topsoil (large amounts of organic material). Organic material biodegrades and uses up water in doing so (Hall & Djerbib, 2004), which leaves pores in the finished block and undermines the characteristic compressive strength.

In the present study, the soil was characterised as per test methods in BS1377-2 (BSI, 1990). The particle size distribution for the soil in Figure 1 indicates a clay and silt content of 9.7% (percentage passing the 0.075 mm sieve). This is marginally less than the recommended minimum value by Pave (2007) of 10%. On the other hand, Pave (2007) suggests maximum plasticity indexes of 10 and 15 for blocks with compressive strength of less than 4MPa and between 4 and 16MPa, respectively. The plastic limit of the soil used in this study is 14%, while the plasticity index was 6. The

Table 1 - Soil requirements for SSB construction (Pave, 2007)

Soil Range	% by mass passing the 0.075mm sieve		Maximum plasticity index	% by volume of cement content	Estimated nominal compressive strength (MPa)
	Min (%)	Max (%)			
A	10	35	15	≤ 7	≤ 4
B	10	25	10	7 – 30	4 – 16

average specific gravity and pH of the soil was 2.6 and 7.9, respectively (Table 2). This suggests that the soil is suitable for making SSBs, but that a soil of greater clay and silt content would yield greater compressive strengths. This is due to the role that clay content plays in cohesion of the blocks. The importance of the clay content of the soil lies in the fact that the clay particles provide cohesion – holding the particles together in the block. Clay also determines the plasticity of the block, which then determines the behaviour of the block in different moisture conditions (Mulenga et al, 2005).

The cement used as a stabiliser was CEM II-A-V 42.5N.

3. SSB Performance

3.1 Compressive Strength

Previous research has shown that the addition of cement to soil leads to an increase in the compressive strength of soil blocks (for example, Bahar et al 2004, Mulenga et al 2005, Pave 2007, Jayasinghe & Mallawaarachchi 2009). The reason for this increase in compressive strength is that products of cement hydration fill the pores that exist in the soil. The reduction of pore space improves the rigidity of the soil by forming bonds between the sand particles in the soil, thereby increasing compressive strength and improving durability characteristics of the blocks made (Bahar et al., 2004).

Stabilised soil with cement contents of 5%, 7.5%, 9% and 10% were tested at NUIG. The soil was air dried and sieved to 6.3mm. Soil and cement were dry mixed and then water was added. The specimens were prepared in accordance with relevant parts of ASTM D1632 (ASTM 2007a) and ASTM D1633 (ASTM 2007b). The mix was compacted in Duriez moulds (cylinder 120mm dia x 250mm high) to a load of 10MPa. The stabilised soil specimen was extruded from the mould after 1 day and immersed in water at 20^{o}C. The specimens were removed from the curing tank and left to dry in the air for 1 day prior to testing. The loss of mass on post-curing drying varied between 1.7 and 2.9%. This reduced to approximately 1.6% for specimens containing straw fibres due to the water absorption capabilities of the straw. The compression strength of specimens was measured at 7, 14 and 28 days by crushing the specimens. As expected, the compression strength increased with curing time and with cement content (Figure 2). An increase in cement content from 5% to 10% resulted in an increase of strength from 3.2MPa to 6MPa. These findings are broadly in agreement with those of Pave (2007), who found that the increase of compressive strength was directly proportional to the cement content of blocks up to a cement content of 10%. That is an increase of cement content from 5% to 10% resulted in an increase in compressive strength of 3 MPa to 8 MPa (Pave, 2007).

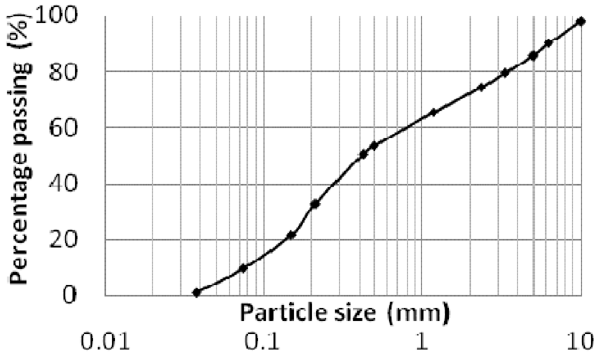

Figure 1 – Particle size distribution curve for soil

Table 2 – Characteristics of soil and cement

	Soil	CEM II
Specific Gravity	2.56	2.79
% passing 0.075*mm*	9.7	68.2
pH	7.9	12.7

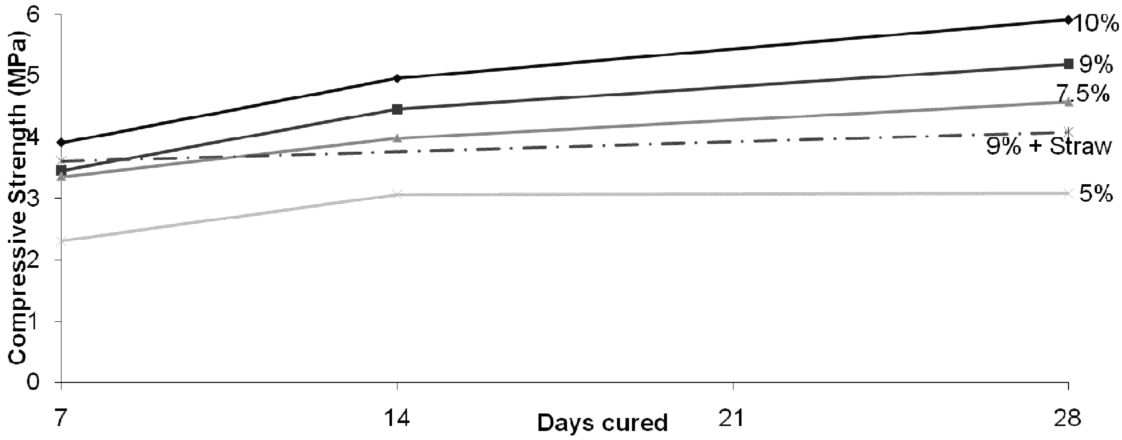

Figure 2 – Compressive strength of SSBs with various amounts of stabilisers

Similarly, Hydraform (2004) suggests a compressive strength of 4 MPa and 6MPa for a 1:20 (5% cement content) mix and 1:12 (8.33% cement content) mix, respectively.

The addition of straw did not significantly affect the 7-day strength, but led to lower strengths at 28 days (Figure 2). On the other hand tests by Bouhicha et al (2005) showed an enhancement of compressive strength, decrease in shrinkage, and reduction in the curing time if an optimal reinforcement ratio of straw was used.

The effect curing has on the compressive strength of SSBs was studied for specimens containing 9% cement content. The specimens stored in normal atmospheric conditions were found to have compressive strengths 1.0 and 1.8 times those stored in a water tank when tested at 7 and 14 days, respectively (Fogarty & Manton, 2010). Similar observations were made by Pave (2007). On the other hand, specimens immersed in water for the first half of the curing period, followed by curing in normal atmospheric conditions were found to have compressive strengths 1.2 and 2.2 times those stored in a water tank when tested at 7 and 14 days, respectively. Pave (2007) found that specimens stored in an oven at 50^{o}C for 24 hours before testing could have compressive strengths up to 2.2 times that of wet specimens. It is recommended to carry out curing under plastic sheeting with daily wetting (Hydraform, 2007).

Most SSBs are used in construction by dry-stacking, i.e. stacking one on top of another, without mortar between the blocks (Figure 3). This technique is complementary to the use of SSBs as it does not require skilled labour or cement for mortar. However, no standards exist that correlate wall strength with masonry unit strength for SSBs. On the other hand, one study found that the compressive strength of wall panels was considerably less than the constituent masonry units (0.85MPa versus 4.4MPa) (Jayasinghe & Mallawaarachchi, 2009). This was attributed to the placing of the blocks and how they fit together. For example, uneven surfaces between blocks leads to stress concentrations meaning that the wall panel fails at a lower compressive stress than the blocks would have had they been individually loaded (Jayasinghe & Mallawaarachchi, 2009).

3.2 Durability

The main concern with SSBs is their ability to withstand climatic actions, such as the effects of wind, rain, extreme temperatures, and changes in moisture and temperature. These actions can result in deteriorations of the blocks due to shrinkage cracking, erosion, swelling and so on (Guettala et al., 2006). These concerns have led to consumer uncertainty about the use of SSBs (Heathcote, 1995).

Shrinkage due to drying is significant in clays but less so in silts and sands. Specimens containing approximately 5% by mass of water and 9% by mass of cement were compacted by hand in layers in a 75x75x280mm steel mould. These were stored inside the laboratory at $20^oC \pm 2^oC$ and 55% RH ± 5% RH and linear shrinkage readings were taken over 14 days (Figure 4). For specimens containing 9% cement, shrinkage stabilised at 0.096% after 14 days. Adding straw fibres slightly reduced the shrinkage (Figure 4). Bahar et al (2004) tested blocks made from clay sandy soil (PI 15, clay and silt content of 62%, sand content of 30%). They found that shrinkage increased rapidly in the first 4 days for both cement-stabilised soil and un-stabilised soil specimens and then at later ages the increase is very slow. Hence, curing for the first 4 days could be beneficial in reducing drying shrinkage. At 25 days cement-stabilised blocks with 6% and 10% cement content had 20% and 44% less linear shrinkage as compared to un-stabilised blocks. Bahar et al (2004) also found that there was minimum shrinkage after 14 days.

The addition of cement reduces water permeability. Bahar et al (2004) noted that water permeability coefficient decreases from 14×10^{-8} to 0.27×10^{-8} m/s when cement content increases from 5% to 20%. This shows that stabilisation of soil with cement could lead to better mechanical strength, lower permeability and, hence, better durability.

Wetting/drying and freeze/thaw tests were carried out in accordance with ASTM D559 (ASTM, 2003a) and ASTM D560 (ASTM, 2003b), respectively. Figure 5(a) shows the mass change for unscratched and scratched stabilised soil specimens containing 5% and 10% cement content after each freeze-thaw cycle. As expected, there is no significant change in mass of the unscratched specimens, whereas specimens with 5% and 10% cement content that were scaped by a wire brush during each cycle experienced 21% and 7% mass loss after 12 cycles of freeze-thaw. Thus, the stabilised soil specimen with 10% cement content shows good durability to freeze-thaw cycles compared to that with 5% cement content, as can be clearly seen from Figure 6. Small increases in mass during some cycles are a result of water absorbed increasing the mass of the cylinder more than the loss of mass from scraping with the wire brush. This can be clearly seen in the moisture content changes in Figure 5(b). Furthermore, the moisture content for a specimen with 10% cement content is much less than that with 5% cement content (Figure 5(b)). The moisture content could be one reason that more soil-cement is lost during the scraping process. The moisture contents fluctuate at the thaw stage as the cylinders soak up moisture during this stage by capillary action.

Figure 3 – House constructed from SSBs

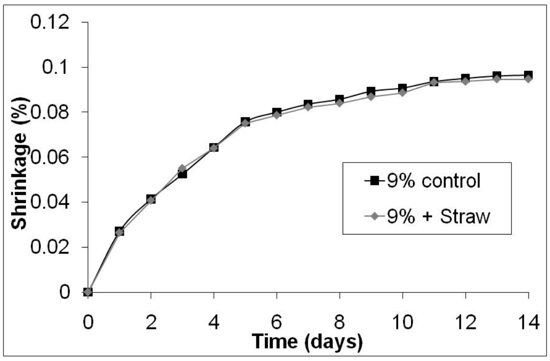

Figure 4 – Linear shrinkage of cement-stabilised soil

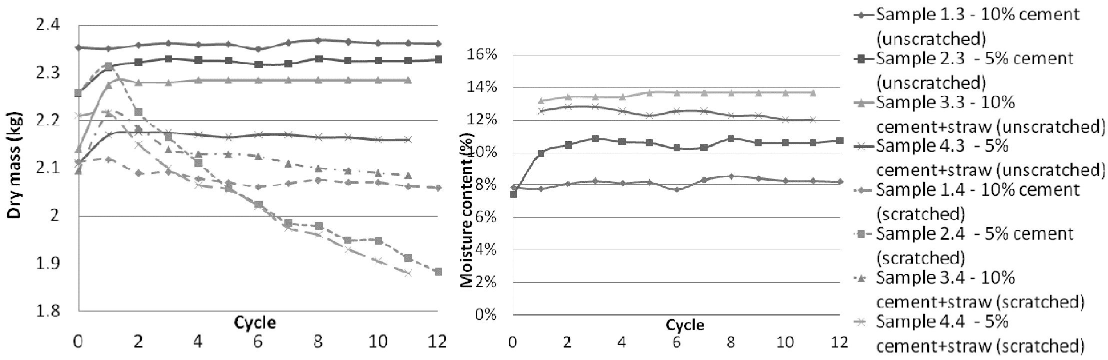

Figure 5 – (a) Mass change after thaw and scratch of stabilised soil specimens over 12 cycles; (b) Moisture content changes of unscratched control mixes.

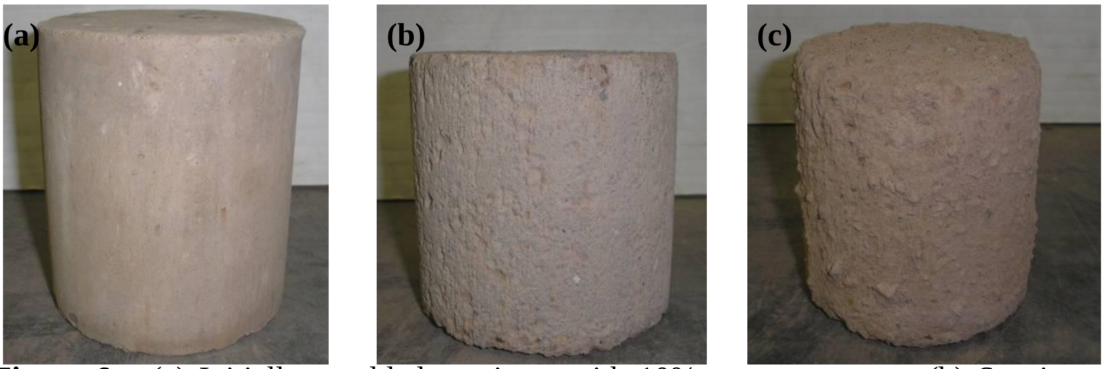

Figure 6 – (a) Initially moulded specimen with 10% cement content, (b) Specimen with 10% cement content after 12 cycles of freeze/thaw, (c) Specimen with 5% cement content after 12 cycles of freeze/thaw.

The straw cylinders show a very similar yet slightly larger percentage of mass loss than those without straw during the test (Figure 5a). These cylinders have the same amount of cement in the mix, so with no improvement in the durability to freeze-thaw cycles suggests it is not a viable option in terms of durability to add straw fibres.

The durability of the stabilised soil specimens to wetting and drying cycles were tested in accordance with ASTM D559 (ASTM 2003a). One sample of each mix design was tested in terms of volume change and the tracking of water content throughout the twelve cycles. The second sample of each mix design was tested in order to calculate the soil-cement loss that occurred during testing. Figure 7a shows the mass loss occurring on the samples over the testing period. The stabilised soil specimens containing 5% and 10% cement content experienced less than 1% and 3% reduction in mass after 12 cycles of wetting and drying, which shows that there is a clear relationship between the soil-cement ratio and the durability of a block. Furthermore, neither sample experienced excessive moisture content fluctuations after the first cycle has been completed (Figure 7b). This is a positive sign as any excess increase or decrease of the moisture content would have a negative impact on the soil block and its performance. The superior performance of the specimen containing 10% cement content in the wetting and drying tests is clearly shown in Figure 8.

The results suggest that soil stabilised blocks with 10% cement content have sufficient durability for use as masonry units for housing construction in the European climate and elsewhere. The straw cylinders show a slightly larger rate of soil-cement loss in comparison with the control cylinders (Figure 7). This may indicate that straw does not improve the binding quality and as a result actually weakens the cylinders durable properties.

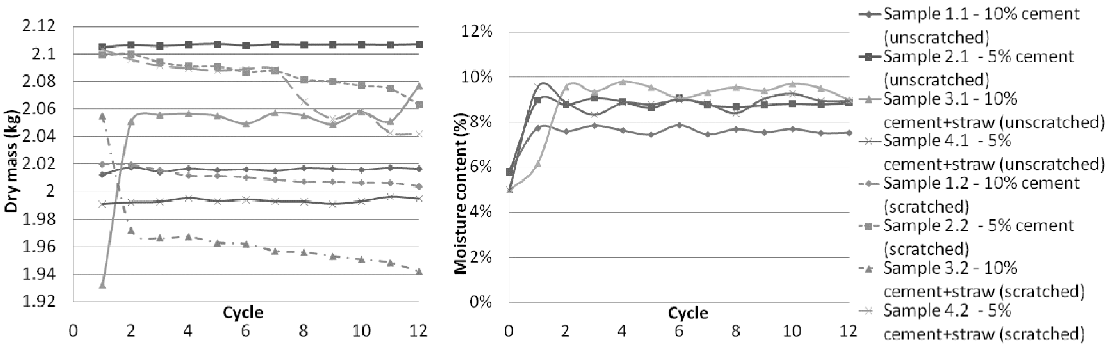

Figure 7 – (a) Soil-stabiliser mass loss and (b) moisture content changes over 12 cycles in wetting & drying test.

Figure 8 – (a) Initially moulded specimen with 10% cement content, (b) Specimen with 10% cement content after 12 cycles of wetting/drying, (c) Specimen with 5% cement content after 12 cycles of wetting/drying.

4. Comparison with other construction technologies

It is important to understand the respective properties of SSBs in relation to other common masonry. Therefore, the following section will explore and compare SSBs to other common masonry such as concrete and clay bricks on topics such as compressive strength, cost effectiveness and environmental impact.

4.1 Comparison of compressive strength

SSBs compare favourably with other common construction materials as regards to the compressive strength of blocks of other materials, such as concrete, clay bricks and compressed earth blocks. The typical compressive strength of concrete masonry block ranges from 3.5MPa to 28MPa. Compressed earth blocks typically have compressive strengths of between 2-3 MPa (Morel et al, 2004). Clay bricks are more difficult to actually specify a typical compressive strength. This is due to the fact that in developing countries the burning of the clay to form the bricks takes place mainly in homemade kilns; this method is undesirable as there is little or no control over the quality and this means that the bricks can range in strength from under 1 MPa to about 16 MPa. In the developed world, the construction of the bricks can be standardised and controlled. As the bricks are manufactured in an industrial environment, they are of a higher quality and generally have a compressive strength of greater than 22 MPa.

4.2 Comparison of cost effectiveness

The cost effectiveness of stabilised soil blocks in comparison to concrete is long established. A study by Tadege (2007) has shown that the construction of a building constructed using just a dry stack of SSBs saves 55.2% of the overall cost of construction when compared to a building constructed of hollow concrete blocks that has been plastered and painted both internally and externally (excluding the labour costs of plastering and painting). A building constructed of SSBs that is internally plastered (excluding labour costs of plastering) saves 36.59% of the overall construction costs in comparison (Tadege, 2007). Fogarty & Manton (2010) found that for a 8m x 8m typical housing unit of 6,400 SSBs in Zambia, by using blocks containing 10% cement substitutes, the cost of a typical housing unit can be reduced by approximately 5%.

4.3 Comparison of environmental impact

SSBs are also much more environmentally friendly than most common construction materials. An investigation by Venkatarama-Reddy & Jagadish (2003) suggests that masonry walls with cement-stabilised soil blocks with 6% and 8% cement have embodied energies of 646 and 810MJ/m^2, respectively, which is 30% and 38% of an equivalent burnt clay brick masonry wall. The energy consumption for clay fired bricks manufactured locally in homemade kilns can be much higher (e.g. 3 times) (Maini & Ayyappan, 2004).

5. Conclusions

This paper has shown that stabilised soil blocks (SSBs) are a cost-effective sustainable masonry unit. SSBs are significantly cheaper than alternative masonry construction and are widely used in developing countries. Furthermore, in many instances their main constituent, the soil, can be obtained on or close to the site, reducing transport costs and environmental impact. Tests carried out at NUIG have shown promising results for the application of SSBs in the European climate. Further tests are ongoing.

Acknowledgements

The author would like to acknowledge the experimental work carried out by R. Creedon, E. Fitzgerald J. Fogarty, and R. Manton, as part of their BE theses, the results from which have been used in this paper. The author would also like to acknowledge the significant input of the Civil Engineering technical staff at NUIG.

References

Adesanya D.A. (1996). 'Evaluation of blended cement mortar, concrete and stabilized earth made from ordinary Portland cement and corn cob ash'. *Construction and Building Materials*, **10**(6), 451-456.

Adesanya D.A. & Raheem A.A. (2009). 'Development of corn cob ash blended cement'. *Construction and Building Materials*, **23**, 347–352.

American Society for Testing and Materials (ASTM). (2003a). '*ASTM D559-03 Standard Test Methods for Wetting and Drying Compacted Soil-Cement Mixtures*.' ASTM, Pennsylvania.

American Society for Testing and Materials (ASTM). (2003b). '*ASTM D560-03 Standard Test Methods for Freezing and Thawing Compacted Soil-Cement Mixtures*.' ASTM, Pennsylvania.

American Society for Testing and Materials (ASTM). (2007a). '*ASTM D1632-07. Standard practice for making and curing soil-cement compression and flexure test specimens in the laboratory'*. Pennsylvania.

American Society for Testing and Materials (ASTM) (2007b). '*ASTM D1633-07. Standard test methods for compressive strength of molded soil-cement cylinders*'. Pennsylvania, USA.

American Society for Testing and Materials (ASTM). (2008). '*ASTM C618-08a. Standard specification for coal fly ash and raw or calcined natural pozzolan for use in concrete*'. USA.

Bahar R., Benazzoug M., Kenai S. (2005). 'Performance of compacted cement-stabilised soil'. *Cement & Concrete Composites*, **26**, 811-820.

Basha E.A., Hashim R., Mahmud H.B., Muntohar A.S. (2004). 'Stabilisation of residual soil with rice husk ash and cement'. *Construction and Building Materials*, **19**, 448-453.

Bouhicha M., Aouissi F., Kenai S. (2005). 'Performance of composite soil reinforced with barley straw'. *Cement & Concrete Composites*, **27**, 617-621.

British standards institute (BSI). 1990. *BS 1377-2: 1990. Methods of test for soils for civil engineering purposes – part 2: classification tests*. London: BSI.

Browne G. (2009). 'Stabilised interlocking rammed earth blocks: alternatives to cement stabilisation'. *Proceedings of NOCMAT 2009*, 6-9 September 2009, Bath, UK

Creedon R. & Fitzgerald E. (2010). 'Examining the durability of stabilised soil blocks'. *BE Thesis*. Civil Engineering, National University of Ireland, Galway.

Fan M., Marshall W., Daugaard D., Brown R.C. (2004). 'Steam activation of chars produced from oat hulls and corn stover', *Bioresource Technology*, **93**, 103-107.

Fogarty J. & Manton R. (2010). 'Cement substitution in stabilised soil blocks: An assessment by compressive strength'. *BE Thesis*. Civil Engineering, National University of Ireland, Galway

Guettala A., Abibsi A., Houari H. (2006).'Durability study of stabilized earth concrete under both laboratory and climatic conditions exposure'. *Construct & Building Materials*,**20**,119-27.

Hall M. & Djerbib Y. (2004). 'Rammed earth sample production: context, recommendations and consistency'. *Construction and Building Materials*, **18**, 281-286.

Heathcote, K.A. (1995). 'Durability of earthwall buildings'. *Construction and Building Materials*, **9**(3), 185-189.

Hydrafrom (2005). '*Hydraform Zambia Manual, Blockmaking*', Lusaka: Hydraform Ltd.

Intermediate Technology Development Group Zimbabwe (ITDGZ) (2008). 'How to Make Stabilised Soil Blocks (SSB's)'. *Technical Advice Notes Number 2*.

Jayasinghe C. & Mallawaarachchi R.S. (2009). Flexural strength of compressed stabilized earth masonry materials. *Materials and Design*, **30**, 3859-3868.

Maini S. & Ayyappan T. (2004). 'Compressed Stabilised Earth Blocks: A Modern Technology', Auroville Earth, Asian representative of the UNESCO Chair "Earthen Architecture, Constructive Cultures and Sustainable Development", Auroville, India

Maslehuddin, M., Al-Amoudi O.S.B., Rahman M.K., Ali M.R., Barry M.S. (2009). 'Properties of cement kiln dust concrete'. *Construction and Building Materials*, **23**, 2357-61.

Morel J.C., Pkalo A., Walker P. (2004). 'Compressive strength testing of compressed earth blocks', *Construction and Building Materials*, **21(**2), 303-309.

Mulenga M.N., Muya M., Tambatamba M.J., Imasiku M., Chinkusu J.M., Shitumbanuma V. (2005). 'Cement and lime stabilized soil blocks and their quality evaluation'. *Research report, Department of Civil and Environment Engineering, UNZA.*

Ogunye F.O. & Boussabaine H. (2002). 'Diagnosis of assessment methods for weatherability of stabilized compressed soil blocks'. *Construction and Building Materials*, **16**, 163-172.

Oti J.E., Kinuthia J.M., Bai J., (2008). 'Developing unfired stabilised building materials in the UK'. *ICE Engineering Sustainability*, **161**(ES4), 211-218.

Pave, R.F. (2007). 'Strength evaluation of dry-stack masonry'. *Research Report, Master of Science*, School of Civil and Environmental Engineering, University of the Witwatersrand, Johannesburg, Republic of South Africa.

Sayah A.I. (1993). 'Stabilisation of a highly expansive clay using cement kiln dust'. *M.Sc. Thesis, University of Oklahoma*, Graduate College, Norman, Oklahoma, USA.

Tadege, M. (2007). 'Study of Compressed Cement Stabilised Soil Block as an alternative wall making material', *M.Sc. Construction Technology thesis*, Addis Ababa University, Ethiopia.

Udoeyo F.F. & Dashibil P.U. (2002). 'Sawdust Ash as Concrete Material', *Journal of materials in Civil Engineering*, **12**(2), 173-176.

Venkatarama-Reddy B.V. & Jagadish K.S. (2003). 'Embodied energy of common and alternative building materials and technologies', *Energy and Buildings*, **35**, 129–137,

Zaman M., Laguros J.G., Sayah A.I. (1992). 'Soil stabilization using cement kiln dust'. *Proceedings of the 7th International Conference on Expansive Soils*, Dallas, Texas, USA.

INFLUENCE OF MORTAR WATER CONTENT ON THE STRENGTH OF LIME MORTAR MASONRY

A. COSTIGAN, S. PAVIA[1]
[1]Dept. of Civil, Structural & Environmental Engineering,
Trinity College Dublin, Ireland

Abstract

Water content affects mortar properties and the quality of the resultant masonry, however, it is often subjectively determined by the mason by assessing workability. This lack of explicit methodology and data, can lead to lack of mortar consistency and field performance, adversely affecting full uptake of lime mortars into mainstream technology. The aim of this research is to assist develop consistent lime mortars of high quality, that would improve the strength and durability of masonry. To this aim, the paper investigates the compressive, flexural and bond strength of clay brick masonry bound with natural hydraulic lime mortar (NHL2), at variable water contents delivering different workabilities. The results evidenced that increasing the water content by 1% yields a 5mm increase in initial flow (from 165 to 170mm). It was found that this water increment significantly increases the mortar's compressive strength simultaneously reducing its flexural strength, but it does not increase stiffness under compression. It was also evidenced that the 1% water increment significantly enhances the masonry's compressive, bond and flexural strengths. From these, it was concluded that mixing NHL2 mortars to produce a 170mm initial flow will result in a consistently adequate strength and mechanical behaviour for mortar and masonry.

Keywords: compressive and flexural strength, flexural bond strength, initial flow, lime mortar masonry, water content, workability.

1. Introduction

Despite their successful role in construction over many centuries, the use of hydraulic limes declined with the introduction of Portland cement in the early part of the twentieth century along with the knowledge of how to use them. The use of lime mortars has revived in the past two decades with the understanding that they are more compatible with historic fabrics than any other mortars.

Water content is one of the main factors that affect mortar properties and, therefore, the quality of the resultant masonry. It can have a stronger influence on the properties of mortar and masonry, than the binder type or the nature of the aggregate. For example, it has been proven that mortar porosity, density and water absorption are more significantly affected by water content than by the aggregate quality (Pavía & Toomey 2008). In addition, excessive water adversely affects mortar properties lowering mechanical strength and increasing the risk of failure due to shrinkage. Water excess can also render a mortar too fluid to be workable and weaken adhesion at the mortar-masonry interface thus lowering bond strength. Chemical processes such as lime leaching can also be related to a water excess.

However, despite the great importance of water content, in practice, it is often subjectively determined by the mason by assessing the mortar's workability. This lack of explicit methodology and data, can lead to a lack of consistency of mortar properties and field performance, and these adversely affect the large scale uptake of lime mortars into new building and mainstream technology.

Water contents cannot be universally specified for site works due to differences in the composition and nature of aggregates, binders and additions as well as differences in the material moisture content that depend on the environment and storage. As a result, adding the same amount of water to a 3:1 calcium lime mortar in two different building sites can produce mortars with different properties, workability and performance. However, water content can be determined by making a mortar flow to a specific diameter in a flow table, this can ensure consistency in the amount of water added and the mortar's workability, avoiding the variation in mortar properties trigered by differences in water content and providing mortars with consistent properties and field performance.

Water content determines mortar workability. Mortars should contain the maximum amount of water consistent with optimum workability (Davison 1974). The influence of workability (measured as initial flow) on the flexural and compressive strength of NHL mortars was studied by Hanley & Pavía (2008). The authors concluded that one universal flow value is inadequate and that, in order to optimize mortar strength, NHL3.5 and 5 mortars should be mixed to attain a high (185 mm) flow whereas NHL2 mixes require a significantly lower value (165 mm).

The influence of mortar water content on the bond strength of masonry was studied by Pavía & Hanley (2009). They established relationships between masonry bond strength and mortar properties, concluding that, for NHL5 mortars, a high (185 mm) flow results in the strongest bond, simultaneously providing the best workability and highest water retention while, in contrast, for lower hydraulic strengths (NHL2/3.5 mortars), the flow that optimises workability (165 and 165–185 mm respectively) does not lead to the strongest bond, but it is the highest workable flow that results in the strongest bond and, mostly, highest water retention.

This paper investigates the influence of water content and hence workability, on the compressive and flexural strength of NHL2 mortar and the compressive, flexural and bond strength of NHL2-mortar masonry. It also studies the mechanical behaviour of mortar and masonry by assessing their elastic modulus and their strength development over time at 28 and 56 days.

2. Materials and Methods

2.1 Materials

Mortars were made with a feebly hydraulic lime (NHL2) complying with EN 459-2: 2001 and a siliceous aggregate (particle size distribution ranging within the standard limits - EN196–1: 2005). They were mixed with water to attain two initial flows (165 and 170mm). Moulded, frogged, fired-clay bricks (Table 1) were used to build the masonry.

2.2 Mixing and curing; initial flow and workability

Water content is the main contributor to mortar workability and determines initial flow, a measurement that takes into account variables affecting workability, such as porosity, size/shape of aggregate, binder type and aggregate/binder. (Hanley & Pavía 2008). Mortars were mixed to two distinct flows, 165±3mm and 170±3mm, measured in accordance with EN459-2, and the water content reported as the ratio of water to total mortar by mass. Mixing, curing and storage was also in accordance with EN 459-2. A binder: aggregate ratio of 1:3 by weight was kept constant. Masonry wallettes and prisms were constructed in accordance with the relevant parts of EN1052 (1999, 2005) for compressive, flexural and bond strength respectively.

Table 1 Brick Characteristics

Property *(Testing standard: EN 771-1 :2003)*	
Compressive Strength (N/mm^2)	≥ 12
Water absorption (%)	Max 15
Unit size (mm) / Size tolerance	215 x 102.5 x 65 /T2 - R1
Gross / net density (kg/m^3)	1630/ 1920
Initial rate of absorption (kg/m^2/minute)	1.0

2.3 Mechanical properties of mortar

Compressive (R_c,) and flexural (R_f,) strength were determined using Equations 1 and 2 (EN196-1:2005, EN459-2:2001). Where: F_c is the max load at fracture (N); 6400-area of the face (mm); F_f -load at fracture (N); b-prism section (mm); l -distance between supports (mm). The mortar's elastic modulus in both compression and flexion were determined from stress vs strain curves. The modulus of elasticity in compression was found using Equation 3. Where: ϵ_c is the strain; σ_c - stress; d_0 - original depth of the prism (mm) and d_i-d_0 - change in prism depth. Equation 3 was also used to determine the modulus of elasticity of masonry. The modulus of elasticity in flexure was found using Equation 4 (EN1052–5:2005). Where: σ_f is the flexural stress (N/mm^2); ε_f is the strain; m the slope of the linear stress-strain plot and D the deflection in mm.

$$R_c = \frac{F_c}{6400} \quad (\text{N/mm}^2) \tag{1}$$

$$R_f = \frac{1.5 \times F_f \times l}{b^3} \quad (\text{N/mm}^2) \tag{2}$$

$$E_c = \frac{\sigma_c}{\varepsilon_c} = \frac{\sigma_c}{\frac{d_i - d_0}{d_0}} \quad (\text{N/mm}^2) \tag{3}$$

$$E_f = \frac{\sigma_f}{\varepsilon_f} = \frac{\sigma_f}{6Dd/l^2} \frac{l^3 m}{4bd_0^{\,3}} \quad (\text{N/mm}^2) \tag{4}$$

2.4 Properties of masonry

Lateral variable displacement transducers recorded strain during compression (EN1052–1:1999). Equation 5 and 6 were used to determine the compressive (f_i) and characteristic compressive strength. Where: $F_{i,max}$-max load (N); A-loaded cross-section (mm^2). Bond strength was determined with five-brick-high bonded prism stacks (EN1052–5:2005).

$$f_i = \frac{F_{i,\max}}{A_i} \quad (\text{N/mm}^2) \tag{5}$$

$$f_k = \frac{f}{1.2} \text{ or } f_k = f_{i,\min} \quad (\text{N/mm}^2) \text{ whichever is smaller} \tag{6}$$

The flexural strength was calculated for both a plane of failure parallel to the bed joints and one perpendicular to the bed joints according to the methodology and equations in EN 1052–2:1999.

3 Results and Discussion

3.1 Influence of water content on mortar properties

As aforementioned, water content is a main factor affecting workability. Water content is reported in Table 2 as the ratio of water to total mortar mass (EN 459-2). The results (Table 2) evidenced that increasing the water content of the NHL2 mortar by 1% yields a 5mm increase in initial flow and a significant increase in compressive strength (a 24% increase at 28 days and a 37% increase at 56 days- Figure1). This agrees with previous authors (Hanley & Pavía 2008) who tested three different flows (165, 185 and 195 mm) concluding that, for a NHL2 mortar, a flow value closer to 165mm produces the greater compressive strength and an optimum workability.

Table 2 Characteristics of mortars

Property	Type of mortar – NHL 2	
Proportion (lime:sand) by weight	1:3	1:3
Initial Flow (mm)	165	170
Water content (% of total mass)	16.9	17.8
Compressive strength R_c (N/mm^2)		
28 days	1.87	2.32
56 days	2.29	3.14
Elastic Modulus E_c (N/mm^2) under compression		
28 days	26	25
56 days	39	32
Flexural strength R_f (N/mm^2)		
28 days	0.51	0.49
56 days	0.73	0.57
Elastic Modulus E_f (N/mm^2) in flexion		
28 days	100	128
56 days	246	153

Surprisingly, the results also suggest that an increase in compressive strength does not lead to an increased stiffness under compression (Figure 2): the mortar's elastic modulus in compression remains nearly constant at 28 days but reduces by 18% at 56 days. This indicates that over time, under compression, the mortar increases strength simultaneously becoming more plastic.

At 28 days, the flexural strength of NHL 2 mortar does not appear to be greatly affected by the water content increase (it reduces by 0.02 N/mm^2). However, at 56 days the flexural strength reduces by 22% (Figure 3). The elastic modulus in flexion does not show a consistent trend (Figure 4).

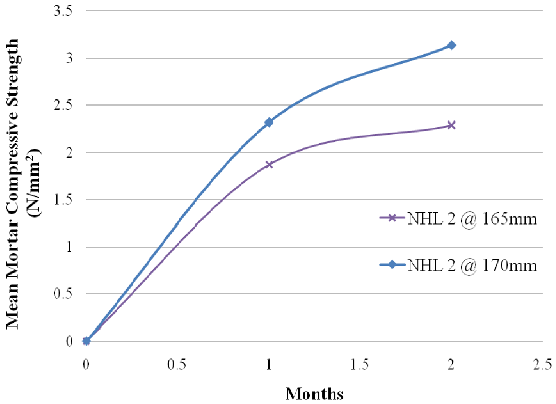

Figure 1 - Compressive strength of mortars

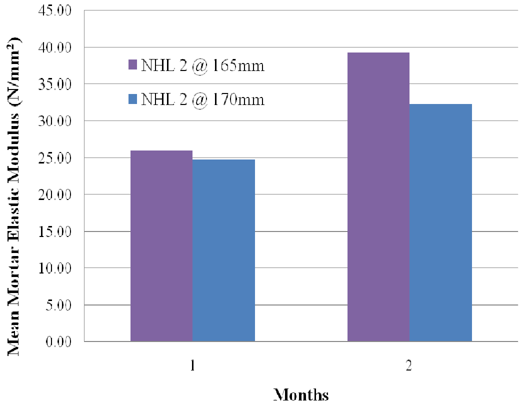

Figure 2 - Elastic modulus of mortars under compression

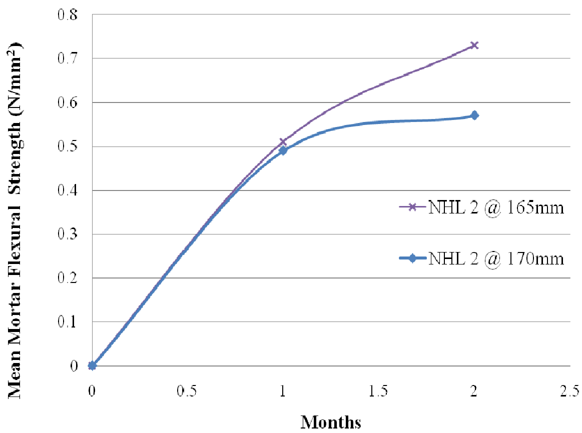

Figure 3 - Flexural strength of mortars

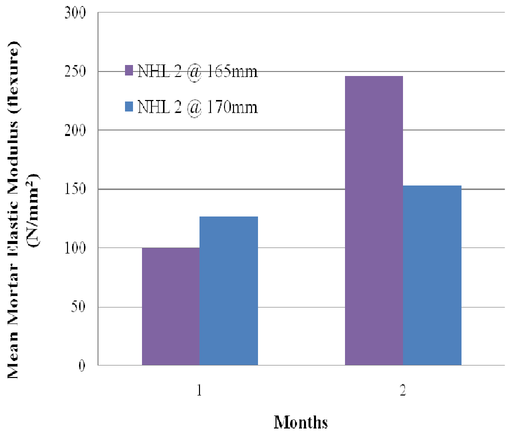

Figure 4-Elastic modulus of mortars in flexion

3.2 Influence of mortar water content on masonry properties

As it can be seen from the results in Table 3 and Figures 5 and 6, increasing the initial flow from 165 to 170mm leads to significant increases in both the bond strength and the compressive strength of the masonry: at 56 days, the compressive strength of the masonry increases by 24% (from 4.59 to 6.53) while the masonry bond strength increases by 29%.

The results also show that, while the mortar's elastic modulus in compression reduces due to the increase in water content (Figure 2), in contrast, the elastic modulus of the masonry increases both at 28 and 56 days, showing an increase of approximately 20% at 56 days (Figure 7). These indicate that, as the water content increases by 1% (from 165 to 170 mm flow), the mortar becomes less stiff while the masonry becomes stiffer. Finally, the masonry's flexural strength both parallel and perpendicular to the joints (Figure 8) increases with the water increment (11% and 22% for the flexural strength parallel to the joints and 2 and 4% for that perpendicular to the joints at 28 and 56 days respectively) in contrast, as aforementioned, the flexural strength of the mortar drops with increasing flow.

This lack of correlation between the strength and mechanical behaviour of the mortar and those of the masonry has been evidenced before (Costigan & Pavía 2009 and 2010). These agree with previous authors concluding that the masonry's compressive strength is more sensitive to the brick-mortar bond strength than to the compressive strength of the mortar (Sarangapani et al. 2005), and that the masonry's bond and compressive strengths are not significantly impacted by the strength of the mortar (Venumadhava Rao et al. 1997).

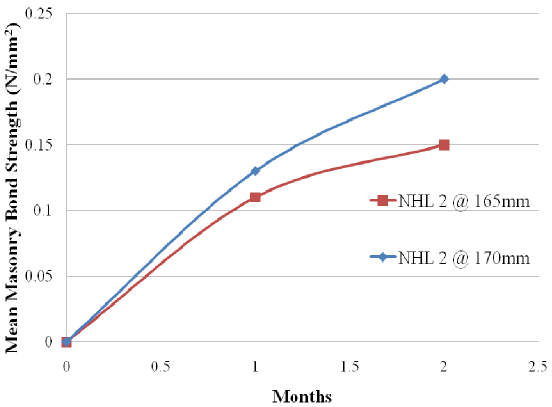

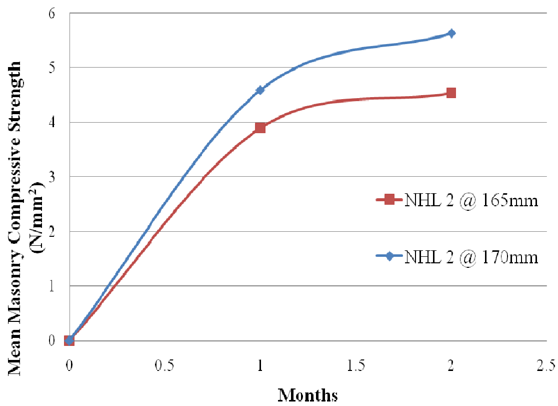

Figure 5 - Influence of mortar's water content on the compressive strength of masonry

Figure 6 - Influence of mortar's water content on masonry's bond strength

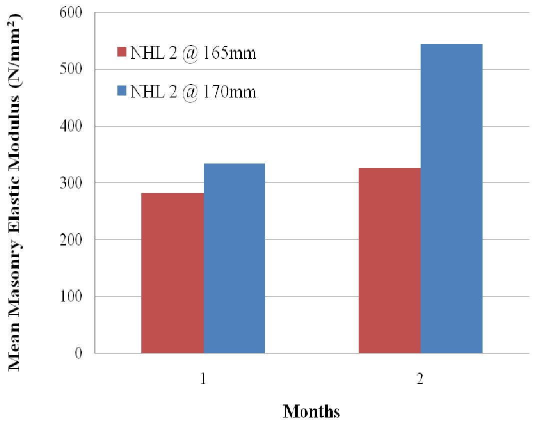

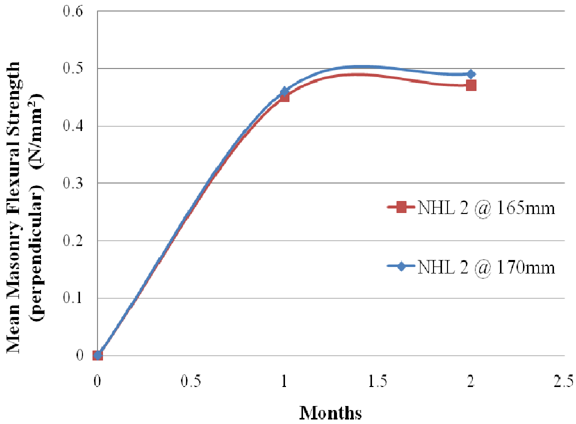

Figure 7 - Influence of mortar's water content on the elastic modulus of masonry

Figure 8 - Influence of mortar's water content on the flexural strength of masonry

Table 3 - Properties of masonry built with NHL 2 mortar with different water contents.

Mortar Initial Flow (mm)	Age (days)	Compressive Strength (N/mm^2)	Elastic Modulus (N/mm^2)	Mean flexural strength parallel to bed joints (N/mm^2)	Mean flexural s. perpendicular to bed joints (N/mm^2)	Mean bond strength (Bond wrench test) (N/mm^2)
165 mm	28	3.90	281	0.08	0.45	0.11
170 mm		4.59	334	0.09	0.46	0.13
165 mm	56	4.54	325	0.14	0.47	0.15
170 mm		5.63	544	0.18	0.49	0.20

(Mean of 3 specimens for compressive/bond strength/elastic modulus; 5 for flexural strength)

4 Conclusions

Increasing the water content of NHL2 mortar by 1% yields a 5mm increase in the initial flow value (from 165 to 170 mm). It was found that, while this increase in water content leads to a significant increase in mortar compressive strength (24% increase at 28 days and 37% at 56 days), it does not lead to an increased stiffness in compression.

Increasing the water content by 1% reduces the flexural strength of the mortar simultaneously raising the masonry's flexural strength both parallel and perpendicular to the joints (by 11% and 22% for the flexural strength parallel to the joints at 28 and 56 days respectively and 2 and 4% for that perpendicular to the joints).The masonry's flexural strength parallel to the bedding joints experiences a greater increase than that perpendicular to the joints.

A 1% increase in mortar water content leads to significant increases in both the bond strength (29% increase at 56 days) and the compressive strength of the masonry: 24% increase at 56 days. Therefore a 170mm flow value enhances NHL 2 mortar masonry strength.

Under compression, as the water content increases by 1%, the mortar becomes more plastic while the masonry becomes stiffer.

Acknowledgements

The authors thank Paul McMahon, National Monuments, Architectural Heritage Division, Office of Public Works, for supporting and funding this project. All testing was carried out in the Dept. of Civil Engineering, Trinity College Dublin. The authors thank Chris O'Donovan, Dr. Kevin Ryan and Dave Mc Auley for their assistance with testing. The authors also thank The Traditional Lime Company, St Astier/CESA Limes, Clogrenanne Lime Ltd and Kingscourt brick for donating materials.

References

Costigan A., Pavía S. (2009) A comparative study of the compressive, flexural and bond strength of brick masonry. Proceedings of PROHITEC 09 – Mazzolani editor, Taylor and Francis Group, London, 1609-1615.

Costigan A., Pavía S. (2010) Mechanical properties of clay brick masonry bound with hydraulic limes and hydrated calcium lime. 8th Int Masonry Conference, Dresden University of Technology.

Costigan A., Pavía S. (2010) Influence of the hydraulic strength of mortar on the mechanical behaviour of lime mortar masonry. HMC 2010. Inst of theoretical and applied mechanics. RILEM Prague.

Davison J. I. (1974) CBD-163 Masonry mortar. Canadian Building Digest.

Hanley R., Pavía S. (2008) A study of the workability of natural hydraulic lime mortars and its influence on strength, *Materials and Structures*, 41 (2), 373 – 381

EN196–1 (2005) Method of testing cement. Part 1 – Determination of strength.

EN459-2 (2001) Building lime. Test methods.

EN1052–1 (1999) Method of testing masonry. Determination of compressive strength.

EN 1052–2 (1999) Method of testing masonry. Determination of flexural strength.

EN1052–5 (2005) Method of testing masonry. Determination of bond strength (Bond wrench method).
Pavía S., Hanley R. (2009) Flexural bond strength of natural hydraulic lime mortar and clay brick, *Materials and Structures*, published with open access.
Pavía S., Toomey B. (2008) Influence of the aggregate quality on the physical properties of natural feebly-hydraulic lime mortars, *Materials and Structures*, 41, 559 – 569
Sarangapani G, Venkatarama Reddy BV, Jagadish KS (2005) Brick–mortar bond and masonry compressive Strength. J Mater Civil Eng (ASCE) 17(2):229–237
Venumadhava Rao, K., Venkatarama Reddy, B. V., Jagadish, K. S. (1995). Influence of flexural bond strength on the compressive strength of masonry. Proc. Nat. Conf. on Civil Eng. Materials and Structures, Osmania Univ., Hyderabad, India, 103–108.

EFFECT OF POZZOLAN PROPERTIES ON THE PROPERTIES OF BUILDING COMPOSITES

R. WALKER, S. PAVÍA
Dept. of Civil Engineering, University of Dublin, Ireland

Abstract
Pozzolans were used by ancient civilizations to enhance the properties of mortars and concrete and are now regaining popularity as sustainable, environmentally-friendly alternatives to cement. This paper studies the relationships amongst some properties of nine pozzolans and their impact on compressive strength and setting time of the resultant composites. Its objective is to assist in making informed choices in the selection of pozzolans for the production of mortars and concrete. Results indicate that each pozzolan has a specific water demand that increases with its specific surface area; and that a high water demand by the pozzolan slows down the setting of the paste but does not undermine the strength of the composite. It was also found that specific surface has a much greater influence on the water demand of the paste than particle size or lime:pozzolan ratio. The results exposed the adverse effect of a small water increase on setting time, and the lack of relationship between setting and reactivity. It was evidenced that the pozzolans accelerate the final set of lime by at least 40%: and that the specific surface area of the pozzolan and its amorphousness are the most important variables affecting reactivity and strength. Pozzolan reactivity was determined by strength development and a chemical activity index.

Keywords: amorphousness, compressive strength, particle size, pozzolan, reactivity, setting time, specific surface, water demand.

1. Introduction

Pozzolans are materials with an amorphous siliceous or siliceous and aluminous content that react with portlandite ($Ca(OH)_2$) in the presence of water to form cementitious hydration products (calcium silicate and calcium silicate aluminate hydrates). They have been used to enhance the properties of composites since antiquity. Pozzolans are often industrial or agricultural by-products and their use has economic and environmental benefits such as lowering the cost of construction and the recycling of waste, while also reducing energy consumption, raw material consumption and CO_2 emissions (Pavía & Regan 2010).

When mixed with lime and water, pozzolans react with portlandite forming hydration products and thereby accelerate the slow hardening process (carbonation) of calcium limes by imparting an hydraulic set. When combined in the right ratio, pozzolans increase the ultimate strength of lime composites: the compressive strength at 2 years can be as high as 3 times the 28-day strength (Massaza 2007).

When mixed with PC and water, pozzolans react with the portlandite, formed during hydration of calcium silicates. As a result, the portlandite content pozzolan-PC pastes is lower than that of the parent PC. In general, replacement of PC by pozzolans lowers early strength and improves the long term one: initially, the pozzolan behaves as an inert material reducing the initial rate of strength gain. However, at greater ages, pozzolanic reaction begins and pozzolan cement attain the same or higher strengths than the parent PC.

Pozzolans can enhance durability of composites so they are used in the production of high performance Portland Cement (PC) concrete with a view to improve the service life of concrete structures. Pozzolans partially replacing PC usually result in materials with higher porosity (especially at early ages due to the reduction of hydration products) but lower permeability and sorptivity and smaller diffusion coefficients than the parent PC (Massazza referring to Day et al. 1989; Ganesan et al. 2008). They also affect the kinetics of hydration, the composition of some hydrates and the heat of hydration of PC composites (Sánchez de Rojas & Frías 1996; Mostafaa & Brown 2005). Some pozzolans reduce the alkalinity of the pore solution, and this impacts on the durability of concrete.

This paper studies the impact of some physical properties of pozzolans including particle size, specific surface, amorphousness, water demand and reactivity, on the density, porosity, compressive strength and setting time of composites, in order to understand and predict the behavior and quality of pozzolan composites for building. Lime pastes were tested but the results are applicable to both PC and lime composites as, in both cases, pozzolanic reaction is based on portlandite consumption.

Particle size, specific surface and amorphousness have been linked to reactivity by former authors. An increase in surface area will expose a greater surface to chemical reaction enhancing reactivity. Amorphous structures are more reactive than crystalline ones on account of the greater mobility and superficial location of their atoms and glassy pozzolans are considered to be active while crystalline material is not.

The setting time of pozzolan cement does not differ from that of PC. Some pozzolans such as fly ash usually delay both initial and final setting times (Massazza 2007 referring to Berry and Malhotra 1987). Finally pozzolans can either increase or reduce water demand depending on the nature of the pozzolan and the properties of the binder with which they are mixed.

2. Materials and Methods

2.1 Materials

Nine pozzolans were studied including Ground Granulated Blastfurnace Slag (GGBS); Leca; Pulverised Fuel Ash (PFA); Calcined Clay (MetaStar); Microsilica (MS); Rice Husk Ash (RHA); Red Brick Dust (RBD); Tile and Yellow Brick Dust (YBD). Two lime:pozzolan ratios 1:1 and 1:3 (by weight) were investigated. The water content was fixed to produce a flow diameter of 165mm. A hydrated commercial lime (CL90s) complying with EN 459-1 was used.

2.2 Properties of the pozzolans

Chemical composition was determined by XRF analysis, using a Quant’X EDX Spectrometer and a UniQuant analysis package. The samples were mixed with Hoescht wax and pressed into aluminum cups using a 10 tonne hydraulic press. Amorphousness was analysed by X-Ray Diffraction (XRD), using a PW1720 XRD with a PW1050/80 goniometer and a PW3313/20 Cu k-alpha anode tube at 40kV and 20mA. Measurements were taken from 3 to 60 degrees (2θ) at 0.02 degrees/second. Particle size was determined with laser diffraction using a Malvern Mastersizer 2000. Specific surface area was measured using a Quantachrome Nova 4200e and the BET method, a model isotherm based on adsorption of gas on a surface.

2.3 Reactivity of pozzolans: chemical activity index

This method follows the pozzolanic reaction indirectly by measuring the changes in the conductivity of a saturated lime and pozzolan solution. The fixation of dissolved $Ca(OH)_2$ reduces portlandite concentration in solution, leading to a decrease in conductivity. 4g of pozzolan were added into a saturated solution of lime (electrical conductivity reading 9.8mS at 20°C). The solution was continuously stirred by a magnetic stirrer and the conductivity and temperature measured at intervals over 125hours using a WTW LF 197 conductivity meter with a Tetracon 325 probe.

2.4 Pozzolan water demand and setting time of the paste

Water demand was assessed by measuring initial flow in accordance with EN459-2 for ratios of 1:1 and 1:3 (lime:pozzolan). The water content was adjusted to produce a 165mm flow diameter. Mixing was in accordance with EN 459 except for the addition of the pozzolan (added after 1 minute and the mixing stopped for 30 seconds). Setting times were measured on the pastes above, including the water required in order to produce a standard consistency (165mm flow).

2.5 Compressive strength development

The prisms were demoulded after 1 day and stored in a curing room at 20°C±3°C temperature under damp hessian to maintain humidity at c.95%. The unconfined compressive test was measured with a Zwick loading machine according to EN 459-2. Water content was determined by fixing the initial flow. The low water demand pozzolans (GGBS, Leca, PFA, RBD, Tile and YBD) were given a lime:pozzolan:sand:water ratio of 1:1:3:1 and therefore a binder: water ratio of 0.5 while the ratio for those with a with a higher water demand (Meta, MS and RHA) was 1:1:3:1.5.

2.6 Bulk/real densities and porosity

These were tested on the compressive strength samples (RILEM 1980). Bulk density (δ) is the ratio of the dry mass of the sample to its bulk volume while real density (δr) is the ratio of the dry mass to its impermeable volume. Both inform on grain packing and compaction and enable calculating the effective or open porosity (P).

3. Results

3.1 Pozzolan particle size, surface area, composition, amorphousness and water demand.

Figure 1 includes the particle size distribution of the pozzolans. According to the results, Metastar, RHA and GGBS are the finest. The microsilica particles flocculated during the laser analysis on account of their extremely small size, therefore, the MS is finer than determined by the laser method. According to the specific surface area results (Table 1), MS, Metastar and RHA have a much greater specific surface than any of the other pozzolans.

The chemical composition and amorphousness of the pozzolans are included in Table 2. Amorphousness was loosely categorised into 4 groups ranging from totally amorphous (displaying a large amorphous hump and no crystalline fraction in the XRD pattern) to slightly amorphous (very small amorphous hump). According to these, GGBS, Meta, MS and RHA are the most reactive; followed by Leca and PFA. Finally, YBD, RBD and Tile are the least active pozzolans.

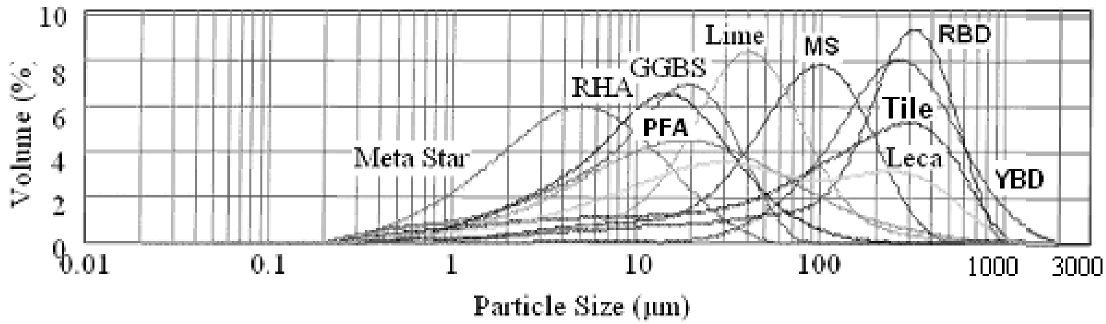

Figure 1 - Particle size distribution of pozzolans.

Table 1 - Specific surface area of pozzolans.

Pozzolan	GGBS	Leca	PFA	Meta	MS	RBD	RHA	Tile	YBD
Surface area m^2/g	2.65	1.28	4.09	18.3	23.6	4.29	13.7	4.16	0.31

The water demand of each pozzolan was calculated based on the water demand of the lime (water:lime ratio for the lime to flow 165mm is 0.862), the amount of lime and pozzolan, and the total water content of the paste. According to the results, the pozzolans were divided into two groups of high (Meta, MS and RHA) and low (GGBS, Leca, PFA, RBD, Tile and YBD) water demand respectively.

Table 2 - Chemical composition and amorphousness of the pozzolans. – not detected.

Pozzolan	**SiO_2**	**Al_2O_3**	**CaO**	**Fe_2O_3**	**SO_3**	**K_2O**	**MgO**	**Rate of amorphousness**
GGBS	34.14	13.85	39.27	0.41	2.43	0.26	8.63	(5) Totally
Leca	52.78	24.39	3.59	11.42	0.39	2.82	2.70	(3) Intermediate
Meta	51.37	45.26	-	0.52	-	2.13	0.55	(4) Mostly
MS	92.10	2.13	1.10	1.62	0.28	1.32	1.05	(4) Mostly
PFA	65.32	24.72	0.94	4.84	0.37	1.37	0.68	(3-2) Intermediate to slightly
RBD	48.24	22.15	10.31	6.67	6.94	2.97	1.17	(2) Slightly
RHA	93.84	1.93	0.68	0.29	-	1.38	0.45	(4) Mostly
Tile	46.61	21.47	11.34	7.19	7.62	3.05	1.12	(2) Slightly
YBD	43.90	44.94	0.36	2.11	-	1.27	6.28	(2) Slightly

3.2 Effect of pozzolan properties on water demand

The results indicate that the water demand depends on the pozzolan’s particle size and specific surface, and on the lime:pozzolan ratio (Figure 2). However, specific surface has a considerably greater influence on water demand than particle size or ratio. As expected, the greater surface pozzolans had a higher water demand. Specific surface has a much greater influence on water demand than particle size (RHA and GGBS have a similar particle size while RHA has a greater surface and a significantly higher water demand). It was noted that replacing lime by pozzolan lowered the water demand of all pastes with the exception of Metastar. This is due to the greater water demand of the Metastar with respect to lime on account of its high specific surface.

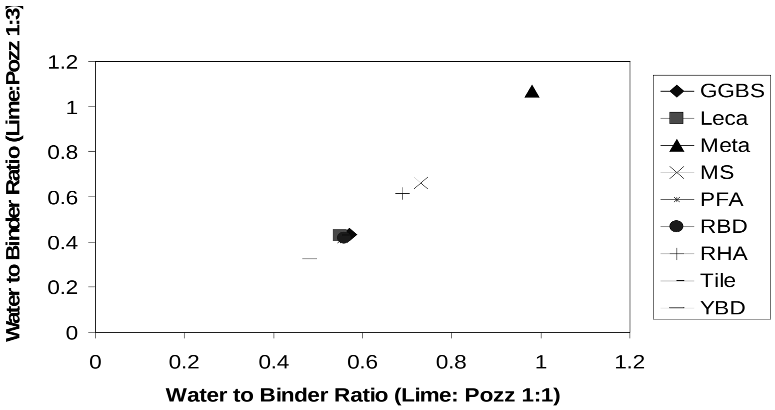

Figure 2 - Water demand of pozzolans in lime:pozzolan pastes of ratios 1:3 and 1:1

3.3 Reactivity of pozzolans and strength development of the paste

A high reactivity (acceleration of the pozzolanic reaction) positively affects strength development because strength builds up with increasing amount of combined lime. Therefore, strength development and reactivity (chemical index) are closely related.

According to the strength and chemical index results (Table 3), Metastar, GGBS, RHA and MS are the most reactive (Walker and Pavía 2010). These pozzolans are either totally (GGBS) or mostly amorphous (Metastar, RHA and MS). In addition, Metastar, RHA and MS have a specific surface much higher than any of the other pozzolans, while GGBS has a lower specific surface but it is amongst the finest. This indicates that specific surface and amorphousness are important variables affecting reactivity and strength development. Although not sensitive to the chemical reactivity index, GGBS has a strength comparable to that of Metastar, much higher than any of the other pozzolans and can therefore be considered amongst the most reactive.

Table 3. Pozzolan reactivity and compressive strength of the paste. (*) ratio of the compressive strength of the lime/pozzolan mix to a standard lime/sand mix.

Pozzolan	Compressive strength	Chemical Activity Index	
		Phase 1 % drop	Latent Period (hrs)
GGBS	29.5	-	-
Leca	4.6	-	-
PFA	3.4	3.4	65.0
Meta	38.1	9.8	18.0
MS	12.5	4.3	39.5
RBD	2.5	2.5	91
RHA	12.0	6.8	55.0
Tile	3.3	3.5	90.0
YBD	1.2	3.9	67.0

Strength increases with decreasing particle size (Figure 3). The well known filler effect of fine pozzolans may be partially responsible for the high strength of the finer pozzolans (GGBS, Metastar and RHA). A clear relationship between increasing amorphousness (Table 3) and increasing reactivity was established for the nine pozzolans (Figure 4). In addition, the higher water demand pozzolans show the greatest 28-day strength. Therefore, water demand of the pozzolan does not affect compressive strength of the paste. Metastar and GGBS displayed higher compressive strength values than any other pozzolans; followed by the high-silica RHA and MS (68% reduction); and finally the PFA, Leca and brick dusts (89% lower than the Metastar).

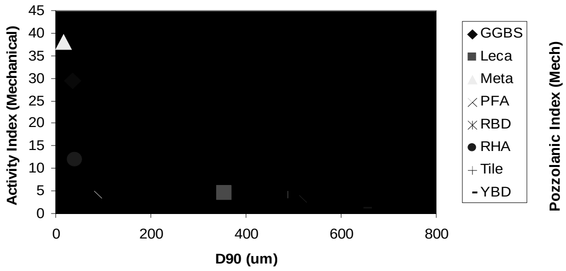

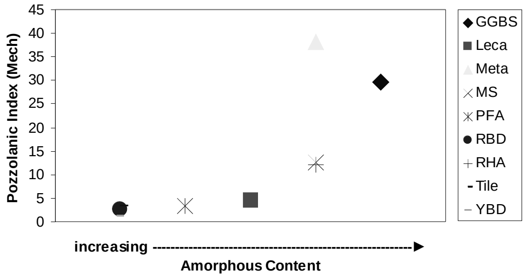

Figure 3- Relationship between particle size and strength development

Figure 4 - Influence of increasing pozzolan amorphousness on strength

3.4 Setting time

All pozzolans reduced the final setting time (when compared to that of the lime alone) by at least 40% (Figure 5). In addition, except for PFA and MS, the pozzolans also accelerated the initial set (Figure 5). The results did not evidence a relationship between setting time and pozzolan reactivity, this may be due to the low speed of the pozzolanic reaction. In addition, a pozzolan can be more reactive than another pozzolan and yet need more time to set if the hydration products initially formed make a smaller contribution to the stiffness of the paste.

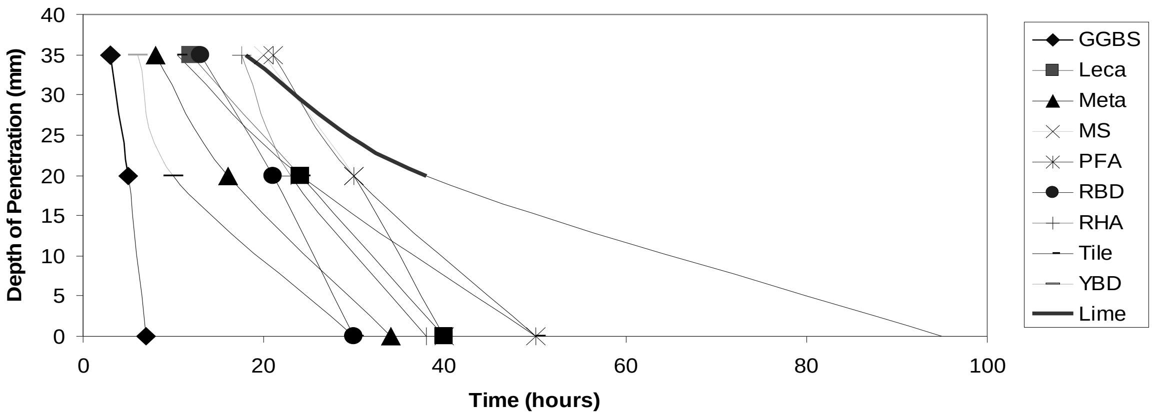

Figure 5. Setting time of lime and lime:pozzolan pastes at ratio 1:3, except for Metastar with a ratio of 1:1 (each value is an average of 3 results).

It was evidenced that a small increase in water content (5%) significantly retards setting. The adverse influence of water increase was also evidenced in the Metastar paste. Here, due to the greater water requirement of this pozzolan, setting time had to be measured in a 1:3 paste, which provided values comparable to those of other pozzolans in 1:1 pastes. It can be seen from the results that the GGBS paste sets significantly faster than any other paste. It is the fastest to develop an initial set and takes only 7 hours to fully set. GGBS can contain calcium silicates and aluminates similar to those found in PC clinkers, thus being a hydraulic rather than a pozzolanic material. Neither silicates nor aluminates were detected with XRD in the GGBS. However small amounts of silicates/aluminates, beneath the limit of detection of the XRD (at 5%) can be present, accelerating the set. In addition, GGBS contains little alumina (13.85%) and is the only pozzolan that is totally amorphous and has a high calcium content (39.27%). These may also contribute to the early set of the GGBS paste.

3.5 Densities and porosity

The high water demand pozzolans (Meta, RHA and MS) display the lowest real density and the greatest difference between real and bulk density thus including the greatest amount of voids. In contrast, the low water demand pozzolans (GGBS, PFA, RBD, Tile and YBD) have a real density greater than that of the reference lime. The results agree with Papayianni, (2006) who determined that, in lime pozzolan mortars, water/binder ratio is the most important factor influencing porosity.

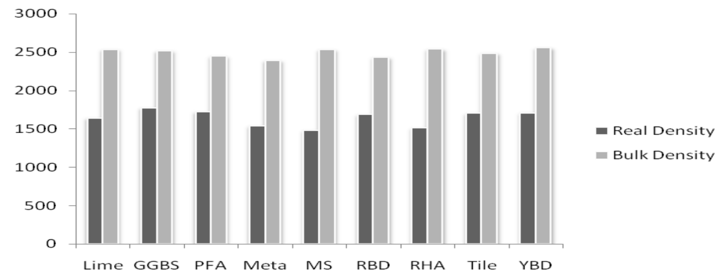

Figure 6. Real and bulk densities of lime:pozzolan mortars.

For both the high and low water demand pozzolans, a relationship between particle size and porosity was evident (figure 7), with porosity reducing as pozzolan particle size decreases. The well established relationship between increasing strength with reducing porosity in lime pozzolan mortars was evident at the two water contents (figure 8). However as noted by Papayianni (2006), strength is also dependant on the pozzolanic reactivity and the Meta, RHA and MS, despite having a higher porosity on account of the high water demand also have a higher strength.

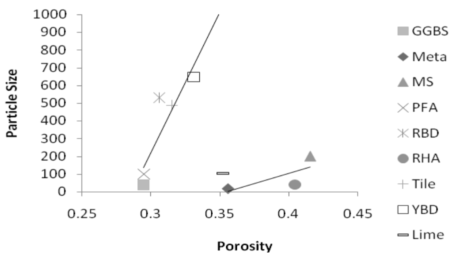

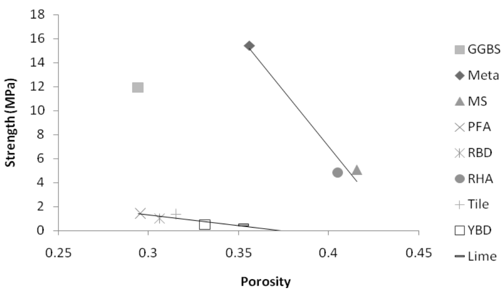

Figure 7- Relationship between porosity and particle size

Figure 8 - Relationship between porosity and strength

4. Conclusion

The conclusions below can contribute to making an informed choice in the selection of pozzolans for the production of building composites.

When high reactivity and a high strength development rate are required, pozzolans of high specific surface area and amorphousness should be used. The fact that strength also increases with decreasing particle size should also be taken into account. According to the strength development and the reactivity results, Metastar, GGBS, RHA and MS are the most reactive pozzolans.

Water content should be carefully determined in the production of pozzolan composites as a small increase in water content will significantly retard the set and will increase the porosity of the composite. Each pozzolan has a specific water demand that is mainly determined by its specific surface area. However, a high water demand by the pozzolan will not undermine the composite's compressive strength

Acknowledgements
The authors thank the EPA for funding this research. They also thank the Traditional Lime Company, Clogrennane Lime, Larsen Building Products and Ecocem for providing materials; Dr R. Goodhue (Geology Dept.) and Ms E. Treacy (Geography Dept.), Trinity College, for their help with the XRD and laser equipment respectively.

References
EN 459–1 (2001), Building lime—part 1. Definitions, specifications and conforming criteria. British Standards Institution, London.
EN 459-2:2001 (2002), Building lime—test methods. British-Adopted European Standard.
Ganesan, K., Rajagopal, K., Thangavel, K, (2008), 'Rice husk ash blended cement: Assessment of optimal level of replacement for strength and permeability properties of concrete', *Construction and Building Materials*, **22**, 1675–1683.
Massazza, F., (2007), 'Pozzolana and pozzolanic cements', in: *Hewlett P.C. Ed. Lea's Chemistry of Cement and Concrete*, Elsevier, UK, 471-602.
Mostafaa, N.Y., Brown, P.W., (2005), 'Heat of hydration of high reactive pozzolans in blended cements: Isothermal conduction calorimetry', *Thermochimica Acta*, **435**, 2, 162-167
Papayianni, I., Stefanidou, M., (2006), 'Strength–porosity relationships in lime–pozzolan mortars, *Construction and Building Materials,* **20**, 700–705
Pavía, S., Regan, D., (2010), 'Influence of cement kiln dust on the physical properties of calcium lime mortars', *Materials and Structures,* **43**, 381-391.
RILEM (1980), 'Essais recommandés pour mesurer l'alteration des pierres et évaluer l'efficacité des méthodes de traitement. Materiaux et Constructions, Bull. Rilem, **13,** 75, 216-220.
Sánchez de Rojas, M. I., Frías, M., (1996), 'The pozzolanic activity of different materials, its influence on the hydration heat in mortars', *Cement and Concrete Research* Volume, **26**, 2, 203-213.
Walker, R., Pavía, S., (2010), 'Behaviour and Properties of Lime-Pozzolan Pastes', in *8th Int Masonry Conference*, Dresden University of Technology.

MODELLING EARTHQUAKE RESISTANT HOLLOW AND FILLED STEEL BRACES

A.D.HUNT & B.M.BRODERICK
Dept. of Civil, Structural & Environmental Engineering, University of Dublin, Trinity College Dublin, Ireland

Abstract

Extensive damage to bridges during the 1995 Hyogo-ken Nanbu earthquake has increased awareness that modern bridges can be seismically vulnerable. Concentrically braced frames (CBFs) are suitable for earthquake resistant design due to their economical strength and stiffness. The seismic performance of steel CBFs is very sensitive to brace behaviour. If the brace sections are thin-walled the onset of local buckling reduces ductility and may lead to brittle failure. In this paper, 2-D idealised brace numerical models developed in the finite element framework OpenSees, are presented to predict the inelastic buckling behaviour of hollow and filled steel braces.

Keywords: Bent; Bracing; Analysis; Earthquake; Substructure.

1. Introduction

Steel moment-resisting frames have long been considered the most suitable structural systems for use in regions of high seismicity. However, unanticipated brittle fracture of connections during the 1994 Northridge and the 1995 Hyogo-ken Nanbu earthquakes were contradictory to the expectations of many structural engineers who anticipated that such systems would undergo large plastic deformation. In particular, the Hyogo-ken Nanbu earthquake caused various kinds of damage to rectangular steel columns in steel bridge piers (Matsumura et al. 2003). An alternative option for lateral resistance is offered by CBFs whose response is characterised by their relatively larger stiffness than that of moment-resisting frames and consequently, their lateral response achieves reduced interstorey drifts. The seismic performance of these frames is sensitive to the pinched hysteretic behaviour of the braces (Ibrahim et al. 1988). As such, energy dissipation in capacity design generally provides allowances for yielding and buckling in the diagonal braces rather than other members of the frame.

Although hollow cold-formed members are effective at resisting compressive axial loads, the onset of local buckling can prevent the steel from developing its full yield strength in compression, reduce ductility and may lead to brittle failure (Uy 1998). Thin-walled sections are most susceptible to local buckling as the occurrence of local buckling in struts is influenced by section properties such as width-to-thickness ratio. Studies have been performed on the hysteretic response of steel braces that examined the effect of brace slenderness, cross-sectional shape and end conditions on buckling capacity (Black et al. 1980; Tremblay et al. 2003). Their main findings showed that the slenderness of a brace appears to be the most important factor in determining the hysteretic behaviour and their ductility is reduced significantly due to local buckling in the sections. If the sections are void-filled with mortar, the thin steel walls are restrained from buckling inward and hence the local buckling pattern is altered to a higher eigenmode. This pattern change delays the onset of local buckling and increases the energy dissipated by up to 85% in thin-walled sections (Zhao et al. 2002). However, Broderick et al. (2005) have shown that energy dissipated decreases with increased member slenderness for both filled and hollow specimens.

(a) (b)

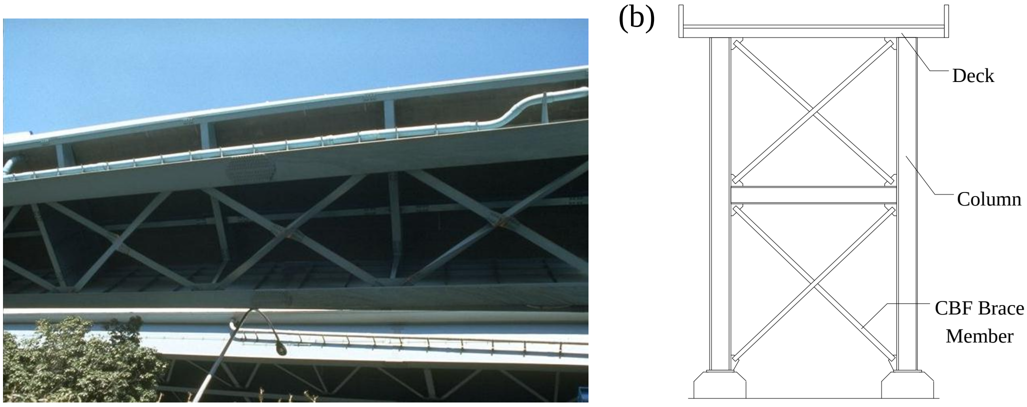

Figure 1 – (a) Brace damage sustained during 1995 Hyogo-ken Nanbu earthquake (Thewalt 1995) and (b) Typical bridge bent with CBF system

Using OpenSees, an object-orientated framework for finite-element analysis, this paper demonstrates the capability of an inelastic beam-column element model in modelling the monotonic and hysteretic response of mortar-filled steel braces for use within CBFs. The beam-column element of this analysis has several limitations; the most significant of which is its dependability on small deformation theory in the basic system. Small deformation theory is based on the assumption that plane sections remain plane and shear distortion has no contribution after deformation so that section shape is retained. In physical terms, this implies that local buckling of braces is not modelled and will affect the numerical correlation to experimental results for sections susceptible to local buckling. It is therefore necessary to investigate the significance of this modelling drawback. However, for compact sections with larger normalised slenderness values and mortar-filled sections it is shown that the OpenSees models demonstrate reasonable fidelity. The inelastic frame element used in the analysis accounts for the distributed inelasticity through integration of material response over the discretised fibre cross section and subsequent integration for a designated number of points along the brace element (Uriz and Mahin 2008b).

This modelling method is validated through a suite of correlation studies with hollow and mortar-filled steel braces and square and rectangular cross-sections tested by Goggins (2004) using a series of monotonic and cyclic complementary tests. These complementary tests form a benchmark for the correlation studies in which the OpenSees inelastic beam-column element models are validated. Having achieved successful validation of the physical fibre theory models, it is envisaged that these will in turn, be utilised in the planning and prediction of a sequence of shake table tests that form a joint research project between researchers in Trinity College Dublin, Imperial College London, University of Ljubljana, National University of Ireland, Galway and University of Liege. The collaborative project entitled ‘Improved European Design and Assessment Methods for Concentrically Braced Frames’ aims to investigate the ultimate response of realistic CBFs, validate numerical models for CBFs and recommend improved design guidance for Eurocode 8 (CEN 2004). The shake table tests will be carried out within the scope of the Seismic Engineering

Research Infrastructures for European Synergies (SERIES) project utilising the AZALEE Shaking Table housed by The Seismic Laboratory of the Commissariat à l'Énergie Atomique (CEA) located in Saclay, France. This paper aims to underpin the modelling capability of the proposed OpenSees physical theory model so that hollow and filled steel brace behaviour within CBFs can be predicted with good confidence for the SERIES project.

2. Correlation Study with Experimental Results

The following correlation studies are intended to demonstrate the capabilities and the limitations of the OpenSees physical theory model for a variety of both hollow and filled cross section shapes as investigated by Goggins (2004). The three section shapes tested were 40x40x2.5SHS, 20x20x2.0SHS and 50x25x2.5RHS and are classified as Plastic, or Class 1 according to Eurocode 3 (CEN 2005). The tests used in the correlation study are scheduled in Table 1. Boundary conditions of the specimens were fully fixed for all of the cyclic displacement tests. The non-dimensional slenderness ratio $\bar{\lambda}$ was calculated about the weak axis (Figure 2) providing a normalised ratio of the slenderness of each specimen. Eurocode 3 (CEN 2005) defines $\bar{\lambda}$ as $(N_{pl,Rd}/N_{cr})^{0.5}$ where $N_{pl,Rd}$ is the plastic section resistance and N_{cr} is the theoretical (Euler) elastic critical buckling force based on the gross section properties and effective length. Stiffener plates with 8 mm thickness and 125 mm height run through the centre of the faces of the hollow steel sections along the y-axis in order to influence the direction of buckling. The length of the specimens (L_T) used for this study was 1100 mm but the stiffener plates provided an unstiffened length (L_0) of 850 mm for all specimens.

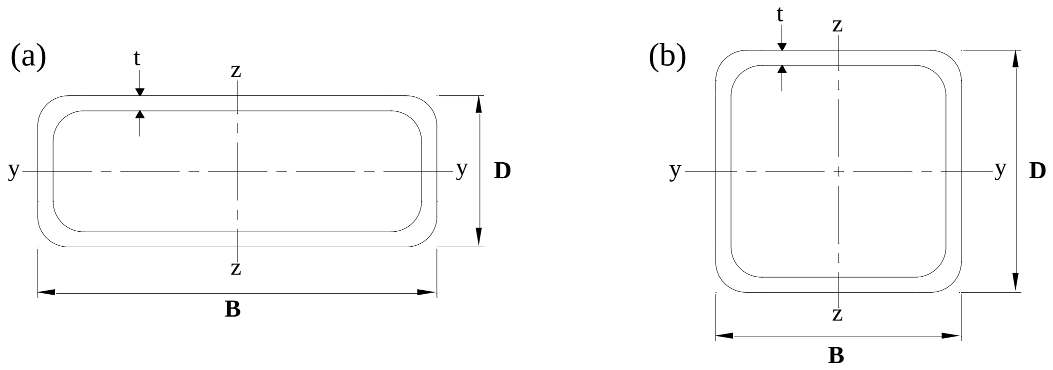

Figure 2 – (a) RHS and (b) SHS dimension definitions

The numerical model consists of seven integration points per inelastic beam-column element and seven elements per strut model. The discretised fibre section model was designed to incorporate both the aforementioned standard sections and also those element sections that include the stiffener plates. As recommended by Uriz and Mahin (2008b), an initial imperfection of 0.1% brace length was assumed mid-brace in the model geometry. In order to model the hysteretic material response of the brace, the Giuffré-Menegotto-Pinto model and Kent-Scott-Park model (Mazzoni et al. 2007) are used to represent the uniaxial stress-strain relationship of the steel and mortar infill, respectively. For the steel model, both the yield strength and the Young's modulus were varied according to the material coupon tests and the mortar model has a compressive strength of 24 N/mm^2 as detailed in the mortar mix design test results in the experimental study. As the brace specimens are represented in a 2-D model only uniaxial buckling is permitted.

Table 1 – Schedule of complementary tests used for correlation study

Specimen	Section Size (*mm*)	Material	L_0 (*mm*)	L_T (mm)	$\bar{\lambda}$
CyIS-40H	40x40x2.5SHS	Steel	850	1100	0.4
CyIS-20H	20x20x2.0SHS	Steel	850	1100	0.9
CyIS-50H	50x25x2.5RHS	Steel	850	1100	0.6
CyIS-40F	40x40x2.5SHS	Composite	850	1100	0.6
CyIS-20F	20x20x2.0SHS	Composite	850	1100	1.0
CyIS-50F	50x25x2.5RHS	Composite	850	1100	0.7

2.1 Hollow Specimens

The three hollow tests are compared in Figures 3 – 5 showing the force-axial displacement hysteresis for the 40x40x2.5SHS, 20x20x2.0SHS and the 50x25x2.5RHS specimens respectively. Each experimental test was performed twice with different specimens to investigate the effect of slightly non-parallel loading patterns and small rotations of the connection (Goggins 2004).

The 40x40x2.5SHS specimens experienced uniaxial buckling and failed by a combination of both overall lateral buckling and local buckling at plastic hinges located at mid-length and close to the end stiffeners. Comparison of the hysteretic response of the 40x40x2.5SHS specimens in Figure 3 shows acceptable agreement.

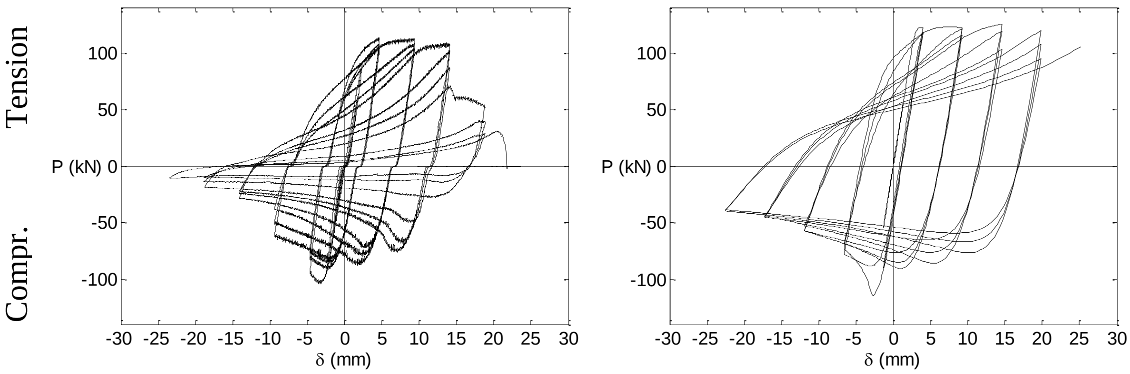

(a) experimental (Goggins 2004) (b) numerical

Figure 3 – Hysteretic response correlation of hollow 40x40x2.5SHS specimens

The numerical analysis shows a notable increase in tensile resistance during the first cycle of increased displacement demand, but in compression the over-estimation of buckling capacity can be accounted for with the model's inability to represent local buckling.

The non-dimensional slenderness value of the 20x20x2.0SHS specimens is higher than that of the other specimens leading to the specimen failing under lateral buckling only (without local buckling). This is reflected in the numerical model with good accuracy observable in Figure 4(b) where both the tension capacity and compressive residual buckling loads correspond with the experimental results. Strength degradation is also reasonably represented during successive loading cycles with the inclusion of the Bauschinger effect in the steel material, where the yield strength of the material decreases following a prestrain in the reverse direction. Although necking resulted in a reduction in cross section in these specimens, this had negligible effects on the numerical model results.

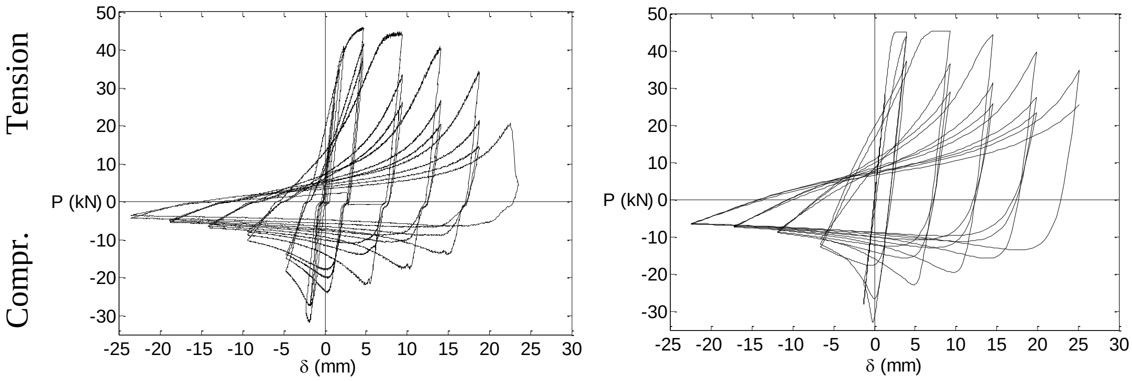

(a) experimental (Goggins 2004) (b) numerical

Figure 4 – Hysteretic response correlation of hollow 20x20x2.0SHS specimens

The response of the 50x25x2.5RHS was very similar to that of the 40x40x2.5SHS specimen. The combination of both overall lateral buckling and local buckling at plastic hinges proved to be difficult to replicate in the numerical model. Similar to the 40x40x2.5SHS specimen, the numerical model shows an overestimation of about 10% in the tensile strength evolution and shows a more significant exaggeration of the residual compressive strength in Figure 5(a) & (b).

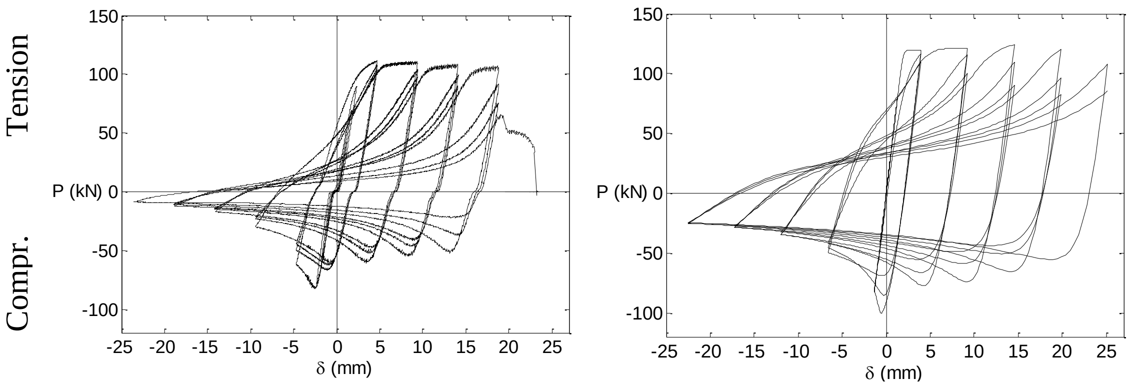

(a) experimental (Goggins 2004) (b) numerical

Figure 5 – Hysteretic response correlation of hollow 50x25x2.5RHS specimens

The series of correlation studies demonstrates that the physical theory model developed in OpenSees is able to replicate the response of compact hollow brace sections with a reasonable degree of fidelity. However, in sections susceptible to local buckling the numerical accuracy can deviate appreciably from the experimental results. For low cycle fatigue of brace members, local strains become significant and hence necessitate an accurate representation of local buckling. The usage of shell or brick elements and modelling parameters (including material properties and nodal geometry) can capture local buckling but at large computational expense. Improvements for the local buckling phenomena require improving the fibre model approach to consider the inaccuracies due to increased yield strength in the corner zones of structural steel sections due to cold working, the presence of a seam weld and variance in the values of yield strength obtained from coupon tests.

2.2 Filled Specimens

To demonstrate the effect of filling the specimens with cement-based mortar the same three pairs of sections are compared in Figures 6 – 8. The same test rig and test procedure was used on pairs of filled sections.

Unlike the hollow specimens, no inward local buckling occurred in the 40x40x2.5SHS specimens (Figure 6). Experimentally, both filled specimens experienced uniaxial lateral buckling and sudden failure. After the first post-buckling excursion, the numerical representation is very accurate. Some discrepancies remain during later cycles but these may be caused by minimal local outward buckling of the steel section.

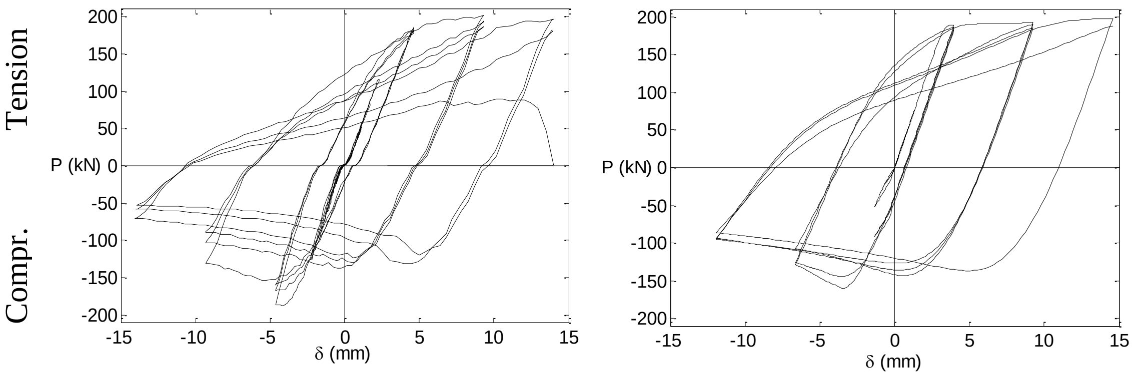

(a) experimental (Goggins 2004) (b) numerical

Figure 6 – Hysteretic response correlation of filled 40x40x2.5SHS specimens

During the experimental tests for the 20x20x2.0SHS specimens, very little local outward buckling occurred in one specimen and during the second test no local buckling was observed. As with the hollow section tests, these specimens buckled biaxially, and failed by fracturing suddenly at mid-height. As predicted, due to the increased $\bar{\lambda}$ value, the OpenSees model of these tests show acceptable fidelity to the experimental hysteresis as shown in Figure 7(b). However, in the post-buckling range the strength degradation is underestimated by about 25% in successive tensile cycles.

In the 50x25x2.5RHS specimens both local inward and outward buckling occurred during the loading cycles. As a result, the tensile range of the loading cycles is exaggerated by the numerical model. However, compared to the hollow specimens, there is a small improvement in the correlation with the experimental results in the compression range. Figure 8(b) demonstrates the improved correlation in the compression cycles, where the small increase in residual compressive strength is more accurately portrayed in the numerical results.

The set of correlation studies shown here demonstrates that the physical theory model using a discretised fibre section in OpenSees can realistically and accurately predict the buckling strength, tensile strength and hysteretic behaviour of hollow and filled compact struts with little local buckling occurring. However, the assumption of the model that cross-section shape is retained limits the accuracy of modelling struts susceptible to local buckling. Mortar infill can delay the onset of local buckling but this has little representation in the numerical model.

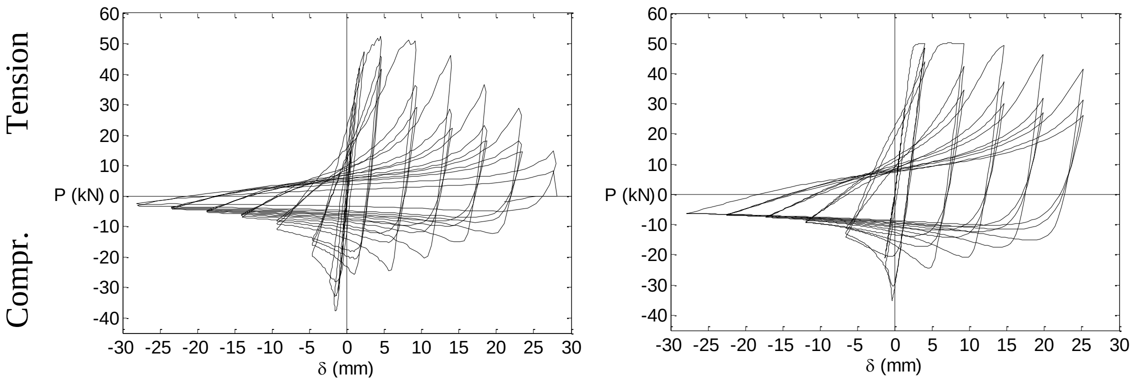

(a) experimental (Goggins 2004) (b) numerical

Figure 7 – Hysteretic response correlation of filled 20x20x2.0SHS specimens

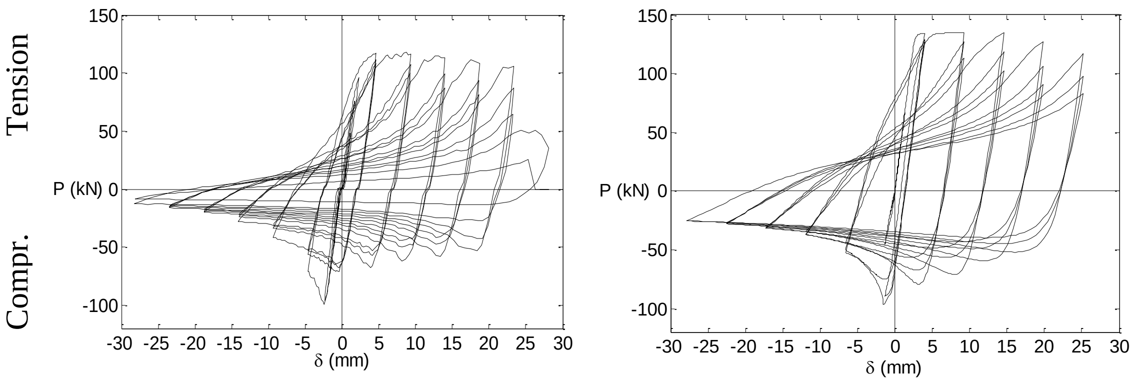

(a) experimental (Goggins 2004) (b) numerical

Figure 8 – Hysteretic response correlation of filled 50x25x2.5RHS specimens

3. Conclusions

This paper presented a model for the inelastic buckling behaviour of hollow and filled steel braces under cyclic loading. The model was validated through a suite of correlation studies with hollow and mortar-filled steel braces of varying cross-section parameters. The conclusions established are summarised as follows:

- The accuracy of the model is directly related to the $\bar{\lambda}$ value. Compact sections that experience little local buckling are modelled with acceptable accuracy. In cases of increased local buckling occurrence, the numerical results begin to diverge from the experimental ones, particularly in the overestimation of post-buckling residual compressive and tensile strength.
- Local buckling inaccuracies are a result of the assumption that section shape is retained after deformation. For low cycle fatigue of brace members it is important to develop improved accountability for local buckling in future studies.
- Mortar-filled specimens can delay the onset of local buckling and necking due to cross section reduction and as such demonstrate greater residual compressive strength in the experimental results. This leads to improved accuracy in the results of the numerical model.

Therefore, to accurately represent local buckling of slender struts in CBF bridge bents it is necessary to improve the OpenSees numerical model. Due to the effect of mortar infill, hollow SHS and RHS struts are more susceptible to numerical error in the analysis process.

Acknowledgements

The Authors wish to acknowledge the financial support of the Dept. of Civil, Struct. & Env. Engineering at Trinity College Dublin and also wish to thank Dr. Jamie Goggins for his permission to reproduce his findings for the purpose of this study.

References

Broderick, B.M., Goggins, J.M. and Elghazouli, A.Y. (2005), 'Cyclic Performance of Steel and Composite Bracing Members', *Journal of Constr. Steel Res.*, **61**, 493-514.
CEN (2004) ENV 1998-1: 'Eurocode 8: Design of Structures for earthquake resistance – Part 1: General rules, seismic actions and rules for buildings', 2004.
CEN (2005), ENV 1993-1-1: 'Eurocode 3: Design of Steel Structures – Part 1.1: General rules and rules buildings', 2005.
Black, R.G., Wenger, W.A.B. and Popov, E.P. (1980), 'Inelastic Buckling of Steel Struts under Cyclic Load Reversals' *UCB/EERC-80/40*, Pacific Earthquake Engineering Research Center, Berkeley, California.
Goggins, J. (2004), 'Earthquake Resistant Hollow and Steel Braces', Ph.D. thesis, Trinity College Dublin.
Ibrahim, F.K., Mahin, S.A. and Pister, K.S. (1988), 'Seismic Behaviour of Concentrically Braced Steel Frames' *UCB/EERC-88/01*, Pacific Earthquake Engineering Research Center, Berkeley, California.
Matsumura, M., Kitada, T. and Nanjyo, A. (2003), 'Seismic Retrofitting Method for Steel Columns Installing Energy Absorption Segment' in *STESSA 2003 Behaviour of Steel Structures in Seismic Areas*, ed F.M. Mazzolani, A.A. Balkema , 737-744.
Mazzoni, S., McKenna, F., Scott, M.H. and Fenves, G.L. (2007), *OpenSees Command Language Manual*, Pacific Earthquake Engineering Center (PEER), UC Berkeley, CA. (http://opensees.berkeley.edu/index.php)
Thewalt, C.R. (1995), 'Twisted Braces under off-ramp', Photograph courtesy of the National Information Service for Earthquake Engineering, EERC, UC Berkeley.
Tremblay, R., Archambault, M.-H. and Filiatrault, A. (2003), 'Seismic Response of Concentrically Braced Steel Frames Made with Rectangular Hollow Bracing Members', *Journal of Structural Engineering*, Am. Soc. Civ. Engnrs, **129**, 1626-1636.
Uriz, P. and Mahin, S.A. (2008a), 'Toward Earthquake-Resistant Design of Concentrically Braced Steel-Frame Structures' *PEER Report 2008/08*, Pacific Earthquake Engineering Research Center, Berkeley, California.
Uriz, P. and Mahin, S.A. (2008b), 'Model for Cyclic Inelastic Buckling of Steel Braces', *Journal of Structural Engineering*, Am. Soc. Civ. Engnrs, **134**, 619-628.
Uy, B. (1998) 'Local and Post-Local Buckling of Concrete Filled Steel Welded Box Columns', *Journal of Constr. Steel Res.*, Am. Soc. Civ. Engnrs, **47**, 47-72.
Zhao, X.-L., Grzebieta, R. and Lee, L. (2002), 'Void-Filled Cold-Formed Rectangular Hollow Section Braces Subjected to Large Deformation Cyclic Axial Loading', *Journal of Structural Engineering*, Am. Soc. Civ. Engnrs, **128**, 746-753.

MODAL ANALYSIS OF A MULTI-SPAN POST TENSIONED REINFORCED CONCRETE BOX GIRDER BRIDGE

J.R.BROWNE[†], P.J.FANNING[†] & M.FENG[††]
[†]School of Architecture, Landscape & Civil Engineering, University College Dublin
[††]Dept. of Civil and Environmental Engineering, University of California, Irvine, USA

Abstract
Vibration based condition monitoring is increasingly being used by bridge owners and managers to monitor the performance of their assets over their design lives and also to help in prioritising the distribution of maintenance budgets. Typically a bridge response is recorded over time and any deviation from a norm is taken as an indicator of change. While recorded data has the ability to identify a change from a norm, the cause of this change often requires a complementary numerical model of the structure being monitored. Fairview Bridge is located on Interstate 405 in the state of California, USA and spans 224m over three intermediary piers. During construction 21 accelerometers were installed, as part of a structural monitoring system, along the length of the bridge deck. The system was configured to trigger once a prescribed response threshold was reached. Modal parameters were extracted from the resulting ambient vibration responses recorded at the 14 accelerometer sites. This paper describes the development of a validated numerical model by cross correlation of numerical predictions with response time histories measured at the bridge site. Particular attention is paid to the sensitivity of the model response to model input parameters. The model was found to be very sensitive to boundary condition assignment at the abutment seats and specific recommendations are advanced for constraining similar constructed box-girder bridges at their respective abutment seats.

Keywords: Bridges, FE Modelling, Modal Analysis, FE Model Updating

1. Introduction

Vibration based condition monitoring methods use measured changes in the dynamic characteristics of a structure to evaluate changes in physical properties that may indicate structural damage or degradation. The basic premise of the technique is that damage to a structure will alter the stiffness, mass or energy dissipation properties of a system, which in turn will alter the measured dynamic response of the system (Farrar et al, 2001). Vibration based monitoring systems aim to facilitate more economical bridge management systems, while trying to overcome shortcomings of visual inspection techniques and providing a method of systematic monitoring which operates on a more global level than other experimental methods.

Early work by Cawley and Adams (1979) proposed using sensitivity matrices to identify defects in structures. Later this concept was developed into the new discipline of model updating (Mottershead and Friswell, 1993). This involves the updating of finite element models of a structure by combining a sensitivity matrix, derived from the sensitivity of eigenvalues, eigenvectors and/or frequency response functions to changes in model input parameters, with the divergence between FEA predictions and results from experimental analysis (Haritos and Owen, 2004). The application of this approach to structural health monitoring for a structure is readily apparent. Given an accurate finite element model of a structure in the undamaged state, it is possible to manipulate the model in an attempt to mirror the modal properties of the structure in the damaged state. The meaning of "damage" in this regard refers to changes in the material and/or geometric properties of the system, including changes to the boundary conditions and system connectivity, which adversely affect the performance of the structure (Farrar et al, 2001).

In the field of civil engineering there exist numerous applications for validated numerical models in the realms of damage detection, health monitoring, structural control, structural evaluation, and assessment (Jaishi and Ren, 2005). This paper discusses the creation of a 3-dimensional finite element model of the Fairview Bridge and the results of a manual, iterative based model updating procedure. Particular emphasis is placed on the modelling process and the assignment of material properties and boundary conditions.

2. Fairview Bridge

Fairview Bridge, Figure 1, is located adjacent to the I-405 freeway in Costa Mesa, California. It is a 224 metre long post-tensioned continuous in-situ concrete box-girder bridge with four spans of 52.500 m, 59.500 m, 59.500 m and 52.500 m respectively. The bridge is supported intermediately by 3 no. bridge piers which are integral with the bridge deck forming a frame structure, a design which is common in the earth quake prone Western United States. The piers are supported by a raft pile cap which sits on approximately 48 no. concrete driven piles.

Figure 1 - Fairview Road On-Ramp Overcrossing Bridge

The box-girder cross-section consists of 3 no. box cells, 2.250 m deep, and a cantilevering deck at each side with a reinforced concrete barrier along each edge of the deck. This section is typical along the bridge length, only altered at the supports where the deck forms a solid diaphragm. The total width at deck level is approximately 8.1m. At each end the bridge sits into an abutment seat and is supported on four elastomeric bridge bearings. The post-tensioning cables of the bridge are encased within the four webs of the box-girder cross-section. When the Fairview Bridge was constructed in 2004, 21 no. accelerometers were installed at 14 no. different locations throughout the bridge as part of a long-term structural monitoring system. The system is configured to trigger, and record the response of the bridge, once a prescribed response threshold was reached. Figure 2 illustrates the accelerometer locations on the Fairview Bridge.

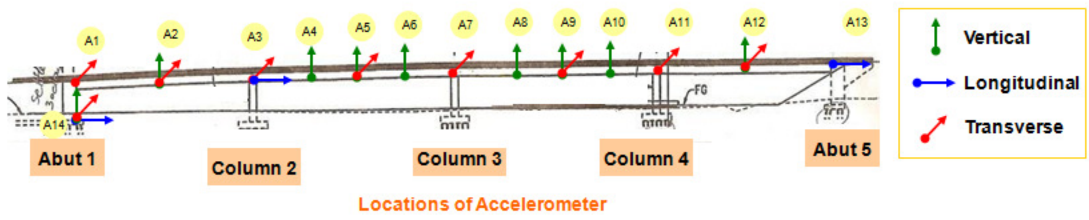

Figure 2 - Accelerometer Locations on the Fairview Bridge

3. FE Modelling

3.1 Geometry and Mesh

The geometry of the FE model was created in Autocad 2010 and Ansys Workbench Design Modeller V12 from construction drawings for the bridge. The deck structure was defined by a 3-dimensional line in space around which the box-girder cross-section twists, with a maximum inclination of 6%. This line, known as the station line, was created in Autocad. The bridge deck profile was then extruded and twisted along this line, as indicated by the construction drawings. Once the deck geometry had been formed it was then imported into Ansys Workbench where the geometry of the piers and pile cap respectively was generated to form a very accurate geometric representation of the complete structural system. The geometry of the FE model created is shown in Figure 3.

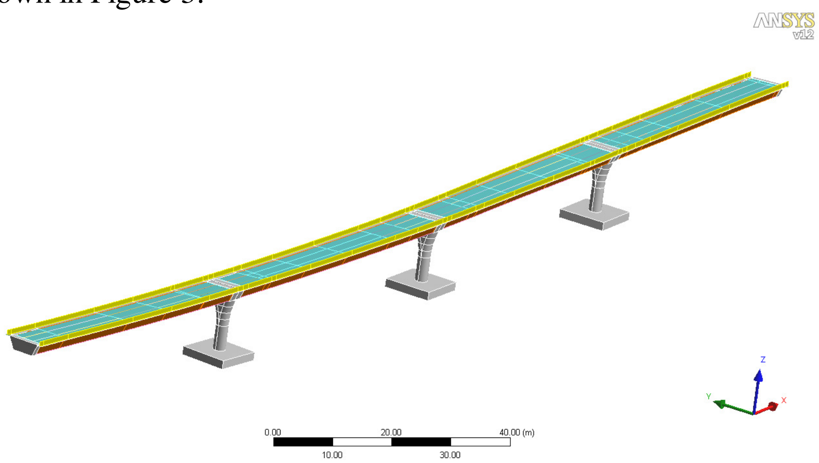

Figure 3 - Fairview Bridge Model Geometry

The box-girder was modelled using iso-parametric shell elements, allowing curved element edges, while the piers were modelled using iso-parametric solid brick elements. Solid brick elements were used for the piers due to their ability to better mimic the support condition provided by the piers to the box-girder. Solid elements were also employed to model the pile caps and solid diaphragm sections of the deck. A series of mesh sensitivity studies were carried out on the model to establish a suitable mesh size. Beginning at an initial element edge length size of 1.0 m the mesh was gradually refined until results of the FE modal analysis began to converge. This was achieved with an element edge length size of 0.35m.

Eriksson (1994) stated that compressive stresses induced as a result of prestressing have the potential to lower natural frequencies however, Pavic et al (2001) argue that 'it is important to note here that this phenomenon cannot be a result of axial forces from internal prestressing'. They go on to describe how for internally prestressed structures, where the prestressing tendons are encased within the concrete either directly or in ducts, the tendon profile follows the deformed shape of the prestressed element. As such no additional eccentricity between the tendon and the centroid of the element can be generated and finally they recommend that the second-order effects due to prestressing should not be taken into consideration when analysing dynamic properties of internally prestressed concrete elements. These recommendations were followed in this model and no specific provision, bar the appropriate mass, was made for the post-tensioning system.

3.2 Material Properties

In order to carry out an investigation into the FE model boundary condition assignment and before any model updating, it was first necessary to establish preliminary density and stiffness estimates. Density estimates were formed by dividing the bridge into a number of sections based on the proportion of steel contained in each section. The quantity of steel in each section was then calculated from reinforcing drawings. The preliminary density estimate for the FE model was then based on a concrete density of 2400 kg/m^3 and a steel density of 7850 kg/m^3. Later density estimates employed in the FE model were based on the possible density variation of normal weight concrete depending on aggregate type, fines content etc. within a sensible range of about 2300-2400 kg/m^3. It is noted further that the density specified in the final FE model was adapted to take into consideration the small discrepancy between the volume of the FE model and the Fairview Bridge due to overlapping shell elements in the FE model and filleted joints in the box-girder cross-section of the Fairview Bridge.

Preliminary estimates for the Modulus of Elasticity of the material in the FE model were based on the concrete strengths specified on construction drawings. Values for the static or secant modulus of elasticity were taken from ACI, BS and EuroCode recommendations. Under dynamic conditions certain material properties are altered and hence these static modulus recommendations were adjusted accordingly. A series of recommendations for the relationship between the static and dynamic moduli were considered. Mehta and Monteiro (2006) state the generally accepted norm to be a 20, 30 and 40% increase on the static modulus for high, normal and low strength concretes respectively. Elsewhere, literature pertinent to the vibration testing of floors typically suggests increasing the static modulus by 10-25 percent (Ammann & Nussbaumer, 1995 and Rainer & Bachmann, 1995). The preliminary estimates for stiffness were based on the lower ACI estimate of the static modulus and a 20% increase to form an approximation to the dynamic modulus of the material.

3.3 Boundary Conditions

A fixed boundary condition was adopted at the pile caps in the FE model. A quasi-fixed condition was investigated, using elastic supports around the pile cap, softening the supports slightly from the fully fixed. However, it was decided that this effect on the natural frequencies exhibited by the FE model was sufficiently small to be neglected and a fully fixed condition was maintained. The boundary condition assignment at the bridge abutments was thus the focus of attention. The main six boundary condition cases examined at the bridge ends are summarised in the table shown in Figure 4 – individual degree of freedom directions were variously fixed or assigned an elastic spring stiffness ("elastic").

	X	Y	Z	Rot-X	Rot-Y	Rot-Z
BC01	Fixed	Fixed	Fixed	Fixed	Fixed	Fixed
BC02	Fixed	Fixed	Fixed	Free	Free	Fixed
BC03	Fixed	Fixed	Free	Free	Free	Fixed
BC04	Elastic	Elastic	Fixed	Elastic	Elastic	Elastic
BC05	Elastic	Elastic	Free	Elastic	Elastic	Elastic
BC06	Elastic	Elastic	Elastic	Elastic	Elastic	Elastic

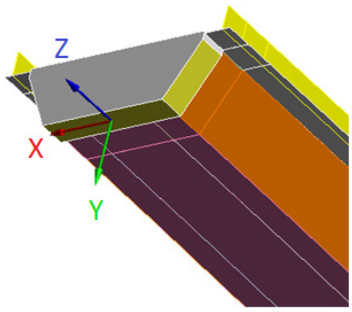

Figure 4 – Abutment Boundary Condition Cases

4.0 FE Model Updating

Carvalho et al (2007) broadly classify current model updating techniques into three categories: (i) direct matrix model updating methods, (ii) iterative methods, and (iii) frequency response methods. Haritos and Owen (2004, p.147) state that while extensive development in the area of finite element model updating in modern times has led to several systematic methodologies which automatically update finite element models, that 'civil engineering structures are not best suited to these approaches because of their indeterminate nature and variable support conditions'. Instead a simplified manual approach is often applied to structures such as bridges. Schlune et al (2009) reinforce this assertion stating that the strength of manually refining models is that all types of modelling errors can be reduced. A manual approach such as that outlined by Haritos and Owen (2004) has been applied in this work.

4.1 Experimentally Derived Natural Frequencies

Over 140 ambient response time-history data sets were processed into frequency response functions using Discrete Fourier Transforms (DFT). From this response data the natural frequencies of the Fairview Bridge were established by identifying consistent peaks in the bridge response and subsequently the mode shapes at each natural frequency were extracted. The first eight natural frequencies of the Fairview Bridge as interpreted from response data, measured on 20 March 2006, are presented in Figure 5 along with a general description of the mode type.

4.2 Identification of Boundary Conditions

The behaviour of the FE model under the various boundary condition cases was compared with the mode shape behaviour as observed from the ambient response data taken from the Fairview Bridge. This investigation examined the first eight modes of vibration in order to establish a reliable basis for validating behaviour of the FE model. It was discovered that boundary condition case BC06, using elastic supports to model partial freedom for each degree of freedom, resulted in the best correlation of the FE model predictions with observed data and this boundary condition configuration was used in all further model updating and sensitivity studies.

Under boundary condition case BC06 the stiffness of the vertical support was specified at an arbitrarily high level to prevent any significant movement of the bridge in the vertical direction. With respect to the support stiffness in the longitudinal and transverse directions, analysis first focused on an elastic stiffness of 3 x 10^7 N/m^2 in the x and z-directions (Figure 4). The boundary conditions at the abutments were hypothesised, not to model any direct stiffness of the deck to move on the elastomeric bearings, but to approximate a combination of effects which result in partial freedom of the deck to move. Accelerometer response data taken at the abutments indicated that a level of freedom was present in the real support condition of the Fairview Bridge.

	Data Frequency (Hz)	Mode Behaviour
Mode 01	1.53	Transverse movement of central bent
Mode 02	1.90	Transverse movement of outer bents
Mode 03	2.05	Vertical movement of spans
Mode 04	2.35	Vertical movement of spans
Mode 05	2.44	Transverse movement- max @ bridge ends and central bent
Mode 06	2.90	Vertical movement of spans
Mode 07	3.02	Transverse movement of deck and bridge ends
Mode 08	3.12	Vertical movement of spans

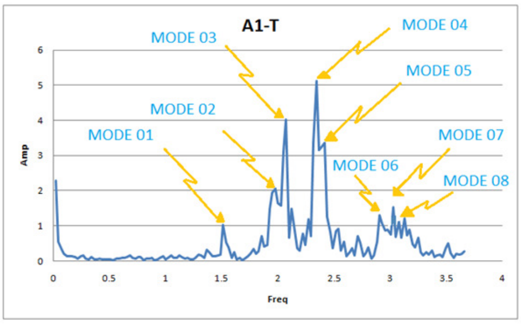

Figure 5 – Natural Frequencies of Fairview Bridge

4.3 Sensitivity Study

The sensitivity of the FE model was examined with respect to three specific variables: (i) variation in the support stiffness at the abutments; (ii) variation in the mass of the bridge (i.e. changes in the material densities specified); and (iii) variation in the stiffness of the bridge model (i.e. changes in the material stiffness specified). Following on from this, a manual iterative based FE model updating procedure was carried out in order to achieve even better correlation of the FE model with the observed natural frequencies of the Fairview Bridge.

4.3 Final Updated Model

The density values employed in the final FE model were based on a concrete density of 2400 kg/m^3. The stiffness values employed in the final model represent a 2 GPa increase on preliminary estimates formed using ACI guidance. This increase moves toward the stiffer estimates established from BS and EuroCode recommendations. It is also in line with the higher relationship between the static and dynamic modulus proposed by Mehta and Monteiro (2006) for normal strength concrete. At the abutments a support stiffness of 5×10^8 N/m^2 was placed in the vertical direction, while supports stiffness of 3×10^7 N/m^2 and 2.6×10^7 N/m^2 was placed in the transverse and longitudinal directions respectively. Figure 6 shows the correlation of the Fairview Bridge Model with observed data taken from the structure. Figure 7 illustrates the mode shapes as extracted from the response data for each natural frequency, using the peak-picking method, as well as the mode shape behavior predicted by the FE model. The numerical mode shapes compare favourably with the measured modes. With respect to predicted frequencies the model is accurate to within 10.3% for the first eight modes. The largest discrepancy is 10.3% for the frequency of mode no. 6, the third vertical bending mode, while all other frequencies are accurate to within 3.8% or less. It is noted that the largest errors are associated with the vertical bending modes (modes 4, 6 and 8) and hence the variance is most probably due to the vertical stiffness of the deck in the FE model.

	FE Model Freq (Hz)	Data Freq (Hz)	%
Mode 01	1.53	1.53	0.00
Mode 02	1.91	1.9	0.53
Mode 03	2.07	2.05	0.98
Mode 04	2.26	2.35	-3.83
Mode 05	2.45	2.44	0.41
Mode 06	2.6	2.9	-10.34
Mode 07	3.01	3.02	-0.33
Mode 08	3.05	3.12	-2.24

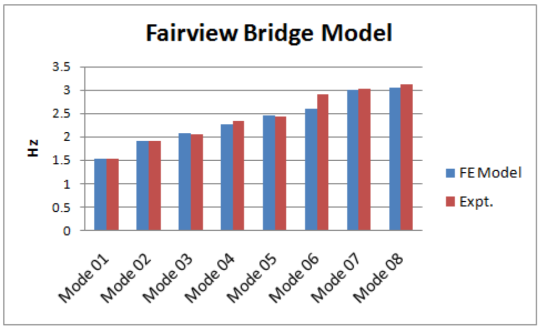

Figure 6 – Fairview Bridge FE Model Correlation with Expt. Data

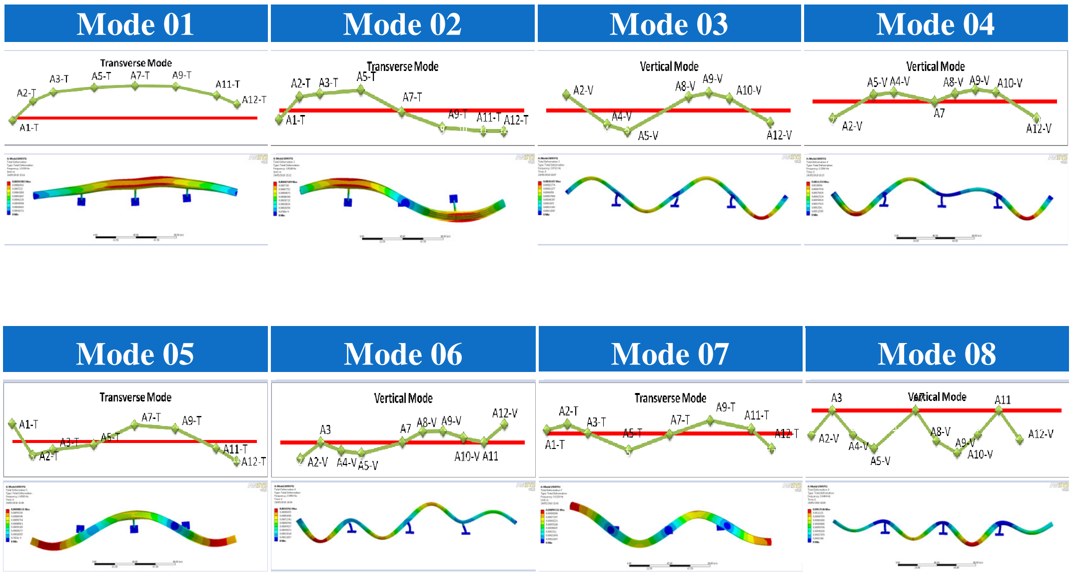

Figure 7 – Mode Shape Correlation: Data and FE Model

5.0 Conclusions

Manual FE model updating was found to be very effective in calibrating the FE model with experimental data. The major strength of manual updating was found to be the flexibility of the process and the ability to explore and minimise all types of modelling error.

An important finding of this work is the sensitivity of the model to boundary condition assignment at the abutment seats. While designed to be only vertically supported at the abutments the seat does provide rotational restraint and also restraint in orthogonal directions also. Linear elastic foundation stiffness type springs were found to be effective in representing this restraint although it is accepted that the specific values will vary from bridge to bridge.

The examination of boundary condition effects on the FE model highlighted the importance of examining a sufficient number of modes of vibration. The first eight modes of vibration were examined in order to establish a reliable basis for validating the predicted response of the FE model. Multiple possible boundary condition solutions were found when only correlation of the first few modes was considered.

However the number of potential boundary conditions, for good correlation with test data, reduces as an increased number of modes are considered. The number of modes that can be used however can be limited by their occurrence at similar frequencies making them difficult to identify precisely from experimental data. In such cases it is recommended that as many modes as are practically identifiable from experimental data be used for model updating studies.

References

Ammann, W. and Nussbaumer, H. (1995), Vibration Problems in Structures: Practical Guidelines - Behaviour of Steel and Concrete under Dynamic Actions. *Basel, Switzerland: Birkhauser.*

Carvalho, J., Datta, B.N., Guptac, A. and Lagadapati, M. (2007), A Direct Method for Model Updating with Incomplete Measured Data and Without Spurious Modes, *Mechanical Systems and Signal Processing*, **21**(7), 2715-2731.

Cawley, P. and Adams, R.D. (1979), The Location of Defects in Structures from Measurements of Natural Frequencies', *Journal of Strain Analysis*, **14**(2), 49-57.

Haritos, N. and Owen, J.S. (2004), The Use of Vibration Data for Damage Detection in Bridges: A Comparison of System Identification and Pattern Recognition Approaches, *Structural Health Monitoring*, **3**(2), 141-163.

Eriksson, P.E. (1994), *Vibration of low-frequency floors - dynamic forces and response prediction*', Ph.D. Thesis, Chalmers University of Technology, Göteborg, Sweden.

Farrar, C.R., Doebling, S.W. and Nix D.A. (2001), Vibration-Based Structural Damage Identification, *Philosophical Transactions: Mathematical, Physical and Engineering Sciences*, **359**(1778), 131-149.

Jaishi, B. and Ren, W.X. (2005), Structural Finite Element Model Updating Using Ambient Vibration Test Results, *Journal of Structural Engineering*, **131**(4), 617-628.

Mehta, P.K. and Monteiro, P.J.M. (2006) Concrete: Microstructure, Properties, and Materials. *New York: McGraw-Hill*.

Mottershead, J.E. and Friswell, M.I. (1993), Model Updating in Structural Dynamics: A Survey', *Journal of Sound and Vibration*, **167**(2), 347–375.

Pavic, A., Reynolds, P., Waldron, P. and Bennett, K.J. (2001), Critical review of guidelines for checking vibration serviceability of post-tensioned concrete floors, *Cement and Concrete Composites*, **23**(1), 21-31.

Rainer, H., Bachmann, H. and Pretlove, A.J. (1995), Vibration Problems in Structures: Practical Guidelines - Floors with Walking People, *Basel, Switzerland: Birkhauser.*

Schlune, H., Plos, M. and Gylltoft, K. (2009), Improved bridge evaluation through finite element model updating using static and dynamic measurements', *Engineering Structures*, **31**(7), 1477-1485.

MULROY BAY BALANCED CANTILEVER BRIDGE ASPECTS OF DESIGN AND CONSTRUCTION

PETER FITZGERALD[1], KENNY MASON[2]
[1]RPS Consulting Engineers, Cork.
[2]RPS Consulting Engineers, Dublin.

Abstract
Mulroy Bay Bridge spans the very scenic and environmentally sensitive Mulroy Bay in County Donegal. The bridge has an elegant 5-span, 340m long box girder deck constructed by the balanced cantilever method, including a main span of 100m length with a vertical clearance of 20m above high water to accommodate shipping. Construction was completed in 2009 at a cost of €15.5m (tender, ex VAT).

This paper presents an overview of key features of the design and the principal aspects of the procurement and construction.

Keywords: Balanced, Bridge, Cantilever, Box girder, post-tensioned

1. Introduction

1.1 Location

Mulroy Bay Bridge is located in northern County Donegal as shown in Figure 1, and provides greatly improved access to the Rosguill Peninsula. It spans the Mulroy Bay estuary at a point previously used as a ferry crossing point, and fulfils a long standing aspiration to restore the link. While the bay is very large, its width reduces to 270m at the bridge site near the mouth of the bay. The site is tidal, with a maximum level variation of 3.35m.

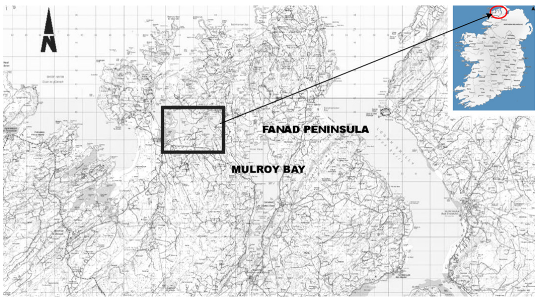

Figure 1 - Site Location

1.2 Site Constraints

Construction of a bridge at this site was subject to several strict environmental constraints, principally,

- The Mulroy Bay estuary and general locality is an area of exceptional scenic merit. It is a designated Special Area of Conservation (SAC), and includes a number of designated scenic routes and is important to tourism in the area. Consequently the architecture of the bridge was of critical importance so that it would blend with and enhance, rather than detract from the landscape.

- The water quality is very high and the bay supports extensive aquaculture and shellfish farms. The design therefore had to be conducive to construction methods which would pose least risk to water quality.
- The main span had to provide passage for commercial shipping, which effectively required a main span length of 100m, and a vertical clearance of 20m above max high water (HW) level.

2. General Arrangement

The bridge has a five span, post-tensioned box girder deck of 340m overall length as shown in Figure 2. The cross section consists of a single cell box as shown in Figure 3. The overall depth of the section varies between 2.2m and 5.1m and the walls of the box are vertical over the variable section to facilitate travelling formwork units.

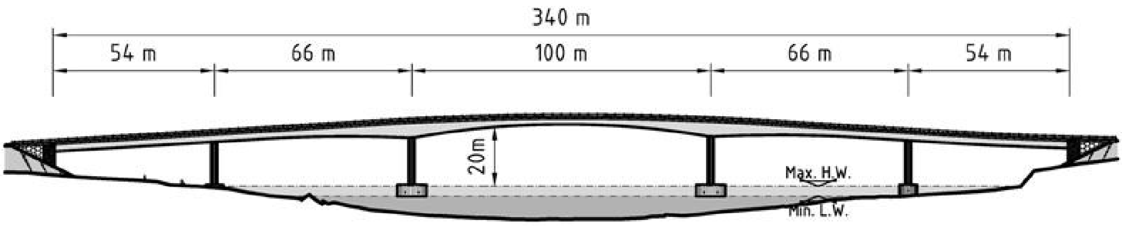

Figure 2 – Elevation

Due to the height of the structure and its exposed coastal location, the wind load on susceptible vehicles such as caravans and high-sided lorries, and the potential need for wind shielding, received consideration. Wind shields would have the disadvantages of adding significant extra wind load to the structure, additional cost, and would negatively affect the external appearance of the bridge and views from the bridge. A risk assessment concluded that other provisions, including signage and warning devices were more appropriate, and thus shielding was not provided.

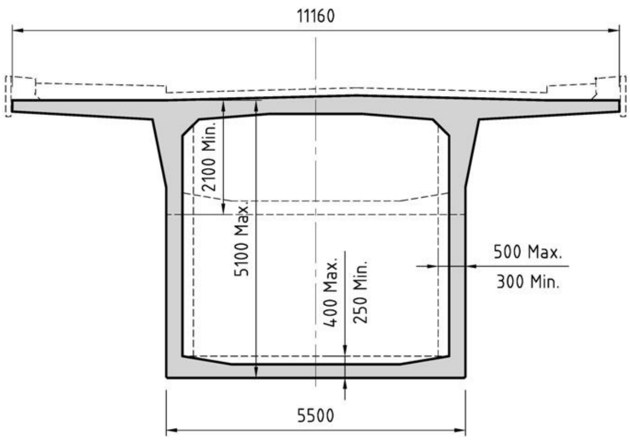

Figure 3 – Deck Cross Section

3. Loading

Applied traffic loading consisted of HA, HB37.5 and pedestrian loads to BD37/01. Wind load, also to BD37/01, was a significant load, particularly during construction.

Horizontal loading due to ship impact on the main piers was the governing load case for the pier foundations, and was the least quantifiable loading. Impact from a specimen commercial vessel of 1060 tonnes displacement moving at 6m/s, which represented the largest vessel using the bay, was adopted for loading purposes. No formal loading guidance was available at the time, and reference was made to various sources, in particular Reference 1, and loadings previously adopted elsewhere. The equivalent static impact loading adopted was 14MN 90º to the bridge centerline and also a separate load case of 10MN at 45° to the bridge centerline. Impact loading was considered only at the main piers, so these foundations are much larger than for the outer piers. By comparison, the loading subsequently checked using the current Eurocode IS EN 1991-1-7 is 17.4MN.

4. Foundations

Site investigation for the bridge involved 23 boreholes, mostly undertaken from a large, floating, jack-up platform. Founding conditions varied across the site. Bedrock on the south side was generally completely weathered schist with significant moderately strong metadolerite intrusions. On the north side, bedrock was highly weathered schist. The river bed over the full site consisted of gravel or boulder-clay layers up to 6m thick.

Two alternative foundation arrangements were considered. The initial preference was for precast caissons, which could have been founded at depths of between 3.5m and 5.5m below river bed level. Caissons for the main piers would have been substantially bigger than for the outer piers to resist impact loading. Construction however would have been complicated by working below water, and by the fast tidal streams at the site of 2.5m/s.

The foundations adopted in the final design consisted of piles, supported mostly by friction, which extended to approximately 11m and 16m below river bed level at the south and north main piers respectively. The piles employed were 900mm cast-in-situ auger piles, temporarily cased below the river bed, and permanently cased above. The piles support a 2.5m thick pilecap which extends to 0.6m above the highest tide level, and thus remains permanently visible to shipping.

The vertical loading at each main pilecap was 41MN permanent, and 5MN live. However, accommodation of the 14MN horizontal impact load required an array of 24 piles, all raked at 1:4 in various orientations as shown in Figure 4. The

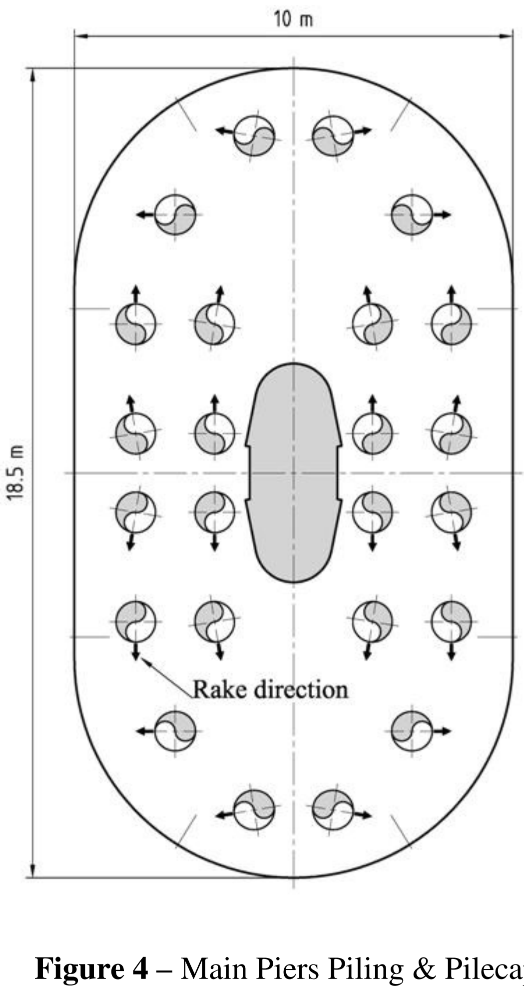

Figure 4 – Main Piers Piling & Pilecap

resultant max pile loads were 2.4MN and 5.3MN with and without impact respectively. Impact loads were considered in a static analysis only, as the level of detail in a dynamic analysis was regarded as inconsistent with the gross uncertainties in the nature and magnitude of the applied loads.

The pilecap cross-section is shown in Figure 5. The skirts are purely aesthetic to conceal the piles at low tide. The skirts and sides were precast, and mounted by means of brackets on a first pour of the pilecap, and then tied in with an in-situ stitch. The remainder of the pilecap was then completed, as shown in the figure.

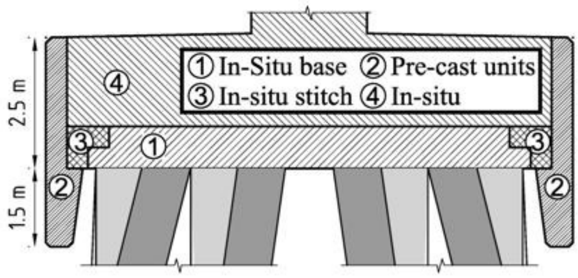

Figure 5 – Main Piers Pilecap Cross Section

In contrast to the main piers, the pile caps for the outer piers are only 10.25m x 6.1m, with 6 piles each. The piers themselves are all reinforced concrete elliptical sections, 5.0m x 2.2m overall dimensions.

Scour around the piles, as a result of the prevailing fast tidal waters of 2.5m/s, was addressed by the provision of rip-rap placed locally on the river bed around the piles.

5. Superstructure

5.1 Span Ratios

The deck cross section is shown in Figure 3, which provides for span/depth ratios of 19.6 and 47.6 respectively at the support and midspan sections of the main span. The ratios for the intermediate spans are 31.4, which was possible only due to the limited extent of cantilever construction proposed at the outer piers.

5.2 Segments

Following the adoption of the balanced cantilever form of the structure, a key question for the design was to select the method of segment construction. Balanced cantilevers are usually constructed from precast segments, which may or may not be bonded together on erection. Alternatively, the segments can be cast in-situ by means of travelling formwork units. As the type of construction would affect both the design and the detailing, a decision could not be left to the construction stage. The overall length of the deck was relatively short in this case, and it was expected that the cost of establishing facilities for precasting and handling the concrete units would not be justified for the number of units required. The design was therefore based on the use of travelling forms. Additionally, travelling forms permit the formation of proper construction joints with continuous reinforcement. This decision and its

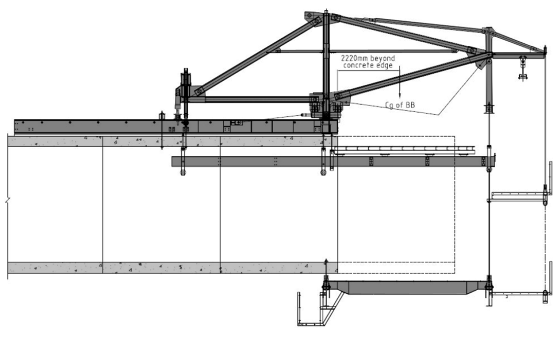

Figure 6 –Travelling Form

rationale were supported later by the Contractor. The travelling form is shown schematically in Figure 6, and the layout of the segments is shown in Figure 7.

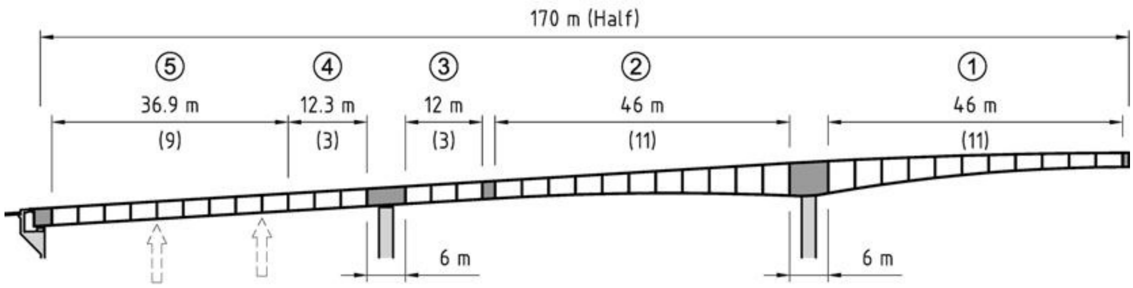

Figure 7 –Segment Layout (half structure)

The design also provided for 6m long deck segments at each pier, cast in conventional forms and incorporating a heavy diaphragm.

5.3 Design Parameters

In addition to the type of segment, assumptions relating to a number of other construction-related inputs were required at the design stage in order to progress the design; principally:

- The ideal segment lengths. These were selected as 4.10m and 4.18m, which turned out to be appropriate.
- The weight of the travelling formwork units. This is a sensitive parameter as the units are located at the tip of the cantilevers. A weight of 70t was allowed, which was significantly more than the 45t weight of the units eventually employed.
- The cycle time of the units. The design assumed units cast alternately each side of the pier at a rate of one unit per week. In the event, the Contractor reduced this to one unit per five days.
- The material properties; key issues here relate to creep and early strength development due to the early application of self-weight and prestressing.

5.4 Support Conditions

The main piers are 16m high, and are integral with the deck, which facilitated the cantilever construction. Expansion and contraction of the main span is thus absorbed by flexibility in the piers. However, reference to Figure 7 shows that cantilever construction extended up to 49m each side of the main piers, and consequently the Contractor elected to stiffen the piers during construction to reduce deflections and oscillations resulting from flexibility of the pier. Stiffening consisted of steel props installed between the pilecap and the deck, which were removed on making the deck continuous.

The outer piers are of a similar section to the main piers, and each incorporate a pair of uni-directional sliding bearings under the deck to facilitate movements during service. However, to accommodate cantilever construction at the outer pier, the design required temporary works to clamp the pier to the deck to provide a rigid connection until the deck was made continuous.

A pair of sliding bearings is provided at each abutment.

5.5 Segmental Construction Sequence

The design provided for simultaneous cantilever construction of sections 1 and 2, and separately sections 3 and 4. Section 5 was designed to be constructed using a travelling form, as an extension of section 4, temporarily propped where indicated in Figure 7 until the deck was completed and made continuous.

A cycle for the construction of a typical pair of segments is shown in Figure 8. The stages indicated are:-

1. Cast segment 4A,
2. Move traveller A,
3. Cast segment 4B,
4. Install and stress tendons,
5. Move traveler B.

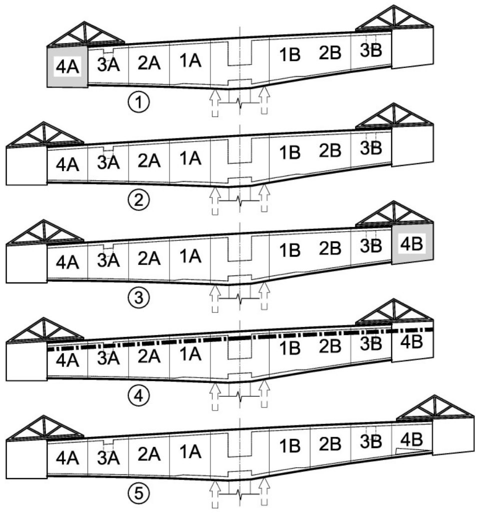

Figure 8 –Segment Construction Cycle

The time achieved for a typical cycle as shown was ten days. The Contractor elected to use four travelling forms in order to construct sections 1 and 2 at both main piers concurrently. He also elected to construct all of sections 3, 4 and 5 on conventional support work and formwork, as this was mostly over relatively shallow water in the inter-tidal zone (refer Figure 2). However, after very successful experience with the travelling forms, the decision not to use the travelling forms for the complete deck was later regretted.

6. Modelling

Modelling of the deck was undertaken with the aid of the SOFiSTiK analysis programme. As the width of the deck is small compared to the spans, it was modelled as a single line beam. Torsion moments due to the eccentricity of live loads were of limited significance and their magnitude and effect on structural stresses could be estimated separately. The main piers were included as members in the model, with full fixity assumed at their bases. Due to the number of piles under the main piers, flexibility of these supports could be neglected. Supports to the deck at the outer piers and abutments locations were pinned. From this point of view, the model was relatively simple.

Stage construction was modelled step by step for the addition of each deck segment, and the stresses and deflections from each stage superimposed to determine the results for the completed structure. This facility was well provided for in the SOFiSTiK software.

The contract required the Contractor to also establish a similar analysis model relating to the construction phase. This model included updated estimates for material properties, actual values for the construction loads, particularly the travelling forms, and the actual stage durations expected and achieved. The input and output of the Contractor's model were monitored by the designers. In this way, stresses and deflections could be controlled during construction, compared to measured values, and the pre-camber adjusted to ensure that the required final geometry was achieved.

7. Prestressing

All prestressing consisted of post-tensioned tendons containing 19x15.7mm low relaxation strand in grouted high-density polyethylene (HDPE) ducts. Three groups of prestressing tendons were employed.

1. Top internal tendons within the top flange of the deck. Tendons were symmetrically arranged in pairs about each pier, with a pair of tendons terminating at the ends of opposing segments. These were stressed before casting the next segments, so the anchors could be contained within the top flange.
2. Bottom internal tendons within the lower flange. These extended only over the sagging region of the spans, and were not continuous through the piers. These terminated in blisters on the bottom flange and were stressed after completion of the deck.
3. External tendons within the box, extending the full length of each span, anchored in the diaphragms at the adjacent pier or abutment, and stressed on completion of the deck. External tendons allow for variable eccentricities, from top to bottom of the section, without having to be placed in the webs. The tendon profiles are achieved by deviators installed at in-span diaphragms.

Table 1 – Prestressing arrangement; number of tendons.

Location	Top Internal	Bott. Internal	External
Main span (at C/L)	0	10	6
Main pier	22	0	6
Intermediate span (at stitch)	0	4	6
Outer pier	8	0	6
Outer span (Section 5)	0	5	6

Generally, the top internal tendons have capacity for the self weight, and the external tendons at the piers have capacity for hogging moments from superimposed dead plus live loads. The bottom tendons (internal and external) have capacity for sagging moments due to super-dead plus live loads, and hogging moments redistributed to the span by creep.

8. Procurement

The construction contract included 2.6km of approach roads and ancillary works and was procured by the restricted procedure. The contract documents were to the NRA Manual of Contract Documents for Road Works, and the conditions of contract were the IEI 3rd edition. The value of the bridge works was €15.5m (tender, excl. VAT).

Key participants were:

Client:	Donegal County County
Designer & Engineer:	RPS Consulting Engineers,
Contractor:	BAM Ltd (formerly ASCON Ltd.),
Piling subcontractor:	Quinn Piling Ltd.
Stressing subcontractor:	VSL Ltd.

The time line for the works was:

Start detail design	January 2003,
Tender issue	May 2006,
Start construction	January 2007
Construction completion	May 2009.

Figure 9 – The Completed Bridge

References:

Larsen, O.D. (1993), Ship Collision with Bridges. IABSE, SED4.

BEHAVIOUR OF SOLID AND HOLLOW VOUSSOIR FLEXIARCH^{TM} SYSTEMS

J.D.BOURKE, S.E.TAYLOR, D.ROBINSON & A.E.LONG
School of Planning, Architecture and Civil Engineering,
Queen's University Belfast,
Northern Ireland, BT9 5AG

Abstract

This paper details research into the behaviour of a FlexiArch bridge system and builds upon previous developmental work at Queen's University and Macrete Ltd. Laboratory tests were carried out on one third-scale arch rings which were backfilled with scaled and carefully graded backfill. The main aim was to investigate the behaviour of similar arches made with hollow and solid voussoirs, as well as varying ring thickness. As the polymeric reinforcement is required during the construction phase, a reduction in self-weight of the arch is highly beneficial. It was found that the behaviour of the arch ring with hollow voussoirs was similar to that with solid voussoirs. Results from both geotechnical tests on the graded backfill and non-linear finite element analyses of the arches are also presented here.

Keywords: arch bridges, voussoirs, backfill, finite element analysis

1. Introduction

Masonry arches form a significant proportion of the road and rail infrastructure in the UK and Ireland. They also provide a sustainable and aesthetical contribution to our history and heritage, having existed for longer periods than most other structures. However, masonry arch bridge design has been in decline in recent years due to high labour costs associated with the skilful building of the timber centring as well as the cutting of the masonry blocks (Long et al., 2007).

In recent years the repair and maintenance of bridge structures has become a major concern (Mulheron, 1999). The UK Highways Agency recommends the use of the arch form where ground conditions permit and also states that "consideration shall be given to all means of reducing or eliminating the use of corrodible reinforcement" (BD57, 1995). Experience has shown that unreinforced arch bridges are very durable structures in comparison to other bridge forms.

Queen's University Belfast in collaboration with Macrete Ltd (under a Knowledge Transfer Partnership) has developed a flat-pack FlexiArch^{TM} bridge made of unreinforced precast concrete voussoirs connected by a polymeric reinforcement and top screed as detailed in previous papers and in Figure 1 (Taylor et al., 2007 and Gupta, 2008). With its quality design, the FlexiArch contains no steel reinforcement or mortar joints and can be transported to site as a flat-pack.

The main aim of the research detailed here is to investigate laboratory arch ring models under a number of variables. These variables relate to the arch ring thickness, backfill type and the comparison of solid and hollow voussoir construction. The intention is to make the arch design more efficient by reducing the self-weight of the system through a reduction in concrete volume.

Research carried out by Fanning and Boothby (2000) used non-linear finite element analysis to predict the behaviour of existing stone arch bridges and found that material property assumptions were key in enabling good predictions of bridge behaviour. Finite element analyses are used here to compare behaviour with that of laboratory tests with the aim of producing a model that accurately captures and predicts the behaviour of the FlexiArch.

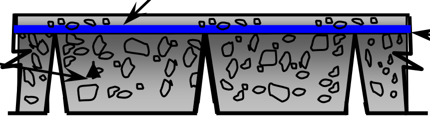

Figure 1 - Components of FlexiArch System (Taylor et al., 2007)

2. Test Set-up and Procedure

Five one third-scale models of a 5m x 2m (internal span x rise) arch rings were constructed in the laboratory (Table 1). The geometry of the voussoir blocks was calculated from the overall span and circular profile of the arch. Twenty-three voussoirs were used to construct each arch, with eight no. moulds used to cast both solid and hollow voussoirs. The variables were the depth of the ring and solid or hollowcore voussoir construction. A third-scale concrete mix was used with a 28-day strength in excess of $30N/mm^2$. After curing, the voussoirs were laid on a flat construction bed, and the polymeric reinforcement placed on top of the blocks. ERS strain gauges were attached to the polymeric reinforcement at the lifting positions and at each end of the arch to enable strain measurement to be recorded at critical locations during the construction phase, backfilling and under load testing. Adhesive was then applied to the surface of the voussoirs to provide a good bond between them and the 13mm top screed thus connecting each voussoir. Vibration was not possible for a screed of this depth, so the top surface was tamped and floated and after one hour crack inducers were then scored into the screed to ensure controlled cracking at the joints during lifting into the arch form.

Table 1 - Summary of variables and experimental results

Arch #	Voussoir Type	Backfill	Deflection (mm)	Load (kN)	Deflection at 11kN
1	66mm Hollow	6mm gravel	28	22.6	2.40
2	66mm Solid	Type 3 GSB	22	34.1	1.50
3	66mm Hollow	Type 3 GSB	16	25.4	2.20
4	50mm Solid	Type 3 GSB	26	20.9	2.40
5	30mm Solid	Type 3 GSB	30	11.1	20.8

After the screed had cured for a minimum of seven days, the arch was lifted three times and the strain measured in the polymeric reinforcement under the self-weight of the arch during lifting and lowering. The maximum strain in the polymer was found to be 1200μ, well below the 67000μ rupture strain of the material.

Each arch was placed on correctly sloped anchor blocks and positioned accurately under the ram of an accurately calibrated load actuator. The formwork was designed and placed with steel on one side and a strong clear plastic on the other side so that deformation and hinge development could be observed during testing. Deflection transducers and vibrating wire strain gauges were then installed under the arch on the intrados at the midspan, third points (under the load point) and near the abutments. The arch was then subjected (without backfill) to a proof load to a limiting deflection of 5mm.

The arch was then backfilled with granular material in equal 100mm layers on both sides of the arch ring to avoid eccentricity and each layer was compacted using a vibro compactor. Deflections under the intrados of the arch were recorded during backfilling operations, but were found to be minimal. Each complete third-scale arch bridge was then tested, with the load applied in 1kN increments across a 150mm wide plate, positioned at the third-span.

3. Results and Discussion

The design variables and results are discussed for each arch below. Each bridge behaved in a similar fashion when loaded. The initial failure was observed as punching shear in the backfill where the granular material deformed greatly due to the high bearing pressure from the load plate. Subsequently the arch deflected downwards under the load point, with an upward deflection at the opposite third-span; observed as the backfill level became raised in this area. Hinge formation was evident in the ring with openings formed between voussoir joints. Each arch was loaded up to a maximum value where it was no longer possible to keep a constant load on the bridge, due to the arch deforming at each load increment and subsequently reducing the applied load. It was impossible to completely break any of the arches, as the internal geotextile kept the blocks connected, even as the deflection (Arch #2) approached the steel floor base.

3.1 Arch #1

This arch was constructed with a ring thickness of 66mm using hollowcore voussoirs with a 45mm void through the centre. This arch system was 20% lighter than an equivalent solid ring (Arch #2) through a reduction in concrete volume from the hollowcore design. A 6mm backfill was used in this bridge and this material sheared greatly under load, due it being poorly graded with only one aggregate size. This produced less resistance in the fill and produced higher deflections at a lower load (Table 1). The maximum load reached was 22.6kN.

3.2 Arch #2

The second arch was constructed with a ring thickness of 66mm using solid voussoirs. A new backfill was constructed using a scaled Type 3 GSB fill (see Section 5.0). This well-graded material was stronger when compacted, and this was evident in the initial deflections as there was less penetration of the load plate into the fill, which gave better load distribution onto the arch. Deflections were noticeably less than the previous arch, and three hinges were clearly visible in this test. This arch sustained the highest load of 34.1kN due to its quality construction and improved backfill (Figure 2).

3.3 Arch #3

The original voussoir blocks from the first arch were used in this bridge, with a new geotextile and top screed applied. This was then tested with the well-graded backfill (used in Arch #2) in order to compare results and determine the effect of the backfill. This backfill performed better as expected, sustaining a load of 25.4kN which was 16% higher than before. The maximum load was less than that of the solid ring (Arch #2) however it should be noted that the well-graded backfill used in both cases is not a perfectly uniform material and will compress at different rates. Test observations in the arch were similar to those above.

3.4 Arch #4

The fourth arch was constructed of solid 50mm voussoirs, achieving an arch ring depth that was three quarters of the previous, resulting in a system 21% lighter than that used in the first arch. The arch was loaded to 20.9kN and both the third-span areas produced fairly symmetrical and opposite responses to load. Although hinges developed as the arch was loaded, a shear failure was observed in a voussoir joint under the loaded area. This was likely due to a debonding that developed in the paragrid under load and also perhaps due to the arch thickness. Load deflection graphs produced similar curves to previous results

3.5 Arch #5

The fifth arch was a thin profile constructed of 30mm solid voussoirs. The shallow ring depth made the system fairly unstable and care was taken during manoeuvring the arch under the load rig, as well as during the backfilling. Deflections of 1.5mm were observed during backfilling due to the movement of the shallow arch ring. The arch was loaded to a maximum value of 11.1kN. Similar responses were found at the third spans with downward deflection under the loaded third span and upward deflection at the opposite third span. A clear hinge was formed under the load which opened to a large extent at failure.

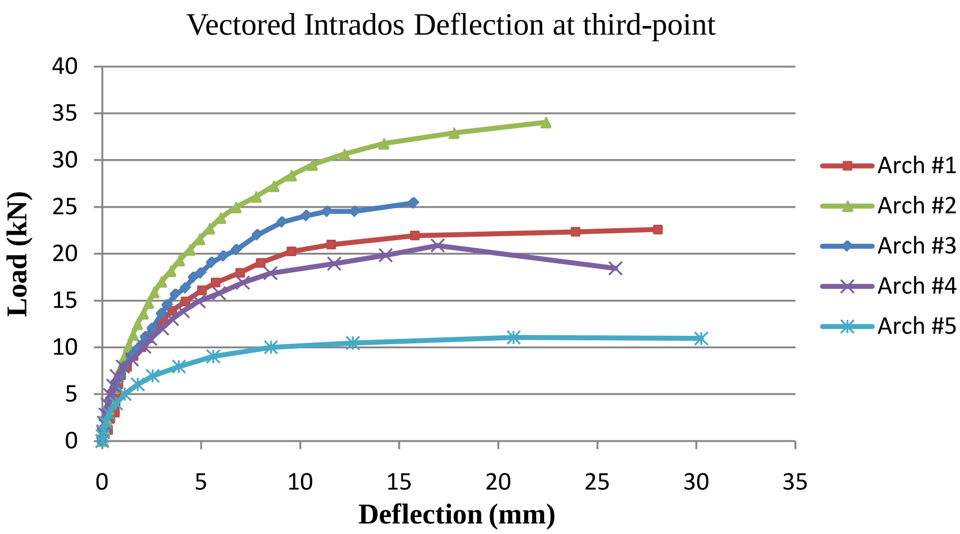

Figure 2 - Load deflection graphs

A comparison of test results for each of the five arches can be seen in Figure 2 and Table 1. The non-linear behaviour of each arch can clearly be seen. This happens due to material and geometric non-linearity as the arch changes shape to resist the increasing load and the line of thrust moves (within the arch ring) towards points where hinges will form. It can be seen that decreasing the ring thickness reduces the load carrying capacity of the arch. The average maximum load taken by arches with 66mm voussoirs was 27.3kN. This value decreased to

20.9kN for a 50mm arch ring, and subsequently to 11.1kN for the fifth arch constructed with 30mm voussoirs. It was clear in the testing that a 30mm ring was too shallow to achieve sufficient stability and the load/deflection results show this. The results for the hollowcore arch (Arch #1) indicated that the solid arch (Arch #2) appeared stronger; however this may not be the case. Both arches failed by hinge formation and no crushing of the voussoirs was evident. Differences in deflection magnitudes can be attributed to the non-uniformity of backfill.

In bridge design, an SV 100 axle load is taken as 165kN (BD91, 2004) which is effectively a 9.17kN wheel load in these scaled tests. The arch tests can be compared more closely for loads up to this value. The difference in the 66mm arches at this level is minimal with deflections of no more than 1.6mm (Fig 3). It should be noted that the tests do not include surfacing which would reduce these deflections further.

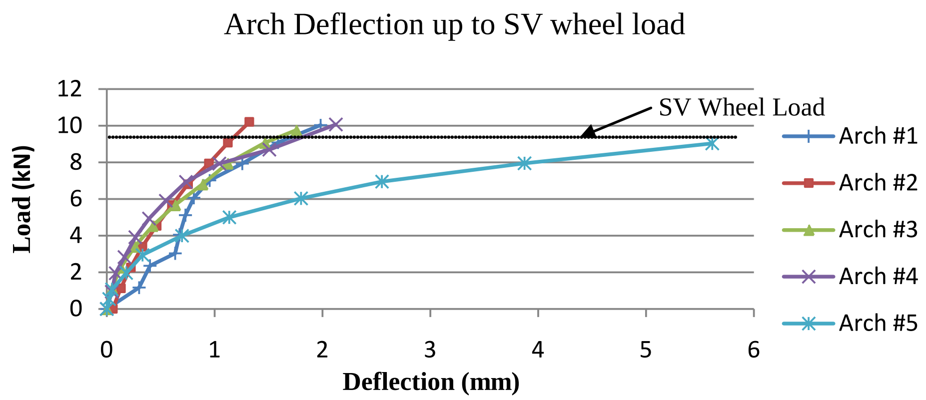

Figure 3 - Vectored Deflection of Arches up to SV wheel load

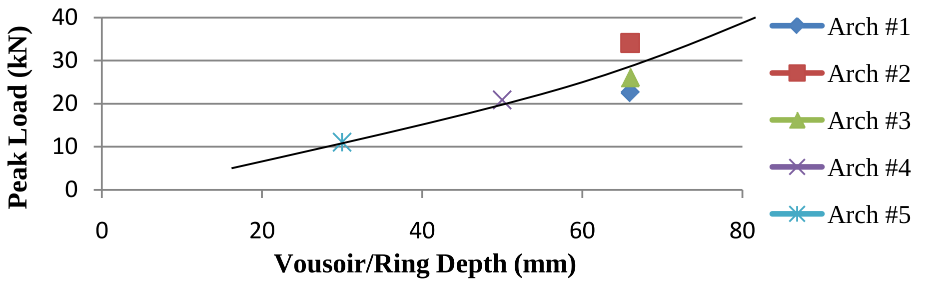

Figure 4 - Relationship between voussoir depth and peak load

The relationship between voussoir depth and peak load has been compared in Figure 4. A further arch test with a voussoir depth of 80mm would be useful to prove whether this relationship is linear or non-linear, however it is hoped that further finite element analysis work will be sufficient to show this. It is clear that halving the ring thickness will typically halve the peak load of the arch in these cases.

4. Influence of Backfill

As stated previously, the backfill type was changed to a fully-graded backfill as it was found that the 6mm aggregate backfill was unsatisfactory in the first test. A backfill was then designed and mix based on a scaled version of the 'Type 3 GSB' fill used in practice. This material is a well-graded fill and provides a higher bearing capacity. The one third scale backfill consisted of 20mm, 10mm, and 6mm aggregates mixed together with sand and grit in proportions to replicate the grading curve of a full-scale Type 3 backfill. It was found that this material did have an effect on the load capacity of the arch model, and the well-graded fill resulted in lower deflections compared to a similar arch model with 6mm aggregate backfill and at the same level of applied load.

In order to determine the shear strength of this well graded fill material, shear box tests were carried out (Fig 5). The main test equipment consists of a steel box with two halves which are slowly moved horizontally against each other until the material contained in the box shears (BS1377, 1990). Proctor compaction tests were carried out on the material to find the optimum moisture content, which was found at 6% (Fig 6). Using this moisture content, the material was compacted in the shear box in three layers, and three shear tests done at loads of 59, 117 and 217kPa. The horizontal load was applied using a proving ring.

Fig 5 - Shear box test equipment

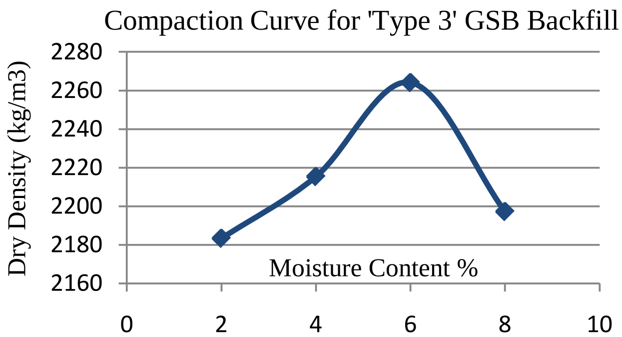

Fig 6 - Optimum Moisture Content for third scale Fill

The load values from the proving ring were translated into shear stress by dividing them by the area of the shear box. The stresses were then plotted against horizontal movement for each test. The peak stresses were then plotted against normal stress to determine peak and ultimate failure angles of 44° and 39° respectively (Fig 7). The lower value of 39° was chosen as the backfill is subjected to a high bearing pressure (as much as 700kN/m^2) from the plate in the test load. This value was used as the strength of the fill for analysis.

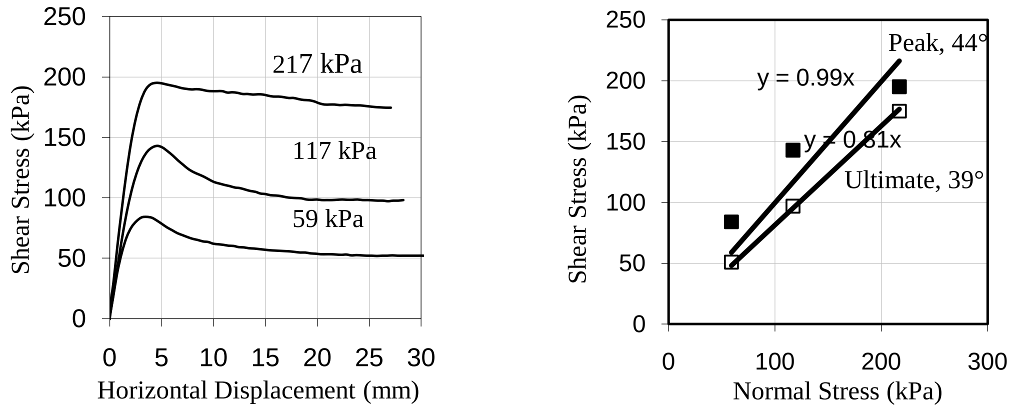

Fig 7 - Shear box test results

5. Non-linear Finite Element Analysis

In recent years a considerable effort has been made to better understand the behaviour of arch bridge up to collapse and to correctly predict the load carrying capacity of masonry arch bridges (Kumar et al., 2004). Non-linear finite element models were constructed to compare different arch bridge tests done in the laboratory and to compare different variables. The FE model was built in steps; which involved construction of the arch geometry, careful selection of material properties, meshing the model, and applying the load progressively in small increments. In non-linear behaviour the stiffness of the structure changes with increasing load as the stresses and strains are modified due to deformation or cracking. The models developed for this research here analysed a third-scale arch ring model with varying strength of backfill. The 'phi' friction angle (ø) is a measure of the strength of granular material. In initial FE models, a nominal value of 30° was used to approximate failure loads, however it was found that the strength of the backfill was greater than this. To determine the effect of this parameter on bridge strength, five arch bridge FE models were constructed and compared, each model representing a third-scale 5m x 2m arch bridge with concrete arch ring and granular backfill.

In all the NLFEA models the backfill failed first through bearing capacity failure before arch deformation led to failure of the bridge. This corresponded to physical observations during laboratory testing. In the first model a failure load of 29.79kN was found using a friction angle of ø=30°. In the second model, the friction angle was modified to ø=40° (representing a stronger fill) and another analysis run. This proved to make the bridge stronger with a failure load of 32.73kN. It could be seen in the contoured deformation output that the backfill had deformed downwards by 547mm at this stage of failure (Fig 8). Subsequently a further three analyses were done with friction angles of 20°, 25°, and 35° in order to produce a range of failure loads. From these, it was possible to determine an estimated failure load of 31.88kN for the friction angle of 39° that had been determined in the geotechnical tests. This value was found to be very close to the value of 34.1kN sustained in Arch Test #2.

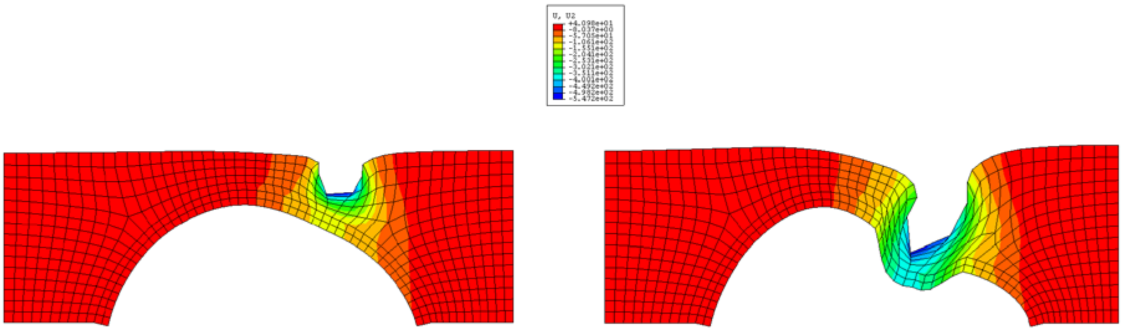

Figure 8 - Failure of backfill in finite element bridge model 1, bridge failure in Model 2

Further finite element modelling will involve a contact analysis, where each block is individually modelled with discrete edges, as well as the inclusion of the geotextile to determine what contribution it may have to the load displacement behaviour of the arch.

6. Conclusions

The results of several third-scale models have been discussed here, showing the effect of the arch variables on the behaviour and load capacity of the bridge concerned. An almost linear relationship was found between arch ring thickness and peak load. Finite element analysis will explore this further. Both geotechnical tests and non-linear finite element analyses have shown the influence of the backfill strength on the predicted failure load of the arch. Further finite element work will continue to compare arch variables with laboratory findings, with the inclusion of the polymeric reinforcement in the model.

7. References

BD91/04. (2004), *Design Manual for Roads and Bridge, Unreinforced Masonry Arch Bridges*. 3.5.1 Vehicles to be considered.

BS1377-7. (1990), *Soils for Engineering Purposes*. Part 4. Determination of shear strength.

Fanning, Paul J, Boothby, Thomas E. 2000. '*Three-dimensional modelling and full-scale testing of stone arch bridges'*. Dept. of Civil Engineering, University College Dublin.

Gupta, Abhey. (2008), *FlexiArch: 'The sustainable option for new crossings and bridge replacement'*. Brochure. Further information at www.macrete.com

Kumar, P, Bhandari, NM. (2004), '*Non-linear finite element analysis of masonry arches for prediction of collapse load'*, p166, Structural Engineering International, March 2005 Issue.

Long, AE, Taylor, SE, Venables, RK, Kirkpatrick, J. (2007), '*Development of Sustainable Forms of Construction'*, Sustainable Construction Materials and Technologies Conference 2007, Coventry, UK.

Mulheron, MJ and Nwaubani SO. (1999), '*Corrosion inhibitors for high performance reinforced concrete structures'*, RILEM TC-AHC:158, The role of admixtures in high performance concrete, Monterey, Mexico.

Taylor, S, Long, A, Robinson, D. (2007), '*Development of a flexible concrete arch'*, p33-37, October 2007 issue of 'CONCRETE'.

UK Highways Agency. (1995), *BD57/95, 'Design for Durability, Design Manual for Roads and Bridges'*. Volume 1, Section 3. Department of Transport , Highway and Traffic. UK.

ASSESSING ASSESSMENT GUIDANCE FOR MASONRY ARCH BRIDGES

N. GIBBONS & P.J. FANNING
Dept. of Architecture, Landscape & Civil Engineering, University College Dublin

Abstract
Masonry arch bridges, most of which have far exceeded modern design lives, have demonstrated themselves to be sustainable structures with low life-cycle costs. However increased traffic loading and material deterioration over time necessitate reassessment of these structures. There are numerous different analytical methods available for the assessment of masonry arch bridges, with an equally diverse range of results. Generally, the expectation would be that for increasing levels of assessment complexity an increase in load capacity would be achieved. However, as the results presented in this paper demonstrate this is not always the case.

This paper describes a programme of research being carried out under the National Road Authority's Research Fellowship Programme to develop a hierarchical assessment framework for masonry arch bridges in order to address this issue. It is envisaged that the assessment framework will include both existing methods and methods developed within this project and will aim to recommend different levels of assessment, specifying limits of applicability for each and providing guidance on their use.

Keywords: assessment, masonry arch bridges

1. General

Masonry arch bridges account for a significant proportion of the bridge stock both in Ireland and throughout Europe. In Ireland there are an estimated 16,000 masonry arch bridges constituting approximately 80% of the national bridge stock (Molloy 1988), and in Europe masonry arches are estimated to account for over 40% of railway bridges.

The results of assessments carried out on 11 single span bridges characteristic of bridges on the Irish road network ranging in span from 2.4 – 15.2m using potential first, second and third level methods are presented and the issues raised in relation to creating an assessment framework are discussed with regard to the current requirements for masonry arch bridge assessment under the Eirspan Bridge Management System.

2. Current Requirements for Stage I Preliminary Assessment

Under the Eirspan Bridge Management System introduced in 2001 to coordinate the maintenance of structures on the national road network (Duffy 2004), many bridges on the national road network have been or are scheduled for assessment as part of Stage I Preliminary Assessments. The Stage I Assessment Methodology Report (NRA 2005) outlines the methodology to be adopted in carrying out inspection, investigation and assessment for a Stage I Preliminary Assessment. Should a Stage II Assessment be required, further analysis or site investigations are determined for each structure and the assessment methodology is to be agreed with the Client.

Stage I Preliminary Assessments cover structures built prior to 1980 and include masonry arch bridges, an example of which can be seen in Figure 1, as well as concrete slabs and prestressed beams. For masonry arch bridges, the Stage I Assessment Methodology Report makes reference to BD 21/01 (Department of Transport 2001) and BA 16/97 (Department of Transport 1997). Additional requirements beyond what is specified in BD 21/01 and BA 16/97 for a Stage I Preliminary Assessment are set out in the Stage I Assessment Methodology Report and are summarized below.

Figure 1 - Glanbehy Bridge

2.1 Inspection and site investigations

Unless site investigations are being carried out an adjoining concrete extension, for masonry arch bridges the site inspection is generally limited to a visual inspection recording the relevant dimensions, the type and condition of the materials, the presence of defects and the general condition of the structure.

Frequently for stone arch bridges, the voussoir stones at the fascia have a greater thickness than across the rest of the arch. For the Stage I Preliminary Assessment site investigation is not required in order to determine the thickness of the arch ring unless site investigation is being carried out on an adjoining concrete structure. Therefore, where site investigation has not been carried out the Stage I Assessment Methodology Report requires that upper bound and lower bound estimates of the ring thickness are made. The upper bound estimate is taken as the thickness of the voussoirs at the fascia and the lower bound estimate is taken as 0.6 of this value.

2.2 Assessment

BD 21/01 requires that masonry arch bridges are assessed using axle load configurations for single, double and triple axle loads for the vehicle configurations set out in The Road Vehicles (Authorised Weight) Regulations 1998 for gross vehicle weights up to 40/44 tonne loading. For a Preliminary Stage I Assessment, the Stage I Assessment Methodology Report specifies that a modified MEXE assessment in accordance with BA 16/97 is carried out, and that where the geometry or the condition of the bridge exclude it from a MEXE assessment a three hinge plastic assessment using the software package Archie is to be carried out.

BD 21/01 states that where the depth of fill is greater than the thickness of the arch ring the modified MEXE method may be unconservative, and consequently the Stage

I Assessment Methodology Report requires that where this is the case that the results of the modified MEXE assessment are corroborated with results from a three hinge plastic assessment using Archie.

For arches where the soffit has been sprayed with concrete, the additional thickness provided by the concrete is not to be taken into account for the Stage I Preliminary Assessment unless the concrete has been dowelled into the arch barrel and founded on abutments.

3. Assessment of bridge set

Properties for eleven bridges, representative of the Irish bridge stock, selected for assessment are listed in Table 1. The bridges ranged in span from 2.4 – 15.2m and covered a variety of bridge shapes including segmental, semi-circular and three-centred/elliptical profiles. As per the Stage 1 Assessment Methodology, where the thickness of the arch ring was not confirmed by site investigation, a lower bound (LB) and upper bound (UB) estimate of ring thickness is required. The resulting ring thickness can be substantial – 0.276m to 0.46m in the case of Glennagevlagh Bridge.

Table 1 - Bridge geometries

Name	Shape	Span m	Rise m	Span/Rise	Width m	Ring thickness m	Depth fill m
Glanlough	Semi-circular	2.4	0.94	2.6	3.1	0.490	0.100
Temple	Segmental	3.0	0.68	4.4	6.525	0.380	0.050
Glennagevlagh LB	Semi-circular	3.05	1.53	2.0	3.6	0.276	0.234
Glennagevlagh UB	Semi-circular	3.05	1.53	2.0	3.6	0.460	0.050
Whistle LB	Segmental	6.21	1.31	4.8	3.65	0.255	0.655
Whistle UB	Segmental	6.21	1.31	4.8	3.65	0.435	0.475
Oghermong LB	Segmental	7.8	2.0	3.9	3.6	0.270	0.400
Oghermong UB	Segmental	7.8	2.0	3.9	3.6	0.550	0.120
Owenmore LB	Segmental	8.6	2.28	3.8	3.82	0.264	0.496
Owenmore UB	Segmental	8.6	2.28	3.8	3.82	0.440	0.320
Killeen	Three-centred	9.29	2.65	3.5	3.15	0.480	0.250
Griffith	Three-centred	9.46	2.71	3.5	3.92	0.446	0.126
Windy	Segmental	10.72	1.97	5.4	4.05	0.670	0.300
Glanbehy	Segmental	13.4	3.40	3.9	6.4	0.625	0.150
Anglesea	Segmental	15.2	1.53	10.0	3.117	0.800	0.300

The bridges were assessed using the two methods that are prescribed in the Stage I Assessment Methodology Report and were also assessed using three further assessment methods which were identified as potential second and third level assessment methods. Each method is described briefly below.

3.1 The modified MEXE method

The Military Engineering Experimental Establishment (MEXE) developed an empirical assessment method for masonry arch bridges (MEXE 1963) based on the work of Pippard (1948). It is now found in its current format in BA 16/97 and is referred to as the modified MEXE method. Pippard assumed a two pinned parabolic arch with a span to rise ratio of 4, loaded at mid-span. Pippard acknowledged that this was not the most onerous loading position for an arch, but argued that it allowed for the least amount of load distribution and therefore a greater concentration of load. Pippard allowed for a small tensile capacity in the masonry and derived an equation for the safe axle load based on a limiting compressive strength.

The modified MEXE method in its present format centres around a nomogram relating the arch span and the total crown thickness to a provisional axle load. This is modified by a number of factors intended to account for variations in bridge geometry and materials and also for defects and deterioration. However, there is a lack of full traceability between Pippard's referenced work and the modified MEXE method which does not promote confidence in its results. There are also a number of limitations to the modified MEXE method stated in BA 16/97 relating to the span length, span to rise ratios, multiple spans and the depth of fill. As will be demonstrated by the results, treating the total crown thickness as a single parameter rather than dividing it into its components of arch barrel and fill material is a major limitation of the MEXE method, as it does not adequately account for variations in ring thickness and the resulting effect on the load capacity of the bridge.

3.2 Plastic Analysis Methods

The two different plastic methods used are based on the plastic analysis methods developed by Heyman (1982). Both identify the location of plastic hinges associated with the line of eccentricity of thrust.

Three hinge plastic method

The three hinge plastic method developed by Harvey (1988) is available as the commercial software package Archie-M. Harvey's method determines the line of thrust associated with the formation of three hinges at which point the arch is still stable. If the line of thrust for a particular load is within the boundaries of the arch ring a fourth hinge cannot form and the ring thickness is deemed to be sufficient to resist the load. If this line of thrust cannot be contained within the thickness of the arch ring the load is deemed to be unsafe.

Rigid block method

The rigid block method developed by Gilbert and Melbourne (1994) is available as the commercial software package ring2.0. This method models the arch ring as a series of rigid blocks with frictional interfaces and therefore can also allow for sliding failure between the blocks. This rigid block method determines the plastic failure load, i.e. the load required for the formation of the fourth hinge to occur. This is expressed as the failure load factor, a multiple of the applied load that has been specified.

3.3 Elastic methods

Two dimensional elastic analysis

The 2D elastic analysis method proposed by Fanning and Boothby (2003) is based on a unit width plane frame model of the arch barrel. The arch is divided into a number of segments running along the centreline of the arch ring and modelled as straight beam elements. A single modulus of elasticity is assumed for the masonry mortar continuum. The support conditions are assumed to be fixed in the vertical direction and against rotation and spring supports are provided in the horizontal direction. This allows the model to account for movement where the abutments are not well founded. Recommended material properties and abutment stiffnesses are derived from full bridge tests. The live loads are assumed to be distributed over a 3m width and a corresponding unit width load is determined. In the longitudinal direction, the live loads are assumed to be applied over a 300mm wheel contact length and distributed longitudinally at a ratio of 1:2, horizontal to vertical. The fill is included in the model as a dead load and does not contribute to the strength or stiffness of the bridge.

The method set out by Fanning and Boothby assumes that the arch ring has a limited tensile capacity and derives an equation for the compressive strength required to resist the axial forces and bending moments based on the ratio of tensile to compressive strength and on the cross section of the arch barrel.

Three dimensional elastic analysis

The 3D elastic analysis method is an extension of the 2D one where the arch barrel is modelled using shell elements. Again a single modulus of elasticity is assumed for the masonry mortar continuum, the fill does not contribute to the strength or stiffness of the bridge, the live loads are assumed to be distributed laterally over a 3m width and in the longitudinal direction at a ratio of 1:2, spring supports are provided in the horizontal direction and it is assumed that the masonry arch has a limited tensile capacity.

All of the assessments methods previously described are based on two dimensional unit width models, and do not directly take account of the transverse structural behaviour of the arch. An advantaged of the 3D elastic method is that by modelling the arch as a three dimensional shell the transverse structural behaviour of the arch is also accounted for and can be assessed.

4. Discussion of Results

The allowable axle loads per axle for a double axle with a 1.8m axle spacing were determined for each of the different assessment methods. For each assessment method, bar the modified MEXE method, the resulting assessed axle loads included factors in accordance with BD 21/01, i.e. a load factor of 1.9 was applied to all of the axles and a further impact factor of 1.8 was applied to the critical axle. For the modified MEXE method there is no explicit inclusion of axle load factors

Normalized results are presented graphically in Figure 2 where the allowable axle load, for each assessment method, has been normalized with respect to the results from the 3D elastic method for each individual bridge.

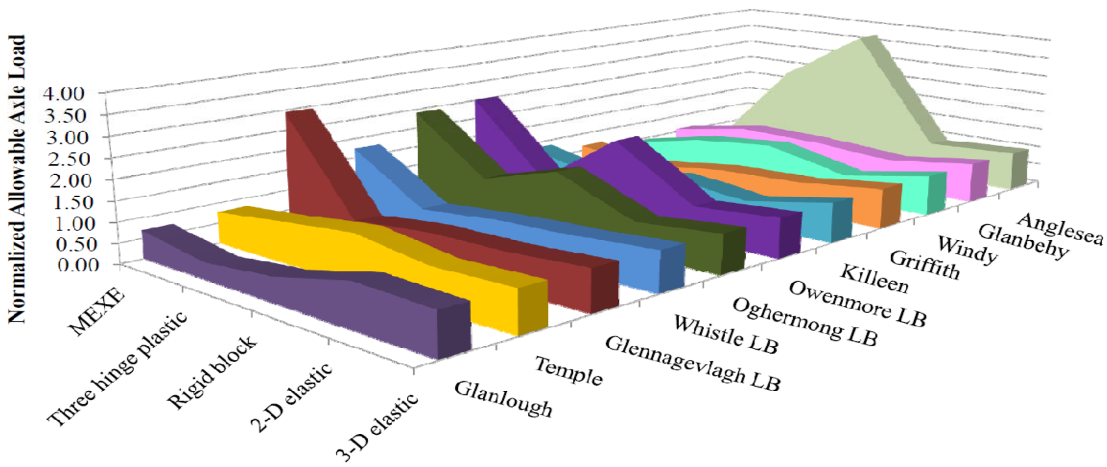

Figure 2 – Normalized Axle Loads

The results for each assessment method are ranked from 1 to 5 in Table 2, with 1 being assigned to the assessment method which gave the highest allowable axle load. There is clear variation in assessed capacity and none of the assessment methods consistently gave either the highest or the lowest allowable axle load.

Table 2 - Ranking of assessment results

Name	MEXE	Three hinge plastic	Rigid block	2-D elastic	3-D elastic
Glanlough	3	5	4	1	2
Temple	5	3	1	4	2
Glennagevlagh LB	1	5	4	3	2
Whistle LB	1*	5	4	3	2
Oghermong LB	1*	3	2	5	4
Owenmore LB	1*	5	2	4	3
Killeen	2	5	3	4	1
Griffith	4	5	3	2	1
Windy	5	3	1	4	2
Glanbehy	5	2	3	4	1
Anglesea	–	2	1	4	3

*MEXE result may be unconservative as depth of fill is greater than arch ring thickness
– Bridge profile too flat for MEXE assessment

There are four bridges for which the modified MEXE method gives a significantly higher result than all other assessment approaches – Glennanevlagh Bridge, Whistle Bridge, Oghermong Bridge and Owenmore Bridge.

The current requirement of the Stage I Assessment Methodology Report is that where the depth of fill is greater than the thickness of the arch ring the results of a MEXE assessment should be corroborated with results from a three hinge plastic assessment. This is supported by a statement saying that MEXE may be unconservative in such cases. However, for the three bridge profiles (Whistle, Oghermong and Owenmore) where this was the case the three hinge plastic method gave a lower result than the MEXE method and was therefore unable to confirm or support the MEXE result. Equally the MEXE result could not be corroborated or confirmed with any of the other assessment methods either. In relation to Glennanevlagh Bridge there would be no basis questioning the rating achieved by MEXE. On the basis of these results there is no evidence to suggest that MEXE can be corroborated by any other assessment method.

A study of the sensitivity of assessments to arch ring thickness was undertaken using these same four bridges. The varying ring thicknesses considered are given as upper (UB) and lower (LB) bound values in Table 1. Normalized axle loads are plotted in Figure 3 – in each case the allowable axle load has been normalised with respect to the allowable axle load determined by the 3D elastic method using an upper bound for the ring thickness. For all methods, bar the modified MEXE method, there is a reduction in allowable axle load due to a reduction in ring thickness. The modified MEXE method is largely insensitive to arch ring thickness. This is an anomaly associated with the MEXE method. The modified MEXE method treats the total crown thickness, i.e. the combined thickness of the arch ring and the fill at the crown, as a single parameter in determining the provisional axle load for a bridge and any variation in the percentage of the total crown thickness which is attributed to the ring thickness is not reflected in the resulting bridge capacity.

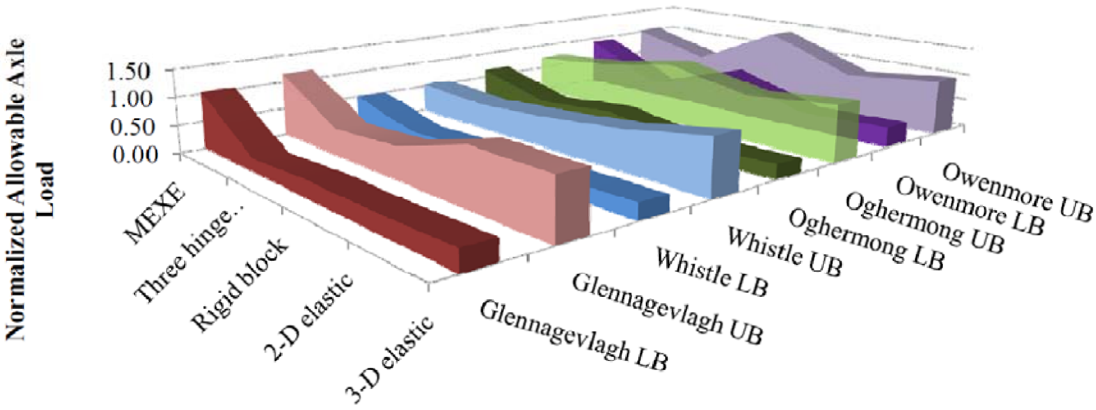

Figure 3 – Normalized Axle Loads for varying Ring Thicknesses

In Figure 4 the assessment ratings for MEXE are excluded as is the flat Anglesea Bridge which is outside the limits of plastic analysis methods due to its span to rise ratio. Immediately there is a consistency of assessment ratings across all bridges and changes in ring thickness are reflected in increased/reduced capacity as expected. Generally the highest rating is achieved with either the rigid block plastic method (which allows four hinges to develop) or the 3D elastic method. The rigid block method produced the highest rating for bridges whose profile reflects the line of thrust when the axles are at the critical location near to the quarter span while the 3D elastic method produces highest ratings for bridges with three-centred arch profiles or semi-circular profiles. Relative to the performance of the three hinge plastic method and the 2D elastic method these trends are consistent with expectations – increased load is required to develop four hinges whereas 3D load dispersion results in less stress demand.

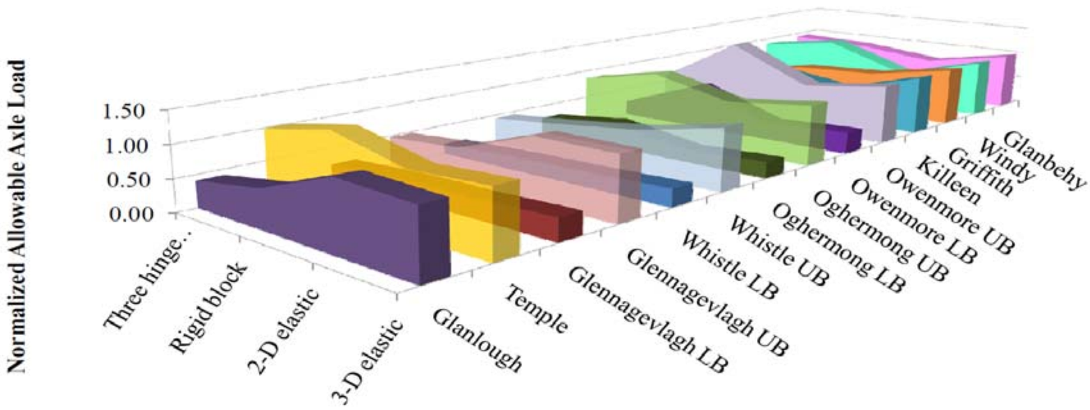

Figure 4 – Normalized Allowable Axle Loads (excluding MEXE & Anglesea Bridge)

5. Conclusions

Eleven different bridge geometries and profiles have been assessed using five different assessment approaches. Current assessment guidelines require the use of the modified MEXE method with corroboration in certain circumstances. No alternative assessment method was found to corroborate the MEXE method. The intuitive expectation of increased capacity as a function of arch ring thickness is not reflected in MEXE assessments. It is using all other assessment approaches.

Plastic analysis methods were found to result in unusually high ratings for flat arches with thick rings. Plastic methods produce the highest rating for bridge whose profiles match the expected line of thrust when the load is applied at its critical location. Elastic methods produce higher ratings for three-centred or semi-circular arch profiles.

Three dimensional elastic methods produced higher ratings than two dimensional ones. Four hinge plastic analysis methods resulted in higher ratings than three hinge methods. Both of these findings are consistent with convergence towards actual bridge capacity as appropriate analysis complexity is increased to reflect real bridge behaviour more faithfully.

The results presented are part of an ongoing research programme directed towards establishing a hierarchical framework of assessment algorithms for masonry arch bridges where increasing analysis effort is reflected in convergence to the expected bridge capacity. At this point it is difficult to see any set of recommendations emerging that would include the continued use of the modified MEXE for masonry arch bridges.

6. Acknowledgements

The authors gratefully acknowledge the National Roads Authority of Ireland for funding this research under the National Roads Authority Research Fellowship Programme 2008.

References

Department of Transport (1997), BA 16/97 The Assessment of Highway Bridges and Structures, *Design Manual for Roads and Bridges*, Volume 3, Section 4, Part 4, London, HMSO.

Department of Transport (2001), BD 21/01 The Assessment of Highway Bridges and Structures, *Design Manual for Roads and Bridges*, Volume 3, Section 4, Part 3, London, HMSO.

Duffy, L. (2004), Development of Eirspan: Ireland's bridge management system, *Proc. Inst. Civ. Eng. Bridge Eng.* **157**(BE3), 139-146.

Fanning, P.J. and Boothby, T.E. (2003), Experimentally-based assessment of masonry arch bridges, *Proc. Inst. Civ. Eng. Bridge Eng.* **156**(BE3), 109-116.

Gilbert, M. and Melbourne, C. (1994), Rigid block analysis of masonry structures, *The Structural Engineer*, **72**(21), 356-361.

Harvey, W.J. (1988), Application of the mechanism analysis to masonry arches, *The Structural Engineer*, **66**(5), 77-84.

Heyman, J. (1982), *The Masonry Arch*, Chichester, Ellis Horwood.

House of Commons (1998), *The Road Vehicles (Authorised Weight) Regulations 1998*, SI 1998/ 3111, London, HMSO.

LimitState (2007) *Theory and modelling guide*, *Version 2.0*, Sheffield, Limit State.

Military Engineering Experimental Establishment (1963), *Military Load Classification of Civil Bridges by the Reconnaissance and Correlation Methods*, Solog Study B38, Christchurch, SRDE.

Molloy, E. (1988), *Report on inspection, assessment and rehabilitation of masonry arch bridges*, Dublin, Department of the Environment.

National Roads Authority (2005), *Stage I Assessment Methodology Report Revision A*, Dublin, National Roads Authority.

Pippard, A.J.S. (1948), The Approximate Estimation of Safe Loads on Masonry Bridges. *The Civil Engineer in War*, **1**, 365-372.

Finite Element Analysis of a Skewed Flexi-Arch

D.J. Robinson, R. Johnston & S.E. Taylor
School of Planning, Architecture and Civil Engineering
Queen's University Belfast

Abstract
The research uses a nonlinear brittle plasticity model to capture the failure mechanism in the arch. The plasticity models can simulate both the behaviour of the ring and the backfill which can either be granular or concrete. However it is notoriously difficult to obtain convergence when using these brittle plasticity models if the traditional implicit approach is adopted. To alleviate these difficulties an explicit approach is used instead, the explicit approach is normally used for transient dynamic problems but if the loading is applied slowly then a pseudo static analysis can be achieved. The skewed nature of the arch requires a fully three dimensional analysis to be undertaken. This provides the opportunity to assess the computational effort needed to undertake the three dimensional analysis of the arch. Where as the use of the explicit method eliminates the convergence problems this is at the expense of having to run the analysis using extremely small time steps in order to keep the analysis numerical stable.

Keywords: Arches, explicit analysis, finite element method

1. Introduction

The paper focuses on the use of the explicit finite element method to analyse arches. The arches under consideration are the flexi-arch systems developed in conjunction with Queen's University and Macrete Ltd (Taylor et. al. 2006). The construction of the flexi-arch simplifies the finite element modelling with the absence of an integral spandrel wall allowing the flexi-arch to be considered as a 2-dimensonal model greatly reducing the computational effort required to perform the analysis. However recent developments with the flexi-arch have introduced a skew to it. From a modelling perceptive this requires the arch to be considered as a fully three dimensional structure. This provides the opportunity to study the performance of the explicit method under these more demanding computational conditions.

The arches presented have been backfilled with both granular and concrete backfill. The behaviour of the granular backfilled arches is more typical of the behaviour of traditional arches and also they are potentially more cost efficient and environmental friendly. The concrete backfilled arches are significantly stronger but do behave differently from conventional arches and this can cause problems if traditional methods are used to analyse the arches as the theory behind the method may not be capable of describing the failure mechanism of the arch. An advantage of adopting the finite element approach is that it can accommodate both the granular and concrete backfilled arches.

2. The finite element approach to analysis arches.

The approach of using the finite element method to capture the behaviour of arches relies on the nonlinear plasticity modelling capabilities of the method (Robinson & Taylor 2008, Ng et.al. 1999, Fanning & Boothby, 2001). The typical failure mode of the arch is through the formation of hinges in the ring of the arch leading to a mechanism occurring when four hinges have formed. These hinges can be simulated through the use of a brittle plasticity model. In addition capturing the spread of the load through the backfill is essential for the accurate prediction of the failure load for the arch. For a granular backfill a Drucker/Prager plasticity model can perform this role. A further complication of the arches studied in this report is the concrete backfill used in some of the arches. The concrete backfill can change the behaviour with the arch effectively behaving as if it has a extremely thick ring. This will inhibit the formation of the hinges and failure will tend to occur as a result of a punching failure through the concrete backfill at a relatively thin section of the arch. A material model which accurately predicts concrete is therefore needed for this type of backfill.

The Abaqus finite element package was used for the analyses presented in this paper. The Abaqus package provides a wide range of material models, two of which have been selected for this work. The concrete damaged model was used for both the arch ring and the concrete backfill. In order to model the ring the tensile strength of the concrete was taken to be extremely small. While for the concrete backfill the parameters defining the material model where selected to match those of the actual concrete used.

A feature of the Abaqus package (ABAQUS 2004), is its ability to undertake both implicit (Abaqus/Standard) and explicit (Abaqus/explicit) analyses. The implicit approach is the method normally associated with the finite element method. For a non-linear static analysis the load is applied in load increments with Newtons/Raphson method being used to solve the non-linear equilibrium equations formed at the start of each increment. This works well for smooth problems however for certain problems it can be extremely difficult to obtain convergence. Both the Drucker/Prager and concrete models fall under this category with the concrete model being particularly difficult to obtain equilibrium at the end of each increment (Molins & Roca 1998).

The explicit method offers a solution to the convergence problems. The explicit method is really a dynamics method where the solution at the next time step can be calculated based on the deformation at the current load increment without the need to solve a system of equations. As a result there are no convergence difficulties and the computational effect for a time increment is extremely small. Although this is essentially a dynamic analysis a quasi-static analysis can be undertaken if the load is applied using a relatively slow loading rate. Unfortunately the method is conditionally stable and the size of the time steps has to below a critical value with the step being a function of the smallest element. This has significant impact on the computational effort required and influences the approach adopted when using a explicit analysis. The smallest element in the model will dictate the length of time the analysis will take to run. For quasi-static analysis a relatively long loading time is required and hence an extremely high number of time increments will be required. A linear analysis will take just as long as a highly nonlinear analysis.

3. Two dimensional finite element analysis of straight arches

Initially 2-dimensional plane stress models for two non-skewed were considered. These analyses provide a useful insight before embarking on the 3-dimenisonal analysis of the skew arches. Experimental test results are available for the 2-dimensional but as yet there are no experimental results available for the skew arch. The test results are important for the validation of the results. For the experimental tests the granular material was held in position by shuttering. The dimensions of the 2-dimensional arches are given in Table 1; one of arches has a granular backfill while the other has a concrete backfill.

Initially a gravity load is applied to the arches; this was followed by a loading applied to the one third position along the arch. There was, however, a difference in the loading for the granular and concrete backfill models to reflect the actual loading of the experimental tests. The granular backfill was loaded over a 150mm x 333mm area; this was necessary to avoid a load bearing failure under the load. The concrete model was on the other hand loaded by a line load across the 333mm width of the arch, as the concrete was capable of withstanding the load.

Table 1 – Dimensions of arch

Dimension	Value mm	Dimension	Value mm
Overall Length	4036	Depth of arch ring	75
Effective span	3333	Width of arch	333
Height to Intrados	667		

The models were run using both implicit and explicit analysis. However when using the implicit analysis is wasn't possible to run the analysis to failure with the increment sizes becoming extremely small causing the analysis to grind to halt well before failure. The implicit analysis were run using 8 node quadrilateral elements however this was changed to 4 node quadrilateral elements for the explicit analysis as the 8 node elements are not permitted because of problems with the mass matrices.

3.1 2-dimensional granular model

The granular material was modelled using a Drucker/Prager plasticity model with no cohesion and an angle of friction of 30^o, while the ring of the arch was modelled using a brittle model with a tensile strength of 0.05 N/mm^2. Figure 1 shows the load-deflection plot for the finite element analysis at the central point of the arch ring.

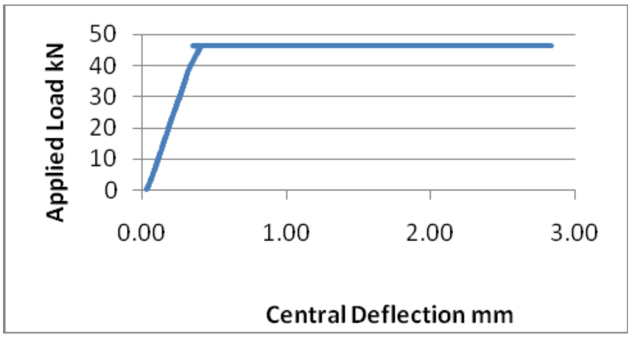

Figure 1- Load/deflection graph for straight arch with granular backfill

With the explicit method the point of failure can be difficult to identify precisely however with the arches it is obvious from the load-deflection plot being represented by the horizontal line given in Figure 1. The failure load predicted form the finite element analysis was 47kN. The deflection of the arch up to this point was extremely small 0.4mm. The deflections from the finite element method are much smaller than the test deflections (Ross 2010) as the finite element isn't able to model the movement that occurs between the individual blocks of the arch. Careful examination of the graph will highlight that the central deflection reverses just before it fails. This is an actual physical occurrence. When the hinges form the arch deforms as a mechanism, the region of the arch ring below the load will continue to sink but the centre will rise. However this occurs only for a short time before the arch completely collapses. In the actual test the arch was loaded to 31.43kN (Ross 2010) at this point the structure was starting to exhibit the formation of hinges. The loading was stopped at this stage as total failure of the arch ring was to be avoided as the same ring was to be used for the concrete backfill test. The actual test failure load of the arch with granular backfill would therefore be a little bigger than the 31.43kN.

Figure 2 shows the plastic stains in the arch just before failure. The presence of four hinges in the arch is apparent, a hinge has formed near each of the supports while two further hinges have formed near each other close to where the load was applied.. The actual arch ring consist of voussiors resting on each other and therefore have no tensile strength, it is therefore important for the material modelling them to have very little tensile strength. The failure load for the arch is fairly constant for tensile values below 0.1 N/mm^2, for values greater than this the arch will become noticeably stronger. A value of 0.05N/mm^2 has been used for the analysis undertaken here.

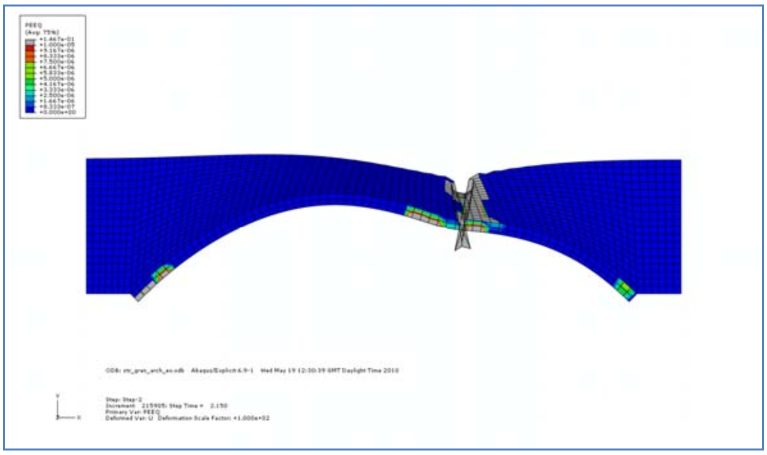

Figure 2 – Plastic tensile strain for straight arch with granular backfill

3.2 2-dimensional concrete backfill model

The backfill consisted of a weak concrete; the compressive strength of the material was taken as 15N/mm^2 and tensile strength of 1N/mm^2, the ring was modelled as in the previous case. Figure 3 shows the load-deflection plot from the finite element analysis for the arch with concrete backfill. The profile of the graph is very similar to the granular backfill with the graph showing a sudden failure at 171kN. On this occasion there wasn't any rising of the centre portion of the ring just before failure. This is in keeping with a different type of failure with the region under the loading punching through. The failure of the actual test arch was at a load of 160kN (Ross 2010).

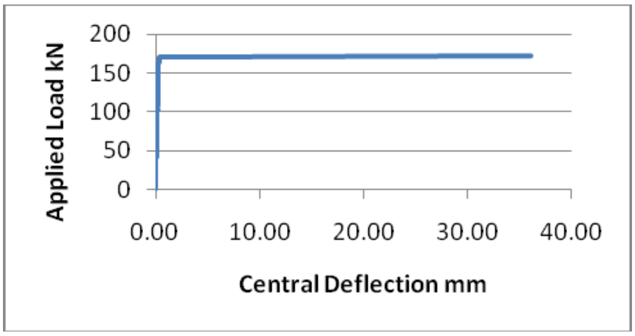

Figure 3- Load/deflection graph for straight arch with concrete backfill

Figure 4 shows the tensile plastic strains in the arch just before failure, there are no hinges at the supports which prevent a mechanism forming and failure occurs as a more localised failure in the vicinity of the loading.

The predicted failure load of 171kN matches with the test load of 160kN very well, however it has been found that the failure load from the finite element model is very sensitive to the tensile strength of the concrete backfill, and not sensitive to its compressive stress. The concrete used for the backfill was a weak mix with compressive strength of 15N/mm^2, which was not compacted when it was placed over the arch ring. A tensile strength of 1N/mm^2 was taken for the finite element analysis. If this value is increased to 1.5N/mm^2 then the failure load will jump up to 234kN.

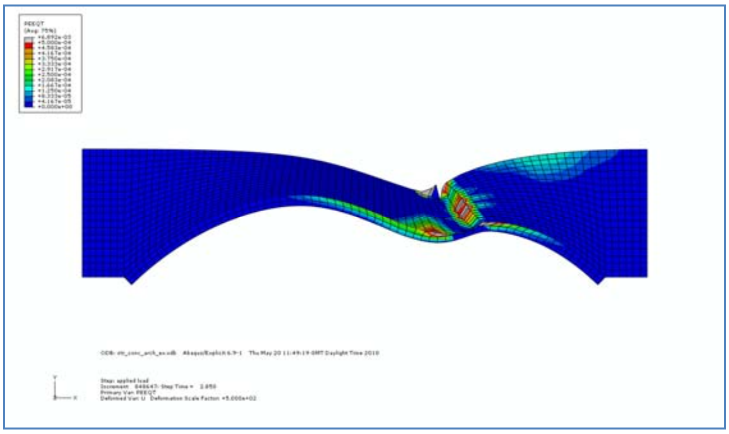

Figure 4 – Plastic tensile strain for straight arch with concrete backfill

4. Finite Element analysis of the skew arch.

The geometry of the skew arch was based on the profile of the straight arch but with a skew of 25°. The 3-dimensional geometry was created in Abaqus by lofting between two planar profiles. The model was meshed using tetrahedral elements rather that hexahedral elements. The hexahedral quadratic elements are not available for the explicit method only the linear element can be used, however there is no restriction on the quadratic tetrahedral element and it was thought that the quadratic tetrahedral would perform better than a linear hexahedral. As for the 2-dimensional models the loading for the granular and the concrete backfill arches was different. The granular model was loaded using a pressure loading over a 150 by 333mm region. A line load across the concrete backfill model was what was intended but the Abacus model doesn't allow a line load to be applied so a concentrated load in the middle of what would have been the line load was used instead. Figures 6 and 9 shows the models used for the analysis.

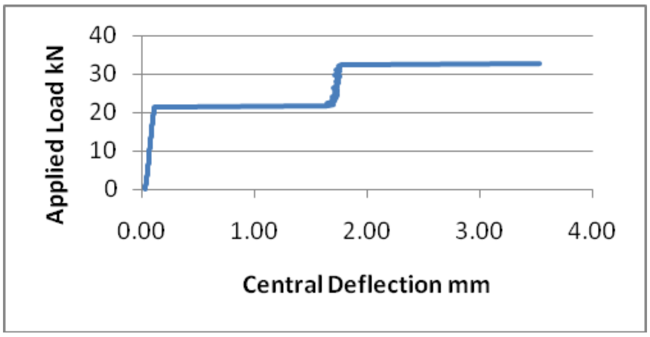

Figure 5- Load/deflection graph for skew arch with granular backfill

4.1 The skew arch with granular backfill

Figure 5 shows the load/deflection plot for the granular skew arch. This plot is very unusual with the arch performing as expected up to 22kN and then there is a sudden increase in deflections as if the arch was collapsing but the arch instead takes further loading up to a failure of 33kN.

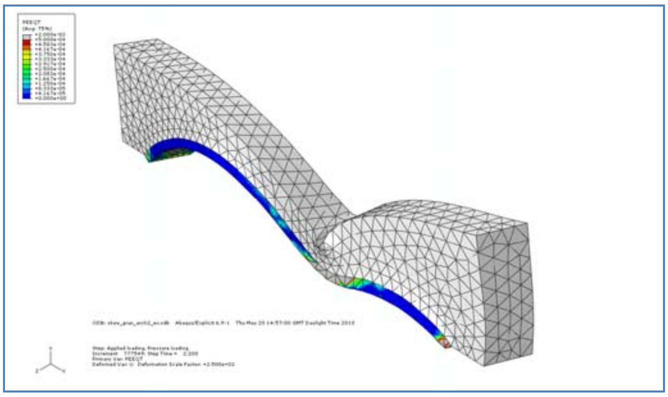

Figure 6 – Plastic tensile strain for skew arch with granular backfill

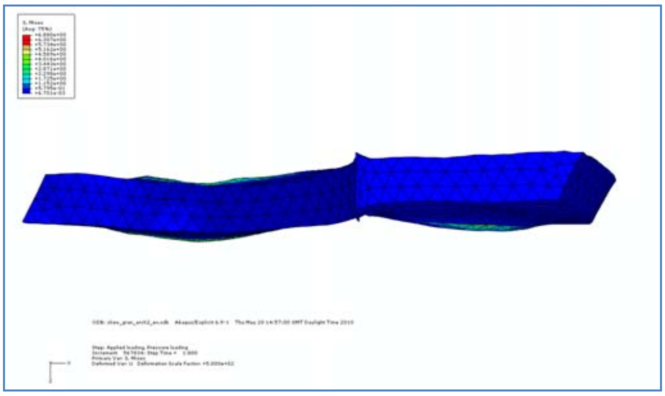

Figure 7 – Twist developed at load of 22kN for skew arch with granular backfill

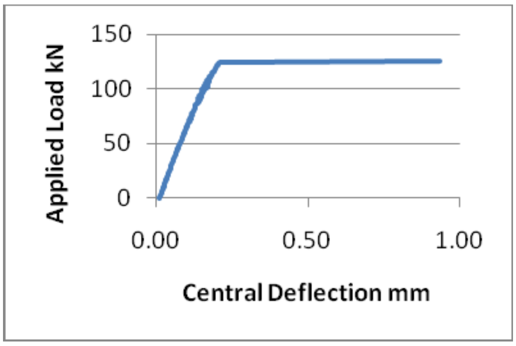

Figure 8- Load/deflection graph for skew arch with concrete backfill

The tensile strains at a load 33kN are shown in Figure 6. As with the 2-dimensional arch the positions of 4 hinges can be observed. The cause of the jump at 22kN can be seen from Figure 7 which is a plot of the arch looking down on it just after a 22kN load was applied. The arch suddenly undergoes a type of lateral torsional buckling at 22kN. The arch is untwisted prior to this load and the twisted shape shown in figure 7 remains to ultimate load of 33kN. Unfortunately experimental tests haven't yet been undertaken on the skew arch so it hasn't been able to validate this behaviour.

4.2 The skew arch with concrete backfill

Figure 8 shows the load/deflection plot for the concrete backfill. The figure shows the arch failing at a load of 122kN, this is compared with 171kN for the straight arch. Unlike the skew arch with granular fill there was no evidence of this arch undergoing major lateral torional buckling behaviour. Figure 8 shows the plastic deformation just before failure. The failure mode is similar to that for the straight arch with more of a punching shear through the concrete rather than a hinge mechanism.

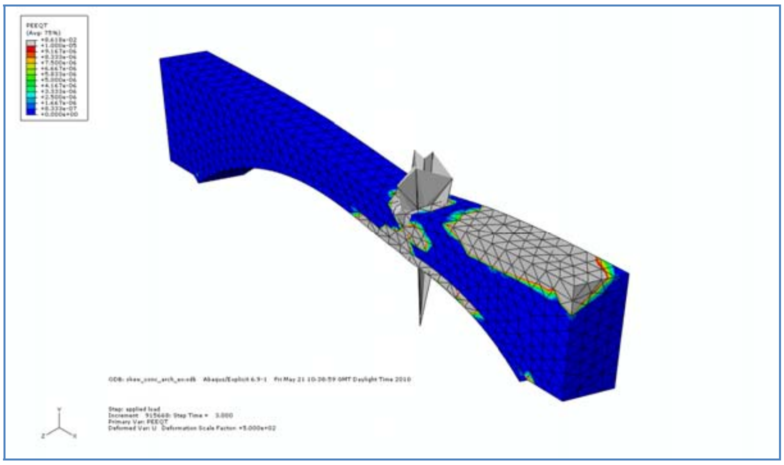

Figure 9 – Plastic tensile strain for skew arch with concrete backfill

5. Conclusions

The severe convergence problems associated with the implicit method particularly when using the concrete backfill makes the explicit method the only viable method for analysing the failure of the arches. The finite element studies on the 2-dimensional arches have indicated that the explicit method can be used to make accurate predictions of the failure load of the arch. However the time step required for the explicit method is extremely small and is a function of the smallest element. Using the explicit method does require the user to model the problem differently; when using the explicit method it is best to avoid local mesh refinement, one small element can make the analysis quadruple its time to run. Also a simple linear analysis will take just as long as a complicated nonlinear analysis for example it is not very efficient to use the explicit method to apply the self weight to the arch, it may therefore be sensible to use a mixture of explicit and implicit methods. Although Abaqus doesn't allow the combination of explicit and implicit in one analysis, the restart facility can be used to combine the two analyses.

The results from the 2-dimensional analysis showed good comparison between the predicted failure loads and those found from the experimental test. The arch geometry used here was a shallower arch than one previously tested (Robinson & Taylor 2008). The finite element results for the early deeper arch were also very encouraging providing further evidence to the explicit finite element method as a means of predicting the failure load for the arch. However the models are sensitive to the tensile strength of ring and concrete back fill material and care needs to be taken when choosing these values. Consistent results will require consistent selection of key material properties.

The results from the skew models indicated that the introduction of the skew caused the ultimate load to decrease by about 28% for both granular and concrete models. The failure modes for the skew arches followed that of the straight arches; however the granular skew did show buckling at a load below the ultimate load which was not evident from the straight arch. This behaviour needs further investigation and it may well be sensible to take the lower load of 22kN to be the failure load rather that the 33kN.

References

Taylor, S. E., Gupta, A., Kirkpatrick, J., Long, A. E., Rankin, G. I. B. and Hogg, I. (2006), 'Developing of a novel flexible concrete arch system' in *11th International Conference on Structural Faults and Repairs*, Edinburgh.

Robinson, D. J., Taylor S. E., (2008) 'A modern analysis for a contemporary arch', Proceedings of CRI08 and BRI08 Joint Symposium, Galway.

Ng, K. H., Fairfield, C. A. and Sibbald, A. (1999), 'Finite-element Analysis of Masonry Arch Bridges', *Proceedings of the Institution of Civil Engineers, Structures & Buildings*, 134, 119-127.

Fanning, P. J. and Boothby, T. E. (2001), 'Three-dimensional modelling and full-scale testing of stone arch bridges', *Computers and Structures*, Vol 79, 2645-2662.

ABAQUS Inc. (2004), ABAQUS/Explicit Users Manual (version 6.5), 2004.

Molins, C. and Roca, P. (1998), 'Capacity of masonry arches and spatial frames', *Journal of Structural Engineering*, 125,653-663.

Ross, J. (2010), 'The development of the skew flexible concrete arch', MEng. project report, Queen's University Belfast.

PARAMETERS AFFECTING THE ALBEDO EFFECT IN CONCRETE

A. SWEENEY[1], R.P. WEST[1] and C. O'CONNOR[2]
[1] TrinityHaus, Department of Civil, Structural and Environmental Engineering, Trinity College, Dublin 2, Ireland
[2] Ecocem Ireland Ltd., Thorncastle Street, Ringsend, Dublin 4, Ireland

Abstract

This paper presents a review of ongoing research at Trinity College into the parameters which affect the albedo effect, that is, solar reflectance of concrete. Some previous research by others considered the effect of the composition of concrete on the solar reflectance. Extending this work, the objective of this research is to quantify the improvement in albedo in concrete containing different aggregates and ground granulated blast furnace slag (GGBS) of varying proportions for different types of concrete finish. The subsequent change in light reflectance and heat absorption will allow one to establish the equivalent reductions in CO_2 by virtue of reduced air conditioning costs in buildings, reduced heat emissions from warm surfaces and increased light reflected back into the universe.

Three aggregate types will be used (crushed limestone, partially crushed limestone and sandstone) with four different percentages of GGBS (0, 30, 50 and 70%). There will be four different surface finishes each to represent certain applications such as a roof area, pavement or car park. A number of devices will be compared in determining an albedo value including a lux meter, solar reflectometer, thermocouples and infrared camera.

Some preliminary research has been conducted to investigate the potential for the use of high solar reflectance concrete within the Trinity College campus. It was found that although the potential surface area which could be used is relatively small (one-third of the total), the corresponding offset in carbon dioxide emissions could be significant (approximately 4,000 tonnes per year).

Keywords: Aggregate types, albedo, carbon dioxide emissions, GGBS, reductions in CO_2, solar reflectance, surface finish

1. Introduction

Solar radiation includes visible light (typically 43% of solar energy), near infrared light (52%), and ultraviolet light (5%). Albedo is the ratio of reflected solar radiation to the total amount that falls on a surface, known as incident solar radiation (ACPA, 2002) and is measured on a scale of 0 to 1. An albedo value of 0 indicates a "black" body that does not reflect any light whereas an albedo value of 1 indicates a "white" perfectly reflective surface (Boriboonsomsin and Reza, 2007).

In developed urban areas, paved surfaces (footpaths, car parks, pavements) account for a large percentage of the total surface area, typically between 30% and 40% (ACPA, 2002). Dark materials such as asphalt are generally used to pave these surfaces and thus absorb the incoming solar radiation. The absorbed solar radiation is converted into heat, causing the surface temperature to become higher than the ambient air temperature and infrared radiation to be reemitted. As the surfaces become warmer, the local ambient air temperature also increases. Where air and surface temperatures are warmer than their surrounding areas, this can create a ‘heat island’ (Gartland, 2008). The heat island effect can cause a number of problems including increased energy demand to cool buildings, which results in large air conditioning bills and an increase in emissions from power plants. It also increases the formation of smog as a higher temperature induces higher rates of photochemical reactions.

In order to reduce the heat island effect by reducing the temperature of the paved surfaces, it is necessary to increase the albedo, or solar reflection. One method would be the use of high solar reflectance concrete as concrete is lighter in colour than asphalt - grey Portland cement concrete typically has an albedo of approximately 0.35 (compared to 0.05 for asphalt). However, by altering the composition of the concrete it is possible to increase this value, in particular by substituting the grey cement with GGBS, which is substantially lighter in colour. Some typical albedo values are given in Table 1.

Table 1 - Typical albedo values (ACPA, 2002)

Surface	**Albedo**
Snow	0.90
Ice Caps	0.80-0.90
White Acrylic Paint	0.80
GGBS Concrete (50%)	0.50
New Concrete (traditional)	0.30-0.40
Aged Concrete	0.20-0.30
Roof Area	0.20
Aged Asphalt	0.10-0.15
Ocean	0.06-0.10
New Asphalt	0.05
Black Paint	0.05

Carbon dioxide is a greenhouse gas and it tends to block radiation from the earth’s atmosphere. Prusinski et al. (2004) conducted research into the carbon dioxide emissions arising from the use of cement and its embodied energy. Although cement makes up only 10% to 20% of the concrete mixture, the cement is responsible for up to 85% of the total embodied energy and 94% of the carbon dioxide emissions.

In order to produce one tonne of Portland cement, approximately 0.9 tonnes of carbon dioxide is generated. GGBS requires nearly 90% less energy to produce than an equivalent amount of Portland cement and the production of carbon dioxide during the manufacture of GGBS is practically negligible. Prusinski’s research is confined to substitution rates of between 35 and 50% GGBS.

2. Materials and Methods

2.1 GGBS

GGBS is a waste product from the blast-furnace production of iron from ore and is used to replace cement in concrete structures. As GGBS is significantly lighter in colour in comparison to conventional Portland cement (Figure 1), its inclusion in concrete subsequently produces a concrete which is lighter in colour. A lighter coloured concrete surface has increased solar reflectivity which results in brighter environments. This increases visibility especially at night time, leading to reduced lighting by approximately 30% (Riley, 2008) and improves safety (SCA, 2003). As it has a higher albedo value it can help to reduce the heat island effect and this can result in achieving LEED (Leadership in Energy and Environmental Design) credits (SCA, 2006). This is a national standard developed by the United States Green Building Council which rates a building's environmental performance and the use of GGBS can have a positive effect on a number of the credit categories. This is the US equivalent of BREEAM in the UK.

Figure 1 - GGBS and Normal Portland Cement (Ecocem, 2009)

A preliminary study carried out by Boriboonsomsin and Reza (2007) using 30%, 60% and 70% GGBS replacement showed that concrete with a high cement replacement achieved a higher albedo. The crude relationship between the albedo and the level of replacement of cement with GGBS can be seen in Figure 2. Although the simplistic approach gives an indication of the effect of GGBS addition, other parameters also affect the albedo value, including concrete moisture content, aggregate type, curing conditions, surface finish and age. These parameters are the focus of the present study.

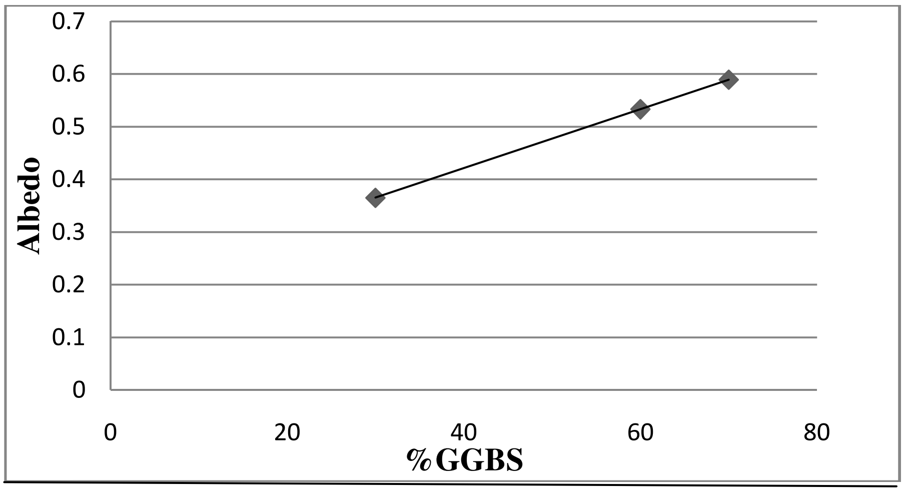

Figure 2 - Relationship between albedo and GGBS content of concrete (Boriboonsomsin and Reza, 2007)

Greyness of Cement

The albedo of concrete made with Normal Portland Cement ranges between 0.20 and 0.40 and can be seen in Table 1. However, as GGBS is much lighter in colour than Normal Portland Cement (Figure 1), its addition increases the albedo value to between 0.40 and 0.60 depending on the substitution rate (Figure 2).

As a result and as part of this study, a colour card will be produced with a wide spectrum of greyness from a white surface to a black surface. The albedo result will then be converted into equivalent reductions in CO_2 emissions.

2.2 Methods

The main aim of this study is to demonstrate enhanced albedo of GGBS concretes compared to a reference concrete with no GGBS present for different concrete constituents and finishes. These mixes will consist of a commonly used cement, CEM II/A-L, with 0%, 30%, 50% and 70% GGBS.

The samples will also comprise three different aggregate types; crushed limestone, partially crushed limestone and sandstone. Different surface finishes will be applied to represent different application types, namely footpath, roof, car park and road areas, thus the surface finishes to be used will be brush, screeded, trowelled and tamped respectively (Table 2).

Table 2 – Proposed testing parameters

	Aggregate 1 Crushed limestone				**Aggregate 2 Partially crushed limestone**				**Aggregate 3 Sandstone**			
	GGBS Level (%)											
Application/Finish	**0**	**30**	**50**	**70**	**0**	**30**	**50**	**70**	**0**	**30**	**50**	**70**
Footpath	X	X	X	X	X	X	X	X	X	X	X	X
Roof	X	X	X	X	X	X	X	X	X	X	X	X
Car Park	X	X	X	X	X	X	X	X	X	X	X	X
Road	X	X	X	X	X	X	X	X	X	X	X	X

The slabs will be 400 x 400 x 60mm in size and there will be two slabs manufactured for each matrix input for repeatability purposes. Thermocouples will be placed in the slabs and once the slabs are poured they will be exposed to a strict and consistent curing regime for the first 24 hours and cured in the air subsequently. They will be placed on a rooftop to be exposed to the environment over the course of at least one year.

2.3 Mechanisms of Measurement

Four independent means will be employed to evaluate albedo. Based on this a recommendation will be made as to the preferred method for measurement.

Temperature

Thermocouples will measure the increase in temperature both on the surface of and inside the samples when exposed to natural sunlight. The ambient temperature will be measured in close proximity to the sample as a reference point. This is being used to independently evaluate the solar light absorption.

Heat Absorption
A thermal imaging camera will be used to measure the uniformity and differences in heat absorbed by the samples once exposed to natural sunlight. The camera records the emittance of infrared radiation from hot bodies and so complements the direct temperature measurements.

Solar Reflectance/Albedo
A portable solar reflectometer will be used to measure the solar reflectance of the samples - this measures the ability of the sample to reflect sunlight off the surface. This is the only method which measures the albedo directly. The samples will be exposed to the environment once placed on the roof, so aging of the samples will be monitored by measuring reflectance at monthly intervals up to one year in order to establish the rate of deterioration of albedo over time.

The reflectometer will obtain measurements of reflectivity at certain wavelengths which can then be integrated to obtain an albedo value. Taha et al. (1992) carried out this procedure which is done by weighting the reflectivities by intensity at each wavelength in order to produce a representative albedo value. This method requires only a small surface area.

Lux Meter
A measure of the light intensity which exists can be achieved by using a lux meter. This measures light in units of “lux” (lumens/m^2) and for light reflected off a surface is an indirect indication of the level of albedo.

Moisture Content
Levinson and Akbari (2002) found that wetting the samples altered the albedo value therefore this parameter will be measured. The greyness of a concrete surface depends to some extent on its dryness - wet surfaces appear darker. To eliminate this parameter, a moisture meter developed by Tramex Ltd. (Holmes and West, 2002), which measures the near surface moisture conditions, will be used on each occasion albedo is measured.

3. Preliminary Research

3.1 Potential for comparison of flat horizontal surfaces

Method
As part of a project to convert Trinity College campus into a greener environment, a study was undertaken into the potential effect of albedo changes to exposed horizontal surfaces on campus.

The objectives were as follows:

- To consider the conversion of four main elements of the campus, namely footpath, roof, car park and pavement areas into whiter surfaces.

- To quantify the total possible surface area within the college which could contain brighter surfaces with the expectation of increasing the overall albedo of the college but without impinging on its historical integrity.
- To calculate the corresponding CO_2 emissions which could be offset as a result.

There are various ways in which to increase the solar reflectance of a surface and one such method is the use of high solar reflectance concrete as described previously. A map of the campus was obtained and the various areas were calculated from this, broken down into categories such as green areas, concrete areas, asphalt car parks, asphalt pavements, asphalt footpaths, horizontal roof areas and miscellaneous.

It was found that just under one-third of the college consisted of green areas, one-third roof areas and the remaining one-third consisting of cobbled areas, asphalt and concrete/paving areas (Figure 3). The asphalt and the concrete/paving slabs around the campus make up 20% of the total surface area. These areas, in conjunction with the roof areas, make up approximately 53% of the campus.

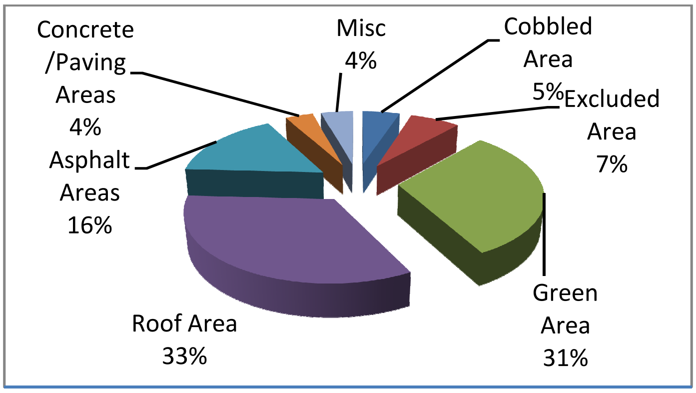

Figure 3 - Breakdown of horizontal areas in Trinity College Dublin

However, of the areas calculated, as demonstrated in the pie chart in Figure 3, there is only 33% of surface area within Trinity College Dublin which has the potential to be used to increase the albedo of the college as areas such as green areas and cobbled areas are excluded. In order to calculate the offset of CO_2 emissions, the current albedo value of the surface in addition to the possible increase in albedo value is required. By using Dublin as a geographic location with an average annual solar radiation, the combined CO_2 saving from the various surfaces within the college was found to be 4,056 tonnes per annum, with the roof area being the largest contributor at 41%. This calculation was based on the increase from the current albedo (ranging from 0.10 to 0.25) to an albedo of 0.60 and was based on research carried out by Akbari et al. (2008). This indicates a potential for CO_2 saving, even on the 40 acre site.

3.2 Test Apparatus for Demonstrating Light Reflection

Before embarking on an extensive testing program, it was necessary to confirm the likelihood of being able to discern changes in albedo of the various concrete specimens. An apparatus was constructed whereby samples of concrete with varying percentages of GGBS (0, 50, 70 and 90%) could be tested with a lux meter to determine the amount of light reflected by the sample. Rectangular prisms (160 x 40 x 40mm in size) are placed in the apparatus in Figure 4. They are inclined at an angle of 45°. A light meter is placed on top of the apparatus which previously had a circular hole cut that was the exact diameter of the light meter receiver so as to exclude peripheral light entering. The receiver on the light meter is parallel to the specimen's surface. The apparatus' surfaces are black inside to exclude any background light. Artificial or natural light enters the front of the testing apparatus and is reflected off the surface of the sample and up towards the light meter where a reading is taken.

This apparatus demonstrated that for each increase in the percentage of GGBS, there was a corresponding increase in the amount of light reflected off the surface which could be seen from the readings on the lux meter. These values ranged from approximately 40 to 75 lux which indicates a reasonable range despite the relatively small reflective surface of the prism. A more refined device is being developed for the specimens listed in Table 2.

Figure 4 - Test apparatus for demonstrating light reflection

4. Conclusions

Albedo, or solar reflectance, is defined as the ratio of reflected solar radiation to the total amount that falls on a surface. The albedo value varies between 1, where 100% of the incoming radiation is reflected, to 0, where no radiation is reflected and it is all absorbed by the surface. Consequently this raises the temperature of the surface and the solar radiation is reemitted as infrared radiation or as heat. A typical surface with a high albedo value would be fresh snow (0.90) and an example of a dark surface with a low albedo would be new asphalt (0.05).

A high albedo concrete surface can be achieved by using a cement replacement such as GGBS which is lighter in colour than Normal Portland Cement. However there are a number of factors which affect the albedo value such as the level of cement replacement, aggregate type, surface finish and the curing regime. As there will be a number of specimens manufactured in order to determine the effect of these parameters, they will be evaluated at regular intervals over the coming year to determine the effect of aging also.

During some preliminary research, the layout of Trinity College campus was examined in order to determine if there were any potential horizontal areas where the albedo value could be increased and to calculate a corresponding offset in carbon dioxide. It was found that a small percentage (33%) of the total area within college could improve its albedo, with the majority of this area being roofs. This would result in an approximate equivalent saving of 4,000 tonnes of carbon dioxide per year.

An experimental apparatus was set up to demonstrate the principle of solar reflection on a GGBS concrete surface using artificial light. A lux meter was used to measure the amount of light reflected off a number of rectangular prism samples containing different levels of GGBS. The results varied between 40 and 75 lux. This confirms that the samples with a higher percentage of GGBS have a higher albedo value and that a lux meter can be used to establish this reliably and repeatedly. This concept will be used in developing the research further.

5. Acknowledgement

The authors wish to gratefully acknowledge the support provided by Mr. John Newell and Mr. Peter Seymour ECOCEM Ireland in the execution of this work.

References

ACPA (2002), ‘Albedo: A Measure of Pavement Surface Reflectance’, American Concrete Pavement Association.

Akbari, H., Menson, S. and Rosenfeld, A. (2008), ‘Global cooling: increasing world-wide urban albedos to offset CO_2’, *Climate Change,* Vol. 95 Joint Issue 3-4 (May-June 2009).

Boriboonsomsin, K. and Reza F. (2007), ‘Mix Design and Benefit Evaluation of High Solar Reflectance Concrete for Pavements’, *Journal of the Transportation Research Board,* No. 2011, Transportation Research Board of the National Academics, Washington D.C., pp. 11-20.

Ecocem (2009), ‘GGBS and Reducing Global Warming-The Albedo Effect’, www.worldcement.com.

Gartland, L (2008), *Heat Islands,* Earthscan.

Holmes, N and West, R.P (2002), ‘Moisture Mitigation in Concrete Slabs During Drying’, Concrete floors and slabs, *Proceedings of the International Congress-challenges of concrete construction*, R.K. Dhir, M.D. Newlands & T.A. Harrison (editors), University of Dundee, pp. 173-180.

Levinson, R. and Akbari, H. (2002), ‘Effects of Composition and Exposure on the Solar Reflectance of Portland Cement Concrete’, *Cement and Concrete Research,* 32, 1679-1698.

Prunsinski, J. R., Marceau, M.L. and Vangeem, M.G. (2004) ‘Life Cycle Inventory of Slag Cement Concrete’, *Proceedings, Eighth CANMET/ACI International Conference on Fly Ash, Silica Fume, Slag and Natural Pozzolans in Concrete*, American Concrete Institute, Farmington Hills, MI.

Riley, R.C. (2008), ‘The Cool Solution to Sustainable Pavements’, *Illinois Chapter* 27.2, Illinois Ready Mixed Concrete Association.

SCA (2003), ‘Slag Cement and the Environment’, *Slag Cement in Concrete*, Slag Cement Association.

SCA (2006), ‘Slag Cement and LEED’, *Slag Cement in Concrete*, Slag Cement Association.

Taha, H., Sailor, D. and Akbari, H. (1992), ‘High Albedo Materials for Reducing Building Cooling Energy Use’, *Energy and Environment Division*, Lawrence Berkeley Laboratory, University of California, Berkeley, CA.

COLOUR VARIATION IN FINISHED CONCRETE

PETER DEEGAN[1], ALAN O'CONNOR[2] & PAUL ARCHBOLD[3]
[1]Banagher Concrete Ltd
[2] Department of Civil, Structural & Environmental Engineering, Trinity College Dublin
[3] STRAIT, Structures & Materials Research Group, Athlone Institute of Technology

Abstract
For more than 20 years engineers have been looking at the variability of colour within concrete elements. Much has been researched and written about this phenomenon and yet there is still a failure to fully understand and control this variation (Monks, 1973; Beijer & Johansson, 1979; Perez-Paret, 2003; Chinchon & Vera, 2004). The result can be of significant cost where units are required to be repaired or replaced prior to being certified as compliant.

Yet it is practically impossible to produce a concrete unit which is completely uniform in colour when one considers that the source of colour variations can result from one/or a combination of a number of factors, including concrete mix design, formwork surface texture, variations in curing conditions, formwork absorbency or stiffness, vibration and/or release agent and leakage of water through joints etc.

Internationally, specifications and codes fail to grasp the true extent of this variability referring rather to the actual required finishes, and providing little or no guidance on acceptable criteria with respect to colour variation.

This paper presents the initial results from an experimental programme aimed at determining further factors which influence colour uniformity and compare colour variations in specimens under different curing conditions with mechanical properties of the concrete samples. Initially strength will be evaluated across the colour variance but the effects of colour on durability will also be addressed at a later stage.

Keywords: Concrete, Colour, Durability, Strength, (SCC) Self Compacting Concrete

1. Introduction

The most consistent thing about concrete colour is its inconsistency. Variation in concrete colour exists both from specimen to specimen and within the same specimen. This variation has become increasingly relevant in recent years, while the architectural and aesthetic value of exposed concrete surfaces has been exploited in tandem with a significant increase in the amount of construction projects in Ireland over the past 15 years.

Anecdotal evidence suggests that this variation in concrete colour has proven contentious in certain instances, primarily due to the fact that assessment of colour and colour variation is presently subjective in nature. Moreover, guidance on controlling colour variation has proven to be inadequate, as variations can occur despite following all recommended best practice techniques in preparing samples. Further, fears have been expressed about potential links between colour variation and short term mechanical properties and long term durability performance. As a result, concrete specimens have been rejected by designers on a subjective basis, which has lead to rather onerous demands on suppliers and inherent increased financial and environmental costs.

1.1 Factors Affecting Concrete Colour

While colour variation in concrete cannot be eliminated, many factors exist, which are known to influence the colour uniformity of the finished product, Table 1. In addition to the basic constituents of the concrete mix, the Concrete Society (2008) list the age at which formwork is removed, the weather, both at time of striking and subsequently, differential contact with polythene sheeting causing differential surface hydration and the use of damp hessian as specific causes of colour variation.

Zhang (2005) states that the following factors affect the colour uniformity of concrete: water/cement ratio; improper curing; release agents; over trowelling; form materials; admixtures and efflorescence.

Monks (1981) provides probable causes for a range of specific types of colour discolouration patterns. In addition to the factors previously mentioned, he also states that differential vibration compaction can be influential in creating colour variation.

Bennett (2008) asks what determines the surface colour of concrete and indicates that the finest particles dominate the surface colour and therefore cement will determine colour.

Table 1 – Causes of colour variation in concrete

Internal Constituents	**External Constituents**
Cement	Mould release agent
Add mixtures	Vibration (type and duration)
Water/Cement ratio	Curing Method
Additions (GGBS, PFA, Micro silica)	Types of formwork
Sand/aggregate	Ambient temperature
Concrete temperatures	Curing time

Best practice techniques exist and are employed to try to eliminate or reduce the impact of these known factors in colour variation. More recently, experience with self-compacting concrete, where vibration compaction has been eliminated, has shown that colour variation still presents within and between samples produced from the same concrete mix.

1.2 Specifications and Codes of Practice

While the finish of concrete specimens can be well defined, specified and measured, the issue of colour is not addressed very clearly in the codes of practice and technical specification documents. Where reference is made to the phenomenon, the literature leaves a lot to interpretation. Table 2 summarises the references made in various guidance documents to colour uniformity.

Table 2 – Design Guidance and Specification on Concrete Colour

Guidance Document	Clause	Reference to Colour
BS8110	Clause 6.2.7.2 b) Type B Finish	"Only very minor surface blemishes should occur, with no staining or discoloration from the release agent"
Specification for Highway Works	(1708)	Class F2 "Fins and surface discoloration shall be made good"
National Building Specification (UK) clauses 610 to 630	620	"Surface to be free from discoloration due to contamination or grout leakage"
Civil Engineering Specification for the water industry	Surface finish produced with formwork	"Only very minor surface blemishes shall be permitted and there shall be no staining or discoloration"
	Fair worked finish	"If the surface is to be exposed in the final work, every effort shall be made to match the colour of the concrete"

One standard encountered, which attempts to objectively rate concrete colour is the French NF P18-503 standard (AFNOR, 1989), which specifies the concrete tint classes and gives a reference of seven grey levels, Figure 1, equivalent to a luminance scale (Lemaire, 2001).

1.3 Concrete Colour Measurement

While the references made to colour variation in design codes and in specifications of contract documents are relatively vague, an issue of real concern is the subjectivity of the assessment of colour variation. Colour variation may present differently depending on aspects such as the viewing distance, the ambient light, the viewing angle, etc. Monks (1981) addressed the first of these factors and recommended that viewing distance be representative of *the typical viewing distance to the specimen in its final location*. Table 3 presents recommended viewing distances to certain concrete applications.

Even employing recommended viewing distances, the determination of colour uniformity is still subjective in current practice. Three factors determine what color an observer perceives: the light source, the object surface and the observer himself (Lemaire, 2005). Nonetheless, several objective methods have been identified in the literature for the evaluation of colour.

Yuzer et al (2004) employed the Munsell Colour System in identifying colour changes in mortars subjected to high temperatures. In this system, the attributes hue, value and chroma of color are divided into equal perceptual intervals and denoted through the use of decimals. Hue is the dimension which distinguishes one color family from another, as red from yellow, or green from blue.

Table 3 – Viewing Distances for Assessing the Quality of Concrete Surfaces (Monks, 1981)

Type of Surface	**Distance**
External surfaces, entrances and building interiors that can be seen from close quarters	1m
External surfaces of buildings generally	3m
Building work above second floor level (except where the surface can be seen from nearby windows) and civil engineering structures generally	6m

Value indicates the lightness of a color, and there are 10 main steps in the value scale. Absolute white and absolute black are given the notations 10 and 0, respectively. Intermediate grays are given notations ranging between 10 and 0. Every hue can be constituted in different values. Chroma, the third attribute of color, can be defined as the degree of departure of a color from a grey having the same Munsell value.

A second method is used by Lemaire (2005) and Zhang (2005). This method is proposed by CIE (International Commission of Lighting) and is referred to as CIELab, due to its use of L (luminance) and a & b (chromatic values) respectively. This effectively defines colour in a three-dimensional light space.

Figure 1 shows the AFNOR standard's seven levels of grey and their corresponding luminance values. Determination of these properties of colour requires the use of specific colourimetry equipment.

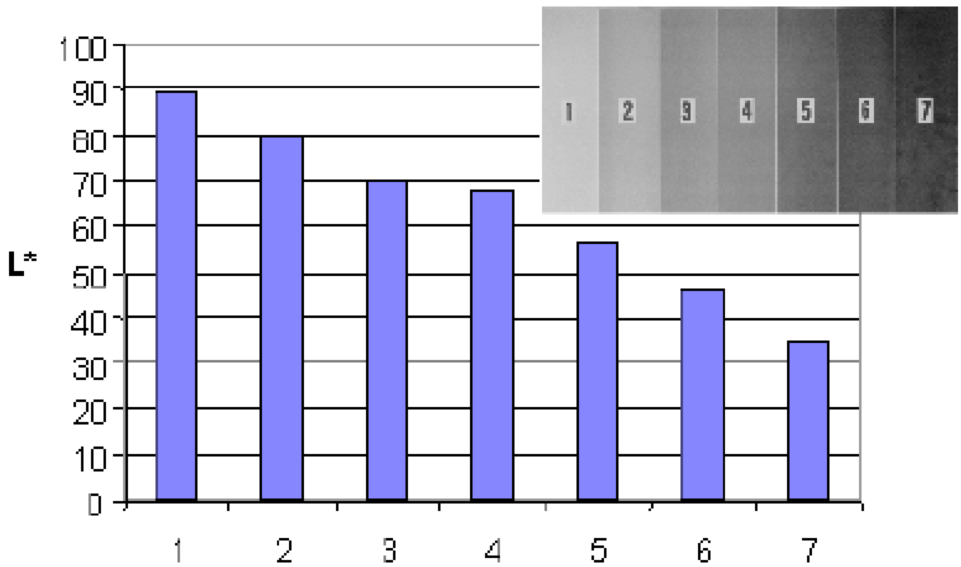

Figure 1 - Grey classes of the standard NFP 18-503 and corresponding luminances (Lemaire, 2001)

This paper reports on the preparation of samples from two concrete mixes, which will serve as a basis for subsequent research, to illustrate the level of colour variation which can occur within each of these sample populations, despite all best practices to eliminate this variation being employed. Results from compressive strength tests are also reported, as a significant portion of the research proposed is related to attempting to characterize if there is a link between finished colour and strength/durability performance.

2. Experimental Programme

The experimental programme consisted of producing concrete samples from two discrete concrete mixes – (i) a self-compacting concrete with a design strength of $60N/mm^2$ (SCC) [Mix A] and (ii) a semi self-compacting concrete with a design strength of $60N/mm^2$, but with 30% GGBS cement replacement (GGBS) [Mix B].

2.1 Sample Preparation

The aggregates for both mixes are locally sourced limestone gravel of a carboniferous age and are both of pale and dark variety in almost equal measure. The concrete has been batched in a 1.5 m^3 pan mixer with microwave moisture control and a computer controlled weigh system accurate to 0.2%. The trial moulds (300mm x 300mm x 100mm) were made from steel to reflect the type of mould most used in an Irish precast operation.

The moulds were cleaned and an application of release agent - Gemleaze, GP Bio - was applied. The concrete mixes were taken to the lab and poured into the moulds. The SCC mix received no vibration but the GGBS samples were placed on a vibrating table for 10 seconds. The samples were then left uncovered to cure overnight in the laboratory and stripped the following morning (approximately 18 hours later). Once stripped, the samples were left for 2 hours before being initially photographed. A total of 72 samples were prepared.

2.2 Curing Conditions

Normal industrial practice offers a variety of curing conditions for precast concrete specimens. Moreover, practical experience has shown that colour variation tends to present more frequently in specimens which are developed and cured in winter months, inferring that ambient curing conditions may be influential in terms of achieving uniformity of colour. In an attempt to replicate these conditions and to examine the effects of curing on the finished colour of the specimens, three different curing scenarios were employed for each of the concrete mix samples as follows:

Curing Tank (Tank)
Samples were placed in a curing tank, with the temperature maintained at 20^oC for the entire period. Samples cured in the curing tank will be denoted as *Tank* hereinafter. A photograph of a curing tank used can be seen in Figure 2(a).

Stacking (Stack)

Samples were stacked on top of one another with the mould face, facing down and placed outside for the test period. These samples will be referred to as *Stack* hereinafter. A photograph of a stack used can be seen in Figure 2(b).

Storage Rack (Rack)

Samples were placed on a storage rack, facing due south to maximize exposure to sunlight. These samples will be referred to as *Rack* hereinafter. A photograph of the rack used can be seen in Figure 2(c).

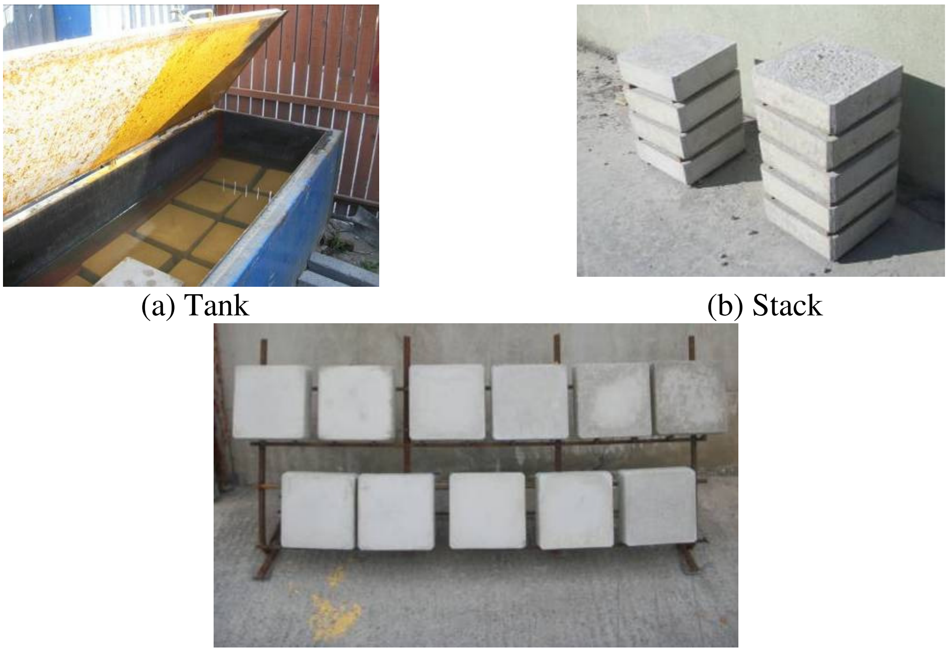

(a) Tank (b) Stack

(c) Rack

Figure 2 – Samples in Curing Regimes Employed

2.3 Sample Photography

At the time of testing, dedicated colourimetry equipment was not available, so in order to control repeatability of sample photography conditions and to eliminate any interference from ambient light, a dedicated photo booth was constructed within the laboratory. This photo booth can be seen in Figure 3 and 4. The booth is approximately 1m wide by 1.5m high by 2m long, constructed from plywood and steel and fitted with amounting apparatus for both the sample and the digital camera, which could be controlled from outside the booth to ensure consistent distance from the sample. The booth is also sealable to prevent any ingress of ambient light. Photographs were taken in this photo booth using a Kodak EasyShare MD41 digital camera. The distance from the camera to the sample is 1.0m.

2.4 Compressive Strength Tests

Each of the test samples was also subjected to compressive strength tests for the aforementioned reason. Cube tests were carried out to determine both 28 and 56 day compressive strengths of the samples. Tests for 90, 118, and 6 month tests were still to be carried out at time of writing. Durability testing using the autoclam apparatus are also proposed in the future.

Figure 3 – Photo booth

Figure 4 – Photo booth interior, showing mounting point for both sample and camera

3. Results

Panels are ordered pale to dark, from left to right, in Figure 5 below. Also indicated in each figure are the respective compressive strengths recorded for each panel. Each individual mould condition is placed together and mix [A] and [B], in the left and right columns respectively, are shown from curing conditions in Figure 2(a) Tank, 2(b) Stack and 2(c) Rack.

From Figure 5 the subjectivity of colour assessment is apparent. Clearly colour variations exist but the selection criteria for determining which are acceptable and which are unacceptable is currently of qualitative rather than a quantitative nature. In assessing whether colour variation can be linked to strength it is apparent that no evidence to confirm or reject this hypothesis is evident from the test results presented. Further work should and is intended to focus in this area. With a more extensive set of experimental results and the development of a quantitative measure to record colour variation, multi-variate regression analysis will be employed to test the aforementioned hypothesis. Similarly, the hypothesis that colour variation can be linked to durability will be investigated.

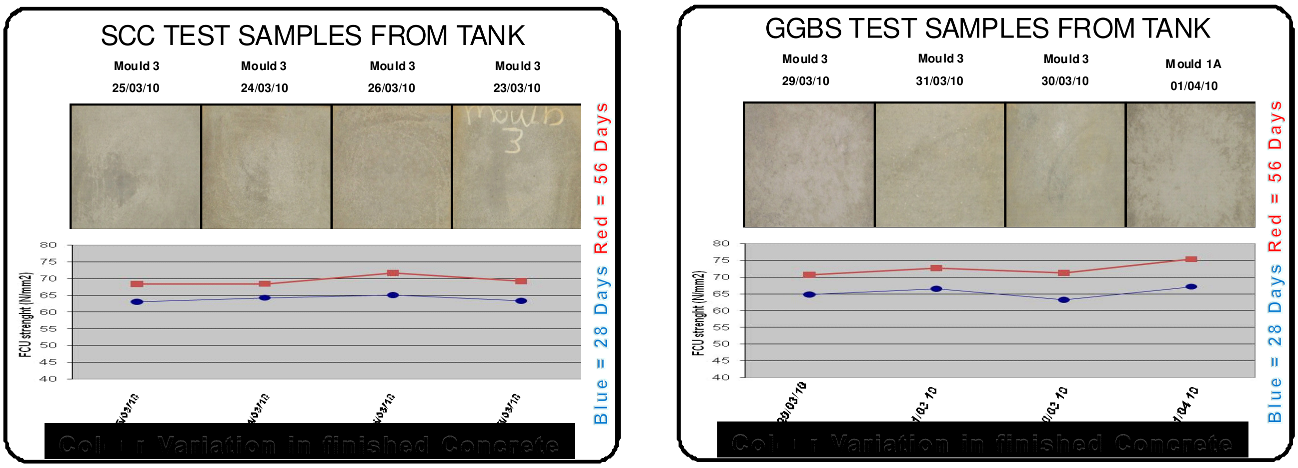

(a) Test Results for *Tank*

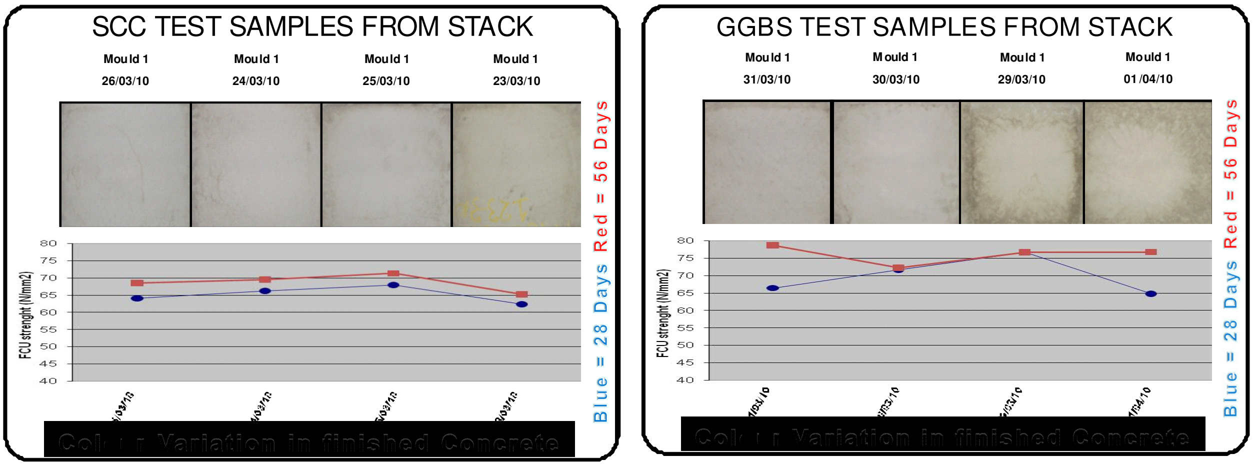

(b) Test Results for *Stack*

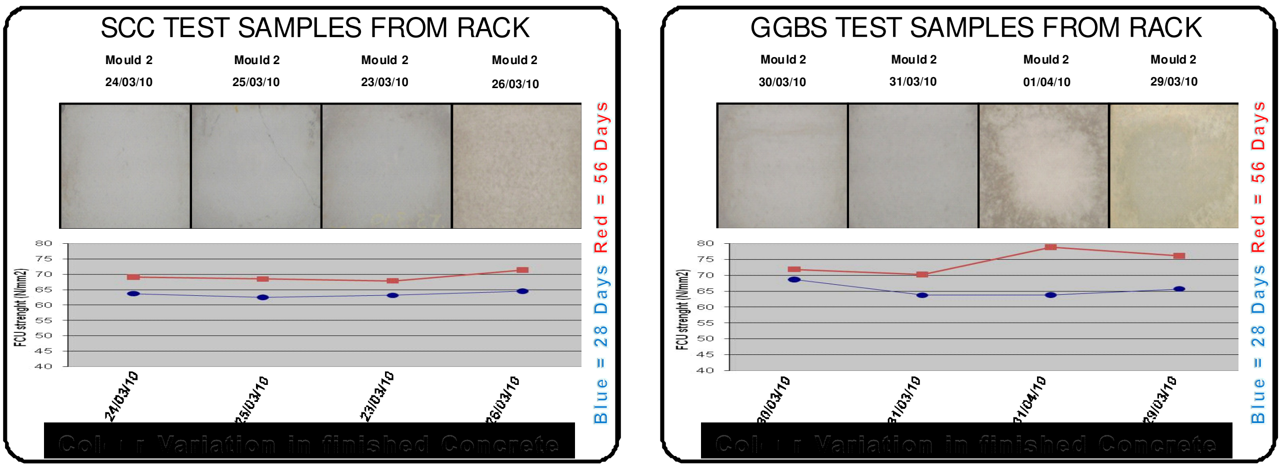

(b) Test Results for *Rack*

Figure 5 - Results of tests carried out to date

4. Conclusions

It is practically impossible to produce a concrete unit which is completely uniform in colour when one considers that the source of colour variations can result from one/or a combination of a number of factors, including concrete mix design, formwork surface texture, variations in curing conditions, formwork absorbency or stiffness, vibration and/or release agent and leakage of water through joints etc. Internationally, specifications and codes fail to grasp the true extent of this variability referring rather to the actual required finishes, and providing little or no guidance on acceptable criteria with respect to colour variation. This paper presents the initial results from a PhD research project currently underway which aims to (i) determine the principal factors which influence colour variation, (ii) quantifiably compare colour variations in specimens under different curing conditions and (iii) to determine if a link exists between colour variation and strength and/or (ii) durability. Initial results of the experimental programme are presented.

References

Monks, W.L., (1973), 'Colour Variations in Smooth Concrete Surfaces', *Concrete*, 8(2), pp. 22-23.

Beijer, O., and Johansson, A., (1979), 'Colour of Concrete Surface – A Discussion on Possible Measurement Methods', *Metal Construction*, Vol. 2., pp 151 – 155.

Perez-Paret, T., (2003), 'Concrete Colours and Pigments', Concrete Engineering International, 7(3), pp 59 – 60.

Chinchon, S., and Vera, R., (2004), 'Cement Paste Colouring in Concretes', Cement and Concrete Research, 34(11), pp 1987 – 1991.

Lopez, A., (2009), Cement & Concrete Composites – Advantages of mortor-based design for self-compacting concrete, pp755.

Yuzer, N., (2004), Cement and Concrete Research – Compressive strength – color change relation in mortars at high temperatures, pp 1804.

Lemaire, G., (2001), Image analysis processing in order to evaluate concrete facings.

Lemaire, G., Ringot., E (2001), Image analysis processing in order to evaluate concrete facings.

Monks, W., (1988), Visual Concrete - Appearance matters, pp 28.

Blake, L., (1967), Technical Advisory Series, Recommendations for the production of high quality concrete surface, pp38.

Monks, W., (1974), An investigation into the incident of colour variation in formed concrete, pp20.

Bennett, David., Architectural Insitu Concrete-Exploring Concrete Architecture. Technical Report 52, Plain Formed Concrete Finishes, Concrete Society

Hurd, M.K,. (1993), Concr. Constr.-Tips for colouring concrete, pp345-351

Monks, W.C., (1974), Cement and Concrete association-An investigation into the incidence of colour variation in form concrete surfaces technical report.

Strehlein, D, Schiebl, P., (2008), Journal of advanced concrete technology-Dark discolouration of fair faced concrete surfaces-transport and crystallization in hardening concrete, pp409.

Lavinson, R, Akbari, H., (2002), Effects of Composition and exposure on the solar reflectance of Portland Cement Concrete.

INVESTIGATION OF FLY ASH FROM PEAT FIRED POWER STATIONS AS A CEMENT REPLACEMENT IN CONCRETE

D. GAVIGAN & J. GOGGINS
College of Engineering & Informatics, National University of Ireland, Galway.

Abstract

Ordinary Portland Cement (OPC) is the most expensive and energy intensive ingredient in concrete. Due to the manufacturing process associated with cement production, for every tonne of cement produced almost as much CO_2 can be released into the atmosphere. Therefore, it is imperative that alternative cement replacements are developed that produce either less greenhouse gas emissions in their production or are waste and/or by-products.

This study investigates the use of two fly ashes from the combustion of peat and the co-firing of peat with wood, which are currently waste products, as alternative binders to OPC. These materials are cost-effective and their use in concrete can benefit the environment, as the alternative may be to dispose of them in landfills. The effects these ashes have on the properties of fresh and hardened concrete is investigated.

Concrete with a cement replacement level of 10% and 20% of both materials is tested in terms of workability and strength at 3, 7, 14, 28 and 56 days. All results are compared to a control mix. Compressive strength testing was carried out on 100mm cubes, 150mm cubes and 150mm x 300mm cylinders. Correlations between compressive strength results from the three different types of specimens are presented. The findings from this study suggest that there is potential for peat fly-ash to be used as a cement replacement.

Keywords: concrete, cement replacements, peat fly ash.

1. Introduction

One of Ireland's most characteristic features is its bogs and peatlands, covering 1,200,000 hectares (17%) of the island. Ireland contains the highest proportion of peatlands than any European country except Finland (Paappanen & Leinonen, 2006). The use of peat for energy production has been used for centuries in Ireland. Peat-fired electricity production in Ireland has changed significantly since 2000, due to changes in the regulation of Irish electricity production and with existing peat-fired power stations built between 1950 and 1980 been decommissioned (Organo et al., 2005). Ireland’s reliance on peat for energy production has declined towards the end of the 1990s, but since stabilised with the opening of two peat-burning power stations in 2004 and 2005, which have a licensed life span of 15 years (Paappanen & Leinonen, 2006). The three remaining peat power stations in Ireland are West Offaly, Lough Ree, and Edenderry (Table 1). In 2005, approximately 8% of Ireland’s electricity requirement was provided through the combustion of peat in these peat power stations (CER, 2007).

Peat power stations burn peat in the form of milled peat to produce energy. In its simplest form, milled peat production involves: milling, harrowing, ridging, harvesting and stockpiling. Peat, which has been milled on the surface of the bog, is air dried to a fine, powder-like material and burned in a boiler to produce steam for the turbine/generator, which in turn produces electricity. Approximately 96-99% of the total ash produced from the combustion of peat is fly ash collected by an electrostatic precipitator. The remainder of the total ash is termed bottom ash, which is a heavier material and is removed beneath the boiler bed. From Table 1, it can be concluded that over 100,000 tonnes of peat fly ash is produced in Ireland every year. Currently, none of this fly ash is being utilised. Considering 5.25 million tonnes of cement was produced in Ireland in 2005 (Motherway & Walker, 2009), then if peat fly ash was used as a cement replacement in concrete, approximately 90,000 tonnes of CO_{2e} would be avoided. In Ireland in 2005, the cement industry emissions totalled to 3.8 million tonnes of CO_{2e}, carbon dioxide equivalent which takes account of all greenhouse gasses, accounting for 5% of the total Irish emissions for that year (Motherway & Walker, 2009). Thus, using peat ash as a replacement would decrease the Irish cement industry emissions by 2.5%.

The effects on the performance of concrete of using fly ash from combustion of peat and the co-firing of peat with wood as cement replacements are investigated in this paper. In particular, the influence on workability and strength gain is discussed, while the effects on durability are part of the on-going study.

Table 1 – Irish peat power stations data (Paappanen & Leinonen, 2006).

Peat Power Station	Output (MW)	Peat consumption per annum (tonnes)	Efficiency (%)	Typical Ash production per annum (tonnes)
West Offaly	150	1,230,000	38	45,000
Lough Ree	100	800,000	38	27,600
Edenderry	120	1,000,000	38.4	32,000

2. Alternative binders

Concrete is the most utilised substance in the world after water. Ordinary Portland Cement (OPC), the most common binder used in concrete, is the most expensive and energy intensive ingredient in concrete. The efficiency with which energy is used is becoming a fundamental question in the energy debate. The global cement production for 2001 was approximately 1200 million tonnes (Coutinho, 2003). This increased to 2540 million tonnes in 2006 and an estimated 2690 million tonnes was produced in 2007 (Russell, 2008). With respect to cement production in Europe, in the 27 European Union countries, total cement production in 2007 was estimated at 283 million tonnes, representing 10.5% of world production (Russell, 2008). 5.25 million tonnes of cement was produced in Ireland in 2005 (Motherway & Walker, 2009).

Due to the manufacturing process associated with cement production, approximately 990kg of CO_2 is released into the atmosphere for every tonne of cement produced in Ireland (McCaffrey et al, 2010). Thus, it is of great interest to reduce the amount of cement being used by the development of new alternative cement replacements. Wide-spread research has been carried out in the development of cement substitutions. Ground granulated blastfurnace slag (GGBS) and fly ash are commonly used in blended cements or as cement replacements across Europe. Goggins & Gavigan (2010) investigated a wide range of alternative binders to OPC, which possessed pozzolanic properties and are mainly waste materials or by-products of no significant value. It was shown that a wide variety of waste products have successfully been tested and used as cement replacements in concrete. In fact, using ashes and other waste materials can significantly increase the useful life of structures through improvements of hardened concrete properties (Goggins & Gavigan, 2010).

When water and cement mix together, a cement paste is formed which acts as an inorganic glue. The reaction of cement and water, which is referred to as hydration, produces three products: **C-S-H** *Calcium silicate hydrated,* **C-A-H** *Calcium* *aluminate hydrated,* **CH** *Calcium hydroxide (Ca(OH)$_2$).* Portland cement contains approximately 80% of calcium silicates [C_3S+C_2S] and 20% of calcium aluminates [C_3A+C_4AF] (Collepardi, 2010). Both C_3A and C_4AF can react with water and produce C-A-H. Similarly, C_3S and C_2S are capable of producing C-S-H in the presence of water. The setting of cement is related with the formation of C-A-H, while the hardening or the strength of cement is primarily due to the formation of C-S-H (Collepardi, 2010).

The third and final product from the reaction of cement and water, calcium hydroxide $Ca(OH)_2$, makes it possible to produce blended cements. Calcium hydroxide doesn't contribute to strength on its own; however it is capable of reacting with other ingredients that contribute to strength. Two forms of silica exist – crystalline silica such as quartz, which is a very well ordered structure, and amorphous silica, which consists of a disordered link of silicon and oxygen i.e. not well crystalline. Alternative cementitious materials do not harden in themselves when mixed with water. However, when finely ground and in the presence of water, they react with dissolved $Ca(OH)_2$ to form extra strength developing calcium silicate compounds C-S-H (Collepardi, 2010).

Pozzolanic materials are substances of siliceous or silico-aluminous composition or a combination as defined in BS EN 197-1 (BSI, 2000a). Pozzolans consist essentially of reactive silicon dioxide (SiO_2) and aluminium oxide (Al_2O_3). Due to the disorder in the arrangement of the atoms, the amorphous silica (SiO_2) within the pozzolan is not stable and is very active, hence reacting with the $Ca(OH)_2$. Natural pozzolans and artificial pozzolans (for example, pulverised fly ash and silica fume) can be used as a cementitious material due to the amorphous silica present. The pozzolanic reaction (Eqn. 1) is much slower than the reaction rate of C_3S, C_2S, C_3A and C_4AF. Thus, the early strength of concrete containing a pozzolanic material is reduced.

$$\mathbf{SiO_2 + Ca(OH)_2 + Water = C - S - H} \tag{1}$$

In a mix containing Portland cement as the only cementitious material, most of the strength gain occurs within about a month. Where the cement has been partly-replaced by other materials, such as fly ash, strength growth may occur more slowly and continue for several months. Final strengths may exceed those from Portland cement-only mixes.

Previous research that was carried out on peat fly ash as a cement replacement concluded that the ash increases the water requirement of the mix significantly, thus reducing the strength (Power et al, 2000; Power et al, 2001). It should be noted that this research was carried out on peat fly ash prior to 2004 and 2005 when the new West Offaly Power station replaced the previous Shannonbridge Power Station.

The new station uses a modern fluidised bed technology to burn peat, and due to higher efficiency the plant produces 30% more electricity for the same fuel input than the older plant that has been replaced. The old power station had a very short residence time, meaning that a complete burn of the peat fuel wasn't being obtained. The new plant has a lot longer residence time and a more complete burn is being achieved. Unburnt carbon within the peat ash is less than 6% in the new plant, in contrast to unburnt carbon levels in the range of 7 to 9% at the old station (Power et al, 2001). This was an undesirable characteristic in the peat fly ash from the old plant regarding high Loss on Ignition (LOI) values reported by Power et al. (2001). Day (1990) reported that high quality peat ash was found to be more reactive than coal ash in concrete.

The main objective of this current study is to see the effect of co-firing peat with wood would have on the ash and comparing this to peat fly ash in the context of using it as a cement replacement. The advantage of co-firing biomass with a fossil fuel is that it gives lower net CO_2 emissions in contrast to burning a fossil fuel on its own (Steenari & Lindqvist, 1999). The peat fly ash produced at the West Offaly Power Station will be compared to the peat ash from the old Shannonbridge station, as the composition and properties of ashes depend on the characteristics of the fuel as well as the combustion conditions (Steenari et al, 1999).

3. Materials and Methods

3.1 Materials

Materials used in this study consisted of cement, fine and coarse aggregate, peat fly ash, fly ash from co-firing peat with wood based materials and water. Irish Cement CEM I Rapid Hardening Cement with a specific gravity of 3.06 was used for all mixes. The coarse aggregate consisted of both single sized 20mm and 10mm crushed limestone aggregate with a specific gravity of 2.72 and 2.71, respectively. The 20mm and 10mm aggregate had a flakiness index of 20 and 17 respectively with a water absorption value of 0.3% for both size aggregates. The fine aggregate used was crushed limestone rock fines (CRF) with a specific gravity of 2.74.

Ashes from West Offaly and Edenderry power stations were used in this study. Both these locations are in Co. Offaly in the midlands of Ireland where the vast majority of the Irish peatlands are situated. Ash ‘A’ is peat fly ash produced from burning peat only in a circulating fluidized bed at 800^{o}C at West Offaly power station. Ash ‘B’ is fly ash from Edenderry Power Plant, which is formed by co-firing 93% peat and 7% wood based material at approximately 850-900^{o}C in a bubbling fluidized bed boiler. The specific gravity of ash A and B is 2.85 and 2.80, respectively. Table 2 presents the chemical composition of both ashes, A and B, in contrast to a similar peat ash from Shannonbridge investigated by Power et al (2001) and cement. From Figure 1 it can be seen that the Edenderry ash (Ash B) is finer than the peat fly ash (Ash A). All these ashes are coarser than a sample presented by Power et al (2001) from the Shannonbridge Station, which has since been decommissioned (Figure 1). All these materials are compared to cement, which is of similar fineness to the Edenderry ash.

The ashes used in this study are shown in Figure 2, including SEM images. The Edenderry ash (Ash B), which is a by-product of co-firing the peat with 7% wood-based material, is slightly darker than the peat fly ash (Ash A). The particle shape of both ashes is mainly spherical which is in agreement with Power et al. (2001).

Table 2- Chemical Composition of peat ashes and cement.

	Rapid Harden-ing Cement	Ash A	Ash B	Peat fly ash (Power et al 2001)
SiO_2	18.75	26.1	35.3	35.1
Al_2O_3	4.66	2.59	3.14	5.70
Fe_2O_3	3.13	5.43	7.75	3.00
CaO	62.2	27.4	36.6	22.7
MgO	2.02	5.79	2.47	5.60
K_2O	0.48	0.40	0.71	0.10
Na_2O	0.10	0.71	0.41	0.40
P_2O_5	0.09	0.96	0.62	--
S	1.19	8.30	1.71	--
SO_3	--	--	--	17.5

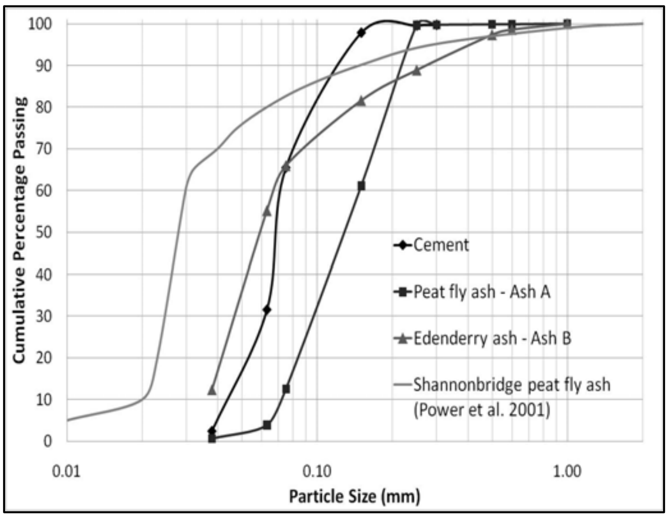

Figure 1- Particle size distribution of various ashes in contrast to cement.

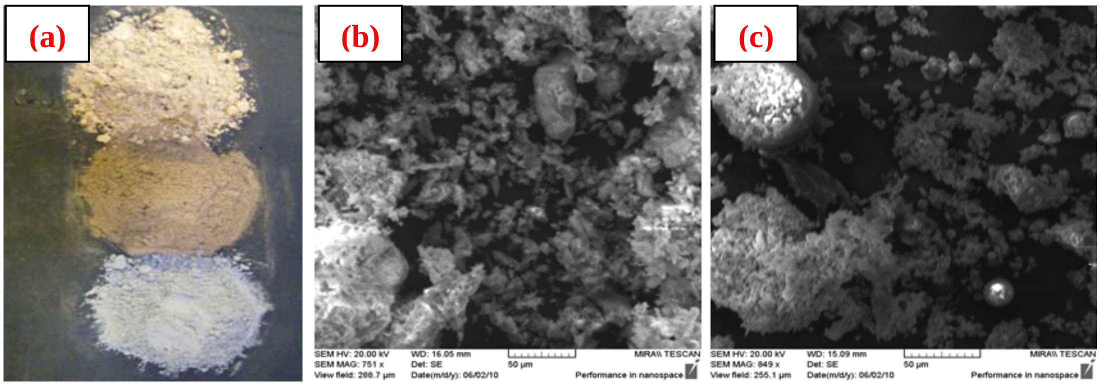

Figure 2- (a) The ashes which were investigated as possible cement replacements, from top, Ash A, Ash B and CEM I Rapid Hardening Cement **(b)** SEM image of peat fly ash (Ash A) and **(c)** SEM image of Edenderry ash from co-firing peat with wood (Ash B).

3.2 Methods

The concrete mix constituents used to investigate the effect of using peat fly-ash in concrete are given in Table 3. Mix 1 is the control mix to which all the mixes were compared. Mixes 2 and 3 contain 20% cement replacement of Ash A and B, respectively, while mixes 4 and 5 contain 10% cement replacement of Ash A and B, respectively.

All mix proportions had the same cementitious materials of 369 kg/m^3 and the water to cementitious materials ratio (w/c) was 0.49 for all mixes. The coarse aggregate content was further divided between both 20mm and 10mm single size aggregate in the ratio of 66:33 by weight. From the workability results, measured by the slump, it is evident that Ash A reduced the workability of the mix significantly, while Ash B had no negative effect on the workability (Table 2). The negative effect the peat fly ash had on the workability was also found by Power et al. (2000; 2001). All mixes were allowed mix for 5 minutes after all mix constituents were added before the concrete specimens were made and cured in accordance with BS EN 12390-2.

Different types and sizes of specimens were used to determine the strength of the concrete. These included 100mm and 150mm standard cubes and cylindrical moulds of diameter 150mm and height 300mm. These concrete specimens were tested at 3, 7, 14, 28 and 56 days, in accordance with BS EN 12390-3 (BSI, 2009), to determine the compressive strengths of the respective mixes.

Table 3 - Concrete mix proportions.

Mix No.	*Mix Proportion (kg/m^3)*						*w/c*	*Slump (mm)*
	Cement	**Ash A**	**Ash B**	**Fine Aggregate.**	**Coarse Aggregate.**	**Water**		
1- Control	369	---	---	712	1160	180	0.49	65
2- 20% Ash A	295	74	---	712	1160	180	0.49	30
3- 20% Ash B	295	---	74	712	1160	180	0.49	65
4- 10% Ash A	332	37	---	712	1160	180	0.49	50
5- 10% Ash B	332	---	37	712	1160	180	0.49	70

4. Results and Discussions

4.1 Strength

The compressive strength of the concrete control mix and those containing the ashes (Ash A and Ash B) of 10% and 20% is presented in Figure 3. Comparing the performance of both ashes, it is clear that mixes containing Ash B (Mixes 3 and 5) performs better than those containing Ash A (Mixes 2 and 4). At the 10% replacement level, concrete mixes containing Ash A (Mix 4) and Ash B (Mix 5) performs very similarly over the 56 day period. Even though Mix 5 exhibits higher early strengths than Mix 4 at 3 and 7 days, both have similar strengths at 14, 28 and 56 days. Mix 4 and Mix 5 established 70% and 100%, respectively, of the strength of the control mix at 7 days. At a later age, both mixes exhibit approximately 94% and 95% of the control strength at 28 and 56 days respectively. At the 20% replacement, concrete mixes containing Ash A (Mix 2) and Ash B (Mix 3) exhibited strengths of 61% and 82% of the strength of the control mix at 7 days and similarly 58% and 81% at 28 days, respectively.

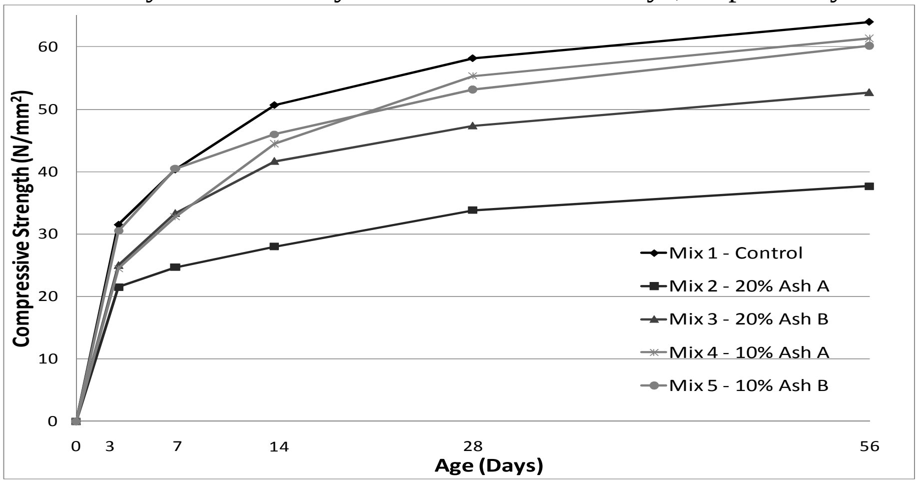

Figure 3: Compressive strength results for the various mixes.

Mix 2 (20% peat fly ash) showed the lowest compressive strengths at all ages, establishing only 61% of the strength of the control mix at 7 days and 58% of the control mix strength at both 28 and 56 days. This emphasises the poor performance of the concrete mix containing Ash A in terms of strength gain.

4.2 Concrete compressive strength using different specimens

There is a difference of opinion as to whether it is better to assess concrete strength by cube or by cylinder. Furthermore, there is no exact mathematical relationship between a concrete cylinder and a cube strength. In addition to size effects, the aggregate size to test size also has an influence. The relationship between 150 x 300mm cylinder strength and 150mm cube strength varies, but on average the cylinder compressive strength is about 80% of that of the cube compressive strength (Collepardi, 2010). The cube has the higher strength because of the difference in aspect ratio affecting lateral restraint to cracking, provided by the test machine platen.

In BS EN 206 Table 7 (BSI, 2000b), compressive strength classes for normal-weight concrete is given in terms of both characteristic cylinder strength $f_{ck,cyl}$ and characteristic cube strength $f_{ck,cube}$. For the most common strength classes, C20/25 to C50/60, the relationship between cylinder strength and cube strength increases from 0.80 to 0.83, as the strength of the concrete increases (BSI, 2000b). From this research, within the same cube strength range of 25N/mm^2 to 60N/mm^2, the relationship between cylinder strength and cube strength was found to range from 0.81 to 0.87 (Figure 4(a)). In contrast, Mansur & Islam (2002) found a correlation between cube and cylinder strength of 0.72 to 0.81 within the same strength range (Figure 4 (a)).

A relationship between the compressive strength obtained from 100mm cubes and 150mm cubes is presented in Figure 4 (b). BS 8500 (BSI, 2006), which is the British complementary standard to BS EN 206 (BSI, 2000b), states *“BS 8500 treats the strength of concrete measured on 100mm and 150mm cubes as being identical”*. It is evident from Figure 4 (b) that the compressive strength obtained from 100mm cubes is higher than that obtained from 150mm cubes. This increase in strength increases from 5% to 8% as the concrete strength increases. The reason for this is again due to the greater lateral restraint to cracking, provided by the test machine platen, on the 100 mm cubes in contrast to the 150mm specimens. Day (1999) stated that the smaller 100mm specimens will give higher strengths in the region of 5% than the larger 150mm specimens. Furthermore, the correlation given by Mansur & Islam (2002) is similar to the relationship developed in this present study.

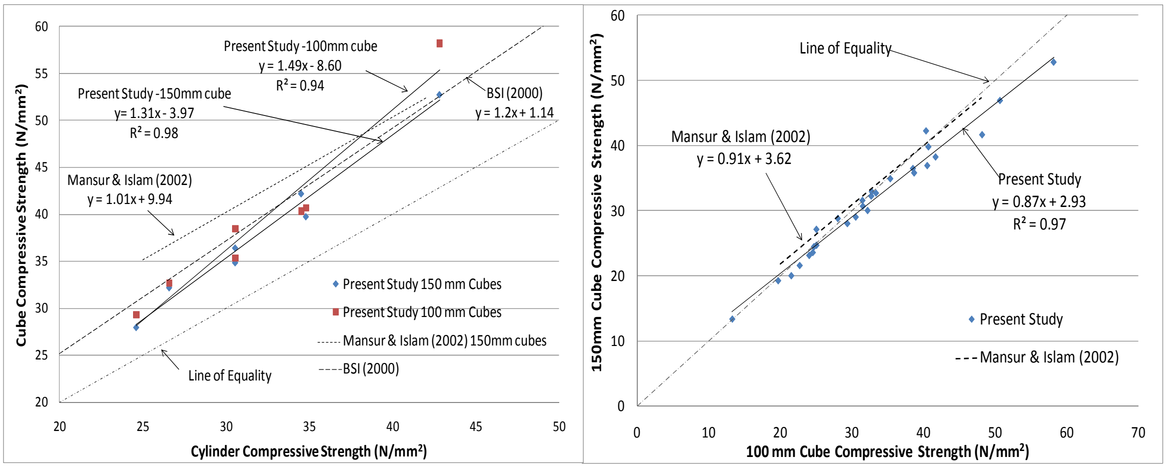

Figure 4 – (a) Comparison of cylinder strength to both 100mm and 150mm cube strength. **(b)** Relationship between 100mm and 150mm cube compressive strength

5. Conclusions

This brief study suggest that peat fly ash and the ash from co-firing peat with wood can be used as a cement replacement with an optimal level of 10% advised. In terms of both workability and strength, it is clear that the Edenderry ash (Ash B), produced from co-firing peat with wood, is a more suitable cement replacement in contrast to the peat fly ash (Ash A). While Ash A decreases the workability of the concrete with increasing replacements levels, Ash B had no such effect and showed the same workability as that of the control at both the 10% and 20% replacement level. This is because ash B has a higher specific surface as it is finer than ash A.

With respect to compressive strength, the concrete containing Ash B performed much better than Ash A at the 20% replacement level, probably due to the fact that Ash B is a finer material than Ash A. Both ashes performed very similarly at the 10% replacement level, exhibiting approximately 94% and 95% of the control strength at 28 and 56 days respectively. The strength of concrete containing a replacement binder highly depends on the fineness of the material due to, firstly, the pozzolanic reaction been potentially highly activated when the particle size is small and, secondly, small particles of fine ash being capable of filling voids in the concrete structure and thus produces denser concrete (Chusilp et al, 2009).

By using the total peat fly ash and co-fired peat fly ash produced in Ireland as cement replacements, approximately 90,000 tonnes of CO_{2e} emissions would be avoided, which would decrease the cement industry emissions by 2.5%. This study suggests that this can be achieved without significant adverse effects on the performance of concrete if 10% replacement levels are used.

Further work is being carried out to investigate the effects using peat fly ash as a binder has on durability of concrete.

Finally, it has been shown that the compressive strengths of 100mm cubes and 150mm cubes are not the same. The compressive strength of 100mmm cubes are 5 to 8% higher than the strength obtained using 150mm cubes. Also, it has been illustrated that the relationship between cylinder compressive strength and cube compressive strength ranges from 81% to 87%.

Acknowledgements

The first author would like to acknowledge support from IRCSET under the Embark Initiative Postgraduate Scholarship Scheme. I would also like to thank the civil engineering technicians for their help and assistance.

References

British Standards Institution, (2000a). BS EN 197-1:2000 Cement - Part 1: Composition, specifications and conformity criteria for common cements. BSI, London.

British Standards Institution, (2000b). BS EN 206-1: 2000, Concrete — Part 1: Specification, performance, production and conformity. BSI, London.

British Standard Institution, (2006). BS 8500-1:2006, Concrete – Complementary British Standard to BS EN 206-1 – Part 1: Method of specifying and guidance for the specifier. BSI, London.

British Standards Institution, (2009). BS EN 12390-3:2009, Testing hardened concrete Part 3: Compressive strength of test specimens. BSI, London.

Chusilp, N., Jaturapitakkul, C. and Kiattikomol, K., (2009). Utilization of bagasse ash as a pozzolanic material in concrete. *Construction and Building Materials*, 23(11): 3352-3358.

Collepardi, M., (2010). *The New Concrete*, Second Edition. Grafiche Tintoretto, Treviso.

Commission for energy regulation, (2007). Disclosure of energy mix figures 2005, CER.

Coutinho, S., (2003). The combined benefits of CPF and RHA in improving the durability of concrete structures. *Cement and Concrete Composites*, 25(1): 51-59.

Day, K.W., (1999). *Concrete mix design, quality control and specification*. E & FN Spon, London.

Day, R.L., (1990). Pozzolans for use in low cost housing. State of the Art Report prepared for: The International Development Research Centre Ottawa, Canada.

Goggins, J. and Gavigan, D., (2010). Low-cost sustainable construction technology for autonomous buildings., *1st International Conference on Structures & Architecture* 21-23 July 2010, Portugal.

Mansur, M.A. and Islam, M.M., (2002). Interpretation of Concrete Strength for Nonstandard Specimens. *Journal of Materials in Civil Engineering,* 14(2): 151-155.

McCaffrey M., Goggins J., Baylor G., (2010). The use of embodied energy and carbon as indicators of the environmental impact of reinforced concrete structures in Ireland. *BCRI*, Cork, 2-3 Sept 2010.

Motherway, B. and Walker, N., (2009). Ireland’s Low-Carbon Opportunity: an analysis of the costs and benefits of reducing greenhouse gas emissions - Technical Appendix, SEI. Dublin.

Organo, C., Lee, E., Menezes, G. and Finch, E., (2005). Investigation of occupational radiation exposures to NORM at an Irish peat-fired power station and potential use of peat fly ash by the construction industry. *J. of Radiological Protection*, 25: 461-474.

Paappanen, T. and Leinonen, A., (2006). Fuel Peat Industry in EU - Country reports - Finland, Ireland, Sweden, Estonia, Latvia and Lithuania., Jyvaskyla, Finland.

Power, E.A., MacCraith, S. and Richardson, M.G., (2001). The influence of peat pulverised fuel ash on the properties of fresh and hardened concrete, *Concrete Research in Ireland*, NUI, Galway.

Power, E.A., Richardson, M.G. and MacCraith, S., (2000). An Investigation of the Potential use of Peat Pulverised Fuel Ash as a Civil Engineering Material. *International Peat Journal*, 10: 57-69.

Russell, A., (2008). A Market / Technology Report for the Cement Industry in Europe and the Middle East. Materials Technology Publications Watford.

Steenari, B.M. and Lindqvist, O., (1999). Fly ash characteristics in co-combustion of wood with coal, oil or peat. *Fuel*, 78(4): 479-488.

Steenari, B., Schelander, S. and Lindqvist, O., (1999). Chemical and leaching characteristics of ash from combustion of coal, peat and wood in a 12MW CFB-comparative study.*Fuel*,78(2): 249-258

CHARACTERISATION AND REACTIVITY INVESTIGATION OF FURNACE BOTTOM ASH FOR FINE AGGREGATE IN CONCRETE

Y. BAI, M.I. RUSSELL & P.A.M. BASHEER
School of Planning Architecture and Civil Engineering, Queen's University Belfast

Abstract
This paper characterises the physical, chemical and mineralogical properties of Furnace Bottom Ash (FBA) and indicates whether FBA sand (FBA with particles smaller than 5mm) is suitable as a fine aggregate in concrete. Moreover, the pozzolanic reactivity of FBA sand was investigated in order to determine whether the limits imposed by various national standards regarding the content of particles smaller than 75µm should be applied to the FBA sand.

The characterisation study indicated that the particle size distribution of FBA sand is similar to that of the natural sand and it is suitable to be used as a fine aggregate in concrete. The pozzolanic study indicated that the FBA sand contains pozzolanically reactive particles and that the inclusion of FBA particles smaller than 75µm as part of the fine aggregate in concrete should benefit the properties of concrete. Therefore, the restrictions imposed by BS 882: 1992 on the amount of fines in fine aggregate should not be applied when the FBA sand is used to replace natural sand in concrete.

Keywords: Compressive strength, Furnace Bottom Ash, Pozzolanic Reactivity, Thermal Analysis, X-ray Diffraction

1. Introduction

As fine material in aggregate is considered detrimental to the properties of concrete (Neville 1995, Popovics, 1992) various national standards (BSI 1992, ASTM C33-93) set limits on the maximum amount of materials passing 75µm. However, with the increase of waste materials and industrial by-products as aggregate, some argue whether these limits should apply.

Furnace Bottom ash (FBA), a by-product from coal-fired thermal power plants, exhibits a particle size distribution similar to that of the natural sand. Although FBA could therefore be suitable as a fine aggregate in concrete, it contains a substantial percentage of fine materials <75µm. Accordingly, concerns arise regarding the possible adverse effects caused to concrete by the fine materials.

Previous research indicated that, when ground, FBA exhibits pozzolanic potential and could therefore be used as a cement replacement material in concrete (Cheriaf et al., 1999, Jaturapitakkul 2003). However, considering the cost related to the grinding process and the fact that large amounts of pulverised fuel ash (PFA) is available; it is not deemed economically viable to replace cement with ground FBA. It has also been reported (Ranganath et al., 1998) that particles of ponded ash below 75µm exhibit pozzolanic reactivity, although the overall ponded ash is not pozzolanically reactive. Both these findings indicate that FBA particles passing 75µm may have pozzolanic reactivity and thus chemically benefit the strength and durability properties of concrete (even though the overall FBA is not that reactive). If that is the case, the limit on the fine material in fine aggregate should perhaps not be applied to a by-product like FBA.

In order to address this problem the properties of FBA, with particles smaller than 5mm (FBA sand), were characterised in terms of physical, chemical and mineralogical composition to indicate the suitability of FBA as a fine aggregate in concrete. In addition, the pozzolanic reactivity of FBA sand and FBA fine (particles passing 75 μm) were investigated in order to determine whether the limits imposed by various national standards on the amount of fine materials passing 75μm should be applied when the FBA sand is used as a fine aggregate to replace natural sand in concrete.

2. Experimental Programme

2.1 Materials

The FBA used in this study was sourced locally (Kilroot Power Station) and supplied by Connexpo (N.I.) Ltd. For the purpose of this paper FBA was classified into three different categories:

- Raw FBA – FBA collected from the disposal sites at the Kilroot Power Station and then dried in an oven at 105^0C for 24 hours and then allowed to cool to room temperature (23^0C) for 24 hours.
- FBA Sand – the raw FBA that passed through the 5 mm BS sieve.
- FBA Fine – the raw FBA that passed through the 75μm BS sieve.

Reagent-grade calcium hydroxide (CH) was used to evaluate the pozzolanic reactivity of the FBA sand and FBA fine samples.

2.2 Mixes Used for Pozzolanic Investigation

Two mixes were cast in order to study the pozzolanic reactivity of the FBA sand and the FBA fine. One mix contained 50% FBA sand and 50% CH (hereafter called FBA mortar) and the other 50% FBA fine and 50% CH (hereafter called FBA paste). The water-to-solid ratio was 0.5 for both the mixes.

2.3 Preparation, Curing and Conditioning of Samples

The mixes were made using a 5 litre capacity bench-mounted mixer. The required quantities were batched by mass, with eighteen 50 mm cubes being cast for each mix.

Immediately after casting, the moulds were sealed with a plastic film and stored in a constant temperature room at 20(±1)^{0}C and 40(±1) % RH for seven days. The specimens were removed from the moulds at the age of 7 days. Each cube was then covered with a damp hessian cloth and put into an air-tight plastic bag, which were again stored in the constant temperature room until the time of testing.

2.4 Details of Test

Sieve analysis, scanning electron microscopy (SEM), X-ray fluorescence (XRF) and X-ray diffraction (XRD) techniques were used to characterise the physical, chemical and mineralogical properties of FBA.

The pozzolanic reactivity of both the FBA sand and the FBA fine was assessed using the following parameters:

i) CH content was investigated by thermogravimetric analysis (TGA) and XRD at 1, 3, 7, 28, 91 and 150 days.

ii) Crystalline hydration products formed during the reaction between CH and the FBA sand/FBA fine were identified by XRD at 1, 3, 7, 28, 91 and 150 days.
iii)Average compressive strength of three 50mm size cubes was determined at the age of 28, 91 and 150 days.

3. Results and Discussion

3.1 Characterisation of FBA Sand

Particle Shape

The SEM images in Figure 1 shows the particle shape of FBA and natural sand. From this it is seen that the particle shape of the FBA sand (as previously reported by Cheriaf et al., 1999) is spherical with a smooth surface texture. In contrast the natural sand particle is somewhat irregular with a rough surface. It is well known that the more spherical the particles, the more workable the resulting concrete will be and, thus less water required for mixing. Moreover, the water requirement of smooth particles is less than that required for rough particles, given that there is less friction between the smooth particles. As a result it is expected when the FBA sand is used to replace the natural sand in concrete, the water demand of the resulting concrete should decrease.

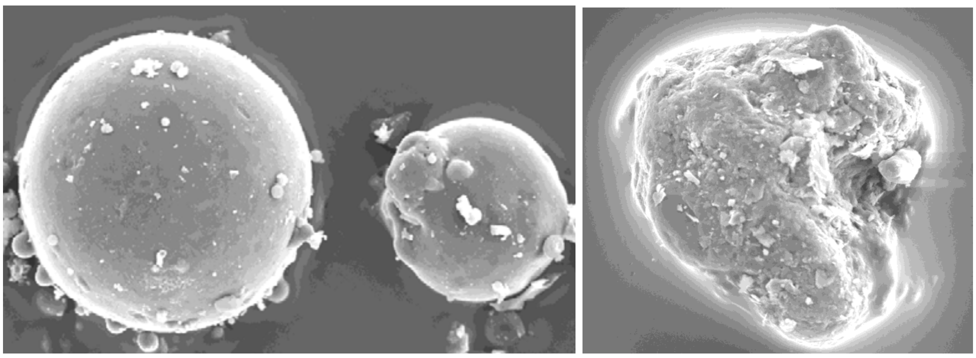

(a) FBA Particles (b) Natural Sand Particle

Figure 1 Particle Nature of FBA and Natural Sand

Particle Size Distribution of FBA Sand

The particle size distributions of the raw FBA, FBA sand, natural sand and PFA are presented in Figure 2. It can be noticed that about half of the particles of raw FBA fall within the boundaries of the medium-sized fine aggregate as per BS 822:1992. However, raw FBA contains particles outside the specified boundaries of medium-sized natural sand that is to be used in concrete (e.g. < 212μm and > 10mm).

Figure 2 also indicates that after sieving the raw FBA through the 5 mm sieve, all of the FBA sand particles coarser than 212μm lie within the boundaries set in BS 882:1992 and the particle size distribution is quite similar to the natural sand. However, all the particles finer than 212μm are outside the lower limit with ~20% of the FBA particles finer than 75μm. Hence, the use of FBA sand in concrete would result in an increase of the fine particles and hence breach the prevailing standards.

In order to identify whether the materials finer than 75µm should be included when the FBA sand is used in concrete, the chemical reactivity of the FBA sand and FBA fine was studied. This is presented and discussed in section 3.2.

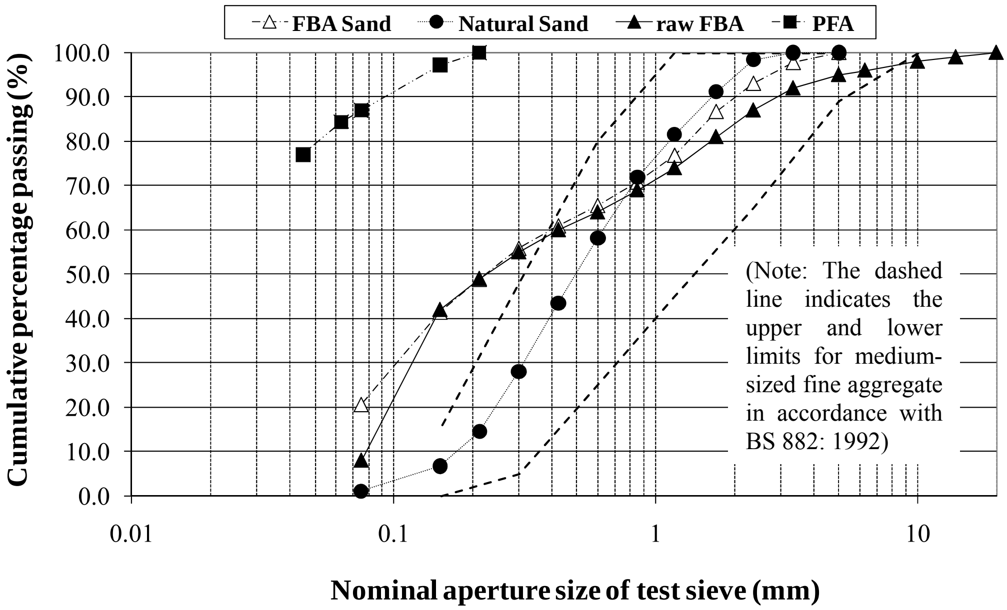

Figure 2 Particle size distribution of the raw materials

Chemical Composition of FBA Sand

The chemical composition of the FBA sand was obtained from the XRF analysis (reported in Table 1). Also presented is the chemical composition of the PFA from the same power plant. It can be observed that the chemical compositions of the FBA sand and the PFA are quite similar. Both of them can be classified as Class F ash in accordance with ASTM C 618-99.

Although FBA and PFA have a similar chemical composition FBA does not have the same pozzolanic potential as PFA. The reason for this can be partly explained by looking at their respective particle size distribution (shown in Figure 2). It can be seen that the majority of the PFA particles are finer than 45µm; whereas the particle distribution of FBA is closer to natural sand. As the fineness of coal ash is believed to influence the pozzolanic reactivity (i.e. the finer the particles the higher the reactivity), it is to be expected that the FBA would be less reactive than the PFA.

Table 1 Chemical composition of the FBA sand and PFA from Kilroot Power Station

Oxide composition (%)	SiO_2	Al_2O_3	Fe_2O_3	CaO	MgO	Na_2O	K_2O	TiO_2	SO_3	P_2O_5	LOI
FBA sand	61.78	17.80	6.97	3.19	1.34	0.95	2.00	0.88	0.79	0.20	3.61
PFA	59.01	22.80	8.80	2.38	1.39	0.74	2.80	1.15	0.27	0.39	6.70

Mineral Composition of FBA Sand
The mineral composition of the FBA sand, obtained from the XRD analysis, is compared with that of the PFA (see Table 2). The results indicate that the FBA sand consists of 26% quartz, 9.8% mullite and 56% amorphous materials, whereas the PFA consists of 5% quartz, 11% mullite, 8.0% lime and 66% amorphous materials.

Table 2 Comparison of the mineral composition of the PFA and the FBA sand

Mineral	Formula	Wt%		Mineral	Formula	Wt%	
		PFA	FBA sand			PFA	FBA sand
Quartz	SiO_2	5.0	26.0	Lime	CaO	8.0	-
Mullite	$Al_6Si_2O_{13}$	11.0	9.8	Portlandite	$Ca(OH)_2$	1.2	-
Hematite	Fe_2O_3	1.2	4.0	Calcite	$CaCO_3$	0.4	3.9
Anhydrite	$CaSO_4$	3.0	-	Sodium Sulphate	Na_2SO_4	1.3	-
Periclase	MgO	2.4	-	Amorphous		66.0	56.0

3.2 Pozzolanic Investigation of FBA Fine and FBA Sand

The pozzolanic reactivity is described as the capacity of siliceous or siliceous and aluminous (pozzolan) materials to enter into the reaction with CH in the presence of water at room temperature to form solid and water-insoluble substances (Wesche 1999). CH reacts with pozzolanic materials in the following ways: firstly with reactive silica to form calcium silicate hydrate (CSH) and secondly with reactive alumina to form calcium aluminate type materials. Accordingly, the depletion of CH in each sample can be used to identify the pozzolanic reactivity of materials. As mentioned in section 2.4, the pozzolanic reactivity of the FBA sand and FBA fine was determined in terms of the depletion of the CH content, the formation of new hydration products and the development of compressive strength of mixes manufactured with these materials. Results are presented and discussed in the following sections.

Depletion of Calcium Hydroxide Content
Thermogravimetric Analysis (TGA) is a technique commonly used in cement hydration studies to determine the presence and quantity of various cement hydrates. During TGA testing a small amount of paste (~30mg) is heated to 1000^0C resulting in the decomposition/dehydration of various hydrates. The amount of weight loss during each decomposition reaction is related to the amount of the hydrate. Figure 3 shows a typical TGA trace for FBA paste at 1 day. Also included in the Figure is the derivative of the TGA trace (DTG). DTG enables a more accurate identification of the temperatures at which weight loss starts and finishes and also distinguishes between overlapping peaks. The sample in Figure 3 exhibits a major decrease in weight between 480-520^0C (highlighted by peak on DTG trace) which can be attributed to the decomposition of CH. From this decrease the amount of CH in each sample can be determined. Another peak around 150^oC can also be observed which could be attributed to the decomposition of monocarbonate phase (Lothenbach et al., 2008). Further details are discussed under XRD results.

A comparison of the weight loss associated with CH depletion for each sample and at all ages (see Figure 4) clearly shows that the pozzolanic reactivity started at an earlier age for the FBA fine than the FBA sand. It can be seen that up to 28 days the amount of CH in both samples is almost the same and the change in CH content is small. However, from 28 days to 91 days, there was a significant decrease in the CH content for the FBA paste, whereas there was a reduced change in the case of the FBA mortar. At 150 days, the CH content in the FBA paste was 8% lower than that of the FBA mortar. Together these results indicate that the FBA fine was more reactive than the FBA sand at these ages.

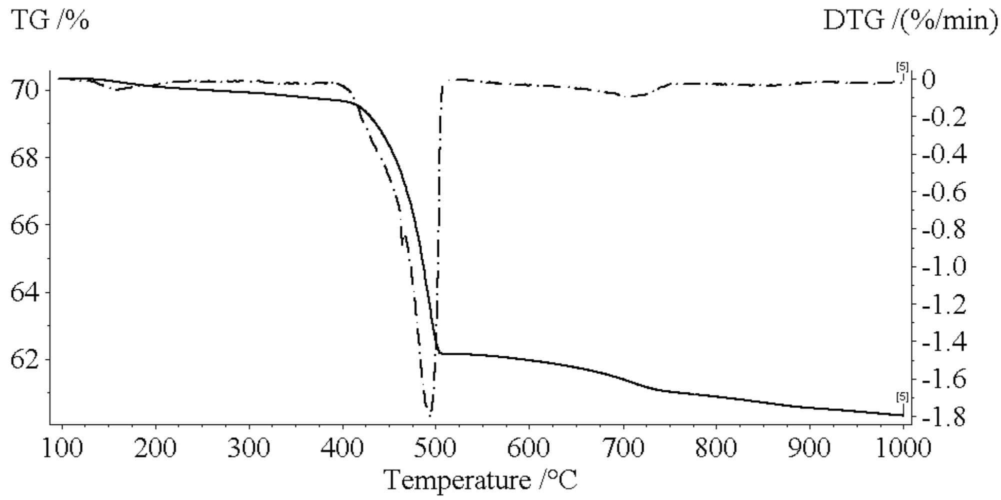

Figure 3 Example of DTG and TGA curves for the FBA paste at 1 day

It is known that the pozzolanic reaction is controlled by the diffusion process and, hence, the particle size or the surface area plays a dominant role in determining the relative rates of reactivity (Mehta 1989). Therefore, the difference in the pozzolanic reactivity between the FBA sand and the FBA fine is attributed in part to the differences in their particle size distribution. The results in Figure 4 would suggest that, as far as the pozzolanic reactivity is concerned, including the fine particles (<75μm) in FBA sand may be beneficial to the properties of concrete.

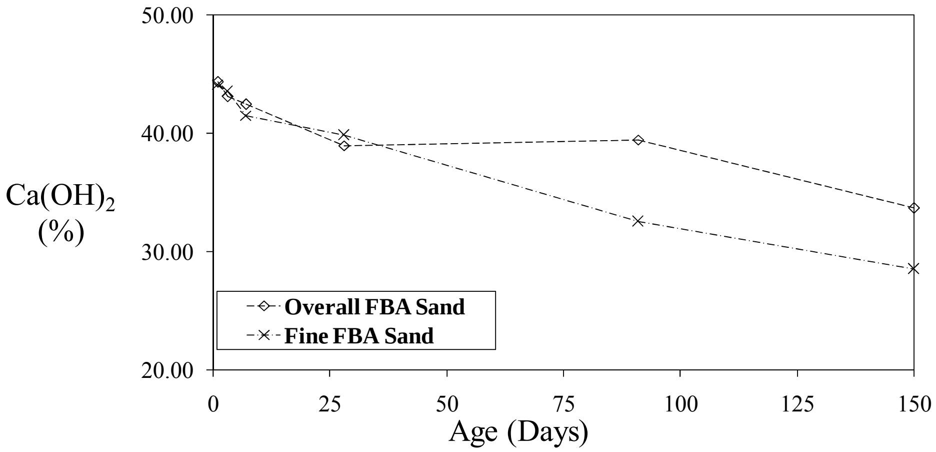

Figure 4 Depletion of CH content for the FBA mortar and the FBA paste

XRD Analysis

Figure 5 shows the XRD patterns for FBA mortar and FBA paste up to the age of 150 days. Results indicate the presence of CH, quartz, mullite and monocarbonate $C_3A{\bullet}CaCO_3{\bullet}11H_2O$ (AFm). Quartz, mullite and CH were already present in the unhydrated sample; whereas monocarbonate is a hydration product. Other hydration products are also likely to form; however they may be amorphous and therefore unable to be identified using XRD.

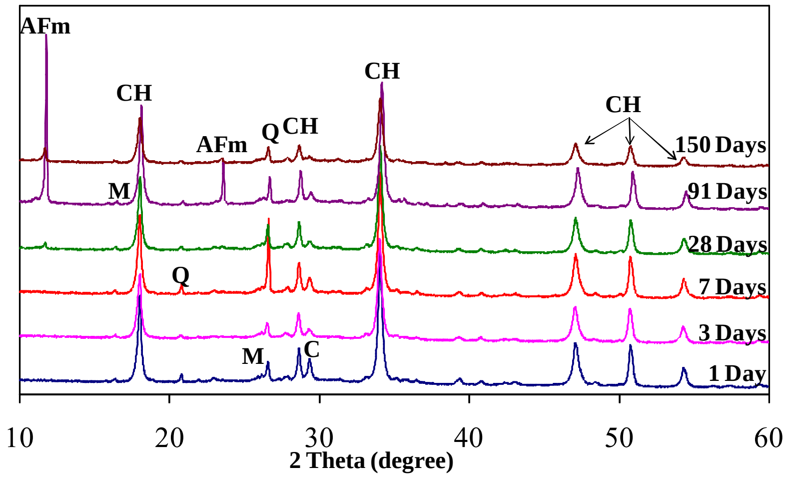

(a) FBA mortar (FBA sand + CH)

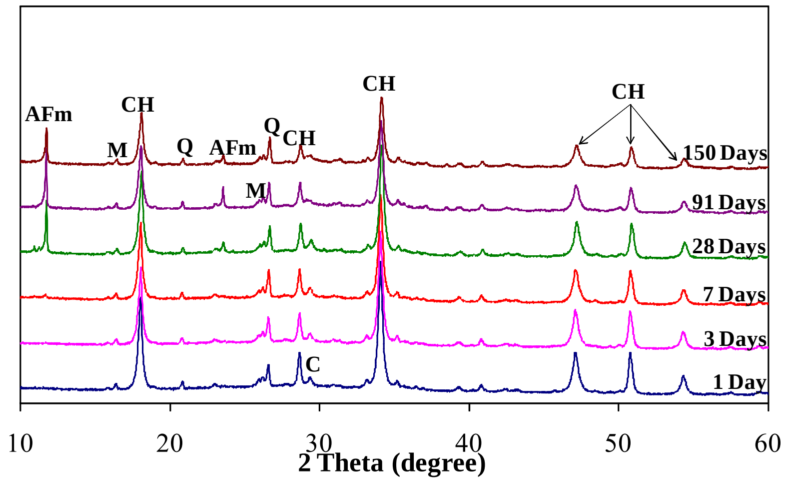

(b) FBA paste (FBA fine + CH)

(AFm=monocarbonate; M=mullite; CH=calcium hydroxide; Q=quartz; C=calcite)

Fig. 5a and b XRD pattern of the FBA mortar and the FBA paste

Like the TGA results, these results indicate a depleting CH content over time which highlights that FBA fine is more reactive than FBA sand.

Two peaks (2θ =11.75^0, 23.56^0) representing AFm can be seen in each sample. The formation of monocarbonate has been well-established in the hydration of Portland cement when limestone is added as a filler, which is mainly attributed to the reaction between C_3A and $CaCO_3$ phases (Hawkins et al., 2003). The formation of monocarbonate has also been reported in some pozzolanic reactions (Hewlett 1998). From Table 2, it can be seen that FBA contains 3.9 wt% $CaCO_3$ whereas PFA only 0.4 wt%. Therefore, the appearance of monocarbonate phase would suggest that the aluminate phase in FBA is chemically reactive. From the XRD pattern, it also can be observed that the reaction of aluminate phase started at the age of 28 days in FBA mortar and 7 days in FBA paste and would imply that the FBA fine has a better reactivity than the FBA sand.

The formation of small amount of AFm in concrete could be beneficial given that any chlorides present in concrete would react with AFm to form Friedel's salt (calcium chloroaluminate). Accordingly the presence of FBA would result in a binding of chlorides and improve the resistance of concrete to chloride attack. Therefore, in contrast to restrictions placed by BS 882:1992, it may beneficial in this instance to include the FBA particles smaller than 75 μm as part of the FBA sand.

Compressive Strength

Compressive strength values are presented in Figure 6. As the mixes did not set sufficiently before 7 days, the compressive strength was tested at 28, 91 and 150 days.

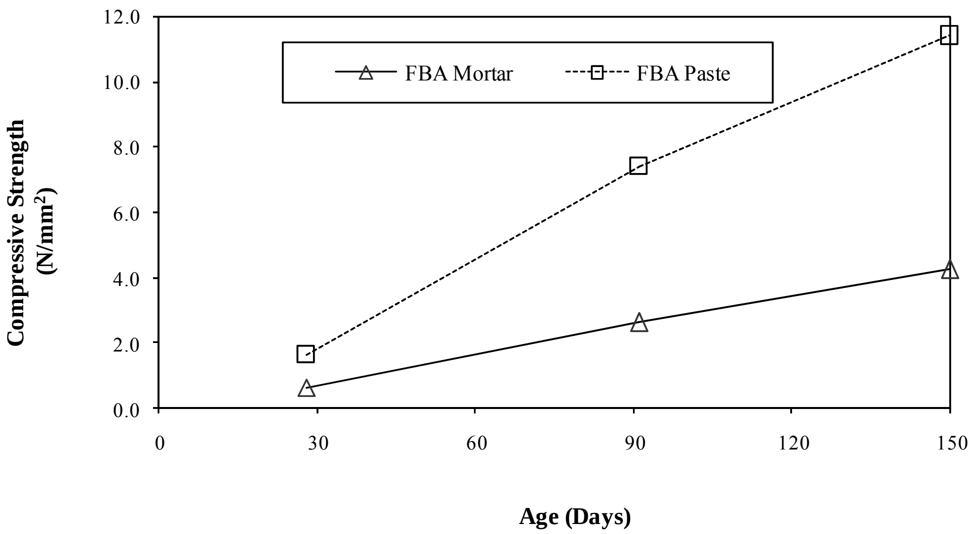

Fig. 6 Compressive strength of the FBA mortar and the FBA paste

Results show that the compressive strength of the FBA paste was higher than that of the FBA mortar and that its strength developed at a greater rate through time. This would again indicate that the FBA fine has better pozzolanic reactivity than the FBA sand. However, considering the compressive strength of the FBA mortar at the age of 150 days reached only 4.2 N/mm2, the contribution of the FBA sand to the compressive strength of concrete would be limited.

Conclusions

Based on the results reported, the following conclusions have been drawn:

i) Physical, chemical and mineralogical characteristics of the FBA:
   a. The FBA particles are spherical and exhibit a smooth surface texture, whereas the natural sand particles are rough and irregular in shape.
   b. The particle size distribution of the raw FBA is similar to that of the natural sand. However, when FBA is sieved through 5 mm sieve (i.e. FBA sand) 50% of its particles are outside the lower limit specified in BS 882:1992.
   c. The chemical and mineralogical compositions of the FBA sand and the PFA in the current study are quite similar. Both could be classified as Class F ash; however, the PFA contains more amorphous phases than the FBA sand.

ii) The TGA and XRD data have indicated that the pozzolanic reactivity of the FBA fine started earlier than that of the FBA sand (typically 7 days against 28 days). The compressive strength of the FBA mortar was 4.2 N/mm^2 at the age of 150 days whereas strength of 11.85 N/mm^2 was obtained for the FBA paste. The difference in behaviour between the two materials is considered to be due to the greater number of fine materials in FBA fine.

iii)FBA fine contained a greater amount of reactive aluminate phase. Hence, the incorporation of the FBA fine (i.e. particles smaller than 75μm) in FBA sand is preferable in the context of chloride binding and improved durability. Therefore, it is concluded that the restrictions imposed by BS 882: 1992 on the amount of fines in fine aggregate from natural sources should not be applied when the FBA sand is used to replace natural sand in concrete.

4. References

ASTM Standard C 33-93, Standard Specification for Concrete Aggregates.
ASTM C618-99, Standard specification for fly ash and raw or calcined natural pozzolan for use as a mineral admixture in Portland cement concrete, 1999.
British Standards Institution, Specification for Aggregates from Natural Sources for Concrete, BSI, London, BS 882.:1992
Cheriaf, M., Rocha, J.C. and Pera, J. (1999), 'Pozzolanic properties of pulverized coal combustion bottom ash', *Cement and Concrete Research 29*, pp. 1387-1391.
Hawkins, P., Tennis, P. D. and Detwiler, R. J. (2003), 'The Use of Limestone in Portland Cement: A State-ofthe-Art Review', EB227, Portland Cement Association, Skokie, Illinois, USA, 44 pp.
Hewlett, P. C. (1998), 'Lea's chemistry of cement and concrete', 4th Edition, London : Arnold, 1053pp.
Lothenbach, B., Saout, G. L., Gallucci, E. and Scrivener, K. (2008), 'Influence of limestone on the hydration of portland cement', *Cement and Concrete Research 38*, pp. 848-860.
Jaturapitakkul, C. and Cheerarot, R. (2003), 'Development of bottom ash as pozzolanic material', *Journal of Materials in Civil Engineering (ASCE)*, Vol. 8, No. 3, pp. 128-137.

Mehta, P.K. (1989), 'Pozzolanic and cementitious by-products in concrete – Another look', *SP-114*, pp. 1-43.
Neville, A.M. (1995), *Properties of Concrete*, Fourth Edition, Longman Group Limited.
Popovics, S. (1992), *Concrete materials: properties, specifications and testing,* 2nd edition, Noyes Publications.
Ranganath, R.V., Bhattacharjee, B. and Krishnamoorthy, S. (1998), 'Influence of size fraction of ponded ash on its pozzolanic activity', *Cement and Concrete Research*, Vol. 28, No. 5, pp. 749-761.
Wesche, K. (1991), 'Fly ash in concrete – properties and performance', *Report of technical committee 67-FAB use of fly ash in building*, RILEM, 1991.

INFLUENCE OF AGGREGATE SIZE AND PROPORTIONS ON FRESH AND HARDENED PROPERTIES OF SELF-COMPACTING CONCRETES

P.W. GREAVES, J. KWASNY, M. SONEBI, P.A.M. BASHEER
School of Planning, Architecture, and Civil Engineering, Queen's University Belfast, Northern Ireland, United Kingdom

Abstract
Both fresh and hardened properties of self compacting concrete (SCC) are heavily dependent on the proportions of fine and coarse aggregates and their sizes. Therefore, an investigation was carried out in which the influence of the fine and coarse aggregate compositions (size and grading) on fresh and hardened properties of SCC was studied. The results were used to develop SCC mixes which are suitable for structural applications.

Three different aggregate compositions were investigated, with three aggregate sizes, viz. sand and 6mm and 14mm coarse aggregates. Each aggregate composition was selected in such a way that it allowed for a conclusion to be drawn on the influence of each of the aggregates on the fresh and hardened properties of the concrete. These properties were measured in accordance with British and ASTM Standards. The results indicated that when the fine aggregate content was at its high level (60% of the total mass of aggregates), workability dramatically decreased, mainly due to high surface area of the fine aggregates and a much lower voids ratio, reducing the volume of paste, hence lowering lubrication effects.

Keywords: Aggregate grading; aggregate size; fresh properties; hardened properties; self-compacting concrete (SCC)

1. Introduction

Japan underwent a post war reconstruction after the 1950's, where speed of construction was the primary concern and the quality of construction was compromised. Within a period of twenty years from construction, many concrete structures had begun to perform so badly that an evaluation was carried out by the government. It was concluded that low quality compaction of the concrete by the unskilled workforce was the source of the poor concrete durability. Therefore, a special type of concrete was developed, the hardened properties of which were independent of the skill of the labourer placing the concrete. This new concrete was called Self-Compacting Concrete (SCC) and it has since been introduced in Europe and around the world (De Schutter *et al.* 2008).

SCC is a highly workable concrete that can self-compact under the action of gravity alone. The major differences between SCC and vibrated concrete (VC) are: the lower coarse aggregate (CA) content, higher powder content and and the prominent use of chemical and mineral admixtures in SCC. These alterations together gave a highly workable concrete that upon pouring and curing would maintain its heterogeneous structure and produce a durable concrete with the required mechanical properties. It is documented that the reduction in volume and size of the CA is critical to reducing the congestion and 'arching' of aggregates as they pass between and around the obstructions within formwork (Khayat, 1999). High powder content is required to maintain the cohesion of the paste within the SCC. This prevents segregation, promotes flowability and facilitates self-compaction (Su *et al.,* 2001).

The chemical admixtures commonly used in SCCs are superplasticisers (SPs) and viscosity-modifying admixtures (VMAs). The SPs are chemical substances which, when added to the concrete mix, will result in more water within the mix being released for lubrication, increasing workability (De Schutter *et al.,* 2008). The main role of the VMAs is to modify the rheology properties of the cement paste (EFCARC, 2006); hence making it more stable, increasing segregation resistance and making the mix more tolerable to slight variations in moisture content.

Alexander and Mindess (2005) reported that for any particular selection of aggregates, there is an optimum blend to achieve the smallest voids ratio. They documented that for a particular 10 mm CA and sand combination there was an optimum value of compaction to be achieved, and that too much sand can have the same consequence as having too little; the voids ratio will be increased. The selection of the aggregate composition, size and grading of both CA and fine aggregates (FA), should desirably be one that has just enough FA to fill the voids between the CA, optimising the room for the paste and hence increasing the workability of the SCC.

The aim of this study was to ascertain the effects of altering the aggregate composition on the rheological and physical properties of SCCs. The objectives were to:

- select suitable aggregate compositions (size and proportions of CA and FA);
- establish a suitable SP dosage to produce SCC mixes with a slump-flow in the range on 600–700 mm;
- test the key fresh properties, including flowability, filling ability, passing ability, and segregation resistance; and
- manufacture concrete specimens and test hardened properties (compressive strength, modulus of elasticity and drying shrinkage).

2. Experimental programme

As the parameters to be investigated were the aggregate composition and the SP dosage, the other constituents of the mix needed to remain constant. The composition of the aggregates would determine the paste volume, as the voids ratio between the aggregates was directly influenced by the composition. For this research the aggregate compositions were set at three different specific values (see section 2.3 for further details) and each mix composition was batched twice. However, to standardise the mixes and limit the influence of water content on the results, the water to powder (w/p) ratio was kept at 0.35.

For the first batch, the SP dosage to obtain a 600–700 mm slump-flow was investigated. After this the rheology characteristics were evaluated by measuring the key fresh properties, *viz.* workability, filling ability, passing ability and segregation resistance. These properties were evaluated using the slump-flow test, V-funnel test, J-ring test and segregation column test, respectively.

For the second batch, only the slump-flow test was carried out to verify that the same workability as the first batch was obtained. Then test specimens (described in section 2.4) were cast to carry out tests for hardened properties, *viz.* tests for compressive strength, modulus of elasticity and drying shrinkage.

2.1. Materials

The aggregates used in the mix were 14 mm and 6 mm crushed basalt as CA and 0 to 4 mm concrete sand as FA, hereafter referred to as 14 mm, 6 mm and sand, respectively. The oven-dry density and 1-hour water absorption of the aggregates are given in Table 1. The cement used was portland cement CEM II/A-L 42,5N (specific gravity of 3.08), as specified by BS EN 197-1:2000. In all mixes the cement was partially replaced with limestone powder (LSP) with specific gravity of 2.75, in the proportion 75% and 25% between them. The particle size distribution (PSD) curves for all aggregates and powders are shown in Figure 1.

Table 1 - Oven-dry density and 1-hour water absorption of the aggregates

Aggregate type	*Oven-dry density [Mg/m^3]*	*1-hour water absorption [%]*
Sand	2.70	0.9
6 mm	2.56	4.6
14mm	2.60	4.0

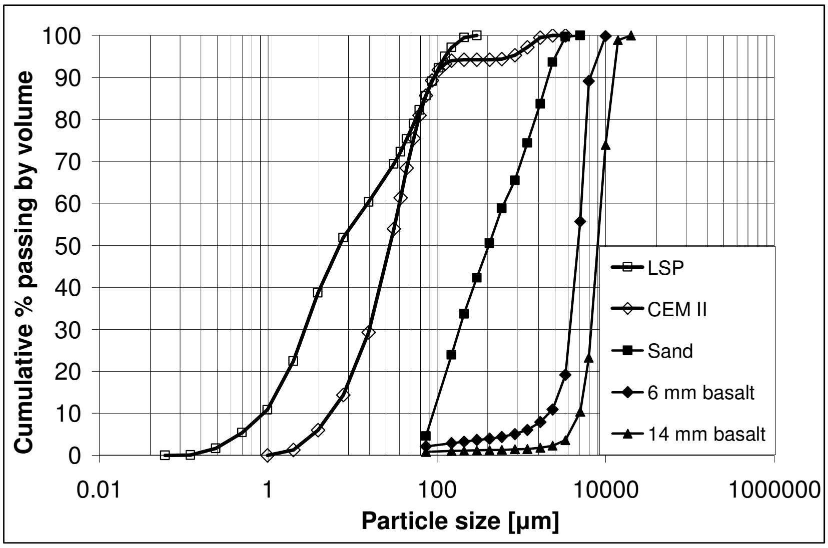

Figure 1 - PSD curves of all powders and aggregates

A commercially available superplasticiser incorporating a stabilising agent was used as SP (specific gravity of 1.10 and solid content of 42%) with the initial dosage kept at 0.9% of total powder mass (*i.e.* cement + LSP). A retarder with specific gravity of 1.22 and solid content of 28% was also incorporated in the mix design at a dosage of 0.3% of the cement mass. Tap water (15 ±2 °C) was used as a mixing water. Noteworthy, the water content in the mixes was adjusted to take into account water in both the SP and the retarder, as well as the water for 1-hour absorption of the aggregates.

2.2. Mix design

Similar to Su *et al.*, the principal consideration of the mix design was to fill the voids between the aggregates with paste. Aitcin's (1998) theory of transforming the proportions of mass of the different ingredients into volumetric quantities was also incorporated into the mix design, which meant that the ingredients could be stated in units of mass per cubic meter of concrete, leading to a yield in the composition of materials.

The mix design process can be summarised as follows:

- determine volume of aggregates from loose bulk density;
- determine volume of paste from volume of aggregates and assuming 1.5% air content;
- evaluate powder mass;
- determine water, SP and retarder content;
- carry out corrections of water mass to be added to allow for 1-hour water absorption of aggregates and water brought into mix by SP and retarder.

2.3. Selection of aggregate composition

Many different mix proportions are proposed by various bodies, including the EFNARC (2005) guidelines. The latter states that the CA (>4–5 mm) content range should be between 27–36% by volume with FA content ranging between 48–55% by weight of total aggregates. De Schutter *et al.* (2008) stated that the FA content is very critical; if the content is too high, the FA particles would interfere with each other during flow and cause blocking; if too low, the resulting higher cement and water content would be detrimental to the hardened concrete properties.

Taking the research data into account, a ternary composition of aggregates, as shown in Table 2 (percentage values in brackets), was created. The maximum and minimum limits to the FA were 60% and 45% of the total aggregate mass. CA contents were limited to 20% and 35% of the total aggregate mass. Taking these boundaries into consideration, the extremes of each case were used as aggregate compositions, namely compositions A, B and C, as shown in Table 2. Also shown in Table 2 are the masses of other ingredients in each mix.

Table 2 - Mix proportion of SCC mixes

Material [kg/m^3]	***Mix A***	***Mix B***	***Mix C***
Sand	1012.1 (60%)	730.3 (45%)	736.0 (45%)
6 mm CA	337.4 (20%)	568.0 (35%)	327.1 (20%)
14 mm CA	337.4 (20%)	324.6 (20%)	572.4 (35%)
CEM II	379.7	400.7	397.3
LSP	126.6	133.6	132.4
SP (initial dosage)	4.6	4.8	4.8
Retarder	1.1	1.2	1.2
Free water	173.7	183.3	181.8

2.4. Mixing and testing procedures

To ensure no other parameters influenced the results of mixes, the cement, LSP, SP and retarder were all stored in dry locations at room temperature prior to all castings. All aggregates were oven dried at 105 ±5 °C. One day before casting they were removed from the oven and kept in sealed polythene bags.

The dry aggregates were placed in the mixer, 2/3rd of the calculated total water was added and they were mixed for two minutes. The mixture was then left for 1 hour, to allow the aggregates to absorb water and reach the 1 hour saturated surface-dry (SSD) state. The remaining 1/3rd of the total water was divided into three parts. After 1 hour aggregates were remixed for one minute, LSP was added with first part of remaining total water and mixed for one minute. Afterwards, cement and second part of remaining water were introduced into the mixer and mixed further for two minutes and the time recorded for rheology tests was taken relative to time of addition of cement; that is time equals zero. Finally, the initial dosage of SP of 0.9%, retarder and the remainder of the water were added to the mixer. After two minutes of mixing, a slump-flow test was carried out. If the result was not in the range of 600–700 mm, an additional quantity of SP was added, and the content was mixed further for 1 minute. This procedure was repeated until the slump-flow spread was in the range of 600–700 mm.

Measurement of fresh properties

The slump-flow of the SCC mix was determined using the slump-flow test in accordance with prEN 12350-8:2007. The fresh SCC concrete was poured into a cone, which was resting on a level PVC board. As the cone was lifted directly upwards, the time (t_{500}) was measured. The largest diameter was then recorded when the concrete had stopped flowing and another measurement was taken in a direction perpendicular to the initial measurement. The average of these two values was reported as the slump-flow spread value.

The V-funnel test was used to examine the filling ability of the mix, in accordance with prEN 12350-9:2007. A V-shaped funnel was filled with fresh SCC in one lift. After filling, the time from opening the gate at the bottom of the V-funnel to that when it was possible to see through the aperture was recorded (escape time).

For analysis of the passing ability of the fresh SCC mix, the J-ring test was used, in accordance with prEN 12350-12:2007. The J-ring consists of a series of vertical reinforcement bars of diameters 12 mm at centres of 70 mm. This test gives a measurable and visual indication of the passing ability of SCC. The average J-ring blocking step was recorded.

The degree of segregation was determined with the segregation column test, similar to ASTM C 1610. After filling, the segregation column comprising of the three 200 mm diameter and 175 mm long PVC pipe sections connected with clamps, the SCC mix was allowed to rest for 15 minutes. The three segments were then separated and the concrete within each segment was washed on a 5 mm sieve to remove all the paste and aggregates <5 mm. Then aggregates from each section were dried (105 ±5 °C) to constant mass and their weight was recorded. Afterwards, following the methodology of Assad *et al.* (2004), the coefficient of variation of the aggregate >5 mm mass along the column was computed and reported as segregation index (I_{seg}).

Measurement of hardened properties

Nine 100 mm cubes were cast for determining the compressive strength. All cubes were de-moulded after exactly 24 hours from the time of introducing cement to water. Just after de-moulding, three cubes were crushed in accordance with BS 1881-116:1983. The remaining six cubes were placed in a water bath (20 ±1 °C) and crushed in sets of three on the 7th day and 28th day after casting.

Three cylinders (100 mm diameter and 200 mm in height) were cast for determining the static modulus of elasticity (BS 1881-121:1983). One day after casting they were de-moulded and placed in a water bath (20 ±1 °C) for 14 days. On the 14th day, the cylinders were removed from the water bath and capped to create two parallel faces on the cylinder for testing. They were then returned to the water bath until they were tested on 28th day.

Three 75×75×255 mm prisms were cast for monitoring of the drying shrinkage. After de-moulded, they were placed in a water bath at 20 ±1 °C for 6 days. Between the third and fifth day after casting, the steel balls were attached to each end of the prisms with cement paste. The length of the prisms was measured initially at 7th day and then at 8, 10, 14, 21, 28, 42 and 56th day after casting, in accordance with ASTM C 490-04. The change of length at 56th day with respect to that at 7th day is reported in this paper as the drying shrinkage (average of the three measurements).

3. Results and discussion

3.1 Fresh properties

As can be seen from Table 3, even after adding 15.3 kg/m^3 of SP, the measured spread for mix A was 565 mm. However, for mixes B and C, a spread of 660 mm was achieved with dosages of 5.5 kg/m^3 and 4.9 kg/m^3, respectively. Mix A had a sand content of >1000 kg/m^3. As reported by Sonebi (2004), mixes with a sand content greater than 900 kg/m^3 would result in a slump-flow less than 580 mm. This is considered to be due to a decreased paste content and increased surface area of sand.

The consequence of the increased sand content is to give a greater aggregate surface area and, therefore, more water being adsorbed onto the surface of the aggregates, leaving less water available for the lubrication.

Mix A also produced the smallest volume of paste per cubic metre (348 l/m^3). Mixes B and C produced similar and relatively higher volumes, 367 l/m^3 and 364 l/m^3, respectively. That is, mix A aggregate composition produced a lower voids ratio compared to the other two mixes, reducing the volume of paste and, as a consequence, compromised lubrication, which had a detrimental effect on the slump-flow spread (workability).

Table 3 - Fresh property results

Mix	*SP required for 600–700 mm spread [kg/m^3]*	*Slump-flow spread [mm]*	*Slump-flow t_{500} flow time [s]*	*V-funnel flow time [s]*	*J-ring blocking step [mm]*	*Segregation index (I_{seg}) [-]*
A	15.3	565	9.4	17.5	14	3.2
B	5.5	660	3.5	12.4	16	3.1
C	4.9	660	4.9	14.4	15	2.1

The low paste content of mix A had a noticeable detrimental effect on its filling ability, as measured by the V-funnel flow time and t_{500}. Mix A produced the poorest filling ability with a V-funnel flow time of 17.5 s. Mix B produced the best V-funnel flow time of 12.4 s. Mix B had the highest paste content. That is, when the paste content is high, the workability and filling ability are better.

Mix A did however give the best results for J-ring passing ability, with a 14 mm difference in height just inside and outside the bars (J-ring blocking step). The reason for this was believed to be a result of 'lack of arching' (ACM centre, 2005) whereby aggregates were unable to form a stable arch in front of an opening due to their shape and/or friction. This increased passing ability can therefore be related to the higher sand content and consequently fewer coarse aggregates present in mix A, which in turn reduces the probability of the formation of 'arch'. It must be noted that none of the three mixes produced a J-ring blocking step smaller than the allowable value of 10 mm, as specified in prEN 206-9:2007. The passing ability of the concretes needs to be improved to conform to the standard.

All mixes showed excellent resistance to segregation. They had I_{seg} in the range of 2–4% which was recommended by Assad *et al.* (2004) as a low risk of segregation range for SCC. The SP used contained both superplasticising admixture and VMA and, hence, as the addition of SP was increased, so was the mass of VMA.

3.2 Hardened properties

Mix A showed poor development of early compressive strength (Table 4), as a result of the high SP addition. That was because overdosing of SP would have a prolonged retardation effect (Higgins, 1984). Furthermore, as there was a smaller volume of paste in mix A, the mass of cement was also smaller. However, the aggregate compositions for mixes B and C produced higher 7^{th} day and 28^{th} day strength, presumably due to better packing and increased paste (and cement) content (Table 2).

All mixes showed similar results for modulus of elasticity (Table 4). A survey carried out by Domone (2007) showed that for a given strength, SCC would have a lower modulus of elasticity than VC. However, De Schutter *et al.* (2008) documented that too few results exist as yet to draw comparisons between the modulus of elasticity of SCC with that of VC.

The 56^{th} day drying shrinkage was 725, 770 and 796 microstrain for mix A, B and C, respectively. It is well documented that drying shrinkage is strongly related to the w/c (w/p) ratio and the paste volume (Bissonnette *et al.*, 1999), apart from storage environment, *i.e.* relative humidity and temperature, size, shape and orientation of the sample. For the three mixes in this study, the w/p remained constant at 0.35, but the paste volume was varied (as discussed before). As a result, the drying shrinkage did not vary much; however, it was higher for the mixes with higher volume of the paste (B and C).

Table 4 - Hardened property results

Mix	*Compressive strength [MPa]*			*Modulus of elasticity [GPa]*	*56^{th} day drying shrinkage [microstrain]*
	1^{st} day	*7^{th} day*	*28^{th} day*		
A	7.7	30.7	42.1	23.3	725
B	10.2	33.5	47.4	23.2	770
C	14.4	33.2	47.4	23.6	796

4. Conclusions

On the basis of materials used in this project and results reported in this paper, the following conclusions have been drawn:

a) It was found that when designing SCC, much consideration needs to be given to the aggregate composition of the mix. An excessively high FA content, in the region of 60% of total percentage of aggregate mass, was found to have a detrimental effect on the workability of the SCC, to such extent that in one case the SCC was not obtained.
b) The results indicated that when combining different sizes of aggregates and sand to manufacture the SCC mixes which would pass the passing ability, the filling ability and the segregation resistance, there is a need to emphasise the paste content and the void ratio. When the void ratio was too low (or the paste content was too low), SCC mixes were not possible. From this study the most favourable percentage of the aggregate composition emerges to be 45% sand, 35% 6 mm and 20% 14 mm for the most of the measured properties, except the passing ability. The approach used in this paper could be further applied to eliminate this limitation, simply by investigation of the different compositions of aggregates.

When the cement type or the admixture type is varied, it is essential to establish the best combination of aggregates to give SCC with the most suitable properties, because the findings of this study are applicable only to cement and admixture types used.

References

ACM Centre (2005), University of Paisley, UK. *'Measurement of properties of fresh self-compacting concrete, Final Report'*.

Aitcin, P.C. (1998), *'High Strength Concrete'*, Spon Press.

Alexander, M., Mindess, S. (2005) 'Aggregates in Concrete', Modern concrete technology 13, MPG Books Ltd, Bodmin.

Assaad, J., Khayat, K.H. and Daczko, J. (2004), ' Evaluation of Static Stability of Self-Consolidating Concrete', *ACI Materials Journal*, **101**, 207-215.

Bissonnette, B., Pierre, P. and Pigeon, M. (1999), ' Influence of key parameters on drying shrinkage of cementitious materials', *Cement and Concrete Research,* **29,** 1655–1662.

De Schutter, G., Batos, P.J.M., Domone, P. and Gibbs, J. (2008) *'Self-Compacting Concrete'*, Whittles Publishing.

Domone, P.L. (2007), 'A review of the mechanical properties of hardened self-compacting concrete', *Cement and Concrete Composites,* **29,** 1-12.

EFNARC European Project Group (2005), *'The European guidelines for Self-compacting concrete: specification, production and use'*.

EFNARC (2006), *'Guidelines for viscosity modifying admixtures for concrete'*.

Higgins, D.D. (1984), *Admixtures for concrete*, Cement and concrete association, Slough.

Khayat, K.H. (1999), 'Workability, testing, and performance of self-consolidating concrete', *ACI Materials Journal*, **96**, 346-353.

Sonebi, M. (2004), 'Medium strength self-compacting concrete containing fly ash: Modelling using factorial experimental plans', *Cement and Concrete Research,* **34,** 1199-1208.

Su, N., Hsu, K.C. and Chai, H.W. (2001), 'A simple mix design method for self-compacting concrete', *Cement and Concrete Research,* **31,** 1799-1807.

ASSESSING THE MODULUS OF ELASTICITY OF HIGH STRENGTH CONCRETE MADE FROM DIFFERENT TYPES OF IRISH AGGREGATES

J. GAO AND R.P. WEST

Department of Civil, Structural and Environmental Engineering

Trinity College Dublin

Abstract

This paper presents a review of a research project which assesses the modulus of elasticity of high strength concrete made from different types of aggregates within Ireland. The paper initially considers the research evidence on the important factors that influence the elastic modulus of concrete, including aggregates types, design strengths and ages. According to EC2, an empirical relationship exists between the concrete strength and elastic modulus. An approximate method is also presented in EC2 to compensate for the variations caused by different aggregate types. The project examines the above methods in EC2 by practical testing with Irish local aggregates. In particular, the modulus of concrete made with limestone will be compared with basalt, sandstone, quartz and granite, because the former is treated in EC2 as a soft limestone, not the dense limestone commonly used in Ireland. A comparison is also made with the recently published *fib* Model Code 2010.

The experimental part of this project is carried out by cylinder and cube testing under the existing standards. 150*300mm cylinders are used to test the elastic modulus E_c according to BS 1881-121. On the other hand, the 100mm cubes are used for strength testing to examine the EC2 predictions involving f_{ck}.

Keywords: Compressive strength, cylinder testing, elastic modulus, Eurocode 2, Irish aggregates, Model Code 2010.

1. Introduction

The modulus of elasticity of concrete is a fundamental property that determines the deformation behaviour of structural concrete, particularly for the design of reinforced and prestressed concrete. However, the direct measurement of the values of the modulus of elasticity E_c is time-consuming and is more complicated than the direct measurement of uniaxial compressive strength. To directly measure this property of concrete, stress and strain of a concrete cylinder with a 150mm diameter and 300mm height are recorded simultaneously until the stress reaches 33% of the ultimate compressive strength, as previously determined (BS 1881-121:1983). The secant modulus of elasticity can be calculated from the mean recorded strains after 3 cycles of loading and unloading procedures.

To avoid time-consuming testing, researchers and design standards have proposed a series of different mathematical formulae to predict the value of modulus of elasticity based on various design factors. The most common method is to express the modulus of elasticity as a function of compressive strength in a given range. There is no precise form of the relationship between the modulus of elasticity and compressive strength, however, it is generally agreed that E_c increases with an increase in compressive strength (Sideris et al., 2003). In this paper, the formulae proposed by IS EN 1992-1-1:2004 (EC2, 2004) and *fib* Bulletins 42 (2008) and

55 (2010) are considered as the main methods for predicting the modulus of elasticity, while there are also formulae from other standards with similar forms but different coefficients and ranges of application.

In EC2 (2004), the modulus of elasticity is determined by the composition of concrete, aggregate type and age. Quartzite aggregates are considered as the standard type for the modulus formula. Limestone and sandstone are treated as weaker aggregates with 10% and 30% reduction factors respectively. On the other hand, basalt has a 20% increase in factor for adjusting the modulus due its stiffer response. However, there is no indication for granite aggregates. All the above types of aggregates are tested in this project to evaluate the compatibility of EC2 and *fib* bulletins 42 and 55 with local Irish aggregates.

2. Research Significance

The modulus of elasticity of concrete is significantly influenced by the characteristics of the coarse aggregates used in the concrete mixture (Baalbaki et al., 1991). Baalbaki et al. tested five different types of aggregates in accordance with British Standards 1881-121 (1983), and compared the results with the theoretical predictions of EC2 (2004), *fib* Bulletin 42 (2008) and *fib* Bulletin 55 (2010). The theoretical formulae give relatively satisfactory results for normal strength concrete, but researchers show that it is not reliable to precisely predict the modulus of elasticity for high strength concrete from its compressive strengths (Baalbaki et al., 1992). Thus, experimental measurement is still necessary to ascertain the modulus of elasticity with appropriate accuracy. This project of research mainly focused on the high strength concrete at ages of 3-day and 28-day to show their compatibility with the code predictions of the modulus of elasticity for different aggregates.

3. Experiment

To find out the relationship between the modulus of elasticity and compressive strength, a series of specimens were made and cured for testing in accordance with IS EN 12390-1 (2000) and IS EN 12390-2 (2009).

3.1 Material and Mix design

Five Irish local aggregate types are chosen for concrete mixes, namely basalt, limestone, sandstone, quartzite and granite. The maximum aggregate sizes are between 14mm and 20mm.

The design strengths applied vary from C40/50 to C70/85 which represents an appropriate range for high strength and pre-stressed concrete in Irish practice – lower strength grades are being considered in a separate research project. The mix designs for the grades used to demonstrate the changes of modulus of elasticity with increasing compressive strengths are given in Table 1.

For the concrete mixture, a bulk CEM I 42.5R cement complying with EN197-1 was used for all concrete mixes. This Rapid Hardening Portland Cement (RHPC) produced specimens with a higher rate of early strength development compared to the CEM I N (Normal Portland Cement or NPC) or CEM IIA-L commonly used.

Table 1. Mix design for four grades

	C40/50	C50/60	C60/75	C70/85
Cement (kg/m^3)	375	425	475	525
Coarse aggregate (kg/m^3)	900	900	900	900
Sand (kg/m^3)	960	900	840	780
Water (l/m^3)	155	155	153	152
Superplasticizer (l/m^3)	2.6	3.0	3.6	4.1

A superplasticizer, CHRYSO®Fluid Premia 196, was added to each concrete mix to achieve appropriate workability. The exact quantity of superplasticizer used for each type of aggregates is varied slightly to deliver a very workable slump of S4 consistency.

For each mix design, two pours were made to acquire results at two different ages, 3 and 28 days, to reflect the practice in the pre-cast industry. 40 pours were planned in total, with four strength grades, 5 aggregate types and two ages at testing.

Six concrete cylinders and 4 cubes were made in plastic moulds for each pour and then cured in a constant temperature curing tank at 20°C until testing.

3.2 Testing Procedures

According to BS 1881-121 (1983), for each valid test, 4 cylinders of 300mm height and 150mm diameter are required for establishing the modulus of elasticity. Three of these are crushed to determine the ultimate compressive strengths in the normal way and the remaining one is tested to 33% of the average ultimate compressive strength result to obtain a single value of elastic modulus. In this case, however, a further two cylinders are tested for each batch so that the variability of modulus results could be estimated. In addition, 4 no. 100mm cubes are made for benchmarking against the compressive strengths of the cylinders poured in different batches and tested at different ages.

4. Results and Discussion

4.1 Strength

Table 2 and Table 3 show the mean cube strengths for each mix at different ages. Unexpectedly, the final results considerably exceeded the initial design strengths. At the lower end, the C40/50 grade has an average of 86.8 MPa compressive strength at 28 days which is much higher than the designed 50 MPa characteristic strength. The C70/85 concrete also has reasonably high 28-day strength at 104.8 MPa. However, it would appear that, without the help of mineral additions such as silica fume for high grades, the magnitude of measured strength for the C70/85 mix is not as high above the grade as for the lower strengths.

Comparing the 3-day and 28-day results, the RHPC provides higher early strengths for most mixes. Since lower w/c ratio mixes have higher early strength, the ratios between 3-day/28-day results increase from 63.8% at C40/50 to 88.2% at C70/85 (see Table 4).

In EC2 (2004), the strength development with time may be predicted by:

$$\beta(t) = \exp\{s(1-(28/t)^{0.5})\} \qquad (1)$$

where $\beta(t)$ is the coefficient of mean compressive strength at age t, that is, $\beta(t) = f_{cm}(t)/f_{cm28}$ and s is a coefficient which depends on the type of cement (s = 0.2 for RHPC). Thus, at 3 days, $\beta(3)$ = 66.3%. The average percentages in Table 4 demonstrate that the percentage strength at 3 days is a higher proportion of the 28 day strength the higher the grade. In fact, using the average $\beta(3)$ values inserted in Equation 1, the range of s values to achieve agreement with the experimental results for RHPC varies from 0.16 for C40/50 to 0.08 for C70/85. This suggests that the performance of these cement types is much better than that predicted by the current EC2 equation, which should be reviewed, accepting that issues of repeatability and reproducability have not been dealt with here.

Table 2. Mean cube compressive strength at 3 days (MPa)

	C40/50	C50/60	C60/75	C70/85
Sandstone	55.8	76.8	72.4	90.1
Basalt	70.4	74.1	85.4	87.7
Limestone	58.6	68.3	75.0	83.3
Quartzite	69.8	75.1	91.2	90.6
Granite	56.7	73.3	76.5	87.9

Table 3. Mean cube compressive strength at 28 days (MPa)

	C40/50	C50/60	C60/75	C70/85
Sandstone	87.4	101.9	101.7	106.9
Basalt	89.6	94.9	99.7	111.1
Limestone	85.2	92.1	97.0	97.0
Quartzite	90.5	99.3	110.8	108.7
Granite	81.4	89.8	95.7	99.7

Table 4. Ratio of 3 to 28 day mean strengths in %

	C40/50	C50/60	C60/75	C70/85
Sandstone	63.8	75.4	71.1	84.3
Basalt	78.6	78.1	85.7	78.9
Limestone	68.8	74.2	77.3	85.9
Quartzite	77.1	75.6	82.3	83.3
Granite	69.7	81.6	80.0	88.2
Average	71.6	77.0	79.3	84.1

4.2 Modulus of Elasticity

Figure 1 contains all the results of modulus of elasticity of granite at 3 days, plotted against compressive strength. Although the variations in results are large for some particular concrete mixes, the general trend clearly shows that the E_c value is ascending with an increase in the compressive strength. Figure 2, based on test results for 28-day basalt aggregate, also demonstrates this point of view.

The formula used to calculate the modulus of elasticity from EC 2 (2004) is given as:

$$E_{cm} = 22(f_{cm}/10)^{0.3} \text{ (GPa)} \qquad (2)$$

where f_{cm} is the mean cylinder strength in MPa.

This standard formula is only applicable for quartzitic aggregates. For other types of aggregates, there is an adjustment coefficients, α, varying in value form from +20% for basalt to -30% for sandstone. However EC 2 (2004) does not give any suggestion for granite, thus granite is presently assumed to have a similar property as quartzite with an adjustment

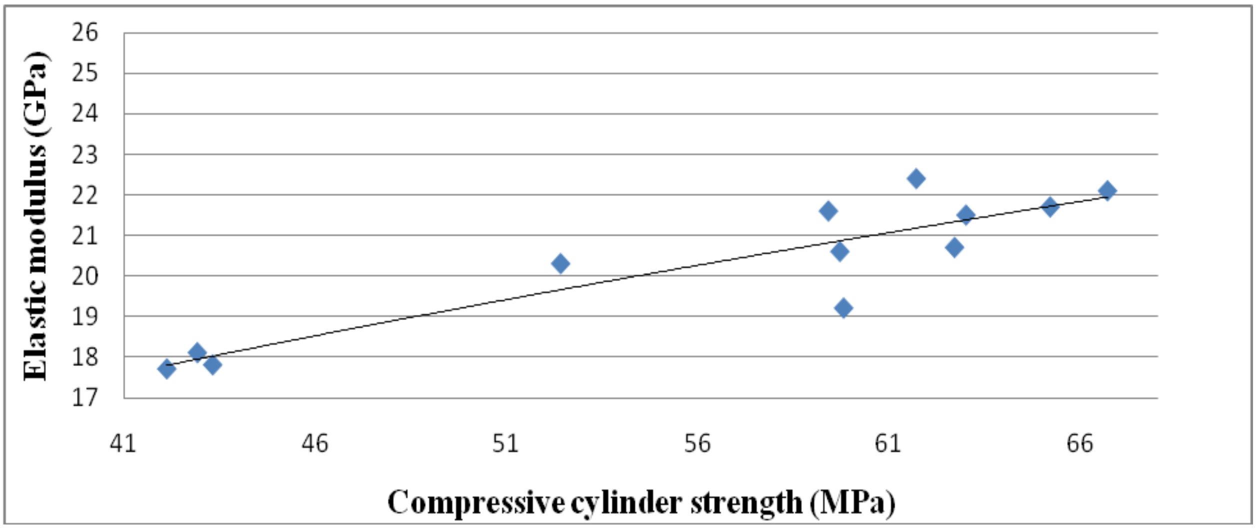

Figure 1. Modulus of elasticity (in GPa) against cylinder strength (in MPa) for 3-day granite samples

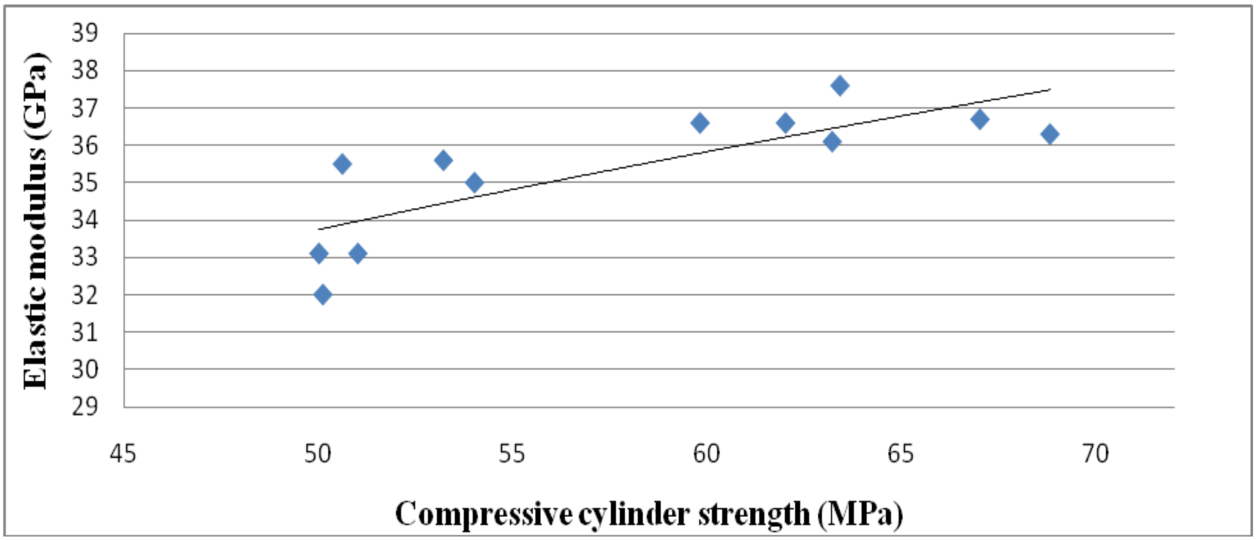

Figure 2. Modulus of elasticity (in GPa) against cylinder strength (in MPa) for 28-day old basalt samples

coefficient of α = 1.

fib bulletin 42 (2008) and the recently released *fib* Bulletin 55 (Model Code 2010) propose a similar formula with relatively small differences in the parameters.

$$E_{cm} = E_{c0}\ \alpha[(f_{ck} + 8\text{MPa})/10]^{0.33}\ \text{(GPa)} \quad (3)$$

where E_{c0} = 20.5GPa in bulletin 42 and 21.5 GPa in bulletin 55, and f_{ck} is the characteristic strength (in MPa); thus (f_{ck} +8MPa) can be assumed to be the same as the mean compressive strength f_{cm}.

The quantitative values α of can be found in Table 5, and are the same as the suggestions given by EC2 (2004). Tables 6 and 7 show the comparisons between the measured modulus of elasticity and the calculated values using the formulae from EC2 (2004), with and without α, and *fib* bulletins 42 and 55 (2008, 2010) at two extreme situations which have the smallest and largest mean cylinder strengths. Table 6, with Grade C40/50 at 3 days, has a minimum f_{cm}, while Table 7, with C70/85 at 28 days, has a maximum f_{cm}. The deviation, σ, between measured and calculated values, as shown in the tables, can be calculated by:

$$\sigma = 100\% \times (E_{cm}' - E_{cm})/\ E_{cm} \quad (4)$$

where E_{cm}' is the calculated value and E_{cm} is the predicted value.

Table 5. Quantitative values of α for different aggregates

Sandstone	Basalt	Limestone	Quartzite	Granite
0.7	1.2	0.9	1	n/a

Table 6. Modulus of elasticity of grade C40/50 at 3 days, assuming α = 1 for granite.

		Sandstone	Basalt	Limestone	Quartzite	Granite
Measure mean value	f_{cm} (MPa)	41.7	47.2	44.8	53.8	41.5
	E_{cm} (GPa)	23.7	32.7	29.8	24.1	17.9
calculated values by EC2 without α	E_{cm}' (GPa)	33.7	35.1	34.4	36.4	33.7
calculated values by EC2 with α	E_{cm}' (GPa)	23.6	42.1	31.0	36.4	33.7
deviation from EC2	σ	-0.4%	+29%	+4%	+51%	+88%
calculated values by *fib* 42	E_{cm}' (GPa)	22.9	41.1	30.3	35.7	32.8
deviation from *fib* 42	Σ	-3%	+26%	+2%	+48%	+83%
calculated values by *fib* 55	E_{cm}' (GPa)	24.0	43.1	31.8	37.4	34.4
deviation from *fib* 55	σ	+1%	+32%	+6.7%	+55%	+92%

Table 7. Modulus of elasticity of grade C70/85 at 28 days.

		Sandstone	Basalt	Limestone	Quartzite	Granite
Measure mean value	f_{cm} (MPa)	73.7	81.5	70.7	77.5	79.0
Measure mean value	E_{cm} (GPa)	29.0	39.7	33.8	30.2	24.1
calculated values by EC2 without α	E_{cm}' (GPa)	40.0	41.3	39.6	40.7	40.9
calculated values by EC2 with α	E_{cm}' (GPa)	28.0	49.5	35.6	40.7	40.9
deviation from EC2	σ	-3%	+24%	+5%	+35%	+70%
calculated values by *fib* 42	E_{cm}' (GPa)	27.7	49.2	35.2	40.3	40.5
deviation from *fib* 42	σ	-4%	+24%	+4%	+33%	+68%
calculated values by *fib* 55	E_{cm}' (GPa)	29.1	51.6	36.9	42.3	42.5
deviation from *fib* 55	σ	+0%	+30%	+9%	+40%	76%

Both of the above tables indicate similar trends the accuracy of the theoretical predictions among different types of aggregates. The introduction of the new Model Code 2010 (*fib* bulletin 55) does not appear to have improved the accuracy of the predictions and so is discarded from further discussion. The calculated results for limestone are slightly higher than the measured values. For basalt and quartzite, the deviations are significantly over the expected range which means the adjustment coefficients are heavily overestimated for these two types of aggregates. Granite has the smallest value of modulus of elasticity compared with other aggregates, thus the previous initial assumption of $\alpha = 1$ by the authors, in the absence of other guidance in EC2, is obviously not valid in this case.

To achieve more accurate results using Equation (2), the adjustment coefficient α can be introduced to this equation. Equation (2) can then be re-written as:

$$E_{cm} = 22\times \alpha\,(f_{cm}/10)^{0.3} \quad \text{(GPa)} \qquad (5)$$

Now Equations (5) and (3) are used in reverse, by substituting in the measured mean strength f_{cm} and measured mean modulus of elasticity E_{cm}, to obtain more practical values of α for Irish conditions. Table 8 and Table 9 show that values of the adjustment coefficient α of sandstone and limestone are close to the reference values from EC2 (2004) and *fib* bulletin 42 (2008, 2010). Basalt and quartzite have significantly lower α compared with reference values 1.2 and 1.0 respectively. The value of α of granite is suggested to be about 0.55 based on the actual results.

If these measured values of α are now normalised against quarzite, with an assumed value of 1, then the relative values of α for the other aggregates are given in the last row of Tables 8 and 9 for 3 and 28 days respectively. Here it can be seen that limestone, for example, has a higher α value than sandstone, quartzite and granite, unlike in the original where quartzite had a higher value. This discrepancy will have significance in higher strength concrete design in Ireland in the coming years.

As a footnote, it should also be recognised that Model Code 2010 recommends a further adjustment, α_i, to the predicted value of modulus, E_c, based on strength, which allows for the initial plastic strain on loading which causes irreversible deformations, as follows:

$$E_c = \alpha_i \,.\, E_{cm}' \qquad (6)$$

where

$$\alpha_i = 0.8 + 0.2 \,.\, f_{cm}/88 \;\; \text{but} \; \leq 1.0 \qquad (7)$$

Typically, for C40/50 α_i = 0.93, while for C70/80, α_i =1. Nonetheless, the observations in this paper are not affected by this secondary matter.

Table 8. Recommended adjustment coefficient α of grade C40/50 at 3 days

		Sandstone	Basalt	Limestone	Quartzite	Granite
Measured mean values	f_{cm} (MPa)	41.7	47.2	44.8	53.8	41.5
	E_{cm}(GPa)	23.7	32.7	29.8	24.1	17.9
Original α in EC2	α	0.7	1.2	0.9	1.0	-
modified α for EC2	α	0.702	0.933	0.864	0.66	0.53
modified α for *fib* 42	α	0.722	0.956	0.886	0.675	0.546
Proposed Irish *α*	α	1.1	1.4	1.3	1.0	0.8

Table 9. Recommended adjustment coefficient α of grade C70/85 at 28 days

		Sandstone	Basalt	Limestone	Quartzite	Granite
Measured mean values	f_{cm} (MPa)	73.7	81.5	70.7	77.5	79.0
	E_{cm}(GPa)	29	39.7	33.8	30.2	24.1
Original α for EC2	α	0.7	1.2	0.9	1.0	-
modified α for EC2	α	0.724	0.962	0.85	0.743	0.589
modified α for *fib* 42	α	0.732	0.969	0.865	0.75	0.594
Proposed Irish α	α	1.0	1.3	1.15	1.0	0.8

5. Conclusions

The prediction of strength gain from 3 to 28 days for high strength RHPC concrete is not currently accurate for Irish conditions and alternative values of s depending on the strength grade increases should be considered when proposing changes to EC2 in the future.

The modulus test results clearly show that the accuracy of theoretical predictions of modulus elasticity by both of EC2 (2004) and *fib* bulletin 42 (2008) strongly depend on the type of aggregates and on concrete strength to a lesser extent. The recently published bulletin 55 (2010) would appear to be less accurate than the original bulletin 42 in Irish conditions.

For Irish local sandstone and limestone, the deviations between practical and theoretical results are small. Such reasonably small errors are acceptable for practical design of structures with respect to deformational behaviour.

On the other hand, the results for basalt and quartzite are overestimated by significant proportions (approximately 30% for basalt and 40% for quartzite). Such large discrepencies have implications for the actual deformation and displacements and are significantly larger than the theoretical calculation of the modulus of elasticity if predicted using the aforementioned standards.

Based on this work, new α values at 28 days are proposed in Table 9 for different aggregates, based on quartzite being normalised to 1, as is current practice. Arising from this, limestone is more favourably positioned such that design of concrete structures with limestone aggregates can now be more accurately assessed for their modulus in Ireland, leading to more economic solutions.

Since granite is mentioned in neither EC2 (2004) nor the *fib* bulletins 42/56 (2008, 2010), a suggested value of α of 0.8 is arrived at by using the theoretical formulae with the experimental results.

Since the aggregates are generally categorised by EC2 (2004) and the *fib* bulletins 42 and 55, further analysis of the different types of aggregates is necessary for better evaluation of these standards by comparing the differences between the Irish local aggregates and aggregates from other European countries. When this work is complete, how such changes might be incorporated in later versions of EC2 and the Model code remains to be seen. If this outcome is to be incorporated into future codes, recognising that these values may be local to Ireland, a case can be made that the value of α should be a Nationally Determined parameter in the Irish National Annex and not a core value given in the main text of EC2.

Acknowledgements

The authors record their sincere thanks to Eamon Stack and Peter Deegan of Banagher Concrete for their technical and financial support for this on-going project. Thanks are also due to Irish Cement Ltd and five aggregate suppliers for providing some of the materials used for the testing programme.

References

British Standard 1881, part 121 (1983), *Method for determination of static modulus of elasticity in compression.* British Standards Institution, London.

Irish Standard 1992-1-1(2004), Eurocode 2: *Design of Concrete Structures -general rules and rules for buildings,* NSAI, Dublin.

CEB-FIP, *fib* Bulletin 42(2008), *Constitutive modelling of high strength / high performance concrete*, CEB-FIP, Lausanne.

CEB-FIP, *fib* Bulletin 56 (2010), *Model Code 2010,* CEB-FIP, Lausanne.

Concrete Society Technical Report No.49 (1998), *Design Guidance for High Strength Concrete,* Camberley.

K.K. Sideris, P. Manita, K. Sideris. (2003), "Estimation of ultimate modulus of elasticity and Poisson's ratio of normal concrete", *Cement & Concrete Composites, 26, 623-631.*

W. Baalbaki, B. Benmokrane, O. Chaallal, and P. Aitcin. (1991),"Influence of Coarse Aggregate on Elastic Properties of High-Performance Concrete" , *ACI Materials Journal, 88 (5), 499-503.*

W. Baalbaki, P.Aitcin, and G. Ballivy. (1992), "On Predicting Modulus of Elasticity in High-Strength Concrete", *ACI Materials Journal, 89 (5), 517-520.*

THE INNOVATIVE REPAIR AND INSTRUMENTATION OF A MARINE BRIDGE AND THE ASSOCIATED RESEARCH

P. RYAN & Dr. A. O CONNOR
Dept. of Civil Engineering, Trinity College Dublin, Ireland

Abstract
This paper presents the repair and instrumentation of a reinforced concrete bridge in a marine environment. The paper also describes a laboratory study which is being carried out at Trinity College Dublin in conjunction with the bridge monitoring scheme. The bridge in question is located in Ferrycarrig, County Wexford, Ireland and was constructed in 1980. The bridge has eight equal spans and is 126m long. Each span consists of 14 prestressed beams with an integral in-situ poured concrete deck. The bridge underwent substantial repairs in 2002. In a move aimed at optimisation of future repairs of structures in this type of environment, it was decided to repair the crosshead beams using five different repair methods and to instrument these repairs to study their relative effectiveness in resisting chloride-ion ingress. The repair and instrumentation of Ferrycarrig Bridge is described in detail in this paper.

The laboratory study, which is currently being carried out at Trinity College Dublin, aims to further investigate the various repair strategies through accelerated chloride ingress testing on concrete samples. The paper describes the laboratory testing which is currently underway at TCD. The testing involves exposing 300mm x 300mm x 120mm concrete slabs and 100mm cubes to a salt spray mist and drying cycles in salt spray chambers. Preliminary results are also presented which give an indication as to the relative efficiencies of the following repair alternatives in an aggressive environment: Ordinary Portland Cement (OPC); Ground Granulated Blastfurnace Slag (GGBS) as a partial replacement; Pulverised Fuel Ash (PFA) as a partial replacement; OPC with a silane treatment applied; and OPC with increased cover.

Keywords: Bridge Deterioration, Chloride-Ion Ingress, Reinforced Concrete.

1. Introduction

In the United Kingdom it has been estimated that the annual cost of management, inspection, maintenance, repair and renewal is up to €545 million (European Co-operation in the Field of Scientific and Technical Research, 2002). According to the 2009 ASCE report on American Bridge Infrastructure, 26% of the United States' bridges are either structurally deficient or functionally obsolete. The ASCE estimates that an annual investment of $17 billion is required to substantially improve current bridge conditions in the United States. At present the total annual investment for the construction of bridges and the maintenance of existing bridges in the United States stands at $10.5 billion (ASCE, 2009).

In a time of global recession funds are simply not available to maintain, repair and/or replace the infrastructure network to the desired level. It is therefore essential that cost-effective bridge management strategies be put in place to allow bridge management bodies obtain maximum return from their budgetary investment. A crucial component of these management strategies is the understanding of how such structures perform throughout their life. Key to this is the ability to predict the deterioration state temporally, i.e. to model the level of deterioration as a function of time. In this context the project presented in this paper was undertaken to improve knowledge of, and reduce uncertainty surrounding, bridge deterioration models as they pertain to different concrete repair materials. The paper presents details of the inspection, repair, and instrumentation of a marine bridge in the South East of Ireland. Following the requirement for major rehabilitation of the crosshead beams it was decided to repair these reinforced concrete elements using different repair materials so that the relative efficiencies of alternative repair approaches could be studied. In this way it was hoped to obtain the information necessary for informed decision making in maintaining the Irish bridge network in the future.

The marine bridge in question is Ferrycarrig Bridge which carries the N11 single carriageway over the River Slaney in Wexford. Built in 1980, the 125.6m long structure consists of 8 spans of precast, prestressed beams with a reinforced in-situ concrete infill deck, supported on intermediate piled pier foundations with reinforced concrete abutments at both ends as seen in Figure 1. The bridge is continuous over all piers except the middle pier where an expansion joint has been provided in the deck. The deck is integral with the abutments. The river piers (intermediate supports) consist of two separate walls encasing steel tubular piles which are driven to rock.

Figure 1 - Ferrycarrig Bridge

2. Inspection and Assessment of Ferrycarrig Bridge

In August 2002 a Principal Inspection of the structure was undertaken in accordance with the EIRSPAN Bridge Management System (Duffy, 2004). This inspection identified extensive cracking on the crossheads and at the South abutment. A Special Inspection of the structure was commissioned in September 2004 in order to determine the cause and extent of cracking of the crossheads and abutments and investigate the severity of the deterioration of Ferrycarrig Bridge. The special inspection included a detailed visual inspection, a crack mapping survey and a chloride penetration study. A structural assessment was also carried out to identify the cause and possible rehabilitation strategies.

The structural assessment and the special inspection led to the following conclusions:

- The deterministic assessment, together with the results of the visual inspections, identified a number of deficiencies that affected the long term serviceability of the structure (British Standards Institution, 1997, 1990, European Standard, 2000, National Roads Authority, 2002).

- The observed cracking in the pier crosshead beams was considered to be due to a lack of reinforcement to resist the serviceability limit state stresses (i.e. shrinkage, thermal, creep). In addition, there was insufficient reinforcement to resist the applied ultimate limit state torsion moments.
- Chloride levels in the concrete indicated a distinct concentration gradient decreasing rapidly through the concrete. The levels of chloride ion concentration in the crosshead beams were considered moderately high.

3. Repair of Ferrycarrig Bridge

Due to its strategic importance, i.e. it lies on the so-called *Euroroute* from Dublin to Rosslare Port, a decision was made to repair and strengthen the structure immediately. The deterioration of Ferrycarrig bridge was not caused by reinforcement corrosion, however the nature of the repair works afforded the NRA a unique opportunity to study the major, worldwide problem of reinforcement corrosion in an Irish marine environment. It was therefore decided to employ five different concrete repair strategies for the seven crosshead beams. Six crossheads would be instrumented and remotely monitored so that the relative efficiency of the various methods in resisting chloride ingress and reinforcement corrosion could be studied over time. For each of the crossheads hydro-demolition was used to remove concrete to a depth of 1.5 times the reinforcement diameter beyond the existing reinforcement before additional steel and repair concrete was put in place. The alternative concrete repair strategies utilised are as discussed below.

3.1 Crosshead 1 - Ordinary Portland Cement (OPC) Mix

This repair option was selected to act as a control for the other repairs with a standard 50mm cover to the new reinforcement. The replacement of the old concrete surrounding the reinforcement with the OPC mix is expected to restore the alkalinity surrounding the reinforcement.

3.2 Crosshead 2 – OPC with Increased Cover

In this option the cover was increased over that employed in option 1 from 50 mm to 70 mm. As increasing the cover increases the distance that chloride ions need to migrate to reach the reinforcement, this option is expected to increase the time to corrosion initiation.

3.3 Crosshead 3 – OPC with a Surface Treatment

For Crosshead 3, an OPC mix was used together with a surface impregnation treatment to prevent penetration of chlorides from the exterior environment. Two coats of monomeric alkyl (isobutyl) trialkoxy-silane, commonly known as silane, were applied to all the surfaces of the crosshead beam.

3.4 Crosshead 4 – Ground Granulated Blast Furnace Slag (GGBS) Mix

For Crosshead 4 it was decided to use GGBS as a partial replacement in the Portland cement mix. Available literature demonstrates that the chloride diffusivity into the concrete significantly decreases when GGBS is used in the range of 50% to 70% per weight of binder (Snidel, 2007). At Ferrycarrig bridge 60% GGBS by weight of total cement was used. It is significant to note that Pier 4 is the location of the expansion joint in the structure and is thus likely to be exposed to a more severe environment than the other crosshead beams.

3.5 Crosshead 5 – OPC with a Mixed-in Corrosion Inhibitors

The corrosion inhibitor used for Crosshead 5 was an organic type inhibitor which addresses both the anodic and the cathodic reactions of the electrochemical corrosion process. A corrosion inhibitor is a substance which when added to the corrosive environment, in this case chloride-contaminated pore solution around the steel, reduces the rate of the metal dissolution. The inhibitor does not prevent the ingress of chlorides; it instead protects the embedded steel from corrosion (Nevile, 1995).

3.6 Crosshead 6 – Identical to Crosshead 4

As discussed above, Crosshead 4 was repaired with an OPC + GGBS concrete mix. The purpose of employing the same repair option for Crosshead 6 was to compare the performance of the GGBS mix at and away from the expansion joint.

3.7 Crosshead 7 – Identical to Crosshead 1

Crosshead 7 was repaired in the same way as Crosshead 1. This was done in order to provide an opportunity to study the spatial variability of chloride ingress for the structure (Kenshel, 2009).

Refurbishment works commenced at Ferrycarrig Bridge in July 2007 and were completed in January 2008.

4. Instrumentation of Ferrycarrig Bridge

Six crosshead beams were instrumented to facilitate monitoring of the relative efficiency of the different repair techniques. The instrumentation scheme design called for the installation of three different types of probes: (i) chloride ion penetration depth probes, (ii) corrosion potential probes and (iii) corrosion rate probes. These were secured to the retrofitted crosshead reinforcement cage. In total ten probes were embedded in each crosshead beam. The southern and northern faces of the crossheads were each instrumented with one chloride ion penetration depth probe, two corrosion potential probes and one corrosion rate probe. The eastern, or seaward, end of the crosshead beams were instrumented with a chloride ion penetration depth probe and a corrosion potential probe. The undersides and western end of the crosshead beams were not instrumented. Temperature and humidity sensors were also installed at three locations on the bridge. A brief description of each of the three corrosion related probes is given below.

4.1 Chloride Ion Penetration Depth Probe

The chloride ion penetration depth probe monitors the penetration of chloride ions through the depth of the concrete cover with time. The chloride ion penetration depth probe employed can be seen labelled *‘A’* in Figure 2. The chloride ion penetration depth probe is secured in all locations perpendicular to the face of the crosshead beams. This means that as the chlorides progress through the depth of concrete cover that they are detected at two depths along the length of the chloride ion penetration depth probe.

4.2 Corrosion Potential Probes

Corrosion potential probes are used to produce reference potential for the assessment of the risk of corrosion of steel reinforcement in concrete structures. The probe can be seen in position on one of the instrumented crossheads of in Ferrycarrig Bridge in Figure 2 labelled '*B*'.

4.3 Corrosion Rate Probes

The corrosion rate probes installed in Ferrycarrig Bridge allow the assessment of instantaneous corrosion rates through the utilisation of the linear polarisation resistance measurement technique. This process involves the monitoring of the relationship between electrochemical potential and current generated between electrically charged electrodes to allow the rate of corrosion to be calculated. A photograph of the corrosion rate probe attached to the crosshead reinforcement in Ferrycarrig Bridge can be seen in Figure 3.

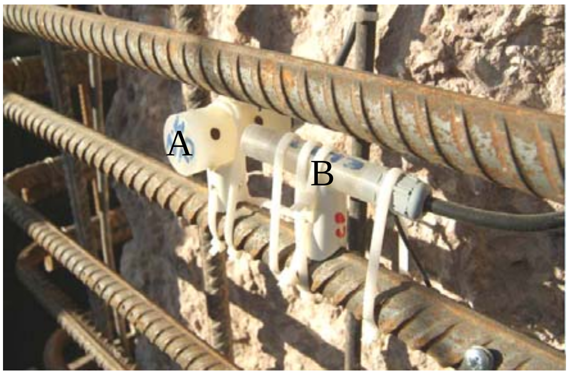

Figure 2 - Chloride ion penetration depth probe (A) and corrosion potential sensor (B)


Figure 3 - Corrosion rate probe at Ferrycarrig bridge

4.4 Instrumentation Results to Date

It may be a number of years before meaningful results on the relative efficiencies of the repair techniques are obtained from Ferrycarrig bridge. The probes are currently in their bedding in period and thus the responses from the probes may be to a greater or lesser degree due to the extensive disruption to the crossheads during the repair sequence. This combined with the slow process of chloride ion ingress means it may be a number of years before meaningful information on the relative efficiencies of the repair techniques are obtained from the instrumentation system.

5. Laboratory Study at Trinity College Dublin

Research is being undertaken at Trinity College Dublin (TCD) in parallel with the Ferrycarrig bridge monitoring project. Part of the PhD research project at TCD is aimed at further investigation into the relative efficiencies of the repair methods utilised at Ferrycarrig Bridge through experimental testing. The experimental testing will give information in the short to medium term on the relative merits of the repair techniques utilised at Ferrycarrig bridge. It is also intended to use these laboratory results in the development of a probabilistic lifetime management plan for Ferrycarrig Bridge. An additional long-term goal is to compare the laboratory results obtained at TCD with the real life results which will be obtained from the Ferrycarrig bridge instrumentation system.

5.1 Description of Experimental Study

The first phase of testing explores the corrosion initiation phase and is aimed at establishing the ability of various repair methods to resist the ingress of chlorides into concrete. The study will also investigate the effect of changes of scale in laboratory experiments through comparison of 100mm cube samples and 300mm x 300mm x 120mm slab sample results.

The testing was carried out at TCD using two salt spray chambers. The chambers subjected the test samples to periodic wetting and drying cycles. The samples were subjected to two days of salt spraying and five days of drying per week. A 5% sodium chloride solution mist fills the chamber during the wetting cycles. For phase one of testing the mix designs and materials utilised were identical to those used in the repair of the crossheads at Ferrycarrig. In addition to the five repair methods used at Ferrycarrig bridge an OPC mix with 30% pulverised fuel ash (PFA) partial replacement was also constructed to investigate the relative merits of PFA in the corrosion initiation phase. The advantages associated with the use of PFA in both the initiation phase and the propagation phase of corrosion have been publicised in the available literature (Bai et al, 2003).

The samples were placed in the chamber on 10^{th} of September 2009 and were exposed to periodic wetting and drying cycles for 33 weeks. The time consuming process of sample analysis has now commenced. This process involves using a profile grinder to grind down the concrete samples to dust and collect the dust at 2mm depth increments. The concrete dust is then analysed using acid soluble potentiometric titration to calculate the total chloride content at 2mm depth increments. Flick’s second law will be fitted to the chloride profiles in order to obtain diffusion coefficients and surface chloride contents for each of the samples. These parameters will allow the relative efficiencies of the six repair methods to be studied and conclusions to be drawn on the relative efficiency of the various repair methods in resisting the ingress of chloride ions.

5.2 Preliminary Results

The lengthy process of sample analysis means that the full set of results comparing the various repair materials are not available to date. However some preliminary results are presented below in the form of Figure 4. The figure shows the total chloride content obtained from acid soluble titration analysis on four slab samples at four depths. The total chloride content by weight of concrete is plotted at 0.5mm 4mm 8mm and 16mm. The samples plotted are OPC, OPC with silane (labelled OPC-S), OPC with GGBS (labelled GGBS) and OPC with PFA labelled (PFA). There are an insufficient number of points in each profile to fit Flick’s law to the data and obtain diffusion coefficients for each of the samples, however the plot gives an indication of the ability of the various repair materials to resist the ingress of chlorides.

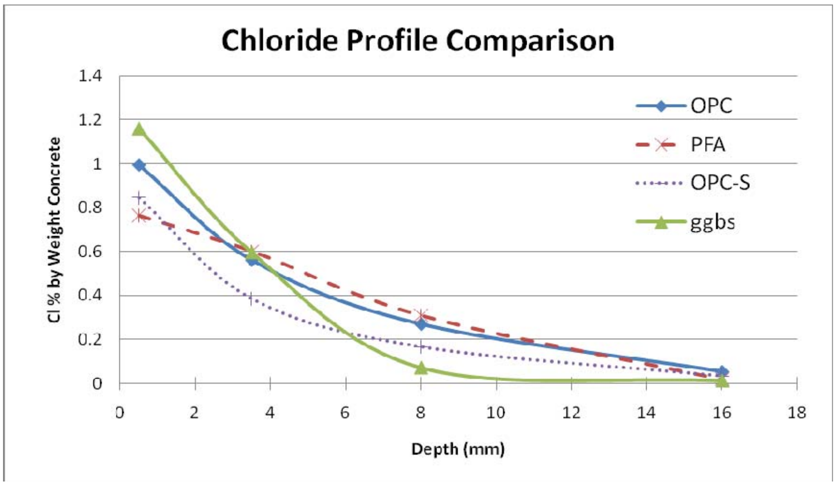

Figure 4 – Plots of chloride content by weight of concrete from 0 to 16mm

As can be seen from the plot the OPC + GGBS mix has the highest surface chloride content with a value of 1.16% by weight of concrete. The OPC + GGBS sample however exhibits the greatest reduction in chlorides with depth signified by the steep slope of the GGBS line. This would indicate that the OPC + GGBS sample will have the lowest diffusion coefficients of the four repair methods considered. The lower the diffusion coefficient of a material, the greater the ability of the material to resist the ingress of chlorides. Consequently, it appears that the OPC + GGBS mix has preformed best of the materials considered.

As can be seen from Figure 4 the OPC and OPC + Silane mixes exhibit similar slope characteristics, however the OPC + Silane sample has a lower surface chloride content than that of OPC mix, as we would expect. This results in lower chloride concentration in the OPC + Silane mix for all the depths plotted. The OPC + PFA mix exhibits a lower surface content than the control OPC mix, however the rate of decrease of chloride content with depth for the OPC + PFA mix is less than that of the OPC mix, resulting in similar chloride contents at the 4mm, 8mm and 16mm depths.

Overall it would appear that GGBS will have the highest surface chloride content but the lowest diffusion coefficient, OPC and OPC + Silane will have very similar diffusion coefficients but OPC + Silane has a lower surface chloride content. PFA has a lower surface chloride content than the OPC control mix, however Figure 5 suggests that the diffusion coefficient for PFA will be greater than that of OPC. It must be noted that these are preliminary results and further investigation is needed before solid conclusions can be drawn from the experimental program.

6. Conclusions

The paper presents information on the assessment, repair, instrumentation and monitoring of a bridge in a marine environment in South East Ireland. Details of an associated laboratory research study are also presented in the paper. The innovative approach to the repair of Ferrycarrig bridge and the subsequent instrumentation will yield informative results on the efficiency of repair techniques in an Irish marine environment in the coming years. In the more immediate future, the accelerated chloride ingress testing being carried out in the TCD laboratory will provide advanced chloride front progression results which would be equivalent to decades of exposure in the real Irish marine environment. Some preliminary laboratory results have been presented in this paper. These results indicate that of the repair methods considered, the OPC + GGBS mix has the greatest ability to resist the ingress of chloride-ions.

Overall the project will provide comparative information on the effectiveness of concrete repair strategies and provide a better understanding of the deterioration of concrete bridges in the Irish marine environment. Advances in understanding of deterioration models will help to improve whole life management plans which rely on the ability of engineers to model bridge deterioration.

7. Acknowledgements

The Irish National Roads Authority and the Irish Research Council for Science Engineering and Technology are gratefully acknowledged for the financial support provided in facilitating this research.

References

American Society of Civil Engineers (ASCE) (2009), *Report Card for America's Infrastructure,– Facts About Transportation - Bridges*, see www.asce.org/reportcard pp76-81

Bai, J., Wild, S., Sabir B.B. (2003), 'Chloride ingress and strength loss in concrete with different PC–PFA MK binder compositions exposed to synthetic seawater', *Cement and Concrete Research* **33**, pp 353–362.

British Standards Institution (1983), *Method of Normal Curing of Test Specimens*, BS 1881-111:1983, HMSO London.

British Standards Institution (1990), *Steel, concrete and composite bridges, Code of practice for design of concrete bridges*, BS 5400-4:1990, HMSO London.

British Standard Institution (1997), *Structural use of Concrete, Part 1 – Code of Practice for Design and Construction*, BS8110-1: 1997. HMSO London

Duffy L. (2004), 'Development of Eirspan; Ireland's Bridge Management System' in *Proceedings of the Institution of Civil Engineers, Bridge Engineering Volume **157** Issue BE3, Pages 139 – 146.*

European Co-Operation in the Field of Scientific and Technical Research, (2002), *Cost 345 Working Group 1, Report on Current Stock of Highway Structures in European Countries*, The Cost of Their Replacement and Annual Cost of Maintaining Repairing and Renewing them, pp 44-46.

European Standard EN 206-1: 2000, Concrete, Part 1: Specification, Performance, production and conformity.

European Standard EN 14629: 2007, Products and systems for the protection and repair of concrete structures - Test methods - Determination of chloride content in hardened concrete.

Kenshel O. and O'Connor A. (2009), 'Assessing Chloride Induced Deterioration in Condition and Safety of Concrete Structures in Marine Environments', *European Journal of Environmental and Civil Engineering*, 2009, **13(5)**, pp. 593-613.

National Roads Authority (2002), *Design Manual for Roads and Bridges, NRA Addendum to BD37/01 Loads for Highway Bridges (and Corrections)*, National Roads Authority, Dublin,

Nevile, A.M. (1995), *Properties of Concrete*, Fourth Edition, Logman Group, pp 571.

Snidel, R. (2007), 'GGBS: A Sustainable Solution for Concrete', *Structural Engineer*, Vol **85(9)**.

EMBEDDED WIRELESS SENSORS FOR STRUCTURAL HEALTH MONITORING

W. QUINN[1], G. KELLY[1] & J. BARRETT[2]
[1]School of Mechanical & Process Engineering & [2]Department of Electronic Engineering, Cork Institute of Technology, Ireland

Abstract
This paper examines the feasibility of embedding wireless sensors into concrete for structural health monitoring purposes. Testing shows that the 433MHz ISM band is suitable for such a system. Steel backed formwork and reinforced concrete was shown to reduce the transmission distance of the sensors to 3.5m which extended to over 5m when the formwork was removed. A second monitoring approach based on embedding a piezoceramic into concrete and employing the electromechanical impedance (EMI) method is described. To enable the piezoceramic to be used on a wireless sensing platform the feasibility of using the AD5933 impedance chip from Analogue Devices is examined. Preliminary results show that monitoring the reactance and the RMSD index successfully indicate the strength development of the concrete. Initial results using the AD5933 impedance chip indicate that it may be used in conjunction with the wireless sensing mote developed to allow the strength development of the concrete be monitored wirelessly using an embedded sensor.

Keywords: Concrete**,** Electromechanical Impedance, Wireless Sensing

1. Introduction

The growing importance of structural health monitoring and the drive towards smarter structures is evident in the number of smart structures being created around the world. Two examples of this trend are the Wind and Structural Health Monitoring (WASHM) in Hong Kong and the recently built 1-35W Saint Anthony Falls Bridge in Minneapolis which contain over 900 and 300 sensors respectively. The use of embedded sensors in the monitoring of the hydration concrete has received increased interest in recent years. These sensors can be wired [1], wireless [2] or a hybrid of the two [3]. Wireless sensors have the potential to reduce the complexity and cost of sensing systems as the requirement of wiring the systems to an external data acquisition system can be eliminated. This paper investigates the feasibility of using wireless sensor nodes in concrete for monitoring concrete curing and structural health. A sensor which monitors the hydration process would be able to produce information on the instantaneous condition of the concrete, which could possibility reduce construction times and also reduce operational and maintenance costs.
This paper is broken into two sections. Section A focuses on the tests carried out on the feasibility of using the 433MHz ISM band for the embedded sensors. A prototype sensing node (mote) is introduced which has the ability to carry out various sensing functions on a single board. Tests were carried out within a construction environment.
Section B advances the Electro Mechanical Impedance (EMI) method so it can be used in an embedded fashion. The possibility of incorporating the method into a wireless sensor is also investigated. The AD5933 allows for analysis of impedance from a single chip with a small footprint and the accuracy of such a system is compared to that of the HP4192A impedance analyser.

2.0 Section A: Development of a Wireless Sensor Node

The developed wireless sensor prototype in this research was designed using the Tyndall 25mm mote [4]. The ISM band used in this particular project was the 433 MHz band as longer wavelengths are less affected by their surroundings which would be required for transmission from concrete. The SHT11 sensor [5] was then applied to the mote to determine if measurement using an embedded sensor was possible. The prototype sensor is powered by batteries with further research into powering methods e.g. electromagnetic coupling, power harvesting to be performed.

2.1 Package Design & Calibration of Sensor Node

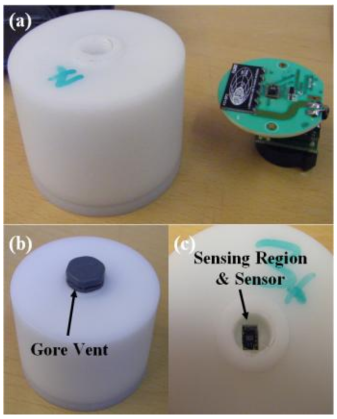

Fig 1 Sensor and Package

To protect the sensor and its circuitry from the aggressive conditions in concrete a protective package was designed. A Gore screw in protective vent [6] was incorporated into the package to expose the SHT11 sensor to the conditions within the concrete. Figure 1 shows the final sensor and package assembly. The suitability of the vent was investigated by placing it into a solution of pH 13 over a 72 hour period. A magnified image of the structure of the vent's membrane was taken using a Hitachi S3700 Scanning Electron Microscope before and after immersing the membrane within the solution. The results indicated that the highly alkaline nature of the pore water would have negligible effect on the transmission properties of the Gore material.

The response of the sensor and package combination was tested within a humidity chamber (Votsch HC7033). The tests were designed to replicate the actual expected humidity of concrete as it cures. After 3 hours the designed sensor comes within 3% relative humidity (RH) of the RH of the chamber. This occurs consistently and the sensor takes less than one hour to fall within 4% RH of the reading of the chamber. The sensor was found to be most accurate and had the quickest response time in the RH 60%-90% range. The response was therefore concluded to be suitable for the purposes of this paper as the hydration of concrete proceeds relatively slowly.

2.2 Feasibility of embedding a wireless sensor into concrete

In each experiment in this paper concrete was made from Ordinary Portland cement, fine aggregate, coarse aggregate and water. A water cement ratio of 0.53 was chosen to ensure an average compressive strength of 25 N/mm^2. LabVIEW programs were designed to communicate with the equipment and to record experimental data.

Experiment 1: 433 MHz transmission through fresh reinforced concrete

A preliminary test was carried out to examine the feasibility of using wireless telemetry from within the concrete. A concrete block of dimensions 600mm x 600mm x 300mm reinforced with a 200mm steel reinforcement cage was created. A transmitter (433 MHz ISM band) using a monopole whip antenna was placed in the centre of the reinforced concrete block. The transmitter was programmed to transmit 100 packets of information at specified time periods. The number of packets received from the concrete indicated if the approach was feasible.

Experiment 2: Impact of formwork on transmission of data

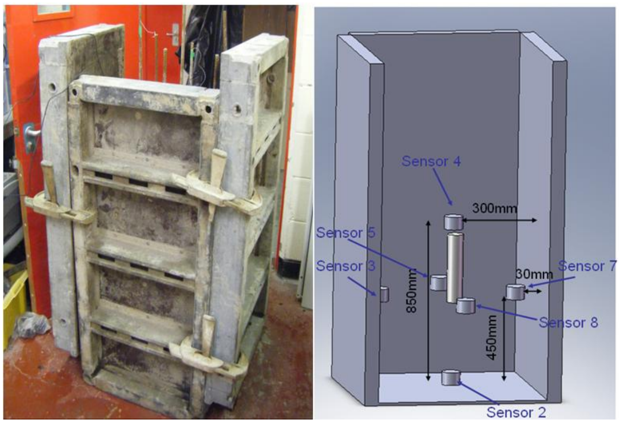

Fig 2 Experimental Setup and location of sensors

A mould was designed using steel backed formwork and filled with reinforced concrete to the dimensions 600mm x 600mm x 900mm (L x W x H). The formwork was removed after 15 days. The sensor deployment was designed so as to be able to determine the accuracy and sensitivity of the SHT11 humidity and temperature sensor. In each sensor the SPLATCH 433 SP2 50Ω grounded line planar antenna replaced the monopole antenna to reduce the overall size of the sensor. In this experiment the top surface was left exposed to test the sensitivity of sensor 4 which was placed below the exposed face of the concrete. This would result in different moisture and RH in this area as heat and moisture would be able to dissipate to the surroundings and result in lower readings. Figure 2 shows the final construction and the location of each of the sensors relative to the formwork. In the centre was the monopole antenna transmitter to compare transmission success with that of the Splatch antenna. To determine the accuracy of the temperature sensor on the SHT11 sensor thermocouples were placed in the concrete with the sensors. The receiver was located 1.5 m from the specimen.

2.3 Results and discussion

Performance of 433MHz whip antenna transmitter in concrete

It was found that the effect of the concrete and rebar on the transmission of data was to reduce the transmission distance of the system from over 25m in unobstructed open air to over 5 m when placed inside the concrete. The concrete and reinforcement were found to have little effect below the minimum transmission range. A similar test was carried out on Experiment 2. The results show that over 95% of the time 100% of the data packages were received with 99% received over 99% of the time. This indicates that data loss is not a problem within the minimum transmission range. The effect of the presence of steel backed reinforcement over the first 15 days of the structures life was to further reduce the transmission distance of the sensor to approximately 3.5m. Removal of the formwork increased the transmission distance again to over 5 m.

Performance of sensor when transmitting data

To examine the ability of the system to transmit readings, the SHT11 sensor was incorporated into the sensor node. Figure 3(a) shows the temperature profile of the sensors embedded within the concrete. It can be seen that the maximum temperature of sensor 4 was lower than that of the others. This was due to the fact that sensor 4 was located at the top of the sample. The temperature profile corresponds with the expected temperature in concrete with a peak in the first 30 hours. The sensors agreed to within 1% of the readings of the thermocouples placed alongside the sensors. The sensor which read the temperature and RH every 5 minutes lasted over 24 days. This indicates that power conservation algorithms combined with power harvesting may

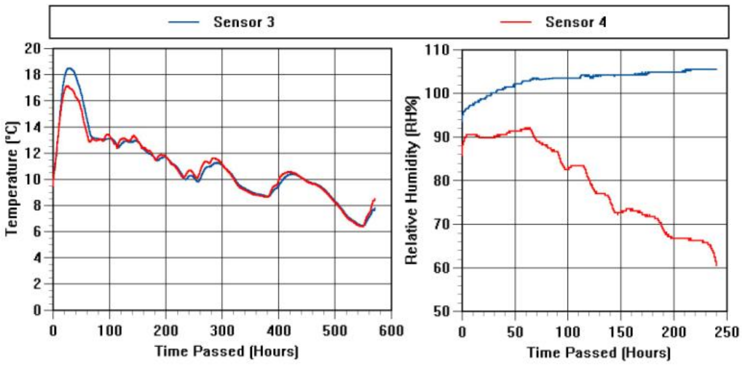

(a) (b)

Fig 3 (a) temperature profile & (b) RH profile of concrete as hydration proceeds

allow for complete monitoring of a structure. The sensor also had the ability to read RH. The RH was expected to reach a maximum when placed inside the concrete and to reduce over time as the concrete cured. All 6 sensors followed the expected response over the first few hours. Figure 3(b) shows how the sensors reached above 95% humidity over the first 3 hours. Sensor 4 reaches a level of 90%. It was expected that sensor 4 would have a lower reading due to the fact that it was located on the exposed side of the concrete. The RH remained around the 90 – 92 RH% mark until 72 hours had passed and then started to reduce significantly. Over the following 170 hours the concrete dried to 65%RH. Over this time the rate of change of the RH was 0.15%RH/hr. This meant that the rate of curing reduced to a minimum and most likely came to a halt at the top of the specimen. After 10 days the sensor ceased to read RH from sensor 4 but continued to read temperature. Sensors 2, 3, 5, 7, and 8 did not read RH as expected. The recorded humidity rose to 100% after 30 hours and it is believed that condensation occurred within the sensing region and caused the sensor to read a value above 100% for the remainder of the experiment. These results show that an indirect measurement of RH using the SHT11 may not be the most suitable method of monitoring the conditions of the concrete. The next section introduces an alternative method of monitoring hydration.

3.0 Section B: Development of the EMI technique for an embedded sensor

This section of the paper presents an advancement of the EMI method to allow it to be applied to the sensor described in section A. The method was developed to monitor the hydration of concrete, the removal of formwork, and subsequent loading cycles. Due to the fact the sensor was being designed to be used in an embedded sensor the suitability of using the AD5933 [7] impedance chip is also examined.

3.1 The EMI Method

The EMI method incorporates the piezoelectric effect to monitor changes in the conditions of the structure to which it is applied. The piezoelectric material produces a mechanical strain when an electric field is applied, which is known as the piezoelectric effect. Piezoelectric materials also show what is termed the inverse piezoelectric effect whereby an induced strain produces an electric field. The EMI method uses both the direct and converse effect in synergy where an electric current is applied causing a deformation but when loaded the induced stress causes an electric current to be produced in the material. This effect can measured using an impedance analyser. The main benefits of the piezoelectric method are that the actuator and sensor are located on one system which reduces the number of components in the system and the amount of wiring required. For sensing purposes advantages include quick response, high linearity, wide frequency ranges, and low power consumption [8]. It has been found that the electrical impedance of the piezoelectric material can be directly related to the mechanical impedance of the host structure [9]. The EMI method has been applied to composite plates, bolted joints, aluminium plates and subsequently applied to concrete for damage detection [8], load sensing and strength monitoring [10].

3.2 Sensor Design

Piezoceramics were specifically selected for use with the AD5933 impedance chip in a wireless sensing system. The AD5933 from Analogue Devices is a high precision impedance converter network analyser with a maximum excitation frequency of 100 kHz. Park et al [8] state that the most useful measurement frequencies are between 70 kHz and 500 kHz. A piezoelectric ceramic was selected with a resonant frequency within the frequency range selected as at resonance the material is most sensitive to changes in its surroundings. The work by Chen et al [11] found that the anti resonance shows greater monotonicity so it was decided to select a material with an anti-resonance located within the 70-100 kHz frequency range. The material chosen was a soft PZT PIC 15. To prevent electrical discharge of the ceramic within the moist concrete and also to protect it from the aggressive conditions within concrete the sensor was packaged within an epoxy which was specifically chosen so as to not introduce any weaknesses into the concrete structure.

The measurement system consisted of an impedance analyser (HP4192A) to prove the concept and also act as a comparison with the AD5933, the sensor and a computer. A frequency sweep of 50 – 150 kHz was chosen with frequency steps of 0.5 kHz. As the packaged piezoelectric material showed a clear resistance peak at 85.5 kHz the sweep of the AD5933 was chosen to be from 80 – 105 kHz in steps of 0.05 kHz. The HP4192A performed a sweep each hour while the AD5933 performed a sweep daily.

3.3 Experimental design & Specimen Preparation

In each test different parameters of the impedance components were examined to monitor changes in the condition of the concrete. The real and imaginary parts of the impedance (Z), Resistance (R) and Reactance (X) (Z = R+jX) were the focus of this investigation. The Root Mean Square Deviation (RMSD) index was used to statistically monitor changes in the graphs as hydration progressed.

$$RMSD(\%) = \sqrt{\frac{\sum_{i=1}^{N}(x_i^1 - x_i^0)^2}{\sum_{i=1}^{N}(x_i^0)^2}} x100 \quad (1)$$

where x_i^1 and x_i^0 are the value of the current condition of the structure and the base value respectively. The RMSD index was calculated for both the Resistance and the Reactance values individually.

The concrete was placed into 150mm moulds and the packaged sensors were placed in the centre of the concrete. The initial sweep was taken as the base value for the RMSD index. The concrete was immediately covered with a waterproof sheet to limit moisture loss after pouring. This covering was removed after 24 hours and the concrete was allowed to cure at room condition.

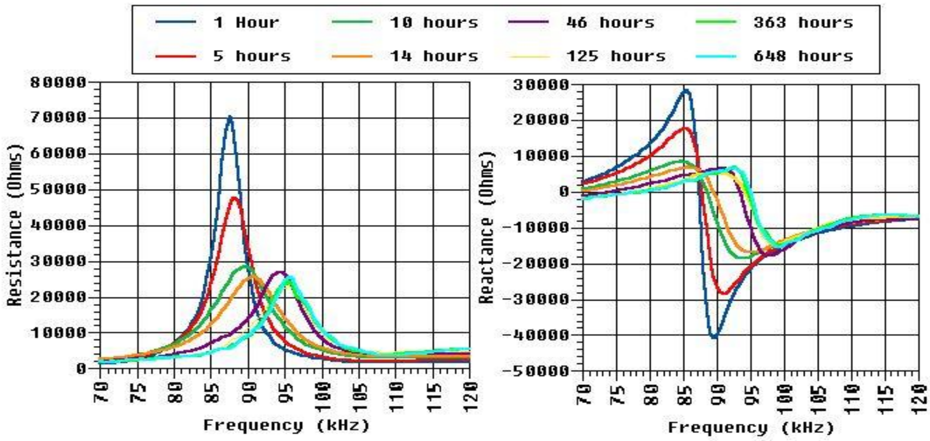

(a) *(b)*

Fig 4 Development of (a) Resistance & (b) Reactance graph as concrete cures

3.4 Results and Discussion of Testing

Figures 4 (a) and (b) show the development of the impedance components, resistance and reactance as the concrete hydrates and hardens around the sensor. It can be clearly seen that as the concrete cures the sweep curve shifts to the right and at 1 hour the peak was at a frequency of between 87 – 88 kHz. The reactance graph also crosses the x – axis at 87 – 87.5 kHz. As the strength develops the peak shifts further to the right After 648 hours (27 days) the resistance peak was between 95 - 96 kHz and the reactance crossed the x axis at between 94.5 – 95 kHz. The shift in the sweep curve is caused by changes in the stiffness of the structure while the change in the shape of the curve is related to damping. Figure 5 (a) and (b) show the results of the development of the peak frequency from the resistance graph and the development of where reactance graph crosses the x-axis. The difference in the graphs is mainly due to the fact that damping of the structure causes the peak position to be less prominent and more difficult to determine exactly. The frequency at which the reactance crosses the x-axis gives a better indication of the changes.

Using the RMSD approach the changes in both the resistance and the reactance graph have been monitored successfully. Figure 6 shows the development of the strength of the concrete using the RMSD index. It is claimed reactance is more sensitive to temperature changes [8], but analysis of the temperature profile of the concrete has shown that the temperature effects cause negligible deviation in the development of the reactance graphs. This indicated that it may be possible to use the reactance as an indicator of the development of the strength of the concrete.

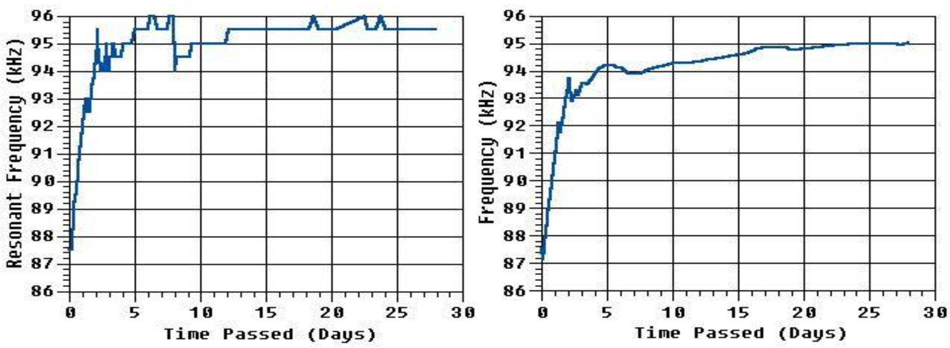

(a) *(b)*

Fig 5 Peak frequency development from (a) resistance graph (b) reactance graph

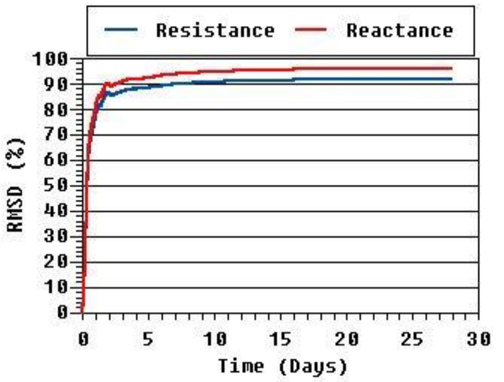

Fig. 6 RMSD index development vs. time

Figure 5 (b) and figure 6 show the development of the strength of the concrete can be broken into 3 stages. Stage 1 is witnessed over the first 1-2 days when the reactions between the cement and the water initially proceed quickly. Stage 2 occurs over the next 3-5 days where the reactions proceed at a slower rate which is followed by stage 3. It is proposed that the beginning of stage 3 is the most suitable time to remove any formwork without affecting structural integrity.

3.5 Analysis of the accuracy of the AD5933 Impedance Chip

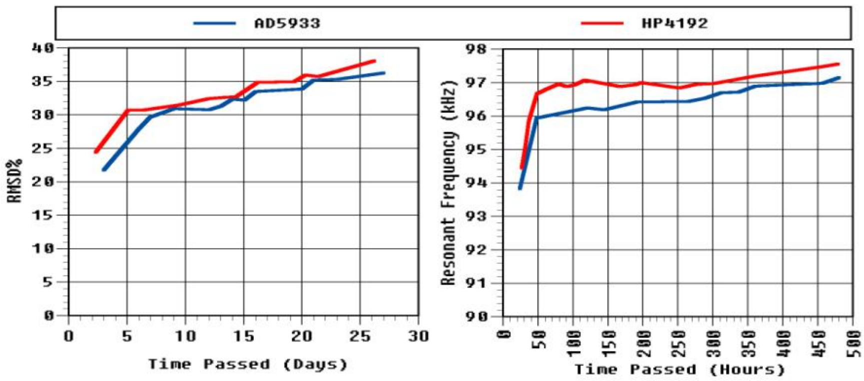

(a) *(b)*

Fig 7 Comparison of HP419A & AD5933 for (a) RMSD (b) Reactance

The AD5933 and HP4192A show a similar response to the hardening concrete when the AD5933 is calibrated using a 12 kΩ resistor. As can be clearly seen from Figure 7 (a) (RMSD index) and (b) (peak frequency) the AD5933 accurately follows the HP4192A. Using RMSD index in conjunction with the peak resonance minimises the data transmitted and thus allows conservation of the battery of the wireless sensor.

4.0 Conclusions

The results of the research have shown that it is feasible to use the 433 MHz ISM band to extract data from sensors embedded within concrete. It was found that as expected the transmission distance of the sensors was greatly reduced but the ISM band chosen was successful in transmitting data out of the concrete from a depth of over 0.5 metres and a further distance of approximately 3.5m. The successful transmission of temperature and relative humidity data further added to confidence in the system to be used as a wireless sensing platform. Only one sensor monitored the RH accurately but failed after 10 days of monitoring. The fact that the temperature readings were not affected indicates that liquid had condensed on the humidity sensor causing early failure. This suggests that the Gore Vent may not be the most suitable protection for the sensor. Furthermore the Gore membrane may deteriorate due to aging of the material so it was decided to look at different methods of monitoring the hydration process and strength development/ deterioration.

The use of piezoelectric ceramics in an embedded sensing platform was subsequently investigated. The sensor was designed to be incorporated with the AD5933 impedance chip and along with the packaging material was designed to mimic a piece of aggregate, and hence, not introduce weaknesses or defects into the concrete. The results of the testing program suggest that it can monitor the strength development of the concrete and also subsequent compressive testing indicated that it does not introduce weaknesses into the structure. When compared with the HP4192A impedance analyser the AD5933 impedance chip shows close correlation. The experimental program shows that it is possible to combine the EMI technique and temperature sensing on a wireless sensor. The combination will result in greater understanding of the hydration process and how to create a long lasting, durable structure while also reducing maintenance costs. The testing programme also suggests that it is possible to determine the occurrence and degree of stress on the concrete and so the system has the potential for realisation as a structural health monitoring system.

5.0 Acknowledgements

This research was funded in part by the Technological Sector Research Strand III 2006 project “Smart Systems Integration” funded by the Higher Education Authority. Access to the humidity chamber and development of the motes was funded under the Tyndall National Access Program project no. 183 “Smart System for Monitoring Concrete Curing & Structural Health”. The authors would like to acknowledge the Centre for Advanced Photonics and Process Analysis in Cork Institute of Technology for providing the SEM facility and John Buckley and Philip Angove of Tyndall.

6.0 References

[1] Grasley ZC, Lange DA, D'Ambrosia MD, "Internal relative humidity and drying stress gradients in concrete", Materials and Structures, Vol. 29, No. 9, (2006)
[2] Saafi M, Romine P, "Embedded MEMS for health monitoring and management of civil infrastructure":, Proceedings of SPIE Vol. 5391, (2004)
[3] Sokoll T, Jacob AF, "In-situ moisture detection system with a vector network analyser", Meas. Sci. Technol. 18 No 4 1088-1093,(2007)
[4] O' Flynn B, Lynch A, Ahearne K, Angove P, Barton J, Harte S, O'Mathuna C, Diamond D, Regan F, "The Tyndall Mote, enabling wireless research and practical sensor application development", Advances in Pervasive computing 2006 Adjunct Proceedings of Pervasive 2006, Vol. 207, (2006)
[5] www.sensirion.com/en/01_humidity_sensors (Accessed 06/10)
[6] www.gore.com/en_xx/products/venting/protective/index.html (Accessed 06/10)
[7]http://www.analog.com/en/rfif-components/direct-digital-synthesis-dds/ad5933/products/product.html (Accessed 06/10)
[8] Park et al, Overview of piezoelectric impedance based health monitoring and path forward, The Shock and Vibration Digest, Vol. 35, Issue: 6, Pages: 451-463 (2003)
[9] Suresh Bhalla *et al*, Structural Health Monitoring by Piezo-Impedance Transducers. I: Modeling.J. Aerosp. Engrg. **17**, 154 (2004)
[10] Soh CK, Bhalla S, Calibration of piezo-impedance transducers for strength prediction and damage assessment of concrete, Smart Mater Struc, 14 671- 684 (2005)
[11] Chen et al, Characterization of PZT ceramic transducer embedded in concrete, Sensors and Actuators A: Physical, Volume 128, Issue 1, 31, Pages 116-124 (2006)

DEVELOPMENT OF DOUBLE RADIUS FLEXIARCH

D. QUINN[1], A. GUPTA[1], D. MCPOLIN[2], S. TAYLOR[2], A. LONG[2]
[1]Macrete, 50 Creagh Rd, Toomebridge, Co. Antrim, BT41 3SE
[2]School of Planning Architecture and Civil Engineering, Queen's University Belfast, Belfast BT9 5AG

Abstract
At present Network Rail use Con Arch units for the replacement of masonry arch bridges along railway routes. These Con Arches resemble a curved shape portal frame that needs intensive steel reinforcement due their structural behaviour. The requirement for high reinforcement leads to serious issues regarding durability, corrosion and cost. Due to the complex shape of the Con Arch, the required profile cannot be achieved using the geometry of existing FlexiArch units. Bearing these issues in mind, there is a tremendous opportunity for a viable, sustainable alternative.

Following consultation, Macrete Ireland Limited and Queen's University Belfast have developed a complex geometry FlexiArch to conform to the precise parameters of Network Rail, a Double Radius FlexiArch (DRA). The shape of this FlexiArch has been finalised and is now ready for casting. Once successfully validated, this could lead to mainstream production of this revolutionary product. It has also emerged from recent enquires by various clients in the UK and Ireland, that the double radius arch shape is favoured for multiple circumstances such as waterways and canals, where more headroom is required for adjoining walkways.

The creation of a DRA has ignited the possibility of widespread adoption by governmental and private bodies. Furthermore, a cost comparison with Con Arch indicates that savings of 15-20% can be achieved using this product in a typical project. These recent innovations in FlexiArch bridge research have led to the advancement of potentially the most superior product to date.

Keywords: arch, bridge, concrete, Flexiarch, masonry arch, railways

1. Introduction

FlexiArch is a modular, unreinforced, precast, concrete arch bridge system, which is based on the same principles as traditional stone masonry built arch bridges dating from Roman times but without the stone mason. Over the last century masonry arches fell out of favour due to the construction time involved, perceived short span and the low headroom nearing the supports limiting travel underneath. At present, FlexiArch in its current form does not lend itself to being adopted for railway bridges due to the traditional arch profile being incompatible with the geometry required for the passage of trains without increasing the span. All of the arches in use by the metropolitan and the metropolitan district railways are of variable geometry, therefore the development a complex geometry FlexiArch is essential. These bridges need to accommodate two trains side by side, and due to the semi circular profile of FlexiArch, a variable geometry profile needs to be developed.

2. Background

2.1 Origin

The original concept for a Double Radius FlexiArch (DRA) was born out of an inquiry from a client in Australia. They wished to assess the suitability of the FlexiArch system for a proposed long span tunnel at Gladstone Airport. The tunnel was designed to allow high volume vehicular access beneath the newly extended runway therefore a key issue was the internal height of the structure. This problem was overcome by the specification of a double curvature arch as shown in Figure 1.

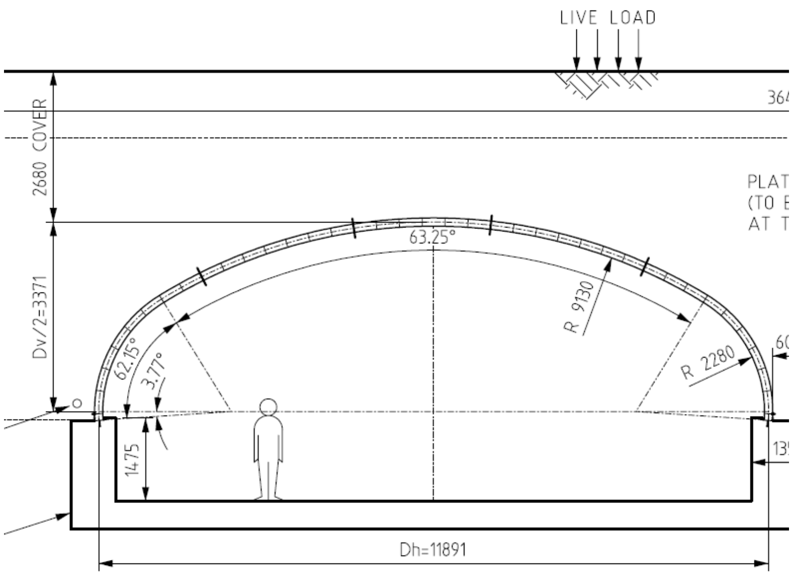

Figure 1 - Double curvature arch

This would increase the headroom within the tunnel, therefore increasing the transport envelope. The double curvature is achieved using shapes of block, for the end radii and middle radius. Following this inquiry, it was decided that model tests should be carried out at Queen's University Belfast to check the load carrying capacity and stability of such a structure.

2.2 Application

As a result of these events, it was deemed that it would be a worthwhile exercise to investigate potential applications of a DRA. At present Network Rail use Con Arch units for the replacement of masonry arch bridges along railway routes, as shown in Figure 2.

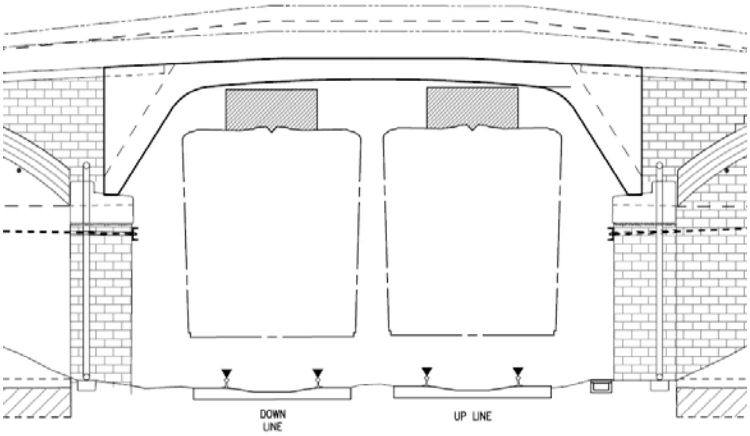

Figure 2 - Con Arch profile

These Con Arches resemble a curved shape portal frame that needs intensive steel reinforcement due their structural behaviour. The requirement for high reinforcement leads to issues regarding durability, corrosion and cost. Bearing these issues in mind, there is a opportunity for a viable, sustainable alternative. In order to investigate if a requirement for the use of a variable geometry FlexiArch in railway bridges exists, the use of a circular FlexiArch in this circumstance must first be evaluated. Due to the complex shape of the Con Arch, the required profile cannot be achieved using the geometry of existing FlexiArch units because of the constraints regarding the raising of the proposed road level. If a semi circular FlexiArch where used it would be necessary to raise the proposed road level an unreasonable and cost ineffective amount, as shown in Figure 3.

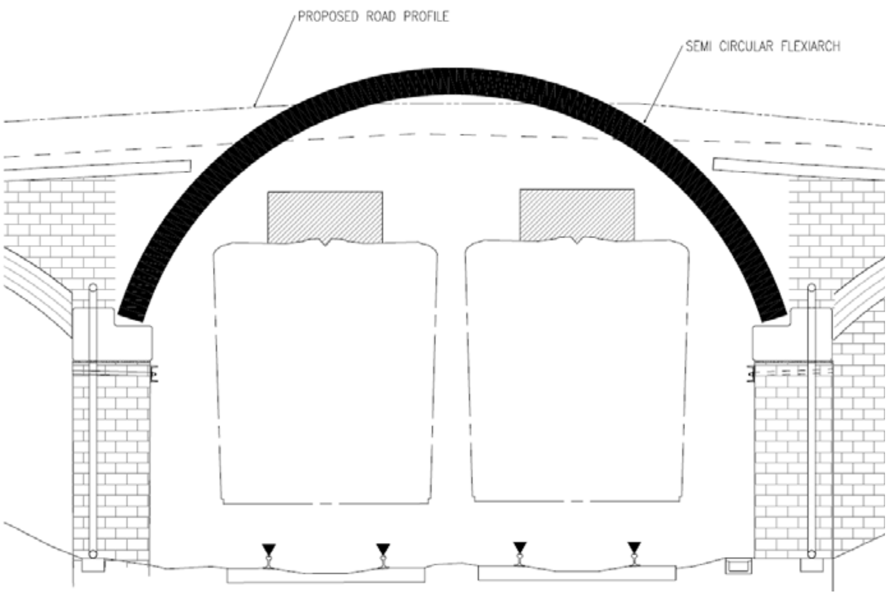

Figure 3 – Profile for semi circular Flexiarch

Following consultation with Network Rail, it was agreed that the development of a DRA for the replacement of masonry over bridges along railway lines would be a viable solution.

3. Development of DRA Geometry

The initial stage for the development of a DRA is the creation of the geometry. Dimensions that the FlexiArch must accommodate in order to comply with a Network Rail standard over bridge necessitated a creation of a process to allow any geometry to be formed. Due to the installation of 8.4m Con Arches being most prevalent, this profile has been selected for development for the purpose of this study.

Due to the complex profile, the provision for an additional 200mm of structural depth was agreed with Network Rail. This is a minimal increase considering the additional cost of road relaying would be countered by the massive savings in the lack of structural steel reinforcement.

In order to achieve the most favourable geometry, a process was undertaken to find a suitable method. This involved a lengthy process of trialling various shapes and eventually arriving at a finalised profile. It was essential throughout to provide adequate headroom while ensuring there was enough room for surfacing above. A key issue was creating an ideal connection between the two radii at the transition point, thereby ensuring the voussoirs are completely closed. Another concern was the angle at the springing, which led to an iterative process of modifying the various parameters, in order to achieve a flat interface with the cill beam. The finalised model is shown in Figure 4.

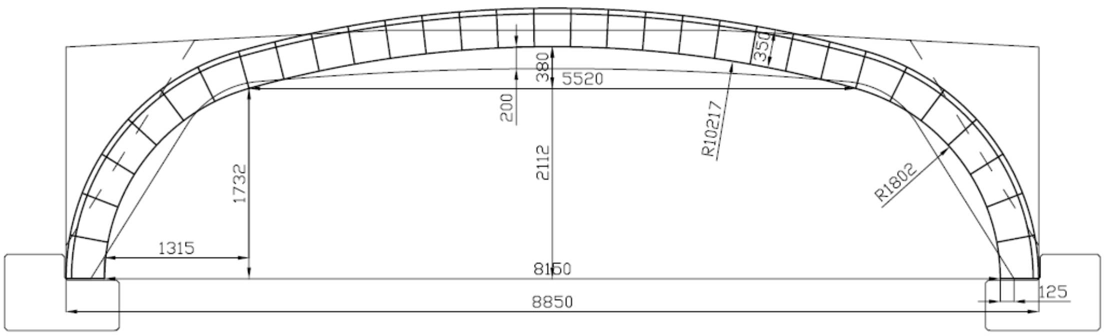

Figure 4 – Finalised model of DRA

The details are as follows:

Span	= 8.15m
Rise	= 2.112m
Number of Voussoirs	= 31
Arch Ring Thickness	= 350mm arch ring (300mm block + 50mm screed)
Total Arch Span:Rise	= 3.86:1
Central Radius Span:Rise	= 14.5:1
Angle at Springing	= 0
Q-rise	= 1906mm

Figure 5 shows the DRA in place on what was a Con Arch project. All the design constraints are met.

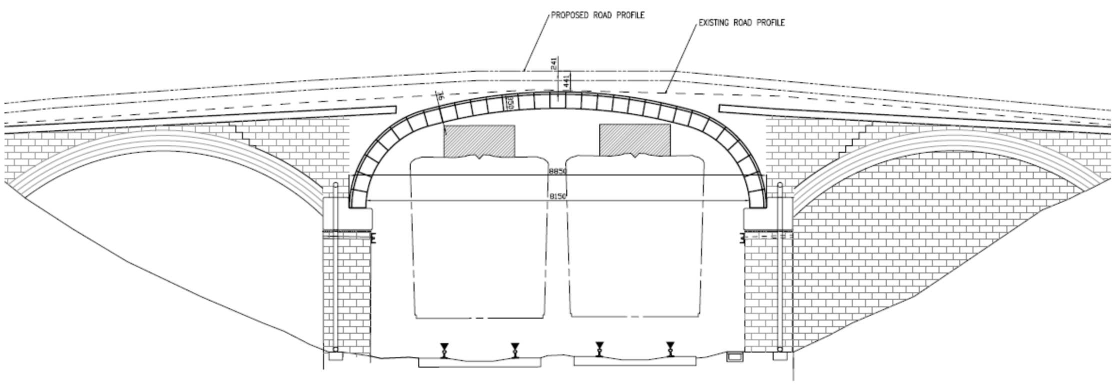

Figure 5 – Use of DRA on typical Con Arch scheme

4. Construction

4.1 Voussoir Production

Figure 6 shows the dimensions of the two sizes of blocks required for casting. As can be seen from Figure. 6 the DRA requires voussoirs of two different geometries to achieve the variation in radius. The larger radius voussoirs (type 1) are used in the central, flat section of the arch while the smaller radius voussoirs (type 2) form the part of the arch nearing the supports.

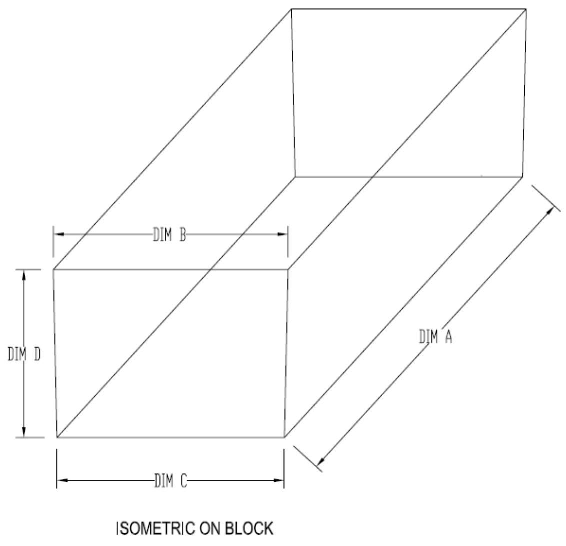

DIMENSIONS OF BLOCKS

	TYPE 1 BLOCK	TYPE 2 BLOCK
DIM A	995.0mm	995.0mm
DIM B	338.5mm	388.5mm
DIM C	328.8mm	333.00mm
DIM D	300mm	300mm
NO.	17	14
VOL	1.00m3	1.07m3

NOTE-
1. 4 no. double moulds required for each type
2. Provide 10mm chamfers along all edges.

Figure 6 – Voussoir dimensions

4.2 Lifting Process

As this is a new shape of FlexiArch, the standard lifting process is likely to require alteration. In order to provide a means of determining the best lifting technique, multiple lifters will be cast in the FlexiArch, as shown in Figure 7.

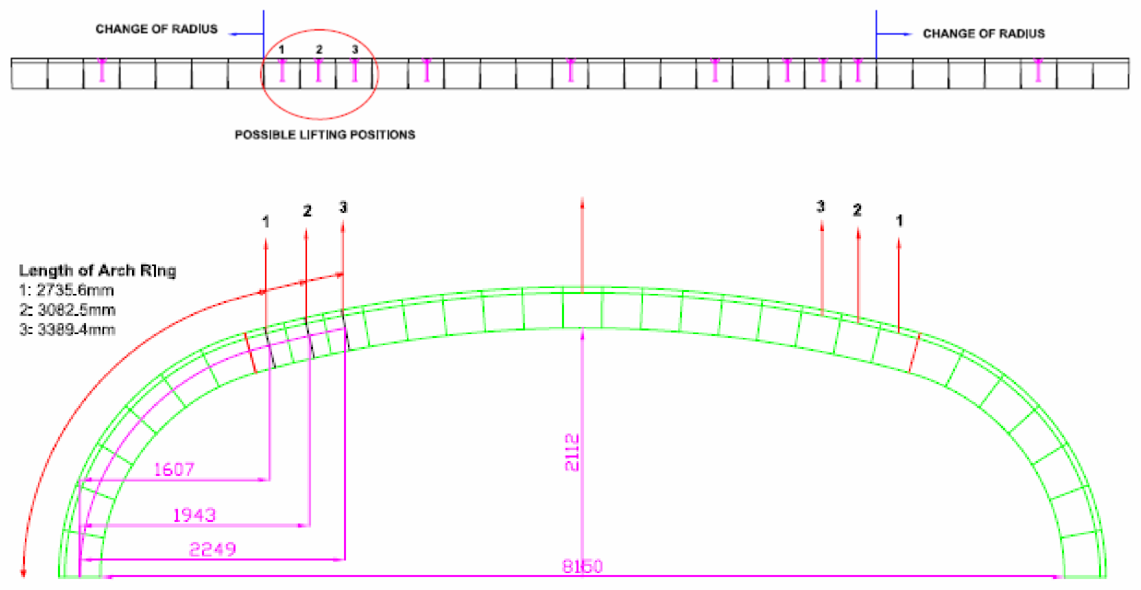

Figure 7 – Lifting point arrangement for DRA

In order to ensure the paragrid reinforcement in the screed can deal with the various lifting points, a series of calculations were done to check the tension produced due to the cantilever moment. The tensile forces for lifting points 1, 2 and 3 are 58.602kN, 79.845kN and 101.625kN respectively. Furthermore, the tensile force created when the FlexiArch was lifted from the middle is 294.05kN. This is the worst case scenario. The paragrid has a capacity of 200kN therefore 2 layers would be required for the DRA. These calculations can be found in the appendix.

4.3 Moving FlexiArch in Factory

It has been observed that slight damage has been caused to the top screed of the larger FlexiArches (>10m span, >23 blocks) as they've being moved from the beam floor to the yard and onto transport. Efforts to maintain a flat profile during the lifting process has allowed the development of excessive compressive forces in the fresh concrete screed due to sagging. It is recommended that consideration is given to inducing a slight hogging curvature during the lifting operation. This can be achieved by adjusting the lengths of the lifting chains as shown below.

It will be necessary to confirm that the tensile forces generated in the screed are within tolerable limits. The crack inducers should ensure a sufficient margin of safety provided the development of the curvature is confined as shown. If the FlexiArch has 7 lifting points as shown in Figure 8, and the central lifting chain has a length "x" then the subsequent chain lengths could be "x + 100mm", "x +300mm", "x+600mm".

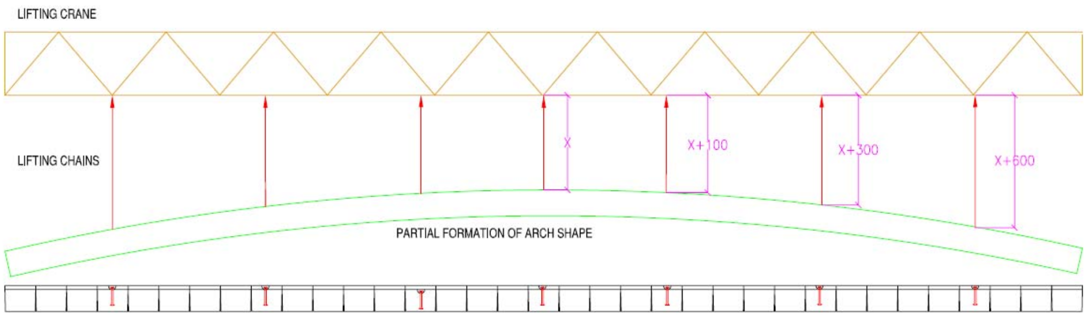

Figure 8 – Lifting process for DRA

4.4 Construction Program

a) Creation of timber moulds for 2 types of voussoir. At present the voussoirs moulds are ready for casting.
b) Cast a master mould in concrete.
c) Commence casting of voussoirs.
d) Manufacture 2 footing units. As the springing angle is zero this will be straightforward.
e) Setting out of Voussoirs
f) Attachment of paragrid reinforcement
g) Pour 50mm screed
h) Provide crack inducers
i) Allow to cure
j) Allocate suitable testing area
k) Move DRA onto transport and bring to site
l) Commence trial lifting process with alternate lifters and document
m) Assess and determine most favourable lifting points
n) Erect DRA
o) Attach shutters and pour backfill
p) Ready for testing

5. Testing

The instrumentation set-up and typical test arrangement for the load test is depicted in Figure 8. Deflection transducers were used to monitor both horizontal and vertical deflections; vibrating wire strain gauges were used to measure crack openings at the joints between voussoirs and discrete optical sensors were used in the arch extrados to measure strain. The arch is going to be tested with minimal fill on top in order to provide a more accurate output.

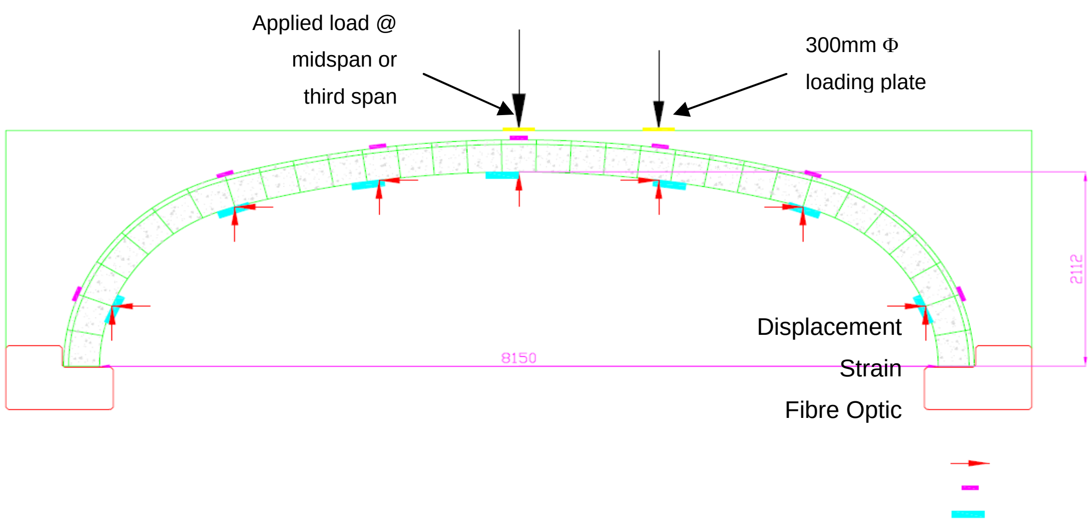

Figure 9 – Testing and monitoring arrangement of DRA

6. Validation / Calibration

The results obtained from the full scale testing of a single arch unit will be calibrated with the output obtained from the FlexiArch design tools.

The DRA was analysed using ARCHIE-M (Obvis, 2006), a numerical analysis package which takes into account the arch backfill and assumes a collapse mechanism type failure (as opposed to ring separation). The arch unit was analysed under different wheel loading conditions but the SV load (EU vehicle axle load from BD91/04) was the most critical. A line of thrust is indicated in Figure 10. Under the design loading, the position of the thrust line in the arch unit gave information about the stability of the unit. Furthermore, ARCHIE was able to demonstrate the change in the thrust line by changing the height of the Backing Material (BM) at the springing level and the effect of changing the Passive Pressure (PP). Therefore, for a particular loading condition, arch ring depth and appropriate passive pressure the load capacity of the bridge was established.

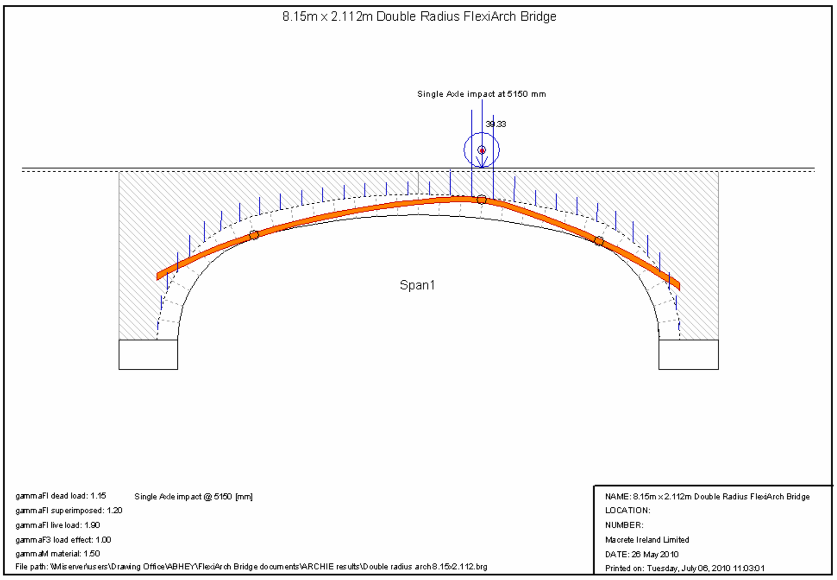

Figure 10 – Thrust line in DRA determined using ARCHIE- M

A Non Linear Finite Element Analysis will be carried out in the future in order to further validate results.

7. Concluding Remarks

The creation of a variable geometry FlexiArch is a large milestone in the development of this product. Already significant progress has been made: the geometry of the arch has been finalised and agreed with Network Rail, computer analysis has been performed, the moulds have be created and the arch is ready for construction. If this study can go on to prove the capability of the Double Radius FlexiArch it would be a great success for all parties involved. The potential for widespread market adoption is significant, particularly if Network Rail embrace the system as a superior alternative to the current Con Arch.

Acknowledgements

The author would like to thank the factory staff, advisors and the Knowledge Transfer Partnership for their contributions to this research.

Referernces

ARCHIE-M: Masonry Arch Bridges and Viaduct Assessment Software, Version 2.0.8, OBVIS Ltd. UK, 2006.

British Standards Institute, BS 8110: Part 2: Structural use of concrete: Code of practice for special circumstances Section 9: Appraisal and testing of structures and components for construction, London, 1985.

British Standards Institute, BS 8110: Part 2: Structural use of concrete: Code of practice for special circumstances Section 9: Appraisal and testing of structures and components for construction, London, 1985.

Highways Agency (UK), BD37/01, Departmental Standard, Loads for Highway Bridges (used with BS5400: Pt2) Design Manual for Roads and Bridges, Volume 1, Section 3, Part 14, Department of Transport, Highway and Traffic, 2001.

Highways Agency (UK), BD44/95, Departmental Standard, The assessment of concrete highway bridges, Design Manual for Roads and Bridges, Volume 1, Section 3, Department of Transport, Highway and Traffic, 1995.

Highways Agency (UK), BD 91/04, Departmental Standard, Unreinforced masonry arch bridges, Design Manual for Roads and Bridges, Volume 2 , Section 2 Special Structures, Part 14, 2004.

Taylor S E, Gupta A, Kirkpatrick J, Long A E, Rankin G I B and Hogg I, Development of a novel flexible concrete arch system, 11th International Conference on Structural Faults and Repairs, Edinburgh, June 2006.

Taylor S E, Gupta A, Kirkpatrick J and Long A E, Testing of a flexible concrete arch system, Proceedings of the seventh New York Bridge Conference, August 2007.

Appendix Cantilever load for construction phase of Double Radius FlexiArch

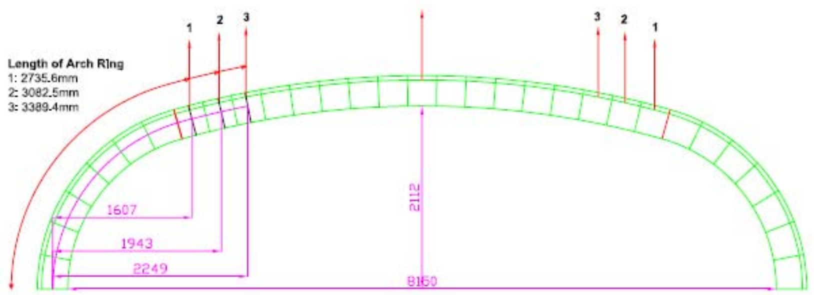

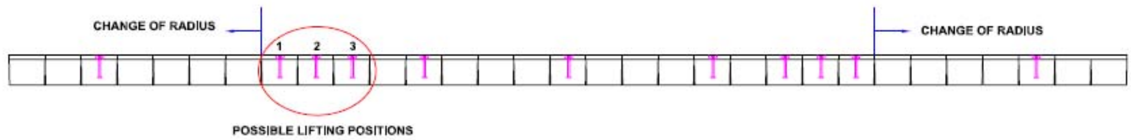

Lifting Point 1

Self–weight:

Length of arch ring = 2.735m

Weight = 0.35m x 1.0m x 24kN/m^3 x 2.735m = 22.974kN

Moment = WL/2 = 22.974 x 1.607/2 = 18.460kN.m

F = M/0.9d = 18.460/(0.9x.35) = 58.602kN

Lifting Point 2

Self–weight:

Length of arch ring = 3.082m

Weight = 0.35m x 1.0m x 24kN/m^3 x 3.082m = 25.889kN

Moment = WL/2 = 25.889 x 1.943/2 = 25.151kN.m

F = M/0.9d = 23.258/(0.9x.35) = 79.845kN

Lifting Point 3

Self–weight:

Length of arch ring = 3.389m

Weight = 0.35m x 1.0m x 24kN/m^3 x 3.389m = 28.468kN

Moment = WL/2 = 28.468 x 2.249/2 = 32.012kN.m

F = M/0.9d = 32.012/(0.9x.35) = 101.625kN

EMERGENCY REHABILITATION OF BROWNSBARN BRIDGE

V.PAKRASHI[1], J.KELLY[1], J.HARKIN[2], A.FARRELL[3] & S.NANUKUTTAN[2]

[1]Roughan & O'Donovan Consulting Engineers, Dublin, Ireland

[2] School of Planning, Architecture and Civil Engineering, Queen's University Belfast, Northern Ireland

[3] National Roads Design Office, Maudlins, Naas, Kildare, Ireland

Abstract

This paper outlines the repair methodology of Brownsbarn Bridge situated over the N7 near Dublin. The repair strategy was formulated following impact damage to the soffit from a low-loader carrying an excavator passing underneath the bridge. Significant damage was observed to one of the beams. The repairs were successfully carried out as emergency works in Ireland in May 2010. The rehabilitation methodology is based on preloading the precast prestressed bridge before repair followed by removal of load after repair to ensure the re-establishment of some of the lost prestress. This paper outlines the various stages of rehabilitation and establishes the timelines of significant events along with practical discussions on the execution of the rehabilitation methodology. The bridge was continuously monitored throughout the refurbishment process. This case study is expected to be of topical interest to researchers, practicing engineers, bridge owners and end-users alike.

Keywords: Bridge, Repair Methods, Durability, Impact Damage, Emergency Works

1. General

An emergency rehabilitation was required to be carried out on Brownsbarn Bridge situated over the national road N7, following an impact damage to its soffit from a low-loader carrying an excavator passing underneath the bridge. The rehabilitation posed a number of theoretical and practical engineering challenges in terms of uncertainty in the stresses, lack of time, liaison among a number of groups working on disparate aspects of the project, the practical execution of rehabilitation strategy and the health and safety aspects of a number of high risk activities. The consulting engineering works were carried out by Roughan & O'Donovan Consulting Engineers for South Dublin County Council on behalf of the National Roads Authority.

The Brownsbarn Bridge is a two span continuous slab – girder bridge comprising of six precast prestressed U8 concrete beams connected by a continuity diaphragm. The reinforced concrete piers are integral to the deck and the ends of the bridge are simply supported. The abutments are made of reinforced concrete. The continuity diaphragm is connected to the U8 beams through steel plates of dimension 300x30x1700 (in mm). These U8 beams date from one of the earliest of their kind of design in the Republic of Ireland.

The impact damage affected two of the prestressed U8 beams the bridge consists of. The edge of the outer beam was damaged in a relatively benign fashion than a more extensively damaged inner beam. The main requirements of the rehabilitation involved detailed repair of both beams including the introduction of some of the lost prestress into the damaged location of the inner beam. Although one of the prestressing strands was severed on the outer beam, it was computed that apart from this isolated severing of a strand, the prestressing tendons were essentially unaffected in both of the damaged beams. Under these circumstances, it was not envisaged that the damaged prestressing strand will be replaced.

Impact damage in bridges is an important (Mallett, 1996), but often academically overlooked problem (Zobel et.al, 1997). Although a number of studies exist on the theoretical aspects of repairs, analysis of partially prestressed beams, exposed tendons, web openings (Zobel and Jirsa,1998; Russo et.al, 2000; Chern et.al, 1992,Au and Du, 2004; Abdala and Kennedy, 1995; Yoo et.al, 2007; Withers and Bhadeshia,2001) or even on the response of prestressed concrete beams to impact loads, (Fujikake et.al, 2009, Ishikawa et.al, 1993) relatively few studies directly attempt to negotiate the problem of vehicle related impact damage to bridges(Zobel et.al, 1997; Civjan et.al, 1995; Zobel and Jirsa,1998).

This paper outlines a successfully executed repair strategy based on a similar nature to (Zobel et.al, 1997) under a number of additional constraints and uncertainties and revisits and revives the problem from a research viewpoint of full scale experimental mechanics and a commercial viewpoint of project management.

Section 1 provides the background to the problem. Section 2 discusses the broad scope of works and the practical ramifications of such a rehabilitation process. Section 3 outlines the emergency rehabilitation in detail and delineates the time zones of significant events through continuous structural health monitoring and Section 4 provides a brief summary of this project of topical interest.

2. Scope of Works

The analytical background to the proposed refurbishment works were constrained to a line beam model and a two dimensional finite element model to qualitatively assess the potential stress hotspots, to distinguish non-structural cracks from structural ones with a high degree of confidence and to establish guidance for monitoring of strains during rehabilitation. Under damaged condition, the bridge was deemed safe under Ultimate Limit State (ULS) but was observed to violate Serviceability Limit State (SLS). Figure 1 provides the as-manufactured drawings of the tendon locations of the prestressed beam obtained from the design archives of Roughan & O'Donovan Consulting Engineers.

The damage extent was assessed and estimated by a number of techniques including an initial visual, photographic and hammer tapping condition survey. The extent was further investigated by incorporating an impact echo test (Tinkey et.al, 2005). In addition, a 3-D visualization was made available through laser scanning. Figure 2 and Figure 3 show the impact damage photograph and the 3-D visualization respectively. Significant damage was established to be extending at least 1.5m on either side of the visually apparent damage.

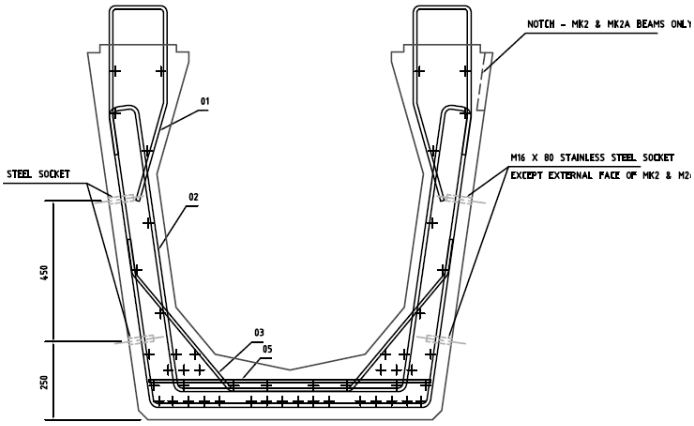

Figure 1 – As Manufactured Tendon Arrangement

Figure 2 – Photograph of Impact Damage

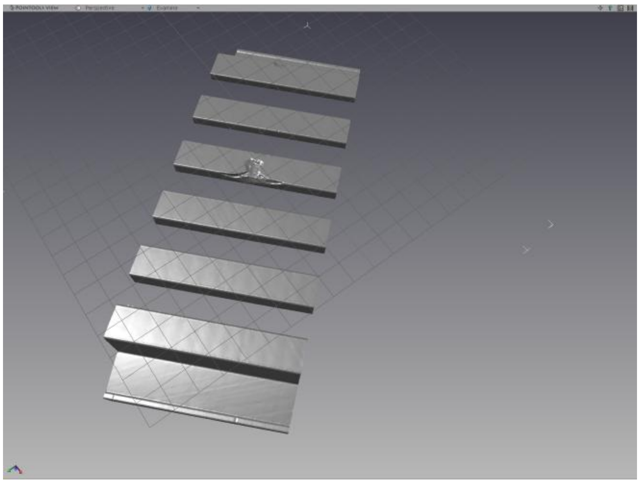

Figure 3 – 3-D Laser Scanning Visualisation

The main elements of the works comprised of site clearance, protective fencing, construction of temporary and permanent safety barriers and guardrails, traffic management, hydrodemolition of damaged concrete, preloading of damaged beam to induce prestrain, repair of concrete beam using an appropriate material and the real time monitoring of the rehabilitation process.

These works were inspired from the fact that the preload, in the form of vertical loading from the top surface on both sides of the damage, would release high prestressing forces at the bottom and will introduce compressive stresses at the top. With uncertainty of the retained stresses within fractured concrete and the redistribution of stresses and the participation of adjacent beams, the prestressing forces alone can be significant. Under such circumstances, the external loads are beneficial. External loads were additionally deemed favourable since a significant section was lost from damage and the hydrodemolition would temporarily increase the stresses even further.

The health and safety aspects of the project were of paramount importance. The rehabilitation involved high risk activities like hydrodemolition. Another important aspect within the management of this project was the severe constraint of time (and of space during the execution of works) where a number of sub-consultants and sub-contractors had to liaise with each other to ensure smooth transition and successful completion of works in a safe and efficient fashion. The works were carried out over the bank holiday weekend of May in the Republic of Ireland. Significantly involved traffic management was required for the completion of the project as one lane of the National Road N7 had to be taken under possession throughout the refurbishment and during the installation and de-installation of monitoring devices.

Real-time online monitoring of strains and deflections were the other important aspects of the project. This required a full instrumentation of the bridge and the monitoring of strain and deflection data continuously in time while the rehabilitation was going on. Instrumentation involved the mounting and zeroing of 16 external strain gauges and three embedded gauges attached to tendons. Five monitoring points were chosen consisting of between two and five strain gauges, this allowed tracking of the strain changes in the repair area itself and of the neighbouring region.

3. Rehabilitation Process

The emergency rehabilitation process on Brownsbarn Bridge can be divided into seven significant zones of activity distributed chronologically. Figure 4 provides a flow chart indicating these stages. The first stage comprises of the installation of gauges. The locations of these gauges correspond to monitoring points of the damaged beam and the two adjacent beams. In total, five monitoring points were selected. Each monitoring point comprised of a number of strain gauges, including sacrificial strain gauges and targets for the measurement of deflection. A vibrating wire strain gauge was used in this regard. The sacrificial strain gauges were used due to the apprehension about the durability of the gauges under mechanically intense activities like hydrodemolition of concrete.

The two ends of the damage were quasistatically and equally patch loaded in 20t increments on each side, using bales of concrete blocks. This loading provided the prestrain in the beam. The loading was carried up to 60t on each side. Consequently, the bridge was preloaded to 120t in total before hydrodemolition was carried out. The organisation of hydrodemolition, including the erection of safety fencing and scaffolding was carried out during this time. Figure 5 shows a photograph after the removal of concrete through hydrodemolition. Although this is a high risk activity and should only be carried out by experts, the process was chosen to be the best for the current project due to its precision and low impact on the existing strands.

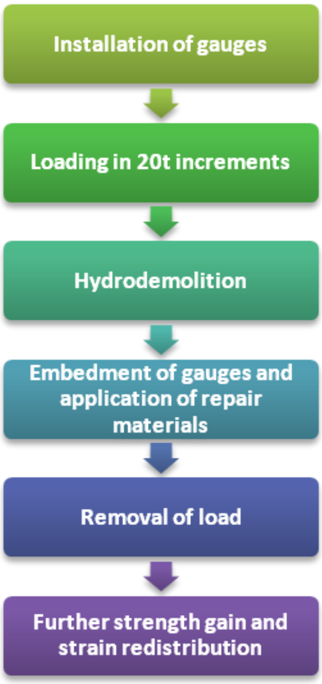

Figure 4 – Brownsbarn Bridge Rehabilitation Flowchart

Figure 5 – Removal of Concrete through Hydrodemolition

Hydrodemolition was followed by the installation of embedded strain gauges within the existing tendons and the application of high strength repair material. The material was expected to gain adequate strength within 12 hours and can take significant tension as well.

The preload was removed from the top of the bridge after the repair material gained adequate strength and some amount of prestress was reinstated following the removal of prestrain. The repaired section is shown in Figure 6 while the removal of preload is shown in Figure 7. A sample photograph of the traffic management provided throughout the rehabilitation is presented as Figure 8.

Figure 6 – Repaired Section of Damaged Beam

Figure 7 – Removal of Preload

Figure 8 – Traffic Management Provided during Rehabilitation

Figure 9 provides the example of outputs from two strain gauges from adjacent beams (damaged and undamaged) during the entire rehabilitation process and zones them into the main activities along the timeline. The strains are in multiples of 10^{-6}. This graph creates the departure point of detailed structural health monitoring analyses including the effects of thermal oscillations, shrinkage characteristics, redistributions of strains, release of entrapped strains, participation and energy flow of adjacent beams and the real mechanics of structures similar to Brownsbarn Bridge. Such analyses are beyond the scope of the current paper and are being currently investigated. It can be seen that initially prior to the application of load that the changes in strain are governed by the diurnal temperature cycle and upon loading the strain level increases representing tensile forces in the soffit of the beams. The hydrodemolition causes some disturbance in the readings followed by another increase in tensile forces as the repair material hardens, the removal of load then reduces the tensile force as the beams fall into their intended state of compression.

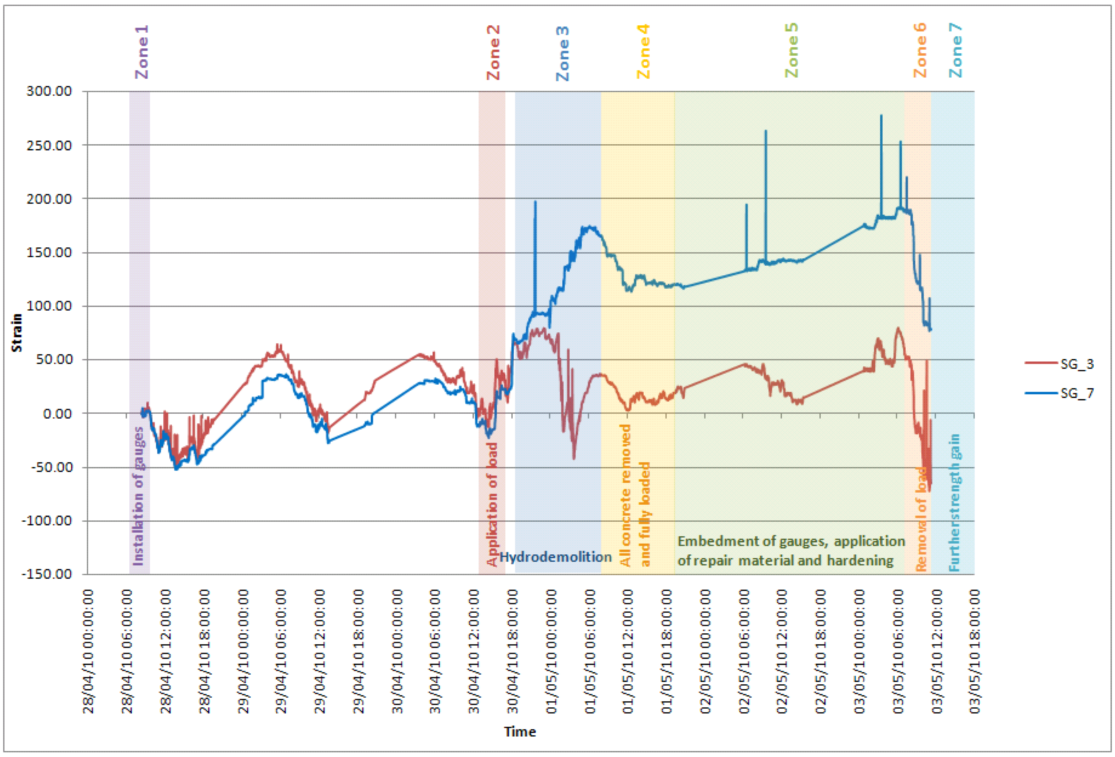

Figure 9 – Activity Footprints in Strain Gauge Monitoring Data and Event Hotspots

4. Conclusions

This paper outlines the emergency rehabilitation of impact damaged Brownsbarn Bridge. The methodology of the emergency repair is discussed along with the theoretical and practical challenges. The various steps of the rehabilitation are detailed and their implications are stated. The footprints of the various stages of the methodology are observed in monitored strain data and are accordingly delineated. The paper create a departure point for a more general and theoretical study in the field of structural health monitoring and experimental engineering mechanics. On the other hand, the general outline of the project is expected to be topical, important and of considerable interest to the engineering committee in general, including academics, engineers and bridge-owners.

Acknowledgements.
The authors gratefully acknowledge the involvement and help of the following:
The National Roads Authority, Maudlins, Naas, Kildare, Ireland
South Dublin County Council, Tallaght, Dublin, Ireland

Coastway, Naas, Kildare, Ireland
Datum Monitoring Services Limited, Moira, Armagh, Northern Ireland
Structural Concrete Bonding Services Limited, Newbridge, Kildare, Ireland
Complete Highway Maintenance Group, Walkinstown, Dublin, Ireland
Testconsult Ireland Limited, Portlaoise, Laose, Ireland

References

Abdalla, H., and Kennedy, J.B. (1995), 'Design Against Cracking at Openings in Prestressed Concrete Beams', *PCI Journal*, Precast/Prestressed Concrete Institute, **40(6)**, 60-75.

Au, F.T.K, and Du, J.S. (2004), 'Prediction of Ultimate Stress in Unbonded Prestressed Tendons', *Magazine of Concrete Research*, **56(1)**, 1-11.

Chern, J.C., You, C.M., and Bazant, Z.P (1992), 'Deformation of Progressively Cracking Partially Prestressed Concrete Beams', *PCI Journal*, Precast/Prestressed Concrete Institute, **37(1)**, 74-84.

Civjan, S.A., Jirsa, J.O., Carrasquillo, R.I., and Fowler, D.W (1995), *Method to Evaluate Remaining Prestress in Damaged Prestress Bridge Girders*, Research Report No. 1370-2, Research Project 3-5-93/5-1370, Centre for Transportation Research, Bureau of Engineering Research, University of Texas, Austin.

Fujikake, K., Li, B., and Soeun, S (2009), 'Impact Response of Reinforced Concrete Beam and its Analytical Evaluation', *JOURNAL OF Structural Engineering, American Society of Civil Engineering*, **135(8)**, 938-950.

Ishikawa, N., Sonada, Y., and Kobayashi, N. (1993), 'Failure Analysis of Prestressed Concrete Beam under Impact Loading', *in Proceedings of the 12th International Conference on Structural Mechanics in Reactor Technology (SMiRT12)*, eds Kussmaul K, Taylor Elsevier Science Publishers, 369-374.

Mallett, G.P. (1996), *State of the Art Review – Repair of Concrete Bridges*, Transport Research Laboratory, Thomas Telford.

Russo, F.M., Wipf, T.J., Klaiber, F.W., and Paradis, R. (2000), 'Evaluation and Repair of Damaged Prestressed Concrete Girder Bridges', *in Proceedings of Mid – Continent Transportation Symposium*, 109-114.

Tinkey, Y., Olson, L.D., and Wiggenhauser, H (2005), 'Impact Echo Scanning for Discontinuity Detection and Imaging in Posttensioned Concrete Bridges and Other Structures', *Materials Evaluation*, **63(1)**, 64-69.

Withers, P.J., and Bhadeshia, H.K.D.H (2001), 'Residual Stress Part 1 – Measurement Techniques', *Materials Science and Technology*, **17**, 355-365.

Yoo, T.M., Doh, J.H., Guan, H., and Fragomeni, S. (2007), 'Experimental Work on Reinforced and Prestressed Concrete Deep Beams with Various Web Openings', *in Proceedings of the 4th Innovations in Structural Engineering and Construction (ISEC-04)*, eds Xie M and Patnaikuni I, Routledge, Taylor and Francis, 413-419.

Zobel, R.S., Carrasquillo R.L, and Fowler, D.W (1997), 'Repair of Impact Damaged Prestressed Girder using a Variety of Materials and Placement Methods', *Construction and Building Materials*, Precast/Prestressed Concrete Institute, **11(5-6)**, 319-326.

Zobel, R.S., and Jirsa, J.O. (1998), 'Performance of Strand Splice Repairs in Prestressed Concrete Bridges', *PCI Journal*, Precast/Prestressed Concrete Institute, **43(5)**, 72-85.

UB500 RIVER SHANNON VIADUCT – SUPERSTRUCTURE RENEWAL

Aidan McAdam, Eoghain Nagle, Kenneth Wade
Structural Design Section, Irish Rail

Abstract

This paper describes the elements of work which were undertaken in the renewal of this large viaduct across the River Shannon on the Dublin – Sligo Railway Line in 2009; being one of only three crossings of Ireland's largest river on the Irish Rail Network.

The paper gives a brief historical overview and sets out the reasons for undertaking the renewal of the viaduct. The design rational and fabrication details are described for the replacement spans. The paper describes the preparation works which were undertaken on and adjacent to the operational railway. Also, the possession planning and logistics of transporting the abnormal loads of the new viaduct spans by road and rail is discussed in some detail.

The paper also explains the logistics for large crane mobilisation and the restrictions for the use of what is believed to be the largest crawler crane ever used in Ireland.

Keywords: Irish Rail, River Shannon, UB500, abnormal, logistics, possession, planning.

1. Introduction

Following the collapse of Cahir Viaduct after a train derailment in October 2003, Irish Rail progressed a programme of works for the replacement and/or upgrade of timber waybeam bridges (IRSC 2005). In railway terminology, timber waybeam bridges are those bridges that have longitudinal timber beams supporting the rail.

In July 2008 the Board of Irish Rail approved the replacement of the superstructure of UB500 River Shannon Viaduct on the main Dublin – Sligo railway line. This line has over six hundred over and under bridges or UB's along its length between the start in Dublin and its finish in Sligo.

2. Brief Historical Overview

This viaduct was original constructed in 1862 by Fox Henderson & Co., Derby, England and was shipped to Ireland for erection into position. The original structure consisted of six spans, with two spans of 9.2 m at each end and two 23 m central spans. Figure 1 shows the general arrangement and typical cross section.

The spans consisted of Howe truss half-through girders, with transverse plate girders supporting longitudinally spanning timber waybeams. The spans were formed from wrought iron and were riveted throughout. The only exception to this form of construction was the pair of spans at the Dublin end of the viaduct. These consisted of a bascule opening in the second span and an underslung lattice truss supporting the longitudinal waybeams in the first span.

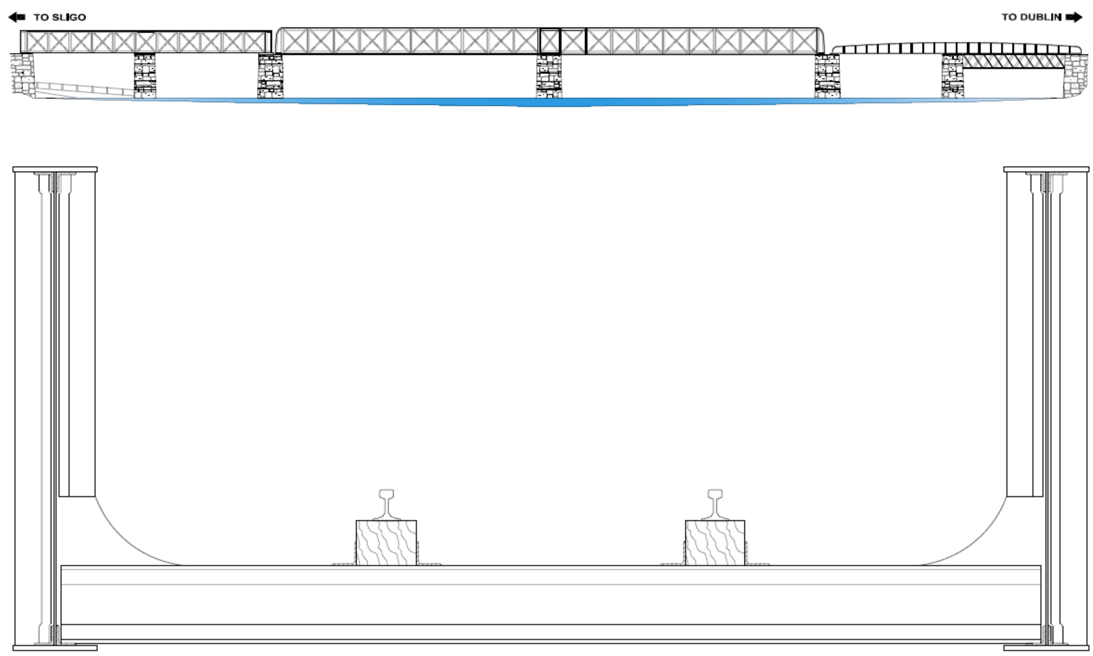

Figure 1 - Original General Arrangement and Typical Cross Section

The lifting span had been provided to allow sailing and larger goods vessels to progress up river, but had fell into disuse and was last recorded opening in 1950. On going maintenance and repairs were carried out over the years with periodic replacement of the timber wayebams. Substantial repairs had been carried out to the original viaduct by the Irish Rail Bridge Gangs during the early 1990's, as substantial corrosion and section loss had taken place to the main transverse girders.

The deterioration of the structure over the years led to the introduction of speed restrictions and in later years a restriction of 16 km/h was in force.

3. Planned Renewal Scheme

The original viaduct had been listed as a protected structure by Leitrim Co. Council in 2005. Consequently, it was necessary to obtain planning permission for the viaduct renewal. When considering the options for a replacement structure it was requested to raise the soffit level by 1.0 m in order to allow larger vessels to pass below the viaduct. Therefore, taking due cognisance of the original lattice truss arrangement, Irish Rail proposed a structural form of a half-through girder but replaced the Howe truss form with a more efficient Warren truss.

Figure 2 shows the general arrangement of the new replacement spans, and the use of structural hollow sections for the main members. These sections were chosen to achieve greater rigidity of the half-through girder form, avoided the use of fabricated sections, achieved shallow construction depths and were available as off-the-shelf structural steel members. The shape of the members would also aid in the application of the new protective treatment system, and the long term maintenance of the protective system throughout the life of the structure.

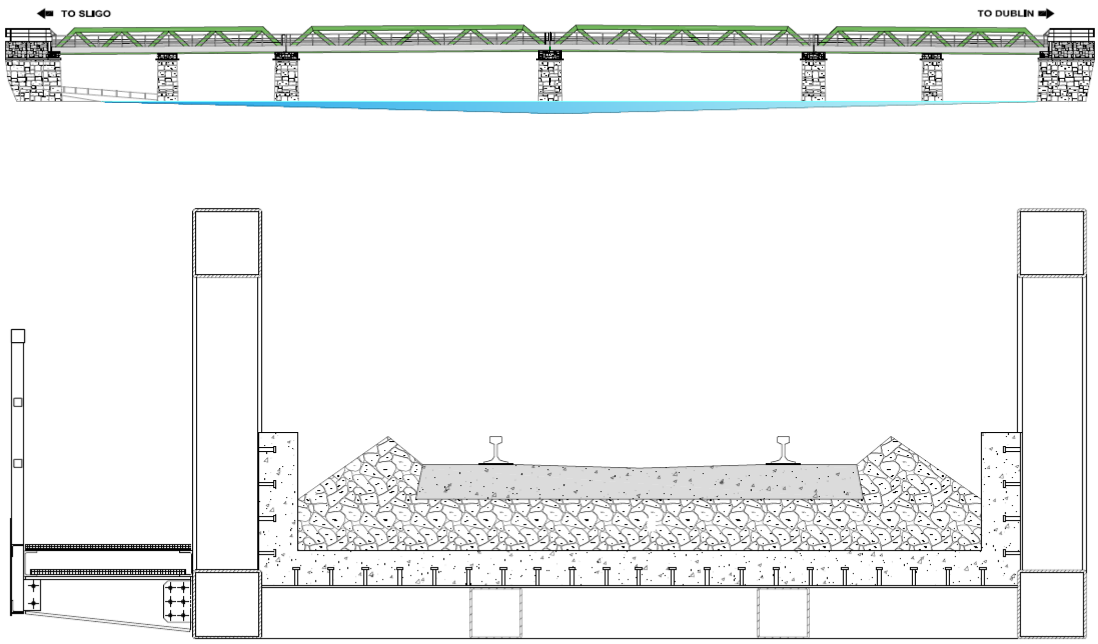

Figure 2 - General Arrangement of Replacement Viaduct Spans and Cross Section

A composite concrete deck was used to increase the transverse and longitudinal stiffness of the deck, and to provide support for the ballasted track.

The overall dimensions of the new truss which exceeded 5.1m in width, meant that the transport of the new spans by road would be difficult. The remote nature of the site meant that the final three miles of the route would be impossible due to the very poor road alignments, and would have required major upgrades and land purchases to make the route passable.

An alternative scheme was developed to transport the new spans to site in two stages: by road to the village of Dromod and by rail over a distance of six miles from Dromod to the site. To facilitate the rail movements, a three dimensional swept path survey was carried out of each of the four masonry arch over-bridges and six under-bridges, and any other structures or signals along the proposed route. It was established that the truss could be transported provided that a maximum height of transport vehicle of 1000 mm was observed. Figure 3 shows the restriction imposed by the existing masonry arch bridges.

Planning permission was sought and granted in 2007. The fabrication contract was awarded to SIAC Butlers Steel Ltd., Portarlington in September 2008. Upon completion of the fabrication process, the spans were moved to a purposely prepared blast-shop where the steelwork was blasted to Sa3 and thermal zinc metal spray was applied, with intermediate MIO coats and polyurethane top coats.

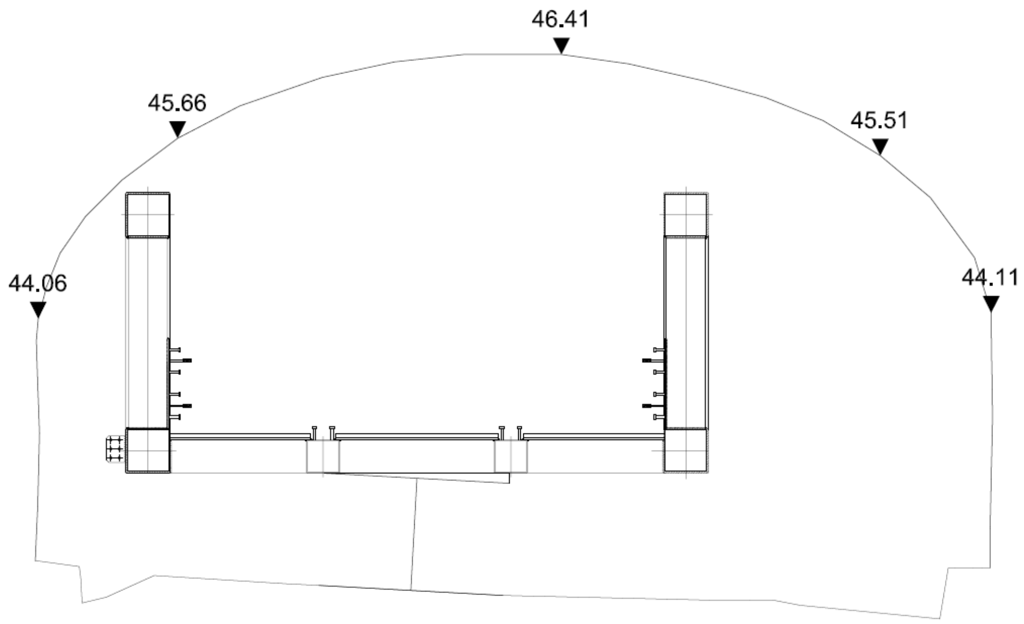

Figure 3 – Swept Path Cross Section for Transportation

Upon final completion in February 2009, the spans were transported as abnormal loads at night by road to the Irish Rail Engineering Sidings in Mullingar. This location was chosen as it provided for safe storage of the spans until the temporary works on site were completed, and also allowed the rail transport system to be tested.

4. Rail Transportation

A balance was sought between optimising the section sizes for the main members of the truss and the maximum clearance envelopes for the passage through the arch bridges. A review of the current fleet of rolling stock found that no chasis arrangement was suitable to transport the viaduct spans.

In March 2009, Irish Rail awarded a contract to Unilokomotive Ltd., Tuam for the fabrication of two special rail trailers for the transport of the new spans. A scheme design for the self-levelling of the spans during transport was proposed by Irish Rail, and this was developed further by Unilokomotive. The self-leveling was controlled by an electronic inclinometer, which through a process controller operated a hydraulic lifting ram. This allowed for a maximum cant of 140 mm transversely across the rail. A central turntable provided for a minimum track curvature of 1500 m.

Due to the stiffness and weight of the spans, no draw or connector bars were used between the front and back trailers when transporting the spans. This meant that adjustments for the variations in the span lengths could be provided for easily.

A trial was carried out at the Mullingar Sidings in July 2009 to verify the operation of the rail transport system. (See Figure 4)

In August 2009, the spans were transported by road to the designated access point just west of Dromod village. Here, the spans were temporarily stored before each was lifted in turn onto the rail trailers and transported to site by rail during a nighttime possession of the line between 10th – 13th August 2009.

Figure 4 – Unilocomotive Rail Trailer and Unilok Traction Unit at Mullingar Sidings

5. River Bank Works

Various options had been considered for the installation of the new spans. The quickest solution was to place a large crane on one of the river banks and remove the original spans by lifting out, and then installing each of the replacement spans in turn. By selecting a sufficiently large crane it was found that the concrete decks of the new spans could be formed before the spans were lifting into place. Having placed each span the crane could then be de-mobilised and in-situ stitches formed between spans. The requirement was for a crane with a lift capacity 130 tonnes at a lift radius of approximately 125 m.

The contract for the supply of the crane was awarded to Mammoet Ltd., who supplied a very large crawler crane which had the ability to move while carrying the new spans. A Liebherr LR11350 (self-weight 1350 tonnes) crawler crane was supplied, and it is believed that this is the largest crane of this type ever used in Ireland.

As the design progressed it was decided to construct a temporary piled crane base close to the river edge. This enabled the crane lift radius to be reduced to 110m.

A total load bearing capacity of over 2200 tonnes was required on the crane base, and due to the depth to satisfactory bearing layers, end bearing piles were installed on a grid of 2.3 m to bed rock at a depth of 15 m.

In June 2009, a contract was awarded to Jons Civil Engineering Ltd. for the construction of the crane support base. Due to the nature of the works and its proximity to the river special navigation measures were put in place adjacent to the original viaduct. A special licensing agreement was put in place with Waterways Ireland to allow the works to take place and a special exclusion zone was set up for vessels moving upstream and downstream through the viaduct.

Jons Civil Engineering adopted driven tubular piles, and a total of 235 No. piles were installed to rock level, with additional raking piles to provide lateral restraint. Upon completion of the piling, the piles were capped and a 750mm deep reinforced concrete bearing slab was formed on top of the piles.

The area adjacent to the crane base was also prepared to temporarily receive the new spans so that concrete works could be carried out for the concrete composite decks before installation into the final postions.

6. Mobilisation Tasks

As outlined in Section 2., the very poor alignment of the existing access road from the adjacent N4 Dublin-Sligo road required special consideration as the limited width and poor verges presented a significant challenge for the transport of the large crawler crane and the smaller cranes required to assemble it to site.

Localised verge widening was undertaken by Leitrim Co. Council to form passing bays along the four mile route from the N4, so that adjacent landowners could gain access safely to their properties while the preparatory works were progressing.

In addition, to facilitate the off loading of the new steelwork spans at the site adjacent to the viaduct, a 500 tonne capacity mobile crane was required. This mobile crane although small in comparison to the large crawler crane, presented a significant challenge to enter the works as it was the largest single load to traverse the road. It was decided to plate the access road with steel plates over short road lengths, moving the plates to adjacent lengths in turn to allow the crane to travel over the full distance. It took a total of twelve hours to complete this movement each way into and out of the site.

Recognising the disruption caused by this method, it was decided to plate the verges of the entire length of road for the transport of two similar cranes to build the large crane in September, and maintain these plates in position for the duration of the works until the crawler crane had completed all its works and been demobilised from site.

It is important to note that considerable logistics were required to transport and assemble the large crawler crane. A total of 87 No. truck movements were required to bring all of the components to site, and a repeat of this number when the crane was later demobilised.

7. Railway Shutdown

The railway shutdown had been programmed in early 2008 to take place from Monday 5th to Friday 16th October and had received the backing of relevant stakeholders affected by this shutdown, including Waterways Ireland, Leitrim Co. Council and the Operations Department of Irish Rail.

Mammoet had arranged for the crawler crane to be shipped from Port Arthur in the Gulf of Mexico, USA. Unfortunately due to strong winds the crane was delayed completing an earlier contract in Houston, Texas and so was delayed departing to Ireland. The mv Edmondgracht, an 8,500 tonne vessel with three 60 tonne derrick cranes, sailed from Port Arthur on 23rd September but was further delayed due to storms in the north atlantic which added a further four days to the delay. In total the ship was delayed by a total of twelve days and had used all of the allotted time for transport and assembly of the crane on site, eventually arriving at Killybegs, Co. Donegal on 8th October.

This information had been conveyed to the project team, and a joint decision was reached to move the shutdown by almost one month.

Line possession was granted at 10.07hrs on Tuesday 27th October between Dromod and Sligo Station. The rails were cut and the Bridge Gang staff began jacking the original spans in preparation for lifting. However due to strong winds no lifting could take place until 22.30hrs when the wind had reduced, the safety requirement for the crane lifting meant that the winds could not exceed 10m/s during any lift.

Original Span No.s 6 & 5 counting from the Sligo side were successfully lifted out at 03.45hrs on Wednesday 28th. Existing Span No. 4 was removed at 05.30hrs and Span No. 3 at 6.30hrs, and this was followed by the bascule span at Span No. 2.

Figure 5 shows the original Span No. 2 being lifted out. This span had been estimated to weight approximately 40 tonnes, however, due to the possible use of lead or pig iron ballasting within the span an actual weight of 53 tonnes was recorded. Due to the various fixing points of the span to the existing pier it was some time before it could be established that there was no concealed fixing. Span No. 2 was not removed until 18.00hrs. The final span No. 1 was lifted out quickly by 19.00hrs.

The new precast concrete bearing shelves were then installed to the tops of each existing abutment and pier, starting at the Sligo abutment and progressing towards the Dublin abutment. The bearing shelves provided for raising the new bridge soffit by 1.0 m above the existing viaduct and so provided a greater clearance for navigation.

Wind speeds strengthened during Thursday morning and all works were stopped until Friday with the installation of the first new viaduct Span No.4 at 17.00hrs. The installation of Span No. 3 followed quickly and was lifted into place at 20.00hrs.

The last two remaining spans were installed with Span No. 2 at 10.00hrs and Span No. 1 at 12.00hrs on Saturday afternoon, and all lifting was finally completed by 14.00hrs on Saturday 31st October. At this stage the crawler crane was disassembled and transported off site over a five day period. At the same time the insitu concrete joints between the spans were formed and waterproofed. The track was reinstated, ballasted and tamped.

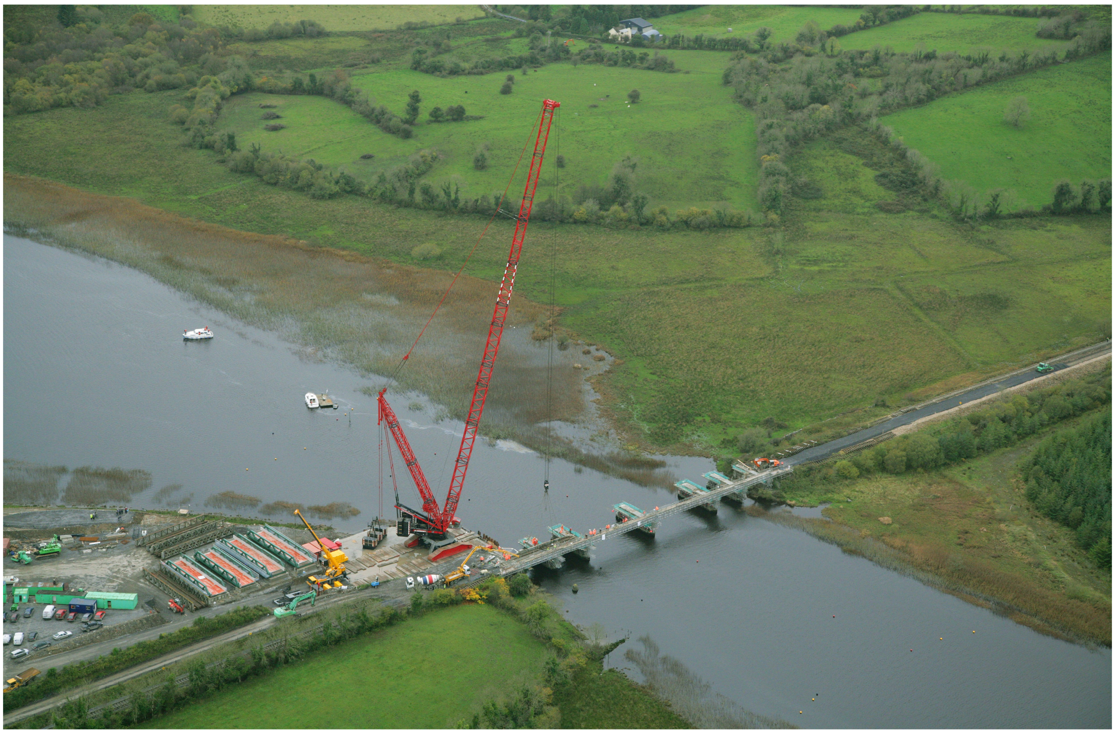

Figure 5 – Removal of Original Bascule Span No.2

The possession was handed back at 10.54hrs on Friday 6th November and the first train across the viaduct was the 9.05am Dublin to Sligo commuter train. A temporary speed restriction of 40 km/h was used initially for the reopening but this later increased to 64 km/h, and then to 120 km/h when final tamping was completed.

Summary

This paper shows how the management of significant logistical challenges can be overcome to lead to the successful delivery of an important piece of civil engineering infrastructure on the Irish Rail Network.

References

IRSC, (2005), Inquiry into the derailment of a freight train at Cahir Viaduct on 7th October 2003, Interim Railway Safety Commission, Dublin, Ireland.

THE NEW ENGINEERING BUILDING AT NUI, GALWAY AS A TEACHING TOOL FOR STRUCTURAL ENGINEERING

E. CANNON, J. GOGGINS
College of Engineering and Informatics, NUI Galway

Abstract:

The New Engineering Building (NEB) at NUIG will consolidate education and research activities in the various engineering disciplines into one building which will not only provide a learning environment, but will itself act as a teaching and learning tool. It will serve as a 'living laboratory' for engineering, where live data sets from numerous types of sensors will be used to illustrate structural engineering and building performance concepts in undergraduate teaching and in the development of full-scale research in structural engineering and energy.

This paper describes the instrumentation of several major structural elements in order to provide the interactivity required of the 'living laboratory'. Three elements were selected for instrumentation: a 40-tonne pre-tensioned box beam, a pre-tensioned double-tee unit and a novel precast two-way flat slab system. The processes of gauge selection, arrangement and installation are presented together some preliminary results.

Keywords: concrete, datalogging, double-tee, gauges, instrumentation, precast, pre-tensioned, prestressed, structural engineering, resistance, teaching, vibrating-wire.

1. Introduction

Figure 1 - Artist's impression of completed New Engineering Building at NUI Galway (NUI Galway, 2010).

The New Engineering Building (NEB) at NUI Galway (Figure 1), presently under construction, will unite all engineering activities on campus in a state of the art academic facility by September 2011. In addition to providing the facilities required of a learning environment, the building will itself function as a teaching and learning tool - it will be a ‘living laboratory’ for engineering. Live data sets from a variety of sensors types will be available for use in illustrating structural engineering and building performance concepts in undergraduate teaching, and in the development of full-scale research in structural engineering and energy. The building contains green-building initiatives which will provide working models for students. Several of the building’s constructional elements have consciously been left exposed, as visual learning tools (RMJM, 2008).

This paper concentrates on an aspect of the development of the NEB as a ‘living laboratory’ for structural engineering, dealing in particular with the embedded sensors – both those requiring to be installed prior to erection of structural elements and those fixed during construction on the NEB site. These are fundamental to the development of the building as an interactive teaching tool, reporting on the evolving dialogue of the structure with its environment (Cannon & Goggins, 2009).

2. The building structure

The gross floor area of the NEB is 14,100m^2. The building structure is composed predominantly of concrete, in-situ and precast, with some elements in structural steel. Superstructure loads are transferred to rock through end-bearing piles, while the ground floor slab rests on engineered fill. Some structural aspects of the project which are of particular interest are:

1. the extensive use of ggbs in place of CEM I concrete;
2. 40-tonne prestressed concrete transfer beams, precast by Banagher Concrete (Figure 2), positioned over the main lecture theatres;
3. prestressed double-tee units, precast by Banagher Concrete;
4. the Cobiax flooring system, a two-way spanning, void-formed, flat slab system utilising slabs manufactured by Oran Precast (Figure 3) and providing a high quality exposed soffitte finish;
5. deep structural steel plate girders, fabricated by Duggan Steel;
6. a highly visible structural steel floor suspension system in one corner of the building.

The instrumentation described in this paper refers principally to items 2 and 3 above.

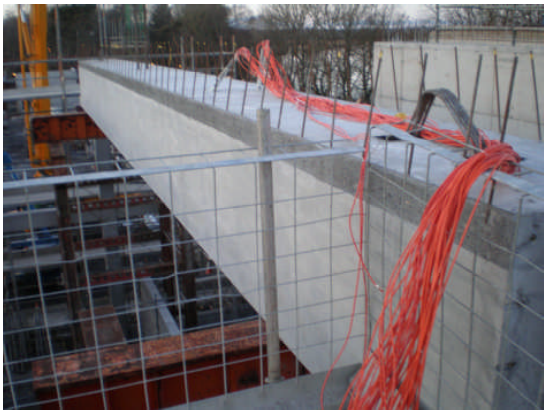

Figure 2 – 40-tonne prestressed concrete transfer beam.

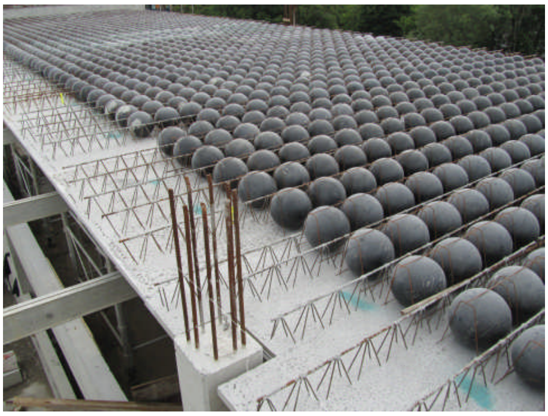

Figure 3 – Void-formed flat slab system prior to installation of top reinforcement mat.

3. Instrumentation:

3.1 Objectives

The general intention was to monitor a many aspects as possible of the response of the selected elements to their environment. This would include response to discrete loading events, time-dependent variation in strain due to creep, shrinkage and temperature change, possible restraint effects in the large transfer beam and in the Cobiax slab, and the load-sharing characteristics of the Cobiax slab.

3.2 Test elements and sensor arrangement

There was a severe time constraint in relation to the purchasing of gauges and datalogging equipment and also a significant time requirement for installation. Due to these factors and to budgetary constraints, instrumentation with embedded sensors was confined to three large-span elements. These were:

(i) a pre-tensioned concrete transfer beam located on the 2nd floor on Grid line L from 3-7 (Figure 4);
(ii) a pre-tensioned double-tee unit located adjacently on the 2nd floor between grid locations D3 to E7 (Figure 5);
(iii) a two-way spanning void-formed flat slab flooring system on third floor between grid locations A9 to C10 (Figure 6);

Elements (i) and (ii) were instrumented with vibrating-wire gauges at Banagher Concrete's premises, while element (iii) was instrumented with both VW and electrical resistance gauges, partly at Oran Precast's premises and partly on the NEB site.

Novel technologies such as fibre-optic sensors and Tensiomag® - for use with prestressing tendons - were explored, but were not feasible in this instance for reasons of time and budget. It is envisaged that additional instrumentation (e.g. accelerometers, inclinometers) will be installed later in the programme to measure aspects of performance in use.

The transfer beam contains 52 VW gauges distributed over 7 sections, five of which are grouped around a concentrated load near midspan, while the other two are near the supports (Figure 4). Most sections contain six gauges - two at top, middle and bottom - but two of the sections contain eleven gauges with the intention of extracting fuller detail regarding strain and temperature variation within the beam. This 970*1200 deep beam is located over one of the main lecture theatres and, given its large mass, its role in the heating and cooling of the space will be of interest.

The double-tee (Figure 5) contains 39 gauges in all - 13 at each of 3 sections. The narrowness of the rib and the arrangement of prestressing strand meant that only one gauge could be placed at any given height within the rib, but there is mirroring of provision between ribs. Nine gauges are arranged across the flange, with the aim of picking up possible variations in compressive strain across the flange, associated with shear lag (Moffatt & Dowling,1975).

Only basic details of the Cobiax units are provided in this paper.

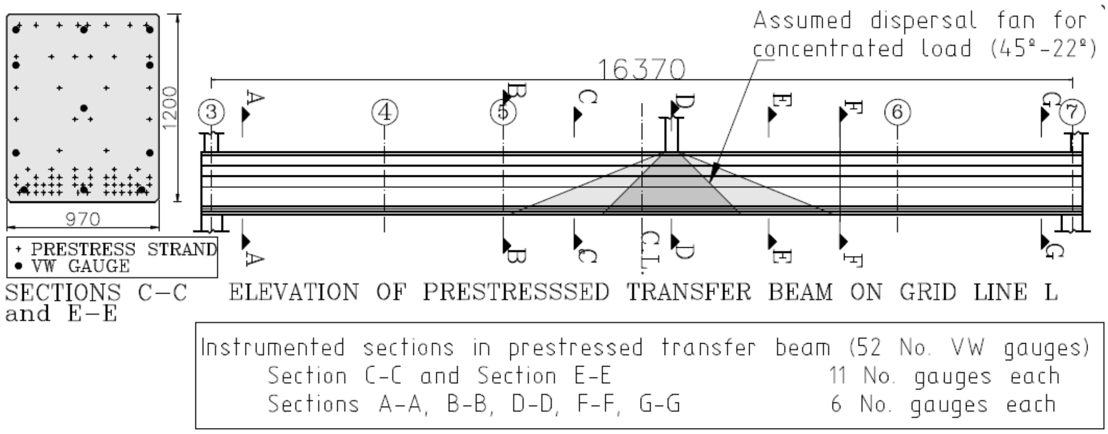

Figure 4 – Instrumentation of the prestressed transfer beam

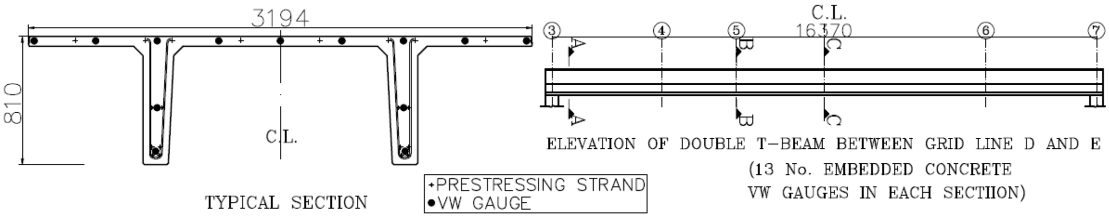

Figure 5 – Instrumentation of the precast double tee unit

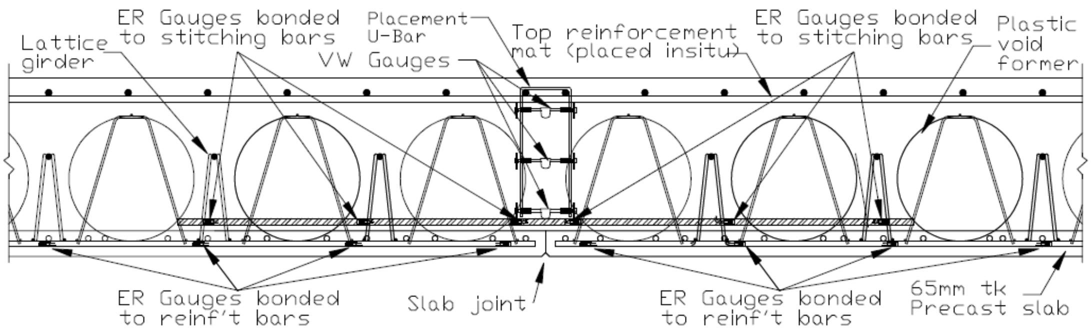

Figure 6 – Typical section of instrumentation in the void-formed flat slab system

3.3 Vibrating-wire gauges

The gauges incorporated in the transfer beam and the double-tee beam are vibrating wire strain and temperature gauges manufactured by Gage Technique, chosen for their robustness and reliability. They are of a type developed originally by the Transport and Road Research Laboratory (TRRL) in the UK (Figure 7) (Tyler, 1968). Vibrating-wire gauges have been extensively used in bridge and tunnelling projects (Tyler, 1973, Mortlock, 1974, Barr et al., 1987, O'Byrne, 1988, Cannon & O'Byrne, 2003). Their long term stability makes them suitable for measuring time dependent phenomena such as creep and shrinkage. Discussions with a specialist structural testing consultant regarding the range of sensor types currently available confirmed the continuing suitability of VW gauges for this task.

The gauge consists of a thin hollow tube of steel with circular flanges at each end. A piano wire inside the tube is stretched between two anchorage points at the ends. A change in the distance between the anchorage points causes a strain change in the wire and a corresponding change in its frequency of vibration. An electromagnet at the centre both plucks the wire and transmits the frequency of vibration of the wire to the recording device, which measures the period for 100 cycles of wire vibration. The gauge is usually operated within the range 500-1000Hz which is equivalent to a range of 2250 microstrain. A 5.5 inch gauge operating at 800 Hz is reported by the manufacturers as having a practical measuring resolution of 1.5 microstrain.

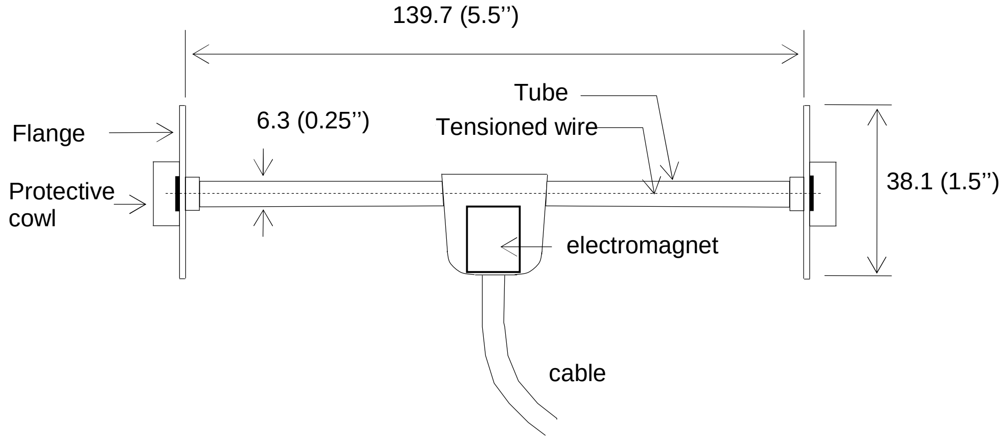

Figure 7 – Vibrating wire gauge.

Figure 8 – Vibrating wire gauges installed in void-formed flat slab in NEB

3.4 Electrical resistance gauges

Electrical resistance gauges (Tokyo Sokki Kenkyujo model FLA-6-120-11-3LT) were used to determine the stresses in reinforcing bars embedded in the Cobiax slabs. These gauges were installed on reinforcing bars in the Civil Engineering laboratory at NUIG at room temperature conditions. The reinforcing bar surface was prepared by removing thee ribs on the bars over a length of 25mm using a milling machine. The gauge was bonded to the bar using P2 TML strain gauge adhesive. A clamp was applied to the gauge and the adhesive was left to dry overnight, after which a VM waterproof tape was applied to protect from moisture and chemicals within the concrete. The reported operational life of the strain gauges and adhesive is a minimum of 30 years. All the gauges were tested in the laboratory before installing the bars on site. The gauges had 3m of 3-wire 0.11mm lead wire pre-connected; up to 15m lengths of 3-wire 0.5mm lead wires were used to connect these to the data acquisition system. The lead wires were installed inside plastic ducting within the concrete.

3.5 Data acquisition system

Campbell Scientific data acquisition system is used to acquire data from both types of gauge. The system for the pre-tensioned beams consists of a Campbell Scientific CR1000 datalogger. This is capable of controlling up to 128 VW gauges or 256 electrical resistance gauges through a series of AM16/32B multiplexers (up to 8 No. off, each capable of controlling up to 16 VW gauges or 32 electrical resistance gauges). In the case of VW gauges, a vibrating wire interface (AVW216) is required for each pair of multiplexers.

3.6 Installation

Installation of VW gauges is a laborious process which has to be fitted in around the work of joiners, steelfixers and general site operatives in preparation for pouring. The time required for installation will limit the scope of the instrumentation project unless the client is prepared for delays which will otherwise occur.

Survival of gauges and cabling is a concern before, during and after pouring. Where possible, cabling was bundled into PVC ducting within the element, and care taken where they emerged from the concrete. In the case of the transfer beam, poker vibrators represented a potential hazard to gauges and cabling, but due to the care taken by Banagher Concrete there was no disablement of gauges on this score. Formwork for the double-tee beam had external vibrators, which presented no risk.

4. Preliminary results

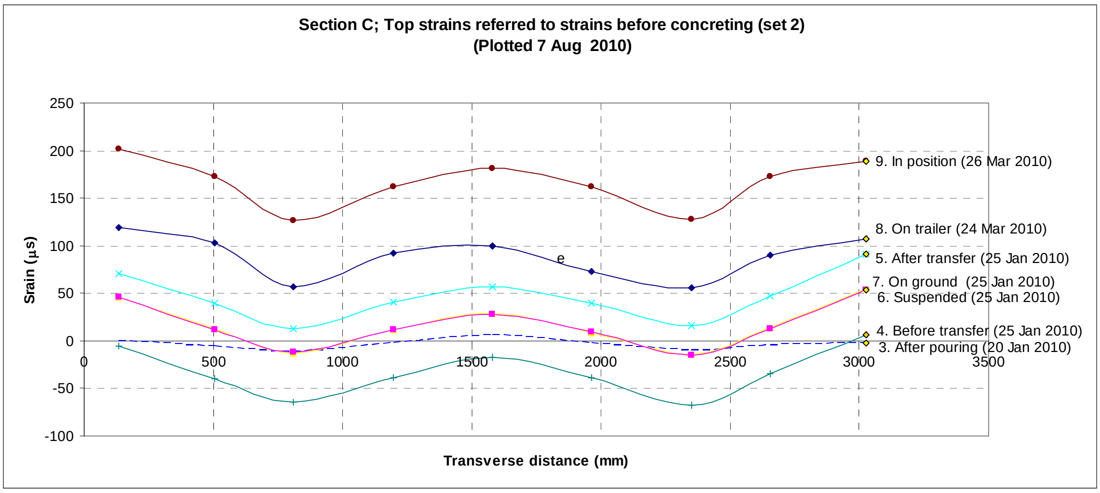

Figure 9. Changes in strain in top slab of double-tee at various dates.

Figure 9 shows strains in the top flange of the double-tee at various times in the first two months after casting. These are referred to a set of readings taken immediately prior to casting on Jan 20th, 2010 (Set No. 2). A set of readings was taken just after concreting, and four sets were taken on Jan 25th, the day on which prestressing transfer occurred and on which the element was lifted from its formwork. Ambient

temperature on this day varied between 1.6°C and 3.1°C. Two further readings were taken two months later, one immediately prior to and the other just after placement of the double-tee in its final position.
No detailed analysis has as yet been carried out of these results, but notable features are:

(i) consistency in the variation of strain across the flange;
(ii) little strain change associated with pouring (broken line; Set No. 3);
(iii) development of tension across slab in the 5 days prior to transfer ((bottom line; Set No. 4). There are a large number of factors at play in this period, including significant changes in concrete temperature associated with heat of hydration; variations in ambient temperature; initial shrinkage, with different rates of development in ribs and flange, restraint from prestressing strand and the possibility of a degree of restraint from formwork. The lateral variation in strain – similar to shear lag – increases with distance from formwork. Further study is required of this phase;
(iv) relatively uniform increase in compression across the section at transfer (Set No. 5). There was a nett upward deflection at midspan at this juncture, indicating that the element was transferring from being continuously supported along its length to being supported at its ends;
(v) a reduction in compression when the element was lifted out of the shutters, associated with a reduction in the effective span (Set No. 6);
(vi) virtually identical strains a short time later when the element was lowered onto timber baulks on the ground, located in proximity of the lifting points (Set. No. 7);
(vii) a marked increase in compressive strain in the two months to March 24^{th}, associated with early creep and shrinkage. These readings were taken when the double-tee was loaded onto a trailer prior to delivery to site and supported on timbers (Set No. 8);
(viii) a further increase in compressive strain two days later when the element was lowered into position and end supported (Set No. 9).

Figure 10 shows the variation in strain for all six gauges in the bottoms of webs i.e. at midspan, quarter point and near ends, for the dates mentioned above and referred to dataset No. 2 as before. The time scale is distorted; reading sets 1-3 occur on the same day (set 1 being a partial set relating to web gauges only and taken 3 hours before set 2), reading sets 4-7 occur 5 days later, and sets 8,9 occur two months later. Drawn to scale, the slope from 7 to 8 would be very much flatter than 4-5. Points worthy of note are:

(i) changes in compressive strain are considerably greater than for the flange;.
(ii) readings are highly consistent, notwithstanding the fact that bending moments at the three sections are different, with the greatest changes being noted between sets 8 and 9, when the element was lifted into its final position on site;
(iii) as occurred with flanges, there was little strain change registered for the webs at any of the sections as a result of concreting (sets 2-3);
(iv) there is some tensile strain developed in the webs over the 5 days prior to transfer (3-4);

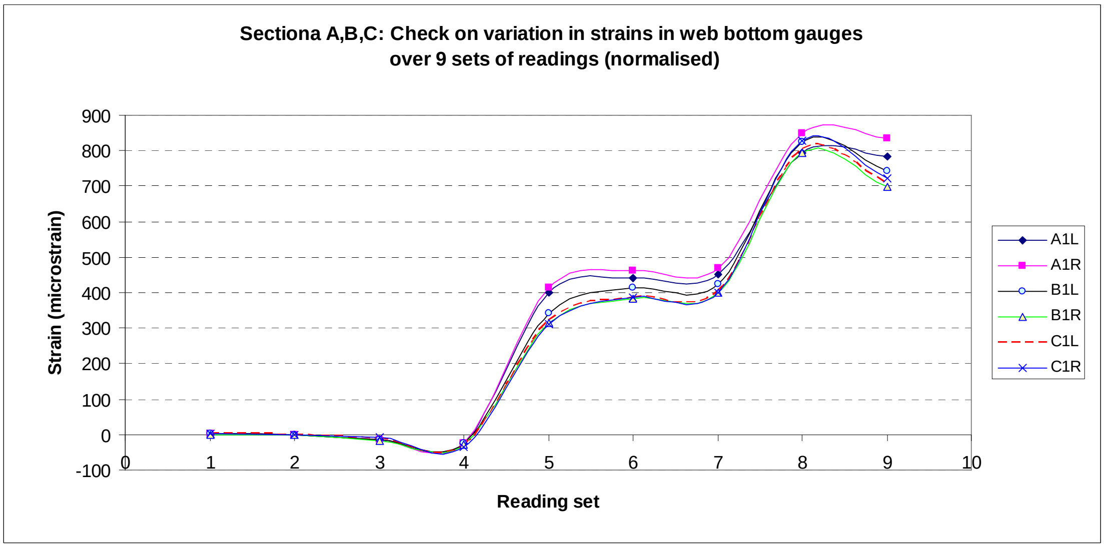

Figure 10. Variation in strain in gauges at bottoms of webs over initial two months.

(v) there is a significant development in compressive strain due to transfer of prestress, notwithstanding that the double-tee assumed its own self-weight loading at this juncture (4-5);

(vi) minor changes in strain resulting from suspension in mid-air (5-6) and lowering onto timber baulks on the ground(6-7);

(vii) significant changes in strain in the following two months, due to creep and shrinkage (7-8). There would not be a corresponding change in concrete stresses;

(viii) a reduction in compressive strain due to the element becoming end-supported on site (8-9).

5. Conclusions

The objective of the project was to instrument several elements in the New Engineering Building so as to provide useful insight into the real time-varying behaviour of concrete structures, for the benefit of undergraduate students and post-graduate researchers. It is considered that the proximity of the instrumented elements to lecturing spaces will confer a degree of immediacy on discussions of structural behaviour and energy performance, encouraging students to actively engage with the underlying engineering issues.

The period to date has been concerned with the completion of the instrumentation scheme, most recently for the Cobiax slab units, as and when the contractor's programme permitted. Instrumentation of the three structural members described in paragraph 3.2 is now complete, and datasets gathered laboriously on Gage Technique's manual data logger have been replaced by frequent and extensive datasets collected on Campbell Scientific dataloggers. Various load tests have been carried out since their installation, and will be reported on later. Whilst analysis of results is at a preliminary stage, results to date display an encouraging level of consistency. Much interesting work remains to be done by way of analysis and ancillary testing before the potential benefits of this project are realised.

Video and photographic records of the process of construction, installation and testing will be of continuing benefit in the education of future engineers in the New Engineering Building at NUI, Galway.

6. Acknowledgements

This support of the New Engineering Building committee, the buildings office and members of the College of Engineering & Informatics (Energy Management Group and Building Structures Group) is gratefully acknowledged. Consultants ARUP and RMJM facilitated us at various stages. The success of a project of this nature is crucially dependent on the cooperation of people on site; in this respect we were most fortunate in relation to the main contractor, BAM Building, subcontractors Banagher Concrete and Oran Precast, and the resident engineer, who facilitated us throughout. The Civil Engineering technicians and postgraduate students at NUI, Galway played major parts in bringing this project to its present state.

References

Barr, B., Waldron, P., Evans, H.R. (1987) 'Instrumentation of glued segmental box girder bridges', *Proceedings IABSE Colloquium, Bergamo*, 1987, Monitoring of large structures and assessment of their safety.

Cannon, E., O'Byrne, C. (2003) 'In-situ instrumentation of concrete structures: a case study'. *Proceedings, Colloquium on Concrete Research in Ireland,* Queen's University, Belfast, 2003

Cannon, E., Goggins, J. (2009) 'Teaching tools – Instrumentation of New Engineering Building – Structural Engineering'. *Internal report*, College of Engineering & Informatics, NUI, Galway, 1 December 2009.

Moffat, K.R., Dowling, P.J. (1975) 'Shear lag in steel box girder bridges'. *The Structural Engineer*, Oct 1975 pp. 439-448 (+ discussion Aug 1976 pp. 285-298)

Mortlock, J. D. (1974) *The instrumentation of bridges for the measurement of temperature and movement*. T.R.R.L. Report LR641, 1974

NUI Galway (2010) *New building*, http://www.nuigalway.ie/civileng/New_Building.html (28th April 2010).

O'Byrne, C. (1988) *The monitoring of strain in a prestressed concrete bridge of box girder construction.* MEngSc thesis, NUI, Galway, 1988

RMJM (2008) '*Teaching Tools'*. Project report, RMJM Architects, Edinburgh, July 2008.

Tyler, R.G. (1968) *Developments in the measurement of strain and stress in concrete bridge structures*. R.R.L. Report LR189, 1968

Tyler, R.G. (1973) *Long term strains in the Medway Bridge*. T.R.R.L. Report LR539, 1973.

THE PERFORMANCE OF LIMESTONE CEMENTS WITH GGBS EXPOSED TO ELEVATED SULFATE ENVIRONMENTS

M. O'CONNELL, C. McNALLY & M.G. RICHARDSON
School of Architecture, Landscape and Civil Engineering, University College Dublin, Ireland

Secondary cementitious materials (SCMs) such as GGBS are being used in increasing quantities as a cement replacement and when used have been shown to possess an inherent sulfate resisting capability. Cements in Ireland have traditionally been supplied as CEM I but in recent years a shift in Irish concrete practice has led to the introduction of CEM II/A-L limestone cement as the primary cement available in this country. While the benefit of a reduced CO_2 footprint through a reduced quantity of clinker has obvious environmental benefits, the change in cement chemistry must be urgently accounted for in concrete specification. This has particular importance when concrete is exposed to chemically aggressive conditions such as elevated sulfate environments.

In an attempt to evaluate the sulfate performance of CEM II/A-L cements with varying amounts of GGBS, twenty-four mortar prisms representing six different binder combinations were prepared and tested according to a modified ASTM C1012 method. Two of these sets consisted of a CEM I cement with 0% and 70% GGBS, three consisted of a CEM II/A-L cement with 0%, 50% and 70% GGBS as a cement replacement and the performance of a commonly used SRPC cement was also evaluated as a reference material.

Results show that for exposure in excess of one year to a 50g/l sodium sulfate (Na_2SO_4) solution the expansion of all specimens containing GGBS, irrespective of the cement used, was minimal and outperformed the SRPC reference cement. The results also show that CEM II/A-L cement appears to have an inherent sulfate-resisting capability and that this is further improved with the use of at least 50% GGBS as a cement replacement. The use of CEM II/A-L in the test programme showed an overall improved performance over specimens containing CEM I.

Keywords: GGBS, sulfate, limestone cement

1. Introduction

With concrete specifications in Ireland having recently shifted from CEM I to CEM II standard, a lack of data exists regarding the performance of GGBS and limestone cements in aggressive sulfate environments. A comparative analysis was carried out using a modified ASTM C1012 sulfate exposure test to examine the behaviour of these materials with sulfate-resisting cement used as a performance benchmark. Further analysis indicated that the diffusion of sulfate ions may form a key part of the degradation mechanism and that CEM II limestone cements may in fact possess an inherent sulfate resisting capability when compared CEM I cements. With GGBS also known to possess similar properties, the investigation attempts to confirm that CEM II with levels of GGBS greater that 50% can equal or exceed the performance of sulfate resisting cement.

2. Experimental programme

Mortar prisms of dimensions 285mm x 25mm x 25mm were prepared with a mix according to EN 196-1 standard. Each mix contained 450g of binder, 1350g of CEN-Normsand (DIN EN 196-1) and 225g of water and produced four prisms. The specimens were placed in a moist air cabinet at 20°C and demoulded after twenty-four hours. Following this they were then placed in a water bath at the same temperature and allowed to cure until twenty-eight days had elapsed. A modified ASTM C1012 standard was used to test the mortar prisms for change of length when exposed to a sulfate solution. The standard exposure solution used in this test method contains 50g of sodium sulfate (Na_2SO_4) per litre of distilled water. Each litre of the solution was prepared with 900ml of distilled water and mechanically stirred until fully dissolved. The solution was then topped up with distilled water until a volume of 1l was achieved. It was then placed into a standard domestic polyethylene container ensuring the quantity was sufficient to cover the prisms by a minimum of 5mm. The prisms were stored for in excess of one year with the solution refreshed on a monthly basis. Measurements were taken every four weeks. The readings consisted of taking an initial reference measurement for each prism and a standard reference bar prior to submersion in the sulfate solution then comparing them with readings of both the reference bar and mortar prism at the designated time intervals. The change of length of the prism from the initial reading is then calculated according to:

$$\Delta L = \frac{L_x - L_i}{L_g} \times 100 \tag{1}$$

ΔL = length change age 'x' (%); $\mathbf{L_x}$ = specimen comparator reading age 'x' – ref. bar comparator reading at age 'x'; $\mathbf{L_i}$ = initial comparator reading of specimen – ref. bar comparator reading at the same time; $\mathbf{L_g}$ = nominal gauge length (250mm used). The percentage change of length of each prism was measured to an accuracy of 0.001% and the average of the four test specimens was recorded.

Table 1 - Mortar mix designations

MA	MB	MC	MD	ME	SR
(CEM II)	(CEMII+50% GGBS)	(CEMII+70% GGBS)	(CEM I)	(CEMI+70% GGBS)	(SRPC)

3. Experimental results

Expansions were obtained for a 420-day period for all six mixes while measurements exist for some up to 532 days (Figure 1). There were some marked differences in visual deterioration of the mixes varying from corrosion related deposits and discoloration to cracking and warping of the specimens, or a combination of both. The severity of the visual deterioration corresponds well to the degree of expansion observed. With regard to the two most expansive mixes, both MA and MD can be seen to have some similarities but also some differences in the way they began to degrade. Common to both were the formation of longitudinal cracks along the length of the specimens as the first form of physical deterioration (Figure 2). For mix MD these became visible at approximately 140 days exposure and at 286 days for mix MA. With the latter however, this manifested initially in the form of the cracks being filled with a white substance (Figure 2).

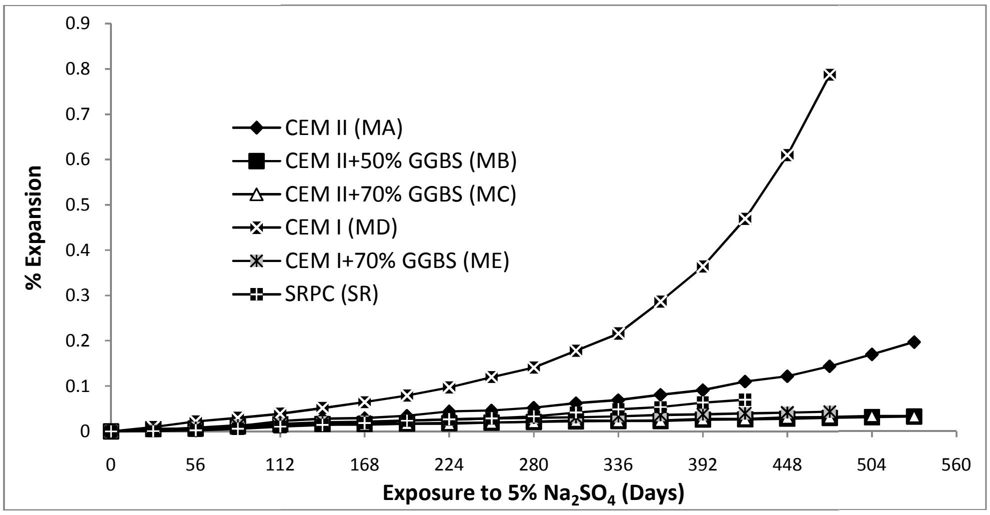

Figure 1 - Sulfate expansion tests

Longitudinal cracking along the length of the specimens was not an exclusive mechanism with radial cracking observed on one of the MA specimens along the boundary of the reference stud (Figure 3). One of the other visual distinctions between MA and MD were notable deposits of a white substance occurring in blotches at random intervals on one of the prisms which can also be seen in Figure 3. These deposits seemed to be an integral part of the paste and were not soft to touch, nor had they the ability to be removed by scratching the surface. Generally however, the appearance of white deposits was less locally concentrated than in Figure 3 and consisted primarily of an intermittent speckled pattern throughout the prisms. This was applicable to all specimens and mixes after one year except those containing 70% GGBS as a cement replacement. The cracking of the mortar prisms appears to commence when approaching an expansion threshold of 0.030 - 0.035% (≈ 0.045% for MA, MD) and the observation has proven true for all specimens approaching this value. This phenomenon continued to progress culminating in a total loss of cohesion and when touched, the prism corners crumbled with ease. This extreme case has thus far only applied to mix MD with expansion readings 300% of the next most expansive mix (MA) after one year. At approximately 0.3% expansion (t = 12 months), the specimens of MD were observed becoming warped, slowly taking a 'banana' shape with the first cracks perpendicular to the surface appearing (Figure 4).

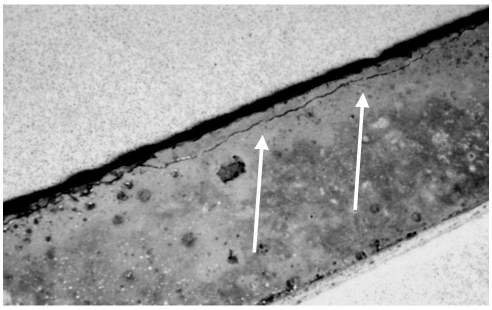

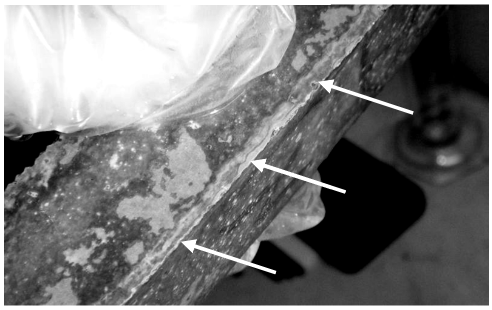

Figure 2 - Cracks visible along the edges of specimens (left), white-filled (right)

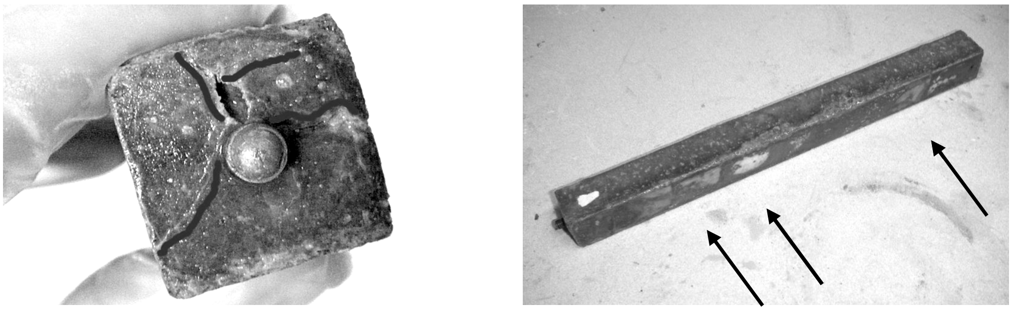

Figure 3 - Radial cracking [enhanced in photo] around the reference studs (left) and white blotches appearing on the surface of the prism (right)

Visually, both mixes MA and MD appear to have suffered the most. Cracking and spalling was widespread after one year for both with white deposits seemingly a prominent feature for the attack on MA while MD exhibited almost exponential expansion. Mixes MB and MC, the CEM II limestone cements with 50% and 70% GGBS respectively, have shown comparatively little expansion. MB has shown some minor discoloration while MC has shown no visual evidence of attack. The sulfate resisting cement specimens (SR) have been outperformed by all mortars containing GGBS either with CEM I or CEM II after one year. Visually it has begun to exhibit the same common degradation phenomenon when approaching the 0.030% – 0.035% expansion threshold, namely cracking, some minor spalling and a white speckled appearance (the latter, however, generally beginning to appear within eight weeks).

4. Effect of the addition of limestone

The results have indicated that the CEM II limestone cement, as used here, appears to possess an inherent sulfate-resisting capability relative to CEM I cement. The recorded expansion readings are still very high but can be reduced further by the addition of 50% or 70% GGBS as a cement replacement. Existing research on the effect of limestone additions to cement has indicated wide-ranging consequences varying from beneficial to detrimental impacts on performance (González and Irassar, 1998, Irassar et al., 2000). Nonetheless a common conclusion seems to centre on an upper limit of limestone additions that provide an improved resistance and this seems to vary between 15% and 20% (Ramezanianpour et al., 2009, Irassar et al., 2005). This varying behaviour has been attributed to several possibilities amongst which are: the dilution effect of cement constituents, the influence of the level of C_3A on the system and the level of calcium hydroxide (CH) in the hydrated cement paste. There are clearly other issues regarding the reaction of limestone with both the cement paste and sulfate ions. Further consequences of its addition surround its effect on permeability, porosity and tortuosity and these are all topics that have been discussed by several authors (Hornain et al., 1995, Tsivilis et al., 2003, Pipilikaki et al., 2009). In the context of these parameters it should also be noted that the effective w/c ratio also increases with an increasing percentage of limestone used which can be attributed to its lack of pozzolanic properties (hence it cannot be considered a cementitious material).

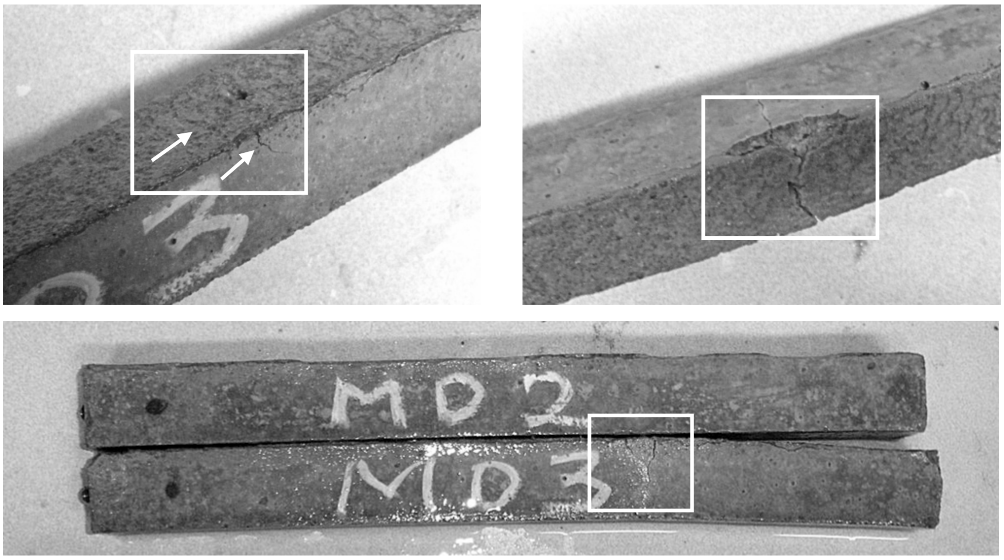

Figure 4 - Perpendicular crack propagation in mix MD. Top left shows onset.

According to Gonzalez and Irassar (1998), the capillary porosity depends not only on the w/c ratio but also the hydration degree and thus this affects the overall porosity of the cement. Tsivilis et al. (2003) showed that a Portland limestone cement exhibited lower water permeability values when compared to an ordinary Portland cement; they added however that permeability is not simply a function of porosity but also of the size, distribution, shape, tortuosity, and continuity of the pores. Their tests were carried out on specimens that contained a range of between 0% and 35% limestone. Pipilikaki et al. (2009) however conducted tests that showed Portland limestone cement containing 35% limestone had a higher porosity than an ordinary Portland cement. The authors then suggested that this may indicate a higher permeability and in turn contradict the findings of Tsivilis et al. (2003). They make the observation however, that CEM II limestone cements have an absence of large capillaries relative to CEM I which may delay the ingress of sulfates and lower initial expansion but stress that the mechanism by which limestone affects the sulfate resistance of cement is far from being well understood.

Portland limestone cements suffer similar chemical reactions from a traditional sulfate attack as ordinary Portland cements resulting primarily in the formation of gypsum and ettringite. The formation of thaumasite may also be of concern given the high level of carbonate in the system. According to Gonzalez and Irassar (1998), during cement hydration carbonate ions from the limestone compete with sulfate ions from gypsum to react with aluminate ions from C_3A forming monocarboaluminate, monosulfoaluminate and ettringite. Irassar et al. (2003) detailed the sequence of a sulfate attack concluding that diffusion of sulfate ions is followed by calcium hydroxide leaching, ettringite formation, gypsum formation and depletion of CH. The latter stages involve the decalcification of C-S-H followed by thaumasite formation. As observed with CEM II limestone mix MA some of these assumptions may be applicable. There was an initial low level expansion detected with very little visual deterioration which could indicate the onset of ettringite or early gypsum formation. As the attack progressed white deposits began forming on the exterior of each prism, followed by a lack of cohesion and spalling at the edges, possibly indicating the decalcification of the C-S-H phase. Irassar et al. (2003) also describe corrosion of edges and corners and attribute it to gypsum formation in parallel veins to the sulfate attack front. As apparent in Figure 2, cracks/veins with a white deposit can be observed around the elapsed exposure time when the specimen began to shed some minor mortar particles.

5. Sulfate resisting capabilities of GGBS

In examining the results of the experimental programme, it is clear that the addition of a relatively high percentage of GGBS to both CEM I and CEM II mortars has had a profound effect on their resistance to a 5% sodium sulfate solution. Both the CEM II mortars (MB and MC) have shown the least amount of expansion and visual deterioration while the CEMI I mortar with 70% GGBS (ME) has shown a resistance equalling SRPC for the majority of the exposure period but eventually exceeding it. The sulfate resisting capabilities of GGBS have been discussed on many occasions (BRE, 2003, Higgins and Crammond, 2003) with much of the benefit being attributed to a denser matrix, decreased permeability and a reduction in calcium hydroxide present in the hydrated system (Pavía and Condren, 2008, Al-Dulaijan et al., 2003, Osborne, 1999). Furthermore, with the formation of a secondary C-S-H phase attributable to the interaction between calcium hydroxide and GGBS, much of the alumina in the system becomes ‘locked up’ in this product and is not available to form ettringite during a sulfate attack (Gollop and Taylor, 1996). The author’s also claim that as the percentage replacement of cement with GGBS increases the proportion which reacts decreases and this limits the quantity of alumina released at high slag contents.

The combination of a reduction in calcium hydroxide, decreased permeability and the ‘locking up’ of potentially reactive alumina may account for the behaviour of the CEM I mortars but it is essential to investigate any further effects of CEM II cements with a limestone addition. The results presented above have indicated the potential increased benefit of using this with at least 50% GGBS as a cement replacement. As previously discussed, CEM II limestone cements have an absence of large capillaries relative to CEM I which may delay the ingress of sulfates (Pipilikaki et al., 2009). When combining this with the more impermeable matrix from GGBS cements, the opportunity for sulfates to interact with the cement compounds is being severely limited. Visually, all specimens containing GGBS have exhibited almost no evidence of a lack of cohesion from exposure to the sulfate solution. Researchers (Brown and Taylor, 1999) have attempted to account for this effect in limestone cements and have put forward a plausible explanation. With an increase in GGBS levels, there is also an increase in hydrated C-S-H in the system. Correspondingly, there is a decrease in the level of calcium hydroxide. Ettringite and gypsum preferentially obtain their calcium from this phase but in the absence of a sufficient quantity available, calcium from the C-S-H phase will serve as a source. This phase constitutes the primary binding capability of a cement matrix and its degradation leads to a major loss in cohesion. The author’s claim that by adding calcium carbonate (limestone) as an additive, this in turn will serve as the source of calcium for ettringite and gypsum thus preserving the integrity of the C-S-H phase.

6. Analysis of sulfate deterioration

It has been observed that many concrete degradation mechanisms (i.e. carbonation, diffusion and chloride phenomena) have a time$^{0.5}$ dependency (Richardson, 2002), thus by applying a similar approach to the obtained expansion data it can be seen that there is a strong proportional relationship between expansion of the mortar prisms and time$^{0.5}$ (Figure 5). It may be claimed that simply plotting against time alone also produces a direct relationship, however by doing so one misses out on an important observation. Of the specimens that have exceeded an expansion of 0.05% or more (MA, MD, SR), there appears to be a divergence from the time$^{0.5}$ proportionality at that point, as illustrated by Figure 5(r), coinciding with the onset of parallel cracking on the prisms surfaces. When simply plotted against time alone however, they merely continue to show a gradual expansion without any apparent differentiation in the curves.

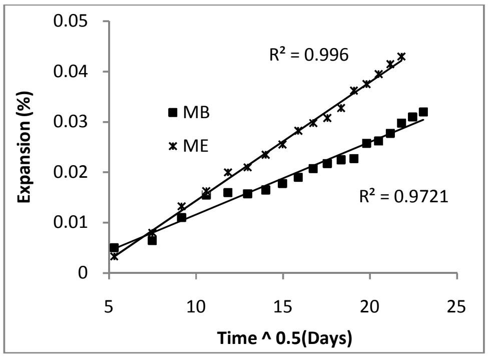

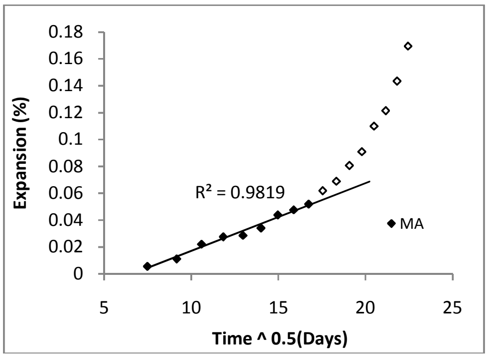

Figure 5 – Time$^{0.5}$ dependencies; deviations begin around expansions of 0.05% (right)

This figure of 0.05% may have significance in that it represents both the six month exposure limit for severe sulfate attack (>10g/l) as determined by the American Concrete Institute (ACI) for ASTM C1012 and the sixth month expansion limit for high sulfate resistance of Portland/slag combination cements as laid out in ASTM C989-06. The other three mortar mixes (MB, MC and ME) have not yet reached the 0.05% threshold and as such are still exhibiting a direct proportionality to time$^{0.5}$ Figure 5(l). Of the mixes that have reached the level of expansion following which a divergence from time$^{0.5}$ dependency is observed, there is clearly a common sequence of corrosion events. Given the time required to observe each specimen to failure in its entirety may require several years, one may hypothesise a sequence of events common to some, if not all, mixes based on those prisms in an advanced stage of corrosion. The degradation process appears to follow four distinct phases: **Stage 1**: A direct proportionality between expansion and time$^{0.5}$ during which no cracking is visible, some surface blemishing may be apparent; **Stage 2**: This stage may represent a transition zone between 0.035% and 0.05% where some longitudinal crack propagation may be observed and the specimen may or may not continue to exhibit a time$^{0.5}$ dependency; **Stage 3**: Expansion>0.05%, divergence from time$^{0.5}$ dependency is observed and longitudinal crack propagation becomes more widespread. Radial cracking may also begin slightly before or after the 0.05% level; **Stage 4**: Expansion ≈ 0.3%, the specimen begins to warp, extensive longitudinal cracking is visible and bulging around the reference studs reaches a critical level. Perpendicular cracking may also become visible. While this sequence of events may be relevant for the non-GGBS specimens (as these are the most advanced stage samples), those that do contain GGBS cannot be assumed to perform in a similar behavior although expansions and observations made to date do not suggest that this will be the case.

7. Conclusions

- The results confirm the CEM II-A/L limestone cement used in this analysis (with limestone additions not exceeding 7%) appears to possess an inherent sulfate-resisting capability relative to CEM I cement. Limestone additions exceeding 15% however, may not be beneficial.
- The inclusion of at least 50% GGBS as a cement replacement further enhances the sulfate resistance of both CEM I and CEM II cements.
- The expansion of specimens up to 0.05% appears to be dependent on time$^{0.5}$. This may confirm that diffusion [of sulfate ions] initially governs the degradation process. Subsequent expansion may depend on the extent of surface cracking and degree of corrosion products formed.

References

Al-Dulaijan, SU, Maslehuddin, M, Al-Zahrani, MM, Sharif, AM, Shameem, M & Ibrahim, M (2003) Sulfate resistance of plain and blended cements exposed to varying concentrations of sodium sulfate. *Cement and Concrete Composites,* **25,** 429-437.

BRE (2003) BRE Special Digest 1, Concrete In Aggressive Ground. . *Part 1: Assessing the Aggressive Chemical Environment.* 2nd Ed, BRE Ltd.

Brown, PW & Taylor, HFW (1999) The role of ettringite in external sulfate attack. In: Marchand, J. & Skalny, J. (Eds.) *Proc. Seminar Sulfate Attack Mechanisms.* Quebec.

Gollop, RS & Taylor, HFW (1996) Microstructural and microanalytical studies of sulfate attack: Comparison of different slag blends. *Cement and Concrete Research,* **26,** 1029-1044.

González, MA & Irassar, EF (1998) Effect of limestone filler on the sulfate resistance of low C3A Portland cement. *Cement and Concrete Research,* **28,** 1655-1667.

Higgins, DD & Crammond, NJ (2003) Resistance of concrete containing GGBS to the thaumasite form of sulfate attack. *Cement and Concrete Composites,* **25,** 921-929.

Hornain, H, Marchand, J, Duhot, V & Moranville-Regourd, M (1995) Diffusion of chloride ions in limestone filler blended cement pastes and mortars. *Cement and Concrete Research,* **25,** 1667-1678.

Irassar, EF, Bonavetti, VL, Trezza, MA & González, MA (2005) Thaumasite formation in limestone filler cements exposed to sodium sulphate solution at 20°C. *Cement and Concrete Composites,* **27,** 77-84.

Irassar, EF, González, M & Rahhal, V (2000) Sulfate resistance of type V cements with limestone filler and Pozzolana. *Cement and Concrete Composites,* **22,** 361-368.

Osborne, GJ (1999) Durability of Portland blast-furnace slag cement concrete. *Cement and Concrete Composites,* **21,** 11-21.

Pavía, S & Condren, E (2008) Study of the durability of OPC vs GGBS concrete on exposure to silage effluent. *Journal of Materials in Civil Engineering,* **20,** 313-320.

Pipilikaki, P, Katsioti, M & Gallias, JL (2009) Performance of limestone cement mortars in high sulfate environment. *Construction Building Materials,* **23,** 1042-1049.

Ramezanianpour, AA, Ghiasvand, E, Nickseresht, I, Mahdikhani, M & Moodi, F (2009) Influence of various amounts of limestone powder on performance of Portland limestone cement concretes. *Cement and Concrete Composites,* **31,** 715-720.

Richardson, MG (2002) *Fundamentals of Durable Reinforced Concrete,* London, Spon Press.

Tsivilis, S, Tsantilas, J, Kakali, G, Chaniotakis, E & Sakellariou, A (2003) The permeability of Portland limestone cement concrete. *Cement and Concrete Research,* **33,** 1465-1471.

DEVELOPMENT OF A NEW MARINE EXPOSURE SITE ON THE ATLANTIC NORTH-WEST COAST OF IRELAND

N. HOLMES[1], L. BASHEER[1], S. NANUKUTTAN[1], S. SRINIVASAN[1], PAM BASHEER[1], J. MCCARTER[2] & M. CHRISP[2]

[1] School of Planning, Architecture and Civil Engineering, Queen's University of Belfast, Northern Ireland

[2] School of the Built Environment, Heriot-Watt University, Edinburgh, Scotland

Abstract

This paper presents a new marine exposure site being developed on the North-west Atlantic coastline of Ireland in Co. Donegal by the Centre for Built Environment Research at Queen's University Belfast. The site will initially contain a number of large precast concrete stems, each 1.5m high, 1.5m wide and 1m thick placed on concrete plinths poured in-situ. The concrete stems will be placed at three levels to achieve different exposure conditions outlined in EN 206, namely atmospheric (XS1), a splash or spray zone (XS3) and a tidal zone (XS3) where the stems will be submerged by the incoming tide twice daily.

The concrete will consist of different cements and appropriate w/b ratios suitable for this type of exposure. The permeability and diffusion properties will be measured using non-destructive tests developed at Queen's University Belfast, namely the Autoclam permeability system and the Permit ion migration test. Other tests to measure the corrosion of the embedded rebar will also be undertaken. In order to monitor the internal concrete properties, electrical sensors will be attached to the rebar and embedded in concrete. The information from these sensors will be relayed back to the office using remote wireless technology.

Such integrated monitoring systems for concrete structures can reduce assessment and repair costs by continuously profiling the covercrete and corrosion for the ingress of various deleterious substances, such as chlorides, in the reinforcing steel in real-time. This approach permits an informed assessment of the performance of the structure throughout its service life. This site will form part of a world-wide exposure study, including similar sites in Scotland, India and China.

Keywords: Exposure Site, EN 206, corrosion, sensors, covercrete, durability

1. Introduction

The introduction of EN 206 (BS EN 206, 2000) now permits concrete to be specified in terms of its performance depending on the environment to which it will be exposed. For a concrete structure in or near to the sea, the exposure class in EN 206 which is relevant is XS; corrosion induced by chlorides from sea water. This exposure class is sub-divided into 3 different sub-classes namely, XS1, XS2 and XS3. These exposures define if the concrete will be exposed to airborne salts, but not in direct contact with sea water (XS1), concrete which will be permanently submerged (XS2) and concrete which will be within a tidal zone or subject to sea water splash or spray (XS3).

It will now be possible to specify concrete both by the historic prescriptive approach (strength, cement quantity, w/c ratio) and/or by its performance in the field, for instance, in terms of an assigned air permeability, absorption rate or chloride diffusivity rate. The concrete must then meet this specification before it is deemed acceptable. Work is currently underway at QUB, in conjunction with Heriot-Watt University (Edinburgh), as part of a EPSRC funded project, to assess if common testing methods are suitable to determine if these specifications/limits have been achieved (Nanukuttan, 2009; Nanukuttan, 2010).

BS 8500 (2006) has prepared prescriptive guidelines, depending on the exposure type, for concrete which, for a particular cover depth, suggests suitable w/c ratios, cement contents (kg/m^3) and strength (N/mm^2). This publication also provides guidelines on which cement type within EN 197 (BS EN 197, 2000) would be appropriate. For instance, for a structure with an intended working life of 50 years, in exposure type XS3, with a cover of 40 + Δc, BS 8500 recommends a minimum strength of C35/45, a maximum w/c ratio of 0.40 and a minimum cement content of 380kg/m^3. BS 8500 also suggests that cement types CEM II/B-V, CEM III/A, CEM III/B and CEM IV/B-V (EN 197, 2000) would be suitable. However, there is little available data on suitable performance specifications for this, or any other exposure type. The Association Francaise de Genie Civil (AFGC, 2007) has published examples of engineering projects where, along with prescriptive specifications, the concrete has been assigned performance-based guidelines for durability. For example, the Channel-Tunnel project assigned a water permeability for some of the concrete of $<10^{-13}$ m/sec. The concrete on sections of the Millau Bridge project had a performance specification of 10^{-17} m^2 and 10^{-12} m^2/s for the gas permeability and an apparent chloride diffusivity rate respectively.

Therefore, QUB, as part of a world-wide concrete exposure study including similar sites in Scotland, India and China, are in the process of setting up a marine exposure site on the North-West Atlantic coastline of Ireland in Co. Donegal. The performance of different concretes will be assessed using non-destructive methods so that performance specifications can be derived for the XS exposure class.

2. The Site

Figure 1 shows the location of the site, near Dungloe, in Co. Donegal. The site is subject to high wave action which will create significant spray as it is situated along a remote section of the Atlantic Ocean coastline. It therefore represents a good test of the concrete that will be located there.

The concrete on the site will be placed at three levels (Figure 2) and exposed to three different environments. The uppermost level (Figure 2(a)) will subject the concrete to atmospheric chlorides but not in direct contact with sea water. This represents the XS1 exposure class. The middle level (Figure 2(a)) will expose the concrete to ocean splash or spray, which will be within the XS3 class. The third level (Figure 2(b)) will be within the tidal zone where the concrete will be fully submerged twice daily, representing the XS3 exposure class. Based on a detailed survey of the site, the concrete will be placed at appropriate levels based on mean neap and spring tides. A similar site (Figure 3), which is also part of the world-wide study, has been in place on the North-East of Scotland since 1992. This site, which is on the North Sea coastline at Dornoch was set up by Heriot-Watt University in Edinburgh. On the site, 9 large, 2m high, octagonal shaped concrete piers are located which are subject to the three exposure types described above (McCarter, *et* al, 2001).

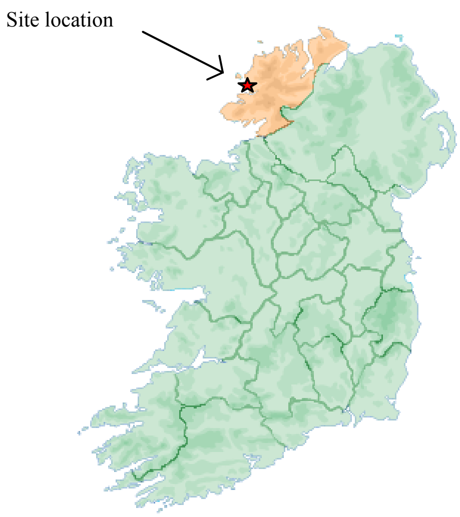

Figure 1 Location of exposure site on North-west coastline of Ireland

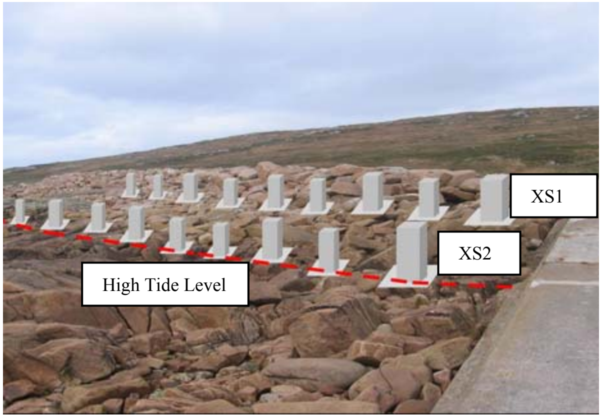

(a)

(b)

Figure 2 Proposed layout of concrete columns on site at the three exposure levels

The Dornoch site is subject to tidal cycles within an estuary (Dornoch Firth) where the Donegal site will be subject to the full force of the Atlantic Ocean. A comparison between the chloride and other aggressive agents (see Table 1) carried out at Queen's using water samples from the two sites confirms that the water in the Atlantic Ocean contains higher levels of aggressive chemicals than the water in Dornoch. For instance, in terms of chlorides, which are responsible for the majority of reinforcement corrosion, the Donegal site has almost twice the chloride content (15,704ppm) than that found in Dornoch (8,826ppm).

At the time of writing, a planning application has been lodged with Donegal County Council to place a number of columns over a 50m zone in the three zones discussed. Also, as the tidal columns will be positioned below the level of the high tide, a foreshore license application will also be lodged to the Department of Agriculture, Fisheries and Food when planning permission is obtained.

3. The Concrete

It is proposed that the concrete will consist of a variation of CEM I, CEM II/B-S, CEM II/B-V and CEM III cements with w/c ratios in the range 0.3 to 0.4. These proportions would be

Figure 3 Existing exposure site at Dornoch, North-East Scotland

Table 1 Comparison between aggressive agents in the water at the Dornoch (North Sea) site and the Donegal (Atlantic Ocean) sites.

Site	Cl ppm	SO_4 ppm	Na ppm	K ppm	Mg ppm	Ca ppm
Dornoch (North Sea)	8826	1384	5600	290	900	310
Donegal (Atlantic Ocean)	15704	2254	9300	360	1800	490

Note: Cl – Chloride, SO_4 –Sulphate, Na – Sodium, K – Potassium, Mg – Magnesium, Ca - Calcium

appropriate for this exposure condition. Figure 4 shows the proposed reinforcement to be embedded into the concrete. The concrete will be positioned on concrete plinths poured on site in and around the rocks. It is intended that these plinths will have a proportion of Ronafit, which is a polymer modified mortar used as a waterproof render. The top of the columns will also have a layer of this material placed in-situ. This prevents water and chloride entering through the tops and bases of the columns.

At Dornoch, six of the stems were made using plain CEM I concrete (with 3 of these having the surface treated with silane); the remaining 3 piers stems had a concrete containing caltite as an additive (McCarter, *et* al, 2001) which can reverse the capillary wicking action and blocks the pores when the concrete surface is subjected to hydrostatic pressure. The reinforcement used in the stems is identical to that used in the bridge piers and is comprised of a combination of 32 mm and 40 mm reinforcing in the form of a circular cage. The cover

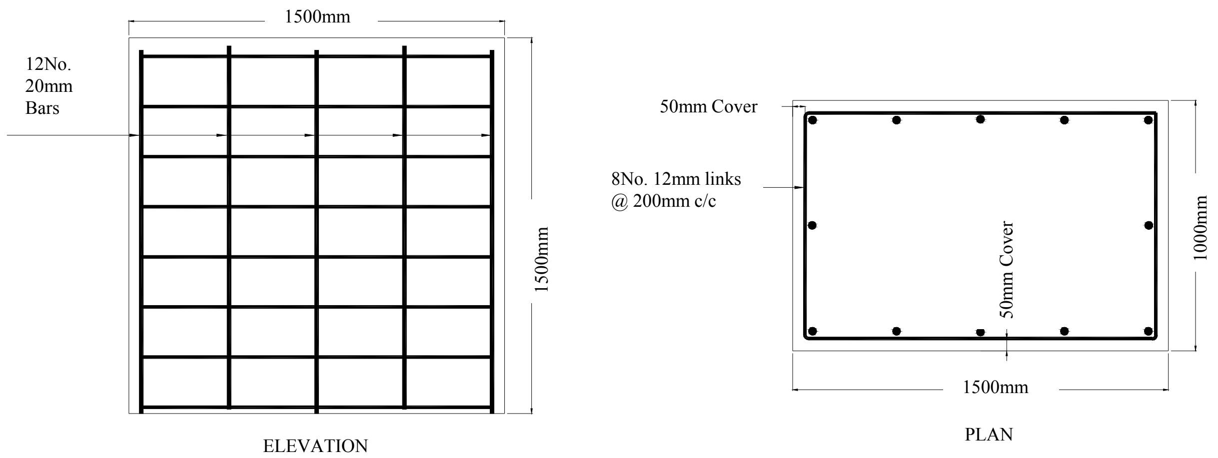

Figure 4 Proposed reinforcement to be embedded in the concrete

to the reinforcement varies due to the circular cage arrangement and the pier stems having an octagonal shape. However, an average cover of 65mm at the centre of each face was achieved.

4. Equipment

The concrete on the site Dornoch contains electrical sensors which will measure the water, ionic and moisture movement with the surface zone using a covercrete electrode-array developed by Prof. John McCarter at Heriot-Watt University, Edinburgh (McCarter *et al*, 2001; McCarter, *et al*, 2001a; Chrisp *et al*, 2002; McCarter & Vennesland, 2004; McCarter *et al*, 2005; McCarter *et al*, 2006). The electrode array, as shown in Figure 5, permits conductance measurements to be obtained at discrete points within the cover zone.

The electrical conductivity readings from the concrete on site are wirelessly transferred back to the laboratory at Heriot-Watt University. Figure 6(a) presents how the two control boxes are positioned on one of the uppermost concrete stems. One of the boxes contains the multiplexer (Figure 6(b)) and the other stores the datalogger (Figure 6(c)). There is also a back-up battery in the multiplexer control box (Figure 6(c)). The power for the logging equipment is provided via a solar panel set on top on one of the stems (Figure 6(d)). Figure 6(e) shows the existing piers on the Dornoch motorway bridge nearby.

In the covercrete electrode array, the sensor comprises 10 electrode pairs mounted on a small perspex former and secured to a reinforcement bar. Cabling is ducted away from the exposed surface. Each electrode comprises a stainless steel pin that is sleeved to expose a 5-mm tip, and in each electrode pair, the pins had a centre to centre spacing of 5 mm. The pairs of electrodes were mounted parallel to the suction surface enabling conductance readings at 10 discrete points. Thermistors are also mounted on the former, thereby enabling temperature profiles through the covercrete to be obtained. Electrode pairs are offset from each other in both the horizontal and vertical directions. The exposed tip of the electrode was positioned remote from the perspex former. A similar setup will be employed on the site in Donegal with the sensors measurements being wirelessly transferred back to the Centre for Built Environment Research (CBER) laboratory at Queen's using remote technology.

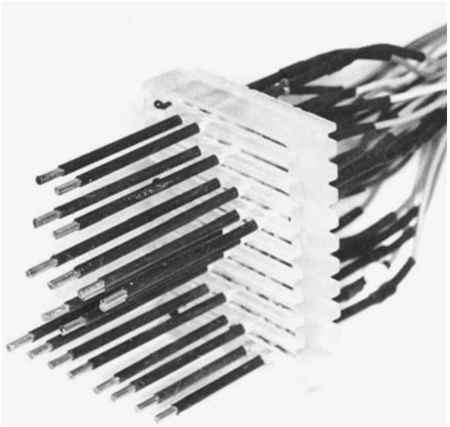

Figure 5 The covercrete electrode array [McCarter *et al*, 2001]

(a)

(b)

(c)

(d)

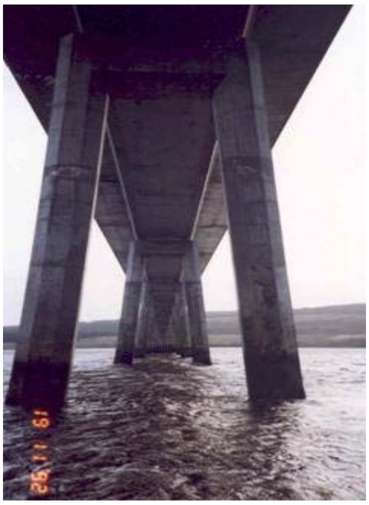

(e)

Figure 6 Remote monitoring of electrical properties at Dornoch exposure site

This represents the new approach to monitoring so-called 'smart structures'. The location of these sensors should be where the exposure to chlorides are at their highest, at structurally critical zones and in an area where exposure is not as severe to act as a control. In terms of a marine structure, the critical area will be in the inter-tidal, heavy splash, and, if the structure is close enough, within the range of wind-borne spray.

5. Non-destructive testing of the covercrete transport properties

In addition to monitoring the internal electrical conductivity, the covercrete transport properties will be measured using non-destructive tests developed at Queens such as the rate of absorption and the air and water permeability properties using the Autoclam apparatus (Basheer *et al*, 1994).

The Autoclam sorptivity test measures the cumulative inflow of water in the first 15 minutes from a water source of 50mm diameter at an applied pressure of 0.02 bars (approximately 200mm water head). A plot of cumulative volume of water verses square root of time gives a linear relationship and the slope obtained from the graph is reported as a sorptivity index. The Autoclam air permeability test depends on the measurement of pressure decay in a test reservoir mounted on the surface of concrete from a pressure of 0.5 bar over a period of 15 min and plotting the natural logarithm of the pressure against time, yielding a straight line graph. The slope of this graph is reported as the Autoclam air permeability index. The Autoclam water permeability test involves a procedure similar to that used for the Autoclam sorptivity test. The main difference is in the test pressure used, i.e. a pressure of 0.5 bar is used for the Autoclam water permeability test compared to 0.02 bar for the Autoclam sorptivity test. The inflow of water through a test area of 50mm diameter through a surface-mounted ring is measured at this pressure for a period of 15 minutes. From a linear plot of the cumulative inflow verses the square root of time, the slope is determined and reported as the Autoclam water permeability index, in $m^3/\sqrt{min}$. The main advantage of the Autoclam is that it is portable, quick and simple to perform.

The chloride diffusion rate will be monitored by the Permit apparatus which is a unique non-destructive test which is capable of determining the chloride migration coefficient of cover concrete. Detailed descriptions of the instrument, test technique and test area preparation are available elsewhere (Basheer *et al*, 2005; Nanukuttan, *et al*, 2006). It has been shown that the in situ migration coefficient from the permit ion migration test on different concrete samples correlate well with the conventional lab-based steady state diffusion and migration tests. The main advantage of this test is that it can provide a migration coefficient without having to remove cores from the structure.

6. Anticipated research findings and significance

The permeation and migration results from the concrete on this site will be compared with those obtained from laboratory testing in QUB and from the exposure site in Dornoch as part of an existing EPSRC funded project. This will demonstrate the significance of the aggressive agents in the water between the two sites, as shown in Table 1. It is anticipated that the permeation and migration properties of the concrete and the corrosion of the embedded steel reinforcement will be heavily influenced by the exposure location, as opposed to that in Dornoch. The results between the two sites will be compared at different seasons which will demonstrate the effect of exposure conditions in the durability performance of reinforced concrete structures.

The degree of deterioration of embedded steel reinforcement increases over time. However, the period before corrosion initiation is not clearly defined, nor is the rate or propagation of deterioration after corrosion begins. By monitoring the corrosion of the steel reinforcement in the concrete columns on this site, a better estimate of the length of time before initiation begins and the rate of corrosion afterwards will be better understood in the XS exposure class. Work will also be undertaken to establish the critical chloride point when corrosion will begin, which is currently assumed to be 0.4% of the cement content by weight for most structures. This is an important criterion for predictive models and site assessment of concrete structures through chloride dust sampling methods.

A new site based electrical sensor will be embedded into the concrete and attached to the reinforcement. This sensor, which is based on the covercrete electrode array, shown in Figure 7, measures both the electrical resistivity and conductivity, but also the corrosion rate of corrosion of a reinforcing steel element. This is achieved by soldering a cable to both the reinforcing steel (working electrode) and the stainless steel (reference electrode) using a silver solder connection. As shown, the length of the stainless steel (the cathode) and the reinforcing steel (the anode) elements are 100 and 25mm respectively. This 4:1 ratio of cathode to anode ensures that the corroding reinforcing steel is over supplied electrically using the stainless steel bar. The sensor is attached to the reinforcement and is positioned so that the edge of the PVC box is flush with the exposed concrete surface. The information from this sensor will be wirelessly transmitted back to QUB using a similar set-up, as shown in Figure 6.

In addition to the electrical sensor being embedded in the concrete, a number of fibre-optic sensors (FOS) will also be placed so that the internal temperature, pH and chloride content can be measured. The use of FOS has been increasing in the field of structural health monitoring during the past few years as they are extremely small; lightweight; robust; corrosion resistant; immune to electro-magnetic interference and can be multiplexed. They also have a high sensitivity and hence suits well for harsh environments encountered in concrete structures. As with the electrical sensors, the information can also be wirelessly transferred to the desktop or laptop allowing for remote analysis will be a great help to monitor existing structures. The inter-relationships between the FOS (internal temperature, humidity, pH and chloride content), the electrical sensors (resistivity, conductivity and corrosion activity) and the AutoClam and Permit (air and water permeability, sorptivity and diffusivity) will be used to establish performance-based specifications for this exposure class.

Both BS 8500 (2006) and Hobbs (1998) have published recommendations regarding concrete strength, w/c ratio, minimum cover and appropriate cements for the exposure classes in EN 206 (BE EN 206, 2000) for 50 and 100-years. An assessment on the appropriateness of these recommendations will be made through life-cycle numerical models and comparisons will be made with experimental results. Using comparisons between the concrete on this site, and from the Dornoch site (Nanukuttan, 2008), the validity of these recommended parameters can be verified along with appropriate laboratory and numerical studies.

The site will also offer an ideal opportunity to further improve existing NDT methods and assess new test methods, which are being developed at QUB. It will also be used to develop new innovative research proposals on concrete durability on real concrete subject to real exposure conditions. Also, a further possibility is the establishment of relationships between the results from accelerated laboratory corrosion methods (namely, ponding and salt-spray

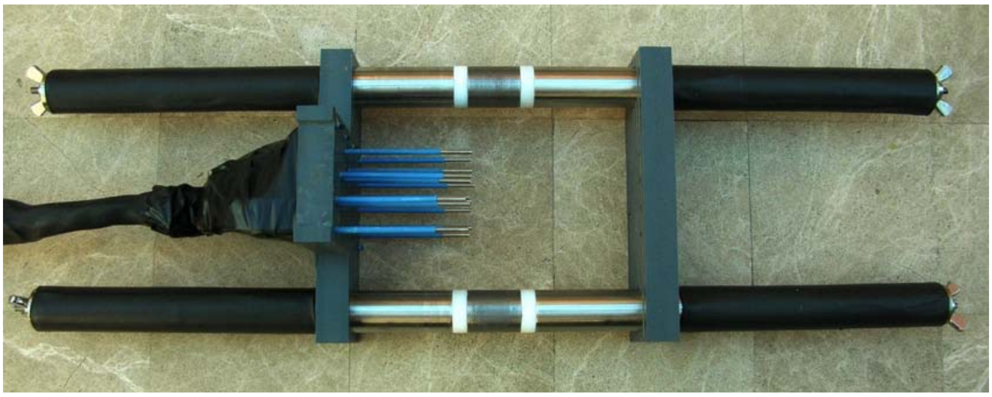

Figure 7 Electrical sensor, manufactured by Amphora Ltd, to undertake a suite of corrosion measurements including rate of corrosion and resistivity.

methods) and site corrosion test results. In the future, therefore, when new materials are produced it can be confirmed whether these laboratory accelerated corrosion tests can be used to give a quick service life picture of the new materials.

7. Conclusions

This paper has presented the setting up of a new marine exposure site on the Co. Donegal Atlantic coastline. A number of concrete columns (1.5m high x 1.5m wide x 1m thick) will be placed on the site where they will be subject to three different exposures within the XS classes in EN206, namely concrete subject to chlorides from airborne salts (XS1), from splash and spray (XS3) and from tidal cycles (XS3). The cement to be used in the concrete columns will consist of CEM I, CEM II/B-S, CEM II/B-V and CEM III/A with w/c or w/b ratios in the range 0.3 – 0.4. These variables are considered appropriate for the three exposure classes above.

This work follows on from a similar site developed by Heriot-Watt University at Dornoch in North-East Scotland which has been in place since 1992. The samples here are exposed to an estuary tidal cycle. A review of the level of chlorides, and other contaminants, between the two sites has shown that the chloride level at the Donegal site is almost twice than in the water at Dornoch.

The concrete on the new site will be cast with steel reinforcement onto which electrical sensors will be attached. These sensors will measure the conductivity and resistivity as well as the ionic and water movement through the coverzone. Half-cell and LPR measurements will also be undertaken. The results from these internal properties will be relayed back to the office through wireless technology through a remote monitoring station set-up on the site, representing ‘smart-structure’ technology. The transport properties (absorption, air permeability, water permeability and the chloride migration coefficient) in the coverzone will also be measured using the non-destructive AutoClam and Permit apparatus. Along with the electrical properties above, these results will be used to set guidelines for suitable performance specifications for concretes in the XS exposure class described here.

8. References

- Association Francaise de Genie Civil (2007) Concrete design for a given structure service life, Scientific and technical documents

- Basheer P. A. M., Long A. E. and Montgomery F. R (1994), 'The Autoclam – a New Test for Permeability. Concrete', Journal of the Concrete Society, July/August, 27–29.
- Basheer P. A. M., Andrews R. J., Robinson D. J. and Long A. E. (2005), 'PERMIT' Ion Migration Test for Measuring the Chloride Ion Transport of Concrete on Site, *NDT & E International*, 38 (3), 219–229.
- BS EN 206 Part 1 (2000), 'Concrete: Specification, performance, production and conformity', British Standard Institute.
- BS 8500 (2006) Concrete: Complementary British Standard to BS EN 206-1, British Standard Institute.
- BS EN 197-1 (2000), Cement: Composition, specification and conformity criteria for common cements, British Standard Institute.
- Chrisp T.M., McCarter W.J., Starrs G., Basheer P.A.M. and Blewett J. (2002), 'Depth related variation in conductivity to study wetting and drying of cover-zone concrete', *Cement and Concrete Composites*, No. 24, Vol. 5, 415-427.
- Hobbs, D.W., (1998) 'Minimum requirements for durable concrete, Carbonation and chloride induced corrosion, freeze-thaw and chemical attack', BCA.
- McCarter, W. J., Chrisp, T. M. and Basheer, P. A. M. (2001a), 'Condition profiling of cover zone concrete', *Proc. COST 521 Workshop*, Tampere, Finland, 105-109 (ISBN 952 15 0364 2).
- McCarter, W.J., Butler, A., Chrisp, T.M., Emerson, M., Starrs, G. and Blewett, J. (2001) 'Field trials on covercrete monitoring sensors', *Proceedings of the Institution of Civil Engineers: Structures and Buildings*, Vol. 146, No. 3, 295-305.
- McCarter, W. J. and Vennesland, Ø. (2004), 'Sensor systems for use in reinforced concrete structures', *Construction and Building Materials*, 18, 351-358.
- McCarter W.J., Chrisp T.M., Starrs G., Blewett J. and Basheer P.A.M. (2005), 'Laboratory to field monitoring of cover-zone concrete', *Cement and Concrete Composites*, 27, 809-817.
- McCarter, W.J., Finnegan L., Linfoot B.T., Basheer P.A.M. and Chrisp T.M. (2006), 'Performance of treated and untreated concrete in a marine environment', *Proceedings of the. 7th CANMET/ACI International Conference on Durability of Concrete*, SP234-5, 71-86 (ISBN 0 87031 207 3).
- Nanukuttan, S.V., Basheer, PAM., McCarter, W.J., Basheer, L., Holmes, N., Starrs, G and Chrisp, M, (2009) 'Testing and monitoring concrete using novel methods for predicting their long term behavior', Concrete Technology Forum organized by the American National Ready Mix Association, Cincinnati, USA, May, CD-ROM.
- Nanukuttan S. V., Basheer P. A. M. and Robinson D. J. (2006), 'Further Developments of the Permit Ion Migration Test for Determining the Chloride Diffusivity of Concrete', *Structural Faults and Repair 2006*, Edinburgh, M. C. Forde (ed.), Vol. CD-ROM, Engineering Technic Press, 2006, June.
- Nanukuttan, S.V., Basheer, P.A.M., Holmes, N., L. Tang, McCarter, J.W. (2010), Use of Performance Specification and Predictive modelling for concretes exposed to a marine environment, Structural Faults & Repair Conference, 15th - 17th June in Edinburgh, CDROM, Pages. 12.
- Nanukuttan S.V., Basheer P.A.M., McCarter W.J., Basheer L. and Robinson D.J. (2008), 'Full-Scale Marine exposure tests on treated and untreated concrete: initial 7-year results', *ACI Materials Journal*, No. 105, Vol. 1, 81-87.

DURABILITY ASPECTS OF MIXER ADDITION BLENDS OF GGBS WITH CEM I AND CEM II/A CEMENTS

C.McNALLY[1] & P.SEYMOUR[2]
[1]School of Architecture, Landscape & Civil Engineering, University College Dublin, Newstead, Belfield, Dublin 4, Ireland.
[2]Ecocem Ireland Ltd, Portview House, 3rd Floor, Thorncastle Street, Ringsend, Dublin 4, Ireland.

Abstract
This paper presents an overview of results of research into the durability characteristics of blends of GGBS with CEM I and CEM II/A cements. Ireland has led the way in Europe in permitting the mixer addition of GGBS to CEM II/A cements in the concrete mixer, in I.S. EN206-1. The development of this Irish standard has been contingent on the demonstration of the durability characteristics of these blends. To demonstrate this durability, specific research has been carried out in Ireland. These results are complemented by the results of similar research in Holland. The results of these studies are presented. Comparisons are made between the durability characteristics of these blends to concretes made with CEM III/A and CEM III/B cements.

Keywords: Carbonation, chloride ingress concrete durability, GGBS

1. Introduction

Concrete is the most-used man-made material on earth. However its main constituent, clinker-based cement, has a relatively high carbon footprint. The construction industry worldwide has embarked on a programme to reduce this carbon footprint, through many measures, in particular the substitution of clinker with supplementary cementitious materials, such as GGBS and fly-ash, and by using inert limestone filler.

As the cement industry in Ireland responded to the imperative to reduce its carbon intensity, new cement types came on to the market. CEM II/A cements replaced the more carbon-intensive CEM I cements, and GGBS became commercially available to Irish concrete manufacturers. With these new cement types, and combinations thereof, it was necessary to demonstrate the performance, in particular durability, of blends of these cements made at the concrete mixer.

In the 2006 revision to the Irish national Annex to EN 206-1, specific suitability had been established for the use of up to 50% GGBS with CEM II/A cements. However there was a growing demand from industry to move the upper limit up to 70% GGBS with CEM II/A cements for technical and environmental reasons.

2. Durability Testing

To determine the durability of combinations of CEM II/A cements with relatively high quantities of GGBS, a series of performance tests were conducted. Specific suitability for the use of up to 50% GGBS with CEM II/A, and up to 70% GGBS with CEM I had previously been established in earlier versions of the National Annex to EN 206-1. Before specific suitability could be established for the use of up to 70% GGBS with CEM II/A cements, supporting research data was required.

A number of key concrete durability aspects were considered: resistance to chloride ingress, resistance to carbonation and strength development. Freeze-thaw testing was not included due to the unavailability of suitable testing equipment at the time. Resistance to sulfate attack is not easily measured using concrete samples and as such is not included in this paper. The results of a separate research programme into the sulfate resistance of GGBS and CEM II/A cements is the subject of a separate paper at this conference.

2.1 Testing Methodology

Based on these concrete durability criteria, a series of tests were required to determine the performance of the concrete mixes. The tests were selected to be conducted in a reasonable time frame to allow direct comparison of the performance of the various concrete mixes.

Resistance to Chloride Ingress

Traditional test methods to quantify this resistance involve the long-term immersion of concrete samples within chloride-rich environments. While these experiments have been shown to produce reliable diffusion coefficients (McNally et al, 2005), they have the disadvantage of being very slow. Tang and Nilsson (1993) developed an accelerated test-method whereby the chloride diffusivity of a concrete sample may be determined by the application of an electric field. The depth of chloride penetration is visually determined by staining with silver nitrate and is used to determine a non-steady state migration coefficient. Tang and Nilsson have also shown how this can be converted to produce the more familiar effective diffusion coefficient, D_{eff}. This easy-to-use method is more commonly known as the Rapid Migration Test (RMT) and was formalised in Nordtest NT Build 492 (1999).

The RMT is typically measured on cylindrical test specimens A series of concrete slabs were cast that were 300 mm square and 100 mm deep. The slabs were cured for 3 weeks in water at 20°C, after which they were moved to a constant temperature room with a relative humidity of approximately 65%. When the samples were 3 months old test specimens were cored from this slab and subsequently cut to produce a test sample that was 100 mm in diameter and 50 mm thick. This was then subjected to the preconditioning and testing procedures as specified in NT Build 492.

Resistance to Carbonation

Resistance to the diffusion of CO_2 into the concrete matrix was determined using an accelerated carbonation testing unit that was built in house at UCD. The test chamber allows the user to set the desired temperature and CO_2 content. Relative humidity is not controlled but experience has shown that the system is constant in this respect. The carbonation chamber is instrumented with sensors to measure CO_2 content, temperature and relative humidity. A LabView programme was written to control the test environment and is connected to a CO_2 supply and an internal heater. A circulation fan is also fitted inside the chamber to ensure a consistent test environment and typical target test conditions are a CO_2 content of 5% and a temperature of 20°C.

The tests were conducted on 100 mm cube samples stored in the test chamber for preset time periods. The cubes were cured for 3 weeks in water at 20°C, after which they were moved to a constant temperature room with a relative humidity of approximately 65% for a further 7 days before testing. Samples were removed from the chamber after 7, 28 and 56 days and split in indirect tension. These were then treated using a phenolphthalein indicator and the carbonation depth measured by callipers on a set of 3 samples.

Compressive Strength
The compressive strength of the various mixes was determined using the standard method of casting concrete cubes and crushing them at preset time intervals up to 90 days.

Materials
For these tests, a series of concrete mixes were designed to reflect the mix designs featured in the National Annex to EN206. These comprised binder contents of 320 and 400 kg/m^3 and water/binder ratios of 0.55 and 0.45 respectively. The full list of combinations tested is shown below in Table 1.

Table 1 - Binder combinations chosen for testing

Mix No	Cement Type	GGBS Replacement Level (%)	Binder Content	Water/Binder Ratio
A1	CEM II/A-L	0	320 kg/m^3	0.55
A2		50		
A3		70		
A4	CEM II/A-V	0		
A5		50		
A6		70		
A7	CEM III/B	0		
B1	CEM II/A-L	0	400 kg/m^3	0.45
B2		50		
B3		70		
B4	CEM II/A-V	0		
B5		50		
B6		70		
B7	CEM III/B	0		

The coarse and fine aggregates used were sourced from a commercial quarry and are commonly used in concrete production. The cementitious binders used in the testing programme were a combination of the following:

- CEM II/A-L: class 42.5 Portland limestone cement
- CEM II/A-V: class 42.5 Portland fly-ash cement
- CEM III/B: class 32.5 Blastfurnace cement
- Ground granulated blast furnace slag (GGBS)

Note: CEM III/A cement has a GGBS content between 36% and 65%; CEM III/B cement has a GGBS content between 66% and 80%.

3. Results

The tests were carried out according to the methodologies previously described and the results are discussed below.

3.1 Resistance to Chloride Ingress

The RMT was conducted on 2 samples per binder combination and the results were processed following the procedures developed by Tang & Nilsson (1993) to produce an effective diffusion coefficient. Average values were calculated and these are presented in Figure 1. It can be seen that the highest diffusion coefficients all correspond to the binder combinations that contained 100% CEM II/A-L or A-V; this is observed for both sets of samples (i.e. 320 and 400 kg/m^3 of binder). In all cases the addition of 50% and 70% GGBS lead to significant reduction in the effective diffusion coefficient. It was observed that the addition of 50% or 70% GGBS produced binder combinations that were approximately equivalent with respect to their resistance to chloride ingress.

3.2 Resistance to Carbonation

Papadakis and Tsimas (2002) studied carbonation testing of concrete and found that the carbonation depth can be calculated from:

$$x_c = \sqrt{\frac{2\,D_{e,CO_2}\left(CO_2/100\right)t}{0.218\left(C+kP\right)}} \tag{1}$$

where:

x_c is the carbonation depth;
t is time;
C is cement content (kg/m^3);
P is the SCM content (kg/m^3);
$D_{e,CO2}$ is the effective CO_2 diffusivity of concrete;
CO_2 is the CO_2 content of air at the concrete surface (%);
k is the efficiency factor of the SCM with respect to CO_2 diffusion

Furthermore Papadakis has shown that the CO2 effective diffusion coefficient is heavily influenced by the relative humidity, (2)

$$D_{e,CO_2} = 6.1x10^{-6}\ f(C,P,k,W)\left(1-\frac{RH}{100}\right)^{2.2} \tag{2}$$

Samples were taken from the carbonation chamber at 7, 28 and 56 days and the depth of carbonation was determined. This was plotted against the square root of time and the slope of the trend line determined. The relative humidity was observed to be approximately 60% for the test duration. By assuming the $D_{e,CO2}$ to be constant with time, the slope of the trend line can be used with Equations (1) and (2) to predict the carbonation depth of concrete at CO_2 = 0.03%, RH = 80% after 50 years. These values are typical of the environment a structure such as a standard urban bridge can expect to encounter in service. The results of this analysis are presented below in Figure 2.

The results are in agreement with previous work done by Papadakis (2000) who found that Supplementary Cementitious Materials (SCM) when used as a cement replacement, lead to increased carbonation depths. This is confirmed in this experimental programme where it is observed that the higher carbonation depths for each cement type corresponds to the use of 70% GGBS.

It should also be noted that the relative humidity of the ambient air plays a significant role on the observed carbonation depths, with increases in RH leading to reductions in carbonation (Papadakis & Tsimas, 2002). The carbonation chamber used for this study does not control humidity, but instead monitors the RH levels; for the duration of these tests the RH level was observed to be consistently around 60%. If these tests were conducted with a variable RH corresponding to field conditions, it is expected that the relative performance of the concrete binder combinations would remain, but the values of the carbonation depths would change.

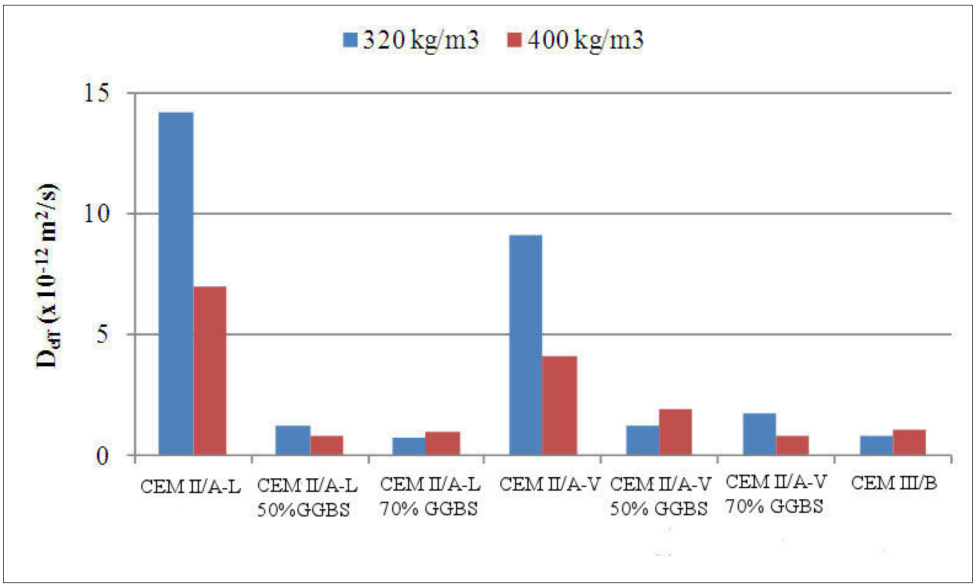

Figure 1 – Effective diffusion coefficients for the various binder combinations tested

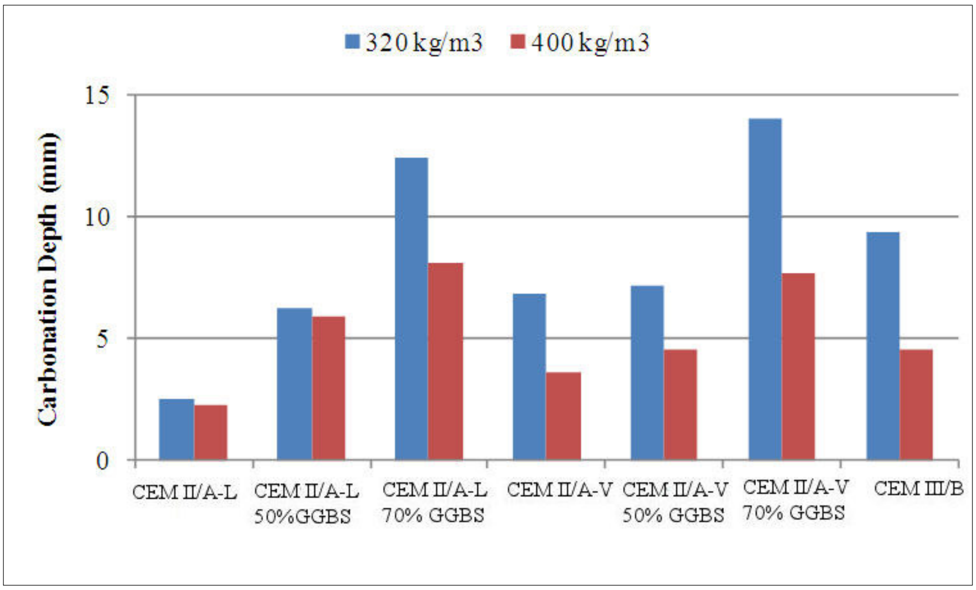

Figure 2 – Predicted 50 yr carbonation depth for the various binder combinations tested, based on Papadakis & Tsimas (2002)

3.3 Compressive Strength

The compressive strength of the various binder combinations was determined and these are presented in Figures 3 and 4. It can be seen that higher strengths were associated with the CEM II/A-L cement and not the CEM II/A-V cement. The use of a 50% GGBS replacement level resulted in almost unchanged strength levels at 28 days for both CEM II/A cement types. The lowest strength for each binder content corresponded to the combination of CEM II/A-V with 70% GGBS.

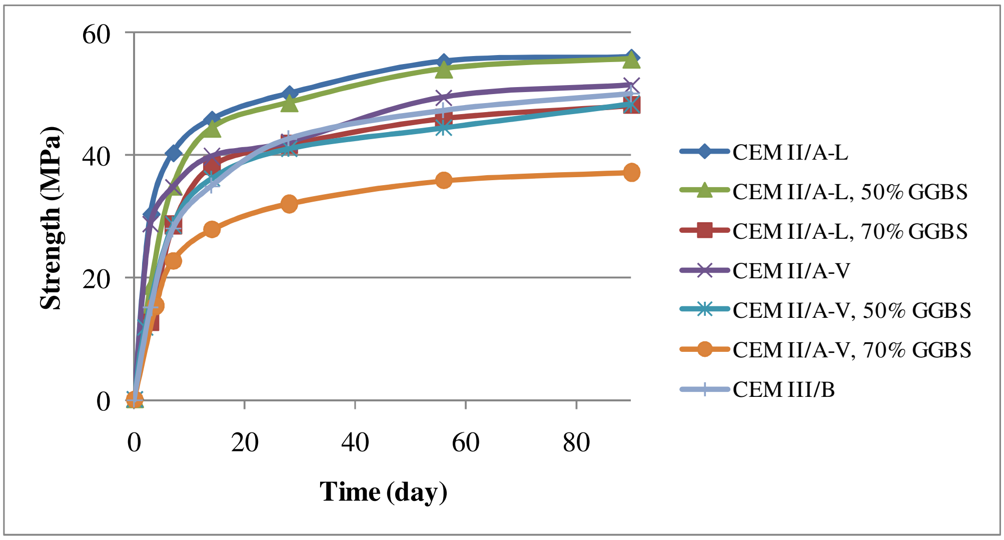

Figure 3 – Compressive strengths for binder contents 320 kg/m^3, w/b ratio 0.55

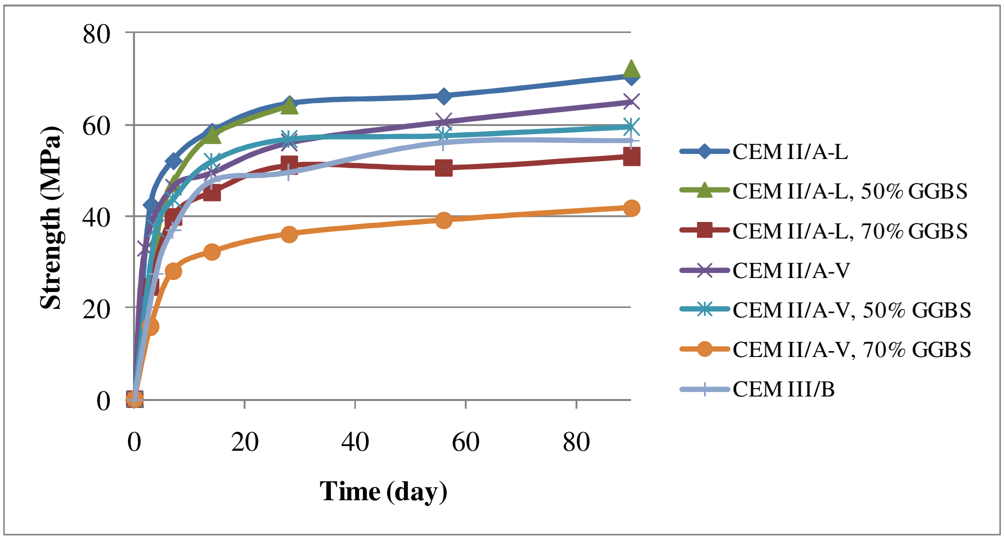

Figure 4 – Compressive strengths for binder contents 400 kg/m^3, w/b ratio 0.45

4. Comparison with International Studies

Mixer addition of GGBS with CEM I cements has been in use in the Netherlands since 2002. Comparative studies have been carried out (Creemers, 2008) to demonstrate the equivalent performance with CEM III cements, for which suitability is generally established in the Dutch market. Studies were carried out on GGBS:CEM I mixer blends at 50:50 and 70:30, to compare to CEM III/A and CEM III/B cements respectively. The results of these tests are summarised below.

4.1 Resistance to Chloride Ingress

The results in Table 2 demonstrate that the performance of mixer addition of GGBS and CEM I cements are comparable to, or even slightly better than the CEM III cements. These tests were carried out on concretes with a binder content of 340 kg/m^3, and a w/c ratio of 0.45. The tests were carried out according to the Nordtest NT-Build 443 testing methodology.

Table 2 – Resistance of binder combinations to chloride ingress

Sample Type	Effective Diffusion Coefficient (x 10^{-12} m^2/s)			
	a	b	c	Mean
CEM III/A (42.5 N)	2.7	4.5	3.6	3.6
50:50 GGBS:CEM I (42.5 R)	1.7	2.8	3.2	2.6
50:50 GGBS:CEM I (52.5 R)	1.9	2.0	2.0	2.0
CEM III/B (42.5 N)	2.8	3.4	1.8	2.7
CEM III/B (42.5 N)	3.2	3.6	3.0	3.3
CEM III/B (32.5 N)	2.6	2.7	2.1	2.5
70:30 GGBS:CEM I (52.5 R)	2.1	1.7	1.5	1.8
70:30 GGBS:CEM I (42.5 R)	1.5	2.1	2.0	1.9
70:30 GGBS:CEM I (52.5 R)	2.0	1.5	2.4	2.0
70:30 GGBS:CEM I (42.5 R)	2.6	2.5	1.7	2.3

Table 3 – Resistance of binder combinations to carbonation

Sample type	Binder content (kg/m^3)	w/c ratio	Average carbonation depth (3 samples, mm)
CEM III/A (42.5 N)	300	0.55	3.0
50:50 GGBS:CEM I (42.5 R)	300	0.55	3.0
50:50 GGBS:CEM I (52.5 R)	300	0.55	2.0
CEM III/B (42.5 N)	300	0.55	5.0
70:30 GGBS:CEM I (52.5 R)	300	0.55	5.0
CEM III/B (42.5 N)	340	0.45	5.0
70:30 GGBS:CEM I (42.5 R)*	340	0.45	4.5
70:30 GGBS:CEM I (52.5 R)	340	0.45	2.3
CEM III/B (32.5 N)	340	0.45	2.5
70:30 GGBS:CEM I (42.5 R)*	340	0.45	2.0

*Note: Results are for two different CEM I (42.5 R) cements

4.2 Resistance to Carbonation

Carbonation tests were carried out on samples made with CEM III cements and with mixer addition of GGBS and CEM I. The tests were carried out according to the CUR 48 methodology, with CO_2 concentrations were 0.04% at a temperature of 20°C and RH of 65%. Concretes with binder contents of 300 kg/m^3 and 340 kg/m^3 were tested. The tests results indicate that there are no adverse effects on resistance to carbonation when concretes are made with mixer additions of GGBS and CEM I, compared to the CEM III cements.

5. Discussion

The test results show that the substitution of up to 50% to 70% GGBS for CEM II/A significantly reduces the chloride diffusion coefficient in concrete compared to the

CEM II/A cements alone. The diffusion coefficient with the blends of GGBS and CEM II/A are similar to those measured in concretes made with CEM III/B cements.

The presence of GGBS in concrete does increase the depth of carbonation as measured under laboratory conditions. However the test data demonstrates that this is still low relative to the concrete cover required by I.S. EN 206-1 to protect against carbonation induced corrosion. This is in agreement with long-term carbonation studies in Germany (Wierig, 1984) that have shown carbonation depths of concretes with up to 75% GGBS to be low in relation to concrete cover. This experience is reflected in the German concrete standard (DIN 1045-2:2008) where the limiting values in the carbonation exposure classes are the same for both CEM I and CEM III/B cements, as is the case for UK, Dutch and French concrete standards.

Data from comparative durability testing conducted in the Netherlands supports the practice of mixer addition of high levels of GGBS with CEM I cements. For a series of binder combinations, it was shown that these mixes produced approximately equivalent durability performance in terms of chloride and carbonation induced corrosion as concretes manufactured using either CEM III/A or CEM III/B factory blended cements.

6. Conclusions

The use of GGBS in concrete, whether added at the concrete mixer or as a factory-blended CEM III cement, improves the resistance of concrete to chloride attack; it will also result in an increase in the carbonation depth in concrete.

The data presented above has been used to support a change in the Irish National Annex to EN 206, which now permits the mixer addition of 70% GGBS with either a CEM II/A-L or CEM II/A-V across all exposure classes. This change now offers more flexibility to concrete manufacturers seeking to produce a product with a reduced carbon footprint.

References

Creemers, H.P.N, (2008) 'Research on cement-GGBS binders for concrete', INTRON, Sittard, Holland.

DIN 1045-2:2008, Concrete, reinforced and prestessed concrete structures – Part 2: Concrete – Specification, properties, production and conformity – Application rules for DIN EN 206-1.

McNally, C., Richardson, M., Evans, C., and Callanan, T. (2005), 'Determination of chloride diffusion coefficients for use with performance-based specifications' in *Proceedings of the 6th international congress on global construction*, eds R.K. Dhir, T.A. Harrison and M.D. Newlands, Dundee, 321-327

Nordtest (1999), *NT Build 492: Chloride Migration Coefficient from Non-Steady-State Migration Experiments*, Nordtest.

Papadakis, V.G. (2000), 'Effect of supplementary cementing materials on concrete resistance against carbonation and chloride ingress', *Cement & Concrete Research*, **30** (10), 291-299.

Papadakis, V.G. & Tsimas, S. (2002), 'Supplementary cementing materials in concrete Part I: efficiency and design', *Cement & Concrete Research*, **32** (10), 1525-1532.

Tang, L. & Nilsson, L.O. (1993), 'Rapid determination of the chloride diffusivity in concrete by applying an electric field', *ACI Materials Journal,* **89** (1), 49-53.

Wierig, H.-J. (1984), 'Longtime studies on the carbonation of concrete under normal outdoor exposure', *Proceedings of RILEM Seminar on Durability*, Hanover.

DEVELOPMENT OF STRUCTURAL LIGHTWEIGHT, CHEMICAL ACTIVATED BLENDED CEMENTITIOUS CONCRETES

K.J. OWENS, Y. BAI, J. KWASNY, P.A.M. BASHEER, D. CLELAND, S. TAYLOR & M. SONEBI
School of Planning, Architecture and Civil Engineering, Queen's University Belfast, BT10 0DU, Northern Ireland.

Abstract
This paper presents results of an ongoing research project on developing structural lightweight and low energy concretes. As the manufacture of Portland cement (PC) is very energy intensive and with an almost equal quantity of carbon dioxide per tonne of PC being released into the atmosphere, high volumes of PC were replaced with Pulverised Fuel Ash (PFA) and Ground Granulated Blast furnace Slag (GGBS) in this project. Aggregates manufactured from sintered PFA were used as lightweight coarse and fine aggregates. A lightweight concrete mix made with lightweight coarse and fine aggregates containing Portland Cement (PC) was manufactured as the control. Another two lightweight concrete mixes were manufactured by replacing 50% of the PC by volume with PFA and GGBS to reduced embodied energy. However, it was noticed the early compressive strength of these PFA and GGBS concretes were low. To improve their early age compressive strength, sodium sulfate, at a dosage of 4% by weight of the binder (PC plus either GGBS or PFA), was used as a chemical activator to activate the PFA and the GGBS mixes. The suitability of these chemically activated lightweight mixes for structural applications was studied initially by assessing the hardened density and compressive strength properties and the results are reported in this paper.

Laboratory results showed that incorporation of large volumes of PFA and GGBS in normal PC based lightweight concrete resulted in significant reduction of compressive strength, especially at early ages but through the use of sodium sulfate activation improved compressive strengths could be achieved. Therefore, this study showed that structural lightweight, low embodied energy concretes can be produced by using lightweight aggregates, large volume replacement of PC with PFA and GGBS along with chemical activation by sodium sulfate.

Keywords: Chemical activators, compressive strength, GGBS, lightweight, PFA, sodium sulfate.

1. Introduction

Concrete made with natural aggregate originating from hard rock has a density with a narrow range because the specific gravity of most rock varies little (Neville, 2002). Consequently, the self-weight of concrete elements is high and can represent a large proportion of the load on a structure. Using concrete with a lower density can have many beneficial results. Topcu (1997) and Al-Khaiat and Haque (1998) reported that structural lightweight concrete has its obvious advantages of higher strength/weight ratio, better tensile strain capacity, lower coefficient of thermal expansion and superior heat and sound insulation characteristics due to air voids in the lightweight aggregate. Furthermore, Topcu (1997) also reported that the reduction in the dead weight of a construction by the use of lightweight aggregates in concrete could result in a decrease in cross section of columns, beams, plates and foundations. It may also be possible to reduce steel reinforcements thus reducing the overall need for virgin materials required for construction. Natural materials such as basaltic-pumice (Kilic, 2003) and also manufactured materials such as expanded shale (Henkensiefken et al. 2009), expanded clay (Chia and Zhang, 2002) and sintered fly ash (Behera et al., 2004) have been commonly used as lightweight aggregate.

The production of Portland cement consumes a lot of natural resources and energy and emits CO_2, SO_2 and NOx. These gases can have a detrimental impact on the environment resulting in acid rain and contributing to the Greenhouse effect. PFA and GGBS have been widely used as a substitute for Portland cement in many applications because of its advantages on fresh, hardened and durability properties of concrete (Lea, 1998). The utilisation of these supplementary materials, especially at high volume replacements of PC (~50%), also has the ability to significantly reduce the embodied energy of concrete (Mehta, 1993). Brocklesby and Davison (2000) showed that the replacement of PC with 50% GGBS and 35% PFA reduced the embodied carbon dioxide of a C40 concrete by 39% and 28% respectively. However, one clear disadvantage in the use of most PFAs and also GGBS for cement-replacement purposes, is that the replacement of PC, especially in high volumes (>40%), decreases the rate of early strength development of the concrete and this is a significant problem for the pre-cast concrete industry (Neville, 2002).

Numerous investigators have utilised chemical activation to activate PFA and GGBS systems (Xu & Sarkar, 1991; Shi, 1996 & 1998). Two different methods commonly utilised include alkali activation and sulfate activation. Alkali activation involved the breaking down of the glass phases of PFA and GGBS in an elevated alkaline environment to accelerate the reaction (Xu & Sarkar, 1991; Ma et al., 1995; Shi, 1996; Shi, 1998; Fraay & Bejen, 1989). Sulfate activation is based on the ability of sulfates to react with aluminium oxide in the glass phase of PFA and GGBS to form sulfates (AFt) that contributes to strength development at early ages (Xu & Sarkar, 1991; Shi, 1996 & 1998). The possibility of PFA and GGBS activation mainly lies in the breaking down of its glassy phases. Fraay considered that the pH value required to dissolve the glassy phases is about 13.3 or higher. The usual way of achieving a high pH is by the addition of NaOH or other alkaline materials into the fly ash system. Studies carried out by Shi (1996 & 1998) compared the addition of Na_2SO_4 and $CaCl_2$ and found that the addition of both increased the cost of raw materials but the cost per unit strength decreased. The addition of 4% Na_2SO_4 increased both the early and later age strength of paste systems whereas the addition of 4% $CaCl_2.2H_2O$ lowered the early age strength but increased the later strength. Owens *et al*., (2010) found Na_2SO_4 to be a better activator of PFA and GGBS pastes when compared to sodium hydroxide and calcium sulfate.

This paper presents an exploratory study on using sintered PFA lightweight aggregate in activated PFA and GGBS concretes. Sodium sulfate was selected as the chemical activator and at a dosage rate of 4% weight of total binder. Fresh and hardened properties of these mixes are presented.

2. Experimental

2.1 Materials used

Portland cement (PC)
A normal hardening Portland cement (CEM I 42.5 according to European Standard EN 197-1, 2002) was used for the manufacture of all concrete specimens.

Pulverised Fuel Ash (PFA)
A Type II PFA, (EN450 complying with European Standard BS EN206 - Part 1:2000) was used for the manufacture of PFA concrete mixes.

Ground Granulated Blast furnace Slag
GGBS conforming to the requirements of BS 6699 (1992) was used for the manufacture of GGBS concrete specimens.

Chemical activator
The sodium sulfate used was an industrial purity chemical.

Chemical admixture
A modified copolymer-based superplasticiser (SP) with dry material content of 40% and relative density at 20^0C of 1.080 was used in the manufacture of mixes. It meets the requirements of BS EN 934-2, 1998.

Lightweight coarse aggregate (LWCA)
The lightweight coarse aggregate used in this study was commercially available sintered PFA. The particle gravity of the dry aggregate was 1.32 and the bulk density was 770 kg/m^3. The particle size ranged from 4 to 14mm. The aggregate had water absorption of 14.9%, 15.1% and 22.1% at 5 minutes, 30 minutes and 24 hours. The LWCA was used in the 'as-received' moisture condition which was 19%. The free moisture content was continually measured to ensure free water contents stayed constant. The free water content in the mixes was adjusted to ensure a consistent water/binder ratio. The material had an Aggregate Crushing Value (ACV) of 41.

Lightweight fine aggregate (LWFA)
The lightweight fine aggregate used in this study was commercially available sintered PFA. The particle density of the dry aggregate was 1.52 and the bulk density was 790 kg/m^3. The particle size ranged from 0 to 4mm. The aggregate had water absorption of 11.8%, 13.4% and 19.8% at 5 minutes, 30 minutes and 24 hours. The LWFA was used in the 'as-received' moisture condition which was 18%. Again, the free moisture content was continually measured to ensure free water contents stayed constant. The free water content in the mixes was adjusted accordingly to ensure a consistent water/binder ratio.

Normal weight fine aggregate (NWFA)
The normal weight fine aggregate used in this study was natural sand. The particle density of the dry aggregate was 2.70 and the bulk density was 1.53 kg/m^3. The particle size ranged from 0mm to 4mm. The aggregate had water absorption of 0.7% at 24 hours. Moisture content was measured before mixing and free water content was adjusted accordingly.

2.2 Mixing and curing

List of mixes

The following mixes were used to assess the effect of high volume PFA and GGBS addition on the compressive strength of concrete mixes incorporating NWA and LWA (mixes 2&3). The influence of sodium sulfate was also assessed for its potential to improve compressive strength of the PFA and GGBS mixes (mixes 4&5, respectively):

(i) 100% PC **(PC)**
(ii) 50% PC + 50% PFA **(PFA)**
(iii) 50% PC + 50% PFA + 4% Na2SO4 **(PFA ACT)**
(iv) 50% PC + 50% GGBS **(GGBS)**
(v) 50% PC + 50% GGBS + 4% Na2SO4 **(GGBS ACT)**

Each mix contained 450 kg/m^3 of PC or PC and the volumetric equivalent of GGBS or PFA, 100% of lightweight coarse aggregates, 60% of light weight fine aggregates and 40% of normal weight fine aggregates (40% normal weight fine aggregates was used as a hardened density of approximately 1800 kg/m^3 was required) . A water/binder (w/b) ratio of 0.42 was used in all mixes. 0.5% SP by weight of total binder was also used in each mix although SP was adjusted, from 0.5% where necessary, in order to obtain workability within the S3 consistency range (100 - 150mm).

Mixing water

In all mixes, tap water at 20^oC (± 2^oC) was used. In the sodium sulfate activated mixes, sodium sulfate was dissolved in the mixing water immediately prior to mixing.

Mixing and casting of concrete

Concrete mixes which were manufactured as per BS EN 206: 1 (2000), were used in this investigation. 12 number 100mm cubes were cast for each mix. Specimens were covered with damp hessian after mixing and were demoulded after 24 hours. All specimens were cured under water at 20^oC (± 2^oC) until required for testing.

2.4 Fresh and hardened tests

Hardened density

The hardened density was determined in accordance with BS EN 12390-7:2009. The test specimens were cured in water until required for testing after 1, 7, 28 and 56 days of curing. Specimens were tested under saturated and surface dry conditions.

Compressive strength

The compressive strength was determined in accordance with BS EN 12390-3: 2002. The test specimens were cured in water until required for testing after 1, 7, 28 and 56 days of curing.

3. Results

3.1 Hardened density

The hardened density was measured after 1, 7, 28 and 56 days of curing. The results recorded after 28 days are presented below in Table 1.

Table 1 - Hardened density measured after 28 days of curing

Mix	PC	PFA	GGBS	PFA ACT	GGBS ACT
Hardened Density (kg/m^3)	1823	1827	1867	1817	1841

It can be seen from Table 1 that the hardened density ranges between 1817 kg/m^3 and 1867 kg/m^3 for all mixes after 28 days of curing. This is a saving of approximately 25% in density of a conventional concrete mix having hardened density of approximately 2400 kg/m^3.

3.2 Compressive strength

The compressive strengths of all concrete mixes were measured after 1, 7, 28 and 56 days of curing. The results of the 5 mixes are presented in Figures 1 to 3.

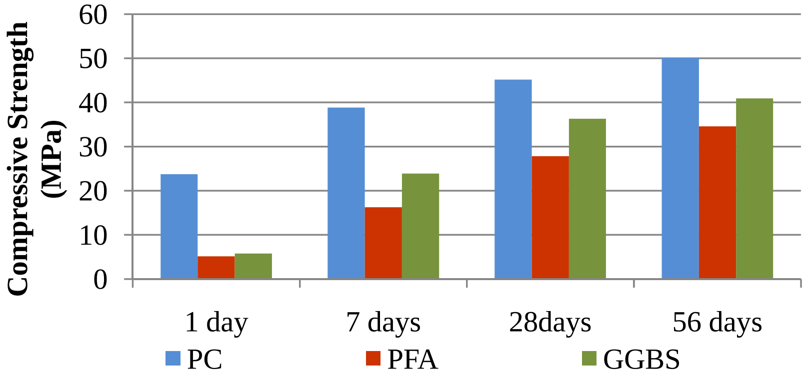

Figure 1 - Compressive strength of PC, PFA and GGBS concrete mixes

The compressive strength data presented in Figure 1 show that the PC mix produced the greatest compressive strength at all test ages when compared to the PFA and GGBS mixes. A compressive strength of 24 MPa was achieved after 24 hours curing. The replacement of PC with PFA and GGBS reduced compressive strength at all ages. Compressive strengths for the PFA and GGBS mixes of 5 MPa and 6 MPa respectively were achieved after 24 hours curing. Whilst these trends are expected with high volume replacements of PC with both PFA and GGBS, these early age compressive strengths are very low and would render these mixes unattractive to the construction industry. Nonetheless, the compressive strength gain of the PFA and GGBS mixes increased at a slow rate, with strengths of 35 MPa and 41 MPa achieved after 56 days of curing. The reduced early age strength is mainly due to the slow reaction of both PFA and GGBS under normal curing conditions, whereby the reaction is heavily rely on the calcium hydroxide generated from the hydration of PC (Mehta, 1993).

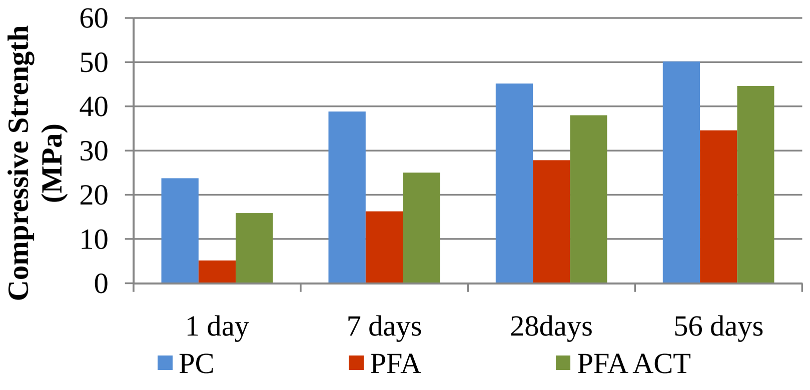

Figure 2 - Compressive strength of PC, PFA and PFA Activated concrete mixes

Significant improvements in compressive strength of PFA mixes were achieved when chemically activated with sodium sulfate as shown in Figure 2. Compressive strengths of 16 MPa for the activated PFA mix were achieved after 24 hours of curing. This is a significant improvement on the 24 hour compressive strength achieved with the non-activated PFA mix, however, it should be noted that this is still approximately 8MPa less than the PC mix at the same test age. The improved compressive strength can be attributed to the ability of sulfates to react with phases such as aluminium oxide in the glass phase of PFA to form Aft phases, such as ettringite that contributes to strength at early ages (Xu and Sarkar, 1991; Shi, 1996; Shi, 1998). Owens *et al.*, (2010) showed, using X-Ray Diffraction and Thermal Analysis techniques, that increased quantities of ettringite were identified in sodium sulfate activated PFA pastes and this was also linked to improved early age compressive strengths.

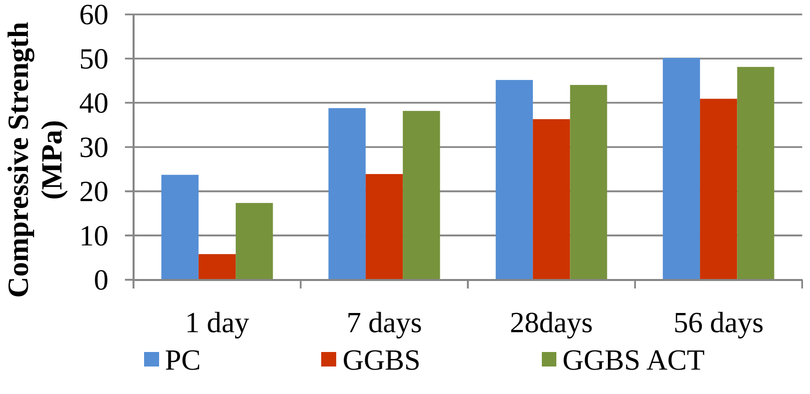

Figure 3 - Compressive strength of all GGBS and GGBS Activated concrete mixes

As with the activated PFA mix, significant improvements in compressive strength of the GGBS mix when activated with sodium sulfate can be seen in Figure 3. Compressive strengths of 17 MPa for the activated GGBS mix were achieved after 24 hours of curing. This is again a significant improvement on the 24 hour compressive strength achieved with the non-activated mixes. As with the PFA mix, the improved compressive strength can be attributed to the ability of sulfates to react with phases such as aluminium oxide in the glass phase of GGBS to form Aft phases that contributes to strength at early ages (Xu and Sarkar, 1991; Shi, 1996; Shi, 1998).

The strength gain of both activated mixes after 24 hours was different. Both the PC and activated GGBS mix provided similar compressive strengths after only 7 days of curing. The compressive strength gain in the activated PFA mix was largest between 7 and 28 days of curing. However, unlike the activated GGBS mix, the activated PFA mix did not match the performance of the PC mix, even after 56 days of curing. A compressive strength of 38 MPa was achieved at 28 days compared to 44 MPa for the activated GGBS mix at the same test age. The activated PFA and GGBS mixes achieved compressive strengths of 45 MPa and 48 MPa respectively after 56 days of curing which are just 5 MPa and 2 MPa respectively lower than the PC mix which achieved 50 MPa. Therefore, this study showed that structural lightweight, low embodied energy concretes can be produced by using lightweight aggregates, large volume replacement of PC with PFA and GGBS along with chemical activation by sodium sulfate.

4. Conclusions

Based on these results the following conclusions can be made;

i. The replacement of Portland cement in lightweight concretes with high volumes of PFA or GGBS, to achieve a low embodied energy concrete mix, had detrimental effects on the compressive strength, especially at early ages.
ii. The utilisation of sodium sulfate as a chemical activator had the ability to significantly improve compressive strength of both the PFA and GGBS mixes at all test ages. The activation effect is especially significant for the one day strength.

5. Acknowledgements

The authors would like to thank the following staff and organisations:
-Technology Strategy Board for their financial support to the project.
-Creagh Concrete, Macrete Ireland, Network Rail and Arup for their financial support and assistance in completing experimental work.
-Geoffrey Davis, QUB, for his assistance and support in carrying out the experimental work.

6. References

Al-Khaiat, H.and Haque, M.N. (1998), 'Effect of internal curing on early strength and physical properties of lightweight concrete', *Cement and Concrete Research,* 28, (6), pp. 859-866.

Behera, J.P., Nayak., B.D. Ray, H.S.and Sarangi, B. (2004), 'Lightweight concrete with sintered fly ash aggregate: A study on partial replacement to normal granite aggregate', *Journal of the Institution of Engineers, India, Civ. Eng. Dept,* 85, pp. 84-87.

Brocklesby, M.W. and Davison, J.B. (2000), ‘The environmental impacts of concrete design, procurement and on-site use in structures’, *Construction and Building Materials*, 14, pp. 179-188.

Chia, K.S. and Zhang, M.H. (2002), ‘Water permeability and chloride penetration of high-strength lightweight aggregate concrete’, *Cement and Concrete Research* 32 639-645.

European Standard EN 197-1:2000, ‘Cement. Composition, specifications and conformity criteria for common cements’.

Fraay, A.L.A.and Bejen, J.M. (1989), ‘The reaction of fly ash in concrete: A critical examination’, *Cement and Concrete Research*, 19, pp. 235-246.

Henkensiefken, R., Castro, J., Bentz, D., Nantung, T.and Weiss, J. (2009), ‘Water absorption in internally cured mortar made with water-filled lightweight aggregate’, *Cement and Concrete Research,* 39, pp. 883-892.

Kilic, A, Atis, C.D., Yasar, E.and Ozcan, F. (2003), ‘High-strength lightweight concrete made with scoria aggregate containing mineral admixtures’, *Cement and Concrete Research*, 33, pp 1595-1599.

Lea, F.M. (1998), *The Chemistry of Cement and Concrete,* fourth ed., Edward Arnold, London.

Ma, W., Liu, C.and Brown, P.W. (1995), Komarneni, S., ‘Pore structures of fly ashes activated by $Ca(OH)_2$ and $CaSO_4.2H_2.O$’, *Cement and Concrete Research* 25 (2) 417-425.

Mehta, P.K. (1993), *Concrete: structure, properties and materials*, Second edition, Prentice-Hall, USA.

Neville, A.M. (2002), ‘*Properties of Concrete’*, fourth ed., Pearson Education Limited, England.

Owens, K.J., Yun, B., Kwasny, J., Basheer, P.A.M., Cleland, D, Taylor, S and Sonebi, M. (2010), ‘Activation of High Volume Fly Ash Pastes using Chemical Activators’, ‘*Second International Conference on Sustainable Construction Materials and Technologies’*, June 28 - June 30, Università Politecnica delle Marche, Ancona, Italy

Shi, C.J. (1996), ‘Early microstructure development of activated lime-fly ash pastes’, *Cement and Concrete Research*, 26, (9) pp. 1351-1359.

Shi, C.J. (1998), ‘Pozzolanic reaction and microstructure of chemical activated lime-fly ash pastes’, *ACI Materials Journal,* 95, (5) 537-545.

Topcu, I.B. (1997), ‘Semi-lightweight concrete produced by volcanic slags’, *Cement and Concrete Research,* 27, (1), pp. 15-21.

Xu, A., Sarkar, S.L. (1991), ‘Microstructural study of gypsum activated fly ash hydration in cement paste’, *Cement and Concrete Research,* 21, 1137-1147.

THE USE OF EMBODIED ENERGY AND CARBON AS INDICATORS OF THE ENVIRONMENTAL IMPACT OF REINFORCED CONCRETE STRUCTURES IN IRELAND

M. McCAFFREY, J. GOGGINS & G. BAYLOR
Dept. of Civil Engineering, National University of Ireland, Galway, Ireland

Abstract

This paper uses embodied energy (EE) and embodied carbon (EC) as indicators of the environmental impact of reinforced concrete (RC). Accuracy and completeness of EE/EC analysis is dependent on the method used. This paper demonstrates that by understanding how energy is consumed in the production of each constituent part and in the manufacture of RC, designers can significantly reduce the overall EE and EC of structures. Both EE and EC of products can vary from country to country. Therefore, to accurately calculate these for RC structures, data specific to the country where they are being constructed must be used. This paper presents the assessment of EE and EC in typical RC structures in Ireland. A case study is presented where it is shown that by replacing ordinary portland cement (OPC) with ground granulated blastfurnace slag (GGBS), savings are achievable in the construction of a multi-megawatt wind turbine in Ireland.

Keywords: (concrete, embodied carbon / energy, life cycle analysis, sustainability)

1 Introduction

The use of natural energy resources has become intrinsic to human behaviour. Today the built environment is responsible for more than 40% of European energy consumption (European-Commission 2002). In recent years there has been a change in public perception as the implications of irresponsible energy usage and resulting climate change have become more evident. However, perceptions and awareness alone are not sufficient factors to convince businesses and industry, who are the main contributors, that a move towards more sustainable use of our resources is required. “Energy” and “Carbon” are two key words which are often used, sometimes interchangeably, in reference to the consumption of available resources. These words are closely linked as the use of energy will have a certain amount of carbon associated with it and is dependent, for example, on whether the source of energy is renewable or not. Studies carried out to date have measured either energy or carbon or both energy and carbon (Bullard et al 1978, Crawford 2008, Hammond & Jones 2008, Acquaye & Duffy 2009, Goggins et al 2010). It is important that both are taken into account.

In the aftermath of the Kyoto protocol (UNFCCC 1998) the ‘Carbon Market’ has incentivised industries to become more sustainable and change their outlook. Currently little attention is being paid to reducing embodied energy (EE) and embodied carbon (EC). These refer to the energy and carbon required for raw material extraction, transport, manufacture, assembly, installation, disassembly, deconstruction and/or decomposition for any product or system. If a drive towards true sustainable use of our resources is to be achieved it is critical that both EE and EC are addressed (Acquaye & Duffy 2009; Goggins et al. 2010).

EE and EC analysis enables informed decision making in relation to the processing methods used and the products purchased in the manufacture and supply of any product or system. This paper outlines how both the EE and EC of reinforced concrete (RC) structures in Ireland can be significantly reduced at potentially little or no extra cost.

2 Embodied Energy & Embodied Carbon in Reinforced Concrete

2.1 Introduction

In the evaluation of the EE and EC there are a number of formally recognised methodologies which exist. These are process analysis, input-output (I-O) analysis and hybrid analysis, which is a combination of both (Bullard et al. 1978; Treloar 1997; Hammond & Jones 2008; Acquaye & Duffy 2009; Goggins et al. 2010). Indirect energy is used to create the inputs of goods and services to the main process, whereas direct energy is the energy used for the main process. The accuracy and extent of an EE/EC analysis is dependent on which of the three main methods is chosen.

Process analysis is a step by step analysis of the inputs to a product. It can, however, suffer from inaccuracy due to truncation and incomplete data. A boundary must be established at some point in order to complete a process inventory analysis.

I-O analysis uses economic I-O tables, which are unique to each economy, to track energy flows through an economy. The Irish I-O tables (CSO 2009a) are separated into 53 sectors. From these the energy sectors are abstracted and disaggregated to calculate energy intensities of manufacturing or service sectors and the products therein. The advantage of using an I-O methodology is that the boundary for the analysis is defined by the economy and, therefore, the completeness of the analysis is improved as the indirect energy inputs are also included (Crawford 2008).

Hybrid analysis takes advantage of both methods and may be primarily process based or I-O based. The energy intensity of typical products from a sector can be accounted for by I-O analysis and incorporated into a process analysis if more detailed data is available for the inventory, and vice versa. This is dependent on the product being assessed.

Three common life cycle (LC) phases include: cradle to gate, cradle to site and cradle to grave (Hammond & Jones 2008). Cradle to gate accounts for all the EE/EC of a product until it leaves the factory gate. Cradle to site includes the additional EE/EC of getting the product to site. This was chosen as the LC phase for this study.

Concrete is the most utilised substance in the world by volume after water. In order to study the EE and EC in reinforced concrete it is necessary to have a comprehensive knowledge of the processes involved in its manufacture and the production of its component materials. RC is divided into its constituent parts of water, binders, aggregate, admixtures and reinforcement. The path of contributing direct EE and EC in concrete is illustrated in Goggins et al. (2010). In the current paper, a process-based hybrid method, based on Irish data, is used to calculate the EE and EC in reinforced concrete structures and the materials used in its construction.

2.2 Water

Combining water with cement forms a binder by the process of hydration (Neville 1995). Generally, water in concrete consists of that added to the mix and that which is carried by the aggregates. Often water is recycled many times in these processes by regular pumping and filtering. As a result, water has a relatively low impact on the CO_2 emissions of concrete.

The I-O total energy intensity of water in Ireland is given in Table 1, and calculated using the ‘water collection, purification and distribution’ economic sector in the 2005 National I-O tables (CSO 2009a) and price indices (CSO 2009b). The primary energy factors (PEF) and the disaggregation constants are evaluated using central statistics office (CSO) data (CSO 2010), along with commission for energy regulation (CER) disclosure of fuel mix figures (CER 2007) and sustainable energy authority of Ireland (SEAI) energy balance statistics (SEAI 2009). An assumed cost of water of 0.16 €/m^3, in 2005 is applied to find the total energy intensity (TEIn) of water in Ireland to be 2.02MJ/m^3, which was evaluated from

$$TEI_n = \sum_{e=1}^{E} T_{RC} \times C_d \times T_e \times PEF \times €_{BP} \quad (1)$$

where T_{RC} is the total requirement coefficients (€/€), C_d is the disaggregation constant (dimensionless), E is the total number of energy supply sectors, e in the I-O table, T_e is the average energy tariff (GJ/€), PEF is the Primary Energy Factor, which is a ratio of the primary energy embodied in a fuel to the delivered energy (dimensionless), and $€_{BP}$ is the basic price of water (€/m^3).

For supplied and treated water in Ireland and assuming average energy mix emissions, Ireland's carbon emissions of 0.36kgCO_2/m^3 for water could be higher than the UK. In the UK, Defra (2009) estimate emissions from full life-cycle of 1m^3 of supplied and treated water as 0.28kg carbon dioxide equivalent (CO_{2e}). CO_{2e} is calculated using the global warming potential (GWP) of the green house gases focused on by the Kyoto protocol (UNFCCC 1998), namely, carbon dioxide (CO_2), methane (CH_4), nitrous oxide (N_2O), hydrofluorocarbons (HFCs), perfluorocarbons (PFCs) and sulphur hexafluoride (SF_6).

Work is ongoing by the authors to obtain more accurate EE and EC values for water. GHG emissions need to be converted to carbon dioxide equivalent CO_{2e} and the assumed price for water also needs to be investigated further. However, in this application water is found to have a negligible effect on the EE and EC of reinforced concrete (Section 3).

Table 1 – I-O Calculation of the total energy intensity of water

Energy supply sector	Primary energy factor, PEF	Average energy tariff, T_e(GJ/€)	Disaggregation constant, C_d	Total requiremet coefficient, T_{RC} (€/€)
Peat	1.05	0.1124	0.341	0.002
Crude Oil	1.00	0.5055	0.136	0.002
Coal	1.00	0.3681	0.015	0.002
Petroleum	1.00	0.1507	0.494	0.008
Natural Gas	1.05	0.227	0.428	0.095
Electricity (non renewable)	1.13	0.0337	0.483	0.095
Renewable Energy	1.00	0.0686	0.089	0.095
Total energy intensity, TEI (MJ/€)				0.0129
Price €/m3 (2005)				0.16
Total energy intensity, TEI (MJ/m^3)				2.02

Table derived from: SEAI (2009), Goggins et al.(2010), CSO(2009;2010), CER(2007).

2.3 Binders

Ordinary Portland Cement (OPC) is the most common binder used in concrete and can contribute up to 65% of the EE in concrete (Section 3). The energy consumed in the cement manufacturing process varies depending on process used (Taylor 1997), but is largely due to the high temperatures required to form clinker. According to Van Puyvelde (2009) the cement industry represents 7% of total global anthropogenic CO_2 emissions. However, with new technologies the cement industry is reducing its CO_2 emissions. For example, the Australian cement sector reduced its reportable CO_2 emission per tonne of cement produced by 20% between 1990 and 2007 (CIF 2007).

Any further cuts are limited to the extent of which cement extenders can be used to produce a material with adequate stress and strength properties (Van Puyvelde 2009). Van Puyvelde (2009) believes that further reductions beyond that will require either a move away from a calcination process (i.e. not using a carbonate as a raw material) or to adopt the use of carbon capture and storage (CCS) for the cement industry.

Using data from CSO (2010) with energy conversion and carbon emission factors (Howley et al. 2008; Defra 2009), and energy prices from SEAI (2005), the direct EE and EC to produce a kg of cement are calculated as 4.03MJ and 0.91kgCO_2, respectively. The chemical reaction is accounted for in the EC, as according to Hendriks et al. (1998) it is said to account for 0.5kgCO_2/kg of cement produced. Using the hybrid I-O methodology, the total EE of cement produced in Ireland for 2005 is calculated as 4.52MJ/kg, which is larger than the direct EE as it includes indirect EE. In Ireland, 637g of CO_2 was produced for every kWh of electricity produced in the year 2005 (Howley et al. 2008). If this is used to convert the indirect EE to EC then the total EC of cement produced in Ireland in 2005 is found to be 0.99kgCO_2/kg. The results compare to values of 4.6MJ/kg and 0.83kgCO_2/kg in the UK (Hammond & Jones 2008), and also EC values of 0.73kgCO_2/kg and 0.99kgCO_2/kg in Japan and the U.S, respectively (Mahasenan et al. 2005).

The breakdown of contributing direct energy sources in relation to EE and EC are given in Figure 1 and Figure 2, respectively. The chemical reaction is the most significant contributor to the direct EC at 55%. A move away from carbonates in the production process is a proposed means of reducing this emission (Van Puyvelde 2009). The direct EE and EC from electricity, for the year 2005, are 10% and 8% respectively. Coal and petroleum coke account for 50% and 38% respectively of the EE, and contribute 18% each to its associated EC total. Therefore, curtailing the use of petroleum coke and coal should significantly reduce emissions, which can be achieved by using fuels with lower associated emissions.

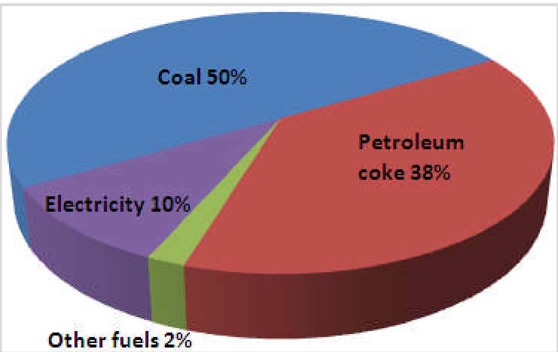

Figure 1 – Breakdown of cement manufacture direct EE (MJ/kg)

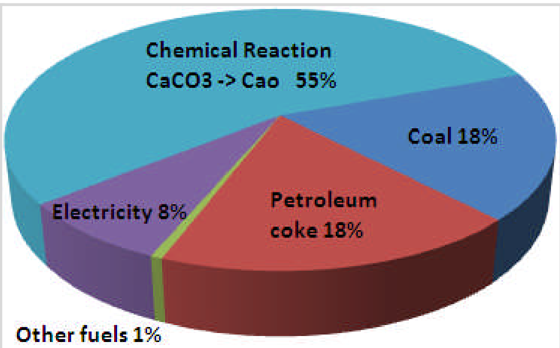

Figure 2 - Breakdown of cement manufacture direct EC (kgCO_2/kg)

While the cement manufacturing process is being re-assessed other solutions to reducing the emissions associated with its use in concrete are being explored. For example, many waste or by-product materials can be used as binders (Goggins & Gavigan 2010) with ground granulated blast furnace slag (GGBS) being one of the most common. Blastfurnace slag is a by-product of the steel industry. Granulated blastfurnace slag (GBS) is obtained by rapidly cooling the slag with water, which is an additional process required to produce GBS for convenient use as a binder material. Therefore, in this study the additional energy required in this granulation process is included in the EE and EC of GBS. It is assumed that water and electrical power consumption in this process is 1m^3/t slag and 8kWh/t slag, respectively (Muñiz 2007). GBS is imported to Ireland from mainland Europe and is grinded in Dublin to give GGBS. The total EE and EC of GGBS from processing and transport to Ireland is 0.715MJ/kg and 0.029kgCO_2/kg, respectively.

Up to 85% of OPC can be replaced with GGBS. Replacement levels vary, but are typically of the order of 40 - 50%. As shown in the case study (Section 3), the use of GGBS reduces the overall EE and EC of concrete. Furthermore, other studies have shown that greenhouse gas emissions are reduced by 40% using a replacement of 50% of cement with GGBS (Higgins 2007). Concrete mixes containing GGBS yield a high ultimate strength and produce a lower heat of hydration (Neville 1995). This makes it ideal for thick sections, such as large foundation pours, where the temperature gradient resulting from the heat of hydration from OPC induces excessive thermal stresses. These thermal stresses may cause micro-cracking, which exposes the concrete to external attack. However, a disadvantage is that the rate of early strength development can be reduced. This may be of concern to contractors when constructing concrete frames, which may delay the time required for curing before striking of formwork can take place.

2.4 Aggregate

Aggregate constitutes up to approximately 80% of a unit of concrete. Quarries process stone by different methods, for example, by drilling boreholes and inserting gelignite which is detonated, dislodging large volumes of rock. A typical aggregate in Ireland is limestone. For the aggregate EE calculations the process based hybrid method is used by including process data compiled by Kennedy (2006). The EE of Irish aggregate is found to be 0.096MJ/kg. For this study, the EC of aggregates is taken as 0.005kgCO_2/kg (Hammond & Jones 2008).

In recent years, aggregates from construction, demolition and excavation waste have been recycled and used as partial replacements for natural aggregates in concrete (Savage 2001; Kwong 2006). There are two methods for including recycled material in an EE analysis; the *recycled content* method and the *substitution* method. The recycled content approach takes into account any recycled materials in a product. The substitution method credits the product with whatever the likely percentage of it to be recycled is. An extreme case of this could see the EE of a concrete structure being drastically reduced as it may be recycled as aggregate at the end of its life. Hammond & Jones (2008) believe that the recycled content approach better serves to accomplish the motivations behind energy analysis and, where possible, these values are used.

2.5 Admixtures

Admixtures are chemicals that are added to concrete to give it certain characteristics, which are not obtainable with a regular concrete mix. Admixtures are added in very small amounts during mixing. Because of the nature of their production, it is difficult to quantify energy involved in production of admixtures. As they account for such a small part of a unit of concrete it is assumed that their contribution is negligible.

2.6 Manufacturing process of concrete

The process based hybrid method is utilised to calculate the EE of concrete with the EE of each of the constituent materials (i.e. indirect inputs) which are then added to the direct energy required during the production of the concrete.

The I-O direct energy intensity for concrete manufacture in Ireland is calculated using the ‘non-metallic minerals’ sector in the I-O tables and wholesale price indices, similar to the process described in Section 2.2 except in this case for the direct energy intensity (DEI_n). Pricing information obtained from suppliers and Spon (2008) are applied, finding the DEI_n for concrete in Ireland to be 0.271MJ/kg, evaluated from

$$DEI_n = \sum_{e=1}^{E} D_{RC} \times C_d \times T_e \times PEF \times €_{BP} \tag{2}$$

where D_{RC} is the direct requirement coefficients (€/€) and C_d, E, e, T_e, PEF and $€_{BP}$ are as defined in Equation 1.

The total embodied energy, EE_t, of concrete is obtained by combining the results from process and I-O based analyses (in other words, a process based hybrid):

$$EE_t = \sum \left(Q_M \times W \times EI_M \right) + DEI_n \tag{3}$$

where Q_M (kg) is the quantity of the material (e.g. cement, aggregate, water), W is the wastage multiplier of the material, EI_M is the energy intensity of the material and DEI_n is the direct energy intensity of the I-O sector containing concrete from Equation 2.

Wastage factors W for concrete and reinforcement are 4.86% and 5.0%, respectively (Tam et al. 2007). Using Equation 3 and mix proportions, by mass, of 12%, 82% and 6% of cement, aggregate (and sand) and water, respectively, the EE of 30MPa concrete is 0.922MJ/kg. Using a similar calculation process to EE, EC is calculated for this mix design as 0.166kgCO_2/kg. However, these figures do not include transport, reinforcement, pouring of concrete or dismantling at end of structure’s life. This is recognised as the cradle to gate figure (Hammond & Jones 2008).

2.7 Concrete & reinforcement transport

A concrete ready mix truck generally carries 6m^3 of concrete with a kerb weight of 21515kg (Iveco 2009). Kennedy (2006) calculates energy usage by various vehicles on different road types. The energy required to transport concrete is 11.04MJ/km for the outbound journey and 8.42 MJ/km for the return. The majority of concrete batching sites in Ireland have an on-site quarry due to the expense of aggregate transport and the calculations are completed using this assumption.

The total time between the beginning of the mixing of concrete and the final pouring of concrete should not exceed 90 minutes. Accounting for outgoing journey time, pouring time, and return time the maximum distance that concrete may be transported in a 6m^3 capacity truck is 53km giving the EE at 0.072MJ/kg, which represents less than 6% of the EE value for concrete. Transport may significantly increase the EE of concrete if partial loads are required. Using Defra (2009) values for trucks emissions, the equivalent EC of these trucks is 0.0064kgCO_2/kg in the aforementioned scenario.

Although all reinforcement used in Ireland is sourced in the UK, it is bent and cut in Ireland. The value of EE and EC of recycled steel is 8.8 MJ/kg and 0.42kgCO_2/kg, respectively (Hammond & Jones 2008). Transport and further processing of the steel must be accounted for. Assuming that a fully loaded truck can carry 24,000 kg of steel (Iveco 2009), the energy used in transport is 0.00046 MJ/km/kg steel for the outbound journey and 0.00035 MJ/km/kg steel for the return. For the purposes of this analysis the energy used to cut and bend the steel is assumed to be negligible considering the high energy use in recycling the steel. Wastage of reinforcement at the bending and cutting facility is, however, not negligible. The standard bar length is 14m. After the bar is cut there are normally sections of bar remaining which are too short to be used. As there is no facility in Ireland to recycle these, they must be returned to the UK for further processing. This analysis will assume that 15% of the steel is returned for further processing. Assuming a total return journey length of 900km from the steel recycling facility in the UK to site (via the processing facility in Ireland) the energy required to transport the steel is 0.365MJ/kg. This is 4.1% of the cradle to gate value for recycled steel. The EC for transport of the reinforcement is 0.033kgCO_2/kg.

3 Case Study

This case study analyses the effects of cement replacements on the EE and EC in the RC foundation of an on-shore wind turbine if it had been constructed in Ireland, for the year 2005. The study is based on the Enercon E126/6MW wind turbine constructed in Emden, Germany (Enercon 2007).

The foundation requires 1500m^3 of concrete and 180 tonnes of steel reinforcement. The batching plant is located 11km from the turbine and a 30MPa concrete mix is used. A comparison is made using two mix designs. The first contains a binder solely of OPC, while in the second mix design 50% of the OPC is replaced with GGBS, which is transported 200km from the grinding plant in Dublin to the batching plant. The resulting EE and EC of the two mixes are given in Table 2, which highlights the positive effect that GGBS can have in reducing the EE and EC of a concrete structure.

As can be seen from Table 2, cement is by far the greatest contributor to the total EE of concrete accounting for 56% and 36% of the EE in the mixes with 0% GGBS and 50% GGBS, respectively. Furthermore it accounts for 65% and 47% of EC of the respective concrete mixes. Replacing 50% of the OPC with GGBS results in reductions of 23% and 31% to the EE and EC of concrete used in the foundation, respectively.

The direct energy refers to the energy required to combine the cement, aggregate and water into concrete. It should also be noted that reinforcement is also a major contributor to the total EE, accounting for 35% and 42% of the EE of the foundation constructed from concrete mixes with 0% GGBS and 50% GGBS, respectively. On the other hand, reinforcement accounts for 13% and 18% of the EC, respectively.

Table 2 – EE & EC of a reinforced concrete wind turbine foundation.

	EE (GJ)		**EC(kgCO_2)**	
***Mix:**	Design 1	Design 2	Design 1	Design 2
Aggregate	296	296	15,477	15,477
Cement	2,046	1,023	410,472	205,236
GGBS	-	162	-	6,568
Water	0	0	81	81
Direct	1,023	1,023	181,017	181,017
Transport concrete	272	272	24,160	24,160
Reinforcement	1,992	1,992	98,460	98,460
Total	5,629	4,796	729,666	533,626

*** Mix design 1: = 100% OPC; Mix design 2: 50% OPC + 50% GGBS**

The total energy saving achieved through the use of GGBS is 833GJ, while 196 tonnes of CO_2 have been saved. The CO_2 savings would equate to 63 cars being taken off the road for one year or the same amount of CO_2 would be absorbed by 25 acres of managed Irish forest for one year. On the other hand, the EE saved is equal to the energy used by 26 average homes in Ireland in one year (Howley et al. 2008).

4 Conclusions

The 'Carbon Market' has incentivised industries to become more sustainable and change their outlook. If a drive towards true sustainable use of our resources is to be achieved both EE and EC need to be addressed. Research is ongoing to develop methods of significantly reducing CO_2 emissions. The first step towards achieving this is to measure, monitor and review all direct and indirect energy use to understand energy demands using formally recognised methodologies.

This paper uses the hybrid I-O methodology to investigate the energy consumed in the production of RC in Ireland. The processes involved in the manufacture of concrete and reinforcement are analysed with the most energy intensive processes being identified. A process based hybrid analysis is performed and the cradle-to-gate EE and EC of a 30MPa concrete mix are found to be 0.922MJ/kg and 0.166kgCO_2/kg, respectively. A case-study on a RC wind turbine foundation in Ireland reveals that by replacing 50% of the cement content with GGBS, results in a 23% reduction in the EE and a 31% reduction in EC. Future studies will be produced with an aim to show all emissions in terms of CO_{2e}, along with more recent emission values and energy intensities. Additionally, it is envisaged to carry out an EE/EC assessment on a pre-cast concrete beam in the new engineering building in NUI, Galway.

Further reductions in the EE and EC of reinforced concrete can be achieved by maximising the use of recycled aggregates and addressing the unsustainable use of coal and petroleum coke (which contribute to 88% of the EE associated with cement).

Acknowledgement

The authors would like to thank Michael Brennan of the CSO for his valuable advice on the Irish Supply and Use and I-O Tables.

References

Acquaye A. A. and Duffy A. P. (2009). "Input-output analysis of Irish construction sector greenhouse gas emissions." *Building and Environment* 45(3): 784-791.

Bullard C. W., Penner P. S. and Pilati D. A. (1978)."Net energy analysis: Handbook combining process and input-output analysis."*Resources and Energy* 1(3):267-313.

Cement-Industry-Federation (2007). Australian Cement Industry Statistics 2007.

Commission for energy regulation (2007). Disclosure of energy mix figures 2005, CER.

Crawford R. H. (2008). "Validation of a hybrid life-cycle inventory analysis method." *Journal of Environmental Management* 88(3): 496-506.

CSO (2009a). Supply and Use and Input-Output Tables for Ireland 2005. Central Statistics Office. Dublin, Stationary Office.

CSO (2009b). Wholesale Price Index, from http://www.cso.ie/releasespublications/pr_pricesarchive2005.htm

CSO (2010). Input-Output analysis statistics. Received by M. McCaffrey. Dublin.

Defra (2009). 2009 Guidelines to Defra / DECC’s GHG Conversion Factors for Company Reporting: Methodology Paper for Emission Factors. London: Defra.

Enercon (2007). World’s most powerful wind turbine installed near Emden. WINDBLATT. Dreekamp 5 · 26605 Aurich · Germany, Enercon GmbH.

European-Commission (2002). Commission directorate 2002/91/EC on the energy performance of buildings. European Commission Official Journal L1**:** p. 65-71.

Goggins J. and Gavigan D. (2010). Low-cost sustainable construction technology for autonomous buildings. *International Conference of Structures and Architecture* (ICSA2010). Guimaraes, Portugal.

Goggins J., Keane T. and Kelly A. (2010). "The assessment of embodied energy in typical reinforced concrete building structures in Ireland." *Energy and Buildings* 42(5): 735-744.

Hammond G. P. and Jones C. I. (2008). Inventory of carbon and energy (ICE) Version 1.6a, from http://www.bath.ac.uk/mech-eng/sert/embodied.

Hendriks C. A., Worrell E., Blok K., de Jager D. and Riemer P. (1998). Emission reduction of greenhouse gases from the cement industry. *Greenhouse gas control technologies conference* (www.ieagreen.org.uk)

Higgins D. (2007). GGBS and sustainability. Proceedings of the Institution of Civil Engineers. Construction Materials.pp:99-101

Howley M., O’Leary F. and Ó Gallachóir B. (2008). SEI Energy in Ireland 1990 - 2007: Trends, issues, forecasts and indicators, Dublin: Sustainable Energy Ireland, Energy Policy Statistical Support Unit.

Iveco. (2009). "Specification Sheets, Iveco." Retrieved 21 March, 2009, from http://www.iveco.com/Uk/Products/Pages/Trakker_Specification_Sheets.aspx.

Kennedy E. (2006). The Integration of the Measurement of Energy Usage into Road Design. Dublin, National Roads Authority.

Kwong C. (2006). The use of recycled concrete aggregate in structural concrete around South East Queensland. *Unpublished BE thesis*.

Mahasenan N., Dahowski R. T., Davidson C. L., Rubin E. S., Keith D. W., Gilboy C. F., Wilson M., Morris T., Gale J. and Thambimuthu K. (2005). The role of carbon dioxide capture and storage in reducing emissions from cement plants in North America. *Greenhouse Gas Control Technologies* 7. Oxford, Elsevier Science Ltd**:** 901-909.

Muñiz M. (2007). Slags: supply and demand, *BMI Symposium*, Madrid

Neville A. M. (1995). Properties of Concrete 4th edn. Essex, Pearson Education.

Savage T. (2001). "Using recycled aggregates: Wessex Water New Operations Centre, Bath." *The Structural Engineer* (79.12).

SEAI (2005). Commercial Fuel Cost Comparisons, from http://www.seai.ie/Publications/Statistics_Publications/Fuel_Cost_Comparison/.

SEAI (2009). Energy Balances 1990 - 2008, from http://www.seai.ie/Publications/Statistics_Publications/Energy_Balance/Previous_Energy_Balances/.

Spon (2008). SPON'S Irish Construction Price Book 3rd Edn. London, Spon Press Taylor & Francis Group.

Tam V. W. Y., Shen L. Y. and Tam C. M. (2007). "Assessing the levels of material wastage affected by sub-contracting relationships and projects types with their correlations." *Building and Environment* 42(3): 1471-1477.

Taylor H. (1997). Cement Chemistry 2nd edn. London, Thomas Telford Ltd.

Treloar G. J. (1997). "Extracting embodied energy paths from input-output tables: Towards an input-output-based hybrid energy analysis method." *Economic Systems Research* 9(4):375-91.

UNFCCC (1998). Kyoto protocol to the United Nations framework convention on climate change. http://unfccc.int/resource/docs/convkp/kpeng.pdf, UNFCCC.

Van Puyvelde D. R. (2009). "CCS opportunities in the Australian "Industrial Processes" sector." *Energy Procedia* 1(1): 109-116.

METHODOLOGY FOR DESIGNING STRUCTURES TO WITHSTAND EXTREME ENVIRONMENTS: PERFORMANCE-BASED SPECIFICATIONS

S.NANUKUTTAN[1], N.HOLMES[1], S.SRINIVASAN[1], L.BASHEER[1], P.A.M. BASHEEER[1], L. TANG[2] & J. McCARTER[3]
[1]Queen's University of Belfast, Belfast
[2]Chalmers University of Technology, Gothenburg, Sweden
[3]Heriot-Watt University, Edinburgh

Abstract
Existing guidelines in BS 8500 allow the selection of concrete mix based on variables such as compressive strength, maximum water to binder ratio, minimum cement content and minimum cover thickness. This approach does not guarantee the durability and expected performance of the concrete structure in a given environment. One alternative is to develop performance- based specifications that supplement the existing guidelines in BS 8500, by specifying the required performance of concrete in terms of measurable properties such as resistance to environmental penetrations. This paper demonstrates one of such methodology for developing performance-based specifications for concretes exposed to marine environments. Chloride ingress related durability problem being critical in a marine environment, the reliability and repeatability of the different test methods for assessing the rate of chloride ingress is discussed first. Furthermore, a numerical simulation model is used to explore the test data to obtain long-term chloride ingress trends. Based on this, guidelines for selecting appropriate concrete mixes for a marine exposure is presented and discussed.

Keywords: Chloride Diffusivity, Chloride Ingress, Concrete Testing, Electrical Resistivity, Modelling, Permit Ion Migration Test, Performance-based Specification

1. General

A significant part of the construction budget is spent for repair and rehabilitation of concrete structures that deteriorates prematurely. As a direct consequence of this, asset owners are often forced to take decisions to repair and maintain an existing ailing infrastructure as opposed to investing in new ones. An effective decision making in this regard requires systematic information about the state of health of an asset (or expected performance), an acceptable level of variance in the ascertained information, an effective maintenance strategy that is linked to its whole life value. In the case of concrete infrastructure, factors such as materials used, design and type of loading on the structure, its location, severity of the exposure condition, etc., all will influence the decision making process due to calculated state of health of the structure. Therefore, it is important to specify the expected performance of a structure in addition to guidelines given in standards, such as BS 8500, which cover the factors defined earlier. At present, there are no performance specifications available for new concrete structures that will ensure the expected state of health of an asset. This paper outlines one of the approaches for developing performance-based specifications for concrete structures exposed to marine environments.

The main objective of this paper is to summarise developments in testing and modelling concrete for chloride ingress and illustrate how progress could be made in developing performance-based specifications with the help of these techniques.

2. Measurement of resistance to chloride ingress in concrete

Although the primary mechanism of chloride transport through unsaturated concrete cover is absorption, the accumulation of chlorides in this layer leads to further penetration of chlorides into concrete by diffusion (Nilsson *et al.*, 1996). As a consequence, diffusion becomes the most dominant mechanism of chloride transport at greater depths, which can be measured in terms of the coefficient of chloride ion diffusion. Different test methods are available to determine the chloride ion diffusion coefficient, e.g. steady-state and non-steady-state chloride diffusion and migration tests.

2.1 Relationship between chloride penetration and concrete diffusivity assessed using different lab based test methods

Figures 1 to 3 show the diffusivity of concrete (assessed using different lab based tests) plotted against the quantity of chloride ions measured at 5 and 10 mm depths from the exposed surface. The chloride ion concentration at these depths was determined by analysing powder samples which were collected from concrete samples immersed in 2.8M NaCl solution for 35days using potentiometric titration method. Data points in the graphs represent ten different concrete mixes. Further details regarding the mixes are available in Table. Results presented in Figures 1 to 3 show that the diffusivity assessed by the different test methods can be used with varying degree of accuracy to predict the quantity of chloride ions at a particular depth.

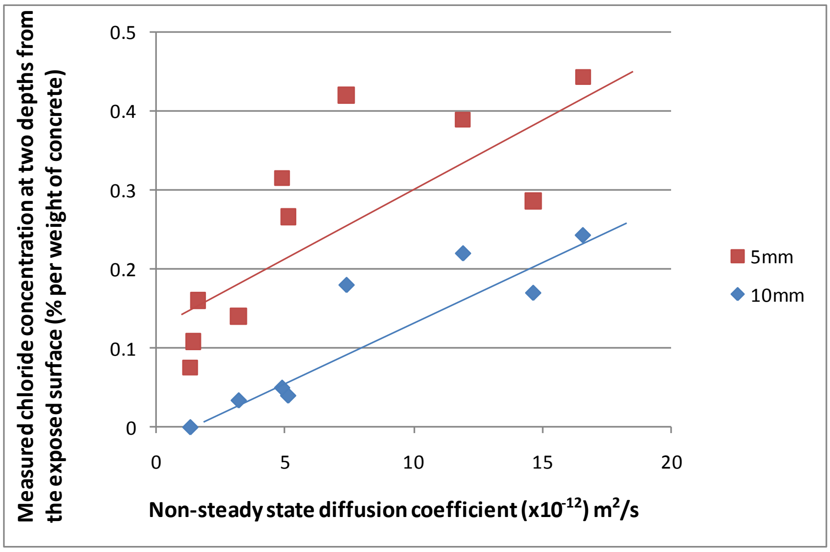

w/cm	Mix detail
0.50	opc
0.45	opc
0.35	opc
0.40	opc + ms
0.42	opc + ms
0.42	opc + pfa
0.45	opc + pfa
0.42	opc + ggbs
0.45	opc + ggbs

Figure 1 – Chloride concentration versus non-steady state diffusion coefficient for 5mm and 10mm depths from the exposed face of concrete specimens (Mix details in Table 1)

Figures 2 and 3 suggest that useful information about penetration of chloride ions can be obtained using rapid test methods. Nordic Test Build 492 (1999) requires on average 24 hours for assessing the diffusivity of concrete whereas electrical resistivity can be measured instantaneously. It is also worth noting that the electrical resistivity in this case was obtained from concrete specimens saturated with calcium hydroxide

($Ca(OH)_2$) solution. However, all these tests require concrete cores with a minimum thickness 50mm to be extracted from the structure. This will considerably limit the number of test that can be performed and frequent testing can leave the structure badly disfigured. It is also worth noting that there are test methods such as Permit Ion Migration test, that can be used on site for assessing the rate of chloride ingress through concrete and eliminates extraction of cores (Nanukuttan, *et.al*, 2006).

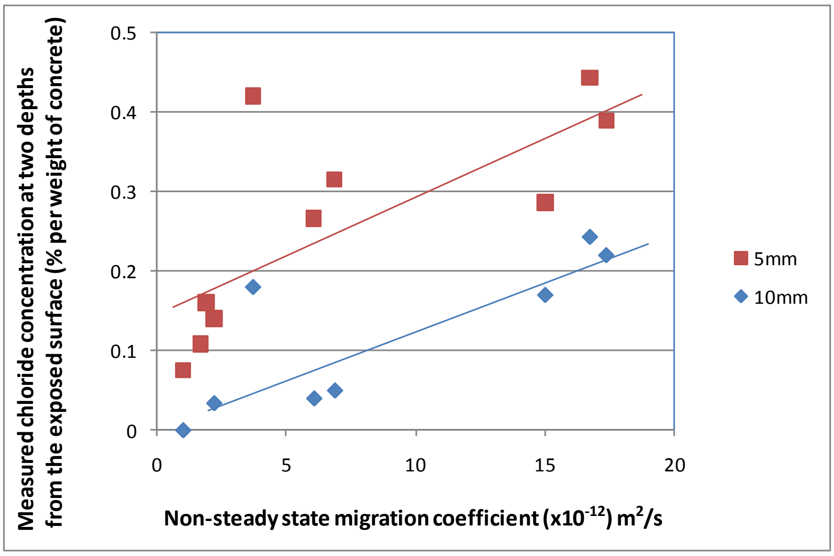

w/cm Mix detail
0.50 opc
0.45 opc
0.35 opc
0.40 opc + ms
0.42 opc + ms
0.42 opc + pfa
0.45 opc + pfa
0.42 opc + ggbs
0.45 opc + ggbs

Figure 2 – Chloride concentration versus non-steady state migration coefficient (Nordic Test Build 492) for depths 5mm and 10mm from the exposed face of concrete specimens

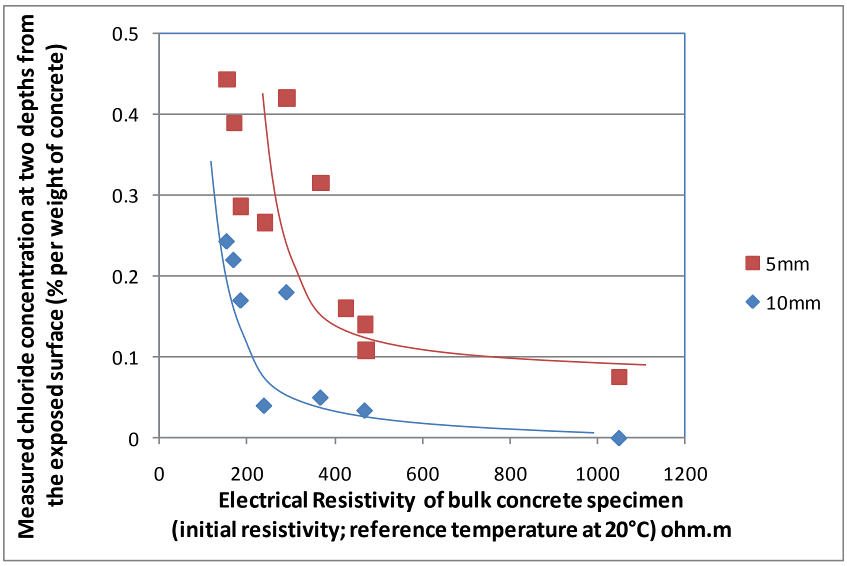

w/cm Mix detail
0.50 opc
0.45 opc
0.35 opc
0.40 opc + ms
0.42 opc + ms
0.42 opc + pfa
0.45 opc + pfa
0.42 opc + ggbs
0.45 opc + ggbs

Figure 3 – Chloride concentration versus electrical resistivity of bulk concrete for 5mm and 10mm depths from the exposed face of concrete specimens (Mix details in Table 1)

2. Effect of concrete mix properties on long term performance

Three test methods that can assess the chloride ingress resistance of concrete were identified in the previous section. It is vital to understand the repeatability and scope of the results in order for the test to be used for qualifying concrete. Table 1 shows mix details of 9 different concretes used in constructions across Europe and data on the chloride diffusivity (or chloride ingress resistance of concrete). The results in Table 1 identify the beneficial effects of using supplementary materials, such as pfa, ggbs and ms, and the influence of w/b on chloride ingress resistance. Most of the results are on average ±20% from the median. The results presented in Table 1 is in agreement with that reported by 11 other participating institutions who compared the repeatability and reproducibility of the test methods as part of an EU funded project (Chlortest, 2006). Hence it can be concluded that the tests are repeatable with 20% variability. To study the scope of these results it is necessary either to study the long-term behaviour of these concrete mixes in a field exposure environment or to simulate the behaviour in a given environment. The former would require long-term study with considerable investment and resources, whereas the latter would depend heavily on the accuracy of the numerical model used for predicting the behaviour. The approach used in this paper is to consider both the aspects. The long-term performance data from a structure exposed to a marine environment (North Sea) is used to validate the numerical models used for prediction. The second aspect is to use the test results along with the validated numerical model to predict the behaviour of different concrete mixes in the same environment.

Figure 4 - Shows the location of the pier stem (right hand side of the picture) near the Dornoch bridge, Scotland

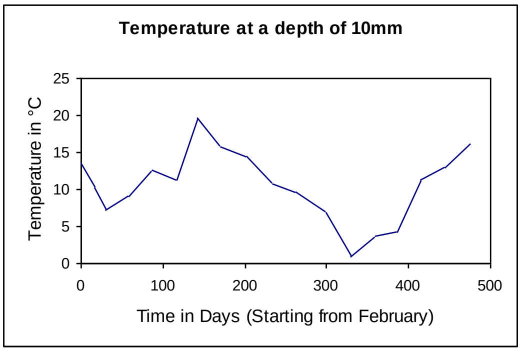

Figure 5 - Temperature of concrete at 10mm depth recorded for 16 months.

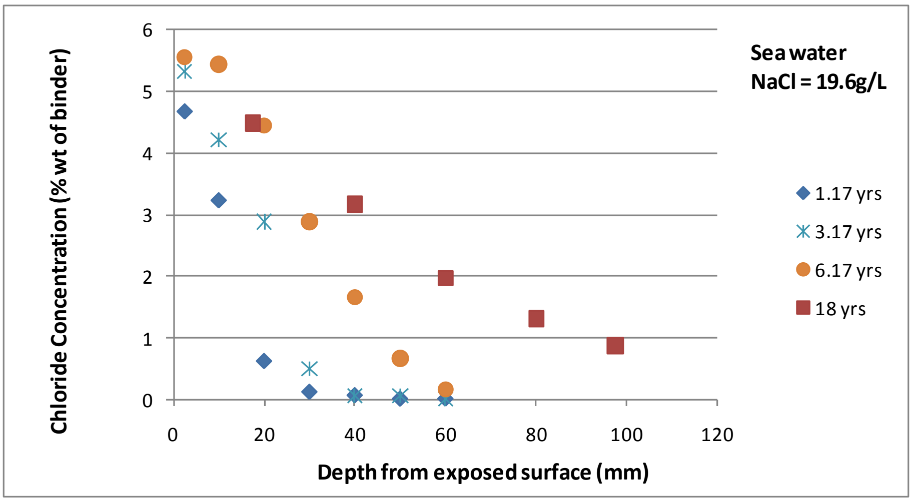

Figure 6 - The chloride profiles from OPC pier stems exposed to tidal low level

Table 1 Details of concrete mixes (Quantities reported in kg/m^3) and their chloride ingress resistance as measured by different test methods

Mix designation	**opc 0.35**	**opc 0.45**	**opc 0.50**	**ms 0.40**	**ms 0.42**	**pfa 0.42**	**pfa 0.45**	**ggbs 0.42**	**ggbs 0.45**
Country of Origin	Sweden	Spain	Sweden			Norway	Portugal	Netherlands	
Cement type (BS EN 197-1, 2000)	CEM I 42.5 N	CEM I-42.5 N	CEM I 42.5 N			(18% PFA) CEM II/A-V 42.5 R	(39% PFA) CEM IV/B 32.5R	(~70% Slag) CEM III/B 42.5 LH HS	
Cement content	450	400	400	399	389.5	410	340	410	350
Microsilica				21	20.5				
Water	157.5	180	200	168	172.2	172.2	153	172.2	157.5
Fine Aggregate (Min size 75μm)	904 (≤8mm)	742 (≤6mm)	920 (≤8mm)	842.5 (≤8mm)	897 (≤8mm)	901 (≤8mm)	62 (≤2mm) 603 (2-4mm)	901 (≤8mm)	70 (≤1mm) 790 (1-4mm)
Coarse Aggregate	904 (5-10mm)	1030 (6-16mm)	816 (5-10mm)	842.5 (8-16mm)	897 (10-15mm)	901 (10-15mm)	619 (4-12mm) 555 (12-25mm)	901 (5-10mm)	1040 (4-16mm)
Superplasticiser % of cement	CemFlux Bro 1.0	Melcret 222 4.8	-	Cementa 92M 3.4	CemFlux Bro 0.5	CemFlux Bro 0.5	Rheobuild 1000 4.1	CemFlux Bro 0.5	Cretoplast 3.9
water/binder (w/b)	**0.35**	**0.45**	**0.5**	**0.4**	**0.42**	**0.42**	**0.45**	**0.42**	**0.45**
Age at test (years)	~0.5	~1.0	~0.5	>1.0	~0.5	~0.5	<1.0	~0.5	<1.0

Measurable performance indicators (chloride diffusivity/bulk electrical resistivity results)

Mix designation	**opc 0.35**	**opc 0.45**	**opc 0.50**	**ms 0.40**	**ms 0.42**	**pfa 0.42**	**pfa 0.45**	**ggbs 0.42**	**ggbs 0.45**
D_{nssd} x 10^{-12} m^2/s (standard error)	5.11 (±0.56)	14.63 (±3.74)	16.56 (±1.82)	1.61 (±0.62)	4.88 (±0.58)	1.44 (±0.27)	7.38 (±2.43)	1.31 (±0.16)	3.19 (±1.35)
D_{nssm} x 10^{-12} m^2/s (standard error)	6.00 (±1.24)	15.00 (±3.02)	16.70 (±0.99)	1.90 (±0.07)	6.90 (±0.50)	1.70 (±0.13)	3.70 (±0.54)	1.00 (±0.05)	2.20 (±0.25)
ρ_{bulk} (ohm.m) (standard error)	175.70 (±16.5)	187.00 (±22.19)	56.00 (±12.77)	426.80 (±21.25)	236.30 (±31.00)	323.70 (±40.07)	291.40 (±4.61)	838.30 (±160.32)	469.80 (±17.25)
$D_{in\ situ}$ x 10^{-12} m^2/s (from Permit Ion Migration Test based on $D_{in\ situ} = 0.11\ D_{nssm}$)	0.66	1.65	1.84	0.21	0.76	0.19	0.41	0.11	0.24
Predicted Chloride concentration at 50mm depth (% wt of binder as in Fig. 10)	For North-Sea tidal low level exposure (constant wetting and drying condition) using ClinConc Service Life Prediction Model [ref]								
	2.56	4.42	4.75	0.77	2.89	0.86	2.37	0.31	1.15

CemFlux Bro is polycarboxylether based superplasticiser; Melcret 222 and Rheobuild 1000 are both napthalene based superplasticisers; Cretoplast is a water reducing superplasticiser; Cementa 92M is melamine formaldehyde based superplasticiser; D_{nssd} is the coefficient from non-steady diffusion test; D_{nssm} is the coefficient from non-steady migration test; $D_{in\ situ}$ is the coefficient from Permit ion migration test; ρ_{bulk} is the saturated bulk electrical resistivity

Long-term performance study on concrete specimens exposed to North Sea

Data from a long-term study conducted on three ordinary Portland cement concrete pier stems exposed to tidal, splash and atmospheric conditions in North Sea are presented below (Nanukuttan *et al.* 2008). The concrete mix details are reported in Table 2. Chloride concentrations from various depths (termed as chloride profile) were determined continuously for a period up to 7 years and then after 18 years. General location of the piers and annual temperature variation at the site is as shown in Figures 4 and 5 respectively. Chloride profiles determined at 1.17, 3.17, 6.17 and 18 years from tidal low level (immersed continuously and rarely dry) are presented in Figure 6.

Table 2. Mix details for OPC pier stems exposed to North Sea

Mix	Cement kg/m^3	20mm kg/m^3	10mm kg/m^3	Fines kg/m^3	w/b	F_{28} MPa	D_{nssm} (10^{-12}m^2/s)
Plain	460	700	350	700	0.4	66	15 (± 3.5)

Several service life prediction models were considered as part of the wider study. However, only data from numerical simulations made using ClinConc service life model (Tang, 2006) is reported in this paper. In any case, this model was selected based on the recommendations by an EU FP5 Growth Programme project (ChlorTest, 2006) which reviewed different test methods and service life models.
The real and numerically simulated chloride profiles are presented in Figures 7-9. The top and bottom lines indicate the level of variation due to the disparity in input parameters including D_{nssm}. Figures 7 and 8 show that numerical simulation can predict the chloride profile with a high degree of accuracy. However, at the age of 18 years (Fig. 9), the simulation has underestimated the chloride ion content at depths greater than 50mm. The cause of this disparity, whether experimental error or error in the simulation, needs to be studied further.

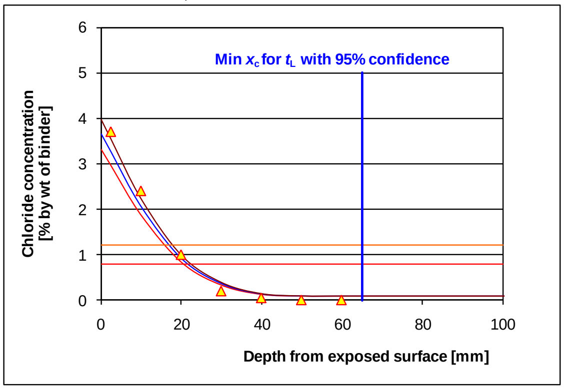

Figure 7 - The real and predicted chloride concentration after 1.17 years of exposure.

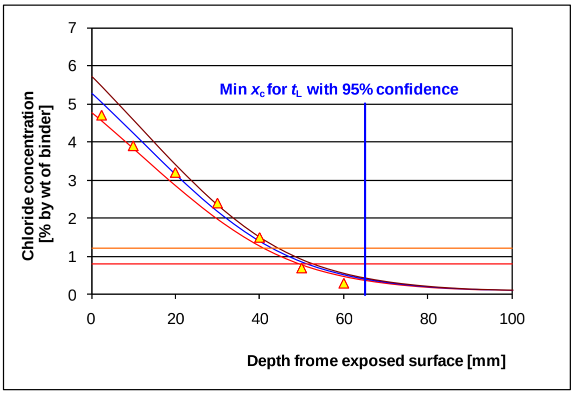

Figure 8 - The real and predicted chloride concentration after 7.17 years of exposure.

Guidelines for selecting concrete mixes for marine exposures

Based on the non-steady state migration coefficient (D_{nssm}) in Table 1, chloride profiles were simulated for the different concrete mixes exposed to the North Sea environment. Figure 10 shows the chloride profiles after 50 years of exposure to tidal low level exposure zone in North Sea. Such information will allow users to select a suitable concrete mix for their exposure condition. Furthermore, the test results such as D_{nssm} identified in Table 1 can be used for defining performance-based specifications for concretes. As an example, in order to keep the chloride concentration at the level of reinforcement that is at a depth of 50mm from the exposure surface to a value below 0.5 % by wt of binder, one should use 0.42 ggbs or any concrete which has a diffusivity D_{nssm} less than 1 x 10^{-12} m^2/s.

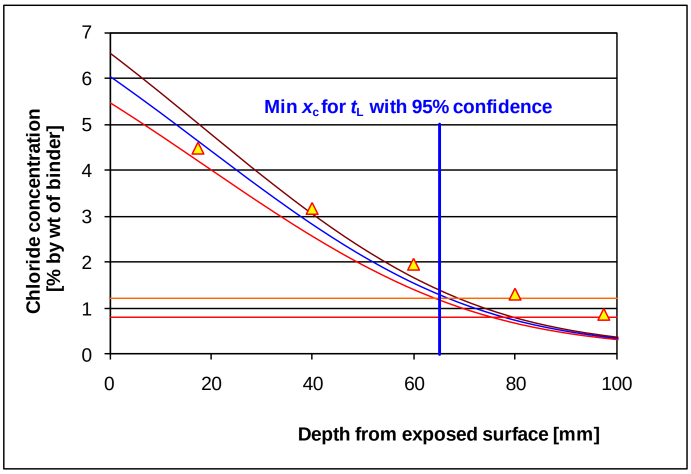

Figure 9 - The real and predicted chloride concentration after 18 years of exposure. [Data points indicate real data collected from the North Sea exposure site]

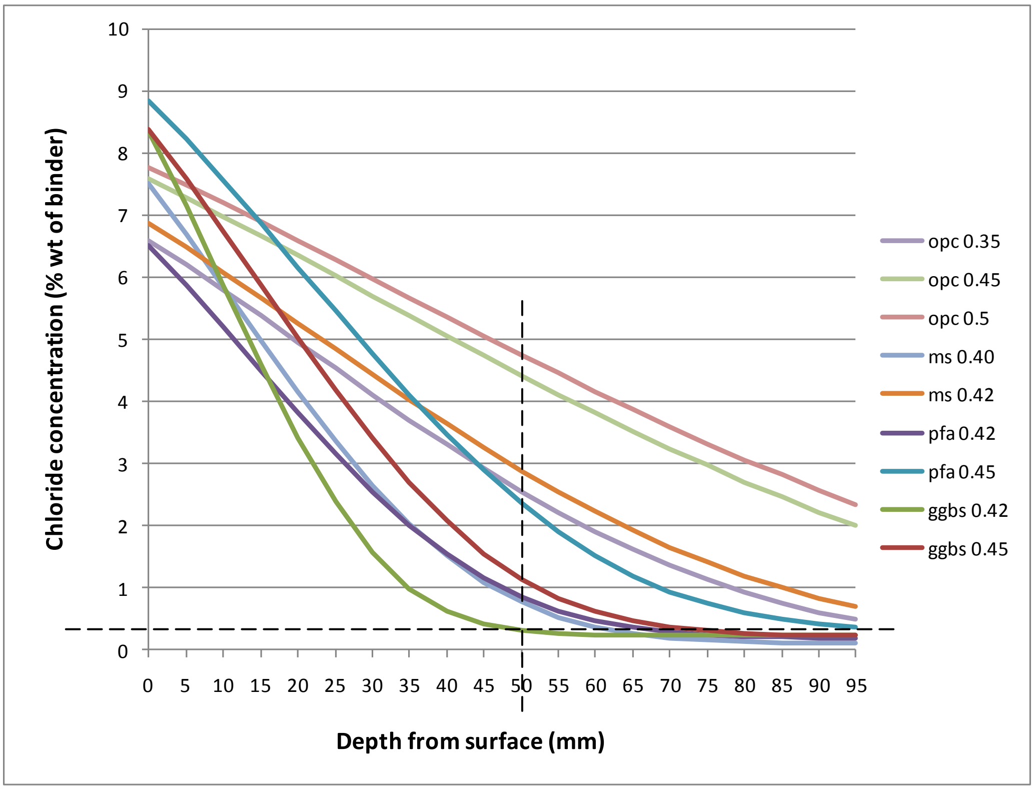

Figure 10 - Numerically simulated chloride profiles for various concretes listed in Table 1

CONCLUDING REMARKS

The usefulness, scope and repeatability of various lab based test methods for assessing the chloride penetration resistance were demonstrated. Data from one of the test method was further exploited to predict the chloride concentration versus depth at different service life of a structure. The accuracy of the prediction was also verified by comparing the predicted data against the field data from a long-term study. It was found that up to 7 years the predictions were accurate, but there was an underestimation of chloride content beyond 50mm depth at 18 years. This means that further refinements of the model are necessary.

The paper shows that a combined use of testing and modelling can be employed to develop performance-based specification for a marine environment. Such an approach can be adopted for any extreme exposure condition provided reliable test methods and numerical models are developed.

Acknowledgements
The authors wish to acknowledge the UK Engineering and Physical Sciences Research Council, Royal Academy of Engineers and Atlantic Area Transnational Programme for the funding provided to carry out this research.

References

British Standard 8500, *Complementary British Standard to BS EN 206-1, Part 1 Method of specifying and guidance for the specifier*, British Standard Institution (BSI), London, 2002.

Chlortest- *Resistance of concrete to chloride ingress-from laboratory test to in-field performance*, CHLORTEST, Final Technical Report EU FP5 Growth Initiative (GRD1-2002-71808), 2006.

Nanukuttan, S.V., Basheer, P. A. M. and Robinson, D. J., “Further developments of the Permit Ion Migration Test for determining the chloride diffusivity of concrete”, Structural Faults and Repair 2006, July 2006, Edinburgh.

Nanukuttan, S.V., Basheer, L., McCarter, W.J., Robinson, D.J. and Basheer, P.A.M., *Full-scale marine exposure tests on treated and untreated concretes: Initial seven year results*, ACI Materials Journal, Vol. 105, No. 1, Jan-Feb 2008, pp. 81-87.

Nilsson, L.-O., Poulsen, E., Sandberg, P., Sorensen, H.E. and Klinghoffer, O. (1996). HETEK, *Chloride penetration into concrete, state-of-the-art-, transport processes, corrosion initiation, test methods and prediction models*, Report No. 53.

Nordic Test BUILD 492, (1999). *Concrete, Mortar and Cement Based Repair Materials: Chloride Migration Coefficient from Non-steady State Migration Experiments*, NORDTEST Method.

Tang, L. (2006). *Service-life prediction based on the rapid migration test and the ClinConc model*, Proceedings of International RILEM workshop on Performance Based Evaluation and Indicators for Concrete Durability, 19-21 March 2006, Madrid, RILEM PRO 47, pp. 157-164.

Author Index